

# NEW TECHNOLOGIES IN CANCER DIAGNOSTICS AND THERAPEUTICS

EDITED BY: Dong-Hua Yang, Pascale Cohen, Haichang Li and Yingyan Yu  
PUBLISHED IN: Frontiers in Pharmacology and Frontiers in Oncology







# frontiers

## Frontiers eBook Copyright Statement

The copyright in the text of individual articles in this eBook is the property of their respective authors or their respective institutions or funders. The copyright in graphics and images within each article may be subject to copyright of other parties. In both cases this is subject to a license granted to Frontiers.

The compilation of articles constituting this eBook is the property of Frontiers.

Each article within this eBook, and the eBook itself, are published under the most recent version of the Creative Commons CC-BY licence.

The version current at the date of publication of this eBook is CC-BY 4.0. If the CC-BY licence is updated, the licence granted by Frontiers is automatically updated to the new version.

When exercising any right under the CC-BY licence, Frontiers must be attributed as the original publisher of the article or eBook, as applicable.

Authors have the responsibility of ensuring that any graphics or other materials which are the property of others may be included in the CC-BY licence, but this should be checked before relying on the CC-BY licence to reproduce those materials. Any copyright notices relating to those materials must be complied with.

Copyright and source acknowledgement notices may not be removed and must be displayed in any copy, derivative work or partial copy which includes the elements in question.

All copyright, and all rights therein, are protected by national and international copyright laws. The above represents a summary only. For further information please read Frontiers' Conditions for Website Use and Copyright Statement, and the applicable CC-BY licence.

ISSN 1664-8714

ISBN 978-2-88971-524-4

DOI 10.3389/978-2-88971-524-4

## About Frontiers

Frontiers is more than just an open-access publisher of scholarly articles: it is a pioneering approach to the world of academia, radically improving the way scholarly research is managed. The grand vision of Frontiers is a world where all people have an equal opportunity to seek, share and generate knowledge. Frontiers provides immediate and permanent online open access to all its publications, but this alone is not enough to realize our grand goals.

## Frontiers Journal Series

The Frontiers Journal Series is a multi-tier and interdisciplinary set of open-access, online journals, promising a paradigm shift from the current review, selection and dissemination processes in academic publishing. All Frontiers journals are driven by researchers for researchers; therefore, they constitute a service to the scholarly community. At the same time, the Frontiers Journal Series operates on a revolutionary invention, the tiered publishing system, initially addressing specific communities of scholars, and gradually climbing up to broader public understanding, thus serving the interests of the lay society, too.

## Dedication to Quality

Each Frontiers article is a landmark of the highest quality, thanks to genuinely collaborative interactions between authors and review editors, who include some of the world's best academicians. Research must be certified by peers before entering a stream of knowledge that may eventually reach the public - and shape society; therefore, Frontiers only applies the most rigorous and unbiased reviews.

Frontiers revolutionizes research publishing by freely delivering the most outstanding research, evaluated with no bias from both the academic and social point of view. By applying the most advanced information technologies, Frontiers is catapulting scholarly publishing into a new generation.

## What are Frontiers Research Topics?

Frontiers Research Topics are very popular trademarks of the Frontiers Journals Series: they are collections of at least ten articles, all centered on a particular subject. With their unique mix of varied contributions from Original Research to Review Articles, Frontiers Research Topics unify the most influential researchers, the latest key findings and historical advances in a hot research area! Find out more on how to host your own Frontiers Research Topic or contribute to one as an author by contacting the Frontiers Editorial Office: [frontiersin.org/about/contact](https://frontiersin.org/about/contact)

# NEW TECHNOLOGIES IN CANCER DIAGNOSTICS AND THERAPEUTICS

Topic Editors:

**Dong-Hua Yang**, St. John's University, United States

**Pascale Cohen**, Université Claude Bernard Lyon 1, France

**Haichang Li**, The Ohio State University, United States

**Yingyan Yu**, Shanghai Jiao Tong University, China

**Citation:** Yang, D.-H., Cohen, P., Li, H., Yu, Y., eds. (2021). New Technologies in Cancer Diagnostics and Therapeutics. Lausanne: Frontiers Media SA.  
doi: 10.3389/978-2-88971-524-4

# Table of Contents

- 07 Editorial: New Technologies in Cancer Diagnostics and Therapeutics**  
Haichang Li, Serena Li Zhao, Pascale Cohen and Dong-Hua Yang
- 10 Construction and Analysis of the Tumor-Specific mRNA–miRNA–lncRNA Network in Gastric Cancer**  
Xiaohao Zheng, Xiaohui Wang, Li Zheng, Hao Zhao, Wenbin Li, Bingzhi Wang, Liyan Xue, Yantao Tian and Yibin Xie
- 24 Targeting B7-H3 Immune Checkpoint With Chimeric Antigen Receptor-Engineered Natural Killer Cells Exhibits Potent Cytotoxicity Against Non-Small Cell Lung Cancer**  
Shuo Yang, Bihui Cao, Guangyu Zhou, Lipeng Zhu, Lu Wang, Li Zhang, Hang Fai Kwok, Zhenfeng Zhang and Qi Zhao
- 34 Feasibility Study of a Modified XELOX Adjuvant Chemotherapy for High-Recurrence Risk Patients With Operated Stage III Colon Cancer**  
Jianhong Peng, Weihao Li, Wenhua Fan, Wenhao Zhou, Ying Zhu, Xueying Li, Zhizhong Pan, Xiaoping Lin and Junzhong Lin
- 42 Increased Tumoral Microenvironmental pH Improves Cytotoxic Effect of Pharmacologic Ascorbic Acid in Castration-Resistant Prostate Cancer Cells**  
Zhoulei Li, Peng He, Ganhua Luo, Xinchong Shi, Gang Yuan, Bing Zhang, Christof Seidl, Andreas Gewies, Yue Wang, Yuan Zou, Yali Long, Dianchao Yue and Xiangsong Zhang
- 54 Prognostic Value of the Modified Systemic Inflammation Score in Patients With Extranodal Natural Killer/T-Cell Lymphoma**  
He Huang, Li Min Chen, Xiao Jie Fang, Cheng Cheng Guo, Xiao Ping Lin, Huang Ming Hong, Xi Li, Zhao Wang, Ying Tian, Mei Ting Chen, Yu Yi Yao, Zegeng Chen, Xiao Qian Li and Fei Pan
- 63 Artificial Intelligence-Based Multiclass Classification of Benign or Malignant Mucosal Lesions of the Stomach**  
Bowe Ma, Yucheng Guo, Weian Hu, Fei Yuan, Zhenggang Zhu, Yingyan Yu and Hao Zou
- 75 Combining <sup>18</sup>F-FDG PET/CT and Serum Lactate Dehydrogenase for Prognostic Evaluation of Small Cell Lung Cancer**  
Xiaoping Lin, Zizheng Xiao, Yingying Hu, Xu Zhang and Wei Fan
- 83 Potential Metabolic Biomarkers for Early Detection of Oral Lichen Planus, a Precancerous Lesion**  
Xiao-Shuang Wang, Zhi Sun, Li-Wei Liu, Qiu-Zheng Du, Zhang-Suo Liu, Yan-Jie Yang, Peng Xue and Hong-Yu Zhao
- 93 External Validation of a Nomogram and Risk Grouping System for Predicting Individual Prognosis of Patients With Medulloblastoma**  
Chengcheng Guo, Dunchen Yao, Xiaoping Lin, He Huang, Ji Zhang, Fuhua Lin, Yonggao Mou and Qunying Yang

- 102 ***Piperlongumine Alleviates Mouse Colitis and Colitis-Associated Colorectal Cancer***  
Jia-Rong Huang, Sheng-Te Wang, Meng-Ning Wei, Kun Liu, Jing-Wen Fu, Zi-Hao Xing and Zhi Shi
- 110 ***MOF Regulates TNK2 Transcription Expression to Promote Cell Proliferation in Thyroid Cancer***  
Danyang Li, Yang Yang, Bo Chen, Xinghong Guo, Shuang Gao, Meng Wang, Mingxiao Duan and Xiangzhi Li
- 121 ***TRPM7 Induces Tumorigenesis and Stemness Through Notch Activation in Glioma***  
Jingwei Wan, Alyssa Aihui Guo, Pendelton King, Shanchun Guo, Talib Saafir, Yugang Jiang and Mingli Liu
- 139 ***LINC00667 Sponges miR-4319 to Promote the Development of Nasopharyngeal Carcinoma by Increasing FOXQ1 Expression***  
Bing Liao, Yun Yi, Lei Zeng, Zhi Wang, Xinhua Zhu, Jianguo Liu, Bingbin Xie and Yuehui Liu
- 149 ***Overexpression of LncRNA BM466146 Predicts Better Prognosis of Breast Cancer***  
Yunxiang Zhang, Xiaotong Dong, Yang Wang, Liquan Wang, Guiyan Han, Lvcheng Jin, Yanping Fan, Guodong Xu, Dawei Yuan, Jie Zheng, Xiangyu Guo and Peng Gao
- 158 ***Network Pharmacology and Molecular Docking on the Molecular Mechanism of Luo-hua-zi-zhu (LHZZ) Granule in the Prevention and Treatment of Bowel Precancerous Lesions***  
Cui Guo, Xingdong Kang, Fang Cao, Jian Yang, Yimin Xu, Xiaoqiang Liu, Yuan Li, Xiumei Ma and Xiaoling Fu
- 172 ***OTS964, a TOPK Inhibitor, Is Susceptible to ABCG2-Mediated Drug Resistance***  
Yuqi Yang, Zhuo-Xun Wu, Jing-Quan Wang, Qiu-Xu Teng, Zi-Ning Lei, Sabrina Lusvarghi, Suresh V. Ambudkar, Zhe-Sheng Chen and Dong-Hua Yang
- 182 ***Mutational Pattern in Multiple Pulmonary Nodules are Associated With Early Stage Lung Adenocarcinoma***  
Shao-wei Dong, Rong Li, Zhiqiang Cheng, Dong-cheng Liu, Jinquan Xia, Jing Xu, Shixuan Li, Jian Wang, Yongjian Yue, Yingrui Fan, Yundi Cao, Lingyun Dai, Jigang Wang, Pan Zhao, Xin Wang, Zhangang Xiao, Chen Qiu, Guang-suo Wang and Chang Zou
- 192 ***Deoxypodophyllotoxin Inhibits Non-Small Cell Lung Cancer Cell Growth by Reducing HIF-1 $\alpha$ -Mediated Glycolysis***  
Yuping Yang, Lingling Liu, Jinghui Sun, Shu Wang, Zhongyuan Yang, Honghui Li, Na Huang and Wei Zhao
- 203 ***Advances in Optical Aptasensors for Early Detection and Diagnosis of Various Cancer Types***  
Qurat ul ain Zahra, Qaiser Ali Khan and Zhaofeng Luo
- 210 ***Advanced Approaches to Breast Cancer Classification and Diagnosis***  
M. Zubair, S. Wang and N. Ali

- 234 Monoamine Oxidase A Inhibits Lung Adenocarcinoma Cell Proliferation by Abrogating Aerobic Glycolysis**  
Yumin Huang, Wei Zhao, Xiaoping Ouyang, Feng Wu, Yujian Tao and Minhua Shi
- 244 Bioinformatics-Based Identification of HDAC Inhibitors as Potential Drugs to Target EGFR Wild-Type Non-Small-Cell Lung Cancer**  
Yizhe Wang, Chunlei Zheng, Wenqing Lu, Duo Wang, Yang Cheng, Yang Chen, Kezuo Hou, Jianfei Qi, Yunpeng Liu, Xiaofang Che and Xuejun Hu
- 256 17 $\beta$ -Estradiol Promotes Apoptosis of HepG2 Cells Caused by Oxidative Stress by Increasing Foxo3a Phosphorylation**  
Yusheng Guo, Xiangsheng Cai, Hanwei Lu, Qiqi Li, Ying Zheng, Zefang Lin, Zexiong Cheng, Maoxiang Yang, Li Zhang, Lei Xiang and Xiaorong Yang
- 267 Combining the Fecal Immunochemical Test with a Logistic Regression Model for Screening Colorectal Neoplasia**  
Feiyuan Liu, Qiaoyun Long, Hui He, Shaowei Dong, Li Zhao, Chang Zou and Weiqing Wu
- 277 LncRNA SNHG8 Promotes Proliferation and Inhibits Apoptosis of Diffuse Large B-Cell Lymphoma via Sponging miR-335-5p**  
Bing Yu, Bo Wang, Zhuman Wu, Chengnian Wu, Juan Ling, Xiaoyan Gao and Huilan Zeng
- 285 Jiyuan Oridonin A Overcomes Differentiation Blockade in Acute Myeloid Leukemia Cells With MLL Rearrangements via Multiple Signaling Pathways**  
Mei Qu, Yu Duan, Min Zhao, Zhanju Wang, Mengjie Zhao, Yao Zhao, Haihua Wang, Yu Ke, Ying Liu, Hong-Min Liu, Liuya Wei and Zhenbo Hu
- 296 MiR-450a-5p Inhibits Gastric Cancer Cell Proliferation, Migration, and Invasion and Promotes Apoptosis via Targeting CREB1 and Inhibiting AKT/GSK-3 $\beta$  Signaling Pathway**  
Ya-Jun Zhao, Jun Zhang, Yong-Cang Wang, Liang Wang and Xin-Yang He
- 308 Autophagy-Related Long Non-coding RNA Is a Prognostic Indicator for Bladder Cancer**  
Jiaming Wan, Cheng Guo, Hongpeng Fang, Zhongye Xu, Yongwei Hu and Yun Luo
- 319 Transcriptomic and microRNA Expression Profiles Identify Biomarkers for Predicting Neo-Chemoradiotherapy Response in Esophageal Squamous Cell Carcinomas (ESCC)**  
Jian Wang, Pengyi Yu, Judong Luo, Zhiqiang Sun, Jingping Yu and Jianlin Wang
- 331 LCT-3d Induces Oxidative Stress-Mediated Apoptosis by Upregulating Death Receptor 5 in Gastric Cancer Cells**  
Menglin Wang, Xinxin Wu, Lu Yu, Zi-yun Hu, Xiaobo Li, Xia Meng, Chun-tao Lv, Gi-Young Kim, Yung Hyun Choi, Zhengya Wang, Hai-Wei Xu and Cheng-Yun Jin
- 340 TP53-Activated lncRNA GHRLOS Regulates Cell Proliferation, Invasion, and Apoptosis of Non-Small Cell Lung Cancer by Modulating the miR-346/APC Axis**  
Ke Ren, Jinghui Sun, Lingling Liu, Yuping Yang, Honghui Li, Zhichao Wang, Jingzhu Deng, Min Hou, Jia Qiu and Wei Zhao

- 354** *PROTAC: An Effective Targeted Protein Degradation Strategy for Cancer Therapy*  
Si-Min Qi, Jinyun Dong, Zhi-Yuan Xu, Xiang-Dong Cheng, Wei-Dong Zhang and Jiang-Jiang Qin
- 367** *Pharmacological Vitamin C Treatment Impedes the Growth of Endogenous Glutamine-Dependent Cancers by Targeting Glutamine Synthetase*  
Yali Long, Jia Qiu, Bing Zhang, Peng He, Xinchong Shi, Qiao He, Zhifeng Chen, Wanqing Shen, Zhoulei Li and Xiangsong Zhang
- 379** *Functionalized Selenium Nanotherapeutics Synergizes With Zoledronic Acid to Suppress Prostate Cancer Cell Growth Through Induction of Mitochondria-Mediated Apoptosis and Cell Cycle S Phase Arrest*  
Yulin An and Jianfu Zhao
- 391** *A Novel Mice Model for Studying the Efficacy and IRAEs of Anti-CTLA4 Targeted Immunotherapy*  
Shengchao Xu, Xi Yan, Gan Dai and Chengke Luo
- 402** *Post-Diagnostic Beta Blocker Use and Prognosis of Ovarian Cancer: A Systematic Review and Meta-Analysis of 11 Cohort Studies With 20,274 Patients*  
Zhao-Yan Wen, Song Gao, Ting-Ting Gong, Yu-Ting Jiang, Jia-Yu Zhang, Yu-Hong Zhao and Qi-Jun Wu
- 412** *Berberine Sensitizes Human Hepatoma Cells to Regorafenib via Modulating Expression of Circular RNAs*  
Kunyu Wang, Ganxiang Yu, Jiaen Lin, Zhilei Wang, Qianting Lu, Chengxin Gu, Tao Yang, Shiming Liu and Hui Yang
- 423** *A PD-1 Inhibitor Induces Complete Response of Advanced Bladder Urothelial Carcinoma: A Case Report*  
Jianzheng Wang, Qingli Li, Huifang Lv, Caiyun Nie, Beibei Chen, Weifeng Xu, Tiejun Yang, Yinping Zhang, Shuiping Tu and Xiaobing Chen
- 430** *Feiyanning Formula Induces Apoptosis of Lung Adenocarcinoma Cells by Activating the Mitochondrial Pathway*  
Li-Min Zhu, Hai-Xia Shi, Masahiro Sugimoto, Kenjiro Bandow, Hiroshi Sakagami, Shigeru Amano, Hai-Bin Deng, Qing-Yu Ye, Yun Gai, Xiao-Li Xin and Zhen-Ye Xu
- 444** *Exploring the Significance of the Exon 4-Skipping Isoform of the ZNF217 Oncogene in Breast Cancer*  
Aur lie Bellanger, Diep T. Le, Julie Vendrell, Anne Wierinckx, L rinc S. Pongor, J r me Solassol, Jo l Lachuer, Philippe Clezardin, Bal zs Gy rffy and Pascale A. Cohen
- 456** *The Role of Long Noncoding RNA AL161431.1 in the Development and Progression of Pancreatic Cancer*  
Gang Ma, Guichen Li, Wufeng Fan, Yuanhong Xu, Shaowei Song, Kejian Guo and Zhe Liu
- 465** *Case Report and Literature Review: Primary Pulmonary NUT-Midline Carcinoma*  
Yunxiang Zhang, Kai Han, Xiaotong Dong, Qian Hou, Tianbao Li, Li Li, Gengyin Zhou, Xia Liu, Guifeng Zhao and Wei Li



# Editorial: New Technologies in Cancer Diagnostics and Therapeutics

Haichang Li<sup>1\*</sup>, Serena Li Zhao<sup>2</sup>, Pascale Cohen<sup>3</sup> and Dong-Hua Yang<sup>4\*</sup>

<sup>1</sup>Department of Surgery, The Ohio State University College of Medicine, Columbus, OH, United States, <sup>2</sup>Department of Medicinal Chemistry and Pharmacognosy, The Ohio State University College of Pharmacy, Columbus, OH, United States, <sup>3</sup>University of Lyon Claude Bernard, INSERM, UMR1033 LYOS, Lyon, France, <sup>4</sup>Department of Pharmaceutical Sciences, College of Pharmacy and Health Sciences, St. John's University, Queens, New York

**Keywords:** cancer, technologies, diagnostics, therapeutics, cancer biology

## Editorial on the Research Topic

### New Technologies in Cancer Diagnostics and Therapeutics

Cancer is a leading public health problem worldwide and is the second leading cause of mortality in the United States (Ferlay et al., 2021; Sung et al., 2021). The burden of cancer incidence and mortality is rapidly growing due to both the aging and the growth of the population. Despite available treatment including surgical, chemotherapeutic, radio- and immunotherapy, there is still a great need for novel diagnostic and therapeutic approaches to meet the challenges of cancer eradication.

Therefore, this research topic “*New Technologies in Cancer Diagnostics and Therapeutics*” focuses on the newly emerging areas of cancer diagnostics, drug development, and molecular signaling pathways involved in tumorigenesis and tumor development. We were excited to receive 65 contributions and finally 42 articles contributed by more than 320 authors from various countries in the fields of cancer biology, pharmacology and therapeutics were selected to be included in this topic collection.

In this topic collection, the systematic review and meta-analysis by Wen et al. summarized the use of post-diagnostic beta blocker for ovarian cancer (OC) prognosis. They screened 11 cohort studies with 20,274 OC patients. Random-effects models were used to calculate overall hazard ratios (HRs) and 95% confidence intervals (CIs). They concluded that HRs did not reveal any statistically significant associations between post-diagnostic beta-blocker use and OC prognostic characteristics, although more prospective cohort studies are necessary to further verify their results. Another three reviews included in this collection review the structures and mechanisms of proteolysis targeting chimeric (PROTACs) and describe several classes of effective PROTAC degraders (Qi et al.), advances approaches to breast cancer diagnosis and therapy (Zubair et al.), and *advances in optical aptasensors for early detection and diagnosis of various cancer types* (Zahra et al.).

Two case reports, one by Zhang et al., on the primary pulmonary NUT-midline carcinoma brought novel insights on the diagnosis of this type of rare tumors; the other by Wang et al. introduced using a *PD-1 inhibitor to induce the complete response of advanced bladder urothelial carcinoma*.

The discovery of long non-coding RNA (lncRNAs) is propelling the future advancement of biomarker development, and cancer diagnosis and treatment (Zhang et al., 2013; Chi et al., 2019; Jiang et al., 2019; Carlevaro-Fita et al., 2020). Zhang et al. analyzed the expression and clinical significance of lncRNA BM466146 in breast cancer and explores the role of BM466146 in immune regulation. Their findings indicated that the lncRNA BM466146 has the tumor suppressor function. Overexpression of BM466146 is associated with a better prognosis. BM466146 could regulate CXCL-13 by adsorbing hsa-miR-224-3p and inducing CD8<sup>+</sup> T cells to accumulate in the tumor area which regulate immune response. Therefore, BM466146 could be a prognostic biomarker and a molecular immune target of breast cancer. Similarly, Ma et al. found that lncRNA AL161431.1 was highly expressed in pancreatic cancer cells and tissues. Knockdown of lncRNA AL161431.1 led to increased cancer cell death and cell cycle arrest. Xenograft

## OPEN ACCESS

### Edited and reviewed by:

Salvatore Salomone,  
University of Catania, Italy

### \*Correspondence:

Haichang Li  
Haichang.Li@osumc.edu  
Dong-Hua Yang  
yangd1@stjohns.edu

### Specialty section:

This article was submitted to  
Experimental Pharmacology and  
Drug Discovery,  
a section of the journal  
Frontiers in Pharmacology

**Received:** 18 August 2021

**Accepted:** 23 August 2021

**Published:** 06 September 2021

### Citation:

Li H, Zhao SL, Cohen P and Yang D-H  
(2021) Editorial: New Technologies in  
Cancer Diagnostics and Therapeutics.  
Front. Pharmacol. 12:760833.  
doi: 10.3389/fphar.2021.760833



growth of SW1990 cells with stable knockdown of lncRNA AL161431.1 in mice was significantly slower than that of SW1990 cells with scrambled control shRNA. Yu et al. investigated the role of lncRNA SNHG8 in regulating diffuse large B-cell lymphoma (DLBCL) cells and uncover its underlying mechanism. Their findings suggested that lncRNA SNHG8 exerted a cancer-promoting effect on DLBCL via targeting miR-335-5p. Liao et al. characterize the molecular mechanism of LINC00667 in nasopharyngeal carcinoma (NPC) progression and found that LINC00667 could be a diagnostic and therapeutic target for NPC patients. Luo et al. investigated the potential prognostic role of autophagy-related lncRNA in patients with bladder cancer (BC) and identified 15 autophagy-related lncRNAs have the prognostic potential for BC, and may play key roles in BC biology. Zheng et al. identified a survival-related gene-based ceRNA network using the WGCNA algorithm, and the constructed lncRNA-miRNA-mRNA ceRNA interactive network to provide novel insights into the treatment of gastric cancer. Taken together, these lncRNAs could be able to predict clinical outcomes, holding great promise in future clinical applications.

Novel targets and biomarkers are essential components in drug developments and treatments, particularly in this era of targeted therapies. Tremendous efforts are being made to interpret the mechanisms of cancer development with the aim of discovery of novel drugs. Li et al. identified MOF as an oncogene in thyroid cancer and found that the expression of MOF was significantly upregulated in most thyroid cancer tissue samples and cell lines. MOF is a well-known histone acetyltransferase, which is involved in diverse biological processes, such as gene transcription, cell cycle, early embryonic development and tumorigenesis. Their findings demonstrated that MOF played an oncogenic role in the development and progression of thyroid cancer and may be a potential novel target for the treatment of thyroid cancer. Bellanger et al. provided insights into the biological and clinical significance of the novel exon4-skipping isoform of the well-established oncogene ZNF217 in breast cancer. They revealed that, in the Luminal subclass, a dual signature combining the expression levels of these two isoforms may serve as a novel prognostic biomarker allowing better stratification of breast cancers with good prognosis and aiding clinicians in therapeutic decisions. They also identified that ZNF217-ΔE4 protein drives cell aggressiveness and that a close interplay exists between the ZNF217-WT and ZNF217-ΔE4 isoforms. Wang et al. identified prognostic biomarkers for patients with EGFR-WT non-small-cell lung cancer and confirmed a novel potential role for HDAC is in the clinical management of EGFR-WT patients. Liu et al. investigated transient receptor potential melastatin-related 7 (TRPM7) mediated glioma stemness. They found that TRPM7 mRNA expression is significantly increased in anaplastic astrocytoma, diffuse astrocytoma, and GBM patients compared to that in healthy brain tissue controls. TRPM7 expression in GBM cells was found to be positively correlated with Notch1 signaling activity and CD133 and ALDH1 expression. Moreover, they found that targeting Notch1 compromises the TRPM7-induced growth and proliferation of glioma cells. Yang et al. demonstrated that *targeting the B7-H3 Immune checkpoint with specific*

*CAR-engineered NK-92 cells exhibits potent cytotoxicity against non-small cell lung cancer*. Wang et al. investigated the role of a novel Indole derivative, named LCT-3d, in inhibiting the growth of gastric cancer cells. LCT-3d modulated the mitochondrial-related proteins and Cleaved-Caspases 3/9, to induce cell apoptosis. Their findings suggested that LCT-3d induces apoptosis via DR5-mediated mitochondrial apoptotic pathway in gastric cancer cells. LCT-3d could be a novel lead compound for development of anti-cancer activity in gastric cancer.

Since the development of drug resistance is a major contributor towards the failure of chemotherapeutic regimens, efforts have been made to develop novel inhibitors that can combat drug resistance and sensitize cancer cells to chemotherapy (Vasan et al., 2019). Yang et al. investigated the interaction of OTS964, a potent T-LAK cell-originated protein kinase (TOPK) inhibitor and multidrug resistance (MDR)-associated ATP-binding cassette sub-family G member 2 (ABCG2). They found that the OTS964 is susceptible to ABCG2-mediated drug resistance, and this effect can be antagonized by a known ABCG2 inhibitor. These findings may serve as a valuable foundation for follow-up clinical investigation on potential use of OTS964. Tumoral microenvironmental is a critical influencing factor for multiple anti-cancer treatments. In this topic collection, Li et al. demonstrated that acidic pH attenuates the cytotoxic activity of pharmacologic ascorbic acid by inhibiting ascorbic acid (AA) uptake in PCa cells. Additionally, they found that the cancer cell-selective toxicity of AA depends on ROS. *In vivo*, the combination of AA and bicarbonate could provide a significantly better therapeutic outcome in comparison with controls or AA single treated mice. Chimeric antigen receptor (CAR)-modified natural killer (NK) cell therapy represents a kind of promising anti-cancer treatment. Yang et al. constructed the second-generation CAR consisting of 4-1BB costimulatory signal domain and a CD3ζ domain, which is similar to the clinically used anti-CD19 CAR-T cells. Compared to unmodified NK-92MI cells, the activity and cytotoxicity of CAR-modified NK-92MI cells were significantly enhanced both *in vitro* and *in vivo*. Those results demonstrate that redirection of anti-B7-H3 CAR promotes activation and antitumor cytotoxicity of NK cells.

In conclusion, this research topic highlights multiple aspects of the emergence of novel modalities that could be of potential application on cancer diagnosis and treatment.

## AUTHOR CONTRIBUTIONS

HL and SZ wrote the first draft. PC and DY provided critical comments and revisions. All authors read and agreed with the submitted version.

## FUNDING

This work was supported by the National Institute of Health (R01-AG056919) and the OSU Lockwood Early Career Development Award to HL.



## REFERENCES

- Carlevaro-Fita, J., Lanzós, A., Feuerbach, L., Hong, C., Mas-Ponte, D., Pedersen, J. S., et al. (2020). Cancer LncRNA Census Reveals Evidence for Deep Functional Conservation of Long Noncoding RNAs in Tumorigenesis. *Commun. Biol.* 3, 56. doi:10.1038/s42003-019-0741-7
- Chi, Y., Wang, D., Wang, J., Yu, W., and Yang, J. (2019). Long Non-coding RNA in the Pathogenesis of Cancers. *Cells* 8 (9), 1015. doi:10.3390/cells8091015
- Ferlay, J., Colombet, M., Soerjomataram, I., Parkin, D. M., Pineros, M., Znaor, A., et al. (2021). Cancer Statistics for the Year 2020: An Overview. *Int. J. Cancer*. doi:10.1002/ijc.33588
- Jiang, M. C., Ni, J. J., Cui, W. Y., Wang, B. Y., and Zhuo, W. (2019). Emerging Roles of lncRNA in Cancer and Therapeutic Opportunities. *Am. J. Cancer Res.* 9, 1354–1366.
- Sung, H., Ferlay, J., Siegel, R. L., Laversanne, M., Soerjomataram, I., Jemal, A., et al. (2021). Global Cancer Statistics 2020: GLOBOCAN Estimates of Incidence and Mortality Worldwide for 36 Cancers in 185 Countries. *CA Cancer J. Clin.* 71 (3), 209–249. doi:10.3322/caac.21660
- Vasan, N., Baselga, J., and Hyman, D. M. (2019). A View on Drug Resistance in Cancer. *Nature* 575, 299–309. doi:10.1038/s41586-019-1730-1
- Zhang, H., Chen, Z., Wang, X., Huang, Z., He, Z., and Chen, Y. (2013). Long Non-coding RNA: a New Player in Cancer. *J. Hematol. Oncol.* 6, 37. doi:10.1186/1756-8722-6-37

**Conflict of Interest:** The authors declare that the research was conducted in the absence of any commercial or financial relationships that could be construed as a potential conflict of interest.

**Publisher's Note:** All claims expressed in this article are solely those of the authors and do not necessarily represent those of their affiliated organizations, or those of the publisher, the editors and the reviewers. Any product that may be evaluated in this article, or claim that may be made by its manufacturer, is not guaranteed or endorsed by the publisher.

Copyright © 2021 Li, Zhao, Cohen and Yang. This is an open-access article distributed under the terms of the Creative Commons Attribution License (CC BY). The use, distribution or reproduction in other forums is permitted, provided the original author(s) and the copyright owner(s) are credited and that the original publication in this journal is cited, in accordance with accepted academic practice. No use, distribution or reproduction is permitted which does not comply with these terms.



# Construction and Analysis of the Tumor-Specific mRNA–miRNA–lncRNA Network in Gastric Cancer

Xiaohao Zheng<sup>1†</sup>, Xiaohui Wang<sup>2†</sup>, Li Zheng<sup>3†</sup>, Hao Zhao<sup>4</sup>, Wenbin Li<sup>5</sup>, Bingzhi Wang<sup>5</sup>, Liyan Xue<sup>5</sup>, Yantao Tian<sup>1</sup> and Yibin Xie<sup>1\*</sup>

<sup>1</sup> Department of Pancreatic and Gastric Surgery, National Cancer Center/National Clinical Research Center for Cancer/Cancer Hospital, Chinese Academy of Medical Sciences and Peking Union Medical College, Beijing, China, <sup>2</sup> Department of General Surgery, Xuanwu Hospital, Capital Medical University, Beijing, China, <sup>3</sup> Department of General Surgery, The First People's Hospital of Dongcheng District, Beijing, China, <sup>4</sup> Department of Cardiovascular Surgery, China-Japan Friendship Hospital, Beijing, China, <sup>5</sup> Department of Pathology, National Cancer Center/National Clinical Research Center for Cancer/Cancer Hospital, Chinese Academy of Medical Sciences and Peking Union Medical College, Beijing, China

## OPEN ACCESS

### Edited by:

Dong-Hua Yang,  
St. John's University, United States

### Reviewed by:

Hua Zhu,  
The Ohio State University,  
United States  
Shanzhi Wang,  
University of Arkansas at Little Rock,  
United States

### \*Correspondence:

Yibin Xie  
yibinxie\_2003@163.com

<sup>†</sup>These authors share first authorship

### Specialty section:

This article was submitted to  
Experimental Pharmacology  
and Drug Discovery,  
a section of the journal  
Frontiers in Pharmacology

**Received:** 03 June 2020

**Accepted:** 08 July 2020

**Published:** 21 July 2020

### Citation:

Zheng X, Wang X, Zheng L, Zhao H,  
Li W, Wang B, Xue L, Tian Y and Xie Y  
(2020) Construction and Analysis of  
the Tumor-Specific mRNA–miRNA–  
lncRNA Network in Gastric Cancer.  
Front. Pharmacol. 11:1112.  
doi: 10.3389/fphar.2020.01112

Weighted correlation network analysis (WGCNA) is a statistical method that has been widely used in recent years to explore gene co-expression modules. Competing endogenous RNA (ceRNA) is commonly involved in the cancer gene expression regulation mechanism. Some ceRNA networks are recognized in gastric cancer; however, the prognosis-associated ceRNA network has not been fully identified using WGCNA. We performed WGCNA using datasets from The Cancer Genome Atlas (TCGA) and the Genotype-Tissue Expression (GTEx) to identify cancer-associated modules. The criteria of differentially expressed RNAs between normal stomach samples and gastric cancer samples were set at the false discovery rate (FDR) < 0.01 and |fold change (FC)| > 1.3. The ceRNA relationships obtained from the RNAinter database were examined by both the Pearson correlation test and hypergeometric test to confirm the mRNA–lncRNA regulation. Overlapped genes were recognized at the intersections of genes predicted by ceRNA relationships, differentially expressed genes, and genes in cancer-specific modules. These were then used for univariate and multivariate Cox analyses to construct a risk score model. The ceRNA network was constructed based on the genes in this model. WGCNA-uncovered genes in the green and turquoise modules are those most associated with gastric cancer. Eighty differentially expressed genes were observed to have potential prognostic value, which led to the identification of 12 prognosis-related mRNAs (*KIF15*, *FEN1*, *ZFP69B*, *SP6*, *SPARC*, *TTF2*, *MSI2*, *KYNU*, *ACLY*, *KIF21B*, *SLC12A7*, and *ZNF823*) to construct a risk score model. The risk genes were validated using the GSE62254 and GSE84433 datasets, with 0.82 as the universal cutoff value. 12 genes, 12 lncRNAs, and 35 miRNAs were used to build a ceRNA network with 86 dysregulated lncRNA–mRNA ceRNA pairs. Finally, we developed a 12-gene signature from both prognosis-related and tumor-specific genes, and then constructed a ceRNA network in gastric cancer. Our findings may provide novel insights into the treatment of gastric cancer.

**Keywords:** gastric cancer, weighted correlation network analysis, competing endogenous RNA, risk score, The Cancer Genome Atlas, Genotype-Tissue Expression, Gene Expression Omnibus

## INTRODUCTION

Gastric cancer is a major cause of cancer-related mortality worldwide (Van Cutsem et al., 2016). It is a serious form of cancer characterized by limited chemotherapy regimens and complex patterns of tumorigenesis and progression in different subtypes (Erdem et al., 2018; Kubota et al., 2020). There have been exceptional advancements in the interpretation of the molecular pattern of gastric cancer through research projects including the Cancer Genome Atlas (TCGA) (Cancer Genome Atlas Research N, 2014) and the Asian Cancer Research Group (ACRG) (Cristescu et al., 2015) in recent years; however, current classifications are not sufficient to describe the vast differences in prognoses and summarize overall genomic characteristics, even for patients who are recognized as belonging to the same molecular subtypes.

Integrated analysis of transcriptomes is believed to provide peculiar insights into diseases; in this respect, weighted gene co-expression network analysis (WGCNA) may be the most popular approach for detecting co-expressed RNAs from RNA-seq data to microarray data (van Dam et al., 2018; Kakati et al., 2019). WGCNA can identify select groups of significant genes with similar biological functions and with strong correlations to specific traits. Many recent surveys have used WGCNA for both non-neoplastic and neoplastic diseases, including gastric cancer.

Salmena et al. (2011) speculated that the expression of many RNA transcripts is regulated by competing endogenous RNAs (ceRNAs) competing for the same sequences in miRNAs. They established the groundwork for a significant discovery of a communication network between coding and non-coding RNAs. Their theory has been supported by studies on the pathological processes of many malignancies, including breast, colon, and gastric cancers (Qi et al., 2015; Shuwen et al., 2018; Abdollahzadeh et al., 2019).

Thus, finding key genes that will serve as drug targets is crucial to the treatment of gastric cancer. In this study, we used WGCNA to construct a solid cancer-associated ceRNA network in gastric cancer for the first time. We hypothesized that identifying gene co-expression patterns would provide additional insight into disease-associated biological pathways. Finally, we explored a lncRNA-miRNA-mRNA network based on the survival-related hallmark genes of gastric cancer, providing candidate targets for its management and surveillance.

## MATERIALS AND METHODS

### RNA-Sequencing and Microarray Data Collection

RNA-seq data were obtained from TCGA repository (<https://portal.gdc.cancer.gov/>) and the Genotype-Tissue Expression (GTEx) portal (<https://www.gtexportal.org/>) and sequenced on the Illumina HiSeq 2000 RNA Sequencing platform. TCGA offers a comprehensive database of cancer genomic profiles of

specific cancer types. GTEx is another project that recruits postmortem donors without diseases, which has made genetic traits of healthy people open to the public. We performed a combined analysis of the stomach data from these two projects in the present study. The transcript per million (TPM) expression values for 625 stomach samples and the RNA-seq by Expectation Maximization (RSEM) expected counts for 624 stomach samples were preserved for further analysis (raw counts data of a patient did not exist).

The microarray data were downloaded from the Gene Expression Omnibus (GEO, <http://www.ncbi.nlm.nih.gov/geo/>). The datasets were obtained from human gene expression microarray profiles of gastric cancer using fresh-frozen specimens. Finally, we included GSE62254 and GSE84433 for further analysis, which are the two largest datasets of microarray-based gene expression profiling. GSE62254 was profiled on the Affymetrix Human Genome U133 Plus 2.0 Array platform (Affymetrix, Inc., Santa Clara, CA, USA), including 300 gastric cancer tumor samples and 100 normal samples, which is the largest number of normal gastric samples among datasets (Cristescu et al., 2015).

We downloaded raw data (CEL files) generated by the Affymetrix platform. The R package oligo was utilized for format conversion, missing data filling, background correction, and data normalization (Parrish and Spencer, 2004). GSE84433 was profiled on the Illumina HumanHT-12 V3.0 Expression Beadchip (Illumina, Inc., San Diego, CA, USA); it includes 357 gastric cancer samples, and thus has the highest number of gastric cancer patients with survival information (Cheong et al., 2018). We downloaded data in the format of raw counts, performed quantile normalization, followed by log transformation.

Annotation of the above datasets was performed according to the different platforms using the official R package downloaded from Bioconductor (<http://www.bioconductor.org/packages/>). When the same RNA name appeared, the probe with the highest signal value was stored. To facilitate the analysis, only the overlapped RNAs qualified for survival-related ceRNA network construction. To keep the data updated, clinical and survival information of patients were obtained from the websites on March 5th, 2020. All original data were retrieved from the open database; thus, the documents of medical ethics were exempted as all had been approved when first published.

### Differentially Expressed RNAs

The Limma package was used for screening differentially expressed RNAs (Ritchie et al., 2015). The RSEM expected counts retrieved from the GTEx database and TCGA database were utilized to discern differentially expressed RNAs between gastric cancer and control groups, which comprised normal stomach tissue both from dead non-cancerous subjects and adjacent stomach tissue in gastric cancer patients. For microarray-based profiling, expression values retrieved from GSE62254 were utilized to distinguish differentially expressed RNAs between 300 gastric cancer samples and 100 normal tissue samples. The R package Limma was used to process the data with

the standard of false discovery rate (FDR) < 0.01, and |fold change (FC)| > 1.3. After filtering out RNAs with low expression values, the overlapping, differentially expressed RNAs were considered suitable for further analysis.

## WGCNA

WGCNA is a bioinformatics method for dealing with high-throughput gene expression data, which can be used for the construction of a co-expression network (Langfelder and Horvath, 2008). The expression values of genes were preprocessed in the form of  $\log_2(\text{TPM} + 0.001)$ . The genes were then chosen in order of descending variance of their expression in the datasets. Finally, 13000 genes were put through WGCNA. Pairwise Pearson coefficients were used to assess the weighted co-expression relationships between all genes to produce an adjacency matrix. The least value for which the scale-free topology fit  $R^2$  index > 0.75 was chosen as the soft-threshold power. Pearson coefficients were produced for all paired genes; thus, the co-expression matrix was rendered into an adjacency matrix using soft-threshold power. The soft-threshold power was selected according to the standard scale-free distribution. Scale-free co-expression networks were created with 30 RNAs as the minimal module size and 0.25 as the dendrogram cut height for module merging. The soft threshold was used to ensure a scale-free network. Genes with high correlations were clustered into the same module after forming a co-expression network.

## Gene Function Analysis

Upregulated and downregulated differentially expressed genes were put into Gene Ontology (GO) and Kyoto Encyclopedia of Genes and Genomes (KEGG), respectively. For the gene set enrichment analysis (GSEA) and KEGG-GSEA, all genes were incorporated into the analysis. A pathway (term) with an adjusted  $p$ -value < 0.05 was considered a functional enriched pathway (term) using the R package ClusterProfiler (Yu et al., 2012).

## ceRNA Network

RNAinter was employed to observe the relationships among mRNA, lncRNA, and miRNA. RNAinter contains 24 databases demonstrated by experiment and 14 databases forecasted by calculation, including miRTarBase and starBase. We used lncRNA-miRNA relationships and mRNA-miRNA relationships with the least confidence score limit of 0.5 for further analysis (Lin et al., 2020). To ensure mRNA-lncRNA competing relationship pairs that have the shared miRNAs in gastric cancer, the Pearson correlation test and the hypergeometric test were utilized using the expression profiles. Quantile normalization and correction of batch effects between TCGA dataset and the GTEx dataset were performed for the expression profiles before further analysis (Leek et al., 2012). If the  $P$ -values of both tests were less than 0.05, the mRNA-lncRNA competing interaction pairs were saved to create the ceRNA network (Paci et al., 2014). The co-expression network with the overlapped lncRNA-miRNA-mRNA relationship was visualized with Cytoscape software (Su et al., 2014).

## Construction and Validation of the Survival Model

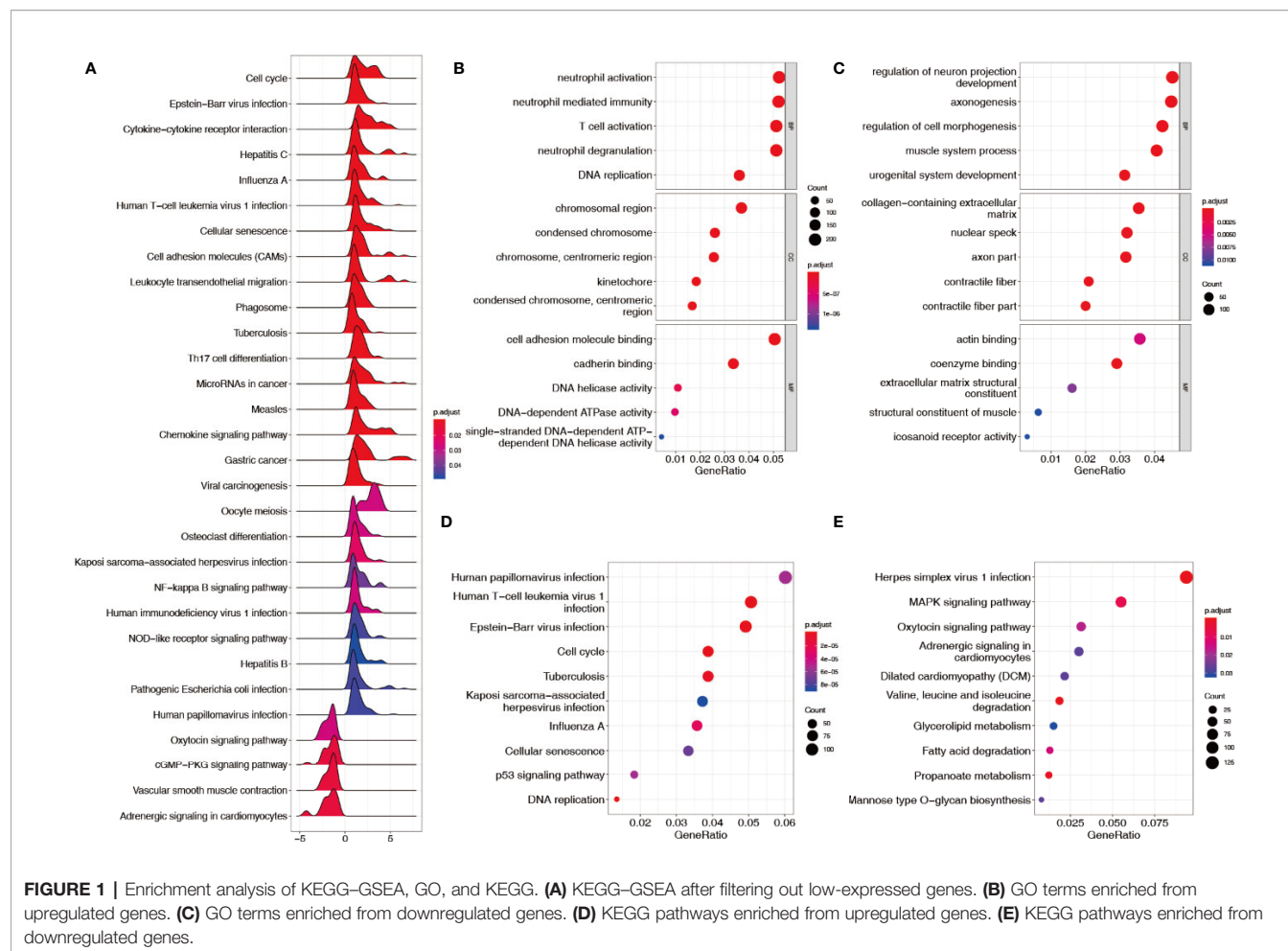
Training datasets for the prognostic score system were performed according to the sequencing data from TCGA. Validation of the prognostic score system was performed on the two microarray datasets (GSE62254 and GSE84433). Patients who died within 30 postoperative days and without 30-day follow-up were excluded. Expression profiles of eligible gastric cancer patients were normalized and non-overlapping genes were removed from the analysis. Before survival analysis, the gene expression values in the datasets were processed with a standardization with 0 mean value and standard deviation of 1. Based on the mRNAs obtained in the clinical cancer-associated modules, univariate Cox regression analysis was performed to identify prognosis-related mRNAs; then, all the survival-related genes were used to perform multivariate Cox regression. The backward selection method was used to select the most suitable survival gene group to construct a risk score system (Donithan et al., 1992). The samples in the datasets were divided into high-risk and low-risk groups according to the universal cutoff value of their risk scores. Kaplan-Meier survival curves were used to evaluate correlations between the overall survival of the two groups in datasets using the survival package (Therneau, 2020).

## RESULTS

### Differential Gene Expression Analysis

Sequencing data (TCGA + GTEx) and microarray data (GSE62254) were downloaded and processed as previously described. A total of 13007 genes and 292 lncRNAs were identified after screening out less-expressed ones. Thirty pathways were generated after the genes were applied to the KEGG-GSEA (**Figure 1A**). A total of 3895 differentially expressed genes and 79 lncRNAs were determined by comparing each gastric cancer group to both control groups. In total, 2347 upregulated and 1548 downregulated genes were subjected to GO term and KEGG pathway enrichment analyses. In the GO analysis for upregulated genes, neutrophil activation, neutrophil mediated immunity, and T cell activation were rendered as the top three terms of biological processes (BP); the chromosomal region, condensed chromosome, and centromeric region on chromosome were rendered as the top three terms of cellular components (CC); cell adhesion molecule binding, cadherin binding, and DNA helicase activity were rendered as the top three terms of molecular functions (MF) (**Figure 1B**). In the GO analysis for downregulated genes, regulation of neuron projection development, axonogenesis, and regulation of cell morphogenesis were rendered as the top three terms of the BP; the collagen-containing extracellular matrix, nuclear speck, and axon part were rendered as the top three terms of CC; actin binding, coenzyme binding, and extracellular matrix structural constituent were rendered as the top three terms of the MF (**Figure 1C**). In the KEGG analysis, human papillomavirus infection, human T-cell leukemia virus 1





infection, and Epstein–Barr virus infection were rendered as the top three enriched pathways for upregulated genes (**Figure 1D**); herpes simplex virus 1 infection, MAPK signaling, and oxytocin signaling were rendered as the top three pathways enriched for downregulated genes (**Figure 1E**).

## WGCNA

WGCNA was performed to ascertain the most strongly cancer-associated genes. When the soft-power  $\beta$  was set to 4, the scale-free topology fit index was over 0.75 (**Figure 2A**). The created network included nine modules (**Figure 2B**). **Figure 2C** shows that the green module was recognized as the most specific module with a coefficient of correlation of 0.89 ( $p = 2 \times 10^{-217}$ ); the turquoise module came in second with a coefficient of correlation of 0.61 ( $p = 8 \times 10^{-65}$ ). Genes in both modules showed a high correlation with each other according to the heatmap of the topological overlap plot (**Figure 2D**).

## Functional Analysis of the Green and Turquoise Modules

A total of 805 genes in the green module and 5213 genes in the turquoise module were subjected to KEGG-GSEA, generating

12 pathways (**Figure 3A**). The GO and KEGG enrichment results of 3312 upregulated differentially expressed genes in both modules are plotted in **Figures 3B, C**, in which enrichment results of the downregulated differentially expressed genes were not found. In total, 817 upregulated and eight downregulated differentially expressed genes were found to be qualified, with appropriate ceRNA relationships in the stomach, and appeared in the two cancer-associated modules (**Figure 3D**).

## Survival Model Construction and Validation

The clinical and pathological data from the construction and validation cohorts are shown in **Table 1**. We used Cox univariate regression analysis for the 825 genes for identifying survival-related genes in 332 TCGA gastric cancer samples. The univariate analysis screened 83 predictors based on prognosis. Because three genes did not appear in GSE84433, 80 genes were included in the multivariate analysis, which further led to the identification of 12 upregulated mRNAs for constructing a risk score model, containing *KIF15*, *FEN1*, *ZFP69B*, *SP6*, *SPARC*, *TTF2*, *MSI2*, *KYNU*, *ACLY*, *KIF21B*, *SLC12A7*, and *ZNF823* (**Table 2**). The risk scores for individual samples was calculated using the formula:

Risk score =  $(0.56321) \times \text{Expression Value (KIF15)} + (-0.24228) \times \text{Expression Value (FEN1)} + (-0.25944) \times \text{Expression Value (ZFP69B)} + (-0.23267) \times \text{Expression Value (SP6)} + (0.18278) \times \text{Expression Value (SPARC)} + (-0.3753) \times \text{Expression Value (TTF2)} + (-0.29728) \times \text{Expression Value (MSI2)} + (0.29177) \times \text{Expression Value (KYNLU)} + (0.45439) \times \text{Expression Value (ACLY)} + (-0.30168) \times \text{Expression Value (KIF21B)} + (-0.23641) \times \text{Expression Value (SLC12A7)} + (-0.22233) \times \text{Expression Value (ZNF823)}$ .

The forest plot of hazard ratios (HRs) is shown in **Figure 4** using TCGA datasets. The HRs of *KIF15* (HR = 1.756), *SPARC* (HR = 1.201), *KYNLU* (HR = 1.339), and *ACLY* (HR = 1.575) were greater than 1; however, the HRs of *FEN1* (HR = 0.784), *ZFP69B* (HR = 0.772), *SP6* (HR = 0.792), *TTF2* (HR = 0.687), *MSI2* (HR = 0.743), *KIF21B* (HR = 0.740), *SLC12A7* (HR = 0.790), and *ZNF82* (HR = 0.801) were less than 1. We further discovered that the best cutoff risk score to differentiate low-risk from high-risk

groups was 0.82. The risk score for each individual were calculated and was categorized into two groups according to the cutoff value. Kaplan-Meier analysis showed that there was a significant difference between high-risk (n=51) and low-risk patients (n=281) in the training dataset (log-rank test,  $p < 0.0001$ , **Figure 5A**). Risk stratification, survival information, and expression values of 12 genes of 332 patients were shown in the risk score panel. We observed that both the survival information and the 12-gene expression of patients in the high-risk group varied from those in the low-risk group (**Figure 5D**). Using GSE62254 and GSE84433 as validation datasets, the survival curves (**Figures 5B, C**) and the risk score panels (**Figures 5E, F**) between the high-risk groups and the low-risk groups were distinctively different. The results in the validation datasets were similar to those in the training dataset, therefore robustness of the 12-gene signature risk score system in predicting sample risk was supported.

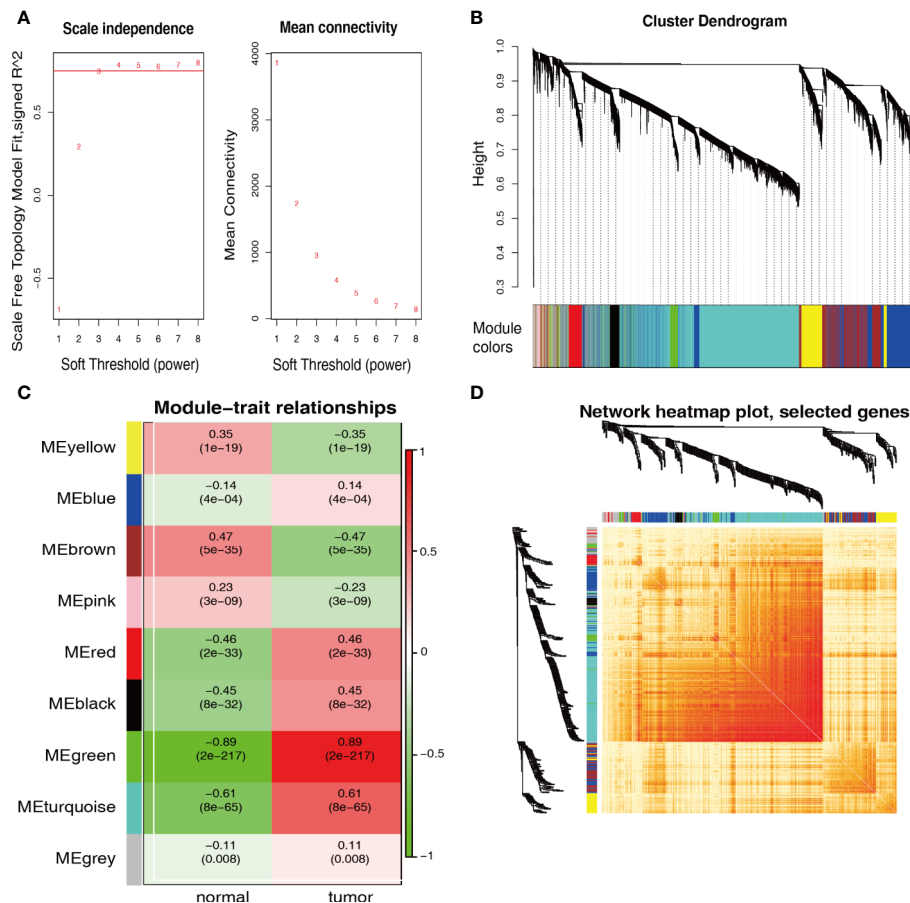


**FIGURE 2 |** WGCNA identification of cancer-associated RNA modules. **(A)** Graphs of soft-threshold power versus scale-free topology model Fit index and mean connectivity. Four was chosen as the appropriate soft-power. **(B)** Cluster dendrogram of the co-expression network modules created according to the dissimilarity of the topological overlap in the selected mRNAs. **(C)** Analysis of relationships between genes in modules between gastric cancer and normal samples. The green and turquoise modules were the most tumor-specific modules. **(D)** Heatmap plot of topological overlap in the mRNA network. Selected genes in the green and turquoise modules showed higher topological overlap. The gene dendrogram and the corresponding module are shown along the left and top.

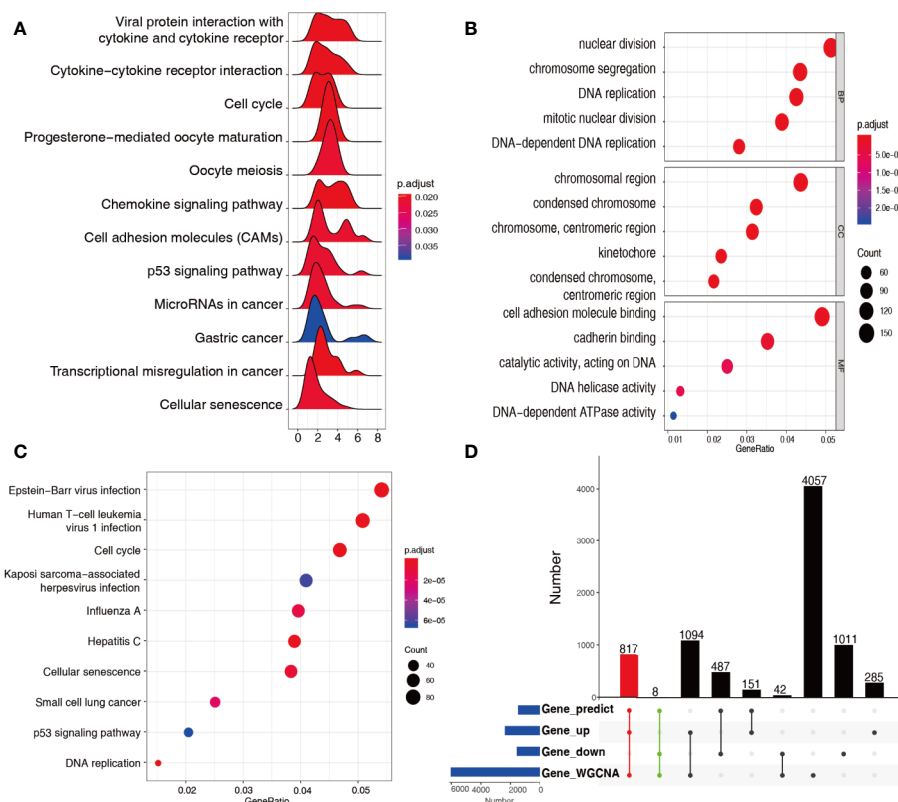


**FIGURE 3 |** Functional analysis of genes in green and turquoise modules. **(A)** KEGG-GSEA for genes in the green and turquoise modules for signaling pathway analysis. **(B)** GO terms enriched from upregulated genes in the green and turquoise modules. **(C)** KEGG pathways enriched from upregulated genes in the green and turquoise modules. **(D)** 825 mRNAs recognized at the intersection of genes predicted, differentially expressed genes, and genes in the green and turquoise modules.

**TABLE 1 |** The baseline characteristics of the construction and validation cohorts.

Variables	TCGA			GSE622554			GSE84433		
	Alive	Dead	N (%)	Alive	Dead	N (%)	Alive	Dead	N (%)
<b>Age</b>									
>=60	122 (64.6)	104 (74.3)	226 (68.7)	91 (61.5)	103 (67.8)	194 (64.7)	85 (46.4)	114 (66.3)	199 (56.1)
<60	67 (35.4)	36 (25.7)	103 (31.3)	57 (38.5)	49 (32.2)	106 (35.3)	98 (53.6)	58 (33.7)	156 (43.9)
<b>Gender</b>									
male	117 (60.9)	97 (69.3)	214 (64.5)	99 (66.9)	100 (65.8)	199 (66.3)	117 (63.9)	123 (71.5)	240 (67.6)
female	75 (39.1)	43 (30.7)	118 (35.5)	49 (33.1)	52 (34.2)	101 (33.7)	66 (36.1)	49 (28.5)	115 (32.4)
<b>pT</b>									
T4	49 (25.5)	38 (27.9)	87 (26.5)	5 (3.4)	16 (10.5)	21 (7.0)	107 (58.5)	135 (78.5)	242 (68.2)
T3	84 (43.8)	70 (51.5)	154 (47.0)	30 (20.3)	61 (40.1)	91 (30.3)	39 (21.3)	28 (16.3)	67 (18.9)
T2	47 (24.5)	27 (19.9)	74 (22.6)	113 (76.4)	75 (49.3)	188 (62.7)	28 (15.3)	7 (4.1)	35 (9.9)
T1	12 (6.3)	1 (0.7)	13 (4.0)	0 (0.0)	0 (0.0)	0 (0.0)	0 (0.0)	0 (0.0)	0 (0.0)
<b>pN</b>									
N3	28 (15.1)	40 (29.6)	68 (21.2)	10 (6.8)	41 (27.0)	51 (17.0)	10 (5.5)	21 (12.2)	31 (8.7)
N2	39 (21.0)	27 (20.0)	66 (20.6)	30 (20.3)	50 (32.9)	80 (26.7)	35 (19.1)	64 (37.2)	99 (27.9)
N1	49 (26.3)	40 (29.6)	89 (27.7)	79 (53.4)	52 (34.2)	131 (43.7)	89 (48.6)	65 (37.8)	154 (43.4)
N0	70 (37.6)	28 (20.7)	98 (30.5)	29 (19.6)	9 (5.9)	38 (12.7)	49 (26.8)	22 (12.8)	71 (20.0)

## Cerna Network Construction

We narrowed interesting lncRNAs to an intersection of lncRNAs predicted by the 12-mRNA model and differentially expressed lncRNAs, with eight upregulated lncRNAs (OIP5-AS1, MCF2L-AS1, TMPO-AS1, HCP5, DLEU1, PPP1R26-AS1, DLEU2, and

ZFAS1) and four downregulated lncRNAs (SH3BP5-AS1, CCDC18-AS1, TTC28-AS1, and TRG-AS1) identified. In total, 35 miRNAs and 12 mRNAs in the risk score system, and 12 differently expressed lncRNAs were identified to create the ceRNA network. The correlation of 12 mRNAs and 12 lncRNAs was confirmed by

**TABLE 2 |** Univariate and multivariate Cox analyses of survival-related genes in the training group.

Gene	univariate					multivariate				
	coef	HR	lower95	upper95	p-value	coef	HR	lower95	upper95	p-value
CKAP2	-0.20	0.82	0.69	0.97	2.11E-02					
F2R	0.22	1.24	1.05	1.47	1.16E-02					
ZNF367	-0.20	0.82	0.70	0.96	1.61E-02					
ASF1B	-0.14	0.87	0.76	1.00	4.71E-02					
UHRF1	-0.18	0.84	0.72	0.98	2.31E-02					
BRIP1	-0.18	0.83	0.71	0.97	1.98E-02					
NDC1	-0.19	0.83	0.71	0.97	2.10E-02					
KIF15	-0.15	0.86	0.74	1.00	4.96E-02	0.56	1.76	1.29	2.39	3.13E-04
DCLRE1B	-0.21	0.81	0.69	0.96	1.53E-02					
TFDP1	-0.19	0.83	0.70	0.98	2.61E-02					
DCK	-0.19	0.83	0.70	0.98	3.31E-02					
RAD54L	-0.15	0.86	0.75	1.00	4.93E-02					
CTHRC1	0.25	1.28	1.08	1.52	4.82E-03					
FEN1	-0.20	0.82	0.70	0.96	1.30E-02	-0.24	0.78	0.62	1.00	4.77E-02
BCL11B	-0.21	0.81	0.69	0.96	1.28E-02					
LMNB2	-0.24	0.79	0.67	0.92	3.53E-03					
TBC1D31	-0.18	0.83	0.70	0.98	2.96E-02					
BORA	-0.18	0.83	0.71	0.97	2.06E-02					
COL10A1	0.19	1.21	1.01	1.44	3.66E-02					
GMCL1	-0.22	0.80	0.67	0.95	1.12E-02					
FGD6	0.19	1.21	1.03	1.43	2.29E-02					
ZFP69B	-0.18	0.83	0.71	0.98	2.58E-02	-0.26	0.77	0.62	0.95	1.62E-02
VCAN	0.28	1.32	1.11	1.57	1.97E-03					
E2F2	-0.19	0.83	0.72	0.96	1.22E-02					
SSX2IP	-0.22	0.80	0.67	0.96	1.44E-02					
RBBP8	-0.19	0.83	0.70	0.98	2.41E-02					
MASTL	-0.19	0.83	0.70	0.97	2.27E-02					
THY1	0.20	1.22	1.03	1.44	2.18E-02					
TIMM8A	-0.19	0.83	0.70	0.98	2.72E-02					
TMEM201	-0.17	0.84	0.71	1.00	4.86E-02					
RMI1	-0.23	0.80	0.68	0.94	6.33E-03					
LRFN4	-0.16	0.85	0.73	1.00	4.98E-02					
SLC7A1	-0.22	0.80	0.67	0.95	1.11E-02					
SLC52A3	-0.25	0.78	0.67	0.90	9.97E-04					
COA7	-0.27	0.76	0.64	0.91	1.96E-03					
COL3A1	0.19	1.21	1.02	1.43	2.83E-02					
SKIL	0.18	1.19	1.00	1.41	4.47E-02					
STRIP2	-0.26	0.77	0.65	0.92	3.64E-03					
TCF3	-0.19	0.82	0.70	0.97	2.00E-02					
PAQR4	-0.16	0.85	0.73	0.99	4.20E-02					
SP6	-0.24	0.79	0.67	0.93	4.16E-03	-0.23	0.79	0.65	0.96	1.92E-02
DPP3	-0.16	0.86	0.74	0.99	4.16E-02					
SPARC	0.26	1.30	1.09	1.54	3.21E-03	0.18	1.20	1.00	1.44	4.69E-02
ANOS1	0.18	1.20	1.01	1.43	4.24E-02					
TTF2	-0.28	0.76	0.64	0.90	1.21E-03	-0.38	0.69	0.53	0.89	3.67E-03
CCDC18	-0.22	0.80	0.68	0.95	9.92E-03					
SMC1A	-0.26	0.77	0.64	0.92	4.51E-03					
TMC6	-0.17	0.84	0.72	0.99	3.92E-02					
PAXIP1	-0.19	0.83	0.70	0.98	3.22E-02					
MFAP2	0.24	1.27	1.07	1.50	6.88E-03					
MSI2	-0.27	0.77	0.65	0.91	2.64E-03	-0.30	0.74	0.61	0.90	2.24E-03
KYNU	0.20	1.22	1.03	1.46	2.35E-02	0.29	1.34	1.11	1.62	2.60E-03
POP1	-0.21	0.81	0.69	0.96	1.53E-02					
WDR4	-0.20	0.82	0.69	0.98	2.44E-02					
ZNF200	-0.18	0.84	0.70	1.00	4.63E-02					
SUSD1	0.17	1.19	1.00	1.41	4.68E-02					
SAC3D1	-0.19	0.83	0.70	0.98	2.64E-02					
MTPAP	-0.19	0.83	0.71	0.98	2.35E-02					
ZMYM1	-0.18	0.83	0.70	0.98	3.04E-02					
CXorf38	-0.19	0.83	0.70	0.99	3.75E-02					
PSMD12	-0.18	0.84	0.71	0.99	4.00E-02					

(Continued)



TABLE 2 | Continued

Gene	univariate					multivariate				
	coef	HR	lower95	upper95	p-value	coef	HR	lower95	upper95	p-value
ACLY	0.17	1.19	1.03	1.38	2.06E-02	0.45	1.58	1.34	1.86	7.02E-08
NSD2	-0.19	0.82	0.69	0.98	3.10E-02					
SLC1A5	-0.18	0.84	0.71	0.98	2.75E-02					
KIF21B	-0.24	0.79	0.66	0.94	9.64E-03	-0.30	0.74	0.62	0.89	1.19E-03
ZNF121	-0.22	0.80	0.69	0.94	7.89E-03					
GPX8	0.24	1.27	1.08	1.49	4.29E-03					
REPIN1	-0.26	0.77	0.65	0.91	2.30E-03					
PRR5	-0.18	0.84	0.72	0.98	2.24E-02					
ZNF557	-0.27	0.76	0.64	0.90	1.67E-03					
VSNL1	-0.17	0.84	0.72	0.99	3.37E-02					
ZNF786	-0.23	0.80	0.68	0.94	6.90E-03					
PLA2G15	0.19	1.21	1.02	1.43	2.50E-02					
ZNF440	-0.19	0.83	0.70	0.98	2.76E-02					
SLC12A7	-0.23	0.80	0.68	0.94	8.33E-03	-0.24	0.79	0.65	0.96	1.64E-02
ZNF823	-0.27	0.76	0.64	0.90	1.40E-03	-0.22	0.80	0.66	0.98	2.88E-02
THOP1	-0.22	0.80	0.67	0.95	1.01E-02					
TNFAIP2	-0.20	0.82	0.70	0.97	1.83E-02					
PLAGL1	0.16	1.18	1.01	1.38	4.19E-02					
ZNF331	0.22	1.25	1.05	1.49	1.06E-02					

both the Pearson correlation test and the hypergeometric test (Table 3). A ceRNA network was constructed using 86 dysregulated lncRNA-mRNA-ceRNA pairs (Figure 6).

## DISCUSSION

Currently, although there have been some investigations concentrating on non-coding RNA-involving gene expression regulation networks in gastric cancer, our research is the first to employ WGCNA to produce a co-expression network of lncRNAs-miRNAs-mRNAs in gastric cancer. Compared with the previous risk score-based system in gastric cancer (Cho et al.,

2011; Cheong et al., 2018; Duan et al., 2019; Hu et al., 2019), the advantages of our ceRNA network are that it provided 12 both cancer-associated and prognosis-related genes and was constructed using rigorous calculation of the ceRNA regulation relationships.

*KIF15* is a gene involved in immune diseases and cancer progression. Whether it is mutated is related to the sensitivity of immune checkpoint inhibitors. Györfy et al. reported that in both wild-type PIK3CA patient groups, individuals with *KIF15* mutations displayed substantially increased expression of PD-L1, whereas those without mutations displayed decreased expression (Menyhart et al., 2018). Zhang et al. found that knockdown of *KIF15* resulted in mitochondrial damage and ROS-JNK-p53 axis

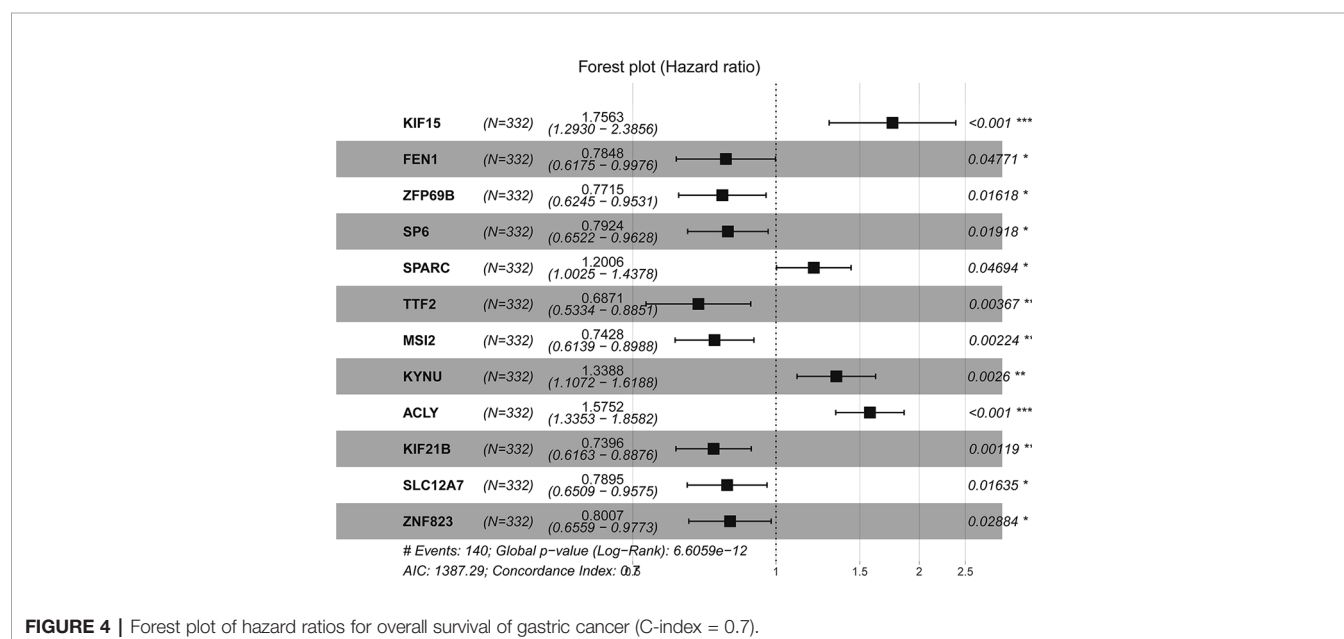
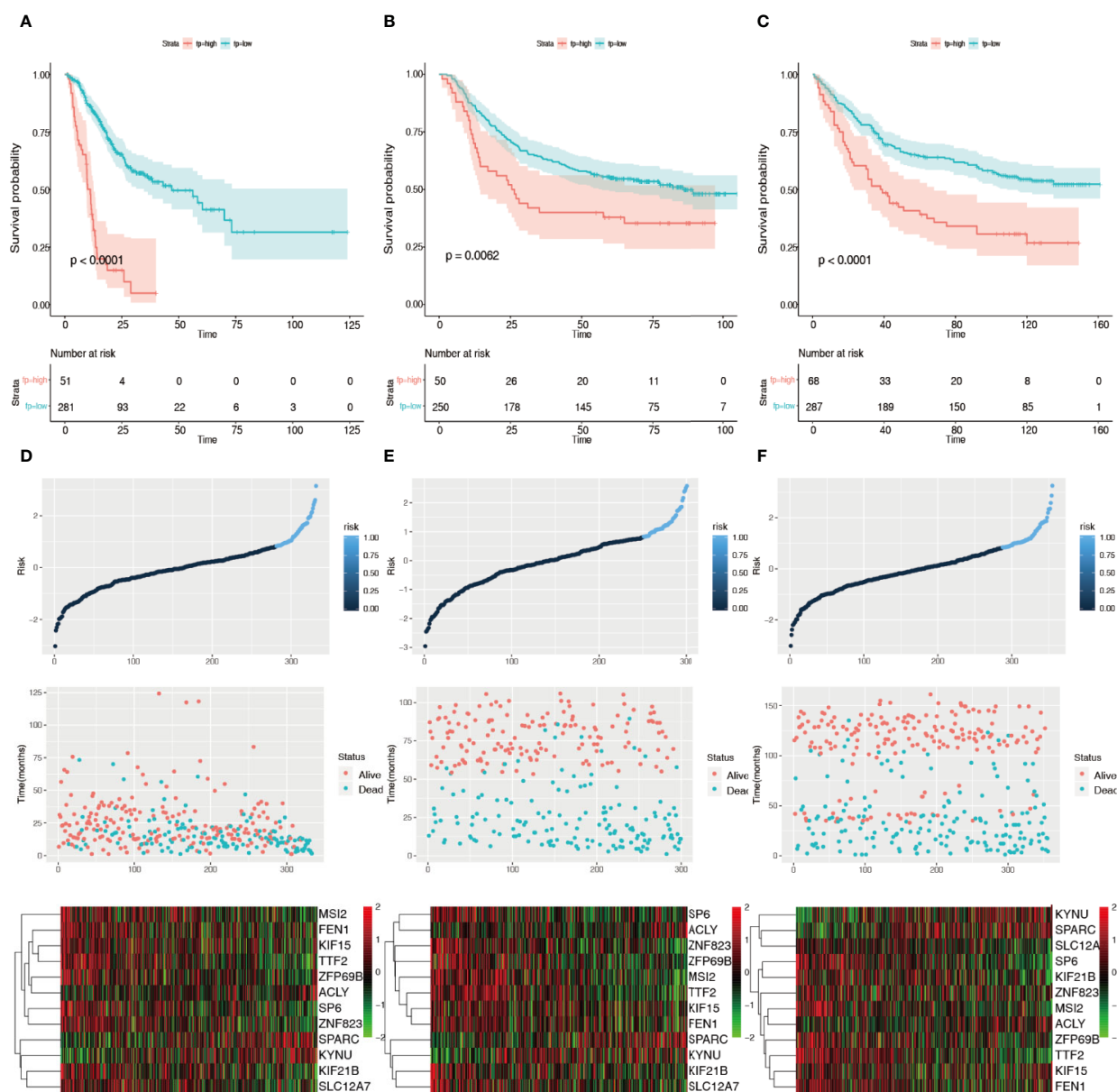


FIGURE 4 | Forest plot of hazard ratios for overall survival of gastric cancer (C-index = 0.7).



**FIGURE 5 |** Validation of the 12 prognosis-related gene risk score system. **(A)** Kaplan–Meier survival curves of the training group using 0.82 as the cutoff value. **(B)** Kaplan–Meier survival curves of the GSE25544 dataset using 0.82 as the cutoff value. **(C)** Kaplan–Meier survival curves of the GSE83344 based on the 12 prognosis-related genes using 0.82 as the cutoff value. **(D)** 12-gene signature risk score panel for the gene signature in the training group. **(E)** 12-gene signature risk score panel for the gene signature in GSE25544. **(F)** 12-gene signature risk score panel for the gene signature in GSE83344.

activation, thus promoting apoptosis and inhibiting cell proliferation in gastric cancer cells (Tao et al., 2020). The DNA replication and repair pathway is an important mechanism in gastric cancer. *FEN1* plays an important role in apoptotic fragmentation of DNA, maintenance of telomere stability, and rescue of stalled replication forks (Shen et al., 2005; Zheng et al., 2011). Unsurprisingly, genetic variants and changes in the expression of *FEN1* will alter patients' sensitivity to chemotherapy and prognosis (Liu et al., 2012; Wang et al.,

2014; Xie et al., 2016). The role of *SPARC* in gastric cancer has not been fully elucidated, although its diagnostic and prognostic value has been confirmed by multiple studies (Zhao et al., 2010; Liao et al., 2018). *SPARC* can act as both an inhibitor and promoter in cancer (Tai and Tang, 2008; Said, 2016; Li et al., 2019); the real effect of *SPARC* can be altered by other genes owing to its epistatic effects (Chen et al., 2018). However, some oncologists have shown that *SPARC* is mostly produced by gastric cancer-associated fibroblasts rather than gastric cancer

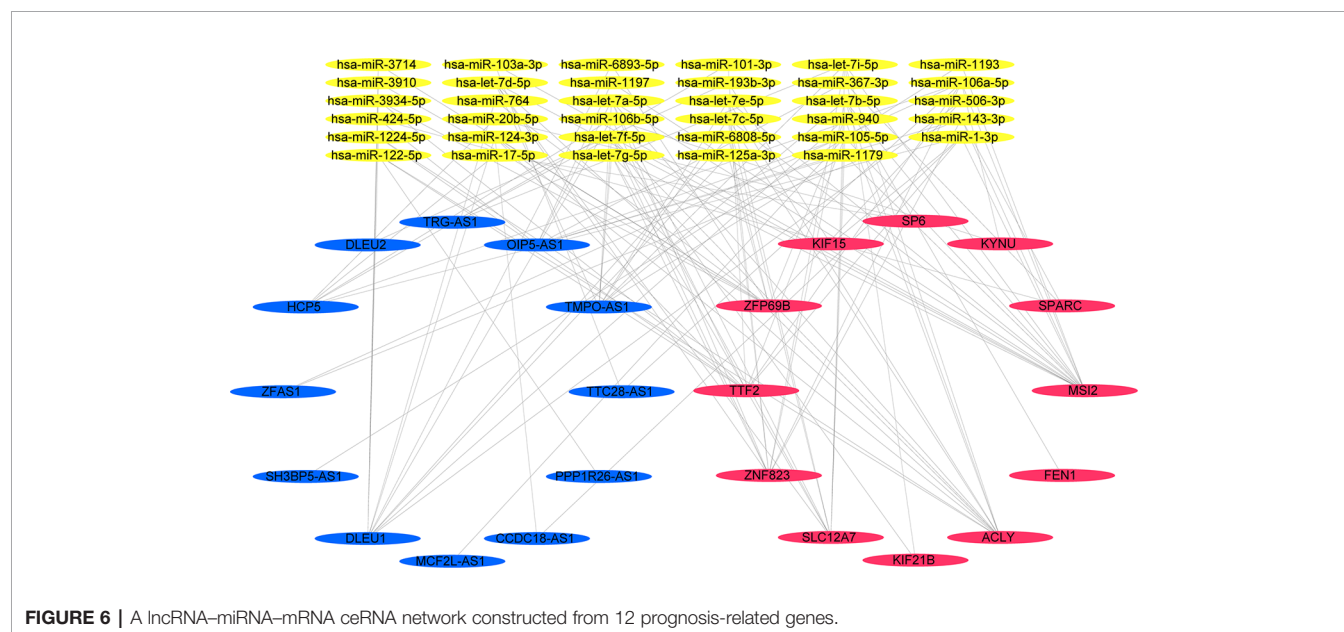
**TABLE 3 |** Pearson correlation tests and hypergeometric tests of the candidate lncRNA-miRNA-mRNA competing endogenous RNA pairs.

Genes	lncRNAs	miRNAs	hyperPValue	Correlation	corPValue
SPARC	OIP5-AS1	hsa-miR-367-3p, hsa-miR-424-5p, hsa-miR-143-3p	3.24E-04	1.23E-01	4.58E-03
SLC12A7	MCF2L-AS1	hsa-miR-105-5p	3.85E-02	2.67E-01	4.97E-09
SLC12A7	TMPO-AS1	hsa-let-7c-5p, hsa-let-7b-5p, hsa-let-7a-5p, hsa-let-7f-5p, hsa-let-7d-5p, hsa-let-7i-5p, hsa-let-7e-5p, hsa-let-7g-5p	3.17E-11	1.07E-01	1.21E-02
KYNU	HCP5	hsa-miR-106b-5p, hsa-miR-106a-5p	2.96E-04	2.33E-01	3.11E-07
TTF2	DLEU1	hsa-miR-106b-5p, hsa-miR-124-3p, hsa-miR-1224-5p, hsa-miR-3934-5p	2.61E-02	4.08E-01	1.31E-19
TTF2	HCP5	hsa-miR-106b-5p, hsa-miR-1-3p, hsa-miR-101-3p, hsa-miR-106a-5p	4.91E-04	1.35E-01	2.18E-03
TTF2	PPP1R26-AS1	hsa-miR-122-5p	3.38E-02	2.94E-01	1.24E-10
TTF2	CCDC18-AS1	hsa-miR-124-3p, hsa-miR-1-3p	3.32E-03	1.47E-01	9.55E-04
TTF2	MCF2L-AS1	hsa-miR-105-5p	3.38E-02	1.78E-01	7.73E-05
KIF21B	TMPO-AS1	hsa-let-7f-5p, hsa-let-7i-5p	1.44E-03	9.07E-02	2.78E-02
KIF21B	TRG-AS1	hsa-let-7f-5p, hsa-let-7i-5p	1.44E-03	2.88E-01	3.04E-10
ACLY	PPP1R26-AS1	hsa-miR-122-5p	1.75E-02	1.79E-01	6.98E-05
ACLY	DLEU1	hsa-miR-124-3p, hsa-miR-1224-5p, hsa-miR-940	2.05E-02	1.05E-01	1.32E-02
ACLY	TMPO-AS1	hsa-let-7c-5p, hsa-let-7b-5p, hsa-let-7a-5p, hsa-let-7f-5p, hsa-let-7d-5p, hsa-let-7i-5p, hsa-let-7e-5p, hsa-let-7g-5p	4.06E-14	1.47E-01	9.60E-04
MSI2	MCF2L-AS1	hsa-miR-105-5p	1.55E-02	1.77E-01	8.64E-05
MSI2	CCDC18-AS1	hsa-miR-1-3p	4.59E-02	1.32E-01	2.68E-03
MSI2	SH3BP5-AS1	hsa-miR-1193	1.55E-02	8.47E-02	3.70E-02
MSI2	OIP5-AS1	hsa-let-7a-5p, hsa-miR-105-5p, hsa-miR-1179, hsa-miR-1197, hsa-miR-143-3p	5.14E-07	9.54E-02	2.20E-02
MSI2	TTC28-AS1	hsa-miR-103a-3p, hsa-miR-106a-5p	1.39E-03	1.11E-01	9.48E-03
MSI2	TMPO-AS1	hsa-let-7c-5p, hsa-let-7b-5p, hsa-let-7a-5p, hsa-let-7f-5p, hsa-let-7d-5p, hsa-let-7i-5p, hsa-let-7e-5p, hsa-let-7g-5p, hsa-miR-1179	2.04E-17	1.26E-01	3.86E-03
KIF15	DLEU2	hsa-miR-193b-3p	7.75E-03	6.38E-01	1.08E-52
KIF15	HCP5	hsa-miR-1-3p	1.85E-02	2.13E-01	2.96E-06

(Continued)

**TABLE 3 |** Continued

Genes	lncRNAs	miRNAs	hyperPValue	Correlation	corPValue
FEN1	TMPO-AS1	hsa-let-7b-5p	3.45E-02	6.20E-01	4.29E-49
ZFP69B	DLEU1	hsa-miR-3714, hsa-miR-125a-3p, hsa-miR-124-3p, hsa-miR-506-3p, hsa-miR-764, hsa-miR-3934-5p, hsa-miR-6893-5p, hsa-miR-3910, hsa-miR-940, hsa-miR-6808-5p	3.02E-08	2.33E-01	3.19E-07
SP6	HCP5	hsa-miR-20b-5p, hsa-miR-17-5p	1.51E-03	1.02E-01	1.58E-02
ZNF823	TMPO-AS1	hsa-let-7c-5p, hsa-let-7b-5p, hsa-let-7a-5p, hsa-let-7f-5p, hsa-let-7d-5p, hsa-let-7i-5p, hsa-let-7e-5p, hsa-let-7g-5p	1.45E-14	3.04E-01	2.57E-11
ZNF823	ZFAS1	hsa-miR-106a-5p, hsa-miR-143-3p	7.92E-03	2.01E-01	9.84E-06

**FIGURE 6 |** A lncRNA-miRNA-mRNA ceRNA network constructed from 12 prognosis-related genes.

cells (Ma et al., 2018; Ma et al., 2019). Thus, the concrete mechanism of *SPARC* in gastric cancer needs further investigation. *MSI2* is an oncogene associated with differentiation, resulting in the preservation of cancer stem cells. According to a previous study based on microarray and RT-PCR, *MSI2* expression increased slightly relative to normal tissue, but it is still used as a biomarker for gastric cancer (Emadi-Baygi et al., 2013; Yang et al., 2019). *SLC12A7* (Solute Carrier Family 12 Member 7) acts as a potassium/chloride co-transporter for maintaining a stable osmotic pressure, which

can be activated by insulin-like growth factor (IGF) resulting in cell invasion and progression in breast cancer, adrenocortical cancer, cervical cancer, and ovarian cancer (Shen et al., 2004; Hsu et al., 2007; Chen et al., 2009; Brown et al., 2019). It has been reported that amplification of *SLC12A7* is mainly within *HER2*-patient samples in gastric cancer, while the precise mechanism of *SLC12A7* is still unknown (Zhou et al., 2018). *ACLY* is the integral enzyme responsible for the formation of cytosolic acetyl-CoA, and high expression of *ACLY* was shown to be associated with a poor prognosis (Qian et al., 2015). Citrate and inhibitors

of ACLY can reduce its expression, thus protecting against gastric cancer cell progression (Guo et al., 2016; Icard et al., 2020). In addition, *ACLY* can be downregulated by miR-133b via PPAR $\gamma$  (Cheng et al., 2017) and lncRNA FLJ22763 (Zhang et al., 2019) in gastric cancer.

The functions of *ZNF823*, *ZFP69B*, *SP6*, *KYNU*, *KIF21B*, and *TTF2* have not been reported in gastric cancer. *KYNU* is a pyridoxal-5'-phosphate dependent enzyme that catalyzes the cleavage of kynurenine into anthranilic acid (AA) and the cleavage of 3-hydroxykynurenine (3-HK) into 3-hydroxyanthranilic acids (3-HAA) (Badawy, 2017). Drugs have been developed to regulate the expression of *KYNU* to suppress tumor growth through the Kynurenine pathways, such as in breast cancer (Liu et al., 2019; Liu et al., 2020) and melanoma (Rad et al., 2019). It has been demonstrated that *TTF2* is able to terminate RNA polymerase II transcription, which has an important function in promoting chromosome segregation and altering protein-DNA interactions (Jiang and Price, 2004; Jiang et al., 2004; Cheng et al., 2012). *KIF21B* is an ATP-dependent microtubule-based motor protein that participates in the intracellular transfer of membranous organelles. *KIF21B* is a potential oncogene that resists the induction of apoptosis and facilitates malignant tumorigenesis, tumor development, intrusion, and metastasis. Patients with high expression of *KIF21B* have been demonstrated to have a poorer prognosis in hepatocellular carcinoma (Zhao et al., 2020) and non-small cell lung cancer (Sun et al., 2020). *SP6* is an important gene that regulates odontogenesis, belonging to a family of transcription factors that contain 3 classical zinc finger DNA-binding domains (Aurrekoetxea et al., 2016; Smith et al., 2020; Nakamura et al., 2020).

In summary, we identified a survival-related gene-based ceRNA network using the WGCNA algorithm, and the constructed lncRNA-miRNA-mRNA ceRNA interactive

network will probably provide a basis for additional inspection of the regulatory mechanisms of gastric cancer. Gastric cancer has high heterogeneity among its different histological and molecular subtypes. Thus, while we have selected the expression profiles with the largest sample size that we could obtain currently, we must admit that further experimental works and large cohorts are needed to verify our results and elucidate the prognostic value of ceRNA networks in gastric cancer.

## DATA AVAILABILITY STATEMENT

The datasets analyzed for this study can be found in The Cancer Genome Atlas (TCGA) data portal (<https://portal.gdc.cancer.gov/>), the Genotype-Tissue Expression (GTEx) portal. (<https://www.gtexportal.org/home/index.html>), and the Gene Expression Omnibus (GEO) repository (<https://www.ncbi.nlm.nih.gov/geo/>).

## AUTHOR CONTRIBUTIONS

XZ and YX contributed to study conception. XZ, XW, LZ, and HZ contributed to data collection and analysis. XZ, WL, BW, LX, and YT contributed to manuscript writing. All authors contributed to the article and approved the submitted version.

## FUNDING

The study was supported by the CAMS Initiative for Innovative Medicine (2016-I2M-1-007) and China International Medical Foundation (CIMF-F-H001-314).

## REFERENCES

- Abdollahzadeh, R., Daraei, A., Mansoori, Y., Sepahvand, M., Amoli, M. M., Tavakkoly-Bazzaz, J., et al. (2019). (ceRNA) cross talk and language in ceRNA regulatory networks: a new look at hallmarks of breast cancer. *J. Cell. Physiol.* 234 (7), 10080–10100. doi: 10.1002/jcp.27941
- Aurrekoetxea, M., Irastorza, I., Garcia-Gallastegui, P., Jimenez-Rojas, L., Nakamura, T., Yamada, Y., et al. (2016). Wnt/beta-Catenin Regulates the Activity of Epiprofin/Sp6, SHH, FGF, and BMP to Coordinate the Stages of Odontogenesis. *Front. Cell Dev. Biol.* 4, 25. doi: 10.3389/fcell.2016.00025
- Badawy, A. A. (2017). Kynurenine Pathway of Tryptophan Metabolism: Regulatory and Functional Aspects. *Int. J. Tryptophan. Res.* 10, 1178646917691938. doi: 10.1177/1178646917691938
- Brown, T. C., Nicolson, N. G., Stenman, A., Juhlin, C. C., Gibson, C. E., Callender, G. G., et al. (2019). Insulin-Like Growth Factor and SLC12A7 Dysregulation: A Novel Signaling Hallmark of Non-Functional Adrenocortical Carcinoma. *J. Am. Coll. Surg.* 229 (3), 305–315. doi: 10.1016/j.jamcollsurg.2019.04.018
- Cancer Genome Atlas Research N (2014). Comprehensive molecular characterization of gastric adenocarcinoma. *Nature* 513 (7517), 202–209. doi: 10.1038/nature13480
- Chen, Y. F., Chou, C. Y., Wilkins, R. J., Ellory, J. C., Mount, D. B., and Shen, M. R. (2009). Motor protein-dependent membrane trafficking of KCl cotransporter-4 is important for cancer cell invasion. *Cancer Res.* 69 (22), 8585–8593. doi: 10.1158/0008-5472.CAN-09-2284
- Chen, L. Z., He, C. Y., Su, X., Peng, J. L., Chen, D. L., Ye, Z., et al. (2018). SPP1 rs4754 and its epistatic interactions with SPARC polymorphisms in gastric cancer susceptibility. *Gene* 640, 43–50. doi: 10.1016/j.gene.2017.09.053
- Cheng, B., Li, T., Rahl, P. B., Adamson, T. E., Loudas, N. B., Guo, J., et al. (2012). Functional association of Gdown1 with RNA polymerase II poised on human genes. *Mol. Cell* 45 (1), 38–50. doi: 10.1016/j.molcel.2011.10.022
- Cheng, Y., Jia, B., Wang, Y., and Wan, S. (2017). miR-133b acts as a tumor suppressor and negatively regulates ATP citrate lyase via PPAR $\gamma$  in gastric cancer. *Oncol. Rep.* 38 (5), 3220–3226. doi: 10.3892/or.2017.5944
- Cheong, J. H., Yang, H. K., Kim, H., Kim, W. H., Kim, Y. W., Kook, M. C., et al. (2018). Predictive test for chemotherapy response in resectable gastric cancer: a multi-cohort, retrospective analysis. *Lancet Oncol.* 19 (5), 629–638. doi: 10.1016/S1470-2045(18)30108-6
- Cho, J. Y., Lim, J. Y., Cheong, J. H., Park, Y. Y., Yoon, S. L., Kim, S. M., et al. (2011). Gene expression signature-based prognostic risk score in gastric cancer. *Clin. Cancer Res.* 17 (7), 1850–1857. doi: 10.1158/1078-0432.CCR-10-2180
- Cristescu, R., Lee, J., Nebozhyn, M., Kim, K. M., Ting, J. C., Wong, S. S., et al. (2015). Molecular analysis of gastric cancer identifies subtypes associated with distinct clinical outcomes. *Nat. Med.* 21 (5), 449–456. doi: 10.1038/nm.3850
- Donithan, M., Van Natta, M., and Tonascia, J. (1992). Cox regression analyses using SAS/PHREG. *Controlled Clin. Trials* 13 (5), 420. doi: 10.1016/0197-2456(92)90146-Q
- Duan, S., Wang, P., Liu, F., Huang, H., An, W., Pan, S., et al. (2019). Novel immune-risk score of gastric cancer: A molecular prediction model combining the value of immune-risk status and chemosensitivity. *Cancer Med.* 8 (5), 2675–2685. doi: 10.1002/cam4.2077



- Emadi-Baygi, M., Nikpour, P., Mohammad-Hashem, F., Maracy, M. R., and Haghighi-Javanmard, S. (2013). MSI2 expression is decreased in grade II of gastric carcinoma. *Pathol. Res. Pract.* 209 (11), 689–691. doi: 10.1016/j.prp.2013.07.008
- Erdem, G. U., Bozkaya, Y., Ozdemir, N. Y., Demirci, N. S., Yazici, O., and Zengin, N. (2018). 5-fluorouracil, leucovorin, and irinotecan (FOLFIRI) as a third-line chemotherapy treatment in metastatic gastric cancer, after failure of fluoropyrimidine, platinum, anthracycline, and taxane. *Bosn. J. Basic Med. Sci.* 18 (2), 170–177. doi: 10.17305/bjbm.2017.2258
- Guo, X., Zhang, X., Wang, T., Xian, S., and Lu, Y. (2016). 3-Bromopyruvate and sodium citrate induce apoptosis in human gastric cancer cell line MGC-803 by inhibiting glycolysis and promoting mitochondria-regulated apoptosis pathway. *Biochem. Biophys. Res. Commun.* 475 (1), 37–43. doi: 10.1016/j.bbrc.2016.04.151
- Hsu, Y. M., Chou, C. Y., Chen, H. H., Lee, W. Y., Chen, Y. F., Lin, P. W., et al. (2007). IGF-1 upregulates electroneutral K-Cl cotransporter KCC3 and KCC4 which are differentially required for breast cancer cell proliferation and invasiveness. *J. Cell Physiol.* 210 (3), 626–636. doi: 10.1002/jcp.20859
- Hu, Z., Yang, D., Tang, Y., Zhang, X., Wei, Z., Fu, H., et al. (2019). Five-long non-coding RNA risk score system for the effective prediction of gastric cancer patient survival. *Oncol. Lett.* 17 (5), 4474–4486. doi: 10.3892/ol.2019.10124
- Icard, P., Wu, Z., Fournel, L., Coquerel, A., Lincet, H., and Alifano, M. (2020). ATP citrate lyase: A central metabolic enzyme in cancer. *Cancer Lett.* 471, 125–134. doi: 10.1016/j.canlet.2019.12.010
- Jiang, Y., and Price, D. H. (2004). Rescue of the TTF2 knockdown phenotype with an siRNA-resistant replacement vector. *Cell Cycle.* 3 (9), 1151–1153. doi: 10.4161/cc.3.9.1151
- Jiang, Y., Liu, M., Spencer, C. A., and Price, D. H. (2004). Involvement of transcription termination factor 2 in mitotic repression of transcription elongation. *Mol. Cell.* 14 (3), 375–385. doi: 10.1016/S1097-2765(04)00234-5
- Kakati, T., Bhattacharyya, D. K., Barah, P., and Kalita, J. K. (2019). Comparison of Methods for Differential Co-expression Analysis for Disease Biomarker Prediction. *Comput. Biol. Med.* 113, 103380. doi: 10.1016/j.compbiomed.2019.103380
- Kubota, Y., Kawazoe, A., Sasaki, A., Mishima, S., Sawada, K., Nakamura, Y., et al. (2020). The Impact of Molecular Subtype on Efficacy of Chemotherapy and Checkpoint Inhibition in Advanced Gastric Cancer. *Clin. Cancer Res.* doi: 10.1158/1078-0432.CCR-20-0075
- Langfelder, P., and Horvath, S. (2008). WGCNA: an R package for weighted correlation network analysis. *BMC Bioinf.* 9 (1), 559. doi: 10.1186/1471-2105-9-559
- Leek, J. T., Johnson, W. E., Parker, H. S., Jaffe, A. E., and Storey, J. D. (2012). The sva package for removing batch effects and other unwanted variation in high-throughput experiments. *Bioinformatics* 28 (6), 882–883. doi: 10.1093/bioinformatics/bts034
- Li, L., Zhu, Z., Zhao, Y., Zhang, Q., Wu, X., Miao, B., et al. (2019). FN1, SPARC, and SERPINE1 are highly expressed and significantly related to a poor prognosis of gastric adenocarcinoma revealed by microarray and bioinformatics. *Sci. Rep.* 9 (1), 7827. doi: 10.1038/s41598-019-43924-x
- Liao, P., Li, W., Liu, R., Teer, J. K., Xu, B., Zhang, W., et al. (2018). Genome-scale analysis identifies SERPINE1 and SPARC as diagnostic and prognostic biomarkers in gastric cancer. *Onco. Targets Ther.* 11, 6969–6980. doi: 10.2147/OTT.S173934
- Lin, Y., Liu, T., Cui, T., Wang, Z., Zhang, Y., Tan, P., et al. (2020). RNAInter in 2020: RNA interactome repository with increased coverage and annotation. *Nucleic Acids Res.* 48 (D1), D189–DD97. doi: 10.1093/nar/gkz804
- Liu, L., Zhou, C., Zhou, L., Peng, L., Li, D., Zhang, X., et al. (2012). Functional FN1 genetic variants contribute to risk of hepatocellular carcinoma, esophageal cancer, gastric cancer and colorectal cancer. *Carcinogenesis* 33 (1), 119–123. doi: 10.1093/carcin/bgr250
- Liu, Y., Feng, X., Lai, J., Yi, W., Yang, J., Du, T., et al. (2019). A novel role of kynureninase in the growth control of breast cancer cells and its relationships with breast cancer. *J. Cell Mol. Med.* 23 (10), 6700–6707. doi: 10.1111/jcmm.14547
- Liu, Q., Zhai, J., Kong, X., Wang, X., Wang, Z., Fang, Y., et al. (2020). Comprehensive Analysis of the Expression and Prognosis for TDO2 in Breast Cancer. *Mol. Ther. Oncolytics* 17, 153–168. doi: 10.1016/j.omto.2020.03.013
- Ma, Y., Zhu, J., Chen, S., Li, T., Ma, J., Guo, S., et al. (2018). Activated gastric cancer-associated fibroblasts contribute to the malignant phenotype and 5-FU resistance via paracrine action in gastric cancer. *Cancer Cell Int.* 18, 104. doi: 10.1186/s12935-018-0599-7
- Ma, Y., Zhu, J., Chen, S., Ma, J., Zhang, X., Huang, S., et al. (2019). Low expression of SPARC in gastric cancer-associated fibroblasts leads to stemness transformation and 5-fluorouracil resistance in gastric cancer. *Cancer Cell Int.* 19 (1), 137. doi: 10.1186/s12935-019-0844-8
- Menyhart, O., Pongor, L. S., and Gyorffy, B. (2018). Mutations Defining Patient Cohorts With Elevated PD-L1 Expression in Gastric Cancer. *Front. Pharmacol.* 9 (1522), 1522. doi: 10.3389/fphar.2018.01522
- Nakamura, T., Iwamoto, T., Nakamura, H. M., Shindo, Y., Saito, K., Yamada, A., et al. (2020). Regulation of miR-1-Mediated Connexin 43 Expression and Cell Proliferation in Dental Epithelial Cells. *Front. Cell Dev. Biol.* 8 (156):156. doi: 10.3389/fcell.2020.00156
- Paci, P., Colombo, T., and Farina, L. (2014). Computational analysis identifies a sponge interaction network between long non-coding RNAs and messenger RNAs in human breast cancer. *BMC Syst. Biol.* 8, 83. doi: 10.1186/1752-0509-8-83
- Parrish, R. S., and Spencer, H. J., III. (2004). Effect of normalization on significance testing for oligonucleotide microarrays. *J. Biopharm. Stat.* 14 (3), 575–589. doi: 10.1081/BIP-200025650
- Qi, X., Zhang, D. H., Wu, N., Xiao, J. H., Wang, X., and Ma, W. (2015). ceRNA in cancer: possible functions and clinical implications. *J. Med. Genet.* 52 (10), 710–718. doi: 10.1136/jmedgenet-2015-103334
- Qian, X., Hu, J., Zhao, J., and Chen, H. (2015). ATP citrate lyase expression is associated with advanced stage and prognosis in gastric adenocarcinoma. *Int. J. Clin. Exp. Med.* 8 (5), 7855–7860.
- Rad, P. S., Morikawa, H., Kiani, N. A., Yang, M., Azimi, A., Shafi, G., et al. (2019). Exhaustion of CD4+ T-cells mediated by the Kynurenine Pathway in Melanoma. *Sci. Rep.* 9 (1), 12150. doi: 10.1038/s41598-019-48635-x
- Ritchie, M. E., Phipson, B., Wu, D., Hu, Y., Law, C. W., Shi, W., et al. (2015). limma powers differential expression analyses for RNA-sequencing and microarray studies. *Nucleic Acids Res.* 43 (7), e47. doi: 10.1093/nar/gkv007
- Said, N. (2016). Role of SPARC in Cancer; Friend or Foe. *Ann. Carcinog.* 1 (1), 1003.
- Salmena, L., Poliseno, L., Tay, Y., Kats, L., and Pandolfi, P. P. (2011). A ceRNA hypothesis: the Rosetta Stone of a hidden RNA language? *Cell* 146 (3), 353–358. doi: 10.1016/j.cell.2011.07.014
- Shen, M. R., Lin, A. C., Hsu, Y. M., Chang, T. J., Tang, M. J., Alper, S. L., et al. (2004). Insulin-like growth factor 1 stimulates KCl cotransport, which is necessary for invasion and proliferation of cervical cancer and ovarian cancer cells. *J. Biol. Chem.* 279 (38), 40017–40025. doi: 10.1074/jbc.M406706200
- Shen, B., Singh, P., Liu, R., Qiu, J., Zheng, L., Finger, L. D., et al. (2005). Multiple but dissectible functions of FEN-1 nucleases in nucleic acid processing, genome stability and diseases. *Bioessays* 27 (7), 717–729. doi: 10.1002/bies.20255
- Shuwen, H., Qing, Z., Yan, Z., and Xi, Y. (2018). Competitive endogenous RNA in colorectal cancer: A systematic review. *Gene* 645, 157–162. doi: 10.1016/j.gene.2017.12.036
- Smith, C. E., Whitehouse, L. L., Poulter, J. A., Wilkinson Hewitt, L., Nadat, F., Jackson, B. R., et al. (2020). A missense variant in specificity protein 6 (SP6) is associated with amelogenesis imperfecta. *Hum. Mol. Genet.* 29 (9), 1417–1425. doi: 10.1093/hmg/ddaa041
- Su, G., Morris, J. H., Demchak, B., and Bader, G. D. (2014). Biological network exploration with Cytoscape 3. *Curr. Protoc. Bioinf.* 47 (1), 8. doi: 10.1002/0471250953.bi0813s47
- Sun, Z. G., Pan, F., Shao, J. B., Yan, Q. Q., Lu, L., and Zhang, N. (2020). Kinesin superfamily protein 21B acts as an oncogene in non-small cell lung cancer. *Cancer Cell Int.* 20, 233. doi: 10.1186/s12935-020-01323-7
- Tai, I. T., and Tang, M. J. (2008). SPARC in cancer biology: its role in cancer progression and potential for therapy. *Drug Resist. Updat.* 11 (6), 231–246. doi: 10.1016/j.drug.2008.08.005
- Tao, J., Sun, G., Li, Q., Zhi, X., Li, Z., He, Z., et al. (2020). KIF15 promotes the evolution of gastric cancer cells through inhibition of reactive oxygen species-mediated apoptosis. *J. Cell. Physiol.* doi: 10.1002/jcp.29743
- Therneau, T. M. (2020). A package for survival analysis in S. version 3.2-3. Available at: <https://CRAN.R-project.org/package=survival>
- Van Cutsem, E., Sagaert, X., Topal, B., Haustermans, K., and Prenen, H. (2016). Gastric cancer. *Lancet* 388 (10060), 2654–2664. doi: 10.1016/S0140-6736(16)30354-3

- van Dam, S., Vosa, U., van der Graaf, A., Franke, L., and de Magalhaes, J. P. (2018). Gene co-expression analysis for functional classification and gene-disease predictions. *Brief Bioinform.* 19 (4), 575–592. doi: 10.1093/bib/bbw139
- Wang, K., Xie, C., and Chen, D. (2014). Flap endonuclease 1 is a promising candidate biomarker in gastric cancer and is involved in cell proliferation and apoptosis. *Int. J. Mol. Med.* 33 (5), 1268–1274. doi: 10.3892/ijmm.2014.1682
- Xie, C., Wang, K., and Chen, D. (2016). Flap endonuclease 1 silencing is associated with increasing the cisplatin sensitivity of SGC-7901 gastric cancer cells. *Mol. Med. Rep.* 13 (1), 386–392. doi: 10.3892/mmr.2015.4567
- Yang, Z., Li, J., Shi, Y., Li, L., and Guo, X. (2019). Increased musashi 2 expression indicates a poor prognosis and promotes malignant phenotypes in gastric cancer. *Oncol. Lett.* 17 (3), 2599–2606. doi: 10.3892/ol.2019.9889
- Yu, G., Wang, L.-G., Han, Y., and He, Q.-Y. (2012). clusterProfiler: an R package for comparing biological themes among gene clusters. *Omics: J. Integr. Biol.* 16 (5), 284–287. doi: 10.1089/omi.2011.0118
- Zhang, G., Wang, Q., Lu, J., Ma, G., Ge, Y., Chu, H., et al. (2019). Long non-coding RNA FLJ22763 is involved in the progression and prognosis of gastric cancer. *Gene* 693, 84–91. doi: 10.1016/j.gene.2019.01.028
- Zhao, Z.-S., Wang, Y.-Y., Chu, Y.-Q., Ye, Z.-Y., and Tao, H.-Q. (2010). SPARC Is Associated with Gastric Cancer Progression and Poor Survival of Patients. *Clin. Cancer Res.* 16 (1), 260–268. doi: 10.1158/1078-0432.CCR-09-1247
- Zhao, H. Q., Dong, B. L., Zhang, M., Dong, X. H., He, Y., Chen, S. Y., et al. (2020). Increased KIF21B expression is a potential prognostic biomarker in hepatocellular carcinoma. *World J. Gastrointest. Oncol.* 12 (3), 276–288. doi: 10.4251/wjgo.v12.i3.276
- Zheng, L., Jia, J., Finger, L. D., Guo, Z., Zer, C., and Shen, B. (2011). Functional regulation of FEN1 nuclease and its link to cancer. *Nucleic Acids Res.* 39 (3), 781–794. doi: 10.1093/nar/gkq884
- Zhou, C., Feng, X., Yuan, F., Ji, J., Shi, M., Yu, Y., et al. (2018). Difference of molecular alterations in HER2-positive and HER2-negative gastric cancers by whole-genome sequencing analysis. *Cancer Manag. Res.* 10, 3945–3954. doi: 10.2147/CMARS172710

**Conflict of Interest:** The authors declare that the research was conducted in the absence of any commercial or financial relationships that could be construed as a potential conflict of interest.

Copyright © 2020 Zheng, Wang, Zheng, Zhao, Li, Wang, Xue, Tian and Xie. This is an open-access article distributed under the terms of the Creative Commons Attribution License (CC BY). The use, distribution or reproduction in other forums is permitted, provided the original author(s) and the copyright owner(s) are credited and that the original publication in this journal is cited, in accordance with accepted academic practice. No use, distribution or reproduction is permitted which does not comply with these terms.



# Targeting B7-H3 Immune Checkpoint With Chimeric Antigen Receptor-Engineered Natural Killer Cells Exhibits Potent Cytotoxicity Against Non-Small Cell Lung Cancer

Shuo Yang<sup>1,2</sup>, Bihui Cao<sup>3</sup>, Guangyu Zhou<sup>1,2</sup>, Lipeng Zhu<sup>1,2</sup>, Lu Wang<sup>3</sup>, Li Zhang<sup>4</sup>, Hang Fai Kwok<sup>1,2</sup>, Zhenfeng Zhang<sup>3\*</sup> and Qi Zhao<sup>1,2\*</sup>

<sup>1</sup> Cancer Centre, Faculty of Health Sciences, University of Macau, Macau, China, <sup>2</sup> Institute of Translational Medicine, Faculty of Health Sciences, University of Macau, Macau, China, <sup>3</sup> Department of Radiology, Translational Medicine Center and Guangdong Provincial Education Department Key Laboratory of Nano-Immunoregulation Tumor Microenvironment, The Second Affiliated Hospital of Guangzhou Medical University, Guangzhou, China, <sup>4</sup> Department of Gynecologic Oncology and Reproductive Medicine, The University of Texas MD Anderson Cancer Center, Houston, TX, United States

## OPEN ACCESS

### Edited by:

Dong-Hua Yang,  
St. John's University, United States

### Reviewed by:

Xiuli Wu,  
Jinan University, China  
Wei Li,  
University of Pittsburgh, United States

### \*Correspondence:

Qi Zhao  
qizhao@um.edu.mo  
Zhenfeng Zhang  
zhangzhf@gzhmu.edu.cn

### Specialty section:

This article was submitted to  
Experimental Pharmacology  
and Drug Discovery,  
a section of the journal  
Frontiers in Pharmacology

**Received:** 17 June 2020

**Accepted:** 03 July 2020

**Published:** 30 July 2020

### Citation:

Yang S, Cao B, Zhou G, Zhu L, Wang L, Zhang L, Kwok HF, Zhang Z and Zhao Q (2020) Targeting B7-H3 Immune Checkpoint With Chimeric Antigen Receptor-Engineered Natural Killer Cells Exhibits Potent Cytotoxicity Against Non-Small Cell Lung Cancer. *Front. Pharmacol.* 11:1089. doi: 10.3389/fphar.2020.01089

Chimeric antigen receptor (CAR)-modified natural killer (NK) cell therapy represents a kind of promising anti-cancer treatment because CAR renders NK cells activation and recognition specificity toward tumor cells. An immune checkpoint molecule, B7-H3, plays an inhibitory role in modulation of NK cells. To enhance NK cell functions, we generated NK-92MI cells carrying anti-B7-H3 CAR by lentiviral transduction. The expression of anti-B7-H3 CAR significantly enhanced the cytotoxicity of NK-92MI cells against B7-H3-positive tumor cells. In accordance with enhanced cytotoxicity, the secretions of perforin/granzyme B and expression of CD107a were highly elevated in anti-B7-H3 CAR-NK-92MI cells. Moreover, compared to unmodified NK-92MI cells, anti-B7-H3 CAR-NK-92MI cells effectively limited tumor growth in mouse xenografts of non-small cell lung cancer and significantly prolonged the survival days of mice. This study provides the rationale and feasibility of B7-H3-specific CAR-NK cells for application in adoptive cancer immunotherapy.

**Keywords:** B7-H3, chimeric antigen receptor, NK-92, immune checkpoint, natural killer cell

## INTRODUCTION

Non-small cell lung cancer (NSCLC) accounts for about 85% of all lung cancers (Oser et al., 2015). Depending on the stages of the cancer, NSCLC patients receive different treatments of surgery, radiation, chemotherapy, targeted therapies, and immunotherapy accordingly. Cancer cells frequently metastasize to some major organs, such as bone, brain, lung, and liver. Metastatic spread of cancer is the reason for most NSCLC deaths (Riihimäki et al., 2014).

The role of programmed cell death protein 1 (PD-1) as an immune checkpoint has been well elucidated in cancer therapy. At present, two anti-PD-1 antibodies (nivolumab and pembrolizumab) have been approved for NSCLC therapy (Forde et al., 2018). B7-H3 is a newly found immune checkpoint



molecule (Picarda et al., 2016; Castellanos et al., 2017). Less is known about the receptor of the B7-H3 molecule. Many studies demonstrate that B7-H3 regulates the function of T cells and natural killer (NK) cells, leading to immune evasion of tumor cells (Hofmeyer et al., 2008). Beyond its inhibitory role, recent studies demonstrate that it is also frequently expressed by tumor vasculature (Kraan et al., 2014; Seaman et al., 2017). It is overexpressed in multiple tumor types, including human lung, breast, and colon cancer (Flem-Karlsen et al., 2019). B7-H3 expression is associated with tumor infiltrating lymphocytes and tumor metastasis in major cancers (Sun et al., 2006; Brunner et al., 2012). B7-H3 is an ideal target for cancer immunotherapy (Yang et al., 2020). Several anti-B7-H3 monoclonal antibodies have been studied in preclinical or clinical trials. The anti-B7-H3 antibody m276 conjugated with small molecule drugs (ADCs) has shown effective for the selective destruction of tumor vasculature in multiple tumor xenografted models (Seaman et al., 2017). Another anti-B7-H3 antibody 8H9 radiolabeled with iodine-131 has improved survival of patients with metastatic central nervous system neuroblastoma (Kramer et al., 2010). Anti-B7-H3 8H9 ADCs further showed the ability of treating NSCLC both *in vitro* and *in vivo* (Zhu et al., 2019). Recently, chimeric antigen receptor (CAR)-modified lymphocytes represent the new therapeutic forms that use artificial receptors, CARs, to redirect lymphocytes against tumor cells (Liu et al., 2019; Ma et al., 2019). Anti-B7-H3 CAR T cell therapy exhibits potent efficacy in preclinical models of tumors, including pediatric tumors, glioblastoma, melanoma, and hematologic malignancies (Du et al., 2019; Majzner et al., 2019; Nehama et al., 2019; Tang et al., 2019; Zhang et al., 2020).

NK cells are critical for innate immunity in preventing tumor metastases, which are associated with the escape from immunosurveillance (Waldhauer and Steinle, 2008). Adoptive transfer of allogeneic NK cells has been used to treat cancer in clinic for the low risk of graft-versus-host-disease (GVHD), which often occurs in the cases of allogeneic T cells (Lorenzo-Herrero et al., 2018). A human NK cell line, NK-92, was derived from patients with malignant non-Hodgkin's lymphoma (Gong et al., 1994). NK-92MI is a derivative cell line of NK-92 with transfection of human interleukin (IL)-2 (Tam et al., 1999). Unlike primary NK cells, which have the variations of expansion capability among different donors, NK-92 and NK-92MI cell lines can be continuously expanded with the similar phenotypical and functional characteristics of primary NK cells. Importantly, lack of most of the inhibitory killer immunoglobulin-like receptors (KIRs) enables NK-92 and NK-92MI cells high cytotoxicity against malignancies (Klingemann et al., 2016). Safety and antitumor activity of infused NK-92 cells have been demonstrated in preclinical models and clinical trials (Klingemann et al., 2016). A number of CAR-modified NK-92 or NK-92MI cells have been constructed toward a panel of tumor-associated antigens, including ErbB2, CD4, CD19, CD20, CD33, CD38, CD138, GD2, and epithelial cell adhesion molecule (EPCAM) (Zhang et al., 2017). These NK constructs have been demonstrated as effective treatments in preclinical models.

In this study, to enhance the potency of NK cells, we modified NK-92MI cells with an anti-B7-H3 CAR that consists of a single

chain variable fragment (scFv) of the anti-B7-H3 antibody 8H9, the intracellular 4-1BB domain, and CD3 $\zeta$  chain. Compared to unmodified NK-92MI cells, the activity and cytotoxicity of CAR-modified NK-92MI cells were significantly enhanced *in vitro* and *in vivo*. Our results demonstrate that redirection of anti-B7-H3 CAR promotes activation and antitumor cytotoxicity of NK cells.

## MATERIALS AND METHOD

### Cell Line and Cell Culture

The human lung cancer cell lines, A549, NCI-H23, HCC827, and Burkitt's lymphoma cell line Daudi, were cultured in RPMI 1640 (Cellgro). The human embryonic kidney (HEK) cell line, 293T, and the breast cancer cell line, MDA-MB-231, were cultured in DMEM (Cellgro). The human colorectal cancer cell lines, DLD-1 and HCT-116, were maintained in DMEM/F-12 medium (GIBCO). All above cell culture media were supplemented with 10% fetal bovine serum (FBS) (GIBCO), 100 U/ml penicillin, and 100  $\mu$ g/ml streptomycin (GIBCO). The human NK-92MI cells were grown in alpha minimum essential medium (GIBCO) supplemented with 0.2 mM inositol (Sigma-Aldrich), 0.1 mM 2-mercaptoethanol (Sigma-Aldrich), 0.02 mM folic acid (Sigma-Aldrich), adjusting to a final concentration of 12.5% horse serum (GIBCO), 12.5% FBS, 100 U/ml penicillin, and 100  $\mu$ g/ml streptomycin. All the above cell lines were maintained in conditions with 5% CO<sub>2</sub> at 37°C. HEK293T, Daudi, NK-92MI, MDA-MB-231, NCI-H23, HCC827, and A549 cell lines were kindly provided by Stem Cell Bank, Chinese Academy of Sciences. DLD-1 and HCT-116 cell lines were provided by Prof. H.F. Kwok in the University of Macau.

### Purification and Expression of Anti-B7-H3 IgG 8H9

The anti-B7-H3 IgG 8H9 was expressed and purified according to the instruction as previously described (Li D. Z. et al., 2018). Briefly, the IgG 8H9 was expressed by transient transfection of the plasmids with polythyleneimine (MW25000, Polyscience) in Free-style 293-F (Invitrogen) cells. The expressed IgG proteins were purified by protein A agarose beads (GE Healthcare).

### Flow Cytometric Analysis of B7-H3 Expression

To detect B7-H3 expression on the surface of target cell lines, the cancer cell lines A549, NCI-H23, HCC827, DLD-1, HCT-116, MDA-MB-231, and Daudi were stained with anti-B7-H3 IgG 8H9 in PBS supplemented with 3% FBS for 30 min at 4°C, respectively. Then cells were rinsed and incubated with PE-conjugated goat anti-human IgG secondary antibody (Thermo Fisher Scientific) for 30 min at 4°C. After washing, cells were analyzed using the Accuri<sup>TM</sup> C6 Flow Cytometer (BD Biosciences). Flow cytometry data were analyzed with FlowJo software.

### Immunoprecipitation Assay

The cancer cell lines, A549, NCI-H23, and Daudi, were collected when grown to ~80% confluence. The lysis buffer [50 mmol/L

Tris-HCl (pH 7.2), 167 mmol/L NaCl, 10% glycerol, 1% Triton X-100, and protease inhibitor cocktail tablets] was used to lyse the collected cells by incubation on ice for 20 min. The lysates were then centrifuged at 14,000 rpm for 20 min at 4°C. For immunoprecipitations, lysates were incubated with anti-B7-H3 IgG 8H9 or control IgG (5 µg/ml) overnight at 4°C. Protein A agarose beads were then added and incubated for 4 h at 4°C. Then, the beads were washed with lysis buffer and boiled with the loading buffer. The supernatants were separated in the SDS-PAGE gel, and transferred onto the PVDF membrane (Bio-Rad). After incubation with PBST containing 5% non-fat milk for 1 h at room temperature (RT), the membrane was probed with the goat anti-human B7-H3 primary antibody MAB1027 (R&D Systems) overnight at 4°C. The membrane was then incubated with the peroxidase-conjugated rabbit anti-goat IgG (H+L) (Jackson ImmunoResearch) for 1 h at RT and visualized using Clarity™ Western ECL Substrate (Bio-Rad).

## Immunohistochemistry

All procedures were in accordance with the ethical standards approved by the Guangzhou Medical University (2019-ks-23). The human lung cancer and normal tissue samples were fixed in 10% formalin and processed for paraffin embedding. The sectioned slices were deparaffined in xylene and rehydrated in graded alcohol, and placed in Tris-buffered saline (TBS) for 15 min. After antigen retrieval and inactivation of endogenous peroxidase, the sections were blocked with animal non-immune serum (Maxvision) and incubated with the goat anti-human B7-H3 primary antibody MAB1027 or 8H9 overnight at 4°C, respectively. After incubated with the corresponding secondary antibodies (Maxvision) for 15 min, the sections were stained by using the detection kit (Maxvision). Cell nucleus was stained with hematoxylin (Sigma). Finally, all sections were dehydrated with absolute ethanol. The pictures of samples were captured by the Olympus TH4-200 microscope.

## Generation of Anti-B7-H3 CAR-Expressing NK-92MI Cells

The anti-B7-H3 CAR is comprised of an immunoglobulin heavy chain signal peptide (SP), an anti-B7-H3 scFv derived from 8H9 antibody, followed by the CD8 transmembrane (TM) region, the intracellular domains of 4-1BB and CD3ζ. The codon-optimized genes were synthesized by BGI and ligated into the lentiviral expression vector, pLVX-EF1-IRES-ZsGreen, to generate a pLVX-8H9-BBζ construct. To produce the lentiviral CAR particles, 95% confluent HEK293T cells were transfected with the pLVX-8H9-BBζ plasmid together with the packaging plasmids, psPAX2 and pMD2.G. The lentiviral supernatants were collected at 72 h post the transfection and filtrated through a 0.45 µm filter (Millipore), followed by centrifugation for 2 h at 28,000 rpm. For titer calculation, HEK293T cells (5×10<sup>5</sup> per well) were seeded into 12-well plate and cultured to reach 80% confluence. The different dilutions of lentiviruses were mixed with polybrene at 5 µg/ml in 1 ml fresh medium. The

culture medium in the wells were replaced by the mixture of lentiviruses and incubated for 2 d. After harvested, the infection percentages of HEK293T cells were counted based on ZsGreen detection by the Accuri™ C6 Flow Cytometer. FlowJo was used to analyze the data. The positive ratio of each well was recorded. The titer can be calculated from cell counting using the following formula:

$$\text{titer}(TU/ml) = \frac{\text{Total cell number} \times \text{positive rate}}{\text{added Volume of lentivirus}(\mu l)} \times 1,000. \quad (1)$$

NK-92MI cells were adjusted to 1×10<sup>5</sup> cells/ml and transduced with the concentrated lentiviral particles at a multiplicity of infection (MOI) of ~5 in the presence of 8 µg/ml polybrene, followed by incubation at 37°C and 5% CO<sub>2</sub>. Transduced cells were expanded and the ZsGreen-positive CAR-expressing NK-92MI cells were further enriched by flow cytometric cell sorting with a FACSaria II cell sorter (BD Biosciences).

## Quantitative Real-Time PCR

Quantitative real-time PCR (qPCR) was performed to evaluate the mRNA expression of B7-H3-specific CAR in the CAR-NK-92MI cells. Total RNA samples were collected using TRIzol reagent (Thermo Fisher Scientific) from CAR-NK-92MI and NK-92MI cells, respectively. Samples were then reverse-transcribed into cDNA with iScript™ cDNA Synthesis Kit (Bio-Rad). GAPDH was used as the internal reference. The PCR was performed with 1 cycle at 94°C for 1 min followed by 45 cycles at 95°C for 30 s, at 59°C for 30 s, and at 72°C for 30 s, in total volumes of 20 µl with all reactions run in duplicate. The primer pairs were B7-H3-specific CAR-F: 5'-GGAAGCACCCAGTACAACGA-3', B7-H3-specific CAR-R: 5'-CCCCAATAGGCGAACCAAGT-3'; GAPDH-F: 5'-TGACTTCA ACAGCGACACCCA-3', GAPDH-R: 5'-CACCTGTGTGCTGTAGCCA A A-3'.

## Cytotoxicity Assay

Cytotoxicity of CAR-NK-92MI cells toward various target cell lines at the different effector to target (E/T) ratios was evaluated using the Calcein-AM efflux assay as described previously with some modifications (Neri et al., 2001). Briefly, A549, HCC827, NCI-H23, DLD-1, HCT-116, MDA-MB-231, and Daudi cells (5,000 cells per well in a 96-well plate) were used as target cells which were labeled with 10 µmol/L Calcein-AM (Invitrogen) for 30 min at 37°C, followed by cocultured with effector cells of amount at different E/T ratios of 10:1, 5:1, and 1:1 in total volume of 200 µl for 2 h at 37°C, respectively. Target tumor cells in the absence of ZsGreen-positive CAR-expressing NK-92MI cells were used for detection of spontaneous release. Target cells added with lysis buffer were used for detection of max lysis. After 2 h, cells were centrifuged and supernatants of cell mixture were harvested for detection. The reading values of fluorescence intensity (FI) in the supernatants were measured at excitation 495 nm and emission 515 nm using a PerkinElmer Victor X3 Microplate Reader (Perkin Elmer). The specific lysis ratios were calculated by the formula:

lysis ratio (%)

$$= \frac{\text{FI (sample wells)} - \text{FI (spontaneous release)}}{\text{FI (max release)} - \text{FI (spontaneous release)}} \times 100\%. \quad (2)$$

## Degranulation and Granule Secretion Analysis

To analyze degranulation of effector cells, the cell-surface expression of CD107a and the secretion of cytotoxic granules by effector cells were analyzed by the Accuri™ C6 Flow Cytometer. Briefly, CAR-NK-92MI or NK-92MI cells were cocultured with target cells at an E/T ratio of 1:1. Monensin (Sigma-Aldrich) was added 4 h prior to 24 h with a final concentration of 2 μmol/L. After 24 h, cells were harvested and washed with PBS supplemented with 3% FBS, followed by labeled with PE-conjugated anti-CD107a antibody (Biolegend). Meanwhile, after the effector cells were cocultured with the target cells at an E/T ratio of 1:1 for 24 h, perforin and granzyme B were determined by fixed/permeabilized with Cytofix/Cytoperm solution (Beyotime), followed by stained with PE-conjugated anti-human perforin (Biolegend) and granzyme B (Biolegend) antibodies for 30 min at 4°C, respectively. The cells were analyzed by flow cytometry and all data were analyzed with FlowJo software.

## In Vivo Tumor Growth Studies

All animal experiments were in accordance with the ethical standards approved by the University of Macau (UMARE-018-2017). NOD/SCID mice (6–7 weeks old) were provided by the animal research core of University of Macau. The A549 xenografts were established by injecting subcutaneously at the right flank of mice with 210<sup>6</sup> cells. Tumor cell engraftments were monitored by caliper measurements. At 10 d post subcutaneous inoculation, tumor-bearing mice received treatments with 5×10<sup>6</sup> of CAR-NK-92MI cells, unmodified NK-92MI cells, and PBS weekly for 4 weeks, respectively. The tumor volumes were measured and calculated according to the formula:

$$\text{tumor volume} = \frac{\text{width}^2 \times \text{length}}{2}. \quad (3)$$

## Statistical Analysis

Statistics was analyzed using the GraphPad Prism software. Data are obtained from duplicate or triplicate samples in 2–3 individual experiments. Significant differences were calculated by two ways ANOVA, t tests, nonparametric Mann-Whitney test, or log-rank test. The values of \**p* < 0.05, \*\**p* < 0.01, and \*\*\**p* < 0.001 were set as the standard for statistical significance levels.

## RESULTS

### Expression of B7-H3 in Human Cancer Tissues and Cell Lines

We firstly assessed the expression of B7-H3 in different cancer cell lines with the anti-B7-H3 IgG 8H9 using flow cytometric

analysis and immunoprecipitation assay. Flow cytometric analyses (**Figure 1A**) demonstrated that B7-H3 was highly expressed on the cell surface of several cancer cell lines, A549, NCI-H23, HCC827, DLD-1, HCT-116, and MDA-MB-231, except the B7-H3-negative cell line (Daudi). Western blot analysis (**Figure 1B**) further confirmed that the 4Ig-B7-H3 protein with ~100 kDa was immunoprecipitated from whole cell lysates of A549 and NCI-H23 but not Daudi by the 8H9 antibody. As shown in **Figure 1C**, immunohistochemistry results showed that both the 8H9 antibody and the commercial anti-B7-H3 antibody (MAB1027) detected B7-H3 in the human NSCLC tissues. No positive staining was detected in the normal lung tissues. Above data suggest that B7-H3 is highly expressed in human solid tumor cell lines and tissues. The 8H9 antibody exhibited the strong reactivity toward B7-H3 without cross-reactivity to normal lung tissues. The antibody 8H9 was thus chosen for the CAR construction.

### Generation of NK-92MI Cells Carrying the Anti-B7-H3 CAR

The anti-B7-H3 scFv was generated by linking heavy and light chain variable domains of the anti-B7-H3 antibody 8H9 *via* a (G4S)<sub>3</sub> linker as previously described (Ahmed et al., 2015). The anti-B7-H3 CAR construct was designed to contain the anti-B7-H3 scFv, the CD8 TM region, the 4-1BB, and CD3ζ intracellular domains (**Figure 2A**). The CAR DNA sequence was inserted into the pLVX lentiviral vector with the co-expression of ZsGreen (**Figure 2B**). The lentiviral particles were subsequently produced and used for transduction of human NK-92MI cells. As shown in **Figure 2C**, transduction efficiency was 24.9%. After several rounds of cell sorting, the percentage of CAR-expressing NK-92MI cells exceeded 95%. Expression of the anti-B7-H3-CAR was examined by qPCR. As shown in **Figure 2D**, the CAR was highly expressed in the transduced CAR-NK-92MI cells compared to untransduced NK-92MI cells.

### Enhanced Cytotoxicity of CAR-NK-92MI Cells Against B7-H3-Positive Tumor Cell Lines

To determine whether B7-H3 recognition could improve the cytotoxicity of NK-92MI cells, we compared CAR-NK-92MI cells and unmodified NK-92MI cells in response to a panel of human cancer cell lines by a Calcein-AM assay. As shown in **Figure 3**, the cytotoxicity abilities of CAR-NK-92MI cells was significantly enhanced at all E/T ratios compared with unmodified NK-92MI cells. However, toward MDA-MB-231, there was no significant difference between the effectiveness of CAR-NK-92MI and unmodified NK-92MI cells at low E/T ratio of 1: 1. B7-H3-negative Daudi cells were not lysed by any of the NK-92 derivatives. When these cell lines were examined, unmodified NK-92MI cells had moderate killing against HCC827 and MDA-MB-231 cell lines at high E/T ratio, which are however lysed by CAR-NK-92MI cells with statistically significant differences. These cell lines are intrinsically sensitive to NK cells, which is consistent with other reports (Dominguez et al., 2016; Shenouda et al., 2017). Taken together, these



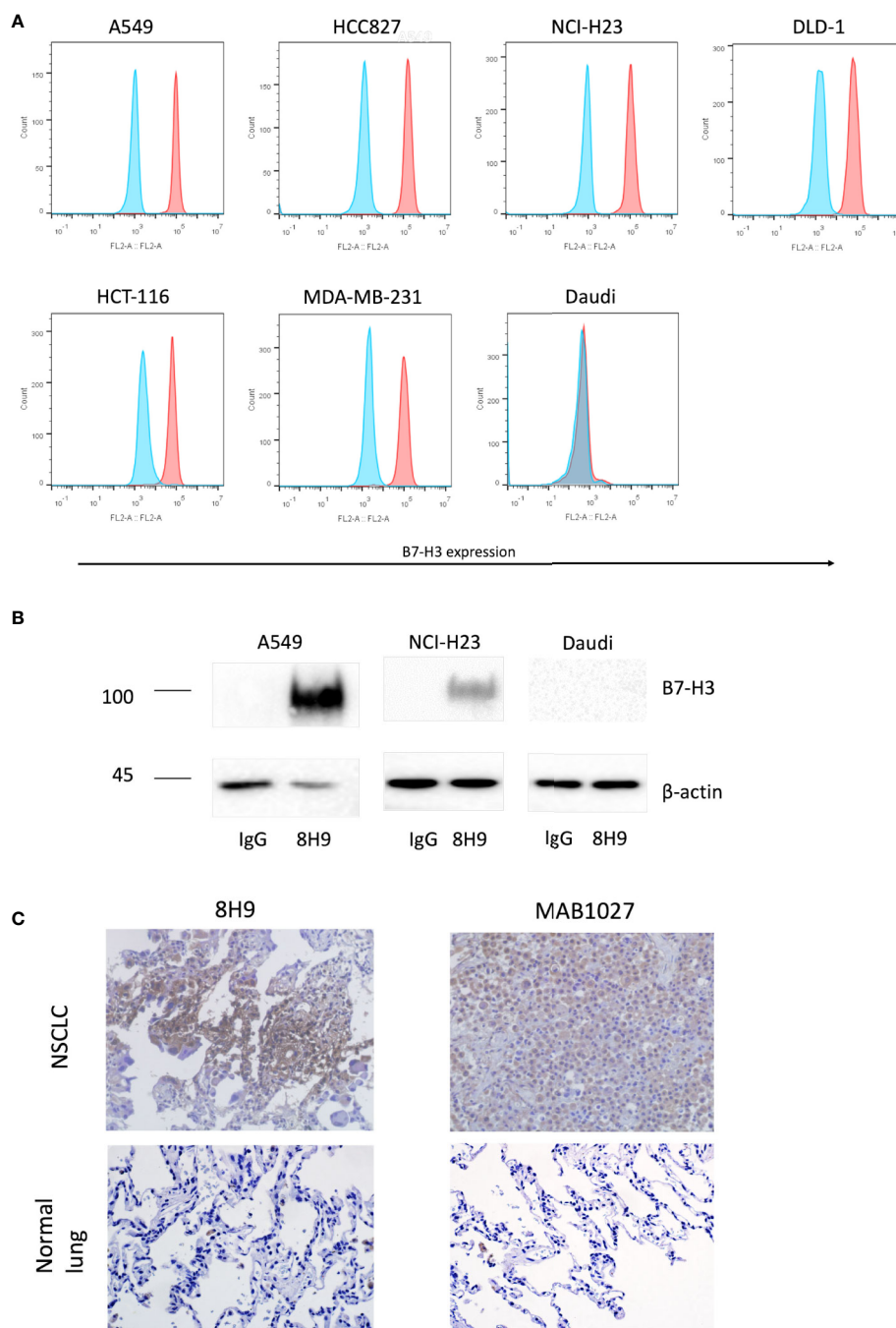


**FIGURE 1 |** Expression of B7-H3 on tumor cell lines and primary human tissues. **(A)** Flow cytometric analysis of B7-H3 expression on the surface of different target cell lines was detected with the anti-B7-H3 8H9 IgG. Red color represents 8H9 IgG staining. Blue color represents control IgG staining. **(B)** Immunoprecipitation of B7-H3 in A549, NCI-H23, and Daudi cell lines. The cell lysates were immunoprecipitated by the 8H9 IgG or control IgG, followed by western blot using the anti-B7-H3 antibody, MAB1027.  $\beta$ -actin levels were utilized as the loading control. **(C)** Immunohistochemistry (IHC) of human NSCLC tissues and normal lung tissues. Tumor tissue sections were stained with the anti-B7-H3 8H9 IgG or the anti-B7-H3 antibody MAB1027. Images were taken under  $\times 400$  magnification.

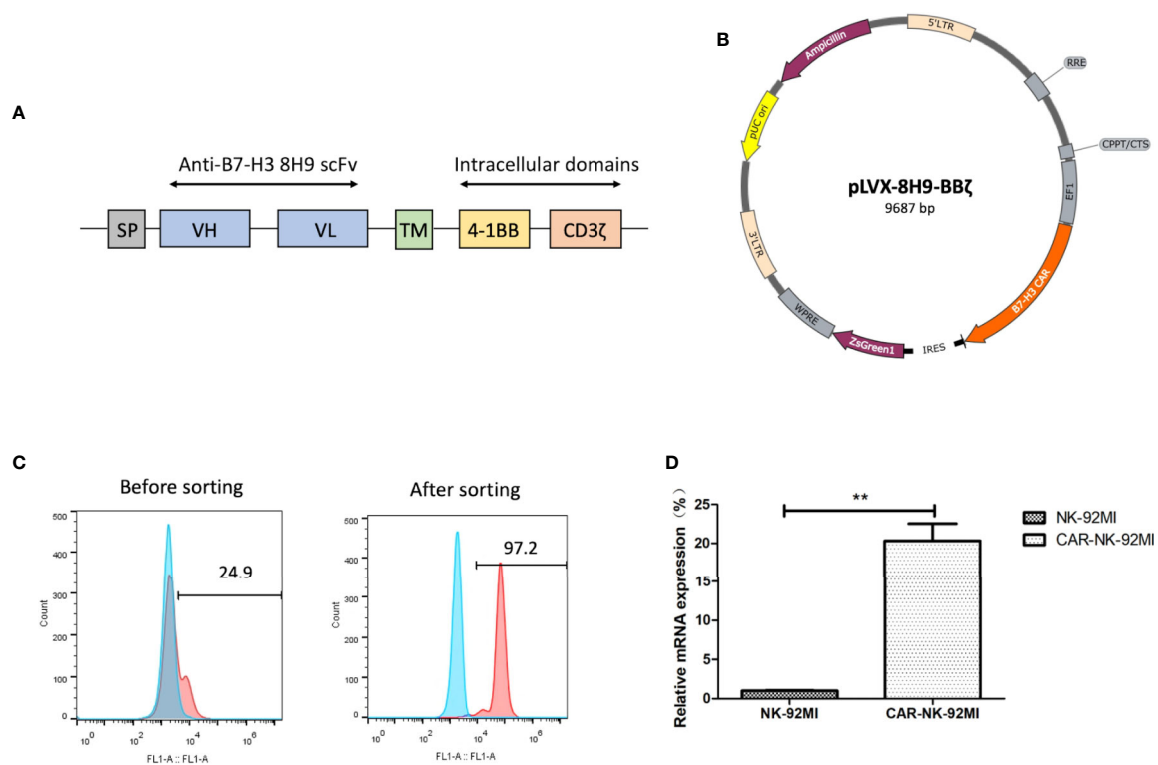


**FIGURE 2 |** Generation of B7-H3-specific CAR-NK-92MI cells. **(A)** Schematic representation of the lentiviral vector loaded with B7-H3-specific CAR. The B7-H3-specific CAR encodes an immunoglobulin heavy chain signal peptide (SP), the anti-B7-H3 scFv derived from 8H9 antibody, followed by the CD8 transmembrane (TM) region, the 4-1BB domain, and the CD3ζ chain. **(B)** Diagram of the B7-H3-CAR lentiviral vector containing the major functional elements. **(C)** Flow cytometric analysis of CAR expression on the surface of transduced NK-92MI cells before and after cell sorting. CAR-NK-92MI cells were sorted by GFP with unmodified NK-92MI cells set as the control. **(D)** Expression of the B7-H3 CAR in NK-92MI cells by qPCR analysis. Primers anchoring in the region of 8H9 scFv were designed to measure relative mRNA expression level in CAR-NK-92MI cells compared to NK-92MI cells. \*\* $p < 0.01$ .

results\_ indicated that the B7-H3 CAR-NK-92MI was cytotoxic specifically against B7-H3-positive tumor cells.

## Elevated Activation of CAR-NK-92MI Cells in Response to B7-H3-Positive Target Cells

A hallmark of NK cell activation is degranulation in which lytic granule contents (perforin and granzymes) are released onto the surface of the target cells. CD107a, granzyme B, and perforin are three major markers in degranulation. To further analyze degranulation of CAR-NK-92MI cells, we examined the expression of CD107a and the secretion of perforin/granzyme B by flow cytometry. CAR-NK-92MI cells were incubated with A549 and NCI-H23 cells at E/T ratio of 1:1 for 24 h, respectively. The significant differences were observed in the CD107a expression on surface of CAR-NK-92MI cells compared to unmodified NK-92MI ( $p < 0.05$ ) (**Figure 4A**). In addition, the B7-H3 CAR strengthened expression of perforin/granzyme B in degranulation of NK-92MI cells. The levels of granzyme B and perforin were significantly elevated in CAR-NK-92MI cells in response to the target cell lines ( $p < 0.05$ ) (**Figures 4B, C**). Although A549 cells express much higher B7-H3 than NCI-

H23 cells, the level of CD107a in A549 seems to be lower than that of NCI-H23, implying cytolytic granule polarization and degranulation are not determined by B7-H3 density above a threshold. We assume that the different receptors control degranulation in the two cell lines. Therefore, the results suggested that degranulation activation played an important role in cytotoxicity of CAR-NK-92MI cells.

## Therapeutic Efficacy of CAR-NK-92MI Cells in NSCLC Xenografts

To assess *in vivo* anti-tumor activity, the subcutaneous model of A549 cells was established. Ten days after the implantation, three groups of A549-xenografted mice received intravenous injections of CAR-NK-92MI cells ( $5 \times 10^6$ /dose), unmodified NK-92MI cells ( $5 \times 10^6$ /dose), and PBS at day 10, 17, 24, and 31, respectively (**Figure 5A**). As shown in **Figure 5B**, the group of CAR-NK-92MI reduced tumor volume by 52.1% and 63.8% at the end of the experiment compared with the NK-92MI group ( $p = 0.002$ ) and the PBS group ( $p = 0.001$ ), respectively. The survival time in the CAR-NK-92MI treated group was significantly longer than the PBS group ( $p < 0.01$ ) and the NK-92MI group ( $p < 0.05$ ) (**Figure 5C**). Therefore, CAR-NK-92MI

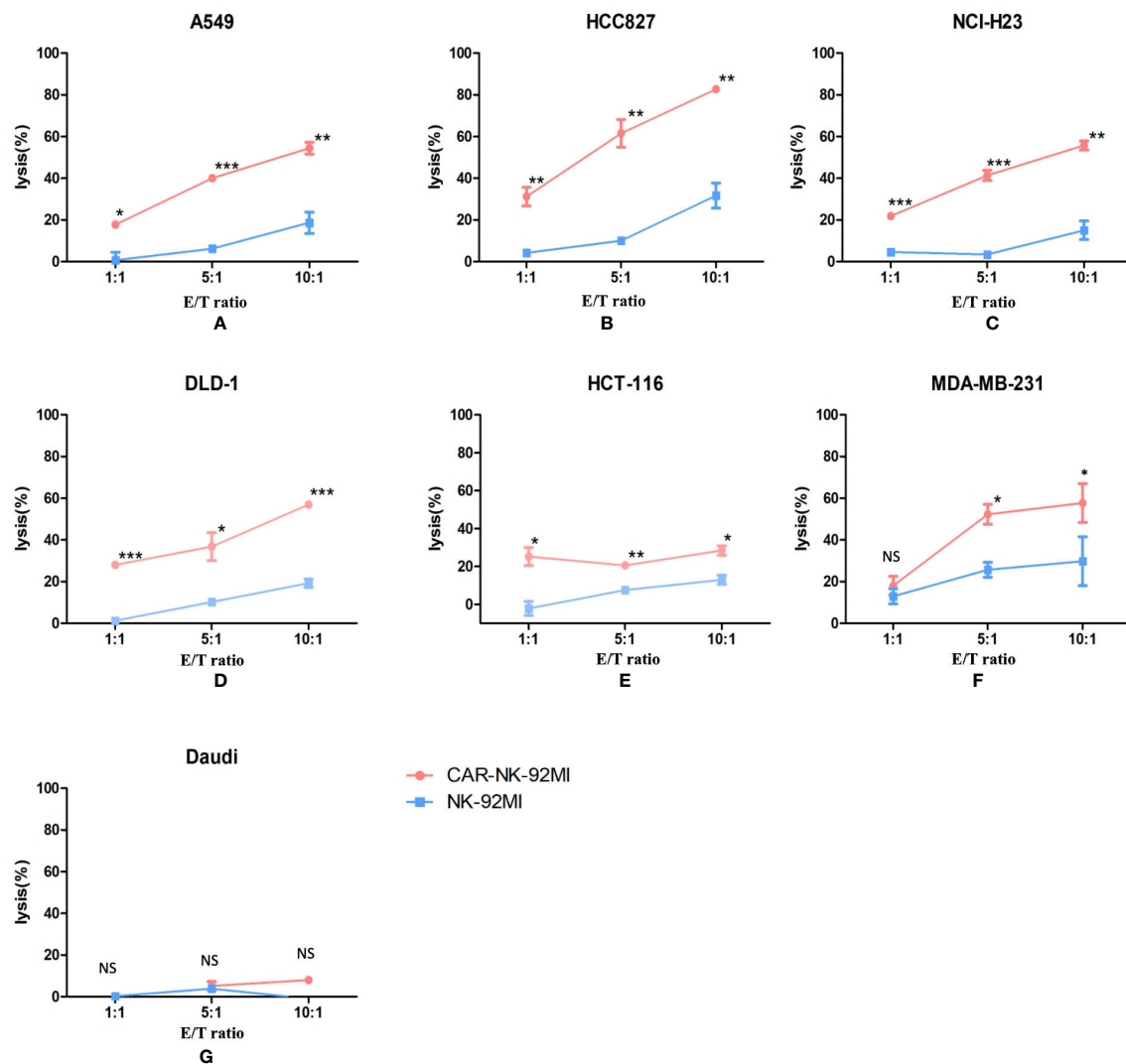


**FIGURE 3 |** Cytotoxicity assay of B7-H3 CAR-NK-92MI cells toward a panel of tumor cell lines *in vitro*. Significant killing was observed in B7-H3-positive cell lines A549, HCC827, NCI-H23, DLD-1, HCT-116, and MDA-MB-231 but not in B7-H3-negative cell line Daudi. The effector cells were co-cultured with target cells for 2 h at different E/T ratios as indicated. Data represent one representative experiment from three individual experiments. \*\*  $p < 0.001$ ; \* $p < 0.01$ ; \* $p < 0.05$ .

cells effectively inhibited tumor growth and prolonged the survival of the tumor-bearing mice.

## DISCUSSION

NK cells are important innate immune effectors in the control of malignancies. Their activation is regulated by the interaction with suppressive and stimulatory receptors (Kwon et al., 2017). B7-H3 plays an inhibitory role in the regulation of NK cells. Recent studies have shown that inhibition of B7-H3 augments tumor eradication by enhancing function of cytotoxic lymphocytes (Lee et al., 2017). Our previous studies demonstrated that the anti-B7-H3 antibody 8H9 inhibited B7-H3-positive tumor cells through the antibody-dependent cell-mediated cytotoxicity (ADCC)

function (Ahmed et al., 2015). ADCC is a mechanism of cell-mediated immune defense through the antibody Fc region (Ochoa et al., 2017). NK cells are key components in the ADCC function of the antibody Fc (Seidel et al., 2013).

Recent studies have shown that the CAR mediates stronger NK cell response than the antibody Fc (Boissel et al., 2013). In this study, we constructed the second-generation CAR consisting of 4-1BB costimulatory signal domain and a CD3 $\zeta$  domain, which is similar to the clinically used anti-CD19 CAR-T cells (Li S. et al., 2018). Our results confirmed that the anti-B7-H3 CAR directly triggered the intrinsic cytolytic function of NK cells through the signals from 4-1BB and CD3 $\zeta$  chain. The *in vitro* cytotoxicity assays demonstrated that CAR-NK-92MI cells specially killed tumor cell lines depending on B7-H3 recognition. In addition, CAR-NK-92MI cells significantly

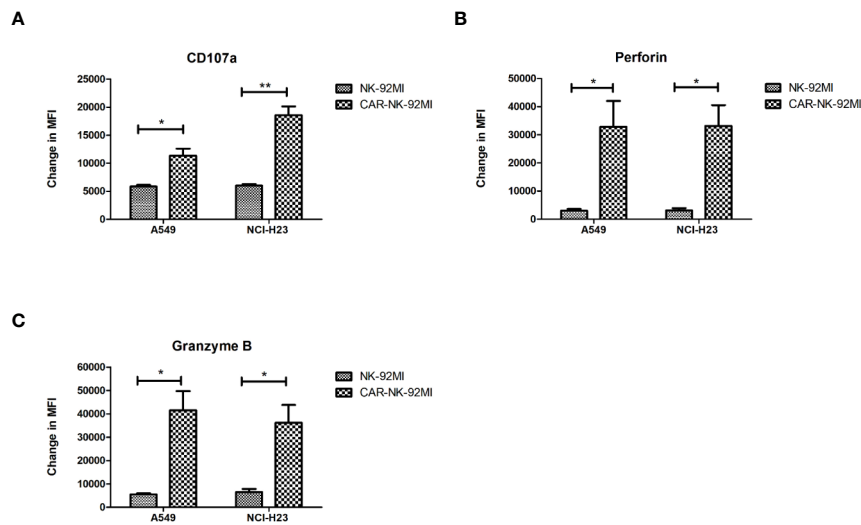


**FIGURE 4 |** Degranulation and granule secretion of B7-H3 CAR-NK-92MI cells. **(A)** Surface expression of CD107a, as measured by mean fluorescence intensity (MFI), detected in CAR-NK-92MI cells compared to NK-92MI cells in response to A549 or NCI-H23 cells. **(B, C)** Secretion of perforin and granzyme B from CAR-NK-92MI cells compared to NK-92MI cells using flow cytometric analysis. Data are presented as mean  $\pm$  SEM of triplicate samples. \*\* $p < 0.01$ ; \* $p < 0.05$ .

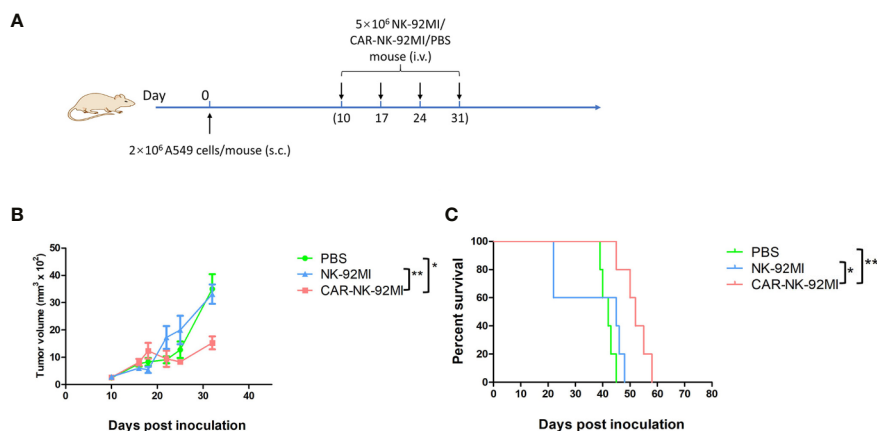


**FIGURE 5 |** Therapy of NSCLC xenografts with B7-H3 CAR-NK-92MI cells. **(A)** Treatment procedures of NOD/SCID mice inoculated subcutaneously with A549 cells. **(B)** Tumor growth in NOD/SCID mice with treatments of CAR-NK-92MI cells compared to NK-92MI cells (\*\* $p < 0.01$ ) and PBS (\*\* $p = 0.001$ ). **(C)** Survival of mice by Kaplan-Meier survival analysis for CAR-NK-92MI cells compared to NK-92MI cells (\* $p < 0.05$ ) and PBS (\*\* $p < 0.01$ ).  $n = 5$  each group.

enhanced cytotoxic ability against all B7-H3-positive cell lines. The redirection of anti-B7-H3 CAR further strengthened NK activation and degranulation. As an important process of NK cell activation, degranulation is triggered to release lytic granule molecules and subsequently induce apoptosis of targeted cells. The secretion of granules, such as granzyme B and perforin, is a significant indicator of immune activation for cytotoxic lymphocytes (Mellor-Heineke et al., 2013). In response to B7-H3-positive target cells, the perforin-granzyme pathway was activated. Surface CD107a is a marker of degranulation in NK cells (Cohnen et al., 2013). Besides perforin/granzyme B, we observed that CD107a expression is highly elevated in CAR-NK-92MI cells. Moreover, in NSCLC xenografts, CAR-NK-92MI

cells exhibited effectively anti-tumor ability and prolonged the survival of the tumor-bearing mice.

Anti-CD19 CAR-T cell therapy shows promising therapeutic activity in hematological malignancies. However, the resistances limit the application of CAR-T therapy in solid tumor due to some mechanisms. Likewise, the solo treatment of the B7-H3 CAR incompletely prevents tumor growth in xenografts of NSCLC and colon cancer (Huang et al., 2020). Although the mechanisms have not been completely elucidated, other immune checkpoint pathways, such as PD-1/PD-L1, may be involved in the activation of anti-B7-H3 CAR-T cells. Although CAR-NK-92MI cells lack the long-term persistence, multiple administrations of CAR-NK-92MI cells can overcome this disadvantage. Because irradiated NK-92MI

cells are necessary for patient infusion to ensure safety, we need to further investigate the effects of irradiation on intrinsic features of CAR-NK-92MI cells before they can be applied in clinical trials.

## CONCLUSION

Taken together, B7-H3 may serve as a target for NSCLC therapy. Anti-B7-H3 CAR-NK-92MI cells showed significant treatment efficacy both *in vitro* and *in vivo*. Our studies support the development of CAR-modified NK-92 as an option for adoptive cancer immunotherapy.

## DATA AVAILABILITY STATEMENT

The datasets generated for this study are available on request to the corresponding authors.

## ETHICS STATEMENT

The studies involving human participants were reviewed and approved by human ethics committee, the Guangzhou Medical University. The animal study was reviewed and approved by Animal Ethics Committee, University of Macau.

## REFERENCES

- Ahmed, M., Cheng, M., Zhao, Q., Goldgur, Y., Cheal, S. M., Guo, H. F., et al. (2015). Humanized Affinity-matured Monoclonal Antibody 8H9 Has Potent Antitumor Activity and Binds to FG Loop of Tumor Antigen B7-H3. *J. Biol. Chem.* 290 (50), 30018–30029. doi: 10.1074/jbc.M115.679852
- Boissel, L., Betancur-Boissel, M., Lu, W., Krause, D. S., Van Etten, R. A., Wels, W. S., et al. (2013). Retargeting NK-92 cells by means of CD19- and CD20-specific chimeric antigen receptors compares favorably with antibody-dependent cellular cytotoxicity. *Oncoimmunology* 2 (10), e26527. doi: 10.4161/onci.26527
- Brunner, A., Hinterholzer, S., Riss, P., Heinze, G., and Brustmann, H. (2012). Immunorepression of B7-H3 in endometrial cancer: relation to tumor T-cell infiltration and prognosis. *Gynecol. Oncol.* 124 (1), 105–111. doi: 10.1016/j.ygyno.2011.09.012
- Castellanos, J. R., Purvis, I. J., Labak, C. M., Guda, M. R., Tsung, A. J., Velpula, K. K., et al. (2017). B7-H3 role in the immune landscape of cancer. *Am. J. Clin. Exp. Immunol.* 6 (4), 66–75.
- Cohnen, A., Chiang, S. C., Stojanovic, A., Schmidt, H., Claus, M., Saftig, P., et al. (2013). Surface CD107a/LAMP-1 protects natural killer cells from degranulation-associated damage. *Blood* 122 (8), 1411–1418. doi: 10.1182/blood-2012-07-441832
- Dominguez, C., Tsang, K. Y., and Palena, C. (2016). Short-term EGFR blockade enhances immune-mediated cytotoxicity of EGFR mutant lung cancer cells: rationale for combination therapies. *Cell Death Dis.* 7 (9), e2380. doi: 10.1038/cddis.2016.297
- Du, H., Hirabayashi, K., Ahn, S., Kren, N. P., Montgomery, S. A., Wang, X., et al. (2019). Antitumor Responses in the Absence of Toxicity in Solid Tumors by Targeting B7-H3 via Chimeric Antigen Receptor T Cells. *Cancer Cell* 35 (2), 221–237 e228. doi: 10.1016/j.ccell.2019.01.002
- Flem-Karlsen, K., Fodstad, Y., and Nunes-Xavier, C. E. (2020). B7-H3 immune checkpoint protein in human cancer. *Curr. Med. Chem.* 27 (24), 4062–4086. doi: 10.2174/0929867326666190517115515

## AUTHOR CONTRIBUTIONS

SY conceived and executed experiments and co-wrote the manuscript. BC and LW conceived and executed IHC assays. GZ executed experiments related to antibody expression and purification. HK assisted cytotoxicity assays. LZhu and LZha assisted flow cytometric analysis. ZZ supervised part of the investigation. QZ supervised all aspects of the investigation and co-wrote the manuscript.

## FUNDING

This study was supported by the National Key R&D Program of China (2019YFA0904400), the Science and Technology Development Fund of Macau (File no. FDCT/131/2016/A3, FDCT/0015/2018/A1, FDCT/0055/2019/A1), and the intramural research program of Faculty of Health Sciences, University of Macau (File no. MYRG2019-00069-FHS).

## ACKNOWLEDGMENTS

The authors would like to appreciate the assistance of Dr. Nainkong V. Cheung (Memorial Sloan-Kettering Cancer Center) for the 8H9 antibody.

- Forde, P. M., Chaft, J. E., and Pardoll, D. M. (2018). Neoadjuvant PD-1 Blockade in Resectable Lung Cancer. *N. Engl. J. Med.* 379 (9), e14. doi: 10.1056/NEJMc1808251
- Gong, J. H., Maki, G., and Klingemann, H. G. (1994). Characterization of a human cell line (NK-92) with phenotypical and functional characteristics of activated natural killer cells. *Leukemia* 8 (4), 652–658.
- Hofmeyer, K. A., Ray, A., and Zang, X. (2008). The contrasting role of B7-H3. *Proc. Natl. Acad. Sci. U. S. A.* 105 (30), 10277–10278. doi: 10.1073/pnas.0805458105
- Huang, B., Luo, L., Wang, J., He, B., Feng, R., Xian, N., et al. (2020). B7-H3 specific T cells with chimeric antigen receptor and decoy PD-1 receptors eradicate established solid human tumors in mouse models. *Oncoimmunology* 9 (1), 1684127. doi: 10.1080/2162402X.2019.1684127
- Klingemann, H., Boissel, L., and Toneguzzo, F. (2016). Natural Killer Cells for Immunotherapy - Advantages of the NK-92 Cell Line over Blood NK Cells. *Front. Immunol.* 7:91. doi: 10.3389/fimmu.2016.00091
- Kraan, J., van den Broek, P., Verhoef, C., Grunhagen, D. J., Taal, W., Gratama, J. W., et al. (2014). Endothelial CD276 (B7-H3) expression is increased in human malignancies and distinguishes between normal and tumour-derived circulating endothelial cells. *Br. J. Cancer* 111 (1), 149–156. doi: 10.1038/bjc.2014.286
- Kramer, K., Kushner, B. H., Modak, S., Pandit-Taskar, N., Smith-Jones, P., Zanzonico, P., et al. (2010). Compartmental intrathecal radioimmunotherapy: results for treatment for metastatic CNS neuroblastoma. *J. Neurooncol.* 97 (3), 409–418. doi: 10.1007/s11060-009-0038-7
- Kwon, H. J., Kim, N., and Kim, H. S. (2017). Molecular checkpoints controlling natural killer cell activation and their modulation for cancer immunotherapy. *Exp. Mol. Med.* 49 (3), e311. doi: 10.1038/emm.2017.42
- Lee, Y. H., Martin-Orozco, N., Zheng, P., Li, J., Zhang, P., Tan, H., et al. (2017). Inhibition of the B7-H3 immune checkpoint limits tumor growth by enhancing cytotoxic lymphocyte function. *Cell Res.* 27 (8), 1034–1045. doi: 10.1038/cr.2017.90



- Li, D. Z., Han, B. N., Wei, R., Yao, G. Y., Chen, Z., Liu, J., et al. (2018). N-terminal alpha-amino group modification of antibodies using a site-selective click chemistry method. *MAbs* 10 (5), 712–719. doi: 10.1080/19420862.2018.1463122
- Li, S., Zhang, J., Wang, M., Fu, G., Li, Y., Pei, L., et al. (2018). Treatment of acute lymphoblastic leukaemia with the second generation of CD19 CAR-T containing either CD28 or 4-1BB. *Br. J. Haematol.* 181 (3), 360–371. doi: 10.1111/bjh.15195
- Liu, J., Zhou, G., Zhang, L., and Zhao, Q. (2019). Building Potent Chimeric Antigen Receptor T Cells With CRISPR Genome Editing. *Front. Immunol.* 10:456. doi: 10.3389/fimmu.2019.00456
- Lorenzo-Herrero, S., Lopez-Soto, A., Sordo-Bahamonde, C., Gonzalez-Rodriguez, A. P., Vitale, M., and Gonzalez, S. (2018). NK Cell-Based Immunotherapy in Cancer Metastasis. *Cancers (Basel)* 11 (1), 29. doi: 10.3390/cancers11010029
- Ma, S., Li, X., Wang, X., Cheng, L., Li, Z., Zhang, C., et al. (2019). Current Progress in CAR-T Cell Therapy for Solid Tumors. *Int. J. Biol. Sci.* 15 (12), 2548–2560. doi: 10.7150/ijbs.34213
- Majzner, R. G., Theruvath, J. L., Nellan, A., Heitzeneder, S., Cui, Y., Mount, C. W., et al. (2019). CAR T Cells Targeting B7-H3, a Pan-Cancer Antigen, Demonstrate Potent Preclinical Activity Against Pediatric Solid Tumors and Brain Tumors. *Clin. Cancer Res.* 25 (8), 2560–2574. doi: 10.1158/1078-0432.CCR-18-0432
- Mellor-Heineke, S., Villanueva, J., Jordan, M. B., Marsh, R., Zhang, K., Bleising, J. J., et al. (2013). Elevated Granzyme B in Cytotoxic Lymphocytes is a Signature of Immune Activation in Hemophagocytic Lymphohistiocytosis. *Front. Immunol.* 4:72. doi: 10.3389/fimmu.2013.00072
- Nehama, D., Di Ianni, N., Musio, S., Du, H., Patane, M., Pollo, B., et al. (2019). B7-H3-redirected chimeric antigen receptor T cells target glioblastoma and neurospheres. *EBioMedicine* 47, 33–43. doi: 10.1016/j.ebiom.2019.08.030
- Neri, S., Mariani, E., Meneghetti, A., Cattini, L., and Facchini, A. (2001). Calcein-acetyoxymethyl cytotoxicity assay: standardization of a method allowing additional analyses on recovered effector cells and supernatants. *Clin. Diagn. Lab. Immunol.* 8 (6), 1131–1135. doi: 10.1128/CDLI.8.6.1131-1135.2001
- Ochoa, M. C., Minute, L., Rodriguez, I., Garasa, S., Perez-Ruiz, E., Inoges, S., et al. (2017). Antibody-dependent cell cytotoxicity: immunotherapy strategies enhancing effector NK cells. *Immunol. Cell Biol.* 95 (4), 347–355. doi: 10.1038/icb.2017.6
- Oser, M. G., Niederst, M. J., Sequist, L. V., and Engelman, J. A. (2015). Transformation from non-small-cell lung cancer to small-cell lung cancer: molecular drivers and cells of origin. *Lancet Oncol.* 16 (4), e165–e172. doi: 10.1016/S1470-2045(14)71180-5
- Picarda, E., Ohaegbulam, K. C., and Zang, X. (2016). Molecular Pathways: Targeting B7-H3 (CD276) for Human Cancer Immunotherapy. *Clin. Cancer Res.* 22 (14), 3425–3431. doi: 10.1158/1078-0432.CCR-15-2428
- Riihimäki, M., Hemminki, A., Fallah, M., Thomsen, H., Sundquist, K., Sundquist, J., et al. (2014). Metastatic sites and survival in lung cancer. *Lung Cancer* 86 (1), 78–84. doi: 10.1016/j.lungcan.2014.07.020
- Seaman, S., Zhu, Z. Y., Saha, S., Zhang, X. M., Yang, M. Y., Hilton, M. B., et al. (2017). Eradication of Tumors through Simultaneous Ablation of CD276/B7-H3-Positive Tumor Cells and Tumor Vasculature. *Cancer Cell* 31 (4), 501–50+. doi: 10.1016/j.ccell.2017.03.005
- Seidel, U. J., Schlegel, P., and Lang, P. (2013). Natural killer cell mediated antibody-dependent cellular cytotoxicity in tumor immunotherapy with therapeutic antibodies. *Front. Immunol.* 4:76. doi: 10.3389/fimmu.2013.00076
- Shenouda, M. M., Gillgrass, A., Nham, T., Hogg, R., Lee, A. J., Chew, M. V., et al. (2017). Ex vivo expanded natural killer cells from breast cancer patients and healthy donors are highly cytotoxic against breast cancer cell lines and patient-derived tumours. *Breast Cancer Res.* 19 (1), 76. doi: 10.1186/s13058-017-0867-9
- Sun, Y., Wang, Y., Zhao, J., Gu, M., Giscombe, R., Lefvert, A. K., et al. (2006). B7-H3 and B7-H4 expression in non-small-cell lung cancer. *Lung Cancer* 53 (2), 143–151. doi: 10.1016/j.lungcan.2006.05.012
- Tam, Y. K., Maki, G., Miyagawa, B., Hennemann, B., Tonn, T., and Klingemann, H. G. (1999). Characterization of genetically altered, interleukin 2-independent natural killer cell lines suitable for adoptive cellular immunotherapy. *Hum. Gene Ther.* 10 (8), 1359–1373. doi: 10.1089/10430349950018030
- Tang, X., Zhao, S., Zhang, Y., Wang, Y., Zhang, Z., Yang, M., et al. (2019). B7-H3 as a Novel CAR-T Therapeutic Target for Glioblastoma. *Mol. Ther. Oncolytics* 14, 279–287. doi: 10.1016/j.omto.2019.07.002
- Waldhauer, I., and Steinle, A. (2008). NK cells and cancer immunosurveillance. *Oncogene* 27 (45), 5932–5943. doi: 10.1038/onc.2008.267
- Yang, S., Wei, W., and Zhao, Q. (2020). B7-H3, a checkpoint molecule, as a target for cancer immunotherapy. *Int. J. Biol. Sci.* 16 (11), 1767–1773. doi: 10.7150/ijbs.41105
- Zhang, C., Oberoi, P., Oelsner, S., Waldmann, A., Lindner, A., Tonn, T., et al. (2017). Chimeric Antigen Receptor-Engineered NK-92 Cells: An Off-the-Shelf Cellular Therapeutic for Targeted Elimination of Cancer Cells and Induction of Protective Antitumor Immunity. *Front. Immunol.* 8:533. doi: 10.3389/fimmu.2017.00533
- Zhang, Z., Jiang, C., Liu, Z., Yang, M., Tang, X., Wang, Y., et al. (2020). B7-H3-Targeted CAR-T Cells Exhibit Potent Antitumor Effects on Hematologic and Solid Tumors. *Mol. Ther. Oncolytics* 17, 180–189. doi: 10.1016/j.omto.2020.03.019
- Zhu, L., Liu, J., Zhou, G., Ng, H. M., Ang, I. L., Ma, G., et al. (2019). Targeting immune checkpoint B7-H3 antibody-chlorin e6 bioconjugates for spectroscopic photoacoustic imaging and photodynamic therapy. *Chem. Commun. (Camb)* 55 (95), 14255–14258. doi: 10.1039/c9cc06839b

**Conflict of Interest:** The authors declare that the research was conducted in the absence of any commercial or financial relationships that could be construed as a potential conflict of interest.

Copyright © 2020 Yang, Cao, Zhou, Zhu, Wang, Zhang, Kwok, Zhang and Zhao. This is an open-access article distributed under the terms of the Creative Commons Attribution License (CC BY). The use, distribution or reproduction in other forums is permitted, provided the original author(s) and the copyright owner(s) are credited and that the original publication in this journal is cited, in accordance with accepted academic practice. No use, distribution or reproduction is permitted which does not comply with these terms.



# Feasibility Study of a Modified XELOX Adjuvant Chemotherapy for High-Recurrence Risk Patients With Operated Stage III Colon Cancer

Jianhong Peng<sup>1†</sup>, Weihao Li<sup>1†</sup>, Wenhua Fan<sup>1</sup>, Wenhao Zhou<sup>1</sup>, Ying Zhu<sup>1</sup>, Xueying Li<sup>1</sup>, Zhizhong Pan<sup>1</sup>, Xiaoping Lin<sup>2\*</sup> and Junzhong Lin<sup>1\*</sup>

## OPEN ACCESS

### Edited by:

Yingyan Yu,

Shanghai Jiao Tong University, China

### Reviewed by:

Rui Zhang,

China Medical University, China

Xianwei Mo,

Guangxi Medical University Cancer

Hospital, China

Shisheng Tan,

Guizhou Provincial People's

Hospital, China

### \*Correspondence:

Junzhong Lin

linjzh@sysucc.org.cn

Xiaoping Lin

linxp@sysucc.org.cn

<sup>†</sup>These authors have contributed  
equally to this work

### Specialty section:

This article was submitted to  
Pharmacology of Anti-Cancer Drugs,  
a section of the journal  
Frontiers in Pharmacology

**Received:** 16 July 2020

**Accepted:** 04 September 2020

**Published:** 18 September 2020

### Citation:

Peng J, Li W, Fan W, Zhou W, Zhu Y,  
Li X, Pan Z, Lin X and Lin J (2020)  
Feasibility Study of a Modified XELOX  
Adjuvant Chemotherapy for High-  
Recurrence Risk Patients With  
Operated Stage III Colon Cancer.  
Front. Pharmacol. 11:583091.  
doi: 10.3389/fphar.2020.583091

<sup>1</sup> Department of Colorectal Surgery, Sun Yat-sen University Cancer Center, State Key Laboratory of Oncology in South China, Collaborative Innovation Center for Cancer Medicine, Guangzhou, China, <sup>2</sup> Department of Nuclear Medicine, Sun Yat-sen University Cancer Center, State Key Laboratory of Oncology in South China, Collaborative Innovation Center for Cancer Medicine, Guangzhou, China

**Background:** Our previous study reported the favorable efficacy and good tolerance associated with a modified XELOX adjuvant chemotherapy with eight cycles of capecitabine and six cycles of oxaliplatin for operated stage III colon cancer. The current study aimed to confirm the feasibility of modified XELOX chemotherapy for treating specific high-risk (T4, N2, or both) stage III colon cancer.

**Methods:** We selected 142 consecutive patients with high-risk stage III colon cancer who received colon tumor resection followed by modified XELOX or standard full-cycle XELOX chemotherapy from November 2007 to June 2016 at Sun Yat-sen University Cancer Center. Disease-free survival (DFS), overall survival (OS), and adverse events of patients treated with the two chemotherapy regimens were compared.

**Results:** Seventy-four (52.1%) patients received standard XELOX chemotherapy, and 68 (47.8%) received modified XELOX chemotherapy. Neurotoxicity was the most common adverse event in 99 (69.7%) patients. Grade 2–3 neurotoxicity, grade 2–4 thrombocytopenia and grade 3–4 leucopenia were the major severe adverse events related to the decision to treat patients with modified XELOX chemotherapy. After a median follow-up of 69 months, the modified XELOX group presented a comparable 5-year DFS rate (79.0 vs. 80.3%,  $P = 0.891$ ) and 5-year OS rate (93.8 vs. 87.8%,  $P = 0.446$ ) as those in the standard XELOX group. Univariate survival analysis indicated that poor tumor differentiation (HR: 2.381, 95% CI: 1.141–4.968,  $P = 0.021$ ) was the only significant risk factor for DFS, but no significant prognostic factor was identified for OS.

**Conclusions:** The modified XELOX adjuvant chemotherapy presented a comparable oncologic efficacy as standard XELOX chemotherapy for high-risk stage III colon cancer. The modified XELOX adjuvant chemotherapy could be an alternative treatment for patients suffering severe adverse events, especially severe neurotoxicity.

**Keywords:** colon cancer, adjuvant chemotherapy, XELOX (CapeOx), high risk, feasibility

## INTRODUCTION

To date, the combination of curative surgery and oxaliplatin-based chemotherapy is recommended as the classical treatment strategy for stage III colon cancer (Andre et al., 2009; Schmoll et al., 2014). A 6-month duration of adjuvant chemotherapy was previously recommended for all stage III colon cancer patients (Labianca et al., 2013; Benson et al., 2014). However, the International Duration Evaluation of Adjuvant Therapy (IDEA) trial introduced individualized durations of adjuvant chemotherapy according to the risk stratification of stage III colon cancer after curative chemotherapy (Grothey et al., 2018). The final results of the IDEA study suggested that a 3-month XELOX adjuvant chemotherapy regimen was sufficient for low-risk patients (T1-3 N1 disease), while 6-month XELOX adjuvant chemotherapy was still recommended for high-risk patients (T4, N2, or both). In fact, chemotherapy-related toxicity, especially neurotoxicity, causes 30–50% of patients to be unable to finish the full planned duration of oxaliplatin-containing adjuvant chemotherapy (Alberts et al., 2012; Lonardi et al., 2016). Therefore, a shorter duration of oxaliplatin-containing adjuvant therapy for stage III patients is warranted, especially for high-risk patients.

Recently, we reported that a modified XELOX (mXELOX) adjuvant chemotherapy with 8 cycles of capecitabine and 6 cycles of oxaliplatin presented a comparable survival outcome and lower incidence of neurotoxicity than a standard full cycle of XELOX chemotherapy for patients with stage III operated colon cancer (Peng et al., 2019). Although the previous study provided the first evidence supporting the administration of the mXELOX adjuvant chemotherapy regimen for stage III colon cancer patients, it did not assess the long-term oncologic efficacy of modified XELOX chemotherapy in those patients by performing a comparison with the standard full cycle of XELOX chemotherapy. Nevertheless, based on the results of the study, we supposed that mXELOX adjuvant chemotherapy could reduce or prevent the aggravation of neurotoxicity in patients with high-risk stage III colon cancer without impairing their oncologic outcomes.

To further demonstrate the feasibility of modified XELOX chemotherapy for treating high-risk stage III colon cancer, the present study aimed to evaluate the oncologic efficacy and safety of modified XELOX chemotherapy for these patients.

## MATERIALS AND METHODS

### Patients

This retrospective study reviewed 448 consecutive patients with colon cancer who underwent primary tumor resection between November 2007 and June 2016 at Sun Yat-sen University Cancer Center, China. The 448 patients met the following criteria: (1) pathologically diagnosed with colon adenocarcinoma, (2) underwent colon tumor curative resection, (3) received adjuvant chemotherapy with the XELOX regimen (oxaliplatin 130 mg/m<sup>2</sup> administered intravenously on day 1 and

capecitabine 1,000 mg/m<sup>2</sup> administered orally twice daily on days 1–14 for a 3-week cycle), (4) received no preoperative anticancer treatment, (5) was categorized as American Society of Anesthesiologists class I–II, (6) attended postoperative follow-up at least 3 months after delivery of the first cycle of chemotherapy, and (7) had a complete record of chemotherapy side effects. Subsequently, we further selected the patients according to the following criteria: (1) high-recurrence-risk patients with stage pT4Nany or pTanyN2 and (2) patients who underwent adjuvant chemotherapy with the full-cycle standard XELOX or the modified XELOX regimen. The clinical information, including demographics, tumor characteristics, treatment details, and follow-up data, was carefully collected from the electronic medical record system. The current study was conducted based on the ethical standards of the World Medical Association Declaration of Helsinki. The study was approved by the Institutional Research Ethics Committee of Sun Yat-sen University Cancer Center (approval number: GZR2017-004). Informed consent was waived by independent ethics committees of Sun Yat-sen University Cancer Center because of the retrospective nature of the study. All patient data were documented confidentially.

### Treatments

All patients underwent curative resection of the colon tumor by the performance of standard complete mesocolic excision and regional lymphadenectomy. The initial adjuvant chemotherapy was performed 3–8 weeks after colon tumor resection for all patients. According to the cycles of oxaliplatin given, patients with adjuvant chemotherapy was grouped into the standard and modified XELOX regimen group. Modified XELOX was defined as six cycles of the XELOX regimen plus two subsequent cycles of capecitabine alone, which consisted of eight cycles of capecitabine and six cycles of oxaliplatin, while the standard XELOX regimen consisted of eight cycles of capecitabine and eight cycles of oxaliplatin. The administration of the two XELOX regimens of adjuvant chemotherapy depended on the toxicity of the chemotherapy, the patient's tolerance, and preferences for the last two cycles of chemotherapy. A complete laboratory assessment was performed before each chemotherapy cycle.

### Definitions

All cases were pathologically staged according to the 8<sup>th</sup> edition of the American Joint Committee on Cancer (AJCC) staging system. Right-sided colon cancer was defined as a tumor located in the cecum, ascending colon, hepatic flexure, or transverse colon. Left-sided colon cancer was recognized as a tumor in the splenic flexure, descending colon, and sigmoid colon (Peng et al., 2018). The lymph node ratio (LNR) was defined as the number of positive lymph nodes divided by the total number of retrieved lymph nodes. Lymphovascular invasion (LVI) was diagnosed based on the presence of tumor cells within the small endothelium-lined lymphatic or vascular channels (Harris et al., 2008). Perineural invasion (PNI) was diagnosed based on tumor invasion in, around, and through nerves and nerve sheaths (Batsakis, 1985). The intensity of the adverse events during adjuvant chemotherapy was graded based on the National

Cancer Institute Common Terminology Criteria for Adverse Events (NCI CTCAE), version 4.0.

## Postoperative Follow-Up

Follow-up was conducted through clinical visits every 3 months for the first 2 years and then semiannually for the subsequent 3 years after surgery. The clinical visit items included abdominal examinations, detection of serum carcinoembryonic antigen (CEA) and carbohydrate antigen 19-9 (CA19-9), chest/abdominal/pelvic CT, and colonoscopy. Disease-free survival (DFS) was the interval from the date of tumor resection to the date of disease recurrence, death or the last follow-up. Overall survival (OS) was the interval from the date of tumor resection to the date of death from any cause or the last follow-up. The final follow-up visit was conducted in July 2019.

## Statistical Analysis

Statistical analyses were conducted using SPSS 20.0 software (IBM, Chicago, IL, USA) and GraphPad Prism 7 software (GraphPad Software, Inc., San Diego, CA, USA). Continuous variables are presented as the median (range), while categorical variables are presented as percentages, which were compared by using the chi-square ( $\chi^2$ ) test. The Kaplan–Meier curve was applied to calculate the survival rates, and the differences in survival between the groups were subsequently compared by using the log-rank test. The hazard ratios (HRs) and 95%

confidence intervals (CIs) were finally generated by univariate Cox proportional hazards analysis. The statistical tests performed above were two sided, and a P value less than 0.05 was considered significant.

## RESULTS

### Patient Characteristics

The participant selection flowchart is presented in **Figure 1**. Among the 448 patients, 306 patients were excluded for the following reasons: low-recurrence risk patients ( $n = 209$ ) and unfinished adjuvant chemotherapy with fewer than eight cycles ( $n = 97$ ). Overall, 142 eligible patients were identified for analysis in the study, with 74 patients in the standard XELOX group and 68 patients in the modified XELOX group. The detailed information of the 142 patients is shown in **Table 1**. The median age of the total sample of patients was 55 years (range, 22–85 years), with 56.3% male patients. The median tumor size was 4.1 cm (range, 1.0–12.0 cm). The median number of retrieved lymph nodes was 15 (range, 2–63), the median number of metastatic lymph nodes was 3 (range, 1–17), and the median LNR was 0.25 (range, 0.09–1.00). According to tumor location, the total sample of patients had 3 (2.1%) cases of cecal cancer, 20 (14.1%) cases of ascending colon cancer, 11 (7.7%) cases of hepatic flexure colon cancer, 10 (7.0%)

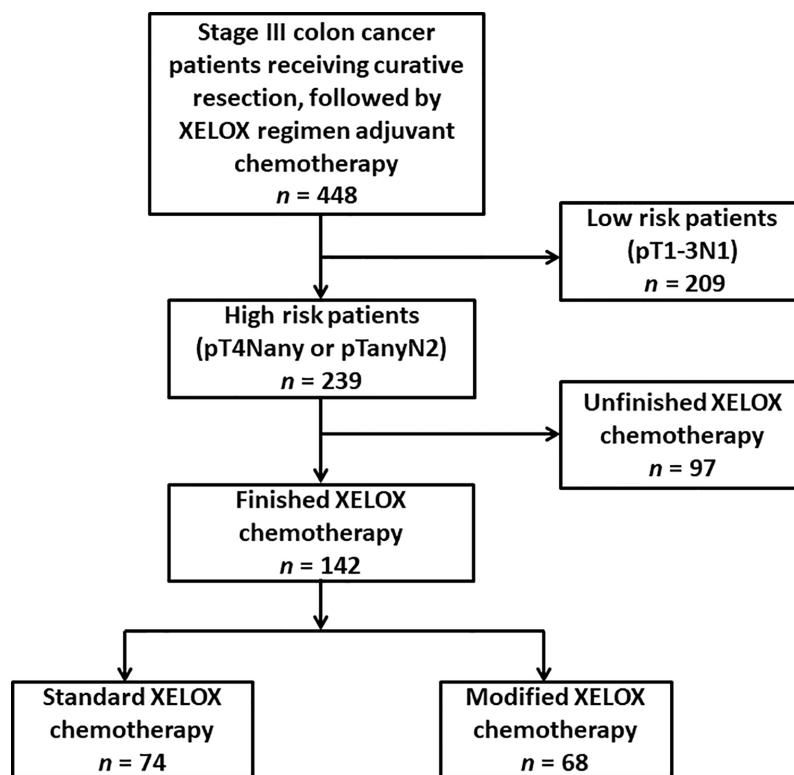


**FIGURE 1** | Flowchart representing the selection of eligible patients for the present study.



**TABLE 1 |** Clinical characteristics of the patients in the standard and modified XELOX groups.

Variable	Overall cases (%)	Standard XELOX (n, %)	Modified XELOX (n, %)	P value
Total	142	74 (52.1)	68 (47.9)	
Age (years)				0.487
≤60	100 (70.4)	54 (73.0)	46 (67.6)	
>60	42 (29.6)	20 (27.0)	22 (32.4)	
Sex				0.657
Male	80 (56.3)	43 (58.1)	37 (54.4)	
Female	62 (43.7)	31 (41.9)	31 (45.6)	
Tumor location				<b>0.031</b>
Right-sided colon	44 (31.0)	17 (23.0)	27 (39.7)	
Left-sided colon	98 (69.0)	57 (77.0)	41 (60.3)	
Baseline hemoglobin (g/L)				0.825
<90	24 (16.9)	13 (17.6)	11 (16.2)	
≥90	118 (83.1)	61 (82.4)	57 (83.8)	
Tumor size (cm)				<b>0.019</b>
≤4	71 (50.0)	30 (40.5)	41 (60.3)	
>4	71 (50.0)	44 (59.5)	27 (39.7)	
Differentiation				0.437
Well/moderate	100 (70.4)	50 (67.6)	50 (73.5)	
Poor/undifferentiated	42 (29.6)	24 (32.4)	18 (26.5)	
T stage				<b>0.002</b>
T1–T3	28 (19.7)	22 (29.7)	6 (8.8)	
T4	114 (80.3)	52 (70.3)	62 (91.2)	
Number of retrieved lymph nodes				0.207
<12	35 (24.6)	15 (20.3)	20 (29.4)	
≥12	107 (75.4)	59 (79.7)	48 (70.6)	
LNR				0.693
<0.25	79 (24.6)	40 (54.1)	39 (57.4)	
≥0.25	63 (75.4)	34 (45.9)	29 (42.6)	
N stage				0.492
N1	73 (55.6)	36 (48.6)	37 (54.4)	
N2	69 (44.4)	38 (51.4)	31 (45.6)	
LVI <sup>a</sup>				0.821
Positive	50 (40.0)	26 (38.2)	24 (42.1)	
Negative	75 (60.0)	42 (61.8)	33 (57.9)	
PNI <sup>b</sup>				0.885
Positive	38 (30.6)	21 (31.3)	17 (29.8)	
Negative	86 (69.4)	46 (68.7)	40 (70.2)	
Mismatch repair protein status <sup>c</sup>				0.970
pMMR	57 (91.9)	46 (92.0)	11 (91.7)	
dMMR	5 (8.1)	4 (8.0)	1 (8.3)	
Preoperative serum CEA (ng/ml)				<b>0.008</b>
≤5	84 (59.2)	36 (48.6)	48 (70.6)	
>5	58 (40.8)	38 (51.4)	20 (29.4)	
Postoperative metastasis				0.643
Yes	29 (20.4)	14 (18.9)	15 (22.1)	
No	113 (79.6)	60 (81.1)	53 (77.9)	

LNR, lymph node ratio; LVI, lymphovascular invasion; PNI, perineural invasion; pMMR, proficient mismatch repair protein; dMMR, deficient mismatch repair protein; CEA, carcinoembryonic antigen. <sup>a</sup>Data from 125 patients were available; <sup>b</sup>Data from 124 patients were available. <sup>c</sup>Data from 62 patients were available. It will be bold when the p-value result is less than 0.05.

cases of transverse colon cancer, 4 (2.8%) cases of splenic flexure colon cancer, 18 (12.7%) cases of descending colon cancer, and 76 (53.5%) cases of sigmoid colon cancer. In total, three (2.1%) patients experienced postoperative complications such as intestinal obstruction.

## Differences in Clinicopathological Parameters Between the Two XELOX Regimens

As shown in **Table 1**, the modified XELOX group presented a significantly higher prevalence of T4 (91.2 vs. 70.3%;  $P = 0.002$ ) and right-sided colon tumors (39.7 vs. 23.0%;  $P = 0.031$ ) than those in the standard XELOX group. However, the standard XELOX group showed a significantly higher prevalence of larger tumors (59.5% vs. 39.7%;  $P = 0.019$ ) and elevated preoperative CEA levels (51.4 vs. 29.4%;  $P = 0.008$ ) than those in the modified XELOX group. The differences in other clinicopathological parameters between the groups did not show statistical significance.

## Adverse Events of Adjuvant Chemotherapy

The major adverse events related to adjuvant chemotherapy with the two regimens are presented in **Table 2**. There were no deaths due to grade 3/4 adverse events. Neurotoxicity was found in 99 (69.7%) patients and was the most common adverse event among all patients. Compared with the standard XELOX group, the modified XELOX group showed a lower incidence of grade 1 hepatic disorder (14.7 vs. 28.4%,  $P = 0.049$ ). There were no significant differences in the total occurrence rates of leukopenia, thrombocytopenia, hepatic disorder, nausea and vomiting, diarrhea, neurotoxicity, or hand-foot syndrome between the two groups. The reasons for the decision to treat patients with modified XELOX chemotherapy are presented in **Figure 2**. The decision to treat patients with modified XELOX chemotherapy was mostly due to severe adverse events in 64.7% (44/68) of patients. Grade 2–3 neurotoxicity (25.0%, 17/68), grade 2–4 thrombocytopenia (20.6%, 14/68), and grade 3–4 leukopenia (13.2%, 9/68) were the major severe adverse events related to the decision to treat patients with modified XELOX chemotherapy. No aggravation of neurotoxicity was observed in the last two chemotherapy cycles in the modified XELOX group.

## Survival Analysis

After a median postoperative follow-up duration of 69 months (range, 7–115 months), 29 (20.4%) patients developed disease recurrence, and 14 (9.9%) patients ultimately experienced cancer-related mortality. Among these patients, 44.8% (13/29) had liver metastases, 31.0% (9/29) had lung metastases, 27.6% (8/29) had abdominal pelvic metastases, and 17.2% (5/29) had metastases to other organs. The 5-year DFS and OS rates were 79.7 and 90.9%, respectively, among all enrolled patients in this study. The 5-year DFS rate was 80.3% for patients in the standard XELOX group and 79.0% for patients in the modified XELOX group; these values were comparable ( $P = 0.891$ ) (**Figure 3A**). Similarly, the 5-year OS rate was 87.8% for the standard XELOX group and 93.8% for the modified XELOX group; these values were not significantly different ( $P = 0.446$ ) (**Figure 3B**). In univariate analysis, poor tumor differentiation (HR: 2.381, 95% CI: 1.141–4.968,  $P = 0.021$ ) was the only significant risk factor for

**TABLE 2 |** Comparison of chemotherapy-related toxicities between the standard and modified XELOX groups.

Toxicity	Total patients (n = 142, %)	Standard XELOX (n = 74, %)	Modified XELOX (n = 68, %)	P value
Leucopenia				
Total	89 (62.7)	47 (63.5)	42 (61.8)	0.830
Grade 1-2	77 (54.2)	41 (55.4)	36 (52.9)	0.768
Grade 3-4	12 (8.5)	6 (8.1)	6 (8.8)	0.878
Thrombocytopenia				
Total	67 (47.2)	35 (47.3)	32 (47.1)	0.977
Grade 1-2	52 (36.6)	29 (39.2)	23(33.8)	0.507
Grade 3-4	15 (10.6)	6 (8.1)	9 (13.2)	0.321
Hepatic disorder				
Total	45 (31.7)	28 (37.8)	17 (25.0)	0.100
Grade 1	31 (21.8)	21 (28.4)	10 (14.7)	<b>0.049</b>
Grade 2-3	14 (9.9)	7 (9.5)	7 (10.3)	0.868
Nausea/vomiting				
Total	38 (26.8)	18 (24.3)	20 (29.4)	0.494
Grade 1	22 (15.5)	11(14.9)	11 (16.2)	0.829
Grade 2-3	16 (11.3)	7 (9.5)	9 (13.2)	0.477
Diarrhea				
Total	22 (15.5)	12 (16.2)	10 (14.7)	0.804
Grade 1	12 (8.5)	6 (8.1)	6 (8.8)	0.878
Grade 2-3	10 (7.0)	6 (8.1)	4 (5.9)	0.605
Neurotoxicity				
Total	99 (69.7)	47(63.5)	52 (76.5)	0.093
Grade 1	64 (45.1)	32 (43.2)	32 (47.1)	0.648
Grade 2-3	35 (24.6)	15 (20.3)	20 (29.4)	0.207
Hand-foot syndrome				
Total	78 (54.9)	37 (50.0)	41 (60.3)	0.218
Grade 1	63 (44.3)	30 (40.5)	33 (48.5)	0.338
Grade 2-3	15 (10.6)	7 (9.5)	8 (11.8)	0.655

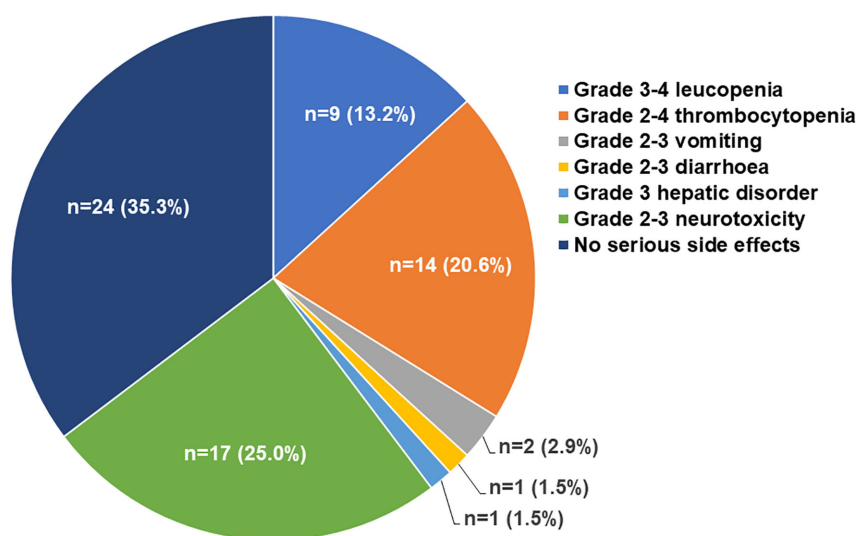
The listed grades of peripheral sensory neurotoxicity represent the maximal levels at any time. It will be bold when the p-value result is less than 0.05.

DFS, while there was no significant prognostic factor for OS (Table 3).

## DISCUSSION

Based on the results of our previous study, the current study further evaluated the long-term efficacy of modified XELOX chemotherapy for the treatment of high-risk stage III colon cancer. In line with our hypothesis, the results indicated that modified XELOX chemotherapy had oncologic efficacy for high-risk patients comparable to that of standard XELOX chemotherapy. Furthermore, modified XELOX showed acceptable safety without aggravating neurotoxicity. The study enhanced the evidence supporting the use of modified XELOX adjuvant chemotherapy for stage III operated colon cancer patients, including the high-risk subgroup.

To our knowledge, the unfavorable prognostic impact of advanced T and N stages for stage III cancer patients has been well identified. Although curative surgery provided temporary evidence of absence of disease for those patients, residual micrometastases probably exist due to the advanced disease stage, which increases the likelihood of disease recurrence postoperatively (Viehl et al., 2017). Based on this theory, these patients warrant aggressive postoperative chemotherapy to maximize the survival benefit from curative treatment. Evidence from the France IDEA trial supported that high-risk patients achieve greater survival benefit from the 6-month full cycle of adjuvant chemotherapy instead of the 3-month duration of adjuvant chemotherapy (Andre et al., 2018). Previous studies have also shown that failure to complete adjuvant chemotherapy impairs long-term survival in stage III colon cancer patients

**Reasons of receiving modified XELOX adjuvant chemotherapy (n=68)****FIGURE 2 |** Reasons of receiving modified XELOX adjuvant chemotherapy.



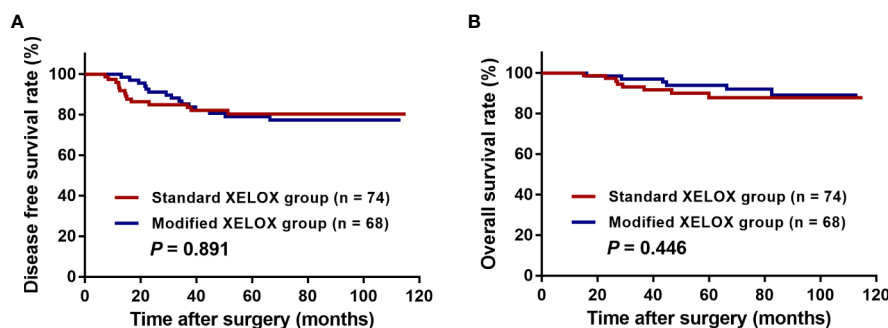


**FIGURE 3** | Kaplan-Meier curves of patients with high-risk stage III colon cancer grouped by standard XELOX and modified XELOX group. **(A)** Comparison of disease-free survival (DFS) between the standard XELOX and modified XELOX group. **(B)** Comparison of overall survival (OS) between the standard XELOX and modified XELOX group.

**TABLE 3** | Univariate analyses of prognostic factors for disease-free survival and overall survival in all patients.

Variable	DFS Univariate		OS Univariate	
	HR (95%CI)	P value	HR (95%CI)	P value
Age, years (>60 vs. ≤60)	2.081 (1.001–24.329)	0.050	0.953 (0.299–3.039)	0.935
Sex (Male vs. Female)	1.952 (0.888–4.288)	0.096	1.546 (0.517–4.621)	0.435
Baseline hemoglobin, g/l (<90 vs. ≥90)	0.493 (0.149–1.630)	0.246	0.035 (0.000–10.900)	0.253
Tumor location (left-sided colon vs. right-sided colon)	1.385 (0.592–3.242)	0.453	0.575 (0.199–1.660)	0.306
Tumor size, cm (>4 vs. ≤4)	0.589 (0.278–1.248)	0.167	0.570 (0.191–1.702)	0.314
Differentiation (Poor vs. Well-moderate)	2.381 (1.141–4.968)	<b>0.021</b>	1.760 (0.585–5.298)	0.315
T stage (T4 vs. T1-3)	1.525 (0.530–4.388)	0.434	2.689 (0.349–20.722)	0.343
Number of retrieved lymph nodes (<12 vs. ≥12)	1.649 (0.767–3.547)	0.201	0.286 (0.792–6.599)	0.126
LNR (≥0.25 vs. <0.25)	2.086 (0.976–4.458)	0.058	1.816 (0.627–5.261)	0.272
N stage (N2 vs. N1)	0.888 (0.427–1.847)	0.427	0.857 (0.296–2.476)	0.775
LVI (positive vs. negative)	1.339 (0.600–2.989)	0.476	1.137 (0.361–3.582)	0.827
PN1 (positive vs. negative)	1.399 (0.612–3.198)	0.426	1.197 (0.360–3.981)	0.769
Preoperative CEA, ng/ml (>5 vs. ≤5)	1.393 (0.672–2.886)	0.373	1.125 (0.390–3.244)	0.827
Adjuvant chemotherapy (modified XELOX vs. standard XELOX)	1.052 (0.507–2.184)	0.891	0.660 (0.226–1.930)	0.448

LNR, lymph node ratio; LVI, lymphovascular invasion; PN1, perineural invasion; CEA, carcinoembryonic antigen. It will be bold when the p-value result is less than 0.05.

(Morris et al., 2007), which demonstrates the necessary of finishing adjuvant 5-FU-based chemotherapy for colon cancer. In our study, the total sample of patients achieved favorable long-term survival, with 79.7% 5-year DFS and 90.9% 5-year OS in both the standard XELOX group and modified XELOX group finishing the 6-month 5-FU-based adjuvant chemotherapy. Therefore, we considered a 6-month duration of 5-FU-based adjuvant chemotherapy to be necessary for disease control in high-risk patients.

On the other hand, the choice of regimen should also be balanced against the additional toxicity associated with longer therapy. Cumulative evidence has reported that approximately 70% of patients develop neurotoxicity during treatment with oxaliplatin-containing chemotherapy (Land et al., 2007). Similarly, nearly 70% of patients suffered oxaliplatin-related neurotoxicity and 24.6% of patients experienced severe neurotoxicity in the current study. It has been proven that neurotoxicity accumulates with the increase in oxaliplatin

administration, leading to poor compliance in the subsequent chemotherapy course (Pachman et al., 2015). More seriously, the neurotoxicity contributing to sensory nerve deficits might persist for years after cessation of oxaliplatin therapy (Kokotis et al., 2016). Obviously, continuous treatment with oxaliplatin increased the risk of developing new neurotoxicity or worsening previous neurotoxicity (Besora et al., 2018). The JSWOG-C2 Study demonstrated the feasibility of a sequential approach to adjuvant chemotherapy with 3 months of an oxaliplatin-based regimen followed by 3 months of capecitabine in stage III and high-risk stage II colorectal cancer patients, which was tolerated by patients and associated with a low incidence of neuropathy (Tsuruta et al., 2016). Another phase 2 Japanese study also reported that intermittent oxaliplatin treatment improved severe neuropathy in a modified FOLFOX6 plus bevacizumab regimen without reducing progression-free survival in patients with inoperable or metastatic colorectal cancer (Kato et al., 2018). In fact, we previously found that a two-cycle shorter duration of oxaliplatin treatment in the

modified XELOX regimen was associated with a significantly lower incidence and severity of adverse events, especially neurotoxicity, without impairing survival (Peng et al., 2019). In the current study, 64.7% (44/68) of patients suffered severe adverse events, of which grade 2–3 neurotoxicity was the most common severe adverse event. Those patients who were initially predicted to fail to finish the full cycle of adjuvant chemotherapy successfully finished the 6-month adjuvant chemotherapy due to the administration of the modified XELOX regimen. This might be explained mostly by the lack of aggravating neurotoxicity in the last two chemotherapy cycles with capecitabine alone. Furthermore, our results revealed that modified XELOX chemotherapy did not impair 5-year survival compared with the survival associated with standard XELOX chemotherapy. Based on the results of the comparable oncologic efficacy, a two-cycle shorter duration of oxaliplatin treatment might be an alternative approach for high-risk stage III colon cancer patients with severe adverse events, especially severe neurotoxicity.

Several limitations to the current study should be acknowledged. First, this retrospective study was performed with an uncontrolled methodology and a limited number of patients in a single cohort. It can not be denied that there exists selective bias such as patients in standard XELOX group tend to have more high-risk clinical characteristics like bigger tumor size, more T4 stage, higher CEA level and have better tolerance to chemotherapy toxicity. Although our study initially indicated the oncologic efficacy of modified XELOX chemotherapy, more work should be done in a prospective, multicenter clinical trial with a large sample size to validate these findings in the future. Second, we failed to evaluate the long-term quality of life effects of the two chemotherapy regimens. As a result, we were unable to compare the occurrence of late effects of oxaliplatin-induced peripheral neuropathy between the two chemotherapy groups. Since persistent neuropathy impaired the survivors' physical and emotional well-being, it is an important parameter to measure the feasibility of an oxaliplatin-containing chemotherapy regimen (Toft-Hagen et al., 2013). Third, although the TNM stage is important for colon cancer management, it seems to be insufficient to determine the authentic high-risk patients with stage III colon cancer. Tumor molecular markers, such as CpG island methylator phenotype (CIMP) status; driver gene mutations, such as KRAS and BRAF; and tumor immune microenvironment, have been linked to different recurrence risks among stage III colon cancer patients (Auclin et al., 2017; Murcia et al., 2018). The above molecular data were unavailable in the current study. Therefore, molecular prognostic markers for risk stratification need to be explored in further works.

## REFERENCES

- Alberts, S. R., Sargent, D. J., Nair, S., Mahoney, M. R., Mooney, M., Thibodeau, S. N., et al. (2012). Effect of oxaliplatin, fluorouracil, and leucovorin with or without cetuximab on survival among patients with resected stage III colon cancer: a randomized trial. *Jama* 307, 1383–1393. doi: 10.1001/jama.2012.385
- Andre, T., Boni, C., Navarro, M., Mahoney, M. R., Mooney, M., Thibodeau, S. N., et al. (2009). Improved overall survival with oxaliplatin, fluorouracil, and leucovorin as adjuvant treatment in stage II or III colon cancer in the MOSAIC trial. *J. Clin. Oncol.* 27, 3109–3116. doi: 10.1200/JCO.2008.20.6771

## CONCLUSION

Our study confirms that modified XELOX chemotherapy presented comparable oncologic efficacy for patients with high-risk stage III colon cancer. These findings indicated that modified XELOX chemotherapy could serve as an alternative regimen for patients suffering severe adverse events, especially severe neurotoxicity.

## DATA AVAILABILITY STATEMENT

The datasets used and analyzed during the current study are available from the corresponding author on reasonable request. The authenticity of this article has been validated by uploading the key raw data onto the Research Data Deposit public platform (<http://www.researchdata.org.cn>), with the Approval Number as RDDA2020001633.

## ETHICS STATEMENT

The studies involving human participants were reviewed and approved by the Institutional Research Ethics Committee of Sun Yat-sen University Cancer Center (approval number: GZR2017-004). Written informed consent for participation was not required for this study in accordance with the national legislation and the institutional requirements.

## AUTHOR CONTRIBUTIONS

All authors listed have made a substantial, direct, and intellectual contribution to the work and approved it for publication.

## FUNDING

The study was funded by grants from the National Natural Science Foundation of China (no. 81772595 and no. 81871991), Natural Science Foundation of Guangdong Province, China (no. 2018A030310239), and Bethune-Ethicon Excellence Surgery Fund Project (no. HZB-20181119-27).

## ACKNOWLEDGMENTS

We greatly appreciate all colleagues of the Department of Colorectal Surgery in Sun Yat-sen University Cancer Center who were involved in performing the treatments for the current study.

- Andre, T., Vernerey, D., Mineur, L., Bannoun, J., Desrame, J., Faroux, R., et al. (2018). Three Versus 6 Months of Oxaliplatin-Based Adjuvant Chemotherapy for Patients With Stage III Colon Cancer: Disease-Free Survival Results From a Randomized, Open-Label, International Duration Evaluation of Adjuvant (IDEA) France, Phase III Trial. *J. Clin. Oncol.* 36, 1469–1477. doi: 10.1200/JCO.2017.76.0355
- Auclin, E., Zaanani, A., Vernerey, D., Douard, R., Gallois, C., Laurent-Puig, P., et al. (2017). Subgroups and prognostication in stage III colon cancer: future perspectives for adjuvant therapy. *Ann. Oncol.* 28, 958–968. doi: 10.1093/annonc/mdx030
- Batsakis, J. G. (1985). Nerves and neurotropic carcinomas. *Ann. Otol. Rhinol. Laryngol.* 94, 426–427.

- Benson, A. B., Venook, A. P., Bekaii-Saab, T., Chan, C., Chen, Y. J., Cooper, H. S., et al. (2014). Colon cancer, version 3.2014. *J. Natl. Compr. Canc. Netw.* 12, 1028–1059. doi: 10.6004/jnccn.2014.0099
- Besora, S., Santos, C., Izquierdo, C., Martinez-Villacampa, M. M., Bruna, J., Velasco, R., et al. (2018). Rechallenge with oxaliplatin and peripheral neuropathy in colorectal cancer patients. *J. Cancer Res. Clin. Oncol.* 144, 1793–1801. doi: 10.1007/s00432-018-2691-8
- Grothey, A., Sobrero, A. F., Shields, A. F., Yoshino, T., Paul, J., Taieb, J., et al. (2018). Duration of Adjuvant Chemotherapy for Stage III Colon Cancer. *N. Engl. J. Med.* 378, 1177–1188. doi: 10.1056/NEJMoa1713709
- Harris, E. I., Lewin, D. N., Wang, H. L., Lauwers, G. Y., Srivastava, A., Shyr, Y., et al. (2008). Lymphovascular invasion in colorectal cancer: an interobserver variability study. *Am. J. Surg. Pathol.* 32, 1816–1821. doi: 10.1097/PAS.0b013e3181816083
- Kato, S., Imai, H., Gamoh, M., Takahata, T., Ohori, H., Yasuda, K., et al. (2018). Intermittent Withdrawal of Oxaliplatin for Alleviating Neurotoxicity during Oxaliplatin-Based Chemotherapy for Japanese Patients with Inoperable or Metastatic Colorectal Cancer: A Phase 2 Multicenter Study. *Tohoku J. Exp. Med.* 245, 21–28. doi: 10.1620/tjem.245.21
- Kokotis, P., Schmelz, M., Kostouros, E., Karandreas, N., and Dimopoulos, M. A. (2016). Oxaliplatin-Induced Neuropathy: A Long-Term Clinical and Neurophysiologic Follow-Up Study. *Clin. Colorectal. Cancer* 15, e133–e140. doi: 10.1016/j.clcc.2016.02.009
- Labianca, R., Nordlinger, B., Beretta, G. D., Mosconi, S., Mandala, M., Cervantes, A., et al. (2013). Early colon cancer: ESMO Clinical Practice Guidelines for diagnosis, treatment and follow-up. *Ann. Oncol.* 24 Suppl 6, vi64–vi72. doi: 10.1093/annonc/mdt354
- Land, S. R., Kopec, J. A., Cecchini, R. S., Ganz, P. A., Wieand, H. S., Colangelo, L. H., et al. (2007). Neurotoxicity from oxaliplatin combined with weekly bolus fluorouracil and leucovorin as surgical adjuvant chemotherapy for stage II and III colon cancer: NSABP C-07. *J. Clin. Oncol.* 25, 2205–2211. doi: 10.1200/JCO.2006.08.6652
- Lonardi, S., Sobrero, A., Rosati, G., Di Bartolomeo, M., Ronzoni, M., Aprile, G., et al. (2016). Phase III trial comparing 3–6 months of adjuvant FOLFOX4/XELOX in stage II–III colon cancer: safety and compliance in the TOSCA trial. *Ann. Oncol.* 27, 2074–2081. doi: 10.1093/annonc/mdw404
- Morris, M., Platell, C., Fritschi, L., and Iacopetta, B. (2007). Failure to complete adjuvant chemotherapy is associated with adverse survival in stage III colon cancer patients. *Br. J. Cancer* 96, 701–707. doi: 10.1038/sj.bjc.6603627
- Murcia, O., Juarez, M., Rodriguez-Soler, M., Hernandez-Illan, E., Giner-Calabuig, M., Alustiza, M., et al. (2018). Colorectal cancer molecular classification using BRAF, KRAS, microsatellite instability and CIMP status: Prognostic implications and response to chemotherapy. *PloS One* 13, e0203051. doi: 10.1371/journal.pone.0203051
- Pachman, D. R., Qin, R., Seisler, D. K., Smith, E. M., Beutler, A. S., Ta, L. E., et al. (2015). Clinical Course of Oxaliplatin-Induced Neuropathy: Results From the Randomized Phase III Trial N08CB (Alliance). *J. Clin. Oncol.* 33, 3416–3422. doi: 10.1200/JCO.2014.58.8533
- Peng, J., Li, C., Wang, F., Zhang, H., Xiao, W., Li, H., et al. (2018). Right- and left-sided stage III colon cancers present different prognostic outcomes of oxaliplatin-based adjuvant chemotherapy after curative resection. *Cancer Manag. Res.* 10, 2095–2103. doi: 10.2147/CMARS.S163520
- Peng, J., Li, W., Zhang, R., Lin, J., Tang, J., Wen, Y., et al. (2019). Safety and efficacy of a modified XELOX adjuvant regimen for patients with operated stage III colon cancer: a Chinese single-center experience. *Cancer Commun. (Lond)* 39, 59. doi: 10.1186/s40880-019-0400-x
- Schmoll, H. J., Twelves, C., Sun, W., O'Connell, M. J., Cartwright, T., McKenna, E., et al. (2014). Effect of adjuvant capecitabine or fluorouracil, with or without oxaliplatin, on survival outcomes in stage III colon cancer and the effect of oxaliplatin on post-relapse survival: a pooled analysis of individual patient data from four randomised controlled trials. *Lancet Oncol.* 15, 1481–1492. doi: 10.1016/S1470-2045(14)70486-3
- Toftagen, C., Donovan, K. A., Morgan, M. A., Shibata, D., and Yeh, Y. (2013). Oxaliplatin-induced peripheral neuropathy's effects on health-related quality of life of colorectal cancer survivors. *Supp. Care Cancer* 21, 3307–3313. doi: 10.1007/s00520-013-1905-5
- Tsuruta, A., Yamashita, K., Tanioka, H., Tsuji, A., Inukai, M., Yamakawa, T., et al. (2016). Feasibility of sequential adjuvant chemotherapy with a 3-month oxaliplatin-based regimen followed by 3 months of capecitabine in patients with stage III and high-risk stage II colorectal cancer: JSWOG-C2 study. *Drug Des. Devel. Ther.* 10, 3827–3835. doi: 10.2147/DDDT.S112322
- Viehl, C. T., Weixler, B., Guller, U., Dell-Kuster, S., Rosenthal, R., Ramser, M., et al. (2017). Presence of bone marrow micro-metastases in stage I–III colon cancer patients is associated with worse disease-free and overall survival. *Cancer Med.* 6, 918–927. doi: 10.1002/cam4.1056

**Conflict of Interest:** The authors declare that the research was conducted in the absence of any commercial or financial relationships that could be construed as a potential conflict of interest.

Copyright © 2020 Peng, Li, Fan, Zhou, Zhu, Li, Pan, Lin and Lin. This is an open-access article distributed under the terms of the Creative Commons Attribution License (CC BY). The use, distribution or reproduction in other forums is permitted, provided the original author(s) and the copyright owner(s) are credited and that the original publication in this journal is cited, in accordance with accepted academic practice. No use, distribution or reproduction is permitted which does not comply with these terms.



# Increased Tumoral Microenvironmental pH Improves Cytotoxic Effect of Pharmacologic Ascorbic Acid in Castration-Resistant Prostate Cancer Cells

Zhoulei Li<sup>1†</sup>, Peng He<sup>1†</sup>, Ganhua Luo<sup>1†</sup>, Xinchong Shi<sup>1</sup>, Gang Yuan<sup>2</sup>, Bing Zhang<sup>1</sup>, Christof Seidl<sup>3</sup>, Andreas Gewies<sup>4</sup>, Yue Wang<sup>1</sup>, Yuan Zou<sup>5</sup>, Yali Long<sup>1</sup>, Dianchao Yue<sup>1</sup> and Xiangsong Zhang<sup>1\*</sup>

## OPEN ACCESS

### Edited by:

Haichang Li,  
The Ohio State University,  
United States

### Reviewed by:

Ana Salomé Pires,  
University of Coimbra, Portugal  
Gagan Deep,  
Wake Forest University, United States

### \*Correspondence:

Xiangsong Zhang  
zhxiangs@mail.sysu.edu.cn

<sup>†</sup>These authors have contributed  
equally to this work

### Specialty section:

This article was submitted to  
Experimental Pharmacology  
and Drug Discovery,  
a section of the journal  
Frontiers in Pharmacology

**Received:** 09 June 2020

**Accepted:** 31 August 2020

**Published:** 23 September 2020

### Citation:

Li Z, He P, Luo G, Shi X, Yuan G,  
Zhang B, Seidl C, Gewies A, Wang Y,  
Zou Y, Long Y, Yue D and Zhang X  
(2020) Increased Tumoral  
Microenvironmental pH Improves  
Cytotoxic Effect of Pharmacologic  
Ascorbic Acid in Castration-Resistant  
Prostate Cancer Cells.  
Front. Pharmacol. 11:570939.  
doi: 10.3389/fphar.2020.570939

<sup>1</sup> Department of Nuclear Medicine, The First Affiliated Hospital of Sun Yat-Sen University, Guangzhou, China, <sup>2</sup> Department of Geriatrics, The First Affiliated Hospital of Sun Yat-Sen University, Guangzhou, China, <sup>3</sup> Department of Nuclear Medicine, Klinikum rechts der Isar, Technical University Munich, Munich, Germany, <sup>4</sup> Institute of Molecular Toxicology and Pharmacology, German Research Center for Environmental Health, Munich, Germany, <sup>5</sup> Sichuan Key Laboratory of Medical Imaging & Ultrasound Medical Center, Affiliated Hospital of North Sichuan Medical College, Nanchong, China

**Background:** The anticancer potential of pharmacologic ascorbic acid (AA) has been detected in a number of cancer cells. However, *in vivo* study suggested a strongly reduced cytotoxic activity of AA. It was known that pH could be a critical influencing factor for multiple anticancer treatments. In this study, we explored the influence of pH on the cytotoxicity of ascorbic acid. We employed castration-resistant prostate cancer (CRPC) cell lines PC3 and DU145 to observe the therapeutic effect of AA on PCa cells that were cultured with different pH *in vitro*. We also analyzed the influence of pH and extracellular oxidation on cytotoxicity of AA in cancer cells using reactive oxygen species (ROS) assay, cellular uptake of AA, and NADPH assay. Male BALB/c nude mice bearing prostate carcinoma xenografts (PC3 or DU145) were used to assess treatment response to AA with or without bicarbonate *in vivo*. The cellular uptake of AA in PCa xenografts was detected using positron emission tomography (PET). Small animal PET/CT scans were performed on mice after the administration of 6-deoxy-6-[<sup>18</sup>F] fluoro-L-ascorbic acid (<sup>18</sup>F-DFA).

**Results:** Our *in vitro* studies demonstrate that acidic pH attenuates the cytotoxic activity of pharmacologic ascorbic acid by inhibiting AA uptake in PCa cells. Additionally, we found that the cancer cell-selective toxicity of AA depends on ROS. *In vivo*, combination of AA and bicarbonate could provide a significant better therapeutic outcome in comparison with controls or AA single treated mice. <sup>18</sup>F-DFA PET imaging illustrated that the treatment with NaHCO<sub>3</sub> could significantly increase the AA uptake in tumor.

**Conclusions:** The alkalinity of tumor microenvironment plays an important role in anticancer efficiency of AA in CRPC. <sup>18</sup>F-DFA PET/CT imaging could predict the



therapeutic response of PCa animal model through illustration of tumoral uptake of AA.  $^{18}\text{F}$ -DFA might be a potential PET tracer in clinical diagnosis and treatment for CRPC.

**Keywords:** ascorbic acid, dehydroascorbate, microenvironmental pH,  $^{18}\text{F}$ -DFA, castration-resistant prostate cancer

## INTRODUCTION

Ascorbic acid (AA, also known as vitamin C) has been proposed as a potential anticancer agent. Intravenous pharmacological dose of AA was repurposed to promote death of therapy-resistant cancer cells, either as a monotherapy or in co-treatment with chemotherapeutic drugs or radiotherapy in various cancers, including melanoma (Hahm et al., 2007), breast cancer (Gan et al., 2019), gastric cancer (Lim et al., 2016), colorectal cancer (Yun et al., 2015), pancreatic cancer (Du et al., 2010), and leukemia (Roomi et al., 1998). However, application of pharmacological dose of AA alone did not inhibit the growth of several xenograft tumors (Chen et al., 2008; Verrax and Calderon, 2009), and randomized controlled clinical trials (RCTs) did not report any statistically significant improvements in overall or progression-free survival of patients (Jacobs et al., 2015). Furthermore, insufficient concentration in blood through oral application was suggested to be one of the reasons of low toxicity of AA *in vivo* (Jacobs et al., 2015). Sodium AA (0–10 mM) decreases the viability of both androgen-independent (DU145) and androgen-dependent (LNCaP) human prostate cancer (PCa) cell lines *in vitro* (Maramag et al., 1997). However, these *in vitro* results were not confirmed in clinical trials following administration of AA *via* infusion in castration-resistant prostate cancer (CRPC) patients and patients with advanced stages of other cancers (Creagan et al., 1979; Chen et al., 2005; Nielsen et al., 2017). So far there was no study investigating whether pH could play a role in the anticancer effect of AA on CRPC. Previous *in vitro* studies were conducted using commercially available cell culture media buffered to physiological pH ranging from 7.2 to 7.4 (Raghuhand et al., 1999a). Metabolic reprogramming in cancer is often accompanied by acidification of extracellular matrix (Szatrowski and Nathan, 1991). Measurements of pH in tumor tissues, using microelectrodes, magnetic resonance, or fluorescence techniques, typically yield an extracellular pH range of 6.5 to 6.9 (Flavell et al., 2016). In most tumors, the pH is more acidic near the surface and less acidic in the tumor center (Stock et al., 2007). The pH at surfaces which consisted of highly metastatic cells was around 6.1 to 6.4. Whereas in non-metastatic tumors, the pH was at a range of 6.7 to 6.9, as measured by positioning a pH-sensitive fluorescent dye (Anderson et al., 2016).

Furthermore, different results from preclinical research and clinical studies indicate that different conditions between tumor cells in a 2D cell culture and the microenvironment of human tumors might be the decisive factor for failure of AA in cancer treatment *in vivo* (Hickman et al., 2014). We proposed that the mild acidic microenvironment of human tumors might be an

important factor for impairing the cytotoxicity of AA. However, the role of microenvironmental pH in the cytotoxicity of AA remains poorly understood.

The cellular transportation of AA is mediated by two transport protein families (Liang et al., 2001), (i) the solute carrier gene family 23, which comprises the sodium-dependent vitamin C transporters (SVCTs) 1 and 2; and (ii) the solute carrier 2 family of glucose transporters (GLUTs). GLUTs transport the oxidized form of AA, dehydroascorbate (DHA) (Wohlrab et al., 2017). SVCT1 and SVCT2 cotransport sodium and ascorbate in a ratio of 2:1 down to an electrochemical sodium gradient, which is maintained by  $\text{K}^+/\text{Na}^+$  exchange mechanisms (Tsukaguchi et al., 1999). SVCTs transport is sensitive to pH changes and the optimum pH is 7.5 (Ormazabal et al., 2010). Acidic pH impairs SVCTs function through a mechanism involving the reversible protonation-deprotonation of five histidine residues in SVCTs (Tsukaguchi et al., 1999). The five histidine residues are central regulators of SVCTs function that modulate pH sensitivity, transporter kinetics,  $\text{Na}^+$  cooperativity, conformational stability, and subcellular localization (Godoy et al., 2007; Ormazabal et al., 2010). In addition, reactive oxygen species (ROS) as a constantly formed normal metabolic product in human body, can induce concentration dependent apoptotic cell death (Circu and Aw, 2010). AA was reported to induce caspase dependent apoptosis in cancer cells through generation of ROS, including superoxide and  $\text{H}_2\text{O}_2$  (Schoenfeld et al., 2017). Recent studies (Schoenfeld et al., 2017; Vissers and Das, 2018) demonstrate that extracellular oxidation of AA is an important influencing factor on its anticancer effect. However, the role of pH in cellular transportation of AA and accumulation of ROS in cancer cells under AA treatment is still unknown.

Prostate cancer is the second most common cancer in men worldwide and the sixth in China (Ren et al., 2013; Teoh et al., 2019). Over the past decade, the incidence of PCa has risen rapidly, reaching an annual growth of 12.07%. However, awareness of PCa is still low, and there are only 20–30% of the public who can correctly recognize high risk factors for PCa and choose early diagnosis and treatment (Teoh et al., 2019). Most patients suffered from PCa with serious metastasis and developed the CRPC at the time of diagnosis. Therefore, treatment of CRPC is extremely important in China because there is no effective therapy available. PC3 and DU145 are the most commonly used CRPC cell lines. The expression of SVCT2 and GLUT1 in PCa cell lines PC3 and DU145 are high (Effert et al., 2004; Godoy et al., 2007). The cellular AA transport is related to SVCT2 and GLUT1 (Welch et al., 1995). Microenvironmental pH could directly influence the transport function of SVCTs (Tsukaguchi et al., 1999; Ormazabal et al., 2010). Therefore, we designed this study to investigate the roles of pH in anti-tumor effect of AA in CRPC using PC3 and DU145.



## METHODS

### Cell Lines

The human PCa cell lines PC3 and DU145 were purchased from the Cell Bank of Chinese Academy of Sciences. They were cultured in RPMI 1640 medium (Gibco, Grand Island, NY, USA) or MEM medium (Gibco) containing 10% Fetal Bovine Serum (FBS; Gibco) and 1% penicillin/streptomycin (MRC, Jintan, China). All cell lines were cultured with 5% CO<sub>2</sub> at 37°C.

### Measurement of Cell Viability of Live Cells

Water-soluble tetrazolium salts (WST-8) assay was carried out according to the manufacturer's instruction (Dojindo Laboratories, Kumamoto, Japan). Briefly,  $5 \times 10^3$  cells per well were seeded into 96-well plate and incubated at 37°C with different concentrations (0, 2, 4, 6, 8, 16 mM) of AA (Sigma-Aldrich, Darmstadt, Germany) for 6 h. Cell culture media were prepared at different pH (6.0, 6.5, 7.0, 7.5, and 8.0, adjusted using HCl and NaOH). Then each well of the plates was supplemented with the WST-8 solution incubated for at least 2 h. Absorbance was measured at 450 nm using a Multiskan FC (Thermo Fisher Scientific, Inc., Waltham, MA).

### Flow Cytometry

PCa cells ( $4 \times 10^5$ /well) were seeded into six-well plates and incubated with AA (0 and 4 mM) at 37°C. Cell culture media were prepared at different pH (6.0, 6.5, 7.0, 7.5, and 8.0), adjusted using HCl and NaOH. After 6 h of culture, cells were collected using 0.05% trypsin solution, washed two times with phosphate buffer solution (PBS; Gibco), and centrifuged at 1,500 r/min for 5 min. Then, cells were stained with fluorescein isothiocyanate-labelled Annexin V apoptosis kit (BD Biosciences, San Jose, CA, USA) and counterstained with propidium iodide (PI; BD Biosciences), resuspended in binding solution for at least 30 min, and then analyzed by CytoFLEX S Flow Cytometer (Beckman Coulter, Inc., Brea, CA, USA).

### Clonogenic Assay

After treatment with AA (4 mM) for 6 h in cell culture medium at different pH (6.0, 6.5, 7.0, 7.5, and 8.0), adjusted using HCl and NaOH, cells were washed with PBS and detached with a 0.05% trypsin/EDTA (MRC) solution. Two hundred cells in each sample were seeded into six-well plates. Following incubation in a 5% CO<sub>2</sub> environment at 37°C for 2 weeks, colonies were

fixed with 100% methanol for 20 min, stained with crystal violet (Beyotime, Shanghai, China) for 5 min, dried overnight, and colonies were counter under Olympus BX51 microscope (Tokyo, Japan).

### ROS Assay

ROS assays were carried out according to the manufacturer's instruction (Sigma-Aldrich). Briefly,  $5 \times 10^3$  PC3 or DU145 cells per well in 96-well plates were incubated at 37°C with different concentrations of AA with different pH (6.0, 6.5, 7, 7.5, and 8.0, adjusted using HCl and NaOH) for 2 h. One hundred microliters of ROS detection reagent diluted in assay buffer was added per well and cells were incubated for 1 h. Florescence intensity ( $\lambda_{\text{ex}} = 640/\lambda_{\text{em}} = 675$  nm) was measured using a SPECTRAmax M5 instrument (Molecular Devices, LLC., San Jose, CA, USA). The relative ROS signal was calculated using the formula: original ROS of cells/cell survival rate obtained from WST-8 assay.

### Immunoblotting

After 16 h treatment with AA, cells were washed, pelleted, and stored at -80°C. Cell culture media were prepared at different pH (6.0, 6.5, 7.0, 7.5, and 8.0, adjusted using HCl and NaOH). The pH of cell culture media was reset four times with HCl and NaOH daily, to maintain a stable pH. Cells were lysed and protein concentration was determined using protein assay dye reagent with bovine serum albumin as standard. For immunoblotting, 30  $\mu$ g protein per lane was separated on 8% gradient readymade SDS-Gel and transferred to a polyvinylidene difluoride membrane (Millipore, Bedford, MA, USA). The primary antibodies, including anti-GLUT1 (ab652; Abcam, Cambridge, MA, USA) and anti-SVCT2 (ab229802; Abcam) were diluted to 1:1,000 into blocking buffer and incubated at 4°C overnight. Then the membranes were washed, and incubated with secondary antibody (Abcam). Blots were developed using Pierce Fast Western Blot Kit (Thermo Scientific) and exposed to film.

### Radiosynthesis of 6-Deoxy-6-[<sup>18</sup>F] Fluoro-L-Ascorbic Acid

6-deoxy-6-[<sup>18</sup>F] fluoro-L-ascorbic acid (<sup>18</sup>F-DFA) was prepared with a two-step radiochemical reaction according to the literature (Yamamoto et al., 1992) (Figure 1). Radiochemical purity was analyzed through analytical HPLC testing. The radiochemical yield was 20–33% (n = 10) with a radiochemical purity of >99%.

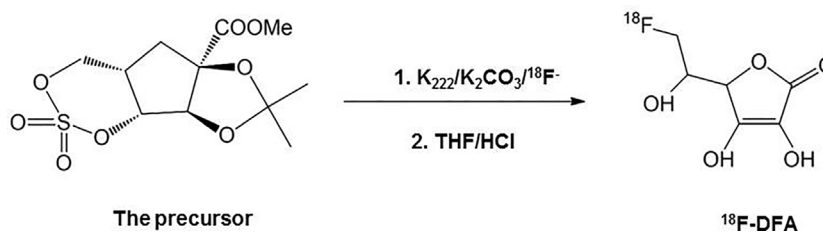


FIGURE 1 | Radiosynthesis scheme of <sup>18</sup>F-DFA.

This part of the work and subsequent related operations strictly comply with the Basic Standards for Protection Against Ionizing Radiation and for Safety of Radiation Sources of the People's Republic of China (GB 18871-2002) and the safety management measures for laboratories of Sun Yat-sen University (NO.2014-34).

## Cellular Uptake of Ascorbic Acid

L-[<sup>14</sup>C]-ascorbic acid (PerkinElmer Life Sciences, Waltham, MA, USA) was solubilized in PBS to 40 mM stock solution and stored at -20°C until used. PC3 and DU145 cells ( $4 \times 10^5$ /well in 24-well plates) were seeded and pre-cultured in conditioned medium of adjusted pH for 24 h. Cell culture was prepared at different pH (6.0, 6.5, 7.0, 7.5, and 8.0, adjusted using HCl and NaOH). The pH of cell culture media was reset with HCl and NaOH four times daily, to maintain with stable pH. The medium was replaced with PBS at the same pH containing Na<sup>+</sup> and 0.1  $\mu$ Ci of L-[<sup>14</sup>C]-ascorbic acid or <sup>18</sup>F-DFA synthesized in the above step. After incubation at 37°C for 30 min, the medium was aspirated and the cells were washed three times with 1 ml of ice-cold PBS. Then 350  $\mu$ l of 1 N NaOH was used to lyse the cells and the lysed cell samples were collected and counted by MicroBeta2 liquid Scintillation detector (PerkinElmer) or 2480 WIZARD2  $\gamma$ -counter (PerkinElmer). One hundred microliters of the cell lysate was used for determination of the protein concentration by modified Lowry protein assay (Thermo Scientific). Finally, the uptake results were normalized as counts per minute (CPM) in relation to 100  $\mu$ g of protein content.

## Animal Experiments

*In vivo* animal studies were approved by the Ethics Committee of Animal Experiments of the First Affiliated Hospital of Sun Yat-sen University and performed strictly according to the Guide for the Care and Use of Laboratory Animals of the Ministry of Science and Technology of the People's Republic of China.

All experimental mice were raised in a sterile environment with a normal light/dark circadian rhythm and access to food and water *ad libitum*. The 4–6 weeks old male BALB/c nude mice (n = 36) were prepared from Nanjing Biomedical Research Institute of Nanjing University (Nanjing, China). Tumor sizes were measured every 3 days with Vernier caliper. Treatment was carried out when the xenografts reached a longest diameter of approximately 6 mm. PCa bearing mice were treated with the following: placebo, AA, bicarbonate, or the combination of AA and bicarbonate. Bicarbonate was provided by Aladdin (Shanghai, China). The AA dose for therapy was 4 g/kg injected intraperitoneally twice daily. Bicarbonate therapy was performed by providing daily 200 mmol/L NaHCO<sub>3</sub> aqueous solution *ad libitum*. All the mice were sacrificed at 2-weeks post initiation of therapy.

## Microdialysis

Two weeks after therapy, microdialysis was performed to evaluate the acidity of the tumor extracellular fluids. Mice bearing the DU145 xenografts were supplied with normal drinking water or bicarbonate water, respectively. Mice were immobilized, the skin was incised, and a trocar was inserted into

the tumor. Then, a probe connected to a syringe pump (BASi, Lafayette, IN, USA) was inserted and 100  $\mu$ l microdialysis solution was collected into a 2 ml centrifuge tube. The pH of microdialysis solution was measured with pH paper (MACHEREY-NAGEL GmbH & Co., Dueren, Germany).

## PET/CT Imaging and Data Analysis

<sup>18</sup>F-DFA (see above for synthesis) was intravenously injected (100  $\mu$ l) at an activity dose of 3.7 MBq per mouse with PC3 xenograft, 1 day before and 3 days after NaHCO<sub>3</sub> treatment. Imaging was performed using an Inveon micro-PET/CT system (Siemens, Munich, Germany), 45 min after initiation of tracer injection. Mice were imaged for a 15 min static acquisition. Tumor-to-background ratios (TBR) were obtained to calculate the <sup>18</sup>F-DFA uptake in tumors. The three-dimensional regions of interest (ROI) were located manually in the area with the highest tracer activity of tumors. The TBR was calculated using the formula: mean <sup>18</sup>F-DFA uptake of tumor/that of the muscle. The PET/CT scan and data analysis were performed according to the reference (He et al., 2019).

## Statistical Analysis

For all analyses, significance was determined at  $p < 0.05$ . \*, \*\*, \*\*\*, or \*\*\*\* representing significance between exposure conditions. All data was tested for normal distribution, and the data consistent with normal distribution was analyzed using parametric tests (independent sample *t*-test), otherwise non-parametric test (*Mann-Whitney test*) was used. All analyses were performed in GraphPad Prism 8.0 (GraphPad Software, Inc., La Jolla, CA, USA). Data were expressed as mean  $\pm$  SD. For each experiment, n represented the number of individual biological replicates. For each biological replicate, n  $\geq$  3 technical replicates were performed for all *in vitro* and *in vivo* studies.

## RESULTS

### The Cytotoxicity of AA on Prostatic Cancer Cells Decreased With Increasing Acidity in the Cell Culture Medium

Extracellular pH regulator such as proton pump inhibitors was reported to supply the anticancer effect in melanoma cells (Lugini et al., 2016). To test whether the extracellular pH could affect the anticancer effect of AA on PCa cells, we treated PC3 and DU145 cells with AA under different pH values. WST-8 assay demonstrated that both PC3 and DU145 cells showed increased sensitivity to AA treatment in cell culture medium with neutral to alkaline pH (pH ranges from 7.0 to 8.0), but not in acidic culture medium (pH = 6.0) after 6 h treatment. The inhibition of cell viability of PC3 and DU145 cells by AA was concentration dependent with a maximum effect at 16 mM AA and pH 7.5. In contrast, acidic pH (6.0) improved the viability of PC3 cells, although they were treated with AA as well (**Figure 2A**). A lowest concentration for 50% inhibition was 2.07 mM for PC3 with pH 7.0 and 4.03 mM for DU145 with pH 7.5,

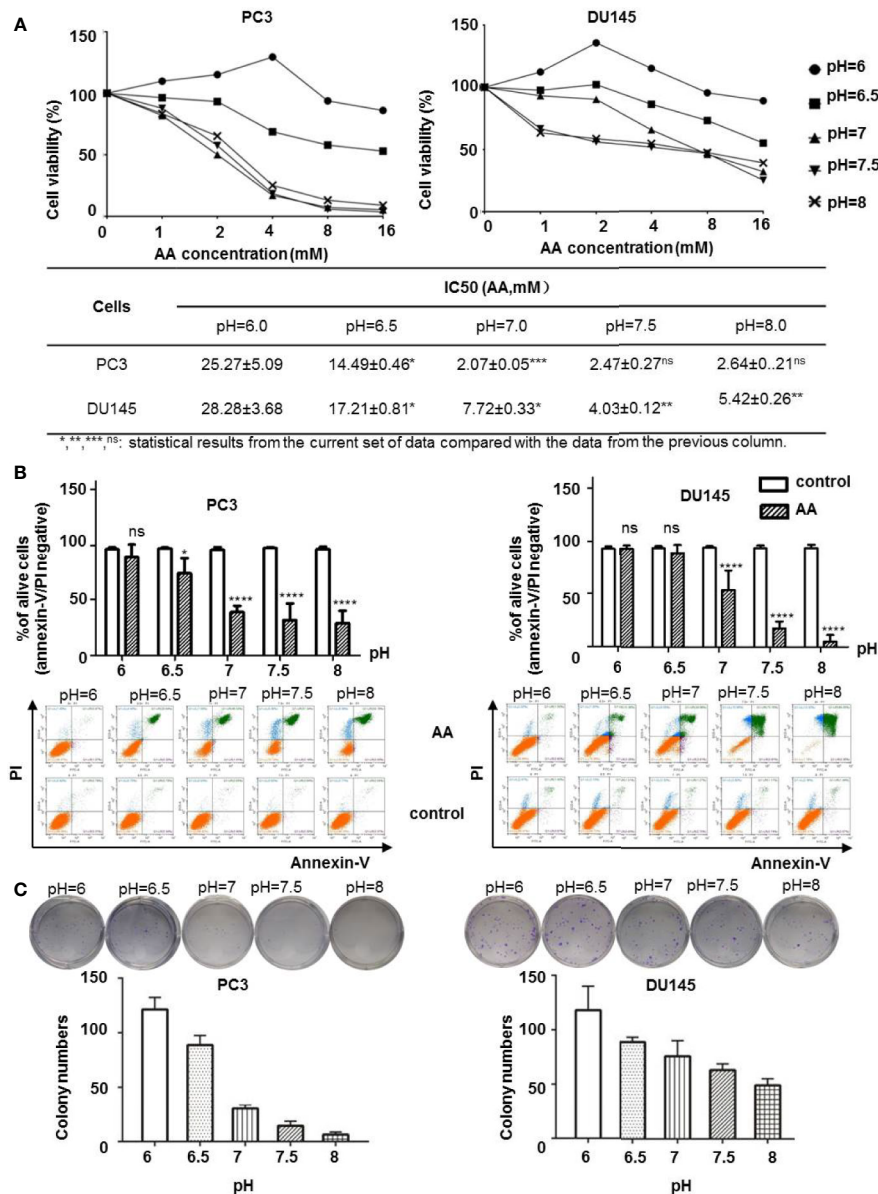


**FIGURE 2** | AA inhibits cell proliferation and induces apoptotic cell death in cancer cells in a pH dependent manner *in vitro*.  $5 \times 10^3$  PC3 or DU145 cells per well (96-well plate) were incubated at 37°C with different concentrations of AA for 2 h: **(A)** Cell viability assessed by WST-8 assay; **(B)** Apoptotic cell death on PCa cells upon AA treatment assessed by flow cytometry for Annexin V positivity; **(C)** Clonogenic Assay on cell proliferation. Two hundred cells in each sample were seeded into six-well plates. The bars represent the mean and SD of the mean,  $n = 3$  (\*, \*\*, \*\*\*, <sup>ns</sup>: statistical results from the current set of data compared with the data from the previous column.  $p < 0.05$ : \*,  $<0.01$ : \*\*,  $<0.001$ : \*\*\* or not significant: <sup>ns</sup>).

respectively. No inhibitory effect was observed at pH 6.0. For DU145 cells, the IC<sub>50</sub> of AA increased to 4.03 mM at pH 7.5 and 28.28 mM at pH 6.0 (Figure 2A). Flow cytometric analysis revealed that AA induced apoptotic cell death as shown by a significant increase of annexin V/PI positive cells as well as a marked decrease in the number of live, annexin V/PI negative cells as observed with an increasing pH from 6.0 to 8.0 in both PC3 and DU145 cells. After 6 h of treatment with 8 mM AA,

59.8% dead PC3 cells and 84.55% dead DU145 cells were detected at pH 8.0, in contrast to 0.9% dead PC3 cells and 1.5% dead DU145 cells at pH 6.0. (Figure 2B and Supplementary Figure 1). Likewise, results of clonogenic assays showed that the cytotoxic effect of AA on both PC3 and DU145 cells was dependent on the pH (Figure 2C, original images in Supplementary Figure 2), and alkaline pH in the culture medium could promote the cytotoxicity of AA.

## AA but Not DHA, Enhanced the Anticancer Effect in PCa Cells Through Induction of Cellular ROS

AA was reported as an important effector of ROS production, which also depends on pH (Teixeira et al., 2018). Induction of ROS generation has turned out to be an effective strategy for the treatment of human PCa (Zhang et al., 2015). In this study, we assessed the cellular ROS content after the addition of 4 mM AA for 2 h. Compared with incubation of PCa cells in acidic culture

medium (pH = 6.0), ROS content increased from 12.71 to 101.55% in DU145 cells and from 20.34 to 166.13% in PC3 cells if the pH was increased from 6.0 to 8.0 (Figure 3A). Then, we compared the cytotoxic effect of AA and DHA. The results demonstrated that AA, but not DHA, exerted the pH dependent cytotoxicity on PCa cells (Figure 3B).

Redox imbalance in tumors may arise from a variety of sources, including mitochondrial or NADPH oxidase-derived reactive oxygen species (Meitzler et al., 2014). We further investigated the

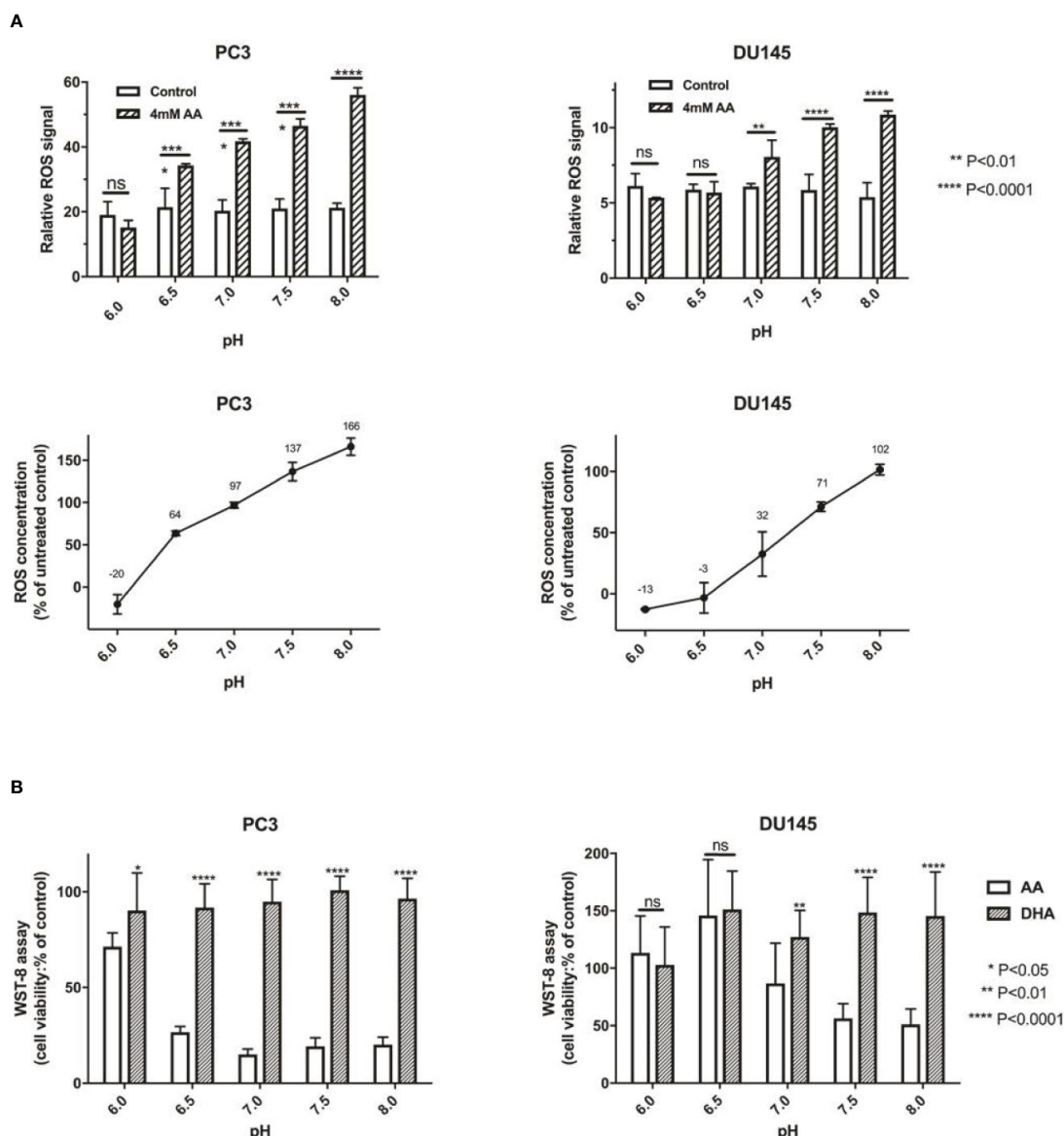


**FIGURE 3** | The pH is an important influencing factor of treatment using AA, but not DHA (the oxidative form of AA). **(A)**  $5 \times 10^3$  PCa cells per well (96-well plates) were incubated at 37°C under 4 mM AA in cell culture medium with different pH for 2 h; ROS was then detected 1 h after addition of ROS detection reagent solution diluted in cell culture medium. Relative ROS of controls are defined as 100%, and change of ROS compared with controls are shown, incubated under different pH (left: PC3 and right: DU145 cells); **(B)**  $5 \times 10^3$  PCa cells per well (96-well plate) were seeded in cell culture medium with different pH (ranging from pH 6.0 to 8.0) and treated under AA with or without ascorbate oxidase (1 U/well) for 2 h. Then cell viability was analyzed using the WST-8 assay; (left: PC3 and right: DU145 cells). The bars represent the mean and SD of the mean,  $n = 3$ .  $p < 0.05$ : \*,  $p < 0.01$ : \*\*,  $p < 0.001$ : \*\*\*,  $p < 0.0001$ : \*\*\*\* or not significant: ns.



relationship between cellular NADPH and the pH of culture medium. After the addition of AA for 2 h, the amount of cellular NADPH decreased along with the elevation of pH from 6.0 to 8.0 in both PC3 and DU145 cells (Supplementary Figure 3).

### Combination of AA and NaHCO<sub>3</sub> Significantly Inhibited the Growth of PCa Xenografts

The above *in vitro* study showed that the extracellular pH played an important role in AA treatment of tumor. We further investigated the effect of pH on tumor treatment with AA *in vivo*. The tumor pH was adjusted by using NaHCO<sub>3</sub>. Following inoculation of DU145 tumor cells, the tumor volume of the DU145 xenografts increased from 111.1 mm<sup>3</sup> (SD = 24.6, n = 5) to 827.2 mm<sup>3</sup> (SD = 256.3, n = 5) in the control animals that received no treatment (Figure 4A). The tumor volume reached 634.3 mm<sup>3</sup> (SD = 240.6, n = 5, p = 0.25) in the animals treated with NaHCO<sub>3</sub> aqueous solution. The tumor volume reached 608.6 mm<sup>3</sup> (SD = 144.5, n = 5, p = 0.14) in animals treated with 4 g/kg AA twice daily, and 354.5 mm<sup>3</sup> (SD = 111.6, n = 5, p = 0.005) that received a combined treatment with 200 mM NaHCO<sub>3</sub> in the drinking water plus intraperitoneal injection of 4 g/kg AA twice daily, as observed 12 days after therapy initiation, respectively (Figure 4A). Additionally, we detected the pH of the tumoral extracellular fluids using microdialysis. Our results showed the acidic tumor microenvironment was almost neutralized by NaHCO<sub>3</sub> alkaline solution (pH increased from 6.59 ± 0.04 to 6.9 ± 0.1, P < 0.01, Figure 4B). These results indicated that combination of AA and NaHCO<sub>3</sub> significantly suppressed tumor growth most likely due to the reducing acidity of tumor extracellular microenvironment. DU145 tumor bearing mice were anatomized after sacrifice. No side effects from normal organs or overall health of the mice were found after two weeks treatment with AA (4 g/kg twice daily) and/or bicarbonate (200 mmol/L NaHCO<sub>3</sub> aqueous solution *ad libitum* daily).

### NaHCO<sub>3</sub> Increased the pH of Extracellular Environment in PCa Xenografts That Improved the Cellular Uptake and the Cytotoxicity of AA in PCa Cells *In Vitro* and *In Vivo*

The above results showed that combined treatment with AA and NaHCO<sub>3</sub> induced a significantly increased inhibition of DU145 tumor growth by regulating tumoral extracellular pH. We further explored the mechanisms of how the pH of extracellular environment influenced the anticancer effect of AA on PC3 xenografts. The results illustrated that in control animals that received no treatment following inoculation of PC3 tumor cells, the tumor volume of the PC3 xenografts increased from 61.0 mm<sup>3</sup> (SD = 6.5, n = 5) to 868.2 mm<sup>3</sup> (SD = 261.5, n = 5). The administration of both 200 mM NaHCO<sub>3</sub> in the drinking water and intraperitoneal injection of with 4 g/kg AA twice daily significantly suppressed tumor growth as observed from the prolongation of the tumor growth of PC3 xenografts to 243.2 mm<sup>3</sup> (SD = 43.4, n = 5), compared to 868.2 mm<sup>3</sup> (SD = 261.5, n = 5) of untreated controls (p = 0.02) 12 days after therapy initiation (Figure 5A). There was no significant inhibition of tumor growth under AA treatment (p = 0.13). In order to understand the mechanisms of extracellular pH that affect the anticancer effect of AA, we examined the expression of GLUT1 and SVCT2 as AA transporters. Western blot analysis showed, except SVCT2 expression in DU145 cells, no significant difference in SVCT2 and GLUT1 expression with respect to different pH (Figure 5B, original images in Supplementary Figure 4). These results demonstrated that pH regulated AA toxicity, did not through changing expression of AA transporters. Furthermore, we analyzed the uptake of L-[<sup>14</sup>C]-ascorbic acid and <sup>18</sup>F-DFA with the addition of glutathione (GSH) in the culture medium, to reduce the oxidative effect on AA (Figure 5C). In comparison with cells incubated in neutral to alkaline medium (pH from 7.0 to 7.5), a significant reduction of AA uptake had been observed in acidic pH (6.5) (Figure 5C).

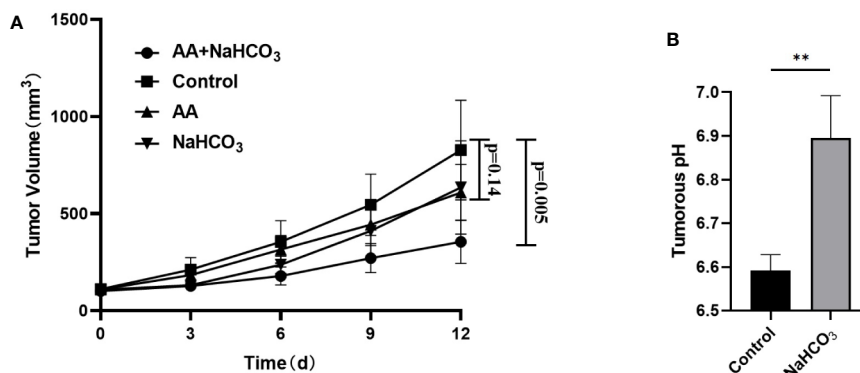


**FIGURE 4** | NaHCO<sub>3</sub> improves the therapeutic effect of AA and significantly inhibits the tumor growth of DU145 xenografts.  $5 \times 10^6$  DU145 cells were subcutaneously injected in to 4–6 weeks old male BALB/c mice. Treatment was carried out when the xenografts reached a longest diameter of approximately 5 mm. Mice were treated with AA (4 g/kg intraperitoneally injected twice daily), NaHCO<sub>3</sub> (200 mmol/L drink water daily) alone or in combination with AA. Animals were monitored for tumor growth until day 12. Then, mice were sacrificed to explant tumors for microdialysis analysis: **(A)** Tumor growth measurements. **(B)** Tumors were obtained 2 weeks after initiation of treatment. The bars represent the mean and SD of the mean, n = 5. p < 0.01: \*\*.



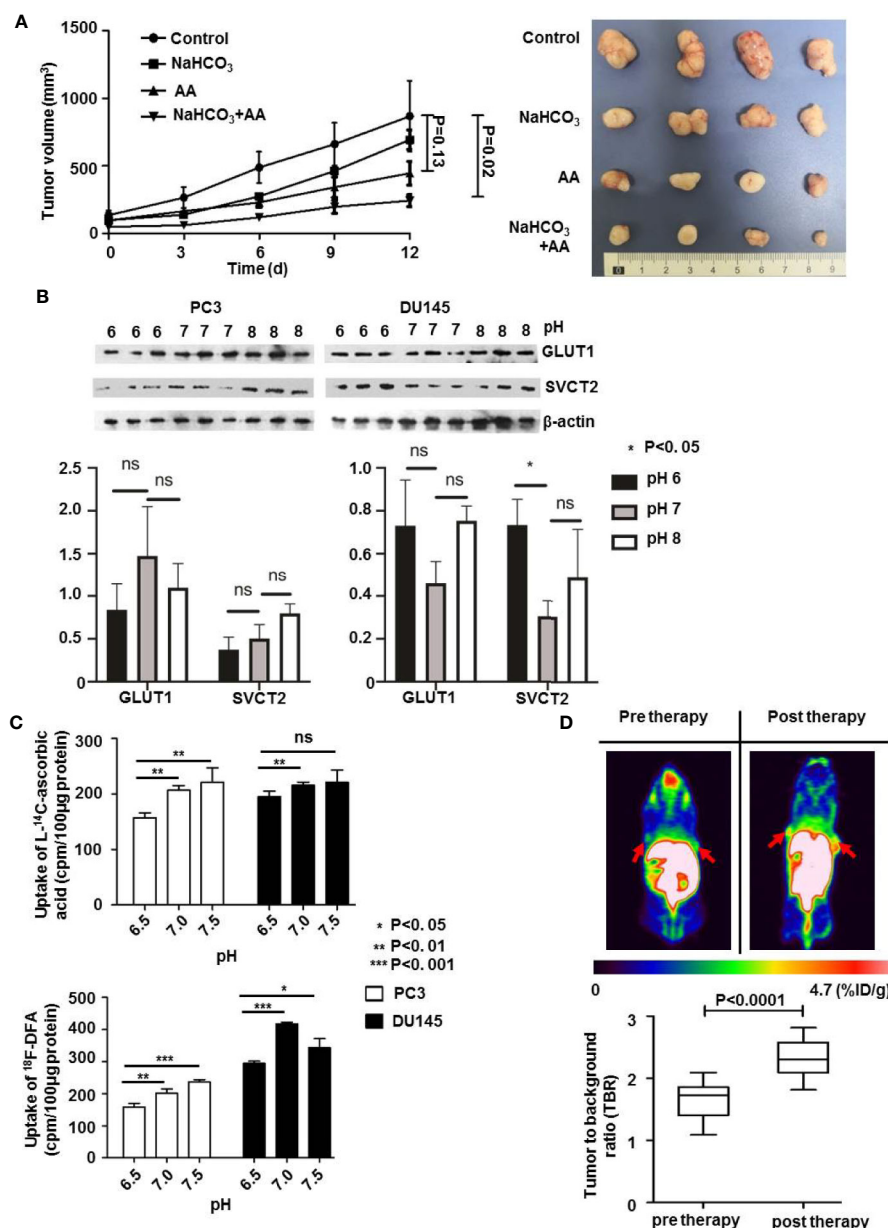


**FIGURE 5** | The pH value affects the therapeutic effect of AA on PC3 tumors through regulation of cellular AA uptake *in vitro* and *in vivo*.  $3 \times 10^5$  PC3 cells were subcutaneously injected into the 4–6 weeks old male Blb/c mice. Treatment was carried out when the xenografts reached a longest diameter of approximately 5 mm. Animals were monitored for tumor growth until day 12. **(A)** Tumor growth measurements (left panel) and tumor were obtained 2 weeks after initiation of treatment (right panel). **(B)** PC3 and DU145 PCa cells were incubated in cell culture medium with pH 6.0, pH 7.0, and pH 8.0, for 16 h and then lysed for Western blot assay. **(C)** After pretreatment of PC3 and DU145 PCa cells with glutathione (GSH) for 24 h, cells were incubated for another 30 min with 4 mM AA in the cell culture medium. Then uptake of L-[<sup>14</sup>C]-ascorbic acid (upper panel) and <sup>18</sup>F-DFA (lower panel) was analyzed. **(D)** <sup>18</sup>F-DFA PET imaging was done 1 day before and 3 days after NaHCO<sub>3</sub> initiation, tracer uptake was calculated with TBR. The bars represent the mean and SD of the mean, n = 5. p < 0.05: \*, <0.01: \*\*, <0.001: \*\*\* or not significant: ns.

Additionally, **Figure 5C** showed that the highest reduction of L-[<sup>14</sup>C]-ascorbic acid uptake was at pH = 7.5. And cellular uptake increased along with increasing of pH from 6.5 to 7.5. Regarding <sup>18</sup>F-DFA uptake and L-[<sup>14</sup>C]-ascorbic acid uptake in PCa cells, similar results were obtained (**Figure 5C**). In the end, we performed small-animal PET imaging to observe the relationship between tumoral <sup>18</sup>F-DFA uptake and NaHCO<sub>3</sub> treatment in PC3

xenografts. Results illustrated that tracer uptake of <sup>18</sup>F-DFA in PC3 tumors was significantly increased two days after NaHCO<sub>3</sub> treatment in comparison with that before treatment. The TBR of <sup>18</sup>F-DFA in PC3 xenografts increased from  $1.65 \pm 0.30$  to  $2.32 \pm 0.30$  ( $P < 0.0001$ ) (**Figure 5D**). PC3 tumor bearing mice were anatomized after sacrifice. No side effects from normal organs or overall health of the mice were found 2 weeks after treatment with

AA (4 g/kg twice daily) and/or bicarbonate (200 mmol/L NaHCO<sub>3</sub> aqueous solution *ad libitum* daily).

## DISCUSSION

The ability of cancer cells to develop resistance to different drugs, known as multiple drug resistance (MDR), remains the key impediment to the successful chemotherapy (Ouar et al., 1999). The mechanism of drug resistance is not clear yet, which may include neutralization of drugs in acidic organelles or extracellular environment, or increasing drug excretion from cells through secretory pathways (Raghunand et al., 1999b; Federici et al., 2014). More and more evidence showed that the change of pH in tumor cells was associated with drug resistance (Taylor et al., 2015). Previous studies have shown that the extracellular pH of malignant solid tumor tissue is acidic, which is between 6.5 and 6.9, while the extracellular pH of normal tissue is mild alkaline, ranging from 7.2 to 7.5 (Vaupel et al., 1989; Griffiths, 1991). In our study, the acidic microenvironment in the tumor has been improved (rise from 6.6 to nearly 6.9) after NaHCO<sub>3</sub> treatment. Therefore, improving the acidic microenvironment in tumors and changing the pH in malignant solid tumors may be a promising anti-tumor strategy. It was demonstrated that oral bicarbonate in mouse models of breast and prostate cancer led to significantly decreased primary tumor activity and the incidence of metastases (Robey et al., 2009).

Previous studies (Creagan et al., 1979; Verrax and Calderon, 2009) have demonstrated that the anticancer effect of AA *in vivo* could not be compared to that *in vitro*. However, studies (Liang et al., 2001; Ormazabal et al., 2010) have reported that the pH can modulate functional activity of the transporter proteins (SVCT1 and SVCT2) involved in cellular transportation of AA. In this study, we observed that with the increase of pH, the effect of AA on PCa cells could be enhanced. The results showed that AA treatment induced a pH dependent cell apoptosis through generation of ROS, accompanied by the reduction of NADPH *in vitro*. Excessive ROS will make the level of redox stress exceed the threshold, which will deplete the antioxidant capacity of cells and lead to apoptosis (Fruehauf and Meyskens, 2007; Gorrini et al., 2013). In addition, studies have shown that membrane translocation of vitamin C transporters (SVCT2, et al.) in tumor cells may occur, resulting in an increase in the efficiency of vitamin C transport into cells (Wu et al., 2007; Acuña et al., 2013). Our study showed cellular uptake of AA increased in the treatment with alkalic pH, but expression of AA transporters such as SVCT2 or GLUT1 was not changed after 16 h incubation under different pH, demonstrating that pH regulates AA toxicity, however does not through changing expression of AA transporters. Moreover, results obtained from L-[<sup>14</sup>C]-ascorbic acid and <sup>18</sup>F-DFA uptake assay in PC3 and DU145 PCa cells demonstrated that cellular uptake of AA increased with the increasing pH from 6.5 to 7.5. Therefore, this study demonstrated that the pH of cell culture medium regulated the cellular uptake of AA in PCa cells, thereby promoting a stronger anticancer effect of AA on PCa cells.

In 1972, Cameron and Rotman (Cameron and Rotman, 1972) first reported the anticancer effect of AA, but the potential mechanism about its cancer cell-selective toxicity is not completely understood. Recently, a preclinical study (Yun et al., 2015) reported that cancer cell-selective toxicity of AA in colorectal cancer with KRAS and BRAF mutation could be enhanced by induction of GLUT-mediated cellular uptake of DHA. However, another research demonstrated (Schoenfeld et al., 2017) that GLUT-mediated DHA uptake played a minimal role in AA toxicity in H292 or H1292 NSCLC cells. Studies (Liou et al., 2016; Cho et al., 2020) also confirmed that AA instead of DHA played a key role in killing cancer cells and explained that SVCT2, not GLUT1, dominated the transport of AA into cells. Consistent with these reports, our findings showed that DHA treatment did not have significant anticancer effect on PC3 or DU145 cancer cells. Moreover, the cancer cell-selective toxicity of AA was improved along with an increase of the pH in the culture media of PC3 and DU145 cells. Our results also showed that the cancer cell-selective toxicity of AA was dependent on ROS, which is consistent with an increase of the mitochondrial-derived ROS in KRAS and BRAF mutant cells (Corazao-Rozas et al., 2013; Liou et al., 2016; Schoenfeld et al., 2017).

Additionally, <sup>18</sup>F-DFA PET/CT imaging illustrated a significant increase in tumor uptake of AA analogues after 2 days of NaHCO<sub>3</sub> administration. Whereas, there was no significant difference in the tumor volume of mice under different treatment strategies in such a short time. Moreover, it takes more than a week before significant changes in tumor size were observed. Therefore, <sup>18</sup>F-DFA PET/CT imaging could specifically detect the increased uptake of AA analogues by tumor cells due to the alkalization of tumor microenvironment. It would be interesting to further explore the role of <sup>18</sup>F-DFA PET/CT in the prediction of the therapeutic effect and prognosis of AA in the treatment of tumors.

## CONCLUSIONS

Our results demonstrate that AA but not DHA enhances PCa cell death through generation of ROS. Alkalinized tumor microenvironment can enhance the uptake of AA by PCa cells, thus enhancing the cytotoxic activity of pharmacological ascorbic acid on tumor cells in both *in vitro* and *in vivo*. This study provides new insights into the anticancer treatment using non-toxic agent and our findings suggest that extracellular pH could be important in anticancer therapy. Because of the predictive ability on therapeutic response of PCa to AA treatment, <sup>18</sup>F-DFA might be a potential PET tracer in cancer diagnosis and treatment.

## DATA AVAILABILITY STATEMENT

The raw data supporting the conclusions of this article will be made available by the authors, without undue reservation, to any qualified researcher.

## ETHICS STATEMENT

The animal study was reviewed and approved by The Ethics Committee of Animal Experiments of the First Affiliated Hospital of Sun Yat-sen University.

## AUTHOR CONTRIBUTIONS

Conceptualization: ZL and XZ. Methodology: ZL, PH, GL, XS, GY, and XZ. Validation: ZL, PH, GL, YZ, and XZ. Formal analysis: ZL, GL, PH, XZ, and ZZ. Investigation: ZL, GL, PH, XS, YW, and YL. Writing—original draft preparation: ZL, GL, XS, and XZ. Writing—review and editing: ZL, GL, PH, CS, AG, XS, GY, YL, YZ, DY, and XZ. Visualization: ZL, PH, CS, GY, and XZ. Supervision: ZL and XZ. Funding acquisition: XZ, DY, ZL, BZ, YZ, and PH. ZL, PH, and GL contributed equally to this work. All authors contributed to the article and approved the submitted version.

## FUNDING

This research was funded by the Science and Technology Planning Project of Guangdong Province (grant number 2017B020210001), the Training program of the Major Research Plan of Sun Yat-Sen University (grant number 17ykjc10), the Science and Technology Program of Guangzhou (grant number 201707010110), the Science and Technology Program of Guangzhou (grant number 201607010353), Young teacher training program of Sun Yat sen University (grant number 19ykpy55), the National Science Foundation for Young Scientists of China (grant numbers 81901793 and 81602701), the Bureau of Science & Technology and Intellectual Property Nanchong City (grant numbers 19SXHZ0263 and 18SXHZ0385). These Funding programs have finically supported our study and contributions from XZ, DY, ZL, BZ, YZ, and PH.

## ACKNOWLEDGMENTS

We are grateful to all members of XZ group for contributions to this project. We thank Qiao Su, Wuguo Li, and all members from animal care facility at the First Affiliated Hospital of Sun Yat-Sen

University for animal management. We thank Yali Tang, Tong Zhang, and Qingqiang Tu from core facility for research equipment at Sun Yat-Sen University for technical supporting with FACS analysis, microdialysis, respectively.

## SUPPLEMENTARY MATERIAL

The Supplementary Material for this article can be found online at: <https://www.frontiersin.org/articles/10.3389/fphar.2020.570939/full#supplementary-material>

### NADPH Assay

NADPH assay was carried out according to the manufacturer's instruction (BioAssay Systems, Hayward, CA, USA). PCa cells ( $4 \times 10^5$ /well in six-well plates) were incubated 1 h at 37°C with 2 mM AA in a pH gradient from 6.0 to 8.0 for cell culture. Cells were washed twice with ice-cold PBS and detached with a 0.05% trypsin/EDTA solution and centrifuged with 1,500 r/min for 5min and discarded the supernatant.

### SUPPLEMENTARY FIGURE 1 | Analysis of AA treatment induced cell death.

PCa cells ( $4 \times 10^5$ /well) were seeded into six-well plates and incubated with AA (0 and 4 mM) at 37°C under AA treatment for 6 h. Cell culture media were prepared at different pH (6.0, 6.5, 7.0, 7.5, and 8.0), then adjusted using HCl and NaOH). Annexin V+ (all apoptotic cells), Annexin V+ PI+ (late apoptotic cells), and only PI+ (original necrotic cells) populations. The bars represent the mean and SD of the mean,  $n = 3$ .

### SUPPLEMENTARY FIGURE 2 | Original images of clonogenic assay.

After treatment with AA (4 mM) for 6 h, 200 cells in each sample were seeded into six-well plates. Following incubation in a 5% CO<sub>2</sub> environment at 37°C for 2 weeks, colonies were fixed with 100% Methanol for 20 min, stained with crystal violet (Beyotime, Shanghai, China) for 5 min, dried overnight, and colonies were counted under Olympus BX51 microscope. Images were set up using camera. (A) PC3, (B) DU145.

**SUPPLEMENTARY FIGURE 3 |** pH is an important influencing factor of AA treatment and cellular activity of NADPH.  $5 \times 10^3$  PCa cells per well (96-well plates) were incubated at 37°C under 4 mM AA in cell culture medium with different pH for 2 h, NADPH activity was then detected 30 min after addition of NADPH detection reagent solution into cell culture medium (left: PC3 and right: DU145 cells). The bars represent the mean and SD of the mean,  $n = 3$ .

### SUPPLEMENTARY FIGURE 4 | Original images of western blot.

For immunoblotting, 30 µg protein per lane was separated on 8% gradient readymade SDS-Gel and transferred to a polyvinylidene difluoride membrane. Then the membrane was cut off to 3 pieces for developing of GLUT1 (between 75 and 50 kDa), SVCT2 (over 75 kDa) and β-actin (between 50 and 37 kDa), respectively. The primary antibodies, including anti-GLUT1 and anti-SVCT2 were diluted to 1:1,000 into blocking buffer and incubated at 4°C overnight. Then the membranes were washed, and incubated with secondary antibody. Blots were developed using Pierce Fast Western Blot Kit and exposed to film.

## REFERENCES

- Acuña, A. I., Esparza, M., Kramm, C., Beltrán, F. A., Parra, A. V., Cepeda, C., et al. (2013). A failure in energy metabolism and antioxidant uptake precede symptoms of Huntington's disease in mice. *Nat. Commun.* 4 (1), 2917. doi: 10.1038/ncomms3917
- Anderson, M., Moshnikova, A., Engelman, D. M., Reshetnyak, Y. K., and Andreev, O. A. (2016). Probe for the measurement of cell surface pH in vivo and ex vivo. *Natl. Acad. Sci. U. S. A.* 113 (29), 8177–8181. doi: 10.1073/pnas.1608247113
- Cameron, E., and Rotman, D. (1972). Ascorbic acid, cell proliferation, and cancer. *Lancet* 1 (7749), 542. doi: 10.1016/s0140-6736(72)90215-2

- Chen, Q., Espey, M. G., Krishna, M. C., Mitchell, J. B., Corpe, C. P., Buettner, G. R., et al. (2005). Pharmacologic Ascorbic Acid Concentrations Selectively Kill Cancer Cells: Action as a Pro-Drug to Deliver Hydrogen Peroxide to Tissues. *Natl. Acad. Sci. U. S. A.* 102 (38), 13604–13609. doi: 10.1073/pnas.0506390102
- Chen, Q., Espey, M. G., Sun, A. Y., Pooput, C., Kirk, K. L., Krishna, M. C., et al. (2008). Pharmacologic doses of ascorbate act as a prooxidant and decrease growth of aggressive tumor xenografts in mice. *Natl. Acad. Sci. U. S. A.* 105 (32), 11105–11109. doi: 10.1073/pnas.0804226105
- Cho, S., Chae, J. S., Shin, H., Shin, Y., Kim, Y., Kil, E., et al. (2020). Enhanced Anticancer Effect of Adding Magnesium to Vitamin C Therapy: Inhibition of

- Hormetic Response by SVCT-2 Activation. *Transl. Oncol.* 13 (2), 401–409. doi: 10.1016/j.tranon.2019.10.017
- Circu, M. L., and Aw, T. Y. (2010). Reactive oxygen species, cellular redox systems, and apoptosis. *Free Radical Bio Med.* 48 (6), 749–762. doi: 10.1016/j.freeradbiomed.2009.12.022
- Corazao-Rozas, P., Guerreschi, P., Jendoubi, M., André, F., Jonneaux, A., Scalbert, C., et al. (2013). Mitochondrial oxidative stress is the Achilles's heel of melanoma cells resistant to Braf-mutant inhibitor. *Oncotarget* 4 (11), 1986–1998. doi: 10.18632/oncotarget.1420
- Creagan, E. T., Moertel, C. G., O'Fallon, J. R., Schutt, A. J., O'Connell, M. J., Rubin, J., et al. (1979). Failure of high-dose(ascorbic acid) therapy to benefit patients with advanced cancer. *A Controlled trial. N. Engl. J. Med.* 301 (13), 687–690. doi: 10.1056/NEJM197909273011303
- Du, J., Martin, S. M., Levine, M., Wagner, B. A., Buettner, G. R., Wang, S., et al. (2010). Mechanisms of ascorbate-induced cytotoxicity in pancreatic cancer. *Clin. Cancer Res.* 16 (2), 509–520. doi: 10.1158/1078-0432.CCR-09-1713
- Effert, P., Beniers, A. J., Tamimi, Y., Handt, S., and Jakse, G. (2004). Expression of Glucose Transporter 1 (Glut-1) in Cell Lines and Clinical Specimens from Human Prostate Adenocarcinoma. *Anticancer Res.* 24 (5A), 3057. <http://ar.iijournals.org/content/24/5A/3057.long>
- Federici, C., Petrucci, F., Caimi, S., Cesolini, A., Logozzi, M., Borghi, M., et al. (2014). Exosome Release and Low pH Belong to a Framework of Resistance of Human Melanoma Cells to Cisplatin. *PLoS One* 9 (2), e88193. doi: 10.1371/journal.pone.0088193
- Flavell, R. R., Truillet, C., Regan, M. K., Ganguly, T., Blecha, J. E., Kurhanewicz, J., et al. (2016). Caged (18)F]FDG Glycosylamines for Imaging Acidic Tumor Microenvironments Using Positron Emission Tomography. *Bioconjug. Chem.* 27 (1), 170–178. doi: 10.1021/acs.bioconjchem.5b00584
- Fruehauf, J. P., and Meyskens, F. L. (2007). Reactive Oxygen Species: A Breath of Life or Death? *Clin. Cancer Res.* 13 (3), 789–794. doi: 10.1158/1078-0432.CCR-06-2082
- Gan, L., Camarena, V., Mustafi, S., and Wang, G. (2019). Vitamin C Inhibits Triple-Negative Breast Cancer Metastasis by Affecting the Expression of YAP1 and Synaptopodin 2. *Nutrients* 11 (12), 2997. doi: 10.3390/nu11122997
- Godoy, A., Ormazabal, V., Moraga-Cid, G., Zúñiga, F. A., Sotomayor, P., Barra, V., et al. (2007). Mechanistic insights and functional determinants of the transport cycle of the ascorbic acid transporter SVCT2. Activation by sodium and absolute dependence on bivalent cations. *J. Biol. Chem.* 282 (1), 615–624. doi: 10.1074/jbc.M608300200
- Gorrini, C., Harris, I. S., and Mak, T. W. (2013). Modulation of oxidative stress as an anticancer strategy. *Nat. Rev. Drug Discovery* 12 (12), 931–947. doi: 10.1038/nrd4002
- Griffiths, J. R. (1991). Are cancer cells acidic? *Brit. J. Cancer* 64 (3), 425–427. doi: 10.1038/bjc.1991.326
- Hahn, E., Jin, D., Kang, J. S., Kim, Y., Hong, S., Lee, S. K., et al. (2007). The molecular mechanisms of vitamin C on cell cycle regulation in B16F10 murine melanoma. *J. Cell Biochem.* 102 (4), 1002–1010. doi: 10.1002/jcb.21336
- He, Q., Zhang, L., Zhang, B., Shi, X., Yi, C., and Zhang, X. (2019). Diagnostic accuracy of 13N-ammonia PET, 11C-methionine PET and 18F-fluorodeoxyglucose PET: a comparative study in patients with suspected cerebral glioma. *BMC Cancer* 19 (1), 198–199. doi: 10.1186/s12885-019-5560-1
- Hickman, J. A., Graeser, R., de Hoogt, R., Vidic, S., Brito, C., Gutekunst, M., et al. (2014). Three-dimensional models of cancer for pharmacology and cancer cell biology: capturing tumor complexity in vitro/ex vivo. *Biotechnol. J.* 9 (9), 1115–1128. doi: 10.1002/biot.201300492
- Jacobs, C., Hutton, B., Ng, T., Shorr, R., and Clemons, M. (2015). Is there a role for oral or intravenous ascorbate (vitamin C) in treating patients with cancer? A systematic review. *Oncologist* 20 (2), 210–223. doi: 10.1634/theoncologist.2014-0381
- Liang, W. J., Johnson, D., and Jarvis, S. M. (2001). Vitamin C transport systems of mammalian cells. *Mol. Membr. Biol.* 18 (1), 87–95. doi: 10.1080/09687680110033774
- Lim, J. Y., Kim, D., Kim, B. R., Jun, J. S., Yeom, J. S., Park, J. S., et al. (2016). Vitamin C induces apoptosis in AGS cells via production of ROS of mitochondria. *Oncol. Lett.* 12 (5), 4270–4276. doi: 10.3892/ol.2016.5212
- Liou, G., Döppler, H., DelGiorno, K. E., Zhang, L., Leitges, M., Crawford, H. C., et al. (2016). Mutant KRas-Induced Mitochondrial Oxidative Stress in Acinar Cells Upregulates EGFR Signaling to Drive Formation of Pancreatic Precancerous Lesions. *Cell Rep.* 14 (10), 2325–2336. doi: 10.1016/j.celrep.2016.02.029
- Lugini, L., Federici, C., Borghi, M., Azzarito, T., Marino, M. L., Cesolini, A., et al. (2016). Proton pump inhibitors while belonging to the same family of generic drugs show different anti-tumor effect. *J. Enzym. Inhib. Med. Ch.* 31 (4), 538–545. doi: 10.3109/14756366.2015.1046062
- Maramag, C., Menon, M., Balaji, K. C., Reddy, P. G., and Laxmanan, S. (1997). Effect of vitamin C on prostate cancer cells in vitro: effect on cell number, viability, and DNA synthesis. *Prostate* 32 (3), 188–195. doi: 10.1002/(sici)1097-0045(19970801)32:3<188::aid-pros5>3.0.co;2-h
- Meitzler, J. L., Antony, S., Wu, Y., Juhasz, A., Liu, H., Jiang, G., et al. (2014). NADPH oxidases: a perspective on reactive oxygen species production in tumor biology. *Antioxid. Redox Sign.* 20 (17), 2873–2889. doi: 10.1089/ars.2013.5603
- Nielsen, T. K., Højgaard, M., Andersen, J. T., Jørgensen, N. R., Zerahn, B., Kristensen, B., et al. (2017). Weekly ascorbic acid infusion in castration-resistant prostate cancer patients: a single-arm phase II trial. *Transl. Androl. Urol.* 6 (3), 517–528. doi: 10.1037/tau.2017.04.42
- Ormazabal, V., Zúñiga, F. A., Escobar, E., Aylwin, C., Salas-Burgos, A., Godoy, A., et al. (2010). Histidine Residues in the Na<sup>+</sup>-coupled Ascorbic Acid Transporter-2 (SVCT2) Are Central Regulators of SVCT2 Function, Modulating pH Sensitivity, Transporter Kinetics, Na<sup>+</sup> Cooperativity, Conformational Stability, and Subcellular Localization. *J. Biol. Chem.* 285 (47), 36471–36485. doi: 10.1074/jbc.M110.155630
- Ouar, Z., Lacave, R., Bens, M., and Vandewalle, A. (1999). Mechanisms of altered sequestration and efflux of chemotherapeutic drugs by multidrug-resistant cells. *Cell Biol. Toxicol.* 15 (2), 91–100. doi: 10.1023/a:1007521430236
- Raghu, N., He, X., Sluis, R. V., Mahoney, B., Baggett, B., Taylor, C. W., et al. (1999a). Enhancement of chemotherapy by manipulation of tumour pH. *Brit. J. Cancer* 80 (7), 1005–1011. doi: 10.1038/sj.bjc.6690455
- Raghu, N., Martinez-Zaguilan, R., Wright, S. H., and Gillies, R. J. (1999b). pH and drug resistance. II. Turnover of acidic vesicles and resistance to weakly basic chemotherapeutic drugs. *Biochem. Pharmacol.* 57 (9), 1047–1058. doi: 10.1016/s0006-2952(99)00021-0
- Ren, S., Chen, R., and Sun, Y. (2013). Prostate cancer research in China. *Asian J. Androl.* 15 (3), 350–353. doi: 10.1038/aja.2013.37
- Robey, I. F., Baggett, B. K., Kirkpatrick, N. D., Roe, D. J., Dosescu, J., Sloane, B. F., et al. (2009). Bicarbonate increases tumor pH and inhibits spontaneous metastases. *Cancer Res.* 69 (6), 2260–2268. doi: 10.1158/0008-5472.CAN-07-5575
- Roomi, M. W., House, D., Eckert-Maksić, M., Maksić, Z. B., and Tsao, C. S. (1998). Growth suppression of malignant leukemia cell line in vitro by ascorbic acid (vitamin C) and its derivatives. *Cancer Lett.* 122 (1–2), 93–99. doi: 10.1016/S0304-3835(97)00376-5
- Schoenfeld, J. D., Sibenaller, Z. A., Mapuskar, K. A., Wagner, B. A., Cramer-Morales, K. L., Furqan, M., et al. (2017). O<sub>2</sub><sup>-</sup> and H<sub>2</sub>O<sub>2</sub>-Mediated Disruption of Fe Metabolism Causes the Differential Susceptibility of NSCLC and GBM Cancer Cells to Pharmacological Ascorbate. *Cancer Cell* 31 (4), 487–500. doi: 10.1016/j.ccell.2017.02.018
- Stock, C., Mueller, M., Kraehling, H., Mally, S., Noël, J., Eder, C., et al. (2007). pH nanoenvironment at the surface of single melanoma cells. *Cell Physiol. Biochem.* 20 (5), 679–686. doi: 10.1159/000107550
- Szatrowski, T. P., and Nathan, C. F. (1991). Production of large amounts of hydrogen peroxide by human tumor cells. *Cancer Res.* 51 (3), 794–798.
- Taylor, S., Spugnini, E. P., Assaraf, Y. G., Azzarito, T., Rauch, C., and Fais, S. (2015). Microenvironment acidity as a major determinant of tumor chemoresistance: Proton pump inhibitors (PPIs) as a novel therapeutic approach. *Drug Resist. Update* 23, 69–78. doi: 10.1016/j.drug.2015.08.004
- Teixeira, J., Basit, F., Swarts, H. G., Forkink, M., Oliveira, P. J., Willems, P. H. G. M., et al. (2018). Extracellular acidification induces ROS- and mPTP-mediated death in HEK293 cells. *Redox Biol.* 15, 394–404. doi: 10.1016/j.redox.2017.12.018
- Teoh, J. Y. C., Hirai, H. W., Ho, J. M. W., Chan, F. C. H., Tsoi, K. K. F., and Ng, C. F. (2019). Global incidence of prostate cancer in developing and developed countries with changing age structures. *PLoS One* 14 (10), e221775. doi: 10.1371/journal.pone.0221775
- Tsukaguchi, H., Tokui, T., Mackenzie, B., Berger, U. V., Chen, X. Z., Wang, Y., et al. (1999). A family of mammalian Na<sup>+</sup>-dependent L-ascorbic acid transporters. *Nature* 399 (6731), 70–75. doi: 10.1038/19986



- Vaupel, P., Kallinowski, F., and Okunieff, P. (1989). Blood flow, oxygen and nutrient supply, and metabolic microenvironment of human tumors: a review. *Cancer Res.* 49 (23), 6449–6465.
- Verrax, J., and Calderon, P. B. (2009). Pharmacologic concentrations of ascorbate are achieved by parenteral administration and exhibit antitumoral effects. *Free Radical Bio. Med.* 47 (1), 32–40. doi: 10.1016/j.freeradbiomed.2009.02.016
- Visser, M. C. M., and Das, A. B. (2018). Potential Mechanisms of Action for Vitamin C in Cancer: Reviewing the Evidence. *Front. Physiol.* 9:809:809. doi: 10.3389/fphys.2018.00809
- Welch, R. W., Wang, Y., Crossman, A. J., Park, J. B., Kirk, K. L., and Levine, M. (1995). Accumulation of vitamin C (ascorbate) and its oxidized metabolite dehydroascorbic acid occurs by separate mechanisms. *J. Biol. Chem.* 270 (21), 12584–12592. doi: 10.1074/jbc.270.21.12584
- Wohlrab, C., Phillips, E., and Dachs, G. U. (2017). Vitamin C Transporters in Cancer: Current Understanding and Gaps in Knowledge. *Front. Oncol.* 7:74:74. doi: 10.3389/fonc.2017.00074
- Wu, X., Zeng, L., Taniguchi, T., and Xie, Q. (2007). Activation of PKA and phosphorylation of sodium-dependent vitamin C transporter 2 by prostaglandin E2 promote osteoblast-like differentiation in MC3T3-E1 cells. *Cell Death Differ* 14 (10), 1792–1801. doi: 10.1038/sj.cdd.4402190
- Yamamoto, F., Sasaki, S., and Maeda, M. (1992). Positron labelled antioxidants: synthesis and tissue biodistribution of 6-deoxy-6-[<sup>18</sup>F]fluoro-L-ascorbic acid. *Int. J. Rad. Appl. Instrum. A.* 43 (5), 633–639. doi: 10.1016/0883-2889(92)90032-a
- Yun, J., Mullarky, E., Lu, C., Bosch, K. N., Kavalier, A., Rivera, K., et al. (2015). Vitamin C selectively kills KRAS and BRAF mutant colorectal cancer cells by targeting GAPDH. *Science* 350 (6266), 1391–1396. doi: 10.1126/science.aaa5004
- Zhang, X., Chen, M., Zou, P., Kanchana, K., Weng, Q., Chen, W., et al. (2015). Curcumin analog WZ35 induced cell death via ROS-dependent ER stress and G2/M cell cycle arrest in human prostate cancer cells. *BMC. Cancer* 15, 866. doi: 10.1186/s12885-015-1851-3

**Conflict of Interest:** The authors declare that the research was conducted in the absence of any commercial or financial relationships that could be construed as a potential conflict of interest.

Copyright © 2020 Li, He, Luo, Shi, Yuan, Zhang, Seidl, Gewies, Wang, Zou, Long, Yue and Zhang. This is an open-access article distributed under the terms of the Creative Commons Attribution License (CC BY). The use, distribution or reproduction in other forums is permitted, provided the original author(s) and the copyright owner(s) are credited and that the original publication in this journal is cited, in accordance with accepted academic practice. No use, distribution or reproduction is permitted which does not comply with these terms.





# Prognostic Value of the Modified Systemic Inflammation Score in Patients With Extranodal Natural Killer/T-Cell Lymphoma

He Huang<sup>1,2,3\*</sup>, Li Min Chen<sup>1,2,3</sup>, Xiao Jie Fang<sup>1,2,3</sup>, Cheng Cheng Guo<sup>2,3,4</sup>, Xiao Ping Lin<sup>2,3,5</sup>, Huang Ming Hong<sup>1,2,3,6</sup>, Xi Li<sup>1,2,3</sup>, Zhao Wang<sup>1,2,3</sup>, Ying Tian<sup>1,2,3</sup>, Mei Ting Chen<sup>1,2,3</sup>, Yu Yi Yao<sup>1,2,3</sup>, Zegeng Chen<sup>1,2,3</sup>, Xiao Qian Li<sup>1,2,3</sup> and Fei Pan<sup>1,2,3</sup>

<sup>1</sup> Department of Medical Oncology, Sun Yat-sen University Cancer Center (SYSUCC), Guangzhou, China, <sup>2</sup> State Key Laboratory of Oncology in South China, Sun Yat-sen University Cancer Center (SYSUCC), Guangzhou, China, <sup>3</sup> Collaborative Innovation Center for Cancer Medicine, Sun Yat-sen University Cancer Center, Guangzhou, China, <sup>4</sup> Department of Neurosurgery, Sun Yat-sen University Cancer Center, Guangzhou, China, <sup>5</sup> Department of Nuclear Medicine, Sun Yat-sen University Cancer Center, Guangzhou, China, <sup>6</sup> Department of Medical Oncology, Sun Yat-sen Memorial Hospital, Guangzhou, China

## OPEN ACCESS

### Edited by:

Dong-Hua Yang,  
St. John's University, United States

### Reviewed by:

Hui Zhou,  
Central South University, China  
Jingxun Wu,  
First Affiliated Hospital of Xiamen  
University, China

### \*Correspondence:

He Huang  
huanghe@sysucc.org.cn

### Specialty section:

This article was submitted to  
Pharmacology of Anti-Cancer Drugs,  
a section of the journal  
Frontiers in Pharmacology

**Received:** 11 August 2020

**Accepted:** 09 September 2020

**Published:** 30 September 2020

### Citation:

Huang H, Chen LM, Fang XJ, Guo CC, Lin XP, Hong HM, Li X, Wang Z, Tian Y, Chen MT, Yao YY, Chen Z, Li XQ and Pan F (2020) Prognostic Value of the Modified Systemic Inflammation Score in Patients With Extranodal Natural Killer/T-Cell Lymphoma. *Front. Pharmacol.* 11:593392. doi: 10.3389/fphar.2020.593392

**Background:** Extranodal natural killer/T-cell lymphoma (ENKTL) is a rare and extremely malignant tumor. The systemic inflammation score (SIS), which is based on the pretreatment level of lymphocyte-to-monocyte ratio (LMR) and serum albumin (Alb), has been shown to be of prognostic value in a number of cancers. We integrate several other pretreatment serum inflammatory indicators, including the neutrophil-to-lymphocyte ratio (NLR), lymphocyte-to-monocyte ratio (LMR), serum C-reactive protein (CRP) and albumin (Alb) level, to establish a modified systemic inflammatory scoring system to predict clinical outcomes of ENKTL.

**Methods:** A total of 184 patients with newly diagnosed ENKTL was retrospectively investigated. Systemic inflammatory indexes, including NLR, LMR, CRP, and Alb level were reviewed. Receiver operating characteristic (ROC) curve analysis was carried out to obtain the optimal cut-off value. The associations between cutoff values and overall survival (OS) were analyzed by Kaplan–Meier curves and Cox proportional models.

**Results:** The median age of patients was 44.0 years, ranging from 15 to 82 years. There were 129 (70.1%) male patient. About 57.1% of patients had stage III or IV disease. The optimal cut-off values of NLR and LMR in predicting OS were 3.1 and 2.4, respectively. The clinical standard of CRP and Alb levels at 10 and 40 mg/L, respectively, were chosen as the optimal cut-off values. By multivariate analysis, hemophilic syndrome (hazard ratio [HR]: 10.540, 95% confidence interval [CI]: 3.440–32.291,  $P < 0.001$ ), advanced Ann Arbor stages (III–IV) (HR: 4.606, 95% CI: 1.661–12.774,  $P = 0.003$ ), paranasal sinus invasion (HR: 2.323, 95% CI: 1.069–5.047,  $P = 0.033$ ),  $NLR \geq 3.1$  (HR: 3.019, 95% CI: 1.317–6.923,  $P = 0.009$ ), Alb level of  $<40$  mg/L (HR: 0.350, 95% CI: 0.134–0.915,  $P = 0.032$ ), and radiation therapy (HR: 0.430, 95% CI: 0.205–0.901,  $P = 0.025$ ) were independent protective factors for ENKTL. We combined two inflammatory indexes

NLR and Alb level to establish a modified systemic inflammation score (mSIS). These 184 patients were divided into 3 groups: group 1 (mSIS score of 0), group 2 (mSIS score of 1), and group 3 (mSIS score of 2). The mean OS of these three groups were 42 months (95% CI: 31.4–53.12), 77 months (95% CI: 68.5–87.5), and 89 months (95% CI: 71.4–82.7), respectively ( $P < 0.001$ ). The Harrell's concordance index (C-index) of mSIS is 0.725. The mSIS could be used to discriminate patients categorized in the low-risk group of International Prognostic Index (IPI) ( $P < 0.001$ ) and the low-risk and intermediate-risk prognostic index of natural killer cell lymphoma (PINK) group ( $P = 0.019$ ).

**Conclusion:** The pretreatment mSIS could be an independent prognostic factor for OS in patients with ENKTL and warrants further research.

**Keywords:** extranodal natural killer/T cell lymphoma, systemic inflammation score, neutrophil-lymphocyte ratio, albumin, prognosis

## INTRODUCTION

Extranodal natural killer/T-cell lymphoma (ENKTL) is a rare and highly malignant lymphoma with heterogeneous clinical behaviors. Most of the tumors occur primarily in the nose and above the throat, and the malignant cells of ENKTL mainly derived from mature NK cells, or T cells, therefore it is named NK/T cell lymphoma (Kwong, 2005; Freud et al., 2006; Sun and Lanier, 2011; Tse and Kwong, 2013; Montaldo et al., 2014). A few cases may occur outside of the nose, such as skin, gastrointestinal tract, lung, etc. Its pathological manifestations are unique, with vascular center of pleomorphic lymphocyte infiltration. The tumor cells infiltrate to destroy the blood vessels and then cause tissue necrosis (Kwong and Khong, 2011). In most cases, there is evidence of Epstein-Barr virus infection (Rickinson et al., 1992).

Systemic inflammation has been shown to play a considerable role in the progression and development of cancers (McMillan et al., 2003). NK/T lymphoma is associated with inflammatory cytokine storm, leading to complications such as hemophagocytic syndrome in later stage.

Potential prognostic values have been shown by pretreatment serum inflammatory indicators like the neutrophil-to-lymphocyte ratio (NLR), lymphocyte-to-monocyte ratio (LMR), the C-reactive protein (CRP), and albumin (Alb) levels in some neoplasms (McMillan, 2013; Kim et al., 2015; Akinci Ozyurek et al., 2017; Lin et al., 2017; Rajwa et al., 2018). However, there is no generally accepted optimal threshold for inflammatory biomarkers and no scoring system to incorporate these indicators in ENKTL. This study aims to look through the prognostic value of some pretreatment serum-based inflammatory biomarkers to establish a scoring system for the prognosis of patients with ENKTL.

## PATIENTS AND METHODS

### Ethical Statement

This study was approved by the Medical Ethics Committees of Sun Yat-sen University Cancer Center. The study procedures were conducted in accordance with the World Medical Association

Declaration of Helsinki. Written informed consents were provided by patients to use data stored in the hospital database.

### Study Population

The database of 204 patients with diagnosed ENKTL from December 28th 2010 to May 1st 2019 in Sun Yat-sen University Cancer Center was surveyed retrospectively. The inclusion criteria include: (1) pathologically diagnosed ENKTL according to the WHO classification of tumors of hematopoietic and lymphoid tissues; (2) no preceding malignant or secondary tumor; (3) no preceding treatment; (4) the subsequent treatment was chemotherapy with or without radiation or radiotherapy alone to achieve the therapeutic intent; (5) complete followed up data and clinical information. The exclusion criteria were: (1) neoadjuvant chemotherapy, (2) no routine blood examination before treatment, (3) incomplete/inaccurate medical records, and (4) acute chronic active inflammatory or infectious diseases.

### Data Collection

The following baseline clinical information were collected by medical record: age, gender; Karnofsky performance status (KPS); Ann Arbor stage; B symptoms; pathological diagnosis; EBV infection status; computed tomography (CT) or magnetic resonance (MR) image of the neck, nasopharynx, abdomen, chest, and pelvis; or positron discharge tomography/computed tomography (PET/CT) of the entire body. All the patients were evaluated with blood cell counts, serum CRP, and Alb levels before treatment and were followed up from the date of diagnosis. They were followed up generally every 3 months in the first year, every 6 months in the second and third year, and every year thereafter. At the last follow-up date, clinical attendance was made by direct communication with the patient or his or her family. Overall survival (OS) was counted from the date of diagnosis to the date of death or the final follow-up.

### Statistical Analysis

We apply Chi-square test or Fisher's exact test to evaluate varying baseline and clinicopathological parameters according to the variety of data. The optimal cut-off value for the systemic inflammatory

indexes NLR and LMR was determined by the receiver-operating-characteristic (ROC) curve. The optimal cut-off value of Alb and CRP are their clinical standard values. The log-rank test was applied to analyze the difference between the curves. Univariate or multivariate death hazard ratios(HRs) were calculated by Cox proportional hazard model. All reported P-values were two-sided, and  $P < 0.05$  was considered to be statistically significant. CIs were calculated at the 95% level. The survival curves were figured by Kaplan-Meier survival analysis. Discrimination was measured by Harrell's concordance index (C-index), which quantifies the likelihood of two random patients. The patient who relapses for the first time had a higher possibility of interest event.

The ROC curve was executed using the MedCalc Statistical Software version 18.2.1 (MedCalc Software bvba, Ostend, Belgium). The C-index was calculated by R version 4.0.2 *via* the survival and design packages, while other analyses were performed using the SPSS software version 25.0 (IBM Corp, Armonk, NY, United States).

## RESULTS

### Patient Characteristics

According to the including and excluding criteria above, 20 patients were excluded. Therefore, 184 patients were enrolled and analyzed in this study. The baseline characteristics of these patients were showed in **Table 1**. The median age was 44.0 years, ranging from 15 to 82 years. The age interquartile range (IQR) was 34.0–54.0 years. There were 129 (70.1%) male and 55 (29.9%) female patients. A total of 146 (79.3%) patients had KPS higher than 80. A total of 113 patients (61.4%) had B symptoms at the initial assess, 57.1% of patients had stage III or IV disease, and 164 (89.1%) of patients had nasal type ENKTL. Thirty-four patients had more than one extranodal involvement. Some patients had metastases to the liver (one case), lung (two case), kidney (one case), adrenal gland (three cases), skin (two cases), and gastrointestinal tract (two cases). The presence of EBV DNA was measured in the plasma or whole blood at diagnosis ( $n = 124$ ). Plasma lactate dehydrogenase(LDH) was found to be elevated in 33 cases (17.9%). According to the International Prognostic Indexs (IPI) (International Non-Hodgkin's Lymphoma Prognostic Factors Project, 1993), the majority of the patients (133 cases, 72.3%) were categorized as low risk (IPI = 0–1) and other patients (51 cases, 27.7%) as low-intermediate/intermediate-high/high risk (IPI = 2–5). The patients with Korean Prognostic Indexs (Lee et al., 2006) (KPI) = 0–1 (117 cases, 63.6%) was significantly more than those with KPI = 2–4 (67 cases, 36.4%). For the prognostic index of natural killer cell lymphoma (PINK) index (Kim et al., 2016), 63 cases (34.2%) were classified as low risk, 42 cases (22.8%) as intermediate risk, and 79 cases (42.9%) as high risk. There are 110 cases (59.8%) of patients had received radiation therapy.

### Optimal Cut-Off Values of Systemic Inflammatory Indexes

According to the ROC curve, the area under curve (AUC) of NLR was 0.669 (95% C: 0.596–0.735;  $P < 0.05$ ) based on a cut-off

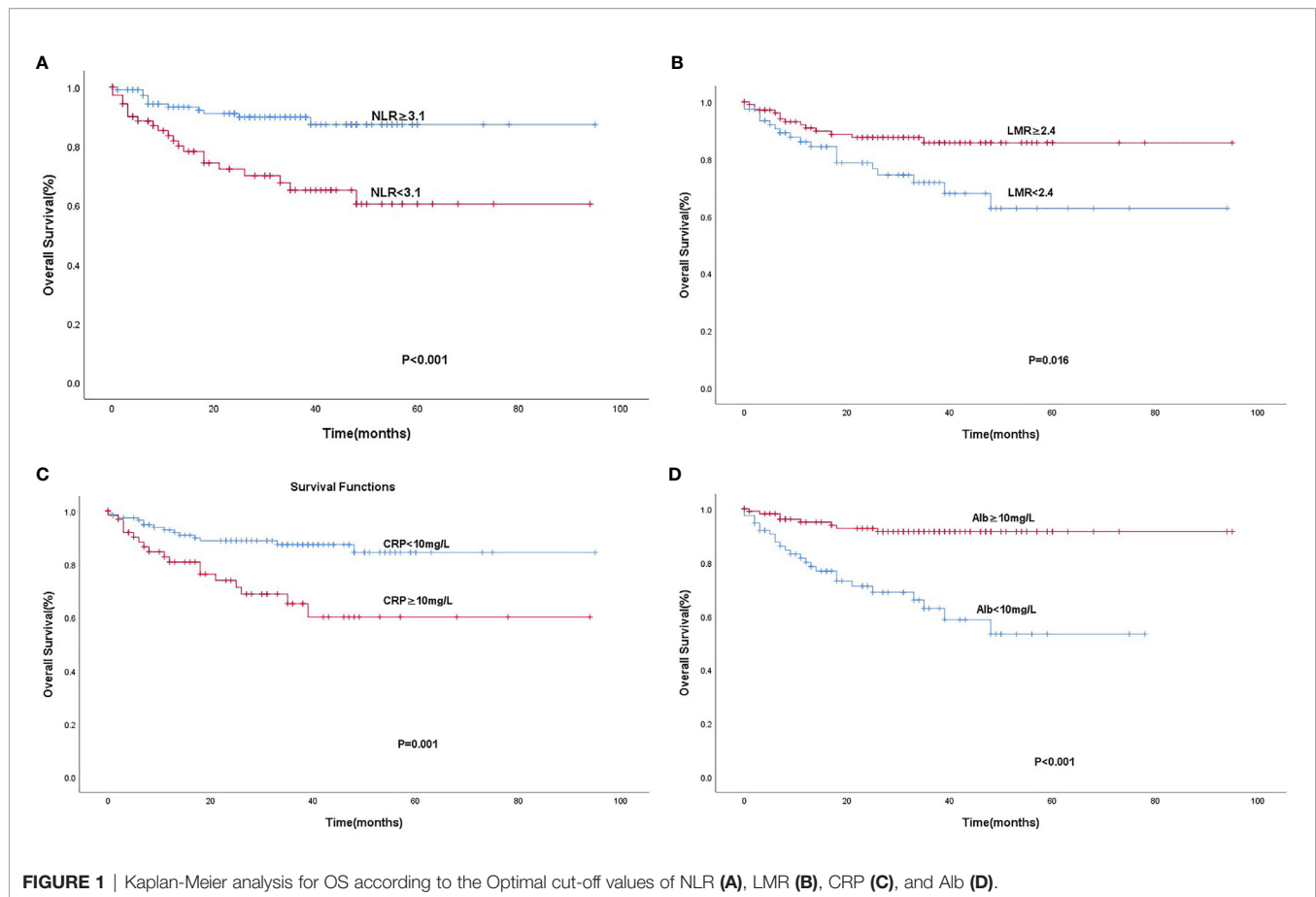
**TABLE 1 |** Baseline characteristics of patients.

Characteristics	No. of patients	%
<b>Age [median (range), years]</b>		
<60	153	83.2
≥60	31	16.8
<b>Gender</b>		
Male	129	29.9
Female	55	70.1
<b>KPS score</b>		
≤80	38	20.7
>80	146	79.3
<b>Ann Arbor stages</b>		
I–II	79	42.9
III–IV	105	57.1
<b>B symptoms</b>	113	61.4
<b>Hemophilic syndrome</b>	9	4.9
<b>Bone marrow involvement</b>	16	8.7
<b>Subtypes</b>		
Nasal	164	89.1
Non-nasal	20	10.9
<b>Extranodal involvement sites</b>		
<2	150	81.5
≥2	34	18.5
<b>Lymph-node involvement</b>	115	62.5
<b>Plasma Epstein-Barr virus</b>	124	67.4
<b>DNA(+)</b>		
<b>LDH elevated</b>	33	17.9
<b>Paranasalsinus invasion</b>	77.2	22.8
<b>Korean Prognostic Indexs (KPI) score</b>		
0–1	117	63.6
2–4	67	36.4
<b>International Prognostic Indexs(IPI) score</b>		
0–1	133	72.3
2–5	51	27.7
<b>The prognostic index of natural killer lymphoma (PINK) model</b>		
Low-risk	63	34.2
Intermediate-risk	42	22.8
High-risk	79	42.9
<b>Radiation therapy</b>	110	59.8

value of 3.1. Similarly, the AUC of LMR was 0.623 (95% CI: 0.548–0.693;  $P < 0.05$ ) based on a cut-off value of 2.4. As mentioned above, the optimal cut-off values of levels of CRP and Alb were 10 and 40 mg/L, respectively. The NLR-low group (60.9%, 112/184) had a higher OS than the NLR-high group (39.1%, 72/184;  $P < 0.001$ ). The OS was significantly poorer in the LMR-high group (57.6%, 106/184) than in the LMR-low group (42.4%, 78/184;  $P = 0.015$ ). The CRP-low group (64.1%, 118/184) had a higher OS than the CRP-high group (35.9%, 66/184;  $P = 0.001$ ), and the OS was significantly shorter in the Alb-low group (41.8%, 77/184) than in the Alb-high group (58.2%, 107/184;  $P < 0.001$ ) (**Figure 1**).

### Association of Systemic Inflammatory Indexes With OS

We evaluated the association of systemic inflammatory indexes with the OS of patients. The median follow-up period was 28.5 months. The 5-year OS rates for the whole cohort were 60.2%. The



univariate and multivariate survival analyses are presented in **Table 2**. In the univariate analysis, the following factors significantly predicted poor outcome: low KPS score ( $\text{KPS} \leq 80$ ), B symptoms, advanced Ann Arbor stage (III/IV), hemophilic syndrome, bone marrow involvement, regional lymph node involvement, paranasal sinus invasion, positive plasma EBV-DNA, CRP of  $\geq 10 \text{ mg/L}$ , Alb level of  $< 40 \text{ mg/L}$ ,  $\text{NLR} \geq 3.1$ ,  $\text{LMR} < 2.4$ , and  $\text{IPI score} \geq 2$ . The multivariate analysis was performed on the clinical parameters related to shorter overall survival and important clinical factors, such as age and serum LDH level. We used conditional Cox regression analysis and found four negative prognostic factors on OS: Hemophilic syndrome (HR: 10.540, 95% CI: 3.440–32.291;  $P < 0.001$ ), advanced Ann Arbor stages (III–IV) (HR: 4.606, 95% CI: 1.661–12.774;  $P = 0.003$ ), paranasal sinus invasion (HR: 2.323, 95% CI: 1.069–5.047;  $P = 0.033$ ),  $\text{NLR} \geq 3.1$  (HR: 3.019, 95% CI: 1.317–6.923;  $P = 0.009$ ), Alb level of  $< 40 \text{ mg/L}$  (HR: 0.350, 95% CI: 0.134–0.915;  $P = 0.032$ ), and radiation therapy (HR: 0.430, 95% CI: 0.205–0.901;  $P = 0.025$ ).

## A Modified Systemic Inflammation Score

In previous studies, we found that the systemic inflammation score (SIS), which is based on the preoperative Alb level and LMR, was a prognostic factor in renal clear cell carcinoma and colorectal cancer. Based on the above results in this study,

LMR could not predict survival in multivariate analysis. Intriguingly, high NLR and low level of Alb had poor overall survival.

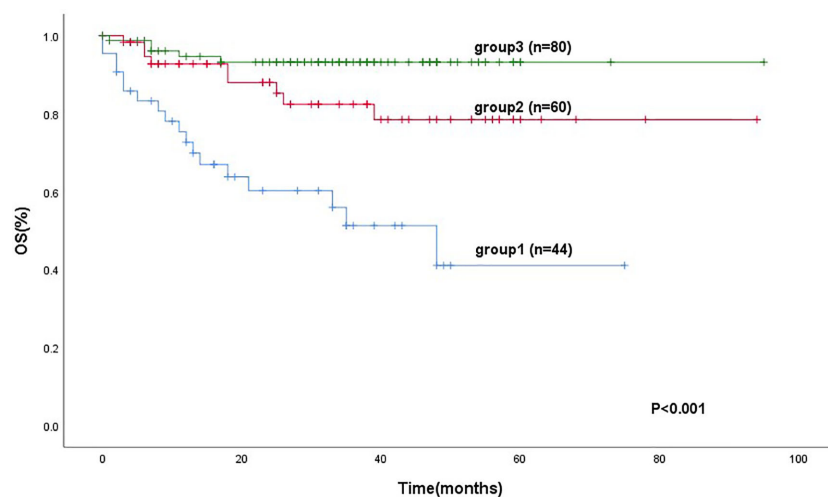
Whether the combination of Alb level and NLR could predict the prognosis of patients with ENKTL remained unclear. Here, we established a modified systemic inflammation score (mSIS) to demonstrate the prognostic value of the combination of Alb level and NLR for the prognosis of ENKTL patients.

184 patients were divided into three groups. Group 1 (mSIS score of 0), patients with  $\text{NLR} \geq 3.1$  and Alb level of  $< 40 \text{ g/L}$  (44 cases, 23.9%). Group 2 (mSIS score of 1), patients with  $\text{NLR} < 3.1$  and Alb level of  $< 40 \text{ g/L}$  or patients with  $\text{NLR} \geq 3.1$  and Alb level of  $\geq 40 \text{ g/L}$  (60 cases, 32.6%). Group 3 (mSIS score of 2), patients with  $\text{NLR} < 3.1$  and Alb level of  $\geq 40 \text{ g/L}$  (80 cases, 43.5%). The mean for OS of these three groups were 42 months (95% CI: 31.4–53.12), 77 months (95% CI: 68.5–87.5), 89 months (95% CI: 71.4–82.7), respectively ( $P < 0.001$ ; **Figure 2**). The C-index of mSIS is 0.725.

We separated our patients according to the IPI, KPI, and PINK. The patients could be stratified into two risk groups based on IPI (IPI, 0–1 vs.  $\geq 2$ ,  $P < 0.001$ ), 133 (72.3%) patients were in the low-risk group, and 51 patients were in the high-risk group. Using the KPI, patients were unable to be distinguished in two risk groups ( $P = 0.084$ ). Using the PINK, there was no difference in the survival

**TABLE 2 |** Univariate and multivariate analyses of potential prognostic factors for OS.

Characteristics	Univariate analysis		Multivariate analysis	
	HR (95% CI)	P	HR (95% CI)	P
<b>Age</b>				
<60				
≥60	2.060 (0.953–4.453)	0.066		0.51
<b>Gender</b>				
Male				
Female	1.190 (0.550–2.574)	0.658		
<b>KPS score</b>				
≤80				
>80	0.426 (0.201–0.904)	0.026		0.297
<b>Ann Arbor stages</b>				
I–II				
III–IV	5.675 (2.177–14.796)	0	4.606(1.661–12.774)	0.003
<b>B symptoms</b>	3.154 (1.297–7.673)	0.011		0.341
<b>Hemophilic syndrome</b>	8.098 (3.290–19.929)	0	10.540(3.440–32.291)	0
<b>Bone marrow involvement</b>	4.390 (1.886–10.215)	0		0.891
<b>Subtypes</b>				
Nasal				
Non-nasal	1.071 (0.325–3.527)	0.91		
<b>Extranodal involvement sites</b>				
<2				
≥2	2.057 (.918–4.611)	0.08		
<b>Lymph-node involvement</b>	4.301 (2.067–8.950)	0		0.354
<b>Epstein-Barr virus infection</b>	3.357 (1.289–8.741)	0.013		0.312
<b>Paranasalsinus invasion</b>	2.303 (1.107–4.789)	0.026	2.323(1.069–5.047)	0.033
<b>CRP ≥ 10mg/l</b>	2.964 (1.470–5.975)	0.002		0.056
<b>NLR ≥ 3.1</b>	3.448 (1.661–7.157)	0.001	3.019(1.317–6.923)	0.009
<b>LMR ≥ 2.4</b>	0.428 (0.211–0.867)	0.018		0.791
<b>ALB &lt; 40 mg/L</b>	5.531 (2.396–11.949)	0	0.350(0.134–0.915)	0.032
<b>LDH elevated</b>	2.112(0.943–4.727)	0.069		
<b>KPI score ≥ 2</b>	1.838 (0.910–3.711)	0.09		
<b>IPI score ≥ 2</b>	2.365 (1.144–4.889)	0.02		0.734
<b>Radiation therapy</b>	0.353(0.175–0.713)	0.004	0.430(0.205–0.901)	0.025

**FIGURE 2 |** Kaplan-Meier analysis for OS according to the mSIS.



difference between the low-risk and intermediate-risk groups ( $P = 0.199$ ) (**Figure 3**). However, the mSIS can classify the patients into the low-risk group of the IPI ( $P < 0.001$ ) and the low-risk and intermediate-risk PINK group ( $P = 0.019$ ; **Figure 4**).

## DISCUSSION

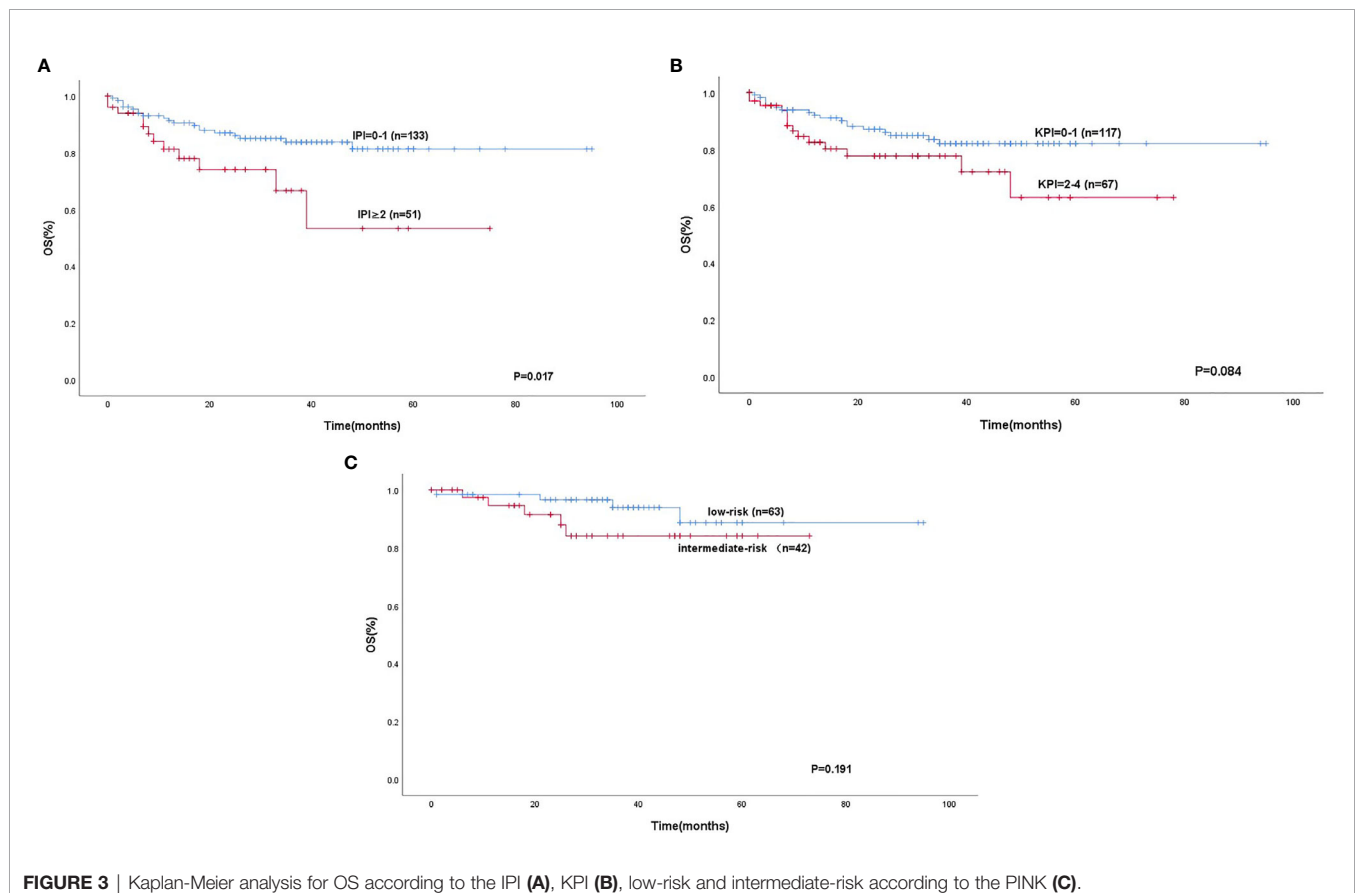
ENKTL is usually associated with poor prognosis. Tremendous efforts have been made in searching valid survival indicators for patients with ENKTL. Numerous studies have demonstrated that cancer progression is caused by the intrinsic properties of tumor cells as well as the systemic and local inflammatory responses. Cancer can cause local and systemic inflammation, which is thought to be associated with cancer and is a hallmark of cancer development and progression (Rajendran et al., 2018). Different systemic inflammatory indicators including NLR, LMR, CRP, and Alb have been analyzed in several malignant tumors with poor outcome and low therapeutic response (Lee et al., 2006; Stotz et al., 2014; Gu et al., 2015; Koh et al., 2015; Kim et al., 2016; Jing et al., 2017; Rajendran et al., 2018). The optimal cut-off values for these systemic inflammatory biomarkers are distinct in a large number of malignancies (Stotz et al., 2014; Chen et al., 2015; Gu et al., 2015; Kim et al., 2015; Koh et al., 2015; Kim et al.,

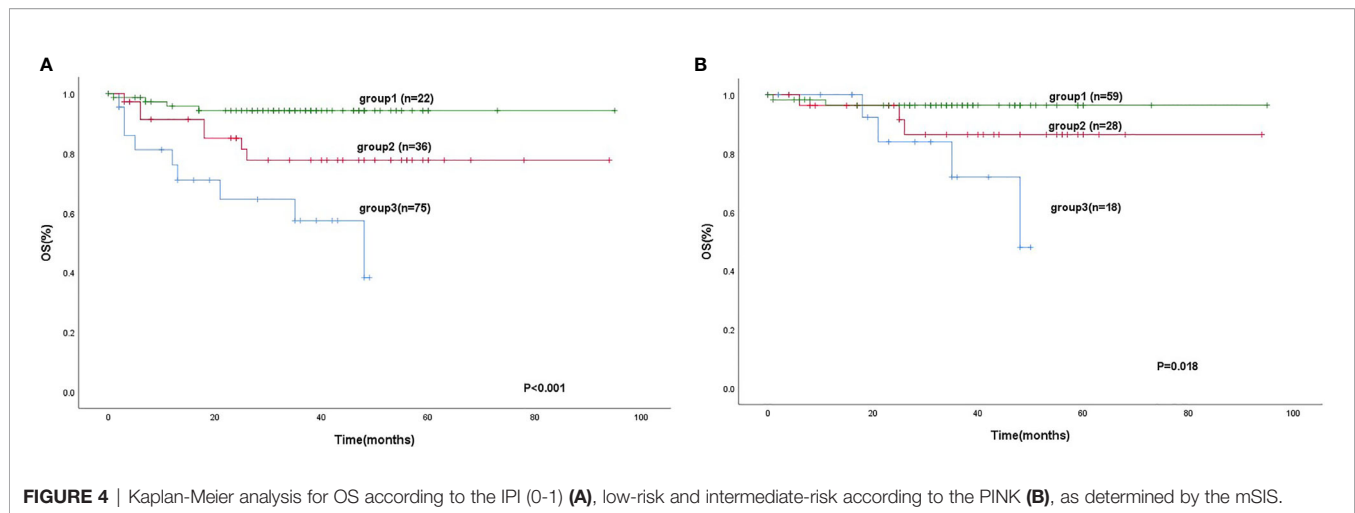
2016; Jing et al., 2017; Tan et al., 2017). We investigated their prognostic significance in ENKTL in this study.

In order to confirm the optimal cutoff value of those indexes in predicting the prognosis of ENKTL, we used a ROC curve analysis. According to the ROC curve and the Youden index, the optimal cut-off values of NLR, LMR in predicting OS were 3.1 and 1.4, respectively. Based on these value, 184 patients were divided into low- and high-risk groups. Based on the results, NLR ( $P = 0.009$ ) and Alb level ( $P = 0.032$ ) were shown to be able to predict the OS in patients with ENKTL. At the same time, hemophilic syndrome ( $P < 0.001$ ), paranasalsinus invasion ( $P = 0.033$ ), advanced Ann Arbor stages (III–IV) ( $P = 0.001$ ), and radiation therapy ( $P = 0.025$ ) also considerably predicted poor survival in multivariate analysis.

The systemic inflammation score (SIS), which is based on the pretreatment level of lymphocyte-to-monocyte ratio (LMR) and serum albumin (Alb). In the current study, we creatively establish a modified systemic inflammation score (mSIS) as a novel, straightforward, and valuable prognostic indicator for OS in for patients with ENKTL, which is based on more than preoperative NLR and serum Alb level.

The mSIS on prognosis of ENKTL is constructed primarily by the NLR and Alb level. Neutrophils and lymphocytes form NLR. Neutrophils can produce chemokines and cytokines to inhibit the





immune activity of lymphocytes and natural killer cells. The interaction between neutrophils and cancer cells could produce inflammatory response, which cause the proliferation, invasion and metastasis of tumors (Petrie et al., 1985). On the contrary, lymphocytes, the basic component of adoptive immune system (Dunn et al., 2004), could enhance tumor immune monitoring and suppress the proliferation, invasion, and metastasis of tumor cells. In our study, NLR  $\geq 3.1$  significantly predicted poor survival in univariate analysis. Therefore, NLR is important in the prognosis of ENKTL. The level of Alb, which is widely applied as an excellent indicator of malnutrition and cachexia in patients with advanced cancer. It has been found that Alb of  $<40$  mg/L was remarkably predict shorter overall survival in univariate analysis. Therefore, the mSIS may enable to assess the impact of tumors on systemic inflammation and malnutrition.

However, although the prognostic value of mSIS has been shown for predicting the survival of patients with ENKTL, the mechanism is still unclear. A lower score of mSIS indicates an elevated NLR and/or low level of albumin, which might indicate immunological response, malnutrition, and cachexia.

On one hand, neutrophils secrete reactive oxygen species that could lead to cellular genetic instability and DNA damage and promote tumor microenvironment to induce carcinogenesis (Weitzman et al., 1990). Neutrophils can also secrete vascular endothelial growth factor (VEGF), which promote tumor cell cycle by activating VEGF receptor 2 (Shamamian et al., 2001; Kusumanto et al., 2003). Lymphocytes are a basal anti-tumor defense line, a reduced number of lymphocytes is associated with unstable host defense to the advanced tumors. There are some subsets of lymphocytes including CD4<sup>+</sup> T helper type 1 lymphocytes, CD8<sup>+</sup> cytotoxic T lymphocytes and natural killer T cells. They were shown to have anticancer abilities detecting precancerous cells and destroying them, directly killing cancer cells, and preventing angiogenesis and tumor metastasis (Lowther and Hafler, 2012; Li et al., 2014). Moreover, neutrophils have been reported to inhibit T cell activation by producing nitric oxide, arginase, and reactive oxygen species,

bringing about the depletion of the lymphocyte immune response (Muller et al., 2009). These may explain the reason that elevated NLR may serve as an independent prognostic factor for OS owing to the counts of increased neutrophils and reduced lymphocytes.

On the other hand, albumin is considered as a nutritional indicator. In recent studies, albumin has become a common indicator for predicting survival of a variety of cancers, such as osteosarcoma, renal cell carcinoma colorectal cancer, hepatocellular carcinoma, and prostate cancer (Yi et al., 2014; Chen et al., 2015; Nazha et al., 2015; Chi et al., 2016; Hiraoka et al., 2016). The mechanisms might involve in malnutrition and tumor microenvironmental imbalance. High concentrations of interleukin 6 (IL-6) and tumor necrosis factor (TNF) regulate liver cells to generate albumin production and increase the permeability of the microvasculature. It has been validated that albumin can maintain cell growth and DNA replication, and produce antioxidant effects on carcinogens (Arroyo et al., 2014). In addition, malnutrition will weaken the human body's cellular immunity, humoral immunity, phagocytosis, and other defense mechanisms, thus leading to an increased possibility of infection and poor anti-tumor treatment effect (Chandra et al., 1999).

This study suggested that mSIS is superior to IPI, KPI and PINK, and could be a new prognostic scoring system model contributes to the risk assessment for patients with ENKTL.

There are some limitation in our study. Firstly, as a retrospective study with a moderate sample size and a single center design, patient selection bias may exist. Secondly, it is difficult to keep the heterogeneity in the treatment used for each patient, which result in different clinical prognosis. Nevertheless, prospective trials are warranted for future study.

In conclusion, our study indicates that mSIS can disclosed the systemic inflammatory reaction and damaged nutritional status and therefore can forecast the survival of patients with ENKTL. Patients with higher mSIS had better OS. mSIS will help direct individual treatment for patients with ENKTL. Patients with low mSIS should be well monitored and treated more seriously to avoid tumor progression.

## DATA AVAILABILITY STATEMENT

The raw data supporting the conclusions of this article will be made available by the authors, without undue reservation, to any qualified researcher.

## ETHICS STATEMENT

The studies involving human participants were reviewed and approved by ClinicalTrials.gov. Written informed consent to participate in this study was provided by the participants' legal guardian/next of kin. Written informed consent was obtained from the individual(s) for the publication of any potentially identifiable images or data included in this article.

## REFERENCES

- International Non-Hodgkin's Lymphoma Prognostic Factors Project (1993). A predictive model for aggressive non-hodgkin's lymphoma. *N. Engl. J. Med.* 329, 987–994. doi: 10.1056/NEJM199309303291402
- Akinci Ozyurek, B., Sahin Ozdemirel, T., Buyukyaylaci Ozden, S., Erdogan, Y., Kaplan, B., and Kaplan, T. (2017). Prognostic value of the neutrophil to lymphocyte ratio (NLR) in lung cancer cases. *Asian Pac. J. Cancer Prev.* 18 (5), 1417–1421. doi: 10.22034/APJCP.2017.18.5.1417
- Arroyo, V., García-Martínez, R., and Salvatella, X. (2014). Human serum albumin, systemic inflammation, and cirrhosis. *J. Hepatol.* 61, 396–407. doi: 10.1016/j.jhep.2014.04.012
- Chandra, R. K. (1999). Nutrition and immunology: From the clinic to cellular biology and back again. *Proc. Nutr. Soc.* 58, 681–683. doi: 10.1017/S0029665199000890
- Chen, K. L., Liu, Y. H., Li, W. Y., Chen, J., Gu, Y. K., Geng, Q. R., et al. (2015). The prognostic nutritional index predicts survival for patients with extranodal natural killer/T cell lymphoma, nasal type. *Ann. Hematol.* 94 (8), 1389–1400. doi: 10.1007/s00277-015-2361-8
- Chen, Z., Shao, Y., Fan, M., Zhuang, Q., Wang, K., Cao, W., et al. (2015). Prognostic significance of preoperative C-reactive protein: Albumin ratio in patients with clear cell renal cell carcinoma. *Int. J. Clin. Exp. Pathol.* 8, 14893–14900.
- Chi, K. N., Kheoh, T., Ryan, C. J., Molina, A., Bellmunt, J., Vogelzang, N. J., et al. (2016). A prognostic index model for predicting overall survival in patients with metastatic castration-resistant prostate cancer treated with abiraterone acetate after docetaxel. *Ann. Oncol.* 27, 454–460. doi: 10.1093/annonc/mdv594
- Dunn, G. P., Old, L. J., and Schreiber, R. D. (2004). The immunobiology of cancer immunosurveillance and immunoediting. *Immunity* 2, 137–148. doi: 10.1016/j.immuni.2004.07.017
- Freud, A. G., Yokohama, A., Becknell, B., Lee, M. T., Mao, H. C., Ferketich, A. K., et al. (2006). Evidence for discrete stages of human natural killer cell differentiation in vivo. *J. Exp. Med.* 203, 1033–1043. doi: 10.1084/jem.20052507
- Gu, X. B., Tian, T., Tian, X.-J., and Zhang, X.-J. (2015). Prognostic significance of neutrophil-to-lymphocyte ratio in non-small cell lung cancer: a meta-analysis. *Sci. Rep.* 5, 12493. doi: 10.1038/srep12493
- Hiraoka, A., Kumada, T., Nouse, T., Tsuji, K., Itobayashi, E., Hirooka, M., et al. (2016). Proposed New sub-grouping for intermediate-stage hepatocellular carcinoma using albumin-bilirubin grade. *Oncology*. 91 (3), 153–161. doi: 10.1159/000447061
- Jing, C. Y., Fu, Y.-P., Shen, H.-J., Zheng, S.-S., Lin, J.-J., Yi, Y., et al. (2017). Albumin to gamma-glutamyltransferase ratio as a prognostic indicator in intrahepatic cholangiocarcinoma after curative resection. *Oncotarget* 8 (8), 13293–13303. doi: 10.18632/oncotarget.14530
- Kim, E. Y., Lee, J. W., Yoo, H. M., Park, C. H., and Song, K. Y. (2015). The platelet-to-lymphocyte ratio versus neutrophil-to-lymphocyte ratio: which is better as a

## AUTHOR CONTRIBUTIONS

These authors contributed equally: HH, LC, and XF. All authors contributed to the article and approved the submitted version.

## FUNDING

This work was supported by Science and Technology Planning Project of Guangdong Province, China (grant number 2017A020215030), Basic and Applied Basic Research Fund Project of Guangdong Province, China (grant numbers 2019A1515010742 and 2019A1515010702). The funders had no role in the study design, data collection and analysis, decision to publish, or preparation of the manuscript.

- prognostic factor in gastric cancer? *Ann. Surg. Oncol.* 22 (13), 4363–4370. doi: 10.1245/s10434-015-4518-z
- Kim, S. J., Yoon, D. H., Jaccard, A., Chng, W. J., Lim, S. T., Hong, H., et al. (2016). A prognostic index for natural killer cell lymphoma after non-anthracycline-based treatment: a multicentre, retrospective analysis. *Lancet Oncol.* 17, 389–400. doi: 10.1016/S1470-2045(15)00533-1
- Koh, Y. W., Park, C. S., Yoon, D. H., Suh, H., and Huh, J. (2014). Should the cut-off values of the lymphocyte to monocyte ratio for prediction of prognosis in diffuse large B-cell lymphoma be changed in elderly patients? *Eur. J. Haematol.* 93 (4), 340–348. doi: 10.1111/ejh.12354
- Koh, C. H., Bhoo-Pathy, N., Ng, K.-L., Jabir, R. S., Tan, G.-H., See, M.-H., et al. (2015). Utility of pre-treatment neutrophil-lymphocyte ratio and platelet-lymphocyte ratio as prognostic factors in breast cancer. *Br. J. Cancer* 113 (1), 150–158. doi: 10.1038/bjc.2015.183
- Kusumanto, Y. H., Dam, W. A., Hospers, G. A., Meijer, C., and Mulder, N. H. (2003). Platelets and granulocytes, in particular the neutrophils, form important compartments for circulating vascular endothelial growth factor. *Angiogenesis* 6, 283–287. doi: 10.1023/B:AGEN.0000029415.62384.ba
- Kwong, Y. L., and Khong, P. L. (2011). Central palatal perforation in nasal natural killer cell lymphoma. *Br. J. Haematol.* 152 (1), 2. doi: 10.1111/j.1365-2141.2010.08461.x
- Kwong, Y. L. (2005). Natural killer-cell malignancies: diagnosis and treatment. *Leukemia* 19 (12), 2186–2194. doi: 10.1038/sj.leu.2403955
- Lee, J., Suh, C., Park, Y. H., Ko, Y. H., Bang, S. M., Lee, J. H., et al. (2006). Extranodal natural killer T-cell lymphoma, nasal-type: a prognostic model from a retrospective multicenter study. *J. Clin. Oncol.* 24, 612–618. doi: 10.1200/JCO.2005.04.1384
- Li, L., Wang, L., Song, P., Geng, X., Liang, X., Zhou, M., et al. (2014). Critical role of histone demethylase RBP2 in human gastric cancer angiogenesis. *Mol. Cancer* 13, 81. doi: 10.1186/1476-4598-13-81
- Lin, J. P., Lin, J. X., Cao, L. L., Zheng, C.-H., Li, P., Xie, J.-W., et al. (2017). Preoperative lymphocyte-to-monocyte ratio as a strong predictor of survival and recurrence for gastric cancer after radical-intent surgery. *Oncotarget* 8 (45), 79234–79247. doi: 10.18632/oncotarget.17058
- Lowther, D. E., and Hafler, D. A. (2012). Regulatory T cells in the central nervous system. *Immunol. Rev.* 248 (1), 156–169. doi: 10.1111/j.1600-065X.2012.01130.x
- McMillan, D. C., Canna, K., and McArdle, C. S. (2003). Systemic inflammatory response predicts survival following curative resection of colorectal cancer. *Br. J. Surg.* 90, 215–219. doi: 10.1002/bjs.4038
- McMillan, D. C. (2013). The systemic inflammation-based Glasgow Prognostic Score: a decade of experience in patients with cancer. *Cancer Treat Rev.* 39 (5), 534–540. doi: 10.1016/j.ctrv.2012.08.003
- Montaldo, E., Vacca, P., Moretta, L., and Mingari, M. C. (2014). Development of human natural killer cells and other innate lymphoid cells. *Semin. Immunol.* 26 (2), 107–113. doi: 10.1016/j.smim.2014.01.006

- Muller, I., Munder, M., Kropf, P., and Hansch, G. M. (2009). Polymorphonuclear neutrophils and T lymphocytes: strange bedfellows or brothers in arms? *Trends Immunol.* 30, 522–530. doi: 10.1016/j.it.2009.07.0077
- Nazha, B., Moussaly, E., Zaarour, M., Weerasinghe, C., and Azab, B. (2015). Hypoalbuminemia in colorectal cancer prognosis: Nutritional marker or inflammatory surrogate? *World J. Gastrointest. Surg.* 7, 370–377. doi: 10.4240/wjgs.v7.i12.370
- Petrie, H. T., Klassen, L. W., and Kay, H. (1985). Inhibition of human cytotoxic T lymphocyte activity in vitro by autologous peripheral blood granulocytes. *J. Immunol.* 134, 230–234.
- Rajendran, P., Chen, Y., Chen, Y., Chung, L., Tamilselvi, S., Shen, C., et al. (2018). The multifaceted link between inflammation and human diseases. *J. Cell. Physiol.* 233 (9), 6458–6471. doi: 10.1002/jcp.26479
- Rajwa, P., Życzkowski, M., Paradysz, A., Bujak, K., and Bryniarski, P. (2018). Evaluation of the prognostic value of LMR, PLR, NLR, and dNLR in urothelial bladder cancer patients treated with radical cystectomy. *Eur. Rev. Med. Pharmacol. Sci.* 22 (10), 3027–3037. doi: 10.26355/eurrev\_201805\_15060
- Rickinson, A. B., Murray, R. J., Brooks, J., Griffin, H., Moss, D. J., and Masucci, M. G. (1992). T cell recognition of Epstein–Barr virus associated lymphomas. *Cancer Surv.* 13, 53–80.
- Shamamian, P., Schwartz, J. D., Pocock, B. J., Monea, S., Whiting, D., Marcus, S. G., et al. (2001). Activation of progelatinase A (MMP-2) by neutrophil elastase, cathepsin G, and proteinase-3: a role for inflammatory cells in tumor invasion and angiogenesis. *J. Cell Physiol.* 189, 197–206. doi: 10.1002/jcp.10014
- Stotz, M., Pichler, M., Absenger, G., Szkandera, J., Arminger, F., Schaberl-Moser, R., et al. (2014). The preoperative lymphocyte to monocyte ratio predicts clinical outcome in patients with stage III colon cancer. *Br. J. Cancer* 110 (2), 435–440. doi: 10.1038/bjc.2013.785
- Sun, J. C., and Lanier, L. L. (2011). NK cell development, homeostasis and function: parallels with CD8+ T cells. *Nat. Rev. Immunol.* 11 (10), 645–657. doi: 10.1038/nri3044
- Tan, Z., Zhang, M., Han, Q., Wen, J., Luo, K., Lin, P., et al. (2017). A novel blood tool of cancer prognosis in esophageal squamous cell carcinoma: the Fibrinogen/Albumin Ratio. *J. Cancer* 8 (6), 1025–1029. doi: 10.7150/jca.16491
- Tse, E., and Kwong, Y. L. (2013). How I treat NK/T-cell lymphomas. *Blood* 121 (25), 4997–5005. doi: 10.1182/blood-2013-01-453233
- Weitzman, S. A., and Gordon, L. I. (1990). Inflammation and cancer: role of phagocyte-generated oxidants in carcinogenesis. *Blood* 76, 655–663. doi: 10.1182/blood.V76.4.655.655
- Yi, J. H., Wang, D., Li, Z. Y., Hu, J., Niu, S.-F., and Liu, X.-L. (2014). C-reactive protein as a prognostic factor for human osteosarcoma: A meta-analysis and literature review. *PLoS One* 9, e94632. doi: 10.1371/journal.pone.0094632

**Conflict of Interest:** The authors declare that the research was conducted in the absence of any commercial or financial relationships that could be construed as a potential conflict of interest.

Copyright © 2020 Huang, Chen, Fang, Guo, Lin, Hong, Li, Wang, Tian, Chen, Yao, Chen, Li and Pan. This is an open-access article distributed under the terms of the Creative Commons Attribution License (CC BY). The use, distribution or reproduction in other forums is permitted, provided the original author(s) and the copyright owner(s) are credited and that the original publication in this journal is cited, in accordance with accepted academic practice. No use, distribution or reproduction is permitted which does not comply with these terms.



# Artificial Intelligence-Based Multiclass Classification of Benign or Malignant Mucosal Lesions of the Stomach

Bowei Ma<sup>1,2†</sup>, Yucheng Guo<sup>1,2†</sup>, Weian Hu<sup>2</sup>, Fei Yuan<sup>3</sup>, Zhenggang Zhu<sup>4</sup>, Yingyan Yu<sup>4\*</sup> and Hao Zou<sup>1,2\*</sup>

<sup>1</sup> Center for Intelligent Medical Imaging & Health, Research Institute of Tsinghua University in Shenzhen, Shenzhen, China, <sup>2</sup> Tsimage Medical Technology, Yantian Modern Industry Service Center, Shenzhen, China, <sup>3</sup> Department of Pathology, Ruijin Hospital, Shanghai Jiao Tong University School of Medicine, Shanghai, China, <sup>4</sup> Department of General Surgery, Ruijin Hospital, Shanghai Institute of Digestive Surgery, Shanghai Key Lab for Gastric Neoplasms, Shanghai Jiao Tong University School of Medicine, Shanghai, China

## OPEN ACCESS

### Edited by:

Salvatore Salomone,  
University of Catania, Italy

### Reviewed by:

Xin Qi,  
Rutgers, The State University of  
New Jersey, United States  
Bruno Annibale,  
Sapienza University of Rome, Italy  
Louis Joseph Vaickus,  
Dartmouth College, United States

### \*Correspondence:

Yingyan Yu  
yingyan3y@sjtu.edu.cn  
Hao Zou  
hzou@tsinghua.edu.cn

<sup>†</sup>These authors have contributed  
equally to this work

### Specialty section:

This article was submitted to  
Experimental Pharmacology  
and Drug Discovery,  
a section of the journal  
Frontiers in Pharmacology

Received: 14 June 2020

Accepted: 08 September 2020

Published: 02 October 2020

### Citation:

Ma B, Guo Y, Hu W, Yuan F, Zhu Z,  
Yu Y and Zou H (2020) Artificial  
Intelligence-Based Multiclass  
Classification of Benign or Malignant  
Mucosal Lesions of the Stomach.  
Front. Pharmacol. 11:572372.  
doi: 10.3389/fphar.2020.572372

Gastric cancer (GC) is one of the leading causes of cancer-related death worldwide. It takes some time from chronic gastritis to develop in GC. Early detection of GC will help patients obtain timely treatment. Understanding disease evolution is crucial for the prevention and treatment of GC. Here, we present a convolutional neural network (CNN)-based system to detect abnormalities in the gastric mucosa. We identified normal mucosa, chronic gastritis, and intestinal-type GC: this is the most common route of gastric carcinogenesis. We integrated digitalizing histopathology of whole-slide images (WSIs), stain normalization, a deep CNN, and a random forest classifier. The staining variability of WSIs was reduced significantly through stain normalization, and saved the cost and time of preparing new slides. Stain normalization improved the effect of the CNN model. The accuracy rate at the patch-level reached 98.4%, and 94.5% for discriminating normal → chronic gastritis → GC. The accuracy rate at the WSIs-level for discriminating normal tissue and cancerous tissue reached 96.0%, which is a state-of-the-art result. Survival analyses indicated that the features extracted from the CNN exerted a significant impact on predicting the survival of cancer patients. Our CNN model disclosed significant potential for adjuvant diagnosis of gastric diseases, especially GC, and usefulness for predicting the prognosis.

**Keywords:** histology, whole-slide imaging, deep learning, convolutional neural network, gastric cancer

## INTRODUCTION

Gastric cancer (GC) is one of the leading causes of cancer-related death worldwide, especially in Asia (Van Cutsem et al., 2016; Thrift and El-Serag, 2019). By 2030, deaths from GC globally are predicted to increase from the 15<sup>th</sup> to the 10<sup>th</sup> leading cause of cancer related death (Mathers and Loncar, 2006). Due to a lack of effective diagnostic methods, early detection of GC is difficult, which can delay optimal surgical treatment.



Based on histology, GC is divided mainly into “intestinal” and “diffuse” types (Lauren, 1965; Liu et al., 2013). In the former, it is often preceded by several decades of chronic gastritis. The intestinal type of GC is responsible for ~60% of GC cases (Tan and Yeoh, 2015). The stomach is an abdominal organ, so the cancer has often reached an advanced stage or may have metastasized to a distant location by the time significant symptoms appear (Orditura et al., 2014). Therefore, studying the diagnosis and evolution of gastric mucosal lesions is important.

Patients suspected of having GC should undergo endoscopy first. Abnormal tissue seen upon endoscopy will be sent for histology to check for cancerous cells. Histology and pathology reports for biopsies are the “gold standard” in the final diagnosis of cancer worldwide (Thrumurthy et al., 2013). Pathologists visually inspect pathology slides to identify abnormalities, which is a prolonged and tedious process. The human eye is limited in recognizing subtle changes and rare high-dimensional features in tissues, which may result in inter- and intra-observer variability (Raab et al., 2005). Nonstandard subjective judgments can also lead to low diagnostic concordance (Stoler and Schiffman, 2001; Elmore et al., 2015). However, the speed, accuracy and consistency of classification could be improved by application of artificial intelligence (AI) (Gurcan et al., 2009; Ghaznavi et al., 2013).

In recent years, models of “deep learning”, especially “convolutional neural networks” (CNNs) have been shown to perform exceptionally well in computer-vision and pattern-analysis tasks, such as image recognition, semantic segmentation, and object detection (Cruz-Roa et al., 2013; LeCun et al., 2015; Schmidhuber, 2015; Shelhamer et al., 2017; Ren et al., 2017). CNNs can “learn” latent representations of one image to capture complex nonlinear relationships in image data. They can discover more abstract and useful features that make it easier to extract useful information for high-level tasks (Bengio et al., 2013; Wang et al., 2014; Guo et al., 2019).

Research on AI-based cancer histopathology has become an important branch of “digital pathology”. The increased availability of many-gigapixel whole-slide images (WSIs) of tissue specimens has enabled AI to aid detection and classification of cancer (Litjens et al., 2017). Studies have shown that various CNN architectures can be implemented and applied to hematoxylin and eosin (H&E)-stained biopsy slides, such as mitosis detection for biopsy slides of breast tissue and automated detection of basal cell carcinoma (Cruz-Roa et al., 2013; Malon and Cosatto, 2013; Wang et al., 2014). Some scholars have made preliminary achievements in digital-pathology images of GC (Sharma, 2017; Sharma et al., 2017a). A simple CNN architecture for automatic classification of GC using WSIs in histopathology has been described by Sharma et al. (Sharma et al., 2017b), thereby revealing the practicability of AI in digital-pathology research for GC. However, their work has rarely focused on how the deep-learning framework identifies GC lesions, nor how the results might influence the prognosis (Droste et al., 2019; Iizuka et al., 2020).

In the present study, we undertook detection and classification of normal mucosa, chronic gastritis, and

intestinal-type GC, which is the most common route of gastric carcinogenesis. This was achieved by proposing a method combining stain normalization, deep CNN, and random forest (RF) classifier. More importantly, we conducted research on how the AI program focused on extracting the morphologic characteristics of gastric mucosal lesions at different stages, which revealed their evolution. Furthermore, we investigated the possible clinical improvement our method could facilitate. We predicted the survival of GC patients by combining the extracted pathologic features from WSIs with clinical follow-up data.

## MATERIALS AND METHODS

### Dataset and Image Annotation

All gastric-tissue sections were stained with H&E. Then, they were digitalized using a KF-pro-400 scanner (Jiangfeng, Ningbo, China) at 400× magnification. A total of 763 WSIs with manual annotations from the stomach (normal mucosa, chronic gastritis, and GC) were enrolled. Of those, 338 cases were normal gastric tissues (including normal mucosa and smooth muscle), and 118 cases were chronic gastritis. Another 307 cases were intestinal-type GC. All these images were authorized by Ruijin Hospital (Shanghai, China). The study protocol was approved by the ethics review board of Ruijin Hospital. Written informed consent was obtained from patients to use their data.

The digitalized slides were annotated by senior pathologists (YY and FY) with ASAP (an open-source platform for visualizing, annotating and analyzing WSIs; <https://computationalpathologygroup.github.io/ASAP/>). The key-components of ASAP are: slide input/output, simple image processing, and image viewer. Irregular curves or polygons were used to encircle normal, chronic-gastritis, and GC regions separately in the images. Human-readable Extensible Markup Language (XML) files were generated automatically after manual annotation with a specific format. Data preprocessing involved use of delicate parsing method to extract the annotation information in the XML files to determine the label positions in the digital image.

### Regions of Interest Extraction and Image Segmentation

The size of each WSI can reach  $5 \times 10^4$  pixels in both width and height, which is usually beyond the processing power of computers. Hence, we segmented the WSIs into image patches, and then carried out operations on the cut patches. The process of regions of interest (RoI) extraction is shown in **Figure S1**. One canonical method to distinguish the background area from foreground objects is to threshold the image with a “binary mask”. Objects in the WSIs presented various colors and it was inappropriate to use a uniform fixed threshold to distinguish the background and target of all images. Instead, several adaptive threshold methods were applied and compared. The Otsu algorithm (Otsu, 1979) was adopted to determine the threshold of binary-image segmentation by minimizing the intra-class

variation (Szegedy et al., 2016a). Then, we undertook a morphologic close operation (which is equivalent to dilation followed by erosion) to close small holes and fill the concave corners in the image. Finally, regions with too small area were abandoned.

In training process, patch-cutting mimics pathologists viewing glass slides from low-power to high-power of a microscope to extract image patches of different sizes: 768×768, 1,024×1,024, 1,495×1,495 and up to 2,048×2,048 pixels. Finally, patches were resized to 299 pixels in weight and height before sending into the CNN. These procedures can train many characteristics at different scales, including the contours of certain lesions and detailed textures. Other too small or too large patches were not adequate for further analyses. The patch size is set as 1,024×1,024 when generating heatmap so that patches can connect to each other by the same side length.

## Stain Normalization and Data Augmentation

To overcome the staining inconsistency of histology slides, multiple researchers have applied operations to standardize specimen colors in histopathological images prior to analysis (Ranefall et al., 1997; Reinhard et al., 2001; Macenko et al., 2009; Tam et al., 2016; Vahadane et al., 2016; Anghel et al., 2019; Ren et al., 2019). One common approach to tackle stain normalization issue is to extract multiple affinities for specific biological substances, and then perform some kind of projection from a preselected reference image to all images. Specifically, color deconvolution methods (Macenko et al., 2009; Vahadane et al., 2016; Anghel et al., 2019) have been utilized extensively in the past decades by transforming the original RGB image into other color space like Lab (Reinhard et al., 2001) and extract the stain vectors. Unsupervised vector estimation methods (Anghel et al., 2019) and generative methods (Ren et al., 2019) have also emerged in the past years. In this study, we applied an internal-feature information of image A to another image B through a specific operation. In brief, a set of characteristic parameters (the RGB color model values of hematoxylin and eosin) are extracted from a reference image, following by a mapping function (Beer-Lambert Law to generate the optical density image and re-assemble the target image's concentration matrix) that converts the appearance of a given image to the reference image. The parameters are, in general, defined to capture the color distribution of H&E images. As a result, the color distribution of a stain-normalized image will have a great resemblance to the reference image. In general, nuclei are dark-purple (hematoxylin dye) and the cytoplasm is light-pink (eosin dye). To eliminate the influence of the void (white) pixels of the background, we applied a threshold on pixel luminosity to isolate different regions (Macenko et al., 2009). In instances of severe fading, brightness standardization of the images was carried out (Tam et al., 2016). The 2×3 stain matrix,  $S$ , was composed of the robust extreme, defined by the two principle eigen-vectors of the optical density (OD) covariance matrix on the angular polar plane. With the extracted stain matrix, the concentration matrix,  $C$ , of a given target image could be solved from the equation  $OD = C \times S$ .

Data augmentation can ease the problem of having few samples. Therefore, we processed affine transformations, such

as 30° rotations, migrations by 20% of the dimension, image flipping horizontally and vertically, and shearing by a factor of 0.2. We did not make any extra adjustment on the brightness and contrast of images to preserve the color and texture features of the images after stain normalization.

## Patch Classification at the WSIs-Level and Features Extraction

Due to the limitation of time and hardware, it was impossible to test multiple models on all patches extracted. Therefore, we made a preliminary attempt with a small amount of data on models before using all patches. Models used included Vgg16 (Simonyan and Zisserman, 2014), Resnet50 (He et al., 2016), InceptionResnet v2 (Szegedy et al., 2016a), Densenet169 (Huang et al., 2017) and Inception v3 (Szegedy et al., 2016b). The result of the preliminary attempt showed that Inception v3 was of great potential in this study.

Inception v3 of the open source of Google™ was selected, which contains the module characteristics suitable for pathology tasks (Ker et al., 2019). Inception v3 has been applied in classification tasks in skin cancer (Esteva et al., 2017) and diabetic retinopathy (Gulshan et al., 2016). We added a global average pooling layer, two fully connected layers, and a soft-max layer on the basis of Inception v3. Thus, a modified deep CNN with 43 layers was applied at patch-level classification. The CNN structure is shown in **Figure S2**.

To test the performance of the CNN model for distinguishing different images from various types of gastric diseases, the CNN was trained “from scratch” for 25 epochs with an exponentially decayed learning rate starting at  $10^{-3}$ . Then, the set of hyper-parameters with the highest accuracy on the validation set was fine-tuned for another 25 epochs with an exponentially decayed learning rate starting at  $10^{-4}$ . In the training process, we used Adam as the optimizer, which has faster convergence speed and can avoid loss function compared with other adaptive learning rate algorithms. The CNN parameters were randomly initialized at the beginning of the first training epoch. Meanwhile, “Cross entropy” was chosen as the loss function corresponding to the soft-max layer.

After obtaining “cancer likelihood maps” from the patches-based classification, we undertook post-processing to extract WSIs-level characteristics. One cancer-likelihood map was created for each WSI, which was an assembled heatmap ( $H$ ) from enormous patches. One pixel ( $x, y$ ) in  $H$  was generated by assembling the malignant probabilities by taking the highest probability of patches containing the point ( $x, y$ ). That is,

$$H(x, y) = \max_{p \in P} (I\{(x, y) \in p\}) * (\Pr(p! = normal)),$$

where  $P$  is the set of all patches extracted from the WSI,  $p$  is one particular patch in the WSI,  $I(\cdot)$  is the indicator function, and  $\Pr(p! = normal)$  is the malignant probability of patch  $p$ . The tumor-probability threshold (denoted as  $P_{tumor}$ ) in the probability section indicates that a pixel in the heatmap is regarded as a tumor pixel if its malignant probability is greater than the threshold.

## RF Classifier for WSIs-Level Classification

To reduce the overfit of the training data due to their randomness, we introduced a RF (Breiman, 2001). A RF is an integrated supervised learning algorithm which ensures that the results of the whole model have high accuracy and considerable generalization performance. The features extracted in the above process are given as the input of the model used for classification at the WSIs-level. The reason that we did not use an end to end approach on WSIs-level classification was that WSIs without preprocessing would cause memory overflow. All the training WSIs were the same as those selected as the training data at the patch-level.

## Visualization of Morphologic Characteristics of Different Gastric Lesions

We wished to construct saliency maps (Simonyan et al., 2013) of the normal mucosa, chronic gastritis, and GC. Hence, we needed to compute the gradients of the unnormalized class score with respect to image pixels, and take the maximum value over red/green/blue (RGB) channels to depict the visually interesting locations in an image. Such topologic representation describes the contribution of each pixel in an image to the confidence of the CNN to classify that image into a specific lesion class. We adopted Grad-CAM (Selvaraju et al., 2020) to produce a coarse localization map highlighting the important regions for predicting the lesions. Grad-CAM takes class-specific gradient information flowing into the penultimate layer of a CNN, and computes an “attention map” showing how intensely the input image activates different channels in the layer with regard to the class. To avoid information loss in the final dense layers, such spatial information in the penultimate layer provides additional guidance. Then, we investigated whether the CNN captured certain cell, nucleus, gland, tissue or stroma features to help identify gastric lesions and make the final decision.

## Survival Analyses

Survival analysis is a crucial ingredient which provides important information about a patient's prognosis status for treatment design and selection. The combination of clinical features as well as clinicopathological features extracted by machine learning methods like Support Vector Machine (Zhang et al., 2011), Random Forest (Liao et al., 2020), Lasso regression (Li et al., 2019) as well as Deep CNN (Ren et al., 2019) has been proved to substantially enhance the accuracy of survival analysis for different kinds of cancers. To expand the clinical usefulness of our CNN system, we undertook survival analyses which combined the features extracted by the CNN with clinical follow-up data for GC. “Survival” was defined as the percentage of people who survived for a specified period of time. The clinicopathologic features used in RF Model 1 are listed in **Table S2**. We discretized survival duration (right-censored) as <1 year, 1–5 years, and >5 years. Then, the WSIs-level features and clinicopathologic data were fed into a RF classifier. We also compared the prediction performance with the model excluding WSIs-level features for evaluating the effects of WSIs-level

features of the CNN system. The Kaplan–Meier estimation method was used (Campos-Filho and Franco, 1988; Miettinen, 2008).

## RESULTS

### Image Patches Produced for CNN Analyses

We used 534 (70%) out of 763 H&E-stained WSIs for the training set, 153 (20%) as the test set, and 76 (10%) as the validation set. The latter was used only to “tune” hyperparameters in the training process of the CNN. The test set was exposed only when evaluating the performance of the CNN model. The dataset covered >1.6 million image patches in the training set, and 0.4 million image patches in the test set (**Table 1**). In the preliminary attempt, about one fifth of the above patches were used.

### Stain Normalization and Extraction of Features

Results of the preliminary attempt are listed in **Table S1**. Inception v3 achieved the highest accuracy in the test set among all models, which indicated that the model had great potential in this study. Therefore, Inception v3 was selected as the final CNN structure.

All patches were included in the results described below. In the binary classification (benign *versus* cancer) without stain normalization, the best prediction accuracy on the test set was 98.1%. The prediction accuracy improved to 98.4% after stain normalization. The specificity and sensitivity increased with stain normalization, from 98.2% to 98.9% and from 97.8% to 98.0%, respectively. Stain normalization helped the classification by unifying the distribution of the pixels in the color spaces. **Figure 1A** shows an example of color distribution of the two image patches with and without stain normalization. Despite the original huge color variation of the two patches, the distribution of pixel color was much alike after stain normalization. The improved performance was attributed to the better morphology observed using digital images, so the CNN model could “grasp” directly the different features between them for identification. The receiver operating characteristic curve (ROC) curve for the patch-level classification as well as the corresponding confusion matrix is shown in **Figure 1B**. We further trained and tested the CNN model on the datasets from three classes (normal mucosa, chronic gastritis, and GC), and the best three-class prediction accuracy of the test set was 94.5%. Stain normalization also showed an improvement in three-class patch classification,

**TABLE 1** | Image numbers at the patch-level of the study.

Images origin	Training set	Test set	Validation set
Normal	544,925	135,446	68,201
Chronic gastritis	544,624	125,783	66,678
Cancer	527,164	138,011	67,452
Total	1,616,713	399,240	202,331



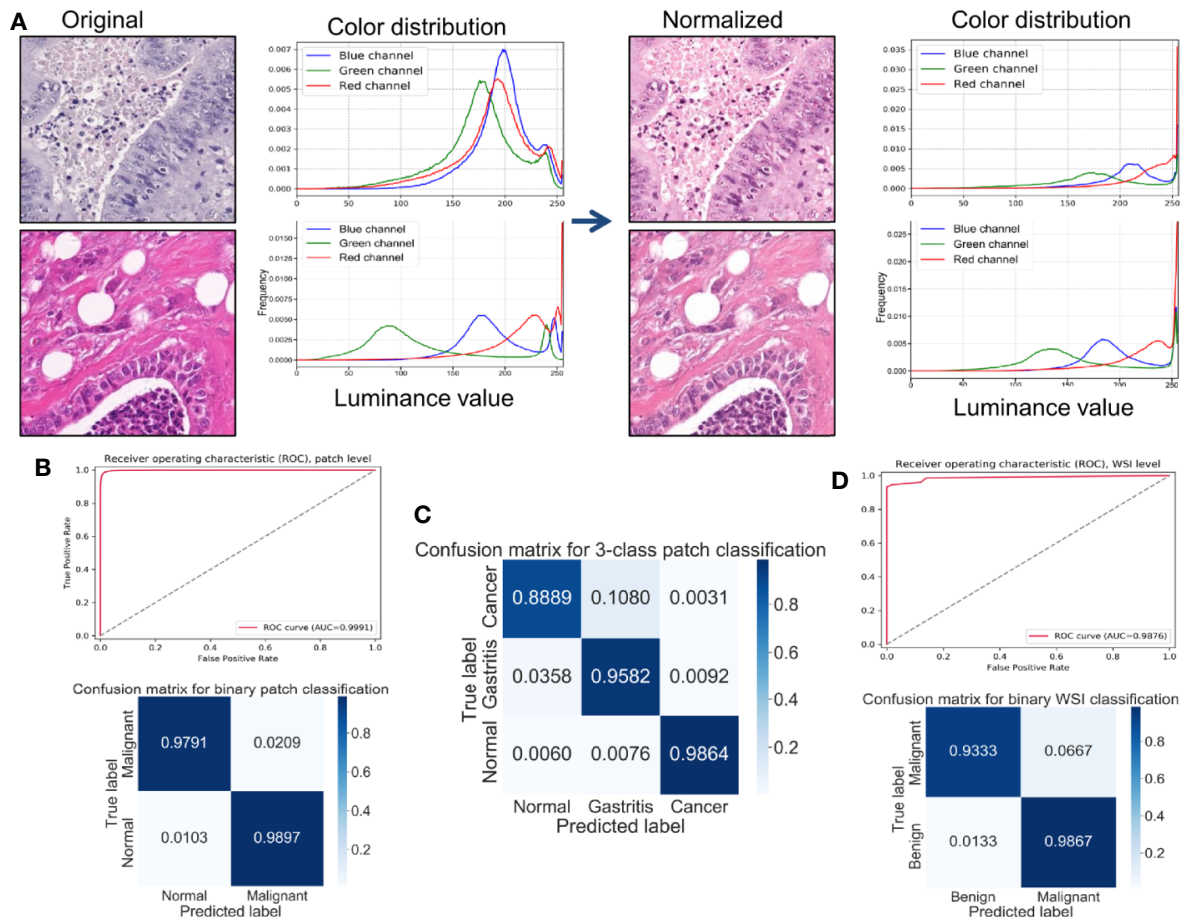


**FIGURE 1** | Stain normalization improves the performance of classification at the patch-level and WSIs-level. **(A)** Example of color distributions with or without stain normalization. Left: Two originally stained image patches with their corresponding pixel-color distribution in red/green/blue (RGB) color channels. Right: The same patches after stain normalization and their corresponding pixel-color distribution in RGB color channels. **(B)** Receiver operating characteristic (ROC) curve and normalized confusion matrix for a convolutional neural network (CNN) binary classification model at the patch-level. **(C)** Normalized confusion matrix of a CNN three-class classification model at the patch-level. **(D)** ROC curve and normalized confusion matrix for a random forest binary classification model at the WSIs-level.

where the prediction accuracy on the test set with a primary stain was 93.8%. The confusion matrix shown in **Figure 1C** indicates that the reduction in test accuracy (compared with the binary classification) was caused mainly by 10.8% of normal mucosa patches being classified as chronic-gastritis patches.

In everyday clinical practice, whole slices from patients are a combination of normal mucosa, chronic gastritis, and GC. We separated all WSIs into categories: “complete normal WSIs” and “mixture WSIs” with gastritis or GC. After generating cancer-likelihood heatmaps from the patch-level classification, we undertook post-processing to extract WSIs-level characteristics. Referring to relevant study (Wang et al., 2018), forty-four features were extracted from the malignant probability (denoted as  $P_{tumor}$ ) heatmap (**Table 2**) in our study, including various morphologic features, such as the long axis length of the largest predicted tumor region. After this feature-extraction process, a RF classifier with 44 extracted features was trained and fine-tuned. The accuracy of the model on the test set was 96.0%, whereas the specificity was 93.3% and sensitivity was

98.7%. The ROC curve for the WSIs-level RF classification as well as the corresponding confusion matrix is shown in **Figure 1D**.

## Visualization of Morphologic Characteristics for Different Gastric Lesions

Visualization of morphologic characteristics is a vital function for a deep-learning model because it can show what the model has learnt. We wished to ascertain if the CNN model had seized certain key characteristics of different gastric lesions. Hence, we undertook gradient-weighted class activation mapping (Grad-CAM) and saliency mapping for presentation of patch-level extracted features from the WSIs of different lesions, which corresponded to the evolutionary route of normal mucosa → chronic gastritis → GC. Both visualization styles are presented as heatmaps at patch-level.

Grad-CAM is able to capture certain object contours, which are shown as an overlaid heatmap by blending the computed

**TABLE 2 |** The 44 features extracted from a heatmap of malignant probability at the whole-slide images (WSIs)-level.

Index	Explanation of feature	Probability remark
1	Total number of tumor regions with an area greater than a threshold	$P_{\text{tumor}} \geq 0.90$ , area threshold $\geq 0.05$ total area
2	Area percentage of tumor region over the whole tissue region	$P_{\text{tumor}} \geq 0.90$
3	Area of the largest tumor region	$P_{\text{tumor}} \geq 0.50$
4	Long axis of the largest tumor region	$P_{\text{tumor}} \geq 0.50$
5	Percentage of pixels with a high probability of malignancy	$P_{\text{tumor}} \geq 0.90$
6	Average prediction across the tumor region	$P_{\text{tumor}} \geq 0.90$
7–11	Max, mean, variance, skewness, and kurtosis of the tumor area	$P_{\text{tumor}} \geq 0.90$
12–16	Max, mean, variance, skewness, and kurtosis of the tumor perimeter	$P_{\text{tumor}} \geq 0.90$
17–21	Max, mean, variance, skewness, and kurtosis of tumor compactness (eccentricity)	$P_{\text{tumor}} \geq 0.90$
22–26	Max, mean, variance, skewness, and kurtosis of tumor rectangularity (extent)	$P_{\text{tumor}} \geq 0.50$
27–35	Mean, variance, standard deviation, median, mode, min, max, range, sum of tumor probabilities	n/a
36	Average of malignant probability	n/a
37	Proportion of tumor patches with $P_{\text{tumor}} > P_{\text{min}}$	$P_{\text{min}} = 0.999$
38	Proportion of tumor patches with $P_{\text{max}} \geq P_{\text{tumor}} > P_{\text{min}}$	$P_{\text{max}} = 0.999$ , $P_{\text{min}} = 0.99$
39	Proportion of tumor patches with $P_{\text{max}} \geq P_{\text{tumor}} > P_{\text{min}}$	$P_{\text{max}} = 0.99$ , $P_{\text{min}} = 0.95$
40	Proportion of tumor patches with $P_{\text{max}} \geq P_{\text{tumor}} > P_{\text{min}}$	$P_{\text{max}} = 0.95$ , $P_{\text{min}} = 0.9$
41	Proportion of tumor patches with $P_{\text{max}} \geq P_{\text{tumor}} > P_{\text{min}}$	$P_{\text{max}} = 0.9$ , $P_{\text{min}} = 0.8$
42	Proportion of tumor patches with $P_{\text{max}} \geq P_{\text{tumor}} > P_{\text{min}}$	$P_{\text{max}} = 0.8$ , $P_{\text{min}} = 0.7$
43	Proportion of tumor patches with $P_{\text{max}} \geq P_{\text{tumor}} > P_{\text{min}}$	$P_{\text{max}} = 0.7$ , $P_{\text{min}} = 0.6$
44	Proportion of tumor patches with $P_{\text{max}} \geq P_{\text{tumor}} > P_{\text{min}}$	$P_{\text{max}} = 0.6$ , $P_{\text{min}} = 0.5$

localization map into the original patch image with 50% transparency. “Warmer” colors correspond to more significant lesions, and *vice versa*. The saliency map was represented by a heatmap indicating the regions whose change would contribute most toward maximizing the predicted probability of that patch belonging to its “true” class (normal, chronic gastritis, or GC). The warmer the color in the heatmap, the higher the possibility the area had to the prediction and *vice versa*.

The most prominent characteristics of normal mucosa was the compactness of lining mucosal cells, as well as the morphologic regularity of the structure. Often, morphologic characteristics were seen with patches extracted with a high-power view (patches with pixels of 1,495×1,495 or larger, as shown in **Figure 2A**). Tubular glands were packed closely and separated from each other by the lamina propria. The contour of assembly of the tubular glands with a regular shape was captured clearly, especially in those patches extracted with a low-power view (patches of pixel size 1495×1495 or smaller, as shown in **Figure 2B**).

In chronic gastritis, the significant characteristics were inflammation and intestinal metaplasia (IM), while atrophic lesion of gastric mucosa is the key intermediate stage of transition and development to early GC. IM was captured at high-power magnification at patch-level (patch dimensionality at pixel size 1,024×1,024 or smaller), which disclosed loss of normal mucous glands, as well as the epithelial cells resembling the glands of the intestinal mucosa. The deformed glands could be seen clearly in Grad-CAM presentation (**Figure 2C**) and irregularly shaped intracytoplasmic mucin droplets were observed in the saliency map (**Figure 2D**).

According to Grad-CAM, GC presented with irregularly shaped glands with nuclear pleomorphism and a disordered structure. Distended tubules surrounded by polymorphous cancer cells can be observed at the patch-level in **Figure 2E**. The cancerous features of irregularly shaped and fused neoplastic glands are captured in **Figure 2F**. These glands tended to be

fused irregularly or expanded, and filled with inflammatory debris or necrotic cells.

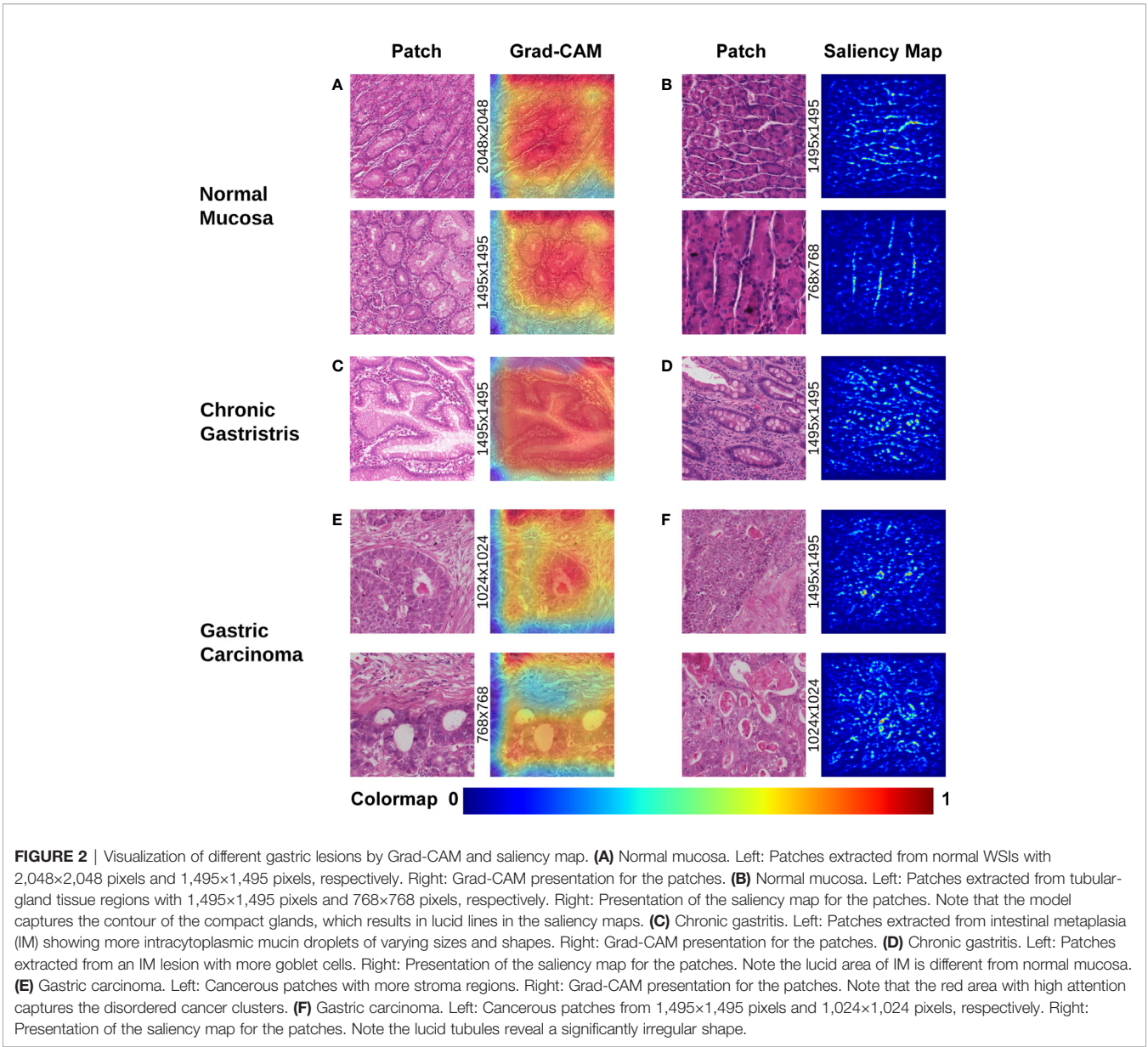
## Features Extracted by CNNs Are Useful for Predicting Outcome

Follow-up data were collected for 273 (88.93%) out of 307 GC patients. The mean duration of follow-up was 46.1 months. The mean age of the study cohort was 61.9 years, and 83.9% of cases were older than 50 years. Clinicopathologic staging was according to the 7<sup>th</sup> TNM staging criteria of the American Joint Committee on Cancer/International Union Against Cancer Classification for gastric adenocarcinoma (Ahn et al., 2010).

The longest living case was first recorded over 12 years ago. Among them, 118 patients had already died whereas 155 cases were alive. The survival time of patients was discretized into three categories with right-censoring, that is, patients who: (i) died within 12 months; (ii) died within 5 years, but survived for  $\geq 12$  months; (iii) survived for  $\geq 5$  years. Three RF models with well-tuned hyper-parameters were trained: (i) RF Model 1 (used only clinicopathologic features) (**Table S2**); (ii) RF Model 2 (used 44 extracted features by CNN) (**Table 2**); (iii) RF Model 3 (used all features, including clinicopathologic features and the 44 features extracted by the CNN). With regard to analyses of the RF model, 75% of the data were used for the training set, whereas the remaining 25% were used for the testing set.

After careful tuning of hyper-parameters, the prediction accuracy increased from 92.7% (RF Model 1) to 97.4% (RF Model 3) with the help of the 44 features extracted by the CNN. Hence, a combination of clinicopathologic features with the 44 features extracted by the CNN resulted in an increase in accuracy for predicting survival by 4.7%. In addition, the prediction accuracy was 90.9% with the 44 features extracted by the CNN only (RF Model 2), which suggested that AI-extracted features were important clinically. To clarify the key features of RF Model 3, we inspected the feature importance by





computing the number of tree splits one feature determined in the model. Among the top-10 important features (**Table 3**), five of those were clinicopathologic features, whereas the others were features extracted by the CNN (**Figure 3A**). The survival function is presented in **Figure 3B** for index 9 (number of cancerous lymph nodes), **Figure 3C** for index 36 (proportion of prediction probability >0.999) as well as **Figure 3D** for index 49 (average of predicted tumor probability). Index 36 represents the proportion of the patches whose prediction probability is greater than 0.999 in all patches, while index 49 represents the average probability prediction of all patches in each WSI. We segmented the data into two groups according to the feature we were interested in. The median value of the feature value was used for the cutoff. Mathematically, if we were studying the

TABLE 3   Top-10 features influencing the prognosis.			
Index	Name of feature	Importance of feature	Category
9	Number of cancerous lymph nodes	0.0624	clinical
5	Distant metastasis	0.0598	clinical
7	Depth of tumor infiltration	0.0334	clinical
0	Age of patient	0.0328	clinical
36	Proportion of prediction probability >0.999	0.0282	AI
49	Average of predicted tumor probability	0.0253	AI
4	Macroscopic type of tumor	0.0237	clinical
47	Area of the largest tumor region	0.0235	AI
52	Proportion of prediction between 0.5 and 0.6	0.0224	AI
13	Long axis of the largest tumor region	0.0223	AI

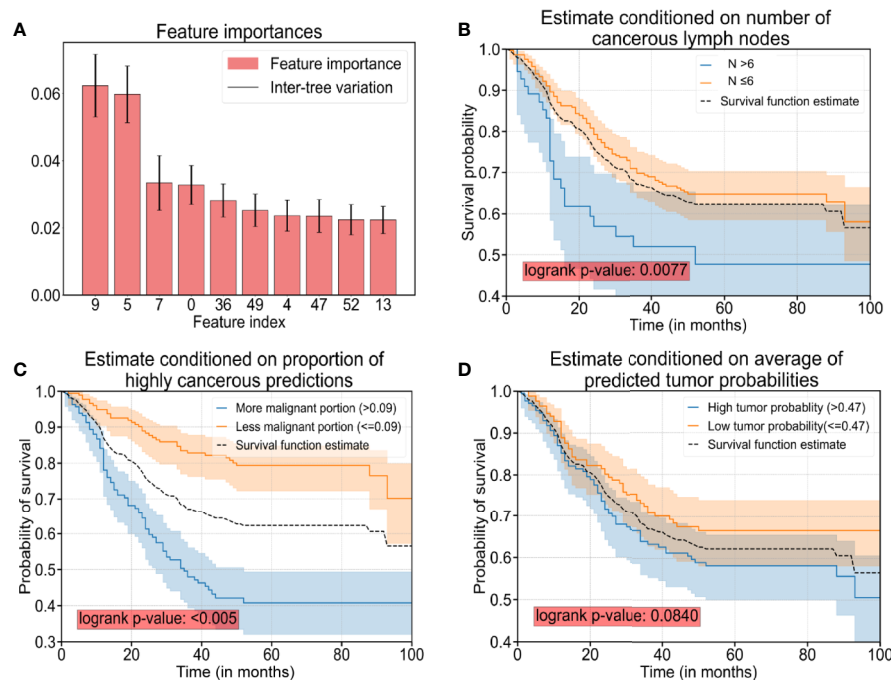


**FIGURE 3 |** The top-10 significant features and survival analyses. **(A)** The top-10 significant features are presented as bar plots (listed in **Table 3**). **(B)** Survival curves conditioned on observed numbers of cancerous lymph nodes (denoted as  $N$ ). **(C)** Survival curves conditioned on the proportion of predicted patches with cancerous probability  $>0.999$ . **(D)** Survival curves conditioned on predicted tumor probability. Note: The black dotted curves in plot **(B–D)** are the same survival curve estimated for all sample cases as a reference.

effect of feature  $x$ , and denoted the median value of  $x$  in the dataset as  $\tilde{x}$ , then we compared the survival function of the two segmented groups using the equations (where  $Pr(X)$  is the probability of event  $X$  and  $T$  denote the survival time of a patient):

$$S(t) = Pr(T > t | x \geq \tilde{x}) \text{ and } S(t) = Pr(T > t | x < \tilde{x})$$

The difference in the two survival distributions was tested by the log-rank test. The 95% confidence interval was presented as the transparent shaded area around the curves.

## DISCUSSION

A deep CNN model for aiding the digital-pathology diagnosis of gastric lesions was designed and implemented. Beyond the classification of histopathologic images, our CNN model also captured features behind the CNN procedure to a certain extent. Currently, CNNs are applied not only in digital pathology, but also in computed tomography (CT) scans, ophthalmoscope images, and ultrasound images (Esteva et al., 2017; De Fauw et al., 2018; Coudray et al., 2018; Philbrick et al., 2018; Falk et al., 2019; Li et al., 2019). Studies (Macenko et al., 2009; Iizuka et al., 2020) have revealed that AI can identify various lesions with a level of competence observed by imaging experts.

Unlike CT scans or ultrasound images, which are grayscale images, WSIs of tissues are color images and more likely to suffer

from color variations due to different staining conditions. Staining inconsistencies may be attributed to multiple factors: dye, staining protocols of laboratories, fading, and digital scanners (Vahadane et al., 2016; Roy et al., 2018). To ease the adverse impact upon the analytic accuracy of AI, multiple scholars have tried various methods to standardize color distribution in images (Khan et al., 2014; Vicory et al., 2015; Bejnordi et al., 2016; Samsi et al., 2018). However, use of a single transformation function for each channel is rarely sufficient. The method of “intensity centering” and histogram equalization enables automatic extraction of reference-stain vectors by finding the fringe of pixel distributions in the optical-density space, but yields poor estimation of the stain vectors in the presence of strong staining variations (Tam et al., 2016). In contrast to the diverse colors of natural images, pathologic images often have a standard staining protocol. The color of pathologic images is affected severely by dyes, storage times, and fading. To tackle such problems, the luminosity of histology slides must be considered because dust and microbes will dim the transparent background and deteriorate the efficacy of stain normalization. We proposed a method involving integration of a brightness-standardization process into stain normalization to filter-out the influence of different levels of brightness and luminosity of the slides.

In analyses of WSIs, considering the gigantic magnitude, Sharma and colleagues designed a program to extract small patches at a fixed scale (e.g.,  $256 \times 256$  pixels) and trained a

deep CNN to classify these small patches (Sharma et al., 2017a). One possible shortcoming of their method is that there are often some spatial correlations between neighboring patches, and discarding such information may result in unstable prediction results.

Here, we proposed a method to remedy such loss in spatial correlation. We combined patches at different scales into the training process: 2,048×2,048, 1,495×1,495, 1,024×1,024, and 768×768 pixels. In this way, not only was the spatial correlation preserved but also the textual contours of different lesions at different scales were captured.

Previously, analyses of the interpretability of pathologic slides of gastric tissue relied merely on simple probability heatmaps (Sharma et al., 2017a). The generated probability loses information about the internal process in deep-learning models.

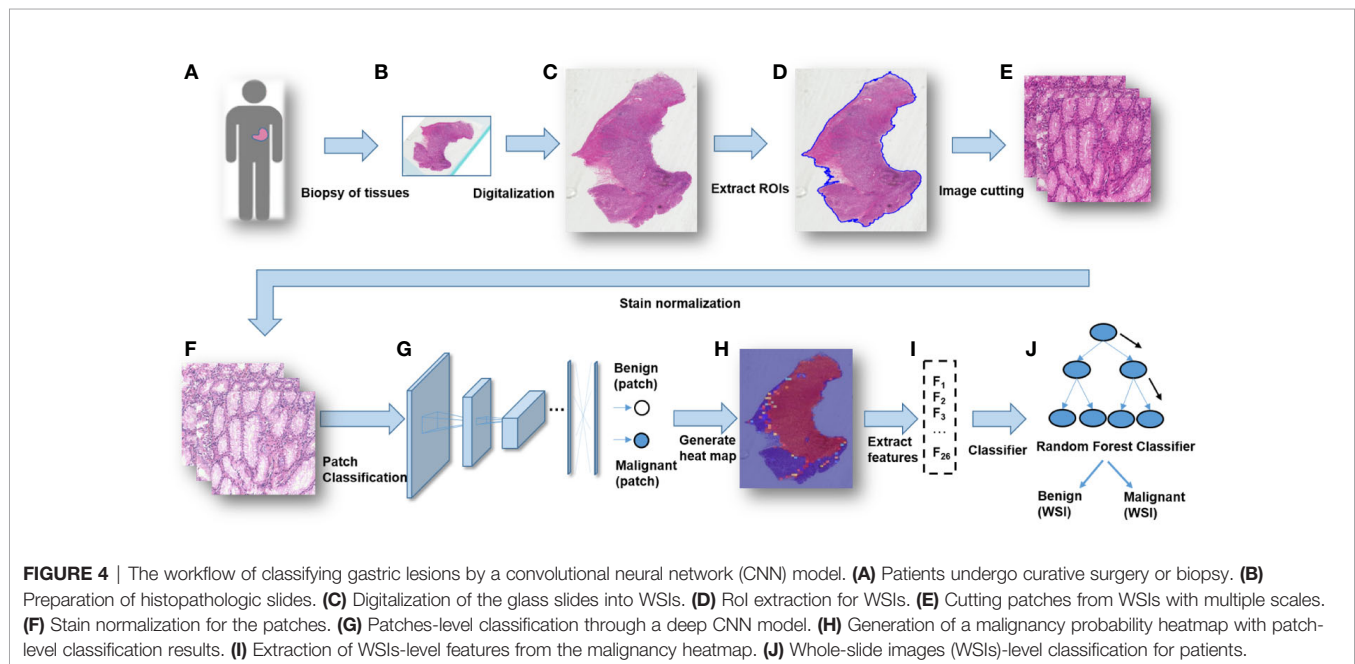
We applied complex visualization methods onto gastric lesions to visualize activation in the deep-learning model and the logic behind its decision. Multiple approaches, including Grad-CAM, saliency maps, and variations in saliency-map computations, such as rectified saliency (Zeiler and Fergus, 2014) and guided saliency (Springenberg et al., 2014), were tested. By examining saliency-map and Grad-CAM visualizations, we showed some morphological features in the figure, which might be of significance in the process of recognition of pathological images by CNN model. Moreover, by carefully inspecting the morphologic features captured by deep-learning models, it is possible to identify various diseases. To uncover the mystery of the CNN model in analyses of medical images, we outlined the key characteristics underlying AI processing, and extracted 44 features, which had roles for discriminating a normal mucosa, chronic gastritis, and intestinal-type GC. Some of those features could be interpreted based on pathologic morphology, others from computing

language. More importantly, the features extracted by the CNN were not only useful for classifying different gastric lesions, they also had a role in predicting the prognosis. This is the first time that crucial features have been revealed for prognostic diagnosis by a CNN model. In the present study, >88% of GC cases were followed up clinically for a long time. Hence, we assessed the possible influencing factors for clinical outcomes. We found that certain features extracted by AI played an important part in assessing disease severity and predicting the prognosis for patients with GC.

Our study had one main limitation. About 30–40% of GCs are classified as diffuse or rare types, which our current system could not identify. The diagnosis of those types of GC, is part of our research which will be carried out in the future and more relevant WSI images have already been prepared. The CNN model we constructed may have a greater role in AI-assisted differential diagnoses for diffuse or rare types of GC in the future. Besides, we will collect cases of different stages between normal type and GC in the next study for better survival analysis.

## CONCLUSIONS

A modified Inception v3 CNN was applied to classify gastric diseases. We segmented WSIs into patches on various scales, and normalized the patches stain. We obtained a good performance for discriminating normal mucosa, chronic gastritis, and intestinal-type GC based on 44 key features at the WSIs-level. The heatmap of malignant probability could provide guidance for pathologists to rapidly notice suspicious regions at the WSIs-level (**Figure 4**). More importantly, certain features extracted from the CNN model revealed clinical importance for predicting disease severity and the prognosis. The future direction of GC study could integrate





clinicopathologic features, extracted AI features, as well as genomic features to guide “precision medicine”.

## DATA AVAILABILITY STATEMENT

All datasets presented in this study are included in the article/**Supplementary Material**.

## ETHICS STATEMENT

This study was approved by the institutional review board of Ruijin hospital, and a written informed consent was obtained from the participants of this study.

## AUTHOR CONTRIBUTIONS

BM, YG, and WH were responsible for the design, implementation and experiments on data preprocessing, data augmentation, training/prediction pipeline, visualization analyses and survival analyses. FY and ZZ collected and assessed clinical information, and YY and HZ supported that

work. All authors contributed to the article and approved the submitted version.

## FUNDING

This project was supported by the Shanghai Science and Technology Committee (18411953100), National Key R&D Program of China (2017YFC0908300, 2016YFC1303200, 2018YFF0301102 and 2018YFF0301105), National Natural Science Foundation of China (81772505), Cross-Institute Research Fund of Shanghai Jiao Tong University (YG2017ZD01), Innovation Foundation of Translational Medicine of Shanghai Jiao Tong University School of Medicine (15ZH4001, TM201617 and TM 201702), and Technology Transfer Project of Science & Technology Department of Shanghai Jiao Tong University School of Medicine.

## SUPPLEMENTARY MATERIAL

The Supplementary Material for this article can be found online at: <https://www.frontiersin.org/articles/10.3389/fphar.2020.572372/full#supplementary-material>

## REFERENCES

- Ahn, H. S., Lee, H. J., Hahn, S., Kim, W. H., Lee, K. U., Sano, T., et al. (2010). Evaluation of the seventh American Joint Committee on Cancer/International Union Against Cancer Classification of gastric adenocarcinoma in comparison with the sixth classification. *Cancer* 116, 24, 5592–5598. doi: 10.1002/cncr.25550
- Anghel, A., Stanisavljevic, M., Andani, S., Papandreou, N., Rüschhoff, J. H., Wild, P., et al. (2019). A High-Performance System for Robust Stain Normalization of Whole-Slide Images in Histopathology. *Front. Med.* 6, 193. doi: 10.3389/fmed.2019.00193
- Bejnordi, B. E., Litjens, G., Timofeeva, N., Otte-Holler, I., Homeyer, A., Karssemeijer, N., et al. (2016). Stain Specific Standardization of Whole-Slide Histopathological Images. *IEEE Trans. Med. Imaging* 35 (2), 404–415. doi: 10.1109/TMI.2015.2476509
- Bengio, Y., Courville, A., and Vincent, P. (2013). Representation learning: a review and new perspectives. *IEEE Trans. Pattern Anal. Mach. Intell.* 35 (8), 1798–1828. doi: 10.1109/TPAMI.2013.50
- Breiman, L. (2001). Random forests. *Mach. Learn* 45 (1), 5–32. doi: 10.1023/A:1010933404324
- Campos-Filho, N., and Franco, E. L. (1988). Microcomputer-assisted univariate survival data analysis using Kaplan-Meier life table estimators. *Comput. Methods Programs Biomed.* 27 (3), 223–228. doi: 10.1016/0169-2607(88)90086-7
- Coudray, N., Ocampo, P. S., Sakellaropoulos, T., Narula, N., Snuderl, M., Fenyo, D., et al. (2018). Classification and mutation prediction from non-small cell lung cancer histopathology images using deep learning. *Nat. Med.* 24 (10), 1559–1567. doi: 10.1038/s41591-018-0177-5
- Cruz-Roa, A. A., Arevalo Ovalle, J. E., Madabhushi, A., and Gonzalez Osorio, F. A. (2013). A deep learning architecture for image representation, visual interpretability and automated basal-cell carcinoma cancer detection. *Med. Image Comput. Comput. Assist. Interv.* 16 (Pt 2), 403–410. doi: 10.1007/978-3-642-40763-5\_50
- De Fauw, J., Ledsam, J. R., Romera-Paredes, B., Nikolov, S., Tomasev, N., Blackwell, S., et al. (2018). Clinically applicable deep learning for diagnosis and referral in retinal disease. *Nat. Med.* 24 (9), 1342–1350. doi: 10.1038/s41591-018-0107-6
- Droste, R., Cai, Y., Sharma, H., Chatelain, P., Drukker, L., and Papageorgiou, A. T. (Eds.) (2019). Ultrasound image representation learning by modeling sonographer visual attention. International conference on information processing in medical imaging. *Inf. Process. Med. Imaging* 2019 (26), 592–604. doi: 10.1007/978-3-030-20351-1\_46
- Elmore, J. G., Longton, G. M., Carney, P. A., Geller, B. M., Onega, T., Tosteson, A. N., et al. (2015). Diagnostic concordance among pathologists interpreting breast biopsy specimens. *JAMA* 313 (11), 1122–1132. doi: 10.1001/jama.2015.1405
- Esteva, A., Kuprel, B., Novoa, R. A., Ko, J., Swetter, S. M., Blau, H. M., et al. (2017). Dermatologist-level classification of skin cancer with deep neural networks. *Nature* 542 (7639), 115–118. doi: 10.1038/nature21056
- Falk, T., Mai, D., Bensch, R., Cicek, O., Abdulkadir, A., Marrakchi, Y., et al. (2019). U-Net: deep learning for cell counting, detection, and morphometry. *Nat. Methods* 16 (1), 67–70. doi: 10.1038/s41592-018-0261-2
- Ghaznavi, F., Evans, A., Madabhushi, A., and Feldman, M. (2013). Digital imaging in pathology: whole-slide imaging and beyond. *Annu. Rev. Pathol.* 8, 331–359. doi: 10.1146/annurev-pathol-011811-120902
- Gulshan, V., Peng, L., Coram, M., Stumpe, M. C., Wu, D., Narayanaswamy, A., et al. (2016). Development and Validation of a Deep Learning Algorithm for Detection of Diabetic Retinopathy in Retinal Fundus Photographs. *JAMA* 316 (22), 2402–2410. doi: 10.1001/jama.2016.17216
- Guo, Y., Bao, C., Ma, D., Cao, Y., Li, Y., Xie, Z., et al. (2019). Network-Based Combinatorial CRISPR-Cas9 Screens Identify Synergistic Modules in Human Cells. *ACS Synth. Biol.* 8 (3), 482–490. doi: 10.1021/acssynbio.8b00237
- Gurcan, M. N., Boucheron, L. E., Can, A., Madabhushi, A., Rajpoot, N. M., and Yener, B. (2009). Histopathological image analysis: a review. *IEEE Rev. BioMed. Eng.* 2, 147–171. doi: 10.1109/RBME.2009.2034865
- He, K., Zhang, X., Ren, S., and Sun, J. (Eds.) (2016). *Deep residual learning for image recognition*. 2016 IEEE Conference on Computer Vision and Pattern Recognition (CVPR), Las Vegas, NV, 770–778. doi: 10.1109/CVPR.2016.90
- Huang, G., Liu, Z., Van Der Maaten, L., and Weinberger, K. Q. (Eds.) (2017). *Densely connected convolutional networks*. 2017 IEEE Conference on Computer Vision and Pattern Recognition (CVPR), Honolulu, HI, 2261–2269. doi: 10.1109/CVPR.2017.243
- Iizuka, O., Kanavati, F., Kato, K., Rambeau, M., Arihiro, K., and Tsuneki, M. (2020). Deep Learning Models for Histopathological Classification of Gastric

- and colonic epithelial tumours. *Sci. Rep.* 10 (1), 1–11. doi: 10.1038/s41598-020-58467-9
- Ker, J., Bai, Y., Lee, H. Y., Rao, J., and Wang, L. (2019). Automated brain histology classification using machine learning. *J. Clin. Neurosci.* 66, 239–245. doi: 10.1016/j.jocn.2019.05.019
- Khan, A. M., Rajpoot, N., Treanor, D., and Magee, D. (2014). A nonlinear mapping approach to stain normalization in digital histopathology images using image-specific color deconvolution. *IEEE Trans. BioMed. Eng.* 61 (6), 1729–1738. doi: 10.1109/TBME.2014.2303294
- Lauren, P. (1965). The Two Histological Main Types of Gastric Carcinoma: Diffuse and So-Called Intestinal-Type Carcinoma. An Attempt at a Histo-Clinical Classification. *Acta Pathol. Microbiol. Scand.* 64, 31–49. doi: 10.1111/apm.1965.64.1.31
- LeCun, Y., Bengio, Y., and Hinton, G. (2015). Deep learning. *Nature* 521 (7553), 436–444. doi: 10.1038/nature14539
- Li, Q., Qi, L., Feng, Q.-X., Liu, C., Sun, S.-W., Zhang, J., et al. (2019). Machine Learning-Based Computational Models Derived From Large-Scale Radiographic-Radiomic Images Can Help Predict Adverse Histopathological Status of Gastric Cancer. *Clin. Trans. Gastroenterol.* 10, 10. doi: 10.14309/ctg.0000000000000079
- Li, X., Zhang, S., Zhang, Q., Wei, X., Pan, Y., Zhao, J., et al. (2019). Diagnosis of thyroid cancer using deep convolutional neural network models applied to sonographic images: a retrospective, multicohort, diagnostic study. *Lancet Oncol.* 20 (2), 193–201. doi: 10.1016/S1470-2045(18)30762-9
- Liao, H., Xiong, T., Peng, J., Xu, L., Liao, M., Zhang, Z., et al. (2020). Classification and Prognosis Prediction from Histopathological Images of Hepatocellular Carcinoma by a Fully Automated Pipeline Based on Machine Learning. *Ann. Surg. Oncol.* 27 (7), 2359–2369. doi: 10.1245/s10434-019-08190-1
- Litjens, G., Kooi, T., Bejnordi, B. E., Setio, A. A. A., Ciampi, F., Ghafoorian, M., et al. (2017). A survey on deep learning in medical image analysis. *Med. Image Anal.* 42, 60–88. doi: 10.1016/j.media.2017.07.005
- Liu, L., Wang, Z. W., Ji, J., Zhang, J. N., Yan, M., Zhang, J., et al. (2013). A cohort study and meta-analysis between histopathological classification and prognosis of gastric carcinoma. *Anticancer Agents Med. Chem.* 13 (2), 227–234. doi: 10.2174/1871520611313020007
- Macenko, M., Niethammer, M., Marron, J. S., Borland, D., Woosley, J. T., and Guan, X. (Eds.) (2009). *A method for normalizing histology slides for quantitative analysis. 2009 IEEE International Symposium on Biomedical Imaging: From Nano to Macro (IEEE)*. (Boston, MA), 2009, 1107–1110. doi: 10.1109/ISBI.2009.5193250
- Malon, C. D., and Cosatto, E. (2013). Classification of mitotic figures with convolutional neural networks and seeded blob features. *J. Pathol. Inform.* 4, 9. doi: 10.4103/2153-3539.112694
- Mathers, C. D., and Loncar, D. (2006). Projections of global mortality and burden of disease from 2002 to 2030. *PloS Med.* 3 (11), e442. doi: 10.1371/journal.pmed.0030442
- Miettinen, O. S. (2008). Survival analysis: up from Kaplan-Meier-Greenwood. *Eur. J. Epidemiol.* 23 (9), 585–592. doi: 10.1007/s10654-008-9278-7
- Orditura, M., Galizia, M., Sforza, V., Gambardella, V., Fabozzi, A., Laterza, M. M., et al. (2014). Treatment of gastric cancer. *World J. Gastroenterol.* 20 (7), 1635–1649. doi: 10.3748/wjg.v20.i7.1635
- Otsu, N. (1979). A threshold selection method from gray-level histograms. *IEEE Trans. Syst. Man Cybern.* 9, 1, 62–66. doi: 10.1109/TSMC.1979.4310076
- Philbrick, K. A., Yoshida, K., Inoue, D., Akkus, Z., Kline, T. L., Weston, A. D., et al. (2018). What Does Deep Learning See? Insights From a Classifier Trained to Predict Contrast Enhancement Phase From CT Images. *AJR Am. J. Roentgenol.* 211 (6), 1184–1193. doi: 10.2214/AJR.18.20331
- Raab, S. S., Grzybicki, D. M., Janosky, J. E., Zarbo, R. J., Meier, F. A., Jensen, C., et al. (2005). Clinical impact and frequency of anatomic pathology errors in cancer diagnoses. *Cancer* 104 (10), 2205–2213. doi: 10.1002/cncr.21431
- Ranefall, P., Egevad, L., Nordin, B., and Bengtsson, E. (1997). A new method for segmentation of colour images applied to immunohistochemically stained cell nuclei. *Anal. Cell. Pathol.* 15 (3), 145–156. doi: 10.1155/1997/304073
- Reinhard, E., Adhikmin, M., Gooch, B., and Shirley, P. (2001). Color transfer between images. *IEEE Comput. Graphics Appl.* 21 (5), 34–41. doi: 10.1109/38.946629
- Ren, S., He, K., Girshick, R., and Sun, J. (2017). Faster R-CNN: Towards Real-Time Object Detection with Region Proposal Networks. *IEEE Trans. Pattern Anal. Mach. Intell.* 39 (6), 1137–1149. doi: 10.1109/TPAMI.2016.2577031
- Ren, J., Hacihaliloglu, I., Singer, E. A., Foran, D. J., and Qi, X. (2019). Unsupervised domain adaptation for classification of histopathology whole-slide images. *Front. Bioeng. Biotechnol.* 7, 102. doi: 10.3389/fbioe.2019.00102
- Ren, J., Singer, E. A., Sadimin, E., Foran, D. J., and Qi, X. (2019). Statistical analysis of survival models using feature quantification on prostate cancer histopathological images. *J. Pathol. Inf.* 10, 10–30. doi: 10.4103/jpi.85\_18
- Roy, S., Kumar Jain, A., Lal, S., and Kini, J. (2018). A study about color normalization methods for histopathology images. *Micron* 114, 42–61. doi: 10.1016/j.micron.2018.07.005
- Samsi, S., Jones, M., Kepner, J., and Reuther, A. (2018). Colorization of H&E stained tissue using Deep Learning. *Conf. Proc. IEEE Eng. Med. Biol. Soc.* 2018, 640–643. doi: 10.1109/EMBC.2018.8512419
- Schmidhuber, J. (2015). Deep learning in neural networks: an overview. *Neural Netw.* 61, 85–117. doi: 10.1016/j.neunet.2014.09.003
- Selvaraju, R. R., Cogswell, M., Das, A., Vedantam, R., and Batra, D. (2020). Grad-CAM: Visual Explanations from Deep Networks via Gradient-Based Localization. *Int. J. Comput. Vision* 128 (2), 336–359. doi: 10.1007/s11263-019-01228-7
- Sharma, H., Zerbe, N., Böger, C., Wienert, S., Hellwich, O., and Hufnagel, P. (Eds.) (2017a). A comparative study of cell nuclei attributed relational graphs for knowledge description and categorization in histopathological gastric cancer whole slide images. *2017 IEEE 30th International Symposium on Computer-Based Medical Systems (CBMS)*, Thessaloniki, 2017, 61–66. doi: 10.1109/CBMS.2017.25
- Sharma, H., Zerbe, N., Klempert, I., Hellwich, O., and Hufnagel, P. (2017b). Deep convolutional neural networks for automatic classification of gastric carcinoma using whole slide images in digital histopathology. *Comput. Med. Imaging Graph.* 61, 2–13. doi: 10.1016/j.compmedimag.2017.06.001
- Sharma, H. (2017). *Medical image analysis of gastric cancer in digital histopathology: methods, applications and challenges* (Germany: Technische Universitaet Berlin).
- Shelhamer, E., Long, J., and Darrell, T. (2017). Fully Convolutional Networks for Semantic Segmentation. *IEEE Trans. Pattern Anal. Mach. Intell.* 39 (4), 640–651. doi: 10.1109/TPAMI.2016.2572683
- Simonyan, K., and Zisserman, A. (2014). *Very Deep Convolutional Networks for Large-Scale Image Recognition. Computer ence.*
- Simonyan, K., Vedaldi, A., and Zisserman, A. (2013). *Deep inside convolutional networks: Visualising image classification models and saliency maps. international conference on learning representations.*
- Springenberg, J. T., Dosovitskiy, A., Brox, T., and Riedmiller, M. (2014). *Striving for simplicity: The all convolutional net.*
- Stoler, M. H., and Schiffman, M. (2001). Atypical Squamous Cells of Undetermined Significance-Low-grade Squamous Intraepithelial Lesion Triage Study G. Interobserver reproducibility of cervical cytologic and histologic interpretations: realistic estimates from the ASCUS-LSIL Triage Study. *JAMA* 285 (11), 1500–1505. doi: 10.1001/jama.285.11.1500
- Szegedy, C., Ioffe, S., Vanhoucke, V., and Alemi, A. (2016a). *Inception-v4, Inception-ResNet and the Impact of Residual Connections on Learning.*
- Szegedy, C., Vanhoucke, V., Ioffe, S., Shlens, J., and Wojna, Z. (2016b). *Rethinking the Inception Architecture for Computer Vision. Proc Cyp IEEE.* 2818–2826.
- Tam, A., Barker, J., and Rubin, D. (2016). A method for normalizing pathology images to improve feature extraction for quantitative pathology. *Med. Phys.* 43 (1), 528. doi: 10.1118/1.4939130
- Tan, P., and Yeoh, K. G. (2015). Genetics and Molecular Pathogenesis of Gastric Adenocarcinoma. *Gastroenterology* 149 (5), 1153–1162. doi: 10.1053/j.gastro.2015.05.059
- Thrift, A. P., and El-Serag, H. B. (2019). Burden of Gastric Cancer. *Clin. Gastroenterol. Hepatol.* 18 (3), 534–542. doi: 10.1016/j.cgh.2019.07.045
- Thrumurthy, S. G., Chaudry, M. A., Hochhauser, D., and Mughal, M. (2013). The diagnosis and management of gastric cancer. *BMJ* 347, f6367. doi: 10.1136/bmj.f6367
- Vahadane, A., Peng, T., Sethi, A., Albarqouni, S., Wang, L., Baust, M., et al. (2016). Structure-Preserving Color Normalization and Sparse Stain Separation for Histological Images. *IEEE Trans. Med. Imaging* 35 (8), 1962–1971. doi: 10.1109/TMI.2016.2529665
- Van Cutsem, E., Sagaert, X., Topal, B., Haustermans, K., and Prenen, H. (2016). Gastric cancer. *Lancet* 388 (10060), 2654–2664. doi: 10.1016/S0140-6736(16)30354-3



- Vicory, J., Couture, H. D., Thomas, N. E., Borland, D., Marron, J. S., Woosley, J., et al. (2015). Appearance normalization of histology slides. *Comput. Med. Imaging Graph.* 43, 89–98. doi: 10.1016/j.compmedimag.2015.03.005
- Wang, H., Cruz-Roa, A., Basavanthally, A., Gilmore, H., Shih, N., Feldman, M., et al. (2014). Mitosis detection in breast cancer pathology images by combining handcrafted and convolutional neural network features. *J. Med. Imaging (Bellingham)* 1 (3), 034003. doi: 10.1117/1.JMI.1.3.034003
- Wang, S., Chen, A., Yang, L., Cai, L., Xie, Y., Fujimoto, J., et al. (2018). Comprehensive analysis of lung cancer pathology images to discover tumor shape and boundary features that predict survival outcome. *Sci. Rep.* 8 (1), 1–9. doi: 10.1038/s41598-018-27707-4
- Zeiler, M. D., and Fergus, R. (Eds.) (2014). Visualizing and Understanding Convolutional Networks. European Conference on Computer Vision. In *Computer Vision, ECCV 2014 - 13th European Conference, Proceedings (PART 1 ed.)*, 818–833. doi: 10.1007/978-3-319-10590-1\_53
- Zhang, X.-P., Wang, Z.-L., Tang, L., Sun, Y.-S., Cao, K., and Gao, Y. (2011). Support vector machine model for diagnosis of lymph node metastasis in gastric cancer with multidetector computed tomography: a preliminary study. *BMC Cancer* 11 (1), 10. doi: 10.1186/1471-2407-11-10
- Conflict of Interest:** The authors declare that the research was conducted in the absence of any commercial or financial relationships that could be construed as a potential conflict of interest.

Copyright © 2020 Ma, Guo, Hu, Yuan, Zhu, Yu and Zou. This is an open-access article distributed under the terms of the Creative Commons Attribution License (CC BY). The use, distribution or reproduction in other forums is permitted, provided the original author(s) and the copyright owner(s) are credited and that the original publication in this journal is cited, in accordance with accepted academic practice. No use, distribution or reproduction is permitted which does not comply with these terms.



# Combining $^{18}\text{F}$ -FDG PET/CT and Serum Lactate Dehydrogenase for Prognostic Evaluation of Small Cell Lung Cancer

Xiaoping Lin<sup>1,2\*</sup>, Zizheng Xiao<sup>1,2</sup>, Yingying Hu<sup>1,2</sup>, Xu Zhang<sup>1,2</sup> and Wei Fan<sup>1,2\*</sup>

<sup>1</sup>Department of Nuclear Medicine, Sun Yat-Sen University Cancer Center, Guangzhou, China, <sup>2</sup>State Key Laboratory of Oncology in South China, Collaborative Innovation Center for Cancer Medicine, Sun Yat-Sen University Cancer Center, Guangzhou, China

**Objective:** To investigate the value of using  $^{18}\text{F}$ -FDG PET/CT in combination with serum lactate dehydrogenase (LDH) for prognostic evaluation of newly diagnosed small cell lung cancer (SCLC).

**Methods:** We reviewed 118 patients with pathologically proven SCLC who underwent  $^{18}\text{F}$ -FDG PET/CT imaging evaluation in our hospital. Among these patients, 64 patients had extensive disease (ED) and 54 patients had limited disease (LD). The maximum standardized uptake value ( $\text{SUV}_{\text{max}}$ ) of primary tumor was measured. A Cox proportional hazards model was used to evaluate age, sex, performance status, serum LDH, tumor stage and  $\text{SUV}_{\text{max}}$  on the prediction of overall survival (OS) and median survival time (MST) of patients. Subgroup analysis was performed based on the  $\text{SUV}_{\text{max}}$  in combination with serum LDH.

**Results:** According to the Receiver Operating Characteristic (ROC) curve, the optimal cut-off value of  $\text{SUV}_{\text{max}}$  was 10.95. The AUC was 0.535 (95% CI: 0.407–0.663). The patients were divided into four groups according to the  $\text{SUV}_{\text{max}}$  (higher or lower than 10.95) and LDH (higher or lower than 245 U/L). The univariate and multivariate analyses showed that curative thoracic radiotherapy, Prophylactic Cranial Irradiation (PCI) and the combination of primary tumor  $\text{SUV}_{\text{max}} \leq 10.95$  and  $\text{LDH} \leq 245$  U/L were prognostic factors of OS in patients with all patients ( $p < 0.05$ ). Smoking status, PCI, the combination of primary tumor  $\text{SUV}_{\text{max}} \leq 10.95$  and  $\text{LDH} \leq 245$  U/L were prognostic factors of OS in patients with LD ( $p < 0.05$ ). N stage and PCI were significant predictors in both of univariate and multivariate analysis of OS for ED SCLC ( $p < 0.05$ ). Among all patients, 27 had low  $\text{SUV}_{\text{max}}$  and normal LDH, and their MST was 36 months (95% CI: 12.98–59.02). Ninety-one patients had high  $\text{SUV}_{\text{max}}$  and/or high LDH, and their MST was 20 months (95% CI: 15.47–24.53). The difference between these two groups was significant ( $p = 0.045$ ). In patients with LD, 16 patients had low  $\text{SUV}_{\text{max}}$  and normal LDH, and their MST was 72 months (95% CI: 26.00–118.0). Thirty-eight patients had high  $\text{SUV}_{\text{max}}$  and/or high LDH, and their MST was 27 months (95% CI: 20.80–33.21). The difference between these two groups was significant ( $p = 0.012$ ). In patients with ED SCLC, 10 patients had low  $\text{SUV}_{\text{max}}$  and normal LDH, with an MST of 18 months (95% CI: 13.69–22.32). Fifty-four patients had high  $\text{SUV}_{\text{max}}$  and/or high LDH, and their MST was 12 months (95% CI: 10.61–13.39). The difference of MST between these two groups was not statistically significant ( $p = 0.686$ ).

## OPEN ACCESS

### Edited by:

Dong-Hua Yang,  
St. John's University, United States

### Reviewed by:

Hubing Wu,  
Southern Medical University, China  
Lijuan Yu,  
Hainan University, China

### \*Correspondence:

Wei Fan  
fanwei@sysucc.org.cn  
Xiaoping Lin  
linxp@sysucc.org.cn

### Specialty section:

This article was submitted to  
Experimental Pharmacology  
and Drug Discovery,  
a section of the journal  
Frontiers in Pharmacology

**Received:** 08 August 2020

**Accepted:** 28 September 2020

**Published:** 28 October 2020

### Citation:

Lin X, Xiao Z, Hu Y, Zhang X and Fan W  
(2020) Combining  $^{18}\text{F}$ -FDG PET/CT  
and Serum Lactate Dehydrogenase for  
Prognostic Evaluation of Small Cell  
Lung Cancer.  
Front. Pharmacol. 11:592768.  
doi: 10.3389/fphar.2020.592768

**Conclusion:**  $^{18}\text{F}$ -FDG PET/CT in combination with serum LDH were prognostic factors of overall survival in patients with SCLC. The prognosis of patients with LD SCLC who had low  $\text{SUV}_{\text{max}}$  of primary tumor and normal LDH was better than those with high  $\text{SUV}_{\text{max}}$  and/or high LDH.

**Keywords:** small cell lung cancer, PET/CT, prognosis, maximum standardized uptake value, lactate dehydrogenase, glycolysis

## INTRODUCTION

Small cell lung cancer (SCLC) is the most common neuroendocrine tumor of the lung. It accounts for 10–15% of lung cancers (Travis, 2012; Torre et al., 2015). SCLC has unique biological behaviors, including rapid growth, short doubling time, invasive and distant metastasis in the early stage of the disease (Rodriguez and Lilenbaum, 2010). Although SCLC is sensitive to radiotherapy and chemotherapy, recurrence or disease progression occurs frequently, and the prognosis is poor. In the past few decades, the overall survival of SCLC has not improved. In recent years, targeted therapy and molecular mechanism of pathogenesis were explored in basic and clinical studies. However, the development of treatments for SCLC is slow because of the heterogeneity of tumor. The pathogenesis and the driving genes of SCLC remain unclear (Kalemkerian and Schneider, 2017).

The main prognostic factors for SCLC include tumor staging, the patient's physical condition, such as physical status, immune function status, etc. and tumor biological characteristics. The principal prognostic factors of SCLC are staging, physical status, weight loss, tumor burden, and elevated serum biomarkers. Staging is the principal consideration for prognosis and treatment strategies. Patients with SCLC are conventionally staged according to a two-stage system as limited disease (LD) and extensive disease (ED). This system was developed by the Veterans Administration Lung Cancer Study Group (VALG) and has been widely used for a long time. LD is defined as disease confined to one hemithorax that can be encompassed in a tolerable radiation field, whereas ED is defined as disease extending outside the thorax or the existence of malignant pleural effusion. The TNM staging is applied in SCLC (Vallières et al., 2009; Carter et al., 2014). Currently, SCLC staging is based on anatomical images, which only reflect the size of the tumor and the range of invasion.

Serum lactate dehydrogenase (LDH) is used as an important prognostic factor in lymphoma, multiple myeloma, lung cancer and nasopharyngeal carcinoma. Serum LDH is elevated in 50–60% of patients with SCLC at diagnosis and is also critical in the prognosis of SCLC (Byhardt et al., 1986; Stahel et al., 1989; Sagman et al., 1991; Quoix et al., 2000; Chen et al., 2018; Hsieh et al., 2018).

With the development of molecular imaging,  $^{18}\text{F}$ -FDG PET/CT is increasingly used for clinical diagnosis and prognosis (Warburg, 1956; Vander Heiden et al., 2009; Liao et al., 2012; Doherty and Cleveland, 2013; Bamji-Stocke et al., 2018).  $^{18}\text{F}$ -FDG PET/CT shows the distribution and metabolism of glucose in the whole body and can be used not only to determine the staging and location of tumors but also to confirm tumor proliferation according to the metabolic index.  $^{18}\text{F}$ -FDG PET/CT can provide metabolic information, tumor biological behavior and characteristics, as well as tumor burden.

Combination of comprehensive  $^{18}\text{F}$ -FDG PET/CT and serum LDH can not only reflect tumor glucose intake, glycolysis inflow and glycolysis effluent but also show the distribution of tumors in the whole body. It can also reveal tumor biological behavior, tumor burden and other prognostic key information in addition to staging.

## MATERIALS AND METHODS

### Ethical Approval

This study was approved by the Ethics committee of the Sun Yat-sen University Cancer Center Institutional Review Board and was conducted following the Declaration of Helsinki.

### Participants

A total of 118 patients were recruited in this study. Patients' age ranges from 30 to 81 years old, mean age 59 years. All patients were pathologically diagnosed with SCLC at Sun Yat-Sen University Cancer Center from June 2005 to December 2016. Patients received no anticancer treatment before enrollment. Whole-body  $^{18}\text{F}$ -FDG PET/CT was carried out 4 weeks before treatment. Serum LDH assessment was performed 2 weeks before or after  $^{18}\text{F}$ -FDG PET/CT scan.

The serum LDH before treatment was assayed based on the spectrophotometric absorbance of nicotinamide-adenine dinucleotide at 340 nm after catalytic oxidation of lactate to pyruvate. The normal reference range was 109–245 IU/L.

Images were acquired with two integrated PET/CT devices (Discovery ST, GE and Biograph mCT; Siemens). PET was performed to cover the identical axial field of view after CT scan. PET images were iteratively reconstructed with CT data for correcting attenuation. For quantitative analysis, irregular regions of interest were placed over the most intense area of  $^{18}\text{F}$ -FDG accumulation. The maximum standardized uptake value ( $\text{SUV}_{\text{max}}$ ) was calculated using the following formula: maximum pixel value with the decay-corrected region-of-interest activity (MBq/kg)/[injected dose (MBq)/body weight (kg)]. The PET images were evaluated by two experienced physicians of nuclear medicine.  $\text{SUV}_{\text{max}}$  of the primary tumor was automatically measured on the workstation.

The general characteristics of the patients, including KPS score, smoking status, body weight, serum LDH, overall survival time (OS), and median survival time (MST) were recorded.

All statistical analyses were performed using SPSS (version 13.0; SPSS Inc.). Statistical difference between the groups were analyzed using one-way ANOVA and t tests where appropriate. *p*

**TABLE 1 |** Characteristics of 118 patients with SCLC.

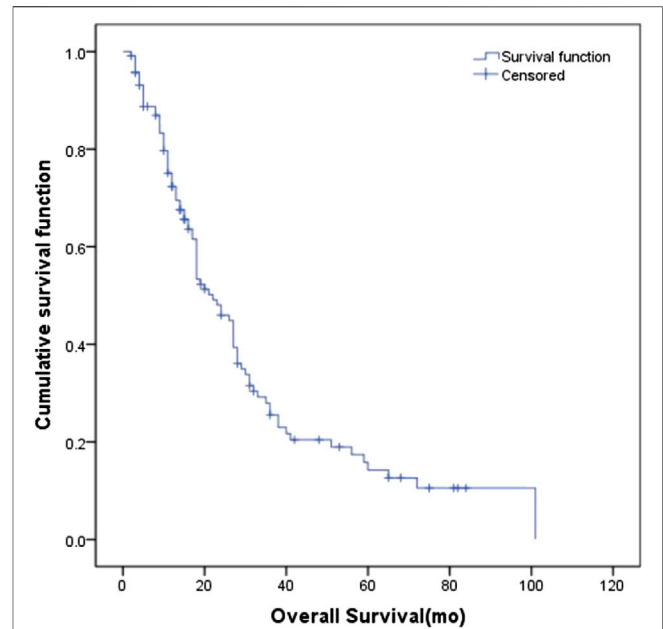
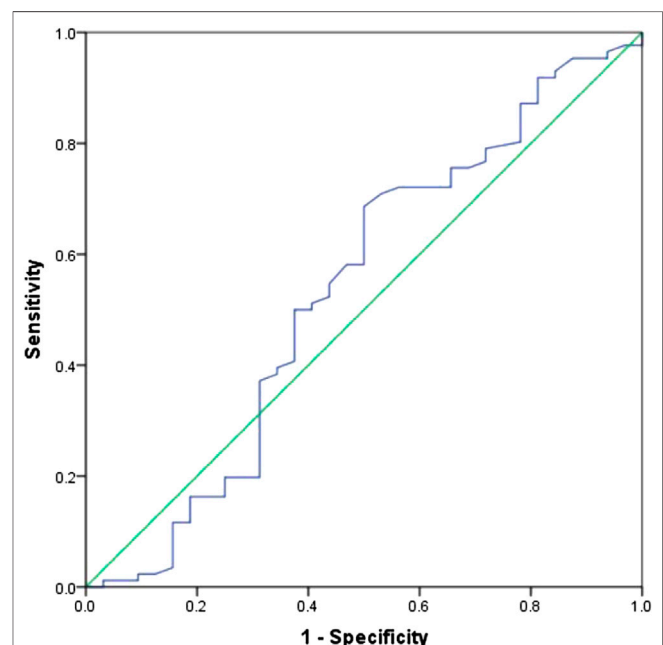
Characteristic	N	%
Gender		
Male	106	89.8
Female	12	10.2
Age, median (range), year	59 (30–81)	
Performance scales (KPS)		
70	2	1.7
80	19	16.1
90	97	82.2
Weight loss		
Yes	31	26.3
No	87	73.7
Smoking status		
Yes	33	28.0
No	85	72.0
VALG stage		
LD	54	45.8
ED	64	54.2
T stage		
T1	16	13.6
T2	54	45.8
T3	21	17.8
T4	27	22.9
N stage		
N0	5	4.2
N1	10	8.5
N2	38	32.2
N3	65	55.1
M stage		
M0	55	46.6
M1	63	53.4
TNM stage		
I	3	2.5
II	7	5.9
III	46	39.1
IV	62	52.5
Initial chemotherapy		
EP	102	86.4
Non-EP	16	13.6
Curative thoracic radiotherapy		
Yes	60	50.8
No	58	49.2
PCI		
Yes	38	32.2
No	80	67.8

values of less than 0.05 were considered statistically significant. Survival curves were calculated by the method of Kaplan and Meier. The log-rank method was used to test the statistical significance of the differences between survival curves and to perform comparisons adjusted for other prognostic factors. *p* values for difference between proportions were calculated with Fisher's exact test (two-tailed). Correlations between LDH levels (normal or elevated) and specific metastatic sites were assessed with the product moment correlation coefficient.

## RESULTS

### Patients Characteristics

The clinical characteristics of the 118 patients including age, gender, performance status (KPS), tumor stage, body weight,

**FIGURE 1 |** The overall survival curve of the 118 patients with SCLC.**FIGURE 2 |** ROC curve of  $SUV_{max}$  of primary tumors in 118 patients with SCLC.

smoking status and treatment management are presented in **Table 1**. The median age of the patients was 59 years (ranges 30–81 years). At the time of analysis, 32 (27.1%) patients were alive, and the other patients had passed away. The median follow-up time was 18 months (2–101 months). The estimated MST for the entire cohort was 22 months (95% CI: 16.8–27.2 months)

**TABLE 2 |** Univariate analysis of prognosis in 118 patients with SCLC.

	OS		
	p Value	HR	95% CI
KPS	0.077	0.956	0.909–1.005
Smoking status	0.297	0.779	0.488–1.245
T stage	0.851	0.979	0.784–1.222
N stage	0.054	1.290	0.995–1.672
M stage	0.000*	2.252	1.443–3.517
Curative thoracic radiotherapy	0.000*	0.417	0.269–0.645
PCI	0.000*	0.313	0.189–0.517
LDH ≤ 245 U/L	0.676	0.913	0.594–1.401
SUV <sub>max</sub> ≤ 10.95	0.116	0.688	0.432–1.096
LDH ≤ 245 U/L + SUV <sub>max</sub> ≤ 10.95	0.032*	0.517	0.284–0.943

\*p &lt; 0.05.

(Figure 1), with 1-year, 2-years, and 3-years cumulative overall survival was 93.1%, 86.9%, and 75.1%, respectively. The estimated MST for patients with LD and ED was 29 months (95% CI: 24.0–33.6 months) and 15 months (95% CI: 2.3–19.5 months), respectively.

## Maximum Standardized Uptake Value and Serum Lactate Dehydrogenase in the Primary Tumors

The median SUV<sub>max</sub> in the primary tumors of all patients was 11.85 (6.0–32.8). The ability of SUV<sub>max</sub> in the primary tumors to predict prognosis was depicted by the ROC curve. The AUC of SUV<sub>max</sub> was 0.535 (95% CI: 0.407–0.663). The point which showed the maximal sum of sensitivity and specificity was determined to be the cut-off point. As a result, the optimal cut-off value of SUV<sub>max</sub> was 10.95. Figure 2 shows the ROC curve of SUV<sub>max</sub>.

The median serum LDH in all patients in this study was 226.6 (118.5–1,266.1) U/L. The median serum LDH in patients with LD was 222.8 (118.5–530.3) U/L, with elevated levels in 19 patients (35.2%, 19/54) and normal levels in 35 patients (64.8%, 35/64). The median serum LDH in patients with ED SCLC was 241.2 (132.0–1,266.1) U/L, with elevated levels in 31 patients (48.4%, 31/64) and normal levels in 33 patients (51.6%, 33/64). Serum LDH was significantly different in patients with LD and ED ( $p = 0.003$ ), with patients with LD had lower LDH level.

## Survival Analysis

Univariate analysis of OS for patients with all SCLC determined that M stage, curative thoracic radiotherapy, PCI and the combination of primary tumor SUV<sub>max</sub> ≤ 10.95 and LDH ≤ 245 U/L were significant predictors, whereas KPS, smoking status, T stage, N stage, SUV<sub>max</sub>, and serum LDH alone, were not significant prognostic factors (Table 2). In multivariate analysis, independent prognostic factors associated with OS included curative thoracic radiotherapy (HR 0.606,  $p = 0.033$ ), PCI (HR 0.325,  $p = 0.000$ ) and the combination of primary tumor SUV<sub>max</sub> ≤ 10.95 and LDH ≤ 245 U/L (HR 2.417,  $p = 0.005$ ) (Table 3).

Univariate analysis of OS for LD SCLC revealed that KPS, smoking status and PCI and the combination of primary tumor

**TABLE 3 |** Multivariate analysis of overall survival in 118 patients with SCLC.

	p Value	HR	95% CI
Curative thoracic radiotherapy	0.033*	0.606	0.382–0.961
PCI	0.000*	0.325	0.188–0.563
LDH ≤ 245 U/L + SUV <sub>max</sub> ≤ 10.95	0.005*	0.414	0.222–0.770

\*p &lt; 0.05.

**TABLE 4 |** Univariate analysis of prognosis in 54 patients with LD SCLC.

	p Value	HR	95% CI
KPS	0.033*	0.901	0.818–0.991
Smoking status	0.023*	0.425	0.203–0.888
T stage	0.436	0.863	0.597–1.219
N stage	0.646	0.925	0.664–1.288
Curative thoracic radiotherapy	0.235	0.609	0.269–1.381
PCI	0.006*	0.351	0.166–0.745
LDH ≤ 245 U/L	0.407	0.733	0.352–1.527
SUV <sub>max</sub> ≤ 10.95	0.099	0.519	0.238–1.132
LDH ≤ 245 U/L + SUV <sub>max</sub> ≤ 10.95	0.018*	0.298	0.110–0.811

\*p &lt; 0.05.

**TABLE 5 |** Multivariate analysis of overall survival in 54 patients with LD SCLC.

	p Value	HR	95% CI
Smoking status	0.013*	0.364	0.163–0.810
PCI	0.000*	0.180	0.075–0.433
LDH ≤ 245 U/L + SUV <sub>max</sub> ≤ 10.95	0.004*	0.182	0.057–0.582

\*p &lt; 0.05.

**TABLE 6 |** Univariate analysis of overall survival in 64 patients with ED SCLC.

	p Value	HR	95% CI
KPS	0.878	0.995	0.934–1.060
Smoking status	0.646	1.159	0.617–2.178
T stage	0.675	1.065	0.793–1.431
N stage	0.010*	1.916	1.171–3.134
Curative thoracic radiotherapy	0.056	0.542	0.289–1.017
PCI	0.007*	0.383	0.1896–0.774
LDH ≤ 245 U/L	0.321	1.310	0.768–2.232
SUV <sub>max</sub> ≤ 10.95	0.980	1.007	0.562–1.807
LDH ≤ 245 U/L + SUV <sub>max</sub> ≤ 10.95	0.650	1.192	0.559–2.538

\*p &lt; 0.05.

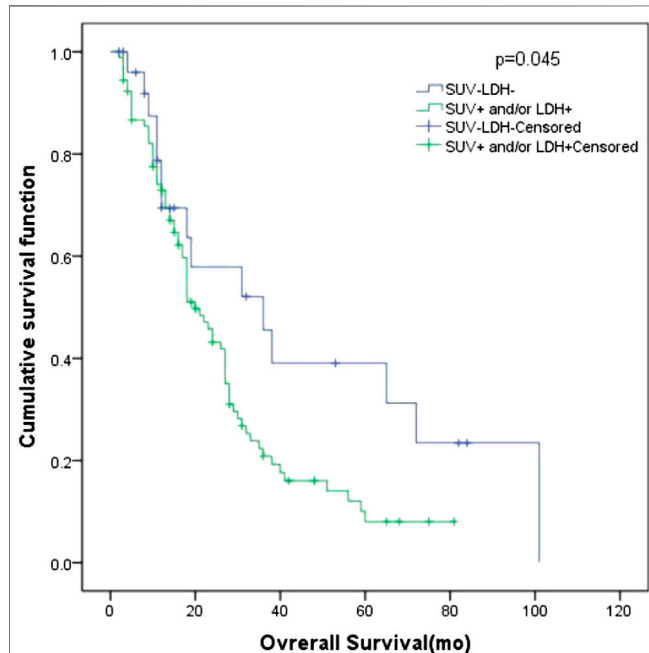
SUV<sub>max</sub> ≤ 10.95 and LDH ≤ 245 U/L were significant predictors, whereas T stage, N stage, curative thoracic radiotherapy, SUV<sub>max</sub>, and serum LDH alone, were not significant prognostic factors (Table 4). In multivariate analysis, independent prognostic factors associated with OS included smoking status (HR 0.364,  $p = 0.013$ ), PCI (HR 0.180,  $p = 0.000$ ), the combination of primary tumor SUV<sub>max</sub> ≤ 10.95 and LDH ≤ 245 U/L (HR 0.182,  $p = 0.004$ ) (Table 5).

Univariate analysis of OS for ED SCLC revealed that N stage and PCI were significant predictors, whereas KPS, smoking status, T stage, curative thoracic radiotherapy, SUV<sub>max</sub>, serum LDH alone, and the combination of primary tumor



**TABLE 7** | Multivariate analysis of overall survival in 64 patients with ED SCLC.

	p Value	HR	95% CI
N stage	0.004*	2.013	1.251–3.239
PCI	0.003*	0.333	0.162–0.684

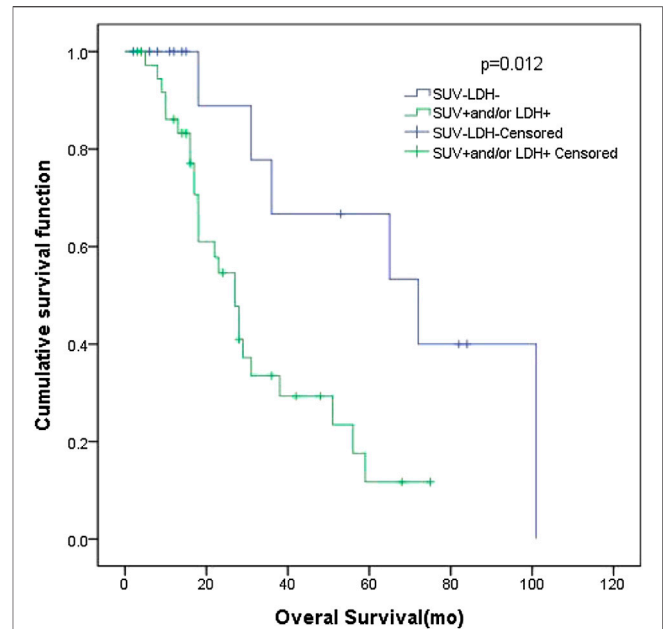
\* $p < 0.05$ .**FIGURE 3** | Survival curves of  $SUV_{max}$  of different primary tumor and LDH in 118 patients with SCLC.

$SUV_{max} \leq 10.95$  and  $LDH \leq 245$  U/L were not significant prognostic factors (Table 6). In multivariate analysis, independent prognostic factors associated with OS included N stage (HR 2.013,  $p = 0.004$ ), PCI (HR 0.333,  $p = 0.003$ ) (Table 7).

### Subgroup Analysis of Maximum Standardized Uptake Value Combined With Serum Lactate Dehydrogenase

Base on the ROC curve, the optimal cut-off value of  $SUV_{max}$  was 10.95. The AUC was 0.535 (95% CI: 0.407–0.663). The patients were divided into four groups according to  $SUV_{max}$  and serum LDH. Group A for primary tumor  $SUV_{max} > 10.95$  and  $LDH > 245$  U/L, Group B for primary tumor  $SUV_{max} > 10.95$  and  $LDH \leq 245$  U/L, Group C for primary tumor  $SUV_{max} \leq 10.95$  and  $LDH > 245$  U/L, and Group D for primary tumor  $SUV_{max} \leq 10.95$  and  $LDH \leq 245$  U/L.

Among the patients with LD, there were 12 patients in group A, with an MST of 28 months (95% CI: 12.92–43.08); 19 patients in group B, with an MST of 28 months (95% CI: 19.33–36.67); seven patients in group C, with an MST of 27 months (95% CI: 11.79–42.21); and 16 patients in group

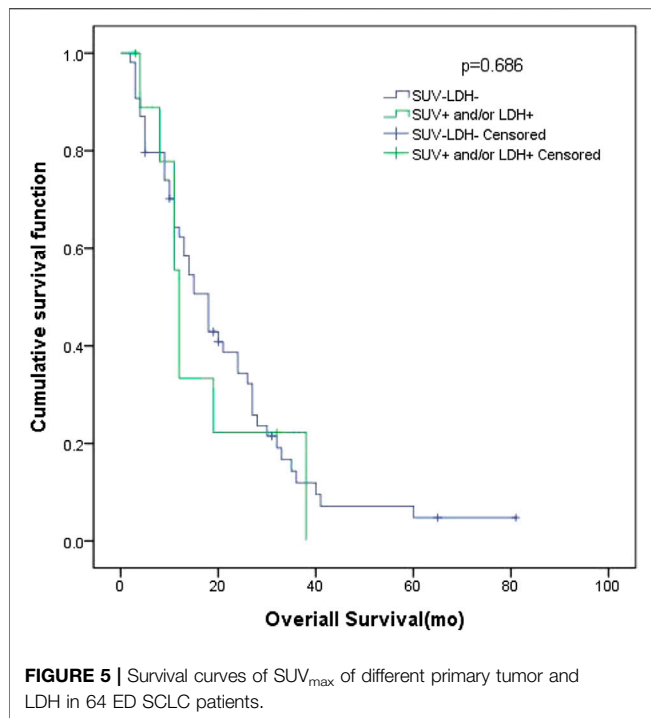
**FIGURE 4** | Survival curves of  $SUV_{max}$  of different primary tumor and LDH in 54 LD SCLC patients.

D, with an MST of 72 months (95% CI: 26.00–118.0). There was no significant difference of MST among the different groups ( $p = 0.057$ ). Among the patients with ED, there were 22 patients in group A, with an MST of 21 months (95% CI: 11.16–30.84); 22 patients in group B, with an MST of 14 months (95% CI: 9.40–18.60); nine patients in group C, with an MST of 14 months (95% CI: 0–33.00); and 11 patients in group D, with an MST of 11 months (95% CI: 8.68–13.32). There was no significant difference of MST among the four groups ( $p = 0.742$ ).

In all patients, there were 27 patients in group D (primary tumor  $SUV_{max} \leq 10.95$  and  $LDH \leq 245$  U/L), with an MST of 36 months (95% CI: 12.98–59.02). There were 91 patients with  $SUV_{max} > 10.95$  and/or  $LDH > 245$  U/L (group A + B + C), and their MST was 20 months (95% CI: 15.47–24.53). The difference of MST between these two groups in the study was statistically significant ( $p = 0.045$ ) (Figure 3).

In patients with LD SCLC, there were 16 patients in group D (primary tumor  $SUV_{max} \leq 10.95$  and  $LDH \leq 245$  U/L), with an MST of 72 months (95% CI: 26.00–118.0). There were 38 patients with  $SUV_{max} > 10.95$  and/or  $LDH > 245$  U/L (group A + B + C), and their MST was 27 months (95% CI: 20.80–33.21). The difference of MST between these two groups was statistically significant ( $p = 0.012$ ) (Figure 4).

In patients with ED SCLC, there were 10 patients in group D (primary tumor  $SUV_{max} \leq 10.95$  and  $LDH \leq 245$  U/L), with an MST of 18 months (95% CI: 13.69–22.32). There were 54 patients with  $SUV_{max} > 10.95$  and/or  $LDH > 245$  U/L (group A + B + C), and their MST was 12 months (95% CI: 10.61–13.39). The difference of MST between these two groups was not statistically significant ( $p = 0.686$ ) (Figure 5).



## DISCUSSION

A number of factors, including tumor stage, performance status, weight loss, tumor burden and elevated tumor biomarkers, have been indicated to affect survival prognosis in SCLC (Kalemkerian and Schneider, 2017). Conventionally, tumor stage is determined by anatomical images, which are used to indicate the tumor size and border. However, the anatomical image-based tumor volume does not represent the tumor burden. Functional imaging can provide metabolic information on malignant tissues and thus more accurately reflects tumor burden. SUV is a semiquantitative index of  $^{18}\text{F}$ -FDG uptake in tumors. SUV can reflect the metabolic information of tumors. Previous studies indicated that the  $SUV_{max}$  of primary tumors is helpful for predicting prognosis of patients with cancers (Warburg, 1956; Romero-García et al., 2016).

The application of  $^{18}\text{F}$ -FDG PET/CT in SCLC remains controversial. Some studies have shown that  $^{18}\text{F}$ -FDG PET/CT imaging can provide prognostic information. (van der Leest et al., 2012) analyzed the correlation of primary tumor  $SUV_{max}$  and survival data, including OS and progression-free survival time (PFS) in SCLC. Compared with stage IV patients, stage I-III patients had lower  $SUV_{max}$  in the primary tumors. In this study,  $SUV_{max}$  alone did not distinguish difference of OS or PFS. However, among patients with stage IV and receiving chemotherapy, patients with higher  $SUV_{max}$  had worse prognosis than those with lower  $SUV_{max}$ . The relationship between  $SUV_{max}$  and prognosis appears to be more complicated in SCLC than in NSCLC.

In a study by Pandit et al. (2003), a high  $SUV_{max}$  was associated with poor survival with significance.  $^{18}\text{F}$ -FDG PET could be important for tumor staging and follow-up, because

there was a significant negative correlation between  $SUV_{max}$  and survival. The overall survival in PET-negative patients was significantly better than that in PET-positive cases. (Lee et al., 2009) also found that tumor metabolic activity as assessed by  $^{18}\text{F}$ -FDG PET is a significant prognostic factor. It could identify high risk of death in both LD and ED SCLC subgroups of patients. Oh et al. (2012) found that WBMTV (whole body metabolism tumor volume), instead of  $SUV_{max}$  or LDH, was an independent predictor of progression and death in 106 patients with SCLC who underwent  $^{18}\text{F}$ -FDG PET/CT before treatment. Incorporation of WBMTV with TNM staging can provide a more detailed prediction of prognosis than WBMTV with conventional staging as well as tumor staging alone. In the subgroup analysis of LD SCLC, Kwon et al. (2016) found that the highest  $SUV_{max}$  was a prognostic factor for PFS with marginal significance (HR: 1.078,  $p = 0.053$ ). After adjusting for age, sex, performance status, tumor stage, and treatment modality, patients with higher  $SUV_{max}$  ( $>11$ ) were characterized by a significantly shorter median OS ( $p < 0.001$ ) and PFS ( $p = 0.002$ ) compared with patients with lower  $SUV_{max}$ . The high  $SUV_{max}$  was an independent prognostic factor for survival in LD-SCLC patients and might be a possible imaging biomarker for risk stratification in LD-SCLC.

In contrast, Ong's study (Ong et al., 2016) suggests that pretreatment PET scans, even with the use of advanced metrics, do not have independent prognostic value for outcomes in LD patients after chemoradiotherapy (CRT). They found that  $SUV_{max}$ ,  $SUV_{mean}$ , MTV, and total lesion glycolysis of the primary tumor were not significantly associated with OS, LRF, and DFS in univariate analysis. MTV was significantly associated with DFS ( $p = 0.024$ ) in univariate but not multivariate analysis in 120 patients with LD who received platinum-based chemotherapy and a median radiation dose of 45 Gy. Kim's study (Kim and Chang, 2015) showed no significant differences in OS and PFS between high and low  $SUV_{max}$  groups in baseline PET/CT in a survival analysis of 82 patients with SCLC.

We performed this retrospective analysis with the following hypotheses. PET/CT reflects the integrated results of glucose transport and the first key enzyme in the process of glycolysis. PET/CT can be recorded with images and has quantitative indexes such as SUV. Serum LDH is the total amount of enzyme released into the blood by cells, reflects the product of glycolysis, and can be tested in peripheral blood. Thus, PET/CT and serum LDH represent the input and output of glycolysis, respectively. Different values of  $SUV_{max}$  and serum LDH could represent different prognoses in patients with SCLC.

This retrospective study shows that  $SUV_{max}$  of the primary tumor combined with serum LDH is an important independent prognostic factor for overall survival and progression-free survival. This parameter is a good predictor of survival in patients with SCLC. The prognosis of LD SCLC patients with primary tumor  $SUV_{max} \leq 10.95$  and a normal level of serum LDH is better than those of patients with primary tumor  $SUV_{max} > 10.95$  and/or serum LDH, with a longer overall survival time (MST of 72 and 27 months, respectively). The prognosis of all SCLC patients with primary tumor  $SUV_{max} \leq 10.95$  and a normal

level of serum LDH was better than that of patients with primary tumor  $SUV_{max} > 10.95$  and/or serum LDH, with longer overall survival time (MST of 36 and 20 months, respectively). These results indicate that the prognosis is better in the cases of low  $SUV_{max}$  and LDH, i.e., when both the input and output of glycolysis are low.

There are some limitations in this study. First, it is a retrospective study with a small sample size. Second, two different PET/CT scanners were used in this study. However, our regular quality control ensured scanning consistency. In addition, volume metabolic parameters (such as MTV and TLG) were not included in the study. Because nearly half of the cases in this study were ED SCLC, it is difficult to achieve a Volume Of Interest (VOI) including all lesions of the whole body excluding physiological or benign avid lesions automatically. Moreover, manual drawing is more likely to be influenced by the operator. Therefore, volume metabolic parameters were not used in this study. Further studies with large sample size and multiple centers and prospective studies are needed.

## CONCLUSION

Combination of  $^{18}F$ -FDG PET/CT and serum LDH could be a prognostic factor of overall survival of patients with SCLC. The prognosis of patients with limited disease of SCLC who have low  $SUV_{max}$  of the primary tumor and normal serum LDH was better than those with high  $SUV_{max}$  and/or high serum LDH.

## REFERENCES

- Bamji-Stocke, S., van Berkel, V., Miller, D. M., and Frieboes, H. B. (2018). A review of metabolism-associated biomarkers in lung cancer diagnosis and treatment. *Metabolomics* 14 (6), 81. doi:10.1007/s11306-018-1376-2
- Byhardt, R. W., Hartz, A., Libnoch, J. A., Hansen, R., and Cox, J. D. (1986). Prognostic influence of TNM staging and LDH levels in small cell carcinoma of the lung (SCCL). *Int. J. Radiat. Oncol. Biol. Phys.* 12, 771–777. doi:10.1016/0360-3016(86)90035-0
- Carter, B. W., Glisson, B. S., Truong, M. T., and Erasmus, J. J. (2014). Small cell lung carcinoma: staging, imaging, and treatment considerations. *Radiographics* 34 (6), 1707–1721. doi:10.1148/rg.346140178
- Chen, C., Zhu, Y. H., and Huang, J. A. (2018). Clinical evaluation of potential usefulness of serum lactate dehydrogenase level in follow-up of small cell lung cancer. *J. Cancer Res. Therapeut.* 14, S336–S340. doi:10.4103/0973-1482.168994
- Doherty, J. R., and Cleveland, J. L. (2013). Targeting lactate metabolism for cancer therapeutics. *J. Clin. Invest.* 123, 3685–3692. doi:10.1172/JCI69741
- Hsieh, A. H.-C., Tahkar, H., Koczwara, B., and Kichenadasse, G., Beckmann, K., Karapetis, C., et al. (2018). Pre-treatment serum lactate dehydrogenase as a biomarker in small cell lung cancer. *Asia Pac. J. Clin. Oncol.* 14 (2), e64–e70. doi:10.1111/ajco.12674
- Kalemkerian, G. P., and Schneider, B. J. (2017). Advances in small cell lung cancer. *Hematol. Oncol. Clin. North Am.* 31 (1), 143–156. doi:10.1016/j.hoc.2016.08.005
- Kim, S.-J., and Chang, S. (2015). Limited prognostic value of  $SUV_{max}$  measured by  $^{18}F$ -FDG PET/CT in newly diagnosed small cell lung cancer patients. *Oncol. Res. Treat.* 38 (11), 577–585. doi:10.1159/000441289
- Kwon, S. H., Hyun, S. H., Yoon, J.-K., An, Y.-S., Oh, Y.-T., Choi, J.-H., et al. (2016). The highest metabolic activity on FDG PET is associated with overall survival in limited-stage small-cell lung cancer. *Medicine* 95 (5), e2772. doi:10.1097/MD.0000000000002772

## DATA AVAILABILITY STATEMENT

The raw data supporting the conclusions of this article will be made available by the authors, without undue reservation.

## ETHICS STATEMENT

The studies involving human participants were reviewed and approved by IRB Sun Yat-Sen University Cancer Center. Written informed consent for participation was not required for this study in accordance with the national legislation and the institutional requirements.

## AUTHOR CONTRIBUTIONS

XL: Conceptualization, methodology, software, data curation, visualization, investigation, writing-original draft preparation, and writing-editing. ZX, YH, and XZ: Data curation and visualization. WF: Conceptualization, supervision, validation, and writing-reviewing.

## FUNDING

This work was supported by the Natural Science Foundation of Guangdong Province, China, No. 2018A030310239.

- Lee, Y. J., Cho, A., Cho, B. C., Yun, M., Kim, S. K., Chang, J., et al. (2009). High tumor metabolic activity as measured by fluorodeoxyglucose positron emission tomography is associated with poor prognosis in limited and extensive stage small-cell lung cancer. *Clin. Cancer Res.* 15 (7), 2426–2432. doi:10.1158/1078-0432.CCR-08-2258
- Liao, S., Penney, B. C., Wroblewski, K., Zhang, H., Simon, C. A., Kampalath, R., et al. (2012). Prognostic value of metabolic tumor burden on  $^{18}F$ -FDG PET in nonsurgical patients with non-small cell lung cancer. *Eur. J. Nucl. Med. Mol. Imaging* 39, 27–38. doi:10.1007/s00259-011-1934-6
- Oh, J.-R., Seo, J.-H., Chong, A., Min, J.-J., Song, H.-C., Kim, Y.-C., et al. (2012). Whole-body metabolic tumour volume of  $^{18}F$ -FDG PET/CT improves the prediction of prognosis in small cell lung cancer. *Eur. J. Nucl. Med. Mol. Imaging* 39 (6), 925–935. doi:10.1007/s00259-011-2059-7
- Ong, L. T., Dunphy, M., Foster, A., Woo, K. M., Zhang, Z., Perez, C. A., et al. (2016). Prognostic value of preradiotherapy  $^{18}F$ -FDG PET/CT volumetrics in limited-stage small-cell lung cancer. *Clin. Lung Cancer* 17 (3), 184–188. doi:10.1016/j.clcl.2015.07.004
- Pandit, N., Gonen, M., Krug, L., and Larson, S. (2003). Prognostic value of [ $^{18}F$ ] FDG-PET imaging in small cell lung cancer. *Eur. J. Nucl. Med. Mol. Imaging* 30, 78–84. doi:10.1007/s00259-002-0937-8
- Quoix, E., Purohit, A., Faller-Beau, M., Moreau, L., Oster, J. P., and Pauli, G. (2000). Comparative prognostic value of lactate dehydrogenase and neuron-specific enolase in small-cell lung cancer patients treated with platinum-based chemotherapy. *Lung Cancer* 30 (2), 127–134. doi:10.1016/S0169-5002(00)00131-8
- Rodriguez, E., and Lilenbaum, R. C. (2010). Small cell lung cancer: past, present, and future. *Curr. Oncol. Rep.* 12 (5), 327–334. doi:10.1007/s11912-010-0120-5
- Romero-Garcia, S., Moreno-Altamirano, M. M. B., Prado-Garcia, H., and Sánchez-García, F. J. (2016). Lactate contribution to the tumor microenvironment: mechanisms, effects on immune cells and therapeutic relevance. *Front. Immunol.* 7, 52. doi:10.3389/fimmu.2016.00052

- Sagman, U., Feld, R., Evans, W. K., Warr, D., Shepherd, F. A., Payne, D., et al. (1991). The prognostic significance of pretreatment serum lactate dehydrogenase in patients with small-cell lung cancer. *J. Clin. Oncol.* 9 (6), 954–961. doi:10.1200/JCO.1991.9.6.954
- Stahel, R. A., Ginsberg, R., Havemann, K., Hirsch, F. R., Ihde, D. C., Jassem, J., et al. (1989). Staging and prognostic factors in small cell lung cancer: a consensus report. *Lung Cancer* 5, 119–126. doi:10.1016/0169-5002(89)90156-6
- Torre, L. A., Bray, F., Siegel, R. L., Ferlay, J., Lortet-Tieulent, J., and Jemal, A. (2015). Global cancer statistics, 2012. *CA A Cancer J. Clin.* 65 (2), 87–108. doi:10.3322/caac.21262
- Travis, W. D. (2012). Update on small cell carcinoma and its differentiation from squamous cell carcinoma and other non-small cell carcinomas. *Mod. Pathol.* 25 (Suppl. 1), S18–S30. doi:10.1038/modpathol.2011.150
- Valli eres, E., Shepherd, F. A., Crowley, J., Van Houtte, P., Postmus, P. E., Carney, D., et al. (2009). The IASLC lung cancer staging project: proposals regarding the relevance of TNM in the pathologic staging of small cell lung cancer in the forthcoming (seventh) edition of the TNM classification for lung cancer. *J. Thorac. Oncol.* 4, 1049–1059. doi:10.1097/JTO.0b013e3181b27799
- van der Leest, C., Smit, E. F., Baas, J., Versteijlen, R. J., van Walree, N., Hoogsteden, H. C., et al. (2012). SUVmax during 18FDG-PET scanning in small cell lung cancer: similar information as in non-small cell lung cancer? *Lung Cancer* 76 (1), 67–71. doi:10.1016/j.lungcan.2011.09.007
- Vander Heiden, M. G., Cantley, L. C., and Thompson, C. B. (2009). Understanding the Warburg effect: the metabolic requirements of cell proliferation. *Science* 324 (5930), 1029–1033. doi:10.1126/science.1160809
- Warburg, O. (1956). On the origin of cancer cells. *Science* 123, 309–314. doi:10.1126/science.123.3191.309
- Conflict of Interest:** The authors declare that the research was conducted in the absence of any commercial or financial relationships that could be construed as a potential conflict of interest.

Copyright   2020 Lin, Xiao, Hu, Zhang and Md. This is an open-access article distributed under the terms of the Creative Commons Attribution License (CC BY). The use, distribution or reproduction in other forums is permitted, provided the original author(s) and the copyright owner(s) are credited and that the original publication in this journal is cited, in accordance with accepted academic practice. No use, distribution or reproduction is permitted which does not comply with these terms.



# Potential Metabolic Biomarkers for Early Detection of Oral Lichen Planus, a Precancerous Lesion

Xiao-Shuang Wang<sup>1,2†</sup>, Zhi Sun<sup>3,4†</sup>, Li-Wei Liu<sup>3,4</sup>, Qiu-Zheng Du<sup>3,4</sup>, Zhang-Suo Liu<sup>5</sup>, Yan-Jie Yang<sup>1,2</sup>, Peng Xue<sup>6\*</sup> and Hong-Yu Zhao<sup>1,2\*</sup>

<sup>1</sup>Stomatological Hospital of Henan Province, The First Affiliated Hospital of Zhengzhou University, Zhengzhou, China, <sup>2</sup>School and Hospital of Stomatology of Zhengzhou University, Zhengzhou, China, <sup>3</sup>Department of Pharmacy, The First Affiliated Hospital of Zhengzhou University, Zhengzhou, China, <sup>4</sup>Henan Key Laboratory of Precision Clinical Pharmacy, Zhengzhou, China, <sup>5</sup>Department of Nephrology, The First Affiliated Hospital of Zhengzhou University, Zhengzhou, China, <sup>6</sup>Health Management Centre, The First Affiliated Hospital of Zhengzhou University, Zhengzhou, China

## OPEN ACCESS

### Edited by:

Dong-Hua Yang,  
St. John's University,  
United States

### Reviewed by:

Honglin Jiang,  
University of California, San Francisco,  
United States  
Longyang Liu,  
Southern Medical University, China

### \*Correspondence:

Peng Xue  
xuepeng1978@hotmail.com  
Hong-Yu Zhao  
zhongyu93@163.com

†These authors have contributed  
equally to this work

### Specialty section:

This article was submitted to  
Experimental Pharmacology  
and Drug Discovery,  
a section of the journal  
Frontiers in Pharmacology

Received: 08 September 2020

Accepted: 05 October 2020

Published: 06 November 2020

### Citation:

Wang X-S, Sun Z, Liu L-W, Du Q-Z, Liu  
Z-S, Yang Y-J, Xue P and Zhao H-Y  
(2020) Potential Metabolic Biomarkers  
for Early Detection of Oral Lichen  
Planus, a Precancerous Lesion.  
Front. Pharmacol. 11:603899.  
doi: 10.3389/fphar.2020.603899

**Background:** Oral lichen planus (OLP) is a T-cell-mediated chronic inflammatory disorder and precancerous oral lesion with high incidence. The current diagnostic method of OLP is very limited and metabolomics may provide a new approach for quantitative evaluation.

**Methods:** The Ultra-Performance Liquid Chromatography-Quadrupole/Orbitrap High Resolution Mass Spectrometry (UHPLC-Q-Orbitrap HRMS) was applied to analyze the change of metabolites in serum of patients with OLP. A total of 115 OLP patients and 124 healthy controls were assigned to either a training set ( $n = 160$ ) or a test set ( $n = 79$ ). The potential biomarkers and the change of serum metabolites were profiled and evaluated by multivariate analysis.

**Results:** Totally, 23 differential metabolites were identified in the training set between OLP group and healthy group. Three prominent metabolites in receiver operating characteristic (ROC) were selected as a panel to distinguish OLP or healthy individuals in the test set, and the diagnostic accuracy was 86.1%.

**Conclusions:** This study established a new method for the early detection of OLP by analyzing serum metabolomics using UHPLC-Q-Orbitrap HRMS, which will help in understanding the pathological processes of OLP and identifying precancerous lesions in oral cavity.

**Keywords:** oral lichen planus, UHPLC-Q-orbitrap HRMS, metabolomics, precancerous lesion, biomarkers

## INTRODUCTION

Oral lichen planus (OLP) is a T-cell-mediated chronic inflammatory disorder and potentially precancerous oral lesion, with a prevalence of 0.5–3% (Warnakulasuriya et al., 2007; Carbone et al., 2009; Kountakis, 2013). About 0.5–12.5% of patients with OLP will progress to malignant transformation (Kountakis, 2013). The diagnosis of OLP is usually based on dental exam, histological examinations and patient history (Alrashdan et al., 2016; Raj and Patil, 2017). Due to the lack of universal diagnostic criteria for OLP and related lesions such as oral epithelial dysplasia (OED), OLP with dysplasia and oral lichenoid lesions (OLL), misdiagnosis often occurs, leading to the incorrect treatment strategy (van der Meij et al., 1999; Au et al., 2013; Raj and Patil, 2017). Therefore, a more efficient, non-invasive and accurate diagnostic method for OLP is urgently needed.



As one of the major components of system biology, metabolomics is a well-established method to assess global metabolic profiles through biomarker discovery in accessible biofluids (Wang et al., 2012; Zhang et al., 2014; Yang et al., 2018). It shows great potential as a way of identifying biomarkers for various diseases (Tohge and Fernie, 2010). In recent years, the application of metabolomics in the diagnosis, etiology, prevention and treatment of oral diseases has attracted attentions in the field of stomatology (Rai et al., 2018). In 2017, Yang *et al.* (Yang et al., 2017) used metabolomics to detect plasma metabolites in 20 erosive OLP patients and successfully found ten differential biomarkers. Subsequently, the urinary metabolome was analyzed and 12 kinds of metabolites were found to have changed (Li et al., 2017). Recently, 16 oral epithelial tissue samples from reticular OLP patients were detected by metabolomics. As a result, 21 metabolites and eight signaling pathways were identified (Yang et al., 2018). These studies provided important references for further understanding the pathogenesis of OLP. However, due to the small sample size and other limitations in studies, further experimental and clinical researches are still needed.

In this study, ultra-performance liquid chromatography-quadrupole/orbitrap high resolution mass spectrometry (UHPLC-Q-Orbitrap HRMS) was used for metabolomic analysis. Serum samples from 160 healthy subjects and OLP patients were assigned as a training set to identify potential biomarkers for the early detection of OLP. To confirm the reliability and accuracy, an independent test sample set ( $n = 79$ ) was used to evaluate the biomarkers panel we identified.

## MATERIALS AND METHODS

### Instruments and Reagents

UHPLC-Q-Orbitrap System: Ultimate 3000 UHPLC (Dionex, United States), Q Exactive high resolution mass spectrometry (Thermo Fisher Scientific, United States); ACQUITY UHPLC® BEH C<sub>18</sub> (100 × 2.1 mm, 1.7 μm) chromatographic column (Waters, United States); AL104 balance with 0.0001 accuracy (Mettler Toledo, Switzerland); Centrifuge CF16RN (HITACHI, Japan); HeraeusFresco17 (Thermo, United States); Acetonitrile and methanol (UPLC-grade, Fisher Scientific, United States); formic acid (UPLC-grade, Aladdin Industrial Co., Ltd., China); Internal standard (L-2-chlorophenylalanine and ketoprofen) (Sigma, United States; J&K Chemical, China); Milli-Q water purification system (Millipore, Shanghai, China); all solutions were filtrated by 0.22 μm pore size filters.

### Participants

A total of 239 participants were recruited including 115 OLP patients (100 patients with reticular OLP and 15 patients with erosive OLP) and 124 healthy individuals from March 1, 2019 to August 30, 2019 at the First Affiliated Hospital of Zhengzhou University. Patients were randomly assigned (by a random-number Generator in Excel) to either a training set ( $n = 160$ ) or a test set ( $n = 79$ ). The distributions of gender, age and other information were listed in **Table 1**. The written informed consent

**TABLE 1 |** The baseline characteristics of 239 participants.

	OLP ( $n = 115$ )	Control ( $n = 124$ )	$p$
Age (years)	50.66 ± 13.73	47.66 ± 13.23	0.870
Gender (male/female)	48/67	56/68	0.596
BMI (kg/m <sup>2</sup> )	24.32 ± 3.79	23.35 ± 3.46	0.059
Smoking history**	50/115	9/124	6.90E-11
Drinking history	25/115	18/124	0.150
Prefer spicy food	45/115	41/124	0.330
Prefer very hot food**	51/115	21/124	3.50E-06
Lack of exercise**	85/115	32/124	3.13E-15
Poor sleep*	19/115	9/124	0.028

Data are presented as the mean ± SD. BMI, body mass index; Smoking history: ≥1 cigarette per day for more than half a year; Drinking history: drinking alcohol more than once a week (alcohol content ≥50 ml) for more than half a year; Prefer very hot food: often intake high-temperature-treated meals within 1 min; Lack of exercise: exercise less than once a week; Poor sleep: sleep less than 6 h per night. \* $p < 0.05$ , \*\* $p < 0.001$ , \*\*\* $p < 0.001$ , student's t-test.

was obtained from all participants. The approval of the Ethical Committees of the First Affiliated Hospital of Zhengzhou University (Name of IRB: Ethics Committee of Scientific Research Project of the First Affiliated Hospital of Zhengzhou University; Date of approval: February 26, 2019; Ethical number: 2019-KY-26) were obtained. This research was conducted in accordance to the ethical guidelines of the 1975 Declaration of Helsinki.

The diagnosis of OLP was made by one oral clinician based on the clinical and pathological criteria and independently confirmed by two pathologists. Excluding criteria: 1) Received any treatment prior to admission; 2) Had other systemic diseases such as cardiovascular diseases, hypertension, kidney disease, diabetes, and other intraoral inflammation, etc.; and 3) Used antibiotics, hormones, or immunomodulator for at least 3 months.

### Sample Collection and Preparation

Blood samples were collected in the morning after fasting at patients' initial visit (Walsh et al., 2006). Samples were put in vacutainer tubes containing coagulant, which is a silica gel blood coagulation activator to promote the coagulation of blood samples, and cooled down in the insulated ice packs, then transferred to the laboratory immediately within half an hour. They were centrifuged at 3,000 ×  $g$  for 10 min at 4°C. Supernatants (serum) were separated and transferred into new vials, and immediately cryopreserved at -80°C until used.

After thawing on ice, the serum (100 μl) sample was added into 300 μl methanol solution (containing 0.05 μg/ml L-2-chlorophenylalanine and 0.5 μg/ml ketoprofen as internal standard). After vortexing for 1 min, the mixture was centrifuged at 16,200 ×  $g$  at 4°C for 10 min 200 μl pipette gun was used to suck out the supernatant and transferred to an auto-sampler vial for analysis.

In order to ensure the reliability, quality control (QC) sample analysis was carried out in the process of metabolomics data collection. Six QC samples were first analyzed, and sample analysis was started after the instrument was stabilized. After that, QC samples were evenly inserted every ten samples in the sequence of sample analysis to monitor the stability of analysis.

Blank samples containing only solvent are inserted after each QC sample to avoid contamination.

### UHPLC-MS/MS System Conditions

An ultra high performance liquid chromatography (UHPLC) system was used to separate the metabolites in serum. Five microliters aliquot from each sample was injected into a ACQUITY UHPLC® BEH C<sub>18</sub> column maintained at 40°C. The mobile phase was the acetonitrile (A) with 0.1% formic acid aqueous solution (B). The gradient elution was as follows: at a flow rate of 0.2 ml/min: 0–0.5 min, 5% A; 0.5–1.0 min, 5–60% A; 1.0–7.0 min, 60–80% A; 7.0–9.0 min, 80–100% A;

9.0–11.0 min, 100% A; 11.0–11.2 min, 100–5% A; 11.2–13.0 min, 5% A.

A Q Exactive high resolution mass spectrometry was tandem to the UHPLC system using a heated electrospray ionization (HESI) source. The temperature of the auxiliary gas, ion source, and capillary were 300°C, 350°C, and 320°C, respectively, the flow rate of the auxiliary gas was 10 arb. Samples were respectively tested in the positive and negative modes by full scan/ddms two scan patterns from 80 to 1,200 *m/z* at the mass resolving power of 17,500 in MS/MS. The gradient collision energy was at 20, 40, and 60 eV. The spray voltage and the sheath gas flow rate were set to 3.50 kV and 40 arb for the positive mode and 2.80 kV and 38 arb

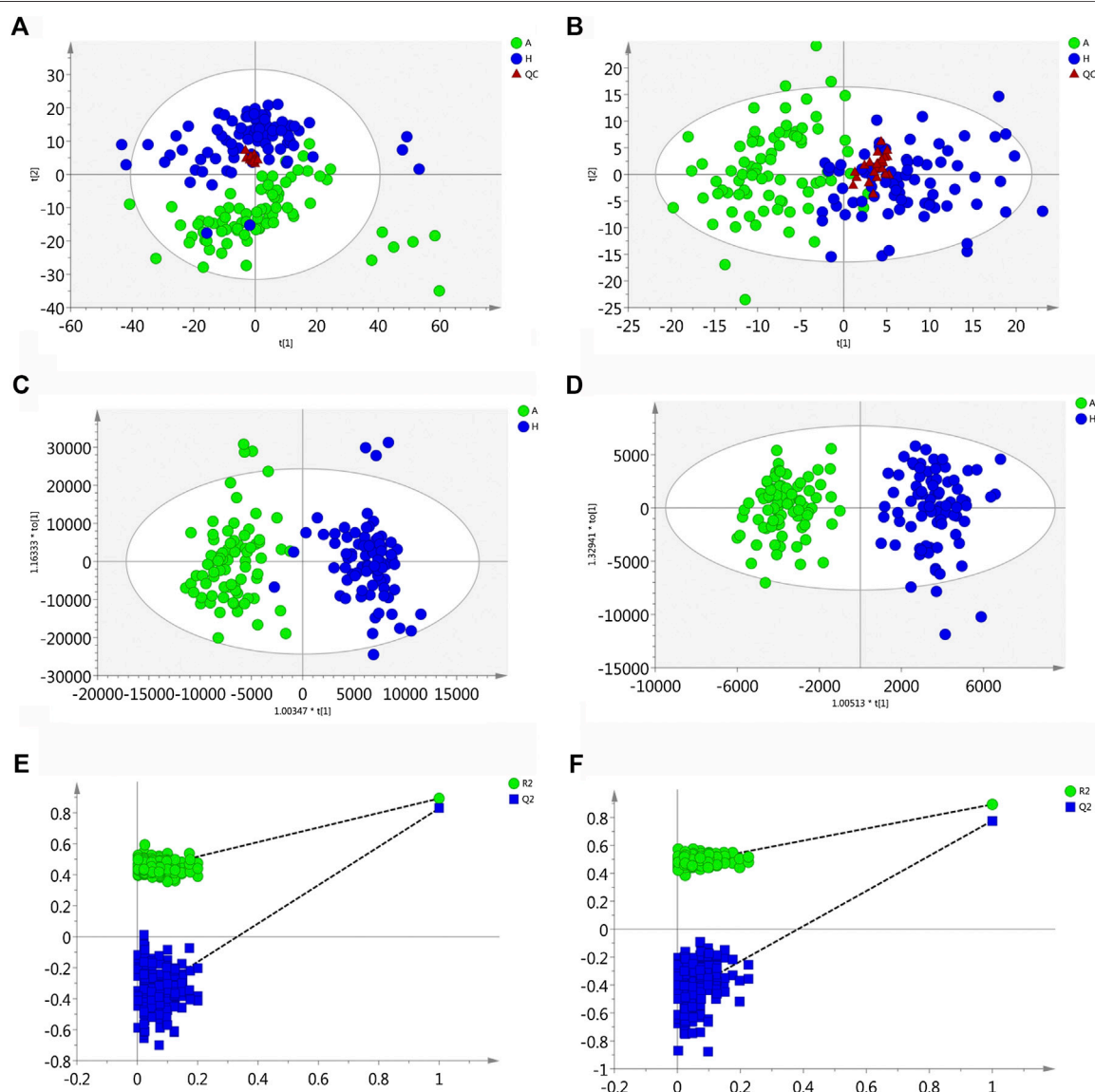


**FIGURE 1 |** Multivariate statistical analysis of two groups. The principal component analysis (PCA) plot of QC and samples in (A) positive ion mode and (B) negative ion mode in the training set. The orthogonal partial least square discrimination analysis (OPLS-DA) score plots of OLP group vs. healthy control group in (C) positive ion mode and (D) negative ion mode in the training set. Cross-validation plot with a permutation test repeated 200 times of OLP group vs. healthy group in (E) positive ion mode and (F) negative ion mode in the training set. A, OLP group; H, healthy control; QC, quality control.

for the negative mode. The order of sample analysis was randomized.

## Data Processing and Statistical Analysis

All data were acquired and processed by Thermo Xcalibur™ software (Version 3.0, Thermo Scientific, United States). Then the peak calibration, peak matching and peak alignment were performed by the Compound Discovery software (Version 3.0, Thermo Scientific) to extract the information. Specific parameters were as follows: the width of Retention Time (RT) is set to 0.1 min and the mass width to 5 ppm. The intensity threshold for filtering ion peak is 1,000,000 in both the positive ion mode and negative ion mode. The data result set which corresponds to the concentration of certain metabolite, contained all the  $m/z$  value, RT and ion peak area of each sample. And they were exported to the multivariate statistical software SIMCA (version 14.0, Umetrics, Umea, Sweden) for the subsequent principal component analysis (PCA) and orthogonal partial least square discrimination analysis (OPLS-DA), and Variable importance in projection (VIP) was obtained from the OPLS-DA model. A 200 times permutation test was performed to assess the risk of overfitting for the model. The preliminary discriminating metabolites were selected by plotting the data set of all the discriminators in a volcano plot. To further screen the significant variables between the two groups, a student's  $t$ -test and fold change of all the detected peaks were carried out by the SPSS 21.0 software (IBM, United States). Finally, the metabolites with statistical significance were selected and identified to distinguish the difference between the two groups. A Heatmap was generated with these screened metabolites by MetaboAnalyst (<https://www.metaboanalyst.ca/>) to show the trend of change. For

each identified differential metabolite, receiver operating characteristic (ROC) curve was drawn and areas under the curve (AUC) were calculated using the SPSS 21.0 software (IBM, United States).

In order to adjust the influence of confounding factors (in **Table 1**) on each differential metabolite, SPSS 21.0 software (IBM, United States) was used to establish a binary logistic regression model by taking groups as dependent variables and each metabolite and each confounding factor as covariables.

## Identification of Differential Metabolites

Compound identification was achieved by comparing the precision  $m/z$ ,  $MS^2$ , RT and other information collected by mass spectrometry with authentic standards or searching the Human Metabolome database (<http://hmdb.ca/>), the PubChem compound database.

## Metabolic Pathway Analysis and Pathological Network Construction

Metabolic pathway analysis of differential metabolites was performed by MetaboAnalyst based on the database source including The Human Metabolome database (HMDB), PubChem and Kyoto Encyclopedia of Genes and Genomes (KEGG).

## RESULTS

### Demographic Characteristics

The baseline characteristics of these 239 participants was showed in **Table 1**. There were more cases had the habit of smoking ( $p < 0.001$ ) and a preference for very hot food in the OLP group

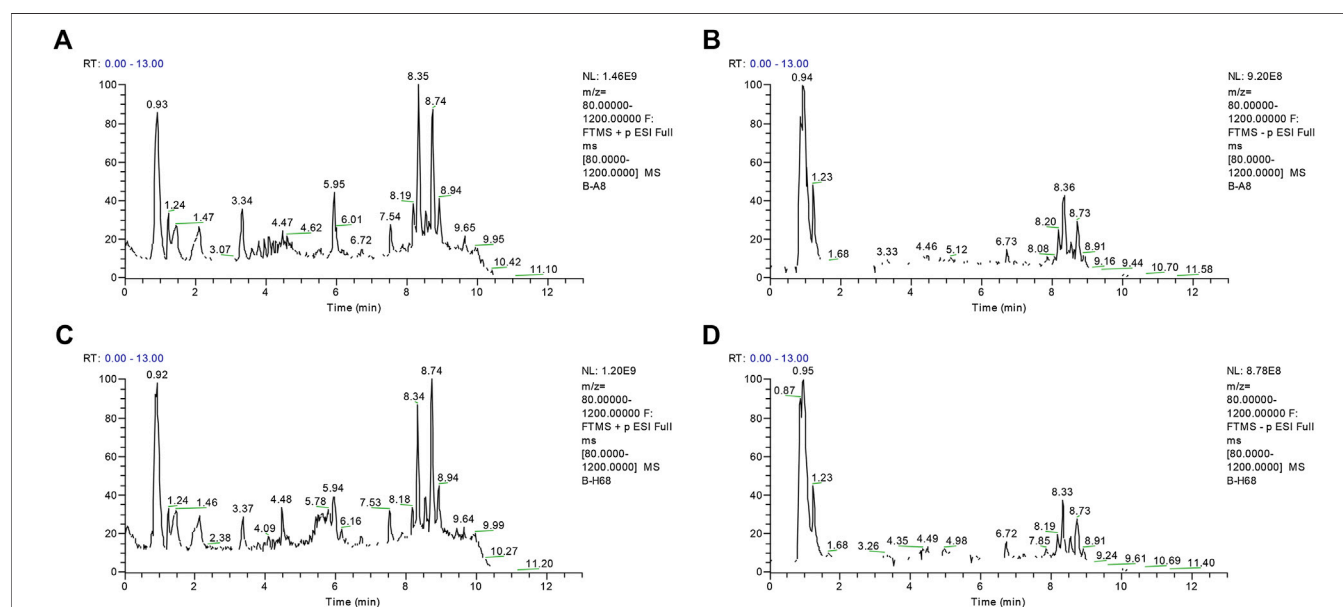


**FIGURE 2 |** The representative total intensity chromatograms (TIC) of OLP and healthy group serum samples. TIC of OLP group obtained from the training set in (A) positive mode and (B) negative mode. TIC of healthy control obtained from the training set in (C) positive mode and (D) negative mode.

compared with the healthy subjects ( $p < 0.001$ ). There was no significant difference among OLP and healthy controls in terms of the habit of drinking ( $p = 0.150$ ) and the preference for spicy food ( $p = 0.330$ ). In addition, most of the subjects in the OLP group lacked exercises ( $p < 0.001$ ), and most of them did not get enough time for sleeping ( $p = 0.028$ ).

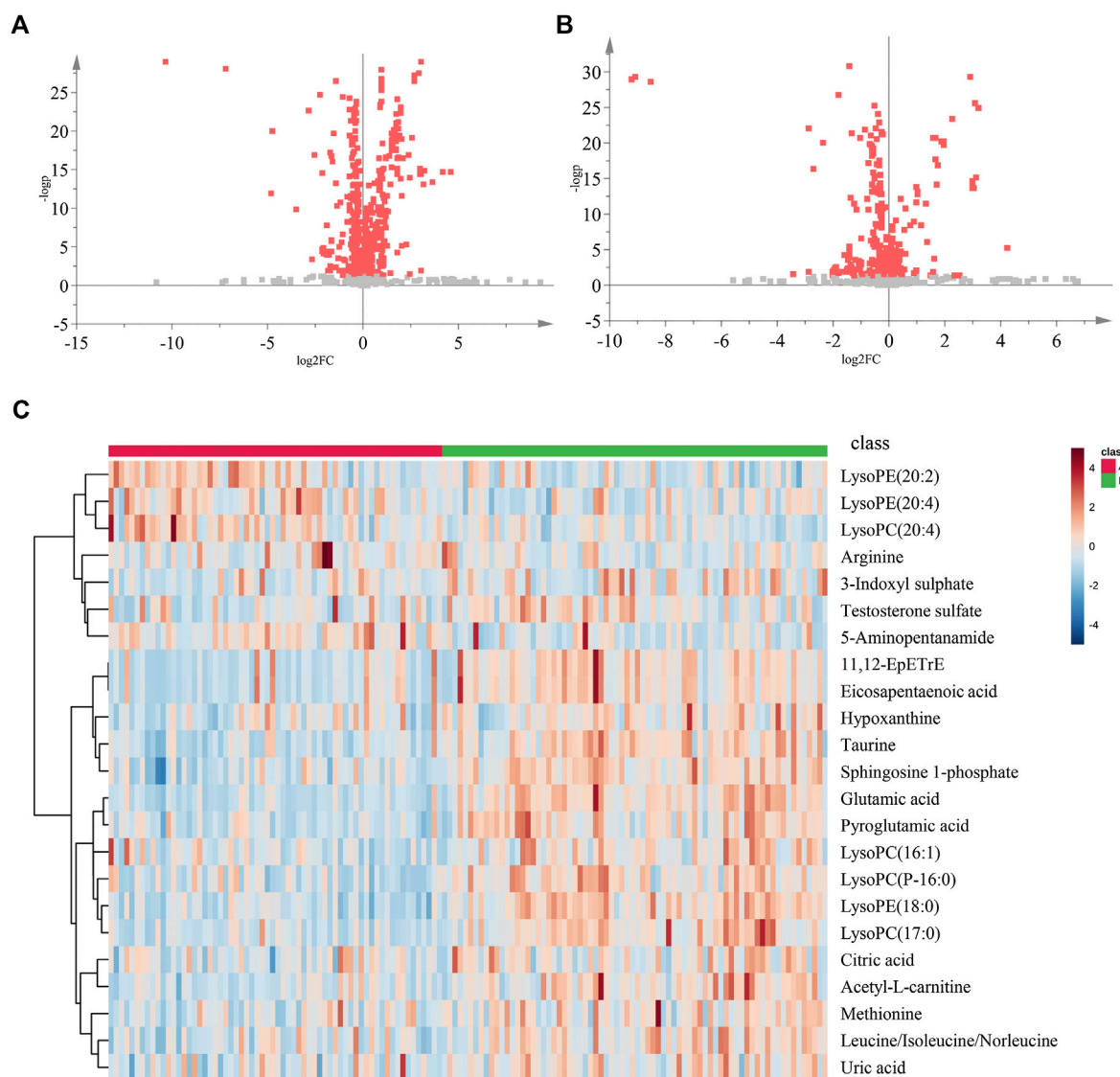
**Supplementary Figure S1** showed the binary logistic regression model established by taking groups as dependent variables and each metabolite and each confounding factor as covariables, in order to adjust the influence of confounding factors on each differential metabolite. It showed that 23 differential metabolites have strong correlation with the occurrence of OLP after adjusting for various risk factors.

## Data Quality Evaluation in Metabolomic Analysis

QC samples in both positive and negative mode were clustered closely in PCA score plots (**Figures 1A,B**), which indicated that the analytical process was stable and reliable.

## Metabolomics Analysis and Biomarkers Identification

Using the alignment software, 1,540 ion peaks in positive and 837 in negative mode and their areas were captured. The total intensity chromatograms (TIC) of serum samples obtained from the training set in both positive and negative ion modes are shown in **Figure 2**, which included the retention time,





precise mass and ion intensity of the detected metabolites. Both PCA and OPLS-DA score plots in training set showed difference of metabolites between the OLP and control groups (Figures 1A–D).  $R^2Y$  at 0.893 and  $Q^2$  at 0.777 in positive ion mode and  $R^2Y$  at 0.892 and  $Q^2$  at 0.828 in the negative ion mode, suggesting that biochemical changes occurred in the blood of patients. The 200 times permutation test in both positive and negative ion modes (Figures 1E,F) demonstrated that the model was not overfitting ( $R^2$  at 0.423 and  $Q^2$  at  $-0.41$  in positive in mode,  $R^2$  at 0.461 and  $Q^2$  at  $-0.482$  in negative in mode). A volcano plot containing the  $p$  values of student's  $t$ -test and fold changes was performed between the two groups to identify the differential metabolites (Figures 3A,B). In the volcano plot, the red dots represented the metabolites with the  $p$  values lower than 0.05 ( $-\log_{10} p > 1.30$ ). In this way, several potential biomarkers were distinguished which showed significant difference between the OLP and healthy group. Heat map of the Pearson correlation coefficients between differential metabolites and groups (Figure 3C) also revealed the distinct difference observed between the OLP and control groups. The metabolites with VIP values  $>1.0$  and  $p$  values  $<0.05$  for each comparison were shown in Table 2.

## Establishment and Evaluation of the Metabolic Biomarkers Panel

Considering the clinical significance of the identified differential metabolites, the combination of Glutamic acid, LysoPE (18:0), Taurine was proposed to be a panel of metabolic biomarkers for

the early detection of OLP in patients. The ROC presentations appear in the logistic regression of the metabolic biomarkers panel from the training set (Figures 4A–D), and the test set (Supplementary Figure S2). The AUC, sensitivity, and specificity are 0.938, 90.5%, and 84.4%, respectively. Supplementary Figure S3 showed the structure and mass fragmentation pattern of these three metabolic biomarkers and mass fragmentation pattern in real samples. The mass fragmentation pattern from the peak in real sample was matched with the pattern of these three metabolic biomarkers.

On the basis of the highest prediction sensitivity and specificity of the ROC in the training set, the optimal cut-off value was 0.461 for OLP and healthy control groups. This cut-off value was then used to distinguish different individuals in the test set and the diagnostic accuracy was 86.1% (Figure 4E).

## Metabolic Pathway Analysis of Potential Biomarkers

The perturbed pathways of metabolites occurred in the serum of patients with OLP were showed in Figure 5, including Taurine and hypotaurine metabolism, Alanine, aspartate and glutamate metabolism, Arginine and proline metabolism, Glutamine and glutamate metabolism and Aminoacyl-tRNA biosynthesis, etc. Based on the differential metabolites, the metabolic pathway network was mapped to display the metabolic disorders in patients with oral lichen planus (Figure 6). These results may provide an important basis for further studies of the pathogenic mechanism of OLP.

**TABLE 2 |** Statistical analysis of potential metabolic biomarkers.

Id	Name	Formula	Retention time (min)	Molecular	VIP	Fold change	$p$	AUC
1	Glutamic acid	$C_5H_9NO_4$	0.992	147.053	2.554	0.551	$1.10E-22$	0.916
2	LysoPE (18:0)	$C_{23}H_{48}NO_7P$	8.749	481.317	8.845	0.826	$3.47E-22$	0.893
3	Taurine	$C_2H_7NO_3S$	0.970	125.014	1.844	0.652	$5.98E-15$	0.850
4	LysoPC (17:0)	$C_{25}H_{52}NO_7P$	9.199	509.347	1.424	0.676	$1.22E-13$	0.847
5	Sphingosine 1-phosphate	$C_{18}H_{38}NO_5P$	7.786	379.248	1.090	0.788	$1.21E-14$	0.837
6	11,12-EpETE	$C_{20}H_{32}O_3$	8.729	320.235	2.269	0.442	$2.96E-12$	0.834
7	Eicosapentaenoic acid	$C_{20}H_{30}O_2$	8.727	302.224	1.296	0.467	$1.77E-11$	0.819
8	Pyroglutamic acid	$C_5H_7NO_3$	1.253	129.042	1.659	0.778	$1.19E-11$	0.815
9	LysoPC (P-16:0)	$C_{24}H_{50}NO_6P$	8.973	479.336	1.150	0.757	$1.05E-11$	0.798
10	Acetyl-L-carnitine	$C_9H_{17}NO_4$	1.247	203.115	1.604	0.666	$4.06E-09$	0.773
11	Leucine/Isoleucine/ Norleucine	$C_6H_{13}NO_2$	1.463	131.094	6.792	0.846	$5.91E-07$	0.730
12	5-Aminopentanamide	$C_5H_{12}N_2O$	3.706	116.095	1.580	1.410	$2.25E-04$	0.719
13	LysoPC (20:4)	$C_{28}H_{50}NO_7P$	8.336	543.331	4.907	1.278	$7.46E-06$	0.704
14	LysoPC (16:1)	$C_{24}H_{48}NO_7P$	8.096	493.316	1.821	0.808	$8.20E-06$	0.698
15	LysoPE (20:2)	$C_{25}H_{48}NO_7P$	8.360	505.316	4.235	1.125	$9.93E-05$	0.690
16	Methionine	$C_5H_{11}NO_2S$	1.253	149.051	1.097	0.869	$6.15E-04$	0.683
17	Uric acid	$C_5H_4N_4O_3$	1.247	168.028	1.698	0.873	0.001	0.668
18	LysoPE (20:4)	$C_{25}H_{44}NO_7P$	8.317	501.285	1.074	1.179	$1.41E-04$	0.668
19	Testosterone sulfate	$C_{19}H_{28}O_5S$	8.194	368.165	2.104	0.724	0.016	0.660
20	Hypoxanthine	$C_5H_4N_4O$	1.251	136.038	1.188	0.866	0.004	0.656
21	Citric acid	$C_6H_8O_7$	1.256	192.027	1.868	0.883	0.002	0.619
22	3-Indoxyl sulfate	$C_8H_7NO_4S$	4.818	213.009	1.934	0.710	0.014	0.604
23	Arginine	$C_6H_{14}N_4O_2$	0.884	174.111	1.238	1.123	0.031	0.567



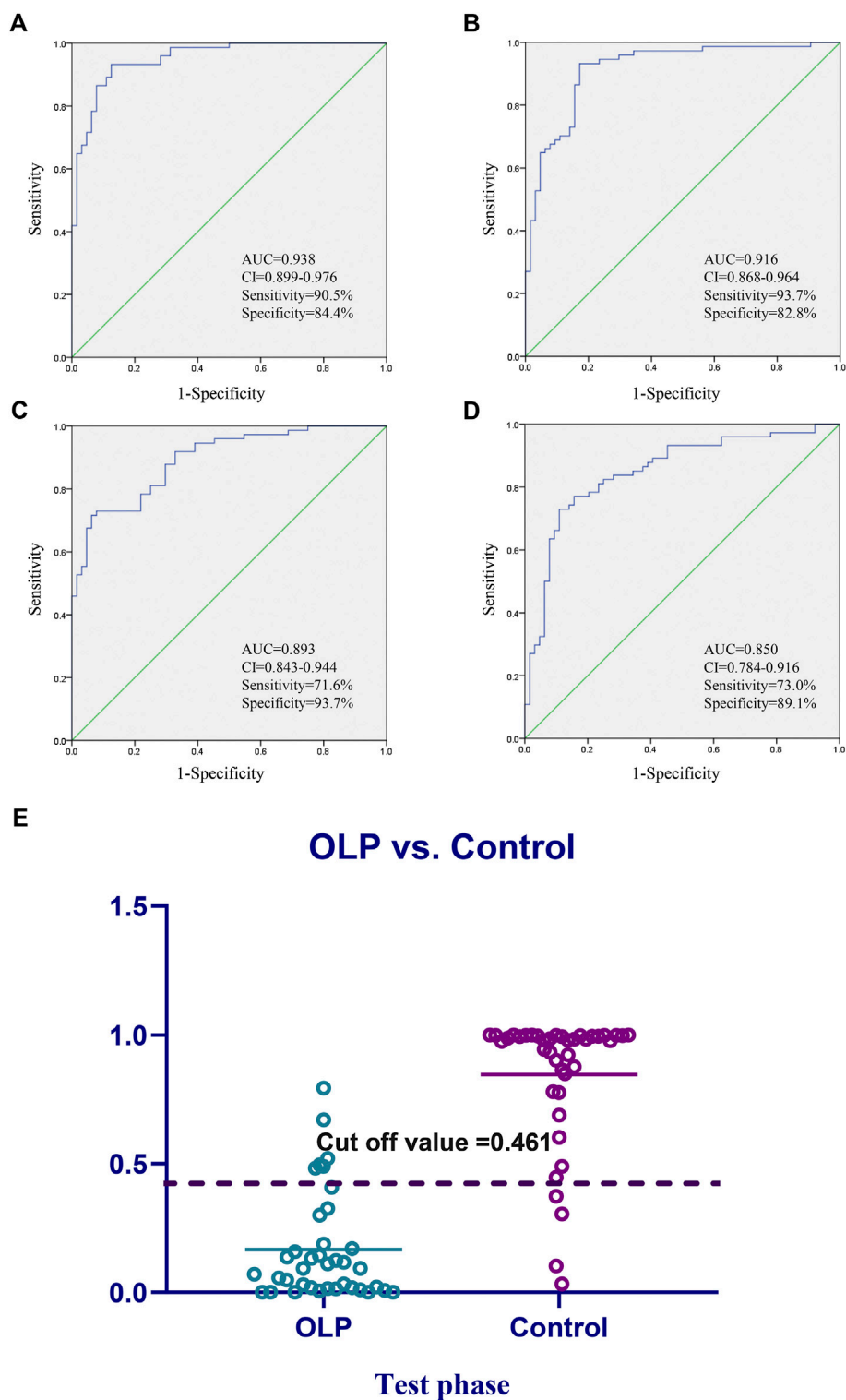
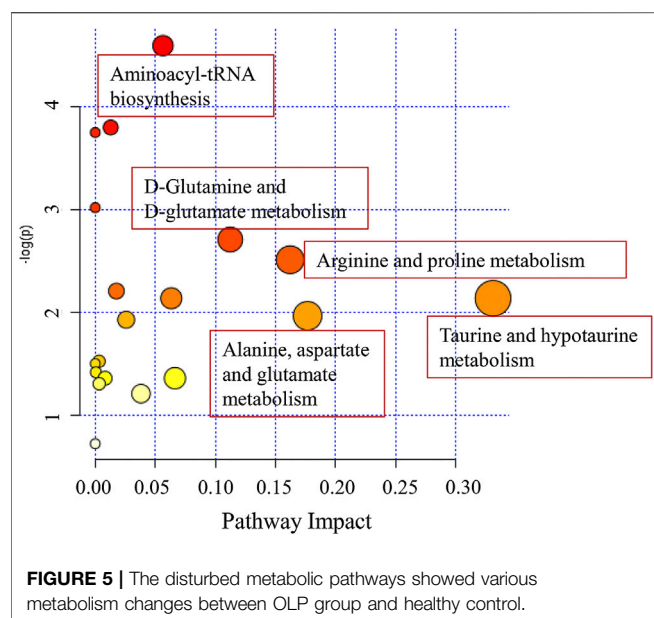


**FIGURE 4 |** Diagnostic outcomes and prediction accuracies. Receiver operating curves (ROC) obtained by the **(A)** biomarkers panel, and **(B–D)** three highest metabolites in the comparisons between OLP group vs. healthy group. **(E)** The prediction accuracies by the biomarkers in test phase compared between OLP group vs. healthy group. AUC, area under curve; 95% CI, 95% confidence interval.



## DISCUSSION

Currently, the identification of potential serum biomarkers for the detection of OLP remains challenged. Studies to date have been conducted on small population and small sample size.

In this study, we demonstrated an untargeted metabolomic evaluation for 115 OLP patients and 124 healthy controls based on UHPLC-Q-Orbitrap HRMS analysis. To our knowledge, this is the largest sample size of metabolomics research to date to investigate the potential biomarkers for early detection of OLP. Metabolic phenotypes revealed significant differences between OLP patients and healthy controls. We established a biomarkers panel for the detection of OLP, which consisted of Glutamic acid, LysoPE (18:0), and Taurine. This panel could be successfully used to reveal the change of metabolites and discriminate OLP from healthy individuals. The ability of this panel to diagnose OLP was excellent, with an accuracy of 87.1% in the test set.

OLP affects females more than males and commonly affects patients of middle age (Wagner et al., 2013). In our study, the mean age of OLP participants was 50.66, and the gender ratio between men and women is 48/67, that are basically consistent with the reported data. We collected the data of personal habits of each patients and healthy controls, and found that smoking was a strong risk factor for OLP. This result was supported by some previous studies (Villa and Gohel, 2014; Feng et al., 2015) indicating that subjects who has a habit of smoking were found to increase almost four-fold risk for oral malignant disorders. Another study showed that drinking alcohol on its own did not seem to increase the risk for oral malignant disorders, which is in consistent with our findings (Hassona et al., 2014). As for food eating habit, 44.3% OLP patients had a preference for very hot food before they got sick, while it was only 17.9% in healthy controls, which showed a significant difference between the two groups. But there was no significant difference for the preference for spicy food before

they got sick. We also found that patients with OLP usually have less exercise and sleeping time than the healthy controls. Most patients claimed to have varying degrees of insomnia and we noticed that insomnia is more likely to lead to psychological problems, and people who are non-depressed subjects with insomnia have a two-fold risk to develop depression (Baglioni et al., 2011). Moreover, psychological factors are thought to play an important role in the pathogenesis of OLP (Liao et al., 2020; Alrashdan et al., 2016). Extensive evidence has indicated that the depression is related to metabolic disturbance in glutamic metabolism (Moriguchi et al., 2019). We found decreased level in Glutamic acid concentration in the serum sample of patients.

Apoptotic cell death may be a contributory cause of basal cell destruction in oral lichen planus (Neppelberg et al., 2001). Phosphatidylcholine (PC) metabolism plays a significant role in the apoptotic program (Wright et al., 2004). In eukaryotic cellular membranes, the most abundant phospholipid moiety is phosphatidylcholine (Raetz, 1986) and apoptosis can be caused by inactivation of phosphatidylcholine biosynthesis (Cui et al., 1996). As a breakdown product of phosphatidylcholine (Zhao et al., 2019), we observed there were changes in four lysophosphatidylcholines including [LysoPC (17:0), LysoPC (P-16:0), LysoPC (16:1), and LysoPC (20:4)]. In addition, lipid-related molecules are often used as biomarkers for tumorigenesis (Defagó and Soria, 2010). Phosphatidylcholine might be the important contributory cause of apoptosis induction in oral precancerous lesions.

Taurine is widely distributed in human body, and it is closely associated with the development of immune system (Piao et al., 2019). It has been suggested that OLP patients might have some immune system dysfunction since the significantly decreased level of Taurine was observed on them. It might be a potential etiological factor of OLP.

Besides, patients with OLP have low defense to oxidative stress (Ergun et al., 2011). Low expression of Glutamic was found to be associated with oxidative stress (Wu et al., 2014). In this study, we found that the level of Glutamic was higher in healthy individuals, which indicated that oxidative stress may have potential biological effect in patients with OLP.

In summary, this study established a new method for the early detection of OLP, using UHPLC-Q-Orbitrap HRMS serum metabolomics analysis, which will help in understanding the pathological processes of OLP and identifying precancerous lesions in oral cavity.

## DATA AVAILABILITY STATEMENT

The raw data supporting the conclusions of this article will be made available by the authors, without undue reservation.

## AUTHOR CONTRIBUTIONS

X-SW and ZS contributed equally to this work. H-YZ and PX designed the research. X-SW, ZS, Z-SL, and Y-JY performed the

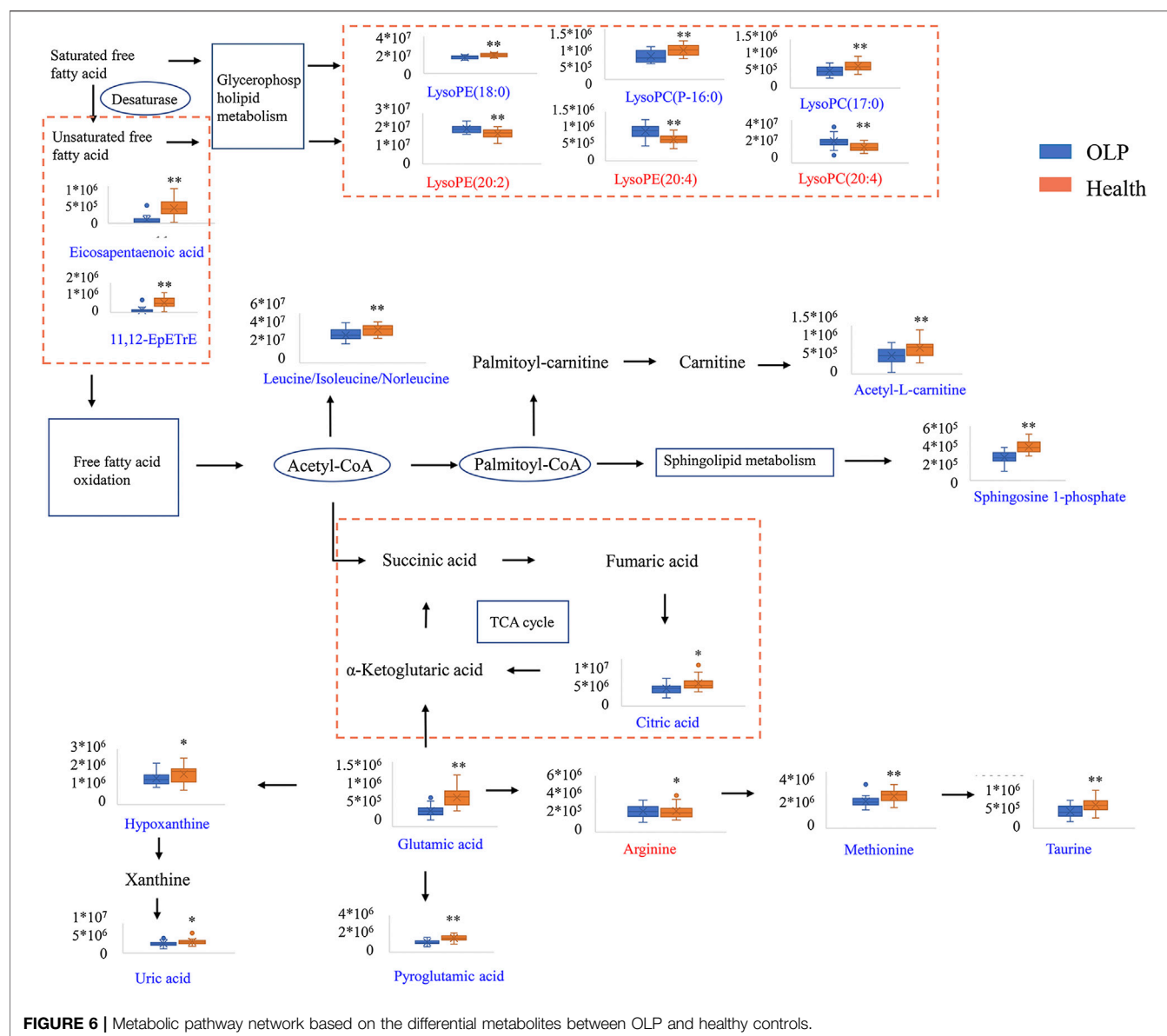


**FIGURE 6 |** Metabolic pathway network based on the differential metabolites between OLP and healthy controls.

experiments. X-SW, ZS, L-WL, and Q-ZD analyzed data. X-SW and ZS wrote the manuscript. L-WL and Q-ZD revised the manuscript. All authors read and approved the final manuscript.

## FUNDING

This work was supported by the National Natural Science Foundation of China (grant no. 81703666), and Kang Meng Medical Research Foundation (grant no. TB204022) by ZS in the author list.

## ACKNOWLEDGMENTS

The authors sincerely thank all personnel who helped with sample collection.

## SUPPLEMENTARY MATERIAL

The Supplementary Material for this article can be found online at: <https://www.frontiersin.org/articles/10.3389/fphar.2020.603899/full#supplementary-material>

## REFERENCES

- Alrashdan, M. S., Cirillo, N., and McCullough, M. (2016). Oral lichen planus: a literature review and update. *Arch. Dermatol. Res.* 308 (8), 539–551. doi:10.1007/s00403-016-1667-2
- Au, J., Patel, D., and Campbell, J. H. (2013). Oral lichen planus. *Oral Maxillofac. Surg. Clin.* 25 (1), 93–100. doi:10.1016/j.coms.2012.11.007
- Baglioni, C., Battagliese, G., Feige, B., Spiegelhalter, K., Nissen, C., Voderholzer, U., et al. (2011). Insomnia as a predictor of depression: a meta-analytic evaluation of longitudinal epidemiological studies. *J. Affect. Disord.* 135 (1–3), 10–19. doi:10.1016/j.jad.2011.01.011
- Carbone, M., Arduino, P. G., Carrozzo, M., Gandolfo, S., Argiolas, M. R., Bertolusso, G., et al. (2009). Course of oral lichen planus: a retrospective study of 808 northern Italian patients. *Oral Dis.* 15 (3), 235–243. doi:10.1111/j.1601-0825.2009.01516.x
- Cui, Z., Houweling, M., Chen, M. H., Record, M., Chap, H., Vance, D. E., et al. (1996). A genetic defect in phosphatidylcholine biosynthesis triggers apoptosis in Chinese hamster ovary cells. *J. Biol. Chem.* 271 (25), 14668–14671. doi:10.1074/jbc.271.25.14668
- Defagó, M. D., and Soria, E. A. (2010). Biomarker assessment in nutritional modulation of oxidative stress-induced cancer development by lipid-related bioactive molecules. *Recent Pat. Anti-Cancer Drug Discov.* 5 (3), 188–196. doi:10.2174/157489210791760481
- Ergun, S., Troşala, S. C., Warnakulasuriya, S., Özel, S., Önal, A. E., Ofluoğlu, D., et al. (2011). Evaluation of oxidative stress and antioxidant profile in patients with oral lichen planus. *J. Oral Pathol. Med.* 40 (4), 286–293. doi:10.1111/j.1600-0714.2010.00955.x
- Feng, J., Zhou, Z., Shen, X., Wang, Y., Shi, L., Wang, Y., et al. (2015). Prevalence and distribution of oral mucosal lesions: a cross-sectional study in Shanghai, China. *J. Oral Pathol. Med.* 44 (7), 490–494. doi:10.1111/jop.12264
- Hassona, Y., Scully, C., Almangush, A., Baqain, Z., and Sawair, F. (2014). Oral potentially malignant disorders among dental patients: a pilot study in Jordan. *Asian Pac. J. Cancer Prev.* 15 (23), 10427–10431. doi:10.7314/apjcp.2014.15.23.10427
- Kountakis, S. E. (2013). *Encyclopedia of otolaryngology, head and neck surgery*. Berlin Heidelberg: Springer. doi:10.1007/9783642234996
- Li, X. Z., Yang, X. Y., Wang, Y., Zhang, S. N., Zou, W., Wang, Y., et al. (2017). Urine metabolic profiling for the pathogenesis research of erosive oral lichen planus. *Arch. Oral Biol.* 73, 206–213. doi:10.1016/j.archoralbio.2016.10.014
- Liao, H., Luo, Y., Long, L., Peng, J., Qiu, X., Yuan, P., et al. (2020). Anxiety and oral lichen planus. *Oral Dis.* doi:10.1111/odi.13569.
- Moriguchi, S., Takamiya, A., Noda, Y., Horita, N., Wada, M., Tsugawa, S., et al. (2019). Glutamatergic neurometabolite levels in major depressive disorder: a systematic review and meta-analysis of proton magnetic resonance spectroscopy studies. *Mol. Psychiatr.* 24 (7), 952–964. doi:10.1038/s41380-018-0252-9
- Neppelberg, E., Johannessen, A. C., and Jonsson, R. (2001). Apoptosis in oral lichen planus. *Eur. J. Oral Sci.* 109 (5), 361–364. doi:10.1034/j.1600-0722.2001.00081.x
- Piao, J., Meng, F., Fang, H., Piao, F., Jin, B., Li, M., et al. (2019). Effect of taurine on thymus differentiation of dex-induced immunosuppressive mice. *Adv. Exp. Med. Biol.* 1155, 381–390. doi:10.1007/978-981-13-8023-5\_36
- Raetz, C. R. (1986). Molecular genetics of membrane phospholipid synthesis. *Annu. Rev. Genet.* 20, 253–295. doi:10.1146/annurev.ge.20.120186.001345
- Rai, V., Mukherjee, R., Ghosh, A. K., Routray, A., and Chakraborty, C. (2018). “Omics” in oral cancer: new approaches for biomarker discovery. *Arch. Oral Biol.* 87, 15–34. doi:10.1016/j.archoralbio.2017.12.003
- Raj, A. T., and Patil, S. (2017). Diagnostic flaws in oral lichen planus and related lesions. *Oral Oncol.* 74, 190–191. doi:10.1016/j.oraloncology.2017.10.003
- Soto Araya, M., Rojas Alcayaga, G., and Esguep, A. (2004). Association between psychological disorders and the presence of Oral lichen planus, Burning mouth syndrome and Recurrent aphthous stomatitis. *Med. Oral* 9 (1), 1–7.
- Tohge, T., and Fernie, A. R. (2010). Combining genetic diversity, informatics and metabolomics to facilitate annotation of plant gene function. *Nat. Protoc.* 5 (6), 1210–1227. doi:10.1038/nprot.2010.82
- van der Meij, E. H., Reibel, J., Slootweg, P. J., van der Wal, J. E., de Jong, W. F., and van der Waal, I. (1999). Interobserver and intraobserver variability in the histologic assessment of oral lichen planus. *J. Oral Pathol. Med.* 28 (6), 274–277. doi:10.1111/j.1600-0714.1999.tb02038.x
- Villa, A., and Gohel, A. (2014). Oral potentially malignant disorders in a large dental population. *J. Appl. Oral Sci.* 22 (6), 473–476. doi:10.1590/1678-775720140254
- Wagner, G., Rose, C., and Sachse, M. M. (2013). Clinical variants of lichen planus. *J. Dtsch. Dermatol. Ges.* 11 (4), 309–319. doi:10.1111/ddg.12031
- Walsh, M. C., Brennan, L., Malthouse, J. P., Roche, H. M., and Gibney, M. J. (2006). Effect of acute dietary standardization on the urinary, plasma, and salivary metabolomic profiles of healthy humans. *Am. J. Clin. Nutr.* 84 (3), 531–539. doi:10.1093/ajcn/84.3.531
- Wang, X., Zhang, A., Han, Y., Wang, P., Sun, H., Song, G., et al. (2012). Urine metabolomics analysis for biomarker discovery and detection of jaundice syndrome in patients with liver disease. *Mol. Cell. Proteomics* 11 (8), 370–380. doi:10.1074/mcp.M111.016006
- Warnakulasuriya, S., Johnson, N. W., and van der Waal, I. (2007). Nomenclature and classification of potentially malignant disorders of the oral mucosa. *J. Oral Pathol. Med.* 36 (10), 575–580. doi:10.1111/j.1600-0714.2007.00582.x
- Wright, M. M., Howe, A. G., and Zarembek, V. (2004). Cell membranes and apoptosis: role of cardiolipin, phosphatidylcholine, and anticancer lipid analogues. *Biochem. Cell. Biol.* 82 (1), 18–26. doi:10.1139/o03-092
- Wu, M., Xiao, H., Ren, W., Yin, J., Tan, B., Liu, G., et al. (2014). Therapeutic effects of glutamic acid in piglets challenged with deoxynivalenol. *PLoS One* 9 (7), e100591. doi:10.1371/journal.pone.0100591
- Yang, X. Y., Li, X. Z., and Zhang, S. N. (2018). Metabolomics analysis of oral mucosa reveals profile perturbation in reticular oral lichen planus. *Clin. Chim. Acta* 487, 28–32. doi:10.1016/j.cca.2018.09.021
- Yang, X. Y., Zhang, S. N., Li, X. Z., Wang, Y., and Yin, X. D. (2017). Analysis of human serum metabolome for potential biomarkers identification of erosive oral lichen planus. *Clin. Chim. Acta* 468, 46–50. doi:10.1016/j.cca.2017.02.010
- Zhang, S. N., Li, X. Z., Wang, Y., Zhang, N., Yang, Z. M., Liu, S. M., et al. (2014). Neuroprotection or neurotoxicity? New insights into the effects of *Acanthopanax senticosus* harms on nervous system through cerebral metabolomics analysis. *J. Ethnopharmacol.* 156, 290–300. doi:10.1016/j.jep.2014.08.037
- Zhao, J., Jung, Y. H., Jin, Y., Kang, S., Jang, C. G., and Lee, J. (2019). A comprehensive metabolomics investigation of hippocampus, serum, and feces affected by chronic fluoxetine treatment using the chronic unpredictable mild stress mouse model of depression. *Sci. Rep.* 9 (1), 7566. doi:10.1038/s41598-019-44052-2

**Conflict of Interest:** The authors declare that the research was conducted in the absence of any commercial or financial relationships that could be construed as a potential conflict of interest.

Copyright © 2020 Wang, Sun, Liu, Du, Liu, Yang, Xue and Zhao. This is an open-access article distributed under the terms of the Creative Commons Attribution License (CC BY). The use, distribution or reproduction in other forums is permitted, provided the original author(s) and the copyright owner(s) are credited and that the original publication in this journal is cited, in accordance with accepted academic practice. No use, distribution or reproduction is permitted which does not comply with these terms.



# External Validation of a Nomogram and Risk Grouping System for Predicting Individual Prognosis of Patients With Medulloblastoma

Chengcheng Guo<sup>1†</sup>, Dunchen Yao<sup>2†</sup>, Xiaoping Lin<sup>3†</sup>, He Huang<sup>4</sup>, Ji Zhang<sup>1</sup>, Fuhua Lin<sup>1</sup>, Yonggao Mou<sup>1\*</sup> and Qunying Yang<sup>1\*</sup>

<sup>1</sup>Department of Neurosurgery/Neuro-Oncology, Sun Yat-Sen University Cancer Center, Collaborative Innovation Center for Cancer Medicine, State Key Laboratory of Oncology in South China, Guangzhou, China, <sup>2</sup>Department of Radiation Oncology, Sun Yat-Sen University Cancer Center, Collaborative Innovation Center for Cancer Medicine, State Key Laboratory of Oncology in South China, Guangzhou, China, <sup>3</sup>Department of Nuclear Medicine, Sun Yat-Sen University Cancer Center, Collaborative Innovation Center for Cancer Medicine, State Key Laboratory of Oncology in South China, Guangzhou, China, <sup>4</sup>Department of Medical Oncology, Sun Yat-Sen University Cancer Center, Collaborative Innovation Center for Cancer Medicine, State Key Laboratory of Oncology in South China, Guangzhou, China

## OPEN ACCESS

### Edited by:

Dong-Hua Yang,  
St. John's University, United States

### Reviewed by:

Jun Su,  
Harbin Medical University Cancer  
Hospital, China  
Xiaoguang Qiu,  
Capital Medical University, China

### \*Correspondence:

Yonggao Mou  
mouyg@sysucc.org.cn,  
Qunying Yang  
yangqy@sysucc.org.cn

<sup>†</sup>These authors have contributed  
equally to this work

### Specialty section:

This article was submitted to  
Pharmacology of Anti-Cancer Drugs,  
a section of the journal  
Frontiers in Pharmacology

**Received:** 19 August 2020

**Accepted:** 28 September 2020

**Published:** 11 November 2020

### Citation:

Guo C, Yao D, Lin X, Huang H, Zhang J, Lin F, Mou Y and Yang Q (2020) External Validation of a Nomogram and Risk Grouping System for Predicting Individual Prognosis of Patients With Medulloblastoma. *Front. Pharmacol.* 11:590348. doi: 10.3389/fphar.2020.590348

**Background:** Medulloblastoma (MB) is one of the most malignant neuroepithelial tumors in the central nervous system. This study aimed to establish an effective prognostic nomogram and risk grouping system for predicting overall survival (OS) of patients with MB.

**Materials and Methods:** The nomogram was constructed based on data from the database of Surveillance, Epidemiology, and End Results (SEER). This database consisted of 2,824 patients with medulloblastoma and was used as the training cohort. The data of another additional 161 patients treated at the Sun Yat-sen University Cancer Center (SYSUCC) were used as the external validation cohort. Cox regression analysis was used to select independent prognostic factors. Concordance index (C-index) and calibration curve were used to predict the prognostic effect of the nomogram for overall survival.

**Results:** In the training cohort, Cox regression analyses showed that the prognostic factors included histopathology, surgery, radiotherapy, chemotherapy, tumor size, dissemination, and age at diagnosis. The internal and external validated C-indexes were 0.681 and 0.644, respectively. Calibration curves showed that the nomogram was able to predict 1-, 3-, and 5-year OS for patients with MB precisely. Using the training cohort, a risk grouping system was built, which could perfectly classify patients into four risk nomogroups with a 5-year survival rate of 83.9%, 76.5%, 64.5%, and 46.8%, respectively.

**Conclusion:** We built and validated a nomogram and risk grouping system that can provide individual prediction of OS and distinguish MB patients from different risk groups. This nomogram and risk grouping system could help clinicians making better treatment plan and prognostic assessment.

**Keywords:** neuroepithelial tumors, training cohort, validation cohort, overall survival, Surveillance, Epidemiology, and End Results



## INTRODUCTION

Medulloblastoma (MB) is one of the most malignant brain tumors in children (Khanna et al., 2017; Leece et al., 2017). Current standard treatment consists of 36 Gy of craniospinal irradiation supplemented with 18–20 Gy of local irradiation (total dose of 54–56 Gy) and adjuvant chemotherapy after surgery (Sirachainan et al., 2011). Although most of the MB cases are curable, around 35% of patients in the average-risk group and 50% in the poor-risk group would relapse in 5 years (Sirachainan et al., 2011; Tamayo et al., 2011). As a result, it is essential to set up an effective prognostic model for accurately identifying such patients for better treatment and surveillance evaluation (He et al., 2018; Wu et al., 2019). In regard to pediatric MB, clinical staging systems including the extent of the tumor, the tumor histology, and age of patients have long been considered as the most powerful stratification system to classify patients into different prognostic risk subgroups (Korshunov et al., 2010; Sirachainan et al., 2011). Children aged older than 3 years had a superior prognosis. As for molecular classification in the 2016 WHO classification, four principal molecular subgroups based on transcriptome and methylome profiling, including Wingless (WNT), Sonic Hedgehog (SHH), group 3 (G3), and group 4 (G4), were identified to be significantly better correlated with different prognosis than traditional subtypes (Taylor et al., 2012; Louis et al., 2016; Liu et al., 2017; Vo et al., 2018). However, the studies on prognosis of MB are still needed to confirm the precise pattern of prognosis.

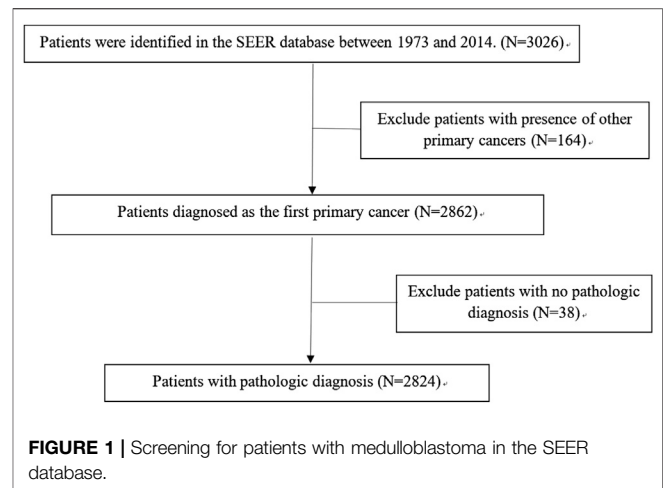
A nomogram was a graphical mathematical algorithm of a statistical predictive model (Kattan et al., 1998) to generate a precise prediction based on the evaluation of important factors for estimating the conditional risk of disease outcomes (Wang et al., 2018). There have been a number of studies using nomograms for prognosis of cancers such as bladder, colorectal, lung, nasopharyngeal, and breast cancer (Mariani et al., 2005; Iasonos et al., 2008; Gold et al., 2009; Valentini et al., 2011; Wang et al., 2013; Chen et al., 2015; OuYang et al., 2018; Tang et al., 2019). However, nomograms for predicting prognosis of MB are limited.

In this study, we aimed to establish a nomogram for predicting the prognosis of MB from two different patient populations and to externally validate it.

## MATERIALS AND METHODS

### Patients and Study Variable

The data of MB patients from the database of the Surveillance, Epidemiology, and End Results (SEER) were extracted using the following specifications: “Incidence—SEER 18 Registries Custom Data (with additional treatment fields), November 2016 Submission (1973–2014 varying).” Inclusion criteria for patient selection included: 1) pathologically proven diagnosis of medulloblastoma; 2) according to the third edition of International Classification of Diseases for Oncology (ICD-O-3) to identify cases of MB, and the following ICD-O-3 codes for histopathology were chosen: 9,470/3 medulloblastoma, NOS;



9,471/3 desmoplastic nodular medulloblastoma; 9,474/3 large cell medulloblastoma; and 3) known survival status and survival time. These data were used as a training cohort.

In addition, to validate the nomogram, we searched the Sun Yat-sen University Cancer Center (SYSUCC) database for patients diagnosed with medulloblastoma between 1971 and 2018. The inclusion criteria for case selection were: 1)

**TABLE 1 |** Clinicopathological variables of training and validation cohort.

Variables	Training cohort (n = 2,824)		Validation cohort (n = 161)		p-Value
	No	%	No	%	
Histopathology					
DMB	299	10.6	21	13.1	0.280
MB, NOS	2,439	86.4	138	85.7	
LC	86	3.0	2	1.2	
Surgery					
Total resection	1,293	45.8	80	49.7	<0.001
Subtotal resection	570	20.2	18	11.2	
Surgery, NOS	828	29.3	63	39.1	
No evidence	133	4.7	0	0.0	
Radiotherapy					
Yes	2,197	77.8	113	70.2	0.025
No evidence	627	22.2	48	29.8	
Chemotherapy					
Yes	1,864	66.0	110	68.3	0.546
No evidence	960	34.0	51	31.7	
Size (cm)					
≤6.5	1,718	60.8	57	35.4	<0.001
>6.5	43	1.5	1	0.6	
Unknown	1,063	37.7	103	64.0	
Dissemination					
Yes	168	5.9	8	5.0	0.586
No evidence	2,656	94.1	153	95.0	
Age					
Median (years)	14.2	—	12.0	—	0.001
≤3	580	20.5	15	9.3	
>3	2,244	79.5	146	90.7	
Sex					
Male	1,753	62.1	105	65.2	0.424
Female	1,071	37.9	56	34.8	

pathologically confirmed diagnosis of medulloblastoma; 2) no prior anticancer therapy; and 3) complete clinicopathologic characteristics, therapeutic records, and complete follow-up data.

## Definition of Variables

Considering some incomplete data variables from the SEER, we redefine the variables for developing the nomogram. In our study, surgery was categorized as: total resection (TR), subtotal resection (SR), surgery, NOS, and no evidence. Histopathology was categorized as: medulloblastoma, NOS, desmoplastic nodular medulloblastoma, and large cell medulloblastoma. For objectively assessing the prognostic value of age and tumor size for MB patients, the patients were stratified into two categories, namely  $\leq 3$  years,  $> 3$  years; or  $\leq 6.5$  cm,  $> 6.5$  cm, and/or unknown, using the X-tile (<https://x-tile.software.informer.com>, Yale School of Medicine, New Haven, CT, United States) software for obtaining the best cutoff value. Moreover, dissemination of tumor cells was defined as findings of distant metastasis based on radiographical images or tumor cells in cerebral spinal fluid (CSF).

## Construction and Validation of the Nomogram

We identified independent prognostic factors by univariate and multivariate Cox regression model in the training cohort, which were then used to construct the nomogram to predict the 1-, 3-,

and 5-year overall survival (OS) rates. Based on the contribution of each factor for the outcome in the model, the nomogram can express the relationship between various variables in the model according to drawing a line segment with certain proportion on the same plane, which transformed the complex regression equation into graphic visualization, and made the results of the prediction model more reifiable and convenient for clinician and patients.

The performance of the nomogram including its discrimination and calibration was validated using the SYSUCC cohort as external validation. Discrimination was assessed using a concordance index (C-index), and the larger the C-index, the more accurate the nomogram. Calibration was performed by comparing predicted survival rate actual survival rate determined using Kaplan–Meier analysis for 1-, 3-, and 5-year overall survival. In addition, we did bootstrap 1,000 resamples to verify the accuracy of the nomogram in the training cohort and external validation cohort from SYSUCC database.

## Risk Grouping

In this study, we defined risk as the harmful factors for prognosis of MB patients. To develop the risk grouping to assess the prognosis of MB patients, we divided patients from the training cohort into four prognostic groups according to the total points of each patient. Furthermore, we used Kaplan–Meier

**TABLE 2 |** Univariate and multivariate Cox regression analysis of variables in the training cohort.

Variables	Univariate analysis		Multivariate analysis	
	HR (95% CI)	p-Value	HR (95% CI)	p-Value
Histopathology				
DMB	Reference	—	Reference	—
MB, NOS	1.344 (1.078–1.676)	0.009	1.306 (1.044–1.635)	0.019
LC	1.688 (1.247–2.284)	0.001	3.245 (2.240–4.701)	<0.001
Surgery				
Total resection	Reference	—	Reference	0.046
Subtotal resection	1.240 (1.037–1.483)	0.018	1.197 (1.001–1.432)	0.049
Surgery, NOS	1.859 (1.619–2.133)	<0.001	1.598 (1.372–1.861)	<0.001
No evidence	4.100 (3.245–5.179)	<0.001	2.668 (2.116–3.365)	<0.001
Chemotherapy				
Yes	Reference	—	Reference	—
No evidence	1.705 (1.514–1.919)	<0.001	2.048 (1.780–2.356)	<0.001
Radiotherapy				
Yes	Reference	—	—	—
No evidence	2.225 (1.954–2.533)	<0.001	1.386 (1.214–1.582)	<0.001
Size (cm)				
$\leq 6.5$	Reference	—	Reference	—
$> 6.5$	1.916 (1.239–2.964)	0.003	1.564 (1.018–2.403)	0.041
Unknown	1.585 (1.405–1.787)	<0.001	1.208 (1.058–1.378)	0.005
Dissemination				
Yes	Reference	—	Reference	—
No evidence	0.591 (0.483–0.725)	<0.001	0.642 (0.522–0.789)	<0.001
Age (years)				
$\leq 3$	Reference	—	Reference	—
$> 3$	0.684 (0.597–0.784)	<0.001	0.855 (0.737–0.992)	0.039
Sex				
Male	Reference	—	—	—
Female	0.982 (0.870–1.107)	0.762	—	—

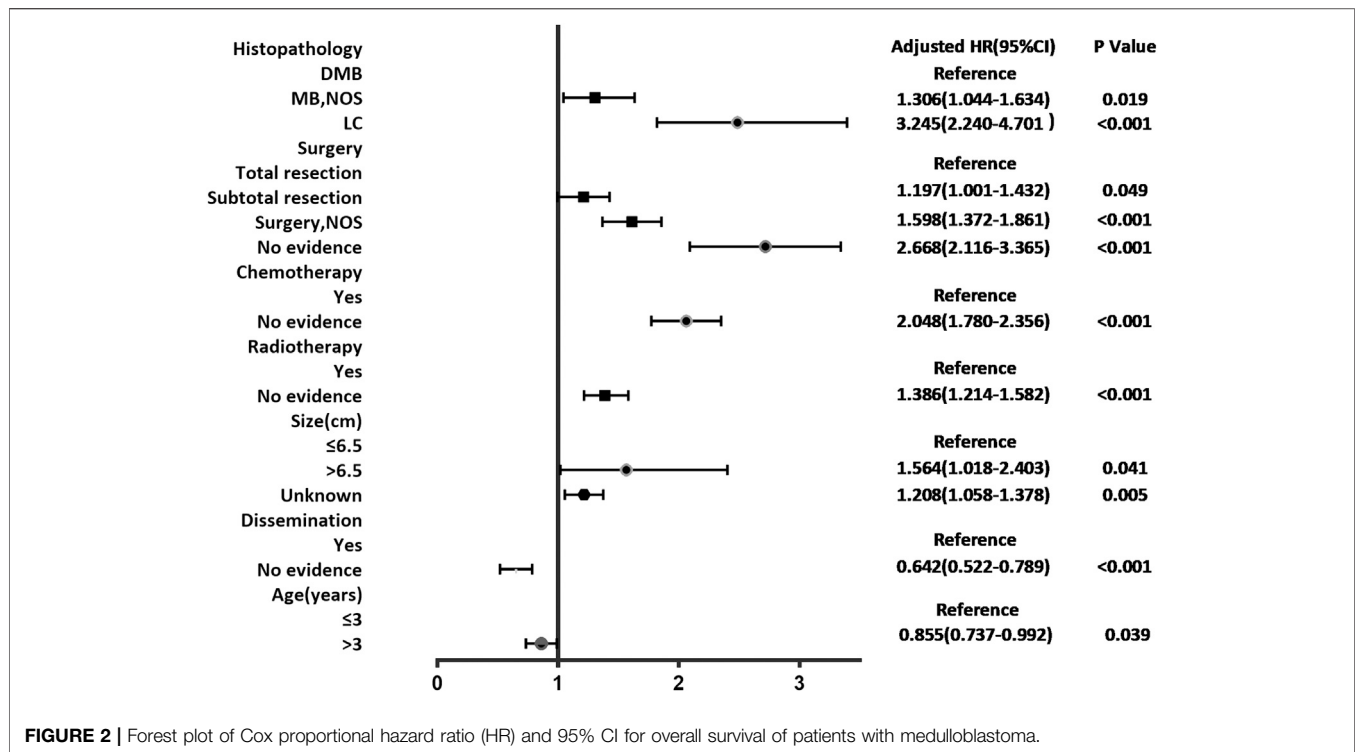
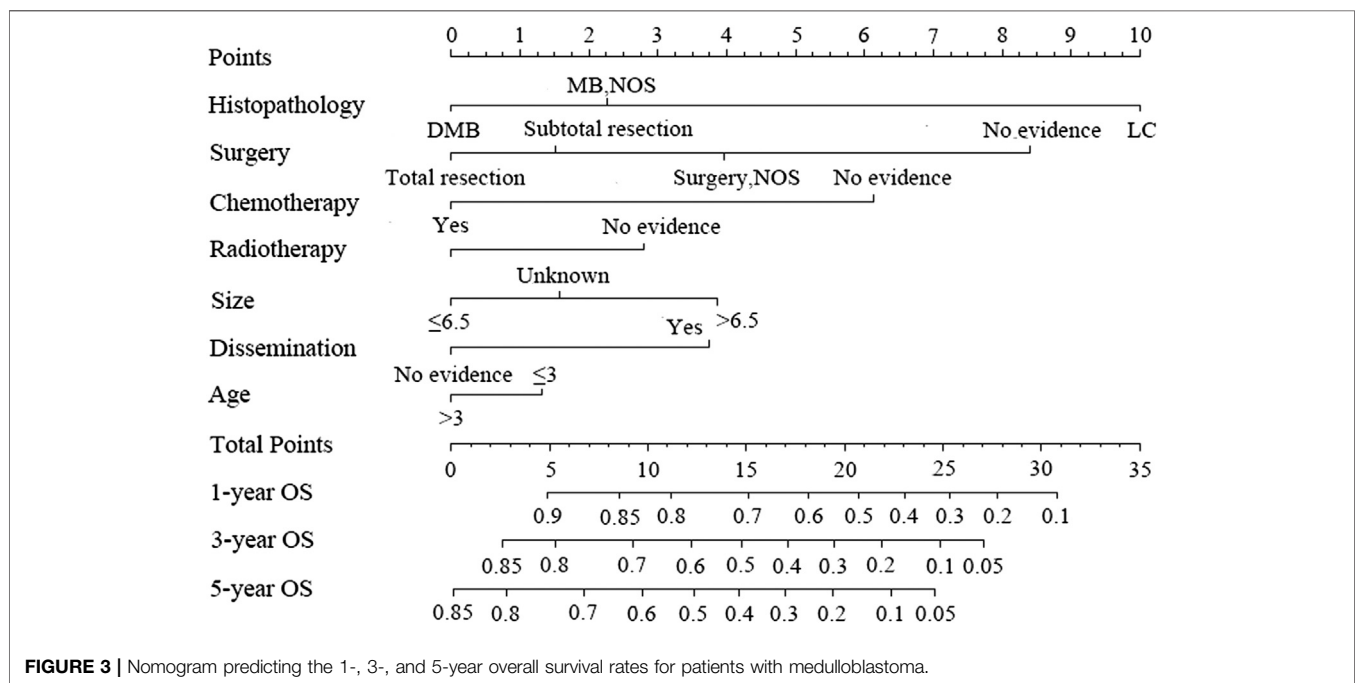


**FIGURE 2 |** Forest plot of Cox proportional hazard ratio (HR) and 95% CI for overall survival of patients with medulloblastoma.



curves to compare the prognosis of patients in the different nomogroups.

## Statistical Analysis

All statistical analyses were performed by the statistical software package of SPSS for Windows, version 22.0 (IBM Corporation,

Armonk, NY, United States), *p*-values were two-sided, and *p*-values <0.05 were considered as statistically significant. The nomogram was constructed by R 3.5.1 (<http://www.r-project.org>) and all diagrams of this study were drawn by GraphPad Prism 8 (<https://www.graphpad.com/scientific-software/prism/>).

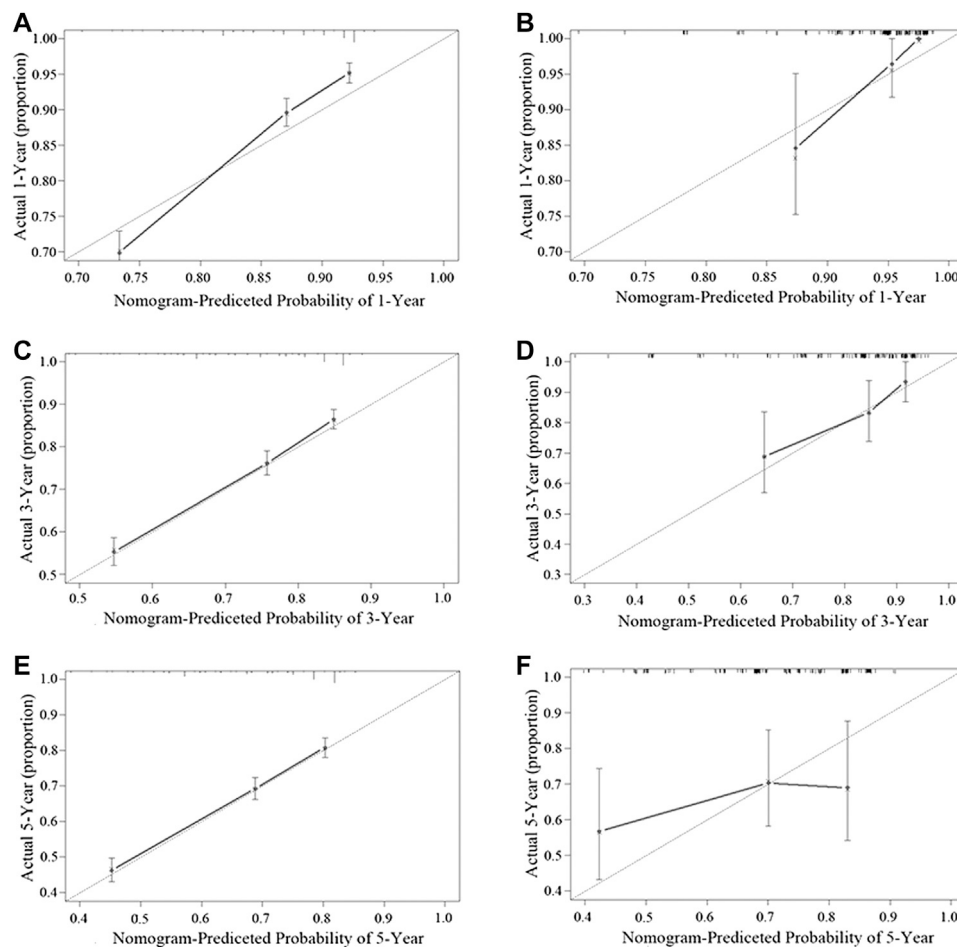


**FIGURE 4 |** Performance of the nomogram in the training cohort (A,C,E) and the validation cohort (B,D,F) was evaluated by the calibration of the nomogram by training cohort and validation cohort. (A), (C), and (E), respectively, stand for the 1-, 3-, and 5-year overall survival rate of the SEER cohort, and (B), (D), and (F), respectively, stand for the 1-, 3-, and 5-year overall survival rate of the SYSUCC cohort (Training cohort: 0.681, 95% CI: 0.663–0.699 Validation cohort: 0.644, 95% CI: 0.551–0.737).

## RESULTS

### Clinicopathological Characteristics of Training and Validation Cohort

A total of 2,824 patients were identified from the SEER database as suitable for inclusion in the study and they were grouped as the training cohort (Figure 1). An additional 161 patients with complete data from SYSUCC database were identified and used as the validation cohort. The clinicopathological characteristics of patients in both cohorts are listed in Table 1.

### Univariate and Multivariate Analyses

According to the cox regression analyses, we identified histopathology, surgery, radiotherapy, chemotherapy, tumor size, dissemination, and age of patients as independent factors correlated with the 1-, 3-, and 5-year OS rates in the training cohort (Table 2). No significant difference between prognosis and

sex was observed. Forest plot was used to illustrate the effect and contribution of each independent prognostic factor in terms of hazard ratio (Figure 2).

### Nomogram

Figure 3 shows the nomogram model established for the 1-, 3-, and 5-year OS rates based on the selected factors. Histopathology was the biggest influencing factor on prognosis, whereas age of patients had the least effect. Validation of the nomogram was performed using bootstrap analyses with 1,000 resamples; internal and external validation cohorts showed favorable discrimination of the nomogram with C-index of 0.681 (95% CI: 0.663–0.699) and 0.644 (95% CI: 0.551–0.737), respectively, demonstrating that the nomogram could be clinically implemented. Internal and external calibration plots indicated high agreement between prediction and actual observation for the 1-, 3-, and 5-year OS rates (Figure 4).

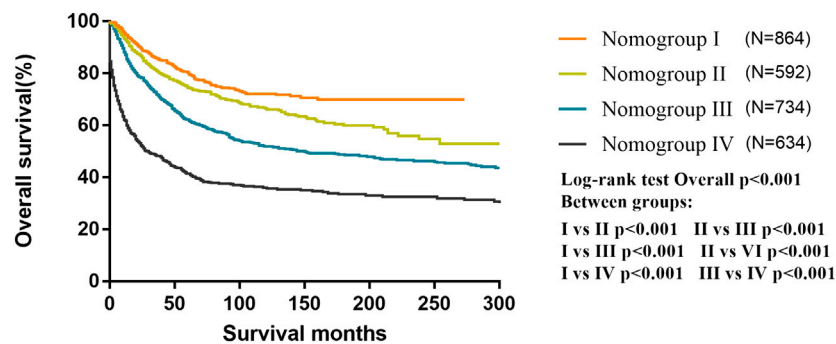


**FIGURE 5 |** Kaplan–Meier curves for overall survival of the different risk nomogroups in the training cohort.

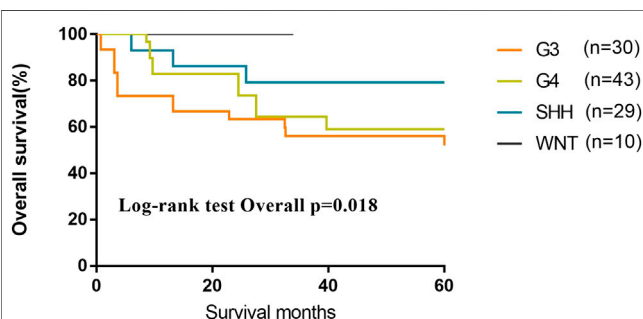


**FIGURE 6 |** Kaplan–Meier curves of different subgroups for overall survival in the validation cohort.

## Nomogroups of Risk Grouping

All patients were classified into four risk nomogroups according to the total score of each factor obtained from the nomogram of the training cohort. The nomogroups of the risk grouping were as follows: nomogroup I, score of 0–3.8 points; nomogroup II, 3.9–6.8 points; nomogroup III, 6.9–11.2 points; and nomogroup IV,  $\geq 11.3$  points. As shown in **Figure 5**, the prognosis between four risk nomogroups and the 5-year OS rate found by Kaplan–Meier analysis was 83.9%, 76.5%, 64.5%, and 46.8%, respectively, with statistically significant differences.

We evaluated 116 patients from the database of SYSUCC to confirm the molecular subgrouping, and 112 MB patients were successfully subgrouped and diagnosed according to the revised WHO classification for brain tumors (2016). As of the last follow-up, the 5-year OS of patients of G3 and G4 subgroups were lower than those of Wnt and SHH subgroups (OS, Wnt 100%; SHH 79.3%; G4 59.1%; G3 56.1%;  $p = 0.018$ ) (**Figure 6**).

## DISCUSSION

As the most common tumor in pediatric central nervous system, MB accounts for 20–25% of all pediatric primary central nervous system tumors, which is classified as WHO grade IV tumor (Srikantha et al., 2010). Although recent studies have indicated that around 60% of MB patients could be curable, 10–15% of

patients die within 2 years after the diagnosis (National Cancer Institute, 2002), indicating that the prognosis varied greatly in different cases. Based on the histopathological features, MBs are classified as classic medulloblastoma, large cell/anaplastic medulloblastoma, desmoplastic/nodular medulloblastoma, and medulloblastoma with extensive nodularity (Fuller and Scheithauer, 2007; Louis et al., 2007; Gilbertson and Ellison, 2008; Quinlan and Rizzolo, 2017). With intensive treatment, such as combined high-dose IV methotrexate and conventional chemotherapy combined with high-dose methotrexate or repeated cycles of myeloablative chemotherapy, the 5-year PFS ranged from 78.6 to 90% in patients with the desmoplastic/nodular and medulloblastoma with extensive nodularity subgroups. However, the severe toxicity of medication required more precise prognostic models to stratify different risk. A study demonstrated that the presence of metastatic disease at presentation, p53, TrkC, and ErbB2 expression in immunohistology were four predictors of overall survival of MB (Srikantha et al., 2010). Other studies suggested that molecular variants of diseases characterized by their gene expression with distinct clinicopathologic and molecular features, named WNT, SHH, G3, and G4, were significantly better associated with prognosis. The prognosis of patients of WNT subgroup has the best prognosis with greater than 90% of 5-year event-free survival. The prognosis of SHH-activated and G4 medulloblastomas is worse than WNT, with 5-year OS rate of 75% and 70%, respectively, whereas that of G3 has the most unfavorable 5-year overall of 50%. Although these four molecular subgroups have become effective predictors and important to divide MB patients into different risk stratification than histology pathology, they are not used comprehensively for all the institutions. In this study, the data of molecular detection were not shown in the SEER database. However, we detected the molecular subgroup in our MB patients as the validation cohort. The survival of SHH, WNT, and G3 in our research was similar to previous research, but the prognosis of G4 in our research was lower than other previous studies. The reason for the poorer G4 survival may be that there were 14.0% cases in G4, which did not receive the standard radiation and systemic chemotherapy as adjuvant therapy in comparison to other subgroups.



Chang staging for MB was introduced in 1960s, which classified MB patients into M0, M1, M2, M3, or M4 and T1, T2, T3a, T3b, or T4 according to their clinical features (Dufour et al., 2012). Although T stage was proved to be not associated with prognosis, M staging is still used for current risk stratification with 5-year OS rate of 47, 51, and 42% from M1 to M3 patients (Quinlan and Rizzolo, 2017). A set of clinical characteristics including the above M staging have classified patients into average-risk and poor-risk groups based on age of onset, extent of tumor resection, and extent of spreading at presentation (Gajjar et al., 2006; Rutkowski et al., 2010). Poor-risk patients were defined as patients with at least one of the following features: age less than 3 years, residual tumor  $\geq 1.5$  cm after maximal safe resection, and histopathological features of large cell or anaplastic MB. The average-risk patients were described as the patients without any of the above features (Quinlan and Rizzolo, 2017). The OS rates for poor-risk patients are 30–40%; for average-risk patients, the OS rates increase to 70–80% (Packer et al., 1999).

In clinical practice, the most commonly used prognosis system is the four molecular subgroup and the high-risk/average-risk system. However, the inconvenience of molecular detection approaches in daily clinical practice limited the application and prognostic evaluation in the majority of centers. However, the poor-risk/average-risk system is inefficient for stratifying patients into accurate prognosis. Biologic and clinical heterogeneity should be considered to stratify different treatment regimen. However, several clinical trials including SJYC07 presented negative risk-adapted therapy, which only confirmed that “reduced-intensity” therapy benefits a subtype SHH in early childhood medulloblastoma that would improve the progression-free survival. Because the aggressiveness, biological characteristics of individual tumors, and the efficacy of the treatment varied from patient to patient, establishing a better stratified and individualized prognostic model would provide a much more significant experience to both clinicians and patients.

However, to the best of our knowledge, there was no nomogram available for the evaluation of MB. The objective of our study is to establish a novel, convenient comprehensive nomogram model to evaluate OS for MB patients. We develop the individual prognostic nomogram from the SEER data set and validate an independent data set from SYSUCC database. Our study shows the value of clinical characteristics predictor of individualized MB prognosis with the nomogram model. The nomograms showed precise and stable prediction when analyzing both the training and the validation cohorts, indicating its good clinical applicability. The traditional prognostic model included the clinical parameters to divide patients into two levels as the poor-risk and average-risk system, which is insufficient for precise prediction. Compared to the previous model, the MB cohort was satisfactorily separated into four distinct prognostic groups with the cutoff point of 3.9, 6.9, and 11.3 in our nomogram model.

According to our nomogram, if an MB patient would have histopathology of LC, received radiotherapy, chemotherapy, and total resection, tumor size greater than 6.5 cm, age older than 3 years, and without dissemination, his total score would be 13.9.

Therefore, as shown in **Figure 5**, we could speculate that this patient was categorized as nomogroup IV with a 44% probability of 5-year OS. In this case, clinician should consider close follow-up because of the poor prognosis.

Seven clinical and pathology factors in our model, including histopathology, surgery, radiotherapy, chemotherapy, tumor size, dissemination, and age, were independently correlated with the OS rates. First, different pathology subtypes may represent distinct biological behaviors of MB, which may affect further treatment strategies. Large-cell and anaplastic MB are regarded as high-risk disease, which demonstrates that patients have a poorer survival and should be received more intensive chemotherapy and higher dose of radiation. However, desmoplastic nodular MB may benefit from a better outcome, because desmoplastic nodular MB shared the best survival in the histopathology in our study, which was consistent with previous study (Packer et al., 1999). We still emphasize that the four main histologic types are essential to the prognostic prediction, although molecular subgroups seem to be more popular than histology subgroups. Second, standard treatment is the therapeutic stratification for medulloblastoma patients. Because relapses of MB are common in patients with nonstandard treatment, the maximal safe resection along with radiation and chemotherapy will benefit the long-term survival of MB patients. Third, recent publications have shown that T stage in the Chang’s operative staging system was not related to survival; however, our model indicated that tumor size could still predict outcome. Although size is not a common risk factor in previous prognostic classification, it is often difficult to separate the residual tumor from normal tissue surgically if the tumor has severe adhesion with large size, which also indicates more probability to have metastasis. As a result, patients with the presence of metastases (M1–M4) or residual disease  $>1.5$  cm<sup>2</sup> belong to the high-risk group according to North American stratification. Last but not least, similar high-risk stratification can be applied to younger MB patients younger than 3 years at diagnosis, who were not recommend to receive radiation instead of prolonged and intensive chemotherapy regimen with the aim of reducing the risk of relapse. As a result, prospective study or evidence from multiple databases is needed to confirm the staging system of MB.

There are several limitations in our study. First, this study was a retrospective analysis although we used reliable databases from the SEER system and that of SYSUCC to investigate the applicability of this nomogram in the Caucasian and Asian populations. Second, some details in the SEER database, such as the molecular subgroups, radiotherapy doses, and chemotherapy regimens, were not provided, and other promising prognostic parameters could not be analyzed. Third, information about several important clinicopathological parameters from SEER such as tumor size, tumor location, and histopathology were not complete. To guard against bias, we have to retain these data, which is defined “unknown or NOS.” Fourth, patient cases from the training and validation cohort spanned for nearly half a century, which may have caused certain statistical biases for not accounting advances in techniques of treatment and diagnosis.

## CONCLUSION

A nomogram, consisting of seven clinicopathological and treatment-related factors, for predicting the 1-, 3-, and 5-year OS of MB patients was constructed from a Caucasian cohort and was successfully validated in an Eastern database. This proposed survival prognostic model could be useful for differentiating patients of different risk groups to better provide individualized treatment decision and surveillance.

## DATA AVAILABILITY STATEMENT

The datasets presented in this study can be found in online repositories. The names of the repository/repositories and accession number(s) can be found in the article/supplementary material.

## ETHICS STATEMENT

Our study was approved by the Ethics Committee of Sun-Yat-Sen University Cancer Center Health Authority (identifier: B2020-

199-01). Written informed consent from the participants' legal guardian/next of kin was not required to participate in this study in accordance with the national legislation and the institutional requirements.

## AUTHOR CONTRIBUTIONS

All authors participated in this research, including conception and design (CG, DY, XL, YM, and QY), data acquisition (CG, XL, and HH), data analysis and interpretation (CG, DY, and XL), material support (JZ, FL, and XL), study supervision (CG, DY, YM, and QY), as well as drafting the article or critically revising (CG, DY, XL, HH, JZ, FL, YM, and QY). The final version is ensured and approved by all authors.

## FUNDING

This research was supported by the Science and Technology Planning Project of Guangdong Province (2017A020215030 and 2014A020212098).

## REFERENCES

- Chen, J. Y., Chen, J. J., Xue, J. Y., Chen, Y., Liu, G. Y., Han, Q. X., et al. (2015). Predicting non-sentinel lymph node metastasis in a Chinese breast cancer population with 1–2 positive sentinel nodes: development and assessment of a new predictive nomogram. *World J. Surg.* 39 (12), 2919–2927. doi:10.1007/s00268-015-3189-z
- Dufour, C., Beaugrand, A., Pizer, B., Micheli, J., Aubelle, M. S., Fourcade, A., et al. (2012). Metastatic medulloblastoma in childhood: Chang's classification revisited. *Int. J. Surg. Oncol.* 2012, 245385. doi:10.1155/2012/245385
- Fuller, G. N., and Scheithauer, B. W. (2007). The 2007 revised World Health Organization (WHO) classification of tumours of the central nervous system: newly codified entities. *Brain Pathol.* 17 (3), 304–307. doi:10.1111/j.1750-3639.2007.00084.x
- Gajjar, A., Chintagumpala, M., Ashley, D., Kellie, S., Kun, L. E., Merchant, T. E., et al. (2006). Risk-adapted craniospinal radiotherapy followed by high-dose chemotherapy and stem-cell rescue in children with newly diagnosed medulloblastoma (St Jude Medulloblastoma-96): long-term results from a prospective, multicentre trial. *Lancet Oncol.* 7 (10), 813–820. doi:10.1016/S1470-2045(06)70867-1
- Gilbertson, R. J., and Ellison, D. W. (2008). The origins of medulloblastoma subtypes. *Annu. Rev. Pathol.* 3, 341–365. doi:10.1146/annurev.pathmechdis.3.121806.151518
- Gold, J. S., Gonen, M., Gutierrez, A., Broto, J. M., Garcia-del-Muro, X., Smyrk, T. C., et al. (2009). Development and validation of a prognostic nomogram for recurrence-free survival after complete surgical resection of localized primary gastrointestinal stromal tumour: a retrospective analysis. *Lancet Oncol.* 10 (11), 1045–1052. doi:10.1016/S1470-2045(09)70242-6
- He, W., Zheng, Y., Zou, R., Shen, J., Yang, J., Qiu, J., et al. (2018). Long- versus short-interval follow-up after resection of hepatocellular carcinoma: a retrospective cohort study. *Canc. Commun.* 38 (1), 26. doi:10.1186/s40880-018-0296-x
- Iasonos, A., Schrag, D., Raj, G. V., and Panageas, K. S. (2008). How to build and interpret a nomogram for cancer prognosis. *J. Clin. Oncol.* 26 (8), 1364–1370. doi:10.1200/JCO.2007.12.9791
- Kattan, M. W., Eastham, J. A., Stapleton, A. M., Wheeler, T. M., and Scardino, P. T. (1998). A preoperative nomogram for disease recurrence following radical prostatectomy for prostate cancer. *J. Natl. Cancer Inst.* 90 (10), 766–771. doi:10.1093/jnci/90.10.766
- Khanna, V., Achey, R. L., Ostrom, Q. T., Block-Beach, H., Kruchko, C., Barnholtz-Sloan, J. S., et al. (2017). Incidence and survival trends for medulloblastomas in the United States from 2001 to 2013. *J. Neuro Oncol.* 135 (3), 433–441. doi:10.1007/s11060-017-2594-6
- Korshunov, A., Remke, M., Werft, W., Benner, A., Ryzhova, M., Witt, H., et al. (2010). Adult and pediatric medulloblastomas are genetically distinct and require different algorithms for molecular risk stratification. *J. Clin. Oncol.* 28 (18), 3054–3060. doi:10.1200/JCO.2009.25.7121
- Leece, R., Xu, J., Ostrom, Q. T., Chen, Y., Kruchko, C., and Barnholtz-Sloan, J. S. (2017). Global incidence of malignant brain and other central nervous system tumors by histology, 2003–2007. *Neuro Oncol.* 19 (11), 1553–1564. doi:10.1093/neuonc/nox091
- Liu, K. W., Pajtl, K. W., Worst, B. C., Pfister, S. M., and Wechsler-Reya, R. J. (2017). Molecular mechanisms and therapeutic targets in pediatric brain tumors. *Sci. Signal.* 10 (470), eaaf7593. doi:10.1126/scisignal.aaf7593
- Louis, D. N., Ohgaki, H., Wiestler, O. D., Cavenee, W. K., Burger, P. C., Jouvett, A., et al. (2007). The 2007 WHO classification of tumours of the central nervous system. *Acta Neuropathol.* 114 (2), 97–109. doi:10.1007/s00401-007-0243-4
- Louis, D. N., Perry, A., Reifenberger, G., von Deimling, A., Figarella-Branger, D., Cavenee, W. K., et al. (2016). The 2016 world Health organization classification of tumors of the central nervous system: a summary. *Acta Neuropathol.* 131 (6), 803–820. doi:10.1007/s00401-016-1545-1
- Mariani, L., Miceli, R., Kattan, M. W., Brennan, M. F., Colechia, M., Fiore, M., et al. (2005). Validation and adaptation of a nomogram for predicting the survival of patients with extremity soft tissue sarcoma using a three-grade system. *Cancer* 103 (2), 402–408. doi:10.1002/cncr.20778
- National Cancer Institute (2002). "Childhood central nervous system embryonal tumors treatment (PDQ®): health professional version," in *PDQ cancer information summaries* (Bethesda, MD: National Cancer Institute).
- OuYang, P. Y., You, K. Y., Zhang, L. N., Xiao, Y., Zhang, X. M., and Xie, F. Y. (2018). External validity of a prognostic nomogram for locoregionally advanced nasopharyngeal carcinoma based on the 8th edition of the AJCC/UICC staging system: a retrospective cohort study. *Canc. Commun.* 38 (1), 55. doi:10.1186/s40880-018-0324-x

- Packer, R. J., Cogen, P., Vezina, G., and Rorke, L. B. (1999). Medulloblastoma: clinical and biologic aspects. *Neuro Oncol.* 1 (3), 232–250. doi:10.1093/neuonc/1.3.232
- Quinlan, A., and Rizzolo, D. (2017). Understanding medulloblastoma. *JAAPA* 30 (10), 30–36. doi:10.1097/01.JAA.0000524717.71084.50
- Rutkowski, S., von Hoff, K., Emser, A., Zwiener, I., Pietsch, T., Figarella-Branger, D., et al. (2010). Survival and prognostic factors of early childhood medulloblastoma: an international meta-analysis. *J. Clin. Oncol.* 28 (33), 4961–4968. doi:10.1200/JCO.2010.30.2299
- Sirachainan, N., Nuchprayoon, I., Thanarattanakorn, P., Pakakasama, S., Lusawat, A., Visudibhan, A., et al. (2011). Outcome of medulloblastoma in children treated with reduced-dose radiation therapy plus adjuvant chemotherapy. *J. Clin. Neurosci.* 18 (4), 515–519. doi:10.1016/j.jocn.2010.08.012
- Srikantha, U., Balasubramaniam, A., Santosh, V., Somanna, S., Bhagavatula, I. D., and Ashwathnarayana, C. B. (2010). Recurrence in medulloblastoma - influence of clinical, histological and immunohistochemical factors. *Br. J. Neurosurg.* 24 (3), 280–288. doi:10.3109/02688691003660558
- Tamayo, P., Cho, Y. J., Tsherniak, A., Greulich, H., Ambrogio, L., Schouten-van Meeteren, N., et al. (2011). Predicting relapse in patients with medulloblastoma by integrating evidence from clinical and genomic features. *J. Clin. Oncol.* 29 (11), 1415–1423. doi:10.1200/JCO.2010.28.1675
- Tang, X., Zhou, X., Li, Y., Tian, X., Wang, Y., Huang, M., et al. (2019). A novel nomogram and risk classification system predicting the cancer-specific survival of patients with initially diagnosed metastatic esophageal cancer: a SEER-based study. *Ann. Surg. Oncol.* 26 (2), 321–328. doi:10.1245/s10434-018-6929-0
- Taylor, M. D., Northcott, P. A., Korshunov, A., Remke, M., Cho, Y. J., Clifford, S. C., et al. (2012). Molecular subgroups of medulloblastoma: the current consensus. *Acta Neuropathol.* 123 (4), 465–472. doi:10.1007/s00401-011-0922-z
- Valentini, V., van Stiphout, R. G., Lammering, G., Gambacorta, M. A., Barba, M. C., Bebenek, M., et al. (2011). Nomograms for predicting local recurrence, distant metastases, and overall survival for patients with locally advanced rectal cancer on the basis of European randomized clinical trials. *J. Clin. Oncol.* 29 (23), 3163–3172. doi:10.1200/JCO.2010.33.1595
- Vo, B. T., Kwon, J. A., Li, C., Finkelstein, D., Xu, B., Orr, B. A., et al. (2018). Mouse medulloblastoma driven by CRISPR activation of cellular Myc. *Sci. Rep.* 8 (1), 8733. doi:10.1038/s41598-018-24956-1
- Wang, W., Sun, Z., Deng, J. Y., Qi, X. L., Feng, X. Y., Fang, C., et al. (2018). A novel nomogram individually predicting disease-specific survival after D2 gastrectomy for advanced gastric cancer. *Canc. Commun.* 38 (1), 23. doi:10.1186/s40880-018-0293-0
- Wang, Y., Li, J., Xia, Y., Gong, R., Wang, K., Yan, Z., et al. (2013). Prognostic nomogram for intrahepatic cholangiocarcinoma after partial hepatectomy. *J. Clin. Oncol.* 31 (9), 1188–1195. doi:10.1200/JCO.2012.41.5984
- Wu, T., Wu, X., Wang, H. Y., and Chen, L. (2019). Immune contexture defined by single cell technology for prognosis prediction and immunotherapy guidance in cancer. *Cancer Commun.* 39 (1), 21. doi:10.1186/s40880-019-0365-9

**Conflict of Interest:** The authors declare that the research was conducted in the absence of any commercial or financial relationships that could be construed as a potential conflict of interest.

Copyright © 2020 Guo, Yao, Lin, Huang, Zhang, Lin, Mou and Yang. This is an open-access article distributed under the terms of the Creative Commons Attribution License (CC BY). The use, distribution or reproduction in other forums is permitted, provided the original author(s) and the copyright owner(s) are credited and that the original publication in this journal is cited, in accordance with accepted academic practice. No use, distribution or reproduction is permitted which does not comply with these terms.



# Piperlongumine Alleviates Mouse Colitis and Colitis-Associated Colorectal Cancer

Jia-Rong Huang<sup>1†</sup>, Sheng-Te Wang<sup>1†</sup>, Meng-Ning Wei<sup>1</sup>, Kun Liu<sup>1</sup>, Jing-Wen Fu<sup>2</sup>, Zi-Hao Xing<sup>1</sup> and Zhi Shi<sup>1\*</sup>

<sup>1</sup>Department of Cell Biology, Institute of Biomedicine, National Engineering Research Center of Genetic Medicine, MOE Key Laboratory of Tumor Molecular Biology, Guangdong Provincial Key Laboratory of Bioengineering Medicine, College of Life Science and Technology, Jinan University, Guangzhou, China, <sup>2</sup>Affiliated High School of South China Normal University, Guangzhou, China

## OPEN ACCESS

### Edited by:

Haichang Li,  
The Ohio State University,  
United States

### Reviewed by:

Zui Pan,  
University of Texas at Arlington,  
United States  
Ashok Kumar Pandurangan,  
B. S. Abdur Rahman Crescent  
Institute of Science and Technology,  
India

### \*Correspondence:

Zhi Shi  
tshizhi@jnu.edu.cn

<sup>†</sup>These authors have contributed  
equally to this work.

### Specialty section:

This article was submitted to  
Experimental Pharmacology  
and Drug Discovery,  
a section of the journal  
Frontiers in Pharmacology

**Received:** 24 July 2020

**Accepted:** 06 October 2020

**Published:** 12 November 2020

### Citation:

Huang J-R, Wang S-T, Wei M-N, Liu K,  
Fu J-W, Xing Z-H and Shi Z (2020)  
Piperlongumine Alleviates Mouse  
Colitis and Colitis-Associated  
Colorectal Cancer.  
Front. Pharmacol. 11:586885.  
doi: 10.3389/fphar.2020.586885

Colorectal cancer is one of the most common and lethal cancers in the world. An important causative factor of colorectal cancer is ulcerative colitis. In this study, we investigated the therapeutic effects of piperlongumine (PL) on the dextran sulfate sodium (DSS)-induced acute colitis and azoxymethane (AOM)/DSS-induced colorectal cancer mouse models. Our results showed that PL could inhibit the inflammation of DSS-induced mouse colitis and reduce the number of large neoplasms (diameter >2 mm) of AOM/DSS-induced mouse colorectal cancer by downregulation of proinflammatory cytokines cyclooxygenase-2 and interleukin-6 and epithelial-mesenchymal transition-related factors,  $\beta$ -catenin, and snail expressions, but fail to improve the colitis symptoms and to decrease the incidence of colonic neoplasms and the number of small neoplasms (diameter <2 mm). These data suggested that PL might be an effective agent in treating colitis and colorectal cancer.

**Keywords:** piperlongumine, Colitis, colorectal cancer

## INTRODUCTION

Colorectal cancer including cancer of the colon or rectum is one of the most common and lethal cancers in the world (Siegel et al., 2020). Although the pathogenesis of colon cancer is unclear, an important causative factor of colorectal cancer is ulcerative colitis (Rogler, 2014). Ulcerative colitis is a chronic and idiopathic inflammatory bowel disease characterized by relapsing and remitting mucosal inflammation of the rectum and colon (Kulaylat and Dayton, 2010). Multiple factors are involved in cancer-related inflammation such as cyclooxygenase-2 (COX-2) and interleukin-6 (IL-6), and are also important for the epithelial-mesenchymal transition (EMT), which is a process whereby epithelial cells are decreased adhesion and enhanced migration or invasion to initiate cancer invasion and metastasis (Cao et al., 2015; West et al., 2015). Therefore, suppression of inflammation is a potential strategy to treat ulcerative colitis and colorectal cancer.

Piperlongumine (PL) isolated from the long pepper (*Piperlongum* L.) is an active alkaloid and exhibits a broad spectrum of biological activities including antiangiogenic, antiatherosclerotic, antibacterial, anti-inflammation, and antitumor, etc (Bezerra et al., 2013; Tripathi and Biswal, 2020). Our previous studies have demonstrated that PL can inhibit cell proliferation and induce cell apoptosis in human ovarian cancer and glioblastoma multiforme cells (Liu et al., 2013; Gong et al., 2014; Nan et al., 2019). In this study, we investigated the therapeutic effects of PL on the DSS-induced acute colitis and AOM/DSS-induced colorectal cancer mouse models.

## MATERIALS AND METHODS

### Reagents

DSS (#60316ES76) was purchased from Yeasen Biotech. AOM (#A5486) was ordered from Sigma-Aldrich. PL (#A4455) was purchased from APExBIO. Anti-IL-6 antibody (#4ab080344) was purchased from 4A Biotech. Anti-COX-2 antibody (#BA0738) was purchased from Boster Biotech. Anti- $\beta$ -catenin antibody (#610154) was ordered from BD Biosciences. Anti-snail antibody (#RLT4351) was purchased from Ruiying Biological. Anti- $\beta$ -tubulin antibody (#KM9003T) was purchased from Sungene Biotech.

### Mice Models of Dextran Sulfate Sodium-Induced Acute Colitis and Acute Colitis and Azoxymethane/Dextran Sulfate Sodium-Induced Colorectal Cancer

Seven-week-old male BALB/c mice were obtained from the Guangdong Medical Laboratory Animal Center. Five mice were randomized into each group. Acute colitis was induced in mice by providing drinking water with 2.5% DSS for 1 week, followed by switching to regular drinking water for another 1 week. Mice were injected with PL (10 mg/kg) or solution control (0.5% methylcellulose) intraperitoneally every day for 2 weeks (**Figure 1A**). Colorectal cancer was induced in mice by intraperitoneal injection of AOM (10 mg/kg), while the mice were maintained with regular drinking water for 1 week and then subjecting the mice to three cycles of DSS treatment, with each cycle including 2.5% DSS treatment for 1 week and regular water for 2 weeks. Mice were injected with PL (10 mg/kg) or solution control (0.5% methylcellulose) intraperitoneally every day for 9 weeks (**Figure 2A**) (Wei et al., 2016).

### Clinical Assessment of Dextran Sulfate Sodium-Induced Acute Colitis and Acute Colitis and Azoxymethane/Dextran Sulfate Sodium-Induced Colorectal Cancer

Body weight, diarrhea degree, and bleeding degree in the rectum were determined in mice every two days. Diarrhea degree was scored 0 for well-formed pellets, 0.3 for soft pellets, 0.6 for pasty stools, 0.9 for liquid stools. Bleeding degree was scored as 0, when there was no blood; 2, for slight bleeding; 4, for gross bleeding (Wei et al., 2016).

### Hematoxylin and Eosin and Immunohistochemistry Staining

Formalin-fixed paraffin-embedded tissue slides were deparaffinized using xylene and graded ethyl alcohol and then stained with haematoxylin and eosin (H&E) solution (**Supplementary Figure S1**). For immunohistochemistry staining, antigen retrieval was performed by boiling the slides in 0.01 M citrate buffer (pH = 6) in a microwave oven for 10 min and cooling at room temperature. The slides were then incubated with 0.05% Triton X-100 in PBS for 5 min, followed by sequential

treatment in a humidified chamber after quenching endogenous peroxides with 3%  $H_2O_2$  in MeOH, blocking serum with avidin for 20 min, first antibody overnight at 4°C, secondary antibody for 20 min, hydrogen peroxidase for 15 min, and peroxidase substrate solution for 20 min at room temperature. The stained slides were then counterstained with hematoxylin and cover slipped. The following formula was used to quantify protein expression: immunohistochemical score = percentage of positive cells  $\times$  intensity score. The intensity was scored as follows: 0, negative; 1, weak; 2, moderate; and 3, intense. An immunohistochemical score of  $\geq 50$  was considered as positive (Zhang et al., 2017).

### Western Blot

Shredded colon tissues were harvested and washed twice with cold PBS, then resuspended and lysed in RIPA buffer (1% NP-40, 0.5% sodium deoxycholate, 0.1% SDS, 10 ng/ml PMSF, 0.03% aprotinin, 1  $\mu$ M sodium orthovanadate) at 4°C for 30 min. Lysates were centrifuged for 10 min at 14,000  $\times$  g and supernatants were stored at -80°C as whole cell extracts. Total protein concentrations were determined with Bradford assay. Thirty  $\mu$ g proteins of each sample were separated on 12% SDS-PAGE gels and transferred to polyvinylidene difluoride membranes. Membranes were blocked with 5% BSA and incubated with the indicated primary antibodies. Corresponding horseradish peroxidase-conjugated secondary antibodies were used against each primary antibody. Proteins were detected using the chemiluminescent detection reagents and Bio-Rad image system. The semiquantitative analysis of protein bands was carried out by software ImageJ (Yuan et al., 2018).

### Statistical Analysis

A student's t-test was used to compare individual data points among each group. A value of  $p < 0.05$  was considered to indicate a significant difference between groups.

## RESULTS

### Piperlongumine Inhibits the Inflammation in Dextran Sulfate Sodium-Induced Acute Colitis Mouse Models

DSS-induced acute colitis mouse model was generated by providing drinking water with 2.5% DSS for 1 week, followed by switching to regular drinking water for another 1 week to evaluate the anti-inflammation efficacy of PL (**Figure 1A**). As shown in **Figures 1B–E**, DSS-treated mice exhibited the colitis symptoms (body weight loss, diarrhea, and rectal bleeding), and PL administration failed to improve these colitis symptoms and to alter the colon length. Histopathologically, DSS-treated mice showed epithelial architecture destruction with loss of crypts and epithelial integrity and inflammatory cell infiltration, and PL administration significantly reduced inflammatory cell infiltration in the mucosa (**Figure 2A**). Moreover, both results of immunohistochemistry staining and Western blot showed that elevated protein expressions of COX-2, IL-6,  $\beta$ -catenin, and snail



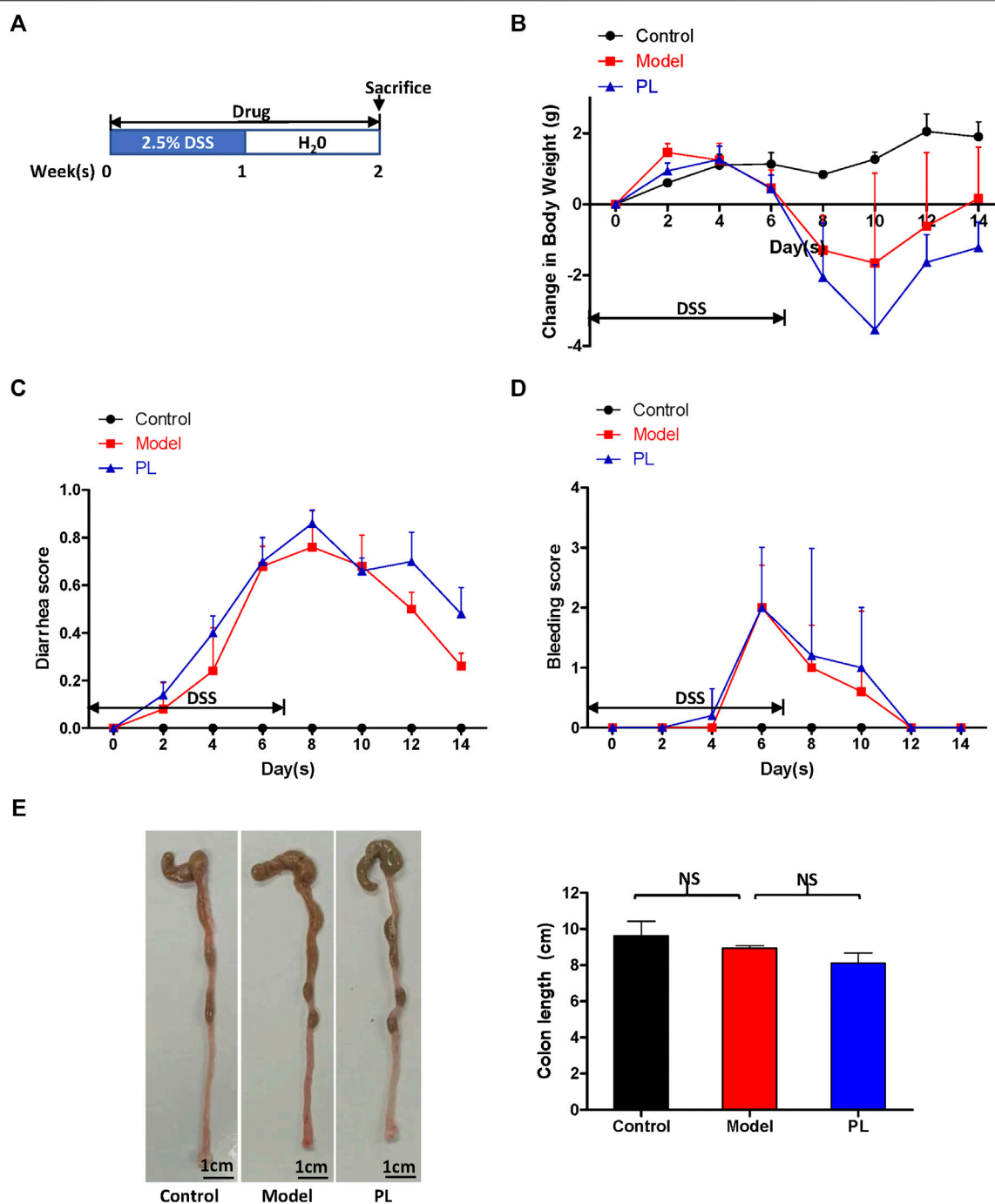


**FIGURE 1 |** Piperlongumine (PL) fails to improve the symptoms and to alter the colon length in dextran sulfate sodium (DSS)-induced acute colitis mouse models (A) The schematic diagram of DSS-induced colitis. The change in body weight of mice (B), diarrhea score (C), bleeding score (D), and the representative whole colons and colon length (E) are shown. Note: Control, no treated group; model, DSS-treated group; PL, DSS in combination with PL-treated group. NS, not significant.

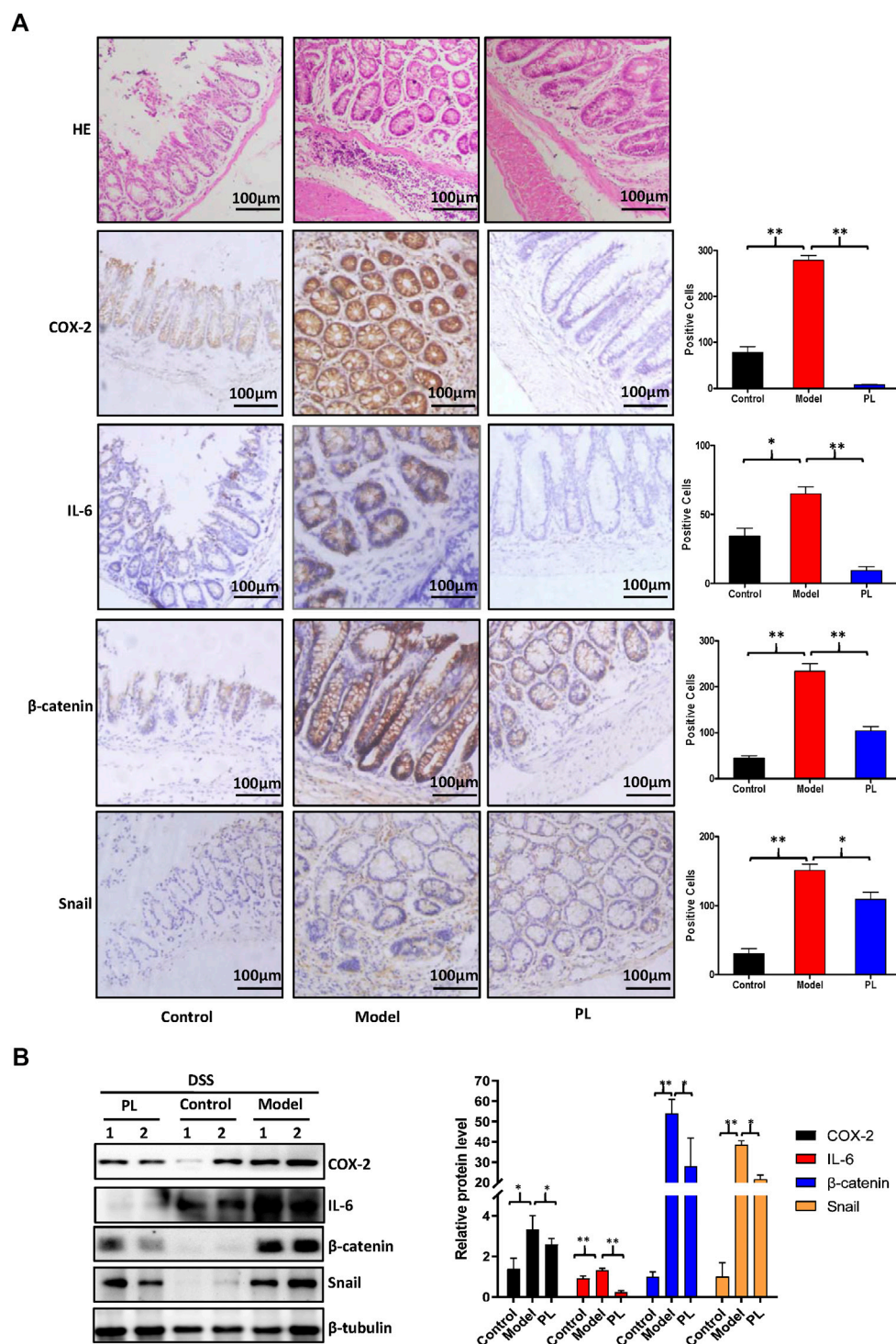


**FIGURE 2 |** Piperlongumine (PL) inhibits the protein expressions of cyclooxygenase-2 (COX-2), interleukin-6 (IL-6), β-catenin, and snail in dextran sulfate sodium (DSS)-induced acute colitis mouse models. **(A)** Colon sections were stained with H&E and the indicated antibodies. **(B)** The protein expression was examined by Western blot with the indicated antibodies after lysing colon tissues from two mice of each group, and β-tubulin was used as loading control. The representative results and quantified data are shown. Note: Control, no treated group; model, DSS-treated group; PL, DSS in combination with PL-treated group. \* $p < 0.05$ , and \*\* $p < 0.01$  vs. corresponding group.

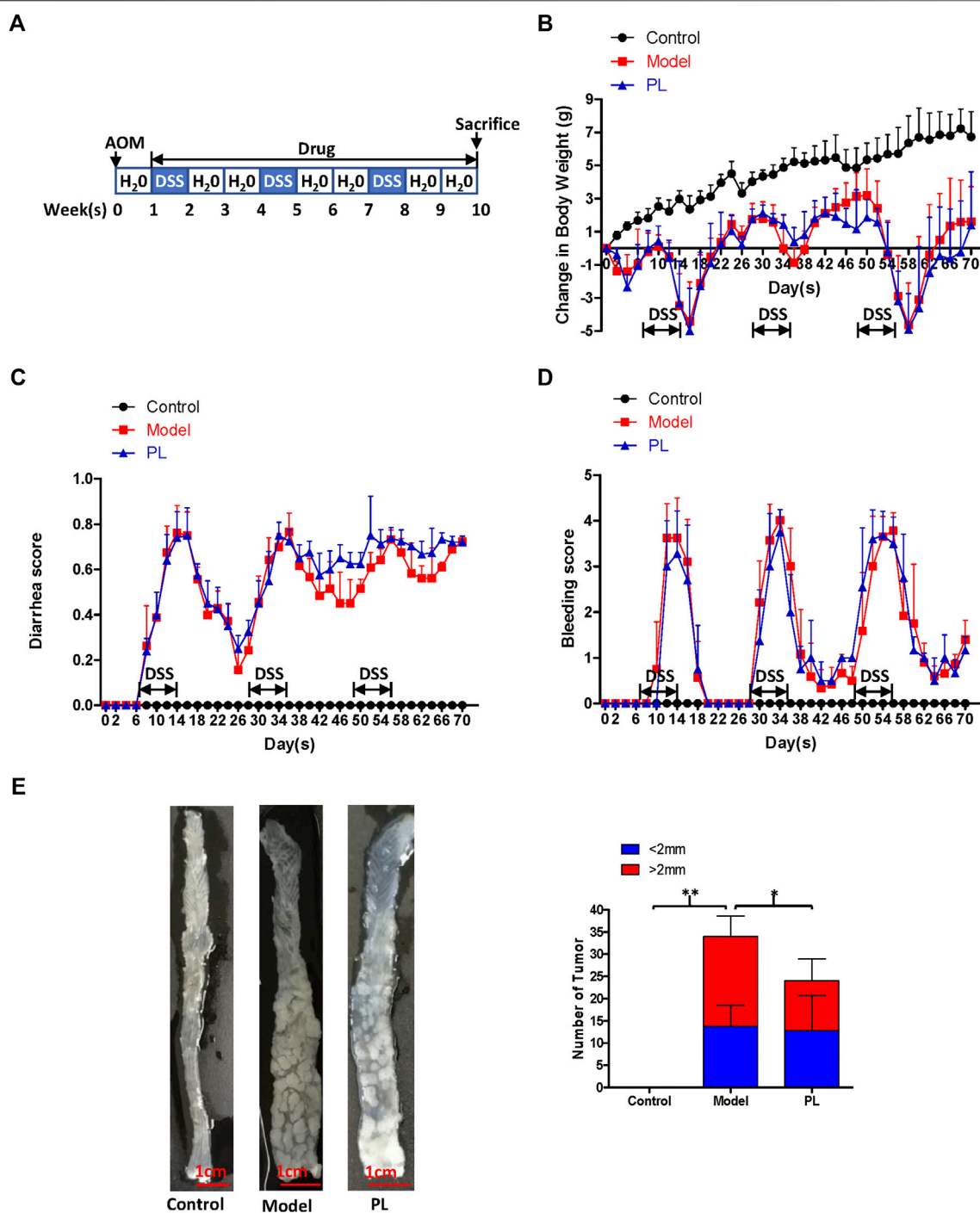


**FIGURE 3 |** Piperlongumine (PL) fails to improve the symptoms, but inhibited the tumor growth in acute colitis and azoxymethane (AOM)/dextran sulfate sodium (DSS)-induced colorectal cancer mouse models **(A)** The schematic diagram of AOM/DSS-induced colorectal cancer. The change in body weight of mice **(B)**, diarrhea score **(C)**, bleeding score **(D)**, and the representative whole colons and number of colon cancer **(E)** are shown. Note: Control, no treated group; model, AOM/DSS-treated group; PL, AOM/DSS in combination with PL-treated group. \* $p < 0.05$ , and \*\* $p < 0.01$  vs. corresponding group.

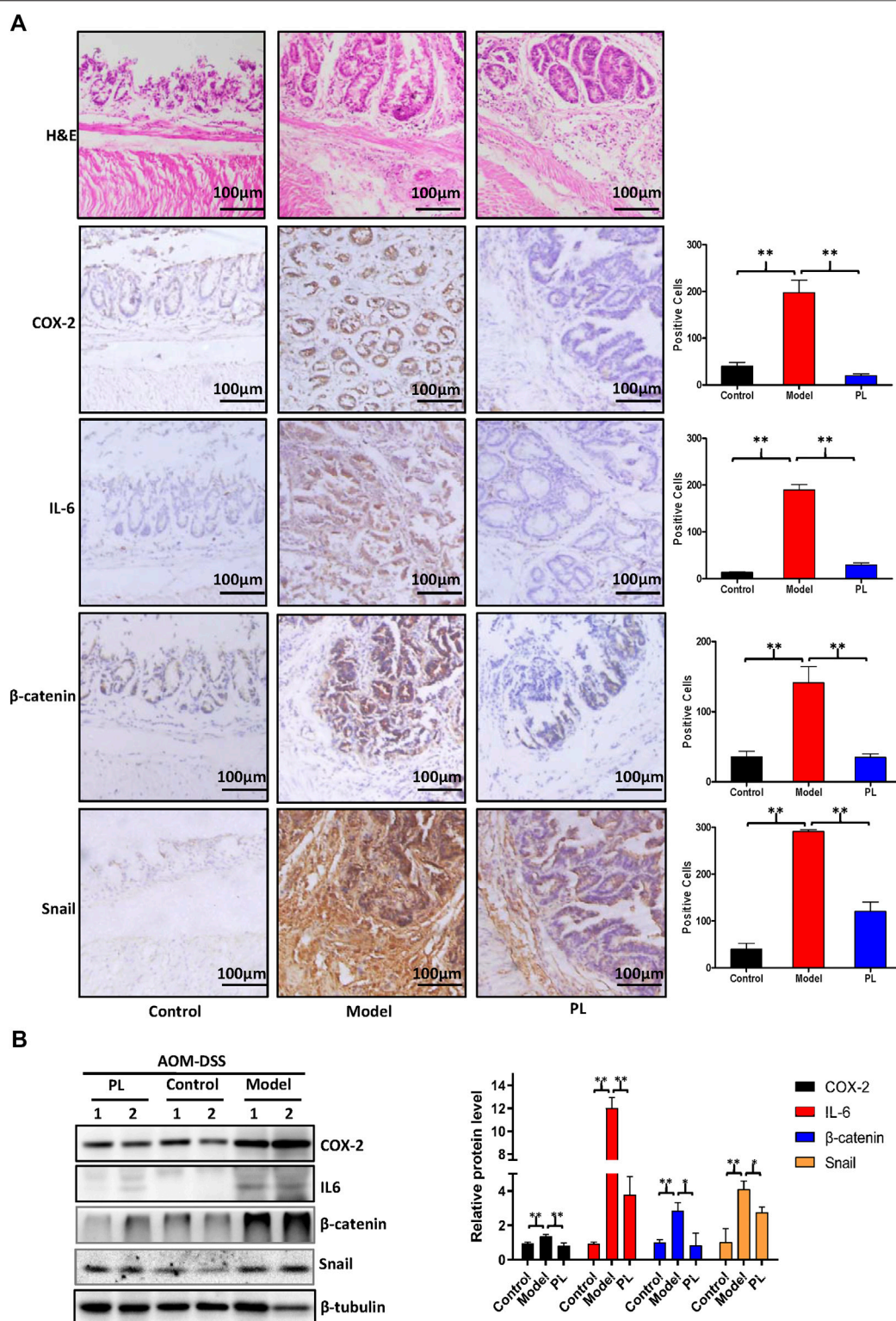


**FIGURE 4 |** Piperlongumine (PL) inhibits the protein expressions of cyclooxygenase-2 (COX-2), interleukin-6 (IL-6), β-catenin, and snail in acute colitis and azoxymethane (AOM)/DSS-induced colorectal cancer mouse models **(A)** Colon sections were stained with H&E and the indicated antibodies **(B)** The protein expression was examined by Western blot with the indicated antibodies after lysing colon tissues from two mice of each group, and β-tubulin was used as loading control. The representative results and quantified data are shown. Note: Control, no treated group; model, AOM/DSS-treated group; PL, AOM/DSS in combination with PL-treated group. \* $p < 0.05$ , and \*\* $p < 0.01$  vs. corresponding group.



were detected in the epithelial cells of DSS-treated mice, and these increases were prevented by PL (Figures 2A,B).

## Piperlongumine Attenuates the Tumor Growth in Acute Colitis and Azoxymethane/Dextran Sulfate Sodium-Induced Colorectal Cancer Mouse Models

As PL could inhibit the inflammation in DSS-induced acute colitis in mice, the therapeutic effect of PL was further evaluated in AOM/DSS-induced colorectal cancer mouse models generated by intraperitoneal injection of AOM (10 mg/kg), while the mice were maintained with regular drinking water for 1 week and then subjecting the mice to three cycles of DSS treatment, with each cycle including 2.5% DSS treatment for 1 week and regular water for 2 weeks (Figure 3A). As show in Figures 3B–D, symptomatic parameters (body weight loss, diarrhea, and rectal bleeding) were observed after DSS administration and decreased after DSS withdrawal in AOM/DSS-treated mice, and PL administration failed to improve these symptoms. AOM/DSS treatment resulted in 100% incidence of colonic neoplasms in mice of all groups. PL administration failed to decrease the incidence of colonic neoplasms and the number of small neoplasms (diameter <2 mm), but significantly reduced the number of large neoplasms (diameter >2 mm) (Figure 3E). The results of H&E staining exhibited colon adenocarcinomas with dysplasia in AOM/DSS-treated mice (Figures 4A). Furthermore, both results of immunohistochemistry staining and Western blot showed that elevated protein expressions of COX-2, IL-6,  $\beta$ -catenin, and snail were also detected in the tumor cells of AOM/DSS-treated mice, and these increases were prevented by PL (Figures 4A,B).

## DISCUSSION

The inflammation–dysplasia–carcinoma is a common development process of colorectal cancer (Lichtenstern et al., 2020). DSS-induced mouse colitis has been demonstrated to be similar to human colitis, and AOM/DSS-induced mouse colorectal cancer has been proven to rapidly mimic the abnormal crypt foci–adenoma–carcinoma sequence of human colorectal cancer (Neurath, 2012). Therefore, the mouse models of DSS-induced colitis and AOM/DSS-induced colorectal cancer have been widely used to explore the pathophysiologic mechanisms and therapeutic strategies of human colitis and colorectal cancer (Snider et al., 2016). In this study, we found that PL could inhibit the inflammation of DSS-induced mouse colitis and reduce the number of large neoplasms (diameter >2 mm) of AOM/DSS-induced mouse colorectal cancer by downregulation of proinflammatory cytokines COX-2 and IL-6 and EMT-related factors  $\beta$ -catenin and snail expressions, but fail to improve the colitis symptoms and to decrease the incidence of colonic neoplasms and the number of small neoplasms (diameter <2 mm). It might be because AOM administration was a week ahead of PL treatment, and PL can affect DSS-induced

inflammation, but not AOM-induced mutagenesis and tumorigenesis. Similarly, a recent report has shown that PL could suppress tumor cell growth and proliferation in DMH/DSS-induced experimental colon cancer by targeting Ras/PI3K/Akt/mTOR signaling axis (Kumar and Agnihotri, 2019). PL-induced Cyclin D1 downregulation and tumor suppression in colorectal cancer cells by suppression of ERKs/Akt-mediated c-Fos expression (Gao et al., 2020). PL could also induce apoptosis by activation of JNK in colorectal cancer HCT116 cells independent of Bax, p21 and p53 status (Li et al., 2015; DA Silva Machado et al., 2018). Additionally, PL increased the sensitivity of colorectal cancer cells to oxaliplatin and radiation by inducing reactive oxygen species production (Chen et al., 2019; Wang et al., 2019). However, the application of PL for human colitis and colorectal cancer treatment need to be further investigated.

In conclusion, our results revealed that PL could inhibit the inflammation of DSS-induced mouse colitis and tumor growth of AOM/DSS-induced mouse colorectal cancer, indicating that PL might be an effective agent to treat colitis and colorectal cancer.

## DATA AVAILABILITY STATEMENT

The raw data supporting the conclusions of this article will be made available by the authors, without undue reservation, to any qualified researcher.

## ETHICS STATEMENT

The animal study was reviewed and approved by the ethics committee of Jinan University.

## AUTHOR CONTRIBUTIONS

JH, SW and ZS designed the experiments, performed the experiments, analyzed the data and wrote the paper. MW, KL, JF and ZX performed the experiments and wrote the paper. All authors read and approved the final manuscript.

## FUNDING

This work was supported by funds from the National Key Research and Development Program of China No. 2017YFA0505104 (ZS), the National Natural Science Foundation of China No. 81772540 (ZS) and the Science and Technology Program of Guangdong No. 2019A050510023 (ZS).

## SUPPLEMENTARY MATERIAL

The Supplementary Material for this article can be found online at: <https://www.frontiersin.org/articles/10.3389/fphar.2020.586885/full#supplementary-material>



## REFERENCES

- Bezerra, D. P., Pessoa, C., De Moraes, M. O., Saker-Neto, N., Silveira, E. R., and Costa-Lotufo, L. V. (2013). Overview of the therapeutic potential of piperlongumine (piperlongumine). *Eur. J. Pharmaceut. Sci.* 48, 453–463. doi:10.1016/j.ejps.2012.12.003
- Cao, H., Xu, E., Liu, H., Wan, L., and Lai, M. (2015). Epithelial-mesenchymal transition in colorectal cancer metastasis: a system review. *Pathol. Res. Pract.* 211, 557–569. doi:10.1016/j.prp.2015.05.010
- Chen, W., Lian, W., Yuan, Y., and Li, M. (2019). The synergistic effects of oxaliplatin and piperlongumine on colorectal cancer are mediated by oxidative stress. *Cell Death Dis.* 10, 600. doi:10.1038/s41419-019-1824-6
- DA Silva Machado, F., Munari, F. M., Scariot, F. J., Echeverrigaray, S., Aguzzoli, C., Pich, C. T., et al. (2018). Piperlongumine induces apoptosis in colorectal cancer HCT 116 cells independent of bax, p21 and p53 status. *Anticancer Res.* 38, 6231–6236. doi:10.21873/anticancer.12978
- Gao, F., Zhou, L., Li, M., Liu, W., Yang, S., and Li, W. (2020). Inhibition of ERKs/Akt-Mediated c-Fos expression is required for piperlongumine-induced cyclin D1 downregulation and tumor suppression in colorectal cancer cells. *Onco. Targets Ther.* 13, 5591–5603. doi:10.2147/ott.s251295
- Gong, L. H., Chen, X. X., Wang, H., Jiang, Q. W., Pan, S. S., Qiu, J. G., et al. (2014). Piperlongumine induces apoptosis and synergizes with cisplatin or paclitaxel in human ovarian cancer cells. *Oxid. Med. Cell Longev.* 2014, 906804. doi:10.1155/2014/906804
- Kulaylat, M. N., and Dayton, M. T. (2010). Ulcerative colitis and cancer. *J. Surg. Oncol.* 101, 706–712. doi:10.1002/jso.21505
- Kumar, S., and Agnihotri, N. (2019). Piperlongumine, a piper alkaloid targets Ras/PI3K/Akt/mTOR signaling axis to inhibit tumor cell growth and proliferation in DMH/DSS induced experimental colon cancer. *Biomed. Pharmacother.* 109, 1462–1477. doi:10.1016/j.biopha.2018.10.182
- Li, W., Wen, C., Bai, H., Wang, X., Zhang, X., Huang, L., et al. (2015). JNK signaling pathway is involved in piperlongumine-mediated apoptosis in human colorectal cancer HCT116 cells. *Oncol. Lett.* 10, 709–715. doi:10.3892/ol.2015.3371
- Lichtenstern, C. R., Ngu, R. K., Shalpour, S., and Karin, M. (2020). Immunotherapy, inflammation and colorectal cancer. *Cells* 9, 618. doi:10.3390/cells9030618
- Liu, J. M., Pan, F., Li, L., Liu, Q. R., Chen, Y., Xiong, X. X., et al. (2013). Piperlongumine selectively kills glioblastoma multiforme cells via reactive oxygen species accumulation dependent JNK and p38 activation. *Biochem. Biophys. Res. Commun.* 437, 87–93. doi:10.1016/j.bbrc.2013.06.042
- Nan, X. W., Gong, L. H., Chen, X., Zhou, H. H., Ye, P. P., Yang, Y., et al. (2019). Survivin promotes piperlongumine resistance in ovarian cancer. *Front. Oncol.* 9, 1345. doi:10.3389/fonc.2019.01345
- Neurath, M. F. (2012). Animal models of inflammatory bowel diseases: illuminating the pathogenesis of colitis, ileitis and cancer. *Dig. Dis.* 30 (Suppl. 1), 91–94. doi:10.1159/000341131
- Rogler, G. (2014). Chronic ulcerative colitis and colorectal cancer. *Canc. Lett.* 345, 235–241. doi:10.1016/j.canlet.2013.07.032
- Siegel, R. L., Miller, K. D., Goding Sauer, A., Fedewa, S. A., Butterly, L. F., Anderson, J. C., et al. (2020). Colorectal cancer statistics, 2020. *CA A Cancer J. Clin.* 70, 145–164. doi:10.3322/caac.21601
- Snider, A. J., Bialkowska, A. B., Ghaleb, A. M., Yang, V. W., Obeid, L. M., and Hannun, Y. A. (2016). Murine model for colitis-associated cancer of the colon. *Methods Mol. Biol.* 1438, 245–254. doi:10.1007/978-1-4939-3661-8\_14
- Tripathi, S. K., and Biswal, B. K. (2020). Piperlongumine, a potent anticancer phytotherapeutic: perspectives on contemporary status and future possibilities as an anticancer agent. *Pharmacol. Res.* 156, 104772. doi:10.1016/j.phrs.2020.104772
- Wang, H., Jiang, H., Corbet, C., De Mey, S., Law, K., Gevaert, T., et al. (2019). Piperlongumine increases sensitivity of colorectal cancer cells to radiation: involvement of ROS production via dual inhibition of glutathione and thioredoxin systems. *Canc. Lett.* 450, 42–52. doi:10.1016/j.canlet.2019.02.034
- Wei, T.-T., Lin, Y.-T., Tseng, R.-Y., Shun, C.-T., Lin, Y.-C., Wu, M.-S., et al. (2016). Prevention of colitis and colitis-associated colorectal cancer by a novel polypharmacological histone deacetylase inhibitor. *Clin. Canc. Res.* 22, 4158–4169. doi:10.1158/1078-0432.ccr-15-2379
- West, N. R., Mccuaig, S., Franchini, F., and Powrie, F. (2015). Emerging cytokine networks in colorectal cancer. *Nat. Rev. Immunol.* 15, 615–629. doi:10.1038/nri3896
- Yuan, M. L., Li, P., Xing, Z. H., Di, J. M., Liu, H., Yang, A. K., et al. (2018). Inhibition of WEE1 suppresses the tumor growth in laryngeal squamous cell carcinoma. *Front. Pharmacol.* 9, 1041. doi:10.3389/fphar.2018.01041
- Zhang, W.-J., Li, Y., Wei, M.-N., Chen, Y., Qiu, J.-G., Jiang, Q.-W., et al. (2017). Synergistic antitumor activity of regorafenib and lapatinib in preclinical models of human colorectal cancer. *Canc. Lett.* 386, 100–109. doi:10.1016/j.canlet.2016.11.011

**Conflict of Interest:** The authors declare that the research was conducted in the absence of any commercial or financial relationships that could be construed as a potential conflict of interest.

Copyright © 2020 Huang, Wang, Wei, Liu, Fu, Xing and Shi. This is an open-access article distributed under the terms of the Creative Commons Attribution License (CC BY). The use, distribution or reproduction in other forums is permitted, provided the original author(s) and the copyright owner(s) are credited and that the original publication in this journal is cited, in accordance with accepted academic practice. No use, distribution or reproduction is permitted which does not comply with these terms.



# MOF Regulates TNK2 Transcription Expression to Promote Cell Proliferation in Thyroid Cancer

Danyang Li<sup>1,2</sup>, Yang Yang<sup>1,3</sup>, Bo Chen<sup>4</sup>, Xinghong Guo<sup>1,5</sup>, Shuang Gao<sup>1</sup>, Meng Wang<sup>1</sup>, Mingxiao Duan<sup>1</sup> and Xiangzhi Li<sup>1\*</sup>

<sup>1</sup> Shandong Provincial Key Laboratory of Animal Cell and Developmental Biology, School of Life Sciences, Shandong University, Qingdao, China, <sup>2</sup> Rehabilitation Center, Qilu Hospital, Cheelo College of Medicine, Shandong University, Jinan, China, <sup>3</sup> School of Pharmacy, Binzhou Medical University, Yantai, China, <sup>4</sup> Department of Thyroid Surgery, Qilu Hospital, Cheelo College of Medicine, Shandong University, Jinan, China, <sup>5</sup> Department of Endocrinology, Qilu Hospital, Cheelo College of Medicine, Shandong University, Jinan, China

## OPEN ACCESS

### Edited by:

Haichang Li,  
The Ohio State University,  
United States

### Reviewed by:

Lin-Yu Lu,  
Zhejiang University, China  
Chunming Cheng,  
The Ohio State University,  
United States

### \*Correspondence:

Xiangzhi Li  
xiangzhi@sdu.edu.cn

### Specialty section:

This article was submitted to  
Experimental Pharmacology and  
Drug Discovery,  
a section of the journal  
Frontiers in Pharmacology

**Received:** 17 September 2020

**Accepted:** 30 October 2020

**Published:** 08 December 2020

### Citation:

Li D, Yang Y, Chen B, Guo X, Gao S,  
Wang M, Duan M and Li X (2020) MOF  
Regulates TNK2 Transcription  
Expression to Promote Cell  
Proliferation in Thyroid Cancer.  
Front. Pharmacol. 11:607605.  
doi: 10.3389/fphar.2020.607605

MOF is a well-known histone acetyltransferase to catalyze acetylation of histone H4 lysine 16 (K16), and it is relevant to diverse biological processes, such as gene transcription, cell cycle, early embryonic development and tumorigenesis. Here, we identify MOF as an oncogene in most thyroid cancer. It is found that expression level of MOF was significantly upregulated in most thyroid cancer tissue samples and cell lines. MOF-deficient in both BHP-10-3 and TT2609 cell lines inhibited cell proliferation by blocking the cell cycle in G1 phase and enhanced cell apoptosis. Mechanistically, MOF bound the TNK2 promoter to activate TNK2 transcription. Furthermore, the expression level of TNK2 was decreased with the histone acetyltransferase inhibitor. Besides, MOF promoted proliferation of thyroid cancer cells through increased phosphorylation of AKT, thus activating the PI3K/AKT pathway. Ultimately, our findings indicated that MOF played an oncogene role in development and progression of thyroid cancer and may be a potential novel target for the treatment of thyroid cancer.

**Keywords:** thyroid cancer, MOF, TNK2, transcription, proliferation

## INTRODUCTION

Thyroid cancer is the most common malignant tumor of the head and neck with high morbidity. According to the statistics of the National Cancer Center in 2018, thyroid cancer has become the fourth most malignant tumor in women. Although most patients have a favored prognosis after surgery and radioactive I<sup>131</sup> treatment, treatment failure and inevitable side effects still exist. Therefore, molecular targeted therapy is of great significance. Current research confirms that some genetic mutations occur in up to 97% thyroid cancer (Cancer Genome Atlas Research Network, 2014). Most thyroid cancers are closely related to MAPK, VEGF, and PI3K signaling pathways, while BRAF, RAS and RET genes have higher mutation rates, which provides molecular targets for thyroid cancer (Thomas et al., 2014). Six molecular targets of thyroid cancer including BRAF, RET, NTRK1, G-GAS, K-RAS, and N-RAS have already been reported (Xing, 2013). Though BRAF inhibitor sorafenib has been used clinically, others are still in the basic research or clinical trial phase (Thomas et al., 2014).

Epigenetics is a hot topic in recent years, and epigenetic modifications have been observed in most tumors (Verma et al., 2014). Epigenetic modifications are also common with thyroid cancer. In follicular thyroid cancer, the promoter of PTEN is usually methylated, and the degree of methylation

is inversely related to the degree of tumor differentiation (Hou et al., 2008). At present, there is no clear explanation for the modification of histone acetylation for thyroid cancer. However, treatment of thyroid cancer cells with HDAC inhibitors alters the expression levels of some genes involved in thyroid cancer differentiation (Sherman et al., 2013). There is still a large gap in the study of non-coding RNA in thyroid cancer compared to other epigenetic modifications. The current study confirmed that PTCSC3 is a thyroid-specific lncRNA whose expression level is significantly down-regulated in papillary thyroid cancer (Fan et al., 2013). Changes in epigenetic modifications are detectable in the early stages of development, progression, eventual recurrence and metastasis. It has a great significance to clarify and use these markers to identify groups of at-risk patients, improve diagnostic criteria, and guide treatment options and predictors (Pan et al., 2018). In addition, the targeted locus of epigenetic modification provides new ideas for changing treatment regimens and provides new treatment options for patients with abnormal epigenetic modifications.

The overall level of acetylation of cells is maintained by histone acetyltransferases (HATs) and histone deacetylases (HDACs), which is in dynamic equilibrium and plays an important role in the regulation of chromatin structure and function (Kouzarides, 2007). HATs are divided into two families. One is GCN5-mediated N-acetyltransferase (GNATs), including GCN5 and PCAF (Dyda et al., 2000). Another is MYST family, including MOF, TIP60, HBO and others.

MOF, also known as MYST1 or KAT8, is a member of MYST family. The highly conserved MYST domain determines its histone acetyltransferase activity. MOF has a strict substrate specificity for the histone H4 at lysine 16 (H4K16), which was first discovered and studied in *drosophila*. As an important component of the *drosophila* X chromosome dose-compensating complex called male special lethal (MSL) (Morales et al., 2004; Gelbart and Kuroda, 2009), MOF was originally purified from a complex containing MSL (Bone and Kuroda, 1996). The MSL complex plays a significant role in balancing X-linked gene expression between male and female *drosophila*. The structure of MOF in mammals is significantly similar to the one in *drosophila*, which contains an acetyl-CoA binding site, a C2H2 zinc finger domain and a histone-binding chromatin region (Avvakumov and Cote, 2007). In mammals, MOF regulates the transcriptional activation through the formation of MSL and MOF-MSL1v1, which are evolutionarily conserved.

As an important histone acetyltransferase, MOF participates in several activities, such as gene transcription, chromatin stability, DNA damage repair, early embryonic development and tumorigenesis (Sharma et al., 2010; Li et al., 2012; Deng et al., 2013; Valerio et al., 2017; Yang et al., 2017). Few studies investigated the function of MOF in cancer. For instance, Valerio et al. (2017) reported that knocking out MOF in AML mice could relieve symptoms and prolong the life span, indicating that MOF may act as an oncogene in AML cells. Nevertheless, the biological effects and related mechanisms of MOF in thyroid cancer cells have not yet been elucidated.

With the increase morbidity and mortality of thyroid cancer, the most common disease in human endocrine system, research on pathogenesis and treatment of thyroid cancer is especially important. Thyroid cancer is a low-grade tumor (Vu-Phan and Koenig, 2014). The Human Epigenetics Association for Cancer Research launched the Human Epigenetic Program in 2003, which is aimed that understanding the epigenetic mechanisms of tumor (Jones and Martienssen, 2005). Gene expression profiling of differentiated thyroid cancer suggests that changes in DNA methylation, histone modifications, lncRNA and microRNA may contribute to tumorigenesis and tumor development (Asa and Ezzat, 2018). Currently, it is believed that HAT (Histone acetyltransferase) and HDAC (Histone deacetylase) are considered as novel anticancer targets (Noureen et al., 2010). Therefore, finding a target for thyroid cancer treatment through histone acetylation modification is promising.

In this study, we reported that MOF, which was upregulated in most thyroid cancer, activated the PI3K/AKT pathway through binding TNK2 promoter. MOF significantly promoted proliferation and inhibited apoptosis in thyroid cancer. Overall, these findings revealed a novel function of MOF in cancer. MOF may be a potential therapeutic target and diagnostic marker for thyroid cancer.

## MATERIALS AND METHODS

### Patients and Tissue Samples

The retrospective research included 20 cases of thyroid cancer which were collected in Qilu Hospital from September, 2016 to June, 2017. The patients already gave written informed consent, which complied with the rules of the Ethics Committee of Shandong University. The thyroid cancer tissue chip was bought from Guge biotechnology company (Wuhan, China).

### Cell Culture and Transfection

N-thy-ori, BHP-10-3, IHH-4, TT2609 and 8505C cell lines were obtained from the American Type Culture Collection (ATCC, United States) and were, respectively, maintained in 1640/1640/DMEM/F12K/MEM with 10% fetal bovine serum (FBS, Gibco, United States). All cells were cultured at 37°C with CO<sub>2</sub> in a humidified incubator. We knocked down MOF in BHP-10-3 and TT2609 cell lines by lentivirus infection. For stable infection, cells were infected with lentivirus for 24 h and then selected for 2 weeks in medium containing 2 µg/ml puromycin to acquire stable expression cells.

### Cell Proliferation Assay

The monoclonal cells and control cells were plated in a 96-well plate at  $2 \times 10^3$  cells/well once a day for 6 days. On the sixth day, these cells were treated with 10 µL of 5 mg/ml CCK8 (APEX BIO, United States) per well for 4 h at 37°C with CO<sub>2</sub> incubator. Viable cells were counted by reading the absorbance at 450 nm using a microplate reader.

## Plate Colony Formation Assay

The two monoclonal cell lines were plated in 10 cm dishes at 200 cells/well. After 10 days of culture, the cells were washed by PBS and stained by Giemsa. The colony number was counted under the light microscope, with one colony containing more than 50 cells. Each experiment was repeated in triplicate.

## EdU Staining Assay

The cells were incubated with EdU labeling solution (Abcam, United States) for 2 h at 37°C with CO<sub>2</sub>, then added with 2 mg/ml glycine to terminate the fixing. The staining was carried out according to the procedure on the kit, and finally the staining was observed with a fluorescence microscope.

## Cell Cycle Assay

The stable expression cells and control cells were collected and washed twice with PBS. Cells were added with 1 ml PI per 10<sup>6</sup> cells protected from light for 30 min. Cell cycle was assessed by flow cytometer.

## Annexin V-FITC/PI Apoptosis Assay

The stable expression cells and control cells were collected and washed twice with PBS. Cells were diluted with 400 µL binding buffer. The cell suspension was then added with Annexin V-FITC and incubated at 4°C for 15 min protected from the light. Then the cell suspension was added with PI for 30 min.

## Western Blot Analysis

In order to detect the relative protein expression, BC200 lysis buffer was used for western blot. The protein samples were separated by SDS-PAGE and electro-transferred onto PVDF membrane, and then incubated with monoclonal anti-human MOF, H4K16ac, p21, p16, Cyclin D1, Cyclin D2, BAX, BCL2, p-BAD, AKT, p-AKT, GAPDH (Abcam, United States) at 4°C overnight. The membranes were probed with anti-mouse/rabbit IgG (Abcam, United States) at 1:5,000 dilution for 1 h, and then added with ECL reagent for examine.

## RNA Isolation and qPCR

Total RNA was extracted from cultured cells or fresh tissues with Trizol (TaKaRa, Japan) reagents following the kit protocol. And then, the total RNA was reverse transcribed into cDNA by using the RevertAid First Strand cDNA Synthesis Kit (Thermo, United States). qRT-PCR was performed to detect mRNA expression by using the Bio-Rad CFX96 real-time PCR detection system and SYBR Premix ExTaq Kit (TaKaRa, Japan). The primer sequences tested for qRT-PCR are shown in **Supplementary Table S1**.

## Immunohistochemistry Staining

To detect the expression level of MOF in thyroid cancer tissues, immunohistochemical staining of thyroid adjacent cancer tissue chips was performed. The tissue sections were deparaffinized in xylene and rehydrated in alcohol. Endogenous peroxidase activity in the tissue sections was blocked in 3% H<sub>2</sub>O<sub>2</sub> for 15 min in the dark. The tissue was subjected to antigen retrieval using sodium citrate buffer by microwave, and naturally cooled to room temperature. 5% BSA was used to block the tissues at 37°C for

1 h. The tissues was incubated with primary antibody (anti-MOF) at 4°C overnight, and then was washed thrice by PBS. Secondary antibody was incubated with the tissues at 37°C for 1 h. After thrice washing with PBS, the tissues was stained by DAB and Hematoxylin. Images of the tissues were taken by using a light microscope (Olympus, Japan).

## Chromatin Immunoprecipitation Assay

ChIP assay was performed by referring to the ChIP kit (CST, United States) protocol. The DNA of cells were then immunoprecipitated with anti-MOF antibody. The purified DNA was analyzed by qRT-PCR. Sequences of all primer pairs used in the research are listed in **Supplementary Table S2**.

## Statistics Analysis

The experimental data were expressed as mean ± standard deviation (Mean SD), analyzed by GraphPad Prism5 software. The data comparison between groups was based on the principle of *t*-test, and *p* value < 0.05 was considered statistically significant standard.

# RESULTS

## MOF Was Upregulated in Most Thyroid Cancer

To ascertain the expression of MOF in thyroid cancer, western blot was performed in 20 thyroid cancer tissue samples and matched corresponding normal tissue. Expression of MOF was significantly up regulated in thyroid cancer tissue (**Figures 1A,B**). We calculated the clinicopathologic features of 20 patients (**Table 1**). Immunohistochemical staining was performed and the results showed that cancer tissues with high MOF expression accounted for 96.6% (28 cases) compared with adjacent tissues, and cancer tissues with low MOF expression accounted for 3.4% (1 case) (**Figure 1C**). We analyzed the clinicopathologic parameters of 29 patients, and found something, which was consistent with the statistical results of these 20 patients (**Table 2**). To further demonstrate the expression of MOF in thyroid cancer, qRT-PCR and western blot were performed in N-thy-ori, BHP-10-3, IHH-4, TT2609, 8505C cell lines. Compared with the normal cell line N-thy-ori, MOF had a high expression in BHP-10-3, IHH-4, TT2609 cell lines (**Figures 1D,E**). The results demonstrated that MOF was upregulated in most thyroid cancer cell lines. Therefore, we suspected that MOF may play an important role in the development of thyroid cancer.

## Knockdown of MOF Inhibited Cell Proliferation

To investigate the functional role of MOF in thyroid cancer, we established two MOF knockdown cell lines by lentivirus infection and examined the effect of MOF on cell proliferation and apoptosis.

MOF was knocked down in BHP-10-3 and TT2609 cells and efficacy was verified (**Figures 2A,B**). It is found that cell



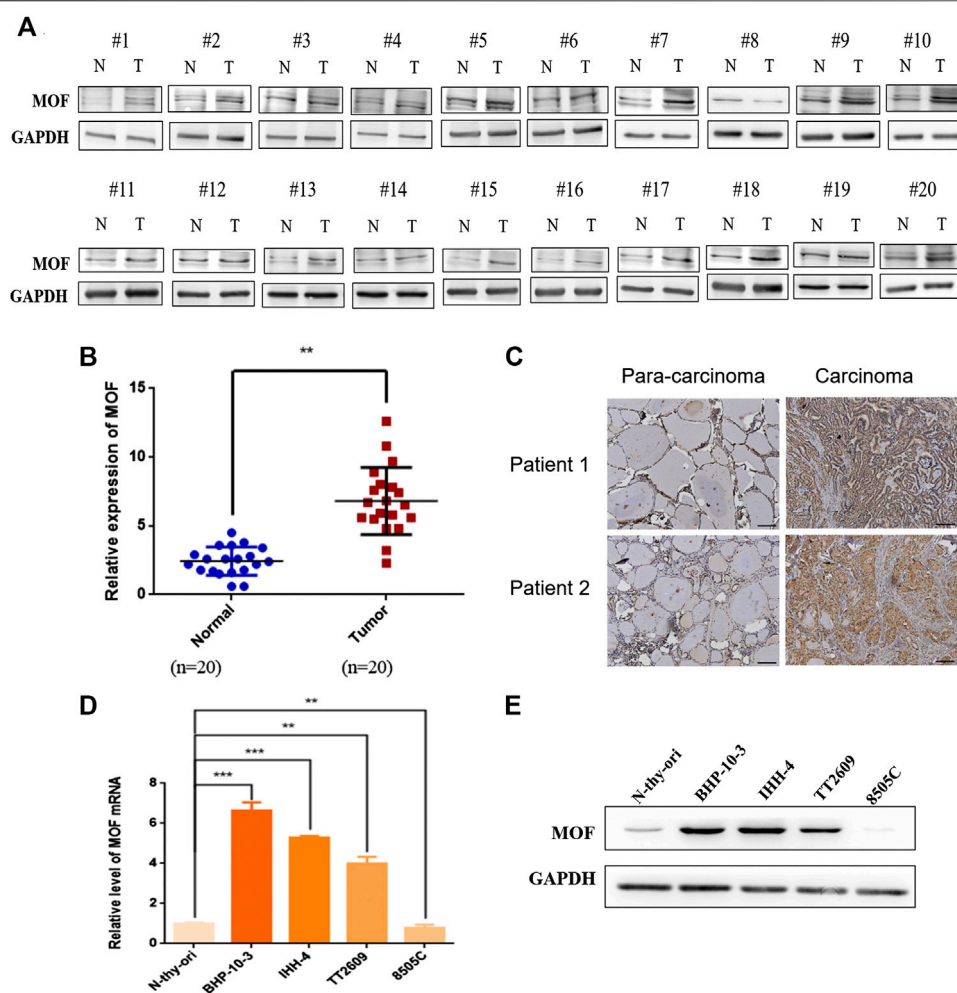


**FIGURE 1 |** Expression analysis of MOF in thyroid cancer. **(A,B)** Western blot analysis of MOF in thyroid cancer tissue samples ( $n = 20$ ) compared with normal fimbria ( $n = 20$ ). **(C)** Representative images of immunohistochemical staining of MOF in tissue chip. **(D)** The MOF expression were measured by qRT-PCR in N-thy-ori, BHP-10-3, IHH-4, TT2609 and 8505C cell lines. **(E)** Western blot analysis of MOF in N-thy-ori, BHP-10-3, IHH-4, TT2609 and 8505C cell lines.  $^{**}p < 0.01$ ,  $^{***}p < 0.001$ .

**TABLE 1 |** Qilu Hospital 20 patients characteristics and association with MOF expression.

Variable	Category	No. of patients	%
MOF expression	High	18	90.0%
	Low	2	10.0%
Sex	Male	4	20.0%
	Female	16	80.0%
Age	<45	9	45.0%
	≥45	11	55.0%
Histology	Typical PTC	18	90.0
	Follicular subtype PTC	2	10.0

**TABLE 2 |** Patient characteristics and association with MOF expression in pathology chip.

Variable	Category	No. of patients	%
MOF expression	High	28	96.6%
	Low	1	3.4%
Sex	Male	8	27.6%
	Female	21	72.4%
Age	<45	15	51.7%
	≥45	14	49.3%
Histology	Typical PTC	28	96.6%
	Follicular subtype PTC	1	3.4%

proliferation ability was decreased after knocking down MOF by CCK8 assay (**Figures 2C,D**). Accordingly, EdU incorporation assay showed that knockdown of MOF reduced the DNA synthesis rate thus inhibits cell proliferation (**Figures 2G,H**). Furthermore, we detected p21, p16, Cyclin D1 and Cyclin D2 by

western blot and qRT-PCR in stable and control cells. Cyclin D1 and Cyclin D2 expression were obviously decreased after knocking down MOF, while p21 and p16 were upregulated (**Figures 2I,J**). Through PI staining by FCM, the G1 phase was significantly blocked in two knockdown cell lines (**Figures**



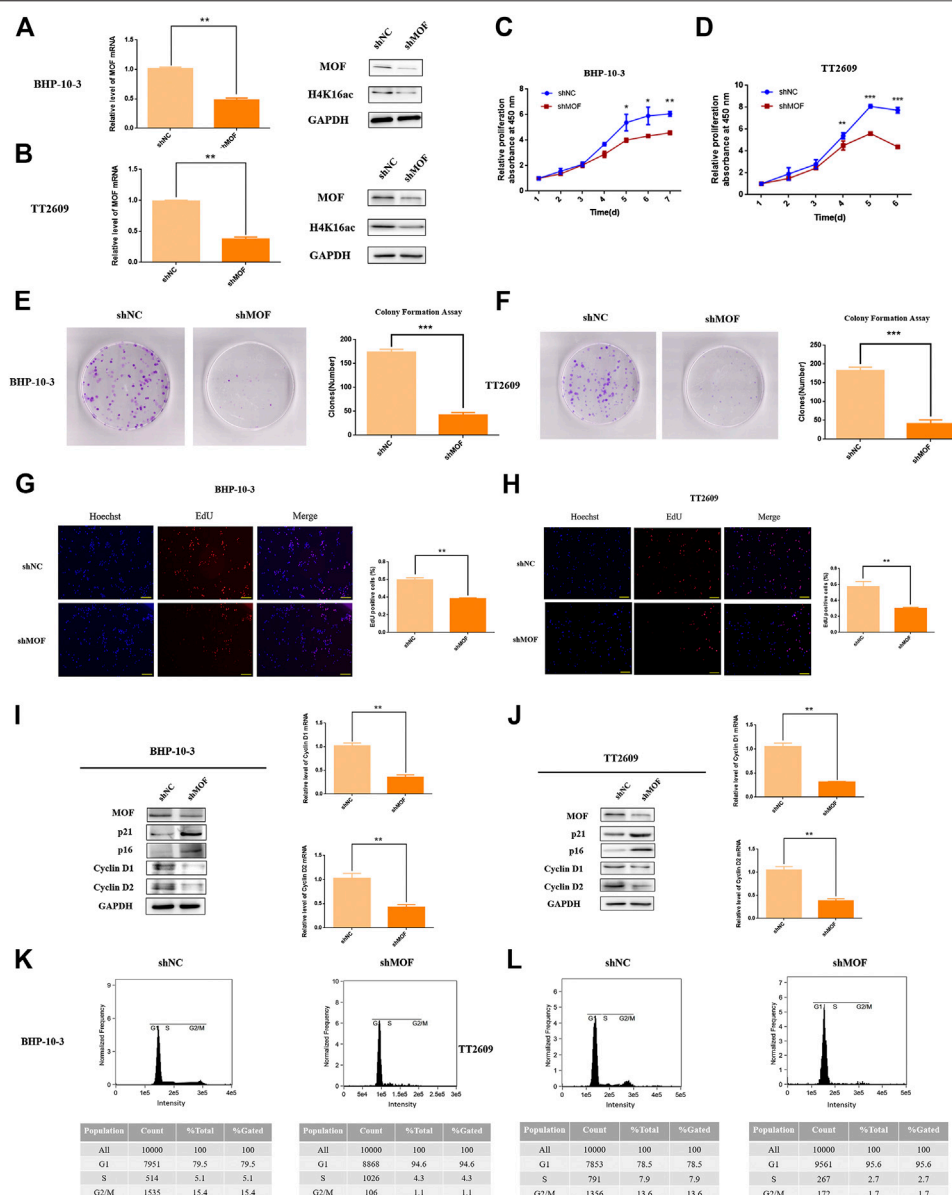


**FIGURE 2 |** MOF inhibited the proliferation and colon formation ability of thyroid cancer cells. **(A,B)** Decreased MOF mRNA and protein expression in stable MOF-knockdown BHP-10-3 and TT2609 cells were detected and verified. **(C,D)** CCK8 assay of stable MOF-knockdown cell line showed decreased proliferation ability. **(E,F)** Colony formation assay of MOF-knockdown or control BHP-10-3 and TT2609 cells. **(G,H)** EdU staining assay of stable MOF-knockdown or control BHP-10-3 and TT2609 cells. **(I,J)** Cyclin D1, Cyclin D2, p21 and p16 mRNA and protein expression in stable MOF-knockdown BHP-10-3 and TT2609 cells were performed by Western blot and qRT-PCR. **(K,L)** Cell cycle was measured using PT staining assay by FCM. \* $p < 0.05$ , \*\* $p < 0.01$ , \*\*\* $p < 0.001$ .

2K,L). Besides, decreasing the expression of MOF also affected the colony formation ability (Figures 2E,F).

## Knockdown of MOF Promoted Apoptosis

Influence of MOF on apoptosis was detected in order to investigate its role on malignant characteristics of the thyroid tumor. Knockdown cell lines with corresponding control groups were stained with PI and FITC, which were analyzed by flow cytometer for apoptosis based on DNA content (Figures 3A,B). It is found that the apoptosis percentage was significantly increased

after knocking down MOF comparing with the control group. What's more, western blot analyze was performed to elevate the levels of apoptosis markers, including caspase 3, cleaved-caspase3, BAX and BCL2 (Figures 3C,D). Overall, knockdown of MOF promoted cell apoptosis and inhibited development of thyroid tumor.

MOF acted as an oncogene function in thyroid cancer. In GEO database, we selected the GO molecular function clustering of MOF expression correlated genes, and annotated the functions of these genes. It was clear that there

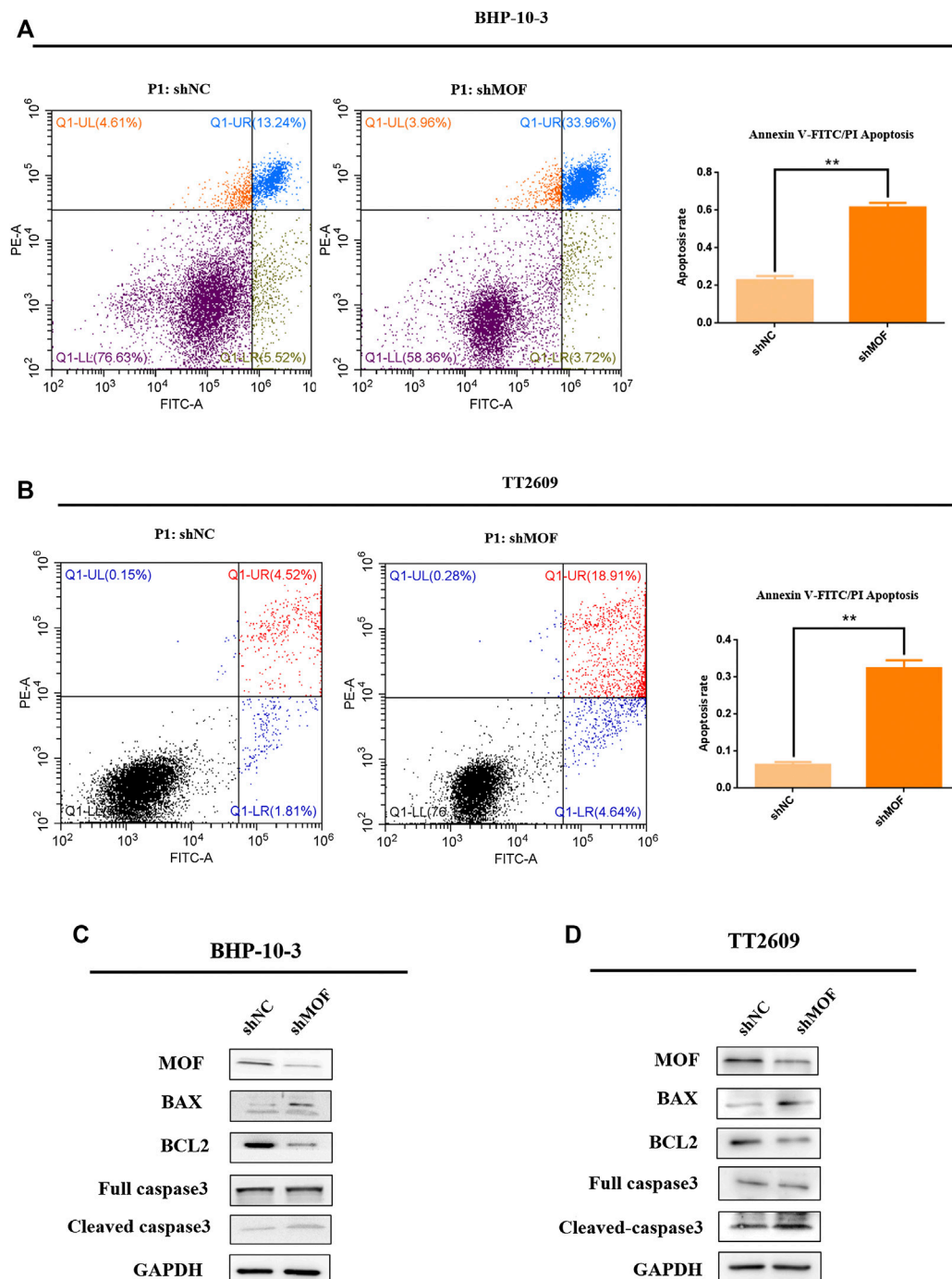


**FIGURE 3 |** Knockdown of MOF promoted the apoptosis of thyroid cancer cells. **(A,B)** In BHP-10-3 and TT2609 cell lines, the effect of knockdown MOF were measured using PI/FITC staining assay. **(C,D)** Western blot assay was performed to detect the protein expression of apoptosis marks including caspase 3, cleaved-caspase 3, BAX, BCL2 in stable MOF-knockdown and control BHP-10-3 and TT2609 cells. MOF regulated TNK2 transcriptional expression in thyroid cancer cells.

are more than 20 genes which was related to protein serine/threonine/tyrosine kinase activity (**Figure 4A**). We screened some phosphokinases that are positively correlated with MOF expression in the cancer genome atlas (TCGA) database, as shown in **Figure 4B**. Through analyzing the previous MOF

transcriptome and ChIP-Seq data in K562 and HepG2 cell lines in Cistrome DB database, several potential MOF targets phosphokinases were discovered, including TNK2, DYK1B and MAP2K2. Both of them had MOF binding peak in their promoter region (**Figure 4C**; **Supplementary Figures S1C,D**).

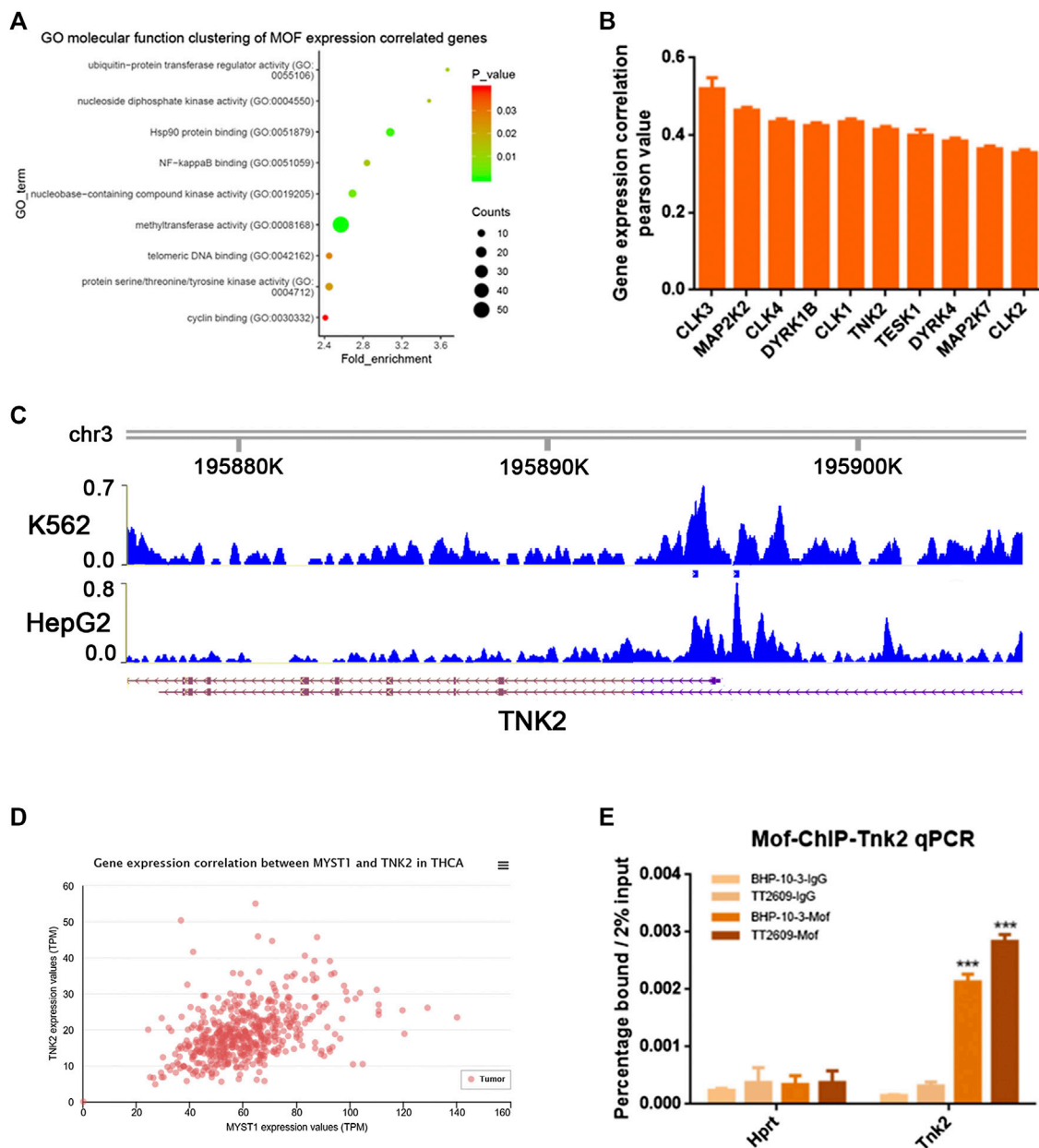
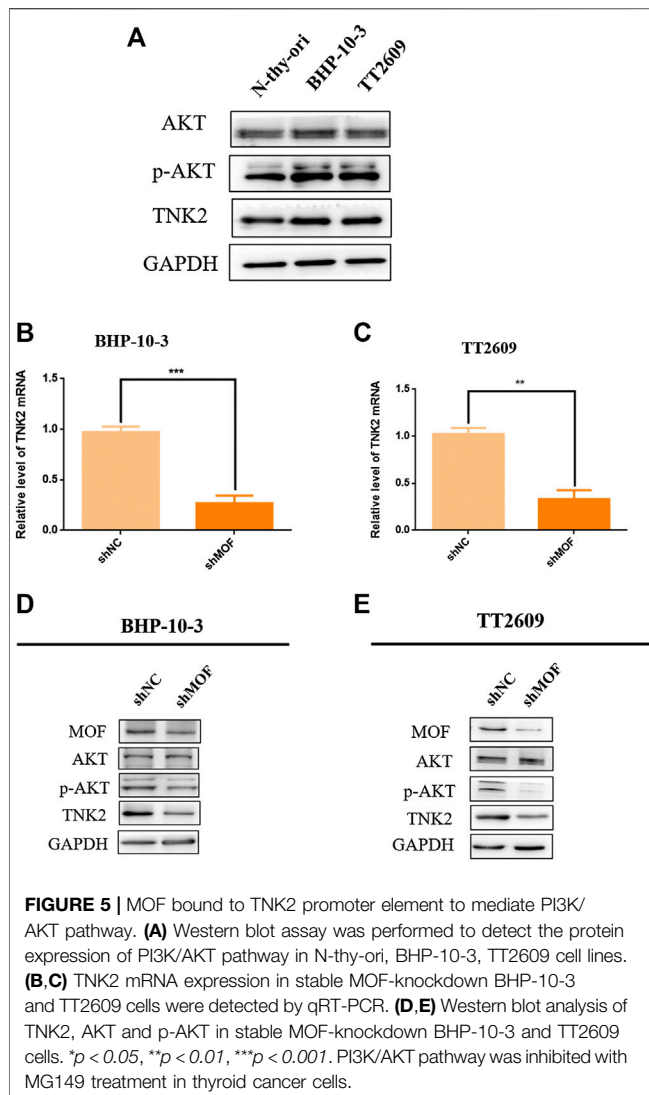


**FIGURE 4 |** MOF bound to the phosphokinase TNK2 promoter. **(A)** Cluster of MOF expression correlated genes were enriched and classified according to GEO molecular functions. **(B)** Analyze the correlation between phosphokinase and MOF expression in TCGA database. **(C)** Screen promoters that might bind to MOF by Cistrome DB database. **(D)** Analyze the correlation between TNK2 and MOF expression in TCGA database. **(E)** ChIP analysis showed the occupancy of MOF on the TNK2 promoter *in vivo*. \* $p < 0.05$ , \*\* $p < 0.01$ , \*\*\* $p < 0.001$  **Table 1.** Qilu Hospital 20 patients characteristics and association with MOF expression.

We verified the correlation between TNK2, DYK1B, MAP2K2 and MOF expression in the TCGA database, and found that in thyroid cancer cells, they all had a strong positive correlation with MOF expression (**Figure 4D**; **Supplementary Figures S1A,B**). With the assumption that MOF could regulate several downstream targets by transcription activation, we supposed that MOF could bind the promoter region of TNK2, DYK1B, MAP2K2. We conducted chromatin immunoprecipitation (ChIP) assay in BHP-10-3 and TT2609 cells. After cross linking and

chromatin fractionations the DNA-protein complex was immunoprecipitated with MOF and IgG antibody. We observed occupancy of MOF at the TNK2 promoter, whereas little signal was amplified from the IgG immunoprecipitated negative control by qRT-PCR (**Figure 4E**). Compared with the negative control, it had little change between DYK1B, MAP2K2 and MOF combination (**Supplementary Figures S1E,F**). In summary, MOF might bind to the promoter of TNK2 and mediate its transcriptional activation.



## MOF Could Mediate the Activation of PI3K/AKT Signaling Pathway Caused by Phosphorylation of AKT by TNK2

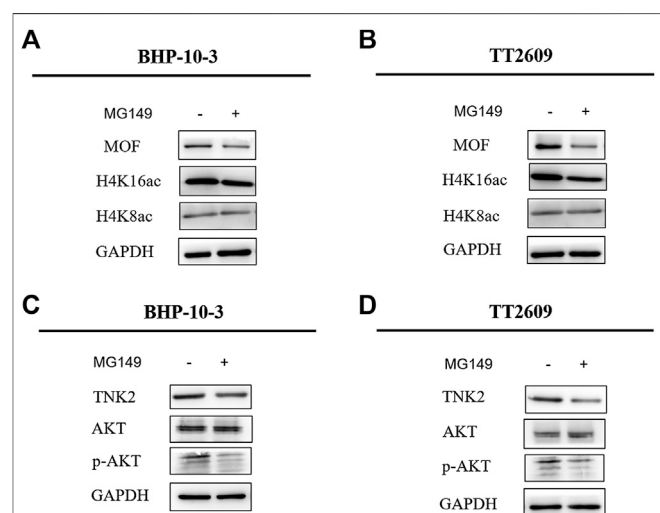
TNK2 is a specific AKT phosphokinase (Mahajan and Mahajan, 2015). Compared with thyroid cell lines N-thy, TNK2 and p-AKT was upregulated in thyroid cancer cell lines BHP-10-3 and TT2609 (Figure 5A). TNK2 mRNA expression was accurately quantified with real-time PCR assay in MOF-knockdown or control cells of BHP-10-3 and TT2609 (Figures 5B,C), which showed considerable down regulation of TNK2 expression after MOF knockdown. What's more, we detected the expression of AKT, p-AKT and TNK2 by western blot in stable MOF-knockdown cell lines. As was shown in Figures 4D,E, knockdown of MOF could inhibit the PI3K/AKT pathway by blocking the protein expression of TNK2 and p-AKT, which was related with the cell proliferation and apoptosis. The conclusion was consistent with our previous results that the proliferative capacity of the cells was reduced

and the level of apoptosis was increased after knocking down MOF in BHP-10-3 and TT2609.

MG149 was a histone acetyltransferase inhibitor, which could act on several histone acetyltransferases like MOF, Tip60 etc. Optimal MG149 concentration for MOF was determined as 33  $\mu$ m. The expression of H4K16ac was obviously inhibited and H4K8ac was constant through Western Blot assay in BHP-10-3 and TT2609 cell lines (Figures 6A,B). What's more, the phosphorylation level of AKT was reduced in the two treated cell lines through western blot assay, which was corresponding to the result after knocking down MOF (Figures 6C,D). It was demonstrated that inhibition of MOF enzyme activity could also decrease the expression of TNK2 and affect the PI3K/AKT signaling pathway represented by the reduced phosphorylation level of AKT. Therefore, our findings revealed the feasibility that MOF could be considered as a target for thyroid cancer treatment.

## DISCUSSION AND CONCLUSION

The present study identified a novel function of MOF in progression of thyroid cancer. MOF is member of the histone acetyltransferase MYST family, which not only specifically acetylates histone H4K16 but also non-specifically acetylates p53, NRF2 and other genes. The acetylation of p53 by MOF leads to the up-regulation of mRNA levels of the apoptotic genes BAX and PUMA (Li et al., 2009). And acetylation of NRF2 leads to nuclear arrest of NRF2, which in turn affects the transcription level of NRF2 target gene (Chen et al., 2014). The biological activity of MOF determines its diverse biological functions, and MOF plays an important role in many life span such as self-renewal of embryonic stem cells, gene transcription,





maintenance of chromosomal stability, immune inflammatory response, and tumorigenesis. The expression of MOF is upregulated in non-small lung cancer. The mechanism is that MOF blocks its nucleation by acetylation of NRF2, affecting the downstream signaling pathway, which is different from that of MOF in thyroid cancer.

In this study, we first analyzed the expression of MOF in thyroid cancer pathology and cell lines, showing that MOF is up-regulated in most thyroid cancers including papillary thyroid cancer and follicular thyroid cancer. So, we uncovered the precise function and mechanism of MOF in thyroid cancer. Results showed that MOF significantly promoted proliferation and inhibited apoptosis. We knocked down MOF in the papillary thyroid cancer cell line BHP-10-3 and the follicular thyroid cancer cell line TT2609 by lentivirus infection, and two monoclonal MOF-knockdown cell lines were screened by puromycin subsequently. After knocking down MOF, the level of acetylation of H4K16 was significantly decreased, which showed its effect on epigenetic modifications. According to CCK8, colony formation and EdU staining we could draw a conclusion that the proliferation ability of knockdown MOF cells was inhibited. Expression of cell proliferation inhibitory proteins p21 and p16 were up-regulated and cyclin D1, cyclin D2 expression were down-regulated. Mammalian cells encodes three D cyclins (D1, D2, D3) that coordinately function as allosteric regulators of cyclin-dependent kinase 4 (CDK4) and CDK6 to regulate cell cycle transition from G1 to S phase (Goel et al., 2017). Cyclin D1 is more frequently abnormal than cyclin D2 or D3 in human tumors, so it has been more widely characterized (Qie and Diehl, 2016). According to the down regulation expression of cyclin D1 and D2 in knockdown MOF cells, We detected the cell cycle by PI staining and flow cytometry. Based on BN Sheikh's research (Sheikh et al., 2016), we speculated that the reason why G1 phase blocked was that MOF directly bound to genes required for cell cycle progression and maintained their transcription. However, further research is needed on the specific mechanism which cyclin D1 regulates the change of thyroid cancer cell cycle.

Apoptosis is a process of programmed cell death, which is regulated through the balance between proapoptotic and antiapoptotic proteins like BCL2 family (Ghobrial et al., 2005). The family has many members including MCL-1, NR-B, BAX, BAD, BIM, BCL-XL, etc. Most members of BCL2 family have two structural homology regions, which play an important role in mediating the dimerization process (Radha and Raghavan, 2017). BAX is an important proapoptotic proteins, and BCL2 is a crucial proapoptotic protein. The ratio of BCL2/BAX can reflect apoptotic activity (Qiao and Wong, 2009). BCL2 can inhibit this process by suppressing the translocation of BAX, decreased the activity of the caspases (Huang et al., 2016). Caspase 3 is type of proteinase. When caspase 3 is activated, it can require proteolytic processing its inactive zymogen into activated p17 and p12 fragments, to play a central role in the execution-phase of cell apoptosis (Nagata, 2018). Flow cytometry showed that the apoptosis level of MOF-knockdown stable cells was significantly increased. What's more, the apoptosis-promoting protein BCL2 was up-regulated, and BAX which could inhibit apoptosis was

down-regulated. Total expression of caspase 3 changed inapparently, but the p17-caspase 3 was obviously up-regulated. However, studies have shown that MOF also plays an important role in autophagy (Füllgrabe et al., 2017), so further research is needed on the effects of excluding autophagy in apoptotic cells.

In order to explore the mechanism of MOF as an oncogene in thyroid cancer, we searched the TCGA database for genes that were positively related to MOF, and annotated the molecular functions of these genes based on the GEO database. We found protein serine/threonine/tyrosine kinase activity was related to MOF. According to that MOF is a well-known transcriptional coactivator for regulating the expression of target genes (Yang et al., 2018), we attempted to confirm that TNK2, DYK1B and MAP2K2 may be a target of MOF at the transcriptional regulation in thyroid cancer. Therefore, ChIP research was performed in BHP-10-3 and TT2609 cell lines, demonstrating that MOF binds to the promoter region of TNK2, thereby directly regulating the transcriptional expression of TNK2. Based on the above results, the downstream signaling pathway PI3K/AKT was further explored. The protein expression of TNK2 and p-AKT were significantly up-regulated in BHP-10-3 and TT2609 cell line compared to normal thyroid cell lines N-thy-ori. Given that TNK2 could directly phosphorylate AKT to activate the PI3K/AKT pathway (Datta et al., 1997), we detected the expression of TNK2 and p-AKT in knock-down MOF cell lines. The TNK2 expression was significantly down-regulated, resulting in a decrease in the level of p-AKT with MOF. Treatment of BHP-10-3 and TT2609 with histone acetyltransferase inhibitor MG149 showed similar results with that knocking down MOF, further illustrating the possibility of MOF as a target in treatment of thyroid cancer. To sum up, our results revealed that MOF could bind to TNK2 promoter which activated the PI3K/AKT pathway, highlighting the extensive significance of MOF on tumor development and treatment.

This study revealed that MOF played a role in thyroid cancer as an oncogene and promoted the development of tumor. However, knocking down MOF in thyroid cancer cell lines only unilaterally verified the changes in proliferation and apoptosis of thyroid cancer cells. Whether overexpression of MOF in thyroid cancer cell lines can accelerate the development of thyroid cancer requires further verification. The research was studied *in vitro*, and further research *in vivo* is needed, such as animal experiments and even clinical trials. It has been reported that VEGFR inhibitors have become the most commonly molecular targeted therapeutic drugs for clinical treatment of differentiated thyroid cancer, which can effectively reduce tumor cell proliferation and angiogenesis (Schlumberger et al., 2015), but are prone to certain side effects and resistance (Cabanillas et al., 2017). Considering our result, the inhibitor of MOF combining with VEGFR inhibitor in treatment of thyroid cancer may reduce the cell proliferation ability and accelerate the apoptosis of cancer cells, leading to less side effect, which also needs further study.

No research provided complete information on roles of MOF in thyroid tumorigenesis and tumor progression. In



summary, our study found that histone acetyltransferase MOF is up-regulated in most thyroid cancers, revealing that MOF plays an important role in the proliferation and apoptosis of thyroid cancer cells. This effect is based on the direct transcriptional activation of TNK2 by MOF and change of downstream PI3K/AKT signaling pathway. Increased MOF expression may be a key event in thyroid cancer progression, such that MOF may be regarded as a potential prognostic marker for thyroid cancer.

## DATA AVAILABILITY STATEMENT

The datasets presented in this study can be found in online repositories. The names of the repository/repositories and accession number(s) can be found in the article/**Supplementary Material**.

## ETHICS STATEMENT

The studies involving human participants were reviewed and approved by School of Life Sciences ethics committee, Shandong

University. The patients/participants provided their written informed consent to participate in this study.

## AUTHOR CONTRIBUTIONS

XL designed the experiments. DL performed the experiments. YY and BC helped perform experiments. XG and SG helped analyze datas. MW and MD offered kind advice.

## FUNDING

This study is supported by the National Key R&D Program of China (2016YFE0129200), the National Natural Science Foundation of China (No. 31571321 No. 81800727 and No. 81873632).

## SUPPLEMENTARY MATERIAL

The Supplementary Material for this article can be found online at: <https://www.frontiersin.org/articles/10.3389/fphar.2020.607605/full#supplementary-material>.

## REFERENCES

- Asa, S. L., and Ezzat, S. (2018). The epigenetic landscape of differentiated thyroid cancer. *Mol. Cell. Endocrinol.* 469, 3–10. doi:10.1016/j.mce.2017.07.012
- Avvakumov, N., and Cote, J. (2007). The MYST family of histone acetyltransferases and their intimate links to cancer. *Oncogene* 26 (37), 5395–5407. doi:10.1038/sj.onc.1210608
- Bone, J. R., and Kuroda, M. I. (1996). Dosage compensation regulatory proteins and the evolution of sex chromosomes in *Drosophila*. *Genetics* 144 (2), 705–713.
- Cabanillas, M. E., de Souza, J. A., Geyer, S., Wirth, L. J., Menefee, M. E., Liu, S. V., et al. (2017). Cabozantinib as salvage therapy for patients with tyrosine kinase inhibitor-refractory differentiated thyroid cancer: results of a multicenter phase II international thyroid oncology group trial. *J. Clin. Oncol.* 35 (29), 3315–3321. doi:10.1200/JCO.2017.73.0226
- Cancer Genome Atlas Research Network (2014). Integrated genomic characterization of papillary thyroid carcinoma. *Cell* 159 (3), 676–690. doi:10.1016/j.cell.2014.09.050
- Chen, Z., Ye, X., Tang, N., Shen, S., Li, Z., Niu, X., et al. (2014). The histone acetyltransferase hMOF acetylates Nrf2 and regulates anti-drug responses in human non-small cell lung cancer. *Br. J. Pharmacol.* 171 (13), 3196–3211. doi:10.1111/bph.12661
- Datta, S. R., Dudek, H., Tao, X., Masters, S., Fu, H., Gotoh, Y., et al. (1997). Akt phosphorylation of BAD couples survival signals to the cell-intrinsic death machinery. *Cell* 91 (2), 231–241. doi:10.1016/S0092-8674(00)80405-5
- Deng, X., Berletch, J. B., Ma, W., Nguyen, D. K., Hiatt, J. B., Noble, W. S., et al. (2013). Mammalian X upregulation is associated with enhanced transcription initiation, RNA half-life, and MOF-mediated H4K16 acetylation. *Dev. Cell* 25 (1), 55–68. doi:10.1016/j.devcel.2013.01.028
- Dyda, F., Klein, D. C., and Hickman, A. B. (2000). GCN5-related N-acetyltransferases: a structural overview. *Annu. Rev. Biophys. Biomol. Struct.* 29, 81–103. doi:10.1146/annurev.biophys.29.1.81
- Fan, M., Li, X., Jiang, W., Huang, Y., Li, J., and Wang, Z. (2013). A long non-coding RNA, PTCSC3, as a tumor suppressor and a target of miRNAs in thyroid cancer cells. *Exp. Ther. Med.* 5 (4), 1143–1146. doi:10.3892/etm.2013.933
- Füllgrabe, J., Lynch-Day, M. A., Heldring, N., Li, W., Struijk, R. B., Ma, Q., et al. (2017). Corrigendum: the histone H4 lysine 16 acetyltransferase hMOF regulates the outcome of autophagy. *Nature* 543 (7647), 742. doi:10.1038/nature22027
- Gelbart, M. E., and Kuroda, M. I. (2009). *Drosophila* dosage compensation: a complex voyage to the X chromosome. *Development* 136 (9), 1399–1410. doi:10.1242/dev.029645
- Ghobrial, I. M., Witzig, T. E., and Adjei, A. A. (2005). Targeting apoptosis pathways in cancer therapy. *CA Cancer J. Clin.* 55 (3), 178–194. doi:10.3322/canjclin.55.3.178
- Goel, S., DeCristo, M. J., Watt, A. C., BrinJones, H., Sceneay, J., Li, B. B., et al. (2017). CDK4/6 inhibition triggers anti-tumour immunity. *Nature* 548 (7668), 471–475. doi:10.1038/nature23465
- Hou, P., Ji, M., and Xing, M. (2008). Association of PTEN gene methylation with genetic alterations in the phosphatidylinositol 3-kinase/AKT signaling pathway in thyroid tumors. *Cancer* 113 (9), 2440–2447. doi:10.1002/cncr.23869
- Huang, F., Huang, M., Zhang, H., Zhang, C., Zhang, D., and Zhou, G. (2016). Changes in apoptotic factors and caspase activation pathways during the postmortem aging of beef muscle. *Food Chem.* 190, 110–114. doi:10.1016/j.foodchem.2015.05.056
- Jones, P. A., and Martienssen, R. (2005). A blueprint for a human epigenome project: the AACR human epigenome workshop. *Cancer Res.* 65 (24), 11241–11246. doi:10.1158/0008-5472.CAN-05-3865
- Kouzarides, T. (2007). Chromatin modifications and their function. *Cell* 128 (4), 693–705. doi:10.1016/j.cell.2007.02.005
- Li, X., Li, L., Pandey, R., Byun, J. S., Gardner, K., Qin, Z., et al. (2012). The histone acetyltransferase MOF is a key regulator of the embryonic stem cell core transcriptional network. *Cell Stem Cell* 11 (2), 163–178. doi:10.1016/j.stem.2012.04.023
- Li, X., Wu, L., Corsa, C. A., Kunkel, S., and Dou, Y. (2009). Two mammalian MOF complexes regulate transcription activation by distinct mechanisms. *Mol. Cell* 36 (2), 290–301. doi:10.1016/j.molcel.2009.07.031
- Mahajan, K., and Mahajan, N. P. (2015). ACK1/TNK2 tyrosine kinase: molecular signaling and evolving role in cancers. *Oncogene* 34 (32), 4162–4167. doi:10.1038/onc.2014.350
- Morales, V., Straub, T., Neumann, M. F., Mengus, G., Akhtar, A., and Becker, P. B. (2004). Functional integration of the histone acetyltransferase MOF into the dosage compensation complex. *EMBO J.* 23 (11), 2258–2268. doi:10.1038/sj.emboj.7600235
- Nagata, S. (2018). Apoptosis and clearance of apoptotic cells. *Annu. Rev. Immunol.* 36, 489–517. doi:10.1146/annurev-immunol-042617-053010

- Noureen, N., Rashid, H., and Kalsoom, S. (2010). Identification of type-specific anticancer histone deacetylase inhibitors: road to success. *Cancer Chemother. Pharmacol.* 66 (4), 625–633. doi:10.1007/s00280-010-1324-y
- Pan, Y., Liu, G., Zhou, F., Su, B., and Li, Y. (2018). DNA methylation profiles in cancer diagnosis and therapeutics. *Clin. Exp. Med.* 18 (1), 1–14. doi:10.1007/s10238-017-0467-0
- Qiao, L., and Wong, B. C. Y. (2009). Targeting apoptosis as an approach for gastrointestinal cancer therapy. *Drug Resist. Updat.* 12 (3), 55–64. doi:10.1016/j.drug.2009.02.002
- Qie, S., and Diehl, J. A. (2016). Cyclin D1, cancer progression, and opportunities in cancer treatment. *J. Mol. Med.* 94 (12), 1313–1326. doi:10.1007/s00109-016-1475-3
- Radha, G., and Raghavan, S. C. (2017). BCL2: a promising cancer therapeutic target. *Biochim. Biophys. Acta Rev. Cancer* 1868 (1), 309–314. doi:10.1016/j.bbcan.2017.06.004
- Schlumberger, M., Tahara, M., Wirth, L. J., Robinson, B., Brose, M. S., Elisei, R., et al. (2015). Lenvatinib versus placebo in radioiodine-refractory thyroid cancer. *N. Engl. J. Med.* 372 (7), 621–630. doi:10.1056/NEJMoa1406470
- Sharma, G. G., So, S., Gupta, A., Kumar, R., Cayrou, C., Avvakumov, N., et al. (2010). MOF and histone H4 acetylation at lysine 16 are critical for DNA damage response and double-strand break repair. *Mol. Cell. Biol.* 30 (14), 3582–3595. doi:10.1128/MCB.01476-09
- Sheikh, B. N., Bechtel-Walz, W., Lucci, J., Karpiuk, O., Hild, I., Hartleben, B., et al. (2016). MOF maintains transcriptional programs regulating cellular stress response. *Oncogene* 35 (21), 2698–2710. doi:10.1038/onc.2015.335
- Sherman, E. J., Su, Y. B., Lyall, A., Schoder, H., Fury, M. G., Ghossein, R. A., et al. (2013). Evaluation of romidepsin for clinical activity and radioactive iodine reuptake in radioactive iodine-refractory thyroid carcinoma. *Thyroid* 23 (5), 593–599. doi:10.1089/thy.2012.0393
- Thomas, L., Lai, S. Y., Dong, W., Feng, L., Dadu, R., Regone, R. M., et al. (2014). Sorafenib in metastatic thyroid cancer: a systematic review. *Oncologist* 19 (3), 251–258. doi:10.1634/theoncologist.2013-0362
- Valerio, D. G., Xu, H., Chen, C.-W., Hoshii, T., Eisold, M. E., Delaney, C., et al. (2017). Histone acetyltransferase activity of MOF is required for leukemogenesis. *Cancer Res.* 77 (7), 1753–1762. doi:10.1158/0008-5472.CAN-16-2374
- Verma, M., Rogers, S., Divi, R. L., Schully, S. D., Nelson, S., Joseph Su, L., et al. (2014). Epigenetic research in cancer epidemiology: trends, opportunities, and challenges. *Cancer Epidemiol. Biomarkers Prev.* 23 (2), 223–233. doi:10.1158/1055-9965.EPI-13-0573
- Vu-Phan, D., and Koenig, R. J. (2014). Genetics and epigenetics of sporadic thyroid cancer. *Mol. Cell. Endocrinol.* 386 (1–2), 55–66. doi:10.1016/j.mce.2013.07.030
- Xing, M. (2013). Molecular pathogenesis and mechanisms of thyroid cancer. *Nat. Rev. Cancer* 13 (3), 184–199. doi:10.1038/nrc3431
- Yang, Y., Guan, J., Shaikh, A. S., Liang, Y., Sun, L., Wang, M., et al. (2018). Histone acetyltransferase Mof affects the progression of DSS-induced colitis. *Cell. Physiol. Biochem.* 47 (5), 2159–2169. doi:10.1159/000491527
- Yang, Y., Han, X., He, J., Guo, X., Shaikh, A. S., Sun, L., et al. (2017). The histone acetyltransferase MOF is required for the cellular stress response. *Sci. Bull.* 62 (23), 1559–1561. doi:10.1016/j.scib.2017.11.012

**Conflict of Interest:** The authors declare that the research was conducted in the absence of any commercial or financial relationships that could be construed as a potential conflict of interest.

Copyright © 2020 Li, Yang, Chen, Guo, Gao, Wang, Duan and Li. This is an open-access article distributed under the terms of the Creative Commons Attribution License (CC BY). The use, distribution or reproduction in other forums is permitted, provided the original author(s) and the copyright owner(s) are credited and that the original publication in this journal is cited, in accordance with accepted academic practice. No use, distribution or reproduction is permitted which does not comply with these terms.



# TRPM7 Induces Tumorigenesis and Stemness Through Notch Activation in Glioma

Jingwei Wan<sup>1,2</sup>, Alyssa Aihui Guo<sup>3</sup>, Pendelton King<sup>1</sup>, Shanchun Guo<sup>4</sup>, Talib Saafir<sup>5</sup>, Yugang Jiang<sup>2</sup> and Mingli Liu<sup>1\*</sup>

<sup>1</sup>Department of Microbiology, Biochemistry and Immunology, Morehouse School of Medicine, Atlanta, GA, United States,

<sup>2</sup>Department of Neurosurgery, The Second Xiangya Hospital, Central South University, Changsha, China, <sup>3</sup>University of South Carolina SOM Greenville, Greenville, SC, United States, <sup>4</sup>Department of Chemistry, Xavier University, New Orleans, LA, United States, <sup>5</sup>Neuroscience Institute, Morehouse School of Medicine, Atlanta, GA, United States

We have reported that transient receptor potential melastatin-related 7 (TRPM7) regulates glioma stem cells (GSC) growth and proliferation through Notch, STAT3-ALDH1, and CD133 signaling pathways. In this study, we determined the major contributor(s) to TRPM7 mediated glioma stemness by further deciphering each individual Notch signaling. We first determined whether TRPM7 is an oncotarget in glioblastoma multiforme (GBM) using the Oncomine database. Next, we determined whether TRPM7 silencing by siRNA TRPM7 (siTRPM7) induces cell growth arrest or apoptosis to reduce glioma cell proliferation using cell cycle analysis and annexin V staining assay. We then examined the correlations between the expression of TRPM7 and Notch signaling activity as well as the expression of GSC markers CD133 and ALDH1 in GBM by downregulating TRPM7 through siTRPM7 or upregulating TRPM7 through overexpression of human TRPM7 (M7-wt). To distinguish the different function of channel and kinase domain of TRPM7, we further determined how the  $\alpha$ -kinase-dead mutants of TRPM7 ( $\alpha$ -kinase domain deleted/M7-DK and K1648R point mutation/M7-KR) affect Notch activities and CD133 and ALDH1 expression. Lastly, we determined the changes in TRPM7-mediated regulation of glioma cell growth/proliferation, cell cycle, and apoptosis by targeting Notch1. The Oncomine data revealed a significant increase in TRPM7 mRNA expression in anaplastic astrocytoma, diffuse astrocytoma, and GBM patients compared to that in normal brain tissues. TRPM7 silencing reduced glioma cell growth by inhibiting cell entry into S and G2/M phases and promoting cell apoptosis. TRPM7 expression in GBM cells was found to be positively correlated with Notch1 signaling activity and CD133 and ALDH1 expression; briefly, downregulation of TRPM7 by siTRPM7 decreased Notch1 signaling whereas upregulation of TRPM7 increased Notch1 signaling. Interestingly, kinase-inactive mutants (M7-DK and M7-KR) resulted in reduced activation of Notch1 signaling and decreased expression of CD133 and ALDH1 compared to that of wtTRPM7. Finally, targeting Notch1 effectively suppressed TRPM7-induced growth and proliferation of glioma cells through cell G1/S arrest and apoptotic induction. TRPM7 is responsible for sustained Notch1 signaling activation, enhanced expression of GSC markers CD133 and ALDH1, and regulation of glioma stemness, which contributes to malignant glioma cell growth and invasion.

**Keywords:** TRPM7, glioma, CD133, Aldehyde dehydrogenase 1, molecular targets, cell cycle, apoptosis

## OPEN ACCESS

### Edited by:

Dong-Hua Yang,  
St. John's University, United States

### Reviewed by:

Giorgio Santoni,  
University of Camerino, Italy  
Rafael Roesler,  
Federal University of Rio Grande do  
Sul, Brazil

### \*Correspondence:

Mingli Liu  
mliu@msm.edu

### Specialty section:

This article was submitted to  
Experimental Pharmacology  
and Drug Discovery,  
a section of the journal  
Frontiers in Pharmacology

**Received:** 02 August 2020

**Accepted:** 19 October 2020

**Published:** 14 December 2020

### Citation:

Wan J, Guo AA, King P, Guo S,  
Saafir T, Jiang Y and Liu M (2020)  
TRPM7 Induces Tumorigenesis and  
Stemness Through Notch  
Activation in Glioma.  
Front. Pharmacol. 11:590723.  
doi: 10.3389/fphar.2020.590723

## INTRODUCTION

GBMs are the most malignant tumors of the central nervous system (CNS) in humans and have an extremely poor prognosis (Sander et al., 2017). The current standard of care for GBM patients includes surgical resection followed by adjuvant radiation therapy and chemotherapy with temozolomide (TMZ), an oral alkylating agent. Chemotherapy with TMZ may suppress tumor growth for a certain period of time; however, invariable tumor recurrence remains virtually inevitable, and most patients ultimately succumb to the disease (Melamed et al., 2018). Accumulating evidence shows that the failure of glioblastoma to current chemo- and radiotherapies and the high tumor recurrence rate are attributed to the presence of a small subpopulation of glioma stem cells (GSC), which is characterized by their stem cell-like properties and aggressive behaviors (Maher et al., 2001). Although controversy remains on the details about the precise GSC identity (Dirks, 2010; Aliferis and Trafalis, 2015), the existence of GSC is widely accepted. GSCs are a small subset of CD133+, and ALDH1+ cells with self-renewal properties and are capable of initiating new tumors, contributing to glioma progression (Lucena-Cacace et al., 2019). CD133+ cells, characterized by high telomerase activities (a sign of stem cell activity) (Ludwig and Kornblum, 2017), have been used as a molecular biomarker for GSC (Cheng et al., 2009; Brown et al., 2017; Lu et al., 2018); the proportion of CD133+ cells is an independent risk factor for tumor growth and time to malignant progression (Zeppernick et al., 2008). Aldehyde dehydrogenase 1 (ALDH1), another functional marker of cancer stem cells (CSC) (Ludwig and Kornblum, 2017), is a cytosolic protein that oxidizes aldehydes to carboxylic acid, and its high activity may contribute to stem cell maintenance. ALDH1 expression in astrocytoma is correlated with a high WHO grade of gliomas and predicts a worse prognosis in glioma patients (Liu et al., 2012; Sullivan et al., 2017; Wang et al., 2017). Because GSCs share neural precursor markers with neural stem cells (NSCs), glioma's high heterogeneity is greatly attribute to the current treatment failures against malignant glioma (Vescovi et al., 2006; Aliferis and Trafalis, 2015).

Notch signaling is highly active in GSCs, inhibits differentiation, maintains stem-like properties, and, therefore, is responsible for glioblastoma tumorigenesis (Bazzoni and Bentivegna, 2019). The Notch system in vertebrates is comprised of four receptors (Notch1–Notch4) and at least five ligands from the families Delta and JAG/Serrate (DSL): JAG1, JAG2, Delta-like (Dll)-1, Dll-3, and Dll-4 (Artavanis-Tsakonas et al., 1999; Miele, 2006; Miele et al., 2006). Notch receptors are activated in gliomas, and their oncogenicity has been confirmed by gain- and loss-of-function studies *in vitro* and *in vivo* (Teodorczyk and Schmidt, 2014). Notch signaling is not only central to the normal development of the CNS, but plays important roles in the proliferation, differentiation, apoptosis, and regulation of GSC. Notch signaling is also involved in regulating responses to hypoxia and angiogenesis, which are typical features for tumors, specifically GBM (Hovinga et al., 2010; Qiang et al., 2012; Stockhausen et al., 2012).

TRPM7 is a non-specific divalent cation channel fused with a functional serine/threonine-protein kinase domain at its C-terminus (Gautier et al., 2016). Physiologically, the TRPM7 channel contributes to calcium, magnesium, and zinc homeostasis, cell survival, gastrulation (Gautier et al., 2016), thymopoiesis, and embryonic development (Jin et al., 2008; Jin et al., 2012; Duan et al., 2018). Pathologically, TRPM7 overexpression is involved in malignancies (Gautier et al., 2016), neuronal death (Asrar and Aarts, 2013), and cardio fibrosis (Yue et al., 2013). The mechanisms by which TRPM7 facilitates the viability of tumor cells vary. TRPM7 is found to interrupt the cell cycle distribution and cell apoptosis in breast and bladder cancer (Cao et al., 2016; Liu et al., 2020), and deregulates senescence in hepatocellular carcinoma (Voring et al., 2019). The TRPM7 kinase domain is cleaved by caspases (Desai et al., 2012; Krapivinsky et al., 2014) and participates in Fas-induced apoptosis (Desai et al., 2012). Given its multifaced function, TRPM7 has been recognized to be a promising drug target. A set of small organic modulators of TRPM7 either activating or inhibiting the TRPM7 channel, or regulating the kinase activity have been identified, and these potential drugs could lay strong foundations for the development of high-affinity *in vivo* drugs targeting TRPM7 (Chubanov et al., 2017).

Our previous report showed that in human glioma cells, TRPM7 expression is upregulated, required for proliferation, migration, and invasion (Liu et al., 2014; Leng et al., 2015), and mediated by multiple mechanisms through Notch, STAT3-ALDH1, and CD133 signaling pathways. In the current study, we further determined the specific component of Notch signaling that is critical in response to altered TRPM7 expression and results in the expression of GSC markers and treatment failure of current chemo- and radiotherapies against glioma.

## MATERIAL AND METHODS

### Antibody and Reagents

The following primary antibodies were used in this study. Rabbit polyclonal anti-TRPM7 (cat no. ab232455) and rabbit polyclonal Notch3 (cat no. ab60087) were purchased from Abcam (Cambridge, MA). Mouse monoclonal Notch1 antibody (cat no. N6786) and rabbit polyclonal Hey2 antibody (cat no. PA5-67647) were purchased from Invitrogen (Waltham, MA). Rabbit monoclonal Notch2 (cat no. 5732), rabbit polyclonal Survivin (cat no. 71 G4B7), and mouse monoclonal anti-HA antibody (cat no. 2367) were purchased from Cell Signaling Technology (Danvers, MA). Rabbit polyclonal Notch4 antibody (cat no. 07-189) and anti- $\beta$ -actin antibody (cat no. A3854) were purchased from Sigma-Aldrich (St. Louis, MO). Rabbit polyclonal CD133 antibody (cat no. NB120-16518) was purchased from Novus Biologicals (Centennial, CO). Rabbit polyclonal ALDH1 was purchased from GeneTex (cat no. GTX123973, Irvine, CA). All secondary antibodies used for Western blot were purchased from Calbiochem (La Jolla, CA).



## Plasmid and siRNA

The wild-type human TRPM7 (wtTRPM7) or constructs in which the  $\alpha$ -kinase domain was deleted ( $\Delta$ kinase) or rendered inactive with a point mutation in the ATP binding site of the  $\alpha$ -kinase domain (K1648R) were provided by Dr. Carsten Schmitz, University of Colorado, Denver, CO. All constructs (wtTRPM7,  $\Delta$ kinase, K1648R) were tagged with a hemagglutinin (HA) at the N-terminal. Control scrambled siRNA (On-TARGETplus Non-targeting siRNA, catalog no. D-001810-01-05) and ON-TARGETplus SMARTpool siRNA (Catalog no. L-005393-000005) targeting TRPM7 were purchased from Dharmacon (Lafayette, CO). Control scrambled siRNA (cat no. sc-37007), and siRNA targeting siNotch1 (cat no. sc-36095) were purchased from Santa Cruz Biotechnology (Santa Cruz, CA). The scrambled siRNAs, with no homology to any known sequence, were used as controls.

## Cell Culture

Human glioblastoma cell lines. A172, was obtained from ATCC (Manassas, VA, USA). Other glioma cell lines, U87MG, U373MG, and SNB19, were kindly provided by Dr. Yancey G. Gillespie at the University of Alabama at Birmingham (UAB), Birmingham, AL. Dr. Hui-Kuo Shu at Emory University, Atlanta, Georgia, kindly provided the human glioblastoma cell line SF767. All cells were cultured in Dulbecco's Modified Eagle's Medium (DMEM, Life Technologies, Waltham, MA) plus 10% fetal bovine serum (FBS), 50 units/ml penicillin, and 50  $\mu$ g/ml streptomycin at 37°C. Human embryonic kidney (HEK293) cells, with inducible expression of human TRPM7 channels (HEK: TRPM7 cells), were cultured in minimal essential medium supplemented with 10% FBS and antibiotics. For TRPM7 induction, cells were treated with 1  $\mu$ g/ml of tetracycline. PDX lines: Tumor tissue cubes stored at liquid nitrogen (provided by Yancey G. Gillespie at UAB) were implanted subcutaneously into the flanks of male or female 6–8 weeks old nude mice under anesthesia (ketamine/Xylazin 90/6 mg/kg Bw). Briefly, cryopreserved tumor tissues were thawed at 37°C and washed with PBS before subcutaneous implantation. To prepare single-cell suspension of viable tumor cells, the xenograft tumor tissues were harvested and minced with scalpel blades followed by passing through cell strainers. The cells were then grown in DMEM/F-12 media plus 10% FBS, 50 units/ml penicillin, and 50  $\mu$ g/ml streptomycin for future use.

Enrichment for glioma stem cells: For tumorsphere culture, glioma cell lines cultured in growth media were grown to confluence, dissociated using 0.1% trypsin, and dispersed by pipetting with a 23-gauge needle. After checking for a single cell, the cells were pelleted and suspended in sphere enrichment medium, specifically in human neurobasal medium supplemented with B27, 20 ng/ml EGF and 20 ng/ml FGF-2 (Invitrogen, Carlsbad, CA), and 5  $\mu$ g/ml heparin (Sigma-Aldrich, St. Louis, MO). These cells were then plated in ultralow attachment surface tissue culture plates (Corning). Following overnight incubation at 37°C with 5% CO<sub>2</sub>, the distinct non-adherent human glioma stem cells were apparent in culture. These spheres were collected, gently centrifuged at low speed (1,000 rpm), passaged, and maintained for growth in the sphere enrichment medium for future use.

## Transfection of siRNA and DNA Constructs

When the glioblastoma cells grew to reach about 50–75% confluency, the appropriate amount of siRNAs specific to TRPM7, Notch1, and control scrambled siRNA with a final concentration of 100 nM, were transfected using Lipofectamine RNAiMAX reagent in serum-free OptiMEM-1 medium (Invitrogen, Carlsbad, CA) according to the manufacturer's instruction. After 6 h of transfection, cells were grown in DMEM containing 10% FBS further for 72 h as indicated in each experiment. 48 or 72 h post-transfection target knockdowns were assessed by RT-PCR or Western blot, respectively. Various glioma cells at 50–75% confluency were transfected with a pcDNA4/TO plasmid that allowed protein expression of wt hTRPM7 or hTRPM7  $\alpha$ -kinase inactive mutants by lipofectamine 3,000 transfection reagent (Invitrogen, Carlsbad, CA) according to the manufacturer's instruction. The transiently transfected glioma cells expressing wt hTRPM7 (M7-wt),  $\Delta$ kinase (M7-DK), and K164R hTRPM7 (M7-KR) constructs were maintained in DMEM containing 10% FBS (Schmitz et al., 2003; Perraud et al., 2011) for further growth for 72 h. The overexpression of TRPM7 and its mutants was assessed by HA expression. All studies were done in triplicates.

## MTT Assay

All glioma cells were seeded at  $1 \times 10^4$  cells in 100  $\mu$ l of medium per well into 96-well plates and were transfected with 100 nM specific siRNA or control using Lipofectamine reagents for the indicated times. 10  $\mu$ l of 3-(4,5-dimethylthiazol-2-yl)-2,5-diphenyltetrazolium bromide (MTT) reagent (Sigma-Aldrich, St. Louis, MO, the ratio of MTT reagent to the medium is 1:10) was added into each well and incubated in the dark at 37°C for 2–4 h. Absorbance at 570 nm was measured using 690 nm as the reference using the CytoFluorTM 2300 plate reader.

## Western Blotting

Cells were lysed with lysis buffer (50 mM HEPES, 150 mM NaCl, 1.5 mM MgCl<sub>2</sub>, 1 mM EGTA, 10% glycerol, 1% Nonidet P-40, 100 mM NaF, 10 mM sodium pyrophosphate, 0.2 mM sodium orthovanadate, 1 mM phenylmethylsulfonyl fluoride, 10  $\mu$ g/ml aprotinin, and 10  $\mu$ g/ml leupeptin). SDS/PAGE separated samples, and separated proteins were transferred to nitrocellulose membranes and identified by immunoblotting. Primary antibodies were obtained from commercial sources and were diluted at the ratio of 1:1,000 according to manufacturer's instruction. Blots were developed with Supersignal Pico or Femto substrate (Pierce). Densitometric analysis of the bands was performed with the ImageQuant program (Bio-Rad).

## Flow Cytometry

Cell cycle analysis and apoptosis assay:  $1 \times 10^6$  cells were harvested, fixed in ice-cold 70% ethanol, and resuspended in PBS for 1 min. After centrifuge at  $450 \times g$  for 5 min with the brake on low at room temperature, the cells were resuspended in 200  $\mu$ l Guava Cell Cycle Reagent (cat no. 4500-0220, Luminex, Austin, TX) and incubated at room temperature for 30 min while shielded from the light. All samples were transferred to 96-well microplate plates with round bottom and acquired on a Guava easyCyte 8HT Base System (Luminex). The percentage of cells in G0/G1, S, and G2/M phases was determined from the



DNA content using guavaSoft 3.1.1. The apoptotic glioma cells were detected by flow cytometry using Annexin V-PE and 7-AAD. The staining procedure was conducted with a Guava Nexin Reagent kit (cat no. 4500-0455, Luminex) according to the manufacturer's protocol. Briefly, after desired treatments, cells were collected and resuspended in 100  $\mu$ l of 1% FBS (Cell concentration should be between  $2 \times 10^5$  and  $1 \times 10^6$  cell/ml) followed by incubation with the 100  $\mu$ l of Guava Nexin Reagent for 20 min at room temperature in the dark. The samples were then acquired on a Guava easyCyte 8HT Base System, which was used to detect apoptotic cells. Data were analyzed using InCyte software. CD133: To evaluate CD133 expression by flow cytometry, cells were harvested, washed with Cell Staining Buffer (cat no. 420201, Biolegend, San Diego, CA), and then incubated with PE-anti-human CD133 antibody (cat no. 372803, Biolegend, San Diego, CA) for 15–20 min on ice in the dark. Cells were then washed and suspended in Cell Staining Buffer for analysis. The data acquired on a Guava easyCyte 8HT Base System were analyzed using the InCyte software. Aldefluor assay: ALDH1 enzymatic activity was measured using the Aldefluor kit (cat no. 01700, Stem Cell Technologies). Cells suspended in the aldefluor assay buffer were incubated with ALDH enzyme substrate, BODIPY-aminoacetaldehyde (BAAA), for 30–60 min at 37°C. As a control for baseline fluorescence, cells were also treated with the ALDH inhibitor, diethylaminobenzaldehyde (DEAB). Fluorescence was detected using a Guava easyCyte 8HT Base System and analyzed using the InCyte software. Statistical significance was determined by the Student's test or one-way ANOVA tests.

## Bioinformatics Analysis

The expression of TRPM7 transcript in brain normal and tumor tissues were obtained from Sun brain samples from Oncomine (<https://www.oncomine.org/>). Statistical analysis of differences was performed using Oncomine algorithms for accounting the multiple comparisons among different studies similar to a meta-analysis.

## Statistical Analysis

The results obtained in this work were expressed as mean  $\pm$  S.D. of at least three independent experiments done in triplicate. Paired Student t-test or one-way ANOVA tests were performed for data analysis, and a significant difference was defined as  $p < 0.05$ .

## RESULTS

### Targeting Transient Receptor Potential Melastatin-Related 7, an Oncotarget in Glioblastoma Multiforme, Suppresses the Growth and Proliferation Through the G1/S Arrest of the Cell Cycle and Promotes the Induction of Apoptosis of Glioma Cells

(1) TRPM7 mRNA is highly expressed in GBM patients compared to that in normal controls, which indicates that

TRPM7 is an oncotarget in GBM. TRPM7 is ubiquitously expressed in all mammalian cells (Penner and Fleig, 2007; Bates-Withers et al., 2011; Runnels, 2011; Paravicini et al., 2012) and is necessary for cell survival, growth, and migration (Jin et al., 2012). Change in TRPM7 expression has been associated to cancers. (Zhou et al., 2014; Yee, 2017). Increasing evidence shows that TRPM7 plays a critical role in tumor cell proliferation and invasion (Prevarskaya et al., 2010), suggesting that TRPM7 could be a therapeutic target in human malignancies (Kim et al., 2008; Yee et al., 2012; Chen et al., 2015; Huang et al., 2017; Rybarczyk et al., 2017). Among brain tumors, our research group pioneered TRPM7's oncogenic function in glioma proliferation, invasion (Wan et al., 2019), and glioma stemness (Liu et al., 2014). To further explore whether or not TRPM7 can be a potential drug target in malignant glioma, we analyzed TRPM7 expression in publicly available glioma microarray studies using the Oncomine database and gene microarray data analysis tool (Rhodes et al., 2004a; Rhodes et al., 2004b). A meta-analysis of microarray gene expression data sets related to human cancer genes revealed that TRPM7 mRNA is highly expressed in glioma patients' tumor tissues compared to that in normal brain tissues (**Figure 1A**). Meta-analysis from published database demonstrated that TRPM7 expression is significantly increased in anaplastic astrocytoma patients ( $t$ -test: 1.928;  $p$ -value: 0.031;  $n = 19$ ; **Figure 1B**), diffuse astrocytoma patients ( $t$ -test: 2.011;  $p$ -value: 0.040;  $n = 7$ ; **Figure 1C**), and glioblastoma patients ( $t$ -test: 3.368;  $P$ -value: 7.72E-4;  $n = 8$ ; **Figure 1D**) compared to that of normal brain controls ( $n = 23$ ). Fifty cases of oligodendroglioma patients were also evaluated using the same Oncomine research platform, and the results showed that TRPM7 mRNA expression is increased but did not reach statistical difference compared to that of the control ( $t$ -test: 1.401;  $P$ -value: 0.084;  $n = 50$ ; **Figure 1E**). These data indicate that TRPM7 mRNA is upregulated in glioma, including GBM patients, and suggests that TRPM7 is an oncotarget in GBM patients.

(2) Targeting TRPM7 suppresses the growth and proliferation of glioma cells through G1/S arrest and the induction of apoptosis. Our previous studies revealed that TRPM7 plays a vital role in glioma cell proliferation (Liu et al., 2014; Wan et al., 2019). To gain further insight into the role of TRPM7 in supporting proliferation, we then investigated whether or not the inhibition of cell proliferation by small interfering RNA against TRPM7 (siTRPM7) could deregulate cell cycle distribution. A172 and U87MG cells were treated with 100 nM of siTRPM7 and corresponding controls for 72 h, followed by flow cytometric cell cycle analysis. The percentage of cells in G0/G1, S, and G2/M phases was determined based on DNA content. The representative histograms and bar graphs of **Figure 2A** show that siTRPM7 significantly changed cell distribution of the cell cycle and is reflected by decreased percentage of cells in S phase (30.9–23.5%) and G2/M phase cells (20.2–13.7%) and concomitantly increased percentage of cells in G0/G1 phase (48.9–62.8%) compared

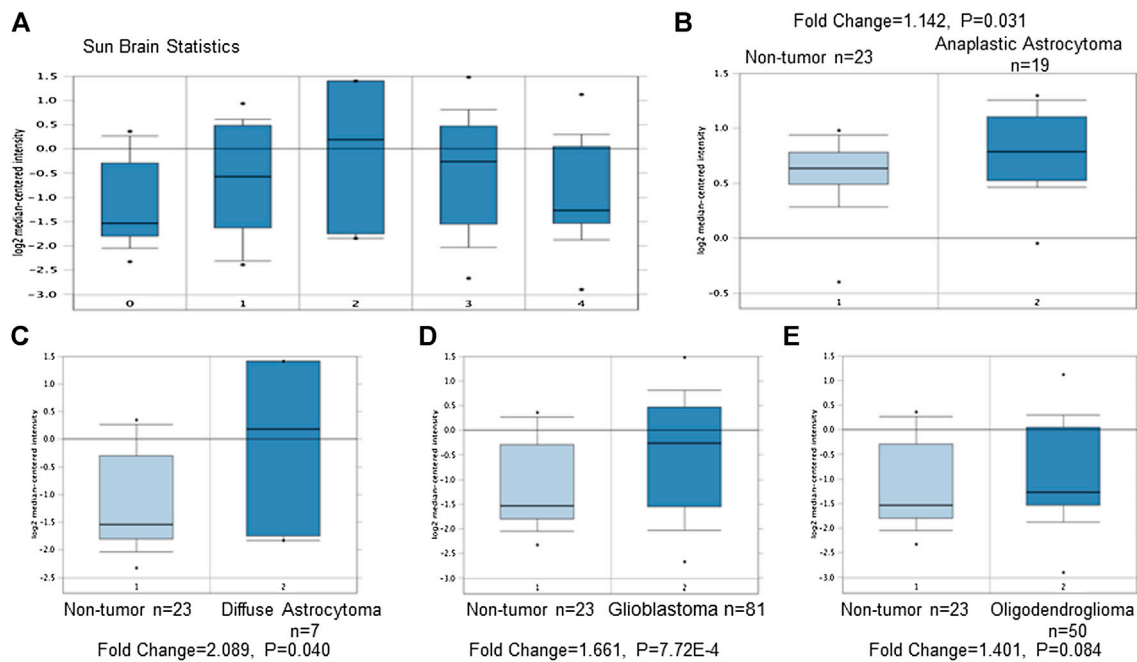
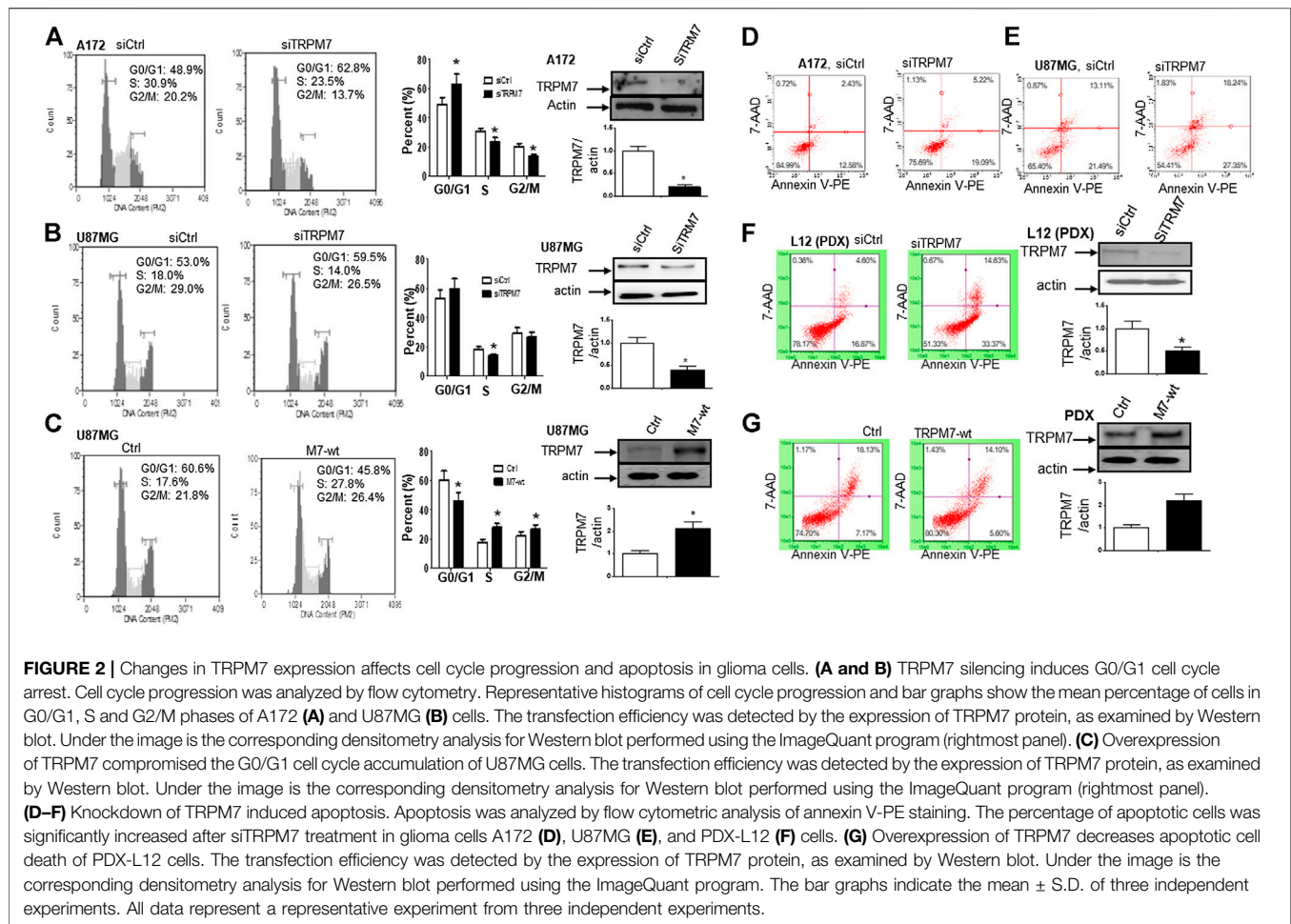


**FIGURE 1 |** TRPM7 expression increases in glioma patients compared to that of healthy brain tissues. Meta-analysis was performed using the Oncomine Research Platform-based microarray studies. **(A)** A general overview of microarray analysis of normal brain tissues (0) and anaplastic astrocytoma (1), diffuse astrocytoma (2), glioblastoma (3), and oligodendroglioma (4). **(B–D)** In detail, microarray analysis of 23 normal brain tissues and 19 anaplastic astrocytomas **(B)**, seven diffuse astrocytomas **(C)**, 81 glioblastomas **(D)**, and 50 oligodendrogliomas **(E)**.

to that of the control. The undetectable TRPM7 protein by Western blot provide confirmative evidence that TRPM7 was effectively silenced by siTRPM7 (**Figure 2A**, rightmost panel). Similarly, in U87MG cells, siTRPM7 treatment significantly decreased the percentage of cells in S phase from 18.0 to 14.0% and G2/M phase from 29.0 to 26.5%, while increased G0/G1 phase cells from 53.0 to 59.5% (**Figure 2B**, the histograms and the bar graphs). The transfection efficiency of siTRPM7 into U87MG is shown on the rightmost panel of **Figure 2B**. In parallel, we transfected 5  $\mu$ g of wild-type TRPM7 constructs (M7-wt) into U87MG cells for 72 h to increase the expression levels of TRPM7. As a result, overexpressed TRPM7 significantly enhanced the percentage of cells in S phase from 17.6 to 27.8% and in G2/M phase from 21.8 to 26.4%, as well as decreased G0/G1 phase cells from 60.6 to 45.8% (**Figure 2C**, histograms and bar graphs). The high transfection efficiency was confirmed by increased TRPM7 protein expression detected by Western blot (**Figure 2C**, rightmost panel). The results indicate that TRPM7 downregulation causes an accumulation of GBM cells in the G0/G1 phase of the cell cycle, and TRPM7 overexpression specifically compromised G0/G1 cell cycle accumulation. Therefore, the functional studies using flow cytometry suggest that TRPM7 is an oncotarget in GBM as well. TRPM7 knockdown-induced suppression of the growth and proliferation of glioma cells could be through G1/S arrest and the inhibition of the tumor cell entry into S and G2/M phase.

The balance between the factors of cell division, cell cycle arrest, differentiation, and apoptosis determines the potential of cell growth and proliferation. Anti-apoptosis is a common mechanism of tumor progression. To further investigate the underlying mechanism in glioma cells with TRPM7 knockdown by TRPM7 siRNA that undergoes a failure of growth, we determined if the apoptotic process is involved in GBM cells when treated with TRPM7 siRNA and employed in an apoptosis assay. Briefly, glioma cells transfected with siTRPM7 for 72 h were stained with annexin V and 7-AAD and subjected to Annexin-FACS to detect apoptotic cell death. The degree of early and late apoptosis was detected as the percentage of cells positive for annexin V-PE without or with 7-AAD staining, respectively. Flow cytometric dot plots of A172 and U87MG cell treated with siTRPM7 displayed increased rates of annexin V positive cells, for A172, from 12.58 to 19.09 and 2.43–5.22%, respectively (**Figure 2D**); for U87MG, from 21.49 to 27.35, and 13.11–18.24%, respectively (**Figure 2E**).

The genetic difference of *in vitro* cell lines only partially mirrors the diversity of individual patient tumors. Due to the limitation of cell lines, the patient-derived xenografts (PDXs) have been widely used because they closely resemble the patient tumors from which they were acquired. PDXs are characterized and classified into four GBM molecular subtypes: Neural, Proneural, Classical, and Mesenchymal. We, therefore, determined whether or not silencing of TRPM7-mediated apoptosis in glioma cell lines can be phenocopied to the PDX model. To this end, the cells isolated from animals with amplified glioma Neural subtype (L12) were grown in regular growth medium and then transfected with either siTRPM7 to

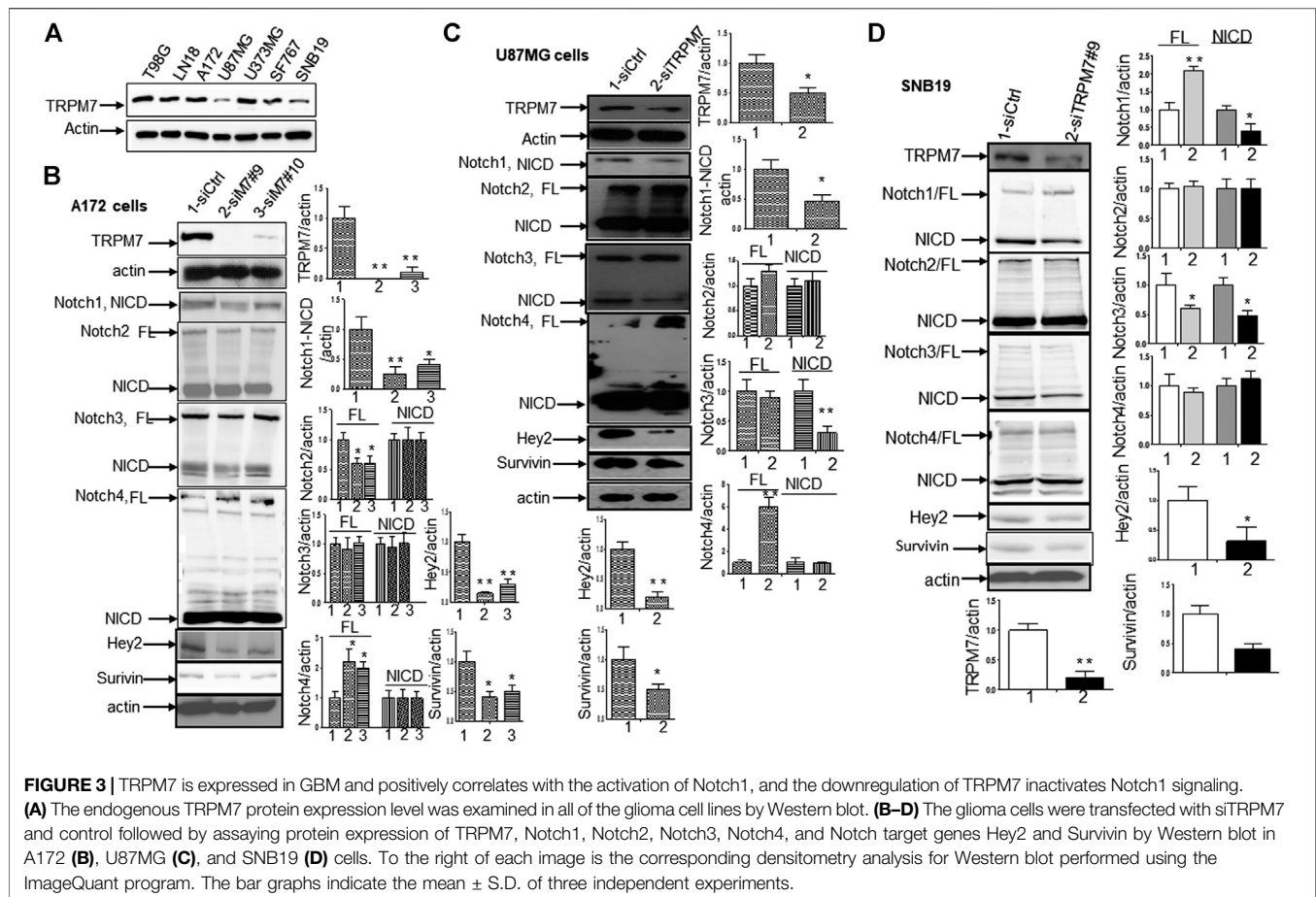


knock down or M7-wt to overexpress the TRPM7 protein. The results clearly show similar patterns as those in A172 and U87MG. The early and late apoptotic cells were increased from 16.87 to 33.37 and 4.60–14.63%, respectively, by silencing TRPM7 (**Figure 2F**). The reduced TRPM7 protein expression detected by Western blot on the right panel of **Figure 2F** confirmed the high transfection efficiency in these cells. Overexpression of TRPM7 resulted in a remarkable decreased late apoptotic cell from 18.13 to 14.10%, while early-stage apoptotic cells slightly decreased from 7.17 to 5.6%. However, it did not reach a significant difference (**Figure 2G**, the right panel demonstrates that M7-wt significantly increases TRPM7 expression). Our data suggest that the downregulation of TRPM7 suppresses glioma proliferation by G0/G1 phase arrest concomitant with apoptosis induction.

## Molecular Studies Indicate That Transient Receptor Potential Melastatin-Related 7 Is Expressed in Glioblastoma Multiforme and Correlated with the Activation of Notch 1 and Stemness

(1) Inhibition of TRPM7 down-regulates Notch1 signaling. High-grade malignant gliomas are devastating, uniformly

fatal tumors for which no effective therapies currently exist. GBM is the most common and aggressive primary brain tumor. We have reported that in the A172 cell line, TRPM7 channels, a subfamily member of the transient receptor potential (TRP), regulate GSC growth and proliferation through STAT3 and Notch1 signaling pathways (Liu et al., 2014). To further explore the mechanism that TRPM7 regulates Notch signaling pathway in the tumorigenesis of glioma, we examined all Notch receptor expressions in response to TRPM7 silencing in various glioma cell lines. To this end, the different glioma cell lines were transfected with either control siRNA (siCtrl) or TRPM7 siRNA (siTRPM7), followed by assaying the expressions of Notch1, Notch2, Notch3 and Notch 4 in each of the following cell lines: A172, U87MG, SNB19, and U373MG. At the mRNA levels, TRPM7 silencing increases Notch 4 mRNA expression in A172, increases Notch 2 mRNA expression in U87MG, decreases Notch 2, 3, and 4 mRNA expression in SNB19, and increases Notch 3 and Notch 4 mRNA in U373MG (Supplementary Figure 1). At the protein levels, we first determined whether or not TRPM7 protein is expressed in these glioma cell lines. As shown by the Western blot, all glioma cell lines A172,



U87MG, U373MG, SF767, and SNB19, as well as two cell lines resistant to TMZ, T98G, and LN18, express an almost equal amount of TRPM7 with U87MG and SNB19 having slightly lower levels of expression (**Figure 3A**). The data show that in A172 cells, upon TRPM7 downregulation, the active form of Notch1, the intracellular domains of Notch1 (NICD), expression along with Notch1 target genes Hey2 and Survivin were decreased (Notch activity is often measured by the expression levels of its direct target genes). Expression of full length (FL) of Notch2 was found to be decreased, while Notch4 was increased (**Figure 3B**). A172 and U87MG both have wild-type *TP53*, *PTEN* mutations, and *p14<sup>ARF</sup>*/p16 deletion (Ishii et al., 1999). However, U87MG cells express high levels of VEGF as compared to A172 expressing high levels of bFGF. Despite the difference in growth factors secretion, identical expression patterns of Notch signaling pathway activation were observed in U87MG cells compared to the A172; Notch1, Hey2, Survivin, and Notch3 NICD decreased, while the full length of Notch4 increased (**Figure 3C**). SNB19 and U373MG (**Figure 4**) have mutated *PTEN* (Memmel et al., 2014; Chakrabarti and Ray, 2015), and share common origins; however, these two cell lines have evolved to exhibit distinct karyotypes and drug sensitivities (Stepanenko and Kavsan, 2014). In SNB19, Notch1 NICD, Notch3 NICD, and Hey2, Survivin

decrease as siTRPM7 downregulated TRPM7 with Notch1 FL increase whereas Notch2 NICD and Notch4 NICD did not change (**Figure 3D**). Interestingly, all three cell lines demonstrate reduced Notch1 and the target genes Hey2 and Survivin expression consistently when the TRPM7 gene was silenced, implying that the decreased expression of TRPM7 is correlated with decreased Notch active component Notch1 NICD in all glioma cell lines even though gliomas are highly heterogeneous with variation in biological characteristics among different glioma cell lines. Moreover, the discrepancy between Notch mRNA (Supplementary Figure 1) and protein expression indicates that the decreased level of active forms NICD in response to siTRPM7 may not be caused by reduced mRNA.

- (2) The upregulation of TRPM7 increases Notch1 signaling. To further investigate the correlation between TRPM7 and Notch receptors, we transfected U87MG cells with (a) wild-type human TRPM7 (wtTRPM7 or M7-wt); (b) constructs that rendered TRPM7 inactive with a point mutation in the ATP binding site of the  $\alpha$ -kinase domain (K1648R, or M7-KR) or the  $\alpha$ -kinase domain was deleted ( $\Delta$ kinase or M7-DK) as described in our previous publication (Wan et al., 2019). We decided U87MG as the cell line to



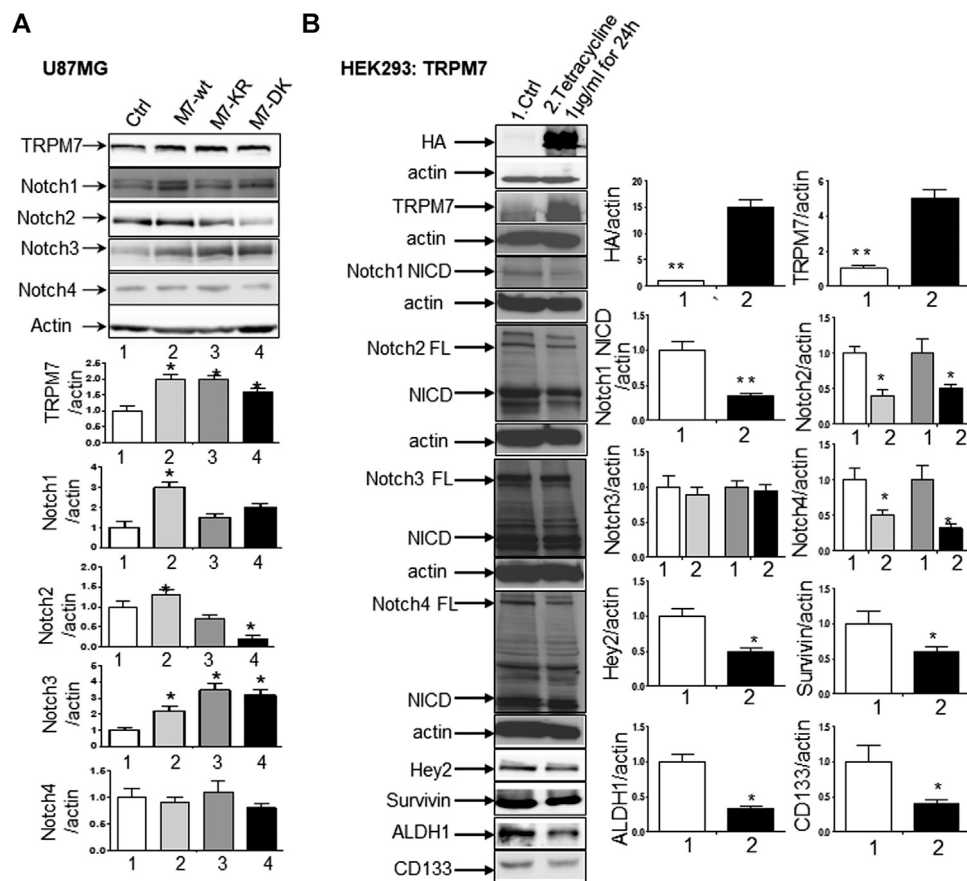


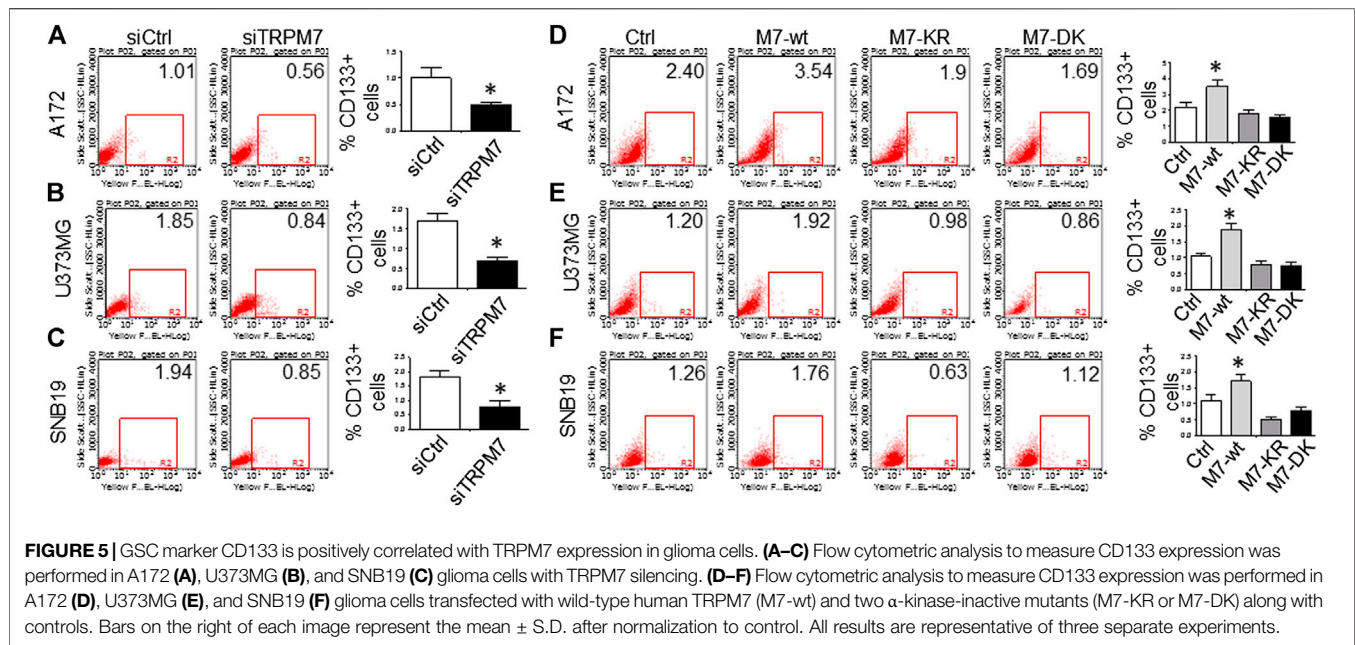
**FIGURE 4 |** TRPM7 is expressed in GBM and positively correlates with the activation of Notch1, and the upregulation of TRPM7 activates Notch1 signaling. **(A)** The U87MG cells were transfected with **(A)** wild-type human TRPM7 (M7-wt); **(B)** two  $\alpha$ -kinase-inactive mutants, “ $\alpha$ -kinase-dead” point mutation (K1648R, or M7-KR) and  $\alpha$ -kinase deleted mutant (M7-DK) along with controls followed by assaying protein expression of TRPM7, Notch1, Notch2, Notch3, and Notch4 by Western blot. **(B)** HEK-293 cells were transfected with a pcDNA4/TO plasmid that allowed tetracycline-inducible protein expression of TRPM7-wt tagged with HA. Then, protein expression of exogenous, endogenous TRPM7, Notch1, Notch2, Notch3, Notch4, and Notch target genes Hey2 and Survivin were determined by Western blot.

investigate the effect of TRPM7 overexpression on Notch1 activation because the endogenous expression of TRPM7 is lowest among all cell lines tested (see **Figure 3A**). The transfection efficiency was first determined by Western blot. U87MG, transfected with M7-wt, M7-KR, and M7-DK constructs, expressed high TRPM7 protein levels compared to that of the control, and this indicates the high transfection efficiency of the system (**Figure 4A**). Considering both TRPM7 and Notch signaling function as oncogenes in glioma formation, it is not surprising to see that U87MG cells, transfected with M7-wt, express increased levels of Notch1 NICD, Notch2 NICD, and Notch3 NICD. By contrast, U87MG cells, transfected with kinase mutants M7-KR and M7-DK (**Figure 4A**), express decreased levels of Notch1 NICD, Notch2 NICD compared with its wild-type partner, indicating TRPM7 with unfunctional kinase activity negatively regulates Notch1 and Notch2 activities. Interestingly, when cells harbor kinase-mutants, their Notch3 NICD are higher, implying a probable feedback regulation by unknown factors due to loss of TRPM7 kinase activities. Notch4 NICD is not significantly affected

by the introduction of neither M7-wt nor the two kinase domain mutants. Our results suggest that Notch1 and Notch2 activities positively correlate with TRPM7 channel activities, where the activities of Notch1 and Notch2 are partly determined by TRPM7 kinase activity. Therefore, our results show that TRPM7 regulates Notch signaling consistently through Notch1 signaling in glioma tumorigenesis.

- (3) To further confirm that TRPM7 regulates Notch signaling, HEK-293 cells, a cell line derived from human embryonic kidney cells, were transfected with a pcDNA4/TO plasmid that allowed tetracycline-inducible protein expression of wild-type of hTRPM7 (HEK293: TRPM7). In brief, when cells were treated with 1  $\mu$ g/ml of tetracycline, TRPM7 protein expression was induced by tetracycline-controlled transcription (Nadler et al., 2001; Jiang et al., 2007). As detected by Western blot in **Figure 4B**, TRPM7 was induced to express in HEK293 cells, either as an exogenous HA-tagged protein or a combination of endogenous and exogenous TRPM7 protein (**Figure 4B**) in the presence of an appropriate tetracycline





concentration. The results show that Notch1, 2, and 4 NICD, Notch target gene Hey2 and Survivin, as well as GSC markers ALDH1 and CD133 are downregulated (**Figure 4B**) in response to increased TRPM7 expression. It is understandable that the changed pattern in Notch Signaling in HEK-293 is different from that of glioma cell lines; This is because of the distinctiveness of normal and tumor cells' biological behaviors. However, this data from the non-tumor cell line, from another point of view, further confirm that TRPM7 is involved in Notch signaling pathway regulation.

- (4) GSC markers CD133 and ALDH1 are correlated with TRPM7 in GBM. We have previously reported that TRPM7 positively regulates the GSC marker CD133 in A172 cells (Liu et al., 2014). To determine whether or not our previous findings are not only limited to A172 cells, we tested the number of CD133 + cells in response to changes in TRPM7 expressions in additional glioma cell (GC) lines. Consistent with our previous results, we found that once TRPM7 was knocked down by siRNA, the amount of CD133 + cells are decreased in A172 cells (**Figure 5A**), U373MG cells (**Figure 5B**), and SNB19 cells (**Figure 5C**). These results indicate that the downregulation of TRPM7 result in a reduced GSC population. When TRPM7 expression levels were increased by introducing M7-wt vectors into GC lines, the number of CD133 + cells increased in A172 (**Figure 5D**, left two panels), U373MG (**Figure 5E**, left two groups), and SNB19 cells (**Figure 5F**, left two panels). However, the kinase-dead mutants M7-KR and M7-KD fail to upregulate the number of CD133 + cells (**Figures 5D–F**, right two groups). In other words, if TRPM7 kinase domain was disrupted, TRPM7 activation would be affected, resulting in reduced expression of CD133, which is an indication of

TRPM7 function loss due to unfunctional kinases. The data represent a representative experiment from three independent experiments performed in duplicate.

- (5) To address the question of whether or not TRPM7 will significantly affect ALDH1, another GSC marker (Rasper et al., 2010; Liu et al., 2014; Sullivan et al., 2017), we chose a similar model of glioma cells as described above, in which TRPM7 is either underexpressed or overexpressed by siTRPM7 or TRPM7-related constructs. The ALDEFLUOR assay was conducted on all glioma cells. TRPM7 knockdown decreases the number of ALDH1-positive cells from 18.10 to 10.87% in U87MG cells (**Figure 6A**), from 3.74 to 1.21% in U373MG (**Figure 6B**), and from 11.2 to 4.4% in SNB19 cells (**Figure 6C**). Consistent with the relationship of TRPM7 and CD133, here, these results provide further evidence that TRPM7 silencing result in a reduced GSC population as characterized by the ALDH1+ population. On the contrary, overexpression of TRPM7 increases the ALDH1-positive cells in all of the three cell lines tested (**Figures 7A–C**). As occurred in CD133-positive cells, the kinase-dead mutants M7-KR and M7-KD fail to upregulate ALDH1+ cells (**Figures 7A–C**), which supports the concept of functional coupling between the TRPM7 channel and a kinase domain. In other words, if TRPM7 kinase domain was disrupted, TRPM7 activation would be affected, resulting in reduced expression of ALDH1, which is an indication of TRPM7 function loss due to unfunctional kinases. The data represent a representative experiment from three independent experiments performed in triplicate. The number of ALDH1- positive cells of the control with diethylaminobenzaldehyde (DEAB), a specific inhibitor of ALDH1, was used to confirm gating areas.

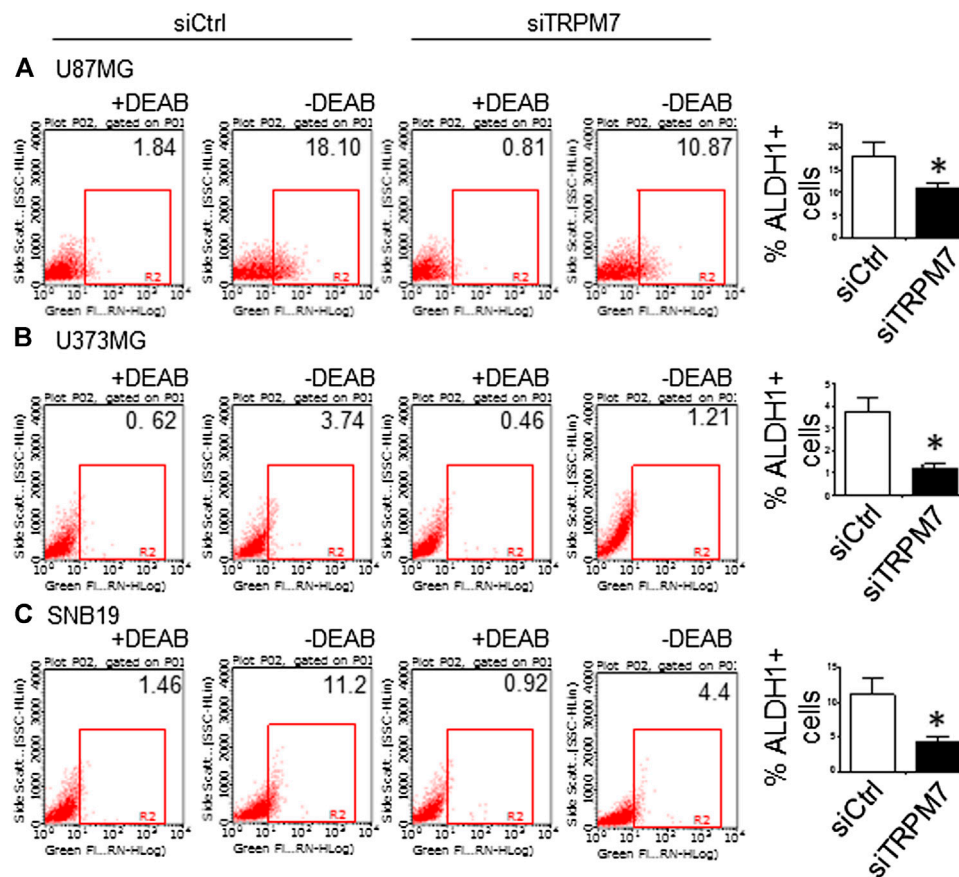


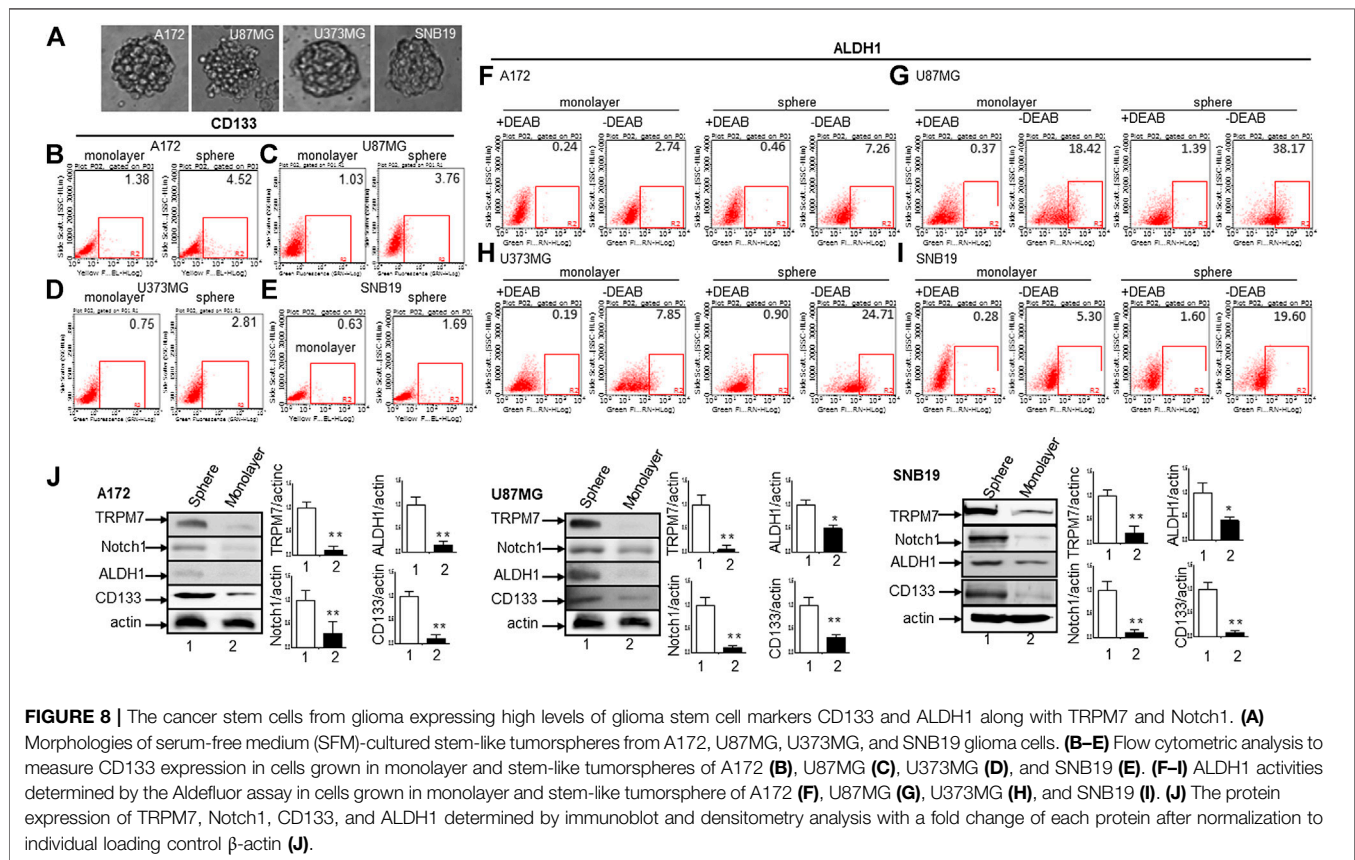
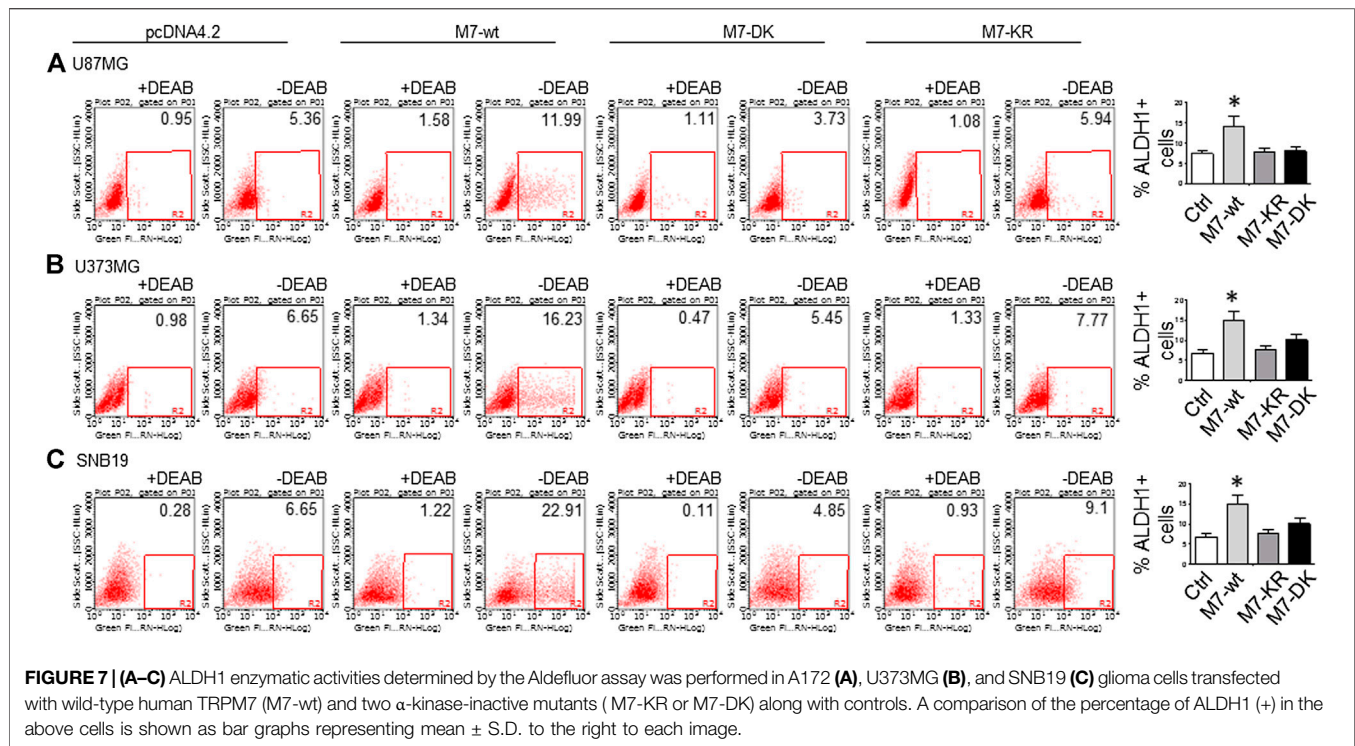
**FIGURE 6 |** GSC marker ALDH1 is positively correlated with TRPM7 expression in glioma cells. (A–C) ALDH1 enzymatic activities determined by the Aldefluor assay was performed in TRPM7 - knockdown of A172 (A), U373MG (B), and SNB19 (C) glioma cell lines.

(6) Glioma neurospheres exhibit high levels of GSC markers CD133 and ALDH1 and express high levels of TRPM7 and Notch1. We placed the glioma cells in non-differentiating medium in non-adherent culture plates, and neurospheres were seen developing in all cell lines tested, including A172, U87MG, U373MG, and SNB19 (Figure 8A). As expected, GSC marker CD133-positive cells increased in GSC compared to glioma cells grown in monolayer: CD133-positive cells increased from 1.38 to 4.52% in A172 (Figure 8B), from 1.03 to 3.76% in U87MG (Figure 8C), from 0.75 to 2.81% in U373MG (Figure 8D), and from 0.63 to 1.69% in SNB19 (Figure 8E). In parallel, ALDH1-positive cells increased from 2.74 to 7.26% in A172 (Figure 8F), from 18.42 to 38.17% in U87MG (Figure 8G), from 7.85 to 24.71% in U373MG (Figure 8H), and from 5.30 to 19.0% in SNB19 (Figure 8I). To further determine the difference in TRPM7 and Notch1 expression in glioma cells grown in monolayer and glioma neurospheres, we compared those indexes between glioma cells grown in monolayer and GSC spheres derived glioma cells by performing Western blot analysis. As expected, TRPM7 and Notch1 are highly correlated with the GSC

markers CD133 and ALDH1 in GSC spheres compared to that in the glioma monolayer cells (Figure 8J).

## Targeting Notch1 Suppresses Transient Receptor Potential Melastatin-Related 7-Induced Growth and Proliferation in Glioma Cells

(1) Targeting Notch1 suppresses TRPM7-induced growth and proliferation in glioma cells. DAPT (2S)-N-[(3,5-difluorophenyl) acetyl]-L-alanyl]-2-phenyl] glycine 1,1-dimethylethyl ester), a typical Notch inhibitor, prevents full-length Notch1 from cleavage by the presenilin- $\gamma$ -secretase complex to generate Notch1 NICD. Failure to release NICD into the nucleus results in the inactivation of Notch1 (Crawford and Roelink, 2007). As supported by our data above, Notch1 acts downstream to TRPM7 and contribute to the malignancy of glioma. Given this, we expect that the Notch1 signaling blockade will reverse the effects of TRPM7 on glioma proliferation. Therefore, first, we tested whether or not the inactivation of Notch1 results in





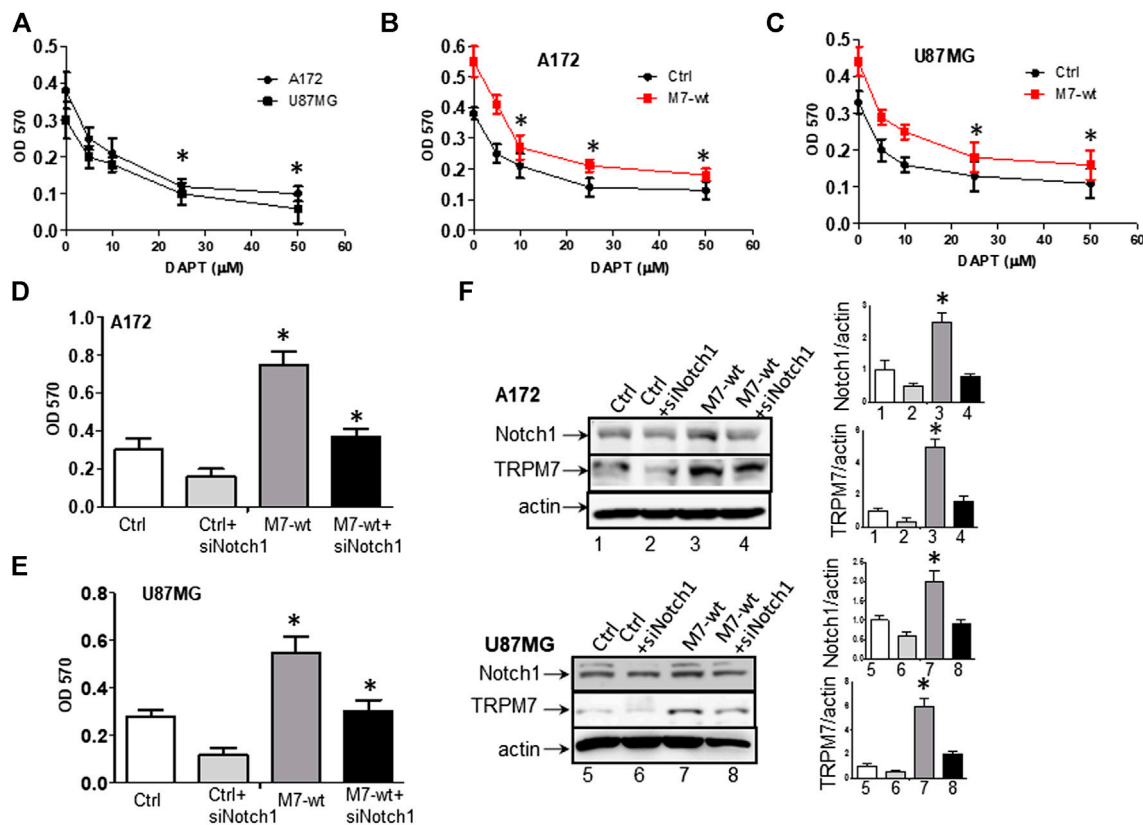
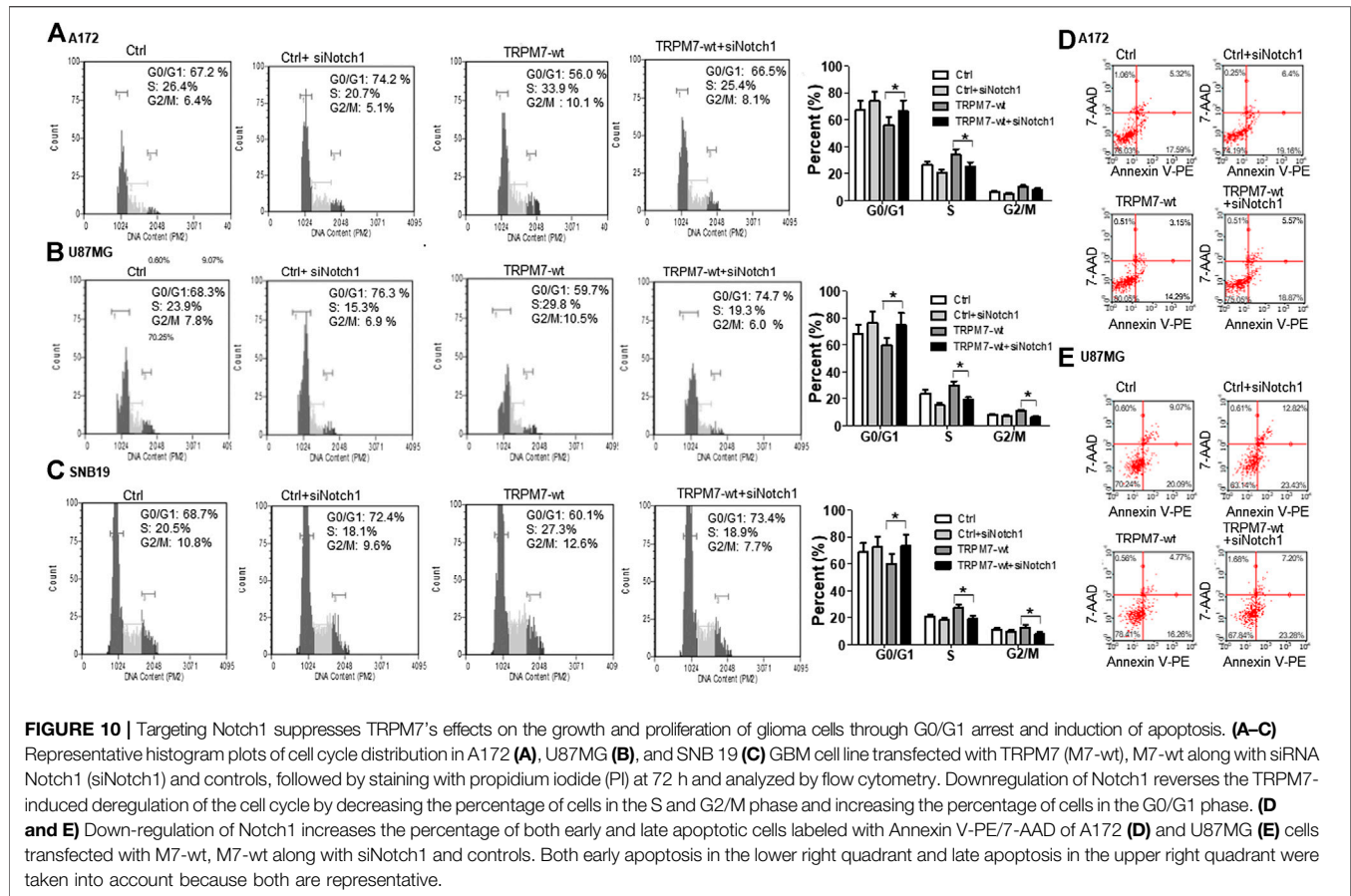


**FIGURE 9 |** Targeting Notch1 suppresses TRPM7-induced growth and proliferation of glioma cells. **(A)** Dose-response curves obtained after 72 h treatment with 5, 10, 25, 50 μM DAPT of A172 and U87MG glioma cell lines grown in growth media. **(B)** Dose-response curves obtained after 72 h treatment with 5, 10, 25, 50 μM DAPT of TRPM7-overexpressed (M7-wt) A172 cells and control. **(C)** Dose-response curves obtained after 72 h treatment with 5, 10, 25, 50 μM DAPT of TRPM7-overexpressed (M7-wt) U87MG cells and control. One-way ANOVA revealed a statistically significant difference between TRPM7-overexpressed glioma cells and controls in both A172 and U87MG cells ( $p < 0.05$ ). **(D and E)** The growth rates obtained from A172 **(D)** and U87MG **(E)** cells at 72 h after transfection with TRPM7 (M7-wt), M7-wt along with siRNA Notch1 (siNotch1) and controls. **(F)** The transfection efficiency was detected by the expression of TRPM7 and Notch1 protein, as examined by Western blot. The corresponding densitometry analysis for Western blot was performed using the ImageQuant program, as shown in bar graphs on the right.

deceased glioma cell proliferation. To this end, A172 and U87MG cells were selected for DAPT treatment from 5 to 50 μM for 72 h, as indicated in **Figure 9A**. The growth rates of both cell lines were inhibited by DAPT in a dose-dependent manner with IC<sub>50</sub> about 25 μM. To strengthen the observation, the post-transfection A172 and U87MG cells with TRPM7 wild type constructs (M7-wt) along with controls were then treated with an increasing dose of DAPT for 72 h. As expected, TRPM7 promotes cell proliferation, which is dose-dependently decreased by DAPT in both A172 (**Figure 9B**) and U87MG (**Figure 9C**). To further support that the inhibition Notch1 reduces TRPM7-mediated cell viability, either small interfering Notch1 RNA (siNotch1) or controls were cotransfected with TRPM7-wt into A172 and U87MG cells. Using this model, we can easily see how genetically silencing Notch1 transcription affects TRPM7-mediated cell viability and growth. Our data show that the growth rates are significantly enhanced by the ectopic introduction of TRPM7 in both A172 (**Figure 9D**) and U87MG cells (**Figure 9E**) as compared to being significantly reduced by

siNotch1 addition. The high transfection efficiency of both TRPM7-wt and siRNA Notch1 is depicted by Western blot assay in **Figure 9F**, where the TRPM7 expression is dramatically enhanced in cells transfected with M7-wt (lane 1 vs. lane 3; lane 5 vs. lane 7), Notch1 NICD expression is remarkably inhibited by siNotch1 (lane 1 vs. lane 2; lane 3 vs. lane 4; lane 5 vs. lane 6; lane 7 vs. lane 8). Of note, when the two cell lines are treated with siNotch1, TRPM7 is downregulated (**Figure 9F**, lane 3 vs. lane 4; lane 7 vs. lane 8), suggesting that TRPM7 functions downstream of Notch1. Considering the data above, we believe there is mutual regulation between TRPM7 and Notch signaling.

- (2) Targeting Notch1 compromises TRPM7-mediated changes in cell cycle progression. To further investigate the effects of Notch1 on TRPM7's function, we investigated whether or not the inactivation of Notch1 could rescue the changes in cell cycle progression caused by TRPM7. To this end, A172, U87MG, and SNB19 glioma cells were cotransfected with siNotch1 and M7-wt for 72 h and then followed by cell cycle distribution analyzation with propidium iodide staining



using flow cytometry to quantify the percentage of cells in different cell cycle phases. Inhibition of Notch1 activity for 72 h by siNotch1 induced a significant decrease in the percentage of cells in S and G2/M phase from 33.9 and 10.1% in A172 cells transfected with M7-wt to 25.4 and 8.1% in those transfected with M7-wt along with siNotch1. There is a concomitant increase in the percentage of cells in the G0/G1 phase (56.0–66.5%) (Figure 10A). These data indicated that when siNotch1 was added into the cell culture system, the increased effects on S and G2/M phase and decreased effects on G0/G1 phase by TRPM7 was compromised. In other works, Notch1 has replaced the TRPM7 function, or TRPM7 function through Notch1 signaling pathway. Similar to the results shown in A172 cells, siNotch1 also decreased in the percentage of cells in S and G2/M phase from 29.8 and 10.5% in U87MG cells transfected with M7-wt to 19.3 and 6.0% in those cotransfected with M7-wt and siNotch1; there was also an increase in G0/G1 phase from 59.7 to 74.7% (Figure 10B). A similar pattern was also observed in SNB19 cells with decreased S (27.3–18.9%) and G2/M phases (12.6–7.7%) and increased G0/G1 phase (60.1–73.4%) when comparing the cells transfected with M7-wt alone to the cells cotransfected with M7-wt and siNotch1 (Figure 10C). These results indicate the downregulation of Notch1 abrogated the deregulated cell cycle distribution caused by TRPM7, in other words, downregulation of

Notch1 compromised increased DNA synthesis and mitosis of tumor cells by TRPM7.

- (3) Targeting Notch1 counteracts the role of TRPM7 in regulating apoptosis in glioma cells. A172 and U87MG glioma cells were treated with siNotch1 along with TRPM7 wild-type constructs for 72 h, followed by Annexin V and 7AAD binding assay. Results show that the percentage of apoptotic glioma cells increased from (17.59 + 5.32) to (19.16 + 6.4)% in the controls compared to those silenced by Notch1; and (14.29 + 3.15) to (18.87 + 5.57)% in TRPM7-wt transfected A172 cells compared to those co-transfected with TRPM7 and siNotch1. Similar to results shown in A172 cells, siNotch1 also induces apoptosis significantly from (20.09 + 9.07) to (23.43 + 12.82)% in the parental U87MG cells and (16.26 + 4.77) to (23.28 + 7.20)% in TRPM7-wt transfected U87MG cells (Figure 10D).

## DISCUSSION

Major findings from the current study include: 1) TRPM7 mRNA expression is significantly increased in anaplastic astrocytoma, diffuse astrocytoma, and GBM patients compared to that in healthy brain tissue controls. 2) TRPM7's channel activity positively correlates with Notch1 activation and GSC markers



CD133 and ALDH1. Downregulation of TRPM7 inactivates Notch1 signaling and its target genes as well as decreases the expression of CD133 and ALDH1, whereas the upregulation of TRPM7 activates Notch1 signaling, and increases the expression of CD133 and ALDH1. TRPM7's role in Notch1 activity, GSC marker CD133, and ALDH1 require functional coupling between TRPM7 channel and a kinase domain. 3) Targeting TRPM7 suppresses the growth and proliferation of glioma cells through G1/S arrests by decreasing the percentage of cells in S and G2/M phases and through glioma cell apoptosis. 4) Targeting Notch1 compromises the TRPM7-induced growth and proliferation of glioma cells.

TRPM7 was first described in 2001 and has been attracting increased attention from many fields due to its multifaceted functions. TRPM7 is involved in various cellular processes such as  $\text{Ca}^{2+}$ ,  $\text{Mg}^{2+}$ , and  $\text{Zn}^{2+}$  homeostasis, mechanosensitivity, exocytosis, immune activation (Romagnani et al., 2017; Schappe et al., 2018), epigenetic modification (Krapivinsky et al., 2014), cell proliferation, migration, and differentiation. Consequentially, TRPM7 plays a causative role in tumorigenesis, ischemic diseases (both heart and brain), and neurodegenerative disorders (Chubanov et al., 2018). The unique molecular structure of TRPM7, which contains a transmembrane channel segment fused to a cytosolic  $\alpha$ -type serine/threonine-protein kinase domain, highlights the functional complexity of this gene (Rios et al., 2020; Trapani and Wolf, 2020). TRPM7 is ubiquitously expressed in all mammalian cells examined so far, and it is well documented that the deletion of the entire *TRPM7* gene is lethal to mouse embryo at an early stage (Trapani and Wolf, 2020; Turlova et al., 2020). Furthermore, the elimination of the kinase domain is also fatal to mouse embryonic development (Ryazanova et al., 2010). It is accepted that TRPM7 signaling does not only depend on channel-mediated  $\text{Mg}^{2+}$  (Rios et al., 2020; Voring et al., 2020) or  $\text{Ca}^{2+}$  influx (Song et al., 2020) but also on phosphorylation of downstream genes that require  $\alpha$ -kinase (Voring et al., 2020). Whether or not the  $\alpha$ -kinase domain is required for TRPM7 channel-mediated ion influx remains controversial with no unanimous conclusion. Some groups reported that a functional  $\alpha$ -kinase domain is required for TRPM7 channel activities (Ryazanova et al., 2004; Ryazanova et al., 2010; Song et al., 2017), others suggested that the  $\alpha$ -kinase domain is not necessary for TRPM7 channel activity and functions in a TRPM7 channel-independent manner (Yogi et al., 2013; Romagnani et al., 2017). The latter was supported by that the specific inactivation of the TRPM7  $\alpha$ -kinase activity with a point mutation in the ATP binding site of the  $\alpha$ -kinase domain (K1648R) did not contribute obvious pathologic phenotypes in homozygous TRPM7 kinase-dead mutant (*TRPM7<sup>K1648R</sup>*) mice (Kaitsuka et al., 2014). Recently, more mechanisms by which TRPM7's contribution to tumor formation have been explored. TRPM7 activates downstream targets annexin-1, calpain, and myosin, contributing to tumor cell migration and invasion. One of the newly found substrates of TRPM7 is RhoA. In hepatocellular carcinoma (HCC), TRPM7 activates RhoA, increases the cellular F-actin expression, increases myocardin-related transcription factors A and B (MRTFs) -Flaming A complex formation, therefore, facilitates

**TABLE 1 |** List of primers used in the study.

Primer set	Forward 5'-3'	Reverse 5'-3'
TRPM7	CTTTGACCAAGAGGGAAT GTG	GACCAAGCGACCAACAAAAAC
GAPDH	GAAGGTGAAGGTCGGAGTC	GAAGATGGTGATGGGATTTC
Notch1	CACTGTGGGCGGGTC C	GTT GTATTGGTTCGGCACCAT
Notch2	AATCCCTGACTOCAGAACG	TGGTAGACCAAGTCTGTGATG AT
Notch3	GGCTGTGAACAACGTGGAAG	TGGCAAAGTGGTCCAACA
Notch4	TAGGGCTCCCCAGCTCTC	GGCAGGTGCCCCCAATT

MRTF nuclear localization and transcriptional activity that lead to cancer cell growth (Voring et al., 2020). The epithelial-mesenchymal transition (EMT) is recognized to promote cancer cell invasiveness because of the high mobility and migratory abilities of mesenchymal cells once converted from carcinoma cells (Lo et al., 2017). Previously, TRPM7 was found to participate in EMT induced by tension (Kuipers et al., 2018) or EGF in breast cancer (Davis et al., 2014), and TGF- $\beta$  in prostate cancer (Sun et al., 2018). Recently, Vanlaeys et al. provided convincing evidence that in mammary epithelial cells exposed to Cadmium ( $\text{Cd}^{2+}$ ), TRPM7 is induced and deregulates cytosolic  $\text{Mg}^{2+}$  balance and enhances cell invasiveness (Vanlaeys et al., 2020). To contribute the mechanism of TRPM7's role in glioma, our current results first decipher that TRPM7 is responsible for sustained Notch1 signaling activation, enhanced expression of GSC markers CD133 and ALDH1, and regulation of glioma stemness, which contribute to malignant glioma cell growth and invasion. Interestingly, wtTRPM7 (M7-wt) increase the CD133 and ALDH1 expression in all glioma cell lines tested, however dead kinase domain of TRPM7 (M7-KR and M7-DK) downregulate the expression of CD133 and ALDH1 compared to controls (M7-wt), which indicates that disruption of kinase domain would reduce the TRPM7 activation resulting in reduced activation of stem cell markers CD133 and ALDH1. In other words, both TRPM7 channel and kinase activity of TRPM7 are required to fulfill its function in the regulation of GSC stemness (Figures 4, 6 and 7).

It is well accepted that Notch signaling activation contributes to human glioma tumorigenesis (Bazzoni and Bentivegna, 2019). Notch1 expression and activation contribute to glial cell transformation and glioma growth/survival, migration/invasion through Ras (Kanamori et al., 2007),  $\beta$ -catenin, NF- $\kappa$ B, AKT activation and downregulation of PTEN (Zhang et al., 2012; El Hindy et al., 2013). Recently, Ulasov et al. found that Temozolomide (TMZ) facilitates nuclear translocation of MMP14, followed by extracellular release of canonical Notch1 and Notch3 ligand Dll4, which in turn promotes cleavage of Notch3 and its nuclear translocation and induces glioma spheroiding ability and stemness (Ulasov et al., 2020). Notch4 is proposed as a less differentiated marker for glioma cells, and Notch4 expression increases from low-grade astrocytoma to high-graded GBM (El Hindy et al., 2013; Dell'albani et al., 2014). The upregulation of Notch ligand JAG1 and targets Hey1, Hey2, Hes1 in brain tissues of glioma patients compared to that of healthy brain tissues also highlight the Notch signaling pathway as a potential therapeutic

target in glioma patients (El Hindy et al., 2013). The cross interaction among Notch and other pathways, such as Hedgehog (Chang and Lai, 2019) and EGF-related pathways (Cristofaro et al., 2020), implicates the molecular targets with overlapping functions should be prioritized as therapeutic targets. As more in-depth research developed, the contribution of Notch signaling in glioma progression is extended to non-canonical Notch ligand 1 (DLK1). DLK1 is a transmembrane protein that can be cleaved by ADAM17 and translocates to the nucleus in glioma cells under hypoxic conditions, leading to p53 and PI3K pathway activation (Grassi et al., 2020). Most recently, Otani provided convincing evidence that oncolytic HSV-infected glioma cells activate Notch signaling in adjacent tumor cells, which sensitizes tumors to gamma-secretase inhibition (Otani et al., 2020). In the current study, we first show that TRPM7-mediated Notch1 signaling activation is a crucial contributor to glioma cell proliferation and GSC stemness. TRPM7 increases the growth and proliferation of glioma cells through unlocking G1/S arrests, stimulating cell entry into S and G2/M phases, and inhibiting glioma cell apoptosis (Figure 2 and Figure 9). Silencing of Notch1 can revert the effects of TRPM7 on cell cycle and programmed cell death in glioma cells (Figure 10), which indicates that Notch1 can replace the TRPM7 function, or TRPM7 functions through Notch1 signaling pathway.

CD133 serves as a GSC marker and has long been used to sort out GSC for further *in vitro* and *in vivo* stem-like characteristics studies (Pollard et al., 2009; Logun et al., 2019; McAbee et al., 2019). ALDH1 is identified as another biomarker for GBM; high levels of ALDH1 usually indicate high invasive features and resistance to EGFR inhibition (Smith et al., 2017; McKinney et al., 2019), characteristics that are used as a measure of stem-like properties for GBM. A recent meta-analysis showed that high expression of ALDH1 is associated with a high WHO grade of glioma and a worse prognosis in glioma patients (Wang et al., 2017). Our data show that TRPM7 expression highly correlates with the expression of CD133 and ALDH1 (Figure 8) in both bulk glioma cells and in GSCs (Figure 8), which indicates that TRPM7 is very important in GSC formation.

High heterogeneous GBM contains GSC and non-stem tumor cells as well as other non-tumor cells, where GSC interact with other cells in the microenvironment can further potentiate the malignancy of GBM (Tao et al., 2020). Targeting GSCs and their interactions with other components may serve as the strategy for current GBM therapy (Kierulf-Vieira et al., 2020). In summary, TRPM7 is responsible for sustained Notch1 signaling activation, enhanced expression of GSC markers, and regulation of glioma stemness, all of which contribute to malignant glioma cell growth and invasion. For the prospects, several siRNA may be combined;

for instance, two siRNAs targeting TRPM7 and Notch1 could be encapsulated together in a single nanoparticle to obtain synergistic therapeutic effects.

## DATA AVAILABILITY STATEMENT

The raw data supporting the conclusions of this article will be made available by the authors, without undue reservation.

## AUTHOR CONTRIBUTIONS

SG and ML designed the study protocol. JW, AG, PK, and TS performed experiments based on glioma cell cultures and evaluated the data with the help of ML. ML performed the biostatistical evaluation of the data. AG and ML wrote the manuscript with contributions and final approval by all authors. SG and YJ contributed to the critical reading and revision of the manuscript.

## FUNDING

This study was supported by the SC3 grant from NIH NIGMS GM121230 to ML and partly supported by the Morehouse School of Medicine Tx Pilot grant. The funding bodies had no role in the design, collection, analysis, and interpretation of the study's data and in writing the manuscript.

## ACKNOWLEDGMENTS

We thank Carsten Schmitz (University of Colorado, Denver, CO) for providing us with all constructs (wtTRPM7,  $\Delta$ kinase, K1648R) that were tagged with a hemagglutinin (HA) at N-terminal. We are grateful to Yancey G. Gillespie at the University of Alabama at Birmingham (UAB) for providing us the U87MG, U373MG, SNB19 cell lines, and PDX lines and to Hui-Kuo Shu at Emory University for providing the SF767 cell line.

## SUPPLEMENTARY MATERIAL

The Supplementary Material for this article can be found online at: <https://www.frontiersin.org/articles/10.3389/fphar.2020.590723/full#supplementary-material>

## REFERENCES

- Aliferis, C., and Trafalis, D. T. (2015). Glioblastoma multiforme: pathogenesis and treatment. *Pharmacol. Ther.* 152, 63–82. doi:10.1016/j.pharmthera.2015.05.005
- Artavanis-Tsakonas, S., Rand, M. D., and Lake, R. J. (1999). Notch signaling: cell fate control and signal integration in development. *Science* 284, 770–776. doi:10.1126/science.284.5415.770
- Asrar, S., and Aarts, M. (2013). TRPM7, the cytoskeleton and neuronal death. *Channels* 7, 6–16. doi:10.4161/chan.22824
- Bates-Withers, C., Sah, R., and Clapham, D. E. (2011). TRPM7, the Mg(2+) inhibited channel and kinase. *Adv. Exp. Med. Biol.* 704, 173–183. doi:10.1007/978-94-007-0265-3\_9
- Bazzoni, R., and Bentivegna, A. (2019). Role of notch signaling pathway in glioblastoma pathogenesis. *Cancers (Basel)* 11, 292. doi:10.3390/cancers11030292

- Brown, D. V., Filiz, G., Daniel, P. M., Hollande, F., Dworkin, S., Amiridis, S., et al. (2017). Expression of CD133 and CD44 in glioblastoma stem cells correlates with cell proliferation, phenotype stability and intra-tumor heterogeneity. *PLoS One* 12, e0172791. doi:10.1371/journal.pone.0172791
- Cao, R., Meng, Z., Liu, T., Wang, G., Qian, G., Cao, T., et al. (2016). Decreased TRPM7 inhibits activities and induces apoptosis of bladder cancer cells via ERK1/2 pathway. *Oncotarget* 7, 72941–72960. doi:10.18632/oncotarget.12146
- Chakrabarti, M., and Ray, S. K. (2015). Synergistic anti-tumor actions of luteolin and silibinin prevented cell migration and invasion and induced apoptosis in glioblastoma SNB19 cells and glioblastoma stem cells. *Brain Res.* 1629, 85–93. doi:10.1016/j.brainres.2015.10.010
- Chang, W. H., and Lai, A. G. (2019). Aberrations in Notch-Hedgehog signalling reveal cancer stem cells harbouring conserved oncogenic properties associated with hypoxia and immunoevasion. *Br. J. Canc.* 121, 666–678. doi:10.1038/s41416-019-0572-9
- Chen, W.-L., Barszczyk, A., Turlova, E., Deurloo, M., Liu, B., Yang, B. B., et al. (2015). Inhibition of TRPM7 by carvacrol suppresses glioblastoma cell proliferation, migration and invasion. *Oncotarget* 6, 16321–16340. doi:10.18632/oncotarget.3872
- Cheng, J.-X., Liu, B.-L., and Zhang, X. (2009). How powerful is CD133 as a cancer stem cell marker in brain tumors? *Canc. Treat Rev.* 35, 403–408. doi:10.1016/j.ctrv.2009.03.002
- Chubanov, V., Ferioli, S., and Gudermann, T. (2017). Assessment of TRPM7 functions by drug-like small molecules. *Cell Calcium* 67, 166–173. doi:10.1016/j.ceca.2017.03.004
- Chubanov, V., Mittermeier, L., and Gudermann, T. (2018). Role of kinase-coupled TRP channels in mineral homeostasis. *Pharmacol. Ther.* 184, 159–176. doi:10.1016/j.pharmthera.2017.11.003
- Crawford, T. Q., and Roelink, H. (2007). The notch response inhibitor DAPT enhances neuronal differentiation in embryonic stem cell-derived embryoid bodies independently of sonic hedgehog signaling. *Dev. Dynam.* 236, 886–892. doi:10.1002/dvdy.21083
- Cristofaro, I., Alessandrini, F., Spinello, Z., Guerriero, C., Fiore, M., Caffarelli, E., et al. (2020). Cross interaction between M2 muscarinic receptor and Notch1/EGFR pathway in human glioblastoma cancer stem cells: effects on cell cycle progression and survival. *Cells* 9 (3), 657. doi:10.3390/cells9030657
- Davis, F. M., Azimi, I., Faville, R. A., Peters, A. A., Jalink, K., Putney, J. W., Jr., et al. (2014). Induction of epithelial-mesenchymal transition (EMT) in breast cancer cells is calcium signal dependent. *Oncogene* 33, 2307–2316. doi:10.1038/onc.2013.187
- Dell'Albani, P., Rodolico, M., Pellitteri, R., Tricarichi, E., Torrisi, S. A., D'antoni, S., et al. (2014). Differential patterns of NOTCH1-4 receptor expression are markers of glioma cell differentiation. *Neuro Oncol.* 16, 204–216. doi:10.1093/neuonc/not168
- Desai, B. N., Krapivinsky, G., Navarro, B., Krapivinsky, L., Carter, B. C., Febvay, S., et al. (2012). Cleavage of TRPM7 releases the kinase domain from the ion channel and regulates its participation in Fas-induced apoptosis. *Dev. Cell* 22, 1149–1162. doi:10.1016/j.devcel.2012.04.006
- Dirks, P. B. (2010). Brain tumor stem cells: the cancer stem cell hypothesis writ large. *Mol Oncol* 4, 420–430. doi:10.1016/j.molonc.2010.08.001
- Duan, J., Li, Z., Li, J., Hulse, R. E., Santa-Cruz, A., Valinsky, W. C., et al. (2018). Structure of the mammalian TRPM7, a magnesium channel required during embryonic development. *Proc. Natl. Acad. Sci. U.S.A.* 115, E8201–E8210. doi:10.1073/pnas.1810719115
- El Hindy, N., Keyvani, K., Pagenstecher, A., Dammann, P., Sandalcioğlu, I. E., Sure, U., et al. (2013). Implications of DLL4-Notch signaling activation in primary glioblastoma multiforme. *Neuro Oncol.* 15, 1366–1378. doi:10.1093/neuonc/not071
- Gautier, M., Perriere, M., Monet, M., Vanlaeys, A., Korichneva, I., Dhennin-Duthille, I., et al. (2016). Recent advances in oncogenic roles of the TRPM7 channel. *Curr. Med. Chem.* 23, 4092–4107. doi:10.2174/0929867323666160907162002
- Grassi, E. S., Pantazopoulou, V., and Pietras, A. (2020). Hypoxia-induced release, nuclear translocation, and signaling activity of a DLK1 intracellular fragment in glioma. *Oncogene* 39, 4028–4044. doi:10.1038/s41388-020-1273-9
- Haddock, A. N., Labuzan, S. A., Haynes, A. E., Hayes, C. S., Kakareka, K. M., and Waddell, D. S. (2019). Dual-specificity phosphatase 4 is upregulated during skeletal muscle atrophy and modulates extracellular signal-regulated kinase activity. *Am. J. Physiol. Cell Physiol.* 316, C567–C581. doi:10.1152/ajpcell.00234.2018
- Hovinga, K. E., Shimizu, F., Wang, R., Panagiotakos, G., Van Der Heijden, M., Moayedpardazi, H., et al. (2010). Inhibition of notch signaling in glioblastoma targets cancer stem cells via an endothelial cell intermediate. *Stem Cell* 28, 1019–1029. doi:10.1002/stem.429
- Huang, J., Furuya, H., Faouzi, M., Zhang, Z., Monteilh-Zoller, M., Kawabata, K. G., et al. (2017). Inhibition of TRPM7 suppresses cell proliferation of colon adenocarcinoma *in vitro* and induces hypomagnesemia *in vivo* without affecting azoxymethane-induced early colon cancer in mice. *Cell Commun. Signal.* 15, 30. doi:10.1186/s12964-017-0188-8
- Ishii, N., Maier, D., Merlo, A., Tada, M., Sawamura, Y., Diserens, A.-C., et al. (1999). Frequent co-alterations of TP53, p16/CDKN2A, p14ARF, PTEN tumor suppressor genes in human glioma cell lines. *Brain Pathol.* 9, 469–479. doi:10.1111/j.1750-3639.1999.tb00536.x
- Jiang, J., Li, M.-H., Inoue, K., Chu, X.-P., Seeds, J., and Xiong, Z.-G. (2007). Transient receptor potential melastatin 7-like current in human head and neck carcinoma cells: role in cell proliferation. *Cancer Res* 67, 10929–10938. doi:10.1158/0008-5472.can-07-1121
- Jin, J., Desai, B. N., Navarro, B., Donovan, A., Andrews, N. C., and Clapham, D. E. (2008). Deletion of Trpm7 disrupts embryonic development and thymopoiesis without altering Mg<sup>2+</sup> homeostasis. *Science* 322, 756–760. doi:10.1126/science.1163493
- Jin, J., Wu, L.-J., Jun, J., Cheng, X., Xu, H., Andrews, N. C., et al. (2012). The channel kinase, TRPM7, is required for early embryonic development. *Proc. Natl. Acad. Sci. U. S. A.* 109, E225–E233. doi:10.1073/pnas.1120033109
- Kaitsuka, T., Katagiri, C., Beesetty, P., Nakamura, K., Hourani, S., Tomizawa, K., et al. (2014). Inactivation of TRPM7 kinase activity does not impair its channel function in mice. *Sci. Rep.* 4, 5718. doi:10.1038/srep05718
- Kanamori, M., Kawaguchi, T., Nigro, J. M., Feuerstein, B. G., Berger, M. S., Miele, L., et al. (2007). Contribution of Notch signaling activation to human glioblastoma multiforme. *J. Neurosurg.* 106, 417–427. doi:10.3171/jns.2007.106.3.417
- Kierulf-Vieira, K. S., Sandberg, C. J., Waaler, J., Lund, K., Skaga, E., Saberniak, B. M., et al. (2020). A small-molecule tankyrase inhibitor reduces glioma stem cell proliferation and sphere formation. *Cancers* 12 (6), 1630. doi:10.3390/cancers12061630
- Kim, B. J., Park, E. J., Lee, J. H., Jeon, J.-H., Kim, S. J., and So, I. (2008). Suppression of transient receptor potential melastatin 7 channel induces cell death in gastric cancer. *Canc. Sci.* 99, 2502–2509. doi:10.1111/j.1349-7006.2008.00982.x
- Krapivinsky, G., Krapivinsky, L., Manasian, Y., and Clapham, D. E. (2014). The TRPM7 channel is cleaved to release a chromatin-modifying kinase. *Cell* 157, 1061–1072. doi:10.1016/j.cell.2014.03.046
- Kuipers, A. J., Middelbeek, J., Vrenken, K., Pérez-González, C., Poelmans, G., Klarenbeek, J., et al. (2018). TRPM7 controls mesenchymal features of breast cancer cells by tensional regulation of SOX4. *Biochim. Biophys. Acta Mol. Basis Dis.* 1864, 2409–2419. doi:10.1016/j.bbdis.2018.04.017
- Leng, T.-D., Li, M.-H., Shen, J.-F., Liu, M.-L., Li, X.-B., Sun, H.-W., et al. (2015). Suppression of TRPM7 inhibits proliferation, migration, and invasion of malignant human glioma cells. *CNS Neurosci. Ther.* 21, 252–261. doi:10.1111/cns.12354
- Liu, D.-y., Ren, C.-p., Yuan, X.-r., Zhang, L.-h., Liu, J., Liu, Q., et al. (2012). ALDH1 expression is correlated with pathologic grade and poor clinical outcome in patients with astrocytoma. *J. Clin. Neurosci.* 19, 1700–1705. doi:10.1016/j.jocn.2012.01.036
- Liu, H., Dilger, J. P., and Lin, J. (2020). The role of transient receptor potential melastatin 7 (TRPM7) in cell viability: a potential target to suppress breast cancer cell cycle. *Cancers* 12 (1), 131. doi:10.3390/cancers12010131
- Liu, M., Inoue, K., Leng, T., Guo, S., and Xiong, Z.-g. (2014). TRPM7 channels regulate glioma stem cell through STAT3 and Notch signaling pathways. *Cell. Signal.* 26, 2773–2781. doi:10.1016/j.cellsig.2014.08.020
- Liu, M., Wilson, N. O., Hibbert, J. M., and Stiles, J. K. (2013). STAT3 regulates MMP3 in heme-induced endothelial cell apoptosis. *PLoS One* 8, e71366. doi:10.1371/journal.pone.0071366
- Lo, U. G., Lee, C. F., Lee, M. S., and Hsieh, J. T. (2017). The role and mechanism of epithelial-to-mesenchymal transition in prostate cancer progression. *Int. J. Mol. Sci.* 18 (10), 2079. doi:10.3390/ijms18102079

- Logun, M. T., Wynens, K. E., Simchick, G., Zhao, W., Mao, L., Zhao, Q., et al. (2019). Surfen-mediated blockade of extratumoral chondroitin sulfate glycosaminoglycans inhibits glioblastoma invasion. *FASEB J.* 33, 11973–11992. doi:10.1096/fj.201802610rr
- Lu, V. M., Phan, K., Yin, J. X. M., and McDonald, K. L. (2018). Older studies can underestimate prognosis of glioblastoma biomarker in meta-analyses: a meta-epidemiological study for study-level effect in the current literature. *J. Neuro Oncol.* 139, 231–238. doi:10.1007/s11060-018-2897-2
- Lucena-Cacace, A., Umeda, M., Navas, L. E., and Carnero, A. (2019). NAMPT as a dedifferentiation-inducer gene: NAD(+) as core Axis for glioma cancer stem-like cells maintenance. *Front Oncol.* 9, 292. doi:10.3389/fonc.2019.00292
- Ludwig, K., and Kornblum, H. I. (2017). Molecular markers in glioma. *J. Neuro Oncol.* 134, 505–512. doi:10.1007/s11060-017-2379-y
- Maier, E. A., Furnari, F. B., Bachoo, R. M., Rowitch, D. H., Louis, D. N., Cavenee, W. K., et al. (2001). Malignant glioma: genetics and biology of a grave matter. *Genes Dev.* 15, 1311–1333. doi:10.1101/gad.891601
- Mcabee, J. H., Rath, B. H., Valdez, K., Young, D. L., Wu, X., Shankavaram, U. T., et al. (2019). Radiation drives the evolution of orthotopic xenografts initiated from glioblastoma stem-like cells. *Cancer Res.* 79, 6032–6043. doi:10.1158/0008-5472.can-19-2452
- McKinney, A., Lindberg, O. R., Engler, J. R., Chen, K. Y., Kumar, A., Gong, H., et al. (2019). Mechanisms of resistance to EGFR inhibition reveal metabolic vulnerabilities in human GBM. *Mol. Canc. Therapeut.* 18, 1565–1576. doi:10.1158/1535-7163.mct-18-1330
- Melamed, J. R., Morgan, J. T., Ioele, S. A., Gleghorn, J. P., Sims-Mourtada, J., and Day, E. S. (2018). Investigating the role of Hedgehog/GLI1 signaling in glioblastoma cell response to temozolomide. *Oncotarget* 9, 27000–27015. doi:10.18632/oncotarget.25467
- Memmel, S., Sukhorukov, V. L., Horing, M., Westerling, K., Fiedler, V., Katzer, A., et al. (2014). Cell surface area and membrane folding in glioblastoma cell lines differing in PTEN and p53 status. *PLoS One* 9, e87052. doi:10.1371/journal.pone.0087052
- Miele, L., Miao, H., and Nickoloff, B. (2006). NOTCH signaling as a novel cancer therapeutic target. *Curr Cancer Drug Targets* 6, 313–323. doi:10.2174/15680090677441771
- Miele, L. (2006). Notch signaling. *Clin. Canc. Res.* 12, 1074–1079. doi:10.1158/1078-0432.ccr-05-2570
- Nadler, M. J. S., Hermosura, M. C., Inabe, K., Perraud, A.-L., Zhu, Q., Stokes, A. J., et al. (2001). LTRPC7 is a Mg ATP-regulated divalent cation channel required for cell viability. *Nature* 411, 590–595. doi:10.1038/35079092
- Otani, Y., Yoo, J. Y., Chao, S., Liu, J., Jaime-Ramirez, A. C., Lee, T. J., et al. (2020). Oncolytic HSV-infected glioma cells activate NOTCH in adjacent tumor cells sensitizing tumors to gamma secretase inhibition. *Clin. Canc. Res.* 26, 2381–2392. doi:10.1158/1078-0432.ccr-19-3420
- Paravicini, T. M., Chubonov, V., and Gudermann, T. (2012). TRPM7: a unique channel involved in magnesium homeostasis. *Int. J. Biochem. Cell Biol.* 44, 1381–1384. doi:10.1016/j.biocel.2012.05.010
- Penner, R., and Fleig, A. (2007). The Mg<sup>2+</sup> and Mg(2+)-nucleotide-regulated channel-kinase TRPM7. *Handb. Exp. Pharmacol.* 179, 313–328. doi:10.1007/978-3-540-34891-7\_19
- Perraud, A.-L., Zhao, X., Ryazanov, A. G., and Schmitz, C. (2011). The channel-kinase TRPM7 regulates phosphorylation of the translational factor eEF2 via eEF2-k. *Cell. Signal.* 23, 586–593. doi:10.1016/j.cellsig.2010.11.011
- Pollard, S. M., Yoshikawa, K., Clarke, I. D., Danovi, D., Stricker, S., Russell, R., et al. (2009). Glioma stem cell lines expanded in adherent culture have tumor-specific phenotypes and are suitable for chemical and genetic screens. *Cell Stem Cell* 4, 568–580. doi:10.1016/j.stem.2009.03.014
- Prevarskaya, N., Skryma, R., and Shuba, Y. (2010). Ion channels and the hallmarks of cancer. *Trends Mol. Med.* 16, 107–121. doi:10.1016/j.molmed.2010.01.005
- Qiang, L., Wu, T., Zhang, H.-W., Lu, N., Hu, R., Wang, Y.-J., et al. (2012). HIF-1 $\alpha$  is critical for hypoxia-mediated maintenance of glioblastoma stem cells by activating Notch signaling pathway. *Cell Death Differ.* 19, 284–294. doi:10.1038/cdd.2011.95
- Rasper, M., Schafer, A., Piontek, G., Teufel, J., Brockhoff, G., Ringel, F., et al. (2010). Aldehyde dehydrogenase 1 positive glioblastoma cells show brain tumor stem cell capacity. *Neuro Oncol.* 12, 1024–1033. doi:10.1093/neuonc/noq070
- Rhodes, D. R., Yu, J., Shanker, K., Deshpande, N., Varambally, R., Ghosh, D., et al. (2004b). ONCOMINE: a cancer microarray database and integrated data-mining platform. *Neoplasia* 6, 1–6. doi:10.1016/s1476-5586(04)80047-2
- Rhodes, D. R., Yu, J., Shanker, K., Deshpande, N., Varambally, R., Ghosh, D., et al. (2004a). Large-scale meta-analysis of cancer microarray data identifies common transcriptional profiles of neoplastic transformation and progression. *Proc. Natl. Acad. Sci. USA.* 101, 9309–9314. doi:10.1073/pnas.0401994101
- Rios, F. J., Zou, Z.-G., Harvey, A. P., Harvey, K. Y., Nosalski, R., Anyfant, P., et al. (2020). Chanzyme TRPM7 protects against cardiovascular inflammation and fibrosis. *Cardiovasc. Res.* 116, 721–735. doi:10.1093/cvr/cvz164
- Romagnani, A., Vettore, V., Rezzonico-Jost, T., Hampe, S., Rottoli, E., Nadoln, W., et al. (2017). TRPM7 kinase activity is essential for T cell colonization and alloreactivity in the gut. *Nat. Commun.* 8, 1917. doi:10.1038/s41467-017-01960-z
- Runnels, L. W. (2011). TRPM6 and TRPM7: a Mul-TRP-PLIK-cation of channel functions. *Curr. Pharmaceut. Biotechnol.* 12, 42–53. doi:10.2174/138920111793937880
- Ryazanova, L. V., Dorovkov, M. V., Ansari, A., and Ryazanov, A. G. (2004). Characterization of the protein kinase activity of TRPM7/ChaK1, a protein kinase fused to the transient receptor potential ion channel. *J. Biol. Chem.* 279, 3708–3716. doi:10.1074/jbc.m308820200
- Ryazanova, L. V., Rondon, L. J., Zierler, S., Hu, Z., Galli, J., Yamaguchi, T. P., et al. (2010). TRPM7 is essential for Mg(2+) homeostasis in mammals. *Nat. Commun.* 1, 109. doi:10.1038/ncomms1108
- Rybarczyk, P., Vanlaeys, A., Brassart, B., Dhennin-Duthille, L., Chatelain, D., Sevestre, H., et al. (2017). The transient receptor potential melastatin 7 channel regulates pancreatic cancer cell invasion through the hsp90a/uPA/MMP2 pathway. *Neoplasia* 19, 288–300. doi:10.1016/j.neo.2017.01.004
- Sander, P., Mostafa, H., Soboh, A., Schneider, J. M., Pala, A., Baron, A.-K., et al. (2017). Vacuolol-1 inducible cell death in glioblastoma multiforme is counter regulated by TRPM7 activity induced by exogenous ATP. *Oncotarget* 8, 35124–35137. doi:10.18632/oncotarget.16703
- Schappe, M. S., Sztajn, K., Stremiska, M. E., Mendu, S. K., Downs, T. K., Seegren, P. V., et al. (2018). Chanzyme TRPM7 mediates the Ca<sup>2+</sup> influx essential for lipopolysaccharide-induced toll-like receptor 4 endocytosis and macrophage activation. *Immunity* 48, 59–74. doi:10.1016/j.immuni.2017.11.026
- Schmitz, C., Perraud, A.-L., Johnson, C. O., Inabe, K., Smith, M. K., Penner, R., et al. (2003). Regulation of vertebrate cellular Mg<sup>2+</sup> homeostasis by TRPM7. *Cell* 114, 191–200. doi:10.1016/s0092-8674(03)00556-7
- Smith, S. J., Diksin, M., Chhaya, S., Sairam, S., Estevez-Cabrero, M. A., and Rahman, R. (2017). The invasive region of glioblastoma defined by 5ALA guided surgery has an altered cancer stem cell marker profile compared to central tumour. *Int. J. Mol. Sci.* 18 (11), 2452. doi:10.3390/ijms18112452
- Song, C., Bae, Y., Jun, J., Lee, H., Kim, N. D., Lee, K.-B., et al. (2017). Identification of TG100-115 as a new and potent TRPM7 kinase inhibitor, which suppresses breast cancer cell migration and invasion. *Biochim. Biophys. Acta Gen. Subj.* 1861, 947–957. doi:10.1016/j.bbagen.2017.01.034
- Song, C., Choi, S., Oh, K. B., and Sim, T. (2020). Suppression of TRPM7 enhances TRAIL-induced apoptosis in triple-negative breast cancer cells. *J. Cell. Physiol.* 235 (12), 10037–10050. doi:10.1158/1538-7445.am2020-367
- Stepanenko, A. A., and Kavsan, V. M. (2014). Karyotypically distinct U251, U373, and SNB19 glioma cell lines are of the same origin but have different drug treatment sensitivities. *Gene* 540, 263–265. doi:10.1016/j.gene.2014.02.053
- Stockhausen, M.-T., Kristoffersen, K., and Poulsen, H. S. (2012). Notch signaling and brain tumors. *Adv. Exp. Med. Biol.* 727, 289–304. doi:10.1007/978-1-4614-0899-4\_22
- Sullivan, K. E., Rojas, K., Cerione, R. A., Nakano, I., and Wilson, K. F. (2017). The stem cell/cancer stem cell marker ALDH1A3 regulates the expression of the survival factor tissue transglutaminase, in mesenchymal glioma stem cells. *Oncotarget* 8, 22325–22343. doi:10.18632/oncotarget.16479
- Sun, Y., Schaar, A., Sukumaran, P., Dhasarathy, A., and Singh, B. B. (2018). TGF $\beta$ -induced epithelial-to-mesenchymal transition in prostate cancer cells is mediated via TRPM7 expression. *Mol. Carcinog.* 57, 752–761. doi:10.1002/mc.22797
- Tao, W., Chu, C., Zhou, W., Huang, Z., Zhai, K., Fang, X., et al. (2020). Dual Role of WISP1 in maintaining glioma stem cells and tumor-supportive macrophages in glioblastoma. *Nat. Commun.* 11, 3015. doi:10.1038/s41467-020-16827-z



- Teodorczyk, M., and Schmidt, M. H. H. (2014). Notching on cancer's door: notch signaling in brain tumors. *Front Oncol* 4, 341. doi:10.3389/fonc.2014.00341
- Trapani, V., and Wolf, F. I. (2020). The TRPM7 channel kinase: rekindling an old flame or not? *Cardiovasc. Res.* 116, 476–478. doi:10.1093/cvr/cvz229
- Turlova, E., Wong, R., Xu, B., Li, F., Du, L., Habbous, S., et al. (2020). TRPM7 mediates neuronal cell death upstream of calcium/calmodulin-dependent protein kinase II and calcineurin mechanism in neonatal hypoxic-ischemic brain injury. *Transl Stroke Res* [Epub ahead of print]. doi:10.1007/s12975-020-00810-3
- Ulasov, I. V., Mijanovic, O., Savchuk, S., Gonzalez-Buendia, E., Sonabend, A., Xiao, T., et al. (2020). TMZ regulates GBM stemness via MMP14-DLL4-Notch3 pathway. *Int. J. Canc.* 146, 2218–2228. doi:10.1002/ijc.32636
- Vanlaeys, A., Fouquet, G., Kischel, P., Hague, F., Pasco-Brassart, S., Lefebvre, T., et al. (2020). Cadmium exposure enhances cell migration and invasion through modulated TRPM7 channel expression. *Arch. Toxicol.* 94, 735–747. doi:10.1007/s00204-020-02674-w
- Vescovi, A. L., Galli, R., and Reynolds, B. A. (2006). Brain tumour stem cells. *Nat. Rev. Canc.* 6, 425–436. doi:10.1038/nrc1889
- Voringe, S., Schreyer, L., Nadoln, W., Meier, M. A., Woerther, K., Mittermeier, C., et al. (2019). Inhibition of TRPM7 blocks MRTF/SRF-dependent transcriptional and tumorigenic activity. *Oncogene* 39 (11), 2328–2344. doi:10.1038/s41388-019-1140-8
- Voringe, S., Schreyer, L., Nadoln, W., Meier, M. A., Woerther, K., Mittermeier, C., et al. (2020). Inhibition of TRPM7 blocks MRTF/SRF-dependent transcriptional and tumorigenic activity. *Oncogene* 39, 2328–2344. doi:10.1038/s41388-019-1140-8
- Wan, J., Guo, A. A., Chowdhury, I., Guo, S., Hibbert, J., Wang, G., et al. (2019). TRPM7 induces mechanistic target of Rap1b through the downregulation of miR-28-5p in glioma proliferation and invasion. *Front Oncol* 9, 1413. doi:10.3389/fonc.2019.01413
- Wang, J., Yang, C. L., and Zou, L. L. (2017). Aldehyde dehydrogenase 1 expression has prognostic significance in patients with glioma. *Mol Clin Oncol* 7, 885–890. doi:10.3892/mco.2017.1396
- Yee, N. S. (2017). Role of TRPM7 in cancer: potential as molecular biomarker and therapeutic target. *Pharmaceuticals* 10 (4), 39. doi:10.3390/ph10020039
- Yee, N. S., Chan, A. S., Yee, J. D., and Yee, R. K. (2012). TRPM7 and TRPM8 ion channels in pancreatic adenocarcinoma: potential roles as cancer biomarkers and targets. *Sci. Tech. Rep.* 2012, 415158. doi:10.6064/2012/415158
- Yogi, A., Callera, G. E., O'Connor, S., Antunes, T. T., Valinsky, W., Miquel, P., et al. (2013). Aldosterone signaling through transient receptor potential melastatin 7 cation channel (TRPM7) and its  $\alpha$ -kinase domain. *Cell. Signal.* 25, 2163–2175. doi:10.1016/j.cellsig.2013.07.002
- Yue, Z., Zhang, Y., Xie, J., Jiang, J., and Yue, L. (2013). Transient receptor potential (TRP) channels and cardiac fibrosis. *Curr. Top. Med. Chem.* 13, 270–282. doi:10.2174/1568026611313030005
- Zeppernick, F., Ahmadi, R., Campos, B., Dictus, C., Helmke, B. M., Becker, N., et al. (2008). Stem cell marker CD133 affects clinical outcome in glioma patients. *Clin. Canc. Res.* 14, 123–129. doi:10.1158/1078-0432.ccr-07-0932
- Zhang, X., Chen, T., Zhang, J., Mao, Q., Li, S., Xiong, W., et al. (2012). Notch1 promotes glioma cell migration and invasion by stimulating  $\beta$ -catenin and NF- $\kappa$ B signaling via AKT activation. *Canc. Sci.* 103, 181–190. doi:10.1111/j.1349-7006.2011.02154.x
- Zhou, W., Guo, S., Xiong, Z., and Liu, M. (2014). Oncogenic role and therapeutic target of transient receptor potential melastatin 7 channel in malignancy. *Expert Opin. Ther. Targets* 18, 1177–1196. doi:10.1517/14728222.2014.940894

**Conflict of Interest:** The authors declare that the research was conducted in the absence of any commercial or financial relationships that could be construed as a potential conflict of interest.

Copyright © 2020 Wan, Guo, King, Guo, Saafir, Jiang and Liu. This is an open-access article distributed under the terms of the Creative Commons Attribution License (CC BY). The use, distribution or reproduction in other forums is permitted, provided the original author(s) and the copyright owner(s) are credited and that the original publication in this journal is cited, in accordance with accepted academic practice. No use, distribution or reproduction is permitted which does not comply with these terms.



# LINC00667 Sponges miR-4319 to Promote the Development of Nasopharyngeal Carcinoma by Increasing FOXQ1 Expression

Bing Liao<sup>1†</sup>, Yun Yi<sup>2†</sup>, Lei Zeng<sup>3</sup>, Zhi Wang<sup>1</sup>, Xinhua Zhu<sup>1</sup>, Jianguo Liu<sup>1</sup>, Bingbin Xie<sup>1</sup> and Yuehui Liu<sup>1\*</sup>

<sup>1</sup> Department of Otorhinolaryngology Head and Neck Surgery, The Second Affiliated Hospital of Nanchang University, Nanchang, China, <sup>2</sup> Department of Gynaecological Oncology, Jiangxi Cancer Hospital, Nanchang, China, <sup>3</sup> Department of Oncology, The Second Affiliated Hospital of Nanchang University, Nanchang, China

## OPEN ACCESS

### Edited by:

Dong-Hua Yang,  
St. John's University, United States

### Reviewed by:

Xingxing Yuan,  
Heilongjiang Academy of Traditional  
Chinese Medicine, China  
Xingfeng Li,  
Guizhou University of Traditional  
Chinese Medicine, China

### \*Correspondence:

Yuehui Liu  
candydd@163.com

<sup>†</sup>These authors have contributed  
equally to this work

### Specialty section:

This article was submitted to  
Pharmacology of Anti-Cancer Drugs,  
a section of the journal  
Frontiers in Oncology

**Received:** 24 November 2020

**Accepted:** 07 December 2020

**Published:** 25 January 2021

### Citation:

Liao B, Yi Y, Zeng L, Wang Z, Zhu X,  
Liu J, Xie B and Liu Y (2021)  
LINC00667 Sponges miR-4319 to  
Promote the Development of  
Nasopharyngeal Carcinoma by  
Increasing FOXQ1 Expression.  
Front. Oncol. 10:632813.  
doi: 10.3389/fonc.2020.632813

Accumulating evidence has indicated that lncRNAs regulate various biological and pathological processes in diverse malignant tumors. The roles of LINC00667 in cancer development have been explored in glioma, hepatocellular carcinoma and non-small cell lung cancer, but not in nasopharyngeal carcinoma (NPC). In the present study, we characterize the role and molecular mechanism of LINC00667 in NPC progression. It was found that LINC00667 was overexpressed in NPC cells compared to normal cells. Silencing LINC00667 suppressed the proliferation, migration, invasion and epithelial mesenchymal transition (EMT) in NPC cells. In addition, bioinformatics analysis revealed that LINC00667 acted as a ceRNA to absorb miR-4319. Further investigations illustrated that miR-4319 had low expression in NPC cells and functioned as a tumor suppressor in the progression of NPC. Mechanistic study identified forkhead box Q1 (FOXQ1) as a functional target of miR-4319. The effect of LINC00667 in NPC development was mediated by the miR-4319/FOXQ1 axis. Analysis on tumor xenograft mouse model demonstrated that knockdown of LINC00667 repressed NPC tumor growth *in vivo* and confirmed the *in vitro* results. Our present study suggested that LINC00667 promoted the malignant phenotypes of NPC cells by competitively binding to miR-4319 to up-regulate FOXQ1 expression. Our results revealed that LINC00667 could be a diagnostic and therapeutic target for NPC patients.

**Keywords:** nasopharyngeal carcinoma, LINC00667, miR-4319, FOXQ1, cancer development

**Abbreviations:** EdU, 5-Ethynyl-20-deoxyuridine; EMT, mesenchymal transition; FOXQ1, fork head box Q1; NPC, nasopharyngeal carcinoma; RIP, RNA immunoprecipitation; RT-qPCR, reverse transcription-quantitative polymerase chain reaction.

## INTRODUCTION

Nasopharyngeal carcinoma (NPC) is one of the most frequent malignant head and neck tumors, which originate from in the surface epithelium of nasopharynx (1, 2). The prevalence of NPC is geographically concentrated in Southeast Asia, especially in Southern China (3). Currently, the most commonly used therapeutic strategies for NPC are chemotherapy and radiation therapy, but the low sensitivity to chemotherapeutic drugs as well as the development of multidrug resistance hinder the treatment efficacy, leading to high recurrence rate and poor outcome of NPC (4–6). The pathogenesis of NPC is complex and involves in a variety of factors including diet, genetic susceptibility, viral infection and carcinogens (7). Thus, exploring the pathological mechanism governing NPC tumorigenesis is urgently needed for the treatment of NPC.

It is well known that long noncoding RNAs (lncRNAs) is a class of ubiquitous transcript greater than 200 nucleotides without protein coding ability (8, 9). Dysregulated lncRNAs have been detected in a wide range of pathological states, including human cancers (10, 11). Accumulating evidence has illustrated that lncRNAs are implicated in the initiation and progression of NPC. For example, up-regulated lncRNA AFAP1-AS1 expression is associated with NPC progression and poor prognosis (12). lncRNA LET repressed by EZH2 suppresses NPC cell proliferation and induces apoptosis (13). The p53-regulated lncRNA LOC401317 restrains cell proliferation and promotes apoptosis in NPC (14). Hence, it is important to identify the expression patterns and functional roles of lncRNAs in the tumorigenesis and development of NPC.

lncRNALINC00667 is located in human chr18 (5238100–5246508) with a full length of 8,409 bps and contains multiple miRNA response element (MRE) regions (15, 16). A number of studies have demonstrated that LINC00667 functions as a key mediator in the processes of diverse malignancies. For instance, LINC00667 facilitates the formation of glioma vasculogenic mimicry and the level of LINC00667 is positively associated with the development of glioma (17). LINC00667 predicts the poor prognosis of hepatocellular carcinoma (18). Moreover, overexpression of LINC00667 is strongly correlated with overall survival of patients with non-small cell lung cancer (NSCLC) (19). However, the role of LINC00667 in NPC and its mechanism have not been clarified. In our study, we explore the expression of lncRNA LINC00667 in NPC and how it affects the malignant phenotypes of NPC cells.

## METHODS

### Cell Culture

Human NPC cell lines (SUNE-1, CNE-1, CNE-2, HONE-1, HNE-1) and human normal nasopharyngeal epithelium cell line NP69 were purchased from the Chinese Academy of Sciences (Shanghai, China). All cell lines were maintained in DMEM/RPMI 1640 medium supplemented with 10% fetal

bovine serum and cultured in a humidified incubator containing 5% CO<sub>2</sub> at 37°C.

### Gene Transfection

The LINC00667-specific shRNA (sh-LINC00667) and the FOXQ1-specific shRNA (sh-FOXQ1) were used to knock down LINC00667 and FOXQ1, respectively. Non-specific shRNA (sh-NC) was used as a negative control. The miR-4319 mimics, inhibitors and the negative controls (NC mimic and NC inhibitor) were synthesized by Invitrogen (Carlsbad, USA). The transfections were carried out by Lipofectamine 3000 reagent as recommended by the vender.

### Reverse Transcription-Quantitative Polymerase Chain Reaction

RT-qPCR was performed to detect the gene expression level. Firstly, the TRIzol reagent was used to extract the total RNA from NPC cells. And then RNA purity was measured by Nano Drop 2000 spectrometer. After that, under the manufacturer's protocols, cDNA was synthesized with the Reverse Transcription System Kit. The PCR reaction was carried out using SYBR qPCR Mix (Toyobo, Osaka, Japan) and results were calculated using 2<sup>-ΔΔCt</sup> method. GAPDH and U6 served as internal controls for normalization.

### Cell Proliferation Assays

Cell viability was assessed using Cell Counting Kit-8 (MedChem Express, Monmouth Junction, USA) according to the manufacturer's protocol. For 5-Ethynyl-20-deoxyuridine (EdU) assay, NPC cells were seeded onto 24-well tissue culture plates, and then detected by the EdU assay kit (Ribo, Guangzhou, China) according to the product manual. The number of EdU-positive cells was counted under a microscope (Olympus, Tokyo, Japan) in three random fields using a 100 × objective (Olympus, Tokyo, Japan).

### Cell Migration and Invasion Assays

The wound healing and transwell chamber assays were performed to examine cell migration and invasion ability. The NPC cells were cultured in six-well plate until >90% confluence. Wounds were created *via* a scratch using pipette tips in the wound healing assay. Besides, NPC cells were cultured in serum-free medium at 37°C for 48 h. The wound healing results were observed under an inverted microscope at 0 and 48 h after cells were scratched.

For transwell chamber assays, transwell chambers (Corning, Cambridge, MA) covered with or without matrigel (BD Biosciences, CA, USA) were used for assessing cell migration and invasion ability. A total of approximately 1 × 10<sup>6</sup> cells was added into the top chamber of 24-well plates, and then the bottom well was complemented with 20% FBS. After incubating for 24 h, the migrated or invaded cells were fixed with 4% paraformaldehyde and then stained with Crystal violet. After that, cells were counted and imaged under an inverted microscope (Olympus, Tokyo, Japan).

## Western Blot Analysis

Cell proteins lysates were separated by 10% SDS-PAGE and transferred to nitrocellulose (NC) membranes. The membranes were blocked with 5% non-fat milk for 1 h at room temperature. Specific primary antibodies against E-cadherin (ab231303, 1:1,000, abcam) and Vimentin(ab20346, 1:1,000, abcam) were added for overnight incubation at 4°C, followed by incubation with HRP-labeled secondary antibodies and Enhanced Chemiluminescence (ECL) Kit (Thermo Scientific, CA, USA) was used to measure the immunoreactivity.

## Subcellular Fractionation

Cytoplasmic and Nuclear RNA Purification Kit (Norgen, Belmont, CA, USA) was used for detection of lncRNA LINC00667 nucleus fraction and cytoplasmic fraction isolated from NPC cells.

## RNA Immunoprecipitation Assay

RNA-Binding Protein Immunoprecipitation Kit (Millipore, Bedford, MA) was applied to conduct RIP experiment. Immunoprecipitation was carried out with Ago2 and IgG utilized as the negative controls. The abundance of LINC00667 and miR-4319 in precipitated RNAs was determined by RT-qPCR analysis.

## Luciferase Reporter Assay

The segments of LINC00667 and FOXQ1 containing miR-4319 binding sites were ligated into pmirGLO vectors. The mutant plasmids were constructed by mutating binding sites with miR-4319. SUNE-1 and HNE-1 cells were co-transfected with indicated reporter vectors and miR-4319 mimics or NC mimics utilizing Lipofectamine 3000 following the manufacturer's procedures. The luciferase activity was measured after transfection.

## RNA Pull-Down Assay

RNA pull-down assay was performed with the Pierce<sup>TM</sup> Magnetic RNA-Protein Pull-Down Kit (#20164, Thermo Fisher Scientific) in line with the manufacturer's recommendations.

## In Vivo Tumor Growth

All animal procedures were approved by the Animal Care Committee of The Second Affiliated Hospital of Nanchang University. BALB/c nude mice were purchased from Vital River Laboratory.  $5 \times 10^6$  HNE-1 cells stably transfected with sh-LINC00667 or sh-NC were subcutaneously injected into the nude mice. Tumor volume was measured every 7 days and calculated by the following formula: volume ( $\text{mm}^3$ ) = (length  $\times$  width<sup>2</sup>)/2. By the end of experiments, mice were euthanized. Tumor tissues from all groups were dissected and weighted. The experimental protocol was established according to the ethical guidelines of the Helsinki Declaration and was approved by the Animal Ethics Committee of the Second Affiliated Hospital of Nanchang University.

## Hematoxylin and Eosin Staining Assay

Tumors from nude mice were fixed with 10% buffered formalin at room temperature for 48 h, then dehydrated and embedded in paraffin. The sections were dyed with H&E solution and photographed using a light microscope.

## Immunohistochemistry Assay

Paraffin-embedded tissue sections were deparaffinized in xylene, dehydrated with ethanol, and blocked by 3% H<sub>2</sub>O<sub>2</sub> for 10 min. Following antigen retrieval in EDTA buffer at 95°C for 15–20 min, sections were incubated with Ki67 antibody (ab92742, 1:1,000, abcam) overnight at 4°C. After washing three times with PBS, the secondary antibody coupled to HRP was incubated at 37°C for 50 min. Then, DAB chromogen was added, sections were washed with water and counterstained with hematoxylin.

## TUNEL Staining

Using a TUNEL assay kit (Roche, USA) to detect the apoptosis of tumor sections. The sections were washed by PBS and then immobilized for 30 min with 4% paraformaldehyde. After washed with PBS once, the slices were added with 0.1% Triton X-100 for 2 min, and then washed with PBS once. Afterwards, 3% H<sub>2</sub>O<sub>2</sub> was used for incubation (5 min). Then the slides incubated with terminal deoxynucleotidyl transferase (TdT) enzyme at 37°C overnight. Then, sections were incubated with antidigoxigenin-peroxidase conjugate and using DAB to evaluate activity. The sections were examined under a light microscope and the TUNEL-positive cells were calculated in Image J software.

## Statistical Analysis

SPSS (18.0 version, SPSS, Inc., USA) and GraphPad (6.0 version) were used to analyze statistical data. Data were represented as mean  $\pm$  SD. Moreover, student's t-test and one-way ANOVA were used for comparison between two or more groups. All the experiments were repeated at least three times.  $P < 0.05$  was considered statistically significant.

## RESULTS

### Down-Regulation of LINC00667 Impedes NPC Cell Proliferation

To determine the abundance of LINC00667 in NPC cells, RT-qPCR analysis was carried out. We observed that the level of LINC00667 in NPC cell lines (CNE-1, CNE-2, HONE-1, SUNE-1 and HNE-1) was markedly higher than that in normal cell line NP69 (**Figure 1A**). As a result, we stably down-regulated LINC00667 expression by shRNA was used to explore the biological role of LINC00667 in NPC development. As shown in **Figures 1B, C**, the efficiency of LINC00667 interference was certified by GFP and RT-qPCR assays. Then, CCK8 assay showed that inhibition of LINC00667 resulted in the decrease of NPC cell viability (**Figure 1D**). Likewise, EdU assay indicated that down-regulation of LINC00667 dramatically inhibited NPC



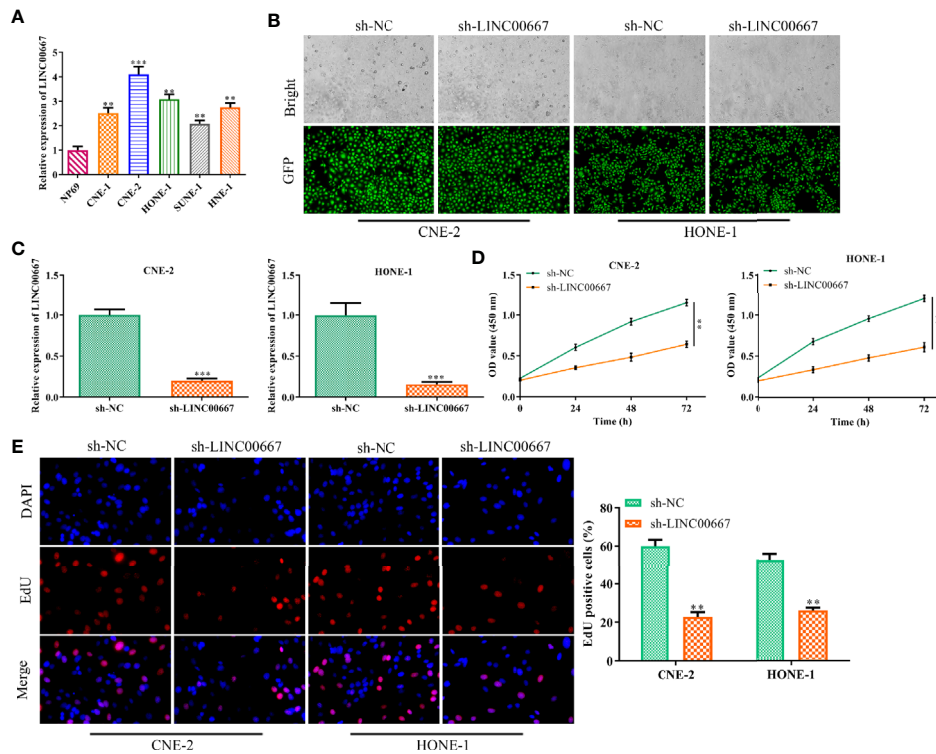


**FIGURE 1 |** Downregulation of LINC00667 impedes nasopharyngeal carcinoma (NPC) cell proliferation. **(A)** Reverse transcription-quantitative polymerase chain reaction (RT-qPCR) analysis of long noncoding RNA (lncRNA) LINC00667 level in human NPC cell lines (SUNE-1, CNE-1, CNE-2, HONE-1, and HNE-1) as well as human normal nasopharyngeal epithelium cell line NP69. **(B)** GFP assay and **(C)** RT-qPCR analysis on the gene transfection efficiency. **(D)** CCK-8 and **(E)** 5-Ethynyl-20-deoxyuridine (EdU) assay detected the impacts of LINC00667 on the proliferative capacity of NPC cells transfected with sh-LINC00667. Magnification 200 $\times$ . All experiments were performed at least in triplicate. \*\* $P < 0.01$ , \*\*\* $P < 0.001$  vs. NP69 group or sh-NC group.

cell proliferation (**Figure 1E**). These results demonstrated that LINC00667 was up-regulated in NPC and promoted cell proliferation of NPC.

### Down-Regulation of LINC00667 Suppresses Nasopharyngeal Carcinoma Cell Migration, Invasion and EMT

Based on the above findings, we further explore the function of LINC00667 in cell migration and invasion. Wound-healing assay illuminated that LINC00667 silencing led to the suppression of cell migration (**Figure 2A**). Similarly, results of transwell chamber assay suggested that the invasion ability of NPC cells was inhibited by attenuation of LINC00667 (**Figure 2B**). For the reason that EMT plays a vital part in cell metastasis, Western blot was used to measure the expression levels of EMT biomarkers so as to identify the effects of LINC00667 on EMT. Results delineated that knockdown of LINC00667 increased the expression of epithelial biomarker E-cadherin and declined the expression level of the mesenchymal biomarker (Vimentin) in SUNE-1 and HNE-1 cells (**Figure 2C**). These results indicated that LINC00667 down-regulation inhibited the migration, invasion and EMT of NPC cells.

### LINC00667 Acts as a Molecular Sponge for miR-4319

To further understand the mechanism of LINC00667 in promoting NPC cell growth, we detected the subcellular localization of LINC00667 and found that LINC00667 was markedly distributed in the cytoplasm of SUNE-1 and HNE-1 cells (**Figure 3A**). Accordingly, we conjectured that LINC00667 exerted its function *via* a competitive endogenous RNA (ceRNA) pattern. By exploring Starbase website, we uncovered that miR-4319 owned the putative binding sites for LINC00667 (**Figure 3B**). Therefore, RIP and luciferase reporter assays were carried out to confirm the interaction between LINC00667 and miR-4319. Results showed that LINC00667 and miR-4319 were highly enriched by Ago2 relative to IgG (**Figure 3C**). In concert with these results, miR-4319 mimics suppressed the luciferase activity of LINC00667-WT reporter in NPC cells, whereas efficacy was lost in response to LINC00667-Mut (**Figure 3D**). Moreover, we observed that miR-4319 expression was significantly higher in cells transfected with sh-LINC00667 than that in sh-NC group (**Figure 3E**). LINC00667 was weakly expressed when miR-4319 was up-regulated (**Figure 3F**). To sum up, these findings suggested that miR-4319 was sponged by LINC00667.

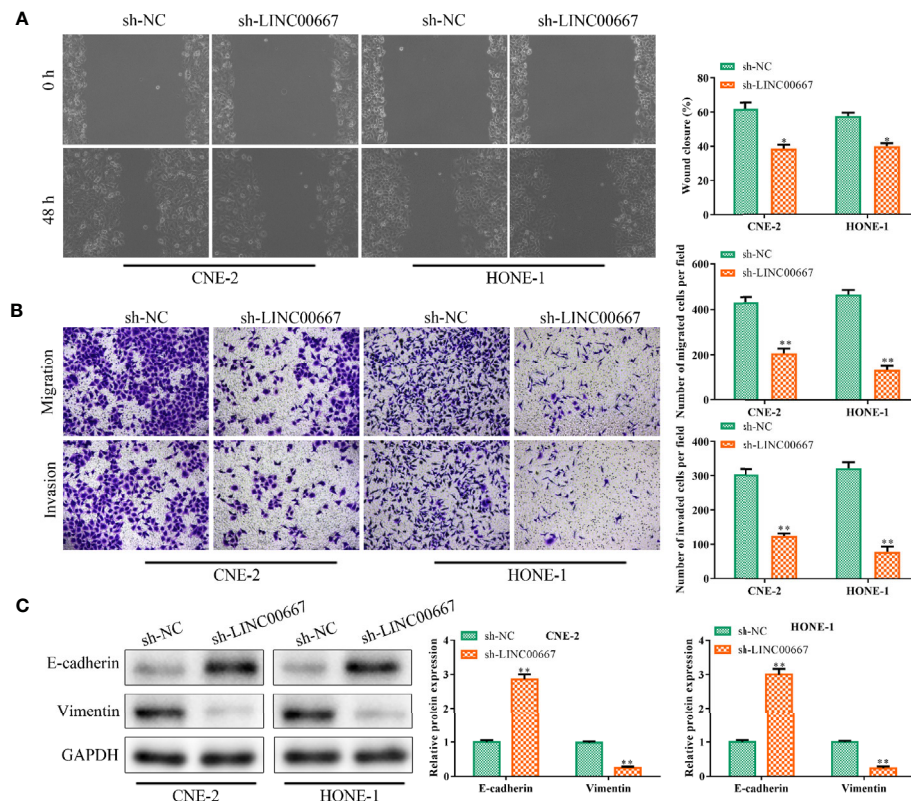


**FIGURE 2 |** Downregulation of LINC00667 suppresses nasopharyngeal carcinoma (NPC) cell migration, invasion and epithelial mesenchymal transition (EMT). **(A)** Wound-healing assay and **(B)** transwell chamber assay to measure the migration and invasion abilities of NPC cells transfected with sh-LINC00667. **(C)** The protein expression levels of EMT biomarkers. All experiments were performed at least in triplicate. \* $P < 0.05$ , \*\* $P < 0.01$  vs. sh-NC group.

## MiR-4319 Inhibits the Malignant Behaviors of Nasopharyngeal Carcinoma Cells

Although miR-4319 has been testified to be a tumor suppressor in various cancers, the role of miR-4319 on NPC cells is not clear. Thus, a series of experiments were conducted to characterize the role of miR-4319 in NPC. In comparison with normal cells, miR-4319 was down-regulated in NPC cells (Figure 4A). Because SUNE-1 and HNE-1 cells presented the lowest expression levels of miR-4319 among the five NPC cell lines, they were selected for transfection with miR-4319 mimics. GFP and RT-qPCR confirmed that miR-4319 was overexpressed in SUNE-1 and HNE-1 cells after transfection (Figures 4B, C). EdU assay showed that overexpression of miR-4319 significantly inhibited NPC cell proliferation (Figure 4D). Moreover, transwell chamber assay indicated that enhanced expression of miR-4319 overtly suppressed the migration and invasion of SUNE-1 and HNE-1 cells, (Figure 4E). These results suggested that miR-4319 played an inhibitory role in NPC progression.

## LINC00667 Elevates FOXQ1 Level in a miR-4319-Mediated Mechanism

Bioinformatics analysis was used to search the downstream genes of miR-4319. It was predicted that FOXQ1 might be a direct target of miR-4319 (Figure 5A). To validate the

association among FOXQ1, miR-4319 and LINC00667, RNA pull-down assay, luciferase reporter assay, RT-qPCR and Western blot were performed. Our observations illustrated that FOXQ1 was abundantly expressed in compounds pulled down by biotin-labeled miR-4319-WT (Figure 5B). Consistently, miR-4319 mimics remarkably impaired the luciferase activity of FOXQ1-WT and overexpression of LINC00667 led to the recovery of FOXQ1-WT activity, while the mutant forms of FOXQ1 had no notable changes (Figure 5C). Results of RT-qPCR and Western blot delineated that the expression level of FOXQ1 was lessened by miR-4319 mimics or depletion of LINC00667 (Figures 5D–G). Collectively, the described findings disclosed that LINC00667 up-regulated FOXQ1 through competing for miR-4319.

## LINC00667 Promotes Nasopharyngeal Carcinoma Progression by Regulating miR-4319/FOXQ1 Axis

In order to further identify whether miR-4319 and FOXQ1 were involved in LINC00667-mediated promotion of the proliferation, migration, invasion and EMT in NPC cells, rescue experiments were carried out. RT-qPCR analysis demonstrated that miR-4319 expression was inhibited after transfection with miR-4319 inhibitor and FOXQ1 was silenced

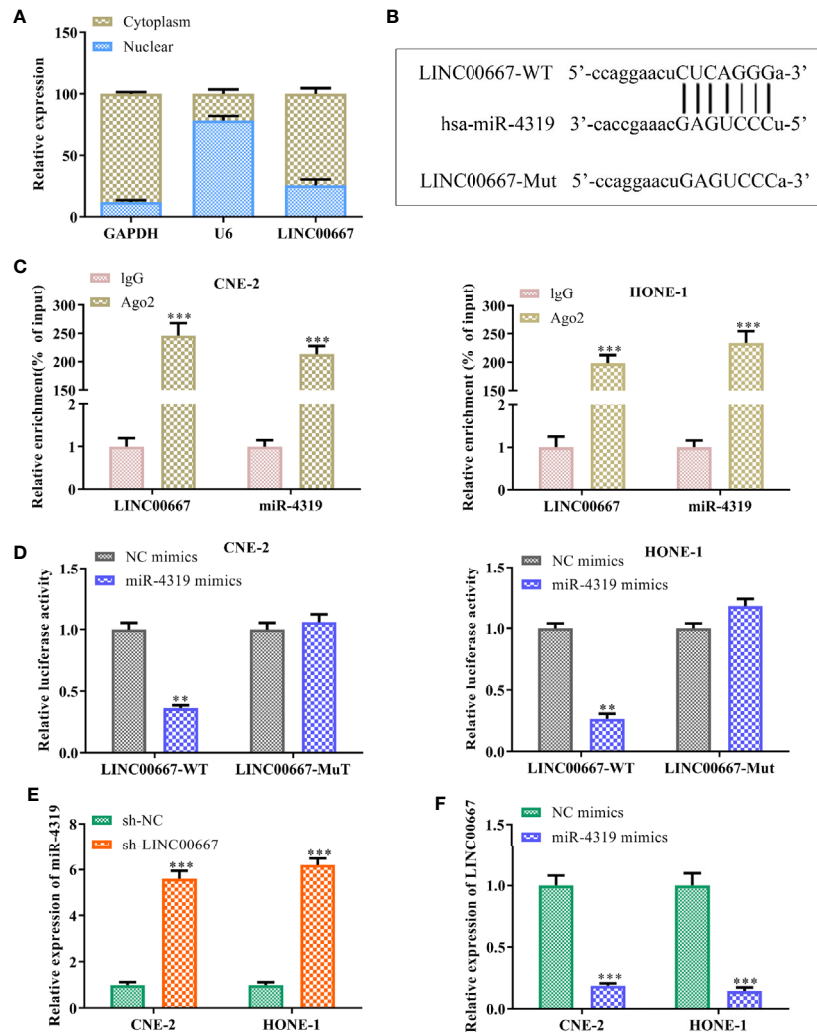


**FIGURE 3 |** LINC00667 acts as a molecular sponge for miR-4319. **(A)** The subcellular localization of LINC00667. **(B)** Bioinformatics analysis on the putative binding sites of LINC00667 in miR-4319. **(C)** RNA immunoprecipitation (RIP) assay. **(D)** Luciferase reporter assay. **(E, F)** RT-qPCR analysis of LINC00667 and miR-4319 expression levels in NPC cells transfected with miR-4319 mimic or sh-LINC00667. Magnification 200 $\times$ . All experiments were performed at least in triplicate. \*\* $P < 0.01$ , \*\*\* $P < 0.001$  vs. IgG group/NC mimic group/sh-NC group.

after transfection with sh-FOXQ1 (Figure 6A). EdU assay revealed that the proliferation of LINC00667-downregulated cells was increased by suppression of miR-4319 and retrieved by knockdown of FOXQ1 (Figure 6B). Furthermore, miR-4319 inhibitors led to the diminution of E-cadherin level and the increase in the expression level of Vimentin in HNE-1 cells transfected with sh-LINC00667, meanwhile, FOXQ1 silence abolished the impacts of miR-4319 inhibitors on the expression levels of E-cadherin and Vimentin (Figure 6C). In agreement with the foregoing findings, transwell chamber assays illuminated that cell migration and invasion suppressed by LINC00667 knockdown were facilitated by miR-4319 inhibitors and then reversed by down-regulation of FOXQ1 (Figure 6D). In a word, the miR-4319/FOXQ1 pathway mediated the function of LINC00667 in NPC.

## LINC00667 Knockdown Inhibits Tumor Growth of Nasopharyngeal Carcinoma *In Vivo*

On the basis of the above findings, we further investigate the impacts of LINC00667 on tumor progression *in vivo*. As shown in Figures 7A–C, the volume and weight of subcutaneous tumors were smaller in mice injected with LINC00667-downregulated cells than those in sh-NC group. In addition, immunohistochemical staining and TUNEL staining showed that the proportion of Ki67 positive cells was reduced and cell apoptosis was increased in the LINC00667 down-regulation group (Figure 7D). To further verify the relationship between LINC00667, miR-4319 and FOXQ1 *in vivo*, we detected their expression levels in xenografts. Results showed that LINC00667 and FOXQ1 were down-regulated, whereas miR-4319 level was

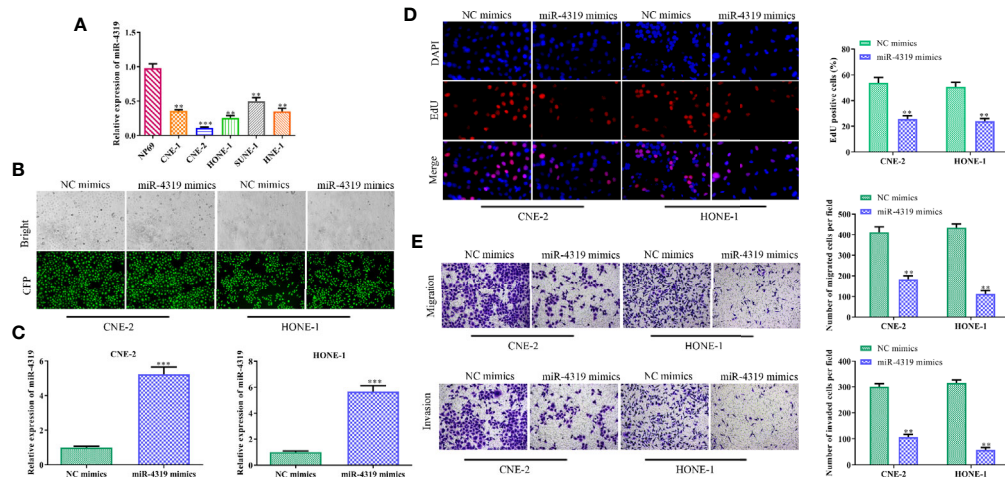


**FIGURE 4 |** MiR-4319 inhibits the malignant behaviors of nasopharyngeal carcinoma (NPC) cells. **(A)** Reverse transcription-quantitative polymerase chain reaction (RT-qPCR) on the expression pattern of miR-4319 in NPC cells. **(B, C)** Determination of the efficiency of miR-4319 overexpression by GFP and RT-qPCR assays. **(D)** EdU assay. **(E)** Transwell chamber assay. Magnification 200 $\times$ . All experiments were performed at least in triplicate.  $^{**}P < 0.01$ ,  $^{***}P < 0.001$  vs. NP69 group or NC mimic group.

enhanced in tumor tissues from sh-LINC00667 group compared with those from sh-NC group (**Figure 7E**). These results suggested that inhibition of LINC00667 impeded NPC cell growth *in vivo*.

## DISCUSSION

A growing number of evidence affirms that lncRNAs play core roles in a wide range of biological and pathological processes (20), and are involved in the initiation and progression of various

types of cancers (10, 11). LncRNALINC00667 has been reported to be a key mediator in the development of glioma (17), hepatocellular carcinoma (18), non-small cell lung cancer (19) and breast cancer (21). In this study, we characterize the expression status of LINC00667 and unravel its molecular mechanism in promoting the development of NPC. Our results revealed that the expression of LINC00667 was prominently elevated in NPC cells compared with normal cells. Loss-of-function assay by knocking down LINC00667 led to the inhibition of NPC cell proliferation, migration, invasion and EMT. These results are in consistent with previous reports that

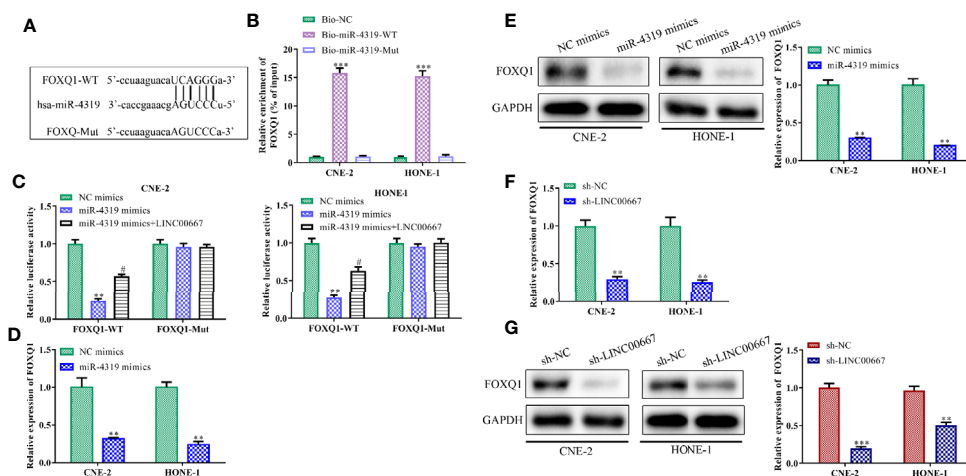


**FIGURE 5 |** LINC00667 elevates FOXQ1 level in a miR-4319-mediated mechanism. **(A)** The predicted binding regions between FOXQ1 and miR-4319. **(B)** RNA pull-down assay. **(C)** Luciferase reporter assay. **(D–G)** Reverse transcription-quantitative polymerase chain reaction (RT-qPCR) and Western blot analyses of FOXQ1 level in nasopharyngeal carcinoma (NPC) cells transfected with miR-4319 mimic or sh-LINC00667. All experiments were performed at least in triplicate.  $^{**}P < 0.01$ ,  $^{***}P < 0.001$  vs. Bio-NC group/NC mimic group/sh-NC group.  $^{#}P < 0.05$  vs. miR-4319 mimic group.



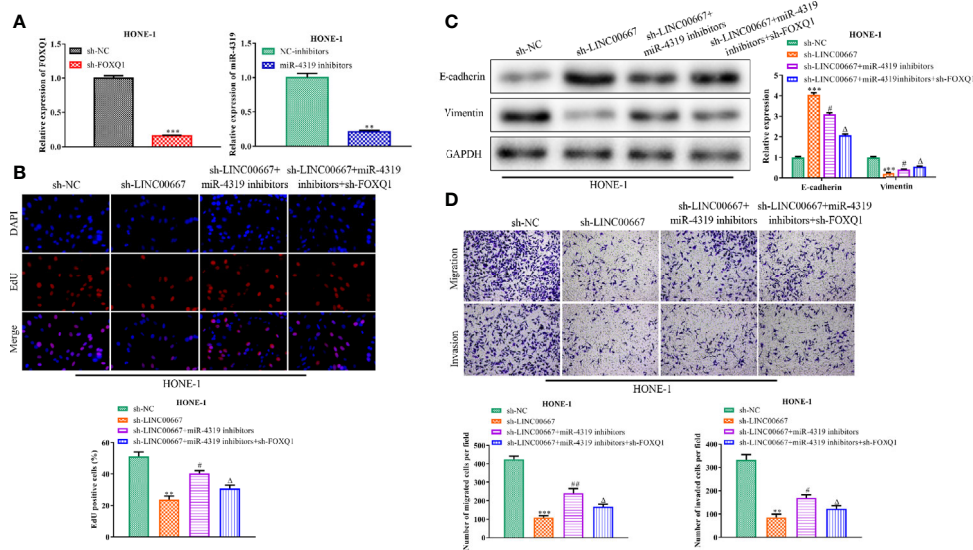


**FIGURE 6 |** LINC00667 promotes nasopharyngeal carcinoma (NPC) progression by regulation of miR-4319/FOXQ1 axis. **(A)** Expression levels of miR-4319 and FOXQ1 detected by reverse transcription-quantitative polymerase chain reaction (RT-qPCR) assay. **(B)** 5-Ethynyl-20-deoxyuridine (EdU) assay assessed the proliferative capacity of NPC cells. **(C)** Western blot analysis of protein levels of EMT-related biomarkers. **(D)** Detection of cell migration and invasion by transwell chamber assay. Magnification 200 $\times$ . All experiments were performed at least in triplicate. \*\* $P < 0.01$ , \*\*\* $P < 0.001$  vs. sh-NC group. # $P < 0.05$ , ## $P < 0.01$  vs. sh-LINC00667 group.  $\Delta P < 0.05$  vs. sh-LINC00667+miR-4319 inhibitor group.

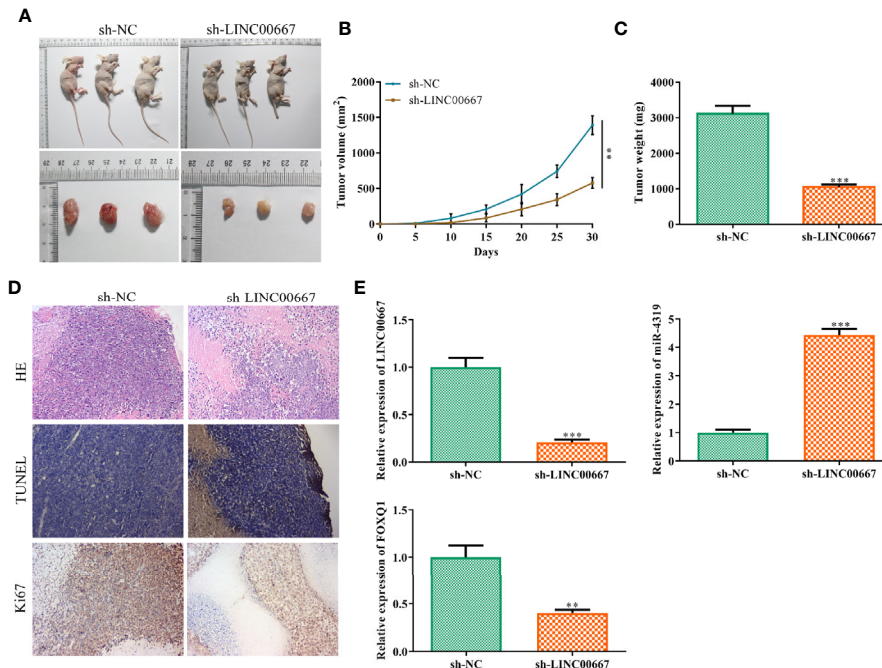


**FIGURE 7 |** LINC00667 knockdown inhibits tumor growth of nasopharyngeal carcinoma (NPC) *in vivo*. **(A)** Macroscopic images of transplanted tumors. **(B, C)** The volume and weight of xenograft tumors. **(D)** Hematoxylin and eosin (H&E) staining, immunohistochemistry (IHC) of Ki-67 and TUNEL in tumor sections. **(E)** reverse transcription-quantitative polymerase chain reaction (RT-qPCR) on the expression levels of LINC00667, miR-4319, and FOXQ1 in tumor tissues. All experiments were performed at least in triplicate. \*\* $P < 0.01$ , \*\*\* $P < 0.001$  vs. sh-NC group.

showed aberrant expression levels of lncRNAs are widely observed in numerous malignancies, including NPC (22–24). In addition, a variety of lncRNAs has been reported to be oncogenes or tumor suppressors in the initiation and evolution of NPC. For instance, overexpression of SOX2-activated lncRNA ANRIL promotes NPC cell growth (25). lncRNA THOR attenuates sensitivity of NPC cells to cisplatin by enhancing cell stemness (26). NKILA restrains NPC carcinogenesis and metastasis *via* suppression of NF- $\kappa$ B pathway (27).

It has been demonstrated that lncRNAs modulate tumorigenesis through diverse molecular mechanisms. Accumulating evidence indicates that competing endogenous RNA (ceRNA) regulates the carcinogenesis of cancers, including NPC (28, 29). A myriad of literatures suggests that lncRNAs can execute their functions in NPC *via* acting as ceRNAs (30, 31). In view of the primary distribution of LINC00667 in the cytoplasm, we speculated that LINC00667 may involve in the tumorigenesis of NPC by working as a ceRNA. Our bioinformatics analysis revealed that LINC00667 has the potential miR-4319 binding sites, indicating that it could be a ceRNA of miR-4319. It has been reported that miR-4319 is a tumor suppressor in multiple cancers, such as esophageal squamous cell carcinoma (ESCC) (32), non-small cell lung cancer (33), thyroid cancer (34), colorectal cancer (35) and prostate cancer (36). Results of our RIP and luciferase reporter assays confirmed that LINC00667 serves as a molecular sponge of miR-4319. Besides, NPC cells have low expression of miR-4319 and overexpression of miR-4319 retarded the proliferation, invasion and metastasis of NPC cells, suggesting that miR-4319 could inhibit the malignant behavior of NPC cells.

Aberrant expression of FOXQ1 has been justified to be associated with the development of diverse cancers (37, 38). More importantly, it is disclosed that the expression of FOXQ1 is significantly elevated in NPC tissues and cells and inhibition of FOXQ1 hindered cell growth, migration and invasion in NPC (39, 40). Among all of the predicted target genes of miR-4319, we identified FOXQ1 as a direct target of miR-4319. Our results of RNA pull-down assay, luciferase reporter assay, RT-qPCR and Western blot analysis suggested that the expression of FOXQ1 was inhibited by miR-4319 mimics or depletion of LINC00667, implicating that LINC00667 might upregulate FOXQ1 by inhibiting miR-4319. Moreover, our xenograft mouse model

validated the role of LINC00667 in promoting NPC cell growth *in vivo*, and the relationship of LINC00667, miR-4319 and FOXQ1. Our results suggest that LINC00667 might serve as an oncogene in the development of NPC *via* targeting miR-4319/FOXQ1 axis.

## CONCLUSIONS

In summary, our study unveiled that lncRNA LINC00667 exerted an oncogenic function in the development and progression of NPC both *in vitro* and *in vivo*. LINC00667 contributed to NPC tumorigenesis as a ceRNA by impairing miR-4319-dependant FOXQ1 down-regulation. Our findings will enhance the understanding of NPC pathogenesis and facilitate the improvement of lncRNA-guided diagnosis and treatment.

## DATA AVAILABILITY STATEMENT

The original contributions presented in the study are included in the article/supplementary materials; further inquiries can be directed to the corresponding author.

## ETHICS STATEMENT

The animal study was reviewed and approved by the Animal Care Committee of The Second Affiliated Hospital of Nanchang University.

## AUTHOR CONTRIBUTIONS

BL, ZW, and BX conceived and designed the study. YY, XZ, and YL performed the literature search and data extraction. LZ and JL drafted the manuscript. All authors contributed to the article and approved the submitted version.

## REFERENCES

1. Zeng Z, Huang H, Zhang W, Xiang B, Zhou M, Zhou Y, et al. Nasopharyngeal carcinoma: advances in genomics and molecular genetics. *Sci China Life Sci* (2011) 54(10):966–75. doi: 10.1007/s11427-011-4223-5
2. Chen YP, Chan ATC, Le QT, Blanchard P, Sun Y, Ma J. Nasopharyngeal carcinoma. *Lancet (London England)* (2019) 394(10192):64–80. doi: 10.1016/S0140-6736(19)30956-0
3. Gao J, Shao Z, Yan M, Fu T, Zhang L, Yan Y. Targeted regulation of STAT3 by miR-29a in mediating Taxol resistance of nasopharyngeal carcinoma cell line CNE-1. *Cancer Biomarkers Section A Dis Markers* (2018) 22(4):641–8. doi: 10.3233/cbm-170964
4. Zhu H, Jiang Z, Gong P, Zhang D, Zou Z, Qian Z, et al. Efficacy of low-protein diet for diabetic nephropathy: a systematic review of randomized controlled trials. *Lipids Health Dis* (2018) 17(1):141. doi: 10.1186/s12944-018-0791-8
5. Peng H, Zhang J, Zhang PP, Chen L, Tang LL, Yang XJ, et al. ARNTL hypermethylation promotes tumorigenesis and inhibits cisplatin sensitivity by activating CDK5 transcription in nasopharyngeal carcinoma. *J Exp Clin Cancer Res CR* (2019) 38(1):11. doi: 10.1186/s13046-018-0997-7
6. Huang Y, Tian Y, Zhao Y, Xue C, Zhan J, Liu L, et al. Efficacy of the hypoxia-activated prodrug evofosfamide (TH-302) in nasopharyngeal carcinoma in vitro and in vivo. *Cancer Commun (London England)* (2018) 38(1):15. doi: 10.1186/s40880-018-0285-0
7. Kong M, Lim YJ, Kim Y. Concurrent Chemoradiotherapy for Loco-regionally Advanced Nasopharyngeal Carcinoma: Treatment Outcomes and Prognostic Factors. *Asian Pacific J Cancer Prev APJCP* (2018) 19(6):1591–9. doi: 10.22034/apjcp.2018.19.6.1591
8. Ponting CP, Oliver PL, Reik W. Evolution and functions of long noncoding RNAs. *Cell* (2009) 136(4):629–41. doi: 10.1016/j.cell.2009.02.006

9. Fatica A, Bozzoni I. Long non-coding RNAs: new players in cell differentiation and development. *Nat Rev Genet* (2014) 15(1):7–21. doi: 10.1038/nrg3606
10. Berger AC, Korkut A, Kanchi RS, Hegde AM, Lenoir W, Liu W, et al. A Comprehensive Pan-Cancer Molecular Study of Gynecologic and Breast Cancers. *Cancer Cell* (2018) 33(4):690–705.e9. doi: 10.1016/j.ccell.2018.03.014
11. Bhan A, Soleimani M, Mandal SS. Long Noncoding RNA and Cancer: A New Paradigm. *Cancer Res* (2017) 77(15):3965–81. doi: 10.1158/0008-5472.Can-16-2634
12. Bo H, Gong Z, Zhang W, Li X, Zeng Y, Liao Q, et al. Upregulated long non-coding RNA AFAP1-AS1 expression is associated with progression and poor prognosis of nasopharyngeal carcinoma. *Oncotarget* (2015) 6(24):20404–18. doi: 10.18632/oncotarget.4057
13. Sun Q, Liu H, Li L, Zhang S, Liu K, Liu Y, et al. Long noncoding RNA-LET, which is repressed by EZH2, inhibits cell proliferation and induces apoptosis of nasopharyngeal carcinoma cell. *Med Oncol (Northwood London England)* (2015) 32(9):226. doi: 10.1007/s12032-015-0673-0
14. Gong Z, Zhang S, Zeng Z, Wu H, Yang Q, Xiong F, et al. LOC401317, a p53-regulated long non-coding RNA, inhibits cell proliferation and induces apoptosis in the nasopharyngeal carcinoma cell line HNE2. *PLoS One* (2014) 9(11):e110674. doi: 10.1371/journal.pone.0110674
15. Chen W, Zhou ZQ, Ren YQ, Zhang L, Sun LN, Man YL, et al. Effects of long non-coding RNA LINC00667 on renal tubular epithelial cell proliferation, apoptosis and renal fibrosis via the miR-19b-3p/LINC00667/CTGF signaling pathway in chronic renal failure. *Cell Signal* (2019) 54:102–14. doi: 10.1016/j.cellsig.2018.10.016
16. Yang Y, Li S, Cao J, Li Y, Hu H, Wu Z. RRM2 Regulated By LINC00667/miR-143-3p Signal Is Responsible For Non-Small Cell Lung Cancer Cell Progression. *OncoTargets Ther* (2019) 12:9927–39. doi: 10.2147/ott.S221339
17. Wang D, Zheng J, Liu X, Xue Y, Liu L, Ma J, et al. Knockdown of USF1 Inhibits the Vasculogenic Mimicry of Glioma Cells via Stimulating SNHG16/miR-212-3p and linc00667/miR-429 Axis. *Mol Ther Nucleic Acids* (2019) 14:465–82. doi: 10.1016/j.omtn.2018.12.017
18. Gu J, Zhang X, Miao R, Ma X, Xiang X, Fu Y, et al. A three-long non-coding RNA-expression-based risk score system can better predict both overall and recurrence-free survival in patients with small hepatocellular carcinoma. *Aging* (2018) 10(7):1627–39. doi: 10.18632/aging.101497
19. Zhou W, Liu T, Saren G, Liao L, Fang W, Zhao H. Comprehensive analysis of differentially expressed long non-coding RNAs in non-small cell lung cancer. *Oncol Lett* (2019) 18(2):1145–56. doi: 10.3892/ol.2019.10414
20. Jarroux J, Morillon A, Pinskaya M. History, Discovery, and Classification of lncRNAs. *Adv Exp Med Biol* (2017) 1008:1–46. doi: 10.1007/978-981-10-5203-3\_1
21. Zhu M, Lv Q, Huang H, Sun C, Pang D, Wu J. Identification of a four-long non-coding RNA signature in predicting breast cancer survival. *Oncol Lett* (2020) 19(1):221–8. doi: 10.3892/ol.2019.11063
22. Huarte M. The emerging role of lncRNAs in cancer. *Nat Med* (2015) 21(11):1253–61. doi: 10.1038/nm.3981
23. Bach DH, Lee SK. Long noncoding RNAs in cancer cells. *Cancer Lett* (2018) 419:152–66. doi: 10.1016/j.canlet.2018.01.053
24. Wu J, Hann SS. Functions and Roles of Long-Non-Coding RNAs in Human Nasopharyngeal Carcinoma. *Cell Physiol Biochem Int J Exp Cell Physiol Biochem Pharmacol* (2018) 45(3):1191–204. doi: 10.1159/000487451
25. Wu JH, Tang JM, Li J, Li XW. Upregulation of SOX2-activated lncRNA ANRIL promotes nasopharyngeal carcinoma cell growth. *Sci Rep* (2018) 8(1):3333. doi: 10.1038/s41598-018-21708-z
26. Gao L, Cheng XL, Cao H. LncRNA THOR attenuates cisplatin sensitivity of nasopharyngeal carcinoma cells via enhancing cells stemness. *Biochimie* (2018) 152:63–72. doi: 10.1016/j.biochi.2018.06.015
27. Zhang W, Guo Q, Liu G, Zheng F, Chen J, Huang D, et al. NKILA represses nasopharyngeal carcinoma carcinogenesis and metastasis by NF-kappaB pathway inhibition. *PLoS Genet* (2019) 15(8):e1008325. doi: 10.1371/journal.pgen.1008325
28. Salmena L, Poliseno L, Tay Y, Kats L, Pandolfi PP. A ceRNA hypothesis: the Rosetta Stone of a hidden RNA language? *Cell* (2011) 146(3):353–8. doi: 10.1016/j.cell.2011.07.014
29. Lian Y, Xiong F, Yang L, Bo H, Gong Z, Wang Y, et al. Long noncoding RNA AFAP1-AS1 acts as a competing endogenous RNA of miR-423-5p to facilitate nasopharyngeal carcinoma metastasis through regulating the Rho/Rac pathway. *J Exp Clin Cancer Res CR* (2018) 37(1):253. doi: 10.1186/s13046-018-0918-9
30. Lan X, Liu X. LncRNA SNHG1 functions as a ceRNA to antagonize the effect of miR-145a-5p on the down-regulation of NUA1 in nasopharyngeal carcinoma cell. *J Cell Mol Med* (2019) 23(4):2351–61. doi: 10.1111/jcmm.13497
31. Zheng YJ, Zhao JY, Liang TS, Wang P, Wang J, Yang DK, et al. Long noncoding RNA SMAD5-AS1 acts as a microRNA-106a-5p sponge to promote epithelial mesenchymal transition in nasopharyngeal carcinoma. *FASEB J Off Publ Fed Am Societies Exp Biol* (2019) 33(11):12915–28. doi: 10.1096/fj.201900803R
32. Hu X, Wang M, Cao L, Cong L, Gao Y, Lu J, et al. miR-4319 suppresses the growth of esophageal squamous cell carcinoma via targeting NLRC5. *Curr Mol Pharmacol* (2019) 144–9. doi: 10.2174/1874467212666191119094636
33. Li Z, Feng C, Guo J, Hu X, Xie D. GNAS-AS1/miR-4319/NECAB3 axis promotes migration and invasion of non-small cell lung cancer cells by altering macrophage polarization. *Funct Integr Genomics* (2020) 20(1):17–28. doi: 10.1007/s10142-019-00696-x
34. Bian S. miR-4319 inhibited the development of thyroid cancer by modulating FUS-stabilized SMURF1. *J Cell Biochem* (2020) 121(1):174–82. doi: 10.1002/jcb.29026
35. Huang L, Zhang Y, Li Z, Zhao X, Xi Z, Chen H, et al. MiR-4319 suppresses colorectal cancer progression by targeting ABTB1. *U Eur Gastroenterol J* (2019) 7(4):517–28. doi: 10.1177/2050640619837440
36. Lin X, Wang Y. Re-expression of microRNA-4319 inhibits growth of prostate cancer via Her-2 suppression. *Clin Trans Oncol Off Publ Fed Spanish Oncol Societies Natl Cancer Institute Mexico* (2018) 20(11):1400–7. doi: 10.1007/s12094-018-1871-y
37. Liu JY, Wu XY, Wu GN, Liu FK, Yao XQ. FOXQ1 promotes cancer metastasis by PI3K/AKT signaling regulation in colorectal carcinoma. *Am J Trans Res* (2017) 9(5):2207–18.
38. Zhang J, Liu Y, Zhang J, Cui X, Li G, Wang J, et al. FOXQ1 promotes gastric cancer metastasis through upregulation of Snail. *Oncol Rep* (2016) 35(6):3607–13. doi: 10.3892/or.2016.4736
39. Zhang Z, Ma J, Luan G, Kang L, Su Y, He Y, et al. MiR-506 suppresses tumor proliferation and invasion by targeting FOXQ1 in nasopharyngeal carcinoma. *PLoS One* (2015) 10(4):e0122851. doi: 10.1371/journal.pone.0122851
40. Peng XH, Huang HR, Lu J, Liu X, Zhao FP, Zhang B, et al. MiR-124 suppresses tumor growth and metastasis by targeting Foxq1 in nasopharyngeal carcinoma. *Mol Cancer* (2014) 13:186. doi: 10.1186/1476-4598-13-186

**Conflict of Interest:** The authors declare that the research was conducted in the absence of any commercial or financial relationships that could be construed as a potential conflict of interest.

Copyright © 2021 Liao, Yi, Zeng, Wang, Zhu, Liu, Xie and Liu. This is an open-access article distributed under the terms of the Creative Commons Attribution License (CC BY). The use, distribution or reproduction in other forums is permitted, provided the original author(s) and the copyright owner(s) are credited and that the original publication in this journal is cited, in accordance with accepted academic practice. No use, distribution or reproduction is permitted which does not comply with these terms.



# Overexpression of LncRNA BM466146 Predicts Better Prognosis of Breast Cancer

Yunxiang Zhang<sup>1,2</sup>, Xiaotong Dong<sup>2</sup>, Yang Wang<sup>3</sup>, Liquan Wang<sup>3</sup>, Guiyan Han<sup>2</sup>, Lvcheng Jin<sup>2</sup>, Yanping Fan<sup>2</sup>, Guodong Xu<sup>2</sup>, Dawei Yuan<sup>4</sup>, Jie Zheng<sup>5</sup>, Xiangyu Guo<sup>6</sup> and Peng Gao<sup>1\*</sup>

<sup>1</sup> Key Laboratory for Experimental Teratology of the Ministry of Education, Department of Pathology, School of Basic Medical Sciences, Shandong University, Jinan, China, <sup>2</sup> Pathology Department, First Affiliated Hospital of Weifang Medical University, (Weifang People's Hospital), Weifang, China, <sup>3</sup> Breast Surgery Department, First Affiliated Hospital of Weifang Medical University, (Weifang People's Hospital), Weifang, China, <sup>4</sup> Precision Medicine Department, Geneis Beijing Co., Ltd., Beijing, China, <sup>5</sup> Department of Diagnostic Pathology, Weifang Medical University, Weifang, China, <sup>6</sup> Department of Pathology, Qilu Hospital, Shandong University, Jinan, China

## OPEN ACCESS

### Edited by:

Dong-Hua Yang,  
St. John's University, United States

### Reviewed by:

De-shen Wang,  
Sun Yat-sen University Cancer Center  
(SYSUCC), China  
Longyang Liu,  
Southern Medical University, China

### \*Correspondence:

Peng Gao  
gaopeng@sdu.edu.cn

### Specialty section:

This article was submitted to  
Pharmacology of Anti-Cancer Drugs,  
a section of the journal  
Frontiers in Oncology

**Received:** 12 November 2020

**Accepted:** 10 December 2020

**Published:** 29 January 2021

### Citation:

Zhang Y, Dong X, Wang Y,  
Wang L, Han G, Jin L, Fan Y,  
Xu G, Yuan D, Zheng J, Guo X and  
Gao P (2021) Overexpression of  
LncRNA BM466146 Predicts Better  
Prognosis of Breast Cancer.  
Front. Oncol. 10:628757.  
doi: 10.3389/fonc.2020.628757

This study analyzes the expression and clinical significance of long non-coding RNA (lncRNA) BM466146 in breast cancer, and explores the role of BM466146 in immune regulation. The expression of BM466146 in 89 cases of breast cancer and their corresponding non-cancerous breast tissues was detected by quantitative real-time polymerase chain reaction (qRT-PCR). Kaplan-Meier survival analysis was applied to evaluate patient survival. EDU and CCK-8 experiments on breast cancer cells were performed to verify the function of BM466146 *in vitro*. The target genes of BM466146 were screened by informatics analysis to predict associated miRNAs and their corresponding mRNAs, immune genes associated with lncRNAs and chemokines associated with CD8. Immunohistochemistry was used to detect the expression of CD8, Ki-67, and CXCL-13 in the 89 breast cancer tissues. It was found that the expression of lncRNA BM466146 in breast cancer tissues was significantly lower than that in normal breast tissues ( $P < 0.001$ ). In breast cancer, tissues that overexpressed BM466146 exhibited a lower Ki-67 index compared with that of low BM466146 expression ( $P = 0.048$ ). Kaplan-Meier survival analysis showed that breast cancer patients with overexpression of BM466146 had longer overall survival. EDU and CCK8 experiments showed that overexpression of BM466146 inhibited the proliferation of breast cancer cells. The hsa-miR-224-3p is associated with BM466146, and its target gene might be CXCL-13. The positive CD8 cells in the BM466146 overexpression group was higher than that in the low BM466146 expression group ( $P=0.027$ ), and the positive CD8 cells in the CXCL-13 positive group was higher ( $P=0.023$ ) than that of the negative group. Our results indicate that the lncRNA BM466146 has the function of tumor suppressor gene. Overexpression of BM466146 is associated with better prognosis. BM466146 could regulate CXCL-13 by adsorbing hsa-miR-224-3p and inducing CD8<sup>+</sup> T cells to accumulate in the tumor area which regulate immune response. Therefore, BM466146 could be a prognostic biomarker and a molecular immune target of breast cancer.

**Keywords:** long non-coding RNA, BM466146, breast cancer, CD8<sup>+</sup> T cells, prognosis



## INTRODUCTION

Breast cancer is the most common malignant tumor that threatens women's health. The latest statistics in recent years show that the incidence and mortality of breast cancer remains high globally (1, 2). Chemotherapy is currently the main treatment modality for breast cancer, but drug resistance of tumor limits the effectiveness of treatment (3). Studies have demonstrated that a large number of immune cells, cytokines and growth factors exist in the tumor microenvironment of breast cancer. These factors play important roles in tumor proliferation, migration, and invasion (4). There is evidence that tumor-infiltrating lymphocytes can affect the prognosis and treatment response of ductal carcinoma *in situ* and invasive breast cancers. The tumor immune environment before treatment can be used as an indicator for the prognosis of individual diseases, as well as treatment guide (5). However, the mechanism of immune system related to the occurrence, metastasis, treatment, and prognosis of breast cancer is not clear. Therefore, exploring the pathogenesis of breast cancer and finding targets for breast cancer immunotherapy is the key to prolong the survival of patients and improve their quality of life (6).

Human genomic DNA is composed of 3 billion base pairs, but only <2% of base pairs encode functional proteins, and about 98% of genomic DNA is transcribed into non-coding RNA (7), of which lncRNA is an important component. At present, the role of lncRNA in various cancers such as liver cancer, breast cancer, bladder cancer and other tumors has been reported (8–10). However, the functions and mechanisms of lncRNA in the development of breast cancer have been less studied. In our preliminary microarray analysis on lncRNA, we found that the expression of lncRNA BM466146 in cancer was significantly reduced compared with normal tissue. We therefore explore the biological function and molecular mechanisms of BM466146 in breast cancer, particularly its role in the development and prognosis of breast cancer.

## MATERIALS AND METHODS

### Specimen Collection

In this study, 89 pairs of fresh breast cancer tissue specimens and matched normal breast tissues ( $\geq 5$  cm from the tumor) were collected from the hospitalized patients in Weifang People's Hospital from February 2019 to June 2019. Each half of the tissues was quickly stored in a  $-80^{\circ}\text{C}$  ultra-low temperature refrigerator for qRT-PCR detection, and the other half of the tissues was placed in 4% neutral formaldehyde solution for HE and immunohistochemical staining. The clinical data of all specimens were complete, and two senior pathologists independently read and evaluated the tissues according to the 2019 version of the WHO diagnostic criteria. The study was approved by the Ethics Committee of Weifang People's Hospital and the participated patients submitted their informed consent.

### Immunohistochemistry

Immunohistochemical staining was used to detect the expression of Ki-67, CD8, CXCL-13 in breast cancer tissues. High temperature and high pressure tissue antigen retrieval method with citrate buffer (PH 9.0) was used to restore the antigens. DAB was used for color development. Neutral gum was used to mount the slides. Positive control was set in each staining. The Ki-67 antibody is a mouse anti-human monoclonal antibody (Ready-to-use antibodies, Fuzhou Maixin, China). The CD8 antibody is a rabbit anti-human monoclonal antibody (Ready-to-use antibodies, Beijing Zhongshan Jinqiao, China). The CXCL-13 antibody is a goat anti-human polyclonal antibody (Ready-to-use antibodies, Fuzhou Maixin, China). A positive result means that there is brownish yellow staining on the nucleus (Ki-67), cell membrane (CD8) or cytoplasm (CXCL-13) of a specific cell in the tissue section, and the number of positive cells is more than 5%.

### RNA Extraction and qRT-PCR

Total RNA of fresh breast cancer and normal breast tissues was extracted using Axygen Total RNA Small Amount Preparation Kit (Corning Life Sciences Co., Ltd., Suzhou, China). UV spectrophotometer (One Drop OD 1000, Nanjing Wuyi Technology Co., Ltd., China) was used to examine the concentration and purity of total RNA by A260/A280 nm ratio. M-MuLV reverse transcriptase (200 U/ $\mu\text{l}$ , purchased from New England Biolabs), RNase inhibitor (Takara), and dNTP (Takara) were used to synthesize cDNA. The kit used for qRT-PCR is KAPA SYBR FAST qPCR Kits (purchased from KAPA). GAPDH is selected as the internal reference. The primer sequence is as follows:

BM466146 forward primer 5'-ACCTGACCCATCTACCTTGC-3',

reversed primer 5'-GTGGTGCTCGCCTGTAATC-3';

GAPDH forward primer 5'-GCACCGTCAA-GGCTGA GAAC-3',

reversed primer 5'-TGGTGAAGACGCCAGTGGA-3'.

The PCR was performed using the Applied Biosystems 7500. All tests were performed in triplicates.

### Cell Culture

The Breast cancer MDA-MD-231 cell line was purchased from Procell Life Science & Technology Co., Ltd. (Wuhan, China) and cultured in RPM1640 medium (Solarbio, USA) containing 10% fetal bovine serum (FBS), and cultivated in an incubator with 5%  $\text{CO}_2$  at  $37^{\circ}\text{C}$ .

### Plasmid Construction and Cell Transfection

The pcDNA3.1-BM466146 overexpression plasmid was constructed by Jinan Boshang Biotechnology Co., Ltd. (Jinan, China), pcDNA3.1-BM466146 overexpressed plasmid was transfected into the MDA-MD-231 cells. The pcDNA3.1 vector was used as the control. The cell function experiments were conducted 24 h after transfection.

## CCK-8 Assay

BBoneBot CCK-8 cell proliferation-cytotoxicity detection kit (Shanghai bestbio Biotechnology Co., Ltd., Shanghai, China) was used to detect the proliferation of the cells. MDA-MD-231 cells after 24 h of transfection was seeded at  $4 \times 10^3$  cells per well in a 96-well plate, with four replicate wells in each group, and the absorbance at 450nm wavelength was measured at 24, 48, 72, and 96 h.

## EDU Assay

BeyoClick EdU-594 cell proliferation detection kit (Shanghai Biyuntian Biotechnology Co., Ltd., Shanghai, China) was used to detect cell proliferation. MDA-MD-231 cells transfected for 24 h was seeded with  $1 \times 10^4$  cells per well in a 96-well plate, with three replicate wells in each group, and the cell proliferation efficiency was calculated after fluorescent staining.

## Cell Migration and Invasion Assay

Transwell chamber (Corning, Cambridge, MA, USA) was used to detect the effect of overexpression of BM466146 on the migration and invasion of MDA-MD-231 cells. In the migration experiment, the cells in serum-free medium ( $3 \times 10^4$  cells/200  $\mu$ l) were added to the inner chamber, and the medium containing 10% FBS was added to the outer chamber. After incubating for 24 h, the cells in the inner chamber were wiped out with a cotton swab. The cells that pass through the membrane and adhere to the bottom of the membrane were fixed and then subjected to Giemsa staining. For the invasion experiment, a transwell chamber coated with Matrigel matrix (BD Bioscience) was used for the experiment.

## Bioinformatics

The RNA-seq datasets of breast cancer patients, along with the clinical information, were downloaded from the TCGA database through GDC data transfer tool. The expression level of each gene was generated by analyzing RNA-seq datasets with reference of the Genome Reference Consortium Human genome build 38 (GRCh38). Then, all gene expression data were combined as the gene expression profile for breast cancer. The data were analyzed in combination with the data from human reference genome 19 (hg19) published by the University of California, Santa Cruz (UCSC). The survival curve was drawn based on the data.

The lncRNA and genes that are related to immune functions, and CD8<sup>+</sup> T cell-related chemokines were searched through The Encyclopedia of RNA Interactomes (ENCORI, <http://starbase.sysu.edu.cn/index.php>) database. The miRNAs and target genes related to BM466146 were searched through miRNA datasets. Target genes were obtained in the intersection of immune genes related to lncRNA, chemokines related to CD8<sup>+</sup>T cells, and target genes of miRNA.

## Statistical Analysis

Statistical analysis was performed using SPSS Statistics 26 software. Mann-Whitney U rank sum was used to test the significance of statistical differences, Receiver Operating Characteristic (ROC curve) was used to determine the cut off

value of lncRNA BM466146 expression. Chi-square test and Fisher exact test were used to analyze the relationship between the expression of lncRNA BM466146, Ki-67 index and CD8. Chi-square test was used to analyze the relationship between CXCL-13 and CD8. Spearman correlation test was used for correlation analysis. Student's t-test was used for the difference between the experimental group and the control group.  $P$  value<0.05 is regarded as statistically significant.

## RESULT

### Expression of lncRNA BM466146 Is Significantly Lower in Breast Cancer Compared With Non-Cancerous Tissues

Data mining from microarray analysis of lncRNA in GEO (GSE72307) showed that the level of BM466146 was significantly lower in cancer compared to normal tissue. We collected 89 pairs of matched specimens from female patients with breast cancer, aged 31–82 years old, with an average age of 55 years. The size of the tumor is 0.8cm–9cm. The pathological types are invasive breast cancer (**Figures 1A, B**). The expression of BM466146 in these 89 pairs of breast cancer tissues and their adjacent tissues was evaluated by qRT-PCR. The specificity of the amplified product was verified by the gene dissolution curve. The experimental results showed that the lncRNA BM466146 is a single peak with good specificity with no non-specific amplification, and no abnormality in the amplification curve. The median expression of BM466146 in breast cancer tissues was 0.034236, and the median expression in normal breast tissues was 0.272265. The difference in the expression of lncRNA BM466146 between the two was 7.95 times. This result confirmed that the expression of BM466146 in breast cancer is significantly lower compared to normal breast tissues ( $U=385.000$ ,  $P<0.001$ , **Figures 1C–E**).

### The Expression of lncRNA BM466146 Is Positively Correlated With CD8<sup>+</sup>T Cells and Negatively Correlated With Ki-67 Proliferation Index in Breast Cancer

Immunohistochemical staining for CD8 antibody was performed. Tumors with 10% or more positive CD8 staining were counted as positive staining, and less than 10% was negative staining. The cut off value of BM466146 expression in breast cancer was determined according to the ROC curve, and was 0.0411913. Based on this value, there were 34 cases of BM466146 high expression, and 55 cases of BM466146 low expression. In the 34 cases of BM466146 high expression group, 27 cases were CD8 positive and seven cases were negative. In the 55 cases of BM466146 low expression group, there were 31 CD8 positive samples and 24 negative samples. The number of CD8-positive T cells was different between the BM466146 high and the low expression group. The CD8 positive T cells was higher in the BM466146 high expression group, and the difference was statistically significant ( $P=0.027$ ,  $\chi^2 = 4.917$ , **Table 1, Figures 2A–C**). Spearman correlation analysis also confirmed that the

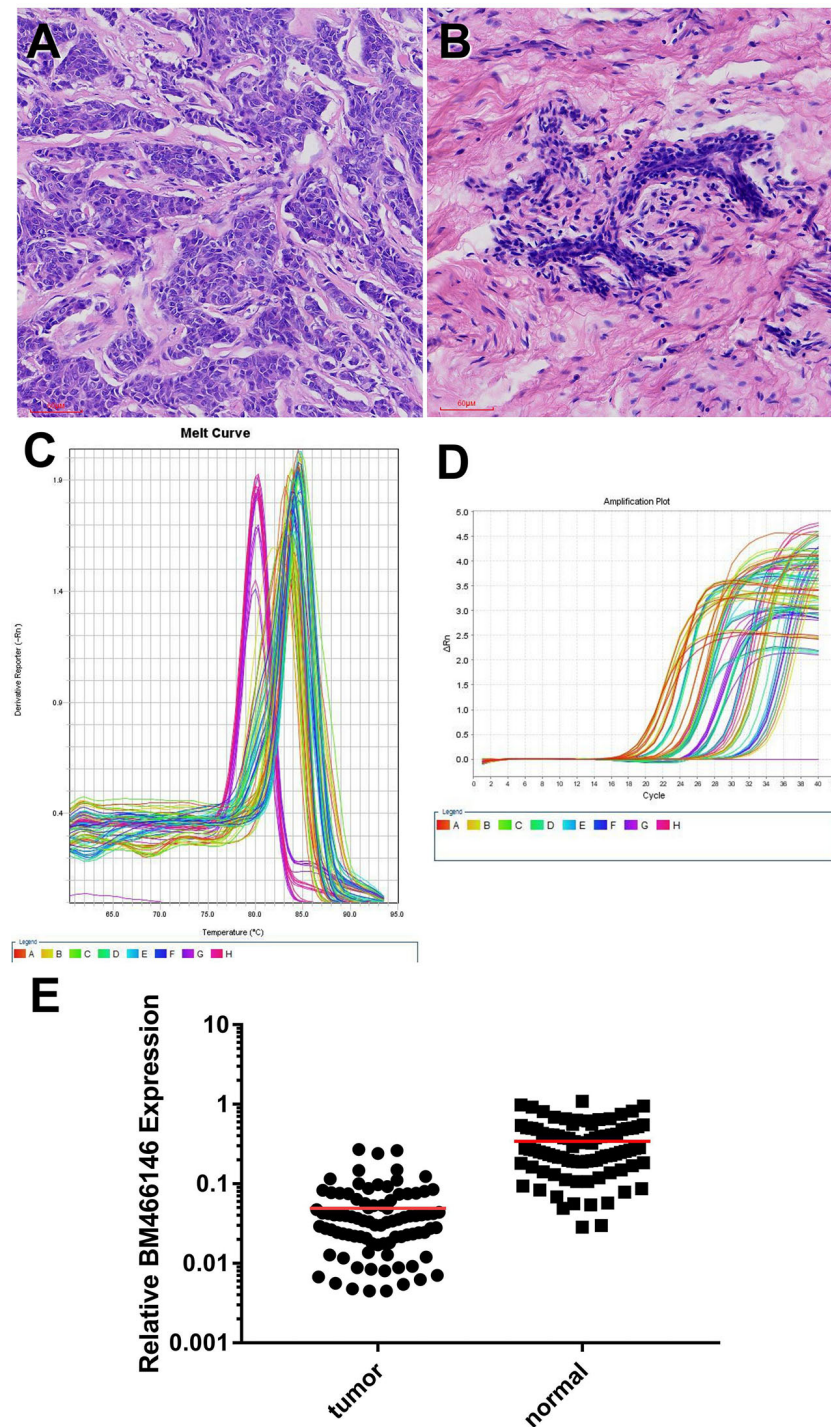


**FIGURE 1** | Expression of lncRNA BM466146 in breast cancer tissues and normal adjacent tissues (A, B) HE images of breast invasive carcinoma and normal breast tissues (HE×200). (C, D) RT-PCR results showed that the melting curves were all single peaks, no abnormal peaks, and no non-specific amplification. The four phases of the amplification curve at baseline phase, exponential growth phase, linear growth phase, and plateau phase are obvious. (E) The expression of lncRNA BM466146 is high in normal breast tissue and low in breast cancer tissue. The difference between the two is about 7.95 times (median change,  $U=385.000$ ,  $P<0.001$ ).



**TABLE 1 |** Relationship between BM466146 and Ki-67 and CD8.

	Number	BM466146		$\chi^2$	P-value
		Low expression	High expression		
CD8				4.917	0.027
Positive	58	31	27		
Negative	31	24	7		
Ki-67 index				3.910	0.048
<30%	38	19	19		
≥30%	51	36	15		

Cut-off  $a=0.05$ .

number of CD8 positive cells was correlated with BM466146 expression ( $P=0.027$ ,  $r=0.235$ ).

According to the Chinese Anti-Cancer Association Breast Cancer Diagnosis and Treatment Guidelines and Standards (2019 edition), 30% of Ki-67 index in breast cancer tissues is a critical value, with 30% or more as a high proliferation index, and less than 30% as a low proliferation index. Immunohistochemistry with Ki-67 antibody was performed. The Ki-67 index of breast cancer cells in BM466146 high expression group is different from that of low expression group. In the 34 cases of BM466146 high expression group, there was 44% cases with high Ki-67 proliferation index and 56% cases had low proliferation index. In the 55 cases of BM466146 low expression group, Ki-67 high proliferation index accounted for 65%, and low proliferation index accounted for 35%. These results indicated that the BM466146 low expression group had a high Ki-67 index and the difference was statistically significant ( $P=0.048$ ,  $\chi^2 = 3.910$ , **Table 1**, **Figures 2D–F**). Spearman correlation test results show that the expression of BM466146 is negatively correlated with Ki-67 index ( $P=0.049$ ,  $r = -0.210$ ).

## Overexpression of BM466146 Reduces the Proliferation of Breast Cancer Cells In Vitro

CCK-8 experiment results showed that overexpression of BM466146 inhibited the proliferation of MDA-MD-231 cells ( $P = 0.048$ , **Figure 3A**), and the EDU experiment also confirmed that, compared with the control group, overexpression of BM466146 significantly reduced the proliferation of MDA-MD-231 cells with a difference of 16% ( $P=0.0067$ , **Figure 3B**). Transwell cell migration and invasion experiments confirmed that overexpression of BM466146 has no significant effect on the migration and invasion of MDA-MD-231 cells (**Supplementary 1**).

## Patients With High Expression of BM466146 Have Better Overall Survival

Kaplan-Meier survival analysis was performed using the combine data from the database of TCGA and hg19 gene and a survival curve was drawn (**Figure 4A**). The results showed that the expression of lncRNA BM466146 is positively associated with the prognosis of patients. Patients with high expression of BM466146 have better prognosis. Compared with patients with low expression of BM466146, patients with high expression of BM466146 have a significantly longer survival time, and the difference is statistically significant ( $P=0.048$ ).

## Bioinformatics

Bioinformatics analysis was performed. A total of 19 miRNAs related to the BM466146 gene, and a total of 922 target genes of these miRNAs were found through chromosome colocalization and sequence identity matching. 373 immune function

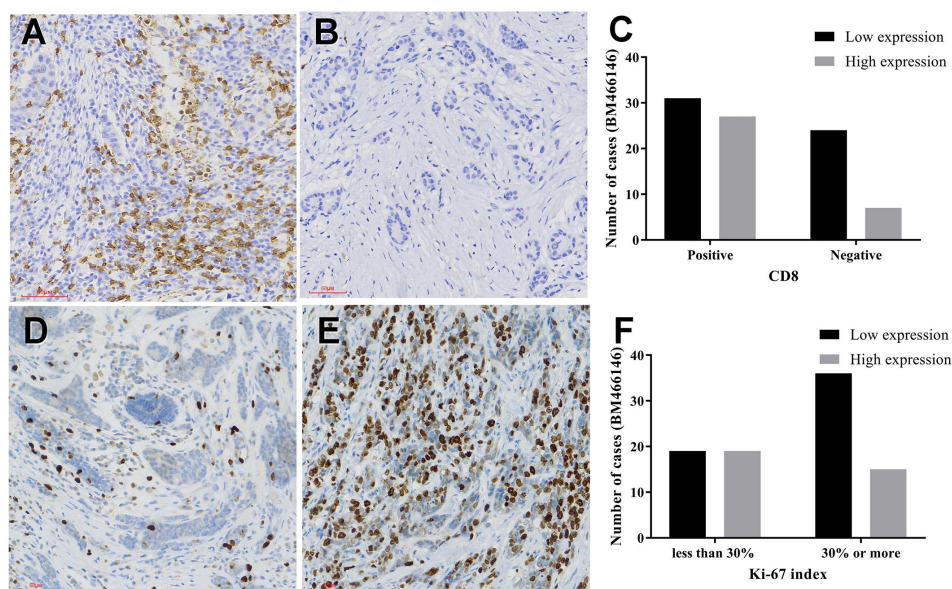


**FIGURE 2 |** Immunohistochemical staining (A, B) CD8 immunohistochemical staining in breast cancer (A positive staining, 200x, B negative staining, 200x), (C) The relationship between BM466146 and CD8. (D, E) Immunohistochemical staining of Ki-67 (D Ki-67 index 5%, 200x, E Ki-67 index 70%, 200x), (F) the relationship between BM466146 and Ki-67 index.



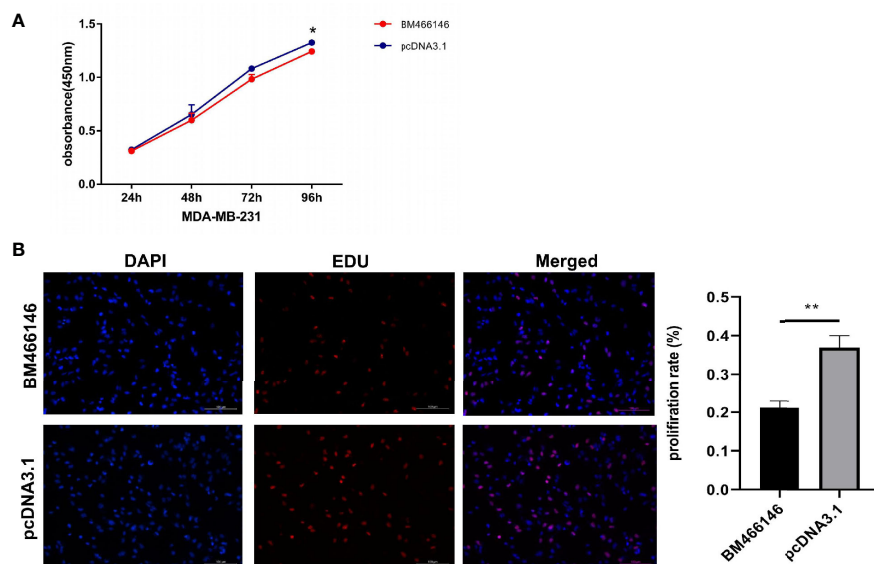


**FIGURE 3 |** Overexpression of BM466146 inhibits breast cancer cell proliferation *in vitro*. **(A)** CCK-8 assay showed overexpression of BM466146 inhibits the proliferation of MDA-MD-231 cells (\*\*P = 0.048); **(B)** EDU analysis showed that overexpression of BM466146 reduces the proliferation of MDA-MD-231 cells. The rate difference is 16% (P=0.0067).

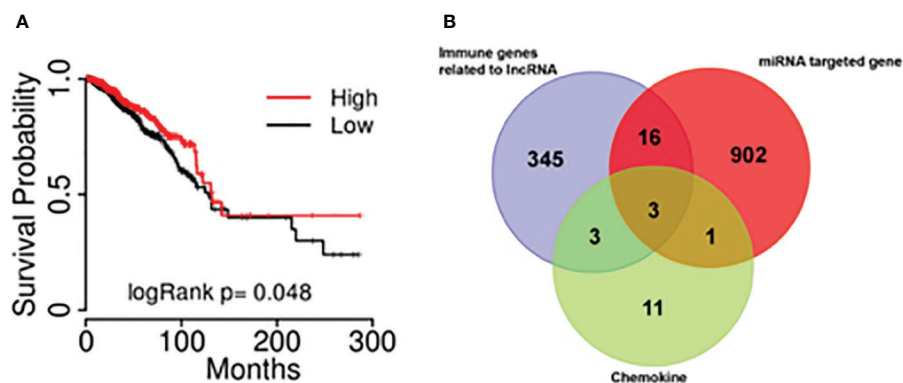


**FIGURE 4 |** The results of bioinformatics **(A)** The association of lncRNA BM466146 expression and the prognosis of breast cancer patients. The prognosis of patients with high expression of BM466146 is better than that of patients with low expression,  $P=0.048$ ; **(B)** Three genes (MIP1A, IL8, and CXCL13) were in the intersection of lncRNA-related immune genes, miRNA target genes, and CD8<sup>+</sup>T cell-related chemokines genes.

regulating genes related to lncRNA were retrieved through the ENCORI database, and there were 18 chemokines related to CD8<sup>+</sup>T cells. The three genes MIP1A, IL8 and CXCL13 were obtained in the intersection of the target gene of miRNA, the immune gene related to lncRNA and the chemokine related to CD8<sup>+</sup>T cell (**Figure 4B**). The CXCL-13 was chosen for further study after consulting with literatures (11, 12).

## The Relationship Between CXCL-13 and CD8

Immunohistochemistry was performed in these breast cancer and normal tissue specimens. In the tumors with CXCL-13

positive staining, 23 samples were CD8 positive and 35 samples were CD8 negative. In the tumors with CXCL13-negative staining, five samples were CD8 positive and 26 samples were CD8 negative. After statistical analysis, there are differences in the expression of CD8 between the CXCL-13 positive group and the negative group. The positive rate of CD8 in the CXCL-13 positive group was significantly higher than that in the CXCL-13 negative group, and the difference was statistically significant ( $\chi^2 = 5.186$ ,  $P=0.023$ , **Table 2**, **Figure 5**). The results of Spearman correlation analysis showed that expression of CXCL-13 was positively correlated with the number of CD8 positive cells ( $P=0.023$ ,  $r=0.241$ ).

## DISCUSSION

Long non-coding RNA (lncRNA) is a type of regulatory RNA with a length of more than 200 nucleotides. It contains very few introns and open reading frames, and is not capable of encoding proteins. Most of them are transcription products of RNA polymerase II (13). According to the type and mode of action, it can be divided into five types: sense lncRNA, antisense lncRNA, bidirectional lncRNA, intergenic lncRNA and intragenic lncRNA (14). lncRNA is mostly located in the nucleus, and can be used as scaffold molecules, guide molecules, enhancers and molecular baits to participate in epigenetic modification, transcription and regulation (15–17). Studies have shown that lncRNA LINC00511 can promote the initiation of breast cancer (18), and lncRNA TINCR can promote epithelial-mesenchymal transition and resistance to trastuzumab in breast cancer (19). With the development of high-throughput sequencing, more and more lncRNAs have been identified playing roles in breast cancer, but their specific roles and mechanisms remain unclear. Currently, there was no specific lncRNA identified to be treatment target of breast cancer.

BM466146 is an intergenic lncRNA located on chromosome 18 and functions mainly in the nucleus. We found that the expression of BM466146 in normal breast tissue is much higher than that in breast cancer tissue. The results of survival analysis showed that patients with high expression of the BM466146 gene is associated with a better prognosis, and have a longer overall survival, which indicating that BM466146 has the effect of tumor suppressor genes. Simultaneously, statistical analysis found that

in breast cancer, the Ki-67 index is low in patients with BM466146 high expression compared with those with low expression, suggesting that high expression of BM466146 can inhibit the proliferation of breast cancer cells. In vitro experiments also showed that BM466146 significantly inhibited the proliferation of breast cancer cells. It is well known that low Ki-67 index is associated with a good prognosis of breast cancer patients (20). Therefore, our study suggests that the high expression of lncRNA BM466146 in tumor tissues might predict improving prognosis of breast cancer.

It was known that lncRNA plays a vital role in mammalian epigenetics and transcriptional regulation, and is a key regulator of immune cell gene expression. It can control the number and homeostasis of immune cells in non-specific and specific immunity (21). The expression of certain lncRNA is associated with the development, differentiation and activation of immune cells (22). Studies have shown that lncRNA CNC-TIM3 exacerbates CD8 T cell failure by binding to TIM-3 in hepatocellular carcinoma (23), and down-regulating lncRNA NEAT1 can inhibit apoptosis of CD8<sup>+</sup> T cells and increase the anti-tumor activity of CD8<sup>+</sup> T cells in hepatocellular carcinoma (24). Therefore, lncRNA can regulate the activation, proliferation, apoptosis, and anti-tumor activity of CD8<sup>+</sup> T cells.

Cytotoxic T Lymphocytes (CTL) are the first line of cancer-targeted immune cells. Tumor-associated fibroblasts, M2 macrophages and regulatory T cells can produce an immune barrier against CD8<sup>+</sup> T cells in the process of tumor development. In anti-tumor immunity, CD8<sup>+</sup> T cells are activated and proliferated, and their anti-tumor function increased to produce a durable and effective anti-tumor immune response (25).

lncRNA represents the largest class of noncoding RNAs (ncRNAs) which are mainly involved in gene regulation. In addition to transcriptional regulation, lncRNA also regulates mRNA splicing, inhibits translation, and plays a role in mRNA processing, maturation and stability (26). MiRNAs are small ncRNAs with a length of about 22 nucleotides. By binding to specific sites of mRNA and miRNA response elements (MRES), they perform post-transcriptional regulation, leading to

**TABLE 2 |** The relationship between CXCL-13 and CD8.

	Number	CXCL-13		$\chi^2$	P-value
		Positive	Negative		
CD8				5.186	0.023
Positive	58	23	35		
Negative	31	5	26		

Cut-off  $\alpha=0.05$ .

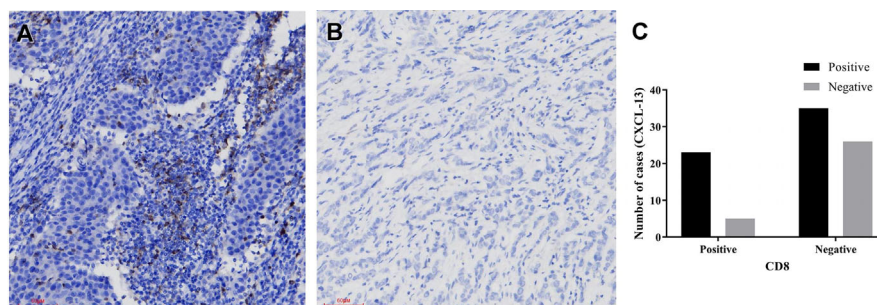


**FIGURE 5 |** The relationship between CXCL-13 and CD8 (A, B) CXCL-13 immunohistochemical staining in breast cancer (A positive staining, 200x, B negative staining, 200x), (C) The relationship between CXCL-13 and CD8.

transcription degradation or translation inhibition. LncRNAs can competitively bind to miRNAs with the same MRES, dilute the concentration of free miRNAs in cells, reduce the inhibition of miRNA on mRNA, and thus increase the expression of downstream genes. This phenomenon is known as the competing endogenous RNA (ceRNA) hypothesis (27). LncRNA can regulate the chemotaxis and activation of CD8<sup>+</sup> T cells by regulating the expression of mRNA, but it cannot directly act on CD8<sup>+</sup> T cells.

Based on the analysis of biogenesis in the TCGA database, the crossover of BM466146-related miRNA target genes, lncRNA-related immune genes and CD8<sup>+</sup> T-cell-related chemokines was performed. And it was found that lncRNA BM466146 may be used as ceRNA to adsorb HSA-Mir-224-3P, up-regulate the expression of CXCL-13 gene, and then generate more CXCL-13 proteins to activate CD8<sup>+</sup> T cells and play its cytotoxic role. CXCL-13 protein is also known as B lymphocyte chemokine 1 (BCA1), a small cytokine belonging to the CXC chemokine family. This chemokine has a selective chemotactic effect on B cells belonging to the B-1 and B-2 subsets, and stimulates its effect by interacting with the only chemokine receptor CXCR5 (11). CD8<sup>+</sup> CXCR5<sup>+</sup> T cells are a subset of CD8<sup>+</sup> T cells, which have potential cytotoxic effects in chronic viral infections and cancers (28, 29). This study found that the number of CD8<sup>+</sup> T cells increased in the breast cancer that overexpressed BM466146. The proportion of CD8<sup>+</sup> T cells in the CXCL-13 positive group was significantly higher than that in the CXCL-13 negative group. In breast cancer, BM466146 might be able to up-regulate the expression of CXCL-13 gene, which in turn activates CD8<sup>+</sup> T cells in the tumor microenvironment and plays a tumor suppressor effect. This result is in consistent with the results of Bai et al. in pancreatic cancer (12). CD8<sup>+</sup> T cells in the tumor microenvironment have higher cytotoxicity than CD8<sup>-</sup> T cells and indicate a better prognosis.

In summary, this study found that lncRNA BM466146 has the function of a tumor suppressor gene. The high expression of lncRNA BM466146 is associated with better prognosis. BM466146 could promote the expression of CXCL-13 gene and increase the number of CD8<sup>+</sup> T cells in tumor microenvironment, and activate their recognition and killing effect on tumor cells.

## REFERENCES

1. Siegel RL, Miller KD, Jemal A. Cancer statistics, 2019. *CA: A Cancer J Clin* (2019) 69(1):7–34. doi: 10.3322/caac.21551
2. Bray F, Ferlay J, Soerjomataram I, Siegel RL, Torre LA, Jemal A. Global cancer statistics 2018: GLOBOCAN estimates of incidence and mortality worldwide for 36 cancers in 185 countries. *CA Cancer J Clin* (2018) 68(6):394–424. doi: 10.3322/caac.21492
3. Moo TA, Sanford R, Dang C, Morrow M. Overview of Breast Cancer Therapy. *PET Clin* (2018) 13(3):339–54. doi: 10.1016/j.cpet.2018.02.006
4. Brady NJ, Chuntova P, Schwertfeger KL. Macrophages: Regulators of the Inflammatory Microenvironment during Mammary Gland Development and Breast Cancer. *Mediators Inflammation* (2016) 2016:4549676. doi: 10.1155/2016/4549676
5. Stanton SE, Disis ML. Clinical significance of tumor-infiltrating lymphocytes in breast cancer. *J Immunother Cancer* (2016) 4:59. doi: 10.1186/s40425-016-0165-6
6. Hayes DF. Further Progress for Patients with Breast Cancer. *N Engl J Med* (2019) 380(7):676–7. doi: 10.1056/NEJMe1816059
7. Consortium EP, Birney E, Stamatoyannopoulos JA, Dutta A, Guigó R, Gingeras TR, et al. Identification and analysis of functional elements in 1% of the human genome by the ENCODE pilot project. *Nature* (2007) 447(7146):799–816. doi: 10.1038/nature05874
8. Huang P-S, Lin Y-H, Chi H-C, Tseng YH, Chen CY, Lin TK, et al. Dysregulated FAM215A Stimulates LAMP2 Expression to Confer Drug-Resistant and Malignant in Human Liver Cancer. *Cells* (2020) 9(4):961. doi: 10.3390/cells9040961
9. Youness RA, Hafez HM, Khallaf E, Assal RA, Abdel Motaal A, Gad MZ. The long noncoding RNA sONE represses triple-negative breast cancer aggressiveness through inducing the expression of miR-34a, miR-15a, miR-16, and let-7a. *J Cell Physiol* (2019) 234(11):20286–97. doi: 10.1002/jcp.28629
10. Feng F, Chen A, Huang J, Xia Q, Chen Y, Jin X. Long noncoding RNA SNHG16 contributes to the development of bladder cancer via regulating miR-98/STAT3/Wnt/β-catenin pathway axis. *J Cell Biochem* (2018) 119(11):9408–18. doi: 10.1002/jcb.27257
11. Kazanietz MG, Durando M, Cooke M. CXCL13 and Its Receptor CXCR5 in Cancer: Inflammation, Immune Response, and Beyond. *Front Endocrinol* (2019) 10:471. doi: 10.3389/fendo.2019.00471

## DATA AVAILABILITY STATEMENT

The original contributions presented in the study are included in the article/**Supplementary Material**. Further inquiries can be directed to the corresponding author.

## ETHICS STATEMENT

The studies involving human participants were reviewed and approved by Ethics Committee of Weifang People's Hospital. The patients/participants provided their written informed consent to participate in this study.

## AUTHOR CONTRIBUTIONS

YZ and PG conceived and designed the study. YZ, XD, YF, and GX performed experiments and analyzed results. GH, LJ, YW, and LW collected clinical samples and analyzed results. DY, JZ, and XG conducted experiments and organized data. YZ wrote the first draft. PG edited the article. All authors contributed to the article and approved the submitted version.

## FUNDING

This study was supported by the National Natural Science Foundation of China (grant nos. 81372856 and 81672842) and the Taishan Scholars Program of Shandong Province (grant no. ts201511096).

## SUPPLEMENTARY MATERIAL

The Supplementary Material for this article can be found online at: <https://www.frontiersin.org/articles/10.3389/fonc.2020.628757/full#supplementary-material>

12. Bai M, Zheng Y, Liu H, Su B, Zhan Y, He H. CXCR5+ CD8+ T cells potently infiltrate pancreatic tumors and present high functionality. *Exp Cell Res* (2017) 361(1):39–45. doi: 10.1016/j.yexcr.2017.09.039
13. Pagano A, Castelnuovo M, Tortelli F, Ferrari R, Dieci G, Cancedda R. New small nuclear RNA gene-like transcriptional units as sources of regulatory transcripts. *PLoS Genet* (2007) 3(2):e1. doi: 10.1371/journal.pgen.0030001
14. St Laurent G, Wahlestedt C, Kapranov P. The Landscape of long noncoding RNA classification. *Trends Genet* (2015) 31(5):239–51. doi: 10.1016/j.tig.2015.03.007
15. Gupta RA, Shah N, Wang KC, Kim J, Horlings HM, Wong DJ, et al. Long non-coding RNA HOTAIR reprograms chromatin state to promote cancer metastasis. *Nature* (2010) 464(7291):1071–6. doi: 10.1038/nature08975
16. Lai F, Orom UA, Cesaroni M, Beringer M, Taatjes DJ, Blobel GA, et al. Activating RNAs associate with Mediator to enhance chromatin architecture and transcription. *Nature* (2013) 494(7438):497–501. doi: 10.1038/nature11884
17. Yan B, Yao J, Liu JY, Li XM, Wang XQ, Li YJ, et al. lncRNA-MIAT regulates microvascular dysfunction by functioning as a competing endogenous RNA. *Circ Res* (2015) 116(7):1143–56. doi: 10.1161/CIRCRESAHA.116.305510
18. Lu G, Li Y, Ma Y, Lu J, Chen Y, Jiang Q, et al. Long noncoding RNA LINC00511 contributes to breast cancer tumorigenesis and stemness by inducing the miR-185-3p/E2F1/Nanog axis. *J Exp Clin Cancer Res* (2018) 37(1):289. doi: 10.1186/s13046-018-0945-6
19. Dong H, Hu J, Zou K, Ye M, Chen Y, Wu C, et al. Activation of lncRNA TINCR by H3K27 acetylation promotes Trastuzumab resistance and epithelial-mesenchymal transition by targeting MicroRNA-125b in breast cancer. *Mol Cancer* (2019) 18(1):3. doi: 10.1186/s12943-018-0931-9
20. Li L, Han D, Wang X, Wang Q, Tian J, Yao J, et al. Prognostic values of Ki-67 in neoadjuvant setting for breast cancer: a systematic review and meta-analysis. *Future Oncol* (2017) 13(11):1021–34. doi: 10.2217/fon-2016-0428
21. Mowle WK, Kotzin JJ, McCright SJ, Neal VD, Henao-Mejia J. Control of Immune Cell Homeostasis and Function by lncRNAs. *Trends Immunol* (2018) 39(1):55–69. doi: 10.1016/j.it.2017.08.009
22. Mumtaz PT, Bhat SA, Ahmad SM, Dar MA, Ahmed R, Urwat U, et al. lncRNAs and immunity: watchdogs for host pathogen interactions. *Biol Proced Online* (2017) 19:3. doi: 10.1186/s12575-017-0052-7
23. Ji J, Yin Y, Ju H, Xu X, Liu W, Fu Q, et al. Long non-coding RNA lnc-Tim3 exacerbates CD8 T cell exhaustion via binding to Tim-3 and inducing nuclear translocation of Bat3 in HCC. *Cell Death Dis* (2018) 9(5):478. doi: 10.1038/s41419-018-0528-7
24. Yan K, Fu Y, Zhu N, Wang Z, Hong JL, Li Y, et al. Repression of lncRNA NEAT1 enhances the antitumor activity of CD8+T cells against hepatocellular carcinoma via regulating miR-155/Tim-3. *Int J Biochem Cell Biol* (2019) 110:1–8. doi: 10.1016/j.biocel.2019.01.019
25. Farhood B, Najafi M, Mortezaee K. CD8(+) cytotoxic T lymphocytes in cancer immunotherapy: A review. *J Cell Physiol* (2019) 234(6):8509–21. doi: 10.1002/jcp.27782
26. Charles Richard JL, Eichhorn PJA. Platforms for Investigating lncRNA Functions. *SLAS Technol* (2018) 23(6):493–506. doi: 10.1177/2472630318780639
27. Chan JJ, Tay Y. Noncoding RNA:RNA Regulatory Networks in Cancer. *Int J Mol Sci* (2018) 19(5):1310. doi: 10.3390/ijms19051310
28. He R, Hou S, Liu C, Zhang A, Bai Q, Han M, et al. Follicular CXCR5-expressing CD8+ T cells curtail chronic viral infection. *Nature* (2016) 537(7620):412–6. doi: 10.1038/nature19317
29. Chu F, Neelapu SS. CXCR5+CD8+ T cells are localized in B cell follicles and germinal centers and exhibit regulatory and anti-tumor function. *J Immunotherapy Cancer* (2015) 3(P321). doi: 10.1186/2051-1426-3-S2-P321

**Conflict of Interest:** Author DY was employed by the company Geneis Beijing Co., Ltd.

The remaining authors declare that the research was conducted in the absence of any commercial or financial relationships that could be construed as a potential conflict of interest.

Copyright © 2021 Zhang, Dong, Wang, Wang, Han, Jin, Fan, Xu, Yuan, Zheng, Guo and Gao. This is an open-access article distributed under the terms of the Creative Commons Attribution License (CC BY). The use, distribution or reproduction in other forums is permitted, provided the original author(s) and the copyright owner(s) are credited and that the original publication in this journal is cited, in accordance with accepted academic practice. No use, distribution or reproduction is permitted which does not comply with these terms.





# Network Pharmacology and Molecular Docking on the Molecular Mechanism of Luo-hua-zi-zhu (LHZZ) Granule in the Prevention and Treatment of Bowel Precancerous Lesions

## OPEN ACCESS

### Edited by:

Dong-Hua Yang,  
St. John's University, United States

### Reviewed by:

Ye Wei,  
Fudan University, China  
Sheau Ching Chai,  
University of Delaware, United States  
Xueqing Hu,  
University of Oklahoma, United States

### \*Correspondence:

Xiaoling Fu  
fuxiaoling111@163.com  
Xiumei Ma  
sallyma@hotmail.com  
Yuan Li  
Livialy@126.com

<sup>†</sup>These authors contributed equally to  
this work and share first authorship.

### Specialty section:

This article was submitted to  
Pharmacology of Anti-Cancer Drugs,  
a section of the journal  
Frontiers in Pharmacology

**Received:** 13 November 2020

**Accepted:** 18 January 2021

**Published:** 15 February 2021

### Citation:

Guo C, Kang X, Cao F, Yang J, Xu Y,  
Liu X, Li Y, Ma X and Fu X (2021)  
Network Pharmacology and Molecular  
Docking on the Molecular Mechanism  
of Luo-hua-zi-zhu (LHZZ) Granule in  
the Prevention and Treatment of Bowel  
Precancerous Lesions.  
Front. Pharmacol. 12:629021.  
doi: 10.3389/fphar.2021.629021

Cui Guo<sup>1,2†</sup>, Xingdong Kang<sup>3†</sup>, Fang Cao<sup>4†</sup>, Jian Yang<sup>5</sup>, Yimin Xu<sup>1</sup>, Xiaoqiang Liu<sup>1,6</sup>,  
Yuan Li<sup>7\*</sup>, Xiumei Ma<sup>8\*</sup> and Xiaoling Fu<sup>1\*</sup>

<sup>1</sup>Second Department of Oncology, Yueyang Hospital of Integrated Traditional Chinese and Western Medicine, Shanghai University of Traditional Chinese Medicine, Shanghai, China, <sup>2</sup>Liaoning University of Traditional Chinese Medicine, Shenyang, China, <sup>3</sup>School of Chinese Materia Medica, Nanjing University of Chinese Medicine, Shanghai, China, <sup>4</sup>Jiangxi University of Traditional Chinese Medicine, Nanchang, China, <sup>5</sup>The Second Military Medical University, Shanghai, China, <sup>6</sup>Department of Pain, Shibe Hospital, Shanghai, China, <sup>7</sup>Infection Prevention and Control Department, Yueyang Hospital of Integrated Traditional Chinese and Western Medicine, Shanghai University of Traditional Chinese Medicine, Shanghai, China, <sup>8</sup>Department of Radiotherapy, Renji Hospital, Shanghai Jiao Tong University, Shanghai, China

The Luo-hua-zi-zhu (LHZZ) granule has been widely used for the treatment of colorectal adenoma (CRA), which is a precursor of colorectal cancer (CRC). However, the active components of LUZZ and its mechanism of action against CRA have not yet been elucidated. This study was designed to investigate the effect of LHZZ on CRA and explore its pharmacological mechanisms. First, a total of 24 chemical constituents were identified in the 50% aqueous methanol extract of LHZZ granule based on the mass fragment patterns and mass spectral library using the high resolution UPLC-Q-TOF MS/MS system. Subsequently, based on a network pharmacology study, 16 bioactive compounds and 28 targets of the LHZZ associated with CRA were obtained, forming a compound-target network. Molecular docking tests showed tight docking of these compounds with predicted targeted proteins. The protein-protein interaction (PPI) network identified AKT1, CASP3, TP53 and EGFR as hub targets. The Kyoto Encyclopedia of Genes and Genomes pathway network and pathway-target-compound network revealed that the apoptosis pathway was enriched by multiple signaling pathways and multiple targets, including the hub targets. Finally, the reliability of the core targets was evaluated using molecular docking technology and *in vitro* studies. Our study indicated that the LHZZ particle has preventive and treatment effect on colorectal adenoma through multi-component, multi-target and multi-pathway.

**Keywords:** network pharmacology, LHZZ granule, colorectal adenoma, molecular mechanisms, AKT1

## INTRODUCTION

Colorectal adenoma (CRA) is the precancerous lesion of colorectal cancer (CRC) (Chen et al., 2020). CRA is characterized with abnormal crypt foci in the intestinal wall, increased inflammatory exudation and proliferation of mucosal epithelial cells in local intestinal tissue (Cho et al., 2006). The incidence of CRA is more than 30% (Dejea et al., 2018). The incidence of cancerous change of a single CRA is 20–30%, and multiple CRA is 30–80% (Chen et al., 2020). Under the theory of Traditional Chinese Medicine (TCM), CRA belongs to the category of "polyps", Polyps in Traditional Chinese medicine is a general concept, and in western medicine, polys can be divided into adenomatous polyps, hyperplastic polyps, infant polyps and so on. Endoscopic excision has become the main treatment of CRA, however, removal of CRA cannot effectively reduce the recurrence (Nishihara et al., 2013). At present, folic acid, metformin, aspirin, celecoxib and other anti-proliferation and anti-inflammatory treatment are applied in clinic as anti-CRA drugs, but the effect is not satisfactory (Liu et al., 2017; Passarelli et al., 2018; Veettil et al., 2019). Therefore, it is urgent to understand the pathogenesis of CRA and find safe and effective drugs.

*Callicarpa nudiflora* Hook, belonging to the family Verbenaceae, is a perennial evergreen shrub or low arbor and its dried leaves and twigs are used as traditional Chinese herbal medicine, Luo-hua-zi-zhu (LHZZ), for the treatment of inflammation and bleeding. LHZZ granule is a Chinese patent medicine, which is included in Chinese Pharmacopoeia 2015 edition. As a drug for anti-inflammation, detoxification, convergence and hemostasis, LHZZ has been widely used in clinical treatment of inflammation caused by bacterial infection, acute infectious hepatitis, respiratory tract and gastrointestinal bleeding (Yang et al., 2021). Recent pharmacological studies suggest that (Wu et al., 2020), LHZZ contains a variety of chemical components that have pharmacological effects such as anti-cancer, anti-mutation, and promotion of immune function. They have inhibitory effects on various malignant tumors, and can improve intestinal inflammation and regulate intestinal flora (Yang et al., 2021).

Previous studies show that LHZZ has anti-inflammatory and hemostatic functions (Wu et al., 2020), suggesting that it may be effective in the prevention and treatment of precancerous lesions of colorectal cancer. However, at present, most of the studies on LHZZ granule in the prevention and treatment of CRA are from systematic perspective, and there are few reports on the mechanism of action (Zhang et al., 2019; Yang et al., 2021). Studies based on molecular targets and related signal pathways will help to better understand the mechanism of action of LHZZ granule against precancerous lesions of colorectal cancer. Therefore, the purpose of this study is to construct a multi-dimensional network of "component-target-pathway-disease" by using network pharmacology (Boezio et al., 2017; Zhou et al., 2020) and molecular docking modality (Park et al., 2018), to explain the biological mechanism of LHZZ granule in the prevention and treatment of CRA. This study will provide a scientific basis for clinical trial research and product development

of LHZZ granule. The idea of this study is shown in the flow chart of Figure 1.

## MATERIALS AND METHODS

### Chemicals and Reagents

HPLC grade acetonitrile was purchased from Merck Company (Darmstadt, Germany), HPLC grade methyl tert-butyl ether from CNW, AR grade acetic acid and GR grade ethanol from Sinopharm Chemical Reagent (Shanghai, China), and Cremophor EL (BR grade) from Shanghai Yuanye (Shanghai, China). Purified water used throughout the study was prepared by a purified water system 611VP (Sartorius, Germany). LHZZ granule was provided by the Jiangxi Puzheng Pharmaceutical Co., Ltd. (Jiangxi, China; batch number: Z20060378). and stored in the laboratory of the Shanghai University of TCM.

### UPLC-MS Analysis

LHZZ granule (25 mg) was accurately weighed and placed in a round bottom flask with 25 ml 50% methanol, mixed well, sealed and soaked for 0.5 h at room temperature, and ultrasonically treated for 30 min using an ultrasonic cleaning instrument (Shenzhen, China). The extract solution was centrifuged at 14,000 rpm for 15 min at room temperature, then filtered through a 0.22- $\mu$ m microporous membrane before qualitative analysis.

A Shimadzu HPLC, consisting of a CBM-20A system controller, a LC-20AD<sub>XR</sub> pump, a SIL-20ACXR autosampler, a CTO-10Avp column oven and a Shiseido C<sub>18</sub> column (2.1  $\times$  150mm, 2.5  $\mu$ m, Shiseido Co., Ltd., Tokyo, Japan) equipped with a guard column (C<sub>18</sub>, 4 mm  $\times$  3.0 mm, Phenomenex Co., Ltd., Torrance, CA, United States) was used for the chromatographic separation of LHZZ granule. A linear gradient program with a mobile phase system including solvent A (0.1% Formic acid + H<sub>2</sub>O, v/v) and solvent B (0.1% Formic acid + acetonitrile, v/v) as follow: 95–5% A at 0.01–18 min, 5% A at 18–19 min, 5–95% A at 19–20 min, and 95% A at 20–25 min. The temperature of the analytical column and autosampler were maintained at 30°C and 4°C respectively. The total run time for a LC-MS/MS analysis was 25 min.

The instrumental settings of Q-TOF-MS/MS were as follow: ion source gas 1 (GSI) and gas 2 (GS2) were both set to 50 psi, curtain gas (CUR) was set to 40 psi, ion spray voltage floating (ISVF) was set to 3500 V in the positive mode while 3200 V was set in the negative mode, ion source temperature (TEM) was 350°C, collision energy (CE) was 60 V, collision energy spread (CES) was 15 V, declustering potential (DP) was 100 V, and nitrogen was used as a nebulizer and auxiliary gas. Samples were analyzed in both positive and negative ionization modes with a scanning mass-to-charge (m/z) range from 120 to 1,500. The quantification was performed via peak area ratio of interest analytes to IS. The Applied Biosystems Analyst version 1.5.1 software was used to control the LC-ESI/MS/MS system as well as collect and process the data.

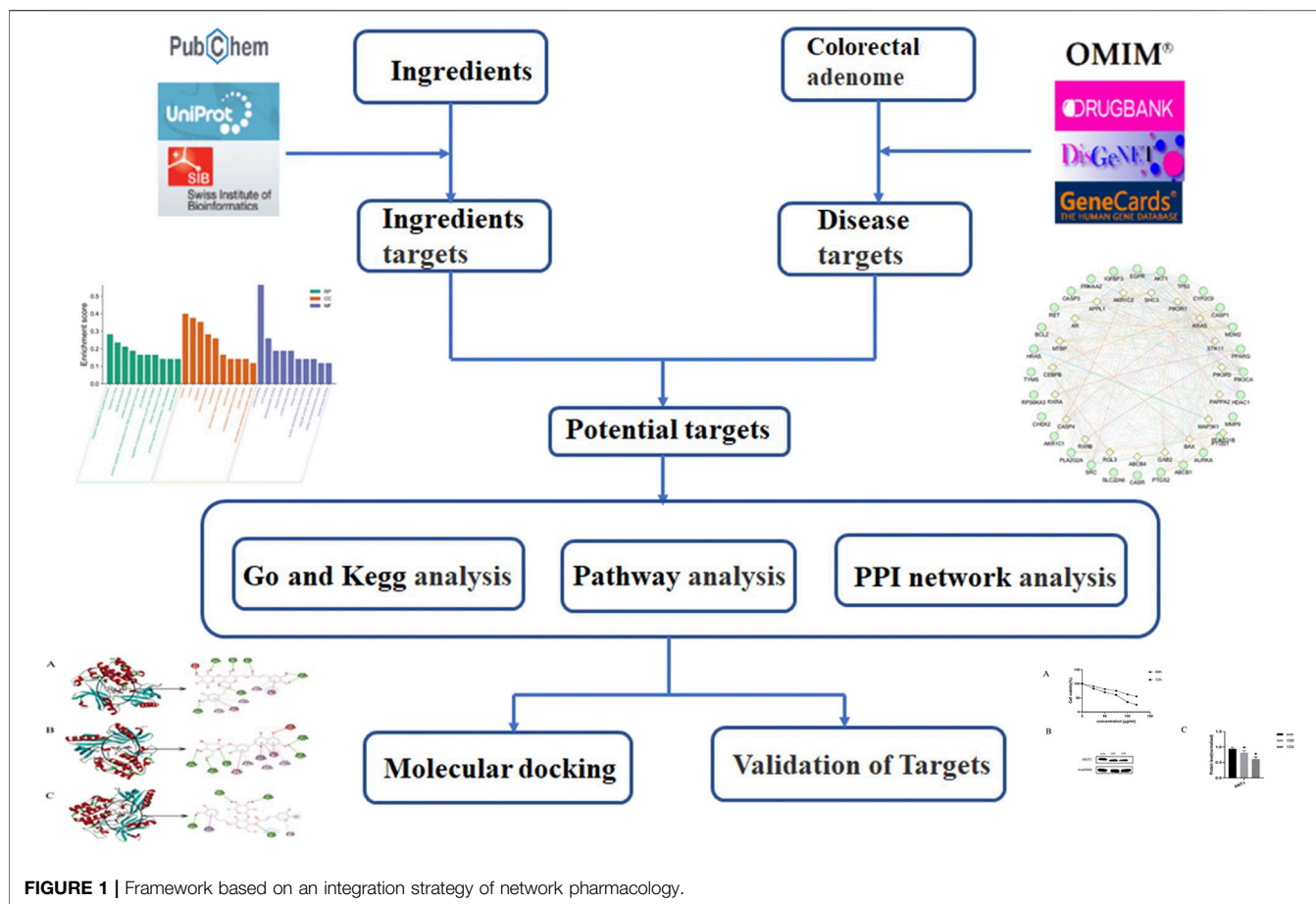


**FIGURE 1 |** Framework based on an integration strategy of network pharmacology.

## Target Prediction of Luo-hua-zi-zhu Active Ingredients

We obtained information on the structure of the bioactive components, including molecular structures, canonical smiles, and their 'sdf' files from the product databases of PubChem (<https://pubchem.ncbi.nlm.nih.gov/>). Then, we predicted the target of bioactive components using public databases, namely the Swiss Target Prediction and STITCH, with the species limited to 'Homo sapiens'. Finally, we standardized the target names using the UniProtKB (<https://www.uniprot.gov/>).

## Construction of Compound-Target Network

The collected traditional Chinese medicine compounds and effective targets are constructed by Cytoscape 3.7.2 software (<http://www.cytoscape.org/>) to construct a compound-target network. The CytoNCA plugin (v2.1.6) was used to measure the topology scores of the nodes, including the betweenness, closeness, and subgraph centrality. The option "without weight" was selected (Zhang et al., 2020).

## Colorectal Adenoma Disease Target Screening

Colorectal adenomas, colon precancerous lesions and Colorectal polyp are search terms used to separately search in the OMIM

database (<https://www.omim.org/>), the DrugBank database (<http://www.drugbank.ca/>), the DisGeNET database (<https://www.disgenet.org/>), and the GeneCards database (<https://www.genecards.org/>). The species "Homo sapiens" was selected and the target gene information related to CRA was collected and integrated.

## Luo-hua-zi-zhu and Colorectal Adenoma Target Screening and Network Construction

The target prediction results of the active ingredients of the LHZZ granule are matched with the search results of the CRA-related targets, and the overlapping target (**Supplementary Table S1**) is selected as the core target of the LHZZ granule for the treatment of CRA. The active ingredient target of the LHZZ granule and CRA target was mapped using Venny 2.1.0 (<http://bioinfogp.cnb.csic.es/tools/venny/index.html>) online tool. The Venn diagram was drawn. A common target network was constructed using the Cytoscape.

## Construction of Protein-Protein Interaction Network (PPI) and Screening of Key Targets

The GeneMANIA tool can not only construct a PPI network, but also find a series of genes related to the input gene based on a large

amount of function-related data, and analyze the interaction between them, such as co-expression and co-localization (Franz et al., 2018). In the current study, GeneMANIA is used to construct the protein-protein interaction network of the cross genes of LHZZ and CRA. Through GeneMANIA analysis, we not only obtained the relationship between the input cross genes, but also obtained the relationship with other closely related targets. In the following analysis, we call this new set of genes "predicted LHZZ targets for CRA". In order to identify the central nodes and key proteins in the PPI network, the topology parameters were calculated by NetworkAnalyzer, and the degree of centrality (betweenness, closeness, and subgraph) was determined by the CytoNCA.

## GO Function and KEGG Pathway Enrichment Analysis

The common target of LHZZ and CRA obtained by the above screening was imported into the DAVID6.8 database (<https://david.ncicrf.gov/>). The species was set to be "Homo Sapiens", and GO function enrichment analysis and KEGG pathway enrichment was performed. GO functional analysis includes biological process (BP, biological process), cellular component (CC, cellular component), molecular function (MF, molecular function). It is visualized as histogram and bubble chart by the OmicShare cloud platform (<http://www.omicshare.com>).

## Target-Path/Functional Network Construction

Ten representative signal pathways, biological processes and molecular functions were screened for further network analysis. The target pathway/functional network was constructed by Cytoscape 3.7.2. In the network, potential targets of LHZZ for treating CRA, biological processes, and signaling pathways obtained through enrichment analysis were represented by nodes, and the interactions between them were represented by edges.

## Molecular Docking Analysis

The core compounds were screened under the condition that the "Degree" parameter of the node in the "active ingredient-target-disease" network was greater than the mean. The mol2 file of the core compound was downloaded from the TCMSP database, imported into the AutoDockTools1.5.6 software, and saved in pdbqt format. The 3D structure of the key target proteins was downloaded from PDB database (<https://www.rcsb.org>). The water molecules and excess inactive ligands were removed by PyMOL software. The proteins were hydrogenated and charged into AutoDockTools1.5.6 software and exported to pdbqt format. According to the published methods, the molecular docking simulation of potential targets and their corresponding components is carried out by using AutoDock vina software. The global optimal binding conformation is obtained, and the docking results are visualized by the DiscoveryStudioVisualizer.

## Experimental Verification in Vitro Cell Culture

IH-CRA cells were obtained from the China Center for Type Culture Collection (CCTCC), whose storage number is C2019307. We have applied for the national invention patent, patent number: 201911261397.9 (Wuhan, China). Cells were cultured in Ham's F 12 nutrient medium (F12, Beyotime Biotechnology, Shanghai, China), supplemented with 10% fetal bovine serum (FBS, Zhejiang, China). Cells were cultured at 37°C and 5% CO<sub>2</sub>.

### Cell Viability Assay

IH-CRA cells in the logarithmic phase were seeded at  $1 \times 10^4$  cells/well in 96-well plates. After incubation for 24 h, IH-CRA cells were exposed to LHZZ (0, 25, 50, 75 and 100 µg/ml). After treatment for 48 h and 72h, 20 ml of Cell Counting Kit (CCK-8) assay solution (Beyotime, Shanghai, China) was added to each well, and cells were incubated for 4 h at 37°C and 5% CO<sub>2</sub>. The absorbance at 450 nm was measured by a microplate reader (FLUOstar Omega, LABTECH, Offenburg, Germany). Cell survival was calculated as: absorbance/absorbance of control  $\times$  100%. The Graphpad prism 7.0 software was used to analyze and plot the data.

### Western Blotting Assay

Total protein was obtained from treated cells in radioimmunoprecipitation assay buffer (P0013B; Beyotime, Shanghai, China) and centrifuged at  $12,000 \times g$  at 4°C for 15 min. Proteins were separated via sodium dodecyl-sulfate polyacrylamide gel electrophoresis and transferred onto polyvinylidene fluoride membranes (Millipore, Bedford, MA, United States). After blocking in 5% bovine serum albumin (Gen-view Scientific Inc., United States) for 1.5 h at room temperature, the membranes were incubated with primary antibodies against AKT1 (cell signal technique) at 4°C overnight. Next, the membranes were incubated with horseradish-peroxidase-conjugated secondary antibodies (proteintech) at room temperature for 1 h. The Enhanced Chemiluminescence Detection Kit (P10100; New Cell & Molecular Biotech Co., Ltd.) was used to detect and visualize protein bands.

## Statistical Analysis

All data are expressed as the mean  $\pm$  standard deviation (SD) and analyzed by one-way analysis of variance (ANOVA) followed by a least-significant difference test. *p*-values of  $<0.05$  or  $<0.01$  were regarded as statistically significant. The statistical analysis was performed by SPSS 20.0 (SPSS Inc., NY, United States).

## RESULTS

### Separation and Identification of Active Components of Luo-hua-zi-zhu

A total of 24 chemical constituents were identified in the 50% aqueous methanol extract of LHZZ granule based on the mass fragment patterns and mass spectral library using the high



**TABLE 1 |** Active ingredient of LHZZ granule.

Number	Molecular formula	PubChem CID	Molecule name	Canonical SMILES
Compound1	C20H32O5	311	(-)-Prostaglandin E2	CCCCC(C=CC1C(CC(=O)C1CC=CCCC(=O)O)O)O
Compound 2	C18H16O7	494583	5,4-Dihydroxy-3,7,3'-trimethoxyflavone	COC1=CC(=C2C(=C1)OC(=C2=O)OC)C3=CC(=C(C=C3)O)OC)O
Compound 3	C20H28O4	66789	5-[2-(Furan-3-yl)ethyl]-8a-(hydroxymethyl)-5,6-dimethyl-3,4,4a,6,7,8-hexahydronaphthalene-1-carboxylic acid	CC1CCC2(C(C1(C)CCC3=COC=C3)CCC=C2C(=O)O)CO
Compound 4	C21H20O12	185766	6-Hydroxyluteolin 7-glucoside	C1=CC(=C(C=C1C2=CC(=O)C3=C(C(=C(C3O2)OC4C(C(C(C(O4)CO)O)O)O)O)O)O)O
Compound 5	C17H26O11	5281788	8-O-Acetylharpagide	CC(=O)OC1(CC(C2(C1C(OC=C2)OC3C(C(C(C(O3)CO)O)O)O)O)C
Compound 6	C21H18O11	23928102	Apigenin 7-glucuronide	C1=CC(=CC=C1C2=CC(=O)C3=C(C(=C(C3O2)OC4C(C(C(C(O4)C(=O)O)O)O)O)O)O
Compound 7	C15 H10 O5	31292	Apigenin	C1=CC(=CC=C1C2=CC(=O)C3=C(C(=C(C3O2)O)O)O
Compound 8	C21H20O10	5280601	Apigenin-7-O-β-D-glucoside	C1=CC(=CC=C1C2=CC(=O)C3=C(C(=C(C3O2)OC4C(C(C(C(O4)CO)O)O)O)O)O
Compound 9	C20H30O12	5280637	Bioside Verbasoside	CC1C(C(C(C(O1)OC2C(C(OC(C2O)OCCC3=CC(=C(C=C3)O)O)CO)O)O)O)O
Compound 10	C16H24O4	6476333	Brefeldin A	CC1CCCC=CC2CC(CC2C(C=CC(=O)O1)O)O
Compound 11	C6H8O7	5280704	Citric acid	C(C(=O)O)C(CC(=O)O)C(=O)O)O
Compound 12	C21H20O11	5319484	Cynaroside	C1=CC(=C(C=C1C2=CC(=O)C3=C(C(=C(C3O2)OC4C(C(C(C(O4)CO)O)O)O)O)O
Compound 13	C34H44O19	5280445	Forsythoside B	CC1C(C(C(C(O1)OC2C(C(OC(C2OC(=O)C=CC3=CC(=C(C=C3)O)O)CO)CO)C(C(C(O4)CO)O)O)O)O)O)O)O)O)O)O)O)O)O
Compound 14	C29H36O15	5280443	Isoacteoside	CC1C(C(C(C(O1)OC2C(C(OC(C2O)OCCC3=CC(=C(C=C3)O)O)CO)C(=O)C=CC4=CC(=C(C=C4)O)O)O)O)O
Compound 15	C21H18O12	5287620	Luteolin 7-glucuronide	C1=CC(=C(C=C1C2=CC(=O)C3=C(C(=C(C3O2)OC4C(C(C(C(O4)C(=O)O)O)O)O)O)O
Compound 16	C15H10O6	5280388	Luteolin	C1=CC(=C(C=C1C2=CC(=O)C3=C(C(=C(C3O2)O)O)O)O
Compound 17	C21H20O11	12310371	Luteolin-3"-O-β-D-glucopyranoside	C1=CC(=C(C=C1C2=CC(=O)C3=C(C(=C(C3O2)O)O)O)OC4C(C(C(C(O4)CO)O)O)O
Compound 18	C21H20O11	5319116	Luteolin-4"-O-β-D-glucopyranoside	C1=CC(=C(C=C1C2=CC(=O)C3=C(C(=C(C3O2)O)O)O)OC4C(C(C(C(O4)CO)O)O)O
Compound 19	C7H13NO3	12309350	N-Acetylvaline	CC(C)C(C(=O)O)NC(=O)C
Compound 20	C24H28O13	5280360	Nudifloside	C1=CC(C2C1C(C3C2(O3)CO)OC(=O)C=CC4=CC(=C(C=C4)O)OC5C(C(C(C(O5)CO)O)O)O
Compound 21	C29H36O16	5281677	Plantamajoside	C1=CC(=C(C=C1CCOC2C(C(C(O2)CO)OC(=O)C=CC3=CC(=C(C=C3)O)OC4C(C(C(C(O4)CO)O)O)O)O)O
Compound 22	C20H32O4	11754080	Prostaglandin B1	CCCCC(C=CC1=C(C(=O)CC1)CCCCCCC(=O)O)O
Compound 23	C18H37NO	5281800	Stearamide	CCCCCCCCCCCCCCCCC(=O)N
Compound 24	C29H36O15	12000883	Verbascoside	CC1C(C(C(C(O1)OC2C(C(OC(C2OC(=O)C=CC3=CC(=C(C=C3)O)O)CO)O)O)O)O)O)O)O)O)O

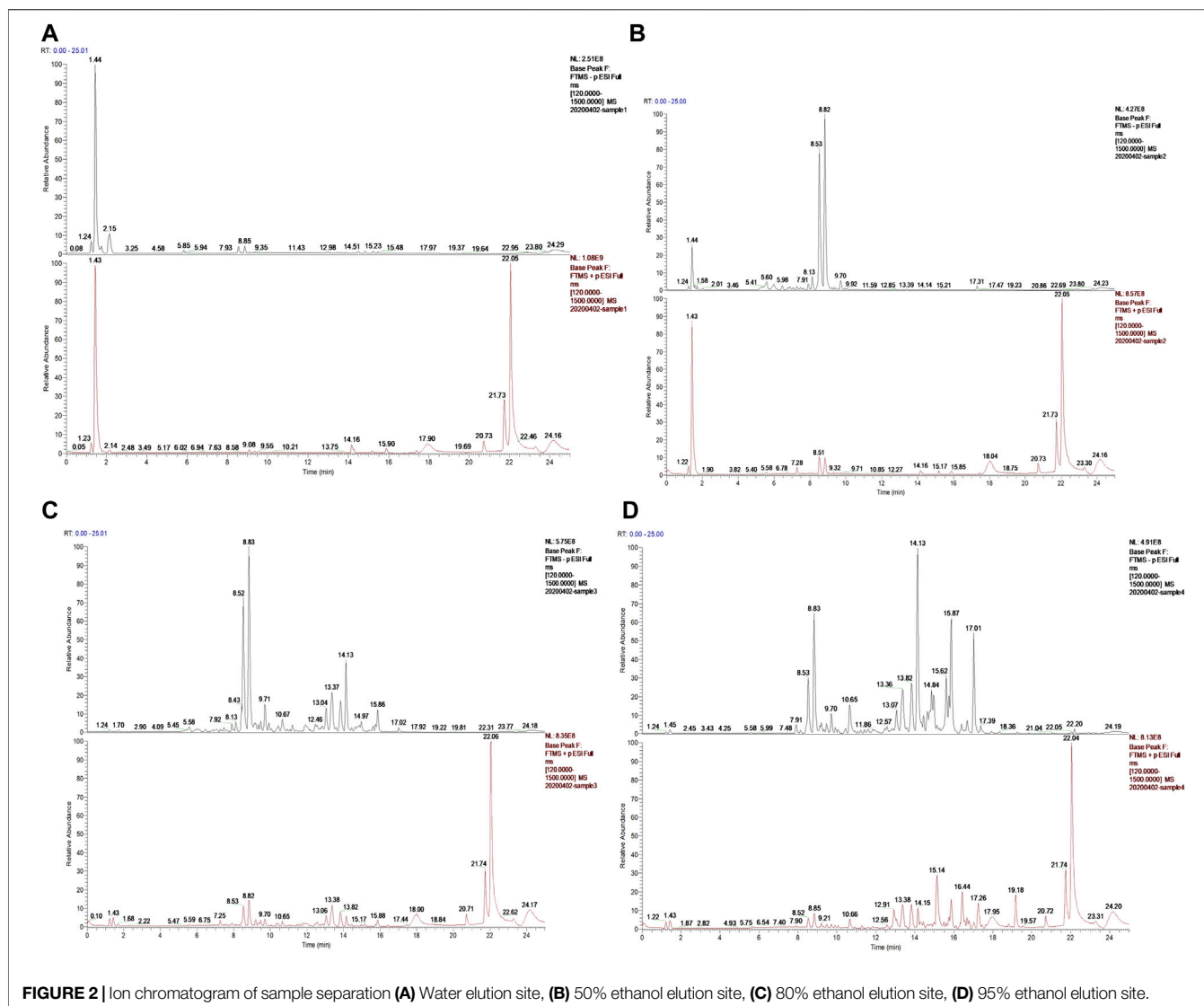
resolution UPLC-Q-TOF MS/MS system. These chemical constituents include Apigenin, luteolin, and Prostaglandin B1 et al. (Table 1). The main components contain verbascoside (8.53 min) and Isoacteoside (8.82 min), of which 80% of ethanol elution has the highest content (Figure 2).

The 24 components isolated from the LHZZ were analyzed by the Swiss Target Prediction database. A total of 359 potential targets were screened after removing duplicates in the target prediction. Subsequently, we used Cytoscape to construct a visual "compound-target" network with 383 nodes and 770 edges (Supplementary Table S1). Nodes represent ingredients and

their corresponding targets. The higher the degree corresponding to the node, the greater the pharmacological effects of this ingredient or target (Table 2).

## Colorectal Adenoma Target and Intersection Target

The intestinal adenoma-related targets were collected from the human genome database. In the OMIM, DisGeNET, DrugBank and GeneCard, with the number of these targets 173, 3, 25 and 111 respectively. A total of 271 LHZZ targets were obtained by



removing duplicates in these four kinds of databases. These targets were intersected with component targets to obtain intersection targets 28, as shown in **Figure 3A**. A "component-intersection target" network diagram with 49 nodes and 64 edges was built using the Cytoscape, as shown in **Figure 3B**.

### Construction of Protein-Protein Interaction Network (PPI) and Key Targets

In order to supplement other related genes in the network and find the key signaling pathways, we imported 28 target genes into the GeneMANIA tool to obtain a PPI network. The percentage in the results stands for the weight of interaction relationship in the network. Our result revealed that in the interaction between targets of the network, 21.82% were co-expression and 32.68% had physical interactions. There were also relationships of co-localization and shared protein domains (**Figure 4A**). The calculated average shortest path length, betweenness centrality,

closeness centrality, and degree of nodes in the network are shown in **Table 3**. According to the network topology properties, the targets are sorted from high to low (degree score  $\geq 17$ ), corresponding to TP53, CASP3, HRAS, EGFR and AKT1. These five targets may be the key targets of LHZZ granule in the prevention and treatment of CRA.

### GO Function and KEGG Pathway Enrichment Analysis

The 28 intersected genes were enriched by GO and KEGG analysis using the analytic tool included in the David database. According to biological process (BP), molecular function (MF) and cellular component (CC) (**Figure 4B**), as well as  $p$ -value  $< 0.05$  and gene number 6 as screening conditions, a total of 30 items related to biological process, molecular function and cellular composition were obtained. It was suggested that LHZZ may play a role in inhibiting CRA through the regulation of metabolic process,

**TABLE 2 |** Topological parameters of the compound.

Compound	Degree	Subgraph	Betweenness	Closeness
Compound7	100	225,335.1	40,899.59	0.409432
Compound22	100	46,496.66	50,719.4	0.411195
Compound10	100	46,093.81	52,926.96	0.413868
Compound2	57	98,829.13	14,967.93	0.374877
Compound5	40	25,103.93	12,349.18	0.347589
Compound9	32	24,252.75	6,896.857	0.343217
Compound8	30	63,206.41	2,961.609	0.356011
Compound16	30	44,007.79	2,837.441	0.356011
Compound20	30	11,373.15	8,202.712	0.341987
Compound19	30	1,448.521	16118.71	0.337754
Compound12	29	61,555.43	2,747.355	0.355349
Compound4	23	45,455.85	1,481.349	0.351426
Compound3	22	1,495.715	10,508.58	0.343217
Compound15	20	36,547.63	1,176.193	0.348858
Compound23	20	2,387.378	9,161.614	0.34016
Compound17	19	35864.06	875.3793	0.348222
Compound18	19	35,864.06	875.3793	0.348222
Compound14	18	11,020.76	1,517.927	0.348222
Compound6	16	23,841.64	705.9578	0.346328
Compound1	12	371.5921	747.7414	0.273443
Compound13	7	2,454.869	213.3352	0.341376
Compound21	7	2,437.616	200.8548	0.341376
Compound24	3	435.55	18.95916	0.304868

inflammatory factors, cell proliferation, protein transport, transcription factor activity and other biological processes. In the KEGG pathway enrichment analysis, a total of 71 enrichment results were obtained. Among them, cancer-related pathway, PI3K-Akt signaling pathway, p53 signaling pathway and cell apoptosis are closely associated with cell proliferation, metabolic disorder and protein transport, that are in consistent with the results of GO enrichment. KEGG pathways and gene pathways with  $p \leq 0.05$  are significantly abundant. The first 20

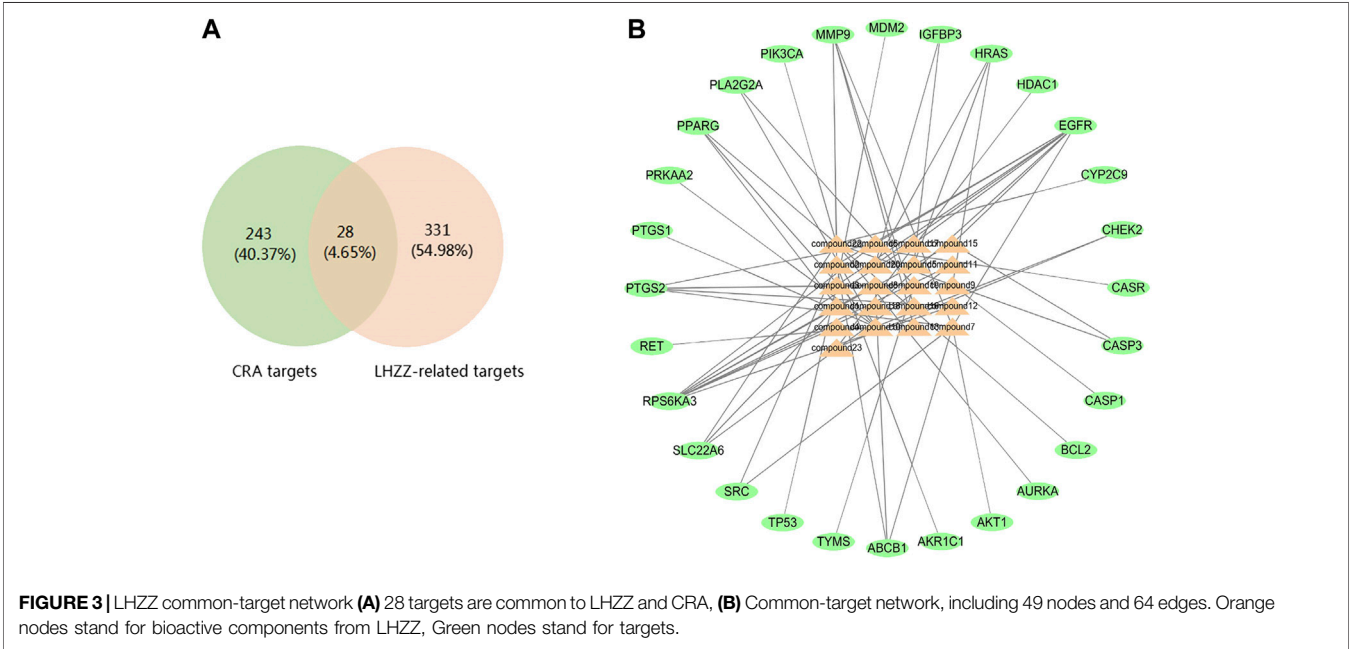
components are graphed using the OmicShare cloud platform (Figure 4C). Statistical analysis showed that five proteins participated in the first 20 pathways with a high frequency ( $\geq 9$  times), which indicated that they played an important role in the enrichment pathway. The five core proteins are AKT1, TP53, CASP3, HRAS and EGFR. Among these enriched pathways, we found that cancer signaling pathways play an important role in CRA. The predictive targets of the cancer signaling pathway are shown in pink in Figure 5A.

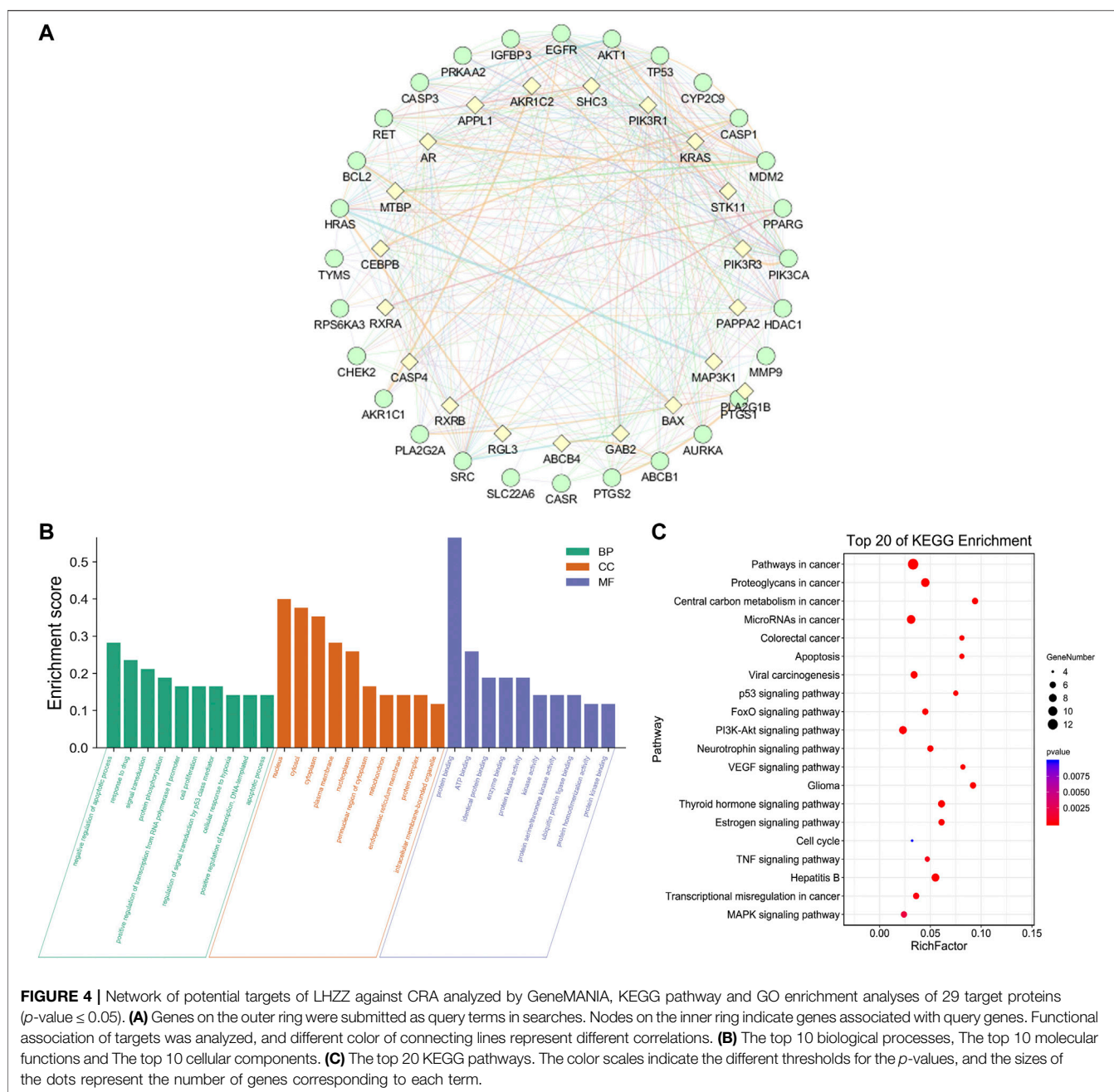
Target-Path/Functional Network

Based on the network analysis of several representative signaling pathways, biological processes and molecular functions, the target pathway/functional network is constructed. There are 28 nodes and 73 edges in the network graph (Figure 5B). Multiple targets participate in multiple biological processes at the same time. For example, AKT1 is involved in the processes of “cancer signaling pathway”, “PI3K-Akt signaling pathway” and “apoptosis”. TP53 belongs to both “central carbon metabolism of cancer” and “viral carcinogenesis”. EGFR participates in many biological processes, such as “MicroRNA in cancer”, “FoxO signaling pathway”, “proteoglycan in cancer” and so on. The above results suggest that LHZZ may play a role in anti-CRA through multiple targets and multiple pathways.

Molecular Docking

In the network analysis of “active ingredient-target-disease”, the target of the top five proteins was docked with the active components of LHZZ granule. They were TP53, CASP3, HRAS, EGFR and AKT1. These targets were chosen because they were not only the key nodes of the PPI network, but also played important roles in KEGG signaling pathways. Folic acid was used as the positive control drug, and the score was used to





evaluate the binding degree between ligand molecule and receptor molecule. The lower the score, the lower the matching energy, indicating that the more stable the conformation of ligand-receptor binding and the greater the possibility of interaction. The results showed that the common target binding energy of the active components and intestinal adenoma was negative, suggesting that the compound had a certain binding activity to the receptor, and the binding energy was less than  $-5$  kJ/mol, indicating strong binding activity. In addition, folic acid, a positive control drug, had a therapeutic effect on CRA. The folic acid target involved in CRA therapy docked with the potential target of LHZZ, and the affinity data obtained were

used as the baseline data of positive control. According to the heat map, all the 15 active components of LHZZ granule had good binding to AKT1, and their binding energies were all less than or equal to folic acid. The highest binding affinity ( $-12.1$  kJ/mol) is Isoacteoside and AKT1, and the second highest binding affinity ( $-11.8$  kJ/mol) is Luteolin-3"-O- $\beta$ -D-glucopyranoside and AKT1 (Figure 6). Using DiscoveryStudio, the two-dimensional plan view and the three-dimensional view of the docking mode of the components and the target AKT1 are shown (Figure 7). It can be seen from Figure 7A that the binding of AKT1 to Isoacteoside is mainly through hydrogen bond interaction with VAL271, GLN79, ASN53, ASN204, ASP292 and THR211, hydrophobic



**TABLE 3 |** Topological parameters of the targets.

	Subgraph	Degree	Betweenness	Closeness
TP53	42,341.098	21	88.14873	0.83871
CASP3	40,129.74	19	39.95825	0.787879
HRAS	36,004.387	18	41.50568	0.764706
EGFR	35,467.51	17	24.41619	0.742857
AKT1	34,581.13	17	28.80135	0.742857
SRC	28,750.186	15	22.94023	0.702703
PTGS2	26,254.316	16	90.85125	0.722222
MDM2	24,656.514	13	7.926167	0.65
PPARG	23,164.822	14	34.5612	0.65
PIK3CA	18,924.707	12	54.69927	0.634146
MMP9	16,088.484	10	1.785714	0.590909
ABCB1	14,378.387	11	68.03709	0.619048
HDAC1	14,345.226	9	1.237302	0.553192
AURKA	13,083.566	9	1.194444	0.553192
TYMS	12,997.974	9	1.65873	0.565217
IGFBP3	11,296.592	8	0.222222	0.565217
CHEK2	10,979.728	9	4.732143	0.577778
RET	9,190.687	7	0.444444	0.541667
CASP1	7,237.4453	7	5.319795	0.553192
BCL2	3,940.878	5	2	0.5
RPS6KA3	1,898.8567	3	0	0.481482
PTGS1	1,169.2216	5	6.203449	0.481482
PRKAA2	1,054.8093	3	0.566667	0.490566
CYP2C9	665.86694	4	4.789682	0.472727
PLA2G2A	297.5576	3	0	0.440678
CASR	114.1672	1	0	0.393939
SLC22A6	87.212425	1	0	0.38806

interaction with LYS268, LEU264 and LEU210, and  $\pi$  bond interaction with TRP80 and THR291. Luteolin-3"-O- $\beta$ -D-glucopyranoside binds to AKT1 (**Figure 7B**) mainly through hydrogen bonding with GLN203, ASP274, ASN204, ASP292 and THR82, hydrophobically with LYS268, VAL270 and LEU210, and  $\pi$  bond with TRP80, TYR272 and LEU264.

The combination of verbascoside and AKT1 (**Figure 7C**) is mainly through hydrogen bonding interaction of TYR272, ASP292, SER205 and TRP80, hydrophobic interaction with ALA58 and  $\pi$  bond interaction with LEU210. The degree of binding between other targets and active components is interpreted in the same way as AKT1.

## Experimental Verification in Vitro CCK-8 Assay

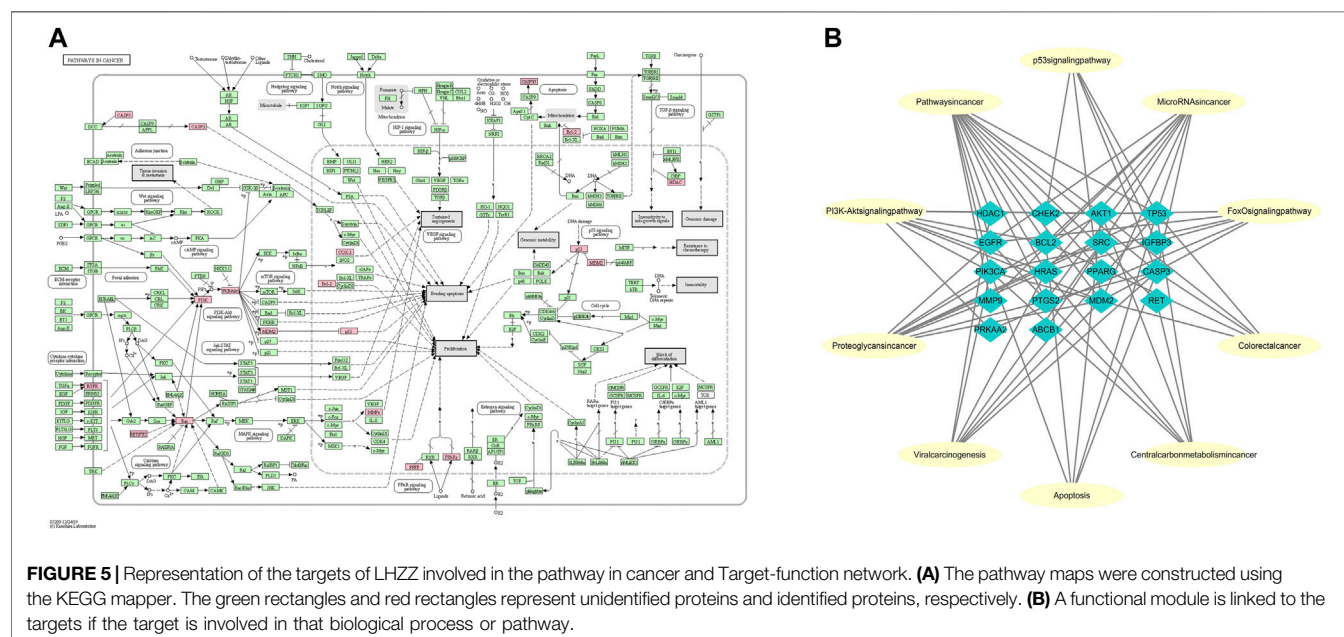
CCK-8 assays were performed to determine the anti-CRA effect of treatment with LHZZ at different concentrations (0, 25, 50, 75, 100 and 120  $\mu$ g/ml) for 48 and 72 h in IH-CRA cells. As shown in **Figure 8A**, the viability of IH-CRA cells was markedly reduced in cells treated with LHZZ in a dose- and time-dependent manner. LHZZ at  $\geq 100$   $\mu$ g/ml had low cell viability (<25%).

## Validation of Targets

We further explored the molecular mechanism of LHZZ involved in inducing apoptosis in IH-CRA cells by Western blotting. As shown in **Figures 8B,C**, the protein levels of AKT1 were significantly decreased in a dose-dependent manner. The results showed that LHZZ could inhibit the proliferation of IH-CRA cells and play a protective role in intestinal tissues.

## DISCUSSIONS

There are approximately 1.4 million new CRC patients, and approximately 700,000 deaths worldwide each year (Cho et al., 2006). About 85% of colorectal cancer is caused by CRA. As the incidence of CRC increases year by year, the treatment and prevention of CRA has become increasingly important. CRA is the key to the pathogenesis of colorectal cancer and has the



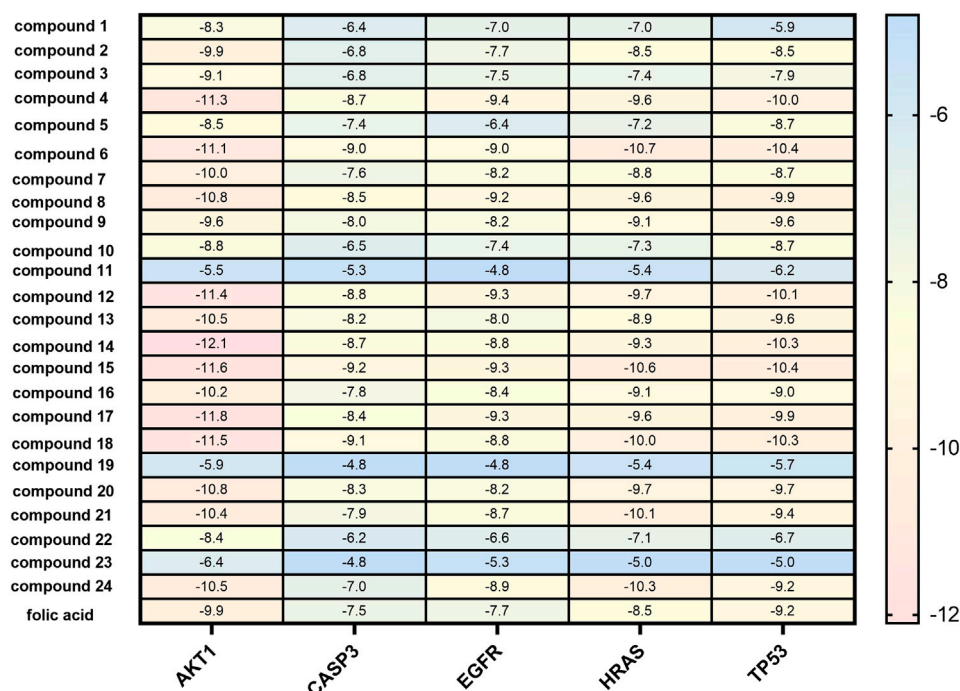


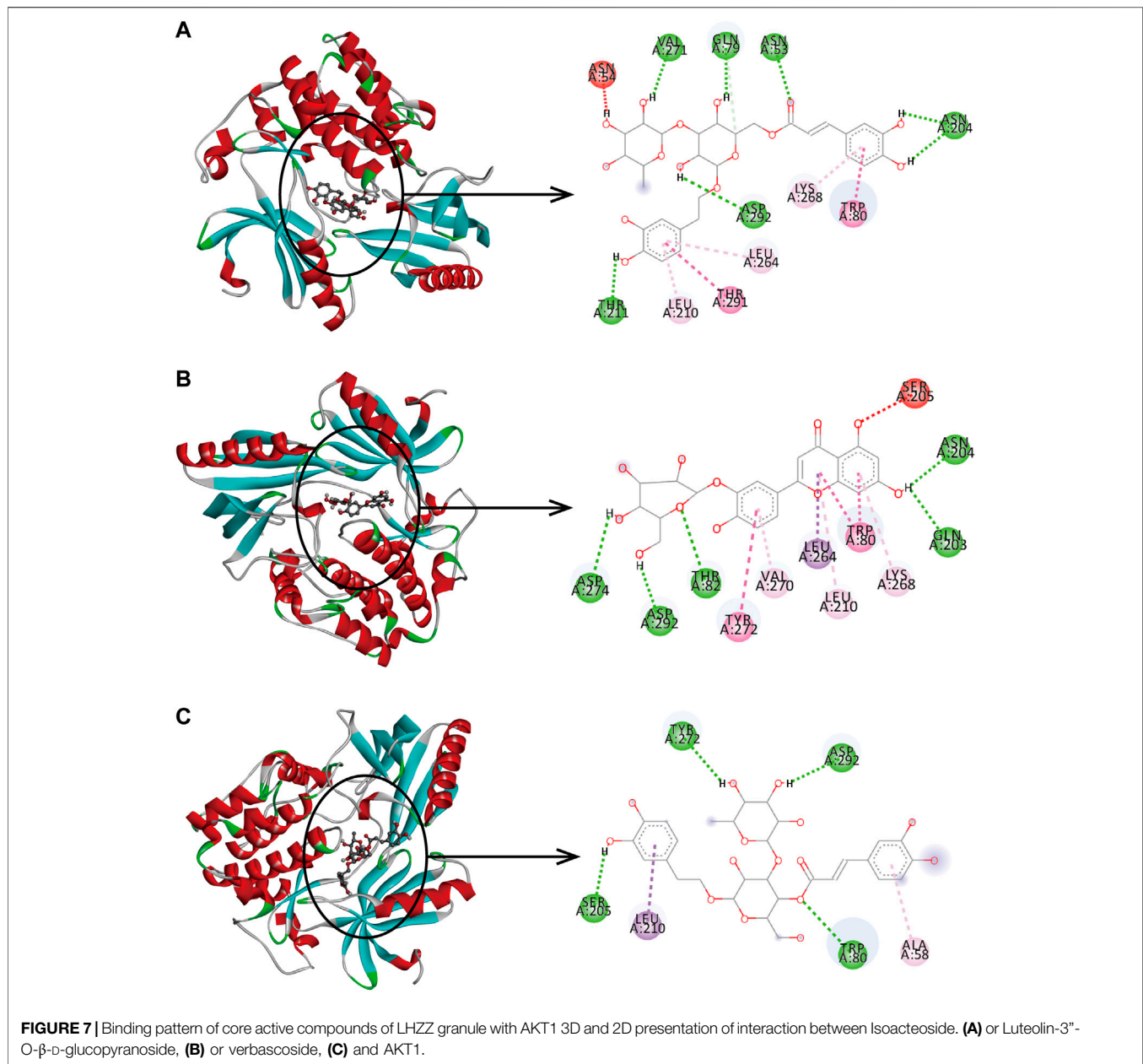
**FIGURE 6 |** Molecular docking results heat map of key active components and key targets. The docking score changes from low to high, from blue to red. Red numbers on the right of the heat map indicate in terms of better molecular docking.

characteristics of two-way transformation, so it is the key point to prevent colorectal cancer (Sánchez-Peralta et al., 2020). According to the TCM, both the large and small intestines belong to the stomach Meridian. Polyps form from the intestinal dregs and the accumulation of dampness and stasis. Therefore, the prevention and treatment of CRA contains the idea of "combined treatment on the spleen and intestine", particularly treating the spleen and stomach Meridian to treat colorectal diseases (Tang et al., 2010). The LHZZ granule can enter the spleen and stomach Meridian.

For complex diseases such as CRA, network pharmacology has unique advantages in predictive analysis (Wang and Dong, 2020). We screened the main anti-intestinal adenoma active components of LHZZ granule by network pharmacology combined with high resolution mass spectrometry analysis. We found that Apigenin, ProstaglandinB1, BrefeldinA, Isoacteoside, verbascoside and Luteolin are the main active ingredients. It was reported that apigenin and luteolin belong to flavonoids, that can inhibit the growth of intestinal adenoma cells by reducing the phosphorylation of AKT and up-regulating the expression of FADD, indicating that apigenin and luteolin can inhibit the invasion and metastasis of tumor cells (Xu et al., 2016; Kang et al., 2019). BrefeldinA is a commonly used protein transport inhibitor. Some studies have confirmed that BrefeldinA can act on the PI3K-Akt pathway and has strong anti-tumor activity (Zhou et al., 2019). As an inflammatory mediator, ProstaglandinB1 can regulate gene expression to drive the pathogenic transformation of these cells and exert its anti-inflammatory effect (Yao and Narumiya, 2019). Both

Isoacteoside and verbascoside belong to phenylpropanoid glycosides and are the main components of LHZZ granule. Verbascoside is an anti-inflammatory factor, has anti-proliferation, anti-inflammatory and anti-cancer effects, that are consistent with the pharmacological action of LHZZ granule (Zhou et al., 2014; Yang et al., 2019).

The top targets in PPI network analysis are TP53, CASP3, EGFR and AKT1. TP53 is a tumor suppressor protein that can induce cell cycle arrest and apoptosis, and its mutations are common in various cancers. Some previous meta analysis show that, TP53 could be used as a biomarker for screening inflammatory bowel disease-related colorectal cancer and dysplasia (Du et al., 2017; Nakayama et al., 2017; Zhao et al., 2019). Caspase-3 is the main executor of cell apoptosis. Specific cleavage of a series of substrates such as poly-ADP ribose polymerase (PARP) and acetyl-DEVD-7-amino-4-methylcoumarin (Ac-DEVD-AMC) leads to the breakdown of DNA in cells (Peterson et al., 2009). The results of gastrointestinal tumor biomarker network analysis show that EGFR (epidermal growth factor receptor) is involved in regulating the proliferation and differentiation of trophoblast cells, and can be used as a predictive biomarker for intestinal cancers (Vaseghi Maghvan et al., 2017). AKT1 is the core member of the proliferation and survival pathway most frequently activated in cancers (Carpenter et al., 2007). It was found that the upstream molecules PHLPP2 and PTEN of Akt1 affect its phosphorylation process, which in turn affects the PI3K/Akt signaling pathway, and exerts an anti-tumor effect. For further experimental verification, AKT1 was selected as a candidate target of LHZZ against CRA. The



molecular docking research showed good affinity of LHZZ to these five targets, among them AKT1 has the highest binding degree. The results of molecular docking and *in vitro* validation experiments confirmed the results of network pharmacology.

According to the GO analysis of LHZZ granule on CRA, 30 biological processes were screened. These processes include those that regulate metabolic processes, inflammatory factors, protein transport, transcription factor activity, regulation of cell proliferation, et al. LHZZ may adjust the microenvironment of intestinal adenomas. In the results of the enrichment analysis of the KEGG pathway of LHZZ on CRA, the top 20 signaling pathways were screened out. Among them, the most enriched targets are cancer pathways that involve in pro-inflammatory carcinogenesis, miRNA

regulatory mechanisms, PI3K-Akt signaling pathways, p53 signaling pathways, etc. According to the previous research findings (Hung et al., 2007; Tewari et al., 2019), PI3K/Akt pathway can activate PI3K by promoting Akt phosphorylation and regulate cell proliferation, thereby promoting tumor growth. The apigenin, luteolin, Isoaeteoside and Brefeldin A can inhibit the progression of intestinal adenoma by affecting Akt phosphorylation, down-regulating Akt kinase and regulating PI3K-Akt pathway and inhibiting intestinal epithelial stromal transformation (Chunhua et al., 2013; Jiang et al., 2018). Dilshar et al. (Dilshara et al., 2019) have confirmed that P53-mediated oxidative stress enhances I3M-induced apoptosis of colon adenoma cells by up-regulating DR5 and inducing apoptosis in their *in vitro* experiments. P53

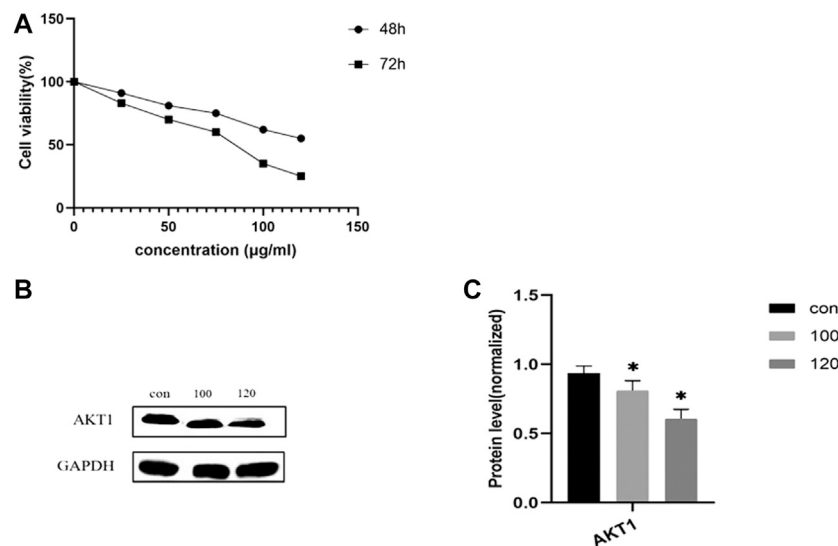


**FIGURE 8 |** LHZZ inhibits the IH-CRA cells. **(A)** IH-CRA cells were treated with various concentrations of LHZZ for 48 and 72 h. Data are presented as the mean  $\pm$  SD from at least three independent experiments. **(B)** LHZZ inhibits the IH-CRA cells. Representative Western blots showing the expression of AKT1 in IH-CRA cells. GAPDH was used as an internal control. **(C)** The protein levels of AKT1 in H-CRA cells. Values are presented as a mean  $\pm$  SEM. \* $p < 0.05$  vs. control.

can prevent CRA by promoting DNA repair, cell cycle control, and programmed cell death. Studies (Granato et al., 2017) have found that verbascoside and apigenin can activate lipid metabolism pathways through the p53 pathway and participate in the apoptosis of adenoma cells. Previous studies have shown that (Mishra et al., 2016; Sabarimurugan et al., 2020), a variety of microRNAs can be used as biomarkers for the prognosis of patients with intestinal adenoma. Traditional Chinese medicine may directly or indirectly target and regulate the corresponding miRNA expression, and then restore the balance between miRNA and oncogenes or tumor suppressor genes, maintain the balance of yin and yang of the body, and achieve the effect of prevention and treatment of colorectal adenoma. Previously, berberine has been reported to reduce the risk of recurrent colorectal adenomas and polypoid lesions after polypectomy, but oral bioavailability has been poor, and LHZZ overcomes this problem (Chen et al., 2020; Wu et al., 2020). The active ingredients of LHZZ granule can treat colorectal adenoma through multiple signaling molecules and multiple signaling pathways. In view of the limitations of network pharmacology, Firstly, the medicine is traditionally prepared might have/yield different amount/concentration of the target compounds and the public databases investigated in the study are constantly updated; thus, some other bioactive ingredients and target genes may not have been included in our analysis. Further studies are warranted to examine the potential involvement of these targets.

In summary, the Apigenin, Prostaglandin, Brefeldin A, Isoacteoside, Verbascoside and luteolin are the main active components LHZZ granule. Their targets of anti-colorectal adenoma are AKT1, TP53, CASP3 and EGFR. LHZZ participates in the regulation of CRA cell proliferation through

cancer pathway, metabolic pathway, PI3K-Akt pathway, p53 pathway and microRNAs. This study provides a rationale for using LHZZ for the treatment of CRA.

## DATA AVAILABILITY STATEMENT

The raw data supporting the conclusion of this article will be made available by the authors, without undue reservation.

## AUTHOR CONTRIBUTIONS

XL, CG contributed to study design, data interpretation, and manuscript preparation. XDK, YL, XMM contributed to sample acquisition. FC, JY contributed to mass spectrometry analysis. YMX contributed to data acquisition and analysis.

## FUNDING

This work was supported by the National Natural Science Foundation of China (81403360). Hospital fund of Yueyang Hospital (2019YYZ08). The funders play no role in data collection and analysis, design, decision to publish, or preparation of the manuscript.

## SUPPLEMENTARY MATERIAL

The Supplementary Material for this article can be found online at: <https://www.frontiersin.org/articles/10.3389/fphar.2021.629021/full#supplementary-material>.



## REFERENCES

- Boezio, B., Audouze, K., Ducrot, P., and Taboureaux, O. (2017). Network-based approaches in pharmacology. *Mol. Inform.* 36, 48. doi:10.1002/minf.201700048
- Carpén, J. D., Faber, A. L., Horn, C., Donoho, G. P., Briggs, S. L., Robbins, C. M., et al. (2007). A transforming mutation in the pleckstrin homology domain of AKT1 in cancer. *Nature* 448, 439–444. doi:10.1038/nature05933
- Chen, Y.-X., Gao, Q.-Y., Zou, T.-H., Wang, B.-M., Liu, S.-D., Sheng, J.-Q., et al. (2020). Berberine versus placebo for the prevention of recurrence of colorectal adenoma: a multicentre, double-blinded, randomised controlled study.
- Cho, N. L., Redston, M., Carothers, A. M., Zaubler, A. G., Wilton, A., and Bertagnoli, M. M. (2006). Predictive role of aberrant crypt foci (ACF) as surrogate endpoint biomarkers of colorectal cancer. *Aacr Meet. Abstr.* 26, A12.
- Chunhua, L., Donglan, L., Xiuqiong, F., Lihua, Z., Qin, F., Yawei, L., et al. (2013). Apigenin up-regulates transgelin and inhibits invasion and migration of colorectal cancer through decreased phosphorylation of AKT. *J. Nutr. Biochem.* 24, 1766–1775. doi:10.1016/j.jnutbio.2013.03.006
- Dejea, C. M., Fathi, P., Craig, J. M., Boleij, A., Taddese, R., Geis, A. L., et al. (2018). Patients with familial adenomatous polyposis harbor colonic biofilms containing tumorigenic bacteria. *Science* 359, 592–597. doi:10.1126/science.aah3648
- Dilshara, M. G., Molagoda, I. M. N., Jayasooriya, R. G. P. T., Choi, Y. H., Park, C., Lee, K. T., et al. (2019). p53-Mediated oxidative stress enhances Indirubin-3'-monoxime-induced apoptosis in HCT116 colon cancer cells by upregulating death receptor 5 and TNF-related apoptosis-inducing ligand expression. *Antioxidants* 8, 423. doi:10.3390/antiox8100423
- Du, L., Kim, J. J., Shen, J., Chen, B., and Dai, N. (2017). KRAS and TP53 mutations in inflammatory bowel disease-associated colorectal cancer: a meta-analysis. *Oncotarget* 8, 22175–22186. doi:10.18632/oncotarget.14549
- Franz, M., Rodriguez, H., Lopes, C., Zuberi, K., Montojo, J., Bader, G. D., et al. (2018). GeneMANIA update 2018. *Nucl. Acids Res.* 46, W60–w64. doi:10.1093/nar/gky311
- Granato, M., Gilardini Montani, M. S., Santarelli, R., D'orazi, G., Faggioni, A., and Cirone, M. (2017). Apigenin, by activating p53 and inhibiting STAT3, modulates the balance between pro-apoptotic and pro-survival pathways to induce PEL cell death. *J. Exp. Clin. Oncol. Res.* 36, 167. doi:10.1186/s13046-017-0632-z
- Hung, S. C., Pochampally, R. R., Chen, S. C., Hsu, S. C., and Prockop, D. J. (2007). Angiogenic effects of human multipotent stromal cell conditioned medium activate the PI3K-Akt pathway in hypoxic endothelial cells to inhibit apoptosis, increase survival, and stimulate angiogenesis. *Stem Cells* 25, 2363–2370. doi:10.1634/stemcells.2006-0686
- Jiang, Q., Pan, D., Yang, Y., Hu, Y., Fang, L., Shang, P., et al. (2018). Luteolin regulates macrophage polarization via the PI3K/Akt pathway to inhibit the apoptosis stimulated by angiotensin II. *Curr. Pharmaceut. Biotechnol.* 19, 428–437. doi:10.2174/1389201019666180629143251
- Kang, K. A., Piao, M. J., Hyun, Y. J., Zhen, A. X., Cho, S. J., Ahn, M. J., et al. (2019). Luteolin promotes apoptotic cell death via upregulation of Nrf2 expression by DNA demethylase and the interaction of Nrf2 with p53 in human colon cancer cells. *Exp. Mol. Med.* 51, 1–14. doi:10.1038/s12276-019-0238-y
- Liu, F., Yan, L., Wang, Z., Lu, Y., Chu, Y., Li, X., et al. (2017). Metformin therapy and risk of colorectal adenomas and colorectal cancer in type 2 diabetes mellitus patients: a systematic review and meta-analysis. *Oncotarget* 8, 16017–16026. doi:10.18632/oncotarget.13762
- Mishra, S., Yadav, T., and Rani, V. (2016). Exploring miRNA based approaches in cancer diagnostics and therapeutics. *Crit. Rev. Oncol. Hematol.* 98, 12–23. doi:10.1016/j.critrevonc.2015.10.003
- Nakayama, M., Sakai, E., Echizen, K., Yamada, Y., Oshima, H., Han, T. S., et al. (2017). Intestinal cancer progression by mutant p53 through the acquisition of invasiveness associated with complex glandular formation. *Oncogene* 36, 5885–5896. doi:10.1038/ncr.2017.194
- Nishihara, R., Wu, K., Lochhead, P., Morikawa, T., Liao, X., Qian, Z. R., et al. (2013). Long-term colorectal-cancer incidence and mortality after lower endoscopy. *N. Engl. J. Med.* 369, 1095–1105. doi:10.1056/NEJMoa1301969
- Park, M., Park, S. Y., Lee, H. J., and Kim, C. E. (2018). A systems-level analysis of mechanisms of platycodon grandiflorum based on A network pharmacological approach. *Molecules* 23, 841. doi:10.3390/molecules23112841
- Passarelli, M. N., Barry, E. L., Zhang, D., Gangar, P., Rees, J. R., Bresalier, R. S., et al. (2018). Risk of basal cell carcinoma in a randomized clinical trial of aspirin and folic acid for the prevention of colorectal adenomas. *Br. J. Dermatol.* 179, 337–344. doi:10.1111/bjd.16571
- Peterson, Q. P., Goode, D. R., West, D. C., Ramsey, K. N., Lee, J. J., and Hergenrother, P. J. (2009). PAC-1 activates procaspase-3 *in vitro* through relief of zinc-mediated inhibition. *J. Mol. Biol.* 388, 144–158. doi:10.1016/j.jmb.2009.03.003
- Sabarimurugan, S., Madhav, M. R., Kumarasamy, C., Gupta, A., Baxi, S., Krishnan, S., et al. (2020). Prognostic value of MicroRNAs in stage II colorectal cancer patients: a systematic review and meta-analysis. *Mol. Diagn. Ther.* 24, 15–30. doi:10.1007/s40291-019-00440-y
- Sánchez-Peralta, L. F., Bote-Curiel, L., Picón, A., Sánchez-Margallo, F. M., and Pagador, J. B. (2020). Deep learning to find colorectal polyps in colonoscopy: a systematic literature review. *Artif. Intell. Med.* 108, 101923. doi:10.1016/j.artmed.2020.101923
- Tang, S., Huang, L., Huang, L., Yang, H., and Zhou, C. (2010). New collection of crude drugs in Chinese Pharmacopoeia 2010. *Zhongguo Zhongyao Zazhi* 35, 539–543. doi:10.5897/JMPR10.012
- Tewari, D., Patni, P., Bishayee, A., Sah, A. N., and Bishayee, A. (2019). Natural products targeting the PI3K-Akt-mTOR signaling pathway in cancer: a novel therapeutic strategy. *Semin. Cancer Biol.* 12, 8. doi:10.1016/j.semcancer.2019.12.008
- Vaseghi Maghvan, P., Rezaei-Tavirani, M., Zali, H., Nikzamir, A., Abdi, S., Khodadoostan, M., et al. (2017). Network analysis of common genes related to esophageal, gastric, and colon cancers. *Gastroenterol. Hepatol. Bed. Bench.* 10, 295–302. doi:10.22037/ghfb.v0i0.1212
- Veettil, S. K., Nathisuwan, S., Ching, S. M., Jinatongthai, P., Lim, K. G., Kew, S. T., et al. (2019). Efficacy and safety of celecoxib on the incidence of recurrent colorectal adenomas: a systematic review and meta-analysis. *Cancer Manag. Res.* 11, 561–571. doi:10.2147/CMAR.S180261
- Wang, K. W., and Dong, M. (2020). Potential applications of artificial intelligence in colorectal polyps and cancer: recent advances and prospects. *World J. Gastroenterol.* 26, 5090–5100. doi:10.3748/wjg.v26.i34.5090
- Wu, Y. S., Shi, L., Liu, X. G., Li, W., Wang, R., Huang, S., et al. (2020). Chemical profiling of Callicarpa nudiflora and its effective compounds identification by compound-target network analysis. *J. Pharmaceut. Biomed. Anal.* 182, 113110. doi:10.1016/j.jpba.2020.113110
- Xu, M., Wang, S., Song, Y. U., Yao, J., Huang, K., and Zhu, X. (2016). Apigenin suppresses colorectal cancer cell proliferation, migration and invasion via inhibition of the Wnt/ $\beta$ -catenin signaling pathway. *Oncol. Lett.* 11, 3075–3080. doi:10.3892/ol.2016.4331
- Yang, X., Guo, F., Peng, Q., Liu, Y., and Yang, B. (2019). Suppression of *in vitro* and *in vivo* human ovarian cancer growth by isoacteoside is mediated via sub-G1 cell cycle arrest, ROS generation, and modulation of AKT/PI3K/m-TOR signalling pathway. *J. Buon.* 24, 285–290.
- Yang, Y., Li, Z. Y., Shao, J. J., Wang, G., Wen, R., Tian, J. Z., et al. (2021). Callicarpa nudiflora Hook. & Arn.: a comprehensive review of its phytochemistry and pharmacology. *J. Ethnopharmacol.* 264, 113123. doi:10.1016/j.jep.2020.113123
- Yao, C., and Narumiya, S. (2019). Prostaglandin-cytokine crosstalk in chronic inflammation. *Br. J. Pharmacol.* 176, 337–354. doi:10.1111/bph.14530
- Zhang, J., Li, H., Zhang, Y., Zhao, C., Zhu, Y., and Han, M. (2020). Uncovering the pharmacological mechanism of stemazole in the treatment of neurodegenerative diseases based on a network pharmacology approach. *Int. J. Mol. Sci.* 21, 145.
- Zhang, X. G., Li, X. M., Zhou, X. X., Wang, Y., Lai, W. Y., Liu, Y., et al. (2019). The wound healing effect of Callicarpa nudiflora in scalded rats. *Evid Based Complement Alternat Med* 2019, 1860680. doi:10.1155/2019/1860680
- Zhao, X., Liu, J., Liu, S., Yang, F., and Chen, E. (2019). Construction and validation of an immune-related prognostic model based on TP53 status in colorectal cancer. *Cancers (Basel)* 11, 1722. doi:10.3390/cancers11111722
- Zhou, L., Feng, Y., Jin, Y., Liu, X., Sui, H., Chai, N., et al. (2014). Verbascoside promotes apoptosis by regulating HIPK2-p53 signaling in human colorectal cancer. *BMC Cancer* 14, 747. doi:10.1186/1471-2407-14-747
- Zhou, L., Gao, W., Wang, K., Huang, Z., Zhang, L., Zhang, Z., et al. (2019). Brefeldin A inhibits colorectal cancer growth by triggering Bip/Akt-regulated autophagy. *Faseb. J.* 33, 5520–5534. doi:10.1096/fj.201801983R

Zhou, Z., Chen, B., Chen, S., Lin, M., Chen, Y., Jin, S., et al. (2020). Applications of network pharmacology in traditional Chinese medicine research. *Evid Based Complement Alternat Med* 20, 1646. doi:10.1155/2020/1646905

**Conflict of Interest:** The authors declare that the research was conducted in the absence of any commercial or financial relationships that could be construed as a potential conflict of interest.

Copyright © 2021 Guo, Kang, Cao, Yang, Xu, Liu, Li, Ma and Fu. This is an open-access article distributed under the terms of the Creative Commons Attribution License (CC BY). The use, distribution or reproduction in other forums is permitted, provided the original author(s) and the copyright owner(s) are credited and that the original publication in this journal is cited, in accordance with accepted academic practice. No use, distribution or reproduction is permitted which does not comply with these terms.



# OTS964, a TOPK Inhibitor, Is Susceptible to ABCG2-Mediated Drug Resistance

Yuqi Yang<sup>1</sup>, Zhuo-Xun Wu<sup>1</sup>, Jing-Quan Wang<sup>1</sup>, Qiu-Xu Teng<sup>1</sup>, Zi-Ning Lei<sup>1</sup>, Sabrina Lusvarghi<sup>2</sup>, Suresh V. Ambudkar<sup>2</sup>, Zhe-Sheng Chen<sup>1\*</sup> and Dong-Hua Yang<sup>1\*</sup>

<sup>1</sup>Department of Pharmaceutical Sciences, College of Pharmacy and Health Sciences, St. John's University, Queens, NY, United States, <sup>2</sup>Laboratory of Cell Biology, Center for Cancer Research, National Cancer Institute, NIH, Bethesda, MD, United States

## OPEN ACCESS

### Edited by:

Joanna Kopecka,  
University of Turin, Italy

### Reviewed by:

De-shen Wang,  
Sun Yat-sen University  
Cancer Center, China  
Dimas Carolina Belisario,  
University of Turin, Italy

### \*Correspondence:

Zhe-Sheng Chen  
chenz@stjohns.edu  
Dong-Hua Yang  
yangd1@stjohns.edu

### Specialty section:

This article was submitted to  
Experimental Pharmacology and  
Drug Discovery,  
a section of the journal  
Frontiers in Pharmacology

**Received:** 24 October 2020

**Accepted:** 08 January 2021

**Published:** 15 February 2021

### Citation:

Yang Y, Wu Z-X, Wang J-Q, Teng Q-X,  
Lei Z-N, Lusvarghi S, Ambudkar SV,  
Chen Z-S and Yang D-H (2021)  
OTS964, a TOPK Inhibitor, Is  
Susceptible to ABCG2-Mediated  
Drug Resistance.  
Front. Pharmacol. 12:620874.  
doi: 10.3389/fphar.2021.620874

OTS964 is a potent T-LAK cell-originated protein kinase (TOPK) inhibitor. Herein, we investigated the interaction of OTS964 and multidrug resistance (MDR)-associated ATP-binding cassette sub-family G member 2 (ABCG2). The cell viability assay indicated that the effect of OTS964 is limited in cancer drug-resistant and transfected cells overexpressing ABCG2. We found that the known ABCG2 transporter inhibitor has the ability to sensitize ABCG2-overexpressing cells to OTS964. In mechanism-based studies, OTS964 shows inhibitory effect on the efflux function mediated by ABCG2, and in turn, affects the pharmacokinetic profile of other ABCG2 substrate-drugs. Furthermore, OTS964 upregulates ABCG2 protein expression, resulting in enhanced resistance to ABCG2 substrate-drugs. The ATPase assay demonstrated that OTS964 stimulates ATPase activity of ABCG2 in a concentration-dependent manner. The computational molecular docking analysis combined with results from ATPase assay suggested that OTS964 interacts with drug-binding pocket of ABCG2 and has substrate-like behaviors. Thus, OTS964 is an MDR-susceptible agent due to its interactions with ABCG2, and overexpression of ABCG2 transporter may attenuate its therapeutic effect in cancer cells.

**Keywords:** TOPK inhibitor, OTS964, ABCG2, ABC transporter, cancer

## INTRODUCTION

T-LAK cell-originated protein kinase (TOPK) is a mitogen-activated protein kinase-like kinase (MAPKK), which plays a critical role in facilitating cell cycle control and mitotic progression (Herbert et al., 2018). TOPK expression is largely confined to tissues with rapid cell proliferation, and TOPK mRNA can be abundantly detected in tissues derived from testis, placenta, brain, and thymus (Herbert et al., 2018). Dysregulated expression of TOPK often results in cancer development and tumor metastasis in various cancer types (Hansel et al., 2009; Shih et al., 2012; Joel et al., 2015; Ikeda et al., 2016; Jiang et al., 2019). TOPK overexpression promotes cell growth and induces tumor formation (Zhu et al., 2007). Conversely, downregulation of TOPK expression suppresses tumor growth, migration, and invasion (Gao et al., 2019). Therefore, TOPK may be a potential cancer-specific biomarker, and serves as a druggable cancer target with minimal harm to normal tissue (Bellay et al., 2016; Hayashi et al., 2018; Herbert et al., 2018; Pirovano et al., 2020).

A small molecule TOPK inhibitor, OTS964, has been reported to have the ability to suppress tumor growth and to induce apoptotic cell death in various cancer models both *in vitro* and *in vivo* (Matsuo et al., 2014; Ikeda et al., 2016; Pirovano et al., 2017). The chemical structure of OTS964 is

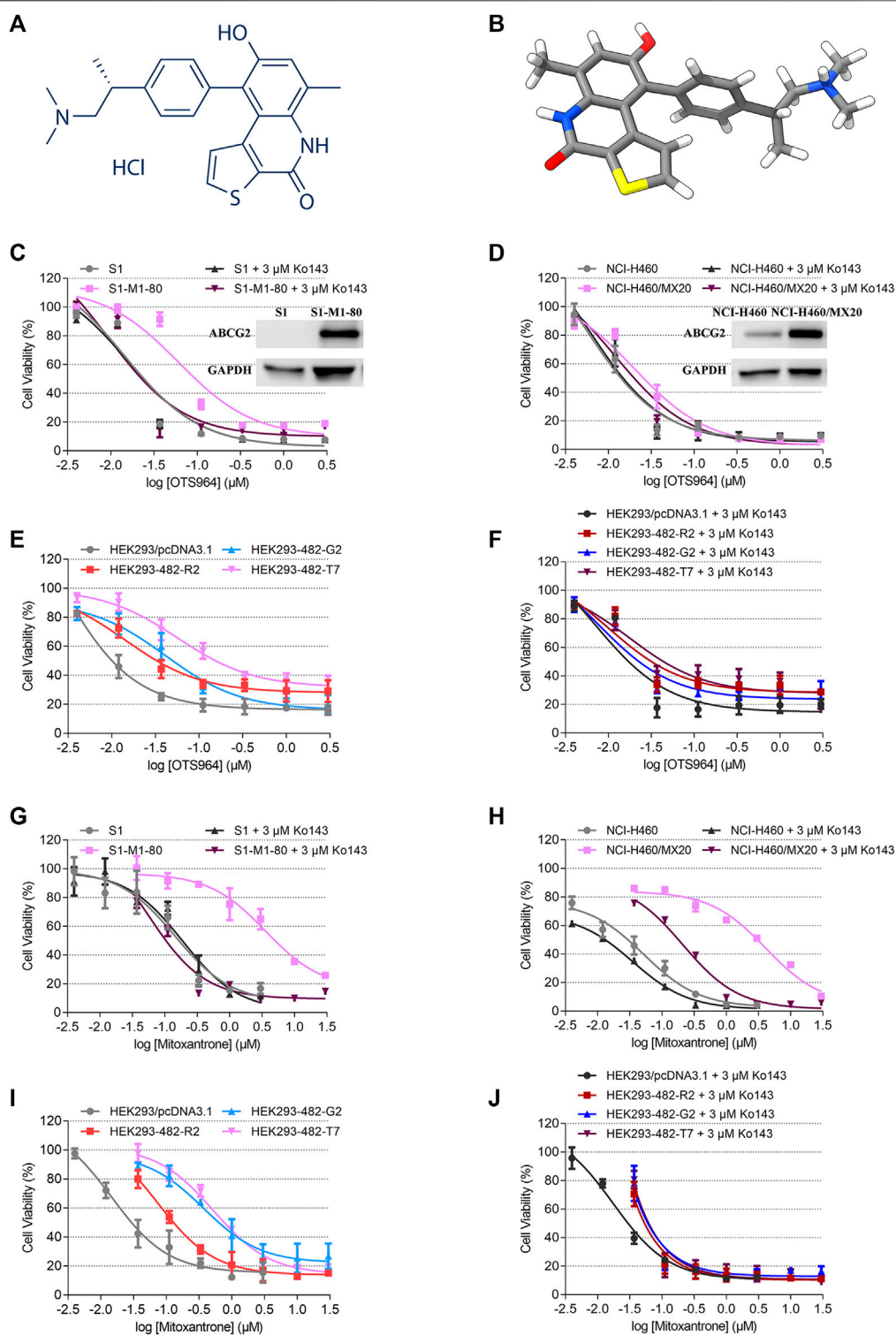


**FIGURE 1 |** Chemical structure of OTS964, and the cell viability-concentration curves for OTS964 and mitoxantrone in MDR cells mediated by ABCG2 and their counterparts in parental cells. **(A)** 2D view of OTS964 structure. **(B)** 3D view of OTS964 structure. OTS964 molecule is exhibited as colored sticks. Gray: carbon; white: hydrogen; red: oxygen; blue: nitrogen; yellow: sulfur. The cytotoxic activity of OTS964 in **(C)** S1-M1-80 and S1, **(D)** NCI-H460/MX20 and NCI-H460, and **(E, F)** ABCG2-transfected HEK293 cells (HEK293/ABCG2-482-R2, HEK293/ABCG2-482-G2, and HEK293/ABCG2-482-T7) and HEK293/pcDNA3.1 co-treated without/with Ko143. The cytotoxic activity of mitoxantrone in **(G)** S1-M1-80 and S1, **(H)** NCI-H460/MX20 and NCI-H460, and **(I, J)** ABCG2-transfected HEK293 cells (HEK293/ABCG2-482-R2, HEK293/ABCG2-482-G2, and HEK293/ABCG2-482-T7) and HEK293/pcDNA3.1 co-treated without/with Ko143. Ko143 served as a known ABCG2 inhibitor. Each dot is displayed as mean  $\pm$  SD obtained from three experiments performed independently.



presented in **Figures 1A,B**. Most recently, Pirovano et al. developed a [ $^{18}\text{F}$ ]-labeled OTS964 and showed that it has acceptable pharmacokinetic profile with favorable biodistribution in a mouse model (Pirovano et al., 2019). Free form of OTS964 has unfavorable hematopoietic toxicity; however, encapsulated OTS964 liposomes could overcome this problem (Gilabert-Oriol et al., 2019). This is a promising step toward clinical use of OTS964.

Evidence from clinical contexts have indicated that the efficacy of anticancer drugs is restricted by multidrug resistance (MDR) (Holohan et al., 2013). Pharmacodynamic and/or pharmacokinetic resistance can further confer limited effectiveness of cytotoxic and targeted drugs (Vagiannis et al., 2020). Dysregulation or mutation of therapeutic target results in pharmacodynamic resistance; while, enhanced efflux function or drug deactivation via an alternative metabolic pathway promotes pharmacokinetic resistance (Holohan et al., 2013). ATP-binding cassette (ABC) transporters, distributed in the lipid raft of certain cells, mediate drug efflux to attenuate intracellular level of chemotherapeutic drugs from accumulating in cancer cells (Klappe et al., 2009). ABC sub-family G member 2 (ABCG2, breast cancer resistance protein/BCRP) is a common factor responsible for MDR (Theodoulou and Kerr, 2015). It is known that ABCG2 is expressed on the breast, ovaries, testis, placenta, intestine, liver, and blood brain barrier (Szakács et al., 2008; Manolaridis et al., 2018).

TOPK and ABCG2 share similar tissue distributions. Hence, we investigated whether ABCG2 could restrict the effectiveness of TOPK inhibitors. In particular, we assessed the antitumor efficacy of OTS964 in the presence of ABCG2 in cancer cells.

## MATERIALS AND METHODS

### Chemicals and Reagents

OTS964 was kindly provided as a gift by ChemieTek company (Indianapolis, IN). The chemical purity of OTS964 is >99.5% (HPLC at 214 and 254 nm). Fetal bovine serum was obtained from Atlanta Biologicals (Minneapolis, MN). Dulbecco's modified Eagle medium, antibiotics (penicillin/streptomycin), and trypsin-EDTA were purchased from Corning (Corning, NY). Topotecan was obtained from Selleckchem (Houston, TX). Ko143, G418, and cisplatin were purchased from Enzo Life Sciences (Farmingdale, NY). SN-38, and mitoxantrone were obtained from Medkoo Biosciences (Morrisville, NC). DMSO, MTT, and anti-BCRP antibody (BXP-21) were purchased from Millipore-Sigma (Burlington, MA). HRP-conjugated secondary antibody was obtained from Cell Signaling Technology (Dancers, MA). [ $^3\text{H}$ ]-Mitoxantrone (11  $\mu\text{Ci}/\text{mmol}$ ) was obtained from Moravék Biochemicals (Brea, CA). Anti-GAPDH antibody (GA1R), liquid scintillation cocktail, and all other reagents were obtained from Thermo Fisher Scientific (Waltham, MA).

### Cell Lines and Cell Culture

Mitoxantrone-selected MDR cell lines expressing ABCG2, NCI-H460/MX20 and S1-M1-80, were developed in medium with

mitoxantrone at 20 nM and 80  $\mu\text{M}$  concentrations, respectively. Their respective parental cell lines are non-small cell lung cancer cell line NCI-H460 and human colon carcinoma cell line S1. NCI-H460/MX20 cells were shown to overexpress wild-type ABCG2 protein (Robey et al., 2001; Henrich et al., 2006), while S1-M1-80 cells were shown to overexpress a mutant allele (R482G) in ABCG2 gene (Miyake et al., 1999; Honjo et al., 2001). HEK293/pcDNA3.1, HEK293/ABCG2-482-R2, HEK293/ABCG2-482-G2, and HEK293/ABCG2-482-T7 were transfected with either an empty vector pcDNA3.1 or a pcDNA3.1 vector containing a full length ABCG2 encoding arginine (R), glycine (G), or threonine (T) at position 482 (Robey et al., 2003). All transfected cell lines were selected with medium containing 2 mg/ml G418. All cells were cultured in complete medium at 37°C in a humidified incubator supplied with 5%  $\text{CO}_2$ . All MDR cells were cultured in drug-free complete medium for at least 3 weeks and passaged for at least three generations before further experimental use.

### Cell Viability Assay

As previously described (Jiang et al., 2019), an MTT assay was used to examine cell viability rate after treatment with OTS964 and other chemotherapeutic drugs. Briefly,  $5 \times 10^3$ – $7 \times 10^3$  cells/well were evenly seeded into a 96-well plate. The next day, serial concentrations of substrate-drugs were added to designated wells with or without 2 h pretreatment of OTS964 or known ABCG2 inhibitor at indicated concentrations. After a 72 h incubation period, an MTT solution was added following 3 h incubation at 37°C in the dark. The supernatant was discarded, and this was followed by the addition of DMSO to dissolve resulting formazan crystals. The absorbance was measured at 570 nm using an UV/Vis microplate spectrophotometer (Fisher Sci. Fair Lawn, NJ). The log scale curves in GraphPad (log inhibitor vs responses) were used to fit cell viability curves. Resistance fold (RF) was calculated by dividing the  $\text{IC}_{50}$  values for antineoplastic drugs of drug-sensitive cells without inhibitor by the  $\text{IC}_{50}$  values for chemotherapeutic drugs of drug-sensitive cells with inhibitor or drug-resistant cells with or without inhibitor.

### Western Blot Analysis

A Western blot was conducted to determine protein expression level by using an established protocol (Ji et al., 2018b). Briefly, following incubation with OTS964 at indicated concentrations for a serial time-course, lysates were collected and quantified by a BCA protein kit. Equal amounts of total protein (10–20  $\mu\text{g}$ ) were loaded and separated by SDS-PAGE, followed by transfer onto a PVDF membrane. After blocking with 5% non-fat milk for 2 h at room temperature, membrane was incubated overnight with primary antibodies at 4°C. The next day, after washing with TBST, the membrane was incubated with an HRP-conjugated secondary antibody for 2 h at room temperature. Subsequently, the chemiluminescence signal of protein-antibody complex was visualized by ECL substrate as per manufacturer's instructions. The relative density of each protein band was analyzed by Fiji software for Windows (NIH, Bethesda, MD).

## Accumulation Assay

Tritium-labeled mitoxantrone accumulation assay was performed to assess the transport function mediated by MDR-associated ABC transporters (Ji et al., 2018a). Each cell line was seeded evenly into a 24-well plate with a density of  $1 \times 10^6$  cells/well. The next day, cells were pretreated for 2 h with or without OTS964 or positive ABCG2 inhibitor at indicated concentrations. Thereafter, tritium-labeled substrate-drug was added to designated wells and incubated for 2 h. Followed by washing with ice-cold PBS, cells were harvested and transferred into scintillation fluid. A Packard TRI-CARB 1900 CA liquid scintillation analyzer (Packard Instrument, Downers Grove, IL) was used to measure radioactivity.

## ATPase Assay

The vanadate-sensitive ATPase activity of ABCG2 was measured, as previously described, based on the amount of inorganic phosphate ( $P_i$ ) produced from hydrolyzed ATP (Yang et al., 2020). The amount of  $P_i$  was quantified by a modified colorimetric method of Murphy and Riley (Ojida et al., 2004).

## Molecular Docking of OTS964 With Human ABCG2 Model

The OTS964 3D structure was constructed for docking simulation as previously described (Wang et al., 2020). Human ABCG2 6VXI (mitoxantrone-bound) (Orlando and Liao, 2020) were obtained from RCSB Protein Data Bank (PDB). The protein model is inward facing. Docking calculations were performed in AutoDock Vina (version 1.1.2) (Trott and Olson, 2010). Hydrogen atoms and partial charges were added using AutoDockTools (ADT, version 1.5.4). Docking grid center coordinates were determined from the bound ligands provided in PDB files. Receptor/ligand preparation and docking simulation were performed using default settings. The top-scoring pose (sorted by affinity score: kcal/mol) was selected for further analysis and visualization.

## Statistics

All data are presented as mean  $\pm$  SD. The  $p$  values were computed by one-way or two-way ANOVA following Tukey post hoc analysis, if appropriate. Data analysis and follow-up statistical evaluation were performed by GraphPad software for Windows (San Diego, CA). The *a priori* significance level was  $p < 0.05$ .

## RESULTS

### Antineoplastic efficacy of OTS964 was compromised by the presence of ABCG2.

An MTT assay was performed to examine the susceptibility of OTS964 to MDR mediated by ABCG2. Herein, RF value was used to evaluate the degree of increased resistance to OTS964 resulting from the presence of ABCG2 transporter. Based on **Figures 1C,D** the drug sensitivity of OTS964 was attenuated in S1-M1-80 and NCI-H460/MX20 cell lines by 4.16- and 3.64-fold, respectively, relative to their corresponding parental cell lines. Also, cells

transfected with wild-type (R482) or mutant (R482T or R482G) ABCG2 were used. This is because Robey et al. showed that variations at amino-acid 482 in the ABCG2 gene affect the substrate specificity of the protein, for example rhodamine 123 and daunorubicin are transported only by mutant ABCG2; also, mutant ABCG2 confers higher level of resistance to certain substrate-drug such as mitoxantrone compared to wild type (Robey et al., 2003). Our results showed that the effectiveness of OTS964 was limited by 6.39-, 18.41-, and 25.41-fold, respectively, in HEK293/ABCG2-482-R2, HEK293/ABCG2-482-G2, and HEK293/ABCG2-482-T7 cells, compared with counterparts in HEK293/pcDNA3.1 cells (**Figure 1E**). Notably, Ko143, a known ABCG2 inhibitor, had the ability to restore sensitivity of OTS964 in ABCG2-overexpressing cell lines (**Figures 1C–F**). Meanwhile, mitoxantrone served as a reference ABCG2 substrate. The RF values for S1-M1-80, NCI-H460/MX20, HEK293/ABCG2-482-R2, HEK293/ABCG2-482-G2, and HEK293/ABCG2-482-T7 cell lines were 19.57, 79.40, 5.03, 24.49 and 38.90, respectively (**Figures 1G–I**). Antineoplastic activity of mitoxantrone was sensitized by Ko143 in MDR cell lines mediated by ABCG2, as shown in **Figures 1G–J**. Considering different responses in wild-type (R482) and mutant (R482G and R482T) ABCG2, gene-transfected HEK293 cell lines were used for further studies. These results implicate that ABCG2 transporter could confer resistance to OTS964.

### OTS964 did not antagonize MDR mediated by ABCG2.

Some repurposed compounds behave as chemosensitizers or substrates based on different cellular settings caused by ABC transporters (Brózik et al., 2011; Beretta et al., 2017). Hence, an MTT assay was performed to examine the ability of OTS964 to restore drug sensitivity in cell lines with MDR mediated by ABCG2. To prevent overlapping impact due to the high cytotoxic nature of OTS964 in drug-sensitive cell lines, this study was conducted only on drug-resistant cell lines. According to the cell viability curves in **Figures 1C–E**, the maximum non-toxic concentration (the concentration at which cell viability rate was more than 80%) was 10 nM in MDR cell lines. In this section, the value of RF was used to assess the ability of OTS964 or known ABCG2 inhibitor to antagonize MDR mediated by ABCG2. **Table 1** summarized the  $IC_{50}$  and RF values of anticancer drugs with or without OTS964 or a known ABCG2 inhibitor Ko143 at non-toxic concentrations. Interestingly, in ABCG2-mediated MDR cells, OTS964 induced resistance to mitoxantrone in S1-M1-80 cell line, as evidenced by increased RF value for mitoxantrone from 19.57-fold to 57.63-fold relative to S1-M1-80 cells without an inhibitor. However, OTS964 at 10 nM did not significantly affect  $IC_{50}$  values for topotecan or SN-38 in S1-M1-80 cells relative to counterparts in S1-M1-80 cells without an inhibitor. Also, OTS964 showed an effect similar to mitoxantrone and SN-38 in ABCG2-transfected cell lines, but not to topotecan. In contrast, Ko143 as a positive ABCG2 inhibitor reversed substrate resistance. Notably, OTS964 and positive inhibitor did not affect cell viability of non-substrate drug cisplatin. These results demonstrated that OTS964 cannot restore

**TABLE 1 |** The effect of OTS964 on the anticancer efficacy of chemotherapeutic drugs in drug-selected and gene-transfected ABCG2-overexpressing cell lines.

Treatment	IC <sub>50</sub> <sup>a</sup> ± SD (μM) (RF <sup>b</sup> )					
	S1	S1-M1-80	HEK293/ pcDNA3.1	HEK293/ABCG2- 482-R2	HEK293/ABCG2- 482-G2	HEK293/ABCG2- 482-T7
Mitoxantrone	0.19 ± 0.13 (1.00)	3.75 ± 0.78 (19.57)*	0.02 ± 0.01 (1.00)	0.08 ± 0.02 (5.03)*	0.37 ± 0.03 (24.49)*	0.59 ± 0.14 (38.90)*
+OTS964 5 nM	-	11.79 ± 0.08 (61.47)*	-	0.09 ± 0.03 (6.10)*	0.51 ± 0.15 (34.11)*	0.77 ± 0.21 (50.81)*
+OTS964 10 nM	-	11.05 ± 0.41 (57.63)*	-	0.14 ± 0.01 (9.07)*	0.66 ± 0.09 (43.77)*	0.80 ± 0.13 (53.29)*
+Ko143 3 μM	0.20 ± 0.07 (1.05)	0.17 ± 0.10 (0.91)	0.02 ± 0.01 (1.20)	0.04 ± 0.01 (2.68)	0.06 ± 0.03 (3.72)	0.07 ± 0.01 (4.48)
Topotecan	0.04 ± 0.01 (1.00)	0.87 ± 0.29 (19.72)*	0.03 ± 0.02 (1.00)	0.19 ± 0.06 (6.05)*	1.21 ± 0.05 (38.44)*	1.85 ± 0.69 (58.74)*
+OTS964 5 nM	-	0.94 ± 0.28 (21.51)*	-	0.17 ± 0.04 (5.25)*	1.35 ± 0.07 (42.69)*	1.85 ± 0.49 (58.67)*
+OTS964 10 nM	-	0.97 ± 0.44 (22.18)*	-	0.19 ± 0.08 (6.01)*	1.23 ± 0.39 (38.85)*	1.95 ± 0.88 (61.87)*
+Ko143 3 μM	0.05 ± 0.01 (1.06)	0.09 ± 0.05 (2.08)	0.03 ± 0.01 (1.01)	0.04 ± 0.07 (1.32)	0.04 ± 0.04 (1.32)	0.05 ± 0.18 (1.72)
SN-38	0.09 ± 0.01 (1.00)	0.61 ± 0.04 (6.72)*	0.02 ± 0.01 (1.00)	0.43 ± 0.21 (20.08)*	0.12 ± 0.05 (5.74)*	0.71 ± 0.86 (32.80)*
+OTS964 5 nM	-	0.67 ± 0.15 (7.36)*	-	0.49 ± 0.26 (22.94)*	0.11 ± 0.01 (5.14)*	0.81 ± 0.42 (37.73)*
+OTS964 10 nM	-	0.69 ± 0.18 (7.59)*	-	0.53 ± 0.09 (24.38)*	0.25 ± 0.12 (11.76)*	1.19 ± 0.74 (55.25)*
+Ko143 3 μM	0.09 ± 0.01 (0.96)	0.14 ± 0.05 (1.53)	0.03 ± 0.01 (1.24)	0.05 ± 0.47 (2.36)	0.03 ± 0.48 (1.21)	0.05 ± 0.03 (2.47)
Cisplatin	1.08 ± 0.23 (1.00)	1.22 ± 0.29 (1.12)	0.61 ± 0.12 (1.00)	0.81 ± 0.21 (1.34)	0.47 ± 0.40 (0.77)	0.93 ± 0.03 (1.53)
+OTS964 5 nM	-	1.22 ± 0.15 (1.13)	-	0.73 ± 0.04 (1.21)	0.40 ± 0.20 (0.65)	1.00 ± 0.13 (1.64)
+OTS964 10 nM	-	1.39 ± 0.13 (1.28)	-	0.82 ± 0.21 (1.34)	0.43 ± 0.04 (0.70)	0.80 ± 0.07 (1.31)
+Ko143 3 μM	1.11 ± 0.02 (1.02)	1.48 ± 0.06 (1.37)	0.71 ± 0.18 (1.17)	0.79 ± 0.36 (1.30)	0.48 ± 0.14 (0.79)	0.72 ± 0.26 (1.18)

\*Indicated that the IC<sub>50</sub> values of chemotherapeutic drugs in drug-resistant cell line had significant statistical difference from the counterparts in corresponding sensitive cell line without inhibitor ( $p < 0.05$ ).

<sup>a</sup>IC<sub>50</sub> values were determined by modified MTT colorimetric assay, and are shown as mean ± SD.

<sup>b</sup>Resistance fold (RF) were calculated by the IC<sub>50</sub> values for chemotherapeutic drugs of drug-sensitive cells without inhibitor, divided by the IC<sub>50</sub> values for chemotherapeutic drugs of drug-sensitive cells with inhibitor or drug-resistant cells in the absence or presence of inhibitor.

drug efficacy in MDR cell lines, but may induce MDR mediated by ABCG2.

## OTS964 Upregulated ABCG2 Protein Expression Level.

It is possible that upregulation of MDR-associated ABC transporters is responsible for increased resistance and reduced efficacy. Hence, a Western blot analysis was conducted to determine the protein expression level. As shown in **Figures 2A–C**, no significant change in ABCG2 expression was observed in HEK293 cells transfected with wild-type or mutant (R482G and R482T) ABCG2, followed by treatment with OTS964 at 5 nM up to 72 h. However, OTS964 at 40 nM had the ability to increase ABCG2 expression level in cells expressing wide-type and R482G-mutant ABCG2 (**Figures 2A,B**). According to **Figure 2C**, OTS964 concentration-dependently enhanced R482T-mutant ABCG2 protein expression followed by 24 h treatment in cells expressing R482T-mutant ABCG2.

## OTS964 Inhibited Transport Function of ABCG2.

To further elucidate the possible interaction between ABC transporter and OTS964, transport function mediated by ABCG2 was analyzed by an accumulation assay. OTS964 at 3 μM significantly increased intracellular accumulation level of [<sup>3</sup>H]-mitoxantrone from 29.6% to 72.6% in HEK293/ABCG2-482-T7 cell line (**Figure 2D**); however, there was no significant difference in [<sup>3</sup>H]-mitoxantrone accumulation in HEK293/ABCG2-482-R2 and HEK293/ABCG2-

482-G2 cell lines relative to HEK293 cells transfected with an empty vector. Together, OTS964 at 3 μM could inhibit ABCG2-mediated efflux of mitoxantrone, which is an established substrate of ABCG2, in R482T-mutant-ABCG2-overexpressing cell line.

## OTS964 Stimulated ABCG2 ATPase.

To further evaluate interaction between OTS964 and MDR-associated ABC transporter, ABCG2-mediated ATP hydrolysis was measured in total membranes after incubation with serial concentrations of OTS964. OTS964 reached a maximum of 139.8% of basal activity for ABCG2 at 20 μM, and achieved 50% maximum stimulatory activity at 0.14 μM (**Figure 2E**). Hence, these results showed that OTS964 had a concentration-dependent stimulation of ATPase activity of ABCG2 transporter.

## Docking simulation of OTS964 in drug-binding pocket of human ABCG2.

According to ATPase results, OTS964 had a stimulatory effect due to its interaction at the drug-binding pocket. To assess this, we applied a docking simulation in the mitoxantrone-binding site of ABCG2 protein (6VXI). The results showed that OTS964 docked into ABCG2 substrate-binding site with an affinity score of -8.4 kcal/mol. Details of the ligand-receptor interaction are displayed in **Figure 3**. OTS964 is positioned and stabilized in a hydrophobic cavity formed by Phe431, Phe432, Phe439 (chain A), and Val442, Phe439, Phe432, Phe405 (chain B). Additionally, OTS964 was stabilized by *pi-pi* stacking interactions formed with Phe439 in both chains. The ionized amine group of OTS964 was stabilized

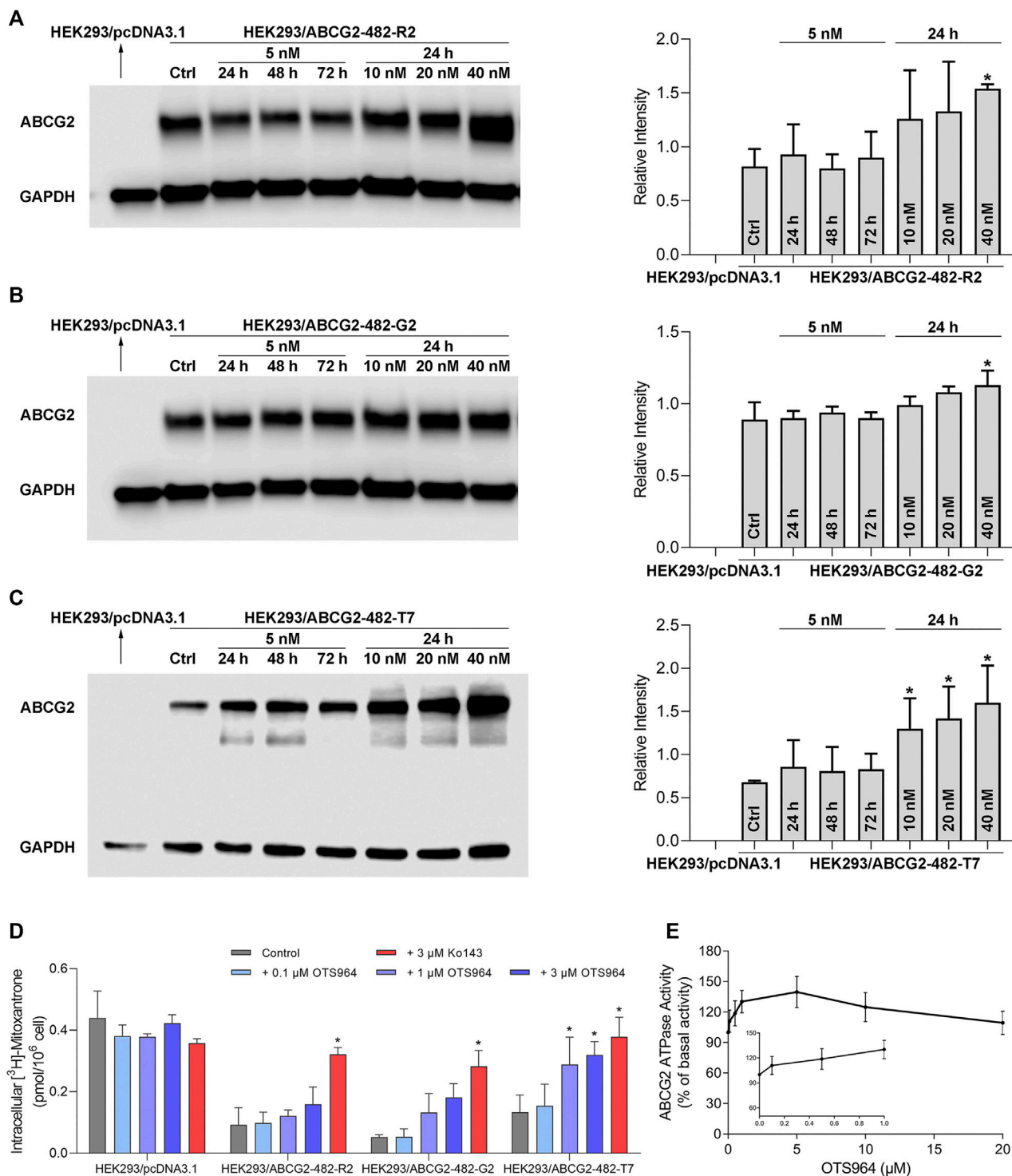
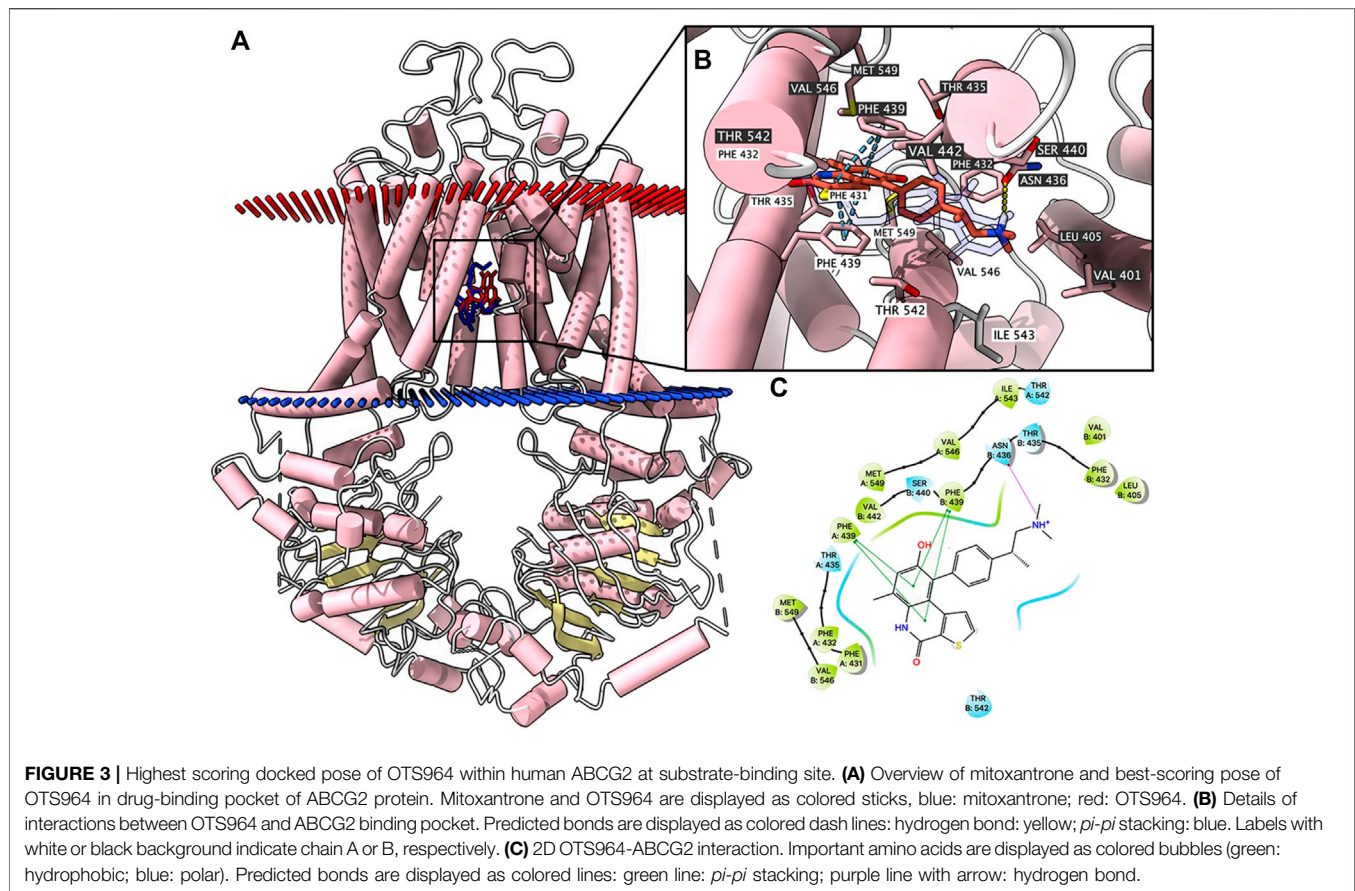


**FIGURE 2 |** OTS964 enhances ABCG2 protein expression in gene-transfected HEK293 cells expressing ABCG2. The protein expression of ABCG2 in (A) HEK293/ABCG2-482-R2, (B) HEK293/ABCG2-482-G2, (C) HEK293/ABCG2-482-T7 cells after treatment with 5 nM OTS964 up to 72 h or incubation for 24 h with OTS964 at 10 nM, 20 nM or 40 nM concentrations. OTS964 inhibits transport function of ABCG2 in gene-transfected HEK293 cell lines. (D) The tritium-labeled mitoxantrone accumulation in ABCG2-transfected HEK293 cells (HEK293/ABCG2-482-R2, HEK293/ABCG2-482-G2, and HEK293/ABCG2-482-T7) and their corresponding drug-sensitive cells HEK293/pcDNA3.1. Ko143 functioned as a known inhibitor for ABCG2. OTS964 concentration-dependently stimulates ATPase activity of ABCG2 within 20 μM. (E) The effect of OTS964 on ATPase activity of ABCG2 in insect cell membrane vesicles was determined as described in materials and methods section. All data are exhibited as mean ± SD. \**p* < 0.05 compared with control group.





by a hydrogen bond formed with Asn436. Similarly, the poses of docked OTS964 and mitoxantrone (docking score:  $-9.2$  kcal/mol) overlapped, indicating that OTS964 possibly shares a similar binding site with ABCG2 substrates.

## DISCUSSION

TOPK has emerged recently as a potential cancer-specific biomarker and a druggable therapeutic target (Herbert et al., 2018). Importantly, TOPK is highly expressed in multiple cancer types, while it is rarely detected in normal tissues except for some fetal tissues and germs cells; hence, TOPK inhibitors may impart minimal damage to normal tissues (Herbert et al., 2018; Hu et al., 2019). OTS964 is a highly potent TOPK inhibitor with tumor suppressive activity in lung cancer (Park et al., 2017) and ovarian cancer (Ikeda et al., 2016), and also serves as a template for synthesizing novel TOPK inhibitors (Hu et al., 2019). Hematologic toxicity, such as anemia and leukocytopenia, has been observed during OTS964 administration; this can be resolved by using a liposomal formulation (Matsuo et al., 2014; Gilabert-Oriol et al., 2019), which provides us with a clue that OTS964 may have off-target effects on indirect targets. In addition to having similar volumes of distribution as ABCG2, we postulated that the expression of ABCG2 might also influence the effectiveness of OTS964.

Our experiments with cell viability assay in drug-selected and gene-transfected cell lines indicated that OTS964 had high potency

with  $IC_{50}$  values at the nanomolar level, which is consistent with previous researches (Matsuo et al., 2014; Pirovano et al., 2017). Furthermore, ABCG2 overexpression could confer resistance to OTS964 in cancer cells. As NCI-H460 is a lung cancer cell line, and S1 is a colon cancer cell line, it might, to some extent, develop other mechanisms of drug resistance apart from overexpressing ABCG2. Therefore, cells transfected with ABCG2 were used, in which ABCG2 was a solo contributor to MDR. Importantly, OTS964 resistance was observed in ABCG2-transfected HEK293 cell lines. It is known that switching arginine to glycine ( $R > G$ ) or threonine ( $R > T$ ) at amino-acid 482 in ABCG2 gene may occur due to drug-induced mutation or genetic polymorphisms, which could cause substrate specificity and different resistance levels to substrate-drugs (Robey et al., 2003; Alqawi et al., 2004; Ejendal et al., 2006). Mitoxantrone is found to be a substrate drug of all ABCG2 variations; however, rhodamine 123, doxorubicin, and daunorubicin are transported by only mutant R482T or R482G but not by the wild-type R482 ABCG2 (Honjo et al., 2001; Robey et al., 2003). Also, compared with wild-type ABCG2, an R482G mutation confers relatively less resistance to SN-38 and topotecan (Honjo et al., 2001). Our results showed that ABCG2 variation at position 482 had some effect on OTS964 resistance. The RF values were higher in cells expressing R482G- and R482T-mutant ABCG2 relative to wild-type ABCG2. Thus, mutant ABCG2 (R482G or R482T) may confer higher level of resistance to OTS964 among all ABCG2 proteins. Together, we hypothesized that the efficacy of

OTS964 could be compromised at the presence of ABCG2. Also, OTS964 induced resistance could be sensitized by an ABCG2 reference inhibitor, suggesting that ABCG2-overexpression is the mechanism of OTS964 resistance.

It is documented that some substrates of ABC transporters (Dai et al., 2008; Eadie et al., 2014), such as lapatinib, imatinib, nilotinib, and dasatinib, can compete with another drug substrate for transport function (Wu et al., 2020); as a result, a repurposed drug substrate has the ability to sensitize MDR-associated ABC transporters to another drug substrate. Considering the cytotoxic nature of OTS964, high concentrations (1 or 3  $\mu\text{M}$ ) used in accumulation assay would be too toxic and not usable clinically. Hence, antagonizing activity of OTS964 at non-toxic concentrations was evaluated only in MDR cell lines to avoid additive toxicity. In repositioning studies, our results indicated that rather than antagonizing MDR, OTS964 may enhance ABCG2-mediated MDR as evidenced by increasing  $\text{IC}_{50}$  values for many antineoplastic drugs after co-treatment with OTS964 at non-toxic concentrations (5 or 10 nM). We postulated that the absence of antagonizing effect on substrate-drug sensitivity might be the result of highly potent nature of OTS964 and high resistance level conferred by ABCG2. Of note, co-treatment with OTS964 did not affect drug sensitivity of cisplatin, which is a non-substrate drug for ABCG2, indicating that failure of sensitizing MDR cell lines to substrate-drugs may be specific to ABCG2. However, these findings do not warrant further testing of OTS964 as a reversal agent.

As different responses to OTS964 were found among ABCG2 variations above, gene-transfected HEK293 cell lines were used for mechanism-based studies. In some cases, upregulating the protein expression of ABCG2 promotes resistance and attenuates efficacy (Wu et al., 2020). Therefore, an immunoblotting analysis was performed to evaluate protein expression after OTS964 treatment. Attempts to circumvent the overlapping effect from additive cytotoxicity and to reduce the extent of off-target activity, cells were treated with a low concentration for a long time or with high concentrations for a short time, separately. At low concentration (5 nM), assuming negligible cytotoxicity, cell viability was more than 80% in MDR cell lines; by contrast, the highest concentration (40 nM) approached  $\text{IC}_{50}$  value in ABCG2-transfected cell lines. As a result, ABCG2 expression was not significantly changed after treatment with OTS964 at 5 nM up to 72 h. However, after 24 h incubation with OTS964 at 40 nM, higher expression level of ABCG2 was observed in MDR cell lines expressing ABCG2. Together, these may, at least in part, be the reason for the limited effectiveness of OTS964 and enhanced ABCG2-mediated MDR.

Tritium-labeled substrate accumulation was performed to investigate the effect of OTS964 on transport function conferred by ABCG2. Our results showed that OTS964 at high concentration (3  $\mu\text{M}$ ) could increase substrate-drug accumulation in MDR cell line (R482T-mutant-ABCG2 overexpression cells), but not in their corresponding parental cell lines. This effect might result from a high concentration of OTS964 competitively inhibiting the efflux of mitoxantrone while impeding the transport function of ABCG2, and in turn increasing intracellular substrate accumulation. The accumulation study was carried out with a short-term treatment (4 h), which protected cells from influence of cell viability and other cellular functions, although concentrations of OTS964 used for these experiments were higher than  $\text{IC}_{50}$  value.

ATP hydrolysis is an energy requirement for transport of substrate-drugs against concentration gradient by ABCG2 (Glavinas et al., 2008). Hence, an ATPase assay was conducted to assess effect of OTS964 on ABCG2 ATPase activity. Our results demonstrated that OTS964 concentration-dependently stimulates the ATPase activity of ABCG2. Subsequently, the *in silico* molecular docking was conducted to explore the interaction of OTS964 with ABCG2. The molecular docking was performed using atomic structures of mitoxantrone-bound ABCG2 (pdb.6VXI). The docking results showed that OTS964 shares similar binding sites with known substrates for ABCG2. Molecular docking combined with ATPase data suggested that OTS964 interacts with drug-binding pocket of ABCG2 and behaves as a substrate for ABCG2 transporter.

## CONCLUSION

OTS964 is susceptible to ABCG2-mediated drug resistance, and this effect can be antagonized by known ABCG2 inhibitor. ABCG2-conferred resistance to OTS964 can be explained by its stimulatory effect on ATPase activity and upregulated protein expression of ABCG2. Additionally, OTS964 at a high concentration inhibits transport function mediated by ABCG2; however, OTS964 at a low concentration promotes ABCG2-mediated MDR rather than antagonizing drug resistance. These findings may serve as a valuable foundation for follow-up clinical investigation on potential use of OTS964.

## DATA AVAILABILITY STATEMENT

The original contributions presented in the study are included in the article/Supplementary Material, further inquiries can be directed to the corresponding authors.

## AUTHOR CONTRIBUTIONS

Conceptualization: YY, DY, and ZC. Methodology: YY, ZW, QT, and JW. Resources: ZL, SL, and SA. Writing-Original Draft: YY. Writing-review and copyediting: YY, DY, SL, SA, and ZC. Supervision: DY and ZC.

## FUNDING

SL and SA were supported by Intramural Research Program of National Institutes of Health, National Cancer Institute, Center for Cancer Research. The research was partially supported by the Department of Pharmaceutical Sciences, St. John's University.

## ACKNOWLEDGMENTS

Authors are grateful to Susan E. Bates and Robert W. Robey (NCI, NIH, Bethesda, MD) for kindly providing cell lines.

## REFERENCES

- Alqawi, O., Bates, S., and Georges, E. (2004). Arginine482 to threonine mutation in the breast cancer resistance protein ABCG2 inhibits rhodamine 123 transport while increasing binding. *Biochem. J.* 382 (Pt 2), 711–716. doi:10.1042/bj20040355
- Bellay, I. H., Marklein, R. A., Lo Surdo, J. L., Bauer, S. R., and Puri, R. K. (2016). Identification of predictive gene markers for multipotent stromal cell proliferation. *Stem Cells Dev.* 25 (11), 861–873. doi:10.1089/scd.2015.0374
- Beretta, G. L., Cassinelli, G., Pennati, M., Zuco, V., and Gatti, L. (2017). Overcoming ABC transporter-mediated multidrug resistance: the dual role of tyrosine kinase inhibitors as multitargeting agents. *Eur. J. Med. Chem.* 142, 271–289. doi:10.1016/j.ejmech.2017.07.062
- Brózik, A., Hegedüs, C., Erdei, Z., Hegedus, T., Özvegy-Laczka, C., Szakács, G., et al. (2011). Tyrosine kinase inhibitors as modulators of ATP binding cassette multidrug transporters: substrates, chemosensitizers or inducers of acquired multidrug resistance? *Expet Opin. Drug Metab. Toxicol.* 7 (5), 623–642. doi:10.1517/17425255.2011.562892
- Dai, C. L., Tiwari, A. K., Wu, C. P., Su, X. D., Wang, S. R., Liu, D. G., et al. (2008). Lapatinib (Tykerb, GW572016) reverses multidrug resistance in cancer cells by inhibiting the activity of ATP-binding cassette subfamily B member 1 and G member 2. *Cancer Res.* 68 (19), 7905–7914. doi:10.1158/0008-5472.Can-08-0499
- Eadie, L. N., Hughes, T. P., and White, D. L. (2014). Interaction of the efflux transporters ABCB1 and ABCG2 with imatinib, nilotinib, and dasatinib. *Clin. Pharmacol. Ther.* 95(3), 294–306. doi:10.1038/clpt.2013.208
- Ejendal, K. F., Diop, N. K., Schweiger, L. C., and Hrycyna, C. A. (2006). The nature of amino acid 482 of human ABCG2 affects substrate transport and ATP hydrolysis but not substrate binding. *Protein Sci.* 15 (7), 1597–1607. doi:10.1110/ps.051998406
- Gao, T., Hu, Q., Hu, X., Lei, Q., Feng, Z., Yu, X., et al. (2019). Novel selective TOPK inhibitor SKLB-C05 inhibits colorectal carcinoma growth and metastasis. *Cancer Lett.* 445, 11–23. doi:10.1016/j.canlet.2018.12.016
- Gilbert-Oriol, R., Sutherland, B. W., Anantha, M., Pallaoro, A., and Bally, M. B. (2019). Liposomal OTS964, a TOPK inhibitor: a simple method to estimate OTS964 association with liposomes that relies on enhanced OTS964 fluorescence when bound to albumin. *Drug Deliv. Transl. Res.* 9 (6), 1082–1094. doi:10.1007/s13346-019-00651-0
- Glavinas, H., Méhn, D., Jani, M., Oosterhuis, B., Herédi-Szabó, K., and Krajcsi, P. (2008). Utilization of membrane vesicle preparations to study drug-ABC transporter interactions. *Expet Opin. Drug Metab. Toxicol.* 4 (6), 721–732. doi:10.1517/17425255.4.6.721
- Hansel, D. E., Nakayama, M., Luo, J., Abukhdeir, A. M., Park, B. H., Bieberich, C. J., et al. (2009). Shared TP53 gene mutation in morphologically and phenotypically distinct concurrent primary small cell neuroendocrine carcinoma and adenocarcinoma of the prostate. *Prostate* 69 (6), 603–609. doi:10.1002/pros.20910
- Hayashi, T., Hayakawa, Y., Koh, M., Tomita, T., Nagai, S., Kashiwazaki, D., et al. (2018). Impact of a novel biomarker, T-LAK cell-originating protein kinase (TOPK) expression on outcome in malignant glioma. *Neuropathology* 38 (2), 144–153. doi:10.1111/neup.12446
- Henrich, C. J., Bokesch, H. R., Dean, M., Bates, S. E., Robey, R. W., Goncharova, E. I., et al. (2006). A high-throughput cell-based assay for inhibitors of ABCG2 activity. *J. Biomol. Screen* 11 (2), 176–183. doi:10.1177/1087057105284576
- Herbert, K. J., Ashton, T. M., Prevo, R., Pirovano, G., and Higgins, G. S. (2018). T-LAK cell-originated protein kinase (TOPK): an emerging target for cancer-specific therapeutics. *Cell Death Dis.* 9 (11), 1089. doi:10.1038/s41419-018-1131-7
- Holohan, C., Van Schaeybroeck, S., Longley, D. B., and Johnston, P. G. (2013). Cancer drug resistance: an evolving paradigm. *Nat. Rev. Cancer* 13 (10), 714–726. doi:10.1038/nrc3599
- Honjo, Y., Hrycyna, C. A., Yan, Q. W., Medina-Pérez, W. Y., Robey, R. W., van de Laar, A., et al. (2001). Acquired mutations in the MXR/BCRP/ABCP gene alter substrate specificity in MXR/BCRP/ABCP-overexpressing cells. *Cancer Res.* 61 (18), 6635–6639.
- Hu, Q. F., Gao, T. T., Shi, Y. J., Lei, Q., Liu, Z. H., Feng, Q., et al. (2019). Design, synthesis and biological evaluation of novel 1-phenyl phenanthridin-6(5H)-one derivatives as anti-tumor agents targeting TOPK. *Eur. J. Med. Chem.* 162, 407–422. doi:10.1016/j.ejmech.2018.11.007
- Ikeda, Y., Park, J. H., Miyamoto, T., Takamatsu, N., Kato, T., Iwasa, A., et al. (2016). T-LAK cell-originated protein kinase (TOPK) as a prognostic factor and a potential therapeutic target in ovarian cancer. *Clin. Cancer Res.* 22 (24), 6110–6117. doi:10.1158/1078-0432.Ccr-16-0207
- Ji, N., Yang, Y., Cai, C. Y., Lei, Z. N., Wang, J. Q., Gupta, P., et al. (2018a). VS-4718 antagonizes multidrug resistance in ABCB1- and ABCG2-overexpressing cancer cells by inhibiting the efflux function of ABC transporters. *Front. Pharmacol.* 9, 1236. doi:10.3389/fphar.2018.01236
- Ji, N., Yang, Y., Lei, Z. N., Cai, C. Y., Wang, J. Q., Gupta, P., et al. (2018b). Ulixertinib (BVD-523) antagonizes ABCB1- and ABCG2-mediated chemotherapeutic drug resistance. *Biochem. Pharmacol.* 158, 274–285. doi:10.1016/j.bcp.2018.10.028
- Jiang, Y., Zhang, J., Zhao, J., Li, Z., Chen, H., Qiao, Y., et al. (2019). TOPK promotes metastasis of esophageal squamous cell carcinoma by activating the Src/GSK3 $\beta$ /STAT3 signaling pathway via  $\gamma$ -catenin. *BMC Cancer* 19 (1), 1264. doi:10.1186/s12885-019-6453-z
- Joel, M., Mughal, A. A., Grieg, Z., Murrell, W., Palmero, S., Mikkelsen, B., et al. (2015). Targeting PBK/TOPK decreases growth and survival of glioma initiating cells *in vitro* and attenuates tumor growth *in vivo*. *Mol. Cancer* 14, 121. doi:10.1186/s12943-015-0398-x
- Klappe, K., Hummel, I., Hoekstra, D., and Kok, J. W. (2009). Lipid dependence of ABC transporter localization and function. *Chem. Phys. Lipids* 161 (2), 57–64. doi:10.1016/j.chemphyslip.2009.07.004
- Manolaridis, I., Jackson, S. M., Taylor, N. M. I., Kowal, J., Stahlberg, H., and Locher, K. P. (2018). Cryo-EM structures of a human ABCG2 mutant trapped in ATP-bound and substrate-bound states. *Nature* 563 (7731), 426–430. doi:10.1038/s41586-018-0680-3
- Matsuo, Y., Park, J. H., Miyamoto, T., Yamamoto, S., Hisada, S., Alachkar, H., et al. (2014). TOPK inhibitor induces complete tumor regression in xenograft models of human cancer through inhibition of cytokinesis. *Sci. Transl. Med.* 6 (259), 259ra145. doi:10.1126/scitranslmed.3010277
- Miyake, K., Mickley, L., Litman, T., Zhan, Z., Robey, R., Cristensen, B., et al. (1999). Molecular cloning of cDNAs which are highly overexpressed in mitoxantrone-resistant cells: demonstration of homology to ABC transport genes. *Cancer Res.* 59 (1), 8–13.
- Ojida, A., Mito-oka, Y., Sada, K., and Hamachi, I. (2004). Molecular recognition and fluorescence sensing of monophosphorylated peptides in aqueous solution by bis(zinc(II)-dipicolylamine)-based artificial receptors. *J. Am. Chem. Soc.* 126 (8), 2454–2463. doi:10.1021/ja038277x
- Orlando, B. J., and Liao, M. (2020). ABCG2 transports anticancer drugs *via* a closed-to-open switch. *Nat. Commun.* 11 (1), 2264. doi:10.1038/s41467-020-16155-2
- Park, J. H., Inoue, H., Kato, T., Zewde, M., Miyamoto, T., Matsuo, Y., et al. (2017). TOPK (T-LAK cell-originated protein kinase) inhibitor exhibits growth suppressive effect on small cell lung cancer. *Cancer Sci.* 108 (3), 488–496. doi:10.1111/cas.13160
- Pirovano, G., Ashton, T. M., Herbert, K. J., Bryant, R. J., Verrill, C. L., Cerundolo, L., et al. (2017). TOPK modulates tumour-specific radiosensitivity and correlates with recurrence after prostate radiotherapy. *Br. J. Cancer* 117(4), 503–512. doi:10.1038/bjc.2017.197
- Pirovano, G., Roberts, S., Brand, C., Donabedian, P. L., Mason, C., de Souza, P. D., et al. (2019). [18F]FE-OTS964: a small molecule targeting TOPK for *in vivo* PET imaging in a glioblastoma xenograft model. *Mol. Imag. Biol.* 21 (4), 705–712. doi:10.1007/s11307-018-1288-6
- Pirovano, G., Roberts, S., and Reiner, T. (2020). TOPKi-NBD: a fluorescent small molecule for tumor imaging. *Eur. J. Nucl. Med. Mol. Imaging.* 47 (4), 1003–1010. doi:10.1007/s00259-019-04608-w
- Robey, R. W., Honjo, Y., Morisaki, K., Nadjem, T. A., Runge, S., Risbood, M., et al. (2003). Mutations at amino-acid 482 in the ABCG2 gene affect substrate and antagonist specificity. *Br. J. Cancer* 89 (10), 1971–1978. doi:10.1038/sj.bjc.6601370
- Robey, R. W., Honjo, Y., van de Laar, A., Miyake, K., Regis, J. T., Litman, T., et al. (2001). A functional assay for detection of the mitoxantrone resistance protein, MXR (ABCG2). *Biochim. Biophys. Acta* 1512 (2), 171–182. doi:10.1016/s0005-2736(01)00308-x

- Shih, M. C., Chen, J. Y., Wu, Y. C., Jan, Y. H., Yang, B. M., Lu, P. J., et al. (2012). TOPK/PBK promotes cell migration *via* modulation of the PI3K/PTEN/AKT pathway and is associated with poor prognosis in lung cancer. *Oncogene* 31 (19), 2389–2400. doi:10.1038/onc.2011.419
- Szakács, G., Váradi, A., Ozvegy-Laczka, C., and Sarkadi, B. (2008). The role of ABC transporters in drug absorption, distribution, metabolism, excretion and toxicity (ADME-Tox). *Drug Discov. Today* 13 (9-10), 379–393. doi:10.1016/j.drudis.2007.12.010
- Theodoulou, F. L., and Kerr, I. D. (2015). ABC transporter research: going strong 40 years on. *Biochem. Soc. Trans.* 43 (5), 1033–1040. doi:10.1042/bst20150139
- Trott, O., and Olson, A. J. (2010). AutoDock Vina: improving the speed and accuracy of docking with a new scoring function, efficient optimization, and multithreading. *J. Comput. Chem.* 31 (2), 455–461. doi:10.1002/jcc.21334
- Vagiannis, D., Novotna, E., Skarka, A., Kammerer, S., Küpper, J. H., Chen, S., et al. (2020). Ensartinib (X-396) effectively modulates pharmacokinetic resistance mediated by ABCB1 and ABCG2 drug efflux transporters and CYP3A4 biotransformation enzyme. *Cancers* 12 (4). doi:10.3390/cancers12040813
- Wang, J. Q., Li, J. Y., Teng, Q. X., Lei, Z. N., Ji, N., Cui, Q., et al. (2020). Venetoclax, a BCL-2 inhibitor, enhances the efficacy of chemotherapeutic agents in wild-type ABCG2-overexpression-mediated MDR cancer cells. *Cancers* 12 (2). doi:10.3390/cancers12020466
- Wu, Z. X., Yang, Y., Teng, Q. X., Wang, J. Q., Lei, Z. N., Wang, J. Q., et al. (2020). Tivantinib, A c-met inhibitor in clinical trials, is susceptible to ABCG2-mediated drug resistance. *Cancers* 12 (1). doi:10.3390/cancers12010186
- Yang, Y., Ji, N., Teng, Q. X., Cai, C. Y., Wang, J. Q., Wu, Z. X., et al. (2020). Sitravatinib, a tyrosine kinase inhibitor, inhibits the transport function of ABCG2 and restores sensitivity to chemotherapy-resistant cancer cells *in vitro*. *Front Oncol.* 10, 700. doi:10.3389/fonc.2020.00700
- Zhu, F., Zykova, T. A., Kang, B. S., Wang, Z., Ebeling, M. C., Abe, Y., et al. (2007). Bidirectional signals transduced by TOPK-ERK interaction increase tumorigenesis of HCT116 colorectal cancer cells. *Gastroenterology* 133 (1), 219–231. doi:10.1053/j.gastro.2007.04.048

**Conflict of Interest:** The authors declare that the research was conducted in the absence of any commercial or financial relationships that could be construed as a potential conflict of interest.

Copyright © 2021 Yang, Wu, Wang, Teng, Lei, Lusvardi, Ambudkar, Chen and Yang. This is an open-access article distributed under the terms of the Creative Commons Attribution License (CC BY). The use, distribution or reproduction in other forums is permitted, provided the original author(s) and the copyright owner(s) are credited and that the original publication in this journal is cited, in accordance with accepted academic practice. No use, distribution or reproduction is permitted which does not comply with these terms.





# Mutational Pattern in Multiple Pulmonary Nodules Are Associated With Early Stage Lung Adenocarcinoma

## OPEN ACCESS

### Edited by:

Haichang Li,  
The Ohio State University,  
United States

### Reviewed by:

Feng Wang,  
Affiliated Hospital of Nantong  
University, China  
Hsian-Rong Tseng,  
University of California, Los Angeles,  
United States

### \*Correspondence:

Chang Zou  
zou.chang@szhospital.com  
Guang-suo Wang  
wgsuwy01@163.com  
Chen Qiu  
szcheater@163.com

<sup>†</sup>These authors have contributed  
equally to this work

### Specialty section:

This article was submitted to  
Pharmacology of Anti-Cancer Drugs,  
a section of the journal  
Frontiers in Oncology

**Received:** 07 September 2020

**Accepted:** 08 December 2020

**Published:** 19 February 2021

### Citation:

Dong S-w, Li R, Cheng Z, Liu D-c,  
Xia J, Xu J, Li S, Wang J, Yue Y, Fan Y,  
Cao Y, Dai L, Wang J, Zhao P,  
Wang X, Xiao Z, Qiu C, Wang G-s and  
Zou C (2021) Mutational Pattern in  
Multiple Pulmonary Nodules Are  
Associated With Early Stage Lung  
Adenocarcinoma.  
Front. Oncol. 10:571521.  
doi: 10.3389/fonc.2020.571521

Shao-wei Dong<sup>1,2†</sup>, Rong Li<sup>3†</sup>, Zhiqiang Cheng<sup>4†</sup>, Dong-cheng Liu<sup>1</sup>, Jinquan Xia<sup>1</sup>,  
Jing Xu<sup>4</sup>, Shixuan Li<sup>5</sup>, Jian Wang<sup>5</sup>, Yongjian Yue<sup>6</sup>, Yingrui Fan<sup>3</sup>, Yundi Cao<sup>3</sup>,  
Lingyun Dai<sup>7</sup>, Jigang Wang<sup>7</sup>, Pan Zhao<sup>1</sup>, Xin Wang<sup>8</sup>, Zhangang Xiao<sup>9</sup>, Chen Qiu<sup>6\*</sup>,  
Guang-suo Wang<sup>5\*</sup> and Chang Zou<sup>1,2\*</sup>

<sup>1</sup> Clinical Medical Research Centre, The First Affiliated Hospital, Southern University of Science and Technology, Shenzhen People's Hospital, Shenzhen, China, <sup>2</sup> Shenzhen Public Service Platform on Tumor Precision Medicine and Molecular Diagnosis, Shenzhen, China, <sup>3</sup> Department of Oncology, Taikang Xianlin Drum Tower Hospital, Nanjing University School of Medicine, Nanjing, China, <sup>4</sup> Department of Pathology, The First Affiliated Hospital, Southern University of Science and Technology, Shenzhen People's Hospital, Shenzhen, China, <sup>5</sup> Department of Thoracic Surgery, The First Affiliated Hospital, Southern University of Science and Technology, Shenzhen People's Hospital, Shenzhen, China, <sup>6</sup> Department of Respiratory and Critical Medicine, Shenzhen People's Hospital, Second Clinical Medical College of Jinan University, Shenzhen, China, <sup>7</sup> Department of Geriatrics, The First Affiliated Hospital, Southern University of Science and Technology, Shenzhen People's Hospital, Shenzhen, China, <sup>8</sup> Department of Biomedical Sciences, City University of Hong Kong, Hong Kong, Hong Kong, <sup>9</sup> Key Laboratory of Medical Electrophysiology of Ministry of Education, School of Pharmacy, Southwestern Medical University, Luzhou, China

The clinical significance of mutation in multiple pulmonary nodules is largely limited by single gene mutation-directed analysis and lack of validation of gene expression profiles. New analytic strategy is urgently needed for comprehensive understanding of genomic data in multiple pulmonary nodules. In this study, we performed whole exome sequencing in 16 multiple lung nodules and 5 adjacent normal tissues from 4 patients with multiple pulmonary nodules and decoded the mutation information from a perspective of cellular functions and signaling pathways. Mutated genes as well as mutation patterns shared in more than two lesions were identified and characterized. We found that the number of mutations or mutated genes and the extent of protein structural changes caused by different mutations is positively correlated with the degree of malignancy. Moreover, the mutated genes in the nodules are associated with the molecular functions or signaling pathways related to cell proliferation and survival. We showed a developing pattern of quantity (the number of mutations/mutated genes) and quality (the extent of protein structural changes) in multiple pulmonary nodules. The mutation and mutated genes in multiple pulmonary nodules are associated with cell proliferation and survival related signaling pathways. This study provides a new perspective for comprehension of genomic mutational data and might shed new light on deciphering molecular evolution of early stage lung adenocarcinoma.

**Keywords:** pulmonary nodules, whole-exome sequencing, mutation, functional analysis, pathway analysis

## INTRODUCTION

Lung adenocarcinoma (LUAD) is the most frequent subtype of lung cancer. Even with regularly performed and thorough radiological and cytological screening in high risk populations, LUAD is usually diagnosed in its middle and late stage (1). Novel therapeutic strategies have been under active research and development to conquer LUAD, but the survival rate of patients has unfortunately kept at a low level (1). The emerging of improved cancer screening methods such as liquid biopsy holds great promise for reversing this serious situation since most of solid tumors are curable in the early stage (2). Unfortunately, this strategy is still limited by the incomplete understandings of the complicated molecular mechanisms of cancer origination and malignant progression as well as intra-tumoral heterogeneity.

Multiple pulmonary nodules (MPNs) contribute to the majority of newly diagnosed LUAD (3). Pathologically, the malignant evolution of early stage LUAD comprises four contiguous steps: atypical adenomatous hyperplasia (AAH), *in situ* pulmonary adenocarcinoma (AIS, also named as bronchioloalveolar carcinoma, BAC), minimally invasive adenocarcinoma (MIA), and invasive adenocarcinoma (IA), all of which could be well exemplified in some patients with MPNs (4). It is well characterized that AAH represents the pre-cancerous lesion of LUAD and AIS is the localized adenocarcinoma without any invasion. MIA and IA are differentiated by the tumor size. MIA is defined as single or multiple invasive neoplasia less than 5 mm and restrained in stage of IA, while IA represents invasive tumor larger than 5 mm (5).

In view of different pathological grades and clinical stages of individual adenoma loci in the same genetic background, MPNs represent an ideal model for biological characterization of molecular evolution of the early stage LUAD. A number of efforts have been made in depicting the molecular diagram of MPNs by using genome-based approaches, e.g., whole genome sequencing, whole exome sequencing (WES) and methylation analysis (6–9). However, the theoretical and clinical significance of these reported mutations are largely limited by the lack of paired validation studies due to the rarity of malignant cells as well as the paucity of neoplasia in MPNs samples (10). In addition, since the origination and malignant progression of solid tumors is a multifaced and multiple-step orchestration, these findings, mostly based on single gene change-directed analysis, needs to be carefully interpreted and reevaluated especially for clinical application.

To better understand the molecular evolution of MPNs, we performed WES in 21 tissues dissected from 4 patients with MPNs and analyzed the somatic mutations using a cell function and pathway converging-directed strategy. Mutated genes e.g., KTM2C and EGFR, and patterns of these mutations were successfully identified and characterized. No ubiquitous mutated genes or mutation loci were discovered in all malignancy or all patients. Interestingly, more mutated genes were found in IA samples than in MIA samples. KEGG (Kyoto Encyclopedia of Genes and Genomes, [www.genome.jp](http://www.genome.jp)) and GO

(Gene Ontology, [www.geneontology.org](http://www.geneontology.org)) analysis indicates that mutated genes tend to converge into cell proliferation and survival related signaling pathways in malignancy in comparison with adjacent normal samples. This converging tendency seems to be more obvious in IA than in MIA. Moreover, the levels of protein structural changes caused by different mutations as well as that of converged signaling pathways are higher in IA than in MIA. The levels of protein structural changes and converged signaling pathways are also higher in all malignant lesions than in adjacent normal tissues, indicating these protein molecules and pathways may be responsible for the malignant evolution of LUAD. Some specific driver genes in cancer development such as EGFR, mutations of this gene are found both in cancer lesions and adjacent normal samples, despite of more severe extent of mutations in malignancy, suggesting driver gene mutations need to be further validated particularly for clinical application. Besides, in comparison with The Cancer Genome Atlas database (TCGA), most of the mutated genes in MIA and IA identified in this study are genes functionally related to the development of lung cancers. Our findings, by function-directed analysis of WES data from MPNs, that a group of functionally converged mutations rather than a single driver gene mutation might be the triggering onset of the origination and malignant progression of lung adenocarcinoma. This study will provide new insights and new strategies to decipher the early development of lung cancer.

## MATERIALS AND METHODS

### Patients and Clinical Information

Tumor samples and their matched normal tissues were obtained from four patients from Shenzhen people's hospital from 2017 to 2019. The clinical information such as age/gender/smoking history was listed in **Supplementary Table 1**. These patients did not receive preoperative chemotherapy or radiotherapy before surgery. Tumor sizes ranged from 0.2 to 3.0 cm according to pathology reports. All patients were free of extra thoracic metastasis. Three of the patients were non-smokers, and one patient had a history of cigarette smoking. The images of CT and hematoxylin-eosin staining were reviewed by experienced pathologists to determine the histopathological subtype and were shown in **Supplementary Figure S1**. The present study was approved by the Ethics Committee of Shenzhen people's hospital. All study procedures were performed according to the Declaration of Helsinki ethical principles. Informed consents were obtained from the patients.

### Sample Preparation

Genomic DNA from formalin-fixed paraffin-embedded (FFPE) samples was extracted using QIAamp DNA FFPE Tissue Kit (Qiagen, Valencia, CA). DNA from fresh tumor tissue and blood was extracted by DNAeasy Blood and Tissue kit (Qiagen, Valencia, CA). Genomic DNA was fragmented into ~250 bp by M220 Focused-ultrasonicator (Covaris, Inc. Woburn, MA)

followed by whole genome library preparation using KAPA Hyper Prep Kit (KAPA Biosystems, Wilmington, MA). Exome capture was performed using the SureSelect Human All Exon V6 panel (Agilent Technologies, Santa Clara, CA).

## Whole Exome Sequencing (WES)

WES was performed by Geneseeq Technology Inc. (Nanjing, China) using an Illumina HiSeq4000 system. The adapters in FASTQ files were cleaned using Trimmomatic-0.36 (11). The alignment was performed using Burrows-Wheeler Aligner (12), and GRCh37 (hg19) downloaded from Ensembl website was used as reference. The exome mutations in pulmonary nodules and para-cancer (PAR) samples were compared with mutations obtained from peripheral blood mononuclear cells (PBMCs), and only somatic specific mutations were retained for further analysis.

## Converging Analysis

Converging index is defined as follows: 1) take any given two samples S1 and S2 with mutated genes from some pathways, KEGG for example 2) the numbers of mutated pathways (pathways with mutated genes) were calculated as P1 and P2; 3) the number of overlapped mutated pathways between two samples (mutated pathways occurred in both samples) is counted as P; and 4) the converging index is calculated as  $(P/P1) \times (P/P2)$ . The converging index in GO biological pathways and GO molecular functions is calculated using the same method.

The ranking of converged pathways/functions was guided by the probability of Poisson distribution, which is calculated using the number of mutations involved in certain pathways in PAR and IA samples. The Poisson distribution is performed in R 3.6.3 using `ppois()` function. The KEGG pathway information of human proteome was downloaded from the KEGG website ([www.genome.jp](http://www.genome.jp)) and the human GO biological pathway and molecular function information were retrieved from the Uniprot website ([www.uniprot.org](http://www.uniprot.org)).

## EGFR Protein Structural Analysis

EGFR protein structure was retrieved from the Protein Data Bank ([www.rcsb.org](http://www.rcsb.org)) using entry 1M17. The protein structures and mutated residues were illustrated by Pymol software (The PyMOL Molecular Graphics System, Version 1.2r3pre, Schrödinger, LLC.) using “cartoon” and “surface” functions.

## Comparison With TCGA Mutation Data

The genomic mutation information in 32 types of cancers was retrieved from the TCGA (The Cancer Genome Atlas) (13) via Xena platform from University of California Santa Cruz. The number of mutations in samples were compared with the TCGA genomic mutation data in each types of cancer, and a paired Wilcoxon test was performed to evaluate the difference between each types of samples.

## Protein-Protein Interaction Network (PPIN) Analysis

The protein-protein interaction information of mutated genes was retrieved from BioGrid (The Biological General Repository

for Interaction Datasets) database (14), and the PPIN in each types of samples were illustrated using Cytoscape (15).

## Statistics

All the statistics are performed by RStudio ([www.rstudio.com](http://www.rstudio.com)) using R version 3.6.1, and a p-value cutoff at 0.05 is used in all the analysis.

## RESULTS

### Characterization of Pulmonary Nodule Samples

A total of 16 nodules with different stages of neoplasia and five para-cancer (PAR) tissues from four patients diagnosed as multiple pulmonary nodules (MPNs) were collected during surgery. After DNA extraction, whole exome sequencing (WES) was performed on these samples and peripheral blood mononucleated cells (PBMCs) of patients. The somatic mutations were retrieved after the filtration against germ-line mutations through a comparison with PBMC mutations, as illustrated in **Figure 1A**.

Among these 21 samples, two were in atypical adenomatous hyperplasia (AAH) stage, four in minimally invasive adenocarcinoma (MIA) stage, 10 in invasive adenocarcinoma (IA) stage, and five were PAR tissues. The histological characteristics of samples together with their IDs from each stage were presented in **Figure 1B**. The locations of all the lesions were indicated in the CT images and the histological image of each tissue were shown in **Supplemental Figure 1**.

### Mutational Analysis of Whole Exome Sequencing Results

WES was performed on these 21 samples from four patients as well as their PBMCs. The somatic mutations in each sample were summarized in **Figure 1C**. Most of the mutations are sample specific, with a small portion of mutations shared in more than one sample (scattered lines in **Figure 1C**). The number of mutations varies among different samples, with the least number of seven mutations (Pa1-1; Pa-2; Pa2-P) and the highest number of 214 mutations (Pa4-1). The average number of mutations in PAR, AAH, MIA, and IA samples are 49.4, 31.5, 29.5, and 53.0, respectively, and the average number of mutated genes in PAR, AAH, MIA, IA samples are 44.2, 25.5, 24.8, and 43.8, respectively, as listed in **Figures 2A, B**. These results indicated that there is no significant difference in the number of mutations or mutated genes between AAH and MIA samples, but there is a dramatic increase in the number of both mutations and mutated genes in IA samples as compared to the rest of samples.

For mutations on individual gene, missense mutation is the most common one across all types of samples (**Supplemental Figure 2**). As for the mutation types, single nucleotide polymorphism (SNP) is the most common type of mutations across all the samples (**Supplemental Figure 3**), which is consistent with the prevalence of missense mutations; referring

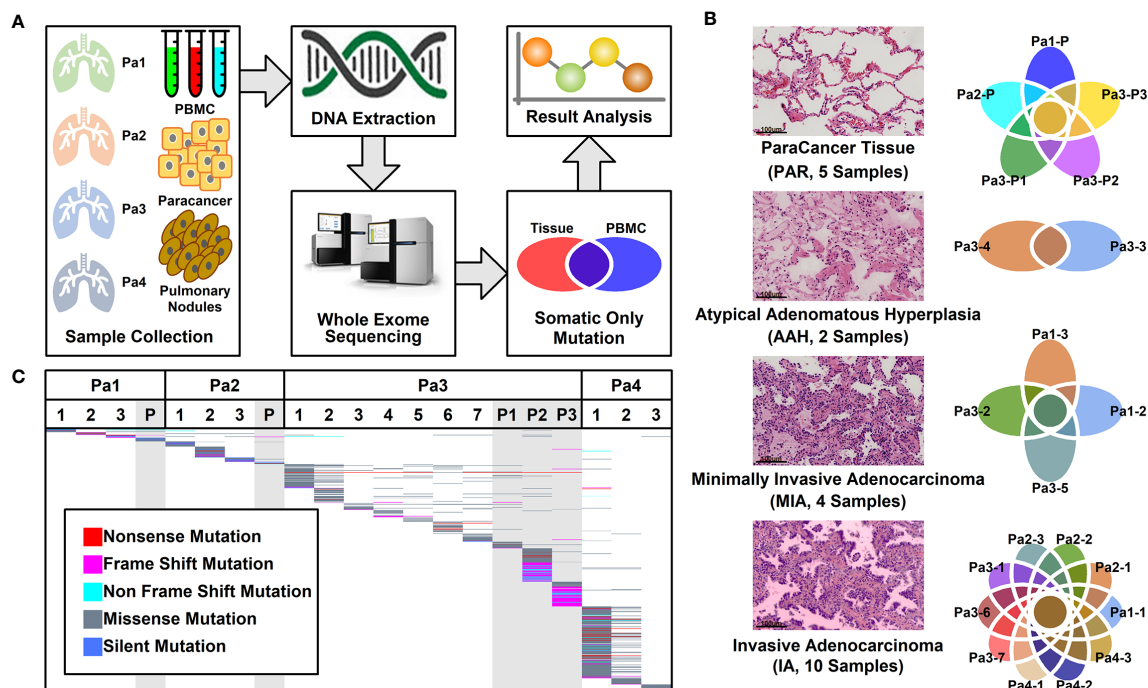


**FIGURE 1 |** Pulmonary nodule sample selection and whole exome sequencing. **(A)** Schematic illustration of research design. Twenty-one tissue samples and PBMC samples were collected. After DNA extraction and whole exome sequencing (WES), somatic mutations in different tissues were further analyzed; **(B)** Histological characteristic representation of samples and patient IDs with histopathological stages; **(C)** Summary of WES results across all samples. Each different-colored line represents a different type of mutations, and the scattered lines represent the shared mutations between different samples.

to SNV (Single Nucleotide Variant) classes in SNPs, C→T and G→A conversions are the top two common SNV types, and these two types of conversions occur most in IA samples (**Supplemental Figure 4**).

## Hotspot Mutated Gene Analysis in Pulmonary Nodules

The frequency of mutated genes in all nodules (AAH, MIA, and IA samples) were further counted and ranked, and the hotspot genes (mutated genes occurred in more than 2 pulmonary nodule samples) were listed in **Figure 2C**. Among these 19 mutated hotspot genes, *KMT2C* (with both missense and nonsense mutations) gene mutation has the highest overall frequency, however, this mutation was only found in the Pa3 samples (including PAR samples); *EGFR* gene mutation, with two types of mutations (missense and in frame deletion mutations), occurs in all four patients and two types of pulmonary samples (MIA and IA); *PRB2* gene mutation, with two types of mutations (missense and nonsense mutations), occurs in two of the patients and two types of pulmonary samples (MIA and IA). Interestingly, some of these hotspot genes with mutation type changes in different types of samples were found and will be further discussed in the following sections.

An interesting phenomenon, as discovered in our study, as well as in many other studies on pulmonary nodules, is the low concurrence of mutated genes between different samples. For example, mutated *EGFR*, the gene with the highest frequency

(*KMT2C* is treated as specific in patient 3, and hence not counted here), only occurs in 37.5% of pulmonary nodules (6 out of 16 samples). The low concurrence of mutated genes indicates the high genetic diversity of pulmonary nodules, and hence we took a step back and tried to explore the commonality among pulmonary nodule samples from a perspective of signaling pathways and cell functions.

## Converging Tendency Towards Functions or Pathways Related to Malignant Transformation in Pulmonary Nodules

To explore whether there is a converging tendency of mutated genes in samples at different nodules, we introduced a converging index, which is defined as the overlapping of signaling pathways or cell functions, including KEGG pathways, GO Biological Pathways (GO\_BP), and GO Molecular Functions (GO\_MF), in which the mutated genes are involved between two samples (detailed in Materials and Methods). The higher converging index between two samples, the higher probability of two samples with same pathways or cell function got affected (pathway or cell function related genes got mutated). To compare the converging status between samples at different stages, we calculated the converging index for KEGG, GO\_BP, and GO\_MF between samples within each nodules and the results are shown in **Figure 3A** (there are only two samples in AAH stage hence only one converging index was generated).



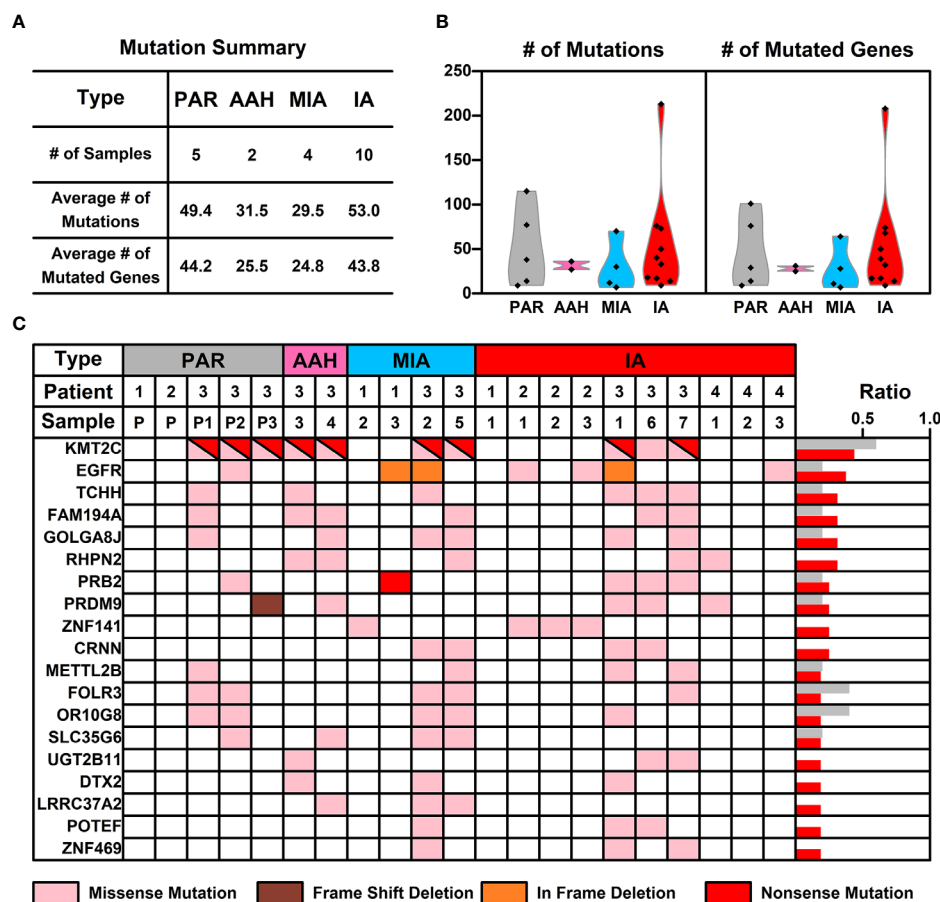


**FIGURE 2** | The mutation status of samples from different nodules. **(A)** List of average numbers of mutations/mutated genes in samples from different stages; **(B)** Violin plot representing the mutations (left) and mutated genes (right) in different samples. Each dot represents the number of mutations (non-synonymous mutations, left) and mutated genes (right) in different samples. **(C)** Chart listing hotspot mutated genes occurring in more than two pulmonary nodules. Each colored rectangle represents a mutated gene with different colors indicating different mutation types.

In all three types of pathway or cell function terms (KEGG, GO\_BP, and GO\_MF), the average converging indexes of lesions are higher than those of PAR tissues, except for the indexes in AAH samples, which might be caused by the limitation of sample numbers. Moreover, the indexes increase with the developmental stages of pulmonary nodules (AAH<MIA<IA).

To further explore the converged status of nodular samples at different stages, we retrieved all converged functions/pathways, ranked them based on the enrichment levels (detailed in Materials and Methods) (**Figure 3B**). Among the top 12 converged KEGG pathways, most of them are cancer related or important signaling pathways such as FoxO/MAPK/Calcium pathways; among the top 12 converged GO biological pathways, most of them are involved in transcription regulation and protein phosphorylation, the aberrant functions of these pathways have been shown directly related to lung cancer development in many studies (16). Moreover, GO:0098609 Cell-cell adhesion, which is directly related to epithelial-mesenchymal transition (EMT), is also converged in

lesions, indicating that the cell-cell adhesion ability has been affected in the pathogenesis of LUAD and might contribute to metastasis. Among the top 12 converged GO molecular functions, many of them are related to regulation of transcription, which is in consistent with GO\_BP results. In addition, GO:0004713, Protein tyrosine kinase activity and GO:0004714 Transmembrane receptor protein tyrosine kinase activity, that are directly involved in cancer-related signaling, have also been affected in pulmonary neoplasia. These findings implicate that multiple cell function disorders in these early stage lesions might trigger and/or accelerate the development of LUAD.

### Effects of Mutation on the Function of the Proteins Encoded by Hotspot Genes

Aside from converging tendency of mutated genes in cancer-related cellular functions and pathways, we also investigated the effect of mutation on the function of hotspot genes at the protein level. The changes of mutation types in pulmonary nodules were

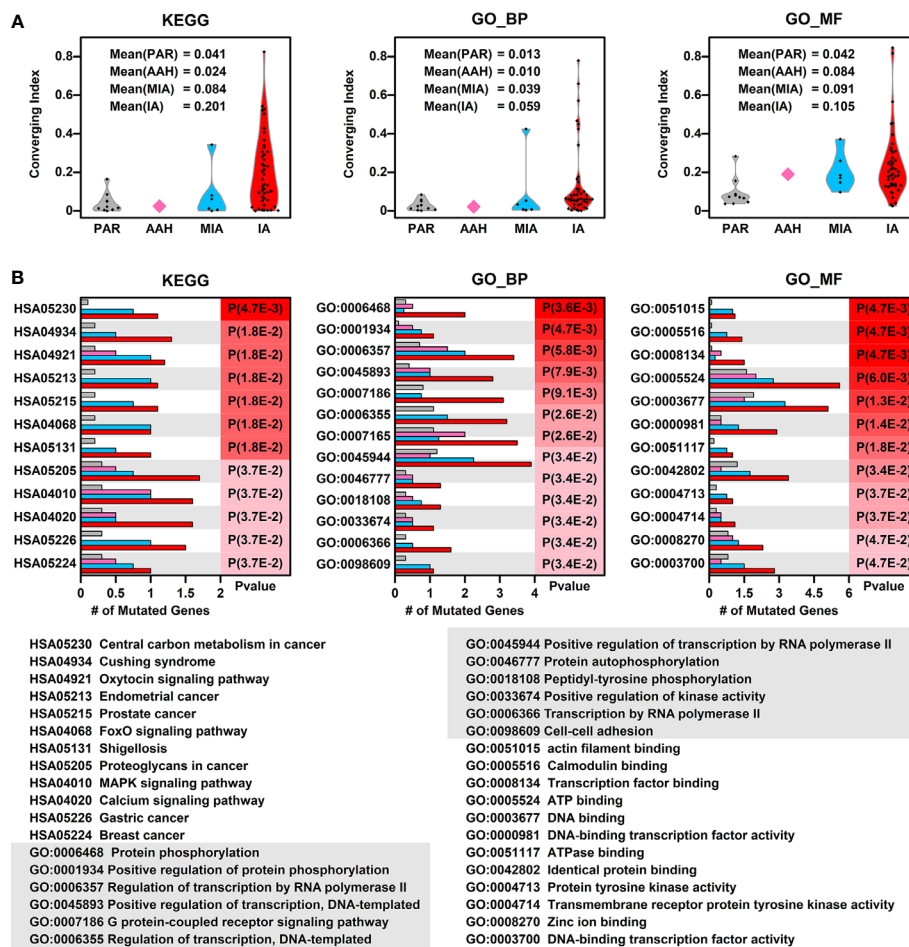


**FIGURE 3 |** Converging status of samples from different nodules. **(A)** The converging ratio of KEGG pathways (left), GO\_BP (GO biological pathways, middle), and GO\_MF (GO molecular functions, right) in samples from different nodules. The converging ratio is defined in Materials and Methods with higher converging index representing the higher tendency of mutated genes converging into the same pathway or function; **(B)** The converged KEGG pathways (left), GO\_BP (middle), and GO\_MF (right) with the number of mutated genes in samples from different stages (PAR, grey; AAH, pink; MIA, cyan; IA, red) and their names (bottom). The converged items were ranked based on the probability calculated by Poisson distribution using the number of mutated genes in PAR samples and IA samples.

compared with mutations in PAR tissues listed in **Figure 4A**. For example, in EGFR protein, there is a point mutation (L858R) in PAR tissues and IA samples; another mutation type, a deletion of 5 amino acids (746-750Del), occurs in both MIA and IA samples. 746-750Del locates in Erlotinib binding region (highlighted in red, **Figure 4B**), and the deletion of this beta3-alphaC loop region has been previously reported in Erlotinib-resistant patient (17).

In PRB2 protein, there is a point mutation of K88R in PAR tissues and IA samples; a nonsense mutation (R1098\*) occur in MIA and IA samples. The nonsense mutation R1098\* is a premature stop codon which might affect the function of PRB2 protein, and might relate to the development of pulmonary nodules.

Missense mutation might also cause dramatic structural changes. For example, in OR10G9 protein, a missense mutation (K3N) occurs in IA samples, leading to conversion of a positively charged amino acid (Lysine) to a polar amino acid

(Asparagine). In PRB2 protein, a missense mutation (Q314K) occurs in IA samples, leading to conversion of a polar amino acid (Glutamine) to a positively charged amino acid (Lysine). In PRDM9 protein, two missense mutations occur in MIA and IA samples (V594D; S814R) leading to conversion of a non-polar amino acid (Valine) to a negatively charged amino acid (Aspartic acid) and a polar amino acid (Serine) to a positively charged amino acid (Arginine). In SLC35G6 protein, a missense mutation occurs in MIA samples (A263D), leading to conversion of a non-polar amino acid (Alanine) to a negatively charged amino acid (Aspartic Acid). In TCHH protein, a missense mutation occurs in MIA samples, (K1394E) leading to conversion of a positively charged amino acid to a negatively charged amino acid (Glutamic Acid). In TXNDC2 protein, a new missense mutation (G207S) occurs in IA samples, leading to conversion of a nonpolar amino acid (Glycine) to a polar amino acid (Serine).

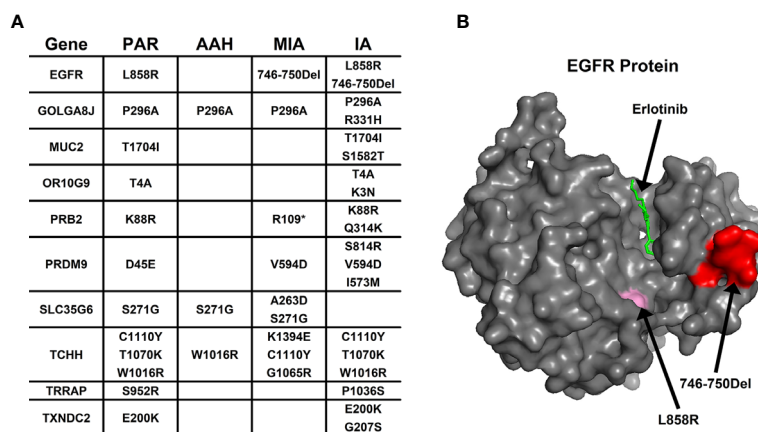


**FIGURE 4** | The mutation change in the same gene from different pulmonary nodules. **(A)** List of genes with different mutation in para-cancer tissues (PAR) and pulmonary nodule tissues (AAH, MIA and IA); **(B)** The 3D surface structure of EGFR in complex with Erlotinib. The different types of mutations are highlighted in pink and red colors.

## Pulmonary Nodule Mutated Genes

To explore the association of cancer related genes and mutated genes in different pulmonary nodules screened in WES, we retrieved the mutational data of these genes in 32 types of cancers from TCGA database, and compared the average number of mutations per gene among different types of cancers. Among 32 types of cancers, IA-related mutated genes have the highest number of mutations per gene in UCEC (Uterine corpus endometrial carcinoma). LUSC (Lung squamous cell carcinoma) and LUAD (Lung adenocarcinoma) ranks among the top #5 and #7, respectively of these 32 types of cancers, indicating the IA-related mutated genes have a higher mutation rate in lung cancers comparing to other types of cancers (**Figure 5A**). Among the four stages of nodules, pulmonary nodule related genes have a higher mutation rate in all types of cancers in comparison with PAR-related genes, and the mutation rate increases with the development of pulmonary nodules (IA>MIA, IA>AAH, AAH>PAR) (**Figure 5B**).

To explore the functional importance of pulmonary nodule related mutated genes, we calculated the number of each mutated gene involved in KEGG pathways (**Figure 5C**), GO\_BP (**Figure 5D**), and GO\_MF (**Figure 5E**). The rationale behind this is that the higher the number of genes involved in the pathways/functions, the more important role one gene could play, and hence the mutation could make bigger impact on cell activities. In general, the average numbers of mutated genes involved in pathways/functions are higher in pulmonary nodules than that of PAR-related mutated genes, suggesting the increased functional importance of mutated genes in pulmonary nodules.

We further constructed the protein-protein interaction (PPI) networks generated by mutated genes from different pulmonary nodules (**Figure 5F**) and compared them with each other (the PPI network of AAH-related genes was not shown due to limited number of mutated genes). The PPI network generated by IA-related mutated genes is more complex when compared with MIA or PAR nodules, indicating a complex function affected in

IA samples. The complexity of PPI network could contribute to the explanation of development of pulmonary nodules.

## DISCUSSION

MPNs is defined as more than one solid nodules in the lung of a single patient. Pathologically, MPNs are commonly identified as AAH, AIS, MIA, and IA. They represent an ideal model of deciphering the clonal evolution of early stage lung adenocarcinoma. Understanding the gene mutations in MPNs holds great promise for prevention and treatment strategy of lung adenocarcinoma.

Accumulating mutations as well as genes were identified by using next generation sequencing on MPNs samples (6, 9, 18). However, these studies mainly used single gene change-directed data analytic strategy and the clinical significance of these findings are largely limited (19). To overcome the limitations of current genome-based data, we analyzed the somatic mutations identified in the WES data from 21 MPNs followed by a cell function and pathway converging-directed analysis. Based on this function-directed analysis, we found that the extent of protein structural changes caused by different mutations as well as the amounts of affected pathways/functions in all lesions are positively correlated with the degree of malignancy, indicating that during the malignant evolution, comprehensive mutations in several key signaling pathways other than single gene are accumulated, which might endow certain cell populations more aggressive phenotype in terms of accelerated proliferation rates and the malignant progression of lesions.

Among the mutated genes identified in all samples, KMT2C other than EGFR was found in 10 out of 21 lesions. This result is in consistent with the recently reported finding from cell line experiments, indicating that KTM2C might be a novel driver gene correlated with KRAS mutation during the development of early stage lung adenocarcinoma (20). However, KMT2C mutation is only found in one of four patient and only one IA out of all 10

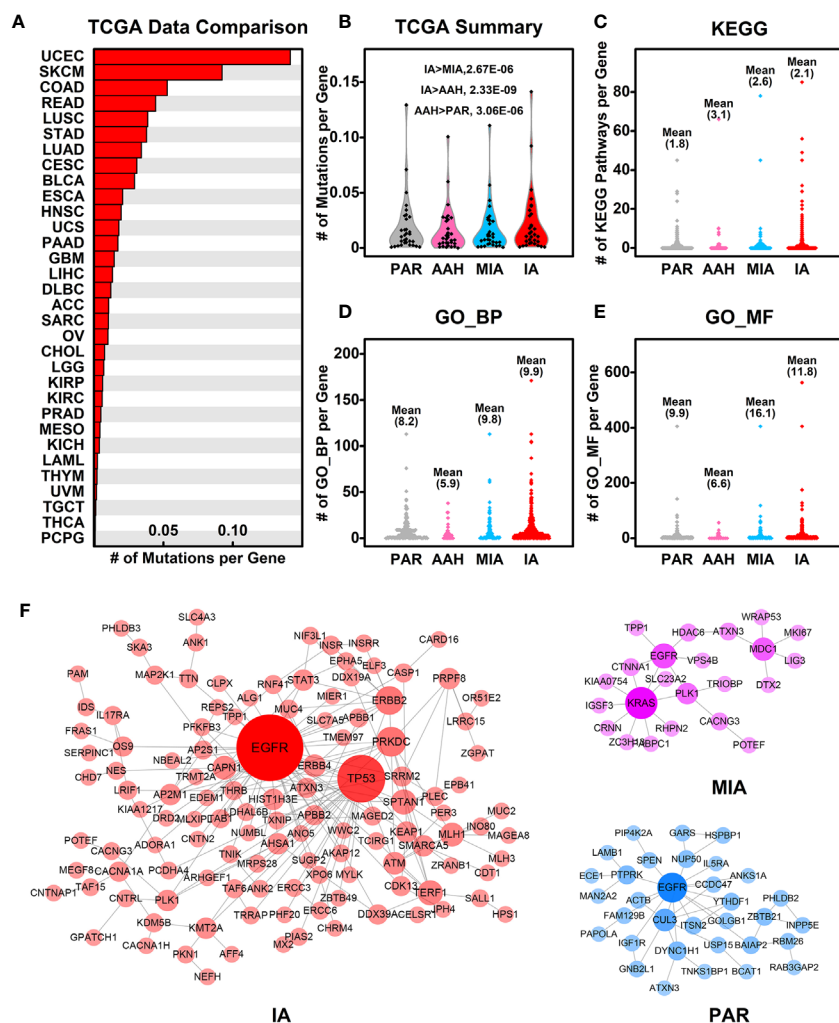


**FIGURE 5 |** Association of mutated genes in pulmonary nodules and other cancer genes. **(A)** The number of mutations per gene in different types of cancers. The mutated genes in IA samples were used here, and the mutation data from different types of cancers were retrieved from TCGA database; **(B)** The summary of mutations per gene in different pulmonary nodules compared with different types of cancers. With the development of pulmonary nodules, the chances of pulmonary nodule related genes that are mutated in different types of cancers increased; **(C–E)** The number of KEGG pathways **(C)**, GO\_BP **(D)**, and GO\_MF **(E)** in which each mutated gene involved is plotted in different nodules. With the development of pulmonary nodules, the average number of mutated gene involved pathways/functions increases, indicating the functional importance of mutated genes; **(F)** The PPI networks generated using mutated genes from PAR, MIA, and IA samples.

samples harbors a missense mutation, all other samples in particular adjacent normal samples harbored with nonsense mutation. Moreover, many of these mutations including those in EGFR were also identified in adjacent normal tissues when germ-line mutations were filtered during the process of analysis. These findings indicate the complicated background of cancer lesions and the clinical significance of single gene mutation in samples except of cancerous tissues should be carefully reevaluated. On the contrary, EGFR mutation are mainly found in malignant lesions, among which in frame deletion is the major mutational pattern. Similar results were obtained in the amounts and patterns of many other gene mutations in this study.

The KEGG signaling pathway analysis indicates that varied mutated genes tend to converge into signaling pathways related

to pivotal cell growth regulation in malignancy in comparison with adjacent normal samples. This converging trend seems to be more obvious in IA than in MIA, indicating a cancer-like microenvironment forced selection of functional mutations during the origination and development of early stage lung adenocarcinoma. Considering the similar number of mutations/mutated genes in PAR and IA samples, the increased converging index indicating mutated genes tend to focus on certain functions/pathways, or only cells with certain impaired functions can survive under these microenvironments. Among the top 12 converged KEGG pathways, most of them are cancer related or important signaling pathways such as FoxO/MAPK/Calcium pathways. Among the top 12 converged GO biological pathways, most of



them are involved in transcription regulation and protein phosphorylation, the aberrant functions of these pathways have been shown directly related to cancer development in many studies. Moreover, the levels of protein structural changes caused by mutations as well as the extent of mutations in these converged pathways are higher in IA as compared with that in MIA tissues, both of which are higher in malignant lesions than in adjacent normal tissues, indicating that these pathways may be responsible for the malignant evolution of pulmonary nodules.

Although whole transcriptional sequencing data from other patients might be available, lacking in-patient paired validation in protein expression levels is the major limitation of exploring WES data in MPNs studies. To circumvent this problem, we used a protein structure predicting strategy to evaluate the functional significance of hot spot gene mutations that are related to carcinogenesis and target therapy resistance (as listed in **Figure 4A**) (21). As shown in our results, 746-750 Del mutation of EGFR was identified, which might induce erlotinib resistance in NSCLC patients (17). PRB2, a tumor suppressor (22, 23), a premature stop codon was identified in our study, suggesting that its down-regulation and dysfunction might occur in patients. The mutation of TCHH is found to be related to platinum resistance in gastric carcinoma (24). In our predicting results, the conversion from positively charged amino acid to negatively charged amino acid (K1394E) of TCHH induced by missense mutation might affect its protein stability as well as the prognosis of this patient (25). Down regulation of TXNDC2, an antioxidant enzyme is directly related to cisplatin resistance in many cancer cells (26, 27). In our findings, conversion from nonpolar amino acid to polar one (G207S) in protein structure is also predicted. These findings are coincide with previous evidences on the mutation analysis in a serial of studies (28–31). Besides, in comparison with The Cancer Genome Atlas database (TCGA), most of mutated genes in MIA and IA identified in this study are genes functionally related to the development of lung cancers.

In this study, the findings by function-directed analysis of WES data from MPNs suggested that a group of functionally converged mutations rather than a single driver gene mutation might be the trigger of the origination and malignant progression of lung adenocarcinoma. Our results indicated that other than well-known genes such as EGFR, KRAS, and TP53, mutations in other genes involved in relating pathways (as listed in **Figure 3B**) deserve more attention, and an involvement of these genes might be necessary in the future screening of early stage lung adenocarcinoma. Besides, our results shed some new insights as well as new strategy to decipher the early development of lung cancer, and also provide many candidate genes which might be used as potential drug targets in the future treatment of lung adenocarcinoma.

## DATA AVAILABILITY STATEMENT

The data presented in the study are deposited in Genome Sequence Archive for Human (“<https://bigd.big.ac.cn/gsa-human/>”) repository, accession number HRA000465.

## ETHICS STATEMENT

The present study was approved by the Ethics Committee of Shenzhen People’s Hospital. The patients/participants provided their written informed consent to participate in this study. Written informed consent was obtained from the individual(s) for the publication of any potentially identifiable images or data included in this article.

## AUTHOR CONTRIBUTIONS

CZ, S-WD, CQ, and G-sW conceived the research idea. CZ, S-WD, ZC, and CQ prepared and wrote the manuscript. D-CL, JXu, SL, PZ, and JAW collected the clinical samples. RL, JXi, YY, JGW, LD, and XW analyzed the WES data. SD, YF, YC, and CZ revised the manuscript. All authors contributed to the article and approved the submitted version.

## FUNDING

This study is funded by The Science and Technology Foundation of Shenzhen (JCYJ20180305164128430); the International Cooperation Foundation of Shenzhen (GJHZ20180928171602104); the Shenzhen Economic and Information Committee “Innovation Chain and Industry Chain” integration special support plan project (20180225112449943); the Shenzhen Public Service Platform on Tumor Precision Medicine and Molecular Diagnosis; Research Grants Council of the Hong Kong Special Administrative Region, China (Project No. CityU 21101115, 11102317, 11103718, 11103619, R4017-18, C4041-17GF), a grant from Guangdong Basic and Applied Basic Research Foundation (Project No. 2019B030302012), Young Scientists Fund of the National Natural Science Foundation of China (81802384); International innovation team for early diagnosis and precise treatment of lung cancer (2016, KQTD2016113015442590); Scientific Research Project of Taikang Xianlin Drum Tower Hospital (TKKY20193805).

## ACKNOWLEDGMENTS

We would like to thank the staffs of Department of Pathology in Shenzhen People’s Hospital for technical support and the nurses of Department of Thoracic Surgery in Shenzhen People’s Hospital for taking care of patients.

## SUPPLEMENTARY MATERIAL

The Supplementary Material for this article can be found online at: <https://www.frontiersin.org/articles/10.3389/fonc.2020.571521/full#supplementary-material>

## REFERENCES

- Siegel RL, Miller KD, Jemal A. Cancer statistics. *CA Cancer J Clin* (2016) 69 (1):7–34. doi: 10.3322/caac.21551
- Santarpia M, Liguori A, D'Aveni A, Karachaliou N, Gonzalez-Cao M, Daffinà MG, et al. Liquid biopsy for lung cancer early detection. *J Thorac Dis* (2018) 10(3):S882–97. doi: 10.21037/jtd.2018.03.81
- Feng RM, Zong YN, Cao SM, Xu RH. Current cancer situation in China: Good or bad news from the 2018 Global Cancer Statistics? *Cancer Commun* (2019) 39(1):1–12. doi: 10.1186/s40880-019-0368-6
- Zheng M. Classification and Pathology of Lung Cancer. *Surg Oncol Clin N Am* (2016) 25(3):447–68. doi: 10.1016/j.soc.2016.02.003
- He P, Yao G, Guan Y, Lin Y, He J. Diagnosis of lung adenocarcinoma in situ and minimally invasive adenocarcinoma from intraoperative frozen sections: an analysis of 136 cases. *J Clin Pathol* (2016) 69(12):1076–80. doi: 10.1136/jclinpath-2016-203619
- Hu X, Fujimoto J, Ying L, Fukuoka J, Ashizawa K, Sun W, et al. Multi-region exome sequencing reveals genomic evolution from preneoplasia to lung adenocarcinoma. *Nat Commun* (2019) 10(1):2978. doi: 10.1038/s41467-019-10877-8
- Li Y, Li X, Li H, Zhao Y, Liu Z, Sun K, et al. Genomic characterisation of pulmonary subsolid nodules: mutational landscape and radiological features. *Eur Respir J* (2020) 55(2):1901409. doi: 10.1183/13993003.01409-2019
- Ren Y, Huang S, Dai C, Xie D, Zheng L, Xie H, et al. Germline Predisposition and Copy Number Alteration in Pre-stage Lung Adenocarcinomas Presenting as Ground-Glass Nodules. *Front Oncol* (2019) 9:288. doi: 10.3389/fonc.2019.00288
- Tailor TD, Rao X, Campa MJ, Wang J, Gregory SG, Patz EFJ. Whole Exome Sequencing of Cell-Free DNA for Early Lung Cancer: A Pilot Study to Differentiate Benign From Malignant CT-Detected Pulmonary Lesions. *Front Oncol* (2019) 9:317. doi: 10.3389/fonc.2019.00317
- Izumchenko E, Chang X, Brait M, Fertig E, Kagohara LT, Bedi A, et al. Targeted sequencing reveals clonal genetic changes in the progression of early lung neoplasms and paired circulating DNA. *Nat Commun* (2015) 6:1–13. doi: 10.1038/ncomms9258
- Bolger AM, Lohse M, Usadel B. Trimmomatic: a flexible trimmer for Illumina sequence data. *Bioinformatics* (2014) 30(15):2114–20. doi: 10.1093/bioinformatics/btu170
- Li H, Durbin R. Fast and accurate short read alignment with Burrows-Wheeler transform. *Bioinformatics* (2009) 25(14):1754–60. doi: 10.1093/bioinformatics/btp324
- Weinstein JN, Collisson EA, Mills GB, Shaw KRM, Ozenberger BA, Ellrott K, et al. The Cancer Genome Atlas Pan-Cancer analysis project. *Nat Genet* (2013) 45(10):1113–20. doi: 10.1038/ng.2764
- Oughtred R, Stark C, Breitkreutz BJ, Rust J, Boucher L, Chang C, et al. The BioGRID interaction database: 2019 update. *Nucleic Acids Res* (2019) 47(D1):D529–41. doi: 10.1093/nar/gky1079
- Shannon P, Markiel A, Owen O2, Baliga NS, Wang JT, Ramage D, et al. Cytoscape: a software environment for integrated models of biomolecular interaction networks. *Genome Res* (2003) 13:2498–504. doi: 10.1101/gr.1239303
- Hanahan D, Weinberg RA. Hallmarks of cancer: The next generation. *Cell* (2011) 144(5):646–74. doi: 10.1016/j.cell.2011.02.013
- Santoni-Rugiu E, Grauslund M, Melchior LC, Costa JC, Sørensen JB, Urbanska EM. Heterogeneous resistance mechanisms in an EGFR exon 19-mutated non-small cell lung cancer patient treated with erlotinib: Persistent FGFR3-mutation, localized transformation to EGFR-mutated SCLC, and acquired T790M EGFR-mutation. *Lung Cancer* (2017) 113:14–7. doi: 10.1016/j.lungcan.2017.08.024
- Liang W, Zhao Y, Huang W, Gao Y, Xu W, Tao J, et al. Non-invasive diagnosis of early-stage lung cancer using high-throughput targeted DNA methylation sequencing of circulating tumor DNA (ctDNA). *Theranostics* (2019) 9(7):2056–70. doi: 10.7150/thno.28119
- Qiu T, Li W, Zhang F, Wang B, Ying J. Major challenges in accurate mutation detection of multifocal lung adenocarcinoma by next-generation sequencing. *Cancer Biol Ther* (2020) 21(2):170–7. doi: 10.1080/15384047.2019.1674070
- Fang B. RAS signaling and anti-RAS therapy: lessons learned from genetically engineered mouse models, human cancer cells, and patient-related studies. *Acta Biochim Biophys Sin (Shanghai)* (2016) 48(1):27–38. doi: 10.1093/abbs/gmv090
- Sigismund S, Avanzato D, Lanzetti L. Emerging functions of the EGFR in cancer. *Mol Oncol* (2018) 12(1):3–20. doi: 10.1002/1878-0261
- Caputi M, Groeger AM, Esposito V, De Luca A, Masciullo V, Mancini A, et al. Loss of pRb2/p130 expression is associated with unfavorable clinical outcome in lung cancer. *Clin Cancer Res* (2002) 8(12):3850–6.
- Cito L, Indovina P, Forte IM, Pentimalli F, Di Marzo D, Somma P, et al. pRb2/p130 localizes to the cytoplasm in diffuse gastric cancer. *J Cell Physiol* (2015) 230(4):802–5. doi: 10.1002/jcp.24805
- Yang Q, Zhu C, Zhang Y, Wang Y, Wang Y, Zhu L, et al. Molecular analysis of gastric cancer identifies genomic markers of drug sensitivity in Asian gastric cancer. *J Cancer* (2018) 9(16):2973–80. doi: 10.7150/jca.25506
- Kuo L-H, Li J-H, Kuo H-T, Hung C-Y, Tsai H-Y, Chiu W-C, et al. Effect of charged amino acid side chain length at non-hydrogen bonded strand positions on  $\beta$ -hairpin stability. *Biochemistry* (2013) 52(44):7785–97. doi: 10.1021/bi400911p
- Pereira L, Igea A, Canovas B, Dolado I, Nebreda AR. Inhibition of p38 MAPK sensitizes tumour cells to cisplatin-induced apoptosis mediated by reactive oxygen species and JNK. *EMBO Mol Med* (2013) 5(11):1759–74. doi: 10.1002/emmm.201302732
- Qiao B, Jiménez-Ángeles F, Nguyen TD, De La Cruz MO. Water follows polar and nonpolar protein surface domains. *Proc Natl Acad Sci U S A* (2019) 116 (39):19274–81. doi: 10.1073/pnas.1910225116
- Betje J, Schneider NI, Harbaum L, Pollheimer MJ, Lindtner RA, Kornprat P, et al. MUC1, MUC2, MUC5AC, and MUC6 in colorectal cancer: expression profiles and clinical significance. *Virchows Arch* (2016) 469(3):255–65. doi: 10.1007/s00428-016-1970-5
- Houle AA, Gibling H, Lamaze FC, Edgington HA, Soave D, Fave MJ, et al. Aberrant PRDM9 expression impacts the pan-cancer genomic landscape. *Genome Res* (2018) 28(11):1611–20. doi: 10.1101/gr.231696.117
- Jethwa A, Slabicki M, Hüllelin J, Jentzsch M, Dalal V, Rabe S, et al. TRRAP is essential for regulating the accumulation of mutant and wild-type p53 in lymphoma. *Blood* (2018) 131(25):2789–802. doi: 10.1182/blood-2017-09-806679
- Martincorena I, Raine KM, Gerstung M, Dawson KJ, Haase K, Van Loo P, et al. Universal Patterns of Selection in Cancer and Somatic Tissues. *Cell* (2017) 171(5):1029–41. doi: 10.1016/j.cell.2017.09.042

**Conflict of Interest:** The authors declare that the research was conducted in the absence of any commercial or financial relationships that could be construed as a potential conflict of interest.

Copyright © 2021 Dong, Li, Cheng, Liu, Xia, Xu, Li, Wang, Yue, Fan, Cao, Dai, Wang, Zhao, Wang, Xiao, Qiu, Wang and Zou. This is an open-access article distributed under the terms of the Creative Commons Attribution License (CC BY). The use, distribution or reproduction in other forums is permitted, provided the original author(s) and the copyright owner(s) are credited and that the original publication in this journal is cited, in accordance with accepted academic practice. No use, distribution or reproduction is permitted which does not comply with these terms.



# Deoxypodophyllotoxin Inhibits Non-Small Cell Lung Cancer Cell Growth by Reducing HIF-1 $\alpha$ -Mediated Glycolysis

Yuping Yang<sup>1†</sup>, Lingling Liu<sup>2,3†</sup>, Jinghui Sun<sup>2†</sup>, Shu Wang<sup>4</sup>, Zhongyuan Yang<sup>5</sup>, Honghui Li<sup>6</sup>, Na Huang<sup>1\*</sup> and Wei Zhao<sup>1,2\*</sup>

<sup>1</sup> Department of Pulmonary and Critical Care Medicine, The First Affiliated Hospital of Chengdu Medical College, Chengdu, China, <sup>2</sup> School of Laboratory Medicine/Sichuan Provincial Engineering Laboratory for Prevention and Control Technology of Veterinary Drug Residue in Animal-origin Food, Chengdu Medical College, Chengdu, China, <sup>3</sup> Development and Regeneration Key Laboratory of Sichuan Province, Chengdu Medical College, Chengdu, China, <sup>4</sup> State Key Laboratory of Natural Medicines, Department of Pharmaceutics, China Pharmaceutical University, Nanjing, China, <sup>5</sup> Cancer Center, Sun Yat-Sen University, Guangzhou, China, <sup>6</sup> Department of Refractive Surgery, Chengdu Aier Eye Hospital, Chengdu, China

## OPEN ACCESS

### Edited by:

Dong-Hua Yang,  
St. John's University, United States

### Reviewed by:

Yunkai Zhang,  
Vanderbilt University Medical Center,  
United States  
Leli Zeng,  
Sun Yat-sen University, China

### \*Correspondence:

Wei Zhao  
zw198626520@126.com  
Na Huang  
717308813@qq.com

<sup>†</sup>These authors have contributed  
equally to this work

### Specialty section:

This article was submitted to  
Pharmacology of Anti-Cancer Drugs,  
a section of the journal  
Frontiers in Oncology

Received: 02 December 2020

Accepted: 11 January 2021

Published: 24 February 2021

### Citation:

Yang Y, Liu L, Sun J, Wang S, Yang Z,  
Li H, Huang N and Zhao W (2021)  
Deoxypodophyllotoxin Inhibits Non-  
Small Cell Lung Cancer Cell Growth by  
Reducing HIF-1 $\alpha$ -Mediated  
Glycolysis.  
Front. Oncol. 11:629543.  
doi: 10.3389/fonc.2021.629543

Cancer cell proliferation is a metabolically demanding process that requires high rate of glycolysis to support anabolic growth. Deoxypodophyllotoxin (DPT) is a natural flavonolignan with various pharmacological activities, including antitumor effect. However, whether DPT affects the metabolic reprogramming of cancer cells is unknown. The purpose of this study is to investigate the role of DPT on non-small cell lung cancer (NSCLC) and to explore whether HIF-1 $\alpha$ -mediated glycolysis is involved in its mechanism of action. The level of HIF-1 $\alpha$  mRNA and protein in NSCLC cells following DPT treatment was detected using qRT-PCR and western blotting, respectively. Cell Counting Kit-8 (CCK-8) and caspase-3 activity assays were performed to analyze cell proliferation and apoptosis. The underlying molecular mechanism was identified by dual luciferase assay, Western blotting, qRT-PCR, glucose consumption, lactate production, and immunoprecipitation. A murine NSCLC model was used to clarify the effect of DPT treatment on tumor cell proliferation. Our findings showed that DPT treatment inhibited NSCLC cell growth in a dose- and time-dependent manner. Further analysis suggested that DPT treatment inhibited HIF-1 $\alpha$  signaling pathway by Parkin-mediated protein degradation in NSCLC cells. DPT treatment significantly decreased glucose consumption and lactate production. In addition, DPT treatment reduced the expression of HIF-1 $\alpha$  target genes, including GLUT1, HK2 and LDHA, resulting in reduction in glycolysis. We further revealed that DPT-induced cell growth inhibition and increased glucose and lactate levels could be reversed by overexpressing HIF-1 $\alpha$ . Additionally, we found that DPT repressed NSCLC growth and GLUT1, HK2 and LDHA expression *in vivo*. Overall, this study suggested that DPT inhibited NSCLC growth by preventing HIF-1 $\alpha$ -mediated glycolysis.

**Keywords:** deoxypodophyllotoxin, non-small cell lung cancer, HIF-1 $\alpha$ , aerobic glycolysis, tumor progression

## INTRODUCTION

Lung cancer is the most frequently diagnosed cancer and its incidence has been increasing in recent years (1, 2). Lung cancer remains a leading cause of cancer-associated mortality for men and women worldwide (1). The development of lung cancer is a multistep process involving alterations in oncogenes and tumor suppressor genes, and also other factors such as alcohol consumption, smoking, pathogenic infections and genetic factors (3–5). NSCLC accounts for over 80% of all lung cancer cases. Because the onset of NSCLC is asymptomatic, NSCLC is usually diagnosed in late clinical stages when surgical resection is not possible. The current prognosis of patients with NSCLC is very poor with a 5-year overall survival (OS) rate of only 10% (6, 7). Thus, there is an urgent need to find novel and effective means for the treatment of NSCLC.

Aerobic glycolysis, also known as the Warburg effect, was discovered almost a century ago (8–10). It has been considered as a hallmark of cancer. Another hallmark of cancer is hyper-cell proliferation. In addition to the high energy requirements of enhanced proliferation, cell division also requires large amounts of biomolecules, including nucleic acids and lipids, for which glucose is an important biosynthetic precursor. Enhanced levels of glucose transporters and enzymes in the glycolytic pathway and upregulated lactate level are often found in NSCLC cells, and inhibition of aerobic glycolysis arrests cancer cell proliferation (11–13).

Hypoxia inducible factor 1 $\alpha$  (HIF-1 $\alpha$ ) is one of the primary glycolytic regulators. HIF-1 $\alpha$  is ubiquitinated by the von Hippel-Lindau protein and degraded *via* the proteasomal pathway under normoxic condition (14, 15). Due to the low oxygen content in most solid tumors, the glycolytic enzymes are consistently upregulated in cancer cells (9, 16, 17). Increased HIF-1 $\alpha$  protein level is induced by activated RAS, loss of p53 or increased heat shock protein 90 (Hsp90) in cancer cells regardless of the availability of oxygen (18–21). The glycolytic proteins, glucose transporter 1 (GLUT1), hexokinase 2 (HK2) and phosphoglycerate kinase 1 (PGK1) are genes that are upregulated by HIF-1 $\alpha$  (22). Therefore, targeting HIF-1 $\alpha$ -mediated metabolic pathways in tumor cells has been hypothesized to be a valuable therapeutic strategy.

Deoxyphylloxytoxin (DPT) is a natural flavonolignan that destabilizes microtubules and has various pharmacological activities, including anti-inflammatory, antiviral and antitumor effects (23–25). Although there have been some studies on DPT (26, 27), the mechanism of its antitumor activity in NSCLC has not been elucidated. This study aims to investigate the potential therapeutic effect of DPT and its mechanism of action in NSCLC and to explore the involvement of HIF-1 $\alpha$ -mediated glycolysis.

## MATERIALS AND METHODS

### Cell Culture and Drug Treatment

The human NSCLC cell lines A549, SK-MES-1, H460, and SPC-A1 were obtained from the Cell Bank of Type Culture Collection

of Chinese Academy of Sciences (Shanghai, China) and were cultured in Dulbecco's modified Eagle's medium (DMEM, Gibco, Waltham, MA) supplemented with 1% penicillin-streptomycin at 37°C with 5% CO<sub>2</sub> and 21% O<sub>2</sub>. Cells were treated with different concentrations (0, 4, 8, 12, 16, and 20 nM) of DPT for 12, 24, and 48 h. Then, the cells were subjected to the following experiments.

### Cell Transfection

For transfection,  $2 \times 10^4$  A549 or SK-MES-1 cells were seeded in each well of a 24-well plate. After 24 h, the cells were transfected with the control or HIF-1 $\alpha$  overexpressing plasmid (pcDNA-HA-HIF-1 $\alpha$ , Mobai Biotech., Nanjing, China) using Lipofectamine 3000 (Thermo Fisher Scientific, Waltham, MA) according to the manufacturer's instructions. Cells were harvested for analysis after 48 h. DPT (16 nM) was added to the medium 48 h before the experiment.

### CCK-8 Assay

Cell viability was assessed by the Cell Counting Kit-8 (CCK-8) assay (DOJINDO, Kumamoto, Japan) at 12, 24, and 48 h of drug treatment. Cells ( $5 \times 10^3$  cells/well) were seeded in 96-well plates and incubated with different concentrations (0, 4, 8, 12, 16, and 20 nM) of DPT for 12, 24, and 48 h. Then, 10  $\mu$ l of CCK-8 assay solution was added to each well and incubated for another 4 h. Finally, the wells were washed with PBS, dried, and 150  $\mu$ l of DMSO was added. Light absorbance was measured by a microplate reader at 490 nm (Thermo Fisher Scientific).

### Caspase-3 Activity Assay

NSCLC cells were cultured in 96-well plates. After DPT treatment for 48 h in DMEM supplemented with 10% FBS, caspase-3 activity was measured. A caspase-3 activity assay kit (Beyotime, China) was used for the measurement of caspase-3 enzymatic activity. Briefly, 50  $\mu$ l of cell lysis buffer was prepared by mixing 10  $\mu$ l Ac-DEVD-pNA (2 mM) and 40  $\mu$ l buffer and was loaded into a 96-well plate. After incubation at 37°C for 4 h, the light absorbance was measured at 405 nm by a microplate reader (Thermo Fisher Scientific). The caspase-3 activity in each sample solution was calculated by the standard curve method. The final results were normalized to the quantity of total protein using a Bradford protein quantitative kit (Beyotime).

### Dual Luciferase Assay

After DPT treatment, the Cignal Finder Cancer 10-Pathway Reporter Array (Qiagen, Shanghai, China; Cat. No.: 336821) was used to characterize the signaling pathways that were altered in NSCLC cells as described previously (28). Then, luciferase assays were performed to confirm the prediction. Briefly,  $1 \times 10^5$  A549 or SK-MES-1 cells were transfected using Lipofectamine 3000 (Thermo Fisher Scientific) with 0.2  $\mu$ g of triple hypoxia response element (3xHRE). A renilla luciferase plasmid was cotransfected as a transfection efficiency control. After 24 h, the cells were harvested, and luciferase activity was measured using the Dual-Luciferase Reporter Assay System (Promega, Madison, WI, USA) according to the manufacturer's protocol.



## Real-Time Quantitative PCR

Total RNA from cells and tissues was extracted using TRIzol reagents (Invitrogen, Carlsbad, CA, USA). RNA was reverse transcribed into cDNA using the Reverse Transcription System Kit (Promega). The reaction mixture was as follows: SYBR Premix Ex Taq II (Bio-Rad, Hercules, CA, USA), 2 µl of cDNA, 5 µl of 2× master mix, 0.5 µl forward/reverse primer and 2 µl of pure water. RT-PCR was performed on an ABI7900HT machine (Applied Biosystems, Foster City, CA) with 3 replicates. Amplification conditions were 95°C for 5 min, followed by 40 cycles of 95°C for 15 s and 60°C for 1 min. Primers were obtained from GeneScript (Nanjing, China), and their sequences were as follows: HIF-1α: Forward 5'-TTGC TCATCAGTTGCCACTTCC-3', Reverse 5'-AGCAATTCATC TGTGCTTTCATGTC-3'; CAIX: Forward 5'-GGATCTACCTA CTGTTGAGGCT-3', Reverse 5'-CATAGCGCCAATGACT CTGGT-3'; GLUT1: Forward 5'-GATTGGCTCCTTCTC TGTGG-3', Reverse 5'-TCAAAGGACTTGCCAGTTT-3'; HK2: Forward 5'-GAGCCACCCTACCCTACT-3', Reverse 5'-CCAGGCATTCGGCAATGTG-3'; LDHA: Forward 5'-AAGCGGTGCAATCTGGATTGAG-3', Reverse 5'-GGTGAA CTCCCAGCCTTTCC-3'; and GAPDH: Forward 5'-TGACGT GGACATCCGCAAAG-3', Reverse 5'-CTGGAAGGTGGA CAGCGAGG-3'. Data were calculated by the  $2^{-\Delta\Delta C_q}$  method after normalization to β-actin mRNA level.

## Western Blot Analysis

Cells were washed with PBS and homogenized in RIPA buffer (Roche, Basel, Switzerland). Proteins were separated by 10% SDS-PAGE (Roche) and transferred to a polyvinylidene fluoride membrane (Millipore, Burlington, MA). Membranes were blocked with 5% skim milk in TBST (TBS with 20% Tween-20) for 2 h at room temperature before incubation with primary antibodies against β-actin (Cell Signaling Technology, Cat. No. 4970; 1:1,000), FLAG (Proteintech, Cat. No. 66008-3; 1:1,000), p21 (Proteintech, Cat. No. 66214-1; 1:1,000), and HIF-1α (Cell Signaling Technology, Cat. No. 36169; 1:1,000) at 4°C overnight. Afterward, the membranes were incubated with a secondary antibody (Cell Signaling Technology, Cat. No. 7074; 1:5,000) for 1 h at room temperature. Bands were visualized by SuperSignalWest Pico Chemiluminescent Substrate (Thermo Fisher). β-actin was used as an internal loading control.

## In vitro Ubiquitination Assay

For *in vitro* ubiquitination assays, NSCLC cells were transfected with pcDNA-HIF-1α (MobaiBiotech.) and the transfected cells were treated with 16 nM DPT for 48 h. Cell lysates were harvested and HIF-1α was purified by immunoprecipitation. Purified HIF-1α protein (0.4 µg) was incubated with reaction mixtures (50 µl) consisting of buffer [5 mM MgCl<sub>2</sub>, 50 mM Tris (pH 7.4), 1 mM DTT, and 2 mM ATP], 0.5 µg of E1 (Boston Biochem, Cambridge, MA, USA), 0.5 µg of E2 (UbcH7; Boston Biochem), 5 µg of Ub (Boston Biochem), and 0.5 µg of PINK1 (Boston Biochem). After incubation for 3 h at 37°C, the postreaction mixtures were used for Western blot analysis with an anti-Ub antibody (sc-8017, Santa Cruz Biotechnology, TX, USA; 1:2,000).

## Immunoprecipitation

Immunoprecipitation assay was performed as described previously. A549 cells were transfected with pcDNA-FLAG-Parkin (MobioTech.) for 24 h with or without DPT (16 nM DPT) and lysed in EBC buffer for 30 min. The precleared soluble supernatants were centrifuged at 12,000 × g for 20 min at 4°C to remove the debris. The lysates were mixed with 1 g of anti-FLAG (Proteintech, Cat. No. 66008-3) antibody for 16 h at 4°C, followed by precipitation of the protein A/G-agarose beads. After washing the immune complexes, the bound proteins were resuspended in sodium dodecyl sulfate sample buffer, separated by sodium dodecyl sulfate-polyacrylamide gel electrophoresis, and incubated with antibodies to HIF-1α, p21, or FLAG. The elution was analyzed by Western blotting.

## Glucose Consumption and Lactate Production Measurements

To determine whether DPT treatment altered glucose utilization or lactate production in A549 and SK-MES-1 cells, cells were plated at 2 × 10<sup>5</sup> cells per flask and incubated at 37°C with 5% CO<sub>2</sub>. After allowing the cells to attach and grow for 24 hr, 16 nM DPT was added to the flasks and incubated at 37°C for 48 hr. The medium was collected by centrifugation to remove the cells, and glucose and lactate levels were detected by standard colorimetric assay kits for glucose (K606-100, BioVision, Milpitas, CA) and lactate (K607-100, BioVision) per the manufacturer's instructions. Glucose consumption and lactate production was calculated as described in the previous report (22).

## Tumor Xenograft Assay

All animal experiments were approved by the Animal Care and Use Committee of Chengdu Medical College (No. 19JY751). Male athymic nude mice (BALB/c<sup>nu/nu</sup>) (6–7 weeks old) were purchased from the Model Animal Research Center (Nanjing, China). To generate subcutaneous tumors, 4 × 10<sup>6</sup> A549 cells were subcutaneously injected into the flanks of the mice. Tumor sizes (calculated by the formula volume = length × width<sup>2</sup>/2) and mouse weights were measured three times per week using a caliper and an electronic balancer. The animals were randomly divided into a vehicle control group and DPT treatment groups (10 or 20 mg/kg DPT, administered three times a week by intravenous injection).

## Statistical Analysis

All experiments were performed at least three times. Statistical analyses were performed with SPSS software version 18.0 (IBM Corp., Armonk, NY). Data are displayed as the mean ± standard deviation (SD). Statistical comparisons between groups were made by one-way analysis of variance with Tukey's *post hoc* test or Student's *t*-test. A *p* value < 0.05 was considered statistically significant.

## RESULTS

### DPT Dose- and Time-Dependently Inhibited the Proliferation and Promoted Apoptosis of Lung Cancer Cells

To assess the effect of DPT on lung cancer cells, A549, SK-MES-1, H460 and SPC-A1 cells were treated with various

concentrations of DPT for the indicated time periods, and CCK-8 assays were performed to measure cell viability. As shown in **Figures 1A–D**, DPT suppressed cell viability in a dose- and time-dependent manner in A549, SK-MES-1, H460, and SPC-A1 cells. To further investigate the mechanisms of DPT toxicity, we assessed apoptosis levels in these NSCLC cells following treatment with 16 nM DPT for 48 h. Caspase-3 activity was detected and found increased in the DPT-treated cells compared with the control cells (**Figures 1E–H**). These data indicated that DPT can inhibit cell proliferation and promote apoptosis of lung cancer cells.

## DPT Decreased Glycolysis in A549 and SK-MES-1 Cells

Metabolic pathways in cancer cells are usually reprogrammed to favor glycolysis, which provides a source of metabolic intermediates needed for cell proliferation (29). A549 and SK-MES-1 lung cancer cells treated with 16 nM DPT showed reduced glucose consumption and lactate production compared with the control cells (**Figures 2A–D**). Furthermore, the mRNA levels of glycolytic pathway genes, including GLUT1, lactate dehydrogenase A (LDHA), and HK2, were significantly decreased in A549 and SK-MES-1 cells following 48 h of DPT treatment (**Figures 2E, F**).

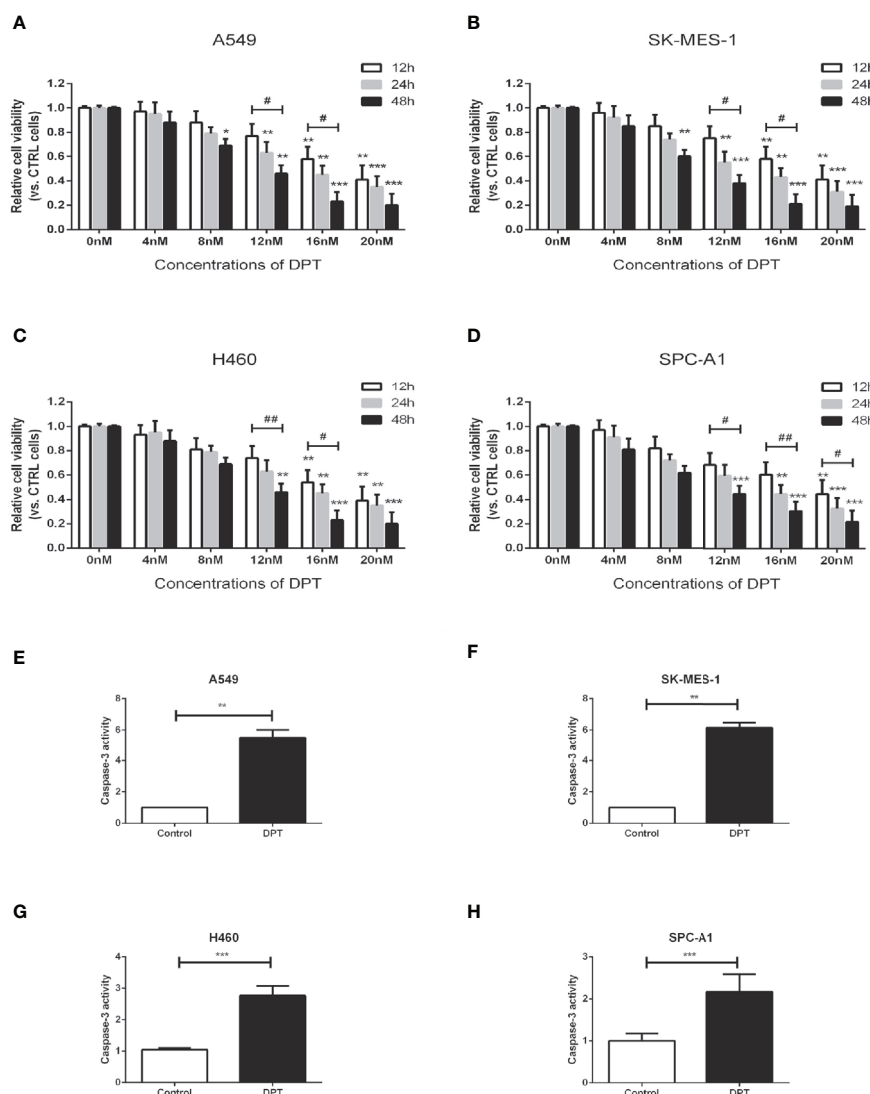


**FIGURE 1 |** DPT dose- and time-dependently inhibited the proliferation and promoted apoptosis of lung cancer cells. (**A–D**) A549, SK-MES-1, H460 and SPC-A1 cells were treated with different concentrations (0, 4, 8, 12, 16, and 20 nM) of DPT for varying lengths of time (12, 24 and 48 h). Cell viability was detected by CCK-8 assay. (**E–H**) Apoptosis of A549 and SK-MES-1 cells following treatment with 16 nM DPT for 48 h, detected using a caspase-3 activity detection kit. \* $P < 0.05$ , \*\* $P < 0.01$ , \*\*\* $P < 0.001$ , compared with the control group; # $P < 0.05$ , ## $P < 0.01$ , compared as indicated.

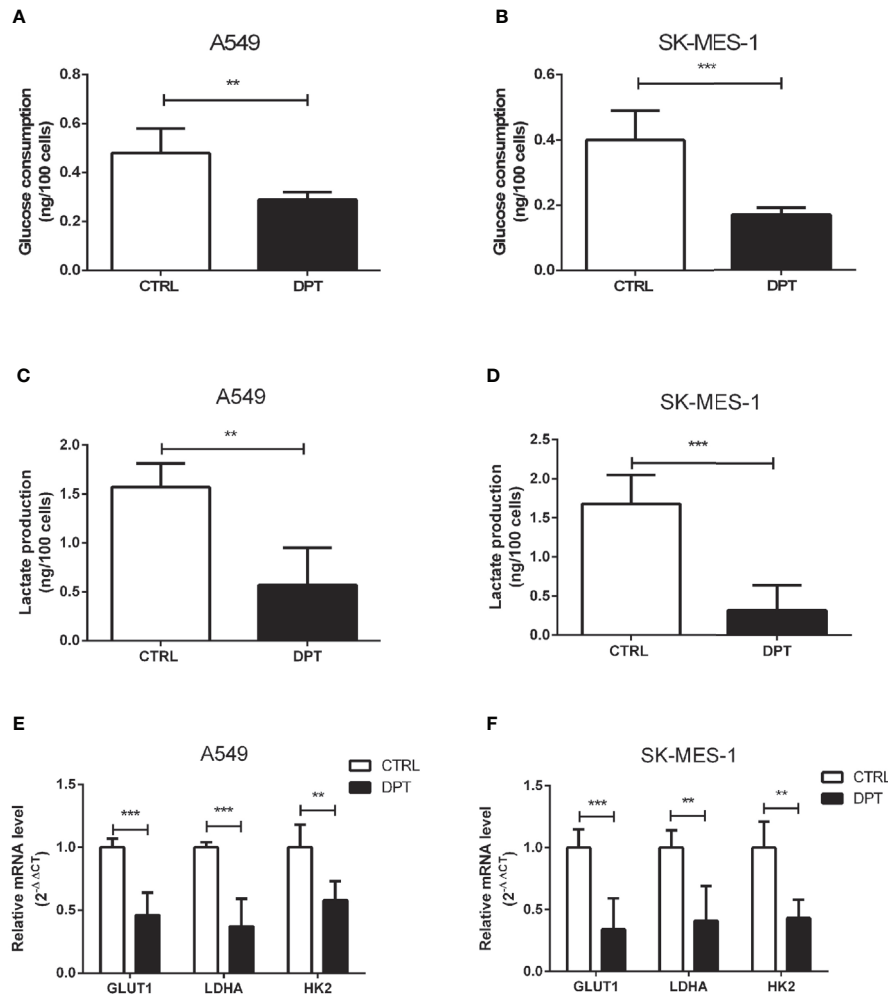


**FIGURE 2 |** DPT reduced glycolysis in A549 and SK-MES-1 cells. A549 and SK-MES-1 cells were treated with 16 nM DPT for 48 h. **(A–D)** Glucose consumption and lactate production detected using specific test kits. The mRNA levels of the glycolytic pathway-related genes including GLUT1, LDHA and HK2 in A549 **(E)** and SK-MES-1 cells **(F)** detected by qRT-PCR. \*\* $P < 0.01$ , \*\*\* $P < 0.001$ .

## DPT Blocked HIF-1 $\alpha$ Signaling in A549 and SK-MES-1 Cells

To further characterize the mechanism by which DPT inhibits A549 and SK-MES-1 cell growth, we performed an analysis on various signaling pathways using Qiagen Cignal Finder. It was found that DPT significantly inhibited HIF-1 $\alpha$  signaling in both lung cancer cell lines, indicating impairment of HIF-1 $\alpha$ -dependent signaling (**Figures 3A, B**). To examine whether DPT treatment affected HIF-1 $\alpha$  protein levels, A549 and SK-MES-1 cells were transfected with pcDNA-HIF-1 $\alpha$  (**Figures 3C, D**) in the presence or absence of DPT for 48 h. As shown in **Figures 3E, F**, DPT significantly decreased HIF-1 $\alpha$ -dependent luciferase activity following hypoxia treatment in both cell lines. Furthermore, we examined the expression of CA IX, which is a specific target gene of HIF-1 $\alpha$  and is a key mediator of tumor progression (30). As shown in **Figures 3G, H**, DPT treatment decreased CA IX mRNA expression compared with the control treatment.

## DPT Promoted HIF-1 $\alpha$ Ubiquitination and Degradation by Increasing the Interaction Between HIF-1 $\alpha$ and Parkin

As shown in **Figures 4A, B**, DPT decreased HIF-1 $\alpha$  protein level but had no effect on the mRNA levels. To investigate whether DPT negatively regulates HIF-1 $\alpha$  through ubiquitin-proteasome degradation, we examined HIF-1 $\alpha$  degradation after DPT treatment. In NSCLC cells transfected with pcDNA-HIF-1 $\alpha$ , DPT decreased HIF-1 $\alpha$  protein level and increased the ubiquitination level (**Figure 4C**). These data indicate that DPT negatively regulates HIF-1 $\alpha$  through ubiquitin-proteasome degradation. Bioinformatic analysis suggested that HIF-1 $\alpha$  is the potential targets of DPT (**Supplementary Data**), and the immunoprecipitation results demonstrated that DPT treatment promoted the interaction of HIF-1 $\alpha$  with Parkin, which is a HIF-1 $\alpha$  interacted E3 ligase (31) (**Figure 4D**), but not p21, which is another substrate of Parkin (32). These data demonstrated that

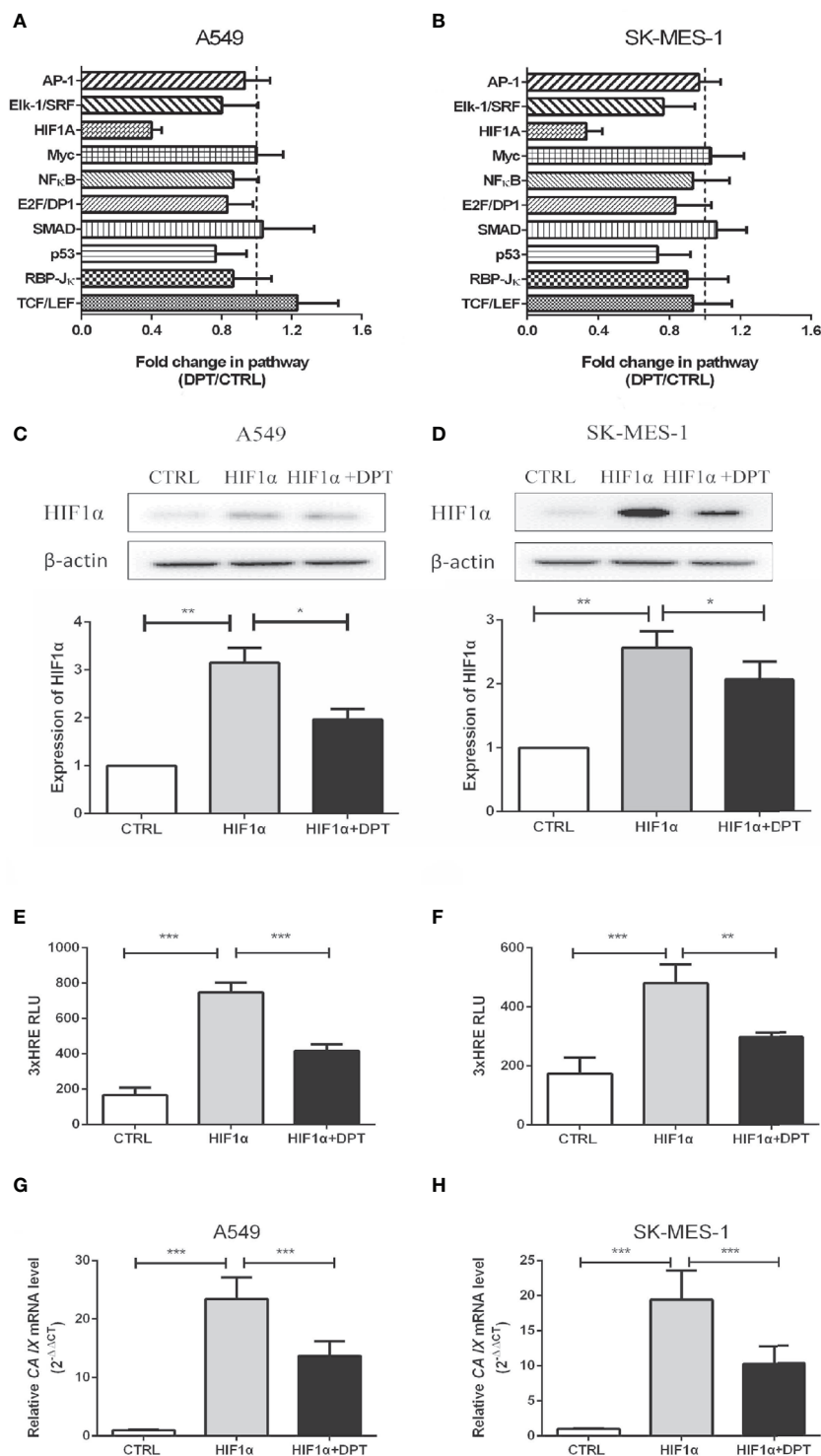


**FIGURE 3** | DPT inhibited HIF-1 $\alpha$  signaling in A549 and SK-MES-1 cells. A549 (**A**) and SK-MES-1 (**B**) cells were treated with 16 nM DPT for 48 h. The various signaling pathways were analyzed using the Signal Finder Cancer 10-Pathway Reporter Array. A549 (**C**) and SK-MES-1 (**D**) cells were transfected with a HIF-1 $\alpha$  expression plasmid in the presence or absence of 16 nM DPT for 48 h. Western blot assay detected HIF-1 $\alpha$  protein and quantified by ImageJ. (**E**, **F**) HIF-1 $\alpha$  luciferase activity detected using luciferase reporter assay. (**G**, **H**) mRNA expression of CA IX in A549 and SK-MES-1 cells detected by qRT-PCR. \* $P < 0.05$ , \*\* $P < 0.01$ , \*\*\* $P < 0.001$ .



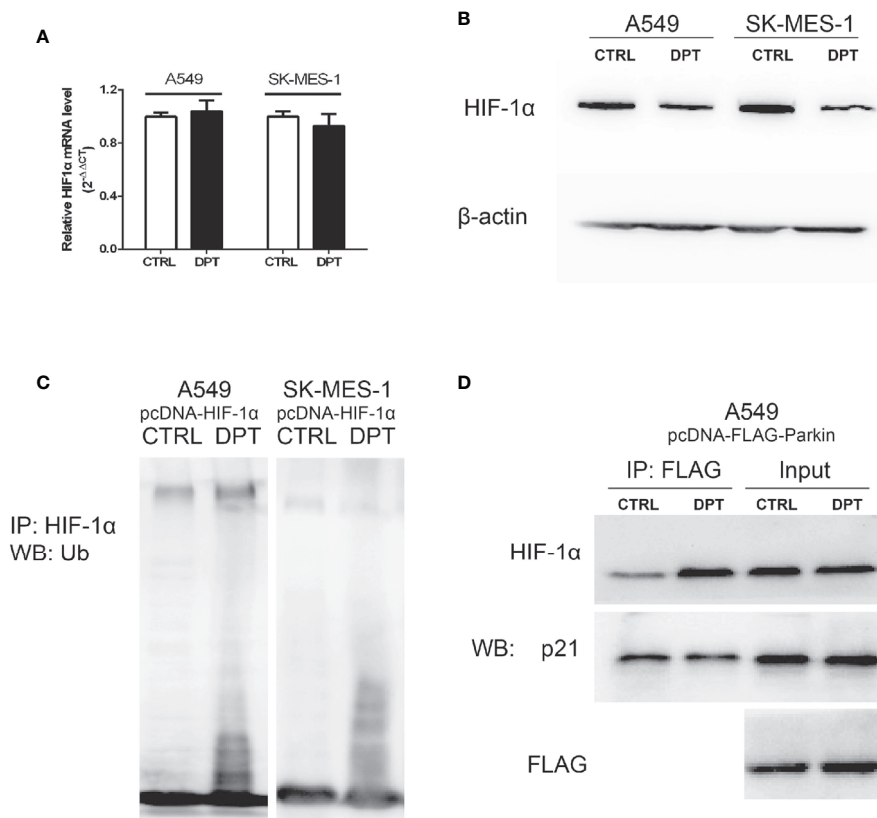


**FIGURE 4** | DPT promoted HIF-1α ubiquitination and degradation by increasing the interaction between HIF-1α and Parkin. A549 and SK-MES-1 cells (transfected with pcDNA-HIF-1α) treated with 16 nM DPT for 48 hr. **(A, B)** HIF-1α mRNA detected by qRT-PCR, and HIF-1α protein detected by Western blot. **(C)** *In vitro* ubiquitination assay detected the effect of DPT on HIF-1α ubiquitination in A549 and SK-MES-1 cells. **(D)** Immunoprecipitation detected the interaction of Parkin with HIF-1α and p21.

DPT targets HIF-1α and increases the interaction between HIF-1α and Parkin, followed by HIF-1α degradation.

## DPT Inhibited HIF-1α Overexpression-Induced Cell Growth and Glycolysis

To confirm whether DPT-induced reduction in cell growth and glycolytic flux is mediated through inhibition of HIF-1α signaling, A549 and SK-MES-1 cells were treated with 16 nM DPT for 48 h after transfection with a HIF-1α expression plasmid. HIF-1α overexpression increased cell viability, glucose consumption and lactate production, all of which could be reversed by DPT treatment (**Figures 5A–C**). These data indicated that HIF-1α is required for the DPT-induced inhibition of cell growth and glycolysis.

## DPT Inhibited A549 Xenograft Growth *In Vivo*

We further examined the effect of DPT on HIF-1α and glycolysis in A549 xenografts in nude mice. The mice were randomly divided into three groups with 5 animals in each group. As shown in **Figures 6A–C**, DPT (10 mg/kg or 20 mg/kg) significantly reduced xenograft volumes and weights. Additionally, DPT (10 or 20 mg/kg) decreased GLUT1, LDHA and HK2 mRNA levels compared with

the control treatment (**Figure 6D**). These findings indicated that DPT inhibited tumor growth and glycolysis *in vivo*.

## DISCUSSION

This study investigated the antitumor effect and potential mechanism of action of DPT in NSCLC both *in vitro* and *in vivo*. The data revealed that DPT has a potent growth-inhibitory effect on A549 and SK-MES-1 cells. Additionally, DPT inhibited the growth of A549 xenograft *in vivo*. These findings indicated that DPT may be a potential drug for NSCLC treatment. Furthermore, our data showed that DPT functions as an anticancer agent in NSCLC by increasing HIF-1α degradation to reduce glycolysis. Here, we showed that DPT suppresses HIF-1α activation at the protein level in NSCLC cells. Moreover, based on the structure of DPT, two state-of-the-art computational methods (33, 34) were employed to predict its potential targets, and HIF-1α was one of the most represented targets. Immunoprecipitation indicated that DPT increased the interaction between HIF-1α and Parkin, and the E3 ubiquitin ligase promoted HIF-1α protein ubiquitination and degradation.

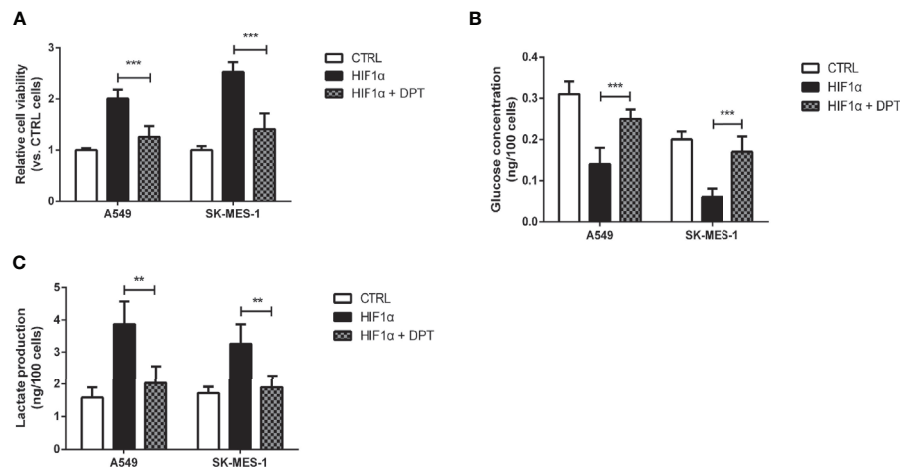


**FIGURE 5 |** DPT inhibited HIF-1 $\alpha$ -induced cell growth and glycolysis. A549 and SK-MES-1 cells treated with 16 nM DPT and the HIF-1 $\alpha$  plasmid for 48 h. **(A)** Cell viability detected by CCK-8 assay. **(B, C)** Glucose consumption and lactate production detected using specific test kits. \*\* $P < 0.01$ , \*\*\* $P < 0.001$ .

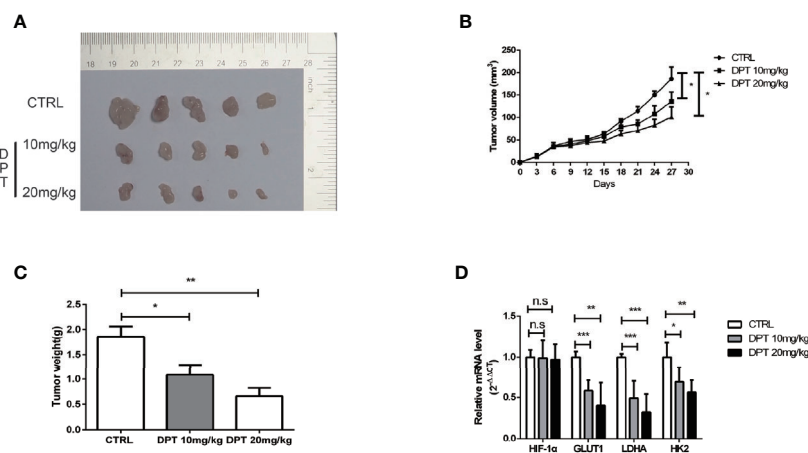


**FIGURE 6 |** DPT inhibited A549 xenograft growth *in vivo*. Mice were randomly divided into the vehicle control group and DPT treatment groups (10 or 20 mg/kg DPT). **(A, B)** *In vivo* A549 tumor and control xenograft growth curve. Tumor sizes were measured three times per week with a calliper and calculated using the formula volume = (length  $\times$  width<sup>2</sup>)/2. **(C)** The average tumor weight of the DPT treatment (10 or 20 mg/kg) and control xenografts at the end point. **(D)** The mRNA level of HIF-1 $\alpha$  and glycolytic pathway-related genes including GLUT1, LDHA, and HK2 detected by qRT-PCR. \* $P < 0.01$ , \*\* $P < 0.01$ , \*\*\* $P < 0.001$ , n.s., not significant.

The role of DPT has been investigated in multiple cancers, including breast cancer (35), osteosarcoma (23), gastric cancer (36) and NSCLC (37). The findings suggested that DPT has a wide range of effect on tumor development, such as inhibiting tumor growth, inducing cell cycle arrest, inhibiting angiogenesis and promoting apoptosis. A previous study also reported that DPT triggers necroptosis in human NSCLC NCI-H460 cells (37). To assess the potential antitumor effect of DPT, this study investigated its time- and dose-dependent activity on lung carcinoma cell lines. Our data demonstrated that DPT inhibited cell viability and induced apoptosis. Additionally, Qiagen Cignal Finder was used to predict the signaling

pathways that were altered following DPT treatment by which we found that HIF-1 $\alpha$  was a DPT target.

HIF-1 $\alpha$  is degraded under normoxic condition *via* the proteasome pathway but is stabilized under hypoxia (38). To date, a series of studies have reported that HIF-1 $\alpha$  expression could be an important predictor of tumor prognosis, including for hepatocellular carcinoma, cervical carcinoma and lung cancer (39–41). A previous study also reported that HIF-1 $\alpha$  is overexpressed in NSCLC and that targeting the HIF pathway may be a promising approach for NSCLC management (42). In other reports, DPT has been shown to inhibit cancer cell cycle/microtubule formation and induce apoptosis/autophagy both *in*

*vitro* and *in vivo* (23, 43–46). Our study supports previous data showing that DPT acts as an anticancer agent through degradation of HIF-1 $\alpha$ .

HIF-1 $\alpha$  is a master transcriptional regulator of glycolysis that controls the expression of a multitude of glycolytic genes, including HK2, GLUT1, PGM, PGK1 and LDHA (38). Cancer cells exhibit significant alterations in glucose metabolism compared with normal cells (47). Previous studies have indicated that cancer cells use aerobic glycolysis (or Warburg metabolism) to facilitate cell proliferation by providing sufficient metabolic intermediates (48). Although some studies have shown that DPT triggers necroptosis in human NSCLC NCI-H460 cells (37), whether DPT inhibits glycolysis in NSCLC cells is unclear. In this study, we demonstrated that HIF-1 $\alpha$  overexpression increased glucose consumption and induced lactate production, both of them could be reversed by DPT treatment. Additionally, DPT decreased the expression of genes in the glycolytic pathway. To exclude mycoplasma infection, which was found to cause major shifts in cellular metabolism (49), mycoplasma testing was performed on the cell lines utilized in this study.

As both HIF-1 $\alpha$  and DPT have been reported to be associated with cancer cell cycle progression (43, 50), cancer cell microtubule destabilization (45, 51), cancer cell necroptosis (37, 52) and autophagy (23, 53), our data suggest that the effect of DPT on cancer cells might occur through the degradation of HIF-1 $\alpha$ . Whether DPT inhibits the NSCLC cell cycle progression, microtubule destabilization, necroptosis and autophagy by abrogating HIF-1 $\alpha$  requires further study.

Taken together, our study demonstrated that DPT inhibits cell proliferation of NSCLC by inhibiting glycolysis *via* downregulation of HIF-1 $\alpha$  expression. Our *in vivo* experiments supported the notion that DPT could be a potential candidate for NSCLC therapy.

## DATA AVAILABILITY STATEMENT

The original contributions presented in the study are included in the article/**Supplementary Material**. Further inquiries can be directed to the corresponding authors.

## REFERENCES

- Bray F, Ferlay J, Soerjomataram I, Siegel R, Torre L, Jemal A. Global cancer statistics 2018: GLOBOCAN estimates of incidence and mortality worldwide for 36 cancers in 185 countries. *CA: Cancer J Clin* (2018) 68(6):394–424. doi: 10.3322/caac.21492
- Siegel RL, Miller KD, Jemal A. Cancer statistics, 2020. *CA: Cancer J Clin* (2020) 70(1):7–30. doi: 10.3322/caac.21590
- Radziszewska A, Karczmarek-Borowska B, Gradalska-Lampart M, Filip A. [Epidemiology, prevention and risk morbidity factors for lung cancer]. *Polski Merkuriusz Lekarski Organ Polskiego Towarzystwa Lekarskiego* (2015) 38(224):113–8.
- Krawczyk P, Nicos M, Ramlau R, Powrozek T, Wojas-Krawczyk K, Sura S, et al. The incidence of EGFR-activating mutations in bone metastases of lung adenocarcinoma. *Pathol Oncol Res POR* (2014) 20(1):107–12. doi: 10.1007/s12253-013-9667-4
- Samet J. Is the Incidence of Adenocarcinoma of the Lung Rising in Never Smokers? *J Natl Cancer Institute* (2017) 109(7). doi: 10.1093/jnci/djw325
- Boloker G, Wang C, Zhang J. Updated statistics of lung and bronchus cancer in United States (2018). *J Thoracic Dis* (2018) 10(3):1158–61. doi: 10.21037/jtd.2018.03.15
- Torre L, Siegel R, Jemal A. Lung Cancer Statistics. *Adv Exp Med Biol* (2016) 893:1–19. doi: 10.1007/978-3-319-24223-1\_1
- Hanahan D, Weinberg R. Hallmarks of cancer: the next generation. *Cell* (2011) 144(5):646–74. doi: 10.1016/j.cell.2011.02.013
- Vander HM, Cantley L, Thompson C. Understanding the Warburg effect: the metabolic requirements of cell proliferation. *Science* (2009) 324(5930):1029–33. doi: 10.1126/science.1160809
- Asgari Y, Zabihpour Z, Salehzadeh-Yazdi A, Schreiber F, Masoudi-Nejad A. Alterations in cancer cell metabolism: the Warburg effect and metabolic adaptation. *Genomics* (2015) 105(5–6):275–81. doi: 10.1016/j.ygeno.2015.03.001
- Li XB, Gu JD, Zhou QH. Review of aerobic glycolysis and its key enzymes - new targets for lung cancer therapy. *Thoracic Cancer* (2015) 6(1):17–24. doi: 10.1111/1759-7714.12148

## ETHICS STATEMENT

The animal study was reviewed and approved by the Animal Care and Use Committee of Chengdu Medical College.

## AUTHOR CONTRIBUTIONS

Conceptualization, WZ. Methodology, YY, LL, and JS. Validation, YY, LL, SW, and JS. Formal analysis, NH and HL. Investigation, NH, YY, and WZ. Resources, HL. Data, YY and LL. Writing—original draft preparation, NH and WZ. Writing—review and editing, YY, WZ, and NH. Supervision, NH and WZ. Funding acquisition, NH and WZ. All authors contributed to the article and approved the submitted version.

## FUNDING

This work was supported by the National Natural Science Foundation of China (81602636), Key project of science of Sichuan Education Department (18ZA0164), Natural Science Foundation of Chengdu Medical College (CYZ18-04), National Key Clinical Specialty Training Program of The First Affiliated Hospital of Chengdu Medical College (CYFY2018GLPHX02), Special key fund of The First Affiliated Hospital of Chengdu Medical College (CYFY2019ZD02), Research Fund of Development and Regeneration Key Laboratory of Sichuan Province (SYS18-08), Scientific Research Project of Sichuan Provincial Administration of Traditional Chinese Medicine (2020JC0021) and Miaozi project of science and Technology Department of Sichuan Province (2018RZ0095).

## SUPPLEMENTARY MATERIAL

The Supplementary Material for this article can be found online at: <https://www.frontiersin.org/articles/10.3389/fonc.2021.629543/full#supplementary-material>

12. Zhao W, Li W, Dai W, Huang N, Qiu J. LINK-A promotes cell proliferation through the regulation of aerobic glycolysis in non-small-cell lung cancer. *OncoTarg Ther* (2018) 11:6071–80. doi: 10.2147/ott.s171216
13. Chen HF, Wu LX, Li XF, Zhu YC, Wang WX, Xu CW, et al. Ginsenoside compound K inhibits growth of lung cancer cells via HIF-1 $\alpha$ -mediated glucose metabolism. *Cell Mol Biol* (2019) 65(4):48–52. doi: 10.14715/cmb/2019.65.4.8
14. Lee K, Kang J, Park S, Jin Y, Chung K, Kim H, et al. LW6, a novel HIF-1 inhibitor, promotes proteasomal degradation of HIF-1 $\alpha$  via upregulation of VHL in a colon cancer cell line. *Biochem Pharmacol* (2010) 80(7):982–9. doi: 10.1016/j.bcp.2010.06.018
15. Kong X, Lin Z, Liang D, Fath D, Sang N, Caro J. Histone deacetylase inhibitors induce VHL and ubiquitin-independent proteasomal degradation of hypoxia-inducible factor 1 $\alpha$ . *Mol Cell Biol* (2006) 26(6):2019–28. doi: 10.1128/MCB.26.6.2019–2028.2006
16. Courtney R, Ngo D, Malik N, Ververis K, Tortorella S, Karagiannis T. Cancer metabolism and the Warburg effect: the role of HIF-1 and PI3K. *Mol Biol Rep* (2015) 42(4):841–51. doi: 10.1007/s11033-015-3858-x
17. Stubbs M, Griffiths J. The altered metabolism of tumors: HIF-1 and its role in the Warburg effect. *Adv Enzyme Regul* (2010) 50(1):44–55. doi: 10.1016/j.advenzreg.2009.10.027
18. Masoud G, Li W. HIF-1 $\alpha$  pathway: role, regulation and intervention for cancer therapy. *Acta Pharm Sin B* (2015) 5(5):378–89. doi: 10.1016/j.apsb.2015.05.007
19. Sang N, Stiehl D, Bohensky J, Leshchinsky I, Srinivas V, Caro J. MAPK signaling up-regulates the activity of hypoxia-inducible factors by its effects on p300. *J Biol Chem* (2003) 278(16):14013–9. doi: 10.1074/jbc.M209702200
20. Bae M, Ahn M, Jeong J, Bae M, Lee Y, Bae S, et al. Jab1 interacts directly with HIF-1 $\alpha$  and regulates its stability. *J Biol Chem* (2002) 277(1):9–12. doi: 10.1074/jbc.C100442200
21. Isaacs J, Jung Y, Mimnaugh E, Martinez A, Cuttitta F, Neckers L. Hsp90 regulates a von Hippel Lindau-independent hypoxia-inducible factor-1  $\alpha$  degradative pathway. *J Biol Chem* (2002) 277(33):29936–44. doi: 10.1074/jbc.M204733200
22. Zhao W, Chang C, Cui Y, Zhao X, Yang J, Shen L, et al. Steroid receptor coactivator-3 regulates glucose metabolism in bladder cancer cells through coactivation of hypoxia inducible factor 1 $\alpha$ . *J Biol Chem* (2014) 289(16):11219–29. doi: 10.1074/jbc.M113.535989
23. Kim S, Son K, Kim K, Yu S, Park S, Kim Y, et al. Deoxypodophyllotoxin induces cytoprotective autophagy against apoptosis via inhibition of PI3K/AKT/mTOR pathway in osteosarcoma U2OS cells. *Pharmacol Rep PR* (2017) 69(5):878–84. doi: 10.1016/j.pharep.2017.04.007
24. Kwak AW, Lee MH, Yoon G, Cho SS, Choi JS, Chae JJ, et al. Deoxypodophyllotoxin, a Lignan from *Anthriscus sylvestris*, Induces Apoptosis and Cell Cycle Arrest by Inhibiting the EGFR Signaling Pathways in Esophageal Squamous Cell Carcinoma Cells. *Int J Mol Sci* (2020) 21(18):6854. doi: 10.3390/ijms21186854
25. Gamage CDB, Park SY, Yang Y, Zhou R, Tas I, Bae WK, et al. Deoxypodophyllotoxin Exerts Anti-Cancer Effects on Colorectal Cancer Cells Through Induction of Apoptosis and Suppression of Tumorigenesis. *Int J Mol Sci* (2019) 20(11):2612. doi: 10.3390/ijms20112612
26. Hu S, Zhou Q, Wu WR, Duan YX, Gao ZY, Li YW, et al. Anticancer effect of deoxypodophyllotoxin induces apoptosis of human prostate cancer cells. *Oncol Lett* (2016) 12(4):2918–23. doi: 10.3892/ol.2016.4943
27. Ma D, Lu B, Feng C, Wang C, Wang Y, Luo T, et al. Deoxypodophyllotoxin triggers parthanatos in glioma cells via induction of excessive ROS. *Cancer Lett* (2016) 371(2):194–204. doi: 10.1016/j.canlet.2015.11.044
28. Wu X, Zhang C, Deng L, Xiao J, Yuan X, Zhang B, et al. Overexpressed D2 Dopamine Receptor Inhibits Non-Small Cell Lung Cancer Progression through Inhibiting NF- $\kappa$ B Signaling Pathway. *Cell Physiol Biochem Int J Exp Cell Physiol Biochem Pharmacol* (2018) 48(6):2258–72. doi: 10.1159/000492644
29. Liu T, Yin H. PDK1 promotes tumor cell proliferation and migration by enhancing the Warburg effect in non-small cell lung cancer. *Oncol Rep* (2017) 37(1):193–200. doi: 10.3892/or.2016.5253
30. Sowa T, Menju T, Chen-Yoshikawa T, Takahashi K, Nishikawa S, Nakanishi T, et al. Hypoxia-inducible factor 1 promotes chemoresistance of lung cancer by inducing carbonic anhydrase IX expression. *Cancer Med* (2017) 6(1):288–97. doi: 10.1002/cam4.991
31. Liu J, Zhang C, Zhao Y, Yue X, Wu H, Huang S, et al. Parkin targets HIF-1 $\alpha$  for ubiquitination and degradation to inhibit breast tumor progression. *Nat Commun* (2017) 8(1):1823. doi: 10.1038/s41467-017-01947-w
32. Park KR, Yun JS, Park MH, Jung YY, Yeo JJ, Nam KT, et al. Loss of parkin reduces lung tumor development by blocking p21 degradation. *PLoS One* (2019) 14(5):e0217037. doi: 10.1371/journal.pone.0217037
33. Gfeller D, Michielin O, Zoete V. Shaping the interaction landscape of bioactive molecules. *Bioinformatics* (2013) 29(23):3073–9. doi: 10.1093/bioinformatics/btt540
34. Keiser M, Roth B, Armbruster B, Ernsberger P, Irwin J, Shoichet B. Relating protein pharmacology by ligand chemistry. *Nat Biotechnol* (2007) 25(2):197–206. doi: 10.1038/nbt1284
35. Khaled M, Belaoui G, Jiang Z, Zhu X, Zhang L. Antitumor effect of Deoxypodophyllotoxin on human breast cancer xenograft transplanted in BALB/c nude mice model. *J Infect Chemother Off J Japan Soc Chemother* (2016) 22(10):692–6. doi: 10.1016/j.jiac.2016.07.017
36. Wang Y, Xu Y, Jiang Z, Guerram M, Wang B, Zhu X, et al. Deoxypodophyllotoxin induces G2/M cell cycle arrest and apoptosis in SGC-7901 cells and inhibits tumor growth in vivo. *Molecules* (2015) 20(1):1661–75. doi: 10.3390/molecules20011661
37. Wu M, Jiang Z, Duan H, Sun L, Zhang S, Chen M, et al. Deoxypodophyllotoxin triggers necroptosis in human non-small cell lung cancer NCI-H460 cells. *Biomed Pharmacother Biomed Pharmacother* (2013) 67(8):701–6. doi: 10.1016/j.biopha.2013.06.002
38. Tickoo S, Milowsky M, Dhar N, Dudas M, Gallagher D, Al-Ahmadie H, et al. Hypoxia-inducible factor and mammalian target of rapamycin pathway markers in urothelial carcinoma of the bladder: possible therapeutic implications. *BJU Int* (2011) 107(5):844–9. doi: 10.1111/j.1464-410X.2010.09517.x
39. Li Y, Zhang N, Hu X, Chen J, Rao M, Wu L, et al. Evodiamine induces apoptosis and promotes hepatocellular carcinoma cell death induced by vorinostat via downregulating HIF-1 $\alpha$  under hypoxia. *Biochem Biophys Res Commun* (2018) 489(3):481–6. doi: 10.1016/j.bbrc.2018.03.004
40. Zhang L, Huang S, Feng Y, Wan T, Gu H, Xu J, et al. The Bidirectional Regulation between MYL5 and HIF-1 $\alpha$  Promotes Cervical Carcinoma Metastasis. *Theranostics* (2017) 7(15):3768–80. doi: 10.7150/thno.20796
41. Zhu J, Huang Z, Zhang M, Wang W, Liang H, Zeng J, et al. HIF-1 $\alpha$  promotes ZEB1 expression and EMT in a human bladder cancer lung metastasis animal model. *Oncol Lett* (2018) 15(3):3482–9. doi: 10.3892/ol.2018.7764
42. Giatromanolaki A, Koukourakis M, Sivridis E, Turley H, Talks K, Pezzella F, et al. Relation of hypoxia inducible factor 1  $\alpha$  and 2  $\alpha$  in operable non-small cell lung cancer to angiogenic/molecular profile of tumours and survival. *Br J Cancer* (2001) 85(6):881–90. doi: 10.1054/bjoc.2001.2018
43. Xiao M, Fan X, Fu Y, Zhou Y, Liu S, Peng S. Deoxypodophyllotoxin induces cell cycle arrest and apoptosis in human cholangiocarcinoma cells. *Oncol Lett* (2018) 16(3):3177–82. doi: 10.3892/ol.2018.8978
44. Chen Y, Zhao K, Liu F, Li Y, Zhong Z, Hong S, et al. Predicting Antitumor Effect of Deoxypodophyllotoxin in NCI-H460 Tumor-Bearing Mice on the Basis of In Vitro Pharmacodynamics and a Physiologically Based Pharmacokinetic-Pharmacodynamic Model. *Drug Metab Disposition: Biol Fate Chem* (2018) 46(6):897–907. doi: 10.1124/dmd.117.079830
45. Zang X, Wang G, Cai Q, Zheng X, Zhang J, Chen Q, et al. A Promising Microtubule Inhibitor Deoxypodophyllotoxin Exhibits Better Efficacy to Multidrug-Resistant Breast Cancer than Paclitaxel via Avoiding Efflux Transport. *Drug Metab Disposition: Biol Fate Chem* (2018) 46(5):542–51. doi: 10.1124/dmd.117.079442
46. Kim S, Kim K, Park S, Yu S, Kim Y, Nam H, et al. Mitochondrial ROS activates ERK/autophagy pathway as a protected mechanism against deoxypodophyllotoxin-induced apoptosis. *Oncotarget* (2017) 8(67):11581–96. doi: 10.18632/oncotarget.22875
47. Vander HM, Lunt S, Dayton T, Fiske B, Israelsen W, Mattaini K, et al. Metabolic pathway alterations that support cell proliferation. *Cold Spring Harbor Symp Quantitative Biol* (2011) 76:325–34. doi: 10.1101/sqb.2012.76.010900



48. Schulze A, Harris A. How cancer metabolism is tuned for proliferation and vulnerable to disruption. *Nature* (2012) 491(7424):364–73. doi: 10.1038/nature11706
49. Geller LT, Barzily-Rokni M, Danino T, Jonas OH, Shental N, Nejman D, et al. Potential role of intratumor bacteria in mediating tumor resistance to the chemotherapeutic drug gemcitabine. *Science* (2017) 357(6356):1156–60. doi: 10.1126/science.aah5043
50. Wang Q, Li L, Gao G, Wang G, Qu L, Li J, et al. HIF-1 $\alpha$  up-regulates NDRG1 expression through binding to NDRG1 promoter, leading to proliferation of lung cancer A549 cells. *Mol Biol Rep* (2013) 40(5):3723–9. doi: 10.1007/s11033-012-2448-4
51. Stengel C, Newman S, Leese M, Thomas M, Potter B, Reed M, et al. The In Vitro and In Vivo Activity of the Microtubule Disruptor STX140 Is Mediated by Hif-1  $\alpha$  and CAIX Expression. *Anticancer Res* (2015) 35(10):5249–61.
52. Huang C, Kuo W, Huang Y, Lee T, Yu L. Resistance to hypoxia-induced necroptosis is conferred by glycolytic pyruvate scavenging of mitochondrial superoxide in colorectal cancer cells. *Cell Death Dis* (2013) 4:e622. doi: 10.1038/cddis.2013.149
53. Seok JY, Jeong YJ, Hwang SK, Kim CH, Magae J, Chang YC. Upregulation of AMPK by 4-O-methylascochlorin promotes autophagy via the HIF-1 $\alpha$  expression. *J Cell Mol Med* (2018) 22(12):6345–56. doi: 10.1111/jcmm.13933

**Conflict of Interest:** The authors declare that the research was conducted in the absence of any commercial or financial relationships that could be construed as a potential conflict of interest.

The reviewer LZ declared a shared affiliation, with no collaboration, with one of the authors ZY to the handling editor at the time of the review.

Copyright © 2021 Yang, Liu, Sun, Wang, Yang, Li, Huang and Zhao. This is an open-access article distributed under the terms of the Creative Commons Attribution License (CC BY). The use, distribution or reproduction in other forums is permitted, provided the original author(s) and the copyright owner(s) are credited and that the original publication in this journal is cited, in accordance with accepted academic practice. No use, distribution or reproduction is permitted which does not comply with these terms.



# Advances in Optical Aptasensors for Early Detection and Diagnosis of Various Cancer Types

Qurat ul ain Zahra<sup>1,2</sup>, Qaiser Ali Khan<sup>3</sup> and Zhaofeng Luo<sup>1\*</sup>

<sup>1</sup> Core Facility Center for Life Sciences, Department of Biochemistry and Molecular Biology, School of Life Sciences, University of Sciences and Technology of China, Hefei, China, <sup>2</sup> Hefei National Lab for Physical Sciences at the Microscale and the Centers for Biomedical Engineering, University of Science and Technology of China, Hefei, China, <sup>3</sup> Institute of Chemistry of New Materials, Universität Osnabrück, Osnabrück, Germany

## OPEN ACCESS

### Edited by:

Yingyan Yu,  
Shanghai Jiao Tong University, China

### Reviewed by:

Tao Bing,  
Institute of Chemistry (CAS), China  
Xinhui Lou,  
Capital Normal University, China

### \*Correspondence:

Zhaofeng Luo  
lzf@ustc.edu.cn

### Specialty section:

This article was submitted to  
Pharmacology of Anti-Cancer Drugs,  
a section of the journal  
Frontiers in Oncology

**Received:** 22 November 2020

**Accepted:** 04 January 2021

**Published:** 25 February 2021

### Citation:

Zahra Qua, Khan QA and Luo Z (2021)  
Advances in Optical Aptasensors for  
Early Detection and Diagnosis of  
Various Cancer Types.  
Front. Oncol. 11:632165.  
doi: 10.3389/fonc.2021.632165

Cancer is a life-threatening concern worldwide. Sensitive and early-stage diagnostics of different cancer types can make it possible for patients to get through the best available treatment options to combat this menace. Among several new detection methods, aptamer-based biosensors (aptasensors) have recently shown promising results in terms of sensitivity, identification, or detection of either cancerous cells or the associated biomarkers. In this mini-review, we have summarized the most recent (2016–2020) developments in different approaches belonging to optical aptasensor technologies being widely employed for their simple operation, sensitivity, and early cancer diagnostics. Finally, we shed some light on limitations, advantages, and current challenges of aptasensors in clinical diagnostics, and we elaborated on some future perspectives.

**Keywords:** optical aptasensors, early cancer diagnostics, cancer biomarkers, fluorescence aptasensors, chemiluminescence, SERS cancer aptasensors, colorimetric aptasensors, SPR aptasensors

## BACKGROUND AND INTRODUCTION

Cancer is one of the main life-threatening concerns both in developed and developing countries around the world. Stomach, breast, liver, colorectal, and lung cancer are the most common cancer types causing a high mortality rate every year (1). Abnormal, uncontrolled cell division, apoptotic resistance, and accumulation of increasing genetic mutations are the leading causes of tumor development. Specific proteins are expressed on the surface of cancerous cells, which are not expressed by healthy normal cells or sometimes expressed in smaller amounts. These surface proteins are known as cancer biomarkers and are used to detect cancer (2). Since cancer is a deadly disease, sensitive and early-stage diagnostics can make it possible for the patients to get through the best available treatment options to combat this menace for longer survival (3). Currently, different cancer diagnostic tests are available including mammography, colonoscopy, cervical cytology, prostate-specific antigen, immunohistochemistry, molecular detection, cancer imaging (IHC), and many more, and all have some associated limitations that may produce unauthentic results (4, 5). Bing et al. screened a novel BG2 (G-rich) aptamer by systematic evolution of ligands by exponential enrichment (cell-SELEX). Their ssDNA aptamer as molecular probe could isolate alkaline phosphatase heterodimers (from cell lysate) present on the surface of various cancer cells

(both *in vivo* and *in vitro*) (6). In another report, Bing et al. introduced a wy-5a aptamer that specifically binds prion proteins (reference markers) on tumor cells and tissues. They demonstrated that it could serve well as a probe in diagnostics and therapy of breast and prostate cancers (7). Consequently, there was an increasing demand to develop a precise, cost-effective, sensitive, and early-stage cancer detection method for various cancer types to prevent malignancies.

Oligonucleotide aptamers are single-stranded, short, nucleic acid (DNA or RNA) sequences with an ability to rearrange into a three-dimensional unique structure for highly specific binding to their particular targets ranging from proteins (8, 9) to even whole cells (10). A variety of aptamers in the last two decades have been screened against different cancer biomarker proteins overexpressed on the tumor surface. Some high-affinity aptamers specific for certain cancer biomarkers are used in early cancer diagnostic sensing platforms (11). The targets are purified for further detection by aptamers, which are used as ligands making targets a potential new biomarker. The binding of aptamers to unknown molecular signatures of a particular cell leads to the discovery of potential biomarkers (12). Aptamers as biorecognition elements in biosensors have shaped a new kind of sensing technology known as aptasensors (13) and exhibit an exceptional recognition ability against their particular target types (14). They can be used in a variety of applications such as the detection of chemicals, disease markers, and foodborne pathogens (15). Aptasensors are classified based on their signal transduction modalities including electrical, micromechanical, mass-sensitive, and optical aptasensors (16). Numerous optical aptasensor types have been developed to bind and identify different cancer biomarkers or cells. In this mini-review, we have focused on recent advances in different types of optical aptasensors being used for early detection of cancer.

## OPTICAL APTASENSORS IN EARLY CANCER DETECTION

Optical methods are advantageous because they show a quick response, simple operation, and high sensitivity. Optical aptasensors involve aptamers as a biorecognition element along with various optical approaches as signal transduction element (17). Optical aptasensors can be classified based on their luminescence changes and light absorption as a result of interaction with different analytes. These aptasensors usually have minute reagent requirements, cost-effectiveness, simple labeling, and swift procedures (18). Optical aptasensors are categorized based on different optical detection methods used to diagnose different cancer types at early stages and are discussed below. Aptamer name, their particular target cancer biomarkers/cells, and the limit of detection/sensitivity have been summarized in **Table 1** for all (2016–2020) reports discussed in this mini-review.

### Fluorescence-Based Optical Aptasensors

Fluorescence is an optical approach commonly employed to construct aptasensors for their low costs, high sensitivity, operation simplicity, and high efficiency (54). Lei et al.

introduced a “nanodoctor” known as “smart split aptamer-based activatable theranostic probe (SATP)” for *in vivo* cancer imaging that not only can activate fluorescence signals as a result of interaction with its analyte but also releases the drug (50). A graphene oxide-based label-free aptasensor for quantitative diagnostics of rare CCRF-CEM cells was employed by Xiao et al. CTCESA-based (cell-triggered cyclic enzymatic signal amplification) fluorescent aptasensors show a better selectivity and sensitivity for clinical and preclinical cancer detection in comparison to normal fluorescence-based aptasensors (32). Hamd-Ghadareh et al. constructed an antibody-ssDNA aptamer-based fluorescence sandwich-type ultrasensitive biosensor for CA125 early detection (22). A fluorescent “turn on” aptasensor based on fluorophore-labeled protein-aptamers and MoS<sub>2</sub> (molybdenum disulfide) nanosheets was assembled by Zhao et al. for a highly sensitive and rapid CEA protein detection (27). In addition, Lai et al., Tan et al., and many others have recently published articles based on fluorescent aptasensors (51, 52). Another label-free, versatile “turn on” fluorescent aptasensor for HER2 early detection was fabricated by Zhang et al. (33). Exosomes for gastric cancer detection can be efficiently identified by a method designed by Huang et al. (37). A multiplex, competitive aptasensor based on fluorescent nanoparticles count was proposed by Pei et al. to detect various cancer biomarkers (30). Li et al. designed a platform not only efficient in exosomal protein profiling but also filling the technological innovation gap to facilitate the exosomal detection assays and shed light on methods for early detection of cancer such as liquid biopsy (47). An aptamer dependent fluorescence polarization technique was established by Zhang et al. that allows direct quantification of exosomes in human plasma without separation. It minimizes the operation time by simplifying the quantification without losing exosomes from the sample during separation (55).

### Chemiluminescence Based Optical Aptasensors

A phenomenon where emitted light from a substance is not because of heat is called luminescence, which can be categorized based on the energy (trigger) sources into electrochemiluminescence (ECL) and chemiluminescence (CL). Both are widely used in the development of aptasensors employed in cancer biomarkers detection (56). Several CL aptasensors for early cancer detection have already been introduced (57). It is considered the most sensitive optical approach because of excellent results (58). Jie and Jie described a quantum dots (QDs) nanocluster based ECL signal probe with a great potential for early cancer diagnosis in clinical samples (34). Wang et al. designed a ratiometric dual-signaling electrochemiluminescence aptasensor exhibiting good reproducibility, high selectivity, and stability against their target cancer cells among non-target cancer cells (35). A simple, all in one, cost-effective, easy to operate, and portable medical platform to be used in hospitals and homes was designed by Khang et al. for early-stage breast cancer diagnostics (31). Another competitive, novel GO@AuNRs-GOD-SA nanoprobe based ECL aptasensor for PSA detection was demonstrated by Cao et al. (44). It is considered to be an excellent advancement for the detection of trace-level disease

**TABLE 1 |** Aptasensors reported for early cancer detection.

Aptamer	Target/Analyte	LOD/sensitivity	Strategy	Reference
AS1411	MCF-7	10 cells	col	(19)
AS1411, and MUC1	MCF-7	5 cells	SERS	(20)
BG2	IAP-PLAP heterodimer proteins on CTRMs	92%	col	(21)
CDs	CA125 marker and OVCAR-3 cells	$5 \times 10^{-7}$ ng/mL, 400 cells/mL	F	(22)
CD63	MCF-7 cells	$5 \times 10^3$ exo/mL	SPR	(23)
CD63	MCF-7 cells	$13.52 \times 10^8$ part/mL	col	(24)
CD63	MCF-7 cells	$5.2 \times 10^8$ part/mL	col	(25)
CD63, HER2, integrin $\alpha v \beta 6$	CD63 cells	$7.7 \times 10^3$ part/mL	col	(26)
CEA	CEA biomarker	0.034 ng/mL	F	(27)
CEA	CEA biomarker	0.56 pM, 18.8 pM	ECL-SPR	(28)
CEA, CD631, H2 and PSMA	SKBR3, T84 and LNCaP biomarker	$32 \times 10^3$ exo/mL for SKBR3, $73 \times 10^3$ exo/mL for T84, and $203 \times 10^3$ exo/mL for LNCaP	SERS	(29)
CEA, PSA, Thr	CEA biomarker	—	F	(30)
<b>CH-1, CH-2</b>	CEA biomarker	0.58 ng/mL	CL	(31)
HAP	CCRF-CEM cells	25 cells	F	(32)
HApt	HER2 biomarker	0.0904 fM	F	(33)
H1, H2	Ramos cells	230 cells/mL	ECL	(34)
HL-60 cell	HL-60 cancer cells	150 cells/mL	ECL	(35)
mamA	MCF-7 cells	49 cell/mL	SPR	(36)
MUC-1	Gastric cancer exo	$4.27 \times 10^4$ mL	F	(37)
MUC-1	MCF-7 cells	100 cells/mL	SPR	(38)
MUC1	MUC1 biomarker	0.1 U/mL	SERS-col	(39)
P1 (EpCAM)	CTCs (on MCF-7 cells)	10 cells	col	(40)
PSA	PSA biomarker	—	PEC	(41)
PSA	PSA biomarker	0.002 ng/mL	LS	(42)
PSA	PSA biomarker	0.00071 ng/mL, 0.77 ng/mL	ECL-SPR	(43)
PSA	PSA biomarker	0.00017 ng/mL	ECL	(44)
PSA, polyA	PSA biomarker	0.02 ng/mL	col	(45)
PSA, Hemin	PSA biomarker	0.1 ng/mL	CL	(46)
PSMA, HER2	HER2 biomarker	92.31%	F	(47)
PSMA, HER2, and AFP	LNCaP, SKBR3, and HepG2 biomarkers	$26 \times 10^3$ part/mL for (LNCaP), $72 \times 10^3$ part/mL (SKBR3), $35 \times 10^3$ part/mL (HepG2)	SERS	(48)
Sgc8c	PTK-7 biomarker on Hela cells	—	SERS-F	(49)
Sgc8c	CEM cells (leukemia)	46 cells	F	(50)
Sgc8c	CCRF-CEM cells	10 cells/mL	F	(51)
TLS11a	HepG2 cells	—	F	(52)
VEGF	VEGF165 biomarker	0.01 ng/mL	col	(53)

F, Fluorescence; CL, chemiluminescence; ECL, electrochemiluminescence; SPR, surface plasmon resonance; CTCs, circulating tumor cells; SERS, surface-enhanced Raman scattering; col, colorimetric; part, particles; Exo, exosomes; CTRMs, circulating tumor-related materials; PEC, photoelectrochemical; LS, light scattering. All units in LOD/sensitivity column are converted to make it more understandable and comparable.

biomarkers. Kim et al. fabricated a fast biosensor, based on a dual aptamer system connected by a 5 adenine linker, to be used for rapid and accurate PSA quantification (46).

## Surface Plasmon Resonance (SPR) Based Aptasensors

Surface plasmon resonance (SPR) based biosensing is advantageous because of label-free and kinetic studies exploring properties that are not offered by many other systems, giving direct and real-time detection of targets. SPR based assays are widely used to detect several types of cancer cells and biomarkers due to their high sensitivity (59). Li et al. proposed that MUC-1 aptamer (Mucin 1 protein) functionalized gold nanorods (AuNRs) have the ability to specially recognize MCF-7 cells *via* specific interactions that can be further processed by their unique localized surface plasmon resonance (LSPR) spectra. Their biosensor can be employed to detect human breast cancer at early stages (38). Electrochemical and SPR assays were combined by Guo et al. to examine the detection kinetics, which revealed significant outcomes for CEA detection by

using their developed aptasensor based on the AgNCs@Apt@UiO-66 nanocomposite. Their SPR aptasensor is considered to have good performance, regenerate ability, selectivity, acceptable reproducibility, high sensitivity, and stability (28). A bi-functional (electrochemical-SPR) aptasensor with exceptional electrochemical action of MoS<sub>2</sub>QDs@g-C<sub>3</sub>N<sub>4</sub> nanosheets and good SPR enactment of CS-AuNPs was combined by Duan et al. to make a 2D MoS<sub>2</sub>QDs@g-C<sub>3</sub>N<sub>4</sub>@CS-AuNPs nanocomposite. The authors expected satisfactory results of their sensor for the detection of cancer markers in clinical applications (43). A highly effective and sensitive SPR aptasensor for exosomal detection was invented by Wang et al., which is based on dual AuNPs assisted signal amplification. The approach finds promising practical applications in clinical and biological studies (23). Loyez et al. devised multiple narrowband resonances (near-infrared wavelength range), an all-fiber SPR aptasensor that takes five minutes for the detection of metastatic breast cancer cells. Supplementary addition of functionalized AuNPs enhances the 2-fold performance of the aptasensor (36).



## Surface-Enhanced Raman Scattering (SERS)-Based Aptasensors

SERS spectroscopy has emerged as a promising tool for characterization in the field of nanoscience, i.e., widely investigated in cancer-related applications (60–62). The major advantages of SERS imaging are the mapping of a sample with a high spatial resolution (< 0.5 microns in the visible range) and the capability of multiplexed analysis (63). The ultrasensitive vibrational spectroscopic technique SERS can be used to detect several target molecules in a single experiment (60, 64). Ning et al. synthesized the aptamer-based SERS detection probes based on gold–silver–silver core-shell–shell nanotrepangs (GSSNTs) nanotags and magnetic beads for simultaneous detection of multiple cancer-related exosomes: the biomarkers (PSMA, Her2, and AFP proteins) for the prostate cancer cell line (LNCaP), breast cancer cell line (SKBR3), and hepatocellular cancer cell line (HepG2) (48). For the simultaneous detection of multiple kinds of exosomes (SKBR3, T84, and LNCaP), three different SERS probes types were designed to have three different types of Raman reporters and aptamers by Weng et al. and the principle of SERS detection (29). Liang et al. fabricated a series of aptamer-charged SERS probes (AS1411 and MUC1) for targeting cancer cells (MCF-7), and their results show the limit of detection (LOD) up to five cancer cells (20). Lately, the SERS spectroscopy method has been combined with other techniques for attaining maximum information from a sample. Li et al. fabricated a SERS-colorimetric dual-mode aptasensor for cancer biomarker MUC1 detection. The SERS probes were fabricated by using modified gold-silver core-shell nanoparticles with Raman reporters and the sequence of MUC1. The SERS probes report both SERS and colorimetric signals simultaneously (39). Bamrungsap et al. combined SERS and fluorescence nanotags assembled-system using a layer-by-layer process. The nanotags consisting of gold-silver nanorods, aptamers, and fluorophore-labeled aptamer for SERS signal generation, targeting ligands and fluorescence imaging, respectively. The dual-mode sensor system was successful for highly sensitive and specific cancer (cervical cancer) diagnostics (49).

## Colorimetric Aptasensors

Colorimetric-based aptasensors have been used for the detection of disease biomarkers, due to their simplicity, ease of use, accessibility, and point-of-care detection (65, 66). The colorimetric method is a promising technique due to the possibility of detection by simply visual color change (67). Xu et al. developed a highly sensitive colorimetric-based aptasensor for the detection of exosomes obtained from breast and pancreatic cancer cells. In this novel approach, the specific detection was accelerated by horseradish peroxidase (HRP) accelerated dopamine polymerization, and sensitivity was enhanced by *in situ* deposition of polydopamine around exosomes particles (26). Shayesteh et al. developed a label-free colorimetric aptasensor, using poly-adenine aptamer and gold nanoparticles for sensitive detection of prostate-specific antigen (PSA) tumor marker. The concentration of PSA (5ng/ml) was detected by the naked eye with the color change (45). Dong et al. proposed a novel highly selective colorimetric based aptasensor strategy for detection of the vascular endothelial growth factor165

(VEGF165) in human serum (53). Colorimetric aptasensor based on gold nanoparticles aggregation developed by Borghei et al. was shown to have good results for the detection of rare circulating cancer cells. In this method, aptamer desorbed from solution due to specific binding of AS1411 aptamer to cancer cells, which resulted in the solution color change from purple to red (19). Xia et al. designed a fast and label-free DNA-capped-Single-Walled Carbon Nanotubes based aptasensor for exosomes detection through visible inspection. The exosomes were obtained from MCF-7 and breast cancer patient's serum. The ability to detect exosomes in a homogenous system in combination with excluding complicated rinsing procedure is the key advantage of this proposed method (25). Wang et al. demonstrated single-stranded DNA (ssDNA) with graphitic carbon nitride nanosheets (g-C<sub>3</sub>N<sub>4</sub> NSs) hybrid aptasensor for the colorimetric detection of exosomes originated by a breast cancer cell line (MCF-7) and a control cell line (MCF-10A). The intrinsic peroxidase-like activity of g-C<sub>3</sub>N<sub>4</sub> NSs was enhanced by ssDNA (24). Shen et al. fabricated a colorimetric aptasensor for the detection and isolation of circulating tumor-related materials and is based on aptamer functionalized magnetic nanoparticles and endogenous alkaline phosphatase signal amplification. Their method exhibited great potential for clinical samples and is considered to find promising applications in point-of-care testing (21).

## Other Optical Aptasensors

Terahertz radiation (THR) finds useful applications in cancer imaging (68). To overcome THR shortcomings regarding cancer cell and biomarkers detection, new technology has recently emerged known as terahertz chemical microscopy (TCM). However TCM has been reported to detect metastatic breast cancer cells, and only limited reports has been published (69). A photoelectrochemical (PEC) aptasensor fabricated by Zhou et al. (2017) is based on reduced graphene oxide-functionalized iron oxyhydroxide (FeOOH-rGO) as the photoactive material for the detection of PSA (prostate-specific antigen). Accuracy, specificity, and stability of the system were comparable to the commercially used PSA ELISA (enzyme-linked immunosorbent assay) kit (41). Liu et al. (2019) reported an ultrasensitive, activatable light-scattering (LS) method for PSA detection in real samples. The working mechanism of the aptasensor is based on target stimuli-responsive aggregation of AuNPs, which are responsible for lighting up the light-scattering signals (42).

## APTASENSORS IN CLINICAL DIAGNOSTICS

An early cancer diagnosis is particularly an active research area because early detection can help to improve patient survival and disease prognosis. For this purpose, very sensitive and stable methods are needed for early cancer diagnosis (70). The main advantages of using aptasensors for clinical diagnostics are high selectivity and specificity, and low cost of production (71). The stability, ability of easy modification, and capability of fast development (animal-free) make nucleic acid aptamers detection

methods widely functional compared to traditional antibody-based detection methods. And the nucleic acid aptamers can be used against a wide spectrum of targets (71, 72). The smaller size of aptamers compared to antibodies improves transport and tissue penetration (72). However one of the main disadvantages of the aptasensor is restricting each aptasensor to one marker or cell type (73). The development of an increasing number of published articles on aptamers for oncological diseases detection shows increased interest and progress in aptamer technology. Despite all the advantages, traditional immunoassays are still the dominant technology in the field of clinical diagnostics (70, 71). Nevertheless, this knowledge utilization for clinical practices has been challenging and the process has been very slow. There are many challenges if the aptasensor based sensing platform is to be used commercially. For example, improved signal-to-noise ratio and a high level of confidence in signal detection must be recognized (74). The compatibility of aptasensor assay with current equipment of diagnostics units is also an issue and is for the reason of the fragility of aptasensors (75). Many published reports investigated the sensing in buffer or diluted biological fluids; however, the goal should be the detection of biomarkers in a raw biological fluid. The cost of the whole sensing system should also be considered, for example, the cost of TCM components (laser) is expensive and uses a bulky femtosecond laser setup (11). Aptasensors after resolving all the above-discussed obstacles can be one of the most important early cancer detection tools (74).

## CONCLUSION AND FUTURE PERSPECTIVES

Since early cancer detection has significant roles to increase available treatment options for the longer survival of patients, advances in various types of optical aptasensors for the detection of cancer cells and biomarkers or exosomes have been comprehensively summarized in this mini-review. Fluorescence-based label-free/labeled (e.g., FRET-based) aptasensors in combination with different nanomaterials/dyes, etc. as fluorophores, and quenchers to quench (change) the fluorescence properties as a result of specific

interactions, have gained increasing attention. ECL and CL owing to their wide-ranging calibration and low background signals have recently been broadly exploited. Other types of optical aptasensors based on SPR, TCM, and SERS, etc. are also highly recommended for early-stage cancer diagnostics. Colorimetric methods combined with several different latest strategies (e.g., nanoparticles, etc.) implicate the simplest aptasensors and can be analyzed easily with the naked eye.

Several optical aptasensors reported for cancer early detection exhibit good performance in terms of selectivity and sensitivity, yet commercially available aptasensors just appear as the tips of some icebergs when we compare them to the mighty academic literature available in this area. Some new methods are still in lab trials with the early results favoring their commercial applications outside labs. However, some important technological issues and challenges still need to be addressed or improved. First, only a limited number of good specificity/sensitivity aptamers are available against a certain type of cancer cells/biomarkers, and more aptamers need to be screened that could target multiple cancer biomarkers without any complexity or off-target recognition in biological samples. Second, aptasensors need further investigations for clinical applications with real, undiluted (raw) biological samples with a primary focus on aptamer specificity, high sensitivity, cost-effectiveness, and simple operation. Overall, it is evident that the full bloom of optical aptasensor technology for cancer diagnostics is still on the way to a bright future.

## AUTHOR CONTRIBUTIONS

All authors listed have made a substantial, direct, and intellectual contribution to the work and approved it for publication.

## FUNDING

We acknowledge the financial support from “the Fundamental Research Funds for the Central Universities (No. YD2070002013)” and the National Natural Science Foundation of China (No. 31570755).

## REFERENCES

1. Cancer molecular markers: A guide to cancer detection and management. *Semin Cancer Biol* (2018) 52(1):39–55. doi: 10.1016/j.semcancer.2018.02.002
2. Hanahan D, Weinberg RA. Hallmarks of cancer: the next generation. *Cell* (2011) 144(5):646–74. doi: 10.1016/j.cell.2011.02.013
3. Crosby D, Lyons N, Greenwood E, Harrison S, Hiom S, Moffat J, et al. A roadmap for the early detection and diagnosis of cancer. *Lancet Oncol* (2020) 21(11):1397–9. doi: 10.1016/S1470-2045(20)30593-3
4. Chen X, Gole J, Gore A, He Q, Lu M, Min J, et al. Non-invasive early detection of cancer four years before conventional diagnosis using a blood test. *Nat Commun* (2020) 11(1):1–10. doi: 10.1038/s41467-020-17316-z
5. Liu M, Yu X, Chen Z, Yang T, Yang D, Liu Q, et al. Aptamer selection and applications for breast cancer diagnostics and therapy. *J Nanobiotechnol* (2017) 15(1):1–16. doi: 10.1186/s12951-017-0311-4
6. Bing T, Shen L, Wang J, Wang L, Liu X, Zhang N, et al. Aptameric Probe Specifically Binding Protein Heterodimer Rather Than Monomers. *Adv Sci* (2019) 6(11):1900143. doi: 10.1002/advs.201900143
7. Bing T, Wang J, Shen L, Liu X, Shanguan D. Prion Protein Targeted by a Prostate Cancer Cell Binding Aptamer, a Potential Tumor Marker? *ACS Appl Bio Mat* (2020) 3(5):2658–65. doi: 10.1021/acsabm.0c00024
8. Tuerk C, Gold L. Systematic evolution of ligands by exponential enrichment: RNA ligands to bacteriophage T4 DNA polymerase. *Science* (1990) 249 (4968):505–10. doi: 10.1126/science.2200121
9. Bock LC, Griffin LC, Latham JA, Vermaas EH, Toole JJ. Selection of single-stranded DNA molecules that bind and inhibit human thrombin. *Nature* (1992) 355(6360):564–6. doi: 10.1038/355564a0
10. Shanguan D, Li Y, Tang Z, Cao ZC, Chen HW, Mallikaratchy P, et al. Aptamers evolved from live cells as effective molecular probes for cancer study. *Proc Natl Acad Sci* (2006) 103(32):11838–43. doi: 10.1073/pnas.0602615103
11. Hassan EM, DeRosa MC. Recent advances in cancer early detection and diagnosis: Role of nucleic acid based aptasensors. *TrAC Trends Anal Chem* (2020) 124:115806. doi: 10.1016/j.trac.2020.115806
12. Bing T, Zhang N, Shanguan D. Cell-SELEX, an Effective Way to the Discovery of Biomarkers and Unexpected Molecular Events. *Adv Biosyst* (2019) 3(12):1900193. doi: 10.1002/adbi.201900193

13. Eivazzadeh-Keihan R, Pashazadeh-Panahi P, Baradaran B, Maleki A, Hejazi M, Mokhtarzadeh A, et al. Recent advances on nanomaterial based electrochemical and optical aptasensors for detection of cancer biomarkers. *TrAC Trends Anal Chem* (2018) 100:103–15. doi: 10.1016/j.trac.2017.12.019
14. Feng C, Dai S, Wang L. Optical aptasensors for quantitative detection of small biomolecules: A review. *Biosens Bioelectron* (2014) 59:64–74. doi: 10.1016/j.bios.2014.03.014
15. Nikhil B, Pawan J, Nello F, Pedro E. Introduction to biosensors. *Essays Biochem* (2016) 60(1):1–8. doi: 10.1042/EBC20150001
16. Lim Y, Kouzani A, Duan W. Aptasensors: a review. *J Biomed Nanotechnol* (2010) 6(2):93–105. doi: 10.1166/jbn.2010.1103
17. Sadeghi AS, Ansari N, Ramezani M, Abnous K, Mohsenzadeh M, Taghdisi SM, et al. Optical and electrochemical aptasensors for the detection of amphenicols. *Biosens Bioelectron* (2018) 118:137–52. doi: 10.1016/j.bios.2018.07.045
18. Pashazadeh P, Mokhtarzadeh A, Hasanzadeh M, Hejazi M, Hashemi M, de la Guardia M. Nano-materials for use in sensing of salmonella infections: recent advances. *Biosens Bioelectron* (2017) 87:1050–64. doi: 10.1016/j.bios.2016.08.012
19. Borghei YS, Hosseini M, Dadmehr M, Hosseinkhani S, Ganjali MR, Sheikhnajad R. Visual detection of cancer cells by colorimetric aptasensor based on aggregation of gold nanoparticles induced by DNA hybridization. *Anal Chim Acta* (2016) 904:92–7. doi: 10.1016/j.aca.2015.11.026
20. Liang D, Jin Q, Yan N, Feng J, Wang J, Tang X. SERS Nanoprobes in Biologically Raman Silent Region for Tumor Cell Imaging and In Vivo Tumor Spectral Detection in Mice. *Adv Biosyst* (2018) 2:1800100. doi: 10.1002/adbi.201800100
21. Shen L, Jia K, Bing T, Zhang Z, Zhen X, Liu X, et al. Detection of circulating tumor-related materials by aptamer capturing and endogenous enzyme-signal amplification. *Anal Chem* (2020) 92(7):5370–8. doi: 10.1021/acs.analchem.0c00051
22. Hamd-Ghadareh S, Salimi A, Fathi F, Bahrami S. An amplified comparative fluorescence resonance energy transfer immunosensing of CA125 tumor marker and ovarian cancer cells using green and economic carbon dots for bio-applications in labeling, imaging and sensing. *Biosens Bioelectron* (2017) 96:308–16. doi: 10.1016/j.bios.2017.05.003
23. Wang Q, Zou L, Yang X, Liu X, Nie W, Zheng Y, et al. Direct quantification of cancerous exosomes via surface plasmon resonance with dual gold nanoparticle-assisted signal amplification. *Biosens Bioelectron* (2019) 135:129–36. doi: 10.1016/j.bios.2019.04.013
24. Wang YM, Liu JW, Adkins GB, Shen W, Trinh MP, Duan LY, et al. Enhancement of the Intrinsic Peroxidase-Like Activity of Graphitic Carbon Nitride Nanosheets by ssDNAs and Its Application for Detection of Exosomes. *Anal Chem* (2017) 89:12327–33. doi: 10.1021/acs.analchem.7b03335
25. Xia Y, Liu M, Wang L, Yan A, He W, Chen M, et al. A visible and colorimetric aptasensor based on DNA-capped single-walled carbon nanotubes for detection of exosomes. *Biosens Bioelectron* (2017) 92:8–15. doi: 10.1016/j.bios.2017.01.063
26. Xu L, Chopdat R, Li D, Al-Jamal KT. Development of a simple, sensitive and selective colorimetric aptasensor for the detection of cancer-derived exosomes. *Biosens Bioelectron* (2020) 169:112576. doi: 10.1016/j.bios.2020.112576
27. Zhao L, Cheng M, Liu G, Lu H, Gao Y, Yan X, et al. A fluorescent biosensor based on molybdenum disulfide nanosheets and protein aptamer for sensitive detection of carcinoembryonic antigen. *Sensors Actuators B: Chem* (2018) 273:185–90. doi: 10.1016/j.snb.2018.06.004
28. Guo C, Su F, Song Y, Hu B, Wang M, He L, et al. Aptamer-templated silver nanoclusters embedded in zirconium metal-organic framework for bifunctional electrochemical and SPR aptasensors toward carcinoembryonic antigen. *ACS Appl Mat Interfaces* (2017) 9(47):41188–99. doi: 10.1021/acsami.7b14952
29. Weng Z, Zong S, Wang Y, Li N, Li L, Lu J, et al. Screening and multiple detection of cancer exosomes using a SERS-based method. *Nanoscale* (2018) 10:9053–62. doi: 10.1039/C7NR09162A
30. Pei X, Wu X, Xiong J, Wang G, Tao G, Ma Y, et al. Competitive aptasensor for the ultrasensitive multiplexed detection of cancer biomarkers by fluorescent nanoparticle counting. *Analyst* (2020) 145(10):3612–9. doi: 10.1039/D0AN00239A
31. Khang H, Cho K, Chong S, Lee JH. All-in-one dual-aptasensor capable of rapidly quantifying carcinoembryonic antigen. *Biosens Bioelectron* (2017) 90:46–52. doi: 10.1016/j.bios.2016.11.043
32. Xiao K, Liu J, Chen H, Zhang S, Kong J. A label-free and high-efficient GO-based aptasensor for cancer cells based on cyclic enzymatic signal amplification. *Biosens Bioelectron* (2017) 91:76–81. doi: 10.1016/j.bios.2016.11.057
33. Zhang M, Gao G, Ding Y, Deng C, Xiang J, Wu H. A fluorescent aptasensor for the femtomolar detection of epidermal growth factor receptor-2 based on the proximity of G-rich sequences to Ag nanoclusters. *Talanta* (2019) 199:238–43. doi: 10.1016/j.talanta.2019.02.014
34. Jie G, Jie G. Sensitive electrochemiluminescence detection of cancer cells based on a CdSe/ZnS quantum dot nanocluster by multibranch hybridization chain reaction on gold nanoparticles. *RSC Adv* (2016) 6(29):24780–5. doi: 10.1039/C6RA00750C
35. Wang Y-Z, Hao N, Feng Q-M, Shi H-W, Xu J-J, Chen H-Y. A ratiometric electrochemiluminescence detection for cancer cells using g-C<sub>3</sub>N<sub>4</sub> nanosheets and Ag-PAMAM-luminol nanocomposites. *Biosens Bioelectron* (2016) 77:76–82. doi: 10.1016/j.bios.2015.08.057
36. Loyez M, Hassan EM, Lobry M, Liu F, Caucheteur C, Wattiez R, et al. Rapid detection of circulating breast cancer cells using a Multiresonant optical fiber Aptasensor with plasmonic amplification. *ACS Sensors* (2020) 5(2):454–63. doi: 10.1021/acssensors.9b02155
37. Huang R, He L, Li S, Liu H, Jin L, Chen Z, et al. A simple fluorescence aptasensor for gastric cancer exosome detection based on branched rolling circle amplification. *Nanoscale* (2020) 12(4):2445–51. doi: 10.1039/C9NR08747H
38. Li Y, Zhang Y, Zhao M, Zhou Q, Wang L, Wang H, et al. A simple aptamer-functionalized gold nanorods based biosensor for the sensitive detection of MCF-7 breast cancer cells. *Chem Commun* (2016) 52(20):3959–61. doi: 10.1039/C6CC01014H
39. Li N, Zong S, Zhang Y, Wang Z, Wang Y, Zhu K, et al. A SERS-colorimetric dual-mode aptasensor for the detection of cancer biomarker MUC1. *Anal Bioanal Chem* (2020) 412:5707–18. doi: 10.1007/s00216-020-02790-7
40. Zhu L, Feng X, Yang S, Wang J, Pan Y, Ding J, et al. Colorimetric detection of immunomagnetically captured rare number CTCs using mDNA-wrapped single-walled carbon nanotubes. *Biosens Bioelectron* (2020) 172:112780. doi: 10.1016/j.bios.2020.112780
41. Zhou Q, Lin Y, Shu J, Zhang K, Yu Z, Tang D. Reduced graphene oxide-functionalized FeOOH for signal-on photoelectrochemical sensing of prostate-specific antigen with bioresponsive controlled release system. *Biosens Bioelectron* (2017) 98:15–21. doi: 10.1016/j.bios.2017.06.033
42. Liu G, Feng D-Q, Li Z, Feng Y. Target-activatable gold nanoparticle-based aptasensing for protein biomarkers using stimuli-responsive aggregation. *Talanta* (2019) 192:112–7. doi: 10.1016/j.talanta.2018.08.034
43. Duan F, Zhang S, Yang L, Zhang Z, He L, Wang M. Bifunctional aptasensor based on novel two-dimensional nanocomposite of MoS<sub>2</sub> quantum dots and g-C<sub>3</sub>N<sub>4</sub> nanosheets decorated with chitosan-stabilized Au nanoparticles for selectively detecting prostate specific antigen. *Anal Chim Acta* (2018) 1036:121–32. doi: 10.1016/j.aca.2018.06.070
44. Cao J-T, Yang J-J, Zhao L-Z, Wang Y-L, Wang H, Liu Y-M, et al. Graphene oxide@ gold nanorods-based multiple-assisted electrochemiluminescence signal amplification strategy for sensitive detection of prostate specific antigen. *Biosens Bioelectron* (2018) 99:92–8. doi: 10.1016/j.bios.2017.07.050
45. Shayesteh OH, Ghavami R. A novel label-free colorimetric aptasensor for sensitive determination of PSA biomarker using gold nanoparticles and a cationic polymer in human serum. *Spectrochim Acta - Part A: Mol Biomol Spectrosc* (2020) 226:117644. doi: 10.1016/j.saa.2019.117644
46. Kim M, Kim K, Lee JH. A cost-effective and rapid aptasensor with chemiluminescence detection for the early diagnosis of prostate cancer. *Microchem J* (2020) 155(2020):104763. doi: 10.1016/j.microc.2020.104763
47. Li B, Liu C, Pan W, Shen J, Guo J, Luo T, et al. Facile fluorescent aptasensor using aggregation-induced emission luminogens for exosomal proteins profiling towards liquid biopsy. *Biosens Bioelectron* (2020) 168:112520. doi: 10.1016/j.bios.2020.112520

48. Ning CF, Wang L, Tian YF, Yin BC, Ye BC. Multiple and sensitive SERS detection of cancer-related exosomes based on gold-silver bimetallic nanotrepangs. *Analyst* (2020) 145:2795–804. doi: 10.1039/C9AN02180A
49. Bamrungsap S, Treetong A, Apiwat C, Wuttikhun T, Dharakul T. SERS-fluorescence dual mode nanotags for cervical cancer detection using aptamers conjugated to gold-silver nanorods. *Microchim Acta* (2016) 183:249–56. doi: 10.1007/s00604-015-1639-9
50. Lei Y, Tang J, Shi H, Ye X, He X, Xu F, et al. Nature-inspired smart DNA nanodotor for activatable in vivo cancer imaging and in situ drug release based on recognition-triggered assembly of split aptamer. *Anal Chem* (2016) 88(23):11699–706. doi: 10.1021/acs.analchem.6b03283
51. Tan J, Lai Z, Zhong L, Zhang Z, Zheng R, Su J, et al. A graphene oxide-based fluorescent aptasensor for the turn-on detection of CCRF-CEM. *Nanoscale Res Lett* (2018) 13(1):1–8. doi: 10.1186/s11671-018-2525-2
52. Lai Z, Tan J, Wan R, Tan J, Zhang Z, Hu Z, et al. An ‘activatable’ aptamer-based fluorescence probe for the detection of HepG2 cells. *Oncol Rep* (2017) 37(5):2688–94. doi: 10.3892/or.2017.5527
53. Dong J, He L, Wang Y, Yu F, Yu S, Liu L, et al. A highly sensitive colorimetric aptasensor for the detection of the vascular endothelial growth factor in human serum. *Spectrochim Acta - Part A: Mol Biomol Spectrosc* (2020) 226:117622. doi: 10.1016/j.saa.2019.117622
54. Musumeci D, Platella C, Riccardi C, Moccia F, Montesarchio D. Fluorescence sensing using DNA aptamers in cancer research and clinical diagnostics. *Cancers* (2017) 9(12):174. doi: 10.3390/cancers9120174
55. Zhang Z, Tang C, Zhao L, Xu L, Zhou W, Dong Z, et al. Aptamer-based fluorescence polarization assay for separation-free exosome quantification. *Nanoscale* (2019) 11(20):10106–13. doi: 10.1039/C9NR01589B
56. Kou X, Zhang X, Shao X, Jiang C, Ning L. Recent advances in optical aptasensor technology for amplification strategies in cancer diagnostics. *Anal Bioanal Chem* (2020) 1–15. doi: 10.1007/s00216-020-02774-7
57. Eivazzadeh-Keihan R, Pashazadeh P, Hejazi M, de la Guardia M, Mokhtarzadeh A. Recent advances in nanomaterial-mediated bio and immune sensors for detection of aflatoxin in food products. *TrAC Trends Anal Chem* (2017) 87:112–28. doi: 10.1016/j.trac.2016.12.003
58. Park L, Kim J, Lee JH. Role of background observed in aptasensor with chemiluminescence detection. *Talanta* (2013) 116:736–42. doi: 10.1016/j.talanta.2013.07.072
59. Nguyen HH, Park J, Kang S, Kim M. Surface plasmon resonance: a versatile technique for biosensor applications. *Sensors* (2015) 15(5):10481–510. doi: 10.3390/s150510481
60. Guerrini L, Alvarez-Puebla RA. Surface-enhanced raman spectroscopy in cancer diagnosis, prognosis and monitoring. *Cancers* (2019) 11(6):748.
61. Vendrell M, Maiti KK, Dhaliwal K, Chang YT. Surface-enhanced Raman scattering in cancer detection and imaging *Trends Biotechnol* (2013) 31(4):249–57.
62. Moisoiu V, Stefanu A, Gulei D, Boitor R, Magdo L, Raduly L, et al. SERS-based differential diagnosis between multiple solid malignancies: Breast, colorectal, lung, ovarian and oral cancer. *Int J Nanomed* (2019) 14:6165–78. doi: 10.2147/IJN.S198684
63. Blanco-Formoso M, Alvarez-Puebla RA. Cancer diagnosis through sers and other related techniques. *Int J Mol Sci* (2020) 21(6):2253. doi: 10.3390/ijms21062253
64. Dougan JA, Faulds K. Surface enhanced Raman scattering for multiplexed detection. *Analyst* (2012) 137(3):545–54.
65. De La Rica R, Stevens MM. Plasmonic ELISA for the ultrasensitive detection of disease biomarkers with the naked eye. *Nat Nanotechnol* (2012) 7:821–4. doi: 10.1038/nnano.2012.186
66. Wang D, Guo R, Wei Y, Zhang Y, Zhao X, Xu Z. Sensitive multicolor visual detection of telomerase activity based on catalytic hairpin assembly and etching of Au nanorods. *Biosens Bioelectron* (2018) 122:247–53. doi: 10.1016/j.bios.2018.09.064
67. Akshaya K, Arthi C, Pavithra AJ, Poovizhi P, Antinate SS, Hikku GS, et al. Bioconjugated gold nanoparticles as an efficient colorimetric sensor for cancer diagnostics. *Photodiagnosis Photodyn Ther* (2020) 30:101699.
68. Walther M, Fischer BM, Ortner A, Bitzer A, Thoman A, Helm H. Chemical sensing and imaging with pulsed terahertz radiation. *Anal Bioanal Chem* (2010) 397(3):1009–17. doi: 10.1007/s00216-010-3672-1
69. Hassan EM, Mohamed A, DeRosa MC, Willmore WG, Hanaoka Y, Kiwa T, et al. High-sensitivity detection of metastatic breast cancer cells via terahertz chemical microscopy using aptamers. *Sensors Actuators B: Chem* (2019) 287:595–601. doi: 10.1016/j.snb.2019.02.019
70. Hong P, Li W, Li J. Applications of aptasensors in clinical diagnostics. *Sensors* (2012) 12(2):1181–93.
71. Hong P, Li W, Li J. Applications of aptasensors in clinical diagnostics *Sensors* (2012) 12(2):1181–93.
72. Mairal T, Cengiz Özalp V, Lozano Sánchez P, Mir M, Katakis I, O’Sullivan CK. Aptamers: Molecular tools for analytical applications. *Anal Bioanal Chem* (2008) 390:989–1007. doi: 10.1007/s00216-007-1346-4
73. Thivyanathan V, Gorenstein DG. Aptamers and the next generation of diagnostic reagents. *PROTEOMICS-Clin Appl* (2012) 6(11-12):563–73.
74. Liu LS, Wang F, Ge Y, Lo PK. Recent Developments in Aptasensors for Diagnostic Applications. *ACS Appl Mat Interfaces* (2020). doi: 10.1021/acsami.0c14788
75. Famulok M, Mayer Gn. Aptamer modules as sensors and detectors. *Acc Chem Res* (2011) 44(12):1349–58. doi: 10.1021/ar2000293

**Conflict of Interest:** The authors declare that the research was conducted in the absence of any commercial or financial relationships that could be construed as a potential conflict of interest.

Copyright © 2021 Zahra, Khan and Luo. This is an open-access article distributed under the terms of the Creative Commons Attribution License (CC BY). The use, distribution or reproduction in other forums is permitted, provided the original author(s) and the copyright owner(s) are credited and that the original publication in this journal is cited, in accordance with accepted academic practice. No use, distribution or reproduction is permitted which does not comply with these terms.





# Advanced Approaches to Breast Cancer Classification and Diagnosis

M. Zubair<sup>1</sup>, S. Wang<sup>2\*</sup> and N. Ali<sup>1\*</sup>

<sup>1</sup>Department of Biology, University of Arkansas at Little Rock, Little Rock, AR, United States, <sup>2</sup>Department of Chemistry, University of Arkansas at Little Rock, Little Rock, AR, United States

## OPEN ACCESS

### Edited by:

Dong-Hua Yang,  
St. John's University, United States

### Reviewed by:

Wenjun Wu,  
Fox Chase Cancer Center,  
United States  
Weijia Wang,  
Peking University First Hospital, China

### \*Correspondence:

S. Wang  
sxwang2@ualr.edu  
N. Ali  
nali@ualr.edu

### Specialty section:

This article was submitted to  
Pharmacology of Anti-Cancer Drugs,  
a section of the journal  
Frontiers in Pharmacology

**Received:** 22 November 2020

**Accepted:** 29 December 2020

**Published:** 26 February 2021

### Citation:

Zubair M, Wang S and Ali N (2021)  
Advanced Approaches to Breast  
Cancer Classification and Diagnosis.  
Front. Pharmacol. 11:632079.  
doi: 10.3389/fphar.2020.632079

The International Agency for Research on Cancer (IARC) has recently reported a 66% increase in the global number of cancer deaths since 1960. In the US alone, about one in eight women is expected to develop invasive breast cancer(s) (breast cancer) at some point in their lifetime. Traditionally, a BC diagnosis includes mammography, ultrasound, and some high-end molecular bioimaging. Unfortunately, these techniques detect BC at a later stage. So early and advanced molecular diagnostic tools are still in demand. In the past decade, various histological and immuno-molecular studies have demonstrated that BC is highly heterogeneous in nature. Its growth pattern, cytological features, and expression of key biomarkers in BC cells including hormonal receptor markers can be utilized to develop advanced diagnostic and therapeutic tools. A cancer cell's progression to malignancy exhibits various vital biomarkers, many of which are still underrepresented in BC diagnosis and treatment. Advances in genetics have also enabled the development of multigene assays to detect genetic heterogeneity in BC. However, thus far, the FDA has approved only four such biomarkers—cancer antigens (CA); CA 15-3, CA 27-29, Human epidermal growth factor receptor 2 (HER2), and circulating tumor cells (CTC) in assessing BC in body fluids. An adequately structured portable-biosensor with its non-invasive and inexpensive point-of-care analysis can quickly detect such biomarkers without significantly compromising its specificity and selectivity. Such advanced techniques are likely to discriminate between BC and a healthy patient by accurately measuring the cell shape, structure, depth, intracellular and extracellular environment, and lipid membrane compositions. Presently, BC treatments include surgery and systemic chemo- and targeted radiation therapy. A biopsied sample is then subjected to various multigene assays to predict the heterogeneity and recurrence score, thus guiding a specific treatment by providing complete information on the BC subtype involved. Thus far, we have seven prognostic multigene signature tests for BC providing a risk profile that can avoid unnecessary treatments in low-risk patients. Many comparative studies on multigene analysis projected the importance of integrating clinicopathological information with genomic-imprint analysis. Current cohort studies such as MINDACT, TAILORx, Trans-aTTOM, and many more, are likely to provide positive impact on long-term patient outcome. This review offers consolidated information on currently available BC diagnosis and treatment options. It further describes advanced biomarkers for the development of state-of-the-art early screening and diagnostic technologies.

**Keywords:** breast cancer, heterogeneity, novel biomarkers, early diagnosis, multigene assays, biosensors

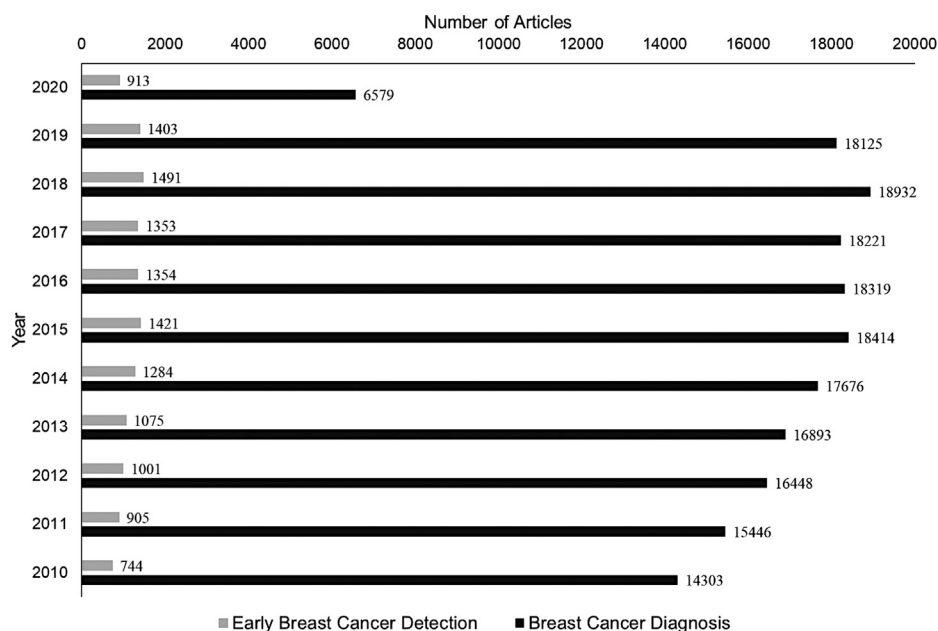


**FIGURE 1 |** A comparative analysis of the number of articles published in the last decade, limiting the search to keywords: “Breast Cancer Diagnosis” and “Early Breast Cancer Detection.” NCBI database was searched as on Nov 1, 2020, to acquire the respective number of publications shown.

## INTRODUCTION

Cancer cells are misbehaving normal cells that are beyond the paradigm of life and death. Some researchers consider their self-sufficiency and self-management as an evolutionary process in the cell division. Like an organism that evolves through a process of natural selection and mutation, cancer cells also progress through selective transformation to malignancy (Casás-Selves and DeGregori, 2011). The current edition of the International Agency for Research on Cancer (IARC) reports a 66% increase in the global number of cancer deaths since 1960. Currently, breast cancer(s) (BC) is the second most common cancer worldwide, after lung cancer. Accordingly, in the US alone, about one in eight women is expected to develop invasive BC at some point in their lifetime. Considering the number of research articles published on BC diagnosis and treatments, research in its early detection is still lagging significantly (Figure 1). In this review, we aim at providing consolidated information on recent advancements in BC diagnosis and therapy.

## BREAST CANCER HETEROGENEITY

BC are heterogeneous in nature, both at the histological and molecular levels. Traditional BC treatments initially depend upon the tumor characteristics such as its clinical stage, histopathologic features, and biomarker profiling. Our understanding of its biological characteristics has improved in the last few decades. We can now subtype it with molecular profiling, hormone indicators, growth factor expressions, and many more. The subtyping of BC is still challenging and very volatile. Different

stem cell populations and progenitor cells in the mammary gland can cause a paradigm shift in our current understanding of its heterogeneity.

## Histopathologic Heterogeneity

Histological analysis of breast tumors considers its anatomical origin, in most instances, from the junction between the terminal duct and lobule, an area further labeled as “atypical lobules” (Oyama et al., 2000) or hyperplastic enlarged lobular unit (HELU) (Lee et al., 2005). These histologically identifiable lesions are also the earliest precancerous ones reflecting hormone-responsive cancer (Lee et al., 2005). This lesion further exhibits an elevation in estrogen and progesterone receptor (ER- $\alpha$ /PR). Such a histological perspective is essential in chemotherapeutic responsiveness and endocrine therapy study.

According to the 2012 WHO classification, BC are primarily categorized into carcinomas and sarcomas (Sinn and Kreipe, 2013) (Figure 2A). If BC's inception is from the breast's epithelial cell-based components, including lobules and terminal ducts (responsible for milk), it falls under carcinomas. It further stretches to the underlying mammary stem cells (MSC) that differentiate into epithelial cells (Liu et al., 2005; Shackleton et al., 2006). Unlike carcinomas that usually ascend from milk ducts, sarcoma originates from the connective tissues, such as blood vessels and myofibroblast, which support the ducts and the lobules. It further represents less than 1% of the total BC.

Significant heterogeneity in breast carcinomas further subcategorizes it into *in situ* and invasive carcinomas. The *in situ* carcinomas are more localized to their prevailing lobules and

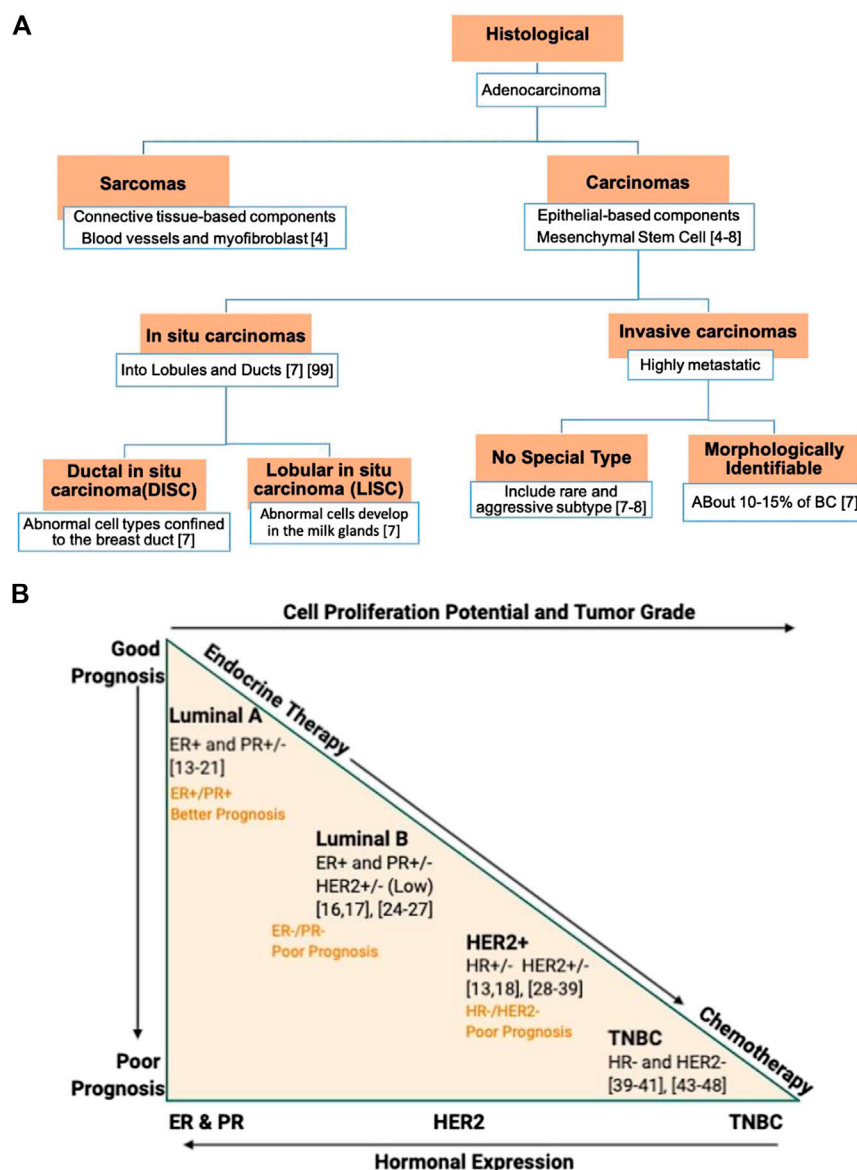


**FIGURE 2 |** Classification of breast cancer (BC) based on: **(A)** The histopathological stratification. **(B)** The molecular stratification, relative grading, therapy requirement, and prognosis. The BC hormone expression reflects an inverse proportion to the tumor grade and cellular proliferation. Luminal A subtype exhibits a better prognosis with a positive response to endocrine therapy. In contrast, TNBC shows no hormonal expression, higher staged and nuclear grade tumor with intense mitotic activity, and poor prognosis. ER, estrogen receptor; HER2, human epidermal growth factor receptor 2; PR, progesterone receptor, and TNBC, triple negative breast cancer.

ducts. In contrast, the invasive carcinomas penetrate the neighboring tissues and, if not intercepted, could metastasize to other body tissues and organs. The invasive carcinomas, based on their morphology, are further categorized into morphologically identifiable types and no special type (NST) or “not otherwise specified” (NOS) type. Of them all, the invasive ductal carcinoma (IDC) (Siegel and Jemal, 2015) of NST represents the most frequent type of invasive carcinoma (about 80% of all BC) followed by invasive lobular carcinomas (ILC) of special-type, representing 10–15% of BC. Additionally, ILC growth involves penetration of single cells or cells segregated

in sheets, with molecular and genetic aberrations different from IDC. Recently, amongst the rare subtypes of invasive carcinomas, two new entities—tall cell carcinoma with reverse polarity (TCCRP) and mucinous cystadenocarcinoma of NST—have been recognized and listed in 2019 WHO BC’s classification (Hoon Tan et al., 2020). Though they both exhibit tall columnar cell morphology, their core contents are different. Mucinous cystadenocarcinoma of NST contains an abundance of luminal mucin with a cytomorphology of pancreatobiliary and ovarian mucinous cystadenocarcinoma. In comparison, TCCRP represents features like papillary thyroid carcinoma and salivary

gland-type tumor. Though they both belong to invasive carcinomas, their malignant potential is low (Hoon Tan et al., 2020).

Additionally, the 3-tier (low, intermediate, and high) grading system further struggles at providing order to the invasive BC-heterogeneity. This grading system analyzes the percentage of tumor in glands and tubular structures (T), degree of nuclear polymorphism or nodes (N), and the mitotic rate (M). However, the stage of a BC is different from its grade. BC staging represents the tumor's gross appearance, whereas TNM grading allows simplification to BC staging by exhibiting BC's spread. However, both are heavily incorporated in clinical tools determining the prognosis during BC surgery, such as in Nottingham Prognosis Index (NPI) (Lee and Ellis, 2008).

## Molecular Heterogeneity

Over time, several molecular biomarkers have been reported subtyping BC based on genomic instability (Kronenwett et al., 2006), cytogenetic pathways (Korsching et al., 2002; Hu et al., 2006), gene expression levels (Perou et al., 2000; Kouros-Mehr et al., 2006), and many more. In modern molecular pathology, high-throughput screening on biomarkers provided a highly desired explanation for BC heterogeneity. It delivers biomarkers—estrogen receptors (ER), progesterone receptors (PR), and human epidermal growth factor receptor 2 (HER2) that categorizes BC into five subtypes (**Figure 2B**): luminal A and B, HER2 enriched, triple-negative or basal-like (BL), and normal-like BC. Stratifying BC will help in expediting the prognosis and treatment selection.

## Estrogen Receptor

ER is the earliest and one of the most prevalent BC biomarkers used (Ellis et al., 2005; Rakha et al., 2010). Many cohorts and cooperative studies with a combined-data set suggest that about 80% of all BC are ER-positive (ER<sup>+</sup>). It is mainly well-differentiated, less aggressive, and great at prognosis than ER-negative (ER<sup>-</sup>) BC (**Figure 2B**). Based on the stem-cell cancer model, the ER<sup>-</sup> BC ascends from the most primitive stem cells, where specific mutations limit its differentiation into ER-positive (ER<sup>+</sup>) cells (Prat and Perou, 2009). A broader gene expression profiling (GEP) on approximately 500 genes' "intrinsic factors" further differentiate ER<sup>+</sup> BC into luminal-A and -B subtypes with different overall survival (Sorlie et al., 2003). Sorlie and his colleagues observed a high expression of luminal genes and ER<sup>+</sup> related genes (such as PR) in the luminal-A subtype (Sorlie et al., 2003) than luminal B subtype (**Figure 2B**). Likewise, the luminal A subtype exhibits a greater prognosis and overall survival than the luminal-B subtype. Consistently, a poor response to endocrine therapies of the luminal-B subtype corroborates with the low ER/PR-expression (Bardou et al., 2003; Creighton et al., 2009; Creighton et al., 2010), high Ki-67 expression (Musgrove and Sutherland, 2009), and an unusual overexpression of HER2 (Ellis et al., 2006) (**Figure 2B**). As such, Ki-67, the proliferative biomarker, is also suggested as an additional clinical biomarker in differentiating luminal-A from luminal-B subtypes.

## Progesterone Receptor

PR is an ER-regulated gene critical for the lobuloalveolar development of mammary glands (Briskin, 2002). Unlike estrogen and its receptor (ER) that induce ductal outgrowth of mammary glands, progesterone and its receptor (PR) regulate ductal morphogenesis (Atwood et al., 2000). A localized PR cluster stimulates the mammary glands' side-branching by inducing insulin-like growth factor1 (IGF-1) (Ruan et al., 2005). It serves as a negative indicator of tumor aggression in that PR<sup>-</sup> BC is more aggressive than PR<sup>+</sup> BC (Cui et al., 2005) (**Figure 2B**). Thus, both ER and PR are functionally intertwined in mammatogenesis, and assessing them together as double receptors will guide the hormonal therapy response.

Taken together, both the receptors have four subclasses under luminal A and B subtypes: ER<sup>+</sup>/PR<sup>+</sup>, ER<sup>+</sup>/PR<sup>-</sup>, ER<sup>-</sup>/PR<sup>-</sup>, and ER<sup>-</sup>/PR<sup>+</sup>. A double-positive subtype—ER<sup>+</sup>/PR<sup>+</sup>—has a better prognosis, and it is more responsive to endocrine therapy (**Figure 2B**). In a study on subclasses that lack PR expression in the ER<sup>+</sup> subset, Rakha and colleagues observed a less receptiveness toward endocrine treatment such as tamoxifen (Rakha et al., 2007) compared to the double-positive subtype (ER<sup>+</sup>/PR<sup>+</sup>) (Dowsett et al., 2006). Double negative—ER<sup>-</sup>/PR<sup>-</sup>—exhibits a higher relapse rate with the worst prognosis and overall survival rate. ER<sup>-</sup>/PR<sup>-</sup> BC acts as an apt candidate for chemotherapy after an unresponsive treatment to endocrine therapy (Bardou et al., 2003). ER<sup>-</sup>/PR<sup>-</sup> BC can further be stratified based on a third biomarker, HER2 (Sorlie et al., 2003), thus introducing triple receptor classification.

## HER2 Receptor

The BC's insensitivity to endocrine therapy in a triple receptor classification is rooted in an unusual overexpression of HER2 receptors on mammary glands. It is a transmembrane protein-tyrosine kinase receptor present on normal mammary gland epithelial cells. However, overexpression of about 20%, which establishes genetic instability and excessive proliferation, is regarded as HER2 positive (HER2<sup>+</sup>) BC subtype (Slamon et al., 1989). Also, intimate crosstalk between HER2 and ER/PR signaling pathways corroborates its resistance to endocrine therapies (Schiff et al., 2004; Rakha et al., 2007). This crosstalk excludes ER/PR expression deletion through selective ER modulators (SERM) (Ellis et al., 2001) inhibitors. Similar to luminal A and B subtype, as defined by GEP (Perou et al., 2000), the three receptor-based immune histochemical/compatibility (IHC) evaluation stratifies BC into ER<sup>+</sup>/PR<sup>+</sup> HER2<sup>+</sup>, ER<sup>-</sup>/PR<sup>-</sup> HER2<sup>+</sup>, ER<sup>-</sup>/PR<sup>-</sup> HER2<sup>-</sup>, and ER<sup>+</sup>/PR<sup>+</sup> HER2<sup>-</sup>, where all HER2<sup>+</sup> cases shared similar genetic variations (Perou et al., 2000; Cheang et al., 2009) and outcomes (Network, 2012), irrespective of their hormonal subsets (**Figure 2B**). Preclinical and clinical studies of patients with HER2 BC reports promising results upon merging chemotherapy with anti-HER2 monoclonal antibodies (trastuzumab and pertuzumab) (Piccart-Gebhart et al., 2005) and tyrosine kinase inhibitor (lapatinib and neratinib) based therapies (Cuzick et al., 2011). Furthermore, HER2<sup>+</sup> BC subtypes, regardless of its ER status, benefit from paclitaxel (a plant alkaloid based chemotherapeutic agent) after adjuvant



treatment with an anthracycline-based regimen such as doxorubicin plus cyclophosphamide, specifically in node-positive breast tumors (Hayes et al., 2007; Blum et al., 2017). In conclusion, ER<sup>+</sup>/PR<sup>+</sup>/HER2<sup>+</sup> BC has the best prognosis and shows an effective treatment response to chemo-hormonal therapy (Cuzick et al., 2011; Lehmann et al., 2011).

### Triple-Negative Breast Cancer

TNBC subtype includes the most aggressive and highly heterogeneous of all BC subtypes. The lack of ER, PR, and HER2 leads to a higher staged nuclear grade cancer with intense mitotic activity and equally poor prognosis (Figure 2B). Due to no hormonal expression, TNBCs are tolerant of endocrine and targeted therapies. Within the last decade, TNBC stratification has been updated frequently. Initially, Lehmann and colleagues, based on GEPs and ontologies from 587 TNBC cases, classified TNBC into six subtypes: BL1, BL2, mesenchymal (M), mesenchymal stem-like (MSL), immunomodulatory (IM), and luminal androgen receptor (LAR) (Lehmann et al., 2011). Whereas, recent findings, based on GEP analysis of most upregulated mRNAs and long non-coding RNAs (lncRNAs) (Liu et al., 2016), merged two subsets IM and MSL into “mesenchymal-like” and Basal1/2 into “BL” to give a most recent classification of four TNBC subtypes (Liu et al., 2016). Though the incursion of LAR assessment into the TNBC subtype requires further investigation, the components involved in the PIK3 pathway is worth considering while developing a targeted therapy (Chia et al., 2015). The IM-TNBC subtype accounts for all the immune-cell associated biomarkers and gene products such as antigen-presenting cells (APCs), chemokines, cytokines signaling components, etc. (Liu et al., 2016). Therefore, in this subtype, targeting immune checkpoints could provide beneficial therapeutic outcome.

Mesenchymal-like TNBC subtype (MES) expresses genes with epithelial-mesenchymal transition (EMT) signature and stem-cell-like properties. It primarily includes cell migration-related signaling pathways such as extracellular matrix-receptor interactions pathways, Wnt pathways, TGF $\beta$  signaling, breast stem cells biomarker, ALDH1A1, and other stem cells-oriented genes. It is also called metastatic BC (Lehmann et al., 2011) and is associated with cell differentiation pathways (Lehmann et al., 2011), which could be due to its high motility-related gene expression. Since MES is associated with growth factors, EMT-targeted chemotherapeutic drugs may benefit the patient (Gibson et al., 2005).

BL subtypes are associated at the mammary gland's basal/myoepithelial level, exhibiting overexpression of cell-proliferative biomarkers such as cell-cycle checkpoints, DNA repair, and replication related genes (Lehmann et al., 2011). Burstein's reclassification of TNBC subtypes highlights BL subtype exhibiting either downregulation of immune regulating genes—BL-immune-suppressive (BLIS)—and an upregulated immune response—BL-immune activated (BLIA)—TNBC subtype (Burstein et al., 2015). The prognosis index recorded the order in disease-free survival of BL-TNBC subtype—BLIA > M > LAR > BLIS (Burstein et al.,

2015). This order could be due to the tumor-infiltrating lymphocytes (TILs) found in the microenvironment of BLIA. The presence of TILs in the BLIA subtype of TNBC could further guide adjuvant chemotherapy treatments. In 2014, the International TILs group proposed facilitating TILs as a stratification factor or one of the significant parameters to assess heterogeneity in BC by hematoxylin and eosin staining evaluation (Salgado et al., 2015).

Traditional BC classifications that include IHC-hormone evaluations, GEP analysis, and examining pathological features have become clinically affordable in routine lab checkups. However, not all transcription synchronizes with the corresponding protein expression. Numerous factors, such as mRNA transcription rate, protein stability, post-translational modifications, and random mutations, affect proteins used as molecular biomarkers. Therefore, for complete knowledge on pathological changes in BC, high-throughput analysis of data extracted from several “omics” studies such as genomic, proteomic, transcriptomic, epigenetics, and Next-Gen Sequencing (NGS)—is needed for analyzing potential biomarkers and pathways involved. However, it still is a long bridge between research findings and its clinical implementations.

### Androgen Receptor

Another potential hormonal receptor—androgen receptor (AR)—is a prevalent sex steroid hormone used in BC subtyping (Labrie et al., 2003). In ER<sup>+</sup> BC, androgen and its receptor promote cell proliferation and spread (Safarpour et al., 2014) by acting at different components of AR-signaling pathways (Rahim and O'Regan, 2017). The AR is highly expressed in the LAR subtype, with mRNA level nine times or more than any other TNBC subtype (Lehmann et al., 2011), reflecting one-third of TNBCs (Mrklič et al., 2013). IHC analysis also detected a high expression of downstream components of AR-signaling (Mrklič et al., 2013). Therefore, anti-AR therapy is recommended for TNBC patients. In April 2020, the phase II trial showed promising results in its anti-androgen hormone—“bicalutamide”—study in treating metastatic BC patients (updated on ClinicalTrials.gov, Identifier NCT00468715). If the results came through as expected, AR assessment could be integrated into the standard test of TNBC subtypes.

### BC BIOMARKERS: ESTABLISHED AND PROMISING

BC's systemic management initially considers the expression level of the cell-proliferation gene (Ki67) and hormonal receptors (HR, PR, and HER2) before assessing its subtype clinicopathological and biological parameters. However, various scientific studies also reported some underrepresented single biomarkers (Figure 3). At present, only four such biomarkers—cancer antigens (CA); CA 15-3, CA 27-29, HER2, and circulating tumor cell (CTC) are approved by FDA in assessing BC in body fluids.

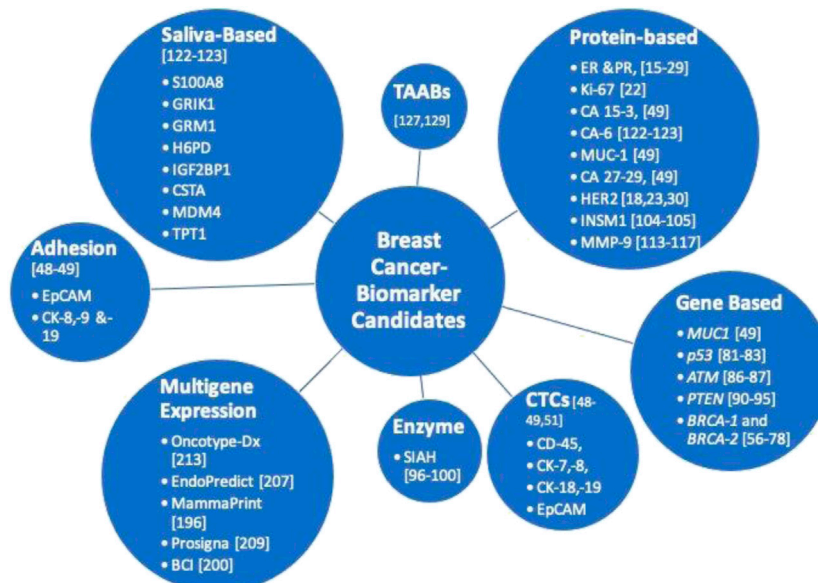


**FIGURE 3 |** Established and promising breast cancer biomarkers for prognosis and diagnosis.

The American society of clinical oncology (ASCO) recommends the gene expression analysis of CA 15-3 (mucin1 (MUC1) gene) and CA 27-29 together with bio-imaging for constant monitoring of treatment's persistence (Van Poznak et al., 2015).

CTCs are approved by the FDA in 2004 to be used in the CellSearch system for measuring and monitoring the metastasis of breast, prostate, and colorectal cancer (Cristofanilli et al., 2007). This CellSearch system analyzes the expression of EpCAM, CD-45, cytokeratin (CK)-8,-18, and CK-19 in body fluids (serum or blood) (Figure 3). In a large cohort of breast carcinoma (575 cases), Shao and colleagues observed that about 90% of all BC exhibit an expression of CK-7, -8, -18, and -19 (Shao et al., 2012). Furthermore, an expression of CK-7 in conjunction with CK-8 showed the utmost sensitivity at detecting BC, especially within high-grade tumors (Shao et al., 2012). Though it promises instant liquid biopsy, the scientific community raises some concerns about the heterogeneity and the low frequency of CTCs, making the detection a bit challenging. However, the addition of more molecular markers such as BSL-2 (Smerage et al., 2013), HER2, EGFR (Zhang L. et al., 2013), CD44, CD47, MET (Baccelli et al., 2013), and many more could assist in rectifying this issue. Nonetheless, this "CellSearch" system is still in its infancy. With a half-life ranging from one to 2 h in BC, CTC fails at guiding subtype-specific therapies (Alix-Panabières and Pantel, 2014).

## BRCA1 and BRCA2

BReast CAncer genes-1/-2 (*BRCA1/2*) are the most common genes implicated in BC risk. Their translated products are phosphoproteins localized in the nucleus (Chen et al., 1996; Bertwistle et al., 1997). BRCA1 protein regulates cellular pathways such as gene-transcription regulation, cell

proliferation, DNA repair response, etc., whereas BRCA2 protein regulates DNA repair pathway (Sharan et al., 1997). Early studies on germline mutation in the *BRCA1* gene found that the normal allele or the wild type (WT) copy was deleted in the event of *BRCA*-related cancers (BC or ovarian cancer). The loss of wild type *BRCA1* (or loss of heterozygosity) gene in tumor samples reveals its role as a tumor suppressor gene (Smith et al., 1992). Moreover, Arizti and colleagues observed regulatory parallels between *BRCA1* and tumor suppressor *p53* (Arizti et al., 2000) (Figure 3). Authors further suggested an interesting pathway connecting *p53* and *BRCA1* genes and that their loss under stress conditions could be integral to tumorigenesis (Arizti et al., 2000). In a separate study, loss of function mutation (frameshift or deletion/duplication) in *BRCA1* shown to result in genomic instability with increased susceptibility to malignancy (Deng, 2006). More than sixteen hundred mutations, predominantly frameshift mutations, have been reported so far in the *BRCA1* gene (Godet and Gilkes, 2017). In circumstances where a mutated copy of the *BRCA1/2* gene gets inherited from either parent, the offspring becomes more susceptible to develop BC. However, a single mutated gene doesn't always result in BC. Only the second mutation or the second defective gene that could affect the wild-type gene triggers BC development. Furthermore, since all cells carry similar genetic imprint, a non-inherited *BRCA* gene mutation is strictly tissue-restricted to the tumor region (breast or ovarian region) (Prevention, 2020; Singh and Yu, 2020). The *BRCA1/2* carriers display a histological characteristic of poorly differentiated high-grade tumors (Musolino et al., 2007). Its metastasis into neighboring vessels indicates a higher risk of contralateral BC (Verhoog et al., 1998; Brekelmans et al., 2007). Mavaddat and his colleagues anticipated the risk to be approximately 83% in *BRCA1* and 62% for *BRCA2* heterozygotes by age 70 (Mavaddat et al.,

2013). Though the contralateral prophylactic mastectomy significantly reduced cancer development risk (Van Sprundel et al., 2005), no survival benefit has been observed from the surgery (Brekelmans et al., 2006). Therefore, its early detection and prevention is now the focus of many studies. Upon molecular stratification, approximately 80% of *BRCA1* (Foulkes et al., 2003; Turner and Reis-Filho, 2006) and 3–17% of *BRCA2* related BC belong to the TNBC subtype (Evans et al., 2011) (Couch et al., 2015). Its prevalence also varies among ethnic groups. In Anglian (Anglian Breast Cancer Study Group, 2000) and US non-Hispanic white families (Whittemore et al., 2004), the frequency of pathogenic *BRCA1/2* variants range between 1:400 and 1:500 in the general population, while the highest observed frequency is about 1:40 in the Ashkenazi-Jewish community (King et al., 2003; Dillenburg et al., 2012). With the advancement of technologies such as NGS and multi-gene analysis, knowing the ethnic origin to estimate the chances of mutation(s) in *BRCA1/2* genes is obsolete. However, the knowledge of recurrent mutation in a particular ethnic group could still expedite the diagnosis and treatment among BC patients and related family members (Karami and Mehdipour, 2013), e.g., the three founders *BRCA1/2* congenital mutations account for up to 99% of pathogenic variants amongst the Ashkenazi-Jewish community (Dillenburg et al., 2012). However, the degree of correlation between *BRCA1/2* carriers and BC prognosis is still under investigation (van den Broek et al., 2015).

### Tumor Protein 53

TP53 is a proline-rich tumor suppressor protein first identified on SDS-PAGE an apparent molecular weight of 53 kDa, which later turned out to be 43.7 kDa based on amino acid composition. In human cancers, the *p53* gene is the most mutated gene that encodes at least 12 TP53 isoforms (p53 $\alpha$ , p53 $\beta$ , p53 $\gamma$ ,  $\Delta$ 40p53 $\alpha$ ,  $\Delta$ 40p53 $\beta$ ,  $\Delta$ 40p53 $\gamma$ ,  $\Delta$ 133p53 $\alpha$ ,  $\Delta$ 133p53 $\beta$ ,  $\Delta$ 133p53 $\gamma$ ,  $\Delta$ 160p53 $\alpha$ ,  $\Delta$ 160p53 $\beta$ , and  $\Delta$ 160p53 $\gamma$ ) of varying sizes from 11 exons (Kim and An, 2016). The mutations, most of which are missense mutations, primarily locate in the central DNA binding domain of the TP53 (Marcel et al., 2011), preventing the activity of TP53 by affecting its binding to DNA. Other mutations can yield truncated isoforms which are associated with different cancers. On the other hand, not all of them have their biological significance reported or investigated utterly. In a cohort of 127 BC cases, of three interdependent TP53 isoforms—p53 $\alpha$ , p53 $\beta$ , p53 $\gamma$ —, only p53 $\gamma$  isoform displayed a good prognosis similar to its wild type TP53 in BC patients (Bourdon et al., 2011). However, regardless of the mutation, approximately 80% of TNBC cases contain a mutated *p53* gene. And, since TNBC is tolerant to endocrine therapies, mutated TP53 highlights its prospective biomarker role (Figure 3) (Shah et al., 2012). Moreover, the first-in-class monoclonal antibodies developed recently recognizes the most common polymorphic region of TP53 (Hwang et al., 2018), i.e., the DNA binding domain. The antibody displays no cross-reactivity against any other p53 isoform. These mutant-specific monoclonal antibodies hold a great clinical diagnostic

potential in targeting minute alterations embedded in various diseased states (Hwang et al., 2018).

### Ataxia Telangiectasia Mutation

*AT* is another tumor suppressor gene, like *p53*, involved in the DNA repair mechanism. Its mutation in women exhibits a greater risk of BC (Thompson et al., 2005). Since it associates with an autosomal recessive disease, patients homozygous for it will be primarily affected. In contrast, the heterozygous patients live an everyday life, but their chances of developing BC are approximately two to four times higher than the general population. An extensive metadata analysis of nineteen heterogeneous cohort studies on relatives of patients suffering from *AT* syndrome suggested that the comparative risk of BC is 6.02% by 50 years of age (95% credible interval: 4.58–7.42%) and 32.83% by 80 years of age (95% credible interval: 24.55–40.43%) (Marabelli et al., 2016) than the general population. Begam and her colleagues also recently concluded their study on aberrant *ATM* promoter methylation as a biomarker to detect BC in patients (Begam et al., 2017) (Figure 3). However, the hurdle in its biomarker role is its relative infrequency of mutation and high prevalence of variants.

### Phosphatase and Tensin Homolog

*PTEN* gene mutation is implicated in a wide variety of sporadic cancers (Milella et al., 2015). It is majorly associated with cellular functions such as genomic stability, cell proliferation, and motility through PI3K dependent/independent pathways. In an invasive BC study on 3,824 patients, an average of 7% exhibited germline mutation in their *PTEN* gene (Gao et al., 2013) (Figure 3). Moreover, although *PTEN*'s mutations aren't prominent, its loss frequency is approximately 30–40% in BC, accounting for about 25% in HER2<sup>+</sup> BC (Zhang H. Y. et al., 2013; Veeraraghavan et al., 2017). Furthermore, its insignificant protein expression levels led to investigating/detecting its mRNA levels much more efficiently than its IHC analysis. Likewise, numerous studies have also highlighted the cases where *PTEN*'s loss status fails to correlate with drug treatment response in BC patients. In the tamoxifen plus everolimus (TAMRAD) and the BC Trials of Oral Everolimus-2 (BOLERO-2) studies, *PTEN*'s status fails to correlate with the response to everolimus treatment in BC patients (Treilleux et al., 2015). Moreover, studies on HER2<sup>+</sup> BC further reported an unsuccessful association between *PTEN* loss and anti-HER therapy response (trastuzumab and lapatinib) (Fujita et al., 2006; Nuciforo et al., 2015). Therefore, clinicians should also combine other pathological parameters of BC besides analyzing *PTEN* gene expression.

### Seven in Absentia Homolog

A growth factor activated RAS pathway is responsible for uncontrolled cell growth, proliferation, and dissemination in various human cancers (Schmidt et al., 2007). In BC, the RAS pathway is an understudied pathway due to an insignificant detection of RAS mutations in mammary tumors (only in about 5% of the BC patients) (Arteaga et al., 2012). Further, it has been observed that the most downstream and an essential component of the EGFR/HER2/RAS pathway is an evolutionarily



conserved E3 ligase— SIAH—that acts as a “gatekeeper” to tumorigenesis (Medhioub et al., 2000; Schmidt et al., 2007). Behling and colleagues found that its expression was proportional to the progression of ductal carcinoma *in situ* (DCIS) to invasive carcinoma (Behling et al., 2011). Though it is the most downstream component of the pathway, inhibiting SIAH expression or its enzymatic activity inhibits the RAS-mediated tumor growth and metastasis in nude mice (Schmidt et al., 2007). The inhibitory effect of reduced SIAH expression may affect the upstream of the pathway, as a feedback loop mechanism. Its enzymatic activity may be nurturing/fostering the tumor cells by modulating its microenvironment. Clinically, it can be recognized in combination with EGFR or alone as a surrogate biomarker guiding chemotherapy treatment by analyzing the depth and recurrence of chemo-resistant tumor clones (van Reesema et al., 2016). Its on and off expression reflects the aggression and repression in post-neoadjuvant chemotherapy patients, a prognostics that outperform the HR/HER/Ki67 as a new biomarker (van Reesema et al., 2016) (**Figure 3**). Furthermore, based on its expression and enzymatic alterations, expectations are to develop a targeted therapy against SIAH, alone or in combination with EGFR, for chemo-resistant, relapsed, late-stage, and metastatic BC.

SIAH is an evolutionarily conserved gene, and its mutations rarely account for any specific disease (Medhioub et al., 2000; Schmidt et al., 2007; Zhao et al., 2016). Some research groups have observed *SIAH1* gene mutations in certain carcinomas such as hepatocellular carcinoma, prostate cancers, breast cancers, etc., whereas the results were hard to interpret because of the interference of other tumor suppressor genes located on the same chromosome (Medhioub et al., 2000; Zhao et al., 2016).

### Insulinoma-Associated Protein 1

In 2003, the WHO incorporated a classification of BC with neuroendocrine (NE) differentiation features (Lakhani et al., 2012), which was first reported in 1963 for its correlation with BC. The classification was further revised to carcinomas of neuroendocrine features in the 2012 WHO classification of BC (Bussolati and Badve, 2012; Lakhani et al., 2012). Its subgroup, invasive breast carcinoma (IBC) with neuroendocrine differentiation (IBC-NE), is a rare subtype predominant in postmenopausal women. In a large IBC cohort, Razvi and his colleagues evaluated a biomarker—INSM1—for NE differentiation using IHC (Razvi et al., 2020). According to the authors, in about 7% of the cases, the INSM1-IHC expression profile was found comparable or more sensitive than predefined NE biomarkers: chromogranin A and CD56, but less sensitive than synaptophysin (Razvi et al., 2020). INSM1 was initially reported, by Goto and colleagues, to be in the fetal pancreas and nervous system as a zinc finger transcription factor (Goto et al., 1992). Most recently, it has been observed in high grade and aggressive breast carcinomas, particularly among luminal-B subtypes (Wachter et al., 2014; Razvi et al., 2020). The authors further suggested INSM1 expression as a favorable prognostic biomarker (**Figure 3**), which could be useful in stratifying NE-tumors (NET) with different prognosis (Razvi et al., 2020).

### Matrix Metalloproteinase-9

Matrix metalloproteinases (MMP) are a family of endopeptidases acting on a broad range of proteins such as gelatin, collagen, and elastin (Kessenbrock et al., 2010). MMP-9, also known as gelatinase B, is an extracellular protease that remodels the tumor environment by degrading the endothelial basement membrane (Kessenbrock et al., 2010). The disrupted membrane enables carcinoma invasion and triggers angiogenic switch, a necessary step in tumor progression (Gialeli et al., 2011; Mehner et al., 2014). MMP-9 also activates soluble factors such as cytokines, which induce EMT and invade microenvironment of distant organs, promoting metastasis (Gialeli et al., 2011; Mehner et al., 2014). Its expression is regulated by various pathways, such as MAPK, ERK, EGFR/PI3K (Dziembowska and Włodarczyk, 2012; Shi et al., 2015), implicated widely in BC. MMP-9 is considered as a potential biomarker in various cancers (Tian et al., 2008; Li et al., 2012; Li L.-N. et al., 2013; Blanco-Prieto et al., 2017; Chen et al., 2018; Zhou et al., 2018) (**Figure 3**). In BC, MMP-9 expression varies with its molecular (intrinsic) subtypes (Yousef et al., 2014). Yousef and colleagues observed a signature expression of MMP-9 in HER2<sup>+</sup> and TNBC subtype with node-positive breast carcinoma (Yousef et al., 2014). Multivariate serum analysis for MMP-9, together with the extracellular domain (ECD) of HER2 (HER2-ECD) and neuron-specific enolase (NSE) (a non-specific NE biomarker), was able to discriminate between BC patients for brain metastasis (Darlix et al., 2016). Furthermore, a non-invasive multivariate exploration could stratify BC patients based on serum MMP-9 expression in conjunction with Rho expression in circulating leukocytes (Golubnitschaja et al., 2017) for BC risk assessment.

MMP-9 polymorphisms have been associated with many diseases such as pancreatic ductal adenocarcinoma (Tian et al., 2008), ovarian and cervical cancer (Li et al., 2012; Li L.-N. et al., 2013), lung cancer (Blanco-Prieto et al., 2017), bone tumor (Varn et al., 2017; Chen et al., 2018), atherosclerosis. However, its relationship with BC's occurrence is still unclear (Felizi et al., 2018).

### Salivary Biomarkers

Investigating the saliva's protein profile for discriminatory cancer biomarkers has been shelved for decades due to technological limitations. Recently, salivary metabolite profiling has received much attention as a noninvasive biomarker for early BC detection. Zhang and colleagues (Streckfus et al., 2006) initiated a *de novo* biomarker discovery approach in saliva (Zhang et al., 2010). The study established a total of nine biomarkers, eight mRNAs (S100A8, GRIK1, GRM1, H6PD, IGF2BP1, CSTA, MDM4, and TPT1) and one CA protein-6 (CA-6), with a clinical diagnostic accuracy of 92% (Zhang et al., 2010) (**Figure 3**). The protein, CA-6, was also found to be a marker in an earlier study on saliva samples of DCIS patients (Streckfus et al., 2006). Subsequent studies found an altered metabolism for approximately 28 different metabolites (Sugimoto et al., 2010), such as valine, proline (Cheng et al., 2015), taurine, lysine, and sialic acid (Ozturk et al., 2011), statistically discriminating BC from healthy controls. Moreover, Laidi and colleagues suggested that salivary



autoantibodies could play a role in BC screening (Laidi et al., 2016). In conclusion, saliva-based biomolecules have shown growing importance in salivary biomarker discovery for future research. However, ASCO has not yet endorsed the use of salivary biomarkers as diagnostic tools for BC.

## Tumor-Associated Autoantibodies

TAABs are antibodies produced by a patient's immune cells against tumor-associated antigens (TAAs) that are comparatively overexpressed in cancer cells (Laidi et al., 2016). The body's immune system recognizes TAAs as foreign entities and triggers an acquired immune response to produce TAABs. These antibodies are an amplified "tumor signal" that may fulfill the biomarker features of cancer, i.e., specificity and sensitivity (Figure 3). With the advancement in technologies, such as serological proteome assay (SERPA), serological analysis of tumor antigens by recombinant DNA (cDNA) expression cloning (SEREX), multiple affinity protein profiling (MAPping), and many more, novel immune biomarkers of BC have been discovered and utilized in the early detection of antigens such as TP53, HSP60, Mn-SOD, cyc-B1, c-myc, and so forth (Hamrita et al., 2008). However, these TAAs are aberrantly expressed or post-translationally modified or irregularly regulated in tumors. It is, therefore, evident that a single TAA-targeted TAAB isn't sufficient for BC detection. A set of multiple TAA-targeted TAABs followed by validation through traditional techniques such as enzyme-linked immunosorbent assay (ELISA), antigen array, and many more could discriminate cancer cells against healthy control. Kim and colleagues successfully devised an autoantibody-based bead array panel of 35 TAAs in a multiplexing assay with an accuracy of approximately 91% (Kim et al., 2009). Noninvasive and simplified detection of TAABs paved the way for its future research as diagnostic biomarkers. Although these TAABs show a strong titer, their heterogeneous nature—due to TAAs' post-translational modification (PTM)—and our inadequate understanding of humoral response, limit their clinical applications.

## BREAST CANCER DIAGNOSTICS

### Mammography

Traditionally, mammography has been used as a gold standard in the screening of BC (Society, 2019). It is a low dosed X-ray exam for each breast, examining breast lumps, skin changes, and nipple discharge or thickening. The digital images, known as a mammogram, are taken both horizontally and vertically to cover a breast to its entirety. These mammograms interpret for mass/lesions, calcifications, and architectural distortions in the breast tissue (Barazi and Gunduru, 2019). Mammography detects such mass/lesions relatively at a stage when the mass has already progressed into a tumor. The interpretations are reported in a Breast Imaging Reporting and Data System (BI-RADS) to communicate with the physician for further assessments (Reporting, 2003). Despite being the gold standard in breast screening, it has significant limitations. The rate of false-

positive is significantly high (Hubbard et al., 2011). An increase in fibro-glandular breast tissue density increases the chance of masking or mimicking the underlying BC in a mammogram because both dense tissue and cancer appear white (Boyd et al., 2007). Also, women may fail to inform about their breast implants, leading to misidentification (Society, 2019). Moreover, though a low dose, radiation generated health concerns among patients (Hauge et al., 2014). Out of these limitations, clinical trials are in session evaluating if mammography can be substituted by other advanced techniques such as MRI (Moy et al., 2009) or digital breast tomosynthesis (DBT) (Society, 2019). DCIS or lobular carcinoma *in situ* (LCIS) and IDC, mammography is the best, superior to MRI and ultrasound. Yet, for detecting ILC, a biopsy is more suitable than mammography (Society, 2019).

### Molecular Imaging

Magnetic Resonance Imaging (MRI) is a standard technique that uses a magnetic field, in contrast to X-rays in mammography, to analyze the lumps in the breast that later need to be biopsied (Society, 2019). Several modifications have been incorporated in MRI over decades. For example, a contrast reagent, such as gadolinium diethylenetriamine penta-acetic acid (GD-DTPA), is injected into the bloodstream, followed by MRI detection to enhance the images in pinpointing the suspected area for further analysis. Similarly, radioactive chemicals (in Breast Specific Gamma Imaging (BSGI) or Scintimammography) or radioactive particle conjugated with a sugar moiety (in Positron Emission Mammography (PEM)) can be injected intravenously to study the spread of BC and to follow up on patients. With technological advancement in MRI based techniques such as dynamic contrast-enhanced MRI (DCE-MRI) (Chang et al., 2016; Rahbar and Partridge, 2016), chemical exchange saturation transfer MRI (CEST-MRI) (Cai et al., 2014), etc., evaluating metabolic heterogeneity within tumors becomes feasible. However, the requirement of sophisticated equipment constraints its availability to all hospitals/clinics. The exposure to radioactive materials and expenses involved further limit a patient's willingness to a yearly checkup. As a result, they are recommended only to high-risk women patients (Society, 2019).

### Ultrasound

As a complementary procedure, ultrasound is a follow-up examination to confirm a positive mammogram (Society, 2019). Several reports have supported the use of automated breast (AB) ultrasonography (ABUS) over mammography for dense breast tissue exams (Kolb et al., 2002; Society, 2019). Contrast-enhanced ultrasonography (CEUS) and microvascular imaging successfully discriminate malignant and benign tumors by analyzing blood flow dynamics in local tissues (Li Y.-J. et al., 2013). CEUS further guides or predicts the effects of neoadjuvant chemotherapy on BC patients (Amioka et al., 2016). As a supplement to mammography, ABUS identifies an additional 1.9 cancer cases per 1,000 women screened (Brem et al., 2015). However, it requires a quality interpretation by an experienced radiologist to minimize false positives.

## Digital Imaging/Spectroscopy

Recently, three new noninvasive technology have emerged promoting BC screening and diagnosis—digital infra-red thermal imaging (DITI), digital image-based elastotomography (DIET), and electrical impedance scanning/spectroscopy (EIS).

DITI measures a localized skin temperature difference to reflect the physiological changes such as vasodilation, neovascularization, inflammation, lymph dysfunction/congestion (Anbar, 1998), and other suspicious activities around the breast borders (sternum or axilla). The changes recorded by the infra-red camera are graphed into a heat map of the breast, also called a thermogram. However, due to its low accuracy, its clinical application is limited. With the recent development of a high-resolution infrared camera, a new interest has been generated in its usage as a BC detection tool.

DIET utilizes the vibrational energy in graphing the location of the tumor (Lee et al., 2014). Sinusoidal waves of low-frequency vibrations (5–100 Hz), as a result of surface motion, are induced in the breast, and the oscillations are recorded by digital cameras tracking fiducial markers (Brown et al., 2007; Peters et al., 2009). Areas with a different surface vibrational response compared to control tissues are considered potentially the tumor infected areas. Feeding these responses to an algorithm allows an evaluation of the phase delay in surface-vibrations, thereby detecting the tumor's angular location, depth, and size (Peters et al., 2008). Clinically, it can detect small tumors that may have gone undetected by an experienced clinician, who depends on manual palpation as the initial diagnosis. Moreover, it can reduce false positives as a screening method, thereby preventing unnecessary radiation and discomfort. However, it cannot provide information on the subtype of BC involved (Ganau et al., 2015).

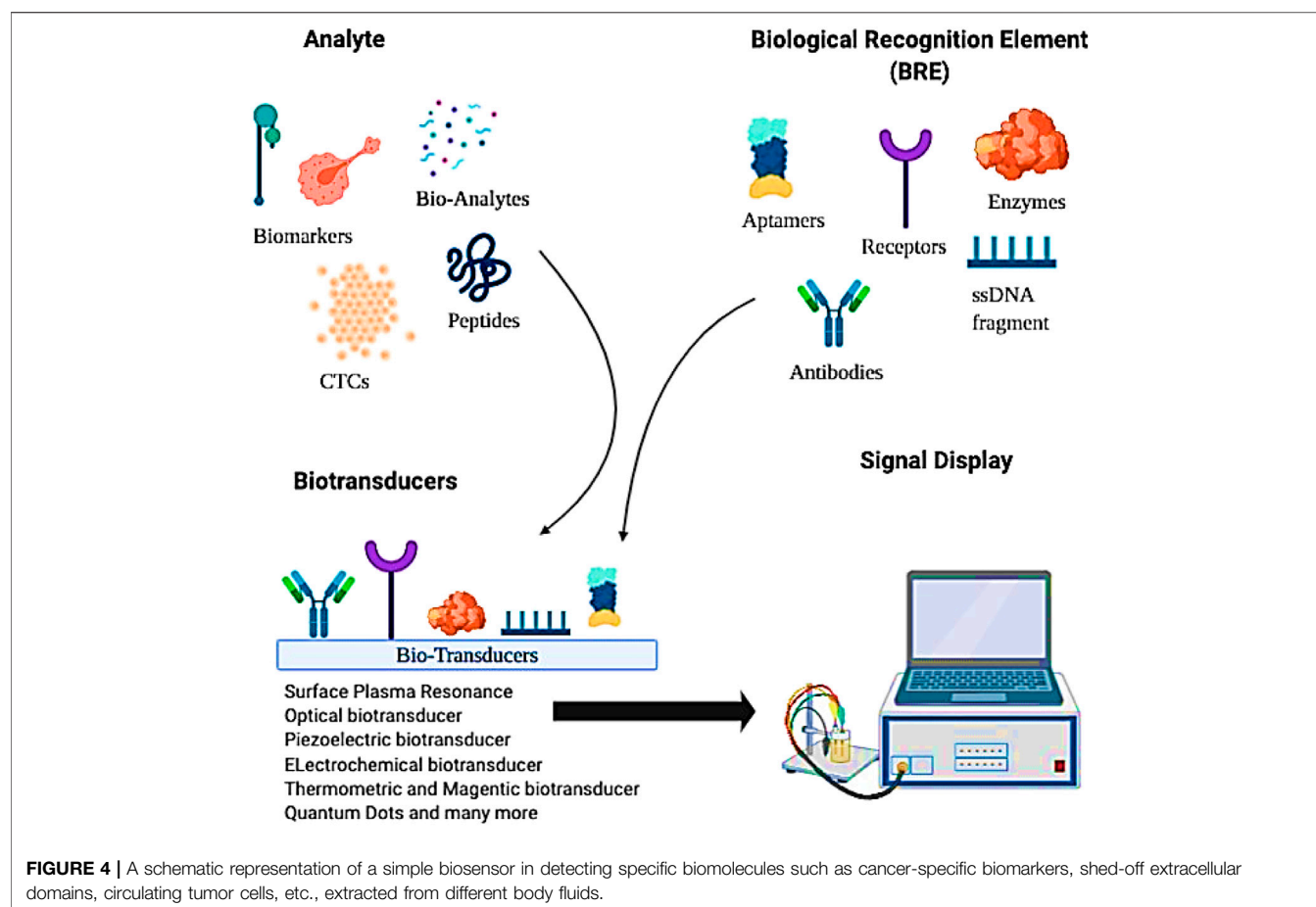
EIS measures the electro resistance (bio-impedance) (Jossinet, 1996) with the principle that tissues have different electrical properties under different metabolic conditions (Morimoto et al., 1990). The multi-frequency EIS measures the tissue's overall bio-impedance/resistance by varying frequencies (50 samples), ranging from 300 Hz to 10 MHz (Jossinet, 1996). Since a disease (like cancer) creates finite metabolic changes in tissues, EIS can discriminate diseased tissues from normal tissues by analyzing the amount of impedance contributed by different cellular components, including the extracellular environment (Alzurq et al., 2016). For example, at low frequency (<1000 Hz), an electric current will pass through the extracellular fluid only, but at higher frequencies (10 kHz–10 MHz), it can conduct through both intracellular and extracellular spaces (Morimoto et al., 1990; Jossinet, 1996; Chauveau et al., 1999). Clinically, the EIS spectrum of higher frequencies is found more relevant at detecting malignancies (Ollmar and Grant, 2016). Using EIS, Haeri and colleagues successfully separated BC patients from healthy patients by accurately measuring the cell shape, structure, depth, intracellular and extracellular environment, and lipid membrane compositions (Haeri et al., 2016).

## Biosensors

Biosensors' inception can be traced back to Leyland's lab in 1956, where the Clark electrodes were invented to detect blood-oxygen (Clark, 1956). Since then, remarkable modifications have been documented in biosensors to sense any abnormality that could result in disease. Biosensors consist of three key components: a receptor, a biomarker, and a transducer (**Figure 4**). Besides cell surface biomarkers, their shed off ECDs also act as potential biomarkers (Marques et al., 2014). Multiple bioreceptor—biochemical recognition elements (BRE)—are employed to detect such biomolecules in a sample. Biotransducer converts positive interactions between biomarker and bioreceptors into measurable signals (Marques et al., 2014). An adequately structured biosensor is portable in nature with user-friendly features. Its non-invasive and inexpensive point-of-care analysis provides a quick response without compromising its specificity and selectivity (Nikhil et al., 2016).

In a biosensor, BRE is the most versatile component. It could be any entity with specificity toward a biomarker such as antibodies, aptamers, enzymes, CTCs, and many more (**Figure 4**). In this regard, antibodies are the most common BREs used in biosensors. Contributing to real nano-sense at detecting BC, antibodies have created a commercial niche in BC diagnosis. With recombinant antibodies—a third-generation antibodies—that contains modified antigen-binding domains, the sensitivity limitations that were previously associated with traditional—poly- or monoclonal—antibodies, can now be overcome (Haurum, 2006). It could detect BC biomarkers directly (Sonuç and Sezgintürk, 2014; Eletxigerra et al., 2015) or indirectly by using enzymatic probes (for example, HRP) (Yang et al., 2011), fluorescence probes (Chang et al., 2011) or cross-linkers (Wang et al., 2014; Arkan et al., 2015). However, the thermal instability of antibodies and the tests' reproducibility are still a challenge and need further research.

Researchers have designed a string of specific nucleotide/peptide sequences, which function on the same principle as antibodies but one-third of the size, as tight target binders known as aptamers. Peptide aptamers and nucleic acid aptamers (NAAs) can bind specifically with high affinity to biomolecules, circulating in body fluids, such as glycoproteins, microRNA (Won et al., 2013), and most recently to whole cells (Rong et al., 2016). Interestingly, nucleotide aptamers are selected from a large DNA/RNA library through a combinatorial process—systemic evolution of ligands by exponential enrichment (SELEX)—used in molecular biology for producing ligand-specific oligonucleotides (Tuerk and Gold, 1990). Aptamers bind because they “fit” their targets. With remarkable folding properties, aptamers make secondary and tertiary structures of ssDNA or RNA interacting with the BC biomarkers (Chambers et al., 2008). Its binding to the target is determined by how the bases are stacked, the intercalations, and the target's hydrophobic interactions. These physical parameters can be chemically refined to bind a variety of targets with specificity. Unlike antibodies, aptamers are easily chemically modifiable by conjugation chemistry to provide greater thermal stability and reduced toxicity. Several researchers have



designed aptamer for HER2 (Chun et al., 2013; Qureshi et al., 2015), EpCAM (Song et al., 2013), MUC1 (He et al., 2012; Hu et al., 2014), VEGF (Zhao et al., 2011) and nucleolin (Feng et al., 2011) for early BC detection.

Besides aptamers and antibodies, cDNA based hybridization biosensor has been investigated in various BC detection studies (Figure 4). In one study, the detection of microRNAs (Zhang et al., 2016) and the *BRCA1* gene (Cui et al., 2017) have been permitted using a modified cDNA hybridization technique. The hybridized complex formed between cDNA and the target was further amplified in real-time by a DNA polymerase enzyme, right at the electrode. The authors additionally observed an exponential increase in the signal, which shortens the analysis time while keeping the sensitivity and selectivity intact (Benvidi et al., 2015).

Similarly, compatibility between BRE and biotransducer is of utmost importance for a useful biosensor. Several modifications have been made in biotransducers to quantify the acquired signal in proportion to the analyte concentration (Nikhil et al., 2016). Modifications such as, optical transducers (Dey and Goswami, 2011), electrochemical (Grieshaber et al., 2008), piezoelectric biotransducers (Pohanka, 2018), thermometric and magnetic-based transducers etc. have been employed by various researchers for targeting *BRCA1* (Culha et al., 2004; Benvidi et al., 2015), HER-2 (Chang et al., 2011; Marques et al., 2014), MUC1 (Chang et al., 2011; Hu et al., 2014), miR-21 (Torrente-

Rodríguez et al., 2015; Li D. et al., 2016), EpCAM (Arya et al., 2013), etc., in early BC detection. Also, nanoparticle enhancers were employed alongside with biotransducers to generate an amplified readout signal. Surface plasmon resonance (SPR) biotransducers that provide real-time sensing by analyzing the changes in refractive index upon interaction with labeled biomolecules has recently been used in conjunction with nanoparticles, resulting in the enhancement of the sensitivity of detecting biomarkers such as CA15-3 (Liang et al., 2012), HR (Neo et al., 2009), and MUC1 (Li Y. et al., 2016). In the past few years, research in quantum dots (QDs)/nanocrystals has gained momentum in early BC detection. QDs as nano-labels, structurally, provide a better platform for antibody/protein/aptamer conjugation that can target biomolecules such as tumor-associated exosomes (Boriachek et al., 2017), CTCs (Wu et al., 2018), etc. In a study, Cheng and colleagues designed a three-component DNA construct containing—MUC1 multi-peptide aptamer stem, QDs-reporter, and a quencher—that detects MUC1 peptide at a nano-molar level (Cheng et al., 2009). Freitas and colleagues successfully screened HER2ECD biomarkers in human serum by combining QDs to electrochemical immunosensing (Freitas et al., 2020). The entire screening was completed within 2 h, with hands-on-time of less than 30 min (Freitas et al., 2020). Compared to enzyme-based label systems, the QD label electrochemical sensing eliminates the

**TABLE 1 |** List of genes/proteins common in the different multigene test analysis. All abbreviations are widely known and are procured following the HGNC and IPNC guidelines. Color coding reflects common genes/proteins included in multiple testing panels.

Oncotype-Dx (21genes)	Prosigna (50genes)	Mammaprint (70genes)	IHC4 (4 proteins)	EndoPredict (12genes)	BCI (7genes)	Mammostrat (5proteins)
<i>BCL2</i>	<i>BCL2</i>	<i>CENPA</i>			<i>CENPA</i>	TP53
<i>BIRC5</i>	<i>BIRC5</i>	<i>ALDH4A1</i>		<i>BIRC5</i>	<i>BUB1B</i>	HTF9C
<i>CCNB1</i>	<i>CCNB1</i>	<i>AA555029_RC</i>		<i>AZGP1</i>	<i>HOXB13</i>	CEACAM5
<i>BAG1</i>	<i>BAG1</i>	<i>AP2B1</i>		<i>CALM2</i>	<i>IL17BR</i>	NDRG1
<i>GRB7</i>	<i>GRB7</i>	<i>AYTL2</i>		<i>DHCR7</i>	<i>NEK2</i>	SLC7A5
<i>MMP11</i>	<i>MMP11</i>	<i>BBC3</i>		<i>HBB</i>	<i>RACGAP1</i>	
<i>MYBL2</i>	<i>MYBL2</i>	<i>C16orf61</i>		<i>IL6ST</i>	<i>RRM2</i>	
<i>PGR</i>	<i>PGR</i>	<i>C20orf46</i>	<i>PGR</i>	<i>MGP</i>		
<i>ESR1</i>	<i>ESR1</i>	<i>ESM1</i>	<i>ESR1</i>	<i>OAZ1</i>		
<i>HER2</i>	<i>KNTC2</i>	<i>KNTC2</i>	<i>HER2</i>	<i>RBBP8</i>		
<i>Ki67</i>	<i>MELK</i>	<i>MELK</i>	<i>Ki67</i>	<i>RPL37A</i>		
<i>RPLPO</i>	<i>ORC6L</i>	<i>ORC6L</i>		<i>STC2</i>		
<i>TRFC</i>	<i>UBE2C</i>	<i>EXT1</i>		<i>UBE2C</i>		
<i>SCUBE2</i>	<i>CDC6</i>	<i>SCUBE2</i>				
<i>ACTB</i>	<i>CXXC5</i>	<i>C9orf30</i>				
<i>CD68</i>	<i>EGFR</i>	<i>CCNE2</i>				
<i>GAPDH</i>	<i>ERBB2</i>	<i>CDC42BPA</i>				
<i>GSTM1</i>	<i>ACTR3B</i>	<i>CDCA7</i>				
<i>GUS</i>	<i>BLVRA</i>	<i>COL4A2</i>				
<i>STK15</i>	<i>CDC20</i>	<i>DIAPH3</i>				
<i>CTSL2</i>	<i>CDCA1</i>	<i>DTL</i>				
	<i>CDH3</i>	<i>EBF4</i>				
	<i>EXO1</i>	<i>FGF18</i>				
	<i>FGFR4</i>	<i>FLT1</i>				
	<i>FOXA1</i>	<i>GMPS</i>				
	<i>FOXC1</i>	<i>GNAZ</i>				
	<i>GPR160</i>	<i>GPR126</i>				
	<i>KIF2C</i>	<i>GPR180</i>				
	<i>KRT14</i>	<i>GSTM3</i>				
	<i>KRT17</i>	<i>HRASLS</i>				
	<i>KRT5</i>	<i>IGFBP5</i>				
	<i>MAPT</i>	<i>JHDM1D</i>				
	<i>MDM2</i>	<i>LGP2</i>				
	<i>MIA</i>	<i>LIN9</i>				
	<i>MKI67</i>	<i>LOC100131053</i>				
	<i>MLPH</i>	<i>LOC100288906</i>				
	<i>MYC</i>	<i>LOC730018</i>				
	<i>NAT1</i>	<i>MCM6</i>				
	<i>UBE2T</i>	<i>MMP9</i>				
	<i>CENPF</i>	<i>MTDH</i>				
	<i>CEP55</i>	<i>NMU</i>				
	<i>CCNE1</i>	<i>NUSAP1</i>				
	<i>ANLN</i>	<i>DCK</i>				
	<i>SFRP1</i>	<i>ECT2</i>				
	<i>SLC39A6</i>	<i>EGLN1</i>				
	<i>TMEM45B</i>	<i>OXCT1</i>				
	<i>TYMS</i>	<i>PALM2</i>				
	<i>PHGDH</i>	<i>PECI</i>				
	<i>PTTG1</i>	<i>PITRM1</i>				
	<i>RRM2</i>	<i>PRC1</i>				
		<i>QSCN6L1</i>				
		<i>RAB6B</i>				
		<i>RASSF7</i>				
		<i>RECQL5</i>				
		<i>RFC4</i>				
		<i>RTN4RL1</i>				
		<i>RUNDC1</i>				
		<i>MS4A7</i>				
		<i>SERF1A</i>				
		<i>SLC2A3</i>				
		<i>STK32B</i>				
		<i>TGFB3</i>				
		<i>TSPYL5</i>				
		<i>UCHL5</i>				
		<i>WISP1</i>				
		<i>ZNF533</i>				



substrate requirement, surpasses enzymes' thermal instability, and provides quick analysis.

In conclusion, by offering a quick, simple, and inexpensive diagnostic tool, especially in BC, the biosensor market is growing exponentially and is expected to surpass approximately US\$40 billion by 2022 (Pfeifer, 2018). Despite all that, further research is needed to increase the detection sensitivity in almost all biosensors.

## ADVANCED BC DETECTION SYSTEMS

### Multiple Gene Prognostic Assays

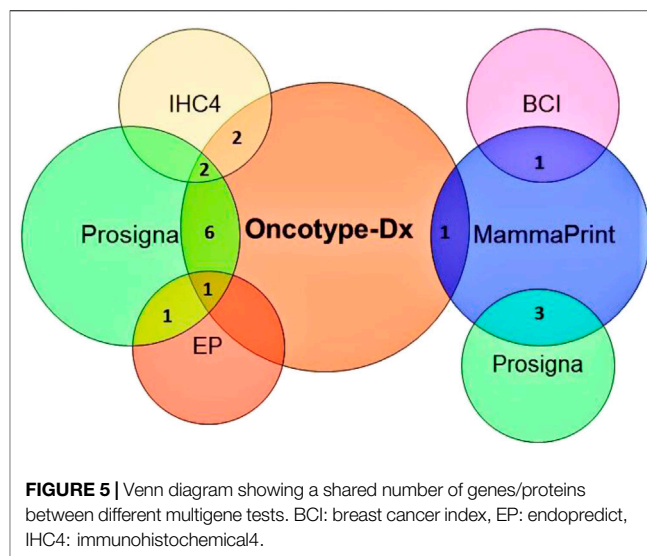
In the era of big data, analyzing the large number of sequences (DNA, RNA, and protein array) from various studies can help devise a systemic strategy combating BC. Several genetic aberrations in women have a predisposition to BC. Incorporating genes that have been implicated in BC as a potential biomarker can provide an advantage in early BC detection and treatment (Walsh et al., 2011). With multigene signature analysis alongside other molecular tools, clinicians can now devise appropriate therapies and predict their outcome while minimizing detrimental effects. Currently, there are seven prognostic multigene signature analyzing tests for BC. However, not all are FDA approved. Some are recommended by agencies, such as the ASCO, American-National Comprehensive Cancer Network (NCCN), and the European Society of Medical Oncology (ESMO) in their guidelines.

### Breast Cancer Index Test

BCI test is a multigene assay developed by Biotheranostics Inc. It records: 1) a set of five proliferative gene expressions (*BUB1B*, *CENPA*, *NEK2*, *RACGAP1*, and *RRM2*), termed as molecular grade index (MGI), and 2) a gene ratio of *HOXB13: IL17BR* (H: I), in predicting the BC outcome (Sgroi et al., 2013) (Table 1). The study compared BCI and IHC4 for their predictive ability in early and late recurrence in postmenopausal-ER<sup>+</sup> patients with node-negative BC who participated in the clinical trial for arimidex, tamoxifen, alone or in combination (Sgroi et al., 2013). The linear BCI model showed significant prognostic value for risk of both early and late distant recurrence. Consistent results were reported in the Stockholm TAM cohort (Zhang et al., 2013), where BCI was able to identify two risk populations in both early and late distant recurrence and aiding in residual risk management after 5 years. In ASCO 2020 meeting, Biotheranostics' Trans-aTTOM study delivered more evidence on BCI as a powerful prognostic tool informing the risk-benefit for extending adjuvant therapy (Bartlett et al., 2020). However, the BCI scores can only be used as an adjunct tool to the operating physician's practice because it relies on the correlation with the patient's clinicopathological study. In conclusion, though its implications are worth considering in clinical research, it has still not been approved by the FDA.

### MammaPrint Test

The MammaPrint test developed by Agendia is a genomic test used for early-stage BC diagnosis. NCCN, ESMO, and ASCO



have recommended molecular signature analysis of 70 genes for primary BC prognosis (Cardoso et al., 2016) (Table 1). Its FDA's approval as a prognostic test stratifies early-staged hormonal BC into low vs. high-risk for relapse (Van De Vijver et al., 2002). The ASCO guidelines of 2017 incorporate MammaPrint test scores to guide on therapy required for high-risk HR<sup>+</sup>/HER2<sup>-</sup> with node-negative breast carcinoma (Krop et al., 2017). The guidelines further state that "MammaPrint assay may assist in decisions on withholding the therapy in patients with one to three positive nodes and high clinical risk, provided that the patient should be informed that a benefit from chemotherapy cannot be excluded" (Krop et al., 2017). Extensive validation studies were performed before the MammaPrint tool became the standard of care. The Microarray In Node negative disease may Avoid Chemotherapy (MINDACT) study on 6,693 women with early-stage BC observed that the 70-genes analysis was able to detect even small aggressive tumors and was able to spare chemotherapy in patients with high clinical risk and low genomic risk of recurrence (ROR) (Cardoso et al., 2016). Therefore, the circumvention of chemotherapy in postmenopausal women with a low-risk of recurrence (as per the MammaPrint test) showcases its clinical utility as a prognostic genomic test (Cardoso et al., 2020). However, in TNBC and HER2<sup>+</sup> BC, MammaPrint tests are not recommended until additional studies and results met the ASCO requirements.

### Mammostrat Test

In contrast to multigene tests, Mammostrat is a five-protein based IHC assay (Table 1). It analyzes proteins (TP53, NDRG1, CEACAM5, HTF9C, and SLC7A5) that have been implicated in BC recurrence (Ring et al., 2006). The test score stratifies early-staged luminal BC with node-negative or positive carcinoma into low-risk to high-risk patients (Bartlett et al., 2010). Mammostrat test evaluates early-stage BC patients on tamoxifen therapy, analyzing and informing them of adjuvant therapy's benefits. Like BCI, it is an adjuvant factor for BC evaluation. As per ASCO

guidelines, patients with HR<sup>+</sup>/HER2<sup>-</sup> with node-positive or negative breast carcinoma are moderately not recommended for the Mammostrat test. But, for TNBC or HER2<sup>+</sup> patients, the Mammostrat test is strictly not recommended.

### IHC4 Test

IHC4 is a hormonal receptor protein-based assay focuses on four primary proteins, ER, PR, HER2, and Ki67 expressions, which were previously used as biomarkers to define surrogate molecular subtypes. Unlike BCI, IHC4 evaluates protein expressions, none of which is translated by BCI associated genes. As an independent tool, IHC4 combines the information from four biomarker proteins (Cuzick et al., 2011) to predict patients' prognosis (Table 1). A modified version of IHC4 (mIHC4) was recently suggested for ER<sup>+</sup>/HER2<sup>-</sup> metastatic BC patients (Jin et al., 2020), guiding on chemo or endocrine therapy. However, IHC4 is not recommended for TNBC and HER2 carcinoma (Harris et al., 2016), and the ASCO guidelines have not endorsed the use of IHC4 due to its unsatisfactory reproducibility (Cuzick et al., 2011).

### EndoPredict Test

EP is a twelve multigene signature assay developed by Myriad Genetics (Table 1). It examines biopsied tumor tissue for eight cancer-related genes, three RNA-reference gene, and one DNA-reference gene (Filipits et al., 2011). The test score (EPclin Risk Score) that reflects tumor size and nodal status stratifies BC as low or high risk for distant metastasis (Filipits et al., 2012). In the GEICAM trial, EPclin Risk Score was used as an independent prognostic parameter for ER<sup>+</sup>/HER2<sup>-</sup> BC with node-negative patients treated with chemotherapy followed by hormonal therapy (Martin et al., 2014). According to the ASCO guidelines, EPclin Risk Score may also be employed in the decision-making process as an adjuvant factor in ER<sup>+</sup>/PR<sup>+</sup> HER2<sup>-</sup> node-negative BC patients. However, for HER2<sup>+</sup> and TNBC with node-positive breast carcinoma, ASCO doesn't recommend EPclin Risk Score due to insufficient evidence for its usefulness (Harris et al., 2016).

### Prosigna/Prediction Analysis of Microarray50 Test

Prosigna, formerly known as Prediction Analysis of Microarray50 (PAM50), is a RNA-based gene molecular signature assay developed by NanoString Technologies (Martin et al., 2014). This assay helps profile a patient's tumor and understand its behavior. It includes analysis models to evaluates relapse/recurrence based on BC's intrinsic hormonal subtyping, developed by Parker et al. (Parker et al., 2009). In Prosigna, the RNA extracted from the biopsied tumor sample is analyzed to provide information on the subtype involved and predict the tumor's recurrence. The analysis is based on the Prediction Analysis of Microarray (PAM) signature assay (Martin et al., 2014) (Table 1), evaluating the activity of 58 genes by integrating NanoString's nCounter technology to simplify the workflow without compromising its efficiency (Nielsen et al., 2014). The fluorescent probes used in nCounter technology bypasses

mRNA amplification, thus saving time and material. The results are digitalized and later fed into an algorithm that translates tumor biology into actionable clinical results (Tibshirani et al., 2002). The algorithm includes hormonal expression and clinicopathological assessment of tumor based on its size and proliferative potential. The results scaled on 0–100, as the risk of relapse/recurrence (ROR) score, classifying node-negative cancers into low (0–40), intermediate (41–60), or high (61–100) risk, and node-positive cancers into low (0–40) or high (41–100) risk. According to the ASCO guidelines, a physician may use this signature assay alongside the clinicopathological parameters for high-risk HR<sup>+</sup>/HER2<sup>-</sup> node-negative BC patients to select an adjuvant therapy (Harris et al., 2016). However, it doesn't recommend using Prosigna score for the low-risk group, HER2<sup>+</sup> and TNBC with node-positive breast carcinoma (Harris et al., 2016).

### Oncotype Dx Test

Oncotype Dx is one of the most validated multigene signature assay, developed by Paik and colleagues (Paik et al., 2004) at Genomic Health, Inc. The ASCO guidelines incorporate it for the early-stage ER<sup>+</sup>/HER2<sup>-</sup> node-negative BC patients with a high risk of recurrence Tian et al. (2008). It analyzes the RNA expression of 21 genes implicated in cancer proliferation and treatment response Tian et al. (2008) (Table 1). In conjunction with the patient's age, the algorithm calculates a score between 0 and 100 as an Oncotype Dx Recurrence Score (RS), stratifying early-stage BC into a group of low, intermediate, and high risk of recurrence. In the low risk (RS < 18) group, chemotherapy benefits outweigh the risk of side effects, wherein high risk (RS > 31) group, chemotherapy benefits should surpass the rise of side effects. In this manner, the intermediate (RS 18–31) groups are the most volatile ones, with uncertainty whether chemotherapy outweighs the side effects or not. With recent technological advancement and research in GEP, an optimization was made in the RS cutoff (Sparano et al., 2015). In the Tailor-Dx phase-3 trial study, Sparano and colleagues confirmed its usefulness in guiding adjuvant systemic therapy (Sparano et al., 2015) in women older than 50 years. According to the authors, chemotherapy can be avoided in 1) women older than 50 years with RS 11–15, 2) women younger than 50-year-old with RS 11–16, and 3) women with RS 0–10. Chemotherapy followed by hormonal therapy were assigned for women with RS > 25. ASCO guidelines advise against the application of chemotherapy for the early-staged HR<sup>+</sup>/HER2<sup>-</sup> node-negative BC patients with low risk of recurrence. The guidelines provide no direct assessment in intermediate RS patients; instead, they refer to TAILORx's recommendation alongside traditional prognostic factors (Andre et al., 2019). The guidelines further indicate that the Oncotype Dx test should not be used in HER2<sup>+</sup> and TNBC (Harris et al., 2016; Krop et al., 2017).

Most of the multigene assays have overlapping target genes in their analysis (Figure 5). Though multigene prognostics are an effective means of detection, different prognostics' results tell a different tale. A comparative study on 1) MammaPrint and Oncotype Dx RS (Nunes et al., 2016; Tsai et al., 2018), 2) Oncotype Dx and Prosigna (Dowsett et al., 2013), 3)

TransATAC study on six different tests: EP, IHC4, Oncotype Dx, BCI, Prosigna, and clinical treatment score (that evaluates nodal status, tumor size, grade, age, and endocrine treatment beyond 5 years) (Sestak et al., 2018), observed different prognostics information in their patients. A discordance in findings reflects the importance of integrating additional factors such as clinicopathological information with genomic imprint analysis (Kwa et al., 2017).

## CONCLUSION AND FUTURE PERSPECTIVES

Despite large number of research articles published on BC diagnosis and treatment, research in its early detection still lags. Although several techniques have been developed in the last decade permitting detection and guidance on specific therapies, individual techniques' pros and cons limit their utilization as a standalone tool. To plan a proper treatment, understanding the tumor's molecular heterogeneity is crucial. An acute stratification is necessary as each group or sub-group exhibits individual prognosis and systemic therapy. Luminal A and B have an overlapping hormonal expression but have different prognosis and treatments. HER2<sup>+</sup> BC has a better prognosis and shows a promising outcome upon merging chemotherapy with anti-HER2 monoclonal antibodies and tyrosine kinase inhibitor-based therapies. TNBC remains a challenge to treat. Recent studies have suggested that analyzing BC molecular subtypes can give better information on recurrence and treatment response.

The traditional classifications that include IHC-hormone evaluations, GEP analysis, and examining pathological features have become clinically more affordable in routine processes. However, gene transcription does not necessarily correlate with protein expression. Numerous factors, such as mRNA transcription rate, protein stability, post-translational modifications, and random mutations, also affect protein biomarkers' therapeutic potential. Several genetic mutations predispose BC in women. Therefore, for a complete understanding of pathological changes in BC, a high-throughput analysis of data extracted from several "omics" studies is needed to interpret biomarkers and pathways involved.

The pursuit of suitable BC biomarkers took us in the era of big data or the era of "BC-Omics." Genomics, metabolomics, and proteomics with predictive and prognostic BC biomarkers have laid the foundation of various multigene assays for early detection and treatment strategy. Currently, there are seven prognostic signature tests available for BC, MammaPrint, Breast Cancer Index, IHC4, EndoPredict, Prosigna, Mammostrat, and Oncotype Dx. Of the seven tests, Mammostrat and IHC4 are protein-based tests, while others are multi-gene-based screening. With multigene signature analysis alongside other molecular tools, clinicians can now select appropriate therapies and predict treatment duration more easily. A prognostic profile developed from multigene tests could better predict recurrence risk. Further, it could help

avoid unnecessary treatments in low-risk patients so that they could resume their daily routines. As per ASCO guidelines, their use for screening BCs have not been approved. Clinical experts' committees request more evidence to support multigene tests' routine usage in HR<sup>+</sup>/HER2<sup>-</sup> with node-positive BC in guiding adjuvant therapy. A comparative analysis of different multigene tests predicts distinct prognostics for the same patient, reflecting the importance of integrating clinicopathological information with genomic imprint analysis. Moreover, the cost of these tests is another obstacle for general use. Also, the expense of training the staff always remains an undervalued proposition that brings the challenge of maintaining the tests' quality and reproducibility. Again, not all the tests are FDA approved. Additional clinical studies and results from large cohorts are needed to meet the ASCO requirements. There remains a gap between research findings and its clinical implementations. Several ongoing extensive cohort studies on BC, such as MINDACT, TAILORx, Trans-aTTOM, and many more, may provide positive impact on long-term patient outcome and guide the therapy.

Several clinical observations have found different treatment responses among diverse ethnic groups. In the era of personalized medicine, individualizing therapy is the next step in cancer treatment's evolution. For a long time, human cell lines' engraftment onto immunocompromized animals (Neve et al., 2006)—cell-derived xenografts (CDX)—have been used to understand BC genetics and its biological processes. With the advancement in understanding the importance of tumor microenvironment (Hanahan and Weinberg, 2011), the development of patient-derived xenografts (PDX) (Hoffman, 2015) circumvents the limitations with CDX. Unlike CDX, PDX models preserve the tumor's heterogeneity, behavioral characteristics (metastasis), the microenvironment, and many other features. A unique advantage of PDX is its response to therapy (Tentler et al., 2012; Hidalgo et al., 2014). New models incorporate rare but aggressive BC (Wurth et al., 2015). Mimicking clinical trials of adjuvant therapy through experimental models such as PDX and syngeneic models will be significantly improved. Currently, these models of BC are amidst scientific debate in various immune-molecular societies (Varn et al., 2017) and are considered as mouse "avatars" for the patient (Holen et al., 2017). Besides, the immense amount of time and capital invested in such models' development limits them to cohort-based preclinical studies. As such, a good *in vivo* model of BC is needed (Holen et al., 2017).

Furthermore, the discovery of the immune checkpoint proteins such as cytotoxic-T-lymphocyte-associated antigen-4 (CTLA-4) and Programmed Death-1 (PD-1) has led to a booming in immune-targeted therapies against tumors. Following targeted therapies' strategy, oncolytic virus therapy (OVT) has shown potential in treating cancers, e.g., melanoma. Unlike gene therapy, where the virus is a carrier, OVT engineered the virus to target, infiltrate, multiply, and kill melanoma cells, leaving the normal cells unharmed. It includes four of the seven classes of viruses in the Baltimore classification system for BC treatment. Several scientific

studies have obtained encouraging results with OVT based immune-targeted therapy. Therefore, mono-therapeutic approaches are rarely the best treatment option for BC. Collaboration across disciplines appears more promising and gaining traction in personalized treatments. With increasing knowledge and the advancement in diagnostics and treatment strategies, BC will become better understood and more manageable.

## AUTHOR CONTRIBUTIONS

MZ wrote the manuscript, SW and NA edited the manuscript.

## REFERENCES

- Alix-Panabières, C., and Pantel, K. (2014). Challenges in circulating tumour cell research. *Nat. Rev. Cancer* 14 (9), 623–631. doi:10.1038/nrc3820
- Alzurq, E., Almaktari, A., Aldin, B., Hamoud, M., and Othman, S. (2016). New system for early breast cancer detection by Electrical impedance spectroscopy. *Recent Adv. Environ. Sci. Biomed.* 4, 142–150.
- Amioka, A., Masumoto, N., Gouda, N., Kajitani, K., Shigematsu, H., Emi, A., et al. (2016). Ability of contrast-enhanced ultrasonography to determine clinical responses of breast cancer to neoadjuvant chemotherapy. *Jpn. J. Clin. Oncol.* 46 (4), 303–309. doi:10.1093/jjco/hyv215
- Anbar, M. (1998). Clinical thermal imaging today. *IEEE Eng. Med. Biol. Mag.* 17 (4), 25–33. doi:10.1109/51.687960
- Andre, F., Ismaila, N., Henry, N. L., Somerfield, M. R., Bast, R. C., Barlow, W., et al. (2019). Use of biomarkers to guide decisions on adjuvant systemic therapy for women with early-stage invasive breast cancer: ASCO clinical practice guideline update-integration of results from TAILORx. *J. Clin. Oncol.* 37 (22), 1956–1964. doi:10.1200/JCO.19.00945
- Anglian Breast Cancer Study Group (2000). Prevalence and penetrance of BRCA1 and BRCA2 mutations in a population-based series of breast cancer cases. *Br. J. Cancer* 83 (10), 1301. doi:10.1054/bjoc.2000.1407
- Arizti, P., Fang, L., Park, I., Yin, Y., Solomon, E., Ouchi, T., et al. (2000). Tumor suppressor p53 is required to modulate BRCA1 expression. *Mol. Cell Biol.* 20 (20), 7450–7459. doi:10.1128/mcb.20.20.7450-7459.2000
- Arkan, E., Saber, R., Karimi, Z., and Shamsipur, M. (2015). A novel antibody-antigen based impedimetric immunosensor for low level detection of HER2 in serum samples of breast cancer patients via modification of a gold nanoparticles decorated multiwall carbon nanotube-ionic liquid electrode. *Anal. Chim. Acta* 874, 66–74. doi:10.1016/j.aca.2015.03.022
- Arteaga, C. L., Sliwkowski, M. X., Osborne, C. K., Perez, E. A., Puglisi, F., and Gianni, L. (2012). Treatment of HER2-positive breast cancer: current status and future perspectives. *Nat. Rev. Clin. Oncol.* 9 (1), 16–32. doi:10.1038/nrclinonc.2011.177
- Arya, S. K., Wang, K. Y., Wong, C. C., and Rahman, A. R. (2013). Anti-EpCAM modified LC-SPDP monolayer on gold microelectrode based electrochemical biosensor for MCF-7 cells detection. *Biosens. Bioelectron.* 41, 446–451. doi:10.1016/j.bios.2012.09.006
- Atwood, C., Hovey, R., Glover, J., Chepko, G., Ginsburg, E., Robison, W., et al. (2000). Progesterone induces side-branching of the ductal epithelium in the mammary glands of peripubertal mice. *J. Endocrinol.* 167 (1), 39–52. doi:10.1677/joe.0.1670039
- Baccelli, I., Schneeweiss, A., Riethdorf, S., Stenzinger, A., Schillert, A., Vogel, V., et al. (2013). Identification of a population of blood circulating tumor cells from breast cancer patients that initiates metastasis in a xenograft assay. *Nat. Biotechnol.* 31 (6), 539–544. doi:10.1038/nbt.2576
- Barazi, H., and Gunduru, M. (2019). *Mammography BI RADS grading. StatPearls*. Treasure Island, FL: StatPearls Publishing.
- Bardou, V. J., Arpino, G., Elledge, R. M., Osborne, C. K., and Clark, G. M. (2003). Progesterone receptor status significantly improves outcome prediction over estrogen receptor status alone for adjuvant endocrine therapy in two large breast cancer databases. *J. Clin. Oncol.* 21 (10), 1973–1979. doi:10.1200/JCO.2003.09.099
- Bartlett, J., Sgroi, D. C., Treuner, K., Zhang, Y., Piper, T., Salunga, R. C., et al. (2020). HER2 status and prediction of extended endocrine benefit with breast cancer index (BCI) in HR+ patients in the adjuvant tamoxifen: to offer more?(aTTom) trial. *J. Clin. Oncol.* 38 (15\_suppl), 522. doi:10.1200/JCO.2020.38.15\_suppl.522
- Bartlett, J. M., Thomas, J., Ross, D. T., Seitz, R. S., Ring, B. Z., Beck, R. A., et al. (2010). Mammostrat as a tool to stratify breast cancer patients at risk of recurrence during endocrine therapy. *Breast Cancer Res.* 12 (4), R47. doi:10.1186/bcr2604
- Begam, N., Jamil, K., and Raju, S. G. (2017). Promoter hypermethylation of the ATM gene as a novel biomarker for breast cancer. *Asian Pac. J. Cancer Prev. APJCP* 18 (11), 3003. doi:10.22034/APJCP.2017.18.11.3003
- Behling, K. C., Tang, A., Freyding, B., Chervoneva, I., Kadakia, S., Schwartz, G. F., et al. (2011). Increased SIAH expression predicts ductal carcinoma in situ (DCIS) progression to invasive carcinoma. *Breast Cancer Res. Treat.* 129 (3), 717–724. doi:10.1007/s10549-010-1254-8
- Benvidi, A., Dehghani Firouzabadi, A., Dehghan Tezerjani, M., Moshtaghian, S. M., Mazloum-Ardakani, M., and Ansarin, A. (2015). A highly sensitive and selective electrochemical DNA biosensor to diagnose breast cancer. *J. Electroanalytical Chem.* 750, 57–64. doi:10.1016/j.jelechem.2015.05.002
- Bertwistle, D., Swift, S., Marston, N. J., Jackson, L. E., Crossland, S., Crompton, M. R., et al. (1997). Nuclear location and cell cycle regulation of the BRCA2 protein. *Cancer Res.* 57 (24), 5485–5488.
- Blanco-Prieto, S., Barcia-Castro, L., Pérez de la Cadena, M., Rodríguez-Berrocal, F. J., Vázquez-Iglesias, L., Botana-Rial, M. I., et al. (2017). Relevance of matrix metalloproteases in non-small cell lung cancer diagnosis. *BMC cancer* 17 (1), 823. doi:10.1186/s12885-017-3842-z
- Blum, J. L., Flynn, P. J., Yothers, G., Asmar, L., Geyer, C. E., Jr, Jacobs, S. A., et al. (2017). Anthracyclines in early breast cancer: the ABC trials-USOR 06-090, NSABP B-46-I/USOR 07132, and NSABP B-49 (NRG oncology). *J. Clin. Oncol.* 35 (23), 2647. doi:10.1200/JCO.2016.71.4147
- Boriachek, K., Islam, M. N., Gopalan, V., Lam, A. K., Nguyen, N. T., and Shiddiky, M. J. A. (2017). Quantum dot-based sensitive detection of disease specific exosome in serum. *Analyst* 142 (12), 2211–2219. doi:10.1039/c7an00672a
- Bourdon, J. C., Khoury, M. P., Diot, A., Baker, L., Fernandes, K., Aoubala, M., et al. (2011). p53 mutant breast cancer patients expressing p53y have as good a prognosis as wild-type p53 breast cancer patients. *Breast Cancer Res.* 13 (1), R7. doi:10.1186/bcr2811
- Boyd, N. F., Guo, H., Martin, L. J., Sun, L., Stone, J., Fishell, E., et al. (2007). Mammographic density and the risk and detection of breast cancer. *N. Engl. J. Med.* 356 (3), 227–236. doi:10.1056/NEJMoa062790
- Brekelmans, C., Seynaeve, C., Menke-Pluymers, M., Brüggerwirth, H., Tilanus-Linthorst, M., Bartels, C., et al. (2006). Survival and prognostic factors in BRCA1-associated breast cancer. *Ann. Oncol.* 17 (3), 391–400. doi:10.1093/annonc/mdj095
- Brekelmans, C., Tilanus-Linthorst, M., Seynaeve, C., vd Ouweland, A., Menke-Pluymers, M. B., Bartels, C. C., et al. (2007). Tumour characteristics, survival and prognostic factors of hereditary breast cancer from BRCA2-, BRCA1- and non-BRCA1/2 families as compared to sporadic breast cancer cases. *Eur. J. Cancer* 43 (5), 867–876. doi:10.1016/j.ejca.2006.12.009
- Brem, R. F., Tabár, L., Duffy, S. W., Inciardi, M. F., Guingrich, J. A., Hashimoto, B. E., et al. (2015). Assessing improvement in detection of breast cancer with three-dimensional automated breast US in women with dense breast tissue: the SomoInsight Study. *Radiology* 274 (3), 663–673. doi:10.1148/radiol.14132832

## FUNDING

This publication was made possible by the Arkansas INBRE program, supported by a grant from the National Institute of General Medical Sciences, (NIGMS), P20 GM103429 from the National Institutes of Health.

## ACKNOWLEDGMENTS

The authors would like to thank Mr. Lauv Patel of University of Arkansas at Little Rock for his help during editing the manuscript.



- Briskin, C. (2002). Hormonal control of alveolar development and its implications for breast carcinogenesis. *J. Mammary Gland Biol. Neoplasia* 7 (1), 39–48. doi:10.1023/a:1015718406329
- Brown, R., Hann, C., Chase, J. G., and Ray, L. (2007). Discrete color-based Euclidean-invariant signatures for feature tracking in a DIET breast cancer screening system. *Med. Imaging 2007: Physiol. Funct. Struct. Med. Images, Int. Soc. Opt. Photon.* 6511, 65110D. doi:10.1117/12.711815
- Burstin, M. D., Tsimelzon, A., Poage, G. M., Covington, K. R., Contreras, A., Fuqua, S. A., et al. (2015). Comprehensive genomic analysis identifies novel subtypes and targets of triple-negative breast cancer. *Clin. Cancer Res.* 21 (7), 1688–1698. doi:10.1158/1078-0432.CCR-14-0432
- Bussolati, G., and Badve, S. (2012). “Carcinomas with neuroendocrine features,” in *WHO Classification of Tumours of the Breast*. Editors S. R. Lakhani, I. O. Ellis, S. J. Schnitt, P. H. Tan, and M. J. van de Vijver (Lyon, France: IARC Press), 62–63.
- Cai, K., Xu, H. N., Singh, A., Moon, L., Haris, M., Reddy, R., et al. (2014). Breast cancer redox heterogeneity detectable with chemical exchange saturation transfer (CEST) MRI. *Mol. Imaging Biol.* 16 (5), 670–679. doi:10.1007/s11307-014-0739-y
- Cardoso, F., van't Veer, L. J., Bogaerts, J., Slaets, L., Viale, G., Delaloge, S., et al. (2016). 70-Gene signature as an aid to treatment decisions in early-stage breast cancer. *N. Engl. J. Med.* 375 (8), 717–729. doi:10.1056/NEJMoa1602253
- Cardoso, F., van't Veer, L., Poncet, C., Lopes Cardozo, J., Delaloge, S., Pierga, J.-Y., et al. (2020). MINDACT: long-term results of the large prospective trial testing the 70-gene signature MammaPrint as guidance for adjuvant chemotherapy in breast cancer patients. *Am. Soc. Clin. Oncol.* 38, 506. doi:10.1200/JCO.2020.38.15\_suppl.506
- Casás-Selves, M., and DeGregori, J. (2011). How cancer shapes evolution and how evolution shapes cancer. *Evo. Edu. Outreach.* 4 (4), 624–634. doi:10.1007/s12052-011-0373-y
- Chambers, J. P., Arulananandam, B. P., Matta, L. L., Weis, A., and Valdes, J. J. (2008). Biosensor recognition elements. *Curr. Issues Mol. Biol.* 10, 1–12. doi:10.1007/978-0-387-75936-4\_1
- Chang, R. F., Chen, H. H., Chang, Y. C., Huang, C. S., Chen, J. H., and Lo, C. M. (2016). Quantification of breast tumor heterogeneity for ER status, HER2 status, and TN molecular subtype evaluation on DCE-MRI. *Magn. Reson. Imaging* 34 (6), 809–819. doi:10.1016/j.mri.2016.03.001
- Chang, Y. F., Hung, S. H., Lee, Y. J., Chen, R. C., Su, L. C., Lai, C. S., et al. (2011). Discrimination of breast cancer by measuring prostate-specific antigen levels in women's serum. *Anal. Chem.* 83 (13), 5324–5328. doi:10.1021/ac200754x
- Chauveau, N., Hamzaoui, L., Rochaix, P., Rigaud, B., Voigt, J., and Morucci, J. (1999). *Ex vivo* discrimination between normal and pathological tissues in human breast surgical biopsies using bioimpedance spectroscopy. *Ann. N. Y. Acad. Sci.* 873 (1), 42–50. doi:10.1111/j.1749-6632.1999.tb09447.x
- Cheang, M. C. U., Chia, S. K., Voduc, D., Gao, D., Leung, S., Snider, J., et al. (2009). Ki67 index, HER2 status, and prognosis of patients with luminal B breast cancer. *JNCI: J. Natl. Cancer Inst.* 101 (10), 736–750. doi:10.1093/jnci/djp082
- Chen, L., Zhang, J., He, Y., and Ding, X. Y. (2018). Matrix metalloproteinase-9 expression of GCTSC in peripheral tissue and central tissue of GCTB. *J. Cell Biochem.* 119 (7), 5805–5812. doi:10.1002/jcb.26766
- Chen, Y., Farmer, A. A., Chen, C. F., Jones, D. C., Chen, P. L., and Lee, W. H. (1996). BRCA1 is a 220-kDa nuclear phosphoprotein that is expressed and phosphorylated in a cell cycle-dependent manner. *Cancer Res.* 56 (14), 3168–3172.
- Cheng, A. K., Su, H., Wang, Y. A., and Yu, H. Z. (2009). Aptamer-based detection of epithelial tumor marker mucin 1 with quantum dot-based fluorescence readout. *Anal. Chem.* 81 (15), 6130–6139. doi:10.1021/ac901223q
- Cheng, F., Wang, Z., Huang, Y., Duan, Y., and Wang, X. (2015). Investigation of salivary free amino acid profile for early diagnosis of breast cancer with ultra performance liquid chromatography-mass spectrometry. *Clin. Chim. Acta* 447, 23–31. doi:10.1016/j.cca.2015.05.008
- Chia, K., O'Brien, M., Brown, M., and Lim, E. (2015). Targeting the androgen receptor in breast cancer. *Curr. Oncol. Rep.* 17 (2), 4. doi:10.1007/s11912-014-0427-8
- Chun, L., Kim, S.-E., Cho, M., Choe, W.-s., Nam, J., Lee, D. W., and Lee, Y. (2013). Electrochemical detection of HER2 using single stranded DNA aptamer modified gold nanoparticles electrode. *Sensors Actuators B: Chem.* 186, 446–450. doi:10.1016/j.snb.2013.06.046
- Clark, L., Jr (1956). Monitor and control of blood and tissue oxygen tensions. *ASAIO J.* 2 (1), 41–48.
- Couch, F. J., Hart, S. N., Sharma, P., Toland, A. E., Wang, X., Miron, P., et al. (2015). Inherited mutations in 17 breast cancer susceptibility genes among a large triple-negative breast cancer cohort unselected for family history of breast cancer. *J. Clin. Oncol.* 33 (4), 304. doi:10.1200/JCO.2014.57.1414
- Creighton, C. J., Fu, X., Hennessy, B. T., Casa, A. J., Zhang, Y., Gonzalez-Angulo, A. M., et al. (2010). Proteomic and transcriptomic profiling reveals a link between the PI3K pathway and lower estrogen-receptor (ER) levels and activity in ER+ breast cancer. *Breast Cancer Res.* 12 (3), R40–R12. doi:10.1186/bcr2594
- Creighton, C. J., Kent Osborne, C., van de Vijver, M. J., Foekens, J. A., Klijn, J. G., Horlings, H. M., et al. (2009). Molecular profiles of progesterone receptor loss in human breast tumors. *Breast Cancer Res. Treat.* 114 (2), 287–299. doi:10.1007/s10549-008-0017-2
- Cristofanilli, M., Broglio, K. R., Guarneri, V., Jackson, S., Fritsche, H. A., Islam, R., et al. (2007). Circulating tumor cells in metastatic breast cancer: biologic staging beyond tumor burden. *Clin. Breast Cancer* 7 (6), 471–479. doi:10.3816/cbc.2007.n.004
- Cui, M., Wang, Y., Wang, H., Wu, Y., and Luo, X. (2017). A label-free electrochemical DNA biosensor for breast cancer marker BRCA1 based on self-assembled antifouling peptide monolayer. *Sensors Actuators B: Chem.* 244, 742–749. doi:10.1016/j.snb.2017.01.060
- Cui, X., Schiff, R., Arpino, G., Osborne, C. K., and Lee, A. V. (2005). Biology of progesterone receptor loss in breast cancer and its implications for endocrine therapy. *J. Clin. Oncol.* 23 (30), 7721–7735. doi:10.1200/JCO.2005.09.004
- Culha, M., Stokes, D. L., Griffin, G. D., and Vo-Dinh, T. (2004). Application of a miniature biochip using the molecular beacon probe in breast cancer gene BRCA1 detection. *Biosens. Bioelectron.* 19 (9), 1007–1012. doi:10.1016/j.bios.2003.09.006
- Cuzick, J., Dowsett, M., Pineda, S., Wale, C., Salter, J., Quinn, E., et al. (2011). Prognostic value of a combined estrogen receptor, progesterone receptor, Ki-67, and human epidermal growth factor receptor 2 immunohistochemical score and comparison with the Genomic Health recurrence score in early breast cancer. *J. Clin. Oncol.* 29 (32), 4273–4278. doi:10.1200/JCO.2010.31.2835
- Darlix, A., Lamy, P. J., Lopez-Crapez, E., Braccini, A. L., Firmin, N., Romieu, G., et al. (2016). Serum NSE, MMP-9 and HER2 extracellular domain are associated with brain metastases in metastatic breast cancer patients: predictive biomarkers for brain metastases? *Int. J. Cancer* 139 (10), 2299–2311. doi:10.1002/ijc.30290
- Deng, C.-X. (2006). BRCA1: cell cycle checkpoint, genetic instability, DNA damage response and cancer evolution. *Nucleic Acids Res.* 34 (5), 1416–1426. doi:10.1093/nar/gkl010
- Dey, D., and Goswami, T. (2011). Optical biosensors: a revolution towards quantum nanoscale electronics device fabrication, *J. Biomed. Biotechnol.*, 2011, 348218. doi:10.1155/2011/348218
- Dillenburg, C. V., Bandeira, I. C., Tubino, T. V., Rossato, L. G., Dias, E. S., Bittelbrunn, A. C., et al. (2012). Prevalence of 185delAG and 5382insC mutations in BRCA1, and 6174delT in BRCA2 in women of Ashkenazi Jewish origin in southern Brazil. *Genet. Mol. Biol.* 35 (3), 599–602. doi:10.1590/S1415-47572012000400009
- Dowsett, M., Houghton, J., Iden, C., Salter, J., Farndon, J., A'hern, R., et al. (2006). Benefit from adjuvant tamoxifen therapy in primary breast cancer patients according oestrogen receptor, progesterone receptor, EGF receptor and HER2 status. *Ann. Oncol.* 17 (5), 818–826. doi:10.1093/annonc/mdl016
- Dowsett, M., Sestak, I., Lopez-Knowles, E., Sidhu, K., Dunbier, A. K., Cowens, J. W., et al. (2013). Comparison of PAM50 risk of recurrence score with oncotype DX and IHC4 for predicting risk of distant recurrence after endocrine therapy. *J. Clin. Oncol.* 31 (22), 2783–2790. doi:10.1200/JCO.2012.46.1558
- Dziembowska, M., and Włodarczyk, J. (2012). MMP9: a novel function in synaptic plasticity. *Int. J. Biochem. Cell Biol.* 44 (5), 709–713. doi:10.1016/j.biocel.2012.01.023
- Eletigerra, U., Martinez-Perdiguero, J., Merino, S., Barderas, R., Torrente-Rodríguez, R., Villalonga, R., et al. (2015). Amperometric magnetoelectrode for ErbB2 breast cancer biomarker determination in human serum, cell lysates and intact breast cancer cells. *Biosens. Bioelectron.* 70, 34–41. doi:10.1016/j.bios.2015.03.017
- Ellis, I., Pinder, S., Bobrow, L., Buley, I., Coyne, J., Going, J., et al. (2005). *Pathology reporting of breast disease*. London, United Kingdom: NHS Publications.

- Ellis, M. J., Coop, A., Singh, B., Mauriac, L., Llombert-Cussac, A., Jänicke, F., et al. (2001). Letrozole is more effective neoadjuvant endocrine therapy than tamoxifen for ErbB-1- and/or ErbB-2-positive, estrogen receptor-positive primary breast cancer: evidence from a phase III randomized trial. *J. Clin. Oncol.* 19 (18), 3808–3816. doi:10.1200/JCO.2001.19.18.3808
- Ellis, M. J., Tao, Y., Young, O., White, S., Proia, A. D., Murray, J., et al. (2006). Estrogen-independent proliferation is present in estrogen-receptor HER2-positive primary breast cancer after neoadjuvant letrozole. *J. Clin. Oncol.* 24 (19), 3019–3025. doi:10.1200/JCO.2005.04.3034
- Evans, D., Howell, A., Ward, D., Lalloo, F., Jones, J., and Eccles, D. (2011). Prevalence of BRCA1 and BRCA2 mutations in triple negative breast cancer. *J. Med. Genet.* 48 (8), 520–522. doi:10.1136/jmedgenet-2011-100006
- Felizi, R. T., Veiga, M. G., Carelli Filho, I., Souto, R. P. D., Fernandes, C. E., and Oliveira, E. (2018). Association between matrix metalloproteinase 9 polymorphism and breast cancer risk. *Rev. Bras Ginecol Obstet.* 40 (10), 620–624. doi:10.1055/s-0038-1673366
- Feng, L., Chen, Y., Ren, J., and Qu, X. (2011). A graphene functionalized electrochemical aptasensor for selective label-free detection of cancer cells. *Biomaterials* 32 (11), 2930–2937. doi:10.1016/j.biomaterials.2011.01.002
- Filipits, M., Rudas, M., Jakesz, R., Dubsy, P., Fitzal, F., Singer, C. F., et al. (2011). A new molecular predictor of distant recurrence in ER-positive, HER2-negative breast cancer adds independent information to conventional clinical risk factors. *Clin. Cancer Res.* 17 (18), 6012–6020. doi:10.1158/1078-0432.CCR-11-0926
- Filipits, M., Dubsy, P. C., Rudas, M., Brase, J. C., Kronenwett, R., Weber, K. E., et al. (2012). Impact of the EndoPredict-clin score on risk stratification in ER-positive, HER2-negative breast cancer after considering clinical guidelines. *Am. Soc. Clin. Oncol.* 30 (15), 542. doi:10.1200/jco.2012.30.15\_suppl.542
- Foulkes, W. D., Stefansson, I. M., Chappuis, P. O., Bégin, L. R., Goffin, J. R., Wong, N., et al. (2003). Germline BRCA1 mutations and a basal epithelial phenotype in breast cancer. *J. Natl. Cancer Inst.* 95 (19), 1482–1485. doi:10.1093/jnci/djg050
- Freitas, M., Neves, M. M. P. S., Nouws, H. P. A., and Delerue-Matos, C. (2020). Quantum dots as nanolabels for breast cancer biomarker HER2-ECD analysis in human serum. *Talanta* 208, 120430. doi:10.1016/j.talanta.2019.120430
- Fujita, T., Doihara, H., Kawasaki, K., Takabatake, D., Takahashi, H., Washio, K., et al. (2006). PTEN activity could be a predictive marker of trastuzumab efficacy in the treatment of ErbB2-overexpressing breast cancer. *Br. J. Cancer* 94 (2), 247–252. doi:10.1038/sj.bjc.6602926
- Ganau, S., Andreu, F. J., Escibano, F., Martín, A., Tortajada, L., Villajos, M., et al. (2015). Shear-wave elastography and immunohistochemical profiles in invasive breast cancer: evaluation of maximum and mean elasticity values. *Eur. J. Radiol.* 84 (4), 617–622. doi:10.1016/j.ejrad.2014.12.020
- Gao, J., Aksoy, B. A., Dogrusoz, U., Dresdner, G., Gross, B., Sumer, S. O., et al. (2013). Integrative analysis of complex cancer genomics and clinical profiles using the cBioPortal. *Sci. Signal.* 6, pl1. doi:10.1126/scisignal.2004088
- Gialeli, C., Theocharis, A. D., and Karamanos, N. K. (2011). Roles of matrix metalloproteinases in cancer progression and their pharmacological targeting. *FEBS J.* 278 (1), 16–27. doi:10.1111/j.1742-4658.2010.07919.x
- Gibson, G. R., Qian, D., Ku, J. K., and Lai, L. L. (2005). Metaplastic breast cancer: clinical features and outcomes. *Am. Surg.* 71 (9), 725–730. doi:10.1177/000313480507100906
- Godet, I., and Gilkes, D. M. (2017). BRCA1 and BRCA2 mutations and treatment strategies for breast cancer. *Integr. Cancer Sci. Ther.* 4. doi:10.15761/ICST.1000228
- Golubnitschaja, O., Yeghiazaryan, K., Abraham, J. A., Schild, H. H., Costigliola, V., Debal, M., et al. (2017). Breast cancer risk assessment: a non-invasive multiparametric approach to stratify patients by MMP-9 serum activity and RhoA expression patterns in circulating leucocytes. *Amino Acids* 49 (2), 273–281. doi:10.1007/s00726-016-2357-2
- Goto, Y., De Silva, M., Toscani, A., Prabhakar, B., Notkins, A., and Lan, M. (1992). A novel human insulinoma-associated cDNA, IA-1, encodes a protein with “zinc-finger” DNA-binding motifs. *J. Biol. Chem.* 267 (21), 15252–15257. doi:10.1016/s0021-9258(18)42173-4
- Grieshaber, D., MacKenzie, R., Vörös, J., and Reimhult, E. (2008). Electrochemical biosensors—sensor principles and architectures. *Sensors (Basel)* 8 (3), 1400–1458. doi:10.3390/s80314000
- Haeri, Z., Shokoufi, M., Jenab, M., Janzen, R., and Golnaraghi, F. (2016). Electrical impedance spectroscopy for breast cancer diagnosis: clinical study. *Integr. Cancer Sci. Ther.* 3 (6), 1–6. doi:10.15761/icst.1000212
- Hamrita, B., Chahed, K., Kabbage, M., Guillier, C. L., Trimeche, M., Chaieb, A., et al. (2008). Identification of tumor antigens that elicit a humoral immune response in breast cancer patients’ sera by serological proteome analysis (SERPA). *Clin. Chim. Acta* 393 (2), 95–102. doi:10.1016/j.cca.2008.03.017
- Hanahan, D., and Weinberg, R. A. (2011). Hallmarks of cancer: the next generation. *Cell* 144 (5), 646–674. doi:10.1016/j.cell.2011.02.013
- Harris, L. N., Ismaila, N., McShane, L. M., Andre, F., Collyar, D. E., Gonzalez-Angulo, A. M., et al. (2016). Use of biomarkers to guide decisions on adjuvant systemic therapy for women with early-stage invasive breast cancer: American Society of Clinical Oncology Clinical Practice Guideline. *J. Clin. Oncol.* 34 (10), 1134. doi:10.1200/JCO.2015.65.2289
- Hauge, I. H., Pedersen, K., Olerud, H. M., Hole, E. O., and Hofvind, S. (2014). The risk of radiation-induced breast cancers due to biennial mammographic screening in women aged 50–69 years is minimal. *Acta Radiol.* 55 (10), 1174–1179. doi:10.1177/0284185113514051
- Haurum, J. S. (2006). Recombinant polyclonal antibodies: the next generation of antibody therapeutics? *Drug Discov. Today* 11 (13–14), 655–660. doi:10.1016/j.drudis.2006.05.009
- Hayes, D. F., Thor, A. D., Dressler, L. G., Weaver, D., Edgerton, S., Cowan, D., et al. (2007). HER2 and response to paclitaxel in node-positive breast cancer. *N. Engl. J. Med.* 357 (15), 1496–1506. doi:10.1056/NEJMoa071167
- He, Y., Lin, Y., Tang, H., and Pang, D. (2012). A graphene oxide-based fluorescent aptasensor for the turn-on detection of epithelial tumor marker mucin 1. *Nanoscale* 4 (6), 2054–2059. doi:10.1039/c2nr12061e
- Hidalgo, M., Amant, F., Biankin, A. V., Budinská, E., Byrne, A. T., Caldas, C., et al. (2014). Patient-derived xenograft models: an emerging platform for translational cancer research. *Cancer Discov.* 4 (9), 998–1013. doi:10.1158/2159-8290.CD-14-0001
- Hoffman, R. M. (2015). Patient-derived orthotopic xenografts: better mimic of metastasis than subcutaneous xenografts. *Nat. Rev. Cancer* 15 (8), 451–452. doi:10.1038/nrc3972
- Holen, I., Speirs, V., Morrissey, B., and Blyth, K. (2017). *In vivo* models in breast cancer research: progress, challenges and future directions. *Dis. Model Mech.* 10 (4), 359–371. doi:10.1242/dmm.028274
- Hoon Tan, P., Ellis, I., Allison, K., Brogi, E., Fox, S. B., Lakhani, S., et al. (2020). The 2019 WHO classification of tumours of the breast. *Histopathology* 77 (2), 181–185. doi:10.1111/his.14091
- Hu, R., Wen, W., Wang, Q., Xiong, H., Zhang, X., Gu, H., et al. (2014). Novel electrochemical aptamer biosensor based on an enzyme-gold nanoparticle dual label for the ultrasensitive detection of epithelial tumour marker MUC1. *Biosens. Bioelectron.* 53, 384–389. doi:10.1016/j.bios.2013.10.015
- Hu, Z., Fan, C., Oh, D. S., Marron, J., He, X., Qaqish, B. F., et al. (2006). The molecular portraits of breast tumors are conserved across microarray platforms. *BMC genomics* 7 (1), 96–12. doi:10.1186/1471-2164-7-96
- Hubbard, R. A., Kerlikowske, K., Flowers, C. I., Yankaskas, B. C., Zhu, W., and Miglioretti, D. L. (2011). Cumulative probability of false-positive recall or biopsy recommendation after 10 years of screening mammography: a cohort study. *Ann. Intern. Med.* 155 (8), 481–492. doi:10.7326/0003-4819-155-8-201110180-00004
- Hwang, L. A., Phang, B. H., Liew, O. W., Iqbal, J., Koh, X. H., Koh, X. Y., et al. (2018). Monoclonal antibodies against specific p53 hotspot mutants as potential tools for precision medicine. *Cell Rep* 22 (1), 299–312. doi:10.1016/j.celrep.2017.11.112
- Jin, L., Chen, K., Tan, C., Li, J., Luo, J., Yang, Y., et al. (2020). Prognostic value of modified IHC4 score in patients with estrogen receptor-positive metastatic breast cancer. *Oncologist* 25 (8), e1170–e1180. doi:10.1634/theoncologist.2019-1006
- Jossinet, J. (1996). Variability of impedivity in normal and pathological breast tissue. *Med. Biol. Eng. Comput.* 34 (5), 346–350. doi:10.1007/BF02520002
- Karami, F., and Mehdi-pour, P. (2013). A comprehensive focus on global spectrum of BRCA1 and BRCA2 mutations in breast cancer. *Biomed. Res. Int.*, 2013, 928562. doi:10.1155/2013/928562
- Kessenbrock, K., Plaks, V., and Werb, Z. (2010). Matrix metalloproteinases: regulators of the tumor microenvironment. *Cell* 141 (1), 52–67. doi:10.1016/j.cell.2010.03.015
- Kim, B. K., Lee, J. W., Park, P. J., Shin, Y. S., Lee, W. Y., Lee, K. A., et al. (2009). The multiplex bead array approach to identifying serum biomarkers associated with breast cancer. *Breast Cancer Res.* 11 (2), R22. doi:10.1186/bcr2247

- Kim, S., and An, S. S. (2016). Role of p53 isoforms and aggregations in cancer, *Medicine (Baltimore)*, 95, e3993. doi:10.1097/MD.0000000000003993
- King, M. C., Marks, J. H., and Mandell, J. B. (2003). Breast and ovarian cancer risks due to inherited mutations in BRCA1 and BRCA2. *Science* 302 (5645), 643–646. doi:10.1126/science.1088759
- Kolb, T. M., Lichy, J., and Newhouse, J. H. (2002). Comparison of the performance of screening mammography, physical examination, and breast US and evaluation of factors that influence them: an analysis of 27,825 patient evaluations. *Radiology* 225 (1), 165–175. doi:10.1148/radiol.2251011667
- Korsching, E., Packeisen, J., Agelopoulos, K., Eisenacher, M., Voss, R., Isola, J., et al. (2002). Cytogenetic alterations and cytokeratin expression patterns in breast cancer: integrating a new model of breast differentiation into cytogenetic pathways of breast carcinogenesis. *Lab. Invest.* 82 (11), 1525–1533. doi:10.1097/01.lab.0000038508.86221.b3
- Kouros-Mehr, H., Slorach, E. M., Sternlicht, M. D., and Werb, Z. (2006). GATA-3 maintains the differentiation of the luminal cell fate in the mammary gland. *Cell* 127 (5), 1041–1055. doi:10.1016/j.cell.2006.09.048
- Kronenwett, U., Ploner, A., Zetterberg, A., Bergh, J., Hall, P., Auer, G., et al. (2006). Genomic instability and prognosis in breast carcinomas. *Cancer Epidemiol. Biomarkers Prev.* 15 (9), 1630–1635. doi:10.1158/1055-9965.EPI-06-0080
- Krop, I., Ismaila, N., Andre, F., Bast, R. C., Barlow, W., Collyar, D. E., et al. (2017). Use of biomarkers to guide decisions on adjuvant systemic therapy for women with early-stage invasive breast cancer: American society of clinical oncology clinical practice guideline focused update. *Jco* 35 (24), 2838. doi:10.1200/jco.2017.74.0472
- Kwa, M., Makris, A., and Esteva, F. J. (2017). Clinical utility of gene-expression signatures in early stage breast cancer. *Nat. Rev. Clin. Oncol.* 14 (10), 595–610. doi:10.1038/nrclinonc.2017.74
- Labrie, F., Luu-The, V., Labrie, C., Bélanger, A., Simard, J., Lin, S. X., et al. (2003). Endocrine and intracrine sources of androgens in women: inhibition of breast cancer and other roles of androgens and their precursor dehydroepiandrosterone. *Endocr. Rev.* 24 (2), 152–182. doi:10.1210/er.2001-0031
- Laidi, F., Bouziane, A., Errachid, A., and Zaoui, F. (2016). Usefulness of salivary and serum auto-antibodies against tumor biomarkers HER2 and MUC1 in breast cancer screening. *Asian Pac. J. Cancer Prev.* 17 (1), 335–339. doi:10.7314/apjcp.2016.17.1.335
- Lakhani, S. R., Ellis, I. O., Schnitt, S., Tan, P. H., and van de Vijver, M. (2012). *WHO classification of tumours of the breast*. Lyon, France: International Agency for Research on Cancer.
- Lee, A. H., and Ellis, I. O. (2008). The Nottingham prognostic index for invasive carcinoma of the breast. *Pathol. Oncol. Res.* 14 (2), 113–115. doi:10.1007/s12253-008-9067-3
- Lee, S., Mohsin, S. K., Mao, S., Hilsenbeck, S. G., Medina, D., and Allred, D. C. (2005). Hormones, receptors, and growth in hyperplastic enlarged lobular units: early potential precursors of breast cancer. *Breast Cancer Res.* 8 (1), R6–R9. doi:10.1186/bcr1367
- Lee, S. H., Moon, W. K., Cho, N., Chang, J. M., Moon, H. G., Han, W., et al. (2014). Shear-wave elastographic features of breast cancers: comparison with mechanical elasticity and histopathologic characteristics. *Invest. Radiol.* 49 (3), 147–155. doi:10.1097/RLI.0000000000000006
- Lehmann, B. D., Bauer, J. A., Chen, X., Sanders, M. E., Chakravarthy, A. B., Shyr, Y., et al. (2011). Identification of human triple-negative breast cancer subtypes and preclinical models for selection of targeted therapies. *J. Clin. Invest.* 121 (7), 2750–2767. doi:10.1172/JCI45014
- Li, D., Cheng, W., Yan, Y., Zhang, Y., Yin, Y., Ju, H., et al. (2016). A colorimetric biosensor for detection of attomolar microRNA with a functional nucleic acid-based amplification machine. *Talanta* 146, 470–476. doi:10.1016/j.talanta.2015.09.010
- Li, L. N., Zhou, X., Gu, Y., and Yan, J. (2013). Prognostic value of MMP-9 in ovarian cancer: a meta-analysis. *Asian Pac. J. Cancer Prev.* 14 (7), 4107–4113. doi:10.7314/apjcp.2013.14.7.4107
- Li, Y., Wu, T., Zhang, B., Yao, Y., and Yin, G. (2012). Matrix metalloproteinase-9 is a prognostic marker for patients with cervical cancer. *Med. Oncol.* 29 (5), 3394–3399. doi:10.1007/s12032-012-0283-z
- Li, Y., Zhang, Y., Zhao, M., Zhou, Q., Wang, L., Wang, H., et al. (2016). A simple aptamer-functionalized gold nanorods based biosensor for the sensitive detection of MCF-7 breast cancer cells. *Chem. Commun. (Camb)* 52 (20), 3959–3961. doi:10.1039/c6cc01014h
- Li, Y. J., Wen, G., Wang, Y., Wang, D. X., Yang, L., Deng, Y. J., et al. (2013). Perfusion heterogeneity in breast tumors for assessment of angiogenesis. *J. Ultrasound Med.* 32 (7), 1145–1155. doi:10.7863/ultra.32.7.1145
- Liang, Y. H., Chang, C. C., Chen, C. C., Chu-Su, Y., and Lin, C. W. (2012). Development of an Au/ZnO thin film surface plasmon resonance-based biosensor immunoassay for the detection of carbohydrate antigen 15-3 in human saliva. *Clin. Biochem.* 45 (18), 1689–1693. doi:10.1016/j.clinbiochem.2012.09.001
- Liu, S., Dontu, G., and Wicha, M. S. (2005). Mammary stem cells, self-renewal pathways, and carcinogenesis. *Breast Cancer Res.* 7 (3), 86. doi:10.1186/bcr1021
- Liu, Y. R., Jiang, Y. Z., Xu, X. E., Yu, K. D., Jin, X., Hu, X., et al. (2016). Comprehensive transcriptome analysis identifies novel molecular subtypes and subtype-specific RNAs of triple-negative breast cancer. *Breast Cancer Res.* 18 (1), 33. doi:10.1186/s13058-016-0690-8
- Marabelli, M., Cheng, S. C., and Parmigiani, G. (2016). Penetrance of ATM gene mutations in breast cancer: a meta-analysis of different measures of risk. *Genet. Epidemiol.* 40 (5), 425–431. doi:10.1002/gepi.21971
- Marcel, V., Dichtel-Danjoy, M. L., Sagne, C., Hafs, H., Ma, D., Ortiz-Cuaran, S., et al. (2011). Biological functions of p53 isoforms through evolution: lessons from animal and cellular models. *Cell Death Differ* 18 (12), 1815–1824. doi:10.1038/cdd.2011.120
- Marques, R. C., Viswanathan, S., Nouws, H. P., Delerue-Matos, C., and González-García, M. B. (2014). Electrochemical immunosensor for the analysis of the breast cancer biomarker HER2 ECD. *Talanta* 129, 594–599. doi:10.1016/j.talanta.2014.06.035
- Martin, M., Brase, J. C., Calvo, L., Krappmann, K., Ruiz-Borrego, M., Fisch, K., et al. (2014). Clinical validation of the EndoPredict test in node-positive, chemotherapy-treated ER+/HER2- breast cancer patients: results from the GEICAM 9906 trial. *Breast Cancer Res.* 16 (2), R38. doi:10.1186/bcr3642
- Mavaddat, N., Peock, S., Frost, D., Ellis, S., Platte, R., Fineberg, E., et al. (2013). Cancer risks for BRCA1 and BRCA2 mutation carriers: results from prospective analysis of EMBRACE. *JNCI: J. Natl. Cancer Inst.* 105 (11), 812–822. doi:10.1093/jnci/djt095
- Medhioub, M., Vaury, C., Hamelin, R., and Thomas, G. (2000). Lack of somatic mutation in the coding sequence of SHAH1 in tumors hemizygous for this candidate tumor suppressor gene. *Int. J. Cancer* 87 (6), 794–797. doi:10.1002/1097-0215(20000915)87:6<794::aid-ijc5>3.0.co;2-b
- Mehner, C., Hockla, A., Miller, E., Ran, S., Radisky, D. C., and Radisky, E. S. (2014). Tumor cell-produced matrix metalloproteinase 9 (MMP-9) drives malignant progression and metastasis of basal-like triple negative breast cancer. *Oncotarget* 5 (9), 2736. doi:10.18632/oncotarget.1932
- Milella, M., Falcone, I., Conciatori, F., Cesta Incani, U., Del Curatolo, A., Inzerilli, N., et al. (2015). PTEN: multiple functions in human malignant tumors. *Front. Oncol.* 5, 24. doi:10.3389/fonc.2015.00024
- Morimoto, T., Kinouchi, Y., Iritani, T., Kimura, S., Konishi, Y., Mitsuyama, N., et al. (1990). Measurement of the electrical bio-impedance of breast tumors. *Eur. Surg. Res.* 22 (2), 86–92. doi:10.1159/000129087
- Moy, L., Elias, K., Patel, V., Lee, J., Babb, J. S., Toth, H. K., et al. (2009). Is breast MRI helpful in the evaluation of inconclusive mammographic findings? *AJR Am. J. Roentgenol* 193 (4), 986–993. doi:10.2214/AJR.08.1229
- Mrklič, I., Pogorelić, Z., Capkun, V., and Tomić, S. (2013). Expression of androgen receptors in triple negative breast carcinomas. *Acta Histochem.* 115 (4), 344–348. doi:10.1016/j.acthis.2012.09.006
- Musgrove, E. A., and Sutherland, R. L. (2009). Biological determinants of endocrine resistance in breast cancer. *Nat. Rev. Cancer* 9 (9), 631–643. doi:10.1038/nrc2713
- Musolino, A., Bella, M. A., Bortesi, B., Michiara, M., Naldi, N., Zanelli, P., et al. (2007). BRCA mutations, molecular markers, and clinical variables in early-onset breast cancer: a population-based study. *Breast* 16 (3), 280–292. doi:10.1016/j.breast.2006.12.003
- Neo, S. J., Su, X., and Thomsen, J. S. (2009). Surface plasmon resonance study of cooperative interactions of estrogen receptor alpha and transcriptional factor Sp1 with composite DNA elements. *Anal. Chem.* 81 (9), 3344–3349. doi:10.1021/ac802543x
- Network, C. G. A. (2012). Comprehensive molecular portraits of human breast tumours. *Nature* 490 (7418), 61. doi:10.1038/nature11412
- Neve, R. M., Chin, K., Fridlyand, J., Yeh, J., Baehner, F. L., Fevr, T., et al. (2006). A collection of breast cancer cell lines for the study of functionally distinct cancer subtypes. *Cancer Cell* 10 (6), 515–527. doi:10.1016/j.ccr.2006.10.008



- Nielsen, T., Wallden, B., Schaper, C., Ferree, S., Liu, S., Gao, D., et al. (2014). Analytical validation of the PAM50-based Prosigna breast cancer prognostic gene signature assay and nCounter analysis system using formalin-fixed paraffin-embedded breast tumor specimens. *BMC Cancer* 14 (1), 177. doi:10.1186/1471-2407-14-177
- Nikhil, B., Pawan, J., Nello, F., and Pedro, E. (2016). Introduction to biosensors. *Essays Biochem.* 60 (1), 1–8. doi:10.1042/EBC20150001
- Nuciforo, P. G., Aura, C., Holmes, E., Prudkin, L., Jimenez, J., Martinez, P., et al. (2015). Benefit to neoadjuvant anti-human epidermal growth factor receptor 2 (HER2)-targeted therapies in HER2-positive primary breast cancer is independent of phosphatase and tensin homolog deleted from chromosome 10 (PTEN) status. *Ann. Oncol.* 26 (7), 1494–1500. doi:10.1093/annonc/mdv175
- Nunes, R. A., Wray, L., Mete, M., Herbolzheimer, P., Smith, K. L., Bijelic, L., et al. (2016). Genomic profiling of breast cancer in African-American women using MammaPrint. *Breast Cancer Res. Treat.* 159 (3), 481–488. doi:10.1007/s10549-016-3949-y
- Ollmar, S., and Grant, S. (2016). Nevisense: improving the accuracy of diagnosing melanoma. *Melanoma Manag.* 3 (2), 93–96. doi:10.2217/mmt-2015-0004
- Oyama, T., Takei, K., Horiguchi, H., Nakajima, J., Koerner, Y., Nakajima, T., et al. (2000). Atypical cystic lobule of the breast: an early stage of low-grade ductal carcinoma *in-situ*. *Breast Cancer* 7 (4), 326–331. doi:10.1007/BF02966399
- Ozturk, L. K., Emekli-Alturfan, E., Kaşıkci, E., Demir, G., and Yarat, A. (2011). Salivary total sialic acid levels increase in breast cancer patients: a preliminary study. *Med. Chem.* 7 (5), 443–447. doi:10.2174/157340611796799230
- Paik, S., Shak, S., Tang, G., Kim, C., Baker, J., Cronin, M., et al. (2004). A multigene assay to predict recurrence of tamoxifen-treated, node-negative breast cancer. *N. Engl. J. Med.* 351 (27), 2817–2826. doi:10.1056/NEJMoa041588
- Parker, J. S., Mullins, M., Cheang, M. C., Leung, S., Voduc, D., Vickery, T., et al. (2009). Supervised risk predictor of breast cancer based on intrinsic subtypes. *J. Clin. Oncol.* 27 (8), 1160. doi:10.1200/JCO.2008.18.1370
- Perou, C. M., Sørlie, T., Eisen, M. B., Van De Rijn, M., Jeffrey, S. S., Rees, C. A., et al. (2000). Molecular portraits of human breast tumours. *nature* 406 (6797), 747–752. doi:10.1038/35021093
- Peters, A., Chase, J. G., and Van Houten, E. E. (2008). Digital image elasto-tomography: combinatorial and hybrid optimization algorithms for shape-based elastic property reconstruction. *IEEE Trans. Biomed. Eng.* 55 (11), 2575–2583. doi:10.1109/TBME.2008.2001132
- Peters, A., Chase, J. G., and Van Houten, E. E. (2009). Estimating elasticity in heterogeneous phantoms using Digital Image Elasto-Tomography. *Med. Biol. Eng. Comput.* 47 (1), 67–76. doi:10.1007/s11517-008-0368-1
- Pfeifer, M. E. (2018). Quo vadis point-of-care diagnostics? Report II of the SWISS SYMPOSIUM in point-of-care diagnostics 2017. *CHIMIA Int. J. Chem.* 72 (1–2), 80–82. doi:10.2533/chimia.2018.80
- Piccart-Gebhart, M. J., Procter, M., Leyland-Jones, B., Goldhirsch, A., Untch, M., Smith, I., et al. (2005). Trastuzumab after adjuvant chemotherapy in HER2-positive breast cancer. *N. Engl. J. Med.* 353 (16), 1659–1672. doi:10.1056/NEJMoa052306
- Pohanka, M. (2018). Overview of piezoelectric biosensors, immunosensors and DNA sensors and their applications. *Materials* 11 (3), 448. doi:10.3390/ma11030448
- Prat, A., and Perou, C. M. (2009). Mammary development meets cancer genomics. *Nat. Med.* 15 (8), 842–844. doi:10.1038/nm0809-842
- Prevention, C. (2020). The BRCA1 and BRCA2 genes. Available at: [https://www.cdc.gov/genomics/disease/breast\\_ovarian\\_cancer/genes\\_hboc.htm](https://www.cdc.gov/genomics/disease/breast_ovarian_cancer/genes_hboc.htm) (Accessed March 25, 2020).
- Qureshi, A., Gurbuz, Y., and Niazi, J. H. (2015). Label-free capacitance based aptasensor platform for the detection of HER2/Erbb2 cancer biomarker in serum. *Sensors Actuators B: Chem.* 220, 1145–1151. doi:10.1016/j.snb.2015.06.094
- Rahbar, H., and Partridge, S. C. (2016). Multiparametric MR imaging of breast cancer. *Magn. Reson. Imaging Clin. N. Am.* 24 (1), 223–238. doi:10.1016/j.mric.2015.08.012
- Rahim, B., and O'Regan, R. (2017). AR signaling in breast cancer. *Cancers* 9 (3), 21. doi:10.3390/cancers9030021
- Rakha, E. A., El-Sayed, M. E., Green, A. R., Paish, E. C., Powe, D. G., Gee, J., et al. (2007). Biologic and clinical characteristics of breast cancer with single hormone receptor positive phenotype. *J. Clin. Oncol.* 25 (30), 4772–4778. doi:10.1200/JCO.2007.12.2747
- Rakha, E. A., Reis-Filho, J. S., and Ellis, I. O. (2010). Combinatorial biomarker expression in breast cancer. *Breast Cancer Res. Treat.* 120 (2), 293–308. doi:10.1007/s10549-010-0746-x
- Razvi, H., Tsang, J. Y., Poon, I. K., Chan, S.-K., Cheung, S.-Y., Shea, K.-H., et al. (2020). INSM1 is a novel prognostic neuroendocrine marker for luminal B breast cancer. *Pathology* 53 (2), 170–178. doi:10.1016/j.pathol.2020.07.004
- Reporting, B. I. (2003). *Data system Atlas (BI-RADS atlas) reston*. Reston, VA: American College of Radiology.
- Ring, B. Z., Seitz, R. S., Beck, R., Shasteen, W. J., Tarr, S. M., Cheang, M. C., et al. (2006). Novel prognostic immunohistochemical biomarker panel for estrogen receptor-positive breast cancer. *J. Clin. Oncol.* 24 (19), 3039–3047. doi:10.1200/JCO.2006.05.6564
- Rong, Y., Chen, H., Zhou, X. F., Yin, C. Q., Wang, B. C., Peng, C. W., et al. (2016). Identification of an aptamer through whole cell-SELEX for targeting high metastatic liver cancers. *Oncotarget* 7 (7), 8282. doi:10.18632/oncotarget.6988
- Ruan, W., Monaco, M. E., and Kleinberg, D. L. (2005). Progesterone stimulates mammary gland ductal morphogenesis by synergizing with and enhancing insulin-like growth factor-I action. *Endocrinology* 146 (3), 1170–1178. doi:10.1210/en.2004-1360
- Safarpour, D., Pakneshan, S., and Tavassoli, F. A. (2014). Androgen receptor (AR) expression in 400 breast carcinomas: is routine AR assessment justified? *Am. J. Cancer Res.* 4 (4), 353.
- Salgado, R., Denkert, C., Demaria, S., Sirtaine, N., Klauschen, F., Pruner, G., et al. (2015). The evaluation of tumor-infiltrating lymphocytes (TILs) in breast cancer: recommendations by an International TILs Working Group 2014. *Ann. Oncol.* 26 (2), 259–271. doi:10.1093/annonc/mdl450
- Schiff, R., Massarweh, S. A., Shou, J., Bharwani, L., Mohsin, S. K., and Osborne, C. K. (2004). Cross-talk between estrogen receptor and growth factor pathways as a molecular target for overcoming endocrine resistance. *Clin. Cancer Res.* 10 (1), 331S. doi:10.1158/1078-0432.ccr-031212
- Schmidt, R. L., Park, C. H., Ahmed, A. U., Gundelach, J. H., Reed, N. R., Cheng, S., et al. (2007). Inhibition of RAS-mediated transformation and tumorigenesis by targeting the downstream E3 ubiquitin ligase seven in absentia homologue. *Cancer Res.* 67 (24), 11798–11810. doi:10.1158/0008-5472.CAN-06-4471
- Sestak, I., Buus, R., Cuzick, J., Dubsy, P., Kronenwett, R., Denkert, C., et al. (2018). Comparison of the performance of 6 prognostic signatures for estrogen receptor-positive breast cancer: a secondary analysis of a randomized clinical trial. *JAMA Oncol.* 4 (4), 545–553. doi:10.1001/jamaoncol.2017.5524
- Sgroi, D. C., Sestak, I., Cuzick, J., Zhang, Y., Schnabel, C. A., Schroeder, B., et al. (2013). Prediction of late distant recurrence in patients with oestrogen-receptor-positive breast cancer: a prospective comparison of the breast-cancer index (BCI) assay, 21-gene recurrence score, and IHC4 in the TransATAC study population. *Lancet Oncol.* 14 (11), 1067–1076. doi:10.1016/S1470-2045(13)70387-5
- Shackleton, M., Vaillant, F., Simpson, K. J., Stingl, J., Smyth, G. K., Asselin-Labat, M. L., et al. (2006). Generation of a functional mammary gland from a single stem cell. *Nature* 439 (7072), 84–88. doi:10.1038/nature04372
- Shah, S. P., Roth, A., Goya, R., Oloumi, A., Ha, G., Zhao, Y., et al. (2012). The clonal and mutational evolution spectrum of primary triple-negative breast cancers. *Nature* 486 (7403), 395–399. doi:10.1038/nature10933
- Shao, M. M., Chan, S. K., Yu, A. M., Lam, C. C., Tsang, J. Y., Lui, P. C., et al. (2012). Keratin expression in breast cancers. *Virchows Arch.* 461 (3), 313–322. doi:10.1007/s00428-012-1289-9
- Sharan, S. K., Morimatsu, M., Albrecht, U., Lim, D. S., Regel, E., Dinh, C., et al. (1997). Embryonic lethality and radiation hypersensitivity mediated by Rad51 in mice lacking Brca2. *Nature* 386 (6627), 804–810. doi:10.1038/386804a0
- Shi, H., Wu, Y., Wang, Y., Zhou, M., Yan, S., Chen, Z., et al. (2015). Liquiritigenin potentiates the inhibitory effects of cisplatin on invasion and metastasis via downregulation MMP-2/9 and PI3 K/AKT signaling pathway in B16F10 melanoma cells and mice model. *Nutr. Cancer* 67 (5), 761–770. doi:10.1080/01635581.2015.1037962
- Siegel, R., and Jemal, A. (2015). *Cancer facts and figures 2015*. Atlanta, GA: American Cancer Society Inc.
- Singh, A. K., and Yu, X. (2020). Tissue-Specific carcinogens as soil to seed BRCA1/2-mutant hereditary cancers. *Trends Cancer* 6 (7), 559–568. doi:10.1016/j.trecan.2020.03.004



- Sinn, H. P., and Kreipe, H. (2013). A brief overview of the WHO classification of breast tumors, 4th edition, focusing on issues and updates from the 3rd edition. *Breast Care* 8 (2), 149–154. doi:10.1159/000350774
- Slamon, D. J., Godolphin, W., Jones, L. A., Holt, J. A., Wong, S. G., Keith, D. E., et al. (1989). Studies of the HER-2/neu proto-oncogene in human breast and ovarian cancer. *Science* 244 (4905), 707–712. doi:10.1126/science.2470152
- Smerage, J. B., Budd, G. T., Doyle, G. V., Brown, M., Paoletti, C., Muniz, M., et al. (2013). Monitoring apoptosis and Bcl-2 on circulating tumor cells in patients with metastatic breast cancer. *Mol. Oncol.* 7 (3), 680–692. doi:10.1016/j.molonc.2013.02.013
- Smith, S., Easton, D., Evans, D., and Ponder, B. (1992). Allele losses in the region 17q12-21 in familial breast and ovarian cancer involve the wild-type chromosome. *Nat. Genet.* 2 (2), 128–131. doi:10.1038/ng1092-128
- Society, A. C. (2019). *Breast cancer facts and figures 2019–2020*. Atlanta, GA: American Cancer Society Inc.
- Song, Y., Zhu, Z., An, Y., Zhang, W., Zhang, H., Liu, D., et al. (2013). Selection of DNA aptamers against epithelial cell adhesion molecule for cancer cell imaging and circulating tumor cell capture. *Anal. Chem.* 85 (8), 4141–4149. doi:10.1021/ac400366b
- Sonuç, M. N., and Sezgentürk, M. K. (2014). Ultrasensitive electrochemical detection of cancer associated biomarker HER3 based on anti-HER3 biosensor. *Talanta* 120, 355–361. doi:10.1016/j.talanta.2013.11.090
- Sorlie, T., Tibshirani, R., Parker, J., Hastie, T., Marron, J., Nobel, A., et al. (2003). Repeated observation of breast tumor subtypes in independent gene expression data sets. *Proc. Natl. Acad. Sci. USA* 100 (14), 8418–8423. doi:10.1073/pnas.0932692100
- Sparano, J. A., Gray, R. J., Makower, D. F., Pritchard, K. I., Albain, K. S., Hayes, D. F., et al. (2015). Prospective validation of a 21-gene expression assay in breast cancer. *N. Engl. J. Med.* 373 (21), 2005–2014. doi:10.1056/NEJMoa1510764
- Streckfus, C. F., Bigler, L. R., and Zwick, M. (2006). The use of surface-enhanced laser desorption/ionization time-of-flight mass spectrometry to detect putative breast cancer markers in saliva: a feasibility study. *J. Oral. Pathol. Med.* 35 (5), 292–300. doi:10.1111/j.1600-0714.2006.00427.x
- Sugimoto, M., Wong, D. T., Hirayama, A., Soga, T., and Tomita, M. (2010). Capillary electrophoresis mass spectrometry-based saliva metabolomics identified oral, breast and pancreatic cancer-specific profiles. *Metabolomics* 6 (1), 78–95. doi:10.1007/s11306-009-0178-y
- Tentler, J. J., Tan, A. C., Weekes, C. D., Jimeno, A., Leong, S., Pitts, T. M., et al. (2012). Patient-derived tumour xenografts as models for oncology drug development. *Nat. Rev. Clin. Oncol.* 9 (6), 338–350. doi:10.1038/nrclinonc.2012.61
- Thompson, D., Duedal, S., Kirner, J., McGuffog, L., Last, J., Reiman, A., et al. (2005). Cancer risks and mortality in heterozygous ATM mutation carriers. *J. Natl. Cancer Inst.* 97 (11), 813–822. doi:10.1093/jnci/dji141
- Tian, M., Cui, Y. Z., Song, G. H., Zong, M. J., Zhou, X. Y., Chen, Y., et al. (2008). Proteomic analysis identifies MMP-9, DJ-1 and A1BG as overexpressed proteins in pancreatic juice from pancreatic ductal adenocarcinoma patients. *BMC cancer* 8 (1), 241. doi:10.1186/1471-2407-8-241
- Tibshirani, R., Hastie, T., Narasimhan, B., and Chu, G. (2002). Diagnosis of multiple cancer types by shrunken centroids of gene expression. *Proc. Natl. Acad. Sci. USA* 99 (10), 6567–6572. doi:10.1073/pnas.082099299
- Torrente-Rodríguez, R. M., Campuzano, S., López-Hernández, E., Montiel, V. R.-V., Barderas, R., Granados, R., et al. (2015). Simultaneous detection of two breast cancer-related miRNAs in tumor tissues using p19-based disposable amperometric magnetobiosensing platforms. *Biosens. Bioelectron.* 66, 385–391. doi:10.1016/j.bios.2014.11.047
- Treilleux, I., Arnedos, M., Cropet, C., Wang, Q., Ferrero, J. M., Abadie-Lacourtoisie, S., et al. (2015). Translational studies within the TAMRAD randomized GINECO trial: evidence for mTORC1 activation marker as a predictive factor for everolimus efficacy in advanced breast cancer. *Ann. Oncol.* 26 (1), 120–125. doi:10.1093/annonc/mdl497
- Tsai, M., Lo, S., Audeh, W., Qamar, R., Budway, R., Levine, E., et al. (2018). Association of 70-gene signature assay findings with physicians' treatment guidance for patients with early breast cancer classified as intermediate risk by the 21-gene assay. *JAMA Oncol.* 4 (1), e173470. doi:10.1001/jamaoncol.2017.3470
- Tuerk, C., and Gold, L. (1990). Systematic evolution of ligands by exponential enrichment: RNA ligands to bacteriophage T4 DNA polymerase. *Science* 249 (4968), 505–510. doi:10.1126/science.2200121
- Turner, N. C., and Reis-Filho, J. S. (2006). Basal-like breast cancer and the BRCA1 phenotype. *Oncogene* 25 (43), 5846–5853. doi:10.1038/sj.onc.1209876
- Van De Vijver, M. J., He, Y. D., Van't Veer, L. J., Dai, H., Hart, A. A., Voskuil, D. W., et al. (2002). A gene-expression signature as a predictor of survival in breast cancer. *N. Engl. J. Med.* 347 (25), 1999–2009. doi:10.1056/NEJMoa021967
- van den Broek, A. J., Schmidt, M. K., van't Veer, L. J., Tollenaar, R. A., and van Leeuwen, F. E. (2015). Worse breast cancer prognosis of BRCA1/BRCA2 mutation carriers: what's the evidence? A systematic review with meta-analysis. *PLoS one* 10 (3), e0120189. doi:10.1371/journal.pone.0120189
- Van Poznak, C., Somerfield, M. R., Bast, R. C., Cristofanilli, M., Goetz, M. P., Gonzalez-Angulo, A. M., et al. (2015). Use of biomarkers to guide decisions on systemic therapy for women with metastatic breast cancer: American Society of Clinical Oncology Clinical Practice Guideline. *J. Clin. Oncol.* 33 (24), 2695. doi:10.1200/JCO.2015.61.1459
- van Reesema, L. L. S., Zheleva, V., Zheleva, J. S., Jansen, R. J., O'Connor, C. F., Isbell, A. J., et al. (2016). SIAH and EGFR, two RAS pathway biomarkers, are highly prognostic in locally advanced and metastatic breast cancer. *EBioMedicine* 11, 183–198. doi:10.1016/j.ebiom.2016.08.014
- Van Sprundel, T., Schmidt, M., Rookus, M., Brohet, R., Van Asperen, C., Rutgers, E. J., et al. (2005). Risk reduction of contralateral breast cancer and survival after contralateral prophylactic mastectomy in BRCA1 or BRCA2 mutation carriers. *Br. J. Cancer* 93 (3), 287–292. doi:10.1038/sj.bjc.6602703
- Varn, F. S., Mullins, D. W., Arias-Pulido, H., Fiering, S., and Cheng, C. (2017). Adaptive immunity programmes in breast cancer. *Immunology* 150 (1), 25–34. doi:10.1111/imm.12664
- Veeraraghavan, J., De Angelis, C., Reis-Filho, J. S., Pascual, T., Prat, A., Rimawi, M. F., et al. (2017). De-escalation of treatment in HER2-positive breast cancer: determinants of response and mechanisms of resistance. *Breast* 34 Suppl 1, S19–S26. doi:10.1016/j.breast.2017.06.022
- Verhoog, L., Brekelmans, C., Seynaeve, C., Van den Bosch, L., Dahmen, G., Van Geel, A., et al. (1998). Survival and tumour characteristics of breast-cancer patients with germline mutations of BRCA1. *Lancet* 351 (9099), 316–321. doi:10.1016/s0140-6736(97)07065-7
- Wachter, D. L., Hartmann, A., Beckmann, M. W., Fasching, P. A., Hein, A., Bayer, C. M., et al. (2014). Expression of neuroendocrine markers in different molecular subtypes of breast carcinoma. *Biomed. Res. Int.*, 2014, 408459. doi:10.1155/2014/408459
- Walsh, T., Casadei, S., Lee, M. K., Pennil, C. C., Nord, A. S., Thornton, A. M., et al. (2011). Mutations in 12 genes for inherited ovarian, fallopian tube, and peritoneal carcinoma identified by massively parallel sequencing. *Proc. Natl. Acad. Sci. USA* 108 (44), 18032–18037. doi:10.1073/pnas.1115052108
- Wang, X., Yu, H., Lu, D., Zhang, J., and Deng, W. (2014). Label free detection of the breast cancer biomarker CA15.3 using ZnO nanorods coated quartz crystal microbalance. *Sensors Actuators B: Chem.* 195, 630–634. doi:10.1016/j.snb.2014.01.027
- Whittemore, A. S., Gong, G., John, E. M., McGuire, V., Li, F. P., Ostrow, K. L., et al. (2004). Prevalence of BRCA1 mutation carriers among U.S. non-Hispanic Whites. *Cancer Epidemiol. Biomarkers Prev.* 13 (12), 2078–2083.
- Won, J. Y., Choi, J.-W., and Min, J. (2013). Micro-fluidic chip platform for the characterization of breast cancer cells using aptamer-assisted immunohistochemistry. *Biosens. Bioelectron.* 40 (1), 161–166. doi:10.1016/j.bios.2012.07.004
- Wu, X., Xiao, T., Luo, Z., He, R., Cao, Y., Guo, Z., et al. (2018). A micro-/nano-chip and quantum dots-based 3D cytosensor for quantitative analysis of circulating tumor cells. *J. Nanobiotechnology* 16 (1), 1–9. doi:10.1186/s12951-018-0390-x
- Wurth, R., Tarn, K., Jernigan, D., Fernandez, S. V., Cristofanilli, M., Fatatis, A., et al. (2015). A preclinical model of inflammatory breast cancer to study the involvement of CXCR4 and ACKR3 in the metastatic process. *Transl. Oncol.* 8 (5), 358–367. doi:10.1016/j.tranon.2015.07.002
- Yang, H., Yuan, R., Chai, Y., Mao, L., Su, H., Jiang, W., et al. (2011). Electrochemical immunosensor for detecting carcinoembryonic antigen using hollow Pt nanospheres-labeled multiple enzyme-linked antibodies as labels for signal amplification. *Biochem. Eng. J.* 56 (3), 116–124. doi:10.1016/j.bej.2011.04.004

- Yousef, E. M., Tahir, M. R., St-Pierre, Y., and Gaboury, L. A. (2014). MMP-9 expression varies according to molecular subtypes of breast cancer. *BMC cancer* 14 (1), 609–612. doi:10.1186/1471-2407-14-609
- Zhang, H. Y., Liang, F., Jia, Z. L., Song, S. T., and Jiang, Z. F. (2013). mutation, methylation and expression in breast cancer patients. *Oncol. Lett.* 6 (1), 161–168. doi:10.3892/ol.2013.1331
- Zhang, J., Wu, D. Z., Cai, S. X., Chen, M., Xia, Y. K., Wu, F., et al. (2016). An immobilization-free electrochemical impedance biosensor based on duplex-specific nuclease assisted target recycling for amplified detection of microRNA. *Biosens. Bioelectron.* 75, 452–457. doi:10.1016/j.bios.2015.09.006
- Zhang, L., Ridgway, L. D., Wetzel, M. D., Ngo, J., Yin, W., Kumar, D., et al. (2013). The identification and characterization of breast cancer CTCs competent for brain metastasis. *Sci. Transl. Med.* 5 (180), 180ra48. doi:10.1126/scitranslmed.3005109
- Zhang, L., Xiao, H., Karlan, S., Zhou, H., Gross, J., Elashoff, D., et al. (2010). Discovery and preclinical validation of salivary transcriptomic and proteomic biomarkers for the non-invasive detection of breast cancer. *PLoS one* 5 (12), e15573. doi:10.1371/journal.pone.0015573
- Zhang, Y., Schnabel, C. A., Schroeder, B. E., Jerevall, P. L., Jankowitz, R. C., Fornander, T., et al. (2013). Breast cancer index identifies early-stage estrogen receptor-positive breast cancer patients at risk for early- and late-distant recurrence. *Clin. Cancer Res.* 19 (15), 4196–4205. doi:10.1158/1078-0432.CCR-13-0804
- Zhao, J., Wu, J., Cai, H., Wang, D., Yu, L., and Zhang, W.-H. (2016). E3 Ubiquitin ligase Siah-1 is down-regulated and fails to target natural HBx truncates for degradation in hepatocellular carcinoma. *J. Cancer* 7 (4), 418. doi:10.1158/1078-0432.CCR-13-0804
- Zhao, S., Yang, W., and Lai, R. Y. (2011). A folding-based electrochemical aptasensor for detection of vascular endothelial growth factor in human whole blood. *Biosens. Bioelectron.* 26 (5), 2442–2447. doi:10.1016/j.bios.2010.10.029
- Zhou, J., Liu, T., and Wang, W. (2018). Prognostic significance of matrix metalloproteinase 9 expression in osteosarcoma: a meta-analysis of 16 studies. *Medicine* 97 (44), e13051. doi:10.1097/md.00000000000013051

**Conflict of Interest:** The authors declare that the research was conducted in the absence of any commercial or financial relationships that could be construed as a potential conflict of interest.

Copyright © 2021 Zubair, Wang and Ali. This is an open-access article distributed under the terms of the Creative Commons Attribution License (CC BY). The use, distribution or reproduction in other forums is permitted, provided the original author(s) and the copyright owner(s) are credited and that the original publication in this journal is cited, in accordance with accepted academic practice. No use, distribution or reproduction is permitted which does not comply with these terms.

## GLOSSARY

<b>AB, ABUS</b> Automated breast ultrasonography;	<b>IBC</b> Invasive breast carcinoma
<b>AI</b> Aromatase inhibitor	<b>IBC-NE</b> Invasive breast carcinoma with neuroendocrine differentiation
<b>APCs</b> Antigen-presenting cells	<b>IDC</b> Invasive ductal carcinoma
<b>AR</b> Androgen receptor	<b>IGF</b> Insulin-like growth factor
<b>ASCO</b> American Society of Clinical Oncology	<b>IHC</b> Immune histochemical/compatibility
<b>AT, ATM</b> Ataxia Telangiectasia, Ataxia Telangiectasia mutation	<b>ILC</b> Invasive lobular carcinoma
<b>BC</b> Breast cancer(s)	<b>IM</b> Immunomodulatory
<b>BI-RADS</b> Breast imaging reporting and data system	<b>INSM1</b> Insulinoma-associated protein 1
<b>BL</b> Basal-like	<b>LAR</b> Luminal androgen receptor
<b>BLIA</b> Basal-like-immune-activated	<b>LncRNA</b> Long non-coding RNAs
<b>BLIS</b> Basal-like-immune-suppressive	<b>LCIS</b> Lobular carcinoma <i>in situ</i>
<b>BRCA1/2</b> Breast cancer genes-1/-2	<b>M</b> Mitotic rate
<b>BRE</b> Biochemical recognition element	<b>MAPP</b> Multiple affinity protein profile
<b>CA</b> Cancer antigen	<b>MGI</b> Molecular grade index
<b>cDNA</b> Complementary DNA	<b>MES</b> Mesenchymal-like triple-negative breast cancer subtype
<b>CDX</b> Cell-derived Xenografts	<b>MMP</b> Matrix metalloproteinase
<b>CES-MRI</b> Chemical exchange saturation transfer MRI	<b>MMP-9</b> Matrix metalloproteinase-9
<b>CEUS</b> Contrast-enhanced ultrasonography	<b>MRI</b> Magnetic resonance imaging
<b>CTCs</b> Circulating tumor cells	<b>MSC</b> Mammary stem cell
<b>CTLA-4</b> Cytotoxic-T-lymphocyte-associated antigen	<b>MUC1</b> Mucin-1
<b>DBT</b> Digital breast tomosynthesis	<b>N</b> Degree of nuclear polymorphism (Nodes)
<b>DCE-MRI</b> Dynamic contrast-enhanced MRI	<b>NAAs</b> Nucleic acid aptamers
<b>DCIS</b> Ductal carcinoma <i>in situ</i>	<b>NCCN</b> American-national comprehensive cancer network
<b>DIET</b> Digital image-based elasto-tomography	<b>NE</b> Neuroendocrine
<b>DITI</b> Digital infrared thermal imaging	<b>NET</b> Neuroendocrine tumor
<b>EIS</b> Electrical impedance scanning/spectroscopy	<b>NGS</b> Next-gene sequencing
<b>ELISA</b> Enzyme-linked immunosorbent assay	<b>NOS</b> Not otherwise specified
<b>EMT</b> Epithelial-mesenchymal transition	<b>NPI</b> Nottingham prognosis Index
<b>EP</b> EndoPredict	<b>NSE</b> Neuron-specific enolase
<b>ER</b> Estrogen receptors	<b>NST</b> No special type
<b>ER-<math>\alpha</math>/PR</b> Estrogen and Progesterone receptor	<b>OVT</b> Oncolytic virus therapy
<b>ER<sup>+</sup>, ER<sup>-</sup></b> ER-positive, ER-negative	<b>PD-1</b> Programmed death-1
<b>ESMO</b> European society of medical oncology	<b>PDX</b> Patient-derived xenografts
<b>GD-DTPA</b> Gadolinium diethylenetriamine pentaacetic acid	<b>PR</b> Progesterone receptors
<b>GEP</b> Gene expression profiling	<b>PTEN</b> Phosphatase and tensin homolog
<b>HELU</b> Hyperplastic enlarged lobular unit	<b>PTM</b> Post-translational modification
<b>HER2</b> Human epidermal growth factor receptor 2	<b>QDs</b> Quantum dots
<b>HER2-ECD</b> Extracellular domain of HER2	<b>SELEX</b> Systemic evolution of ligands by exponential enrichment
<b>IARC</b> International Agency for Research on Cancer	<b>SEREX</b> Serological analysis of tumor antigens by recombinant cDNA expression cloning
	<b>SERM</b> Selective estrogen receptor modulators

**SERPA** Serological proteome assay

**SIAH** Seven in absentia homolog

**SPR** Surface plasmon resonance

**T** Tubular structures

**TAABs** Tumor-associated autoantibodies

**TAA**s Tumor-associated antigens

**TCCRP** Tall cell carcinoma with reverse polarity

**TIL**s Tumor-infiltrating lymphocytes

**TNBC** Triple-negative breast cancer

**WT** Wild type





# Monoamine Oxidase A Inhibits Lung Adenocarcinoma Cell Proliferation by Abrogating Aerobic Glycolysis

Yumin Huang<sup>1,2</sup>, Wei Zhao<sup>3</sup>, Xiaoping Ouyang<sup>2</sup>, Feng Wu<sup>2</sup>, Yujian Tao<sup>2</sup> and Minhua Shi<sup>1\*</sup>

<sup>1</sup> Department of Respiratory Medicine, The Second Affiliated Hospital of Soochow University, Suzhou, China, <sup>2</sup> Department of Respiratory Medicine, The Affiliated Hospital of Yangzhou University, Yangzhou, China, <sup>3</sup> School of Laboratory Medicine/Sichuan Provincial Engineering Laboratory for Prevention and Control Technology of Veterinary Drug Residue in Animal-Origin Food, Chengdu Medical College, Chengdu, China

## OPEN ACCESS

### Edited by:

Dong-Hua Yang,  
St. John's University, United States

### Reviewed by:

An Zhao,  
University of Chinese Academy of  
Sciences, China  
Na Xie,  
Independent Researcher,  
Chengdu, China

### \*Correspondence:

Minhua Shi  
smhsuda@163.com

### Specialty section:

This article was submitted to  
Pharmacology of Anti-Cancer Drugs,  
a section of the journal  
Frontiers in Oncology

Received: 24 December 2020

Accepted: 04 February 2021

Published: 08 March 2021

### Citation:

Huang Y, Zhao W, Ouyang X, Wu F,  
Tao Y and Shi M (2021) Monoamine  
Oxidase A Inhibits Lung  
Adenocarcinoma Cell Proliferation by  
Abrogating Aerobic Glycolysis.  
Front. Oncol. 11:645821.  
doi: 10.3389/fonc.2021.645821

Lung adenocarcinoma (LUAD) accounts for ~30% of all lung cancers and is one of the causes of cancer-related death worldwide. As the role of monoamine oxidase A (MAOA) in LUAD remains unclear, in this study, we examine how MAOA affects LUAD cell proliferation. Analyses of both public data and our data reveal that the expression of MAOA is downregulated in LUAD compared with non-tumor tissue. In addition, the expression of MAOA in tumors correlates with clinicopathologic features, and the expression of MAOA serves as an independent biomarker in LUAD. In addition, the overexpression of MAOA inhibits LUAD cell proliferation by inducing G1 arrest *in vitro*. Further mechanistic studies show that MAOA abrogates aerobic glycolysis in LUAD cells by decreasing hexokinase 2 (HK2). Finally, the expression of HK2 shows a negative correlation with MAOA in LUAD, and high HK2 predicts poor clinical outcome. In conclusion, our findings indicate that MAOA functions as a tumor suppressor in LUAD. Our results indicate that the MAOA/HK2 axis could be potential targets in LUAD therapy.

**Keywords:** lung adenocarcinoma, monoamine oxidase A, aerobic glycolysis, hexokinase 2, cell proliferation

## INTRODUCTION

Lung cancer is one of the most common cancers and the leading cause of cancer-related death globally (1). Lung adenocarcinoma (LUAD) accounts for more than 30% of all lung cancers and for about half of all non-small cell lung cancer (NSCLC) (2, 3). Alterations of gene expression and abnormal signal pathways affect the proliferation of lung cancer (4–7), which greatly limit the treatment options. The identification of molecules associated with LUAD tumor growth may not only shed light on the underlying biological mechanisms involved in the development or progression of the disease but also reveal potential novel targets for the LUAD therapy.

Monoamine oxidase A (MAOA) is an enzyme which breaks down adrenergic neurotransmitters, such as norepinephrine and dopamine, and is widely expressed in the liver, the digestive tract, the placenta, and the lung, among other tissues (8). MAOA is overexpressed in prostate tumors, and it promotes cancer cell proliferation, stemness, and tumorigenesis (9, 10). Clinical and *in vitro* data indicate that MAOA functions as a tumor suppressor in hepatocellular carcinoma (11), cholangiocarcinoma (12), pheochromocytoma (13), neuroblastoma (14), renal cell carcinoma (15),

and oral and pharyngeal cancers (16). MAOA is overexpressed in NSCLC and stimulates the epithelial–mesenchymal transition in cancer cells (17, 18). An inhibitor of MAOA repressed paclitaxel-resistant NSCLC metastasis and growth (19). However, MAOA is expressed at a low level in LUAD compared to non-tumor tissues, and the overexpression of MAOA correlates with poor outcome for LUAD according to the samples from Gene Expression Profiling Interactive Analysis (GEPIA) (20), The Cancer Genome Atlas (TCGA), and The Genotype-Tissue Expression (GTEx). Thus, the expression and role of MAOA in LUAD needs further study.

Aerobic glycolysis provides abundant ATP, sufficient biomolecules (e.g., nucleotides, amino acids, and lipids), and signaling pathways that are regulated by glycolysis metabolites (21, 22). Reprogrammed aerobic glycolysis promotes the proliferation of bladder cancer cells (23), breast cancer cells (24), and LUAD cells (25, 26). Hexokinase 2 (HK2) is the key rate-limiting enzyme in glycolysis and is overexpressed in NSCLC tumors and promotes cancer cell proliferation (27). Moreover, the repression of HK2 abrogates NSCLC tumor growth (28). These reports suggest that HK2 and its related molecules may be promising therapeutic targets in LUAD.

In the present study, we found a low level of MAOA in LUAD tumors and cell lines. The expression of MAOA correlated with LUAD clinicopathological factors and the clinical outcome. Aerobic glycolysis in LUAD cells was inhibited by MAOA in an HK2-dependent manner. Our results reveal the tumor suppressive role of MAOA in LUAD growth.

## MATERIALS AND METHODS

### Specimen Collection

This study recruited 108 patients with lung cancer who received surgery in the Second Affiliated Hospital of Soochow University. The patients received no chemotherapy or radiotherapy before surgery. Samples from lung cancer tissues and non-tumor lung tissues (>5 cm from the tumor margin) were dissected, snapped frozen in liquid nitrogen after surgery, and stored at  $-80^{\circ}\text{C}$ . Clinicopathological data, such as sex, age, smoking status, size of tumor, lymph nodal status, pathological differentiation, and clinical stage, were obtained at the time of surgery. The postoperative staging was determined according to the 7th Edition of the TNM classification (29). Pathological type was determined according to the classification by the WHO (30). This study was approved by the Research Ethics Committee of the Second Affiliated Hospital of Soochow University (ID: RD2019X011). Written informed consent was obtained from all patients.

### Immunohistochemistry (IHC) and Evaluation

Collected samples were fixed in 10% neutral buffered formalin and embedded in paraffin. Sections were cut at  $5\ \mu\text{m}$  and placed on slides coated with poly-L-lysine. Sections were deparaffinized in xylene and rehydrated in descending concentrations of alcohol. Antigen retrieval was achieved by boiling the sections in a 10 mm citric acid buffer (pH 6.0) for 25 min. Endogenous

peroxidase activity was blocked by incubating sections with 3% hydrogen peroxide for 15 min. The sections were incubated with 10% normal goat serum for 15 min after two washes in a phosphate buffered saline (PBS). The sections were incubated with the rabbit anti-human MAOA polyclonal antibody (1:300, Bioworld, China) at  $4^{\circ}\text{C}$  overnight. Later, the sections were incubated with biotinylated goat anti-rabbit IgG antibody (1:100, Bioworld, China) at room temperature for 15 min, followed by incubating with streptavidin-biotinylated peroxidase at room temperature for another 15 min. The sections were washed in PBS, and the diaminobenzidine (DAB) solution was used to develop color. Color development was monitored under a bright-field microscope, and the reaction was stopped by dipping the sections in water. Hematoxylin was used for nuclear counterstaining.

The IHC staining was evaluated independently by two pathologists at the Second Affiliated Hospital of Soochow University in a double-blinded manner, as described previously (31). In cases of disagreement, a consensus was made through discussion. The stained tumor cells in four randomly selected high magnification fields were counted. The percentage of positively stained tumor cells was graded as 0, 1, 2, and 3, with 0 equals 0% or  $< 5\%$  tumor cells, 1 equals 5–25% tumor cells, 2 equals 25–50% tumor cells, and 3 equals  $> 50\%$  tumor cells. High expression of MAOA was defined as the IHC score  $\geq$  mean of total of tumors IHC score, whereas the low expression of MAOA was defined as the IHC score  $<$  mean IHC score of total tumors.

### Western Blotting Assay

Protein samples (20  $\mu\text{g}$ ) were electrophoresed on a 10% SDS-PAGE gel and transferred onto polyvinylidene difluoride membranes. The membranes were blocked and incubated overnight with antibodies against MAOA (Bioworld), HK2 (Bioworld), proliferating cell nuclear antigen (PCNA) (Santa Cruz, CA, USA), or  $\beta$ -actin (Bioworld, Nanjing, China). The membranes were then incubated with the corresponding horseradish peroxidase-conjugated secondary antibodies for 2 h at room temperature. Protein bands were detected using the Pierce SuperSignal West Pico Chemiluminescent Detection System (Thermo Fisher Scientific Inc., Rockford, IL, USA) and visualized in a G: BoxiChem Imager (Syngene, Cambridge, UK).

### Quantitative RT-PCR Analysis

Total RNAs were extracted using the TRIzol<sup>®</sup> Reagent (Invitrogen Inc., Carlsbad, CA, USA). Quantitative RT-PCR was used to examine the mRNA expression of MAOA using 2  $\mu\text{g}$  total RNA, and  $\beta$ -actin was used as an internal control. The sequences of primers are as follows: MAOA forward 5'-TCCCCGAGCTTCTAAACCAA-3' and reverse 5'-GGAGAATCAAGAGAAGGCGA-3'; HK2 forward 5'-GGCTCTGGACAGGTGGTAAAGA-3' and reverse 5'-CGGTAATGCCACCTTGGTGT-3';  $\beta$ -actin forward 5'-AGCGAGCATCCCCCAAAGTT-3' and reverse 5'-GGGCACGAAGGCTCATCATT-3'. The qRT-PCR was performed on the ABI StepOne Sequence Detection System using the SYBR<sup>®</sup> Green (TaKaRa Biotechnology Co. Ltd., Dalian, China). The conditions used include  $95^{\circ}\text{C}$  for 10 min, followed by 40 cycles of  $95^{\circ}\text{C}$  for

5 s and 55°C for 31 s. The  $\Delta CT$  (CT value of target gene—CT value of internal control) was used for the quantification of the transcripts.

## Cell Lines and Stable Cell Line Construction

The human NCSLC cell lines NCI-H1975 and A549 were obtained from the Cell Bank of Type Culture Collection of Chinese Academy of Sciences (Shanghai, China). The cells were cultured in RPMI 1640 Medium containing 10% FBS (Hyclone). The overexpression of MAOA in LUAD cell lines (NCI-H1975

and A549) was conducted using a lentivirus containing MAOA cDNA or control lentivirus (constructed by GeneChem, Shanghai, China). Lentivirus infection was performed as previously reported (32).

## Cell Viability Assay

Cells ( $1.0 \times 10^3$ ) were plated into each well of a 96-well-plate. A10  $\mu$ l MTT solution was added to each well after 0, 24, 48, and 72 h of culture and incubated in the dark at 37°C for 4 h. After that, the medium was discarded. A 100  $\mu$ l dimethyl sulfoxide (DMSO) was used to dissolve the formazan crystals. Light absorbance was

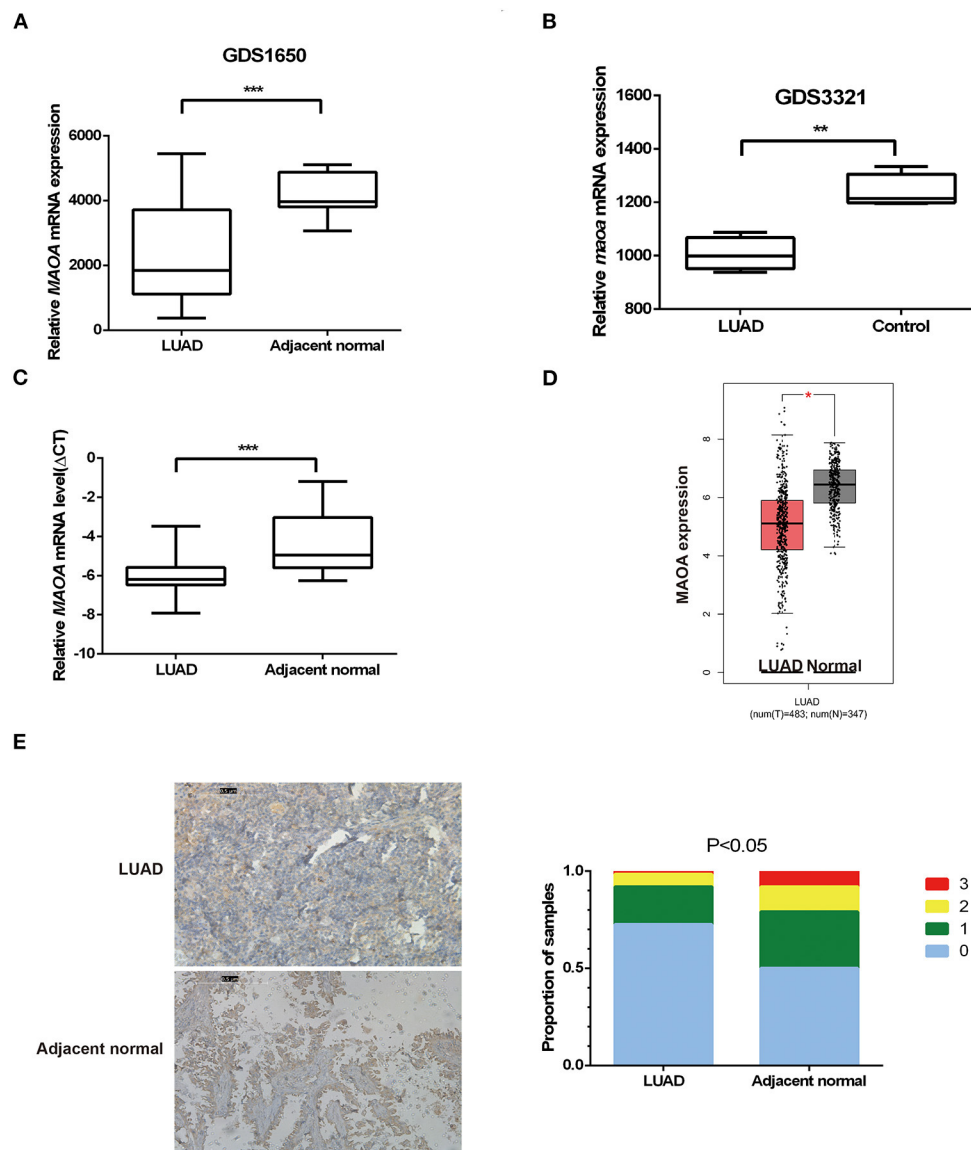


**FIGURE 1 |** The expression of monoamine oxidase A (MAOA) in lung adenocarcinoma (LUAD). The expression of MAOA in gene expression omnibus (GEO) data **(A)**, 19 pairs of human LUAD specimens **(B)**, 15 pairs of mice induced LUAD, 108 human LUAD specimens **(C)**, and the gene expression profiling interactive analysis (GEPIA) database **(D)**. The immunohistochemistry (IHC) detection of MAOA in human LUAD specimens **(E)**. \* $p < 0.05$ , \*\* $p < 0.01$ , and \*\*\* $p < 0.001$ , compared with non-tumor tissues.

read at 490 nm. The growth curves were determined from each experiment, which was repeated three times.

## Cell Cycle Analysis

The cell cycle was evaluated by flow cytometric analysis with propidium iodide (PI) for DNA staining. In brief, cells were harvested and washed in PBS. Later, the cells were fixed in cold 70% ethanol for 30 min at 4°C. Next, 50  $\mu$ l of a 100  $\mu$ g/ml stock of RNase (Sigma, St. Louis, MO, USA) was added, followed by the addition of 1 mg/ml PI (Sigma). The cells were incubated at 37°C for 30 min. The cells were then evaluated by a flow cytometer (BD FACS Calibur, BD Biosciences, San Jose, CA, USA).

## Aerobic Glycolysis and Detection of HK2 Activity

Agilent Seahorse XFe96 Analyzers (Beijing, China) were used to measure the extracellular acidification rate (ECAR) of cancer cells in a 96-well-plate followed the manufacturer's manual.

The glucose consumption and lactate production in stable MAOA overexpressing cells and the corresponding control cells were detected as follows. Cells were seeded into 35-mm dishes for 36 h. The supernatants of cell culture medium were collected by centrifugation at 800 rpm for 5 min. The Glucose Assay Kit (Sigma, Shanghai, China) and the Lactate Assay kit (BioVision, Milpitas, CA, USA) were used to determine the level of glucose and lactate, respectively. The PicoProbe™ Hexokinase Activity Assay Kit (BioVision, CA, USA) was used to detect HK2 activity, as previously reported (5).

## Colony Formation Assay

Non-small cell lung cancer cells (300) were plated into 6-well-plates. Cells were incubated for 14 days. The colonies were fixed using 100% methanol and stained with 0.5% crystal violet solution. Colonies with >50 cells were counted. Each experiment was performed in triplicate.

## Statistical Analysis

Results are expressed as mean  $\pm$  SD. The significance of the difference between the experimental groups, expression correlation, and MAOA correlation with clinicopathologic features were evaluated by the  $\chi^2$  analysis. The Kaplan–Meier curve and the log-rank test were used to analyze the survival of the patients. A value of  $p < 0.05$  was considered significant for all analyses.

## RESULTS

### MAOA Expression Is Decreased in LUAD

The open database of cancer gene expression was examined for the expression of MAOA in gene expression omnibus (GEO) profile datasets (GDS1650 and GDS3321) (33, 34). The results showed that the MAOA mRNA level of LUAD tumor in both human (GDS1650) and mice (GDS3321) was significantly lower than the normal tissue (Figures 1A,B). We performed qRT-PCR to evaluate the MAOA mRNA expression in 108 paired LUAD samples and adjacent normal tissues. It was found that the MAOA mRNA level was significantly decreased in tumors compared with adjacent normal tissues (Figure 1C). Similar findings were observed in the GEPIA (20) database (Figure 1D). The IHC staining showed that the MAOA expression was reduced in LUAD specimens compared with non-tumor controls (Figure 1E), which was inconsistent with the mRNA results. These results suggest that both mRNA and the protein level of MAOA were decreased in LUAD, indicating that MAOA has a tumor suppressive role in LUAD cells.

### The Expression of MAOA Is Associated With Clinicopathologic Factors and the Survival of Patients With LUAD

We investigated the correlation of the expression of MAOA with the overall survival in the GEPIA database of patients

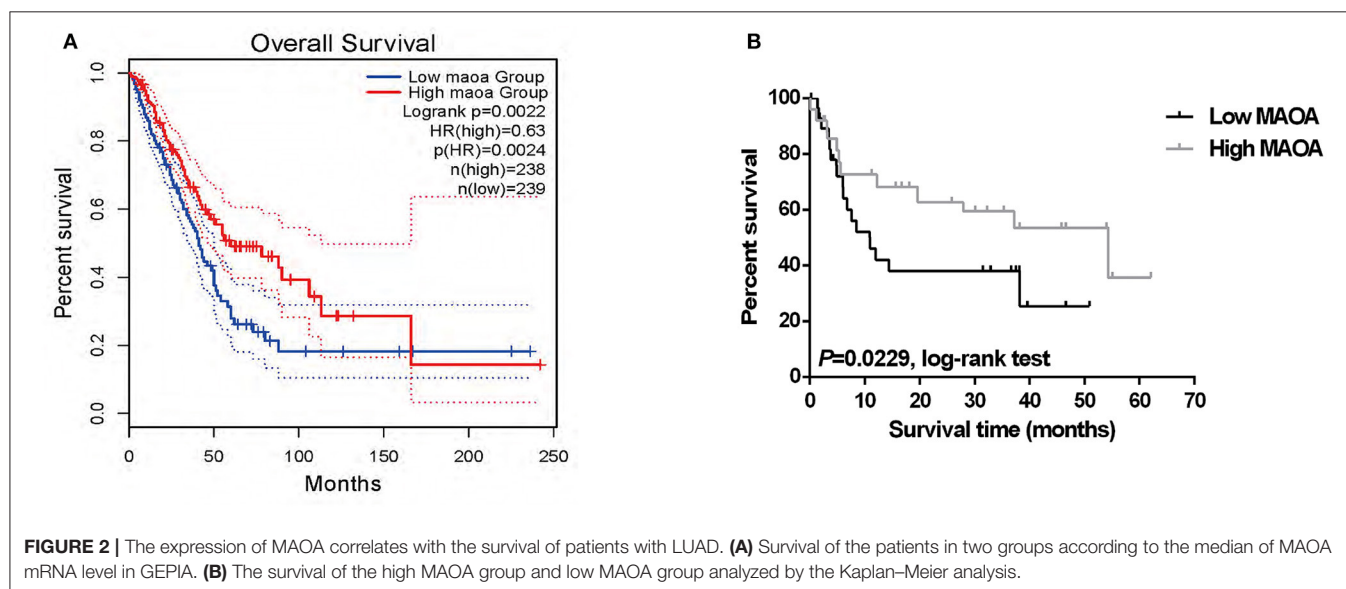




**TABLE 1 |** MAOA IHC scores and clinicopathological factors in LUAD patients.

Characteristic	Number of patients (%)	MAOA IHC scores		
		Low	High	P-value
All patients	108	71	37	
Gender				0.042*
Male	85 (78.7)	60	25	
Female	23 (21.3)	11	12	
Age				0.505
<65	66 (61.1)	45	21	
≥65	42 (38.9)	26	16	
Size of tumor				0.438
≤3 cm	30 (27.8)	18	12	
>3 cm	78 (72.2)	53	25	
Smoking status				0.009*
No Smoking	40 (37.0)	20	20	
Smoking	68 (63.0)	51	17	
Lymph node metastasis (pN)				0.003*
N0	65 (60.2)	50	15	
N1+N2+N3	43 (39.8)	21	22	
p-TNM stages				0.013*
I	51 (47.3)	40	11	
II	40 (37.0)	22	18	
III	16 (14.8)	8	8	
IV	1 (0.9)	1	0	

\*Statistically significant difference ( $P < 0.05$ ).

**TABLE 2 |** Multivariate analyses of MAOA expression and other clinical prognostic factors in 108 patients with LUAD.

Factors	HR (95%CI)	P
Age (>65/≤65 Years)	0.585 (0.330–1.039)	0.068
Gender (Female/Male)	0.689 (0.351–1.353)	0.279
Smoking status (Yes/No)	2.452 (0.414–14.537)	0.743
Size of tumor (>3 cm/≤3 cm)	0.735 (0.414–1.303)	0.291
N stage (N <sub>1+2+3</sub> /N <sub>0</sub> )	1.734 (1.383–2.665)	0.023*
Stage (I and II vs. III and IV)	1.932 (1.312–2.675)	0.005*
MAOA expression (high/low)	2.125 (1.644–2.760)	0.008*

HR, hazard ratio; 95% CI, 95% confidence interval.

\*Statistically significant difference ( $P < 0.05$ ).

with LUAD. The results showed that high MAOA mRNA level indicated good clinical outcome compared to low MAOA mRNA level (**Figure 2A**). We classified 108 LUAD tumors according to MAOA expression and examined the low and high MAOA expression groups. The Kaplan–Meier survival analysis showed that higher MAOA predicted better clinical benefit (**Figure 2B**). Moreover, the expression of MAOA was significantly correlated with the lymph node metastasis status, tumor stage, gender, and smoking status (**Table 1**). Finally, multivariate analysis uncovered that the expression of MAOA is

an independent prognostic biomarker for LUAD (**Table 2**). These results demonstrate that reduced expression of MAOA could be a promising prognostic biomarker for LUAD.

## MAOA Inhibits LUAD Cell Colony Formation and Proliferation

To further examine the biological effect of MAOA, we overexpressed MAOA by a lentivirus in NCI-H1975 and A549 cells (**Figure 3D**). Colony formation assay revealed that the number of colonies of LUAD cells was significantly decreased by the overexpression of MAOA (**Figure 3A**). MAOA also significantly reduced cell proliferation at 72 h after the infection of the lentivirus (**Figure 3B**). Flow cytometry revealed that MAOA induced G1 arrest in LUAD cells (**Figure 3C**), suggesting that cell cycle arrest may be the major cause of MAOA in inhibiting cell proliferation and growth. Moreover, the cell cycle molecule PCNA was decreased in LUAD cells with the overexpression of MAOA (**Figure 3D**).

## MAOA Abrogates Aerobic Glycolysis in LUAD Cells

As aerobic glycolysis plays a critical role in LUAD growth and proliferation, we examined whether MAOA affects aerobic glycolysis in LUAD cells by detecting the ECAR. As shown in **Figure 4A**, the ECAR was reduced by the overexpression of MAOA in NCI-H1975 and A549 cells at around 60 min, and the difference was increased at 120 min. Consistent with these findings, glucose consumption and lactate production (**Figures 4B,C**) were significantly abrogated in LUAD cells with the overexpression of MAOA. Furthermore, the expression and enzymatic activity of HK2, a key rate-limiting enzyme in aerobic glycolysis, was reduced by the overexpression of MAOA (**Figure 4D**). These results suggest that MAOA regulates LUAD cell growth and proliferation by reducing aerobic glycolysis.

## HK2 Expression Negatively Correlates With MAOA Expression and Poor Clinical Outcome in LUAD

Analyses of the GEO profile dataset (GDS3627) and GEPIA database revealed a negative correlation of the mRNA level between HK2 and MAOA in clinical specimens (**Figures 5A,B**). In our collected LUAD tissue samples, HK2 and MAOA have negatively correlated the expression in LUAD tumors (**Figure 5C**). Investigation of the GEPIA database also showed that LUAD cases with high expression of HK2 had a poor survival rate (**Figure 5D**). These results indicate that the MAOA/HK2 axis plays an important role in the progression of LUAD.

## DISCUSSION

Lung adenocarcinoma accounts for ~30% of lung cancers. LUAD is the most common cancer and the leading cause of cancer-related death globally (35, 36). Thus, the identification of reliable predictive biomarkers and potential therapeutic

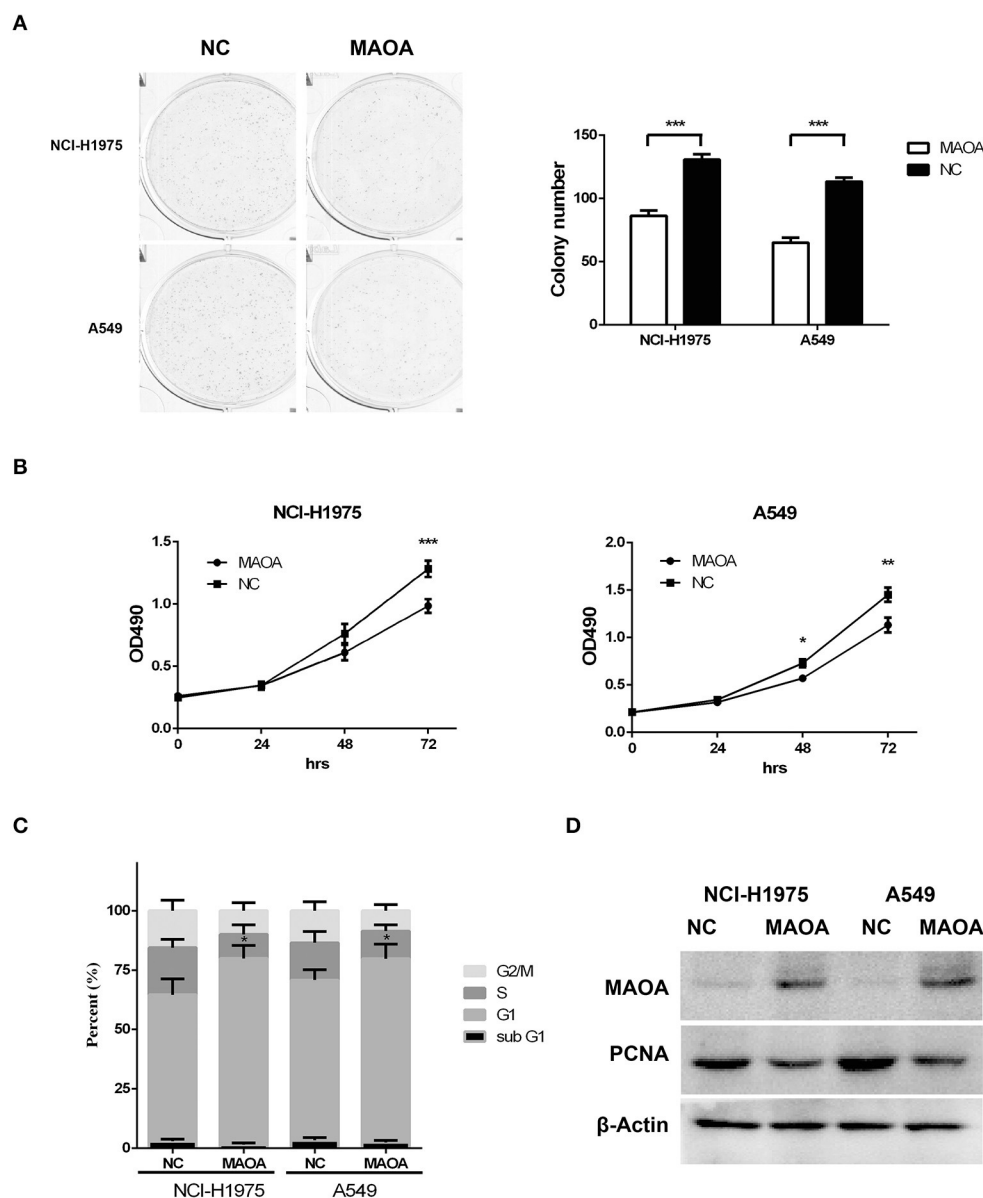


**FIGURE 3 |** Overexpressed MAOA affects LUAD cancer cell proliferation and growth *in vitro*. Colony formation **(A)** and MTT **(B)** assays performed to evaluate the effects of MAOA on LUAD cells (NCI-H1975 and A549). Flow cytometry **(C)** and Western blot **(D)** performed to analyze LUAD cell cycle and the G1/S cell cycle-related protein proliferating cell nuclear antigen (PCNA), respectively. Data are presented as mean + SD ( $n = 3$ ). \* $p < 0.05$ , \*\* $p < 0.01$  and \*\*\* $p < 0.001$ , compared to the control group.

targets for LUAD is urgently needed. In the present study, we demonstrated that the expression of MAOA was decreased in LUAD and correlated with the overall survival of patients. Additionally, we showed that MAOA abrogates cancer cell growth and serves as an independent biomarker for LUAD.

Monoamine oxidase A was reported to be an oncogene in NSCLC (17, 37). Tang's group found positive expression of MAOA in 9 out of 12 LUAD tumors by IHC (18).

Recently, we reported that MAOA plays a critical role in NSCLC migration and HPV-16 E7 induced-HIF-1 $\alpha$  protein accumulation in NSCLC cells (17). Another group found that a potential inhibitor of MAOA, G11, increases the sensitivity of chemotherapy drug and metastasis of NSCLC cells (19). However, we found that MAOA was downregulated in LUAD in an open public database and 108 clinical specimens. Both the database and our results show that high expression of MAOA in LUAD correlated with better clinical outcome of patients

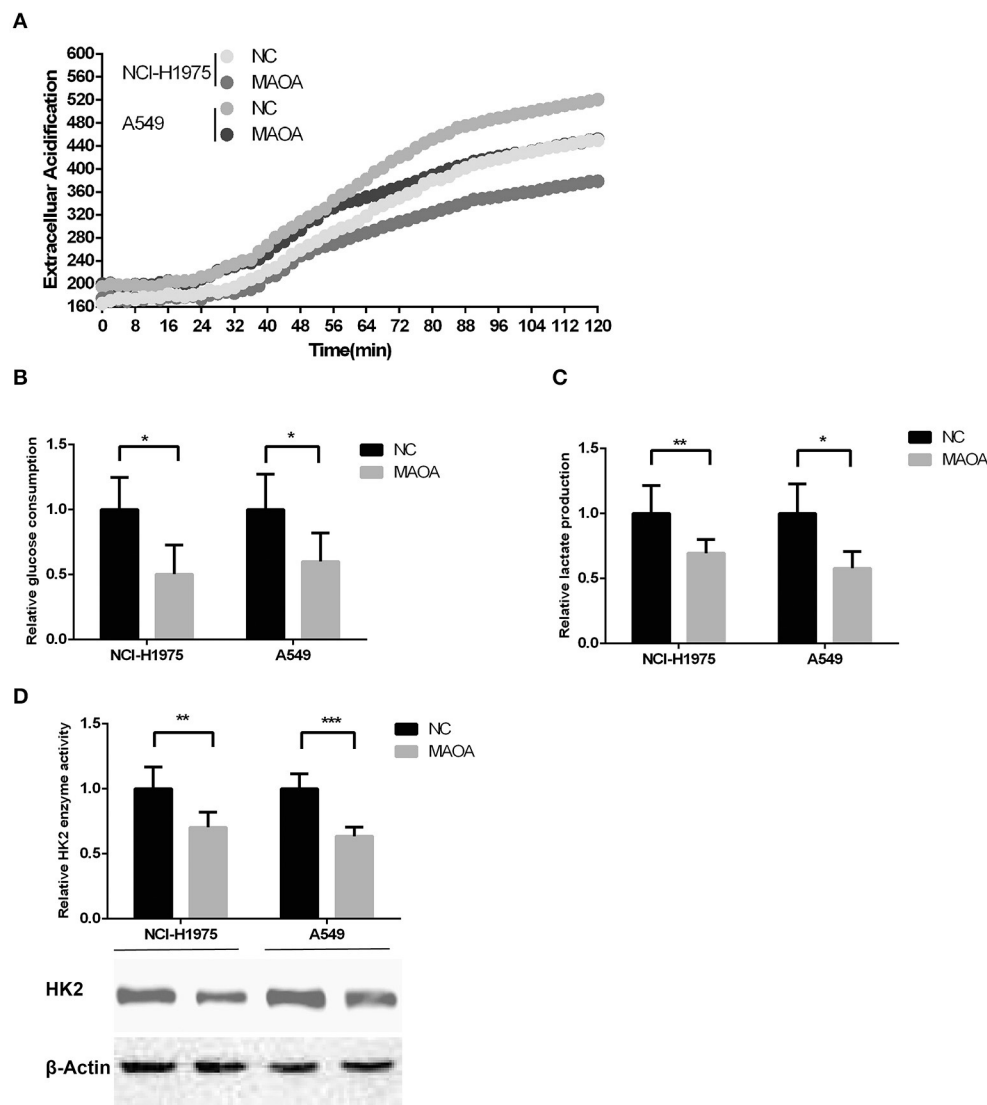


**FIGURE 4 |** Aerobic glycolysis in MAOA-overexpressing LUAD cells. **(A)** Extracellular acidification rate [ECAR, **(B)** glucose consumption, and **(C)** lactate production were analyzed in MAOA-overexpressing and control LUAD cells. **(D)** The enzymatic activity and protein level of hexokinase 2 (HK2) were detected by hexokinase activity assay and Western blot, respectively. Data are presented as mean + SD ( $n = 3$ ). \* $p < 0.05$ , \*\* $p < 0.01$ , and \*\*\* $p < 0.001$ , compared to the control group.

with LUAD. Furthermore, MAOA works as an independent biomarker for LUAD prediction. The contradictory results on findings of this study and others might have arrived due to differences in the number of clinical specimens or detection methods.

Our results showed that the expression of MAOA correlates with the smoking status. Previous reports showed that MAOA is inhibited by tobacco smoke (38, 39), and smoking is the major cause of LUAD (40). These findings suggest that smoking may cause the downregulation of MAOA in LUAD.

In this study, overexpressed MAOA reduced LUAD cell growth and proliferation by inducing G1 cell cycle arrest.

Emerging evidence indicates that enhanced aerobic glycolysis promotes transcription in the G1 phase and furnishes more ATP, which is necessary for the G1/S transition (41). Consistent with these findings, we found that the aerobic glycolysis of cancer cells was abrogated by MAOA. Moreover, MAOA reduced the protein level and enzyme activity of HK2, a key rate-limiting enzyme in glycolysis. These data suggest that MAOA inhibits LUAD cell growth and proliferation by abrogating HK2-dependent aerobic glycolysis.

In conclusion, the expression of MAOA showed a negative correlation with HK2 in LUAD tumors, and overexpressed MAOA reduced the expression of HK2 and the enzymatic

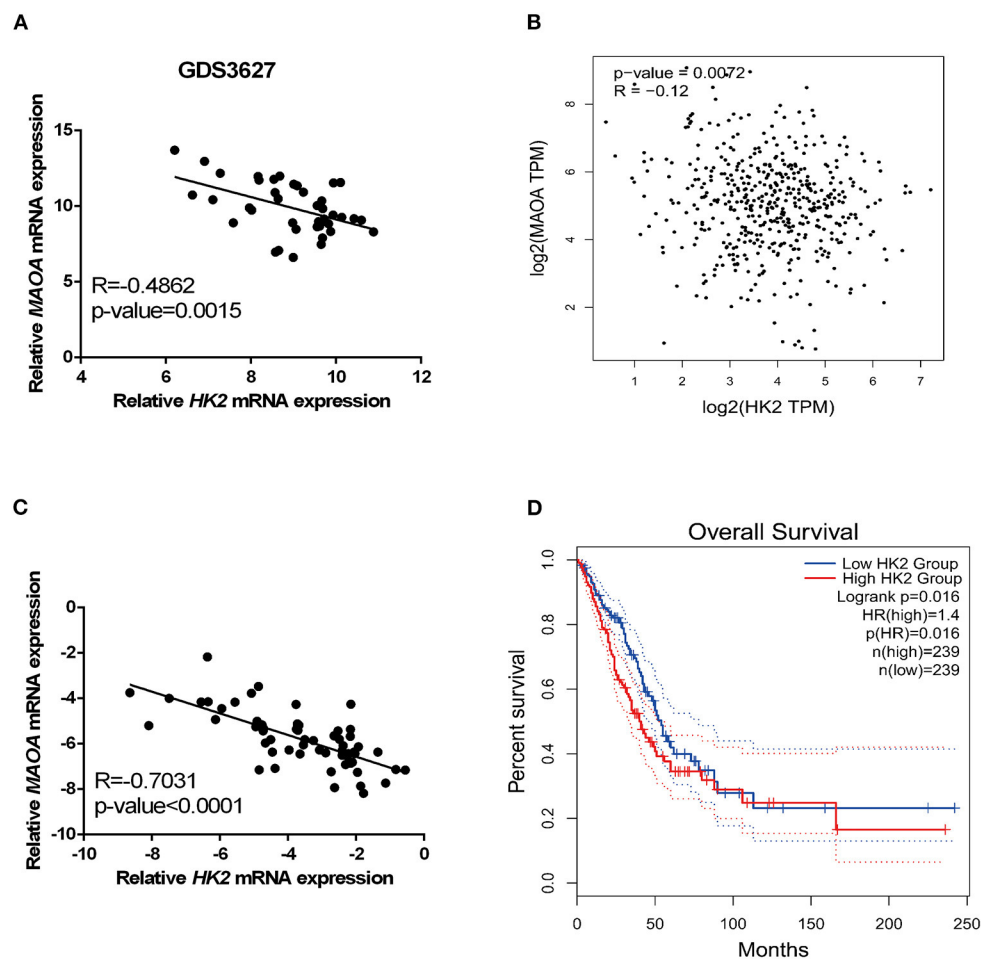


**FIGURE 5 |** HK2 correlates negatively with MAOA in LUAD. The correlation between HK2 and MAOA was analyzed in the GEO dataset (A), GEPIA (B), and our collected LUAD tumors (C). The survival rate of patients with LUAD was analyzed in GEPIA according to the expression of HK2 (D).

activity. MAOA could be a potential therapeutic target for LUAD treatment.

## DATA AVAILABILITY STATEMENT

The original contributions generated for the study are included in the article/supplementary material, further inquiries can be directed to the corresponding author/s.

## ETHICS STATEMENT

The studies involving human participants were reviewed and approved by The Research Ethics Committee of the Second Affiliated Hospital of Soochow University. The patients/participants provided their written informed consent to participate in this study.

## AUTHOR CONTRIBUTIONS

MS: conceptualization. YH, WZ, and XO: methodology. YH, WZ, FW, and YT: validation. WZ: formal analysis. MS, YH, and WZ: investigation and writing—original draft preparation. YH: resources. MS and YH: data and supervision. YH, WZ, and XO: writing, reviewing, and editing. MS and WZ: funding acquisition. All authors have read and agreed to the final version of the manuscript.

## FUNDING

This research was supported by the National Natural Science Foundation of China (81602636), Nanjing Medical Science and Technology Development Project (ZKX15049), Jiangsu Postdoctoral Research Grant (1601182B), a key project of science of Sichuan Education Department (18ZA0164), and Natural Science Foundation of Chengdu Medical College (CYZ18-04).



## REFERENCES

- Bray F, Ferlay J, Soerjomataram I, Siegel R, Torre L, Jemal A. Global cancer statistics 2018: GLOBOCAN estimates of incidence and mortality worldwide for 36 cancers in 185 countries. *CA Cancer J Clin.* (2018) 68:394–424. doi: 10.3322/caac.21492
- Goodgame B, Viswanathan A, Zoole J, Gao F, Miller CR, Subramanian J, et al. Risk of recurrence of resected stage I non-small cell lung cancer in elderly patients as compared with younger patients. *J Thoracic Oncol.* (2009) 4:1370–4. doi: 10.1097/JTO.0b013e3181b6bc1b
- Siegel RL, Miller KD, Jemal A. Cancer statistics, 2020. *CA Cancer J Clin.* (2020) 70:7–30. doi: 10.3322/caac.21590
- Zhao X, Li X, Zhou L, Ni J, Yan W, Ma R, et al. LncRNA HOXA11-AS drives cisplatin-resistance of human LUAD cells via modulating miR-454-3p/Stat3. *Cancer Sci.* (2018) 109:3068–79. doi: 10.1111/cas.13764
- Zhao W, Li W, Dai W, Huang N, Qiu J. LINK-A promotes cell proliferation through the regulation of aerobic glycolysis in non-small-cell lung cancer. *OncoTargets Therap.* (2018) 11:6071–80. doi: 10.2147/OTT.S171216
- Zhang K, Wang J, Yang L, Yuan YC, Tong TR, Wu J, et al. Targeting histone methyltransferase G9a inhibits growth and Wnt signaling pathway by epigenetically regulating HP1 $\alpha$  and APC2 gene expression in non-small cell lung cancer. *Mol Cancer.* (2018) 17:153. doi: 10.1186/s12943-018-0896-8
- Lee SS, Cheah YK. The interplay between MicroRNAs and cellular components of Tumour Microenvironment (TME) on Non-Small-Cell Lung Cancer (NSCLC) progression. *J Immunol Res.* (2019) 2019:3046379. doi: 10.1155/2019/3046379
- Grimsby J, Chen K, Wang LJ, Lan NC, Shih JC. Human monoamine oxidase A and B genes exhibit identical exon-intron organization. *Proc Natl Acad Sci USA.* (1991) 88:3637–41. doi: 10.1073/pnas.88.9.3637
- Liao CP, Lin TP, Li PC, Geary LA, Chen K, Vaikari VP, et al. Loss of MAOA in epithelia inhibits adenocarcinoma development, cell proliferation and cancer stem cells in prostate. *Oncogene.* (2018) 37:5175–90. doi: 10.1038/s41388-018-0325-x
- Kim WY, Won M, Salimi A, Sharma A, Lim JH, Kwon SH, et al. Monoamine oxidase-A targeting probe for prostate cancer imaging and inhibition of metastasis. *Chem Commun.* (2019) 55:13267–70. doi: 10.1039/C9CC07009E
- Li J, Yang XM, Wang YH, Feng MX, Liu XJ, Zhang YL, et al. Monoamine oxidase A suppresses hepatocellular carcinoma metastasis by inhibiting the adrenergic system and its transactivation of EGFR signaling. *J Hepatol.* (2014) 60:1225–34. doi: 10.1016/j.jhep.2014.02.025
- Huang L, Frampton G, Rao A, Zhang KS, Chen W, Lai JM, et al. Monoamine oxidase A expression is suppressed in human cholangiocarcinoma via coordinated epigenetic and IL-6-driven events. *Lab Invest.* (2012) 92:1451–60. doi: 10.1038/labinvest.2012.110
- Grouzmann E, Matter M, Bilz S, Herren A, Triponez F, Henzen C, et al. Monoamine oxidase A down-regulation contributes to high metanephrine concentration in pheochromocytoma. *J Clin Endocrinol Metab.* (2012) 97:2773–81. doi: 10.1210/jc.2012.1557
- Fitzgerald JC, Ugun-Klusek A, Allen G, De Girolamo LA, Hargreaves I, Ufer C, et al. Monoamine oxidase-A knockdown in human neuroblastoma cells reveals protection against mitochondrial toxins. *FASEB J.* (2014) 28:218–29. doi: 10.1096/fj.13-235481
- Hodorova I, Rybarova S, Vecanova J, Solar P, Domorakova I, Adamkov M, et al. Comparison of expression pattern of monoamine oxidase A with histopathologic subtypes and tumour grade of renal cell carcinoma. *Medl Sci Monitor.* (2012) 18:BR482–6. doi: 10.12659/MSM.883592
- Chen PH, Huang B, Shieh TY, Wang YH, Chen YK, Wu JH, et al. The influence of monoamine oxidase variants on the risk of betel quid-associated oral and pharyngeal cancer. *ScientificWorldJournal.* (2014) 2014:183548. doi: 10.1155/2014/183548
- Huang B, Zhou Z, Liu J, Wu X, Li X, He Q, et al. The role of monoamine oxidase A in HPV-16 E7-induced epithelial-mesenchymal transition and HIF-1 $\alpha$  protein accumulation in non-small cell lung cancer cells. *Int J Biol Sci.* (2020) 16:2692–703. doi: 10.7150/ijbs.46966
- Wu H, Pang H, Chen Y, Huang L, Liu H, Zheng Y, et al. Anti-inflammatory effect of a polyphenol-enriched fraction from acahypha wilkesiana on lipopolysaccharide-stimulated RAW 264.7 macrophages and acetaminophen-induced liver injury in mice. *Oxidative Med Cell Longevity.* (2018) 2018:7858094. doi: 10.1155/2018/7858094
- Yang X, Zhao D, Li Y, Li Y, Cui W, Li Y, et al. Potential monoamine oxidase A inhibitor suppressing paclitaxel-resistant non-small cell lung cancer metastasis and growth. *Thoracic Cancer.* (2020) 11:2858–66. doi: 10.1111/1759-7714.13617
- Tang Z, Li C, Kang B, Gao G, Li C, Zhang Z. GEPIA: a web server for cancer and normal gene expression profiling and interactive analyses. *Nucleic Acids Res.* (2017) 45:W98–W102. doi: 10.1093/nar/gkx247
- Vander Heiden MG, Cantley LC, Thompson CB. Understanding the Warburg effect: the metabolic requirements of cell proliferation. *Science.* (2009) 324:1029–33. doi: 10.1126/science.1160809
- Ganapathy-Kanniappan S. Molecular intricacies of aerobic glycolysis in cancer: current insights into the classic metabolic phenotype. *Crit Rev Biochem Mol Biol.* (2018) 53:667–82. doi: 10.1080/10409238.2018.1556578
- Zhao W, Chang C, Cui Y, Zhao X, Yang J, Shen L, et al. Steroid receptor coactivator-3 regulates glucose metabolism in bladder cancer cells through coactivation of hypoxia inducible factor 1 $\alpha$ . *J Biol Chem.* (2014) 289:11219–29. doi: 10.1074/jbc.M113.535989
- Li R, Li J, Huang Y, Li H, Yan S, Lin J, et al. Polydatin attenuates diet-induced nonalcoholic steatohepatitis and fibrosis in mice. *Int J Biol Sci.* (2018) 14:1411–25. doi: 10.7150/ijbs.26086
- Prado-Garcia H, Campa-Higareda A, Romero-Garcia S. Lactic acidosis in the presence of glucose diminishes warburg effect in lung adenocarcinoma cells. *Front Oncol.* (2020) 10:807. doi: 10.3389/fonc.2020.00807
- An S, Huang L, Miao P, Shi L, Shen M, Zhao X, et al. Small ubiquitin-like modifier 1 modification of pyruvate kinase M2 promotes aerobic glycolysis and cell proliferation in A549 human lung cancer cells. *OncoTargets Therap.* (2018) 11:2097–109. doi: 10.2147/OTT.S156918
- Ma Y, Yu C, Mohamed EM, Shao H, Wang L, Sundaresan G, et al. A causal link from ALK to hexokinase II overexpression and hyperactive glycolysis in EML4-ALK-positive lung cancer. *Oncogene.* (2016) 35:6132–42. doi: 10.1038/ncr.2016.150
- Zhou L, Li M, Yu X, Gao F, Li W. Repression of hexokinases II-Mediated glycolysis contributes to piperlongumine-induced tumor suppression in non-small cell lung cancer cells. *Int J Biol Sci.* (2019) 15:826–37. doi: 10.7150/ijbs.31749
- Paleri V, Mehanna H, Wright RG. TNM classification of malignant tumours 7th edition: what's new for head and neck? *Clin Otolaryngol.* (2010) 35:270–2. doi: 10.1111/j.1749-4486.2010.02141.x
- Travis WD, Brambilla E, Geisinger KR. Histological grading in lung cancer: one system for all or separate systems for each histological type? *Europ Respir J.* (2016) 47:720–3. doi: 10.1183/13993003.00035-2016
- Zhou J, Bi H, Zhan P, Chang C, Xu C, Huang X, et al. Overexpression of HP1 $\gamma$  is associated with poor prognosis in non-small cell lung cancer cell through promoting cell survival. *Tumour Biol.* (2014) 35:9777–85. doi: 10.1007/s13277-014-2182-8
- Li C, Zhao W, Pan X, Li X, Yan F, Liu S, et al. LncRNA KTN1-AS1 promotes the progression of non-small cell lung cancer via sponging of miR-130a-5p and activation of PDPK1. *Oncogene.* (2020) 39:6157–71. doi: 10.1038/s41388-020-01427-4
- Kuner R, Muley T, Meister M, Ruschhaupt M, Buness A, Xu EC, et al. Global gene expression analysis reveals specific patterns of cell junctions in non-small cell lung cancer subtypes. *Lung Cancer.* (2009) 63:32–8. doi: 10.1016/j.lungcan.2008.03.033
- Reymann S, Borlak J. Transcription profiling of lung adenocarcinomas of c-myc-transgenic mice: identification of the c-myc regulatory gene network. *BMC Syst Biol.* (2008) 2:46. doi: 10.1186/1752-0509-2-46
- Jemal A, Bray F, Center MM, Ferlay J, Ward E, Forman D. Global cancer statistics. *CA Cancer J Clin.* (2011) 61:69–90. doi: 10.3322/caac.20107
- Yu Y, He J. Molecular classification of non-small-cell lung cancer: diagnosis, individualized treatment, and prognosis. *Front Med.* (2013) 7:157–71. doi: 10.1007/s11684-013-0272-4
- Liu F, Hu L, Ma Y, Huang B, Xiu Z, Zhang P, et al. Increased expression of monoamine oxidase A is associated with epithelial to mesenchymal transition and clinicopathological features in non-small cell lung cancer. *Oncol Lett.* (2018) 15:3245–51. doi: 10.3892/ol.2017.7683

38. Sari Y, Khalil A. Monoamine oxidase inhibitors extracted from tobacco smoke as neuroprotective factors for potential treatment of parkinson's disease. *CNS Neurol Disord Drug Targets*. (2015) 14:777–85. doi: 10.2174/1871527314666150325235608
39. Herraiz T, Chaparro C. Human monoamine oxidase is inhibited by tobacco smoke: beta-carboline alkaloids act as potent and reversible inhibitors. *Biochem Biophys Res Commun*. (2005) 326:378–86. doi: 10.1016/j.bbrc.2004.11.033
40. Sui Q, Liang J, Hu Z, Chen Z, Bi G, Huang Y, et al. Genetic and microenvironmental differences in non-smoking lung adenocarcinoma patients compared with smoking patients. *Trans Lung Cancer Res*. (2020) 9:1407–21. doi: 10.21037/tlcr-20-276
41. Fu H, Gao H, Qi X, Zhao L, Wu D, Bai Y, et al. Aldolase A promotes proliferation and G1/S transition via the EGFR/MAPK

pathway in non-small cell lung cancer. *Cancer Commun*. (2018) 38:18. doi: 10.1186/s40880-018-0290-3

**Conflict of Interest:** The authors declare that the research was conducted in the absence of any commercial or financial relationships that could be construed as a potential conflict of interest.

Copyright © 2021 Huang, Zhao, Ouyang, Wu, Tao and Shi. This is an open-access article distributed under the terms of the Creative Commons Attribution License (CC BY). The use, distribution or reproduction in other forums is permitted, provided the original author(s) and the copyright owner(s) are credited and that the original publication in this journal is cited, in accordance with accepted academic practice. No use, distribution or reproduction is permitted which does not comply with these terms.



## OPEN ACCESS

## Edited by:

Dong-Hua Yang,  
St. John's University, United States

## Reviewed by:

Wenliang Li,  
University of Texas Health Science  
Center at Houston, United States  
Gloryn Chia,  
National University of Singapore,  
Singapore  
Jun Chen,  
Second Affiliated Hospital of Dalian  
Medical University, China

## \*Correspondence:

Xuejun Hu  
xjhu@cmu.edu.cn  
Xiaofang Che  
xfche@cmu.edu.cn

<sup>†</sup>These authors have contributed  
equally to this work

## Specialty section:

This article was submitted to  
Pharmacology of Anti-Cancer Drugs,  
a section of the journal  
Frontiers in Oncology

Received: 22 October 2020

Accepted: 26 January 2021

Published: 08 March 2021

## Citation:

Wang Y, Zheng C, Lu W,  
Wang D, Cheng Y, Chen Y,  
Hou K, Qi J, Liu Y,  
Che X and Hu X (2021)  
Bioinformatics-Based Identification  
of HDAC Inhibitors as Potential  
Drugs to Target EGFR  
Wild-Type Non-Small-Cell  
Lung Cancer.  
Front. Oncol. 11:620154.  
doi: 10.3389/fonc.2021.620154

# Bioinformatics-Based Identification of HDAC Inhibitors as Potential Drugs to Target EGFR Wild-Type Non-Small-Cell Lung Cancer

Yizhe Wang<sup>1†</sup>, Chunlei Zheng<sup>2,3,4†</sup>, Wenqing Lu<sup>2,3,4</sup>, Duo Wang<sup>2,3,4</sup>,  
Yang Cheng<sup>1</sup>, Yang Chen<sup>1</sup>, Kezuo Hou<sup>2,3,4</sup>, Jianfei Qi<sup>5</sup>, Yunpeng Liu<sup>2,3,4</sup>,  
Xiaofang Che<sup>2,3,4\*</sup> and Xuejun Hu<sup>1\*</sup>

<sup>1</sup> Department of Respiratory and Infectious Disease of Geriatrics, The First Hospital of China Medical University, Shenyang, China, <sup>2</sup> Department of Medical Oncology, The First Hospital of China Medical University, Shenyang, China, <sup>3</sup> Key Laboratory of Anticancer Drugs and Biotherapy of Liaoning Province, The First Hospital of China Medical University, Shenyang, China, <sup>4</sup> Liaoning Province Clinical Research Center for Cancer, Shenyang, China, <sup>5</sup> Marlene and Stewart Greenebaum Comprehensive Cancer Center, University of Maryland, Baltimore, Baltimore, MD, United States

Patients with EGFR-mutant non-small-cell lung cancer (NSCLC) greatly benefit from EGFR-tyrosine kinase inhibitors (EGFR-TKIs) while the prognosis of patients who lack EGFR-sensitive mutations (EGFR wild type, EGFR-WT) remains poor due to a lack of effective therapeutic strategies. There is an urgent need to explore the key genes that affect the prognosis and develop potentially effective drugs in EGFR-WT NSCLC patients. In this study, we clustered functional modules related to the survival traits of EGFR-WT patients using weighted gene co-expression network analysis (WGCNA). We used these data to establish a two-gene prognostic signature based on the expression of CYP11B1 and DNALI1 by combining the least absolute shrinkage and selection operator (LASSO) algorithms and Cox proportional hazards regression analysis. Following the calculation of risk score (RS) based on the two-gene signature, patients with high RSs showed a worse prognosis. We further explored targeted drugs that could be effective in patients with a high RS by the connectivity map (CMap). Surprisingly, multiple HDAC inhibitors (HDACis) such as trichostatin A (TSA) and vorinostat (SAHA) that may have efficacy were identified. Also, we proved that HDACis could inhibit the proliferation and metastasis of NSCLC cells *in vitro*. Taken together, our study identified prognostic biomarkers for patients with EGFR-WT NSCLC and confirmed a novel potential role for HDACis in the clinical management of EGFR-WT patients.

**Keywords:** non-small cell lung cancer, histone deacetylase inhibitor, WGCNA, EGFR wild type, metastasis, proliferation

## INTRODUCTION

Lung cancer has the highest morbidity and mortality in China and around the world. Most patients presented with lung cancer at a late stage owing to hidden onset and unspecific symptoms associated with the disease (1, 2). Lung cancer is generally classified into non-small-cell lung cancer (NSCLC) and small cell lung cancer (SCLC). However, this traditional classification according to histological assessment fails to account for the complex prognosis and drug resistance associated with the disease (3).

Radiotherapy combined with chemotherapy is the major treatment strategy for SCLC, whereas targeted therapy has become the first-line treatment for NSCLC patients carrying specific driver mutations (4–6). Epidermal growth factor receptor (EGFR)-tyrosine kinase inhibitors (TKI) such as gefitinib and erlotinib were the first targeted therapy for NSCLC. They have been widely applied in the clinical application for NSCLC patients carrying EGFR-sensitive mutations such as in-frame deletions at exon 19 and exon 21 point mutations (L858R). Also, EGFR-TKIs have significantly prolonged disease-free survival (DFS) compared with platinum-based chemotherapy (7, 8). However, only 20–30% of all NSCLC patients with EGFR-sensitive mutations can benefit from EGFR-TKIs. For patients with no EGFR gene mutations or an unknown mutation status, platinum-based doublet chemotherapy regimens remain the standard first-line therapy (9, 10). In these cases, the tumor response rate is estimated to be less than 10% and overall survival (OS) is only slightly improved (11). There is an unmet need to develop a novel therapy and to improve the prognosis for patients with EGFR wild-type (EGFR-WT) NSCLC.

The rapid development of bioinformatics analysis has allowed the development of novel biomarkers that can predict prognosis in patients with lung cancer (such as PD-L1 (12, 13), GLUT1 (14), and Ki-67 (15, 16)). However, little effort has been focused

on the identification of specific biomarkers for EGFR-WT patients. Thioredoxin reductases 1 (TrxR1) has been reported to be related to the poor prognosis in EGFR-WT and ALK-negative NSCLC (17). As the statistical power of individual biomarkers is considered to be weak, it is necessary to establish a gene signature biomarker to improve the accuracy of prognosis prediction (18–20). Weighted gene co-expression network analysis (WGCNA) is a systems biology approach that clusters genes with a high co-expression relationship into the same module (21). WGCNA has been widely used to assess the functions of transcriptome systems (22), to identify gene modules related to clinical parameters and to investigate cancer biomarkers (23–25). However, WGCNA has not yet been reported to reveal the prognostic prediction of biomarkers in EGFR-WT NSCLC patients.

In this study, WGCNA was conducted on the expression profiles of EGFR-WT NSCLC patients and a two-gene prognosis signature was obtained by LASSO COX regression. We performed connectivity map (CMap) database analysis to identify HDACis as potential drugs to effectively target EGFR-WT NSCLC patients with a high risk score (RS). Our findings provided a further understanding for prognosis prediction and clinical treatment of EGFR-WT NSCLC patients.

## MATERIALS AND METHODS

The flow chart for this research is shown in **Figure 1**.

### Data Acquisition and Consolidation

GSE31852 database expression profile and clinical data were downloaded from the GEO database (**Table S1**) as a training set, and 62 EGFR-WT patients with complete survival data were

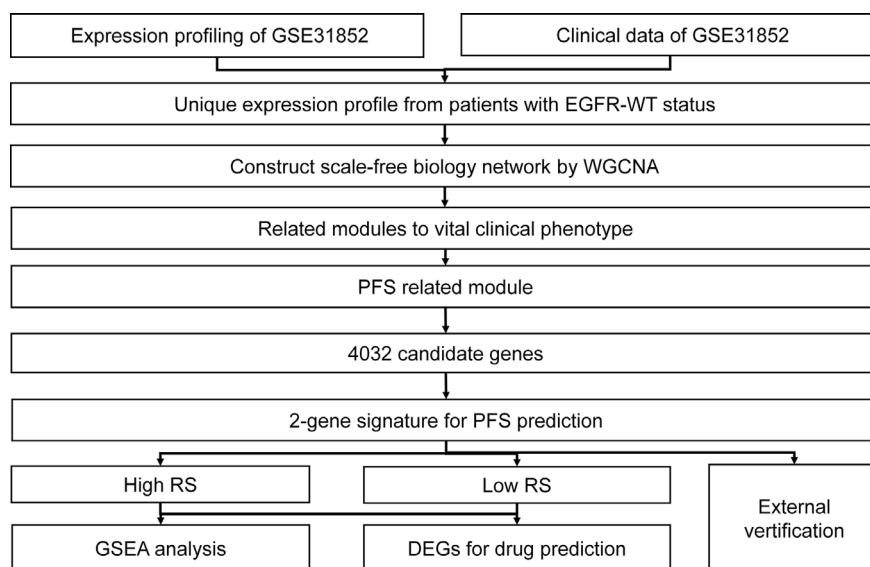


**FIGURE 1** | Schematic diagram of the bioinformatics process used for the analysis in this study.



selected for further analysis (Table S2). Gene expression profiles of these samples were annotated by using the Human Gene 1.0 ST Array (Table S3, Affymetrix, Santa Clara, CA) according to Affymetrix protocols (Table S4). Probes with no gene or duplicate-gene annotation were excluded.

GSE31210 database (Tables S5–S8) was selected as the validation set, which contains the expression profile information, gene mutation status, and progression-free survival (PFS) of 226 NSCLC expression profiles (127 EGFR mutations, 20 KRAS mutations, 11 EML4-ALK fusion mutations, and 68 EGFR/KRAS/ALK-WT cases). Samples of 423 EGFR-WT and 75 EGFR-mutant LUAD patients from The Cancer Genome Atlas Program were downloaded from The Cancer Genome Atlas (TCGA) database (<https://portal.gdc.cancer.gov/>) as another validation dataset (Table S9).

## WGCNA Network Construction

R package “WGCNA” was used for the automatic construction of a co-expression network. Firstly, a hierarchical clustering analysis of the samples was undertaken to ensure that there is little difference between the samples in the GSE31852 dataset (Figure S1A). The co-expression similarity matrix of gene expression was defined according to the Pearson correlation coefficient. Following the selection of an appropriate soft threshold  $\beta$ , the unweighted co-expression similarity matrix was converted into a weighted adjacency matrix. Then, the topological overlap matrix (TOM) was constructed using the degree of dissimilarity between the nodes and the dissimilarity index was defined between the nodes (26). Finally, by using the dynamic tree-cutting algorithm, the TOM was modified and the network modules were initially identified by satisfying conditions such that the difference between these modules is less than 0.25, or the similarity exceeds 0.75 (Table S10).

R package “WGCNA” was used sequentially to visualize the constructed network module and elucidate the correlation between external information. Modules with a significance  $P < 0.05$  in the correlation test were defined being related to the trait. All genes in modules related to prognosis (time and status) were included in the construction of a prognostic risk signature for EGFR-WT patients.

## LASSO Regression and Multivariate COX Regression

R packages “glmnet” and “survival” were used to perform COX regression analysis through the LASSO algorithm. Those parameters with non-zero regression coefficients in the LASSO regression results were further included in the multivariate COX regression analysis. Genes with statistical significance in the multivariate Cox regression analysis were used to calculate their weighted gene expression values to establish RSs for each patient. The RS formula was established as follows:

$$RS = \text{Exp}_{mRNA1} \times \beta_{mRNA1} + \text{Exp}_{mRNA2} \times \beta_{mRNA2} + \dots + \text{Exp}_{mRNA_n} \times \beta_{mRNA_n}$$

$\text{Exp}_{mRNA}$  represents the expression level of each gene, and  $\beta_{mRNA}$  denotes the regression coefficient of the gene in the multi-factor COX regression model.

## Internal and External Verification of the Prognostic Risk Score Signature

X-tile software was used to calculate the best cut-off value of the patient's RS. According to the best cut-off value, all patients were divided into a high-RS group and a low-RS group. Kaplan–Meier survival analysis was performed using the “survival” package with the “log-rank” method. Both the consistency parameter C-index of the survival model and the accuracy of the prediction model in the training set were validated by the resampling method for internal cross-validation using R package “boot.” R package “survivalROC” was used to plot the ROC curve and calculate the area under the curve (AUC).

## Gene Set Enrichment Analysis for Biological Function

GSEA Version 3.0 software was employed to enrich the main biological function pathways in the high-RS group, referring to “c2.cp.kegg.v6.2.symbols.gmt” and “h.all.v7.1.symbols.gmt” gene sets taken from the MsigDB database. All processes were performed according to the default parameters of the GSEA software. The number of random combinations was set to 1,000 and the results were sorted according to normalized enrichment scores (NES).

## Differential Gene Screening and Targeted Drug Prediction

Differentially expressed genes (DEGs) of the high-RS group *versus* low-RS group with  $|\log \text{fold change} (\log FC)| > 0.585$  and  $p\text{-value} < 0.05$  were analyzed by the R package “limma” (Table S11). Then, to find those drugs targeting high-RS patients, the differential gene sets were input into the CMap drug database (<http://www.broadinstitute.org/cmap>). The results included genes, diseases, or drug networks that were similar with, or opposite to, the expression profile. A positive score meant that the change in the expression profile caused by a drug was similar to the input gene expression profile. Conversely, a negative score indicated that the change in the expression profile caused by a drug was opposite that in the input gene expression profile. A drug with a negative score may reverse the corresponding gene expression in the disease and thus serves as a potential targeting drug for the disease (Table S12). Potential compound drugs were selected for verification according to the correlation score (less than 90) of the drugs (Table S12) based on published data from the literature (26).

## Cell Culture and Reagents

Lung adenocarcinoma cell lines A549 and H1299 without EGFR mutations were purchased from the Type Culture Collection of the Chinese Academy of Sciences (Shanghai, China), and cultured in RPMI-1640 (GibcoBRL, USA) supplemented with 10% fetal bovine serum (FBS), penicillin (100 U/ml), and streptomycin (100 mg/ml), in a humid atmosphere containing 5% CO<sub>2</sub> at 37°C. Trichostatin A (TSA, HY-15144) and vorinostat (SAHA, HY-10221) were purchased from MedChem Express (Monmouth Junction, NJ, USA).

## MTT Assay

Approximately 2,000 cells per well in 96-well plates were treated with various concentrations of TSA or SAHA for 48 or 72 h. Then, we added 20  $\mu$ l of 3-(4,5-dimethylthiazolyl-2-yl)-2,5-diphenyltetrazolium bromide (MTT) (5 mg/ml) to each well and the cells were incubated for another 4 h at 37°C. After removing the medium, cells were lysed in 200  $\mu$ l dimethylsulfoxide (DMSO) at room-temperature, and the optical density (OD) was measured at a wavelength of 570 nm with a microplate reader (Bio-Rad Laboratories, Hercules, CA, USA).

## Transwell Assay

Cells were treated with HDACis for 24 h, collected, and resuspend in serum-free media. Transwell chambers (Corning, NY, USA) were plated into a 24-well plate;  $2 \times 10^4$  cells in 200  $\mu$ l of serum-free medium were seeded onto the upper chamber and 500  $\mu$ l of medium with 10% FBS was added to the lower chamber with or without HDACis. After incubation for 24 h, the chambers were fixed with methanol and cells on the upper membrane were removed. Cells in the lower membrane were stained with Wright-Giemsa dye and the number of cells counted.

## Statistical Analysis

All statistical analyses and visualization were performed using GraphPad Prism 7.0 and R (version 3.6.2). Student's *t*-test was used to compare the differences between the two groups:  $P < 0.05$  was considered statistically significant.

## RESULTS

### Data Collation and Patient Characteristics

In order to identify the key prognostic biomarkers for EGFR-WT NSCLC patients, we performed a systematic analysis of the GSE31852 dataset that included 62 patients with complete progression-free survival (PFS) information. The general information of these patients is summarized in **Table 1**. These patients included 24 lung adenocarcinomas, accounting for 38.7% of the samples, and six lung squamous cell carcinomas, accounting for 9.7% of the sample. The cohort consisted of 21 men and 16 women, accounting for 33.9 and 25.8% of the samples respectively. Six patients had no previous history of smoking, and 31 patients were former smokers. According to the expression profiles, all of the patients were clustered gene expression datasets (**Figure S1A**). As no obvious outliers in the expression profiles were observed, all of the 62 EGFR-WT patients were included in the subsequent analysis.

### Construction of a Scale-Free Network by WGCNA

WGCNA was conducted on the gene expression profile data to identify the gene network modules co-expressed in EGFR-WT patients and to explore the relationship between these gene network modules and prognosis. Firstly, a soft threshold ( $\beta = 18$ ) with an  $R^2 > 0.9$  was defined to establish an adjacency matrix

**TABLE 1** | Characteristics of patients of GSE31852.

Characteristic	Number (%)
Gender	
Male	21 (33.9)
Female	16 (25.8)
Unknown	25 (40.3)
Smoking status	
Never	6 (9.7)
Former	31 (50.0)
Unknown	25 (40.3)
Pathological stage	
I	1 (1.6)
II	2 (3.2)
III	7 (11.3)
IV	27 (43.5)
Unknown	25 (40.3)
Histology	
Adenocarcinoma	24 (38.7)
Squamous carcinoma	6 (9.7)
Unknown	32 (51.6)

(**Figures 2A, B**). All genes were clustered into 21 modules with different colors (**Figure 2C**). The gray module in which the genes were not clustered was excluded from the analysis. The similarity between each module was less than 0.75 (**Figures 2D, E**).

We calculated the module eigengenes (ME) value of the samples which represented the gene expression pattern of each module. We found that the gene expression of every sample in each module was different whereas the gene expression of each sample in every module was similar. These results suggested that the modules composed of genes with similar expression patterns may have important biological functions (**Figure S1B**). Then, according to gene significance (GS) which was defined as the association of a single gene with external information (clinical pathology parameters), the correlation between the survival parameters (PFS time and state) and related modules was explored (**Table S10, Figure 2F**). Among each of the 20 modules, the turquoise and green modules were both significantly associated with PFS ( $P < 0.05$ ) compared to the other traits. These modules were most closely related to PFS time and PFS status with correlation coefficients of  $-0.42$  ( $P < 0.0001$ ) and  $-0.35$  ( $P < 0.0001$ ), respectively. These results indicated that the gene expression patterns in the turquoise and green modules were most closely correlated with prognosis in the EGFR-WT patients.

### Construction of Two-Gene Prognostic Signature-Based RS for EGFR-WT NSCLC Patients

As each module in the WGCNA network based on gene expression profiles could be regarded as a characteristic for EGFR-WT patients, the turquoise module (**Figure S2A**) and green modules (**Figure S2B**) may contain the prognostic prediction genes for EGFR-WT patients. The genes of these two modules were combined as candidate gene sets for prognostic markers in EGFR-WT patients. To further select the key genes related to prognosis, we performed the Least Absolute Shrinkage and Selection Operator (LASSO)

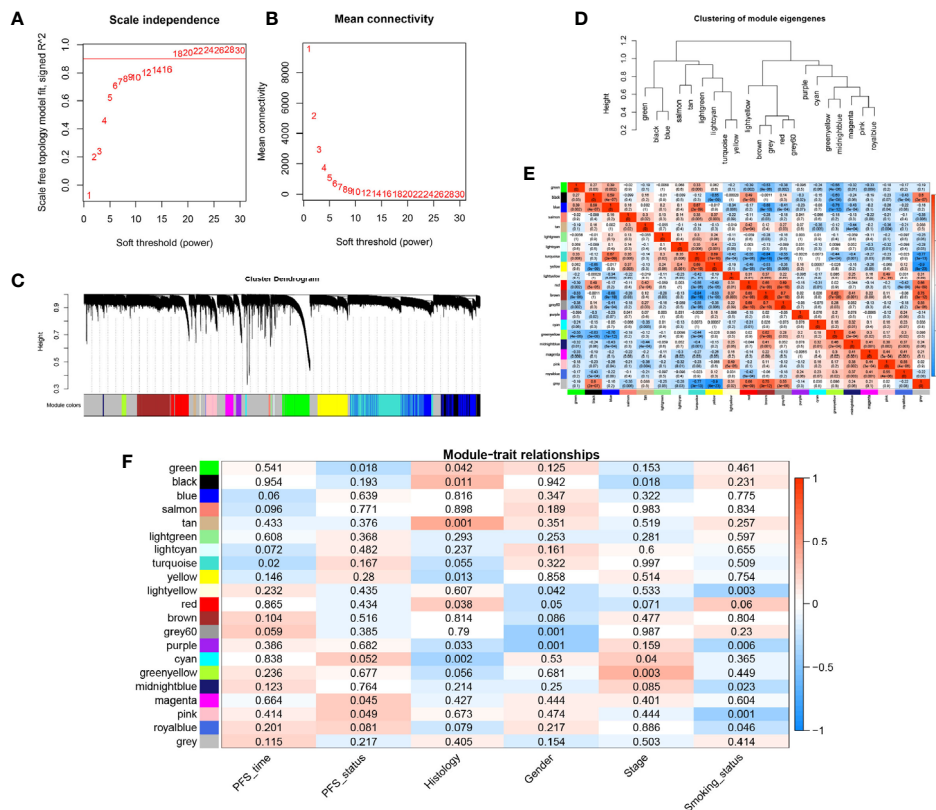


**FIGURE 2** | Construction of the weighted gene co-expression network analysis (WGCNA) network in EGFR-WT NSCLC patients and module identification.

(A) Network topology for different soft-threshold powers. (B) The mean connectivity for different soft threshold powers. (C) One-step network construction by weighted gene co-expression network analysis (WGCNA). (D) Hierarchical clustering tree for clustering modules. (E) Heatmap of the correlation between identified modules (F) Correlation of modules and traits. Colors represent the correlation coefficient, while the number on each module represents the associated *P*-value.

regression combined with multivariate COX regression analysis (Figures 3A and S2C, D). CYP11B1 and DNALI1 were identified as independent prognostic factors for PFS of EGFR-WT NSCLC patients by univariate and multivariate Cox regression (Table 2). Based on the expression of independent prognostic factors and their corresponding coefficients in the regression analysis, the two-gene signature-based RS of each EGFR-WT patient was derived based on the following formula:

$$\text{RS} = [\text{Exp}_{(\text{CYP11B1})} \times 3.3531005] + [\text{Exp}_{(\text{DNALI1})} \times (-0.6605697)]$$

According to the best cut-off value (RS = 19.1), the patients were divided into high- and low-RS groups (Figure 3B). Kaplan-Meier survival analysis showed that the PFS of patients in the high-RS group was significantly shorter than that in the low-RS group (Figure 3C, HR = 3.99, 95% CI = 2.04–7.82,  $P < 0.0001$ ). The C-index was 0.8625 (95% CI = 0.7579–0.9671,  $P < 0.001$ ) by internal cross-validation.

To assess the predictive ability of the model for short-term PFS, the receiver operating characteristic (ROC) curves of the two-gene signature-based on the RS and gene expression were

drawn at 1, 2, and 6 months, and the AUC was determined. The results showed that the two-gene RS model was a good indicator of short-term PFS (Figure 3D). The AUCs for the two-gene RS at 1, 2, and 6 months were 0.736, 0.781, and 0.848, respectively. These values were significantly better than those obtained based on simple gene expression for predicting PFS at each time point (Figures S2E, F).

Taken together, these results indicated that the two-gene RS signature established by the PFS-related modules of WGCNA reflected the survival of EGFR-WT patients and had better predictive power than independent prognostic gene expression.

## External Validation of Two-Gene RS for EGFR-WT Patients

To validate the significance of the two-gene signature for the prognosis of PFS in EGFR-WT NSCLC patients, the GSE31210 database was selected for external verification. All patients were divided into high- or low-RS groups according to the best cut-off value (RS = 10.1) and analyzed based on the Kaplan-Meier survival curves. In patients with EGFR mutations, the PFS of low-RS group was significantly shorter than that of high-RS group (Figures S3A, B). In contrast, in patients with EGFR-WT

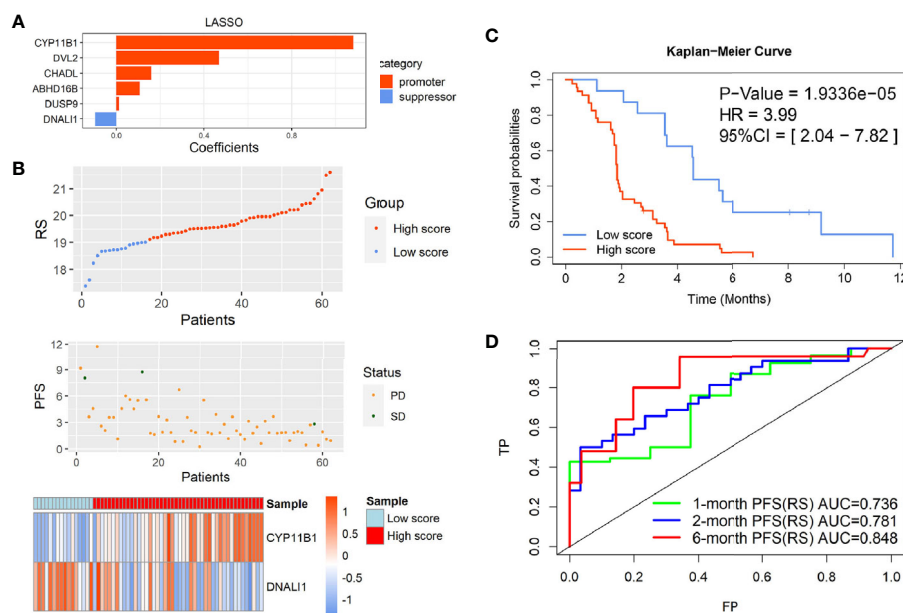


**FIGURE 3** | Identification of the two-gene prognostic signature-based risk score (RS) for EGFR-WT NSCLC patients. **(A)** Six robust markers obtained by LASSO regression. **(B)** The distribution of RSs in GSE31852. Top: two groups for EGFR-WT patients according to the best cut-off of risk score. Middle: relationship between RS (X-axis) and PFS time (Y-axis). Bottom: heatmap plot for the expression of genes in the two-gene signature. **(C)** Kaplan-Meier curve of PFS probability based on the RS in EGFR-WT NSCLC. **(D)** ROC curves were used to compare the predictive ability of the two-gene prognostic signature for 1, 2, and 6-month survival probabilities. PFS status: SD, stable disease; PD, progressive disease.

**TABLE 2** | Univariate and multivariate Cox regression analysis between six candidate markers and progression-free survival (PFS) after Least Absolute Shrinkage and Selection Operator (LASSO) analysis.

Genes	Univariate COX				Multivariate COX			
	HR	95% CI	P-value		HR	95% CI	P-value	
ABHD16B	23.5951	3.5311–157.6667	0.00111	**	3.5896	0.4189–30.7607	0.2436	
CHADL	22.49484	5.13425–98.5573	0.00004	***	7.8693	0.6556–94.4554	0.1037	
CYP11B1	25.99976	5.63712–119.9172	0.00003	***	6.5785	1.2655–34.1969	0.0251	*
DNALI1	0.54419	0.33607–0.88118	0.01335	*	0.2759	0.1472–0.5174	0.0001	***
DUSP9	10.75214	3.09879–37.30756	0.00018	***	4.7842	0.6875–33.2923	0.1138	
DVL2	10.39295	2.73054–39.55755	0.0006	***	3.066	0.6193–15.1795	0.1698	

\* $P < 0.05$ , \*\* $P < 0.01$ , \*\*\* $P < 0.001$ .

(including KRAS mutations, ALK fusion, and none of three mutations named as triple-negative type), the PFS of high-RS patients tended to be shorter although it failed to reach statistical significance ( $P > 0.05$ ) potentially due to the small sample size (Figures 4A, B). Further refinement of the grouping indicated that the two-gene RS signature had better performance in predicting PFS for patients with triple-negative disease (HR = 3.11, 95% CI = 1.35–7.19,  $P < 0.01$ ) (Figures 4C, D). The C-index results of the prognostic model in the three classifications of populations also showed that the RS could fit the true situation of PFS for patients with triple-negative lung cancer (Table 3). However, no significant difference in the long-term OS was found between the high- and low-RS groups regardless of the types of mutations (Figure S4).

Our results demonstrated that the two-gene RS was significant for survival prediction in EGFR-WT patients

particularly in those who did not have EGFR/KRAS/ALK mutations. The two-gene signature was also verified in TCGA database (Figures S3C, D and 4E, F). All NSCLC patients were also divided into high- and low-RS groups and analyzed from the Kaplan-Meier survival curves. The survival time of high-RS patients was significantly shorter than that of low-RS patients (HR = 2.1, 95% CI = 1.51–2.91,  $P < 0.0001$ ), suggesting that the two-gene signature had a generalized and adaptive capacity in predicting the prognosis of EGFR-WT NSCLC patients.

## Verification of HDAC Inhibitors as Potential Targeted Drugs for EGFR-WT NSCLC

To clarify the biological characteristics of high-RS populations, we performed GSEA on the gene expression profile of EGFR-WT NSCLC patients using the tumor-related HALLMARK pathway



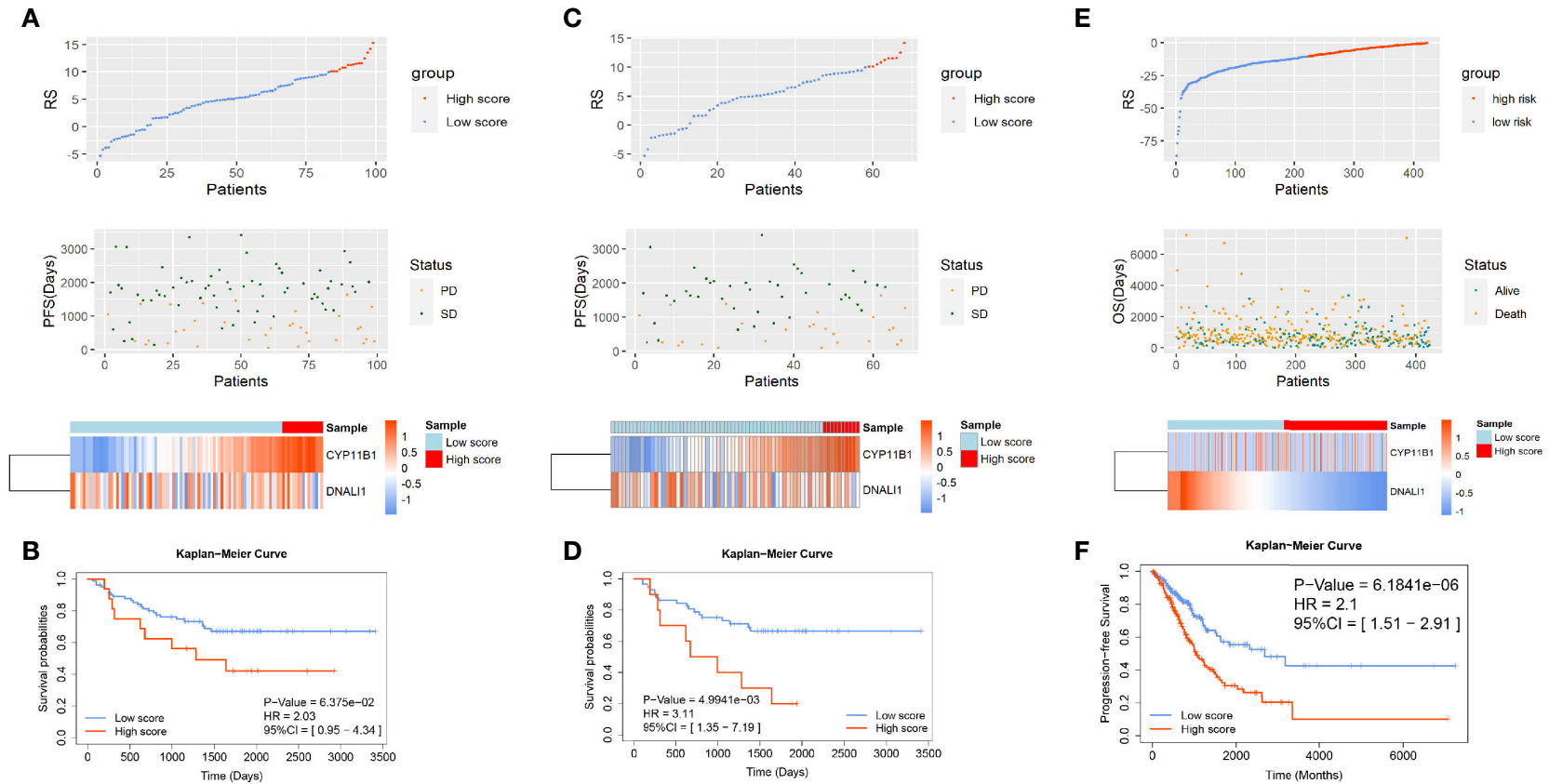


**FIGURE 4 |** The verification of the two-gene prognostic signature for non-small-cell lung cancer (NSCLC) patients with EGFR-WT in GSE31210 and The Cancer Genome Atlas (TCGA) databases. The distribution of RSs in patients with **(A)** EGFR-WT, **(C)** EGFR/ALK/KRAS wild type in GSE31210, and **(E)** EGFR-WT in TCGA. Top: two groups for patients according to the best cut-off of RS. Middle: relationship between RS and PFS information. Bottom: heatmap plot for the expression of genes in the two-gene signature. Kaplan-Meier curve of PFS probability based on the RS in patients with **(B)** EGFR-WT, **(D)** EGFR/ALK/KRAS wild type in GSE31210, and **(F)** EGFR-WT in TCGA.

**TABLE 3** | C-index of the two-gene risk score (RS) signature in three different mutation populations.

Mutant	C-index	95% CI	P-value
EGFR-mutant	0.7051	0.4933–0.9169	0.0578
EGFR-WT	0.6600	0.4933–0.8268	0.0599
EGFR/KRAS/ALK-WT	0.7330	0.5887–0.8774	0.0016

gene set and the classic Kyoto Encyclopedia of Genes and Genomes (KEGG) pathway gene set. Our results showed that both pathways were enriched in metastasis-related pathways including epithelial-mesenchymal transition, apical junction, focal adhesion, ECM receptor interaction and regulation of actin cytoskeleton. These data indicated that the poor prognosis of high-RS patients may be attributed to the enhancement of tumor metastatic ability (**Figure 5A**).

To ascertain potential drug targeting in the EGFR-WT high-RS population, we performed differential gene analysis between the high- and low-RS groups, and identified 25 up-regulated differential expression genes (DEGs) and 36 down-regulated DEGs (**Table S11, Figure 5B**). We compared these DEGs with the CMap database, aiming to identify the drugs that interacted with the DEGs as detailed in the *Materials and Methods* (**Figure 5C**). Twenty-four candidate drugs were identified, and

**TABLE 4** | Candidate drugs targeting EGFR-WT patients with high risk score (RS).

No.	Score	Name	Description
1	−98.94	Tracazolate	GABA receptor modulator
2	−95.3	SB-202190	p38 MAPK inhibitor
3	−95.14	Vemurafenib	RAF inhibitor
4	−94.88	THM-I-94	HDAC inhibitor
5	−94.76	Trichostatin-a	HDAC inhibitor
6	−94.58	NCH-51	HDAC inhibitor
7	−93.9	ISOX	HDAC inhibitor
8	−93.89	AZD-7762	CHK inhibitor
9	−93.84	TG-101348	FLT3 inhibitor
10	−93.81	HG-5-113-01	Protein kinase inhibitor
11	−93.62	Vorinostat	HDAC inhibitor
12	−93.59	Droxinostat	HDAC inhibitor
13	−93.16	SB-590885	RAF inhibitor
14	−93.09	Dasatinib	BCR-ABL kinase inhibitor
15	−92.74	Scriptaid	HDAC inhibitor
16	−92.61	HC-toxin	HDAC inhibitor
17	−92.39	Fostamatinib	SYK inhibitor
18	−92.11	KU-0063794	MTOR inhibitor
19	−91.53	TPCA-1	IKK inhibitor
20	−91.21	TWS-119	Glycogen synthase kinase inhibitor
21	−90.68	GSK-1070916	Aurora kinase inhibitor
22	−90.64	Pyroxamide	HDAC inhibitor
23	−90.41	PI-828	PI3K inhibitor
24	−90.13	PP-2	SRC inhibitor

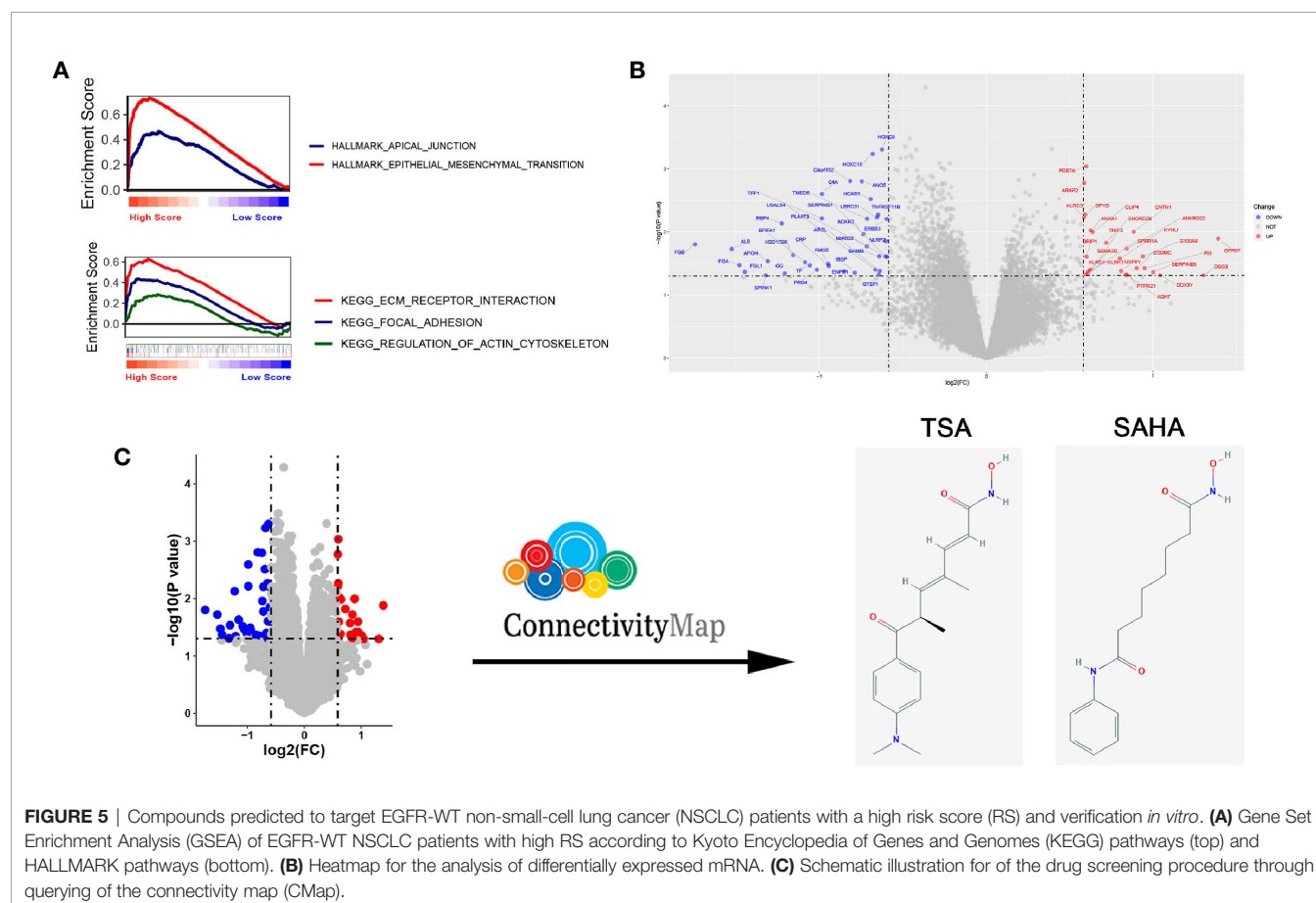


**FIGURE 5** | Compounds predicted to target EGFR-WT non-small-cell lung cancer (NSCLC) patients with a high risk score (RS) and verification *in vitro*. **(A)** Gene Set Enrichment Analysis (GSEA) of EGFR-WT NSCLC patients with high RS according to Kyoto Encyclopedia of Genes and Genomes (KEGG) pathways (top) and HALLMARK pathways (bottom). **(B)** Heatmap for the analysis of differentially expressed mRNA. **(C)** Schematic illustration for the drug screening procedure through querying of the connectivity map (CMap).

interestingly, nine were classified as HDACi (Tables 4, S12). Considering the safety and feasibility of HDACis for clinical applications, we verified two common HDACis, TSA, and SAHA in EGFR-WT lung cancer cells (A549 and H1299). Both HDACis significantly inhibited the proliferation and migration of these cell models (Figures 6A, B), indicating the potential of TSA and SAHA as novel treatment strategies in EGFR-WT lung cancer.

## Discussion

In the current study, we established a RS based on a two-gene signature for EGFR-WT NSCLC patients and found that EGFR-WT patients with a high RS had a worse prognosis. Mechanistically, a high RS might cause poor prognosis by activating multiple metastasis-related pathways such as epithelial-mesenchymal transition and ECM receptor interaction. Furthermore, HDACis were screened out as potential targeted drugs for EGFR-WT NSCLC and found to inhibit cell proliferation and migration of EGFR-WT NSCLC cells.

Although well-known driver genes such as EGFR and ALK with sensitive mutations could strongly predict the efficacy of targeted drugs in NSCLC patients, about 50% of NSCLC patients without driver gene mutations do not benefit from the personalized targeted therapy (27, 28). For those patients that do not have corresponding mutations or have unknown mutation status, platinum-based doublet chemotherapy remains the standard first-line regimen which has poor efficacy (9, 10). In these patients, docetaxel or pemetrexed could be used as second-line single-agent chemotherapies. However, the tumor response rate was less than 10% and the OS was only slightly improved with these treatments (11). The current known tumor-driver mutations are not sufficient to fully predict the drug response of lung cancer. This study aimed to ascertain the characteristics of gene expression profiles in EGFR-WT

NSCLC patients and provide evidence for the clinical treatment for NSCLC patients without specific mutations.

The rapid development of NGS technology and bioinformatics has allowed major progress in the prediction of NSCLC prognosis. In addition to the TNM stage, multi-gene prognostic signatures based on transcriptome sequencing have been developed for prognosis. However, the majority of studies of gene signatures for predicting prognosis in lung cancer have focused on RSs related to specific mechanisms, starting with functional molecules or cell components, such as immune infiltration (29–31), EMT scores (32), hypoxic or metabolic catabolites (33, 34), and non-coding RNA (35, 36). Little research has considered specific mutations.

Few gene signature studies have considered a scale-free property of the gene interaction network using WGCNA (37). WGCNA bridges the gap from individual genes to systems biology networks and can be utilized to identify hub genes that play key roles in the disease by converting the relationship between genes from a constant probability to the value adding a correlation weight (38). This allows the conversion from a random network to a scale-free network (39). Unfortunately, WGCNA on EGFR-WT NSCLC patients has not yet been reported.

In the present study, we used WGCNA to cluster the gene expression pattern of the EGFR-WT population, studied the co-expressed gene modules and correlated the gene modules with patient prognostic information for the first time. Due to the limited omics data containing information on mutations, the accuracy and comprehensiveness of our two-gene signature need to be validated in a large cohort of lung cancer patients. Also, we observed that the two-gene signature predicted the prognosis of patients without known driver gene mutations (EGFR/KRAS/ALK-WT) better than that of patients with EGFR-WT alone. Thus, the accumulation of next-generation sequencing (NGS)

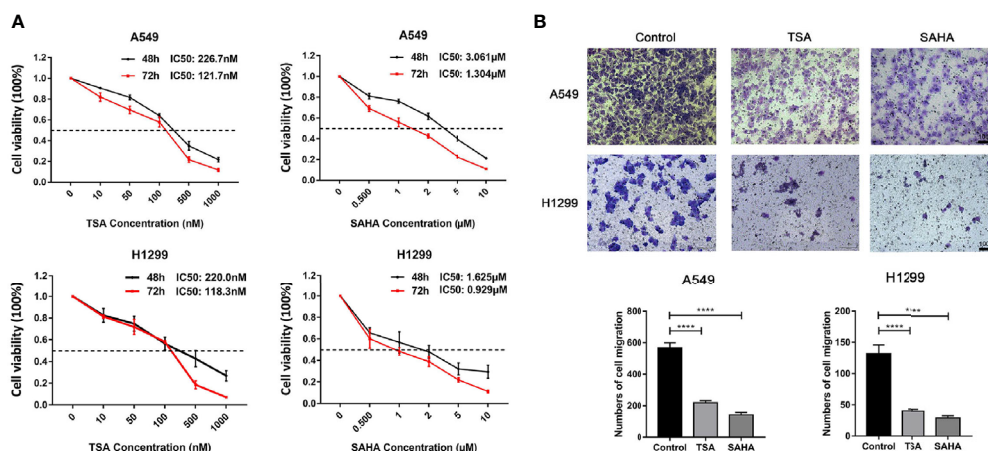


**FIGURE 6 |** Verification of the effect of HDACis on EGFR-WT non-small-cell lung cancer (NSCLC) cells *in vitro*. **(A)** Inhibition of cell proliferation of trichostatin A (TSA) and vorinostat (SAHA) as assessed by MTT assay in A549 and H1299 cells. **(B)** Inhibition of migration ability by TSA and SAHA as assessed by Transwell assays in A549 and H1299 cells. \*\*\*\* $P < 0.0001$ .

data in clinical tumor assessment and treatment may allow the further verification of a two-gene signature in a larger multi-omics database.

Considering the genes in WGCNA modules might be interrelated, they were not suitable for direct prognostic signature construction as this may result in multi-collinearity. We performed LASSO regression on the genes in the WGCNA modules to screen for the prognostic factors for the subsequent multivariate COX regression model. These analyses led to the selection of CYP11B1 and DNALI1 genes to construct a prognostic risk signature for EGFR-WT patients.

CYP11B1 encodes the cytochrome P450 family 11 subfamily B member 1 protein that is mostly expressed in the adrenal glands and is related to excessive cortisol secretion (40). In cancer, CYP11B1 is not only related to aldosterone- and cortisol-co-secreting adrenal tumors (41, 42), but it also affects the drug response of breast cancer (43), gastrointestinal tumors (44), leukemia (45), and other tumors. DNALI1 encodes dynein axonemal light intermediate chain 1 protein which is a human homologue of p28 in Chlamydia. DNALI1 is widely expressed in the human testis, ovaries and other tissues (28, 46), but the functions of DNALI1 in physiological processes and tumor development remain unclear. Limited studies have reported that DNALI1 is down-regulated in breast cancer (47) and negatively correlated with poor prognosis (48, 49). However, the expression pattern and function of both genes in lung cancer, as well as their influence on prognosis are unknown.

In this study, we analyzed the predictive significance of both molecules in the prognosis of NSCLC patients from online databases (**Figure S5**). The prognosis of patients with high expression of CYP11B1 or low expression of DNALI1 was significantly poor ( $P < 0.0001$ ). Furthermore, the efficiency of prognostic prediction in the EGFR-WT population from RS based on the two-gene signature was better than that by individual genes (**Figures S2E, F**). The RS based on the two-gene signature had good predictive significance for the prognosis of EGFR-WT patients. This may provide a good reference value for clinical decision-making in EGFR-WT patients, particularly in patients without known driver mutations.

From the online drug database named CMap, HDACs were screened out as potential drugs to improve the prognosis of EGFR-WT patients with a high RS based on the two-gene signature.

CMap is a database developed by Broad Research Institute to reveal the functional relationships between small molecule compounds, genes, and disease states (50). CMap was employed to compare the differentially expressed gene list with the reference gene sets after specific treatments in the database. A correlation score (–100 to 100) was obtained according to the enrichment of differentially expressed genes in the reference gene expression profile. A positive score indicated that the up-regulation or down-regulation pattern of input genes was similar to the pattern of reference gene expression treated with different drugs. In contrast, a negative score indicated that the drugs regulated the expression of genes in an opposite direction. Finally, all treatments in the database were ranked according to the correlation score with the reference gene expression profile.

We found that among a total of 24 drug candidates with scores less than –90, 9 were HDACs, accounting for more than one-third of those identified. HDACs, such as romidepsin and vorinostat, are approved by the Food and Drug Administration (FDA) in cutaneous T cell lymphoma therapy (51, 52). However, although multiple preclinical studies have shown that HDAC inhibitors play a significant anti-cancer role *in vitro* or in animal models (53, 54), HDACs monotherapy clinical trials for lung cancer have failed (55–57). The results in the present study independently predicted that HDACs may be potential drugs for patients with high-RS EGFR-WT NSCLC and implicated the possibility of HDACs as single drugs for lung cancer therapy. Furthermore, HDACs were found to inhibit the proliferation and migration capacity of EGFR-WT NSCLC cells which was consistent with previous studies. Our research provides support for the independent application of HDAC inhibitors in EGFR wild-type NSCLC. Large-scale clinical trials should be carried out to confirm the efficacy of HDACs in EGFR-WT NSCLC patients.

In conclusion, the current study showed that a two-gene signature could effectively predict the survival of EGFR-WT patients, especially in NSCLC patients without known gene mutations. Our data also indicate that HDACs, such as TSA or SAHA, might be potentially effective clinical drugs for high-RS EGFR-WT patients. This study may fill the gap in lung cancer data analysis on one-specific mutant population, highlights the need for differential analysis of different oncomutations in cancer and also provides clues for the clinical treatment of EGFR-WT NSCLC patients.

## DATA AVAILABILITY STATEMENT

The original contributions presented in the study are included in the article/**Supplementary Material**. Further inquiries can be directed to the corresponding authors.

## AUTHOR CONTRIBUTIONS

YW and CZ analyzed the data and drafted the manuscript and all figures. WL and DW helped interpreted the data. YCheng and YChen completed analysis of drug prediction. KH and YL completed the *in vitro* experiments. JQ edited language grammars and all tables. XC and XH designed the study and revised the manuscript. All authors contributed to the article and approved the submitted version.

## FUNDING

This study was supported by the National Natural Science Foundation of China (Grant No. 81972197; No. 81472193), the Key Research and Development Program of Liaoning Province (2018225060), the Natural Science Foundation of Liaoning



Province (2019-ZD-777), the Technological Special Project of Liaoning Province of China (2019020176- JH1/103), the Science and Technology Plan Project of Liaoning Province (No. 2013225585), Science and Technology Plan Project of Shenyang City (19-112-4-099).

## REFERENCES

- Chen W, Zheng R, Baade PD, Zhang S, Zeng H, Bray F, et al. Cancer statistics in China, 2015. *CA Cancer J Clin* (2016) 66(2):115–32. doi: 10.3322/caac.21338
- Carney DN. Lung cancer—time to move on from chemotherapy. *N Engl J Med* (2002) 346(2):126–8. doi: 10.1056/NEJM200201103460211
- Gridelli C, Rossi A, Carbone DP, Guarize J, Karachaliou N, Mok T, et al. Non-small-cell lung cancer. *Nat Rev Dis Primers* (2015) 1:15009. doi: 10.1038/nrdp.2015.9
- Mok TS, Wu YL, Thongprasert S, Yang CH, Chu DT, Saijo N, et al. Gefitinib or carboplatin-paclitaxel in pulmonary adenocarcinoma. *N Engl J Med* (2009) 361(10):947–57. doi: 10.1056/NEJMoa0810699
- Wu YL, Zhou C, Hu CP, Feng J, Lu S, Huang Y, et al. Afatinib versus cisplatin plus gemcitabine for first-line treatment of Asian patients with advanced non-small-cell lung cancer harbouring EGFR mutations (LUX-Lung 6): an open-label, randomised phase 3 trial. *Lancet Oncol* (2014) 15(2):213–22. doi: 10.1016/S1470-2045(13)70604-1
- Ramalingam SS, Vansteenkiste J, Planchard D, Cho BC, Gray JE, Ohe Y, et al. Overall Survival with Osimertinib in Untreated, EGFR-Mutated Advanced NSCLC. *N Engl J Med* (2020) 382(1):41–50. doi: 10.1056/NEJMoa1913662
- Zhong WZ, Wang Q, Mao WM, Xu ST, Wu L, Shen Y, et al. Gefitinib versus vinorelbine plus cisplatin as adjuvant treatment for stage II-IIIa (N1-N2) EGFR-mutant NSCLC (ADJUVANT/CTONG1104): a randomised, open-label, phase 3 study. *Lancet Oncol* (2018) 19(1):139–48. doi: 10.1016/S1470-2045(17)30729-5
- Yue D, Xu S, Wang Q, Li X, Shen Y, Zhao H, et al. Erlotinib versus vinorelbine plus cisplatin as adjuvant therapy in Chinese patients with stage IIIA EGFR mutation-positive non-small-cell lung cancer (EVAN): a randomised, open-label, phase 2 trial. *Lancet Respir Med* (2018) 6(11):863–73. doi: 10.1016/S2213-2600(18)30277-7
- Azzoli CG, Temin S, Aliff T, Baker Jr, Brahmer J, Johnson DH, et al. 2011 Focused Update of 2009 American Society of Clinical Oncology Clinical Practice Guideline Update on Chemotherapy for Stage IV Non-Small-Cell Lung Cancer. *J Clin Oncol* (2011) 29(28):3825–31. doi: 10.1200/JCO.2010.34.2774
- Scagliotti GV, Parikh P, von Pawel J, Biesma B, Vansteenkiste J, Manegold C, et al. Phase III study comparing cisplatin plus gemcitabine with cisplatin plus pemetrexed in chemotherapy-naïve patients with advanced-stage non-small-cell lung cancer. *J Clin Oncol* (2008) 26(21):3543–51. doi: 10.1200/JCO.2007.15.0375
- Hanna N, Shepherd FA, Fossella FV, Pereira JR, De Marinis F, von Pawel J, et al. Randomized phase III trial of pemetrexed versus docetaxel in patients with non-small-cell lung cancer previously treated with chemotherapy. *J Clin Oncol* (2004) 22(9):1589–97. doi: 10.1200/JCO.2004.08.163
- Takada K, Toyokawa G, Shoji F, Okamoto T, Maehara Y. The Significance of the PD-L1 Expression in Non-Small-Cell Lung Cancer: Trenchant Double Swords as Predictive and Prognostic Markers. *Clin Lung Cancer* (2018) 19(2):120–9. doi: 10.1016/j.clcc.2017.10.014
- Aguiar PN Jr, De Mello RA, Hall P, Tadokoro H, Lima Lopes G. PD-L1 expression as a predictive biomarker in advanced non-small-cell lung cancer: updated survival data. *Immunotherapy* (2017) 9(6):499–506. doi: 10.2217/imt-2016-0150
- Zhang B, Xie Z, Li B. The clinicopathologic impacts and prognostic significance of GLUT1 expression in patients with lung cancer: A meta-analysis. *Gene* (2019) 689:76–83. doi: 10.1016/j.gene.2018.12.006
- Wei DM, Chen WJ, Meng RM, Zhao N, Zhang XY, Liao DY, et al. Augmented expression of Ki-67 is correlated with clinicopathological characteristics and prognosis for lung cancer patients: an up-dated systematic review and meta-analysis with 108 studies and 14,732 patients. *Respir Res* (2018) 19(1):150. doi: 10.1186/s12931-018-0843-7
- Grant L, Banerji S, Murphy L, Dawe DE, Harlos C, Myal Y, et al. Androgen Receptor and Ki67 Expression and Survival Outcomes in Non-small Cell Lung Cancer. *Horm Cancer* (2018) 9(4):288–94. doi: 10.1007/s12672-018-0336-7
- Chen G, Chen Q, Zeng F, Zeng L, Yang H, Xiong Y, et al. The serum activity of thioredoxin reductases 1 (TrxR1) is correlated with the poor prognosis in EGFR wild-type and ALK negative non-small cell lung cancer. *Oncotarget* (2017) 8(70):115270–9. doi: 10.18632/oncotarget.23252
- Chen HY, Yu SL, Chen CH, Chang GC, Chen CY, Yuan A, et al. A five-gene signature and clinical outcome in non-small-cell lung cancer. *N Engl J Med* (2007) 356(1):11–20. doi: 10.1056/NEJMoa060096
- Kadara H, Behrens C, Yuan P, Solis L, Liu D, Gu X, et al. A five-gene and corresponding protein signature for stage-I lung adenocarcinoma prognosis. *Clin Cancer Res* (2011) 17(6):1490–501. doi: 10.1158/1078-0432.CCR-10-2703
- Okayama H, Schetter AJ, Ishigame T, Robles AI, Kohnno T, Yokota J, et al. The expression of four genes as a prognostic classifier for stage I lung adenocarcinoma in 12 independent cohorts. *Cancer Epidemiol Biomarkers Prev* (2014) 23(12):2884–94. doi: 10.1158/1055-9965.EPI-14-0182
- Zhang B, Horvath S. A general framework for weighted gene co-expression network analysis. *Stat Appl Genet Mol Biol* (2005) 4:Article17. doi: 10.2202/1544-6115.1128
- Langfelder P, Horvath S. WGCNA: an R package for weighted correlation network analysis. *BMC Bioinformatics* (2008) 9:559. doi: 10.1186/1471-2105-9-559
- Link VM, Duttke SH, Chun HB, Holtman IR, Westin E, Hoeksema MA, et al. Analysis of Genetically Diverse Macrophages Reveals Local and Domain-wide Mechanisms that Control Transcription Factor Binding and Function. *Cell* (2018) 173(7):1796–809 e17. doi: 10.1016/j.cell.2018.04.018
- Zhang XJ, Cheng X, Yan ZZ, Fang J, Wang X, Wang W, et al. An ALOX12-12-HETE-GPR31 signaling axis is a key mediator of hepatic ischemia-reperfusion injury. *Nat Med* (2018) 24(1):73–83. doi: 10.1038/nm.4451
- Doering TA, Crawford A, Angelosanto JM, Paley MA, Ziegler CG, Wherry EJ. Network analysis reveals centrally connected genes and pathways involved in CD8+ T cell exhaustion versus memory. *Immunity* (2012) 37(6):1130–44. doi: 10.1016/j.immuni.2012.08.021
- Subramanian A, Narayan R, Corsello SM, Peck DD, Natoli TE, Lu X, et al. A Next Generation Connectivity Map: L1000 Platform and the First 1,000,000 Profiles. *Cell* (2017) 171(6):1437–52 e17. doi: 10.1016/j.cell.2017.10.049
- Riely GJ, Politi KA, Miller VA, Pao W. Update on epidermal growth factor receptor mutations in non-small cell lung cancer. *Clin Cancer Res* (2006) 12(24):7232–41. doi: 10.1158/1078-0432.CCR-06-0658
- Fukuoka M, Wu YL, Thongprasert S, Sunpawaravong P, Leong SS, Sriuranpong V, et al. Biomarker analyses and final overall survival results from a phase III, randomized, open-label, first-line study of gefitinib versus carboplatin/paclitaxel in clinically selected patients with advanced non-small-cell lung cancer in Asia (IPASS). *J Clin Oncol* (2011) 29(21):2866–74. doi: 10.1200/JCO.2010.33.4235
- Li B, Cui Y, Diehn M, Li R. Development and Validation of an Individualized Immune Prognostic Signature in Early-Stage Nonsquamous Non-Small Cell Lung Cancer. *JAMA Oncol* (2017) 3(11):1529–37. doi: 10.1001/jamaoncol.2017.1609
- Song Q, Shang J, Yang Z, Zhang L, Zhang C, Chen J, et al. Identification of an immune signature predicting prognosis risk of patients in lung adenocarcinoma. *J Transl Med* (2019) 17(1):70. doi: 10.1186/s12967-019-1824-4
- Chen F, Yang Y, Zhao Y, Pei L, Yan H. Immune Infiltration Profiling in Nonsmall Cell Lung Cancer and Their Clinical Significance: Study Based on

## SUPPLEMENTARY MATERIAL

The Supplementary Material for this article can be found online at: <https://www.frontiersin.org/articles/10.3389/fonc.2021.620154/full#supplementary-material>

- Gene Expression Measurements. *DNA Cell Biol* (2019) 38(11):1387–401. doi: 10.1089/dna.2019.4899
32. Chae YK, Chang S, Ko T, Anker J, Agte S, Iams W, et al. Epithelial-mesenchymal transition (EMT) signature is inversely associated with T-cell infiltration in non-small cell lung cancer (NSCLC). *Sci Rep* (2018) 8(1):2918. doi: 10.1038/s41598-018-21061-1
  33. Heiden BT, Chen G, Hermann M, Brown RKJ, Orringer MB, Lin J, et al. 18F-FDG PET intensity correlates with a hypoxic gene signature and other oncogenic abnormalities in operable non-small cell lung cancer. *PloS One* (2018) 13(7):e0199970. doi: 10.1371/journal.pone.0199970
  34. Lim SL, Jia Z, Lu Y, Zhang H, Ng CT, Bay BH, et al. Metabolic signatures of four major histological types of lung cancer cells. *Metabolomics* (2018) 14(9):118. doi: 10.1007/s11306-018-1417-x
  35. Lin T, Fu Y, Zhang X, Gu J, Ma X, Miao R, et al. A seven-long noncoding RNA signature predicts overall survival for patients with early stage non-small cell lung cancer. *Aging (Albany NY)* (2018) 10(9):2356–66. doi: 10.18632/aging.101550
  36. Wang X. Improving microRNA target prediction by modeling with unambiguously identified microRNA-target pairs from CLIP-ligation studies. *Bioinformatics* (2016) 32(9):1316–22. doi: 10.1093/bioinformatics/btw002
  37. Xie H, Xie C. A Six-Genes Signature Predicts Survival of Adenocarcinoma Type of Non-Small-Cell Lung Cancer Patients: A Comprehensive Study Based on Integrated Analysis and Weighted Gene Coexpression Network. *BioMed Res Int* (2019) 2019:4250613. doi: 10.1155/2019/4250613
  38. Duan H, Ge W, Zhang A, Xi Y, Chen Z, Luo D, et al. Transcriptome analyses reveal molecular mechanisms underlying functional recovery after spinal cord injury. *Proc Natl Acad Sci U S A* (2015) 112(43):13360–5. doi: 10.1073/pnas.1510176112
  39. Barabasi AL, Oltvai ZN. Network biology: understanding the cell's functional organization. *Nat Rev Genet* (2004) 5(2):101–13. doi: 10.1038/nrg1272
  40. Zhu W, Chen Z, Li Q, Tan G, Hu G. Inhibitors of 11 $\beta$ -Hydroxylase (CYP11B1) for Treating Diseases Related to Excess Cortisol. *Curr Med Chem* (2016) 23(6):623–33. doi: 10.2174/0929867323666160122114947
  41. Murakami M, Rhyam Y, Kunzke T, Sun N, Feuchtinger A, Ludwig P, et al. In situ metabolomics of aldosterone-producing adenomas. *JCI Insight* (2019) 4(17):e130356. doi: 10.1172/jci.insight.130356
  42. Fallo F, Castellano I, Gomez-Sanchez CE, Rhyam Y, Pilon C, Vicennati V, et al. Histopathological and genetic characterization of aldosterone-producing adenomas with concurrent subclinical cortisol hypersecretion: a case series. *Endocrine* (2017) 58(3):503–12. doi: 10.1007/s12020-017-1295-4
  43. Brixius-Anderko S, Scott EE. Structure of human cortisol-producing cytochrome P450 11B1 bound to the breast cancer drug fadrozole provides insights for drug design. *J Biol Chem* (2019) 294(2):453–60. doi: 10.1074/jbc.RA118.006214
  44. Ravegnini G, Urbini M, Simeon V, Genovese C, Astolfi A, Nannini M, et al. An exploratory study by DMET array identifies a germline signature associated with imatinib response in gastrointestinal stromal tumor. *Pharmacogenomics J* (2019) 19(4):390–400. doi: 10.1038/s41397-018-0050-4
  45. Haznedaroglu IC, Malkan UY. Local bone marrow renin-angiotensin system in the genesis of leukemia and other malignancies. *Eur Rev Med Pharmacol Sci* (2016) 20(19):4089–111.
  46. Fagerberg L, Hallstrom BM, Oksvold P, Kampf C, Djureinovic D, Odeberg J, et al. Analysis of the human tissue-specific expression by genome-wide integration of transcriptomics and antibody-based proteomics. *Mol Cell Proteomics* (2014) 13(2):397–406. doi: 10.1074/mcp.M113.035600
  47. Parris TZ, Danielsson A, Nemes S, Kovacs A, Delle U, Fallén G, et al. Clinical implications of gene dosage and gene expression patterns in diploid breast carcinoma. *Clin Cancer Res* (2010) 16(15):3860–74. doi: 10.1158/1078-0432.CCR-10-0889
  48. Tian W, Li Y, Zhang J, Li J, Gao J. Combined analysis of DNA methylation and gene expression profiles of osteosarcoma identified several prognosis signatures. *Gene* (2018) 650:7–14. doi: 10.1016/j.gene.2018.01.093
  49. Ye Z, Wang F, Yan F, Wang L, Li B, Liu T, et al. Bioinformatic identification of candidate biomarkers and related transcription factors in nasopharyngeal carcinoma. *World J Surg Oncol* (2019) 17(1):60. doi: 10.1186/s12957-019-1605-9
  50. Lamb J, Crawford ED, Peck D, Modell JW, Blat IC, Wrobel MJ, et al. The Connectivity Map: using gene-expression signatures to connect small molecules, genes, and disease. *Science* (2006) 313(5795):1929–35. doi: 10.1126/science.1132939
  51. Mann BS, Johnson JR, Cohen MH, Justice R, Pazdur R. FDA approval summary: vorinostat for treatment of advanced primary cutaneous T-cell lymphoma. *Oncologist* (2007) 12(10):1247–52. doi: 10.1634/theoncologist.12-10-1247
  52. Grant C, Rahman F, Piekarz R, Peer C, Frye R, Robey RW, et al. Romidepsin: a new therapy for cutaneous T-cell lymphoma and a potential therapy for solid tumors. *Expert Rev Anticancer Ther* (2010) 10(7):997–1008. doi: 10.1586/era.10.88
  53. Shieh JM, Tang YA, Hu FH, Huang WJ, Wang YJ, Jen J, et al. A histone deacetylase inhibitor enhances expression of genes inhibiting Wnt pathway and augments activity of DNA demethylation reagent against non-small-cell lung cancer. *Int J Cancer* (2017) 140(10):2375–86. doi: 10.1002/ijc.30664
  54. Wu YF, Ou CC, Chien PJ, Chang HY, Ko JL, Wang BY. Chidamide-induced ROS accumulation and miR-129-3p-dependent cell cycle arrest in non-small lung cancer cells. *Phytomedicine* (2019) 56:94–102. doi: 10.1016/j.phymed.2018.09.218
  55. Traynor AM, Dubey S, Eickhoff JC, Kolesar JM, Schell K, Huie MS, et al. Vorinostat (NSC# 701852) in patients with relapsed non-small cell lung cancer: a Wisconsin Oncology Network phase II study. *J Thorac Oncol* (2009) 4(4):522–6. doi: 10.1097/jto.0b013e3181952478
  56. Reid T, Valone F, Lipera W, Irwin D, Paroly W, Natale R, et al. Phase II trial of the histone deacetylase inhibitor pivaloyloxymethyl butyrate (Pivanex, AN-9) in advanced non-small cell lung cancer. *Lung Cancer* (2004) 45(3):381–6. doi: 10.1016/j.lungcan.2004.03.002
  57. Schrupp DS, Fischette MR, Nguyen DM, Zhao M, Li X, Kunst TF, et al. Clinical and molecular responses in lung cancer patients receiving Romidepsin. *Clin Cancer Res* (2008) 14(1):188–98. doi: 10.1158/1078-0432.CCR-07-0135

**Conflict of Interest:** The authors declare that the research was conducted in the absence of any commercial or financial relationships that could be construed as a potential conflict of interest.

Copyright © 2021 Wang, Zheng, Lu, Wang, Cheng, Chen, Hou, Qi, Liu, Che and Hu. This is an open-access article distributed under the terms of the Creative Commons Attribution License (CC BY). The use, distribution or reproduction in other forums is permitted, provided the original author(s) and the copyright owner(s) are credited and that the original publication in this journal is cited, in accordance with accepted academic practice. No use, distribution or reproduction is permitted which does not comply with these terms.



# 17 $\beta$ -Estradiol Promotes Apoptosis of HepG2 Cells Caused by Oxidative Stress by Increasing Foxo3a Phosphorylation

Yusheng Guo<sup>1,2†</sup>, Xiangsheng Cai<sup>1,3†\*</sup>, Hanwei Lu<sup>1</sup>, Qiqi Li<sup>2</sup>, Ying Zheng<sup>2</sup>, Zefang Lin<sup>2</sup>, Zexiong Cheng<sup>2</sup>, Maoxiang Yang<sup>3</sup>, Li Zhang<sup>1</sup>, Lei Xiang<sup>3,4\*</sup> and Xiaorong Yang<sup>1,2\*</sup>

<sup>1</sup>Clinical Laboratory, First Affiliated Hospital/School of Clinical Medicine, Guangdong Pharmaceutical University, Guangzhou, China, <sup>2</sup>Department of Medical Laboratory, School of Clinical Medicine, Guangdong Pharmaceutical University, Guangzhou, China, <sup>3</sup>Center for Medical Experiments, University of Chinese Academy of Science-Shenzhen Hospital, Shenzhen, China, <sup>4</sup>Department of Integrative Chinese and Western Medicine, The First Affiliated Hospital of Guangdong Pharmaceutical University, Guangzhou, China

## OPEN ACCESS

### Edited by:

Yingyan Yu,  
Shanghai Jiao Tong University, China

### Reviewed by:

Michele De Bortoli,  
University of Turin, Italy  
Ran Zhao,  
Zhengzhou University, China

### \*Correspondence:

Xiaorong Yang  
122424818@qq.com  
Lei Xiang  
xianglei9527@163.com  
Xiangsheng Cai  
xiangshengcai@gdpu.edu.cn

<sup>†</sup>These authors have contributed  
equally to this work

### Specialty section:

This article was submitted to  
Pharmacology of Anti-Cancer Drugs,  
a section of the journal  
Frontiers in Pharmacology

**Received:** 17 September 2020

**Accepted:** 13 January 2021

**Published:** 15 March 2021

### Citation:

Guo Y, Cai X, Lu H, Li Q, Zheng Y,  
Lin Z, Cheng Z, Yang M, Zhang L,  
Xiang L and Yang X (2021) 17 $\beta$ -  
Estradiol Promotes Apoptosis of  
HepG2 Cells Caused by Oxidative  
Stress by Increasing  
Foxo3a Phosphorylation.  
Front. Pharmacol. 12:607379.  
doi: 10.3389/fphar.2021.607379

Liver cancer is associated with high mortality, particularly in patients infected with the hepatitis B virus. Treatment methods remain very limited. Here, we explored the effects of 17 $\beta$ -estradiol (E2) on apoptosis of various liver cell lines (LO2, HepG2, and HepG2.2.15 cells). Within a certain concentration range, 17 $\beta$ -estradiol induced oxidative stress and apoptosis of HepG2 cells, downregulated ER $\alpha$ -36 expression, and increased Akt and Foxo3a phosphorylation. *p*-Foxo3a became localized around the nucleus but did not enter the organelle. The levels of mRNAs encoding manganese superoxide dismutase (MnSOD) and catalase, to the promoters of which Foxo3a binds to trigger gene expression, were significantly reduced in HepG2 cells. 17 $\beta$ -estradiol had no obvious effects on LO2 or HepG2.2.15 cells. We speculate that 17 $\beta$ -estradiol may induce oxidative stress in HepG2 cells by increasing Foxo3a phosphorylation, thus promoting apoptosis. This may serve as a new treatment for hepatocellular carcinoma.

**Keywords:** 17 $\beta$ -estradiol, hepatocellular carcinoma, oxidative stress, apoptosis, foxo3a phosphorylation

## INTRODUCTION

Liver cancer is common and associated with high mortality (Mak et al., 2018); hepatocellular carcinoma (HCC) is the most common cancer type (Liu and Suo, 2020). Chronic HBV infection is an important risk factor for HCC (Nayagam et al., 2020). Traditional treatments include surgical resection, liver transplantation, local ablation, and transcatheter arterial chemoembolization. The clinical effects on, and prognoses of, patients with advanced liver cancer are very poor; more effective therapies are needed (Bruix et al., 2019). Primary liver cancer occurrence and development is complex, involving multiple factors and several regulatory steps. Molecularly targeted therapy exploiting the abnormal signaling pathways of primary liver cancer are being intensively researched (Rossetto and De Re, 2019). However, as cancer occurrence and development remain poorly understood, and as the pathophysiological mechanism remains unclear, such therapies are not yet advanced. Sorafenib was the first such oral drug approved by the European Medicines Agency and Food and Drug Administration to treat primary liver cancer. However, sorafenib used as first-line treatment for HCC exhibits several side-effects, high-level drug-resistance development, and is associated with poor patient tolerance (Moawad et al., 2020).

Epidemiologically, the incidence of, and mortality from, liver cancer in males are much higher than in females (Mak et al., 2018), suggesting that estrogen may be protective. Estrogen regulates reproductive physiology and function (Satirapod et al., 2020), cell growth and proliferation, apoptosis, the immune response, and metabolism (Guerra et al., 2020; Jehle et al., 2020). The liver is targeted by estrogen (Clegg et al., 2017; Kur and Kolasa-Wołoskiuk, 2020). Estrogen and estrogen receptor (ER) agonists inhibit the growth of liver cancer HepG2 cells by downregulating proliferation and promoting apoptosis (Shen et al., 2018). Estrogen binds to its receptor to inhibit the activity of NF- $\kappa$ B, thereby regulating tumor growth (Pelekanou et al., 2016). Thus, the estrogen signal transduction pathway (involving the Era receptor and estrogen *per se*) may inhibit the occurrence and development of liver cancer.

Chronic HBV infection is an important risk factor for HCC in our country; we encounter many such patients. Here, we used HepG2.2.15 cells harboring the hepatitis B virus to explore whether estrogen might exert a therapeutic effect. LO2 cells are human normal liver cells derived from human embryos; HepG2 cells were derived from the liver cancer tissue of a 15-year-old Caucasian teenager and are widely used in liver cancer-related *in vitro* studies; the HepG2.2.15 cell line is derived from the HepG2 human liver cancer cell line transfected with HBV genes (Xia et al., 2016; Li et al., 2020). Therefore, we explored the effects of 17 $\beta$ -estradiol on LO2, HepG2, and HepG2.2.15 cells, and the mechanisms in play, to derive a theoretical basis for biotherapy of hepatomas with 17 $\beta$ -estradiol.

## MATERIALS AND METHODS

### Reagents

17 $\beta$ -estradiol, dihydroethidium (DHE), and 2',7'-dichloro dihydro fluorescein diacetate (DCFH-DA) were purchased from Sigma-Aldrich (St. Louis, MO, United States). Antibodies (rabbit anti-human) against ER $\alpha$ , Akt, *p*-Akt, Foxo3a, *p*-Foxo3a, and  $\beta$ -actin were purchased from Cell Signaling Technology (Beverly, MA, United States). The 17 $\beta$ -estradiol was dissolved in dimethyl sulfoxide (DMSO) to prepare a stock solution at a concentration of 50 mg/ml, and was stored at  $-20^{\circ}\text{C}$ . Complete Dulbecco's modified Eagle medium (DMEM; Gibco, Gaithersburg, MD, United States) was added to dilute the 17 $\beta$ -estradiol to the appropriate concentrations prior to use.

### Cell Culture and Treatment

LO2, HepG2, and HepG2.2.15 cells were cultured in DMEM supplemented with 10% fetal bovine serum (Gibco or CellMax, Sunnyvale, CA, United States) at  $37^{\circ}\text{C}$  in a humidified atmosphere of 5%  $\text{CO}_2$ . After digestion and counting, cells were seeded into 96-well plates (5,000 cells/well) or 6-well plates (50,000 cells/well). When grown to 70–80% confluence, 17 $\beta$ -estradiol was added to various levels and the cells were cultured further until they were used for the MTT assay or other detection methods.

**TABLE 1** | The primers used in the qPCR.

Name	Primers sequence (5'-3')
MnSOD-forward	ACAAAGATGGTGTGGCCGAT
MnSOD-reverse	AACGACTTCCAGCGTTTCCT
Catalase-forward	AGTGATCGGGGATTCCAGA
Catalase-reverse	GAGGGGTACTTTCCTGTGGC
GAPDH-forward	GAAGGTGAAGGTCGGAGTC
GAPDH- reverse	GAAGATGGTGATGGGATTTC

### MTT Assay

First, 17 $\beta$ -estradiol of different concentrations was added to each well, and the cells were cultured for 24, 48, or 72 h, followed by incubation with 5 mg/L MTT for 0.5–4 h. Then, the medium was discarded and 200  $\mu\text{L}$  of DMSO was added to each cell. Finally, absorbance at a wavelength of 490 nm was measured using a microplate reader (Multiscan-GO, Thermo Fisher Scientific, Waltham, MA, United States).

### qPCR and Ribonucleic Acid-Seq Analysis

Total RNA was isolated using the TRIzol reagent and reverse transcribed into cDNA using a commercial kit (Takara (Dalian), Shiga, Japan). Relative mRNA abundances were calculated as the differences between the thresholds of target genes and the housekeeping gene (GAPDH). The average of three replicates was calculated. The primers are listed in **Table 1**.

Construction of the cDNA library, Illumina sequencing (paired-end on Illumina HiSeq<sup>TM</sup>2000), and RNA-Seq analysis were performed by a commercial gene-sequencing company (Gene Denovo, Guangdong, China). Low-quality sequence reads with >5% N bases and reads containing adaptor sequences were removed before data analysis. The sequencing data are available on the NCBI BioProject website (accession no. PRJNA664533). Sequencing reads were mapped to the reference sequence using SOAPaligner/soap2 (Li et al., 2009). The gene expression level was measured by the number of uniquely mapped reads per kilobase of exon region per million mappable reads (RPKM;  $\text{RPKM} = 106C/(\text{NL}/103)$ , where C is the number of reads uniquely mapped to the given gene, N is the number of reads uniquely mapped to all genes, and L is the total length of exons from the given gene). For genes with more than one alternative transcript, the longest transcript was selected to calculate the RPKM. All statistical analyses and visualization with expression data were conducted using R software (<http://www.r-project.org/>). After the expression level of each gene was calculated, differential expression analysis was conducted using edgeR (Robinson et al., 2010). The false discovery rate (FDR) was used to determine the *p*-value threshold for multiple tests, and for the analysis,  $\text{FDR} \leq 0.001$  and an absolute  $\log_2$  ratio value  $\geq 1$  were used to determine the significance of differences in gene expression. Gene Ontology (GO) enrichment analysis provides all GO terms that significantly enriched in the differentially expressed genes (DEGs) comparing to the genome background and filters the DEGs that correspond to biological functions. GO enrichment analysis was conducted using OmicShare tools.



## Reactive Oxygen Species Detection

After treatment with 17 $\beta$ -estradiol, cells were washed with PBS and stained with DHE or DCFH-DA for 10–90 min in the dark at 37°C or room temperature. Then the cells were observed under a fluorescence microscope (Olympus FV1000, Japan) and analyzed using Image-Pro Plus software after being washed with PBS. Fluorescence intensity was determined using flow cytometry (BD Biosciences, San Jose, CA, United States) after cells were trypsinized and collected.

## Detection of Apoptosis by Flow Cytometry

Apoptosis was detected with the aid of an AnnexinV-FITC/PI Kit (KeyGen, Nanjing, China). After trypsin digestion and resuspension in PBS,  $1 \times 10^5$  cells/group were mixed with Annexin V-FITC (5  $\mu$ L) and propidium iodide (5  $\mu$ L) in turn, and incubated in the dark for 15 min. Flow cytometry (BD Biosciences, San Jose, CA, United States) followed.

## Immunofluorescence Staining

Cells were fixed in 4% (w/v) paraformaldehyde for 20 min and washed with PBS three times for 5 min each time. After treatment with 0.2% (v/v) Triton X-100 for 15 min, the cells were incubated with goat serum at 37°C for 30 min and the medium discarded. The first antibody (1:100 dilution) was added, and the cells washed with PBS three times at 4°C for 5 min each time. Next, 1:100-diluted Cy3-labeled donkey anti-mouse secondary

antibody and FITC-labeled goat anti-rabbit secondary antibody were added, followed by incubation for 60 min at 37°C. After washing the slides with PBS, DAPI staining solution was added; the nuclei were stained at 37°C for 15 min and then washed twice with distilled water for 5 min each time. The fluorescence buffer did not contain glycerin. Six random fields were imaged using a fluorescence microscope and the fluorescence intensity analyzed with the aid of Image-Pro plus ver. 6.0 software.

## Western Blotting

Samples were lysed in RIPA buffer, homogenized, cracked, and centrifuged to obtain total protein extracts; protein concentrations were measured with the bicinchoninic acid assay. Proteins were subjected to SDS-PAGE and then transferred to PVDF membranes under a constant current (200 mA for 1 h). The membranes were placed into TBST sealing solution with 5% (w/v) skim milk powder for 1 h, the primary antibody added, followed by shaking at 4°C overnight. After washing, the second antibody was added and incubation proceeded at 37°C for 1 h. After washing, the light-emitting solution was added; and the membranes compressed, exposed, and fixed. A Labworks model 4.5 image acquisition and analysis system was used to determine the optical densities of protein bands. Actin served as the internal standard. Each experiment was repeated at least three times.

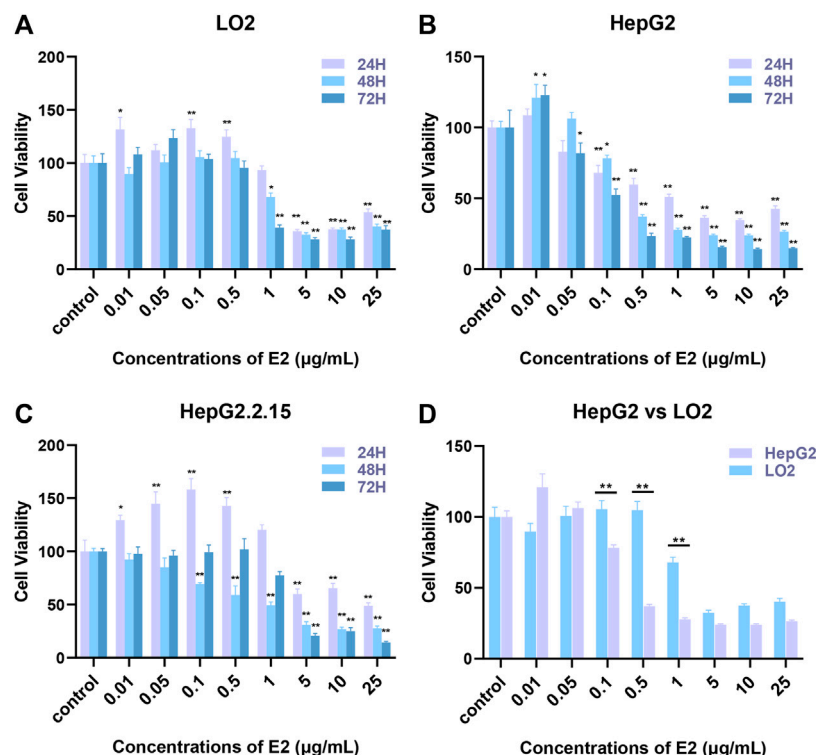


**FIGURE 1 |** The effects of 17 $\beta$ -estradiol on the proliferation of HepG2, HepG2.2.15, and LO2 cells. **(A–C)** The histograms show the effects of various levels of the hormone at different times, compared to control groups. \* $p < 0.05$ , \*\* $p < 0.01$ . **(D)** The histogram compares HepG2 and LO2 cell proliferation during 17 $\beta$ -estradiol treatment over 48 h, \*\* $p < 0.01$ .

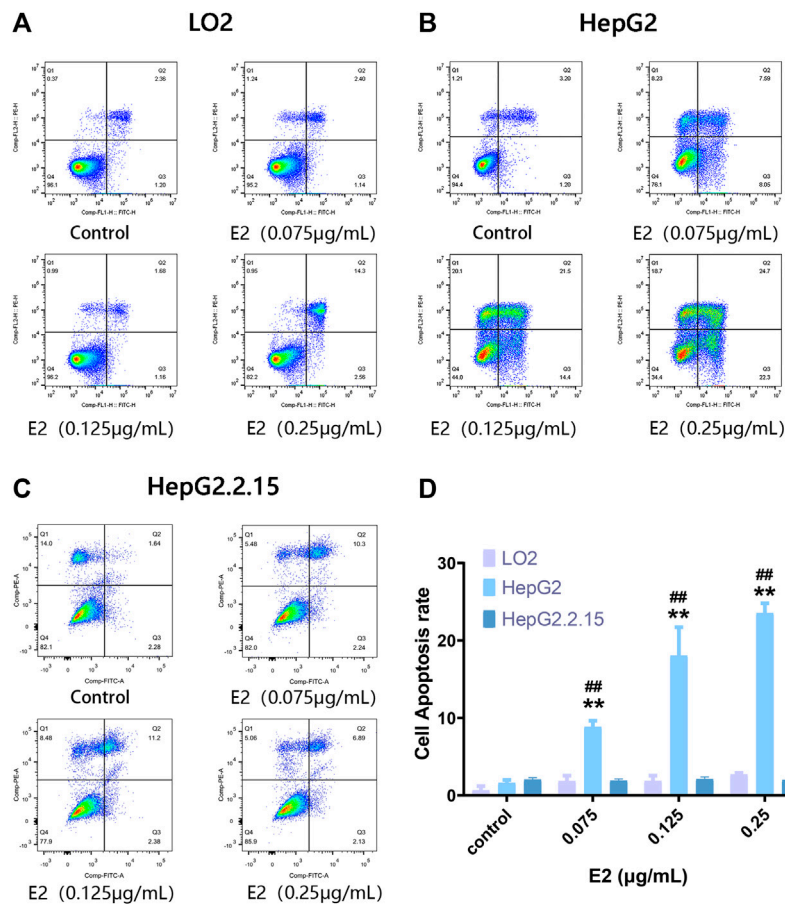


**FIGURE 2 |** The extent of apoptosis of HepG2, HepG2.2.15, and LO2 cells treated with 17 $\beta$ -estradiol. **(A–C)** Tetrad plots showing the effects on the three cell types after 48 h. Annexin V-FITC/PI double-staining was used to measure the proportions of apoptotic cells. **(D)** The histogram shows the apoptotic proportions of HepG2 and LO2 cells. All experiments were performed in triplicate. \*\* $p < 0.01$  compared to the control group, <sup>##</sup> $p < 0.01$  compared to LO2 cells at the same dose.

## Statistical Analysis

SPSS ver. 20.0 software was used to analyze data and GraphPad Prism ver. 6.0 software for statistical mapping. The ANOVA test was employed to analyze data and the chi-squared test for comparisons. A  $p$ -value  $< 0.05$  was taken to indicate statistical significance.

## RESULTS

### Effects of 17 $\beta$ -Estradiol on Human Hepatocyte Proliferation

HepG2, HepG2.2.15, and LO2 cells were treated with 17 $\beta$ -estradiol (0.01  $\mu$ g/ml to 25  $\mu$ g/ml) for 24, 48, and 72 h (Figure 1A). 17 $\beta$ -estradiol at 0.01–0.5  $\mu$ g/ml had no effect on LO2 cell proliferation but significantly inhibited proliferation at 5–25  $\mu$ g/ml ( $p < 0.01$ ). Figure 1B shows that 17 $\beta$ -estradiol had no effect on HepG2 proliferation at 0.01  $\mu$ g/ml but significantly inhibited proliferation at 0.1–25  $\mu$ g/ml at 24, 48, and 72 h (Figure 1B,  $p < 0.01$ ). The IC<sub>50</sub> values were 0.7968, 0.3446, and 0.1256  $\mu$ g/ml, respectively, at these times. For HepG2.2.15

cells, 17 $\beta$ -estradiol at 0.01–1  $\mu$ g/ml did not inhibit proliferation to 24 or 72 h, but significantly inhibited proliferation at 1–25  $\mu$ g/ml. However, at 48 h, 17 $\beta$ -estradiol at levels over 0.1  $\mu$ g/ml significantly inhibited proliferation (Figure 1C,  $p < 0.01$ ). To explore whether the inhibitory effect of 17 $\beta$ -estradiol was tumor-specific, we compared the inhibitory effects of 17 $\beta$ -estradiol on HepG2 and LO2 cells at 48 h. The results (Figure 1D) showed that the inhibitory effect of 17 $\beta$ -estradiol on HepG2 cells was significantly higher than that on LO2 cells at relatively low concentrations (0.01–1  $\mu$ g/ml). 17 $\beta$ -estradiol thus strongly inhibited hepatoma cell proliferation in a tumor-specific manner.

### 17 $\beta$ -Estradiol Promotes Apoptosis of HepG2 Cells

To explore a possible specific apoptotic effect of 17 $\beta$ -estradiol on HepG2 cells, we used the Annexin V-FITC/PI double-staining method to evaluate apoptosis (via flow cytometry) after treatment of cells with 7 $\beta$ -estradiol for 48 h. Compared to the control groups, 17 $\beta$ -estradiol did not induce apoptosis of LO2 or HepG2.2.15 cells (Figures 2A,C). 17 $\beta$ -estradiol

dose-dependently induced significant apoptosis of HepG2 cells by 48 h (**Figure 2B**); the apoptotic cell percentages are compared in **Figure 2D**. The results of Annexin V-FITC/PI double-staining were consistent with these results; 17 $\beta$ -estradiol specifically inhibited hepatoma cell proliferation and triggered apoptosis.

## 17 $\beta$ -Estradiol Increases Oxidative Stress in HepG2 Cells

We used the DCFH-DA and DHE fluorescent probes to explore whether 17 $\beta$ -estradiol induced oxidative stress in

hepatoma cells. After treatment with 17 $\beta$ -estradiol for 48 h, the probes were used for *in vitro* staining; fluorescence intensity detected by flow cytometry reflected the levels of intracellular ROS (**Figures 3A–C**). As shown in **Figures 3D,E**, compared to control LO2 cells, the ROS level in HepG2 cells was significantly increased by treatment with 17 $\beta$ -estradiol for 48 h ( $p < 0.01$ ). Under the fluorescence microscope, HepG2 cells (compared to controls) exhibited obvious green or red fluorescence (**Figure 4**). This further confirmed that 17 $\beta$ -estradiol increased ROS levels in HepG2 cells.

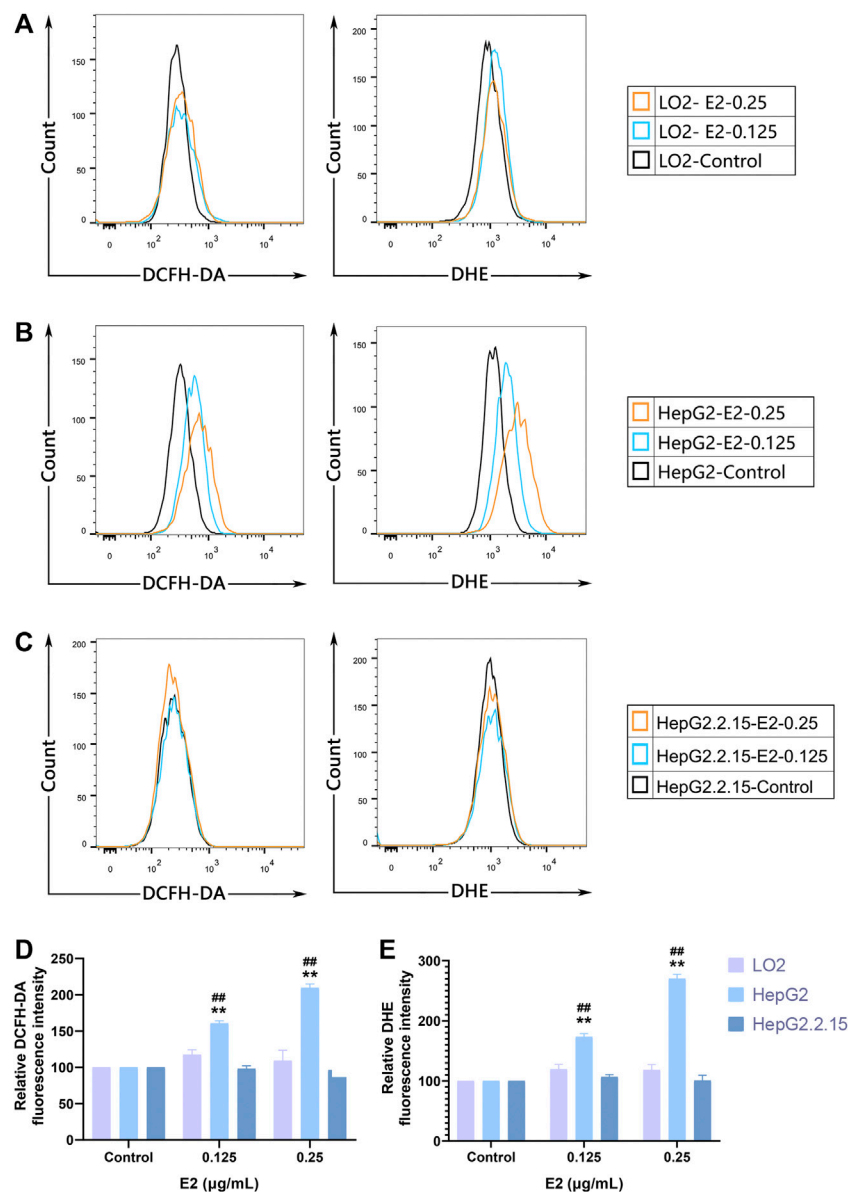


**FIGURE 3 |** ROS accumulation in cells as assessed by flow cytometry. **(A–C)** Fluorescent ROS peaks of HepG2, HepG2.2.15, and LO2 cells, respectively, induced by 17 $\beta$ -estradiol. After treatment with 17 $\beta$ -estradiol for 48 h, cells were stained using DCFH-DA and DHE fluorescent probes and examined by flow cytometry. **(D,E)** The histograms show the differences in the ROS levels of HepG2 and LO2 cells. All experiments were performed in triplicate, \*\* $p < 0.01$  compared to the control group, ## $p < 0.01$  compared to LO2 cells at the same dose.

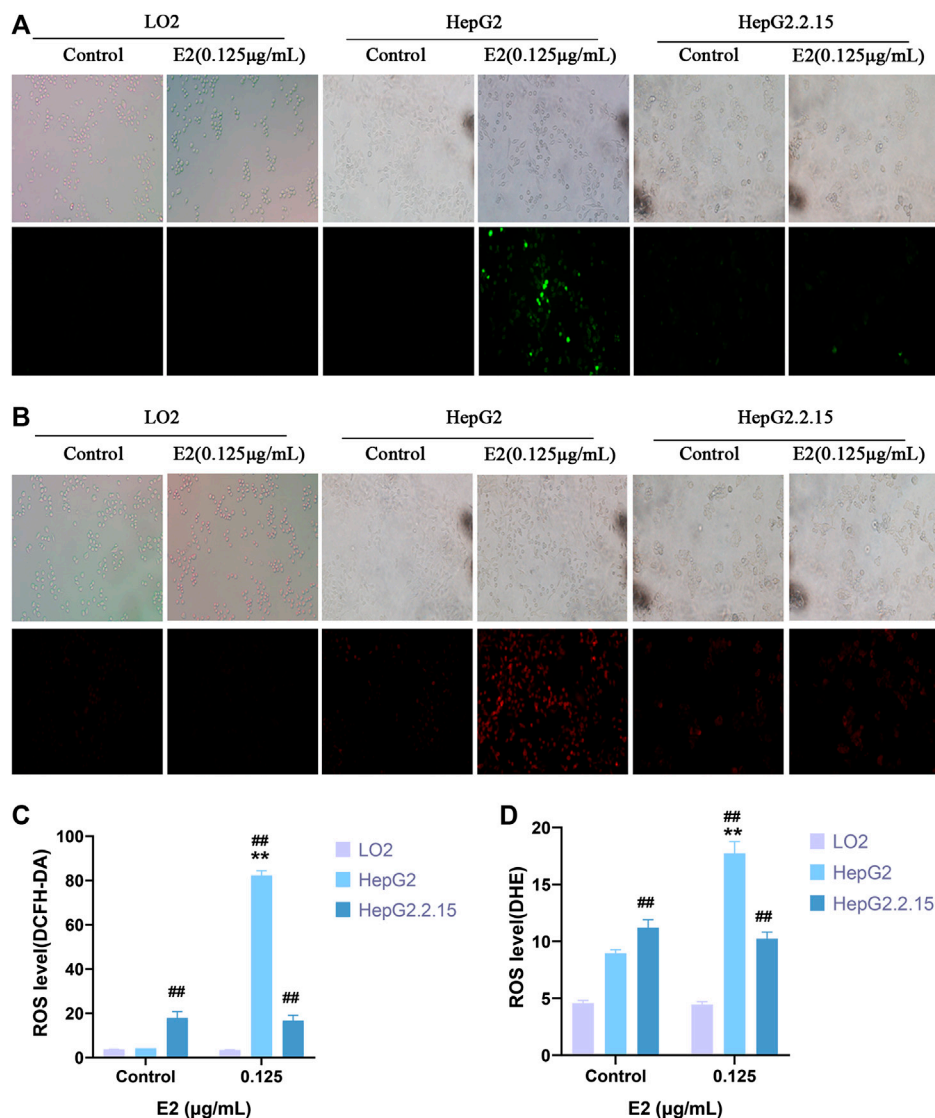


**FIGURE 4 |** ROS levels in cells as evaluated by immunofluorescence staining. (A,C) DCFH-DA. (B,D) DHE. Fluorescence microscopy was used to observe and record fluorescence levels.  $^{**}p < 0.01$  compared to the control group,  $^{##}p < 0.01$  compared to LO2 cells at the same dose.

## Changes in ER $\alpha$ /Akt/Foxo3a Signaling Induced by 17 $\beta$ -Estradiol

ER $\alpha$  and *p*-Foxo3a levels were evaluated by immunofluorescence staining. As shown in **Figures 5A,B**, after treatment with 17 $\beta$ -estradiol for 48 h, ER $\alpha$  was downregulated in HepG2 cells, but the level of phosphorylated Foxo3a increased and the protein was localized around the nucleus (**Figure 5B**). The phosphorylated protein could not enter the nucleus to trigger the expression of Mn-SOD and catalase. ER $\alpha$  and phosphorylated Foxo3a levels in LO2 and HepG2.2.15 cells were not affected by 17 $\beta$ -estradiol treatment, and the Foxo3a protein was not significantly localized around the nucleus.

Western blotting showed that the levels of ER $\alpha$ -66 and ER $\alpha$ -36 in HepG2 cells were significantly reduced after 24 h of 17 $\beta$ -estradiol treatment (both  $p < 0.05$ ); such treatment notably increased the levels

of phosphorylated AKT and Foxo3a (both  $p < 0.05$ ). The levels of ER $\alpha$ -66 and ER $\alpha$ -36 in LO2 and HepG2.2.15 cells were not affected after 24 h of 17 $\beta$ -estradiol treatment. ER $\alpha$ -46 levels in the three liver cell lines were not affected after 24 h of 17 $\beta$ -estradiol treatment. The *p*-Akt level did not change in the LO2 cells and HepG2.2.15 cells, and *p*-Foxo3a expression was not affected in LO2 and HepG2.2.15 cells after 24 h of 17 $\beta$ -estradiol treatment (**Figure 6**).

## Changes in the Levels of Enzymes Related to Oxidative Stress Induced by 17 $\beta$ -Estradiol

Transcriptome sequencing was performed to an average depth of 48 million reads per sample using 150-base, paired-end reads. Quality



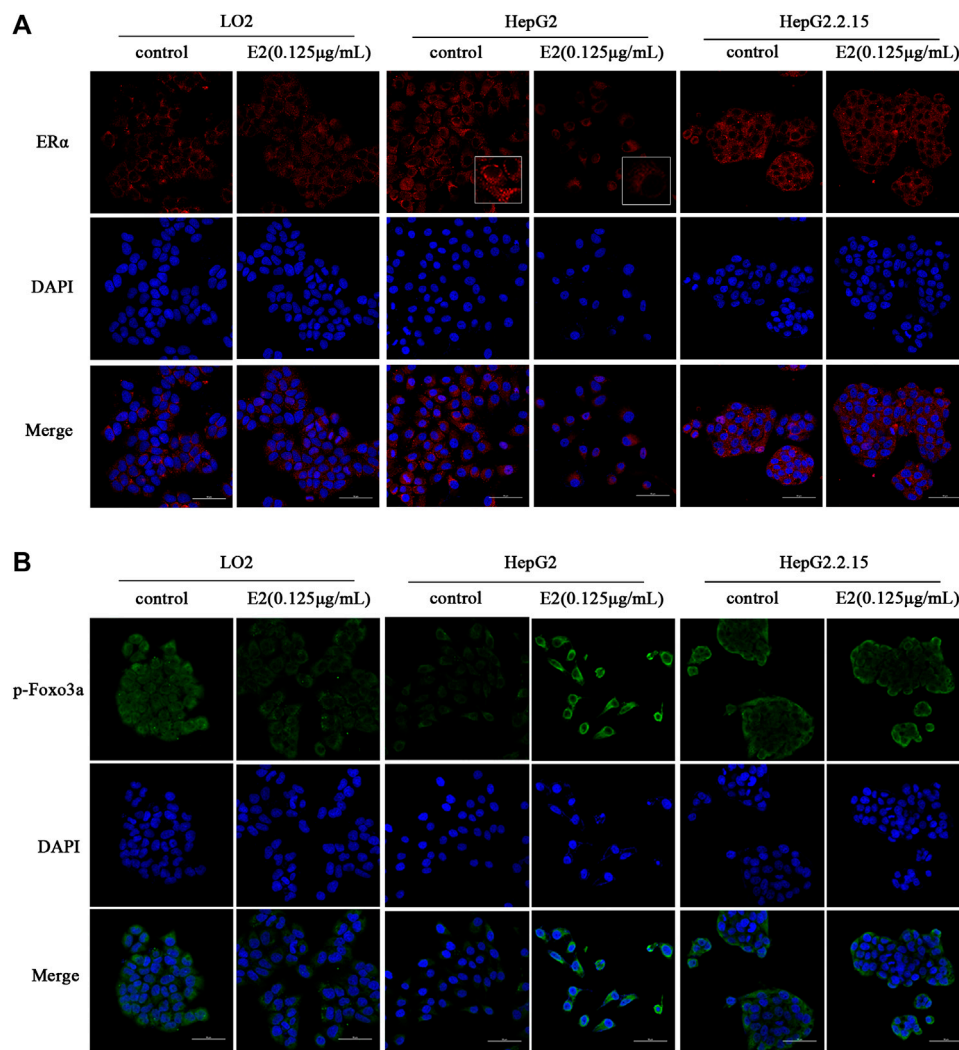


**FIGURE 5 |** The effects of 17 $\beta$ -estradiol (0.125  $\mu$ g/ml for 48 h) on ER $\alpha$  (A) and p-Foxo3a (B) expression and localization. The effects on HepG2, HepG2.2.15, and LO2 cells, respectively, as revealed by fluorescence microscopy.

control analysis indicated that the Phred nucleotide quality score was  $>30$  (indicating 95% accuracy of the base call) across the length of the reads. The number of trimmed reads ranged from  $3.8$  to  $6.1 \times 10^7$  with an average of 84% of reads mapping to the *Homo sapiens* genome. A total of 17,860 known mRNAs in cells were detected quantitatively. And 3,682 differentially expressed mRNAs were obtained.

Then, we performed an analysis on the GO terms of DEGs in three cell lines with E2 treatment. The DEGs in HepG2-E2 groups were mainly concentrated in the following biological processes: “apoptotic process”, “protein phosphorylation”, “peroxisome”, “superoxide metabolic process”, “autophagy”, and “protein ubiquitination”. Besides, DEGs in the “peroxisome” and “superoxide metabolic process” were significantly downregulated. There is no particular functional class of genes overrepresented in DEGs in LO2-E2 group and HepG2.2.15-E2 group (Figure 7A).

To verify that 17 $\beta$ -estradiol increased Foxo3a phosphorylation in HepG2 cells, rendering the protein unable to enter the nucleus

to initiate transcription of Mn-SOD and catalase, we analyzed the expression levels of enzymes associated with oxidative stress. The heatmap showed that Mn-SOD, Cu-SOD, Fe-SOD, and catalase were downregulated in HepG2 cells after 17 $\beta$ -estradiol treatment (Figure 7B). To confirm these results, we employed RT-qPCR to analyze the mRNA expression levels of Mn-SOD and catalase. As shown in Figures 7C,D, after addition of 17 $\beta$ -estradiol, the Mn-SOD (SOD1) level in HepG2 cells became significantly higher than that in control cells. However, the levels of mRNAs encoding Mn-SOD and catalase in LO2 cells did not change and, indeed, decreased slightly in HepG2.2.15 cells.

## DISCUSSION

Liver cancer is common and is associated with a high mortality rate. Several molecular-targeting drugs have been used as treatments

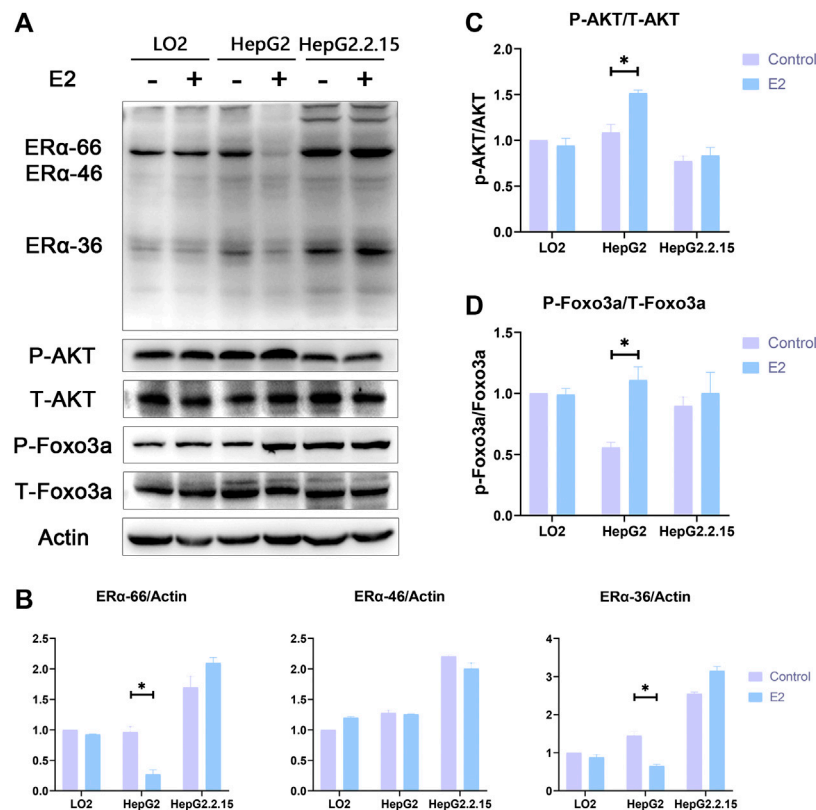


**FIGURE 6 | (A)** The effects of 17 $\beta$ -estradiol on the expression levels of ER $\alpha$ , *p*-Akt, *p*-Foxo3a, ER $\alpha$ -36, t-Akt, and t-Foxo3a in HepG2, HepG2.2.15, and LO2 cells treated with 17 $\beta$ -estradiol (0.125  $\mu$ g/ml) for 48 h, as revealed by Western blotting. **(B–D)** The effects of 17 $\beta$ -estradiol on ER $\alpha$ -36, ER $\alpha$ -46, ER $\alpha$ -66, *p*-Akt/t-Akt, and *p*-Foxo3a/t-Foxo3a levels, respectively. \* $p < 0.05$  compared to the control groups.

(Dabney et al., 2019; Anwanwan et al., 2020); sorafenib was the first such oral drug to be approved. However, sorafenib exhibits several side-effects, and is associated with high-level drug-resistance and poor patient tolerance. It is essential to discover targeted drugs that are more efficacious, have fewer side-effects, and are cheaper (Dutta and Mahato, 2017). The aims of this study were to observe differences in the apoptosis-promoting effects of 17 $\beta$ -estradiol in three liver cell lines and to determine the mechanism by which 17 $\beta$ -estradiol promotes HepG2 apoptosis, to aid the development of hepatoma drugs targeting this pathway. 17 $\beta$ -estradiol expression affects breast cancer development (Sreekumar et al., 2020); the effects of 17 $\beta$ -estradiol on liver cancer and other tumors is less well understood. We found that 17 $\beta$ -estradiol (at different concentrations) promoted apoptosis of HepG2 cells, but not LO2 or HepG2.2.15 cells. To the best of our knowledge, this is the first such report. Because the concentration of the 17 $\beta$ -estradiol drug was high, we will consider administering it via local interventions according to current interventional treatments for liver cancer in future studies.

We evaluated the mechanism underlying the effect of 17 $\beta$ -estradiol on apoptosis in HepG2 cells and found that 17 $\beta$ -estradiol increases the ROS levels in HepG2 cells through flow cytometry analysis and immunofluorescence staining. Oxidative stress can cause apoptosis (Wang et al., 2015). 17 $\beta$ -estradiol had

no obvious effects on LO2 or HepG2.2.15 cells. To the best of our knowledge, this is the first report on oxidative stress induced by 17 $\beta$ -estradiol in three liver cell lines.

We then explored how 17 $\beta$ -estradiol induced oxidative stress. There are two estrogen signal transduction pathways, the classical pathway mediated by the estrogen nuclear receptor (*ner*, including ER $\alpha$ -66 and ER $\beta$ ) and the rapid pathway mediated by the estrogen membrane receptor (GRER, EGFR, ER $\alpha$ -36). The former is a slow-response pathway that functions via genomic effects; the latter is a fast-reaction pathway that operates by changing protein conformations, and is also termed the stress conduction pathway (Zhao et al., 2019). ER $\alpha$ -36 rapidly activates non-genomic signaling pathways when it binds to estrogen-related receptors (ERRS) including those of the mitogen-activated protein kinase (MAPK)/extracellular signal-regulated kinase (ERK) pathways, and the PI3K/Akt pathway that regulates cell proliferation, differentiation, apoptosis, invasion, and migration (Liu et al., 2015). In this study, we found that 17 $\beta$ -estradiol specifically decreased the levels of ER $\alpha$ -36 and ER $\alpha$ -66 in HepG2 cells. Combined with the results from a previous study (Liu et al., 2015), these data show that the reduction in ER $\alpha$ -36 triggers an increase in *p*-Akt levels in HepG2 cells.

Foxo3a is an important downstream signal molecule of the PI3K/Akt pathway; Foxo3a activity is strongly linked to the

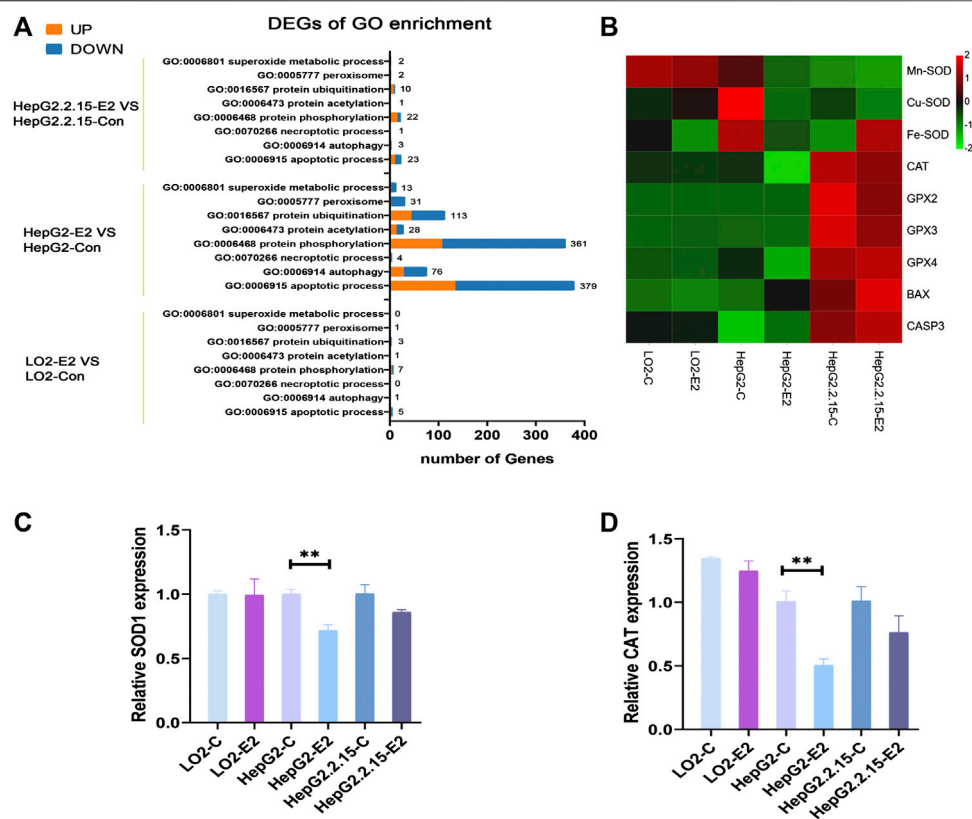


**FIGURE 7 |** 17 $\beta$ -estradiol decreased the expression levels of SODs and catalase in HepG2 cells. **(A)** Enriched Gene Ontology (GO) biological process **(B)** A heatmap of the enzyme expression levels in the three cell lines. qRT-PCR was used to measure the expression levels of mRNAs encoding SOD1 **(C)** and catalase **(D)** in HepG2 cells. \*\* $p < 0.01$  compared to the control group.

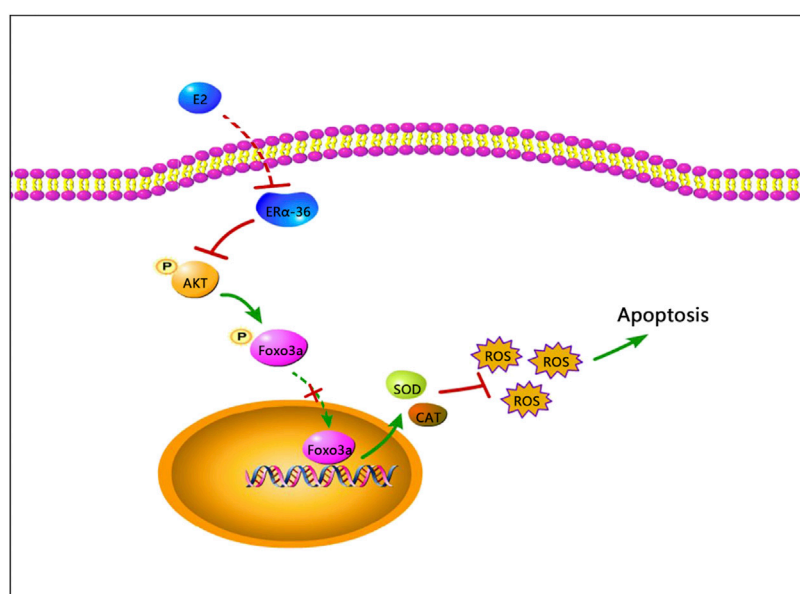


**FIGURE 8 |** A schematic of a possible mechanism whereby apoptosis may be induced by 17 $\beta$ -estradiol in HepG2 cells.

intracellular oxidative stress response. Activated Foxo3a reduces this response by binding to the promoters of genes encoding manganese superoxide dismutase (Mn-SOD) and catalase (Liu et al., 2018; Link, 2019). Foxo3a activity is closely related to its subcellular localization. On stimulation by growth and other factors, Akt directly phosphorylates Foxo3a, which then complexes with the 14-3-3 nuclear efflux protein to transfer from the nucleus to the cytoplasm, resulting in inhibition of transcriptional activity. Inactivation of Foxo3a transcription is common in many tumors, including those of liver, breast, and prostate cancer (Barthel et al., 2005; Fukunaga et al., 2005; Zhang et al., 2017; Link, 2019).

We found that 17 $\beta$ -estradiol downregulated ER $\alpha$  expression in HepG2 cells and increased phosphorylation of Akt and Foxo3a, preventing nuclear entry by Foxo3a and thus the synthesis of Mn-SOD and catalase, triggering oxidative stress and ultimately apoptosis (Figure 8). To the best of our knowledge, this is the first study to investigate the role of Foxo3a phosphorylation induced by 17 $\beta$ -estradiol in three liver cell lines.

However, 17 $\beta$ -estradiol had no effect on the expression levels of ER $\alpha$ , phosphorylated Akt, or Foxo3a in LO2 or HepG2.2.15 cells; the mechanism of action on HepG2 cells thus remains unclear. 17 $\beta$ -estradiol had no effects on normal cells within a certain concentration range, but promoted apoptosis of HepG2 cells; this may be therapeutically valuable. However, 17 $\beta$ -estradiol therapy alone may not be ideal for liver cancer patients infected with the hepatitis B virus. The mechanism of action of 17 $\beta$ -estradiol should be explored further; effective treatment may also require genetic modification.

We investigated the apoptotic effects of 17 $\beta$ -estradiol on three different cell types and elucidated the mechanism in play. Our study provides a new theoretical basis for biotherapy of liver cancer.

## REFERENCES

- Anwanwan, D., Singh, S. K., Singh, S., Saikam, V., and Singh, R. (2020). Challenges in liver cancer and possible treatment approaches. *Biochim. Biophys. Acta Rev. Canc* 1873 (1), 188314. doi:10.1016/j.bbcan.2019.188314
- Barthel, A., Schmoll, D., and Unterman, T. G. (2005). FoxO proteins in insulin action and metabolism. *Trends Endocrinol. Metab.* 16 (4), 183–189. doi:10.1016/j.tem.2005.03.010
- Bruix, J., da Fonseca, L. G., and Reig, M. (2019). Insights into the success and failure of systemic therapy for hepatocellular carcinoma. *Nat. Rev. Gastroenterol. Hepatol.* 16 (10), 617–630. doi:10.1038/s41575-019-0179-x
- Clegg, D., Hevener, A. L., Moreau, K. L., Morselli, E., Criollo, A., Van Pelt, R. E., et al. (2017). Sex hormones and cardiometabolic Health: role of estrogen and estrogen receptors. *Endocrinology* 158 (5), 1095–1105. doi:10.1210/en.2016-1677
- Dabney, R. S., Khalife, M., Shahid, K., and Phan, A. T. (2019). Molecular pathways and targeted therapy in cholangiocarcinoma. *Clin. Adv. Hematol. Oncol.* 17 (11), 630–637.
- Dutta, R., and Mahato, R. I. (2017). Recent advances in hepatocellular carcinoma therapy. *Pharmacol. Ther.* 173, 106–117. doi:10.1016/j.pharmthera.2017.02.010
- Fukunaga, K., Ishigami, T., and Kawano, T. (2005). Transcriptional regulation of neuronal genes and its effect on neural functions: expression and function of forkhead transcription factors in neurons. *J. Pharmacol. Sci.* 98 (3), 205–211. doi:10.1254/jphs.fmj05001x3
- Guerra, D. D., Bok, R., Breen, K., Vyas, V., Jiang, H., MacLean, K. N., et al. (2020). Estrogen regulates local cysteine metabolism in mouse myometrium. *Reprod. Sci.* 28 (1), 79–90. doi:10.1007/s43032-020-00284-6

## DATA AVAILABILITY STATEMENT

Illumina sequencing reads were uploaded to the SRA under accession number PRJNA664533. The rest of the data that support the conclusions of this study are available from the corresponding author upon request.

## AUTHOR CONTRIBUTIONS

XC, XY, and LX conceived and designed the study. YG and XC conducted the experiments. HL, QL, YZ, ZL, ZC, MY, and LZ participated in completing the experiments. HL and LX analyzed the data. XC wrote the manuscript. XY and LX revised the manuscript. All authors have read and approved the final version of this manuscript for publication.

## FUNDING

This study was supported by the Guangzhou Health Care Co-innovation Major Plan Fund (grant no. 201803040014) and the Innovation and Entrepreneurship Training Program of Guangdong Pharmaceutical University (grant no. 202010573014).

## ACKNOWLEDGMENTS

We thank the Guangzhou Genedenovo Biotechnology Co. Ltd. for assisting with sequencing and bioinformatics analysis.

- Jehle, J., Tiyerili, V., Adler, S., Groll, K., Nickenig, G., and Becher, U. M. (2020). Atheroprotective effects of 17 $\beta$ -oestradiol are mediated by peroxisome proliferator-activated receptor  $\gamma$  in human coronary artery smooth muscle cells. *Arch. Med. Sci. Atheroscler. Dis.* 5, e118–e126. doi:10.5114/amsad.2020.96103
- Kur, P., and Kolasa-Wolosiuk, A. (2020). Sex hormone-dependent physiology and diseases of liver. *J. Environ. Res. Public Health* 17, 2620. doi:10.3390/ijerph17082620
- Li, F., Wang, Z., Hu, F., and Su, L. (2020). Cell culture models and animal models for HBV study. *Adv. Exp. Med. Biol.* 1179, 109–135. doi:10.1007/978-981-13-9151-4\_5
- Li, R., Yu, C., Li, Y., Lam, T. W., Yiu, S. M., Kristiansen, K., et al. (2009). SOAP2: an improved ultrafast tool for short read alignment. *Bioinformatics* 25 (15), 1966–1967. doi:10.1093/bioinformatics/btp336
- Link, W. (2019). Introduction to FOXO biology. *Methods Mol. Biol.* 1890, 1–9. doi:10.1007/978-1-4939-8900-3\_1
- Liu, J., Xu, Z., Ma, X., Huang, B., and Pan, X. (2015). Role of ER- $\alpha$ 36 in breast cancer by typical xenoestrogens. *Tumour Biol.* 36 (10), 7355–7364. doi:10.1007/s13277-015-4006-x
- Liu, Y., Ao, X., Ding, W., Ponnusamy, M., Wu, W., Hao, X., et al. (2018). Critical role of FOXO3a in carcinogenesis. *Mol. Cancer* 17 (1), 104. doi:10.1186/s12943-018-0856-3
- Liu, Z., and Suo, C. (2020). Global incidence trends in primary liver cancer by age at diagnosis, sex, region and etiology, 1990–2017. *Cancer* 126 (10), 2267–2278. doi:10.1002/cncr.32789
- Mak, L. Y., Cruz-Ramón, V., Chinchilla-López, P., Torres, H. A., LoConte, N. K., Rice, J. P., et al. (2018). Global epidemiology, prevention, and management of hepatocellular carcinoma. *Am. Soc. Clin. Oncol. Educ. Book* 38, 262–279. doi:10.1200/edbk\_200939



- Moawad, A. W., Szklaruk, J., Lall, C., Blair, K. J., Kaseb, A. O., Kamath, A., et al. (2020). Angiogenesis in hepatocellular carcinoma; pathophysiology, targeted therapy, and role of imaging. *J. Hepatocell. Carcinoma* 7, 77–89. doi:10.2147/jhc.s224471
- Nayagam, S., Chan, P., Zhao, K., Sicuri, E., Wang, X., Jia, J., et al. (2020). Investment case for a comprehensive package of interventions against hepatitis B in China: applied modeling to help national strategy planning. *Clin. Infect. Dis.* [Epub ahead of print]. doi:10.1093/cid/ciaa134
- Pelekanou, V., Kampa, M., Kiagiadaki, F., Deli, A., Theodoropoulos, P., Agrogiannis, G., et al. (2016). Estrogen anti-inflammatory activity on human monocytes is mediated through cross-talk between estrogen receptor ER $\alpha$ 36 and GPR30/GPER1. *J. Leukoc. Biol.* 99 (2), 333–347. doi:10.1189/jlb.3A0914-430RR
- Robinson, M. D., McCarthy, D. J., and Smyth, G. K. (2010). edgeR: a Bioconductor package for differential expression analysis of digital gene expression data. *Bioinformatics* 26 (1), 139–140. doi:10.1093/bioinformatics/btp616
- Rossetto, A., and De Re, V. (2019). Carcinogenesis and Metastasis in Liver: Cell Physiological Basis. *Cancers (Basel)* 11 (11), 1731. doi:10.3390/cancers11111731
- Satirapod, C., Wang, N., MacDonald, J. A., Sun, M., Woods, D. C., and Tilly, J. L. (2020). Estrogen regulation of germline stem cell differentiation as a mechanism contributing to female reproductive aging. *Aging (Albany NY)* 12 (8), 7313–7333. doi:10.18632/aging.103080
- Shen, M., Cao, J., and Shi, H. (2018). Effects of estrogen and estrogen receptors on transcriptomes of HepG2 cells: a preliminary study using RNA sequencing. *Int. J. Endocrinol. Metab.* 2018, 5789127. doi:10.1155/2018/5789127
- Sreekumar, S., Levine, K. M., Sikora, M. J., Chen, J., Tasdemir, N., Carter, D., et al. (2020). Differential regulation and targeting of estrogen receptor turnover in invasive lobular breast carcinoma. *Endocrinology* 161 (9), bqaa109. doi:10.1210/endo/bqaa109
- Wang, F., Reece, E. A., and Yang, P. (2015). Advances in revealing the molecular targets downstream of oxidative stress-induced proapoptotic kinase signaling in diabetic embryopathy. *Am. J. Obstet. Gynecol.* 213 (2), 125–134. doi:10.1016/j.ajog.2015.01.016
- Xia, J., Inagaki, Y., Song, P., Sawakami, T., Kokudo, N., Hasegawa, K., et al. (2016). Advance in studies on traditional Chinese medicines to treat infection with the hepatitis B virus and hepatitis C virus. *Biosci. Trends* 10 (5), 327–336. doi:10.5582/bst.2016.01110
- Zhang, X., Zhuang, T., Liang, Z., Li, L., Xue, M., Liu, J., et al. (2017). Breast cancer suppression by aplysin is associated with inhibition of PI3K/AKT/FOXO3a pathway. *Oncotarget* 8 (38), 63923–63934. doi:10.18632/oncotarget.19209
- Zhao, L., Zhou, S., and Gustafsson, J. (2019). Nuclear receptors: recent drug discovery for cancer therapies. *Endocr. Rev.* 40 (5), 1207–1249. doi:10.1210/er.2018-00222

**Conflict of Interest:** The authors declare that the research was conducted in the absence of any commercial or financial relationships that could be construed as a potential conflict of interest.

Copyright © 2021 Guo, Cai, Lu, Li, Zheng, Lin, Cheng, Yang, Zhang, Xiang and Yang. This is an open-access article distributed under the terms of the Creative Commons Attribution License (CC BY). The use, distribution or reproduction in other forums is permitted, provided the original author(s) and the copyright owner(s) are credited and that the original publication in this journal is cited, in accordance with accepted academic practice. No use, distribution or reproduction is permitted which does not comply with these terms.



# Combining the Fecal Immunochemical Test with a Logistic Regression Model for Screening Colorectal Neoplasia

Feiyuan Liu<sup>1†</sup>, Qiaoyun Long<sup>2,3†</sup>, Hui He<sup>4†</sup>, Shaowei Dong<sup>2,3</sup>, Li Zhao<sup>4</sup>, Chang Zou<sup>2,3\*</sup> and Weiqing Wu<sup>4\*</sup>

<sup>1</sup>Department of Scientific Research, The First Affiliated Hospital, Southern University of Science and Technology, Shenzhen People's Hospital, Shenzhen, China, <sup>2</sup>Department of Clinical Research Center, The First Affiliated Hospital, Southern University of Science and Technology, Shenzhen People's Hospital, Shenzhen, China, <sup>3</sup>Shenzhen Public Service Platform on Tumor Precision Medicine and Molecular Diagnosis, Shenzhen, China, <sup>4</sup>Department of Health Management, The First Affiliated Hospital, Southern University of Science and Technology, Shenzhen People's Hospital, Shenzhen, China

## OPEN ACCESS

### Edited by:

Dong-Hua Yang,  
St. John's University, United States

### Reviewed by:

Hsian-Rong Tseng,  
UCLA Department of Molecular and  
Medical Pharmacology, United States  
Xin Wang,  
City University of Hong Kong,  
Hong Kong

### \*Correspondence:

Chang Zou  
zou.chang@szhospital.com  
Weiqing Wu  
wweiqing007@szhospital.com

<sup>†</sup>These authors have contributed  
equally to this work

### Specialty section:

This article was submitted to  
Pharmacology of Anti-Cancer Drugs,  
a section of the journal  
Frontiers in Pharmacology

**Received:** 02 December 2020

**Accepted:** 19 January 2021

**Published:** 17 March 2021

### Citation:

Liu F, Long Q, He H, Dong S, Zhao L,  
Zou C and Wu W (2021) Combining  
the Fecal Immunochemical Test with a  
Logistic Regression Model for  
Screening Colorectal Neoplasia.  
Front. Pharmacol. 12:635481.  
doi: 10.3389/fphar.2021.635481

**Background:** The fecal immunochemical test (FIT) is a widely used strategy for colorectal cancer (CRC) screening with moderate sensitivity. To further increase the sensitivity of FIT in identifying colorectal neoplasia, in this study, we established a classifier model by combining FIT result and other demographic and clinical features.

**Methods:** A total of 4,477 participants were examined with FIT and those who tested positive (over 100 ng/ml) were followed up by a colonoscopy examination. Demographic and clinical information of participants including four domains (basic information, clinical history, diet habits and life styles) that consist of 15 features were retrieved from questionnaire surveys. A mean decrease accuracy (MDA) score was used to select features that are mostly related to CRC. Five different algorithms including logistic regression (LR), classification and regression tree (CART), support vector machine (SVM), artificial neural network (ANN) and random forest (RF) were used to generate a classifier model, through a 10X cross validation process. Area under curve (AUC) and normalized mean squared error (NMSE) were used in the evaluation of the performance of the model.

**Results:** The top six features that are mostly related to CRC include age, gender, history of intestinal adenoma or polyposis, smoking history, gastrointestinal discomfort symptom and fruit eating habit were selected. LR algorithm was used in the generation of the model. An AUC score of 0.92 and an NMSE score of 0.076 were obtained by the final classifier model in separating normal individuals from participants with colorectal neoplasia.

**Conclusion:** Our results provide a new “Funnel” strategy in colorectal neoplasia screening via adding a classifier model filtering step between FIT and colonoscopy examination. This strategy minimizes the need of colonoscopy examination while increases the sensitivity of FIT-based CRC screening.

**Keywords:** fecal immunochemical test, colorectal neoplasia screening, logistic regression model, funnel strategy, classifier model

## INTRODUCTION

Colorectal cancer (CRC) is the fourth most common cancer, and accounts for around 10% of the newly diagnosed cases of cancers (Siegel et al., 2020). In 2019, CRC caused approximately 900,000 deaths worldwide (Dekker et al., 2019). CRC screening is a process of detecting adenomatous polyps or early cancerous change that are highly treatable (Atkin et al., 2010; Schoen et al., 2012) and is currently one of the most realistic approaches that reduce CRC-related mortalities (Oort et al., 2010).

Three main types of CRC screening strategies have been suggested by various international guidelines, which are physical-based, blood-based and faecal-based methods. Among them, physical-based methods such as colonoscopy are currently the most sensitive tests in CRC screening. However, due to its invasiveness and complexity, colonoscopy may not be acceptable as a population-based screening test (Gupta et al., 2013). Blood-based screening methods or liquid biopsies are a type of non-invasive screening methods which detect biomarkers in a patient blood sample (Hauptman and Glavač, 2017). Currently some available and innovative (published but not yet commercially available) blood-based CRC screening strategies include carcinoembryonic antigen (CEA) (Locker et al., 2006), carbohydrate antigen 19-9 (CA 19-9) (Kim et al., 2017), circulating tumor cells (CTCs) (Baek et al., 2019), cell-free DNA (cfDNA) (Vymetalkova et al., 2018), microsatellite instability (MSI) (Zeinalian et al., 2018), aberrant DNA methylation (*SEPT9* gene methylation status) (Warren et al., 2011), mRNAs (*ANXA3*, *CLEC4D*, *LMNB1*, *PRRG4*, *TNFAIP6*, *VNN1* and *IL2RB*) from peripheral blood (Marshall et al., 2010), microRNAs (miR-601, miR-760, miR-15b, miR-19a, miR-19b, miR-29a, miR-335) (Wang et al., 2012; Ahmed et al., 2013; Giráldez et al., 2013; Kanaan et al., 2013) and long noncoding RNAs (lncRNAs CRNDE-h, CCAT, HOTAIR) (Graham et al., 2011; Zhao et al., 2015). Faecal-based methods detect biomarkers in patients' stool samples including guaiac-based faecal occult blood test (gFOBT), fecal immunochemical test (FIT) and multitargeted stool DNA test (FIT-DNA). Of these, gFOBT uses chemical guaiac to detect blood in stool. Due to its high false positive and negative rate, it requires three home-based stool samples per test (Kościelniak-Merak et al., 2018); FIT-DNA detects altered DNA in stool sample, and is more expensive than the other two tests. FIT uses antibodies specific to hemoglobin, and has the ability to detect low level of bleeding in stool samples. In comparison with physical-based screening methods, FIT is a non-invasive test and can be done without dietary or medication restrictions; in comparison with blood-based screening methods, FIT is cheaper and faster in the report generation process while yielding fairly reliable results. Hence FIT is recommended as a population level screening strategy (Chiu et al., 2013).

FIT-based CRC screening has now been widely applied in many Asia and European countries (Chen et al., 2011; Stegeman et al., 2012). However, there are some limitations in this strategy, such as low sensitivity for identifying certain types of polyps and some false-positive cases. The reported FIT sensitivity ranged

from 25% to 100% and the specificity usually exceeded 90%, as summarized by Lee et al. (Lee et al., 2014). To increase the sensitivity of FIT-based screening, in this study, we established a funnel strategy via adding a model filtering step between FIT and colonoscopy examination. This filtering model was established by a logistic regression analysis using FIT results and six other features, and an AUC score of 0.92 was reached in discriminating colorectal neoplasia participants from normal ones.

## MATERIALS AND METHODS

### Data Collection

This study was conducted in the Early Cancer Screening Center (ECSC) of the Health Management Department in Shenzhen People's hospital, Guangdong, China. A total of 4,477 participants were recruited from customers who came for physical examination in the period from March 2019 to June 2020. No specific inclusion or exclusion criteria was applied. The demographic characteristics from all participants including age, sex, BMI (Body Mass Index), clinical history, diet habits and life styles were collected through a questionnaire survey.

### Fecal Immunochemical Test and Colonoscopy

A FIT testing was performed in all these 4,477 participants using a fully automated fecal occult blood analyzer (OC-SENSOR io, EIKEN Chemical Co., Ltd., Japan), and a value of 100 ng/ml was used as a cut-off based on the manufacturer's instructions (FIT positive: >100 ng/ml). For FIT positive participants, colonoscopy examination (CSE) was performed by gastroenterologists from the Department of Anorectal Surgery in Shenzhen People's Hospital. The following situations were considered as colorectal neoplasia (CSE Positive): colorectal polyps, adenoma and colorectal cancer. The rest including inflammation were considered as CSE Negative.

### Data Pre-Processing

The demographic and clinical characteristics of participants were divided into four domains that consist of 15 variables. The information of all 4,477 participants was listed in **Supplementary Table S1** and the summary information of 155 FIT positive participants who went through colonoscopy examination was listed in **Table 1**. A series of data conversion were performed to facilitate subsequent analysis. For "Age," a z-score was performed to avoid overfitting; for "BMI," value < 20 was defined as 0,  $20 \leq \text{value} \leq 25$  was defined as 1, and value > 25 was defined as 2; for "Gender," male was defined as 0 and female was defined as 1; for binary variables in clinical history category including tumor, family tumor, IAP (Intestinal adenoma or polyposis) and GDS (Gastrointestinal discomfort, including symptoms such as abdominal pain or discomfort, increased defecation frequency, black stool, blood/pus/mucus in the stool, constipation) and in life style category including smoking, drinking and pressure (here the pressure is defined

**TABLE 1 |** Features of FIT positive participants and their correlation with colorectal neoplasia.

Category			Total	CSE positive	CSE negative	p value
Basic information	Gender	Male	96	61	35	0.0026
		Female	59	22	37	
	Age	>55	48	34	14	0.0062
		≤55	107	49	58	
	BMI	20–25	88	45	43	0.6
Else		67	38	29		
Clinical history	Tumor	YES	2	0	2	0.42
		NO	153	83	70	
	Family tumor	YES	45	24	21	1
		NO	110	59	51	
	IAP	YES	17	16	1	0.00098
		NO	138	67	71	
	GDS	YES	56	25	31	0.13
NO		99	58	41		
Diet habits	Fruits	Rarely	44	20	24	0.27
		Regularly	111	63	48	
	Vegie	Rarely	6	2	4	0.55
		Regularly	149	84	68	
	Meat	Rarely	12	6	6	1
Regularly		143	77	66		
Life styles	Smoking	YES	54	37	17	0.01
		NO	101	46	55	
	Drinking	YES	37	19	18	0.91
		NO	118	64	54	
	Sports	Rarely	71	31	40	0.035
		Regularly	84	52	32	
	Pressure	YES	83	43	40	0.76
NO		72	40	32		

as living or working pressure, which is the subjective judgment of the participants regarding to their mental status including anxiety and depression), a “yes” was defined as 1 and a “no” was defined as 0; For diet habit category including fruits, vegie and meat and for life style category including sports, “< 3 times/week” was defined as 0 (rarely) and “≥ 3 times/week” was defined as 1 (regularly).

## Feature Selection

After data pre-processing, the number of participants in each category was summarized and listed in **Table 1**. A chi-square test was used to explore the correlation between each feature and CSE results, and a *p* value of 0.05 was used as the cutoff for statistical significance.

To filter features for model building, a random forest process was performed and a Mean Decrease Accuracy (MDA) score was used to evaluate the feature contribution value. In this step, a 10-fold cross validation process was used and 10 iterations were performed. The average MDA scores of all 15 features were ranked and listed (**Figure 1A**), and the frequencies of the appearances of top 10 important features were also ranked and listed (**Figure 1B**).

## Model Selection

Five classical algorithms were used in the model selection step, including LR (Logistic regression), CART (Classification and regression tree), SVM (Support vector machine), ANN (Artificial neural network) and RF (Random forest). In this

study, R function `glm()` was used to perform LR analysis with all parameters set as default except connection (set to “binomial”) (Dobson 1990); R function `rpart()` was used to perform CART analysis with all parameters set as default (Breiman et al., 1984); R function `svm()` was used to perform SVM analysis with the kernel parameter set as “linear” and scale parameter set as “FALSE” (Fan et al., 2005); R function `nnet()` was used to perform ANN analysis with the size parameter set as 1, maxit parameter set as 1,000 and entropy parameter set as “TRUE” (Ripley, 2008); R function `randomForest()` was used to perform RF analysis with the ntree parameter set as iterative manner and optimal 67 selected (Breiman 2001). All the parameters were set based on the manuals of each R function.

For the features ranked based on their MDA scores, different combinations (top N) of features were tested in all five algorithms and their AUC (Area Under Curve) values in all 10 iterations were calculated using R function `pROC()` and illustrated as violin plots (**Figure 1C**). Average AUC was used to select the best algorithm + best feature combinations (top N).

## Model Evaluation

Six features including “Age,” “IAP,” “Gender,” “Smoking,” “GDS” and “Diet Habit: Fruit” were used in the final model generation. AUC score and NMSE (Normalized mean squared error) value were used in the evaluation of model performance. R package `pROC` was used in the calculation of AUC. The NMSE value was calculated using formula:  $\text{mean}((\text{predicted value} - \text{observed value})^2) / \text{mean}((\text{mean}(\text{observed value}) - \text{observed value})^2)$ .



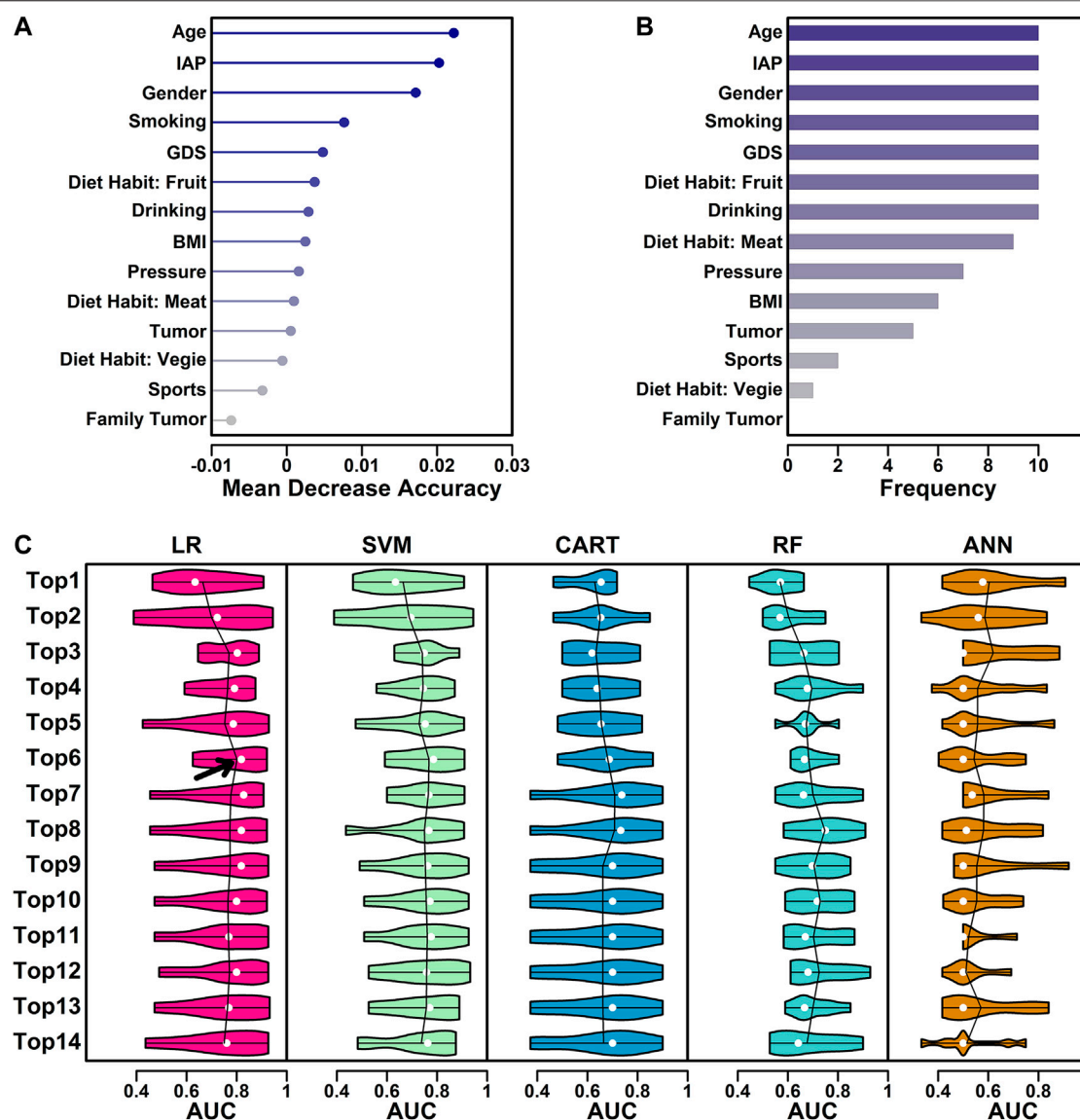


**FIGURE 1 |** Feature selection process. **(A)** MDA values of all 15 features. **(B)** The number of the appearances in top 10 ranked variables in every iteration. **(C)** Performance of five different algorithms using different combinations of features. The AUC values from 10 iterations were illustrated as violin plot, with mean value highlighted in lines and median value highlighted in white dots.

## Ethical Considerations

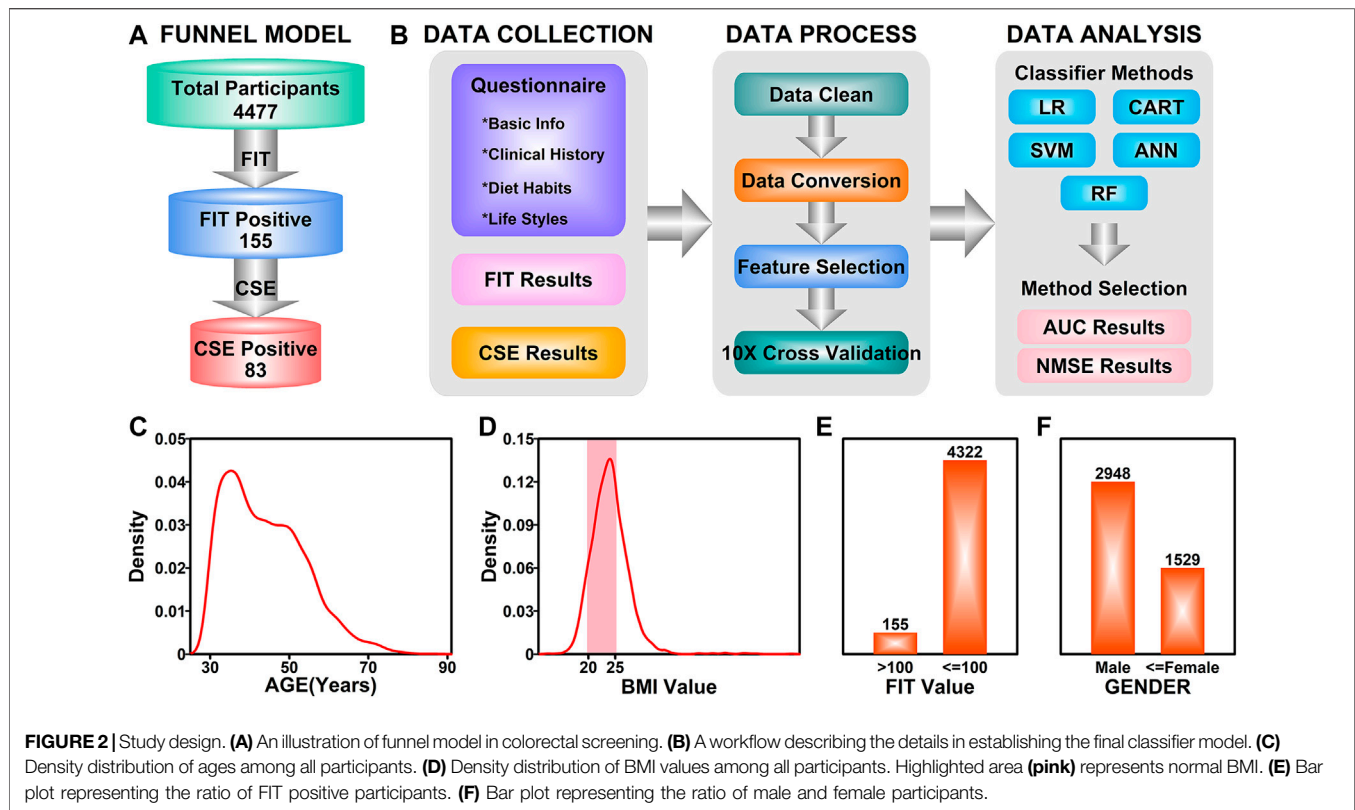
This study was approved by the Ethical Committee Board of the Shenzhen People's hospital. All the participants were provided with a cover letter containing information regarding the research purpose and methods. Written consents were obtained from all participants.

## RESULTS

### Study Design

The number of participants in each step were illustrated in **Figure 2A**. The aim of this study is to generate a classifier

model to evaluate the likelihood of colorectal neoplasia based on FIT results and a cohort of other features. The workflow of this study was illustrated in **Figure 2B**. For the 155 FIT positive participants, the CSE results together with the information from questionnaires were collected. After data cleaning and data conversion steps, all the features were evaluated and the top ranked features were selected and used in the following 10-fold cross validation process. Five analytical methods including LR, SVM, CART, ANN and RF were used in the data analysis step, and the AUC and NMSE scores were used in judging the performance of the classifier model.



## Characteristics of Participants

These 4,477 participants have the age ranging from 30 to 86 years (Figure 2A). The age distribution of the participants was illustrated in Figure 2C, with a peak in 35 years. The BMI value distribution of the participants was illustrated in Figure 2D, with a majority of values (56.7%, pink field) falling in the 20–25 ( $20 \leq \text{BMI} \leq 25$  is defined as normal) normal range. Among these 4,477 participants, 155 of them have a FIT score over 100 ng/ml (Positive), while the rest of the participants were FIT negative, as illustrated in Figure 2E; 2,948 of the participants were males (65.8%) and 1,529 of them were females (34.2%). After colonoscopy examination of the 155 FIT positive participants, 83 of them (53.5%) were diagnosed with colorectal neoplasia (CSE Positive).

## Features of Fecal Immunochemical Test Positive Participants

In this study, after data preprocess, only features with relatively high data integrity were selected, which yields 15 features, as listed in Supplementary Table S1. Information relating to these 15 features was further extracted from the raw data of 155 FIT positive participants, and the details of these features were illustrated in Figure 3. Among these 155 FIT positive participants, 83 of them were CSE positive (53.5%), and 72 were CSE negative (46.5%). These features were further divided into four categories including “Basic information,” “Clinical History,” “Diet Habits” and “Life Styles.”

Among all the 15 features, five of them showed a significant correlation with colorectal abnormal symptoms ( $P$  value  $< 0.05$ , as listed in Table 1), which are “Gender,” “Age,” “IAP,” “Smoking” and “Sports.” Regarding to “Gender,” among 96 FIT positive male participants, 61 of them were diagnosed as CSE positive (63.5%); among 59 FIT positive female participants, 22 of them were diagnosed as CSE positive (37.3%), indicating a higher incidence of colorectal neoplasia in FIT positive males ( $p$  value = 0.0026). Regarding to “Age,” 48 of FIT positive participants were over 55 years old, with 34 of them diagnosed as CSE positive (70.8%); 107 of FIT positive participants were less than 55 years old, with 49 of them diagnosed as CSE positive (45.8%), indicating a higher incidence of colorectal neoplasia in older FIT positive participants ( $p$  value = 0.0062). Regarding to the “IAP,” 17 of the FIT positive participants had a history of intestinal adenoma or polyps, in which 16 of them were diagnosed as CSE positive (94.1%); for the rest of the FIT positive participants with no history of intestinal adenoma or polyps, 67 of them were diagnosed as CSE positive (48.6%), indicating a higher incidence of colorectal neoplasia in FIT positive participants with a history of intestinal adenoma or polyps ( $p$  value = 0.00098). Regarding to “Smoking,” 54 of the FIT positive participants had a smoking history, in which 37 of them were diagnosed as CSE positive (68.5%); for the rest of FIT positive participants with no smoking habits, 45 of them were diagnosed as CSE positive (44.6%), indicating a higher incidence of colorectal neoplasia in smoking FIT positive participants ( $p$  value = 0.010). Regarding to “Sports,” 71 of the FIT positive participants rarely played sports (less than two times/week), in which 31 of them were diagnosed as CSE positive (43.7%); for the

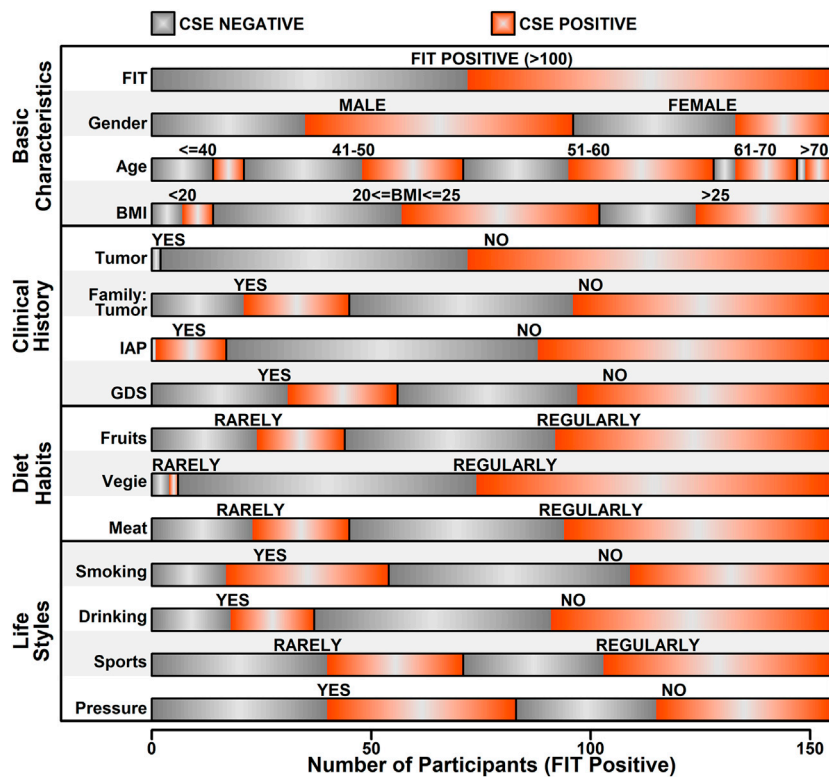


**FIGURE 3 |** Summary of the features of FIT positive participants.

rest of FIT positive participants who regularly played sports (more than two times/week), 52 of them were diagnosed as CSE positive (61.9%), indicating a higher incidence of colorectal neoplasia in FIT participants playing sports regularly ( $p$  value = 0.035).

## Feature Selection

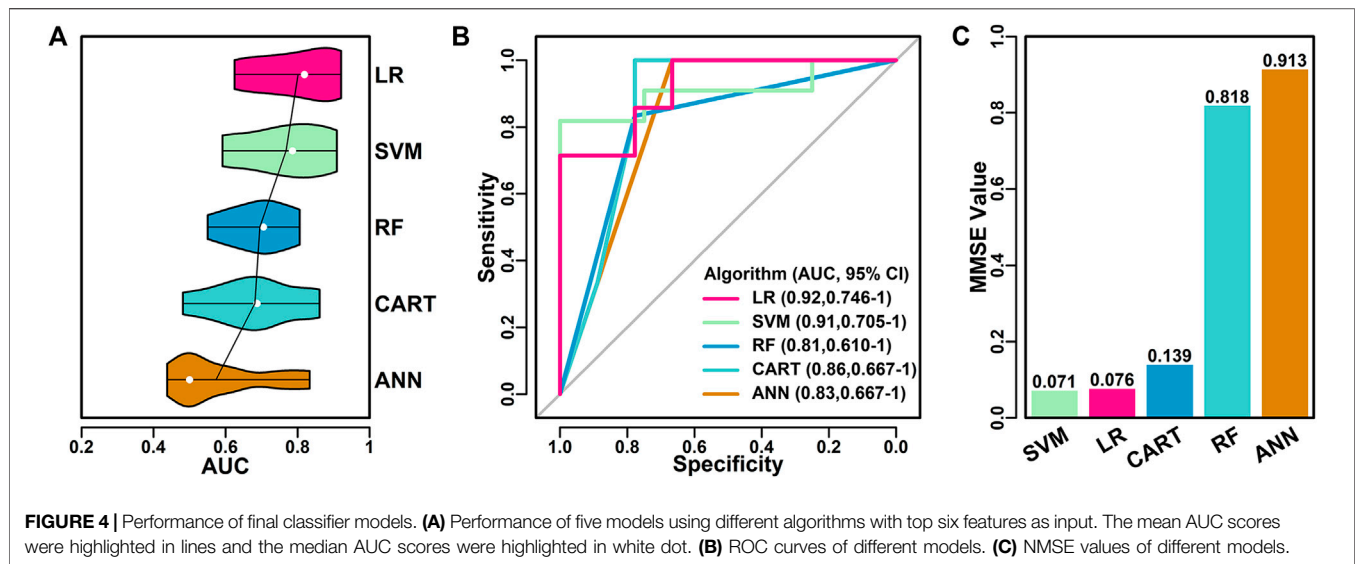
These 15 features were further screened based on the contributions to the final models. In this step, a random forest process was used in the screening, and a 10-fold cross-validation process was used to eliminate the difference caused by sample randomness. These 15 features were first ranked based on the average MDA scores from 10 iterations, and the results were listed in **Figure 1A**. These 15 features were further ranked by the number of the appearances in top 10 ranked variables in every iteration, and the results were listed in **Figure 1B**.

The feature selection process was further performed using five classical algorithms including logistic regression (LR), support-vector machine (SVM), classification and regression tree (CART), random forest (RF) and artificial neural network (ANN). LR utilizes the logistic function to estimate a binary dependent variable, which is, in this study, CSE positive or CSE negative (Tolles and Meurer, 2016); SVM uses a set of training examples to build an algorithm which assigns new examples to one of the two categories (positive/negative) (Cortes and Vapnik, 1995); CART utilizes a predictive model (decision tree) to generate a conclusion (tree leaves, positive/negative) based on the observations (tree

branches, training sets) (Barlin et al., 2013); RF is an ensemble method combining multiple learning algorithms such as classification and regression, to output the class of individual trees (positive/negative) based on a multitude of decision trees constructed during training (Breiman, 2001). ANN is based on an artificial neural network constructed by neurons (nodes) and connections (edges). During a training process, a probability-weighted association was generated between input (different characteristics) and result (CSE results) (Renganathan, 2019). These five machine learning methods are currently most widely used algorithms, and they were all included in this study. Their performance was summarized in **Figure 1**. The ranked features from **Figure 1A** was used as the input, and the AUC scores were used as the judgements. The performance was summarized and illustrated in **Figure 1C**. Among all the five algorithms and different combinations of features, the LR algorithm with top six features yielded the highest mean AUC value (highlighted with arrow), indicating a combination of these six features has the best separating ability in discriminating CSE positive participants from CSE negative ones, hence these six features, “Age,” “IAP,” “Gender,” “Smoking,” “GDS” and “Diet Habit: Fruit” were chosen in the final model generation.

## Model Performance

The top six features were further applied in five algorithms for model building, and the performance of these models were evaluated and compared with each other. The AUC score



distribution of each model was shown in **Figure 4A**. The highest, lowest, mean and median AUC values for each model were listed as follows:

LR (0.92, 0.63, 0.80, 0.82); SVM (0.91, 0.59, 0.77, 0.79); RF (0.81, 0.55, 0.69, 0.71); CART (0.86, 0.48, 0.68, 0.69); ANN (0.83, 0.44, 0.57, 0.50).

Among all five algorithms, LR model performed the best, with the highest AUC score of 0.92 in one of the 10 iterations. ROC curves of the best models using different algorithms were shown in **Figure 4B**. LR model has the highest AUC value (0.92), followed by SVM model (0.91), RF model (0.81), CART model (0.86) and ANN model (0.83).

The performance of the best models using different algorithms were also evaluated using the average NMSE value, as shown in **Figure 4C**. SVM and LR models have the lowest scores (0.071 and 0.076), followed by CART (0.139), RF (0.818) and ANN (0.913), which was in consistent with the results of AUC evaluations.

## DISCUSSION

FIT has been recommended as a non-invasive strategy in CRC screening, and the sensitivity varies between 25 and 100% in many reports, as summarized by Lee et al. (2014). To further increase the sensitivity of FIT in identifying colorectal neoplasia, we combined FIT results with six other demographic and clinical characteristics, and established a LR classifier model, which yields an AUC of 0.92 in distinguishing colorectal neoplasia participants from false positive ones.

In this study, 83 FIT positive participants were diagnosed with colorectal neoplasia, with a sensitivity of 53.5%. The cut off value for FIT positive was set at 100 ng/ml, as suggested by the FIT equipment manufacturer. 100 ng/ml was widely used as FIT positive judgment standard (Chen et al., 2011; Crotta et al., 2012), and different cut off values do not have too much effects on final results, as discussed by Wilschut et al. (2011), in which FIT values ranging from 50 to 200 ng/ml were used as

cutoffs, and the sensitivities varies a little around 60%, which is comparable to our sensitivity result. Multiple rounds of FITs might improve the screening results, as discussed in many studies (Crotta et al., 2012; Kapidzic et al., 2014; Jensen et al., 2016), however, in this study, due to the limitations of time and cost, only one round of FIT was performed to all participants. In the future, multiple rounds of FITs might help in generating a better and more accurate classifier model.

Six features were involved in establishing the final classifier model. Among them, Age, Gender, IAP and Smoking showed significant correlations with development of colorectal neoplasia ( $p$  value <0.05), as listed in **Table 1**. Regarding to age and sex, it has long been observed that these two factors are directly associated with the occurrence of colorectal cancer (Siegel et al., 2019; Siegel et al., 2020). Siegel et al. (2014) showed that the number of new CRC cases and deaths associated with CRC increases with age, and these numbers are higher in males in comparison with that in females, which is in consistent with our results. Regarding the IAP, the correlation between personal history of polyps or adenomas and colorectal cancer or neoplasia have also been reported. Stark et al. (2006) showed that colon polyp was a risk factor associated with CRC. Saini et al. (2006) showed that patients with a history of adenoma were more likely to have recurrent adenomas. As of smoking, there is consistent evidence of relationships between dose-responsive smoking and colorectal neoplasia Fagunwa et al. (2017) or CRC (Kozma et al., 2012; Akter et al., 2020), even in a passive smoking manner (Yang et al., 2016). Regarding to drinking, although there were studies reported the relationship between drinking and occurrence of CRC (Zisman et al., 2006; Fagunwa et al., 2017), the correlation between drinking and colorectal neoplasia is not significant in our study, which might be caused by the limited number of participants.

The relationship between sports (Physical activity) and CRC incidence is controversial in many studies. Papadimitriou et al. (2020) showed an inverse association between physical activity and incidence of colorectal cancer, indicating that the higher level



of physical activity, the lower risks of colorectal cancer, and this result is supported by many other studies including Simons et al. (2013) and Des Guetz et al. (2013). Harriss et al. (2009), however, showed that physical activity did not affect the incidence of colorectal cancer. In this study, more frequent sports are correlated with higher incidence of colorectal neoplasia, which is different from the results of previous studies. The reason for this might be from different standards in estimating the frequency, duration and intensity of activities, as suggested in a review by Slattery et al. (2003). Limited number of participants might also cause this inconsistent result, hence this feature is not included in the final model generation.

## CONCLUSION

In this study, we developed a funnel strategy in FIT based colorectal neoplasia screening with the addition of a filtering step between FIT and colonoscopy. This filtering step was performed through a classifier model based on FIT results and a cohort of six other features using logistic regression algorithm, with a yielding of 0.92 (AUC score) in discriminating colorectal neoplasia participants from normal participants. This study will help increasing the sensitivity of FIT-based CRC screening and reducing the need of colonoscopy examination.

## DATA AVAILABILITY STATEMENT

The original contributions presented in the study are included in the article/Supplementary Material, further inquiries can be directed to the corresponding authors.

## ETHICS STATEMENT

The studies involving human participants were reviewed and approved by the Ethical Committee Board of the Shenzhen People's Hospital. The patients/participants provided their written informed consent to participate in this study.

## REFERENCES

- Ahmed, F. E., Ahmed, N. C., Vos, P. W., Bonnerup, C., Atkins, J. N., Casey, M., et al. (2013). Diagnostic MicroRNA markers to screen for sporadic human colon cancer in stool: I. Proof of principle. *CGP* 10 (3), 93–113.
- Akter, S., Islam, Z., Mizoue, T., Sawada, N., Ihira, H., Tsugane, S., et al. (2021). Smoking and colorectal cancer: a pooled analysis of 10 population-based cohort studies in Japan. *Int. J. Cancer* 148 (3), 654–664. doi:10.1002/ijc.33248
- Atkin, W. S., Edwards, R., Kralj-Hans, I., Wooldrage, K., Hart, A. R., Northover, J. M., et al. (2010). Once-only flexible sigmoidoscopy screening in prevention of colorectal cancer: a multicentre randomised controlled trial. *Lancet* 375 (9726), 1624–1633. doi:10.1016/S0140-6736(10)60551-X
- Baek, D. H., Kim, G. H., Song, G. A., Han, I. S., Park, E. Y., Kim, H. S., et al. (2019). Clinical potential of circulating tumor cells in colorectal cancer: a prospective study. *Clin. Transl. Gastroenterol.* 10 (7), e00055. doi:10.14309/ctg.0000000000000055

## AUTHOR CONTRIBUTIONS

FL, CZ and WW conceived the research idea; HH and LZ performed the FIT tests and collected the samples; QL and SD performed the statistical analysis; FL and CZ prepared and wrote the manuscript; WW revised the manuscript. All authors read and approved the final version of the manuscript.

## FUNDING

This study is funded by The Science and Technology Foundation of Shenzhen (JCYJ20180305164128430); the International Cooperation Foundation of Shenzhen (GJHZ20180928171602104); the Shenzhen Economic and Information Committee "Innovation Chain and Industry Chain" integration special support plan project(20180225112449943); the Shenzhen Public Service Platform on Tumor Precision Medicine and Molecular Diagnosis; Research Grants Council of the Hong Kong Special Administrative Region, China (Project No. CityU 21101115, 11102317, 11103718, 11103619, R4017-18, C4041-17GF), a grant from Guangdong Basic and Applied Basic Research Foundation (Project No. 2019B030302012) and Young Scientists Fund of the National Natural Science Foundation of China (81802384); International innovation team for early diagnosis and precise treatment of lung cancer (2016, KQTD2016113015442590).

## ACKNOWLEDGMENTS

We would like to thank the nurses from Department of Health Managements in Shenzhen People's Hospital.

## SUPPLEMENTARY MATERIAL

The Supplementary Material for this article can be found online at: <https://www.frontiersin.org/articles/10.3389/fphar.2021.635481/full#supplementary-material>.

- Barlin, J. N., Zhou, Q., St Clair, C. M., Iasonos, A., Soslow, R. A., Alektiar, K. M., et al. (2013). Classification and regression tree (CART) analysis of endometrial carcinoma: seeing the forest for the trees. *Gynecol. Oncol.* 130 (3), 452–456. doi:10.1016/j.ygyno.2013.06.009
- Breiman, L., Friedman, J., Stone, C. J., and Olshen, R. A. (1984). *Classification and regression trees*. 1st Edn. Wadsworth: Chapman and Hall.
- Breiman, L. (2001). Random forests. *Machine Learn.* 45, 5–32. doi:10.1023/a:1010933404324
- Chen, L. S., Yen, A. M., Chiu, S. Y., Liao, C. S., and Chen, H. H. (2011). Baseline faecal occult blood concentration as a predictor of incident colorectal neoplasia: longitudinal follow-up of a Taiwanese population-based colorectal cancer screening cohort. *Lancet Oncol.* 12 (6), 551–558. doi:10.1016/S1470-2045(11)70101-2
- Chiu, H. M., Lee, Y. C., Tu, C. H., Chen, C. C., Tseng, P. H., Liang, J. T., et al. (2013). Association between early stage colon neoplasms and false-negative results from the fecal immunochemical test. *Clin. Gastroenterol. Hepatol.* 11 (7), 832–838.e2. doi:10.1016/j.cgh.2013.01.013

- Cortes, C., and Vapnik, V. (1995). Support-vector networks. *Mach Learn* 20 (3), 273–297. doi:10.1007/bf00994018
- Crotta, S., Segnan, N., Paganin, S., Dagnes, B., Rosset, R., and Senore, C. (2012). High rate of advanced adenoma detection in 4 rounds of colorectal cancer screening with the fecal immunochemical test. *Clin. Gastroenterol. Hepatol.* 10 (6), 633–638. doi:10.1016/j.cgh.2012.02.030
- Dekker, E., Tanis, P. J., Vleugels, J. L. A., Kasi, P. M., and Wallace, M. B. (2019). Colorectal cancer. *Lancet.* 394 (10207), 1467–1480. doi:10.1016/S0140-6736(19)32319-0
- Des Guetz, G., Uzzan, B., Bouillet, T., Nicolas, P., Chouahnia, K., Zelek, L., et al. (2013). Impact of physical activity on cancer-specific and overall survival of patients with colorectal cancer. *Gastroenterol. Res. Pract.* 2013, 1–6. doi:10.1155/2013/340851
- Dobson, A. J. (1990). “An introduction to generalized linear models,” in *An introduction to generalized linear models*. 3rd Edn (London: Chapman, Hall).
- Fagunwa, I. O., Loughrey, M. B., and Coleman, H. G. (2017). Alcohol, smoking and the risk of premalignant and malignant colorectal neoplasms. *Best Pract. Res. Clin. Gastroenterol.* 31 (5), 561–568. doi:10.1016/j.bpg.2017.09.012
- Fan, R. E., Chen, P. H., and Lin, C. J. (2005). Working set selection using the second order information for training support vector machines. *J. Mach Learn Res.* 6, 1889–1918. doi:10.1109/TNN.2008.2003299
- Giráldez, M. D., Lozano, J. J., Ramírez, G., Hijona, E., Bujanda, L., Castells, A., et al. (2013). Circulating microRNAs as biomarkers of colorectal cancer: results from a genome-wide profiling and validation study. *Clin. Gastroenterol. Hepatol.* 11 (6), 681–e3. doi:10.1016/j.cgh.2012.12.009
- Graham, L. D., Pedersen, S. K., Brown, G. S., Ho, T., Kassir, Z., Moynihan, A. T., et al. (2011). Colorectal neoplasia differentially expressed (CRNDE), a novel gene with elevated expression in colorectal adenomas and adenocarcinomas. *Genes Cancer* 2 (8), 829–840. doi:10.1177/1947601911431081
- Gupta, S., Halm, E. A., Rockey, D. C., Hammons, M., Koch, M., Carter, E., et al. (2013). Comparative effectiveness of fecal immunochemical test outreach, colonoscopy outreach, and usual care for boosting colorectal cancer screening among the underserved: a randomized clinical trial. *JAMA Intern. Med.* 173 (18), 1725–1732. doi:10.1001/jamainternmed.2013.9294
- Harris, D. J., Atkinson, G., Batterham, A., George, K., Cable, N. T., Reilly, T., et al. (2009). Lifestyle factors and colorectal cancer risk (2): a systematic review and meta-analysis of associations with leisure-time physical activity. *Colorectal Dis.* 11 (7), 689–701. doi:10.1111/j.1463-1318.2009.01767.x
- Hauptman, N., and Glavač, D. (2017). Colorectal cancer blood-based biomarkers. *Gastroenterol. Res. Pract.* 2017, 1–11. doi:10.1155/2017/2195361
- Jensen, C. D., Corley, D. A., Quinn, V. P., Doubeni, C. A., Zauber, A. G., Lee, J. K., et al. (2016). Fecal immunochemical test program performance over 4 rounds of annual screening: a retrospective cohort study. *Ann. Intern. Med.* 164 (7), 456–463. doi:10.7326/M15-0983
- Kanaan, Z., Roberts, H., Eichenberger, M. R., Billeter, A., Ocheretner, G., Pan, J., et al. (2013). A plasma microRNA panel for detection of colorectal adenomas: a step toward more precise screening for colorectal cancer. *Ann. Surg.* 258 (3), 400–408. doi:10.1097/SLA.0b013e3182a15bcc
- Kapidzic, A., Grobbee, E. J., Hol, L., Van Roon, A. H., Van Vuuren, A. J., Spijker, W., et al. (2014). Attendance and yield over three rounds of population-based fecal immunochemical test screening. *Am. J. Gastroenterol.* 109 (8), 1257–1264. doi:10.1038/ajg.2014.168
- Kim, N. H., Lee, M. Y., Park, J. H., Park, D. I., Sohn, C. I., Choi, K., et al. (2017). Serum CEA and CA 19-9 levels are associated with the presence and severity of colorectal neoplasia. *Yonsei Med. J.* 58 (5), 918–924. doi:10.3349/ymj.2017.58.5.918
- Kościelniak-Merak, B., Radosavljević, B., Zajac, A., and Tomasik, P. J. (2018). Faecal occult blood point-of-care tests. *J. Gastrointest. Cancer* 49 (4), 402–405. doi:10.1007/s12029-018-0169-1
- Kozma, D., Simon, I., and Tusnády, G. E. (2012). CMWeb: an interactive on-line tool for analysing residue-residue contacts and contact prediction methods. *Nucleic Acids Res.* 40 (W1), W329–W333. doi:10.1093/nar/gks488
- Lee, J. K., Liles, E. G., Bent, S., Levin, T. R., and Corley, D. A. (2014). Accuracy of fecal immunochemical tests for colorectal cancer: systematic review and meta-analysis. *Ann. Intern. Med.* 160, 171–181. doi:10.7326/M13-1484
- Locker, G. Y., Hamilton, S., Harris, J., Jessup, J. M., Kemeny, N., Macdonald, J. S., et al. (2006). ASCO 2006 update of recommendations for the use of tumor markers in gastrointestinal cancer. *J. Clin. Oncol.* 24 (33), 5313–5327. doi:10.1200/JCO.2006.08.2644
- Marshall, K. W., Mohr, S., Khattabi, F. E., Nossova, N., Chao, S., Bao, W., et al. (2010). A blood-based biomarker panel for stratifying current risk for colorectal cancer. *Int. J. Cancer* 126 (5), 1177–1186. doi:10.1002/ijc.24910
- Oort, F. A., Terhaar Sive Droste, J. S., Van Der Hulst, R. W., Van Heukelem, H. A., Loffeld, R. J., Wesdorp, I. C., et al. (2010). Colonoscopy-controlled intra-individual comparisons to screen relevant neoplasia: faecal immunochemical test vs. guaiac-based faecal occult blood test. *Aliment. Pharmacol. Ther.* 31 (3), 432–439. doi:10.1111/j.1365-2036.2009.04184.x
- Papadimitriou, N., Dimou, N., Tsilidis, K. K., Banbury, B., Martin, R. M., Lewis, S. J., et al. (2020). Physical activity and risks of breast and colorectal cancer: a Mendelian randomisation analysis. *Nat. Commun.* 11 (1), 597. doi:10.1038/s41467-020-14389-8
- Renganathan, V. (2019). Overview of artificial neural network models in the biomedical domain. *Bratisl Lek Listy* 120 (7), 536–540. doi:10.4149/BLL\_2019\_087
- Ripley, B. D. (2008). *Pattern recognition and neural networks*. 1st Edn. Cambridge, United Kingdom: Cambridge University Press.
- Saini, S. D., Kim, H. M., and Schoenfeld, P. (2006). Incidence of advanced adenomas at surveillance colonoscopy in patients with a personal history of colon adenomas: a meta-analysis and systematic review. *Gastrointest. Endosc.* 64 (4), 614–626. doi:10.1016/j.gie.2006.06.057
- Schoen, R. E., Pinsky, P. F., Weissfeld, J. L., Yokochi, L. A., Church, T., Laiyemo, A. O., et al. (2012). Colorectal-cancer incidence and mortality with screening flexible sigmoidoscopy. *N. Engl. J. Med.* 366 (25), 2345–2357. doi:10.1056/NEJMoa1114635
- Siegel, R., DeSantis, C., and Jemal, A. (2014). Colorectal cancer statistics, 2014. *CA Cancer J. Clin.* 64 (2), 104–117. doi:10.3322/caac.21220
- Siegel, R. L., Miller, K. D., Goding Sauer, A., Fedewa, S. A., Butterly, L. F., Anderson, J. C., et al. (2020). Colorectal cancer statistics, 2020. *CA Cancer J. Clin.* 70 (3), 145–164. doi:10.3322/caac.21601
- Siegel, R. L., Miller, K. D., and Jemal, A. (2019). Cancer statistics, 2019. *CA A. Cancer J. Clin.* 69 (1), 7–34. doi:10.3322/caac.21551
- Simons, C. C., Hughes, L. A., Van Engeland, M., Goldbohm, R. A., Van Den Brandt, P. A., and Weijenberg, M. P. (2013). Physical activity, Occupational sitting time, and colorectal cancer risk in The Netherlands cohort study. *Am. J. Epidemiol.* 177 (6), 514–530. doi:10.1093/aje/kws280
- Slattery, M. L., Edwards, S., Curtin, K., Ma, K., Edwards, R., Holubkov, R., et al. (2003). Physical activity and colorectal cancer. *Am. J. Epidemiol.* 158 (3), 214–224. doi:10.1093/aje/kwg134
- Stark, J. R., Bertone-Johnson, E. R., Costanza, M. E., and Stoddard, A. M. (2006). Factors associated with colorectal cancer risk perception: the role of polyps and family history. *Health Educ. Res.* 21 (5), 740–749. doi:10.1093/her/cyl049
- Stegeman, I., de Wijkerslooth, T. R., Mallant-Hent, R. C., de Groot, K., Stroobants, A. K., Fockens, P., et al. (2012). Implementation of population screening for colorectal cancer by repeated Fecal Immunochemical Test (FIT): third round. *BMC Gastroenterol.* 12, 73. doi:10.1186/1471-230X-12-73
- Tolles, J., and Meurer, W. J. (2016). Logistic regression: relating patient characteristics to outcomes. *JAMA* 316 (5), 533–534. doi:10.1001/jama.2016.7653
- Vymetalkova, V., Cervena, K., Bartu, L., and Vodicka, P. (2018). Circulating cell-free DNA and colorectal cancer: a systematic review. *IJMS* 19 (11), 3356. doi:10.3390/ijms19113356
- Wang, Q., Huang, Z., Ni, S., Xiao, X., Xu, Q., Wang, L., et al. (2012). Plasma miR-601 and miR-760 are novel biomarkers for the early detection of colorectal cancer. *PLoS One* 7 (9), e44398. doi:10.1371/journal.pone.0044398
- Warren, J. D., Xiong, W., Bunker, A. M., Vaughn, C. P., Furtado, L. V., Roberts, W. L., et al. (2011). Septin 9 methylated DNA is a sensitive and specific blood test for colorectal cancer. *BMC Med.* 9 (9), 133. doi:10.1186/1741-7015-9-133
- Wilschut, J. A., Hol, L., Dekker, E., Jansen, J. B., Van Leerdam, M. E., Lansdorp-Vogelaar, I., et al. (2011). Cost-effectiveness analysis of a quantitative immunochemical test for colorectal cancer screening. *Gastroenterology* 141 (5), 1648–1655.e1. doi:10.1053/j.gastro.2011.07.020
- Yang, C., Wang, X., Huang, C. H., Yuan, W. J., and Chen, Z. H. (2016). Passive smoking and risk of colorectal cancer: a meta-analysis of observational studies. *Asia Pac. J. Public Health* 28 (5), 394–403. doi:10.1177/1010539516650724

- Zeinalian, M., Hashemzadeh-Chaleshtori, M., Salehi, R., and Emami, M. (2018). Clinical aspects of microsatellite instability testing in colorectal cancer. *Adv. Biomed. Res.* 16, 7–28. doi:10.4103/abr.abr\_185\_16
- Zhao, W., Song, M., Zhang, J., Kuerban, M., and Wang, H. (2015). Combined identification of long non-coding RNA CCAT1 and HOTAIR in serum as an effective screening for colorectal carcinoma. *Int. J. Clin. Exp. Pathol.* 8 (11), 14131–14140.
- Zisman, A. L., Nickolov, A., Brand, R. E., Gorchow, A., and Roy, H. K. (2006). Associations between the age at diagnosis and location of colorectal cancer and the use of alcohol and tobacco: implications for screening. *Arch. Intern. Med.* 166 (6), 629–634. doi:10.1001/archinte.166.6.629

**Conflict of Interest:** The authors declare that the research was conducted in the absence of any commercial or financial relationships that could be construed as a potential conflict of interest.

Copyright © 2021 Liu, Long, He, Dong, Zhao, Zou and Wu. This is an open-access article distributed under the terms of the Creative Commons Attribution License (CC BY). The use, distribution or reproduction in other forums is permitted, provided the original author(s) and the copyright owner(s) are credited and that the original publication in this journal is cited, in accordance with accepted academic practice. No use, distribution or reproduction is permitted which does not comply with these terms.



# LncRNA SNHG8 Promotes Proliferation and Inhibits Apoptosis of Diffuse Large B-Cell Lymphoma via Sponging miR-335-5p

Bing Yu<sup>††</sup>, Bo Wang<sup>††</sup>, Zhuman Wu<sup>2</sup>, Chengnian Wu<sup>1</sup>, Juan Ling<sup>1</sup>, Xiaoyan Gao<sup>1</sup> and Huilan Zeng<sup>1\*</sup>

<sup>1</sup> Department of Hematology, The First Affiliated Hospital of Jinan University, Guangzhou, China, <sup>2</sup> Emergency Department, The First Affiliated Hospital of Jinan University, Guangzhou, China

## OPEN ACCESS

### Edited by:

Dong-Hua Yang,  
St. John's University, United States

### Reviewed by:

Shanzhi Wang,  
University of Arkansas at Little Rock,  
United States  
Xingqi Li,  
Stony Brook University, United States

### \*Correspondence:

Huilan Zeng  
thlz@jnu.edu.cn

<sup>††</sup> These authors have contributed  
equally to this work

### Specialty section:

This article was submitted to  
Pharmacology of Anti-Cancer Drugs,  
a section of the journal  
Frontiers in Oncology

**Received:** 06 January 2021

**Accepted:** 04 February 2021

**Published:** 19 March 2021

### Citation:

Yu B, Wang B, Wu Z, Wu C, Ling J,  
Gao X and Zeng H (2021) LncRNA  
SNHG8 Promotes Proliferation and  
Inhibits Apoptosis of Diffuse Large  
B-Cell Lymphoma via Sponging  
miR-335-5p.  
Front. Oncol. 11:650287.  
doi: 10.3389/fonc.2021.650287

Long-chain non-coding RNAs (LncRNAs) are expressed in diffuse large B-cell lymphoma (DLBCL) tissues and have played a regulatory role in DLBCL with a cancer-promoting effect. In this study, the role of LncRNA SNHG8 in the regulation of DLBCL cells is investigated, and its underlying mechanism is explored. The database of the Gene Expression Profiling Interactive Analysis (GEPIA) was searched, and the expression of SNHG8 in DLBCL and normal tissues was examined. The expression of SNHG8 was evaluated in several DLBCL cell lines and a normal lymphocyte cell line. It was found that SNHG8 was overexpressed in DLBCL tissues and cells in comparison with their normal counterparts. The short hairpin RNA (shRNA) plasmids of SNHG8 were transfected into DLBCL cells to knockdown the expression of SNHG8, followed by assays of proliferation, colony formation, apoptosis, and related protein expression. The results showed that the knockdown of SNHG8 significantly inhibited DLBCL cell proliferation and colony formation while promoting cell apoptosis. Moreover, the knockdown of SNHG8 reduced the expression of Ki-67, proliferating cell nuclear antigen (PCNA), and Bcl-2 and enhanced the expression of Bax and cleaved caspase 3/9. MiR-335-5p was predicted to be a potential target of SNHG8 by using the bioinformatics analysis, and the interaction between the two was validated by using the dual luciferase assay. In addition, the knockdown of SNHG8 increased the level of miR-335-5p, whereas miR-335-5p mimic decreased the expression of SNHG8. Finally, U2932 cells were co-transfected with or without sh-SNHG8 and miR-335-5p inhibitors, whose proliferation, colony formation, and apoptosis were determined subsequently. It was demonstrated that the presence of an miR-335-5p inhibitor partially canceled the inhibitory effects of the knockdown of SNHG8 on DLBCL cell proliferation and colony formation and the stimulating effects of the knockdown of SNHG8 on cell apoptosis. Taken together, our study suggests that LncRNA SNHG8 exerts a cancer-promoting effect on DLBCL via targeting miR-335-5p.

**Keywords:** diffuse large B cell lymphoma, apoptosis, long non-coding RNA, SNHG8, MiR-335-5p



## INTRODUCTION

Being an aggressive malignant B-cell lymphoma, diffuse large B-cell lymphoma (DLBCL) is the most common subtype of non-Hodgkin lymphoma (NHL). DLBCL accounts for about 40% of newly diagnosed NHL cases in western countries (1). The lesions of DLBCL occur mainly on the lymph nodes, and some of them are found in the gastrointestinal tract, bone, and the central nervous system (2). The lymph nodes of patients with DLBCL enlarge rapidly at an early stage, and symptoms such as fever and night sweat can occur. With the progression of DLBCL, the lesions show aggressive growth, resulting in poor treatment outcome (3). Although the advancement of medicine contributes to a great progress in the therapeutic approach for the treatment of DLBCL, up to 40% of patients die from a relapse (4). So far, the molecular mechanism of the pathogenesis of DLBCL remains unclear, which seriously hinders the management of DLBCL.

Long-chain non-coding RNA (lncRNA) is a type of RNA that has a length >200 nucleotides. lncRNA was initially thought to be the noise of gene transcription because it does not have an open reading frame and rarely participates in encoding proteins. However, lncRNAs have been confirmed in recent years for the regulation of various diseases by binding to microRNAs or proteins, thereby participating in the occurrence, progression, and prognosis of diseases (5). The abnormal expression of lncRNA plays an important role in various cancers, such as hepatocellular carcinoma, breast cancer, prostate cancer, and non-small-cell lung cancer (NSCLC) (5–7). Therefore, it has been proposed that lncRNAs can become tumor biomarkers.

Long-chain non-coding RNAs also play a key role in the occurrence, progression, drug resistance, and prognosis of DLBCL (8). Verma et al. identified 2,632 novel multi-exonic lncRNAs that are expressed in more than one tumor. Two-thirds of the identified lncRNAs are not expressed in normal B cells, and one-thirds of them are differentially expressed in DLBCL subtypes (9). A study showed that lncRNA MALAT-1 is upregulated in DLBCL cell lines, and the downregulation of MALAT-1 inhibits the proliferation and migration of DLBCL cells, induces a cell cycle arrest, activates autophagy, and blocks doxorubicin-induced epithelial–mesenchymal transition, thereby reducing the doxorubicin resistance in DLBCL (10).

Long-chain non-coding RNA SNHG8 was demonstrated to have a cancer-promoting effect in various cancers such as lung cancer, liver cancer, colorectal cancer, pancreatic cancer, and endometrial cancer (11–13). However, the involvement of SNHG8 in DLBCL has not been reported.

The objective of this study is to investigate the role of lncRNA SNHG8 in DLBCL cells and uncover the potential mechanism.

## MATERIALS AND METHODS

### Cell Culture and Treatment

Human B lymphocytes GM12878 and human DLBCL cell lines, including OCI-Ly10, OCI-Ly7, OCI-Ly3, and U2932 (ATCC, Virginia, USA), were cultured in RPMI-1640 medium (Thermo Fisher Scientific, Massachusetts, USA), supplemented with 10%

fetal bovine serum (FBS) and 1% penicillin/streptomycin with an atmosphere of 5% CO<sub>2</sub> at 37°C.

The short hairpin RNA (shRNA) targeting SNHG8 and negative scrambled control shRNA (sh-NC) were synthesized by GenePharma (Shanghai, China). MiR-335-5p mimic, inhibitor, and its NC; SNHG8 mutant (MUT); and wild type (WT) were obtained from GenePharma (Shanghai, China) and cloned into pcDNA3.1 vector. After reaching 80% confluence, cells were transfected with the indicated sh-RNAs, an miR-335-5p mimic or inhibitor, and SNHG8 MUT or WT using lipofectamine 2000 (Invitrogen, California, USA) according to the manufacturer's instructions. All transfected cells were then cultured for 48 h before the following experiments.

### Cell Counting Kit-8 Assay

Cells were seeded at a density of  $3 \times 10^3$  cells per well in a 96-well plate. After treatment with the indicated conditions for 24, 48, and 72 h, cells were incubated with 10  $\mu$ l of the cell counting kit-8 (CCK-8) solution (MedChemExpress, MCE, New Jersey, USA) for 2 h at 37°C. The light absorbance of cells was measured at 450 nm using a microplate reader.

### Colony Formation Assay

For colony formation assays, cell suspension was resuspended in 1 ml medium. Samples were plated in a 24-well plate and incubated for 2 weeks. Crystal violet was used to stain cells, and a colony with >50 cells was counted as a colony.

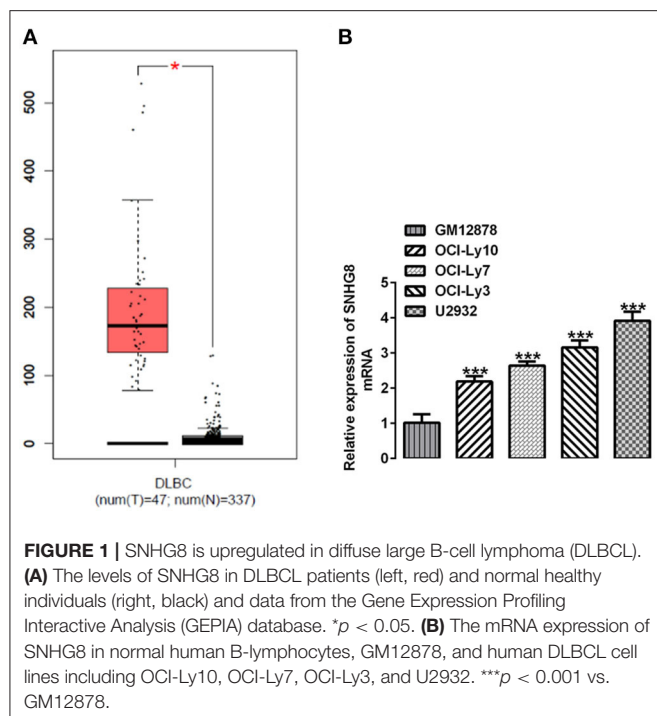
### Real-Time Quantitative PCR

Total RNA was extracted using an RNeasy Mini Kit (QIAGEN, Maryland, USA) and reverse-transcribed into cDNA with SuperScript III First-Strand Synthesis SuperMix (Invitrogen, California, USA) according to the manufacturer's instructions. Quantitative PCR was performed by following the instructions of the HotStarTaq Master Mix Kit (QIAGEN). The reactions were performed in accordance with the following conditions: 95°C for 15 min, 25 cycles of 95°C for 15 s, 58°C for 30 s, and 72°C for 30 s, followed by 72°C for 10 min. The RT-PCR primers used were as follows:

SNHG8: forward, 5'-CCCGAGAACCGTCAGTTTGA-3', reverse, 5'-ACACCCGTT-TCCCCAACTAC-3';  
MiR-335-5p: forward, 5'-TGTTTTGAGCGGGGGTCAAG-3', reverse, 5'-TGAATAT-AGCAAATGAGAGG-3'; and  
GAPDH: forward, 5'-ACCTGACCTGCCGTCTAGAA-3', reverse, 5'-TCCACCAC-CCTGTTGCTGTA-3'.

### Western Blotting

Total proteins from the cells were extracted by RIPA buffer with protease inhibitors (Beyotime Institute of Biotechnology, Jiangsu, China) on ice. Sodium dodecyl-sulfate–polyacrylamide gel electrophoresis (SDS–PAGE) was performed using equal amounts of protein samples for transferring the proteins to polyvinylidene difluoride (PVDF) membranes. On the first day, the membranes were incubated in 5% non-fat milk for 2 h at 37°C and then with primary antibodies against Ki-67, proliferating cell nuclear antigen (PCNA), Bcl-2, Bax, caspase-3/9, and GAPDH



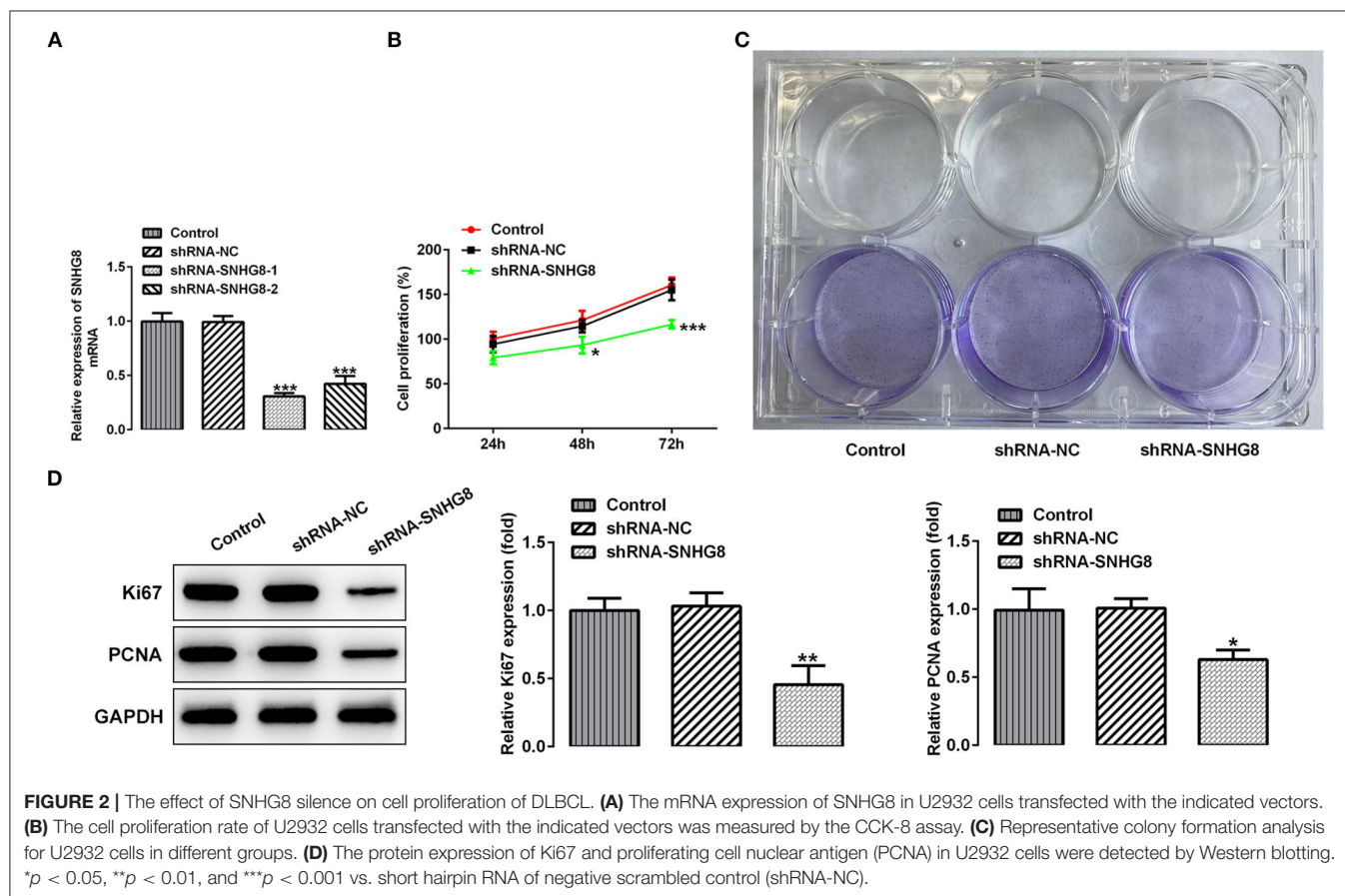
(1:1,000, Proteintech) at 4°C overnight. On the second day, the membranes were incubated with secondary antibodies (goat anti-mouse, 1:10,000; Proteintech) at 37°C for 2 h. Immunoblots were visualized by enhanced chemiluminescence (Santa Cruz Biotechnology, Texas, USA) and analyzed using ImageJ software.

## Flow Cytometry

Cell apoptosis was assessed by flow cytometry using the Annexin V-FITC Apoptosis Detection Kit (Beyotime, Shanghai, China). Briefly, cells were collected, washed with phosphate buffered saline (PBS), and then stained with APC-conjugated anti-Annexin V antibody and propidium iodide (PI) according to the manufacturer's protocol. The percentage of Annexin V<sup>+</sup> PI<sup>+</sup> cells was determined by using a flow cytometer (Becton Dickinson, New Jersey, USA).

## Luciferase Reporter Assay

Direct interactions between miR-335-5p and SNHG8 were predicted by Starbase 3.0 software (14). A luciferase reporter assay was performed by co-transfecting firefly luciferase reporter plasmids containing WT or MUT SNHG8 and renilla luciferase control reporter vectors (Promega, Wisconsin, USA) and the miR-335-5p mimic or miR-335-5p NC *via* lipofectamine 2,000 into U2932 cells. The luciferase assay was conducted at 48 h



after transfection by using the Dual Luciferase Reporter Assay System (Promega, Wisconsin, USA) according to the previously described manufacturer's instructions (15).

## Statistical Analysis

The data are presented as the mean  $\pm$  SD from three independent experiments. The Student's *t*-test was used for statistical comparisons between the two groups, and a one-way ANOVA was used for comparisons among multiple groups. A *p*-value  $<0.05$  was considered significant.

## RESULTS

### SNHG8 Is Upregulated in DLBCL Cells

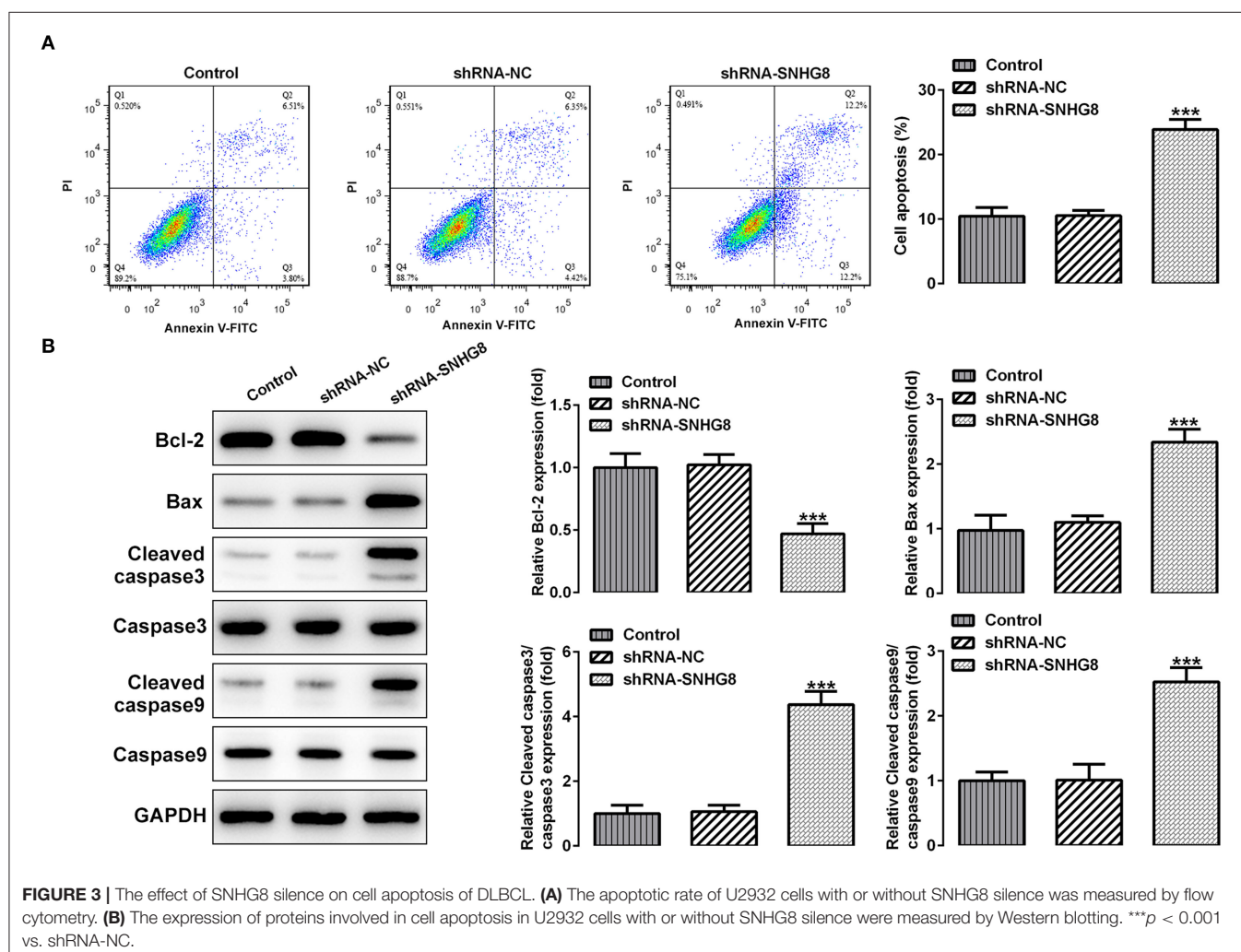
We searched the database of the Gene Expression Profiling Interactive Analysis (GEPIA) and found that SNHG8 was significantly upregulated in the tissues of patients with DLBCL in comparison with that of normal healthy individuals (Figure 1A). We detected the mRNA levels of SNHG8 in normal human B lymphocytes, GM12878, and human DLBCL cell lines, including OCI-Ly10, OCI-Ly7, OCI-Ly3, and U2932. As shown

in Figure 1B, the mRNA levels of SNHG8 in DLBCL cell lines were remarkably higher than those in GM12878. This result was consistent with the data from the GEPIA and suggested that lncRNA SNHG8 might play a role in DLBCL. Among these DLBCL cell lines, the U2932 cell line showed the highest level of SNHG8 and was, therefore, chosen for subsequent experiments.

### Knockdown of SNHG8 Inhibits Proliferation and Promotes Apoptosis of DLBCL Cells

To investigate the effects of SNHG8 on the cellular behaviors of DLBCL cells, two pairs of chemically synthesized shRNAs (shRNA-1 and shRNA-2) targeting SNHG8 and negative control (sh-NC group) were transfected into U2932 cells. The results from RT-qPCR showed that the expression of SNHG8 was inhibited by both shRNAs in comparison with the control and NC groups. The inhibitory efficiency of shRNA-1 was better than that of shRNA-2 (Figure 2A). Therefore, the cells transfected with shRNA-SNHG8-1 was chosen for subsequent experiments.

It was found that the cells that were transfected with shRNA-SNHG8 showed an obviously depressed cell proliferation in





comparison with the cells that were transfected with shRNA-NC (**Figure 2B**). The results obtained from the colony formation assay also showed that the knockdown of SNHG8 inhibited DLBCL cell colony formation (**Figure 2C**). Moreover, the expression of proliferation-related proteins, Ki-67, and PCNA was significantly decreased by the knockdown of SNHG8 (**Figure 2D**).

As shown in **Figure 3A**, the percentage of apoptotic cells was remarkably higher in cells that were transfected with shRNA-SNHG8 than the cells that were transfected with shRNA-NC. At the same time, a decreased expression of the anti-apoptotic protein Bcl-2 and an increased expression of pro-apoptotic proteins, such as Bax, cleaved caspase 9, and cleaved caspase 3, were observed in the shRNA-SNHG8 group in comparison with the shRNA-NC group (**Figure 3B**). These data indicated that the knockdown of SNHG8 suppressed the proliferation and induced apoptosis in DLBCL cells.

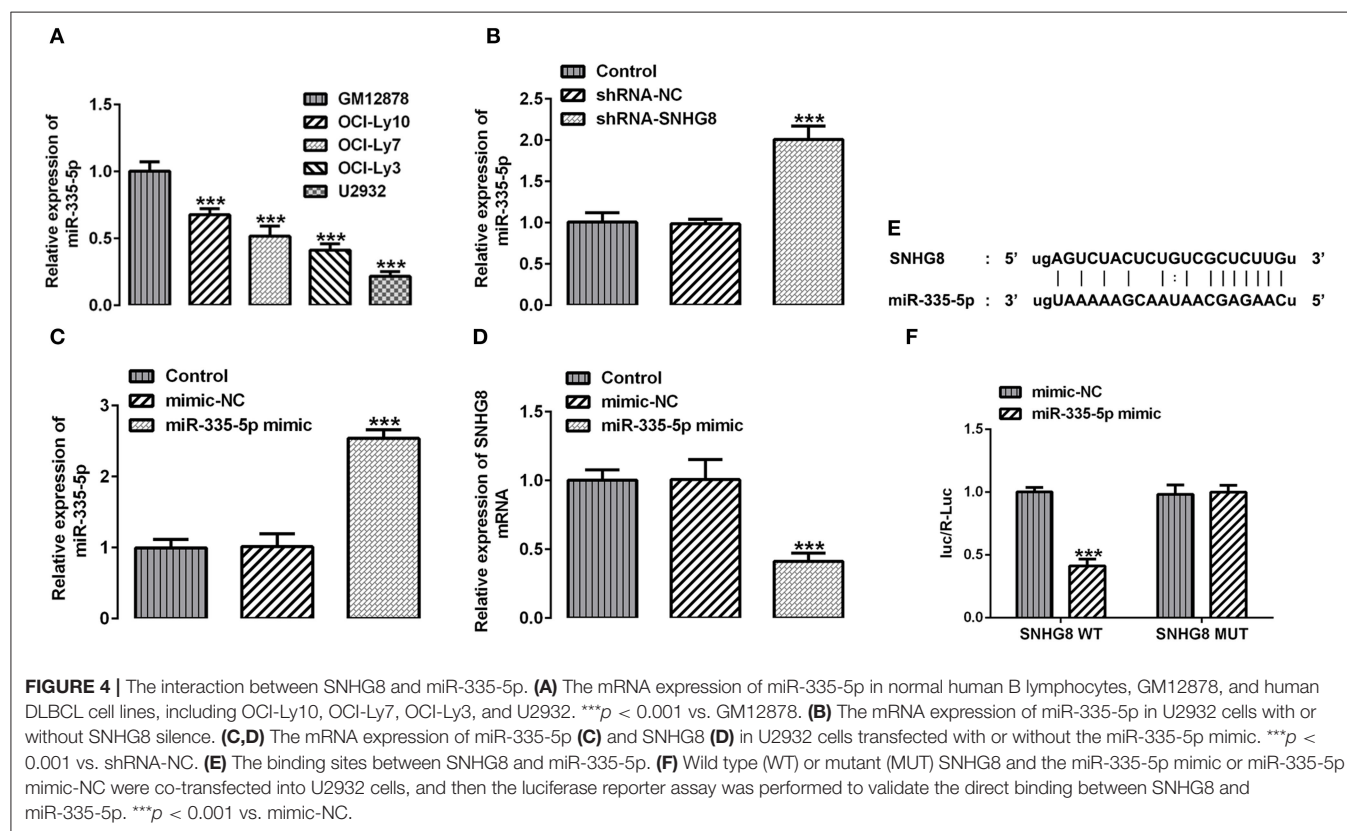
### MiR-335-5p Is Downregulated in DLBCL Cell Lines and Can Interact With SNHG8 to Affect Reciprocal Expression

With the help of the bioinformatics analysis using the StarBase software, we found that miR-335-5p might be a target of SNHG8. MiR-335-5p was reported to inhibit the invasion and metastasis of various cancers, such as thyroid cancer, colorectal cancer, and NSCLC (16–18). To evaluate the role of miR-335-5p in DLBCL

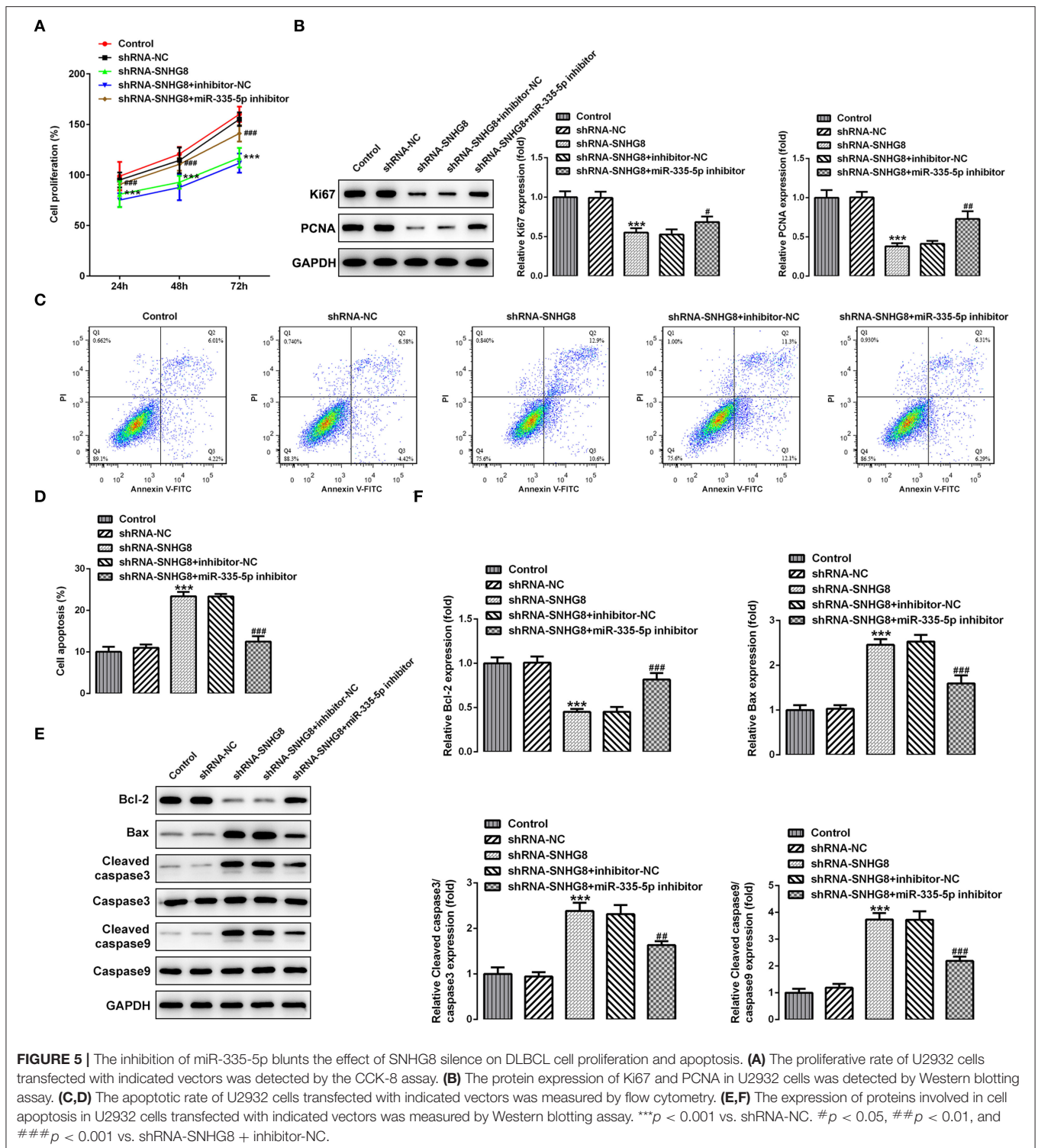
cells, we examined the expression of miR-335-5p in the DLBCL cell lines. Contrary to SNHG8, the mRNA levels of miR-335-5p were significantly lower in DLBCL cell lines in comparison with normal human B lymphocytes GM12878 (**Figure 4A**). In addition, the silencing of SNHG8 increased the expression of miR-335-5p (**Figure 4B**), suggesting the interaction between SNHG8 and miR-335-5p in DLBCL cells. Then, we constructed the miR-335-5p mimic, which was transfected into U2932 cells. The upregulation of miR-335-5p was confirmed by qRT-PCR (**Figure 4C**). Further studies found that the overexpression of miR-335-5p reduced the expression of SNHG8 (**Figure 4D**). Moreover, WT or MUT SNHG8 and the miR-335-5p mimic or miR-335-5p mimic-NC were co-transfected into U2932 cells for the luciferase reporter assay. The result suggested the direct binding between SNHG8 and miR-335-5p (**Figures 4E,F**).

### Inhibition of the Expression of miR-335-5p Reverses the Effects of SNHG8 Knockdown on DLBCL Cell Proliferation and Apoptosis

Finally, determining whether the actions of SNHG8 were associated with the binding to miR-335-5p, cells with SNHG8 knockdown were exposed to the miR-335-5p inhibitor or inhibitor-NC. It was found that the cells co-treated with shRNA-SNHG8 and the miR-335-5p inhibitor exhibited a significantly higher rate of proliferation in comparison with







the cells co-treated with shRNA-SNHG8 and the miR-335-5p inhibitor-NC (Figure 5A). Furthermore, the presence of the miR-335-5p inhibitor increased the expression of Ki-67 and PCNA (Figure 5B) and reduced the ratio of apoptotic cells

increased by the knockdown of SNHG8 (Figures 5C,D). A Western blot analysis confirmed that the decreased expression of Bcl-2 and the increased expression of Bax and cleaved caspase 3/9 in cells with SNHG8 knockdown were

partially reversed by co-treatment of the miR-335-5p inhibitor (Figures 5E,F).

## DISCUSSION

Non-Hodgkin lymphoma has a high degree of heterogeneity and can occur in many sites of the body. DLBCL is the most common NHL pathological type, with an incidence as high as 30–40%. It is reported that DLBCL has a variety of histomorphology, clinical characteristics, and epigenetics (19). Usually, patients with stages I or II of DCBCL are treated with chemotherapy in combination with a comprehensive treatment, and those with stages III or IV of DLBCL are mainly treated with chemotherapy (20). The common chemotherapeutic drugs for DLBCL include methyl-benzylhydrazine, cyclophosphamide, nitrogen mustard, and other alkylating agents (21). The comprehensive treatment is to control distant metastasis of the tumor. Radiotherapy can effectively control the recurrence of local lesions and can cure about 50% of the patients (22, 23). However, the treatment efficacy in patients at an advanced stage is unsatisfied, and some patients are prone to relapse after treatment (24). Therefore, finding biomarkers that can detect DLBCL at earlier stages and identifying the risk factors for prognosis are the current focal points of the clinical management of DLBCL.

Long-chain non-coding RNAs can regulate the epigenetics, gene transcription, and gene post-transcription and play a significant role in the occurrence and development of tumors. lncRNA SNHG8 has been demonstrated to have a cancer-promoting effect in various cancers whose overexpression may be an independent risk factor for poor tumor prognosis (25). In addition, lncRNA SNHG8 can also be used as an early diagnostic biomarker for tumors (13, 25). So far, the role of lncRNA SNHG8 in DLBCL has not been elucidated. Therefore, this study takes the lead in analyzing the association between lncRNA SNHG8 and the pathological features of DLBCL.

Our results revealed an upregulated expression of SNHG8 in DLBCL tissues in comparison to the expression in healthy tissues and normal cell lines. Furthermore, the knockdown of SNHG8 could remarkably inhibit the proliferation and colony formation and promote the apoptosis of DLBCL cells, indicating that SNHG8 aggravates the progression of DLBCL and the knockdown of SNHG8 exerts an opposite effect. It is well-known that lncRNAs usually function as competing endogenous RNAs of specific microRNAs for the regulation of target genes. For example, SNHG8 has been identified as a key regulator in the progression of NSCLC *via* sponging miR-542-3p (11). Moreover, SNHG8 has been found to be upregulated in esophageal squamous cell carcinoma and to directly sponge miR-411 to increase oncogenicity (13). In this study, miR-335-5p was predicted by the GEPIA database to be a target microRNA of SNHG8 whose downregulation was also detected in DLBCL cell lines. Importantly, it has been demonstrated

that miR-335-5p inhibits cell invasion and metastasis in thyroid cancer (18), an epithelial–mesenchymal transition in NSCLC (16), cell proliferation and metastasis in osteosarcoma (26), and cancer cell growth in colorectal cancer (17). Moreover, miR-335-5p acts as a target of lncRNAs to play a regulatory role in various cancers, such as osteosarcoma (27), cervical cancer (28), and bladder cancer (29). However, whether miR-335-5p regulates DLBCL remains to be investigated. In this study, we explored the interaction between SNHG8 and miR-335-5p and the role of miR-335-5p in DLBCL. Our results confirmed that miR-335-5p interacts with SNHG8 to regulate reciprocal expression. To further determine whether the actions of SNHG8 knockdown were dependent on an increased expression of miR-335-5p, we treated the cells with the miR-335-5p inhibitor in the presence of the knockdown of SNHG8. Our results demonstrated that the introduction of the miR-335-5p inhibitor significantly blunted the inhibitory effect of the knockdown of SNHG8 on cell proliferation and the stimulating effect of that on cell apoptosis. These results implied that SNHG8 sponges miR-335-5p to act on DLBCL. Furthermore, the effects of the miR-335-5p inhibitor on DLBCL suggested that miR-335-5p might inhibit the proliferation and promote the apoptosis of DLBCL cells. These data were inconsistent with the previous studies (16–18). However, the fact that the effects of the knockdown of SNHG8 were incompletely blocked by the miR-335-5p inhibitor, indicating the possible participation of other targets in the mechanism of SNHG8 in DLBCL. The mechanisms involved in the influence of miR-335-5p on cancers may be related to regulation of downstream signaling, such as ROCK1 and mitogen-activated protein kinase (MAPK) (30, 31), which was not clarified in this study. In addition, this study only focused on the *in vitro* cell model, lacking the validation of results from animal experiments. Therefore, further investigations on the above limitations shall be conducted in future studies.

In conclusion, the present study demonstrated that lncRNA SNHG8 can decoy miR-335-5p to facilitate the proliferation and inhibit the apoptosis in DLBCL cells. This study provides a better understanding of DLBCL and a novel therapeutic target for its treatment strategy.

## DATA AVAILABILITY STATEMENT

The original contributions presented in the study are included in the article/supplementary material, further inquiries can be directed to the corresponding author/s.

## AUTHOR CONTRIBUTIONS

HZ conceived the study and edited the manuscript. BY and BW performed the experiments and analyzed the results. ZW, CW, JL, and XG collected the samples and analyzed the results. BY wrote the first draft. All authors read and approved the final version of the manuscript.

## REFERENCES

- Li S, Young KH, Medeiros LJ. Diffuse large B-cell lymphoma. *Pathology*. (2018) 50:74–87. doi: 10.1016/j.pathol.2017.09.006
- Sukswai N, Lyapichev K, Khoury JD, Medeiros LJ. Diffuse large B-cell lymphoma variants: an update. *Pathology*. (2020) 52:53–67. doi: 10.1016/j.pathol.2019.08.013
- Ollila TA, Olszewski AJ. Extranodal diffuse large B cell lymphoma: molecular features, prognosis, and risk of central nervous system recurrence. *Curr Treat Options Oncol*. (2018) 19:38. doi: 10.1007/s11864-018-0555-8
- Caro P, Kishan AU, Norberg E, Stanley IA, Chapuy B, Ficarro SB, et al. Metabolic signatures uncover distinct targets in molecular subsets of diffuse large B cell lymphoma. *Cancer Cell*. (2012) 22:547–60. doi: 10.1016/j.ccr.2012.08.014
- Fu D, Shi Y, Liu JB, Wu TM, Jia CY, Yang HQ, et al. Targeting long non-coding RNA to therapeutically regulate gene expression in cancer. *Mol Ther Nucleic acids*. (2020) 21:712–24. doi: 10.1016/j.omtn.2020.07.005
- Martens-Uzunova ES, Böttcher R, Croce CM, Jenster G, Visakorpi T, Calin GA. Long noncoding RNA in prostate, bladder, and kidney cancer. *Eur Urol*. (2014) 65:1140–51. doi: 10.1016/j.eururo.2013.12.003
- Gutschner T, Diederichs S. The hallmarks of cancer: a long non-coding RNA point of view. *RNA Biol*. (2012) 9:703–19. doi: 10.4161/rna.20481
- Kang J, Yao P, Tang Q, Wang Y, Zhou Y, Huang J. Systematic analysis of competing endogenous RNA networks in diffuse large B-cell lymphoma and Hodgkin's lymphoma. *Front Genet*. (2020) 11:586688. doi: 10.3389/fgene.2020.586688
- Jiang YY, Du W, Fairchild L, Melnick A, Elemento O. Transcriptome sequencing reveals thousands of novel long non-coding RNAs in B cell lymphoma. *Genome Med*. (2015) 7:110. doi: 10.1186/s13073-015-0230-7
- Li LJ, Chai Y, Guo XJ, Chu SL, Zhang LS. The effects of the long non-coding RNA MALAT-1 regulated autophagy-related signaling pathway on chemotherapy resistance in diffuse large B-cell lymphoma. *Biomed Pharmacother*. (2017) 89:939–48. doi: 10.1016/j.biopha.2017.02.011
- Chen C, Zhang Z, Li J, Sun Y. SNHG8 is identified as a key regulator in non-small-cell lung cancer progression sponging to miR-542-3p by targeting CCND1/CDK6. *Onco Targets Ther*. (2018) 11:6081–90. doi: 10.2147/OTT.S170482
- Song Y, Zou L, Li J, Shen ZP, Cai YL, Wu XD. LncRNA SNHG8 promotes the development and chemo-resistance of pancreatic adenocarcinoma. *Eur Rev Med Pharmacol Sci*. (2018) 22:8161–8. doi: 10.26355/eurrev\_201812\_16508
- Song H, Song J, Lu L, Li S. SNHG8 is upregulated in esophageal squamous cell carcinoma and directly sponges microRNA-411 to increase oncogenicity by upregulating KPNA2. *Onco Targets Ther*. (2019) 12:6991–7004. doi: 10.2147/OTT.S214881
- Chen X, Zhao S, Li Q, Xu C, Yu Y, Ge H. LncRNA NEAT1 knockdown inhibits retinoblastoma progression by miR-3619-5p/LASP1 axis. *Front Genet*. (2020) 11:574145. doi: 10.3389/fgene.2020.574145
- Wang QM, Lian GY, Song Y, Huang YF, Gong Y. LncRNA MALAT1 promotes tumorigenesis and immune escape of diffuse large B cell lymphoma by sponging miR-195. *Life Sci*. (2019) 231:116335. doi: 10.1016/j.lfs.2019.03.040
- Du W, Tang H, Lei Z, Zhu J, Zeng Y, Liu Z, et al. miR-335-5p inhibits TGF- $\beta$ 1-induced epithelial-mesenchymal transition in non-small cell lung cancer via ROCK1. *Respir Res*. (2019) 20:225. doi: 10.1186/s12931-019-1184-x
- Zhang D, Yang N. MiR-335-5p inhibits cell proliferation, migration and invasion in colorectal cancer through downregulating LDHB. *J BUON*. (2019) 24:1128–36.
- Luo L, Xia L, Zha B, Zuo C, Deng D, Chen M, et al. miR-335-5p targeting ICAM-1 inhibits invasion and metastasis of thyroid cancer cells. *Biomed Pharmacother*. (2018) 106:983–90. doi: 10.1016/j.biopha.2018.07.046
- Liu Y, Barta SK. Diffuse large B-cell lymphoma: 2019 update on diagnosis, risk stratification, and treatment. *Am J Hematol*. (2019) 94:604–16. doi: 10.1002/ajh.25460
- Wong J, Pickles T, Connors J, Parsons A, Sehn L, Freeman C, et al. Efficacy of palliative radiation therapy (RT) for chemotherapy relapsed or refractory diffuse large B-cell lymphoma: a population-based retrospective review. *Pract Radiat Oncol*. (2020) 11:203–9. doi: 10.1016/j.prro.2020.11.003
- Vercellino L, Di Blasi R, Kanoun S, Tessoulin B, Rossi C, D'Aveni-Piney M, et al. Predictive factors of early progression after CAR T-cell therapy in relapsed/refractory diffuse large B-cell lymphoma. *Blood Adv*. (2020) 4:5607–15. doi: 10.1182/bloodadvances.2020003001
- Tilly H, Gomes da Silva M, Vitolo U, Jack A, Meignan M, Lopez-Guillermo A, et al. Diffuse large B-cell lymphoma (DLBCL): ESMO clinical practice guidelines for diagnosis, treatment and follow-up. *Ann Oncol*. (2015) 26(Suppl. 5):v116–25. doi: 10.1093/annonc/mdv304
- Van Den Neste E, Schmitz N, Mounier N, Gill D, Linch D, Trneny M, et al. Outcome of patients with relapsed diffuse large B-cell lymphoma who fail second-line salvage regimens in the International CORAL study. *Bone Marrow Transplant*. (2016) 51:51–7. doi: 10.1038/bmt.2015.213
- Wang Y, Farooq U, Link BK, Larson MC, King RL, Maurer MJ, et al. Late relapses in patients with diffuse large B-cell lymphoma treated with immunochemotherapy. *J Clin Oncol*. (2019) 37:1819–27. doi: 10.1200/JCO.19.00014
- Liu J, Yang C, Gu Y, Li C, Zhang H, Zhang W, et al. Knockdown of the lncRNA SNHG8 inhibits cell growth in Epstein-Barr virus-associated gastric carcinoma. *Cell Mol Biol Lett*. (2018) 23:17. doi: 10.1186/s11658-018-0070-8
- Wang Y, Zeng X, Wang N, Zhao W, Zhang X, Teng S, et al. Long noncoding RNA DANCER, working as a competitive endogenous RNA, promotes ROCK1-mediated proliferation and metastasis via decoying of miR-335-5p and miR-1972 in osteosarcoma. *Mol Cancer*. (2018) 17:89. doi: 10.1186/s12943-018-0837-6
- Wang Y, Yang T, Zhang Z, Lu M, Zhao W, Zeng X, et al. Long non-coding RNA TUG1 promotes migration and invasion by acting as a ceRNA of miR-335-5p in osteosarcoma cells. *Cancer Sci*. (2017) 108:859–67. doi: 10.1111/cas.13201
- Liang H, Zhang C, Guan H, Liu J, Cui Y. LncRNA DANCER promotes cervical cancer progression by upregulating ROCK1 via sponging miR-335-5p. *J Cell Physiol*. (2019) 234:7266–78. doi: 10.1002/jcp.27484
- Yang Y, Wang F, Huang H, Zhang Y, Xie H, Men T. LncRNA SLCO4A1-AS1 promotes growth and invasion of bladder cancer through sponging miR-335-5p to upregulate OCT4. *Onco Targets Ther*. (2019) 12:1351–8. doi: 10.2147/OTT.S191740
- She JK, Fu DN, Zhen D, Gong GH, Zhang B. LINC01087 is highly expressed in breast cancer and regulates the malignant behavior of cancer cells through miR-335-5p/ROCK1. *Onco Targets Ther*. (2020) 13:9771–83. doi: 10.2147/OTT.S255994
- Gao Y, Wang Y, Wang X, Zhao C, Wang F, Du J, et al. miR-335-5p suppresses gastric cancer progression by targeting MAPK10. *Cancer Cell Int*. (2021) 21:71. doi: 10.1186/s12935-020-01684-z

**Conflict of Interest:** The authors declare that the research was conducted in the absence of any commercial or financial relationships that could be construed as a potential conflict of interest.

Copyright © 2021 Yu, Wang, Wu, Wu, Ling, Gao and Zeng. This is an open-access article distributed under the terms of the Creative Commons Attribution License (CC BY). The use, distribution or reproduction in other forums is permitted, provided the original author(s) and the copyright owner(s) are credited and that the original publication in this journal is cited, in accordance with accepted academic practice. No use, distribution or reproduction is permitted which does not comply with these terms.



# Jiyuan Oridonin A Overcomes Differentiation Blockade in Acute Myeloid Leukemia Cells With MLL Rearrangements via Multiple Signaling Pathways

Mei Qu<sup>1,2†</sup>, Yu Duan<sup>1,2†</sup>, Min Zhao<sup>1,2</sup>, Zhanju Wang<sup>1</sup>, Mengjie Zhao<sup>1,2</sup>, Yao Zhao<sup>1</sup>, Haihua Wang<sup>1</sup>, Yu Ke<sup>3</sup>, Ying Liu<sup>3</sup>, Hong-Min Liu<sup>3</sup>, Liuya Wei<sup>1,2\*</sup> and Zhenbo Hu<sup>1\*</sup>

## OPEN ACCESS

### Edited by:

Haichang Li,  
The Ohio State University,  
United States

### Reviewed by:

Jian-Ye Zhang,  
Guangzhou Medical University, China  
Nan Wang,  
Fynn Biotechnologies, China

### \*Correspondence:

Liuya Wei  
xiaoyawfmc@163.com  
Zhenbo Hu  
huzhenbo@wfmc.edu.cn

<sup>†</sup>These authors have contributed  
equally to this work

### Specialty section:

This article was submitted  
to Pharmacology of  
Anti-Cancer Drugs,  
a section of the journal  
Frontiers in Oncology

**Received:** 28 January 2021

**Accepted:** 04 March 2021

**Published:** 26 March 2021

### Citation:

Qu M, Duan Y, Zhao M, Wang Z,  
Zhao M, Zhao Y, Wang H, Ke Y, Liu Y,  
Liu H-M, Wei L and Hu Z (2021) Jiyuan  
Oridonin A Overcomes Differentiation  
Blockade in Acute Myeloid Leukemia  
Cells With MLL Rearrangements via  
Multiple Signaling Pathways.  
Front. Oncol. 11:659720.  
doi: 10.3389/fonc.2021.659720

<sup>1</sup> Laboratory for Stem Cell and Regenerative Medicine, Affiliated Hospital of Weifang Medical University, Weifang, China,  
<sup>2</sup> School of Pharmacy, Weifang Medical University, Weifang, China, <sup>3</sup> School of Pharmacy, Zhengzhou University,  
Zhengzhou, China

Differentiation therapy with all-trans-retinoic acid (ATRA) in acute promyelocytic leukemia (APL), a subtype of acute myeloid leukemia (AML), has been extremely successful in inducing clinical remission in APL patients. However, the differentiation therapy of ATRA-based treatment has not been effective in other subtypes of AML. In this study, we evaluated a small molecule of *ent*-kaurene diterpenoid, Jiyuan oridonin A (JOA), on the differentiation blockade in AML cells with the mixed lineage leukemia (MLL) gene rearrangements (MLLr) in MV4-11, MOLM-13 and THP-1 cells. We found that JOA could significantly inhibit the proliferation of MOLM-13, MV4-11 and THP-1 cells. Moreover, JOA promoted cell differentiation coupled with cell-cycle exit at G0/G1 and inhibited the colony-forming capacity of these cells. We showed that the anti-proliferative effect of JOA attributed to cell differentiation is most likely through the martens tretinoin response up pathway in the MOLM-13 cell line, and the hematopoietic cell lineage pathway by the inhibition of c-KIT expression and cell adhesion pathway in the THP-1 cell line. Our findings suggest that JOA could be a novel therapeutic agent against human MLLr acute myeloid leukemia.

**Keywords:** differentiation therapy, acute myeloid leukemia with MLL gene rearrangements, Jiyuan oridonin A, martens tretinoin response up pathway, hematopoietic cell lineage pathway, cell adhesion pathway

## INTRODUCTION

Acute myeloid leukemia (AML) is the most common acute leukemia in adults and the second most common form of acute leukemia in children. AML is a malignancy of hematopoietic stem cell, with distinctive features of excessive proliferation and impaired differentiation (1, 2). The biology of AML cells is complex and involves multiple interdependent molecular pathways. The traditional chemotherapies are the mainstay of treatment for the past 50 years. However, a 5-year overall survival (OS) for patients younger than 60 years is about 40%. For those older than 60 years, the



5-year OS of only 10~20% has been achieved (3). In AML, the normal differentiation pathway is impaired and the cells persistently proliferate without undergoing terminal apoptosis (4, 5). If the leukemic cells could be forced to stop proliferating and turned to differentiation, the malignancy would be controlled. Hence, the idea toward eliminating the maturation block and inducing differentiation contributes to the development of the differentiation therapy (6, 7). Differentiation therapy is easily monitored because hematopoietic cells have a broad range of surface biomarkers and specific morphological features (8). The differentiation-inducing agent, All-trans retinoic acid (ATRA, tretinoin) is effective in the treatment of acute promyelocytic leukemia (APL), the M3 subtype of AML (9). However, there has been no remarkable progress in the treatment of the other 90% of AML cases. Moreover, AML with the mixed lineage leukemia (MLL) gene rearrangements (MLLr) found in about 10% of AML often associated with subtypes M4 and M5 of AML, that are associated with poor prognosis (10, 11). Therefore, finding new differentiation inducers against MLLr of AML is urgently needed. Natural products have been shown to possess multi-faceted mechanism that can target multiple pathways that are deregulated in cancer cells to achieve greater therapeutic efficacy.

Our previous work had shown that OGP46 have been shown to have anti-proliferative effect in leukemic cells such as BaF3-T315I and K562 cells (12). OGP46 also possessed anti-proliferative activity in solid tumor cells including SMMC-7721.25, A549, Eca-109, and MCF-7 cells (13–15). Jiyuan oridonin A (JOA), a kaurene diterpenoid compound isolated from *Isodon rubescens*, has similar structure to OGP46. In the current study, we explored whether JOA possesses anti-leukemia activity against MLLr AML cells including MV4-11, MOLM-13 and THP-1.

## MATERIALS AND METHODS

### Chemicals

We have prepared JOA with purity of 98.5% by isolating it from *Isodon rubescens* (15), which is similar to OGP46. The sole difference of the two compounds is the substituent of the C20. The chemical structure of JOA with a molecular weight of 348.2 and OGP46 were shown in **Figure 1A**. JOA and Cytosine arabinoside (Ara-C) were dissolved in dimethyl sulfoxide (DMSO) to 10 mM stock solutions and stored at -20°C. The same concentration of DMSO as corresponding to JOA solution diluted in RPMI 1640 medium was used as the control. The final DMSO concentrations during all incubations were not more than 0.1%, which had no observable toxic effects to cells. Fluorescein Isothiocyanate (FITC)/Annexin V Apoptosis Detection Kit and Propidium iodide (PI)/RNase staining solution were obtained from BD Biosciences (San Jose, CA, USA). Cell Counting Kit-8 (CCK-8) was purchased from Solarbio (Beijing, China). PE anti- CD13 (cat #301704 RRID: AB\_314180), FITC anti- CD14 (cat #301804, RRID: AB\_314186) and PE anti- CD15 (cat #301906, RRID: AB\_314198) were obtained from Biolegend (Inc, San Diego, CA, USA). MethoCult H4100 (cat #04100) and H4435 (cat #04435) were obtained from STEMCELL Technologies Inc. (Vancouver, BC, Canada). Antibodies against GAPDH (Cat #5174) was obtained from Cell Signaling Technology (Beverly, MA, USA). Antibodies against ALDH3A1 (EPR7406) and c-KIT (EPR22566-344) were obtained from Abcam (Cambridge, MA, USA). Antibody against CALML6 (SAB 1402033) was purchased from Sigma-Aldrich. The 2×SYBR Green qPCR Mix (cat #AH0104-B), SPARKscript II RT Plus kit (cat #AG0304-B), Spark ECL Plus A (cat #ED0015-C), Spark ECL Plus B (cat #ED0016-C) and RIPA

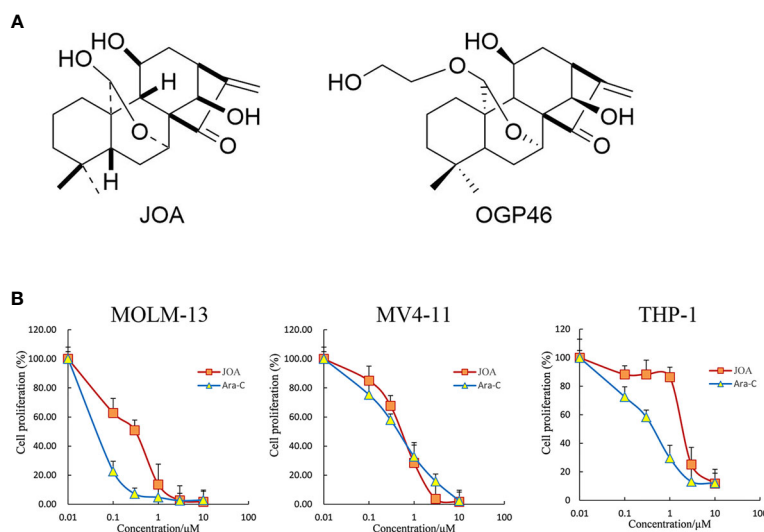


**FIGURE 1** | JOA reduces the proliferation of MV4-11, MOLM-13 and THP-1 cells. **(A)** The chemical structure of JOA and OGP46. **(B)** The effect of JOA in inhibiting cellular proliferation. Cells were treated with different concentrations of JOA or Ara-C (0–10 μM) for 72 h, and subjected to CCK-8 assay. Error bars represent the mean ± SD. The CCK-8 assay was carried out for four times in triplicate.

buffer (SparkJade EA0002) were purchased from SPARKJADE (Shandong, China).

## Cell Lines and Cell Culture

MOLM-13 (AML with MLLr expressing FLT3/ITD mutation, DSMZ No.: ACC 554), MV4-11 (AML with MLLr expressing FLT3/ITD mutation, DSMZ No.: ACC 102), and THP-1 (AML with MLLr expressing wild -type FLT3, DSMZ No.: ACC 16) cell lines were used. These cell lines were grown in RPMI-1640 medium containing 10% FBS and streptomycin/penicillin (1%) with 5% CO<sub>2</sub> at 37°C.

## Cell Proliferation Assay

The proliferation of MV4-11, MOLM-13, and THP-1 cells was evaluated by CCK-8 assay. Briefly, cells were seeded in 96-well plate with about  $5 \times 10^3$  cells in each well. The cells were treated with JOA or Ara-C (0–10  $\mu$ M) after 24 h of incubation. 72 h later, CCK-8 reagent (10  $\mu$ L) was added to each well, and cells were incubated at 37°C for 4 h. The light absorbance at 450 nm was measured by using an Osys microplate reader (Dynex Technologies, Chantilly, VA, USA). Results are expressed as percent of cell viability normalized to DMSO-treated control cells.

## Colony Formation Assay

MV4-11, MOLM-13 and THP-1 cells were cultured with JOA (0–2  $\mu$ M) in 2.6% methycellulose medium containing 10% FBS in a 24-well flat-bottomed plate for 12 days. The number of individual colonies consisting of more than approximately 50 cells was counted by a CX43 microscope (Olympus, Shinjuku-ku, Tokyo, Japan) with an Olympus EP50 camera (Olympus, Shinjuku-ku, Tokyo, Japan).

## Cell Cycle Analysis

MV4-11, MOLM-13 and THP-1 cells were incubated with JOA for 48 or 72 h. After treatment, cells were collected and fixed with 70% pre-cold ethanol in PBS and stored at -20°C for at least 24 h. Then the cells were stained with 50 mg/mL PI and 100 mg/mL RNase A for 30 min in the dark at room temperature. Finally, flow cytometry was used to detect the percentage of cells in the sub-G1, G0/G1, S, and G2/M phases with a Beckman Coulter DxFLX flow cytometer (Florida, Miami, USA). The data was analyzed and fitted by ModFit software.

## Cell Apoptosis Analysis

MV4-11, MOLM-13 and THP-1 cells were treated with JOA (0.25–4  $\mu$ M) or Ara-C (0.5–4  $\mu$ M) for 72 h, collected and resuspended in 1× binding buffer. Cells were incubated with FITC Annexin V and PI double labeling for 30 min in the dark at room temperature and measured by flow cytometry.

## Analysis of Cell Morphology

MV4-11, MOLM-13 and THP-1 cells were incubated with JOA or Ara-C for 72 h and then collected. Slides were made by cytospin and subsequently air dried. The cells were stained with Wright-Giemsa and observed for morphological features using a light microscope.

## Cell Surface Antigens Measurement

After treatment with JOA for 72 h, the cells were centrifuged, collected and washed, and incubated with different antibodies for 30 min at room temperature in the dark. Cell surface antigens analysis was carried out by using a flow cytometer.

## mRNA-Sequencing Analysis

mRNA-Sequencing (mRNA-seq) was performed for MOLM-13 and THP-1 cells. As described in a previous work [12], after incubating with JOA for 48 h, cells were collected for RNA extraction. Sequencing libraries were prepared and then sequenced using 150 bp pair-end strategies with an Illumina HiSeq X10 instrument (Annoroad Genomics, Beijing, China). The mRNAs levels were estimated using FPKM (fragments per kilobase of exon per million fragments mapped). Differential expression analysis was performed using DESeq R packages. A corrected p value of 0.05 and absolute value of log<sub>2</sub> FC (fold change)  $\geq 0.58$  was set as a threshold of differential expression of genes (DEGs). Gene Set Enrichment Analysis (GSEA) was conducted and C2 curated functional gene sets from the Molecular Signature Database (<http://www.gsea-msigdb.org/gsea/msigdb>) for MOLM-13 cell line. In addition, the method of geometric test was used to enrich the DEGs from the Gene Ontology and Kyoto Encyclopedia of Genes and Genomes (KEGG) databases in THP-1 cell line. The clusterProfiler package of R software was used to the enrichment analysis of DEGs in both methods. The pathways with an adjusted p value of  $< 0.05$  were considered significantly enriched.

## Verification of Expression Difference Genes by Real-time PCR (RT-PCR)

The total RNAs of MOLM-13 and THP-1 cells treated with JOA were extracted using the Trizol reagent. Reverse transcription for first strand of cDNA was performed using the Primerscript RT reagent kit with gDNA Eraser. The following primers were used to amplify cDNA: forward GAPDH 5'-TGGGTGTGAA CCATGAGAAGT-3', reverse GAPDH 5'-TGAGTCCTTCC ACGATACCAA-3'; forward c-KIT 5'-TGACTTACGACA GGCTCGTG-3', reverse c-KIT 5'-CCACTGGCAGTA CAGAAGCA-3'; forward ALDH3A1 5'-TGTGTCAAAGG CGCCATGAGCAAG-3', reverse ALDH3A1 5'-GGCGTTCC ATTCATTCTTGTGCAG-3'; forward CALML6 5'-GGGCTACATTGACTGG AACACAC-3', reverse CALML6 5'-CCTCATAGTCGATGGTCTCTGTC-3'.

## Western Blotting Analysis

After treatment with JOA for 72 h, the MOLM-13 and THP-1 cells were lysed by RIPA buffer with proteinase inhibitors. The protein lysates were separated by sodium dodecyl sulfate polyacrylamide gel (SDS-PAGE), then transferred to PVDF membrane. After blocked by 10% skimmed milk, the membranes were incubated with specific primary antibodies overnight at 4°C, followed by the incubation with goat anti-rabbit or goat anti-mouse immunoglobulin G (IgG) antibodies for 1 hour at room temperature. The expression of proteins was visualized using an enhanced chemiluminescence (ECL) reagent

detection system (Amersham Imager 600; GE Healthcare Biosciences, Pittsburgh, PA, USA).

## Statistical Analysis

All experiments were repeated at least three times unless otherwise stated. The data were represented as mean  $\pm$  SD. Statistical analysis were performed with Student's *t* test for two-group comparisons and using one-way ANOVA with Tukey's *post hoc* test for multigroup comparisons, and  $p < 0.05$  or  $p < 0.01$  were considered statistically significant.

## RESULTS

### JOA Possesses Anti-Leukemic Activity Against MLLr AML Cell Lines

Cells were treated with different concentrations of JOA or Ara-C (0–10  $\mu$ M) for 72 h, and CCK-8 assay was carried out to test the effect of JOA on cell proliferation as compared to Ara-C. As shown in **Figure 1B**, JOA significantly reduced the proliferation of MV4-11, MOLM-13 and THP-1 cells with the  $IC_{50}$  value of 0.62, 0.42, 2.19  $\mu$ M, respectively, that were comparable with those of Ara-C which was 0.52, 0.07 and 0.50  $\mu$ M, respectively. This finding revealed that JOA has the activity against the proliferation of MLLr AML cells. Moreover, JOA has similar anti-proliferative effect as Ara-C on MV4-11 cells. In addition,

MOLM-13 and MV4-11 cells, that carried FLT3/ITD mutation, are more sensitive to JOA than THP-1 cells that had wild-type FLT3.

### JOA Inhibits Colony Formation of MLLr AML Cells

The effect of JOA on the colony forming capacity of MV4-11, MOLM-13 and THP-1 cells was next investigated. Cells were treated with JOA at the concentrations of 0.25–2  $\mu$ M for 12 days and the formation of colonies was observed under a microscope. It was found that JOA significantly decreased the number of colonies in a concentration-dependent manner. Moreover, the MV4-11, MOLM-13 and THP-1 cells failed to form colonies when treated with 1–2  $\mu$ M JOA (**Figure 2**). This result indicated that the colony-forming capacity of MLLr AML cells was significantly inhibited by JOA treatment.

### JOA Induces Cell Cycle Arrest at G0/G1 in MLLr AML Cell Lines

The effect of JOA on cell-cycle progression was evaluated in MOLM-13, MV4-11 and THP-1 cells. MV4-11, Cells were treated with 0.5, 0.5, 1 or 2  $\mu$ M JOA, respectively for 48 h or 72 h, and the percentage of cells in various phase of cell cycle was analyzed with flow cytometry. As shown in **Figure 3**, the percentage of cells in G0/G1 phase increased in a time-dependent manner in these cells. This result suggested that

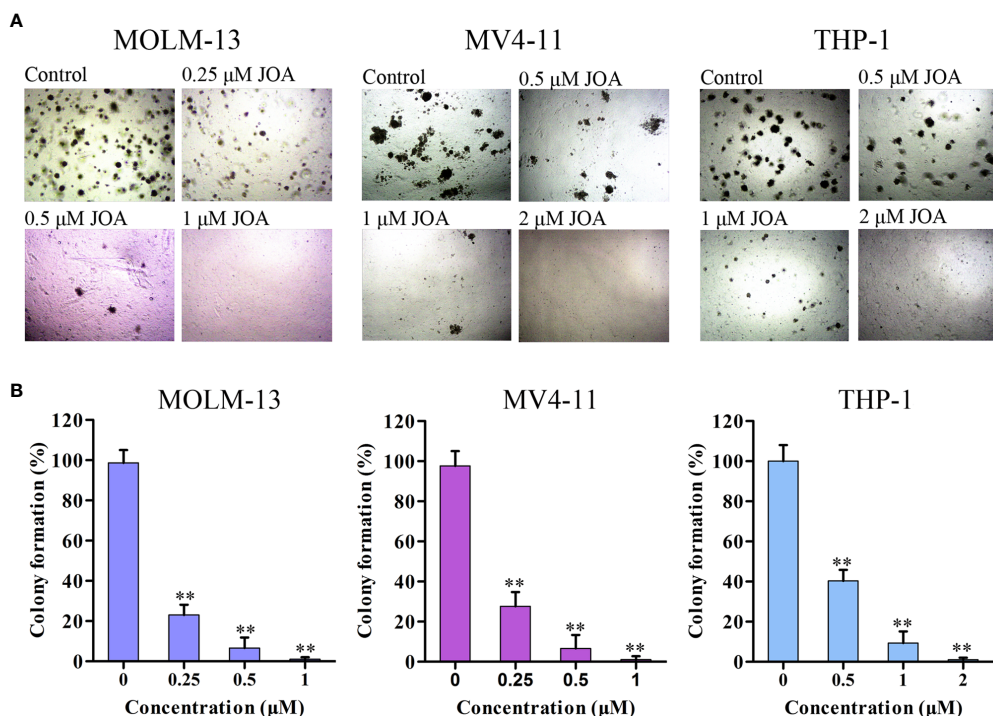


**FIGURE 2 |** JOA suppresses the colony formation in MV4-11, MOLM-13 and THP-1 cells. **(A)** Cells were treated with JOA at the concentrations of 0.25–2  $\mu$ M for 12 days then the cell morphology was observed under light microscopy. **(B)** Graph bars show the number of colonies (\*\* $p < 0.01$ ). The colony formation assay was performed for three times.

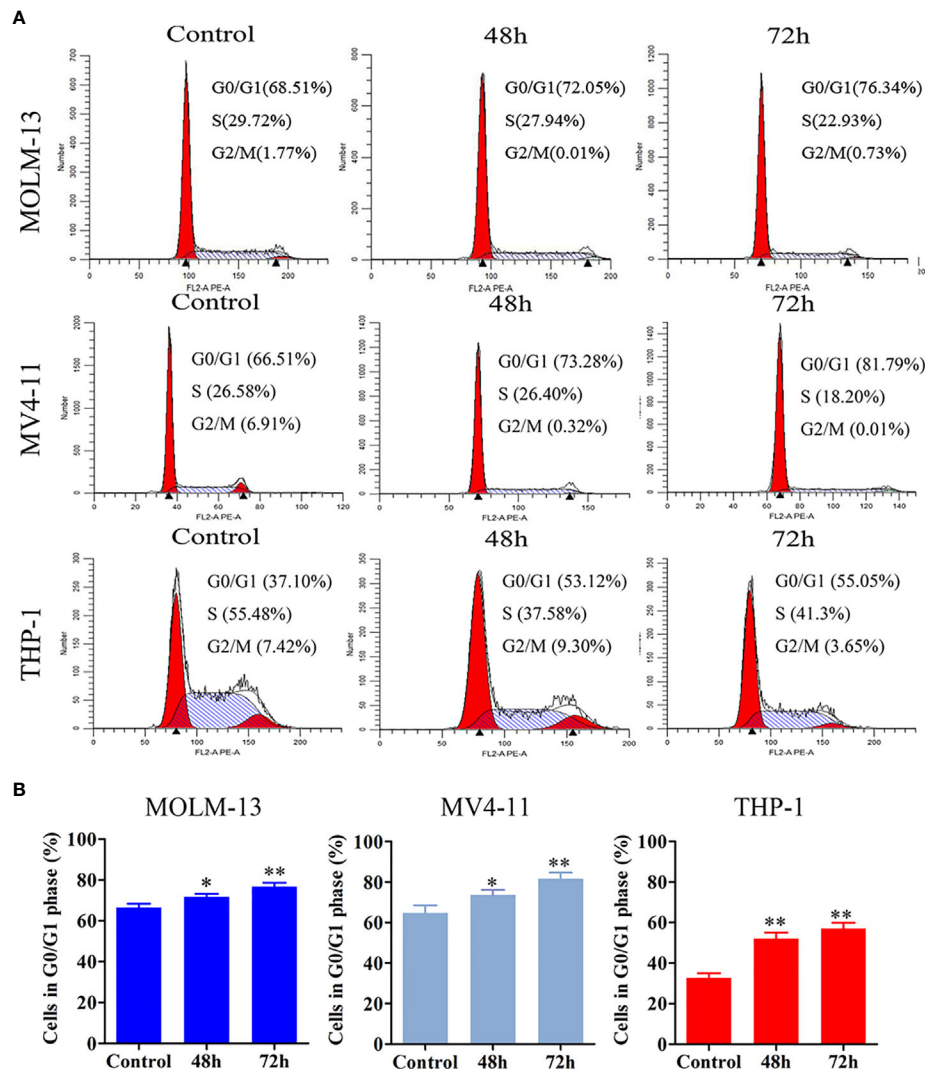


**FIGURE 3 |** JOA induces cell cycle exit in MV4-11, MOLM-13 and THP-1 cells. **(A)** MV4-11, MOLM-13 and THP-1 cells were treated with 0.5, 0.5 or 2  $\mu$ M JOA, respectively for 48 h or 72 h, then flow cytometry was used to detect the percentage of cells in various phase of the cell cycle. **(B)** Graph bars show the percentage of cells in G0/G1 phase. (\* $p < 0.05$ , \*\* $p < 0.01$ ). The cell cycle analysis was performed for four times.

JOA inhibits cell proliferation through inducing a G0/G1 cell cycle exit in MLLr AML cells.

### JOA Induces Minimal Signs of Apoptosis in MLLr AML Cell Lines

In order to examine whether the anti-proliferation of JOA is associated with the induction of apoptosis, MV4-11, MOLM-13, and THP-1 cells were treated with different concentrations of JOA or Ara-C for 72 h and cell apoptosis was determined by flow cytometric analysis. As shown in **Figures 4A, B**, no significant apoptosis was observed when MOLM-13 and MV4-11 cells were incubated with JOA (0.25, 0.5, or 1  $\mu$ M). Similarly, minimal signs of apoptosis were found in THP-1 cells treated with 1 or 2  $\mu$ M JOA. In contrast, Ara-C led to the obvious apoptosis in all three cell lines at indicated concentration. This data revealed that the

cell-cycle exit was not associated with cell apoptosis in MV4-11, MOLM-13 and THP-1 cells treated with JOA at 0.5, 0.5, 2  $\mu$ M, respectively. The concentration of JOA will be used to treat the cell lines in subsequent experiment.

### JOA Promotes Cell Differentiation in MLLr AML Cell Lines

Because JOA did not cause the apoptosis of MV4-11, MOLM-13 and THP-1 cells at the indicated concentration, morphology and flow cytometry analysis were carried out to assess the differentiation of these cells treated with JOA. A set of four myeloid biomarkers (CD11b, CD13, CD14 and CD15) were assessed to analyze the cell phenotype. It was seen that all the three cell lines showed increased cell size with a decrease in the nuclear-cytoplasmic ratio, indicating that JOA induced the cell



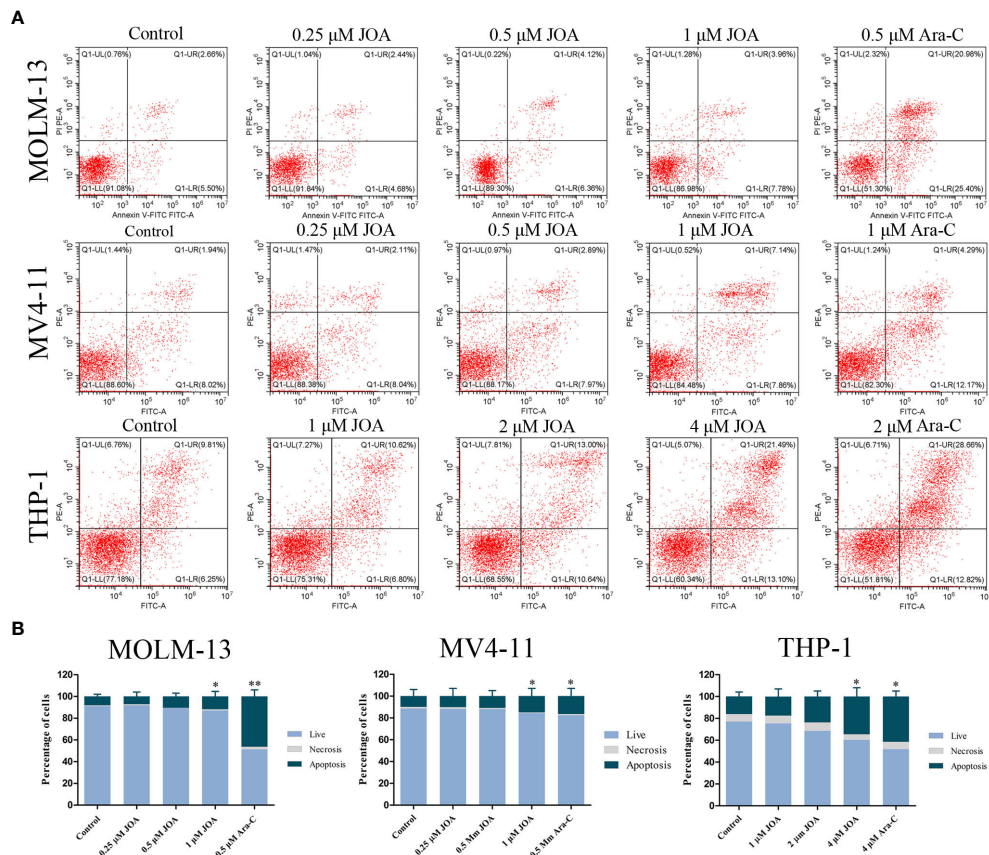


**FIGURE 4 |** JOA does not induce significant apoptosis in MV4-11, MOLM-13 and THP-1 cells. **(A)** Cells were treated with JOA or Ara-C for 72 h and cell apoptosis was determined by flow cytometric analysis. **(B)** Graph bars show the percentage of living cells and cells undergoing necrosis/apoptosis. MOLM-13, MV4-11 cells were treated with 0.25, 0.5, 1  $\mu$ M JOA or Ara-C (0.5 or 1  $\mu$ M) and THP-1 were treated with 1, 2, 4  $\mu$ M JOA or 4  $\mu$ M Ara-c for 72h. (\* $p$  < 0.05, \*\* $p$  < 0.01). The cell apoptosis analysis was performed for four times.

differentiation accompanied with morphological changes, while Ara-C did not promote cell differentiation (**Figure 5A**). Moreover, JOA increased the expression of CD15 (a monocyte/macrophage biomarker) in all these three leukemia cell lines (**Figures 5B, C**). In addition, JOA significantly increased the expression of CD11b (ITGAM, a monocyte/granulocyte biomarker) in THP-1 cells. These results suggested that JOA induces cell differentiation in MLLr AML cells.

### JOA Induces Cell Differentiation Is Associated With Multiple Signaling Pathways Depending on Cell Type

To elucidate the molecular mechanism of cell differentiation-mediated by JOA, we performed global gene expression analyses by mRNA-seq in MOLM-13 and THP-1 cells. The volcano plots of MOLM-13 and THP-1 cells were shown in **Figure 6A**. A total of 14 genes were down-regulated and 13 genes were up-regulated in MOLM-13 cells. Similarly, the expression of 165 genes decreased, and 83 genes increased in THP-1 cells, indicating that the different effect of JOA on the expression of different genes. This result suggested that JOA does not universally affect

the mRNA expression of all genes in these cells. As shown in **Figure 6B**, aldehyde dehydrogenase 3A1 (ALDH3A1) was markedly down-regulated, whereas the calcium binding protein calmodulin (CALML6) and LPIN3 were significantly up-regulated in MOLM-13 cells incubated with JOA. Simultaneously, genes such as ITGAM (CD11b), CR1, FCER2, OCLN, HMOX1 were significantly up-regulated and genes including c-KIT, cell adhesion molecules (CD99, HLA-DQA1, HLA-DRA, HLA-DPA1, HLA-DPB1) were significantly down-regulated in THP-1 cells after JOA treatment. GSEA analysis showed that the most optimal pathway induced by JOA was martens tretinoin response up (AML-induced differentiation) pathway in MOLM-13 cells. In contrast, the DEGs were enriched in the hematopoietic cell lineage, cell adhesion molecules and phagosome pathways in THP-1 cells (**Figure 6C**).

The DEGs identified by mRNA-seq play important role in cell differentiation. To confirm their expression in the MLLr AML cells, RT-PCR and Western blotting were carried out in MOLM-13 and THP-1 cell lines. It was found that JOA treatment markedly changed the expression of mRNA and protein of ALDH3A1 and CALML6 in MOLM-13 cells and the

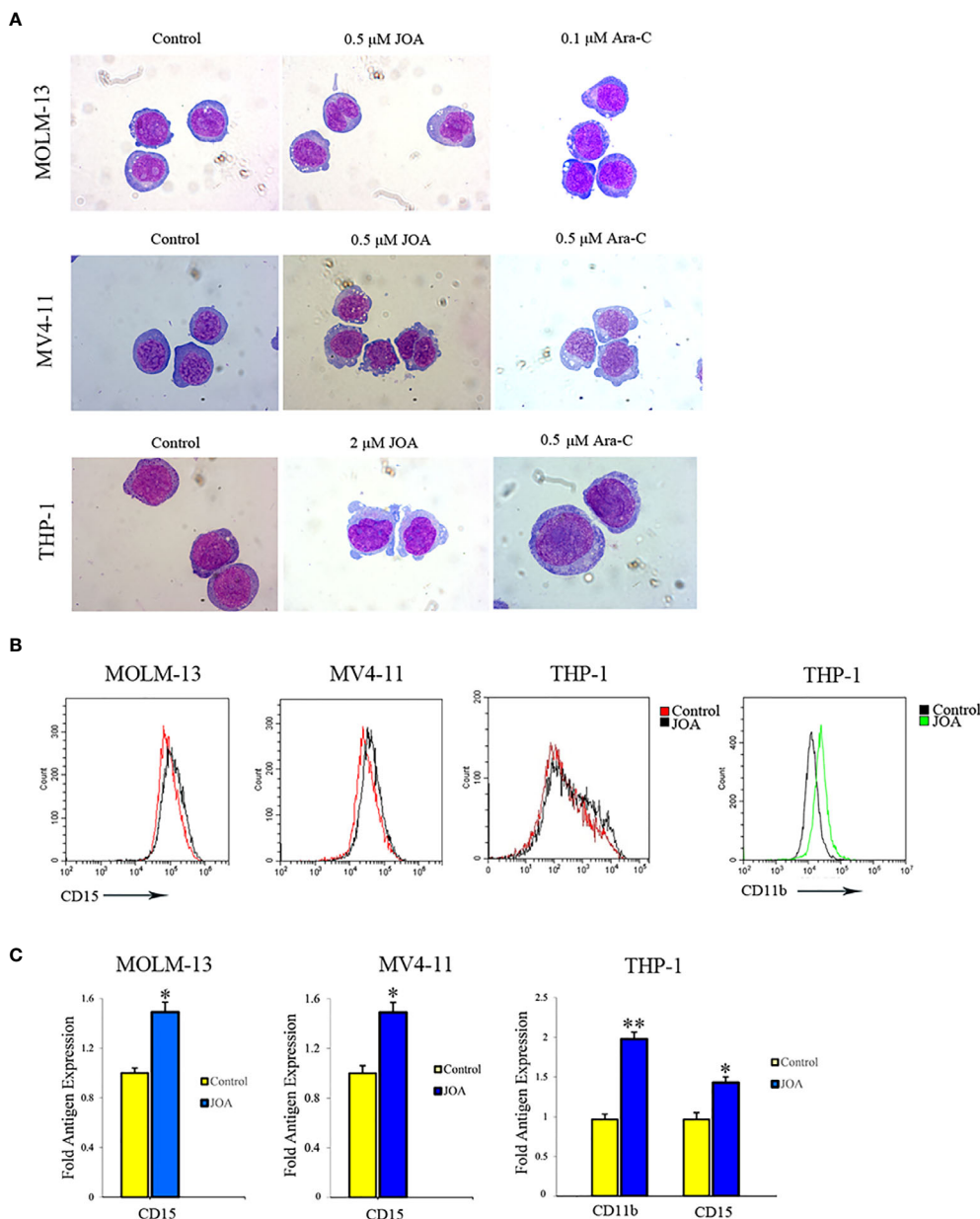


**FIGURE 5 |** JOA induces differentiation of MV4-11, MOLM-13 and THP-1 cells. **(A)** Wright-Giemsa staining images of cells captured by oil immersion lens ( $\times 1,000$ ). **(B)** The expression of cell-surface antigens was measured by flow cytometry. **(C)** Graph bars show the mean fluorescence intensity (MFI) of antigens. MV4-11, MOLM-13 and THP-1 cells were incubated with 0.5, 0.5 or 2  $\mu$ M JOA, or Ara-C at the concentration of 0.1, 0.5 or 0.5  $\mu$ M for 72 h, respectively (\* $p < 0.05$ , \*\* $p < 0.01$ ). The figures are representative of three independent experiments.

expression of c-KIT was significantly down-regulated at both transcription and protein level in THP-1 cells (**Figure 7**). These results were in consistent with the results of mRNA-seq.

## DISCUSSION

AML accounting for 75% of acute leukemia, is a heterogeneous disease characterized by accumulation of immature myeloid

cells in bone marrow and peripheral blood with abnormal proliferation and differentiation blockade (9, 16). In the past decades, chemotherapy consisting of Ara-C and anthracycline is used for the first-line treatment of AML (17). Although the complete remission rate is high initially, the adult five-year overall survival of AML patients is less than 40% because of chemotherapy resistance (18). Recently, the recognition of origins and drivers of the pathogenesis of AML enabled the development of novel therapeutics in targeting multiple

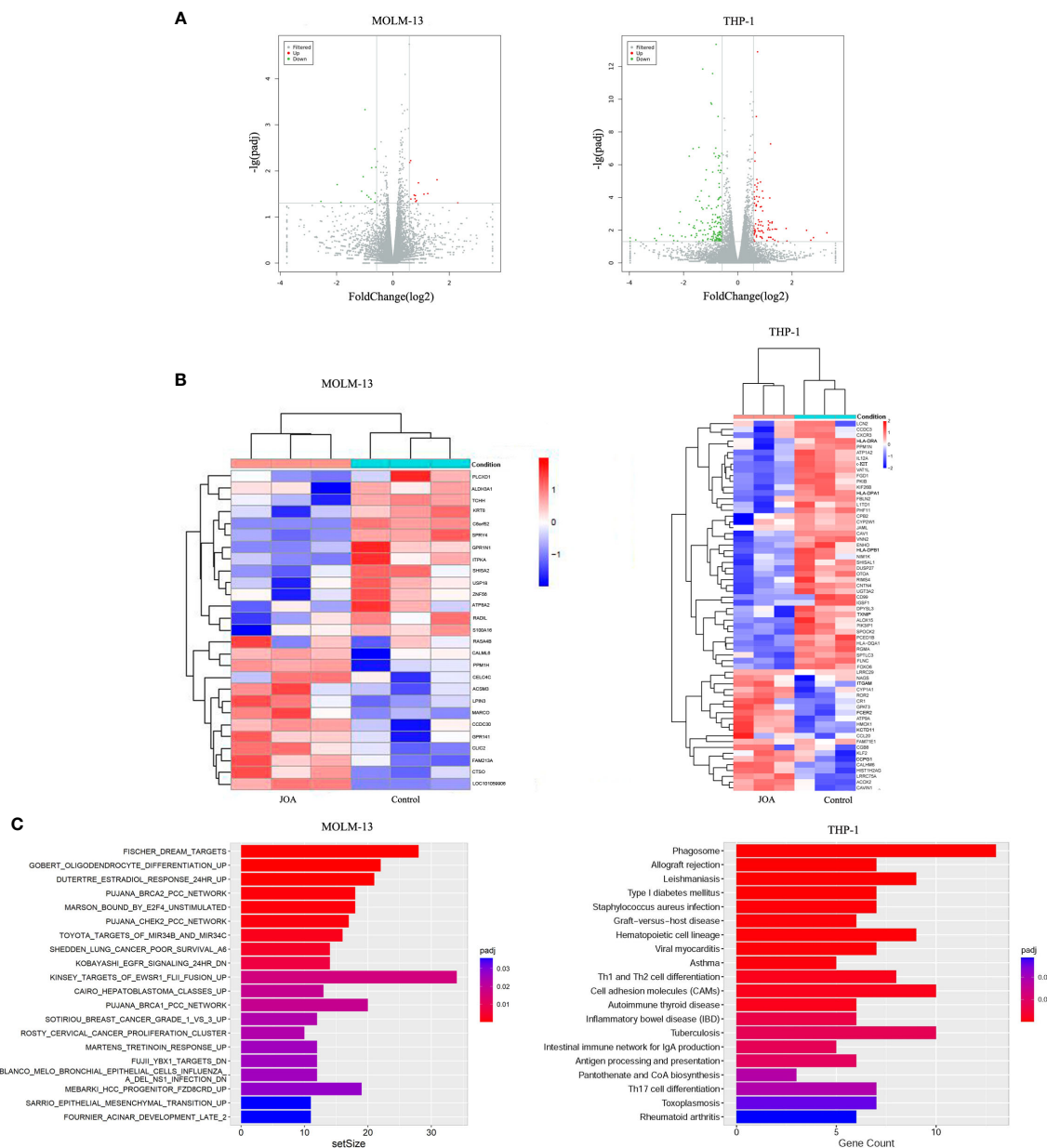


**FIGURE 6** | JOA promotes cell differentiation *via* multiple pathways depending on cell type. MOLM-13 and THP-1 Cells were incubated with 0.5 or 2  $\mu$ M JOA, respectively for 72 h. **(A)** Volcano plots of MOLM-13 and THP-1 cells. **(B)** The heatmap of DEGs. The heatmap bars from blue to red represents the expression levels of genes from lower to higher. (100 genes with  $p < 0.05$  and  $|\log_2 FC| > 0.58$  based on their  $p$  value in the THP-1 cells). **(C)** KEGG pathway analyses on the differentially expressed genes. MOLM-13 and THP-1 cells were incubated with 0.5, or 2  $\mu$ M JOA for 72 h, respectively. The figures are representative of two independent experiments.

signaling pathways such as proteasome pathway, apoptosis, c-Myc signaling and hedgehog pathway (19, 20). The differentiation therapy using ATRA dramatically improved the long-term clinical outcome for APL patients, which attributed to the ATRA-induced degradation of PML/RAR $\alpha$  by the proteasome pathway. Moreover, ATRA treatment converted the AML subtype from a bad prognostic leukemia to a curable one (21). However, clinical effectiveness of ATRA-

based differentiation therapy has no effect in other AML subtypes (22). In addition, MLL-rearranged AML has been associated with poor outcome despite intensive chemotherapy. Therefore, the development of potent small molecules to overcome these drawbacks may be offer alternative or complementary therapies. In the current study, we investigate the role of a novel diterpenoid compound JOA on the differentiation of MLLr AML cells.

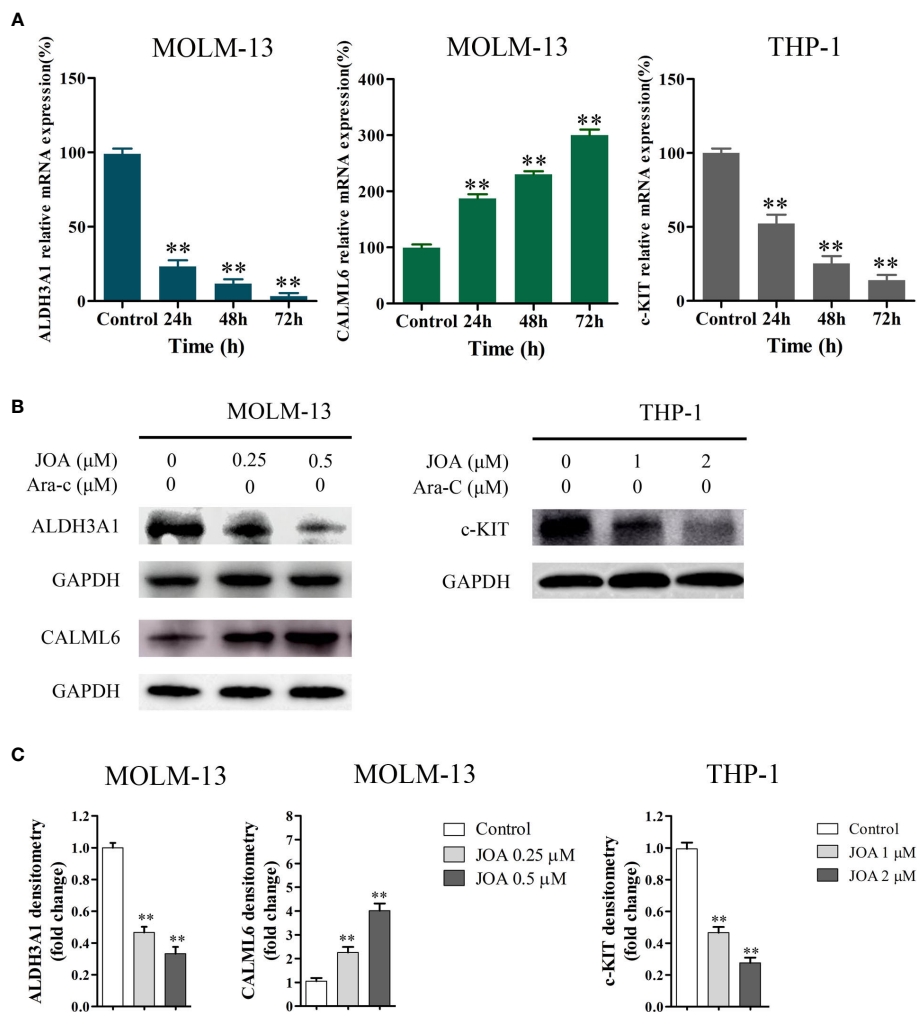


**FIGURE 7** | The RT-PCR and Western blotting analysis of DEGs in MOLM-13 and THP-1 cells. **(A)** The effects of JOA on the mRNA expression of ALDH3A1, CALML6 and c-KIT evaluated by RT-PCR **(B)** ALDH3A1, CALML6 and c-KIT protein levels measured by Western blotting analysis. **(C)** Graph bars show the protein expression visualized and quantified by Al600 imager. MOLM-13 and THP-1 cells were incubated with 0.5, or 2 μM JOA for 72 h, respectively. (\*\*p < 0.01). The figures are representative of four independent experiments.

The analog of JOA, OGP46, have been found to exert antileukemic effect on various CML cell lines, such as K562 and BaF3 cells that expressed BCR-ABL wild-type or mutations, by cell differentiation (12). Here, we found that JOA significantly inhibited cell proliferation, colony formation by cell differentiation of MLLr AML cells, as evidenced by the morphological changes, increasing expression of the cell surface antigen CD15 or CD11b. We found that the cell differentiation was coupled with cell-cycle exit at G0/G1. Furthermore, JOA significantly up-regulated the expression of CALML6 at both mRNA and protein level in MOLM-13 cells, and it remarkably down-regulated the expression of c-KIT at both transcription and protein levels in THP-1 cells. Taken together, we found that JOA is effective against MLLr AML cells by inducing cell differentiation. Moreover, MOLM-13 and MV4-11 cells are more sensitive to JOA than THP-1 cells.

It is revealed that martens tretinoin response up pathway was involved in the treatment of MOLM-13 cells with JOA (**Figure 6C**). Genes including CALML6 (calcium binding protein calmodulin [CAM]), LPIN3, SEMA6B, FGR, LRFN3, SCIMP and TREM2 were enriched in this pathway, which regulates AML cell differentiation, RAR signaling, and epigenetic control (23). In this study, we showed that JOA had an anti-proliferative effect on MLLr AML cells by inducing cell differentiation. In addition, the expression of CALML6 were significantly up-regulated in MOLM-13 cells with JOA treatment. In addition, it is revealed that  $Ca^{2+}$ /CaM activation is involved in dendritic cell-like differentiation of U937 cells (24). Therefore, it may be concluded that JOA up-regulated the expression of CALML6 which may induce cell differentiation of MOLM-13 cells. The detailed mechanism need to be further investigated. Hence, these results indicate that the differentiation of MOLM-13 cells occurs



perhaps *via* a martens tretinoin response up pathway activated by JOA.

Hematopoietic cell lineage is critical for the differentiation of basophils, eosinophils, macrophages, neutrophils, and myeloid-derived dendritic cells (25, 26). The lineage differentiation is down-regulated by c-KIT (CD117). c-KIT is a typical biomarker for undifferentiated hematopoietic cells and plays an important role in the differentiation and proliferation of leukemia cells (27, 28). Our present study showed that JOA treatment induced cell differentiation with morphological changes, increased the expression of CD11b and CD15, and alteration of cell adhesion molecules such as CD99, HLA-DRA, HLA-DQA1, HLA-DPA1, and HLA-DPB1 in THP-1 cells. JOA treatment also down-regulated the mRNA and protein level of c-KIT. Therefore, JOA-mediated differentiation of THP-1 cells might be through the alteration of lineage-specific target genes, and be related to hematopoietic cell lineage pathway *via* inhibition of c-KIT expression.

Cell adhesion molecules are a group of membrane glycoproteins and carbohydrate molecules that mediate cells to communicate with one another and their environment (29). They play important role in cellular functions, including proliferation and differentiation. Here, JOA treatment resulted in the alteration of cell adhesion molecules such as CD11b and CD99 (less expression of them indicating the more differentiated leukemia cells) (30), CD15 and major histocompatibility complex (MHC) class II genes (immune regulation antigens including HLA-DRA, HLA-DQA1, HLA-DPA1, HLA-DPB1) in THP-1 cells. Hence, the alteration of cell adhesion molecules combined with the change of cell morphology and increasing expression of CD11b and CD15 indicates that the cell differentiation induced by JOA is associated with cell adhesion molecules pathway.

As describe above, JOA treatment increased expression of CD15 and CD11b, that are biomarkers of monocyte/macrophage and monocyte/granulocyte differentiation, respectively, suggesting that treatment with JOA promoted the commitment of THP-1 cells into the monocyte/macrophage or monocyte/granulocyte lineage. Moreover, JOA treatment altered the expression of genes including CD11b, HLA-DRA, HLA-DRB5, HLA-DQA1, HLA-DPA1, HLA-DPB1, NCF2, MARCO, TLR6, HLA-F, TUBB4A, FCAR, and TUBA8. These genes were enriched in the phagosome pathway. It was revealed that monocyte/macrophages are involved in phagocytosis in enteritis through the phagosome pathway (31, 32). Therefore, it suggested that JOA induces monocyte/macrophages differentiation of THP-1 cells, and activates the phagosome pathway. The result is in accordance with that phagosome pathway was commonly activated in both MV4-11 and

Kasumi-1 AML cell lines treated with differentiation inducers, trichostatin A and 5-azacytidine (33).

Hence, the signaling pathways triggered in response to JOA treatment are different in MOLM-13 and THP-1 cells. It was shown that JOA mainly targeted the genes in the martens tretinoin response up pathway in the MOLM-13 cells, whereas it targeted the genes in cell adhesion molecules and hematopoietic cell lineage pathways in the THP-1 cells. These differences might be due to their different molecular characteristics (FLT3/ITD mutation vs wild -type FLT3).

In conclusion, our findings reveal that JOA possess anti-proliferation effect on MLLr AML cells perhaps through martens tretinoin response up pathway involving the CALML6 up-regulations, or hematopoietic cell lineage by depletion of c-KIT and cell adhesion molecules pathways depending on the cell type, which results in cell differentiation. JOA could overcome differentiation block in MLLr AML cells, suggesting that JOA could be a potential compound that merits further development to overcome differentiation blockade in MLLr AML patients.

## DATA AVAILABILITY STATEMENT

The datasets presented in this study can be found in online repositories. The names of the repository/repositories and accession number(s) can be found here: GEO of NCBI, <https://www.ncbi.nlm.nih.gov/geo/query/acc.cgi?acc=GSE167083> repository, accession number is GSE167083.

## AUTHOR CONTRIBUTIONS

MQ: Conceptualization, methodology, and writing—original. YD: performed flow cytometry analysis. MZ: performed MTT assay. ZW: Data analysis. MJZ: performed Western blotting analysis. YZ: cell cycle analysis. HW: prepared the chemical reagent solutions. YK, YL, and H-ML: preparation of JOA. LW: Writing—review, editing, and supervision. ZH: Conceptualization and supervision. All authors contributed to the article and approved the submitted version.

## FUNDING

This work was supported by the National Natural Science Foundation of China (grants 8170016, 781370628 and 81570157) and Natural Science Foundation of Shandong Province (grant ZR2016HM47).

## REFERENCES

1. Cornell RF, Palmer J. Adult acute leukemia. *Disease-a-month: DM* (2012) 58 (4):219–38. doi: 10.1016/j.disamonth.2012.01.011
2. Wiseman DH, Greystoke BF, Somerville TC. The variety of leukemic stem cells in myeloid malignancy. *Oncogene* (2014) 33(24):3091–8. doi: 10.1038/onc.2013.269
3. Döhner H, Weisdorf DJ, Bloomfield CD. Acute myeloid leukemia. *N Engl J Med* (2015) 373:1136–52. doi: 10.1056/NEJMra1406184
4. Friend C, Scher W, Holland JG, Sato T. Hemoglobin synthesis in murine virus-induced leukemic cells in vitro: stimulation of erythroid differentiation by dimethyl sulfoxide. *Proc Natl Acad Sci United States America* (1971) 68 (2):378–82. doi: 10.1073/pnas.68.2.378
5. de Thé H. Differentiation therapy revisited. *Nat Rev Cancer* (2018) 18(2):117–27. doi: 10.1038/nrc.2017.103

6. Tsiftoglou AS, Pappas IS, Vizirianakis IS. Mechanisms involved in the induced differentiation of leukemia cells. *Pharmacol Ther* (2003) 100 (3):257–90. doi: 10.1016/j.pharmthera.2003.09.002
7. Ferrero D, Pessano S, Pagliardi GL, Rovera G. Induction of differentiation of human myeloid leukemias: surface changes probed with monoclonal antibodies. *Blood* (1983) 61(1):171–9. doi: 10.1182/blood.V61.1.171.171
8. Sachs L. The control of hematopoiesis and leukemia: from basic biology to the clinic. *Proc Natl Acad Sci* (1996) 93(10):4742–9. doi: 10.1073/pnas.93.10.4742
9. Mi JQ, Li JM, Shen ZX, Chen SJ, Chen Z. How to manage acute promyelocytic leukemia. *Leukemia* (2012) 26(8):1743–51. doi: 10.1038/leu.2012.57
10. Gole B, Wiesmüller L. Leukemogenic rearrangements at the mixed lineage leukemia gene (MLL)-multiple rather than a single mechanism. *Front Cell Dev Biol* (2015) 3:3389/fcell.2015.00041:41. doi: 10.3389/fcell.2015.00041
11. Wuchter C, Harbott J, Schoch C, Schnitter S, Borkhardt A, Karawajew L, et al. Detection of acute leukemia cells with mixed lineage leukemia (MLL) gene rearrangements by flow cytometry using monoclonal antibody 7.1. *Leukemia* (2000) 14(7):1232–8. doi: 10.1038/sj.leu.2401840
12. Wei L, Yang Y, Gupta P, Wang A, Zhao M, Zhao Y, et al. A Small Molecule Inhibitor, OGP46, Is Effective against Imatinib-Resistant BCR-ABL Mutations via the BCR-ABL/JAK-STAT Pathway. *Mol Ther Oncolytics* (2020) 18:137–48. doi: 10.1016/j.omto.2020.06.008
13. Ke Y, Wang W, Zhao LF, Liang JJ, Liu Y, Zhang X, et al. Design, synthesis and biological mechanisms research on 1,2,3-triazole derivatives of Jiyuan Oridonin A. *Bioorg Med Chem* (2018) 26(17):4761–73. doi: 10.1016/j.bmc.2017.11.005
14. Ke Y, Liang JJ, Hou RJ, Li MM, Zhao LF, Wang W, et al. Synthesis and biological evaluation of novel Jiyuan Oridonin A-1,2,3-triazole-azole derivatives as antiproliferative agents. *Eur J Med Chem* (2018) 157:1249–63. doi: 10.1016/j.ejmech.2018.08.056
15. Liu HM, Zhu WC, Zhu CG, Wang QD, Ke Y, Liu ZZ, et al. Novel entkaurene diterpene compound and its derivatives, their preparation and their use. Washington, DC: U.S. Patent and Trademark Office (2011). U.S. Patent No 8,084,430.
16. Estey E, Döhner H. Acute myeloid leukaemia. *Lancet (London England)* (2006) 368(9550):1894–907. doi: 10.1016/S0140-6736(06)69780-8
17. van Gils N, Verhagen H, Smit L. Reprogramming acute myeloid leukemia into sensitivity for retinoic-acid-driven differentiation. *Exp Hematol* (2017) 52:12–23. doi: 10.1016/j.exphem.2017.04.007
18. Kakizuka A, Miller WH Jr, Umesono K, Warrell RP Jr, Frankel SR, Murty VV, et al. Chromosomal translocation t (15;17) in human acute promyelocytic leukemia fuses RAR alpha with a novel putative transcription factor, PML. *Cell* (1991) 66(4):663–74. doi: 10.1016/0092-8674(91)90112-c
19. Carter JL, Hege K, Yang J, Kalpage HA, Kalpage HA, Kalpage H, et al. Targeting multiple signaling pathways: the new approach to acute myeloid leukemia therapy. *Sig Transduct Target Ther* (2020) 5:288–316. doi: 10.1038/s41392-020-00361-x
20. Yao JF, Zhao MJ, Wang JY, Wei LY. Advances in New Targets for Differentiation Therapy of Acute Myeloid Leukemia. *J Cancer Res Updat* (2020) 9:88–95. doi: 10.30683/1929-2279.2020.09.10
21. Wang ZY, Chen Z. Acute promyelocytic leukemia: from highly fatal to highly curable. *Blood* (2008) 111(5):2505–15. doi: 10.1182/blood-2007-07-102798
22. Olsson I, Bergh G, Ehinger M, Gullberg U. Cell differentiation in acute myeloid leukemia. *Eur J Haematol* (1996) 57(1):1–16. doi: 10.1111/j.1600-0609.1996.tb00483.x
23. Martens JHA, Brinkman AB, Simmer F, Francois K-J, Nebbioso A, Ferrara F, et al. PML-RAR $\alpha$ /RXR Alters the Epigenetic Landscape in Acute Promyelocytic Leukemia. *Cancer Cell* (2010) 17:173–85. doi: 10.1038/sj.leu.2403826
24. Kandilci A, Grosveld GC. SET-induced calcium signaling and MAPK/ERK pathway activation mediate dendritic cell-like differentiation of U937 cells. *Leukemia* (2005) 19(8):1439–45. doi: 10.1038/sj.leu.2403826
25. Tenen DG. Disruption of differentiation in human cancer: AML shows the way. *Nat Rev Cancer* (2003) 3(2):89–101. doi: 10.1038/nrc989
26. De Marchis ML, Ballarino M, Salvatori B, Puzzolo MC, Bozzoni I, Fatica A. A new molecular network comprising PU.1, interferon regulatory factor proteins and miR-342 stimulates ATRA-mediated granulocytic differentiation of acute promyelocytic leukemia cells. *Leukemia* (2009) 23 (5):856–62. doi: 10.1038/leu.2008.372
27. Tokuhisa M, Kadowaki T, Ogawa K, Yamaguchi Y, Kido MA, Gao W, et al. Expression and localisation of Rab44 in immune-related cells change during cell differentiation and stimulation. *Sci Rep* (2020) 10(1):10728. doi: 10.1038/s41598-020-67638-7
28. Ashman LK, Griffith R. Therapeutic targeting of c-KIT in cancer. *Expert Opin Invest Drugs* (2013) 22(1):103–15. doi: 10.1517/13543784.2013.740010
29. Freemont AJ, Hoyland JA. Cell adhesion molecules. *Clin Mol Pathol* (1996) 49 (6):M321–30. doi: 10.1136/mp.49.6.m321
30. Chung SS, Eng WS, Hu W, Khalaj M, Garrett-Bakelman FE, Tavakkoli M, et al. CD99 is a therapeutic target on disease stem cells in myeloid malignancies. *Sci Trans Med* (2017) 9(374):eaaj2025. doi: 10.1126/scitranslmed.aaj2025
31. Grainger JR, Konkel JE, Zangerle-Murray T, Shaw TN. Macrophages in gastrointestinal homeostasis and inflammation. *Pflugers Archiv: Eur J Physiol* (2017) 469(3-4):527–39. doi: 10.1007/s00424-017-1958-2
32. Landsverk OJ, Bakke O, Gregers TF. MHC II and the endocytic pathway: regulation by invariant chain. *Scand J Immunol* (2009) 70(3):184–93. doi: 10.1111/j.1365-3083.2009.02301.x
33. Asmaa MJS, Al-Jamal HA, Hussein AR, Yahaya BH, Hassan R, Hussain FA, et al. Transcriptomic Profiles of MV4-11 and Kasumi 1 Acute Myeloid Leukemia Cell Lines Modulated by Epigenetic Modifiers Trichostatin A and 5-Azacytidine. *Int J Hematol Oncol Stem Cell Res* (2020) 14(1):72–92. doi: 10.18502/ijhoscr.v14i1.2362

**Conflict of Interest:** The authors declare that the research was conducted in the absence of any commercial or financial relationships that could be construed as a potential conflict of interest.

Copyright © 2021 Qu, Duan, Zhao, Wang, Zhao, Zhao, Wang, Ke, Liu, Liu, Wei and Hu. This is an open-access article distributed under the terms of the Creative Commons Attribution License (CC BY). The use, distribution or reproduction in other forums is permitted, provided the original author(s) and the copyright owner(s) are credited and that the original publication in this journal is cited, in accordance with accepted academic practice. No use, distribution or reproduction is permitted which does not comply with these terms.



# MiR-450a-5p Inhibits Gastric Cancer Cell Proliferation, Migration, and Invasion and Promotes Apoptosis *via* Targeting CREB1 and Inhibiting AKT/GSK-3 $\beta$ Signaling Pathway

Ya-Jun Zhao<sup>1</sup>, Jun Zhang<sup>1</sup>, Yong-Cang Wang<sup>1</sup>, Liang Wang<sup>2</sup> and Xin-Yang He<sup>3\*</sup>

<sup>1</sup> Department of Gastrointestinal Oncology Surgery, The First Affiliated Hospital of University of Science and Technology of China, Division of Life Sciences and Medicine, University of Science and Technology of China, Hefei, China, <sup>2</sup> Center for Diagnostic Pathology, The First Affiliated Hospital of University of Science and Technology of China, Division of Life Sciences and Medicine, University of Science and Technology of China, Hefei, China, <sup>3</sup> Department of General Surgery, The First Affiliated Hospital of University of Science and Technology of China, Division of Life Sciences and Medicine, University of Science and Technology of China, Hefei, China

## OPEN ACCESS

### Edited by:

Dong-Hua Yang,  
St. John's University, United States

### Reviewed by:

Wei Zhao,  
Chengdu Medical College, China  
Fengli Gao,  
The First Affiliated Hospital of  
Heilongjiang University of Chinese  
Medicine, China

### \*Correspondence:

Xin-Yang He  
hexinyang6699@163.com

### Specialty section:

This article was submitted to  
Pharmacology of Anti-Cancer Drugs,  
a section of the journal  
Frontiers in Oncology

**Received:** 25 November 2020

**Accepted:** 08 January 2021

**Published:** 29 March 2021

### Citation:

Zhao Y-J, Zhang J, Wang Y-C, Wang L  
and He X-Y (2021) MiR-450a-5p  
Inhibits Gastric Cancer Cell  
Proliferation, Migration, and Invasion  
and Promotes Apoptosis *via*  
Targeting CREB1 and Inhibiting  
AKT/GSK-3 $\beta$  Signaling Pathway.  
Front. Oncol. 11:633366.  
doi: 10.3389/fonc.2021.633366

Gastric cancer seriously affects human health and research on gastric cancer is attracting more and more attentions. In recent years, molecular targets have become the research focus. Accumulating evidence indicates that miR-450a-5p plays a critical role in cancer progression. However, the biological role of miR-450a-5p in gastric carcinogenesis remains largely unknown. In this study, we explore the effects and mechanisms of miR-450a-5p on the development and progression of gastric cancer. We used gain-of-function approaches to investigate the role of miR-450a-5p on gastric cancer cell proliferation, migration, invasion, and apoptosis using biological and molecular techniques including real-time quantitative PCR (RT-qPCR), CCK-8, colony formation, flow cytometry, Western blot, wound healing, transwell chamber, dual luciferase reporter, and tumor xenograft mouse model. We found that gastric cancer cells have low expression of miR-450a-5p and overexpression of miR-450a-5p inhibited gastric cancer cell proliferation, migration and invasion, and induced apoptosis *in vitro*. Moreover, we demonstrated that ectopic expression of miR-450a-5p inhibited gastric cancer growth *in vivo*. At the molecular level, overexpression of miR-450a-5p significantly increased the expression of pro-apoptotic proteins, including caspase-3, caspase-9, and Bax, and inhibited the expression of anti-apoptotic protein Bcl-2. Luciferase reporter experiment suggested that camp response element binding protein 1 (CREB1) had a negative correlation with miR-450a-5p expression, and knockdown of CREB1 alleviated gastric cancer growth. Furthermore, we also found that miR-450a-5p inhibited the activation of AKT/GSK-3 $\beta$  signaling pathway to inhibit the progression of gastric cancer. Collectively, miR-450a-5p repressed gastric cancer cell proliferation, migration and invasion and induced

apoptosis through targeting CREB1 by inhibiting AKT/GSK-3 $\beta$  signaling pathway. MiR-450a-5p could be a novel molecular target for the treatment of gastric cancer.

**Keywords:** gastric cancer, proliferation, apoptosis, CREB1, AKT/GSK-3 $\beta$  signaling pathway, miR-450a-5p

## INTRODUCTION

Human gastric cancer is one of the common malignancies around the world. Approximately 1,000,000 cases of gastric cancer are diagnosed and 783,000 deaths occur in 2018 (1). Different treatment strategies, including surgery, chemotherapy, and radiation, have achieved remarkable advance. However, the overall therapeutic outcome for advanced disease remains poor (2, 3). Thus, it is critical to better understand the molecular mechanisms and explore new treatment strategies for improving the treatment of gastric cancer.

MicroRNAs (miRNAs) are a kind of endogenous small RNA with a length of about 20–24 nucleotides, that have a variety of important regulatory roles in cells. Previous studies showed that miRNAs are involved in regulating the development of gastric cancer. MiR-4317 inhibits cell proliferation and blocks the conversion of S-G2/M phase in gastric cancer cells, and is a promising therapeutic molecular target (4). MiR-455 suppresses cell proliferation and migration by inhibiting EGFR, acting as a potential target for treatment of gastric cancer (5). MiR-582-5p inhibits cell proliferation and promotes apoptosis by regulating AKT3 (6). Other studies have also shown the inhibitory effect of miRNAs on the progression and development of gastric cancer, including miR-744, miR-140-5p, miR-181a, miR-182, miR-802, miR-21, and miR-149 (7–14). On the other hand, miR-450, as a novel miRNA, functions as a tumor suppressor in colorectal cancer (15). However, its specific role in gastric cancer and the underlying mechanism remain unknown.

The role of CAMP-response element binding protein (CREB1) has been reported previously. For instance, aberrant expression of CREB1 affects proliferation and invasion of cancer cells, and has been highlighted in various pathologies (16, 17). Yang et al. demonstrated that CREB1 was a target of miR-134-5p and affected infarct-induced cardiomyocyte apoptosis (18).

In the present study, we found that gastric cancer cells have low expression of miR-450a-5p. Overexpression of miR-450a-5p inhibited cell proliferation, migration, and invasion and induced cell apoptosis in gastric cancer cells both *in vitro* and *in vivo*. Furthermore, we found that CREB1 is targeted by miR-450a-5p and mediated the anti-tumor effects of miR-450a-5p by inhibiting AKT/GSK-3 $\beta$  signaling pathway. Our study indicated that miR-450a-5p could be a potential molecular target for the treatment of gastric cancer.

## MATERIALS AND METHODS

### Cell Culture

The human gastric cancer cell lines (BGC-823, SGC7901) and human gastric epithelial cell (GES-1) were purchased from the Cell Bank of the Chinese Academy of Science (Shanghai, China).

Cells were maintained in Dulbecco's modified Eagle's Medium (DMEM) containing 10% fetal bovine serum (FBS, Gibco, NY, USA) in a humidified chamber with 5% CO<sub>2</sub> atmosphere at 37°C.

### RNA Extraction and RT-qPCR Assay

RNA was isolated using TRIzol (Invitrogen, CA, USA) reagent according to the manufacturer's protocols. RNAs were reverse transcribed to cDNA by using PrimeScript RT Master Mix (Takara, Dalian, China) following the manufacturer's protocol. PCR amplification was conducted with the SYBR Premix Ex Taq™ Kit (Takara, Dalian, China). GAPDH and U6 were used to normalize the expression. The relative expression was calculated using the  $2^{-\Delta\Delta Ct}$  method.

### Oligonucleotides and Transfection

The plasmid carrying the CREB1 CDS domain was used to overexpress the CREB1 in gastric cancer cells and a pcDNA (pcDNA3.1) vector was used as a negative control (GenePharma, Guangzhou, China). The cDNA encoding CREB1 CDS domain was amplified by PCR, and then sub-cloned into the pcDNA3.1 vector (Invitrogen, CA, USA) to obtain the pcDNA-CREB1. Short hairpin RNA (shRNA) against CREB1 (sh-CREB1), their corresponding negative control (sh-NC), miR-450a-5p mimic, and the negative control (NC) were synthesized and purchased from GenePharma (Guangzhou, China). The transfection was performed by using Lipofectamine 3000 Reagent (Life Technologies, Carlsbad, CA, USA).

### Cell Proliferation Assay

Cell Counting Kit-8 (CCK-8) and colony formation assays were performed to examine gastric cancer cell proliferation. In brief, BGC-823 or SGC7901 cells ( $1 \times 10^4$ /well) were seeded in 96-well plates and incubated for 0, 24, 48, and 72 h. Then BGC-823 or SGC7901 cells were incubated with 10  $\mu$ l CCK-8 solution for 4 h at 37°C. The optical density (OD) was recorded at 490 nm using a microplate reader (Multiskan MK3, Thermo Scientific, USA). For colony formation assay, BGC-823 and SGC7901 cells ( $2 \times 10^4$  cells/well) were seeded in 24-well plates. After incubation for 12 days, the cells were immobilized with paraformaldehyde for 30 min, and stained with 10% crystal violet for another 30 min. Colonies were counted and photographed with a light microscope (Olympus, Tokyo, Japan).

### Cell Apoptosis Assay

Flow cytometry was conducted to investigate the gastric cancer cell apoptosis. Cells ( $1 \times 10^4$  cells/well) were seeded in six-well plates and culture for 48 h. Thereafter, cells were washed using PBS, treated with 5  $\mu$ l of annexin V-FITC and 5  $\mu$ l of PI in the dark for 15 min at room temperature. Then apoptotic cells were detected through a FACSCalibur Flow Cytometry (BD Biosciences, CA, USA).



## Cell Migration and Invasion Assays

Wound healing and transwell chamber (5- $\mu$ m pore size, Costar, Cambridge, MA, USA) assays were conducted to examine gastric cancer cell migration and invasion. For wound healing assay, cells were seeded into six-well plates. The supernatant fluid was removed when BGC-823 or SGC7901 cells were highly confluent (> 90%). Scratches were made using a sterile pipette tip, with the scratch width remaining the same. After continuous culture for 48 h, the width of the scratch was photographed and recorded under a microscope (100 $\times$ ). The distance was assessed by ImageJ software (ImageJ Software Inc., MD, USA). Wound healing rate = (scratch width at 0–48 h)/scratch width at 0 h  $\times$  100%.

Cell invasion assay was performed using transwells. In short, transfected BGC-823 or SGC7901 cells were added to the upper chamber loaded with Matrigel (Corning, Cambridge, MA) and the bottom of the chamber were supplemented with complete medium containing 1% FBS. 48 h later, cells on the surface of membranes were wiped out. Invaded cells were fixed in 10% formaldehyde, dyed with 0.1% crystal violet and then counted under a light microscope (Olympus, Tokyo, Japan) (200 $\times$ ).

## Dual Luciferase Reporter Assay

A putative 3'-untranslated regions (3'-UTR) of CREB1 was mutated using mutagenesis kit (Promega, USA). Wild type and mutant sequences were amplified and inserted into the vector to construct luciferase reporter plasmids according to the manufacturer's instructions (Promega, USA). The luciferase activities were detected with the dual luciferase reporter kit (Promega, USA). Luciferase activity was measured by dual-luciferase reporter assay system (Promega) and presented as firefly luciferase intensity normalized to Renilla luciferase activity.

## Western Blotting Analysis

Total proteins in tissues or cells were extracted with RIPA lysate buffer (Beyotime Inc, Shanghai, China). The protein was quantified using BCA protein assay Kit (Thermo Scientific, CA, USA). The protein samples were separated by 12% polyacrylamide gel, which were transferred onto the PVDF membrane, sealed with 5% skim milk powder. The membrane was incubated with the primary antibody at 4°C overnight and then incubated with HRP coupled secondary antibody (Santa Cruz Inc, CA, USA) at room temperature for 1 h. The protein signal was detected by ECL detection reagents (Thermo Scientific, CA, USA) and GAPDH was used as the internal reference.

## Xenograft Tumors in Nude Mice

Female nude mice (6-week-old, 18–22 g) were provided by Nanjing Medical University and housed under germ free conditions. Animal care and use were carried out according to the ethical guidelines by the First Affiliated Hospital of USTC Animal Care and Use Committee and approved by the Ethics Committee of the First Affiliated Hospital. Nude mice were maintained in a 12h light/12 dark cycle in a temperature- and humidity-controlled environment. To detect the effect of miR-450a-5p on tumor growth *in vivo*, BGC-823 cells ( $1 \times 10^6$  cells) were injected subcutaneously into the right axilla of the nude mice. Following a 30-day period, nude mice were sacrificed, and

tumors were isolated for further analyses. Note that the tumor volumes were recorded every week and calculated with the formula: volume =  $0.5 \times \text{length} \times \text{wide}^2$ .

## Statistical Analyses

All data are presented as the mean  $\pm$  SD. Each bar expressed the mean  $\pm$  SD of three independent experiments. Statistical significance between two or multiple groups was analyzed by t-test or one-way ANOVA using SPSS 17.0 (SPSS Inc, Chicago, IL, USA). Experiments were repeated three times independently. Statistical significance was assumed when  $P < 0.05$ .

## RESULTS

### Effect of miR-450a-5p on Gastric Cancer Cell Proliferation and Apoptosis

RT-qPCR analysis was employed to examine the expression of miR-450a-5p in gastric cancer cells. As shown in **Figure 1A**, gastric cancer cells (BGC-823 and SGC7901) had low expression of miR-450a-5p compared with the human gastric epithelial cell (GES-1). To further evaluate the roles of miR-450a-5p in the regulation of gastric cancer, miR-450a-5p mimic was transfected into BGC-823 and SGC7901 gastric cancer cells for gain-of-function assays. The efficiency of transfection was validated by RT-qPCR assay (**Figure 1B**). CCK-8 and colony formation assays were performed to evaluate cell viability and proliferation of BGC-823 and SGC7901 cells. The results indicated that the cell viability and number of colonies were significantly decreased in BGC-823 and SGC7901 cells transfected with miR-450a-5p mimic, compared with that in NC group (**Figures 1C, D**). Subsequently, flow cytometry assay was conducted to examine cell apoptosis of these cells. We found that cell apoptosis was significantly increased in miR-450a-5p mimic group, compared with NC group (**Figure 1E**). Consistent with these findings, Western blot analysis revealed that the expression levels of apoptosis-associated proteins, including caspase-3, caspase-9, and Bax, were significantly increased, whereas the anti-apoptotic protein Bcl-2 was decreased in BGC-823 and SGC7901 cells transfected with miR-450a-5p mimic (**Figure 1F**). These results indicated that miR-450a-5p overexpression inhibited cell proliferation and induced cell apoptosis of gastric cancer.

### Overexpression of miR-450a-5p Inhibits Tumor Growth *In Vivo*

To confirm whether miR-450a-5p inhibit gastric cancer growth *in vivo*, we generated BGC-823/miR-450a-5p mimic cells and their negative control, then injected them into nude mice to establish tumor xenograft mouse models. Representative images of tumors with miR-450a-5p mimic and NC in the nude mice were shown in **Figure 2A**. Tumor volume and tumor weight were significantly decreased in miR-450a-5p mimic group compared with that in NC group (**Figures 2B, C**). Furthermore, Western blot assay suggested that the expression of apoptosis-associated proteins, including caspase-3, caspase-9, and Bax, were significantly decreased in miR-450a-5p mimic group compared with that in NC group. On the contrary, the

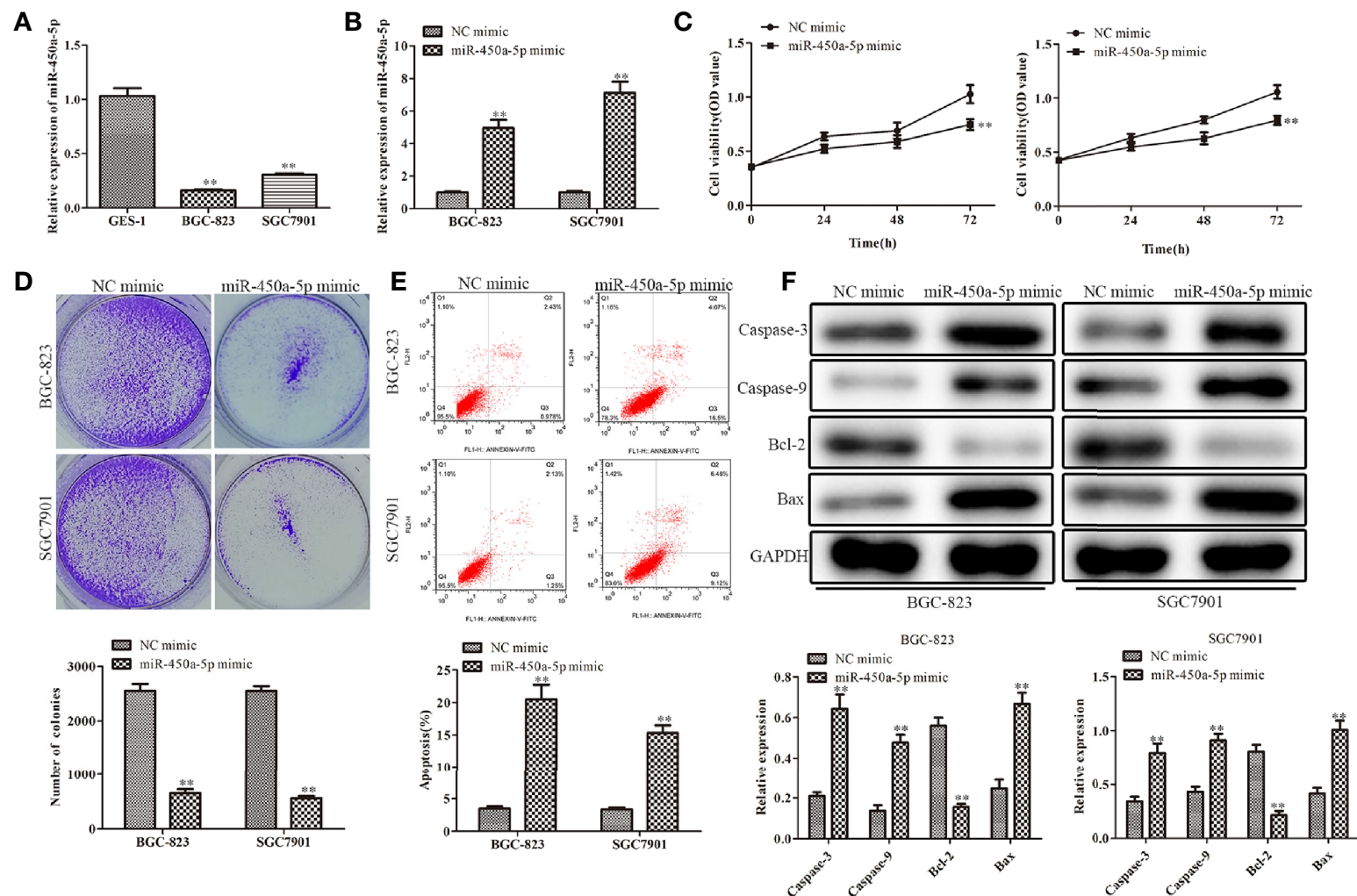


**FIGURE 1** | Overexpression of miR-450a-5p inhibits cell proliferation and promotes apoptosis of gastric cancer. **(A)** The expression of miR-450a-5p measured by RT-qPCR in gastric cancer cell lines (BGC-823 and SGC-7901) and a human gastric epithelial cell line (GES-1). \*\* $P < 0.01$  vs. GES-1 group. **(B)** The expression of miR-450a-5p assessed by RT-qPCR assay. \*\* $P < 0.01$  vs. miR-NC group. **(C–E)** CCK-8, colony formation, and flow cytometry assays detected the cell proliferation and apoptosis in BGC-823 and SGC-7901 cells. \*\* $P < 0.01$  vs. miR-NC group. **(F)** Western blot analysis evaluated the expression of apoptosis-associated proteins in BGC-823 and SGC-7901 cells. \*\* $P < 0.01$  vs. miR-NC group.

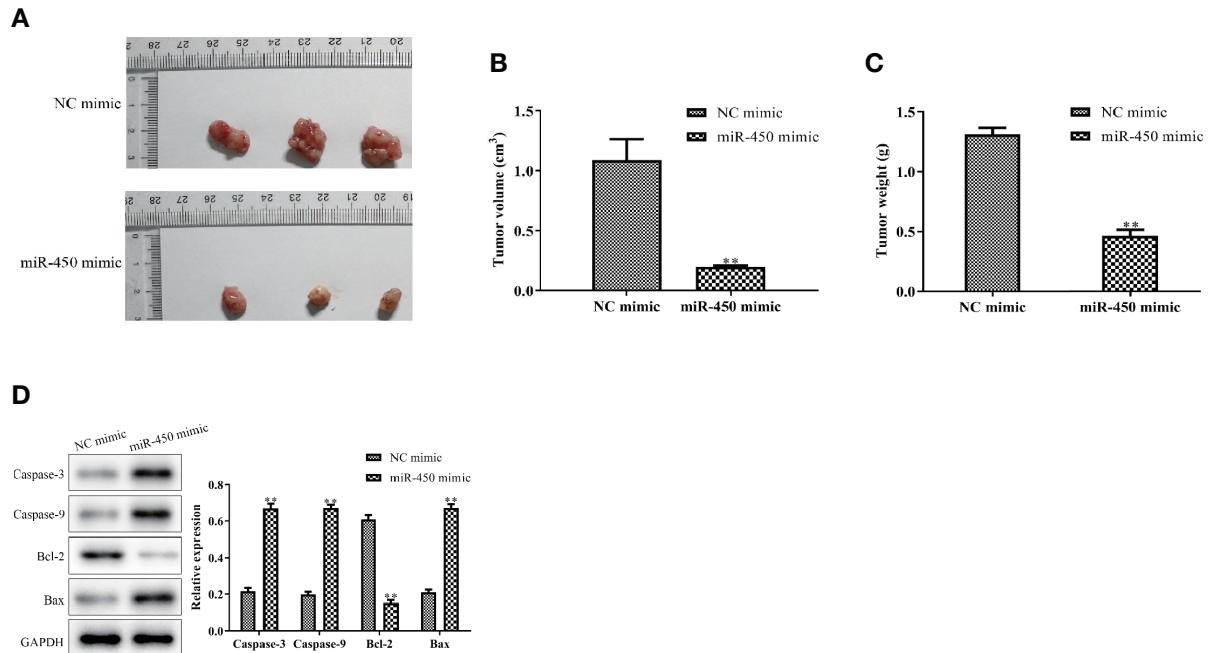


**FIGURE 2 |** Overexpression of miR-450a-5p inhibits tumor growth. **(A–C)** Tumor phenotype, tumor volume, and weight. **(D)** Western blot analysis on the expression of apoptosis-associated proteins in tumor tissues. \*\* $P < 0.01$  vs. miR-NC group.

expression of Bcl-2 increased in miR-450a-5p mimic group compared with that in NC group (**Figure 2D**). These results indicated that overexpression of miR-450a-5p suppressed gastric cancer growth *in vivo*.

### Overexpression of miR-450a-5p Inhibits Gastric Cancer Cell Migration and Invasion

Cell migration and invasion play important role in the pathogenesis of cancer metastasis. To evaluate the effect of miR-450a-5p on tumor migration and invasion, wound healing assay, and transwell assay were carried out. The results showed that the wound closure rate was significantly decreased in miR-450a-5p-overexpressed BGC-823 and SGC7901 gastric cancer cells, compared with that in NC group (**Figure 3A**). Moreover, the results of transwell invasion assay showed that ectopic expression of miR-450a-5p limited the invasive capability of BGC-823 and SGC7901 cells, compared with that in NC group (**Figure 3B**). Furthermore, Western blot assay suggested that the expression of matrix proteins that are associated with migration and invasion, such as MMP-2 and MMP-9, were significantly decreased in both BGC-823 and SGC7901 cells transfected with miR-450a-5p mimic, compared with that in NC group (**Figure 3C**). These results suggested that overexpression of miR-450a-5p inhibits migration and invasion of BGC-823 and SGC7901 cells.

### MiR-450a-5p Negatively Regulates CREB1

To study the possible targets of miR-450a-5p involved in the occurrence of gastric cancer, TargetScan was carried out.

Then, result predicted that CREB1 was a potential candidate of miR-450a-5p (**Figure 4A**). The expression of CREB1 in gastric cancer cells was investigated. It was found that BGC-823 and SGC7901 gastric cancer cells have overexpression of CREB1 (**Figure 4B**). The luciferase reporter assay showed that miR-450a-5p mimic repressed the relative luciferase activities containing the WT 3'-UTR of CREB1, but had no obvious effect on Mut 3'-UTR of CREB1 (**Figure 4C**). Moreover, RT-qPCR and Western blot analysis were adapted to evaluate the expression of CREB1 in BGC-823 and SGC7901 cells transfected with miR-450a-5p mimic or NC, and the data revealed that up-regulation of miR-450a-5p decreased the expression of CREB1 (**Figures 4D, E**). These results indicated that miR-450a-5p negatively regulates CREB1.

### Knockdown of CREB1 Inhibits Gastric Cancer Cell Proliferation, Migration, Invasion, and Promotes Apoptosis

The above results indicated that CREB1 is a target of miR-450a-5p in gastric cancer. We then examined whether CREB1 regulate the progression of gastric cancer. We knocked-down CREB1 in BGC-823 and SGC7901 cells and evaluated the knockdown efficiency by RT-qPCR analysis (**Figure 5A**). CCK-8 and colony formation assays were performed and the results showed that the cell viability and the number of colonies were significantly decreased in BGC-823 and SGC7901 cells transfected with sh-CREB1 compared with that in cells transfected with sh-NC (**Figures 5B, C**). Subsequently, flow cytometry was conducted to examine cell apoptosis after



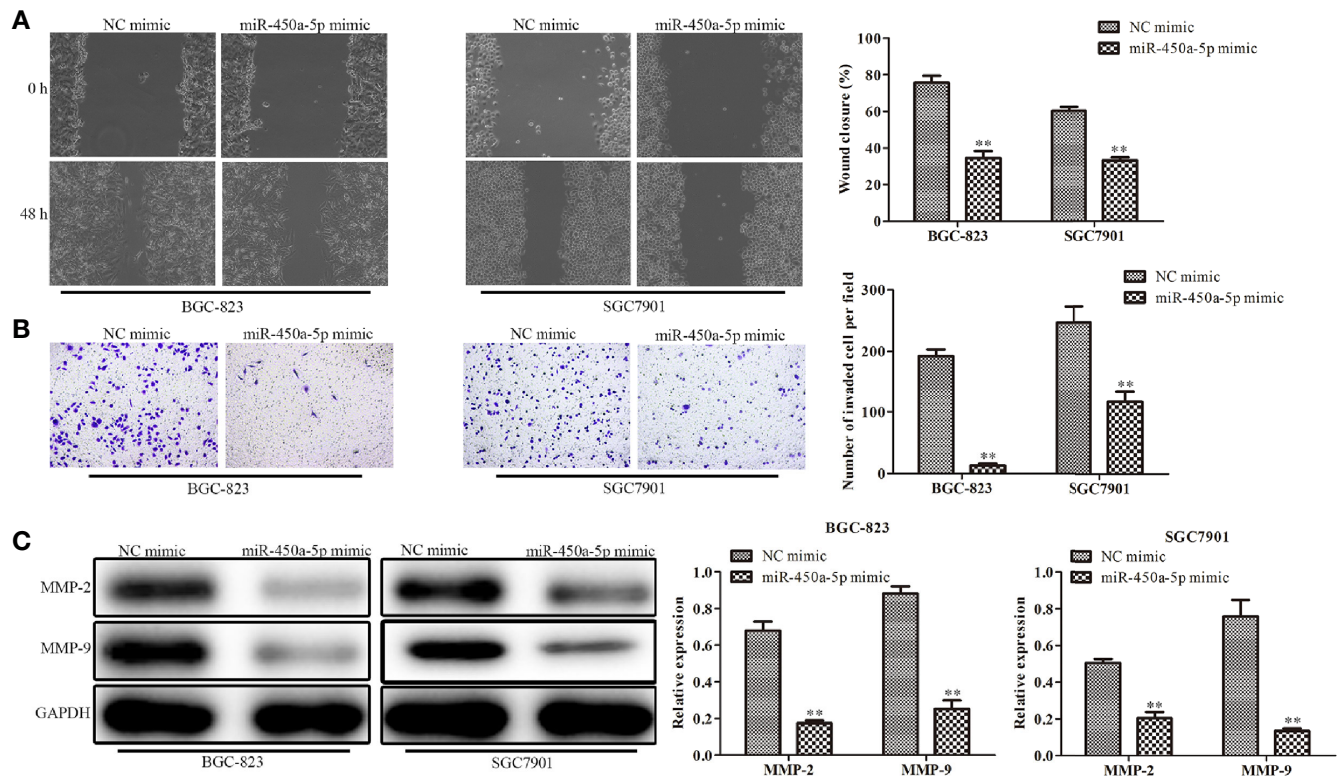


**FIGURE 3 |** Overexpression of miR-450a-5p inhibits gastric cancer cell migration and invasion. **(A)** Wound healing assay on the cell migration capability of BGC-823 and SGC-7901 gastric cancer cells after transfection of miR-450a-5p mimic. **(B)** Transwell chamber assay on the cell invasion capability of BGC-823 and SGC-7901 gastric cancer cells after transfection of miR-450a-5p mimic. **(C)** Western blot assay on the expression of matrix proteins in BGC-823 and SGC-7901 gastric cancer cells after transfection of miR-450a-5p mimic. \*\* $P < 0.01$  vs. miR-NC group.

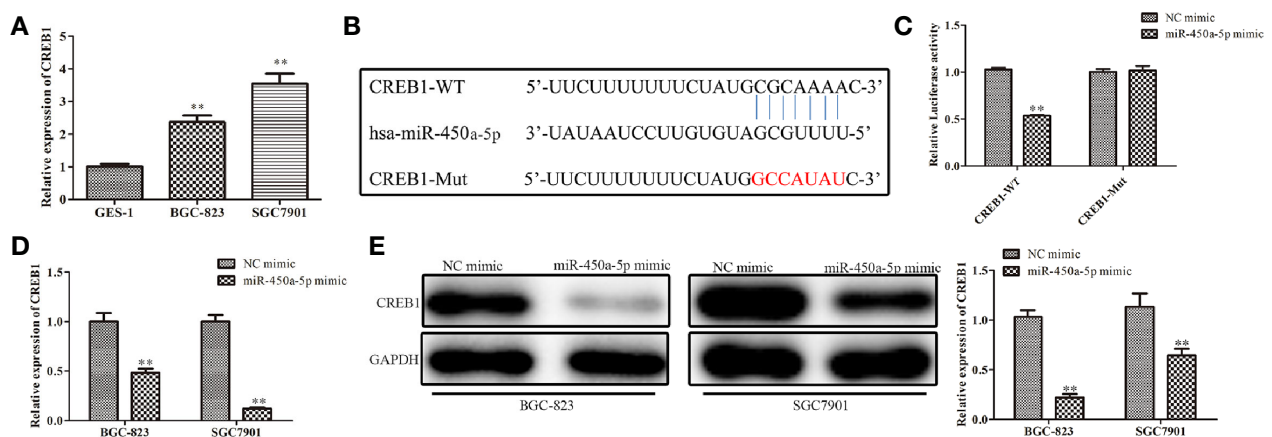


**FIGURE 4 |** MiR-450a-5p targets and negatively regulates CREB1. **(A)** The expression of CREB1 determined by RT-qPCR in GES-1, BGC-823, and SGC7801 cells. \* $P < 0.05$  vs. GES-1 group. **(B)** The binding sites between miR-450a-5p and CREB1 were predicted. **(C)** Dual luciferase reporter assay performed in HEK-293T cells to detect the interaction between miR-450a-5p and CREB1. \*\* $P < 0.01$  vs. miR-NC group. **(D)** RT-qPCR on the CREB1 expression after transfection of miR-450a-5p mimic. \*\* $P < 0.01$  vs. miR-NC group. **(E)** Western blot assay on the CREB1 expression after transfection of miR-450a-5p mimic. \*\* $P < 0.01$  vs. miR-NC group.



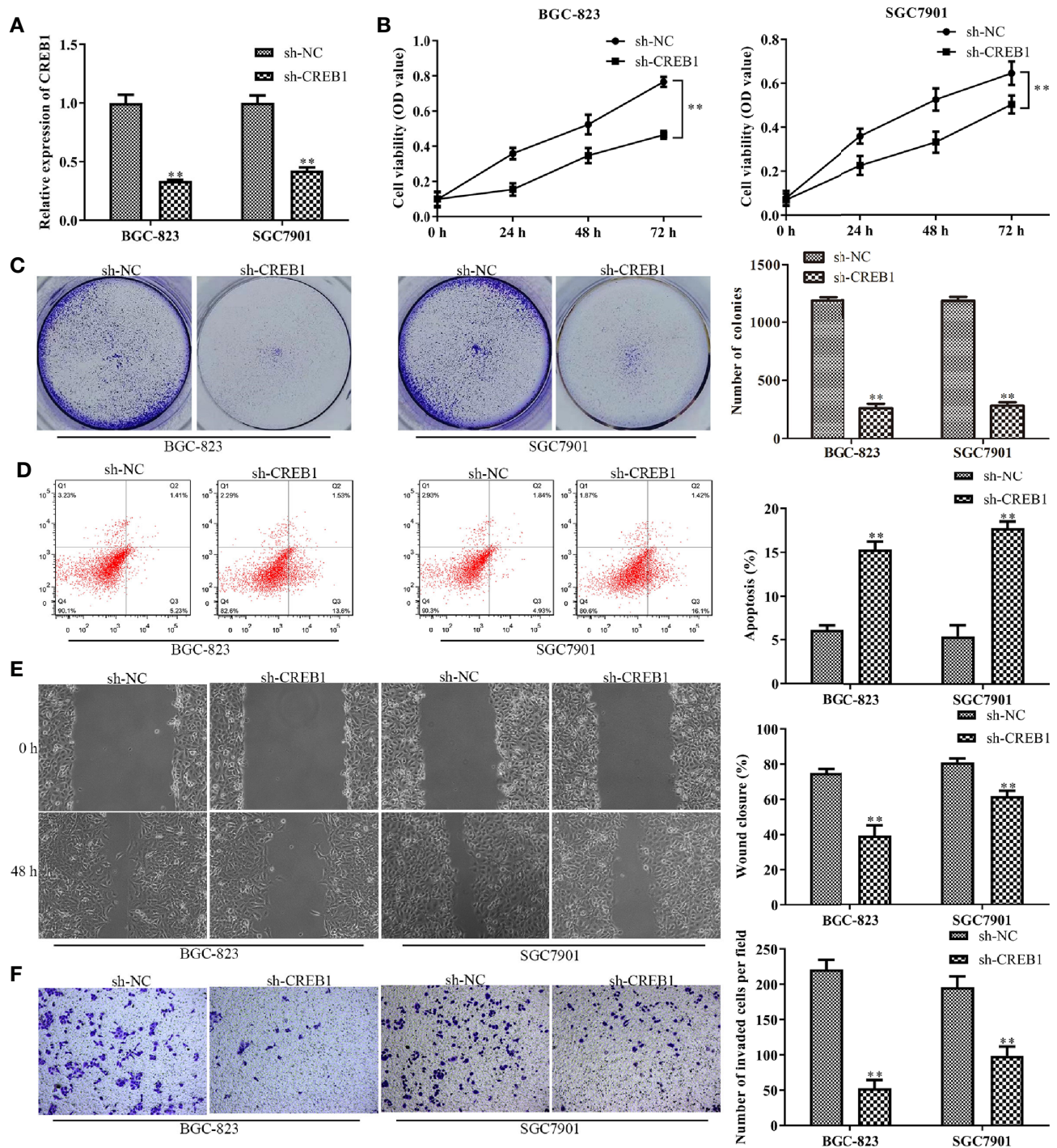


**FIGURE 5 |** Knockdown of CREB1 affects gastric cancer cell proliferation, apoptosis, migration, and invasion. **(A)** RT-qPCR evaluated the efficiency of CREB1 knockdown in BGC-823 and SGC7901 cells. **(B, C)** CCK-8 and colony formation assays on the cell proliferation of BGC-823 and SGC7901 cells after knockdown of CREB1. **(D)** Flow cytometry on the cell apoptosis of BGC-823 and SGC7901 cells after knockdown of CREB1. **(E, F)** Wound healing and transwell chamber assays on the cell migration and invasion of BGC-823 and SGC7901 cells after knockdown of CREB1. \*\* $P < 0.01$  vs. sh-NC group.

knocking-down of CREB1 expression in BGC-823 and SGC7901 cells. The results indicated that cell apoptosis was significantly increased in CREB1-knockdown BGC-823 and SGC7901 gastric cancer cells, compared with that in NC group (Figure 5D).

Wound healing and transwell chamber assays showed that the gastric cancer cell migration and invasion capability was significantly inhibited in CREB1-knockdown BGC-823 and SGC7901 gastric cancer cells, compared with that in NC group

(Figures 5E, F). These results showed that knockdown of CREB1 suppressed gastric cancer cell proliferation, migration, and invasion and induced apoptosis.

## CREB1 Overexpression Partially Restores the Effects of miR-450a-5p on Gastric Cancer

To further explore the role of CREB1 in mediating the inhibitory effect of miR-450a-5p on gastric cancer, BGC-823 and SGC7901 gastric cancer cells were overexpressed with CREB1 and co-transfected with miR-450a-5p mimic. CCK-8 and colony formation assays indicated that the cell viability and the number of colonies was significantly decreased in BGC-823 and SGC7901 cells in the miR-450a-5p mimic-treated group, compared with that in NC + pcDNA 3.1 group, suggesting that CREB partially abolished the inhibitory effects of miR-450a-5p mimic on cell proliferation of BGC-823 and SGC7901 gastric cancer cells (Figures 6A, B). Flow cytometric analysis indicated that miR-450a-5p mimic-induced promotion of cell apoptosis was prominently abrogated by CREB1 overexpression (Figure 6C).

At the molecular level, Western blot analysis indicated that the expression of apoptosis-associated proteins, including caspase-3, caspase-9, and Bax, were significantly increased in BGC-823 and SGC7901 gastric cancer cells treated with miR-450a-5p mimic, compared with that in NC + pcDNA 3.1 group, whereas the overexpression of CREB similarly abolished the activation effects of miR-450a-5p mimic on the expression of apoptosis-associated proteins, including caspase-3, caspase-9, and Bax. In contrast, the expression of anti-apoptotic protein of BCL-2 were decreased (Figure 6D). These results demonstrated that CREB1 overexpression partially restored the effects of miR-450a-5p on proliferation and apoptosis of gastric cancer.

## MiR-450a-5p Regulates Gastric Cancer Progression Through Inhibiting AKT/GSK-3 $\beta$ Signaling Pathway

Given the importance of AKT/GSK-3 $\beta$  in the regulation of gastric cancer, we investigated the expression of proteins in the AKT/GSK-3 $\beta$  signaling pathway by Western blot assay (Figure 7). We found that the expression of the AKT/GSK-3 $\beta$  pathway-associated

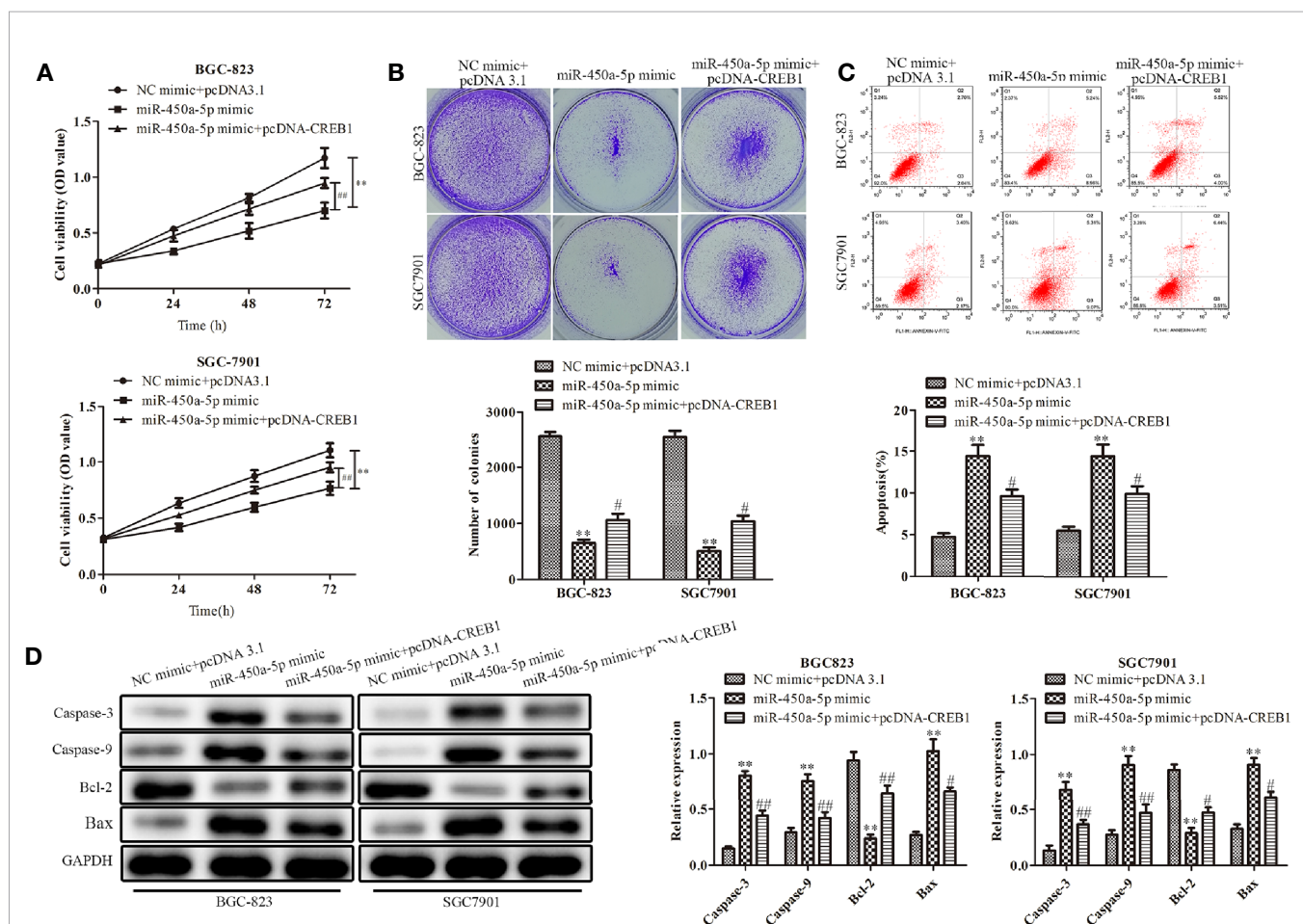


**FIGURE 6 |** CREB1 overexpression partially restores the effects of miR-450a-5p on gastric cancer. (A, B) CCK-8 assay and colony formation assay on the cell proliferation of BGC-823 and SGC7901 cells. (C) Flow cytometry on the cell apoptosis of BGC-823 and SGC7901 cells. (D) Western blot analysis evaluated the expression of apoptosis-associated proteins in BGC-823 and SGC7901 cells. \*\* $P < 0.01$  vs. NC + pcDNA3.1 group. \* $P < 0.05$ , ## $P < 0.05$  vs. miR-450a-5p mimic group.

protein, including GSK-3 $\beta$  and AKT, had no significantly change. However, the phosphorylated proteins in this pathway were markedly decreased in response to the overexpression of miR-450a-5p, while CREB overexpression increased AKT/GSK-3 $\beta$  phosphorylated proteins in BGC-823 cells treated with miR-450a-5p mimic. To further identify the role of AKT/GSK-3 $\beta$  in mediating the anti-gastric cancer role of miR-450a-5p, we use SC79 as an activator of the AKT/GSK-3 $\beta$  signaling pathway. As shown in **Figures 8A, B, D, E**, CCK-8, colony formation, wound healing, and transwell chamber assays showed that the gastric cancer cell proliferation, migration, and invasion abilities were significantly decreased in the miR-450a-5p mimic-treated group, while significantly increased in the miR-450a-5p mimic + SC79 group compared with that in miR-450a-5p mimic group. These results were further confirmed by flow cytometry, which showed that the apoptosis rate markedly increased in miR-450a-5p mimic group, while significantly decreased in miR-450a-5p mimic + SC79 group (**Figure 8C**). These results suggested that miR-450a-5p represses gastric cancer progression by targeting CREB1 through inhibiting AKT/GSK-3 $\beta$  signaling pathway.

## DISCUSSION

Over the past years, more and more evidence indicated that microRNAs are involved in regulating various biological and

pathological processes. In this study, we found that miR-450a-5p was significantly downregulated in gastric cancer cells. Gain-of-function analysis indicated that overexpression of miR-450a-5p inhibited cell proliferation, migration, and invasion, and facilitated cell apoptosis in gastric cancer cells *in vitro*, and suppressed tumor growth *in vivo*. Moreover, we found that overexpression of miR-450a-5p increased the expression of apoptosis-associated proteins, including caspase-3, caspase-9, and Bax, while inhibited the expression of anti-apoptotic protein Bcl-2. In addition, overexpression of miR-450a-5p suppressed the expression of matrix protein enzymes MMP-2 and MMP-9, and promoted cancer cell migration and invasion. Our results suggested that miR-450a-5p could function as a tumor suppressor to inhibit gastric cancer cell growth. Although the public data shows miR-450a-5p has a bit higher expression in gastric tumors (**Supplementary Data**), the role of miR-450a-5p in clinic tissues still need further study.

A number of studies have been focused on trying to identify effective new targets for the treatment of gastric cancer. MiRNAs have been attracted great attention. Various miRNAs were found to be associated with cancer development and progression, and therefore, they could be potential molecular targets for cancer treatment. In the area of gastric cancer, Feng et al. reported that miR-518 suppresses the progression of gastric cancer by promoting cell apoptosis *via* targeting MDM2 (19). Therefore, miR-518 may be a promising therapeutic target for gastric

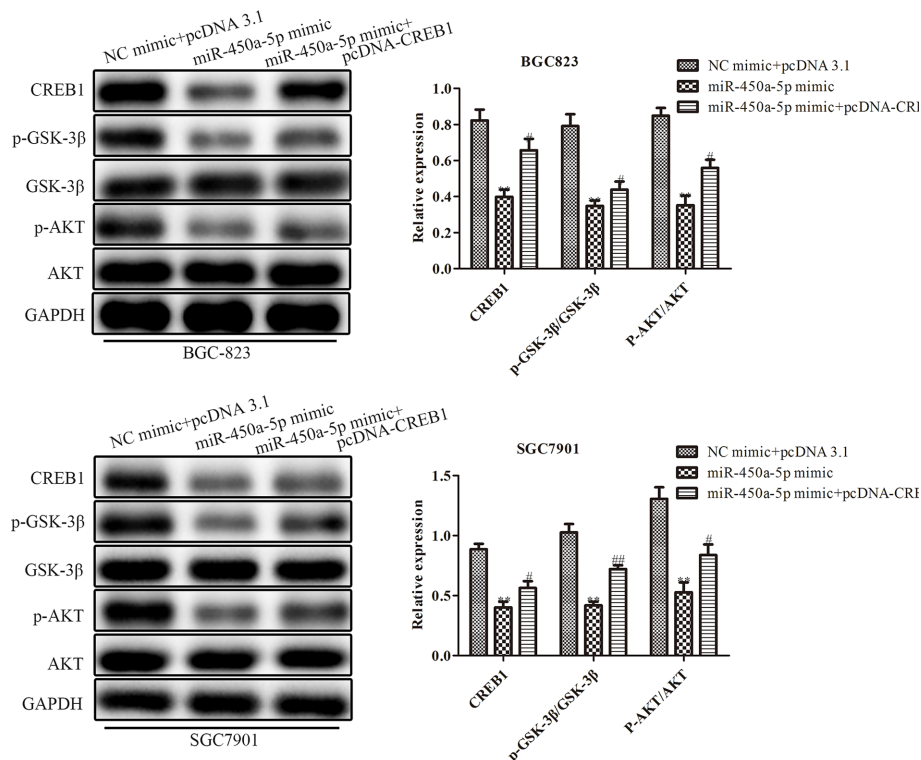


**FIGURE 7 |** MiR-450a-5p regulates the AKT/GSK-3 $\beta$  signaling pathway. Western blotting evaluated the protein expression of CREB1, GSK-3 $\beta$ , AKT, p-GSK-3 $\beta$ , p-AKT. \*\* $P < 0.05$  vs. NC + pcDNA3.1 group. # $P < 0.05$ , ## $P < 0.01$  vs. miR-450a-5p mimic group.



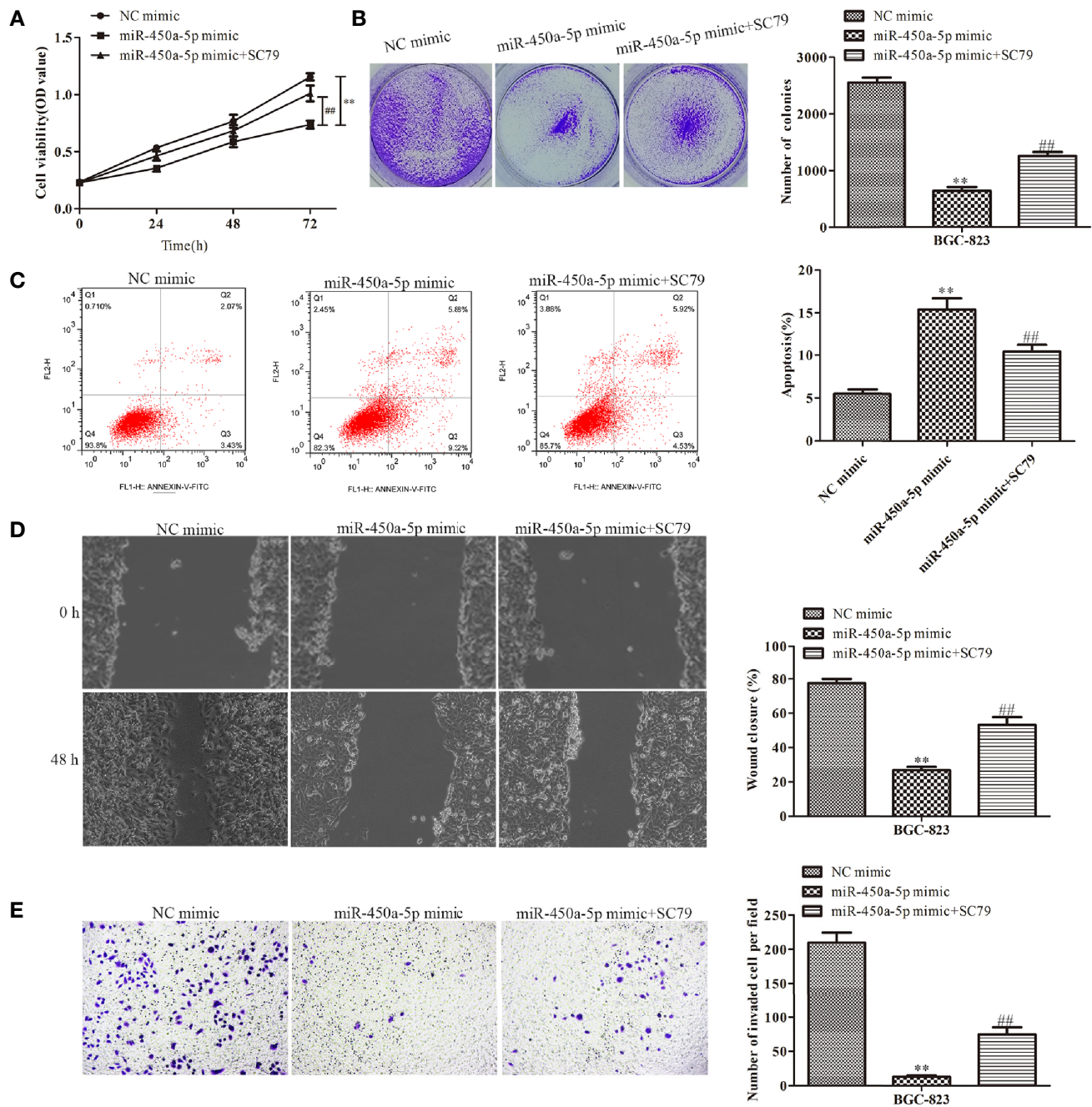


**FIGURE 8 |** MiR-450a-5p inhibits the progression of gastric cancer by inhibiting the AKT/GSK-3 $\beta$  signaling pathway. **(A, B)** CCK-8 and colony formation assays on the cell proliferation of BGC-823 cells. **(C)** Flow cytometry on the cell apoptosis of BGC-823 cells. **(D)** Wound healing assay on the cell migration of BGC-823 cells after knockdown of CREB1. **(E)** Transwell chamber assay on the cell invasion of BGC-823 cells after knockdown of CREB1. \*\* $P < 0.01$  vs. NC mimic group. ## $P < 0.01$  vs. miR-450a-5p mimic group.

cancer. Liu et al. demonstrated that miR-204 modulates the EMT process to inhibit gastric cancer cell migration and invasion *via* regulating snail both *in vitro* and *in vivo* (20). Wang et al. confirmed that miR-129-5p inhibits gastric cancer cell proliferation and EMT by high-mobility group box 1 (HMGB1), and could be a potential target for the treatment of

gastric cancer (21). Wang et al. showed that overexpression of miR-128b inhibits cell proliferation, migration, and invasion, and promotes apoptosis in gastric cancer cells *via* down-regulating adenosine 2b receptor (A2bR) (22). Wu et al. reported that up-regulation of miR-449c suppresses gastric cancer cell growth and promotes apoptosis, while down-regulation of miR-449c



promotes gastric cancer cell growth and inhibits apoptosis (23). Wang et al demonstrated that over-expression of miR-217 inhibits gastric cancer cell proliferation, invasion and promotes apoptosis *via* regulating geriatric palliative care 5 (GPC5), and could be a potential therapeutic target (24). In addition to the above mentioned miRNAs, other miRNAs, for instance, miR-376c-3p (25), miR-133b (26), miR-99b-5p and miR-203a-3p (27), miR-491-5p (28), miR-143 (29) are involved in the regulation of the development and progression of gastric cancer. Our study suggested that miR-450a-5p plays critical roles in inhibiting the development and progression of gastric cancer.

Multiple lines of evidence have proofed that miRNAs exert their diverse biological functions, such as acting as key signal transduction mediators and regulating cell activities, mainly by degrading mRNA or suppressing mRNA translation. Therefore, we further explored the potential downstream target of miR-450a-5p by bioinformatic analysis. TargetScan revealed that CREB1 could be a potential candidate of miR-450a-5p. Dual luciferase reporter assay, RT-qPCR and Western blot analysis confirmed that CREB1 is negatively regulated by miR-450a-5p. Therefore, miR-450a-5p might alleviate the development and progression of gastric cancer *via* targeting CREB1. In this study, we also found that CREB overexpression increased the phosphorylated proteins of AKT/GSK-3 $\beta$  signaling pathway, promoting cell proliferation, migration, and invasion, and suppressed apoptosis. Simultaneously, knockdown of CREB1 suppressed gastric cancer cell growth.

It was well known that the AKT/GSK-3 $\beta$  signaling pathway is closely associated with cancer development and progression. Hua et al. reported that knockdown of ANXA11 suppressed gastric cancer cell proliferation, invasion, and migration through the AKT/GSK-3 $\beta$  signaling pathway (30). Pan et al. demonstrated that CD36 regulated palmitate acid-induced metastasis in gastric cancer by AKT/GSK-3 $\beta$ / $\beta$ -catenin signaling pathway (31). Targeting AKT/GSK-3 $\beta$  signaling pathway might be critical for cancer intervention. In our study, we found that miR-450a-5p blocked the AKT/GSK-3 $\beta$  signaling pathway to inhibit the growth of gastric cancer cells and the level of miR-450a-5p were related to the inhibitory ability of the AKT/GSK-3 $\beta$  signaling pathway.

Previous study reported that miR-21, miR-450 and miR-149 participate in the regulation of cancers (13, 15). Moreover, miR-21 and miR-149 are associated with the development of gastric cancer (12, 14). As miR-21 and miR-149 play a role in other cancers, for instance, colorectal cancer (32), ovarian cancer (33), breast cancer (34), bladder cancer (35), and hepatocellular

carcinoma (36), it is worthy to investigate whether miR-450a-5p also plays a role in these cancers. Future study will be directed to understand the role of miR-450a-5p in various cancers, which will provide the advantages of using miR-450a-5p as a molecular therapeutic target.

In conclusion, miR-450a-5p targets CREB1 and inhibits the AKT/GSK-3 $\beta$  signaling pathway to repress the development and progression of gastric cancer. Our study suggests that miR-450a-5p is a tumor suppressor and could be a new molecular target for the treatment of gastric cancer.

## DATA AVAILABILITY STATEMENT

The raw data supporting the conclusions of this article will be made available by the authors, without undue reservation.

## ETHICS STATEMENT

The animal study was reviewed and approved by Use Committee and approved by the Ethics Committee of the First Affiliated Hospital of USTC.

## AUTHOR CONTRIBUTIONS

X-YH conceived the study. Y-JZ and X-YH designed the study. JZ, Y-CW, and LW performed the literature search and data extraction. Y-JZ and X-YH drafted the manuscript. All authors contributed to the article and approved the submitted version.

## FUNDING

This work was supported by the Youth Fund Project of The First Hospital of USTC (West District, No. 2018YJQN002).

## SUPPLEMENTARY MATERIAL

The Supplementary Material for this article can be found online at: <https://www.frontiersin.org/articles/10.3389/fonc.2021.633366/full#supplementary-material>

## REFERENCES

- Bray F, Ferlay J, Soerjomataram I, Siegel RL, Torre LA, Jemal A. Global cancer statistics 2018: GLOBOCAN estimates of incidence and mortality worldwide for 36 cancers in 185 countries (vol 68, pg 394, 2018). *Ca-Cancer J Clin* (2020) 70(4):313–. doi: 10.3322/caac.21609
- Song ZY, Wu YY, Yang JB, Yang DQ, Fang XD. Progress in the treatment of advanced gastric cancer. *Tumor Biol* (2017) 39(7):1010428317714626. doi: 10.1177/1010428317714626
- Sasako M. Progress in the treatment of gastric cancer in Japan over the last 50 years. *Ann Gastroent Surg* (2020) 4(1):21–9. doi: 10.1002/ags3.12306
- Hu XY, Zhang M, Miao JY, Wang XF, Huang C. miRNA-4317 suppresses human gastric cancer cell proliferation by targeting ZNF322. *Cell Biol Int* (2018) 42(8):923–30. doi: 10.1002/cbin.10870
- Ning T, Peng ZJ, Li S, Qu YJ, Zhang HY, Duan JJ, et al. miR-455 inhibits cell proliferation and migration via negative regulation of EGFR in human gastric cancer. *Oncol Rep* (2017) 38(1):175–82. doi: 10.3892/or.2017.5657
- Jin Y, Tao LP, Yao SC, Huang QK, Chen ZF, Sun YJ, et al. MicroRNA-582-5p suppressed gastric cancer cell proliferation via targeting AKT3. *Eur Rev Med Pharmacol Sci* (2017) 21(22):5112–20. doi: 10.26355/eurev\_201711\_13827

7. Liu JX, Wei YL, Li SY, Li YJ, Liu HX, Liu JM, et al. MicroRNA-744 promotes cell apoptosis via targeting B cell lymphoma-2 in gastric cancer cell line SGC-7901. *Exp Ther Med* (2018) 16(4):3611–6. doi: 10.3892/etm.2018.6602
8. Sun YH, Han CY. Long Non-Coding RNA TMPO-AS1 Promotes Cell Migration and Invasion by Sponging miR-140-5p and Inducing SOX4-Mediated EMT in Gastric Cancer. *Cancer Manag Res* (2020) 12:1261–8. doi: 10.2147/CMAR.S235898
9. Lu Q, Chen YC, Sun D, Wang SK, Ding K, Liu MY, et al. MicroRNA-181a Functions as an Oncogene in Gastric Cancer by Targeting Caprin-1. *Front Pharmacol* (2019) 9:1565. doi: 10.3389/fphar.2018.01565
10. Tang L, Chen F, Pang EJ, Zhang ZQ, Jin BW, Dong WF. MicroRNA-182 inhibits proliferation through targeting oncogenic ANUB1 in gastric cancer. *Oncol Rep* (2015) 33(4):1707–16. doi: 10.3892/or.2015.3798
11. Zhang XY, Mu JH, Liu LY, Zhang HZ. Upregulation of miR-802 suppresses gastric cancer oncogenicity via targeting RAB23 expression. *Eur Rev Med Pharmacol Sci* (2017) 21(18):4071–8.
12. Gu YF, Fei ZW, Zhu RH. miR-21 modulates cisplatin resistance of gastric cancer cells by inhibiting autophagy via the PI3K/Akt/mTOR pathway. *Anti-cancer Drugs* (2020) 31(4):385–93. doi: 10.1097/CAD.0000000000000886
13. Obermannova R, Redova-Lojova M, Vychytilova-Faltejskova P, Grell P, Cho WC, Sachlova M, et al. Tumor Expression of miR-10b, miR-21, miR-143 and miR-145 Is Related to Clinicopathological Features of Gastric Cancer in a Central European Population. *Anticancer Res* (2018) 38(6):3719–24. doi: 10.21873/anticancer.12651
14. Wang XY, Zhou YC, Wang Y, Liu YY, Wang YX, Chen DD, et al. miR-149 contributes to resistance of 5-FU in gastric cancer via targeting TREM2 and regulating beta-catenin pathway. *Biochem Biophys Res Commun* (2020) 532(3):329–35. doi: 10.1016/j.bbrc.2020.05.135
15. Jin YH, Jiang Z, Guan X, Chen YG, Tang QC, Wang GY, et al. miR-450b-5p Suppresses Stemness and the Development of Chemoresistance by Targeting SOX2 in Colorectal Cancer. *DNA Cell Biol* (2016) 35(5):249–56. doi: 10.1089/dna.2015.3120
16. Lihua G, Min Y, Yixuan WJOL. CREB1, a direct target of miR-122, promotes cell proliferation and invasion in bladder cancer. (2018) 16:3842–8. doi: 10.3892/ol.2018.9118
17. Rodón L, Svensson RU, Wiater E, Chun MGH, Montminy M. The CREB coactivator CRT2 promotes oncogenesis in LKB1-mutant non-small cell lung cancer. *Sci Adv* (2019) 5(7):eaaw6455. doi: 10.1126/sciadv.aaw6455
18. Yang J, Liu S, Wang H, Liu Y, Liu Y, Diseases C. miR-134-5p inhibition reduces infarct-induced cardiomyocyte apoptosis via Creb1 upregulation. *Stroke Cerebrovasc Dis* (2020) 29(8):104850. doi: 10.1016/j.jstrokecerebrovasdis.2020.104850
19. Feng CJ, Xian QJ, Liu ST. Micro RNA-518 inhibits gastric cancer cell growth by inducing apoptosis via targeting MDM2. *Biomed Pharmacother* (2018) 97:1595–602. doi: 10.1016/j.biopha.2017.11.091
20. Liu Z, Long J, Du RX, Ge CL, Guo KJ, Xu YH. miR-204 regulates the EMT by targeting snail to suppress the invasion and migration of gastric cancer. *Tumor Biol* (2016) 37(6):8327–35. doi: 10.1007/s13277-015-4627-0
21. Feng J, Guo J, Wang JP, Chai BF. MiR-129-5p inhibits proliferation of gastric cancer cells through targeted inhibition on HMGB1 expression. *Eur Rev Med Pharmacol Sci* (2020) 24(7):3665–73. doi: 10.26355/eurrev\_202004\_20829
22. Wang P, Guo XY, Zong W, Song B, Liu GS, He SX. MicroRNA-128b suppresses tumor growth and promotes apoptosis by targeting A2bR in gastric cancer. *Biochem Biophys Res Commun* (2015) 467(4):798–804. doi: 10.1016/j.bbrc.2015.10.062
23. Chen X, Wang AP, Yue XX. miR-449c inhibits migration and invasion of gastric cancer cells by targeting PFKFB3. *Oncol Lett* (2018) 16(1):417–24. doi: 10.3892/ol.2018.8609
24. Wang H, Dong XL, Gu X, Qin R, Jia HP, Gao JP. The MicroRNA-217 Functions as a Potential Tumor Suppressor in Gastric Cancer by Targeting GPC5. *PLoS One* (2015) 10(6):e0125474. doi: 10.1371/journal.pone.0125474
25. Tu L, Zhao EH, Zhao WY, Zhang ZZ, Tang DF, Zhang YQ, et al. hsa-miR-376c-3p Regulates Gastric Tumor Growth Both In Vitro and In Vivo. *BioMed Res Int* (2016) 2016:9604257. doi: 10.1155/2016/9604257
26. Guo LH, Bai H, Zou DL, Hong T, Liu J, Huang JQ, et al. The role of microRNA-133b and its target gene FSCN1 in gastric cancer (vol 33, pg 99, 2014). *J Exp Clin Cancer Res* (2020) 39(1). doi: 10.1186/s13046-014-0099-0
27. Wang ZZ, Zhao ZH, Yang Y, Luo M, Zhang M, Wang XF, et al. MiR-99b-5p and miR-203a-3p Function as Tumor Suppressors by Targeting IGF-1R in Gastric Cancer. *Sci Rep* (2018) 8:10119. doi: 10.1038/s41598-018-27583-y
28. Yu T, Wang LN, Li W, Zuo QF, Li MM, Zou QM, et al. Downregulation of miR-491-5p promotes gastric cancer metastasis by regulating SNAIL and FGFR4. *Cancer Sci* (2018) 109(5):1393–403. doi: 10.1111/cas.13583
29. Liu JJ, Yang F, Li WL, Wan HX, Gao NN, Chen SY, et al. Mir-143 Suppresses Tumorigenesis and Progression of Gastric Cancer through Targeting Irbt. *Gastroenterology* (2019) 156(6):S375–S. doi: 10.1016/S0016-5085(19)37780-7
30. Hua KL, Li Y, Zhao Q, Fan LQ, Tan BB, Gu JB. Downregulation of Annexin A11 (ANXA11) Inhibits Cell Proliferation, Invasion, and Migration via the AKT/GSK-3 beta Pathway in Gastric Cancer. *Med Sci Monit* (2018) 24:149–60. doi: 10.12659/MSM.905372
31. Pan JM, Fan ZY, Wang ZQ, Dai QQ, Xiang Z, Yuan F, et al. CD36 mediates palmitate acid-induced metastasis of gastric cancer via AKT/GSK-3/-catenin pathway. *J Exp Clin Cancer Res* (2019) 38. doi: 10.1186/s13046-019-1049-7
32. Wu Y, Song Y, Xiong Y, Wang X, Xu K, Han B, et al. MicroRNA-21 (Mir-21) Promotes Cell Growth and Invasion by Repressing Tumor Suppressor PTEN in Colorectal Cancer. *Cell Physiol Biochem: Int J Exp Cell Physiol Biochem Pharmacol* (2017) 43(3):945–58. doi: 10.1159/000481648
33. Baez-Vega PM, Echevarria Vargas IM, Valiyeva F, Encarnacion-Rosado J, Roman A, Flores J, et al. Targeting miR-21-3p inhibits proliferation and invasion of ovarian cancer cells. *Oncotarget* (2016) 7(24):36321–37. doi: 10.18632/oncotarget.9216
34. Wu X. Expressions of miR-21 and miR-210 in Breast Cancer and Their Predictive Values for Prognosis. *Iran J Public Health* (2020) 49(1):21–9. doi: 10.18502/ijph.v49i1.3048
35. Yang D, Du G, Xu A, Xi X, Li D. Expression of miR-149-3p inhibits proliferation, migration, and invasion of bladder cancer by targeting S100A4. *Am J Cancer Res* (2017) 7(11):2209–19.
36. Luo G, Chao YL, Tang B, Li BS, Xiao YF, Xie R, et al. miR-149 represses metastasis of hepatocellular carcinoma by targeting actin-regulatory proteins PPM1F. *Oncotarget* (2015) 6(35):37808–23. doi: 10.18632/oncotarget.5676

**Conflict of Interest:** The authors declare that the research was conducted in the absence of any commercial or financial relationships that could be construed as a potential conflict of interest.

Copyright © 2021 Zhao, Zhang, Wang, Wang and He. This is an open-access article distributed under the terms of the Creative Commons Attribution License (CC BY). The use, distribution or reproduction in other forums is permitted, provided the original author(s) and the copyright owner(s) are credited and that the original publication in this journal is cited, in accordance with accepted academic practice. No use, distribution or reproduction is permitted which does not comply with these terms.



# Autophagy-Related Long Non-coding RNA Is a Prognostic Indicator for Bladder Cancer

Jiaming Wan<sup>1†</sup>, Cheng Guo<sup>2†</sup>, Hongpeng Fang<sup>1†</sup>, Zhongye Xu<sup>1</sup>, Yongwei Hu<sup>1</sup> and Yun Luo<sup>1\*</sup>

<sup>1</sup> Department of Urology, The Third Affiliated Hospital of Sun Yat-sen University, Guangzhou, China, <sup>2</sup> Department of Otorhinolaryngology Head and Neck Surgery, The Third Affiliated Hospital of Sun Yat-sen University, Guangzhou, China

## OPEN ACCESS

### Edited by:

Dong-Hua Yang,  
St. John's University, United States

### Reviewed by:

Kang Le,  
George Washington University,  
United States  
Litu Zhang,  
Guangxi Medical University Cancer  
Hospital, China  
Wen Zhong,  
First Affiliated Hospital of Guangzhou  
Medical University, China

### \*Correspondence:

Yun Luo  
luoyun8@mail.sysu.edu.cn

<sup>†</sup>These authors have contributed  
equally to this work and share first  
authorship

### Specialty section:

This article was submitted to  
Pharmacology of Anti-Cancer Drugs,  
a section of the journal  
Frontiers in Oncology

**Received:** 29 December 2020

**Accepted:** 12 February 2021

**Published:** 01 April 2021

### Citation:

Wan J, Guo C, Fang H, Xu Z, Hu Y  
and Luo Y (2021) Autophagy-Related  
Long Non-coding RNA Is a Prognostic  
Indicator for Bladder Cancer.  
Front. Oncol. 11:647236.  
doi: 10.3389/fonc.2021.647236

Bladder cancer (BC) is one of the most common malignant urinary system tumors, and its prognosis is poor. In recent years, autophagy has been closely linked to the development of BC. Therefore, we investigated the potential prognostic role of autophagy-related long non-coding RNA (lncRNA) in patients with BC. We obtained the lncRNA information and autophagy genes, respectively, from The Cancer Genome Atlas (TCGA) data set and the human autophagy database (HADb) and performed a co-expression analysis to identify autophagy gene-associated lncRNAs. Then, we divided the data into training group and testing group. In the training group, 15 autophagy-related lncRNAs were found to have a prognostic value (AC026369.3, USP30-as1, AC007991.2, AC104785.1, AC010503.4, AC037198.1, AC010331.1, AF131215.6, AC084357.2, THUMPD3-AS1, U62317.4, MAN1B1-DTt, AC024060.1, AL662844.4, and AC005229.4). The patients were divided into low-risk group and high-risk group based on the prognostic lncRNAs. The overall survival (OS) time for the high-risk group was shorter than that for the low-risk group [risk ratio (hazard ratio, HR) = 1.08, 95% CI: 1.06–1.10;  $p < 0.0001$ ]. Using our model, the defined risk value can predict the prognosis of a patient. Next, the model was assessed in the TCGA testing group to further validate these results. A total of 203 patients with BC were recruited to verify the lncRNA characteristics. We divided these patients into high-risk group and low-risk group. The results of testing data set show that the survival time of high-risk patients is shorter than that of low-risk patients. In the training group, the area under the curve (AUC) was more than 0.7, indicating a high level of accuracy. The AUC for a risk model was greater than that for each clinical feature alone, indicating that the risk value of a model was the best indicator for predicting the prognosis. Further training data analysis showed that the gene set was significantly enriched in cancer-related pathways, including actin cytoskeleton regulation and gap junctions. In conclusion, our 15 autophagy-related lncRNAs have a prognostic potential for BC, and may play key roles in the biology of BC.

**Keywords:** autophagy, TCGA, bladder cancer, prognostic indicator, lncRNA

## INTRODUCTION

Global Cancer Observatory (GCO) data (<https://gco.iarc.fr/>) (1) show that ~550,000 people were diagnosed with bladder cancer (BC) in 2018, making BC the 10th common and 13th most fatal tumor worldwide. Of all patients with BC, ~77% are male and BC is the sixth most common cancer in males worldwide. Furthermore, 53% of the patients with BC are more than 70 years old and the mortality is as high as 47%. The diagnosis of BC is mainly dependent on the findings of specimen biopsy, and the treatments for BC have generally included radical/partial cystectomy, neoadjuvant chemotherapy, adjuvant chemotherapy/radiation, and checkpoint inhibitor-based targeted therapies (2–6). BC is considered to be one of the tumors possessing the greatest economic burden on its treatment because of the difficulty of an accurate diagnosis and a precise treatment, inevitable frequent surveillance strategies, and the high recurrence risk (7, 8). Therefore, timely diagnosis and clinical staging of BC for enabling reasonable and effective treatment measures become an urgent problem.

Autophagy is a process of elemental catabolism responsible for intracellular degradation. In the process of autophagy, excessive,

aggregated, or damaged proteins and organelles are transferred to lysosomes for the degradation and reuse, thereby producing macromolecular molecules and energy (9, 10). Ishaq and his colleagues (11) provided a good overview of the role of autophagy in tumors, describing that autophagy can exert anticancer and pro-cancer dual effects by affecting the web of inter-organelle membrane contact sites, cancer stem cells, cancer metabolism, and tumor immunity (11). Moreover, autophagy is also involved in gene repair and supports the synthesis of DNA in response to oncogenes (12, 13). Few studies show that microRNA (miRNA) 516a exerts carcinogenic effects in BC by attenuating beclin-1 (BECN1)-dependent autophagy (14), the miR-139-5p/Bmi-1 axis is closely related to AMP activated protein kinase (AMPK) and mammalian target of rapamycin (mTOR) pathway-dependent autophagy in human BC cells (15), and autophagy-related gene 7 (ATG7) promotes the invasion of BC *via* an autophagy-mediated increase in the rho GDP dissociation inhibitor beta (*ARHGDIB*) messenger RNA (mRNA) stability (16). Although the role of autophagy and targeted therapy strategies based on this process have gradually become a research hotspot in BC in recent years, the involvement of specific mechanisms and checkpoints remains controversial.

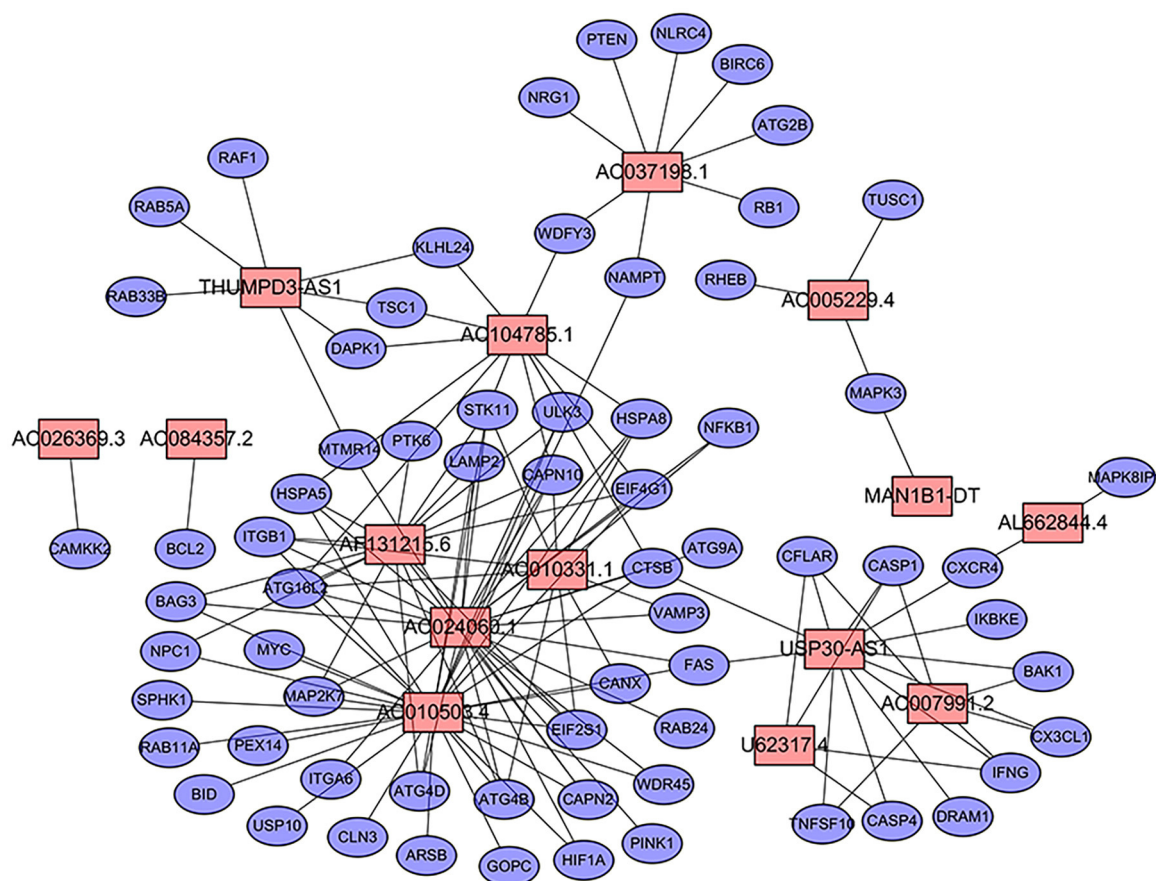


**FIGURE 1 |** Prognostic network of long non-coding RNAs (lncRNAs) and co-expressed autophagy genes in bladder cancer (BC). In the center, the red node represents lncRNA, and the blue represents autophagy genes. The co-expression network was constructed by using CYTOSCAPE 3.7.2 software.



**TABLE 1 |** Autophagy-related long non-coding RNAs (lncRNAs) (*n* = 45) significantly associated with the prognosis of bladder cancer (BC).

ID	HR	95% CI	P-value
AC026369.3	0.285	0.120–0.675	0.004
USP30-AS1	0.601	0.447–0.806	<0.001
AC025165.4	0.360	0.178–0.729	0.005
AC007991.2	0.609	0.436–0.851	0.004
AC104785.1	0.389	0.202–0.747	0.005
AC112721.2	1.376	1.148–1.649	<0.001
AC010503.4	0.754	0.639–0.889	<0.001
AC037198.1	1.475	1.141–1.907	0.003
LINC00942	1.278	1.102–1.481	0.001
AC116914.2	0.521	0.337–0.807	0.004
TNFRSF14-AS1	0.516	0.336–0.791	0.002
MAFG-DT	1.464	1.128–1.900	0.004
AC010331.1	0.481	0.297–0.776	0.003
MANCR	1.524	1.199–1.938	<0.001
AF131215.6	0.582	0.410–0.824	0.002
LINC00324	0.529	0.348–0.803	0.003
SPINT1-AS1	0.738	0.599–0.910	0.005
AC005840.4	0.438	0.274–0.701	<0.001
DBH-AS1	0.427	0.246–0.742	0.003
AC112721.1	1.362	1.133–1.638	0.001
AC016957.2	0.394	0.209–0.745	0.004
AC104825.1	0.663	0.499–0.880	0.004
AC022150.2	0.514	0.359–0.736	<0.001
LINC01871	0.707	0.576–0.867	<0.001
ASB16-AS1	0.461	0.284–0.749	0.002
MIR200CHG	0.777	0.673–0.897	<0.001
AC008610.1	0.555	0.382–0.807	0.002
CARD8-AS1	0.406	0.229–0.719	0.002
AC084357.2	2.242	1.397–3.597	<0.001
LINC01356	1.430	1.138–1.797	0.002
AL033397.1	1.402	1.148–1.714	<0.001
AC009283.1	0.660	0.496–0.878	0.004
ATP1B3-AS1	1.786	1.215–2.626	0.003
AC005291.2	1.509	1.137–2.003	0.004
THUMPD3-AS1	0.546	0.366–0.815	0.003
AL450384.2	0.601	0.441–0.818	0.001
LINC02446	0.615	0.453–0.834	0.002
AC087741.1	0.547	0.365–0.821	0.004
IPO5P1	0.696	0.551–0.880	0.002
U62317.4	0.521	0.340–0.798	0.003
MAN1B1-DT	1.865	1.225–2.839	0.004
AC024060.1	0.628	0.458–0.861	0.004
AL662844.4	0.324	0.152–0.694	0.004
AC011374.2	0.482	0.296–0.784	0.003
AC005229.4	1.948	1.249–3.038	0.003

HR, hazard ratio; CI, confidence interval.

Since the development of high-throughput genomics, long non-coding RNA (lncRNA) has been validated as a non-protein coding RNA comprising different types of RNA polymerase II

**TABLE 2 |** Multivariate cox analysis revealed 15 autophagy lncRNAs that were significantly associated with BC prognosis.

ID	COEF	HR	95% CI
AC026369.3	−0.886	0.412	0.182–0.937
USP30-AS1	−0.329	0.720	0.469–1.105
AC007991.2	−0.488	0.614	0.398–0.947
AC104785.1	−0.739	0.478	0.205–1.115
AC010503.4	−0.308	0.735	0.570–0.946
AC037198.1	0.776	2.173	1.515–3.116
AC010331.1	−0.529	0.589	0.325–1.067
AF131215.6	−0.657	0.518	0.328–0.818
AC084357.2	0.978	2.659	1.686–4.192
THUMPD3-AS1	−0.715	0.489	0.247–0.967
U62317.4	−0.465	0.628	0.341–1.158
MAN1B1-DT	1.185	3.269	1.918–5.573
AC024060.1	0.796	2.216	1.240–3.958
AL662844.4	−2.014	0.133	0.042–0.427
AC005229.4	0.800	2.225	1.254–3.947

COEF, coefficient; HR, hazard ratio; CI, confidence interval.

(Pol II)-transcribed molecules longer than 200 nucleotides (17, 18). lncRNA participates in the occurrence and development of cancer by regulating biological processes including cell growth, cell cycle, cell metastasis, cell death, angiogenesis, metabolic disorders, drug resistance, immune escape, DNA damage, and cell stemness (19, 20). Many reports have corroborated the association between lncRNA and autophagy in cancer. BLACAT1, MALAT1, XIST, SNHGs, HULC, CASC2, GAS5, H19, and HOTAIR all are lncRNAs that mediate chemoresistance in the tumor by modulating autophagy (19). The expression of lncRNA maternally expressed 3 (MEG3) leads to a reduced autophagy activation, which reduces the proliferation of BC cells (21). lncRNA urothelial cancer associated 1 (UCA1) acts as an oncogene and promotes malignant progression of BC through the UCA1-miR-582-5p-ATG7 autophagy signaling pathway (22). Therefore, autophagy-related lncRNAs may be used as prognostic factors in patients with BC and also as potential therapeutic targets. Here, we strived to establish a prognostic system for autophagy-related lncRNA in BC and to promote the targeted therapy of BC.

## MATERIALS AND METHODS

### The Extraction of Information About Patients With BC

The Cancer Genome Atlas (TCGA; <https://cancergenome.nih.gov/>) microarray was used as a training group to establish an autophagy-related lncRNA signature in patients with BC. TCGA is a cancer and tumor gene mapping program launched in the USA in 2006 (23). TCGA includes thousands of samples that have been sequenced by the whole transcriptome sequencing, DNA methylation microarray detection, miRNA, mRNA, and other sequencing. The training data set includes TCGA RNA sequencing (RNA-seq) [fragments per kilobase of transcript

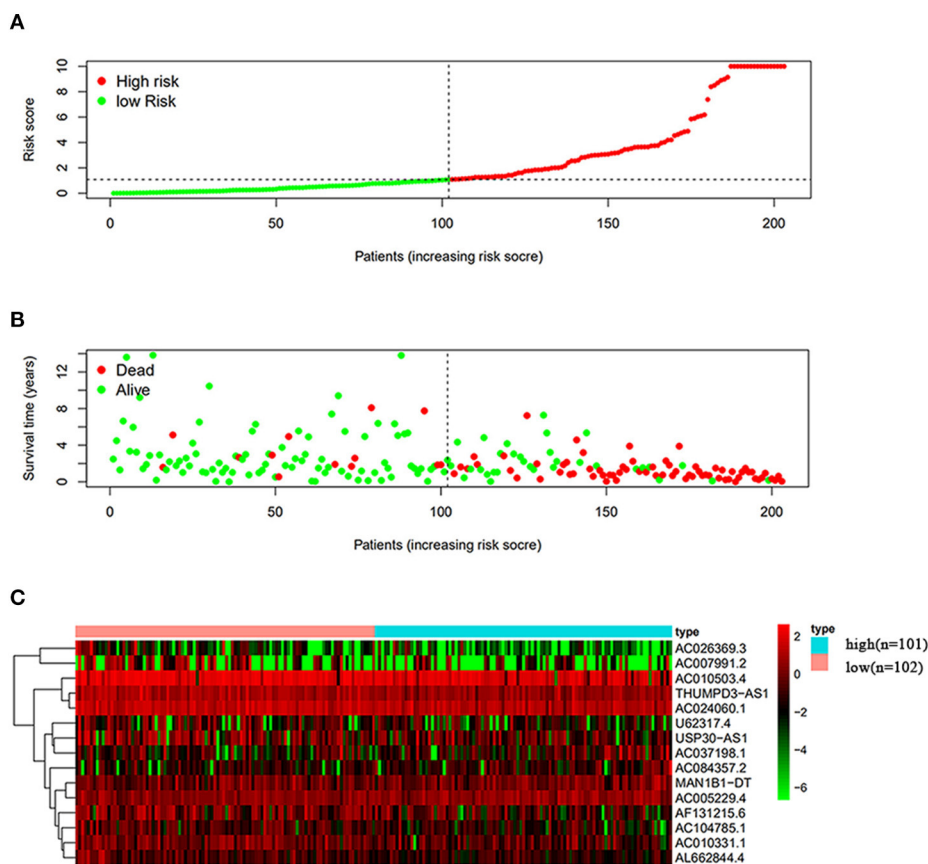


**FIGURE 2 |** Analysis of autophagy-related lncRNA risk scores of patients with BC in The Cancer Genome Atlas (TCGA) training group. **(A)** Patients with BC were divided into low-risk group ( $n = 102$ ) and high-risk group ( $n = 101$ ) based on the median-risk score. **(B)** Survival status and duration of the survival in patients with BC. **(C)** Heat map of the expression of 15 key lncRNAs in BC. The color from green to red shows the expression trend from low level to high level.

per million (FPKM)] from 411 patients with bladder urothelial carcinoma (BLCA), a type of BC, and related clinical data. Transcriptome data and clinical information were downloaded from the data set website.

### Screening for lncRNA Co-expressed With Autophagy-Related Genes

Autophagy-related genes were extracted from the human autophagy database (HADb, <http://autophagy.lu/clustering/index.html>). The Limma R package was used to extract the autophagy-related gene expression information from the TCGA-BLCA RNA sequencing data. To identify the lncRNAs-targeting autophagy-related genes, we analyzed the Pearson correlation between the lncRNA and autophagy-related gene expression levels using the screening criteria: ( $|R2| > 0.3$  and  $p < 0.001$ ). Finally, 1435 lncRNAs co-expressed with autophagy-related genes were identified in a TCGA-BLCA data set.

### Establishment of a Risk Score Model and Building a Risk Curve

We use the survival R package to construct the lncRNA signature. The BLCA sample criteria for identifying and

verifying lncRNA characteristics were: (1) complete lncRNA expression value; and (2) complete clinical characteristics (the survival time and survival status). A total of 406 BLCA samples were included for further construction of lncRNA characteristics. We randomly divided the 406 BLCA samples into the training group ( $n = 203$ ) and testing group ( $n = 203$ ). The training cohort was used to develop the lncRNA features. The experimental cohort was used to verify the lncRNA characteristics.

Secondly, 406 lncRNAs were selected from a training cohort for univariate Cox regression analysis to identify prognosis-related lncRNAs ( $p < 0.005$ ). Univariate Cox regression analysis identified 45 prognostic lncRNAs. We used the Akaike information criterion (AIC) method to select the optimal model from 45 prognostic lncRNAs. Finally, we selected 15 lncRNAs with the lowest AIC values to build a prediction model.

Multivariate Cox regression analysis was performed on 15 prognostic lncRNAs to determine their prognostic characteristics and calculate the correlation coefficient (24, 25). The risk score for the prognostic lncRNA characteristics of each patient was

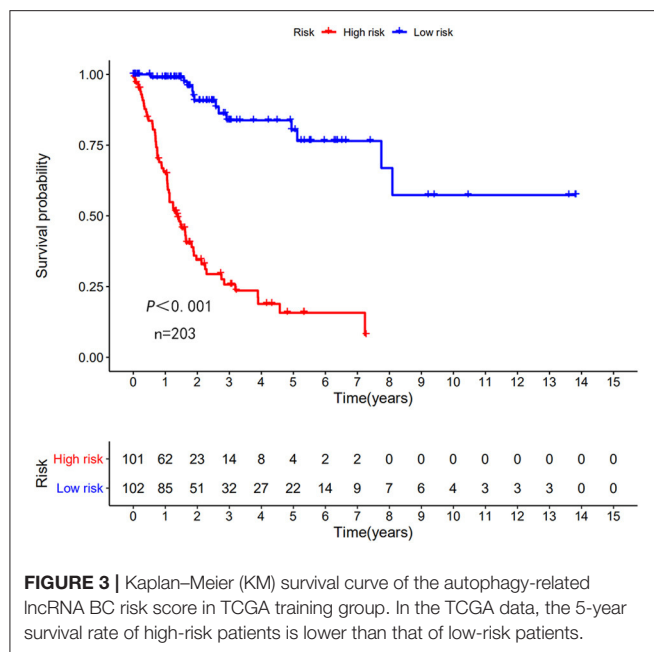


**FIGURE 3 |** Kaplan-Meier (KM) survival curve of the autophagy-related lncRNA BC risk score in TCGA training group. In the TCGA data, the 5-year survival rate of high-risk patients is lower than that of low-risk patients.

**TABLE 3 |** Multivariate Cox regression analysis of characteristics and risk score in BC.

ID	B	SE	z	HR	95% CI	P-value
Age	0.040	0.014	2.906	1.040	1.013–1.069	0.004
Gender	−0.176	0.275	−0.637	0.839	0.489–1.440	0.524
Grade	1.910	1.099	1.738	6.754	0.784–58.181	0.082
Stage	0.268	0.323	0.830	1.307	0.694–2.459	0.407
T	0.462	0.239	1.935	1.588	0.994–2.536	0.053
M	0.226	0.139	1.628	1.253	0.955–1.645	0.103
N	0.138	0.215	0.640	1.148	0.753–1.749	0.522
Risk score	0.076	0.010	7.679	1.079	1.058–1.100	<0.001

B, regression coefficient; SE, standard error; HR, hazard ratio; CI, confidence interval; stage, union for international cancer control (UICC) stage; T, pT stage; M, pM stage; N, pN stage.

calculated by using the following formula:

$$\text{Risk score} = \text{expression lncRNA1} \times \text{coefficient lncRNA1} \\ + \text{expression lncRNA2} \times \text{coefficient lncRNA2} + \dots \\ + \text{the expression lncRNA}_n \times \text{coefficient lncRNA}_n.$$

The risk score of prognostic lncRNAs was calculated by using a linear combination of lncRNA expression levels weighted by a regression coefficient ( $\beta$ ).  $\beta$  was calculated by a log conversion of the hazard ratio (HR) obtained from multivariate Cox regression analysis (26). Low-risk group and high-risk group were determined by using the median-risk score.

## Risk Model Prediction Ability in Training Group and Testing Group

Survival and phopmap packages were used to evaluate the predictive value of the risk model in a training cohort ( $n = 203$ ).

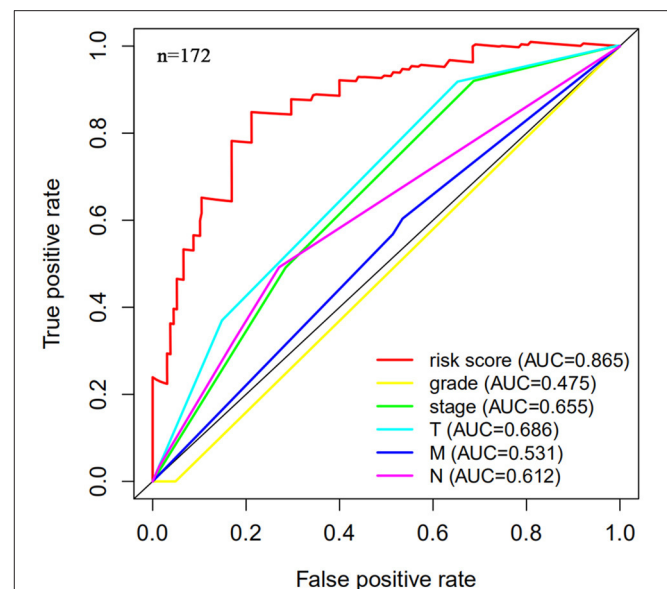


**FIGURE 4 |** Multi-factor receiver operating characteristic (ROC) curve. The area under the curve (AUC) value of the model established in the training group is significantly more than 0.7, and is greater than the predicted value of clinical data.

**TABLE 4 |** lncRNA clinical correlation analysis.

Clinical	Group	N	Mean	SD	t	P-value
Age	>65	106	4.528	9.902	0.855	0.394
	≤65	66	3.287	8.838		
Gender	Female	54	5.305	12.264	1.003	0.319
	Male	118	3.478	7.921		
Grade	High	165	4.179	9.678	3.547	0.001
	Low	7	1.053	1.209		
Stage	I-II	47	1.17	1.374	−3.974	<0.001
	III-IV	125	5.135	10.929		
T	T1-2	52	1.163	1.323	−4.012	<0.001
	T3-4	120	5.303	11.123		
M	M0	78	4.203	11.032	0.185	0.853
	M1	94	3.926	8.073		
N	N0-1	138	3.663	8.909	−0.921	0.362
	N2-3	34	5.627	11.620		

Clinical, clinical characteristics; Mean, arithmetic mean; SD, standard deviation; t, t-value; stage, UICC stage; T, pT stage; M, pM stage; N, pN stage.

The training cohort was divided into low-risk group and high-risk group based on the median risk score. The Kaplan-Meier (KM) survival curve was drawn to compare the difference in the overall survival (OS) between the two groups and a risk curve was drawn.  $p < 0.05$  was considered as statistically significant.

Subsequently, the training group was used to sort the complete data ( $n = 172$ ) for each clinical feature. These clinical features include age, gender, union for international cancer control (UICC) stage, histologic grade, and pathological TNM (pTNM) stage. Univariate and multivariate Cox regression analyses were

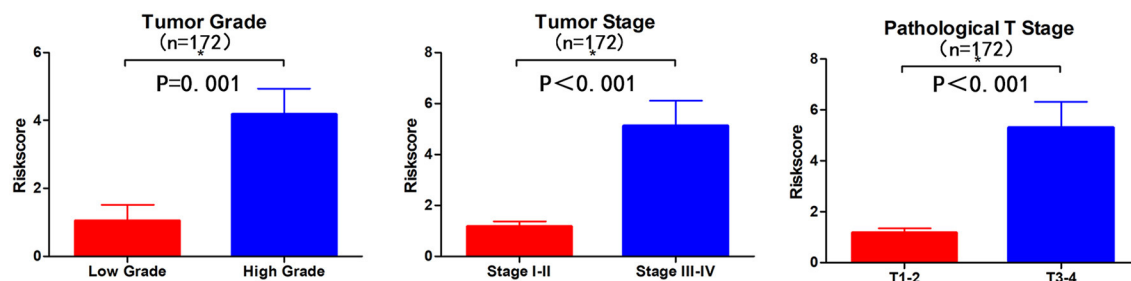


**FIGURE 5 |** Visualization of the clinical correlation between autophagy-related lncRNA model and patients with BC. The risk score is closely related to grade, union for international cancer control (UICC) stage, and pathological T stage (\* $p < 0.05$ ).

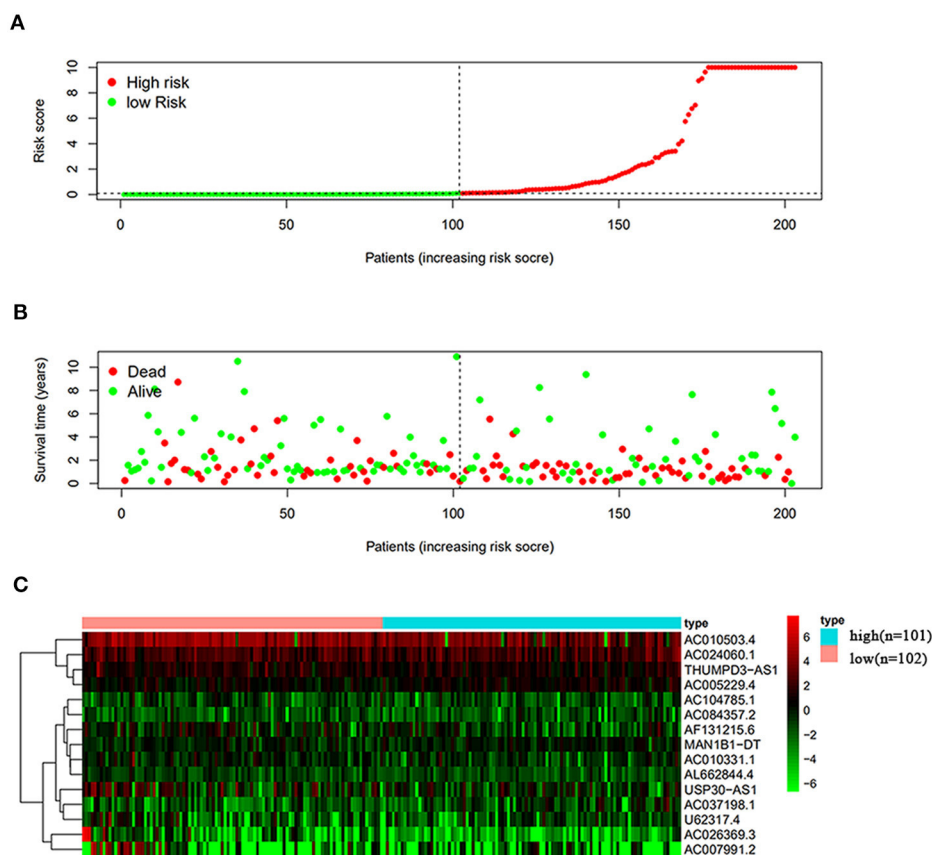


**FIGURE 6 |** Analysis of autophagy-related lncRNA risk scores of patients with BC in TCGA testing group. **(A)** Autophagy-related lncRNA low-risk group ( $n = 102$ ) and high-risk group ( $n = 101$ ) in patients with BC. **(B)** Survival status and duration of BC cases. **(C)** Heat map of the expression of 15 key lncRNAs in BC. The color from green to red shows the expression trend from low level to high level.

used to evaluate the predictive power of the risk model. Then, survrroc was used to draw the time-dependent receiver operating characteristic (ROC) curve and area under the curve (AUC) values to evaluate the predictive value of the comparative risk model and the assessed clinical features.  $p < 0.05$  was considered as statistically significant. We then conducted a correlation analysis between the model risk score and the clinical characteristics of the training group. Each clinical feature was

divided into two categories (e.g., dividing age into  $> 65$  and  $\leq 65$ , and dividing the grade into high and low). SPSS 25 software was used for statistical analyses.

The same method was used in the testing group to verify the stability and reliability of the risk model. The testing group ( $n = 203$ ) was divided into low-risk group and high-risk group based on the median risk. The KM survival and risk curves were drawn. The testing group data with complete clinical data was selected ( $n$



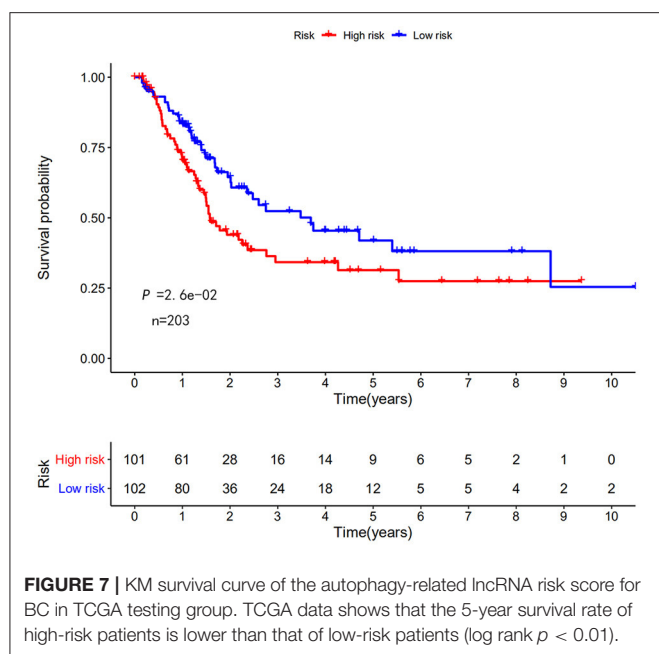


**FIGURE 7 |** KM survival curve of the autophagy-related lncRNA risk score for BC in TCGA testing group. TCGA data shows that the 5-year survival rate of high-risk patients is lower than that of low-risk patients (log rank  $p < 0.01$ ).

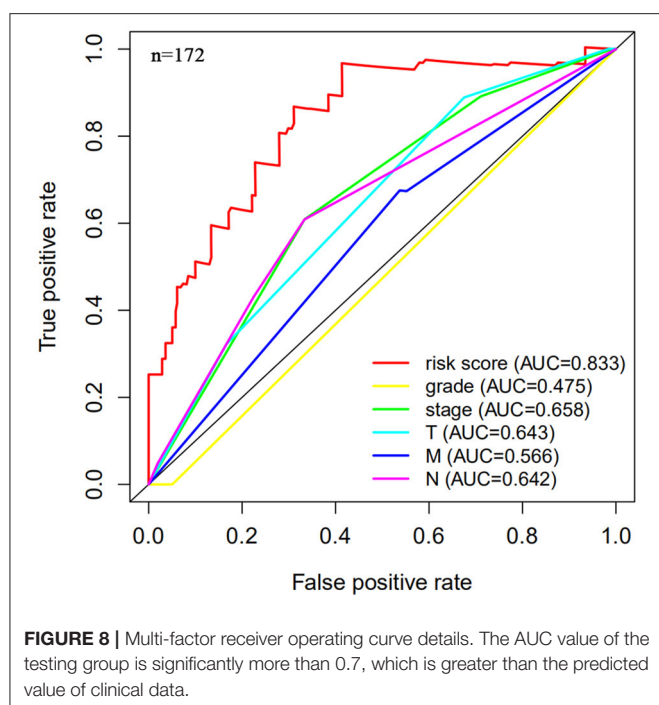


**FIGURE 8 |** Multi-factor receiver operating curve details. The AUC value of the testing group is significantly more than 0.7, which is greater than the predicted value of clinical data.

= 172), and the time-dependent ROC curve and AUC value were determined to evaluate the predictive value of the comparative risk model and these clinical features.

## Gene Set Enrichment Analysis

Gene set enrichment analysis (GSEA) was used to determine the gene set functions. The aim was to use a predefined set of genes, sort the genes according to the differential expression levels in the

two sample groups, and check whether the gene set was enriched at the top or bottom of this sorting table.

## Statistical Analysis

Cytoscape software (version 3.7.2) was used to construct an autophagy-related lncRNA co-expression network. R language (version x64 3.6.3, survival library) was used to estimate the survival rate, generate a survival curve, and perform the Cox regression analysis. We used the R language (pheatmap library) to generate the risk value, survival time, and risk heat maps. We used the R language (survival ROC library) to draw a multi-index ROC curve. GSEA (version 4.0.3) was used to distinguish between the two sets of functional annotations. SPSS 25 was used to analyze the correlation between the risk model and clinical features. Statistical significance was set at the threshold of  $p < 0.05$  for both tails.

## RESULTS

### Autophagy-Related Gene lncRNAs Co-expression Network Construction

We extracted the lncRNA data from the TCGA database transcriptome data set. A total of 232 autophagy-related genes were extracted from the HADb (<http://autophagy.lu/clustering/index.html>). We constructed an autophagy-related lncRNA co-expression network and performed a co-expression analysis to identify autophagy-related lncRNAs. The screening criteria were ( $|R2| > 0.3$  and  $p < 0.001$ ). A co-expression network diagram with autophagy genes was drawn by using the 15 prognostic-related lncRNAs identified by multivariate Cox analysis (Figure 1).

### Selection of 15 Autophagy-Related Prognostic lncRNAs for Patients With BC

First, we used univariate Cox regression analysis based on the identified autophagy-related lncRNAs to initially screen the prognostic genes. We used a value of  $p = 0.005$  as a cutoff value, and the lncRNAs that met this criterion were used to judge prognostic indicators. Our training set included 203 patients with BC from the TCGA data set. A total of 45 lncRNAs had a prognostic value for patients with BC ( $p < 0.01$ ) (Table 1). Then, we used the AIC method to select the best model from the 45 prognostic lncRNAs. About 15 autophagy-related lncRNAs were found to be suitable for model building. Of these lncRNAs, 5 were unfavorable prognostic factors (AC037198.1, AC084357.2, MAN1B1-DT, AC024060.1, and AC005229.4) and 10 were favorable prognostic factors (AC026369.3, USP30-as1, AC007991.2, AC104785.1, AC010503.4, AC010331.1, AF131215.6, THUMPD3-AS1, U62317.4, and AL662844.4) for BC (Table 2). These 15 autophagy-related lncRNAs were used as a prognostic model.

### The Effect of Autophagy-Related lncRNA on BC Prognosis

The risk scoring method was used to assess the prognosis of BC in the training group ( $n = 203$ ). We divided patients with BC into low-risk group and high-risk group based on the median risk

**TABLE 5 |** Gene set enrichment analysis (GSEA) results based on 15 autophagy lncRNA markers.

Name	ES	NES	NOM <i>P</i> -val	FDR <i>q</i> -val	FWER <i>P</i> -val	RANK AT MAX	Leading edge
KEGG_FOCAL_ADHESION	0.629	2.287	<0.001	0.002	0.003	5254	Tags = 46%, list = 10%, signal = 50%
KEGG_GLIOMA	0.592	2.201	<0.001	0.006	0.007	6855	Tags = 45%, list = 12%, signal = 51%
KEGG_GAP_JUNCTION	0.552	2.060	0.002	0.012	0.039	6855	Tags = 42%, list = 12%, signal = 48%
KEGG_ECM_RECEPTOR_INTERACTION	0.691	2.112	0.002	0.012	0.023	5559	Tags = 56%, list = 10%, signal = 62%
KEGG_REGULATION_OF_ACTIN_CYTOSKELETON	0.515	2.078	<0.001	0.012	0.03	5731	Tags = 38%, list = 10%, signal = 42%
KEGG_WNT_SIGNALING_PATHWAY	0.474	1.927	<0.001	0.025	0.111	11144	Tags = 48%, list = 20%, signal = 60%
KEGG_SMALL_CELL_LUNG_CANCER	0.488	1.864	0.004	0.041	0.181	5555	Tags = 35%, list = 10%, signal = 38%

ES, enrichment score; FDR, false discovery rate; FWER, familywise-error rate; NES, normalized enrichment score; NOM *p*-value, nominal *p*-value.

score (**Figure 2**). The risk score can significantly predict the OS in patients with BC, with OS being longer in the low-risk group than in the high-risk group. Additionally, a KM survival curve for BC autophagy-related lncRNA risk scores was plotted (**Figure 3**). The KM survival curve showed that the 5-year survival rate was greater in the low-risk group than that in the high-risk group (log rank  $p < 0.01$ ). We screened the training group data with complete clinical characteristics for the next analysis ( $n = 172$ ) and used multivariate Cox regression analysis to explore if the risk score is an independent predictor of prognosis in patients with BC. The HR was 1.080, which indicates that the risk score model can significantly help predict the survival in patients with BC, and eliminates the effects of other factors (such as age, gender, and grade; **Table 3**). Next, the ROC curve of clinical data and risk score was drawn. The AUC of the ROC curve of the risk score was 0.865, which is  $> 0.7$  and indicates that the model has good accuracy. The AUC of the model is greater than that of any other clinical characteristics, which indicate that the model is superior to other clinical traits in prognostic prediction (**Figure 4**).

### Clinical Correlation Between Autophagy-Related lncRNAs and Patients With BC

Subsequently, we determined the clinical value of the 15 autophagy-related lncRNAs in terms of age, gender, grade, and pTNM stage (**Table 4**). The risk score is closely related to grade, UICC stage, and pT stage (**Figure 5**), but is not strongly related to age, gender, pN stage, and pM stage. Additionally, the risk score tends to increase in higher grades, which indicates that the lncRNA signature may be related to BC progression.

### Validation in the TCGA Data Set

Next, this model was validated by using the TCGA testing group. A total of 203 patients with BC were recruited to verify the lncRNA characteristics (**Figure 6**). We divided the patients with BC into low-risk group and high-risk group based on the median

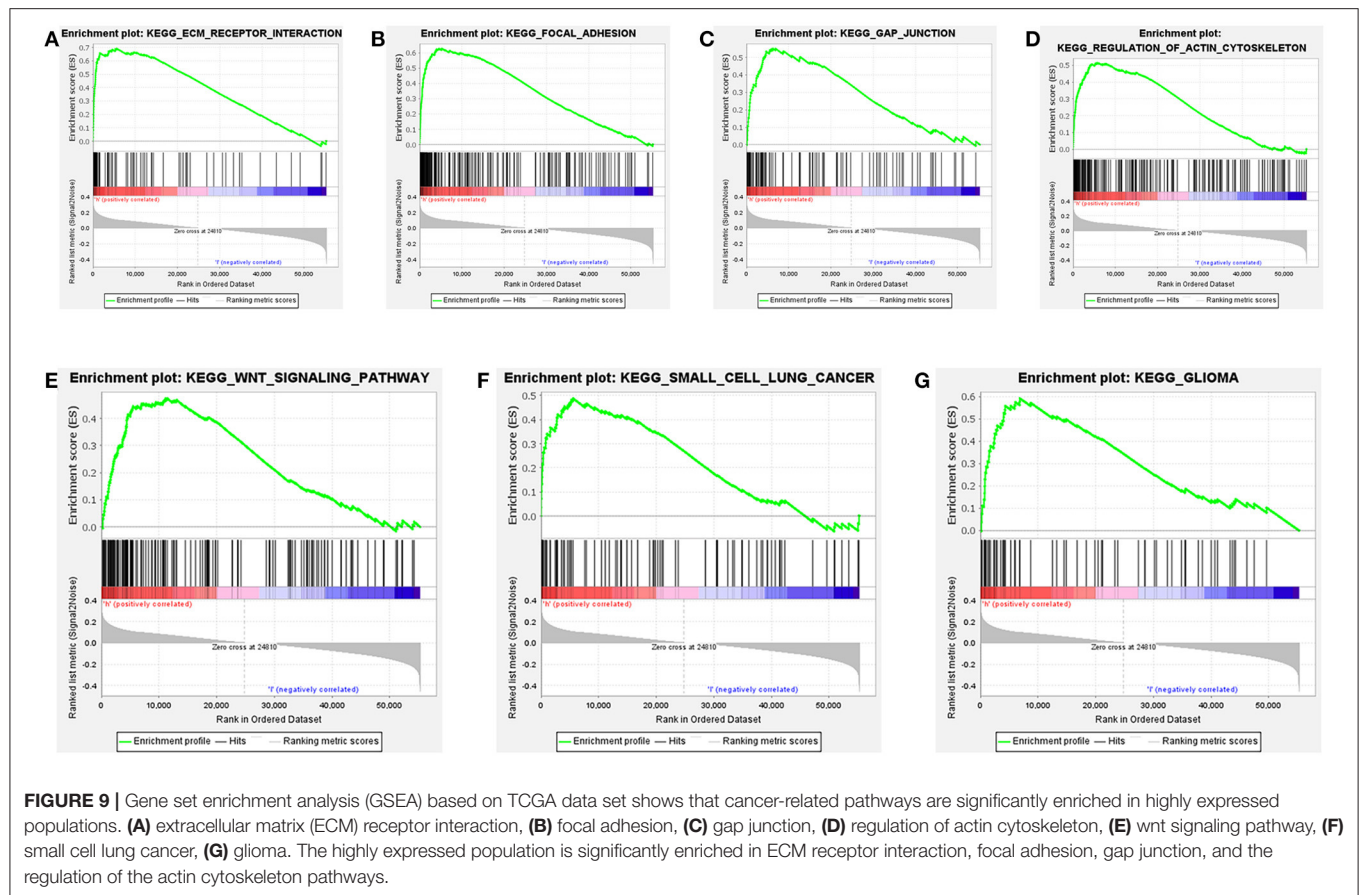
risk score. Consistent with the results obtained from the TCGA data set training group, the survival time was shorter in high-risk patients than in low-risk patients (**Figure 7**). Testing group data were then screened with complete clinical characteristics ( $n = 172$ ), and the time-related ROC curve was drawn (**Figure 8**). The AUC value was 0.833, which is  $> 0.7$ , and indicates that the risk model has great predictive ability and that the predictive ability of the risk model is greater than that of other clinical features. Together, these results show that the established lncRNA signature provides reliable prognostic predictions for patients with BC.

### Gene Set Enrichment Analysis

Further functional annotations were made through GSEA. The results showed that differentially expressed genes between the two groups were enriched in tumor-related pathways. A total of 11 gene sets were significantly enriched when the nominal value of  $p < 0.05$ . We selected seven pathways closely related to tumor metastasis and invasion, including actin cytoskeleton regulation, gap junctions, focal adhesion, and extracellular matrix (ECM) receptor interaction (**Table 5**). These are important signaling pathways related to tumorigenesis and cancer progression, including in small cell lung cancer, which is highlighted by the relationship between the Wnt signaling pathway and glioma (**Figure 9**). In conclusion, the identified autophagy-related genes contribute to important cancer pathways. This may provide a new direction for the treatment of BC.

### DISCUSSION

Bladder cancer is defined as malignant tumors that occur on the bladder mucosa. BC is the most common malignant tumor of the urinary system (27). There are currently some BC prognostic indicators, including tumor grade, UICC stage, and pTNM stage (28). However, additional prognostic factors are required to more accurately predict and analyze the survival rate in patients with



BC. At present, a large number of lncRNAs have been analyzed in the diagnosis and prognosis of various cancers.

Long non-coding RNA *ErbB4-IR* is downregulated in prostate cancer and can predict the prognosis (29). Overexpression of lncRNA *ROR1AS1* predicts a poor prognosis and promotes cervical cancer metastasis by activating the Wnt/ $\beta$ -catenin/EMT signaling cascade (30). lncRNA-D16366 is a potential biomarker for the diagnosis and prognosis of hepatocellular carcinoma (31). lncRNA *PVT1* can predict a prognosis in patients with prostate cancer and regulate the tumor growth (32). lncRNA *FENDRR* and *FOXF1* are also prognostic factors for the survival in patients with lung adenocarcinoma (33). In addition, many reports confirm a link between lncRNA and autophagy in cancer.

Reduced expression of lncRNA *PRRT3-AS1* can inhibit the prostate cancer cell proliferation and promote apoptosis and autophagy (34). In acute myeloid leukemia, lncRNA *UCA1* promotes autophagy by targeting miR-96-5p (35). lncRNA *MALAT1* activates autophagy and promotes the cell proliferation by downregulating the miRNA-204 expression in gastric cancer (36). However, to-date, there has been no systematic and comprehensive analysis of autophagy-related lncRNA in BC. This study is the first to use bioinformatics to analyze the value of autophagy-related lncRNA in the diagnosis and prognosis of BC. These results are expected to provide new

ideas and research directions for the diagnosis and treatment of BC.

In this study, we collected TCGA data sets and divided them into training group and testing group. In the training group, autophagy-related lncRNAs were used to investigate the prognosis of BC in patients. We identified autophagy-related lncRNAs by constructing a lncRNA autophagy gene co-expression network. We identified a signature of 15 autophagy-related lncRNAs and divided the patients with BC into low-risk group and a high-risk group based on the median risk score. The 5-year survival rate of patients in the high-risk group was shorter than that of patients in the low-risk group. Using univariate and multivariate Cox regression analyses, we showed that the risk score is an independent BC prognostic prediction factor. Subsequently, a multi-factor ROC curve was made, and its AUC was 0.865, which was greater than the AUC of each clinical feature. Together, these results show that the lncRNA signature can better predict a prognosis in patients with BC than can other clinical features. Then, the model was used to predict a prognosis in the testing group, and satisfactory results were obtained, which prove the effectiveness of the model.

Among the 15 autophagy-related lncRNAs, 5 were unfavorable diagnostic factors (*AC037198.1*, *AC084357.2*, *MAN1B1-DT*, *AC024060.1*, and *AC005229.4*) and 10 were

favorable diagnostic factors for BC (AC026369.3, USP30-as1, AC007991.2, AC104785.1, AC010503.4, AC010331.1, AF131215.6, THUMP3-AS1, U62317.4, and AL662844.4). The results of GSEA revealed that differentially expressed lncRNAs in high-risk people are enriched in the Wnt signaling, small cell lung cancer, and glioma pathways, gap junctions, focal adhesion, actin cytoskeleton regulation, and ECM receptor interaction.

Previous studies have shown that THUMP3-AS1 is associated with non-small cell lung cancer and regulates self-renewal through miR-543 and ONECUT2 (37). The Wnt/ $\beta$ -catenin signaling pathway promotes the progression of liver cancer through the activation of SUMO1P3 lncRNA by targeting miR-320a (38). A large number of studies also indicate that lncRNA can directly or indirectly regulate the development of cancer through the regulation of miRNA. Therefore, lncRNA-mRNA co-expression analyses are essential to fully evaluate the function of lncRNAs in cancer. Additionally, the autophagy-related functions of lncRNAs occur through the regulation of mRNA. Therefore, it is important to analyze the specific function of lncRNAs by examining the co-expression of lncRNA-mRNA (39, 40). Ultimately, our results indicate that the 15 autophagy-related lncRNAs identified in this study are potential BC therapeutic targets.

By constructing an autophagy lncRNA co-expression network, we identified a risk model of 15 autophagy-related lncRNAs. Using this model, we were able to separate the group as low risk and high risk based on the median-risk score. This risk score has a prognostic value for patients with BC. In the future, this lncRNA model can be used for risk scoring to predict the prognosis of a patient. However, our research contains several limitations. Bioinformatics methods and public databases were used for this study. Although the stability

of the autophagy-related lncRNA signature was successfully validated, the exact molecular mechanisms of these lncRNAs have not been experimentally investigated and their prognostic values have not been experimentally proven. Therefore, further experimental studies using a larger sample size are required to verify these results.

## DATA AVAILABILITY STATEMENT

The data that support the findings of this study are available from the corresponding author upon reasonable request.

## AUTHOR CONTRIBUTIONS

JW and CG: conceptualization, methodology, validation, formal analysis, investigation, data curation, writing of the original draft, and reviewing and editing. HF, ZX, and YH: validation, formal analysis, investigation, data curation, and visualization. YL: conceptualization, methodology, investigation, data curation, reviewing and editing the manuscript, visualization, supervision, and project administration. All authors: agree to be accountable for the content of the work.

## FUNDING

The authors acknowledge financial support from the Science and Technology Planning Project of Guangzhou no. 201610010016 (YL), the Foundation of the 3rd Affiliated Hospital of Sun Yat-sen University (YL), and the Natural Science Foundation of Guangdong Province no. 2018A030313459 (YL).

## REFERENCES

- Bray F, Ferlay J, Soerjomataram I, Siegel RL, Torre LA, Jemal A. Global cancer statistics 2018: GLOBOCAN estimates of incidence and mortality worldwide for 36 cancers in 185 countries. *CA Cancer J Clin.* (2018) 68:394–424. doi: 10.3322/caac.21492
- Davis AA, Patel VG. The role of PD-L1 expression as a predictive biomarker: an analysis of all US Food and Drug Administration (FDA) approvals of immune checkpoint inhibitors. *J Immunother Cancer.* (2019) 7:278. doi: 10.1186/s40425-019-0768-9
- Segovia C, San Jose-Eneriz E, Munera-Maravilla E, Martinez-Fernandez M, Garate L, Miranda E, et al. Inhibition of a G9a/DNMT network triggers immune-mediated bladder cancer regression. *Nat Med.* (2019) 25:1073–81. doi: 10.1038/s41591-019-0499-y
- Wang L, Gong Y, Saki A, Szabo PM, Martini A, Necchi A, et al. Fibroblast growth factor receptor 3 alterations and response to PD-1/PD-L1 blockade in patients with metastatic urothelial cancer. *Europ Urol.* (2019) 76:599–603. doi: 10.1016/j.eururo.2019.06.025
- Morales-Barrera R, Suarez C, Gonzalez M, Valverde C, Serra E, Mateo J, et al. The future of bladder cancer therapy: optimizing the inhibition of the fibroblast growth factor receptor. *Cancer Treat Rev.* (2020) 86:102000. doi: 10.1016/j.ctrv.2020.102000
- Casadei C, Dizman N, Schepisi G, Cursano MC, Basso U, Santini D, et al. Targeted therapies for advanced bladder cancer: new strategies with FGFR inhibitors. *Therap Adv Med Oncol.* (2019) 11:1758835919890285. doi: 10.1177/1758835919890285
- Dason S, Cha EK, Falavolti C, Vertosick EA, Dean LW, McPherson VA, et al. Late recurrences following radical cystectomy have distinct prognostic and management considerations. *J Urol.* (2020) 204:460–5. doi: 10.1097/JU.0000000000001028
- Ravva K, Weissert JA, Downs TM. American urological association nonmuscle invasive bladder cancer risk model validation—should patient age be added to the risk model? *J Urol.* (2019) 202:682–8. doi: 10.1097/JU.0000000000000389
- Yang Z, Klionsky DJ. Mammalian autophagy: core molecular machinery and signaling regulation. *Curr Opin Cell Biol.* (2010) 22:124–31. doi: 10.1016/j.ceb.2009.11.014
- Mizushima N, Komatsu M. Autophagy: renovation of cells and tissues. *Cell.* (2011) 147:728–41. doi: 10.1016/j.cell.2011.10.026
- Ishaq M, Ojha R, Sharma AP, Singh SK. Autophagy in cancer: recent advances and future directions. *Semin Cancer Biol.* (2020) 66:171–81. doi: 10.1016/j.semcancer.2020.03.010
- Vanzo R, Bartkova J, Mercht-May JM, Hall A, Bouchal J, Dyrskjot L, et al. Autophagy role(s) in response to oncogenes and DNA replication stress. *Cell Death Different.* (2020) 27:1134–53. doi: 10.1038/s41418-019-0403-9
- Hewitt G, Korolchuk VI. Repair, reuse, recycle: the expanding role of autophagy in genome maintenance. *Trends Cell Biol.* (2017) 27:340–51. doi: 10.1016/j.tcb.2016.11.011
- Jin H, Ma J, Xu J, Li H, Chang Y, Zang N, et al. Oncogenic role of MIR516A in human bladder cancer was mediated by its attenuating PHLPP2 expression and BECN1-dependent autophagy. *Autophagy.* (2020) 16:1–15. doi: 10.1080/15548627.2020.1733262



15. Wang F, Wu H, Fan M, Yu R, Zhang Y, Liu J, et al. Sodium butyrate inhibits migration and induces AMPK-mTOR pathway-dependent autophagy and ROS-mediated apoptosis via the miR-139-5p/Bmi-1 axis in human bladder cancer cells. *FASEB J.* (2020) 34:4266–82. doi: 10.1096/fj.201902626R
16. Zhu J, Tian Z, Li Y, Hua X, Zhang D, Li J, et al. ATG7 promotes bladder cancer invasion via autophagy-mediated increased ARHGAP10 mRNA stability. *Adv Sci.* (2019) 6:1801927. doi: 10.1002/adv.201801927
17. Chen LL. Linking long noncoding RNA localization and function. *Trends Biochem Sci.* (2016) 41:761–72. doi: 10.1016/j.tibs.2016.07.003
18. Ponting CP, Oliver PL, Reik W. Evolution and functions of long noncoding RNAs. *Cell.* (2009) 136:629–41. doi: 10.1016/j.cell.2009.02.006
19. Jin KT, Lu Z. B, Lv JQ, Zhang JG. The role of long non-coding RNAs in mediating chemoresistance by modulating autophagy in cancer. *RNA Biol.* (2020) 17:1727–40. doi: 10.1080/15476286.2020.1737787
20. Zhang Y, Tao Y, Liao Q. Long noncoding RNA: a crosslink in biological regulatory network. *Briefings Bioinform.* (2018) 19:930–45. doi: 10.1093/bib/bbx042
21. Ying L, Huang Y, Chen H, Wang Y, Xia L, Chen Y, et al. Downregulated MEG3 activates autophagy and increases cell proliferation in bladder cancer. *Mol Biosyst.* (2013) 9:407–11. doi: 10.1039/c2mb25386k
22. Wu J, Li W, Ning J, Yu W, Rao T, Cheng F. Long noncoding RNA UCA1 targets miR-582-5p and contributes to the progression and drug resistance of bladder cancer cells through ATG7-mediated autophagy inhibition. *Oncotargets Therap.* (2019) 12:495–508. doi: 10.2147/OTT.S183940
23. Sharpless Norman “Ned”, Liang H, Hutter C, Zenklusen JC, Shen H, Giordano TJ. The TCGA legacy. *Cell.* (2018) 173:281–2. doi: 10.1016/j.cell.2018.03.049
24. Zhang CB, Zhu P, Yang P, Cai JQ, Wang ZL, Li QB, et al. Identification of high risk anaplastic gliomas by a diagnostic and prognostic signature derived from mRNA expression profiling. *Oncotarget.* (2015) 6:36643–51. doi: 10.18632/oncotarget.5421
25. Cai J, Zhang W, Yang P, Wang Y, Li M, Zhang C, et al. Identification of a 6-cytokine prognostic signature in patients with primary glioblastoma harboring M2 microglia/macrophage phenotype relevance. *PLoS ONE.* (2015) 10:e0126022. doi: 10.1371/journal.pone.0126022
26. Zhang W, Zhang J, Yan W, You G, Bao Z, Li S, et al. Whole-genome microRNA expression profiling identifies a 5-microRNA signature as a prognostic biomarker in Chinese patients with primary glioblastoma multiforme. *Cancer.* (2013) 119:814–24. doi: 10.1002/cn.127826
27. Antoni S, Ferlay J, Soerjomataram I, Znaor A, Jemal A, Bray F. Bladder cancer incidence and mortality: a global overview and recent trends. *Eur Urol.* (2017) 71:96–108. doi: 10.1016/j.eururo.2016.06.010
28. Alfred Witjes J, Lebrecht T, Comperat EM, Cowan NC, De Santis M, Bruins HM, et al. Updated 2016. EAU guidelines on muscle-invasive and metastatic bladder cancer. *Eur Urol.* (2017) 71:462–75. doi: 10.1016/j.eururo.2016.06.020
29. Zhou J, Song Q, Liu X, Ye H, Wang Y, Zhang L, et al. lncRNA Erbb4-IR is downregulated in prostate carcinoma and predicts prognosis. *Oncol Lett.* (2020) 19:3425–30. doi: 10.3892/ol.2020.11464
30. Zhang L, Yao HR, Liu SK, Song LL. Long noncoding RNA ROR1AS1 overexpression predicts poor prognosis and promotes metastasis by activating Wnt/beta-catenin/EMT signaling cascade in cervical cancer. *Eur Rev Med Pharmacol Sci.* (2020) 24:2928–37. doi: 10.26355/eurrev\_202003\_20656
31. Chao Y, Zhou D. lncRNA-D16366 is a potential biomarker for diagnosis and prognosis of hepatocellular carcinoma. *Med Sci Monitor.* (2019) 25:6581–6. doi: 10.12659/MSM.915100
32. Yang J, Li C, Mudd A, Gu X. lncRNA PVT1 predicts prognosis and regulates tumor growth in prostate cancer. *Biosci Biotechnol Biochem.* (2017) 81:2301–6. doi: 10.1080/09168451.2017.1387048
33. Herrera-Merchan A, Cuadros M, Rodriguez MI, Rodriguez S, Torres R, Estecio M, et al. The value of lncRNA FENDRR and FOXF1 as a prognostic factor for survival of lung adenocarcinoma. *Oncotarget.* (2020) 11:1172–85. doi: 10.18632/oncotarget.22154
34. Fan L, Li H, Wang W. Long noncoding RNA PRRT3-AS1 silencing inhibits prostate cancer cell proliferation and promotes apoptosis and autophagy. *Exp Physiol.* (2020) 105:793–808. doi: 10.1113/EP088011
35. Li JJ, Chen XF, Wang M, Zhang PB, Zhang F, Zhang JJ. Long non-coding RNA UCA1 promotes autophagy by targeting miR-96-5p in acute myeloid leukaemia. *Clin Exp Pharmacol Physiol.* (2020) 47:877–85. doi: 10.1111/1440-1681.13259
36. Shao G, Zhao Z, Zhao W, Hu G, Zhang L, Li W, et al. Long non-coding RNA MALAT1 activates autophagy and promotes cell proliferation by downregulating microRNA-204 expression in gastric cancer. *Oncol Lett.* (2020) 19:805–12. doi: 10.3892/ol.2019.11184
37. Hu J, Chen Y, Li X, Miao H, Li R, Chen D, et al. THUMP3-AS1 is correlated with non-small cell lung cancer and regulates self-renewal through miR-543 and ONECUT2. *Oncotargets Therap.* (2019) 12:9849–60. doi: 10.2147/OTT.S227995
38. Wu S, Chen S, Lin N, Yang J. Long non-coding RNA SUMO1P3 promotes hepatocellular carcinoma progression through activating Wnt/beta-catenin signalling pathway by targeting miR-320a. *J Cell Mol Med.* (2020) 24:3108–16. doi: 10.1111/jcmm.14977
39. Guo Q, Cheng Y, Liang T, He Y, Ren C, Sun L, et al. Comprehensive analysis of lncRNA-mRNA co-expression patterns identifies immune-associated lncRNA biomarkers in ovarian cancer malignant progression. *Sci Rep.* (2015) 5:17683. doi: 10.1038/srep17683
40. Li H, Wang W, Zhang L, Lan Q, Wang J, Cao Y, et al. Identification of a long noncoding RNA-associated competing endogenous RNA network in intracranial aneurysm. *World Neurosurg.* (2017) 97:684–92 e4. doi: 10.1016/j.wneu.2016.10.016

**Conflict of Interest:** The authors declare that the research was conducted in the absence of any commercial or financial relationships that could be construed as a potential conflict of interest.

Copyright © 2021 Wan, Guo, Fang, Xu, Hu and Luo. This is an open-access article distributed under the terms of the Creative Commons Attribution License (CC BY). The use, distribution or reproduction in other forums is permitted, provided the original author(s) and the copyright owner(s) are credited and that the original publication in this journal is cited, in accordance with accepted academic practice. No use, distribution or reproduction is permitted which does not comply with these terms.



# Transcriptomic and microRNA Expression Profiles Identify Biomarkers for Predicting Neo-Chemoradiotherapy Response in Esophageal Squamous Cell Carcinomas (ESCC)

Jian Wang<sup>1</sup>, Pengyi Yu<sup>2</sup>, Judong Luo<sup>3</sup>, Zhiqiang Sun<sup>3</sup>, Jingping Yu<sup>3</sup> and Jianlin Wang<sup>3\*</sup>

<sup>1</sup>Department of Radiotherapy, Jiangyin People's Hospital, Jiangyin, China, <sup>2</sup>Department of Cardiothoracic Surgery, The Third Affiliated Hospital of Soochow University, Jiangsu, China, <sup>3</sup>Department of Radiotherapy, The Affiliated Changzhou Second People's Hospital of Nanjing Medical University, Jiangsu, China

## OPEN ACCESS

### Edited by:

Yingyan Yu,  
Shanghai Jiao Tong University, China

### Reviewed by:

Chenjing Zhu,  
Nanjing Medical University, China  
Qiang Shen,  
Louisiana State University,  
United States

### \*Correspondence:

Jianlin Wang  
wangjianlin@njmu.edu.com

### Specialty section:

This article was submitted to  
Pharmacology of Anti-Cancer Drugs,  
a section of the journal  
Frontiers in Pharmacology

**Received:** 10 November 2020

**Accepted:** 10 February 2021

**Published:** 15 April 2021

### Citation:

Wang J, Yu P, Luo J, Sun Z, Yu J and  
Wang J (2021) Transcriptomic and  
microRNA Expression Profiles Identify  
Biomarkers for Predicting Neo-  
Chemoradiotherapy Response in  
Esophageal Squamous Cell  
Carcinomas (ESCC).  
Front. Pharmacol. 12:626972.  
doi: 10.3389/fphar.2021.626972

Neo-chemoradiotherapy (nCRT) before surgery is a standard treatment for locally advanced esophageal cancers. However, the treatment outcome of nCRT varied with different patients. This study aimed to identify potential biomarkers for prediction of nCRT-response in patients with esophageal squamous cell carcinoma (ESCC). Microarray datasets of nCRT responder and non-responder samples (access number GSE45670 and GSE59974) of patients with ESCC were downloaded from Gene Expression Omnibus (GEO) database. The mRNA expression profiles of cancer biopsies from four ESCC patients were analyzed before and after nCRT. Differentially expressed genes (DEGs) and miRNAs were screened between nCRT responder and non-responder ESCC samples. Functional enrichment analysis was conducted for these DEGs followed by construction of protein-protein interaction (PPI) network and miRNA-mRNA regulatory network. Finally, univariate survival analysis was performed to identify candidate biomarkers with prognostic values in ESCC. We identified numerous DEGs and differentially expressed miRNAs from nCRT responder group. GO and KEGG analysis showed that the dysregulated genes were mainly involved in biological processes and pathways, including “response to stimulus”, “cellular response to organic substance”, “regulation of signal transduction”, “AGE-RAGE signaling pathway in diabetic complications”, and “steroid hormone biosynthesis”. After integration of PPI network and miRNA-mRNA network analysis, we found eight genes, TNF, AKR1C1, AKR1C2, ICAM1, GPR68, GNB4, SERPINE1 and MMP12, could be candidate genes associated with disease progression. Univariate cox regression analysis showed that there was no significant correlation between dysregulated miRNAs (such as hsa-miR-34b-3p, hsa-miR-127-5p, hsa-miR-144-3p, and hsa-miR-486-5p, et al.) and

**Abbreviations:** GO, gene ontology; KEGG, Kyoto encyclopedia of genes and genomes; OS, overall survival; BP, biological process; CC, cellular component; ESCC, esophageal squamous cell carcinomas; GEO, gene expression omnibus; DEGs, differentially expressed genes; nCRT, Neo-chemoradiotherapy; PPI, protein-protein interaction network; log2 FC, log2 fold change/logarithm of fold change.

overall survival of ESCC patients. Moreover, abnormal expression of MMP12 was significantly correlated with pathological degree, TNM stage, lymph nodes metastasis, and overall survival of ESCC patients ( $p < 0.05$ ). Taken together, our study identified that MMP12 might be a useful tumor biomarker and therapeutic target for ESCC.

**Keywords:** esophageal neoplasms, differentially expressed genes, prognosis, MMP12, neo-chemoradiotherapy

## INTRODUCTION

Esophageal squamous cell carcinoma (ESCC) is a primary histological type of esophageal cancer worldwide. In the United States, approximately 18,440 new cases were diagnosed and 13,100 deaths occurred in 2020 (Siegel et al., 2020). China is one of the areas with highest incidence of esophageal cancer. According to the cancer statistics in China, an estimate of 477,900 newly diagnosed esophagus carcinoma cases were found in China, and 375,000 individuals died of this disease (Chen et al., 2016). Over the past decades, the incidence of esophageal cancer has been decreased slightly in the United States, whereas most cases of this disease occurred in developing countries. ESCCs in China bear more than half of global burden (Bray et al., 2018; He et al., 2019).

Esophageal cancer has a poor prognosis when it is diagnosed at advanced stage. The 5 years survival rate would decrease to 4% when metastasis occurred (Shaheen et al., 2017). As for locally advanced ESCC, neo-chemoradiotherapy (nCRT) before surgery is the primary management. However, patients always suffer from disease recurrence after resection. Also, the outcome of nCRT varied among patients. Patients who response to nCRT acquire superior survival time while those with no response suffer a poor prognosis (Berger et al., 2005). Besides, nCRT may increase postoperative complications, and clinical parameters (TNM classification, tumor location) could not predict response to nCRT (Rohatgi et al., 2005; Wen et al., 2014). Therefore, identification of novel biomarkers that could predict response to nCRT would be beneficial for ESCC management. In addition, it would help clinical doctors to discontinue non-effective treatments, and thereby avoid overtreatment for non-responders.

In recent years, the development of microarray analysis and RNA sequencing technology provided favorable information for exploring the association of gene expression and clinical outcomes (Meyerson et al., 2010; Ross and Cronin, 2011). In this study, based on RNA sequencing and bioinformatics analysis, we identified differentially expressed genes (DEGs) or differentially expressed miRNA between nCRT responders and non-responders in patients with ESCC. Additionally, protein-protein interaction (PPI) network integrated with miRNA-mRNA network were constructed to explore the candidate genes related to disease progression. Cox regression analysis was finally conducted to investigate the correlations between survival times and candidate genes or miRNAs in ESCC patients. A schematic diagram of bioinformatics analysis for ESCC datasets were shown in **Figure 1**. Our study investigated the transcriptomic expression patterns of ESCC, and identified novel biomarkers with prognostic values that could provide a better understanding of ESCC progression.

## MATERIALS AND METHODS

### Data Source and Data Processing

The gene expression profile GSE45670 (Wen et al., 2014) and miRNA expression profile GSE59974 (Fu et al., 2016) were downloaded from the Gene Expression Omnibus (GEO) database. The two datasets were derived from the same clinical samples that consist of 17 treatment non-responders and 11 responders. GSE45670 dataset were tested on platform of hgu133\_plus\_2 Affymetrix Human Genome U133 Plus 2.0 and GSE45670 was analyzed on Agilent-038169 human miRNA novirus v18.0 platform.

In addition, cancer biopsies were taken from four patients before and after nCRT in Changzhou No.2 People's Hospital, the Affiliated Hospital of Nanjing Medical University. This study was approved by the Ethical Research Committee of hospital. Transcriptomics data (under access number GSE137867, <https://www.ncbi.nlm.nih.gov/geo/query/acc.cgi?acc=GSE137867>) were obtained by RNA sequencing technology and mRNA expression was analyzed for these clinical specimens.

GSE137867 were considered as validation datasets. DEGs were screened from the three datasets and overlapped genes were considered as candidate genes related to ESCC.

Data normalization was performed for these microarray data. We extracted the gene expression values from series matrix files, and converted corresponding probe ID into gene symbols. After removal of abnormal information, we selected the expressed values from ESCC responders or non-responders to conduct Principal Components Analysis (PCA).

### PCA Analysis and DEGs Screening

PCA is a multivariate technique that converted multiple correlated variables into cohort of values linearly, and uncorrelated variables represented principal components. It has been extensively used to explore high-dimensional data, such as genomic and transcriptomic expression data (Ringnér, 2008; Ellsworth et al., 2017). In this study, we used PCA method to investigate distribution of samples between the experimental group and control groups. After detection and removal of abnormal samples, we finally obtained a series of specimen with high similarity.

The miRNA matrix and mRNA expression profiles were normalized based on quantile normalization method. Limma package (Ritchie et al., 2015) was used to screen DEGs and miRNAs between experimental group and normal control group by setting thresholds as  $p < 0.1$  and fold change  $> 1.5$  ( $|\log_2\text{FC}| > 0.585$ ). Moreover, with the same cutoff criteria, we screened the overlapped DEGs of GSE137867 and GEO datasets to conduct further analysis.

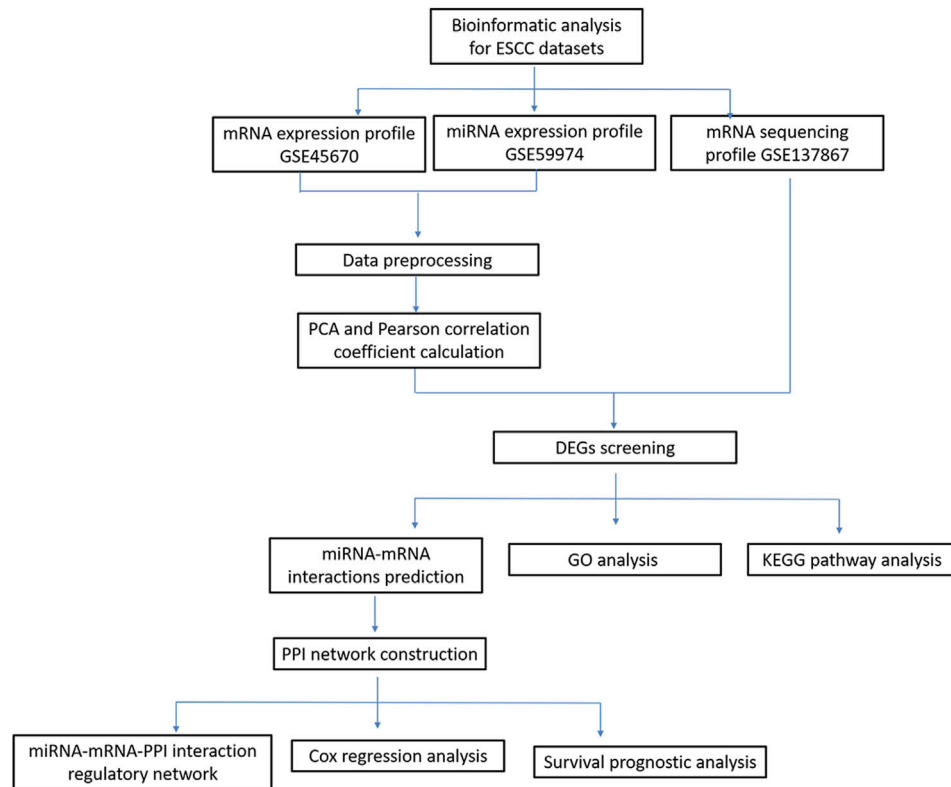


**FIGURE 1** | A schematic diagram of bioinformatics analysis for ESCC datasets.

## Functional Enrichment Analysis for DEGs Associated with ESCC

Gene Ontology (GO) (Ashburner et al., 2000) and Kyoto Encyclopedia of Genes and Genomes (KEGG) (Ogata et al., 2000) signaling pathway enrichment analysis were conducted for DEGs. Using Fisher's exact test, we screened a cohort of biological processes and pathway categories enriched by DEGs.  $p < 0.05$  was considered as significant difference, and the column with smaller  $p$  value represented a closer association between DEGs and pathway categories.

## Prediction of miRNA-mRNA Interactions

We further predicted the miRNA-mRNA interactions by examining various databases [TargetScan (Agarwal et al., 2015), miRTarBase (Chih-Hung et al., 2017), miRDB (Nathan and Wang, 2014) and miRanda (Doron et al., 2008)]. As for the upregulated miRNAs, we explored their correlations with down-regulated target genes. Subsequently, we focused on the downregulated miRNAs, and investigated their correlations with upregulated target genes in nCRT responders. Cytoscape software was used to visualize the relationships of differentially expressed miRNAs and mRNAs.

## Construction of Regulatory Network

The online tool STRING (<https://string-db.org/>) (Christian et al., 2003) was used to analyze the interactions of proteins. Interaction

score  $> 0.7$  (high confidence) was set as the cut-off criteria. After screening the correlation pairs, Cytoscape (Shannon et al., 2003) was used to analyze the topological properties (connectivity degree, closeness degree and betweenness degree) of PPI network. The proteins with high scores were considered as hub factors in network and might be key candidate genes in disease progression.

In addition, we integrated the PPI network and miRNA-mRNA regulatory network by using Cytoscape software to predict the candidate miRNAs involved in ESCC progression.

## Survival Analysis

Survival package (Cox, 1972) in R software was used to construct cox regression model. Univariate cox regression analysis and survival analysis were performed to identify crucial genes and miRNAs related to ESCC survival based on the TCGA datasets.

## RESULTS

### Screening DEGs From nCRT Responders of ESCCs

PCA analysis and correlation analysis on samples were conducted for mRNA expression dataset GSE45670. Under the threshold of  $p < 0.1$  and fold change  $> 1.5$  ( $|\log_2FC| > 0.585$ ), we screened a



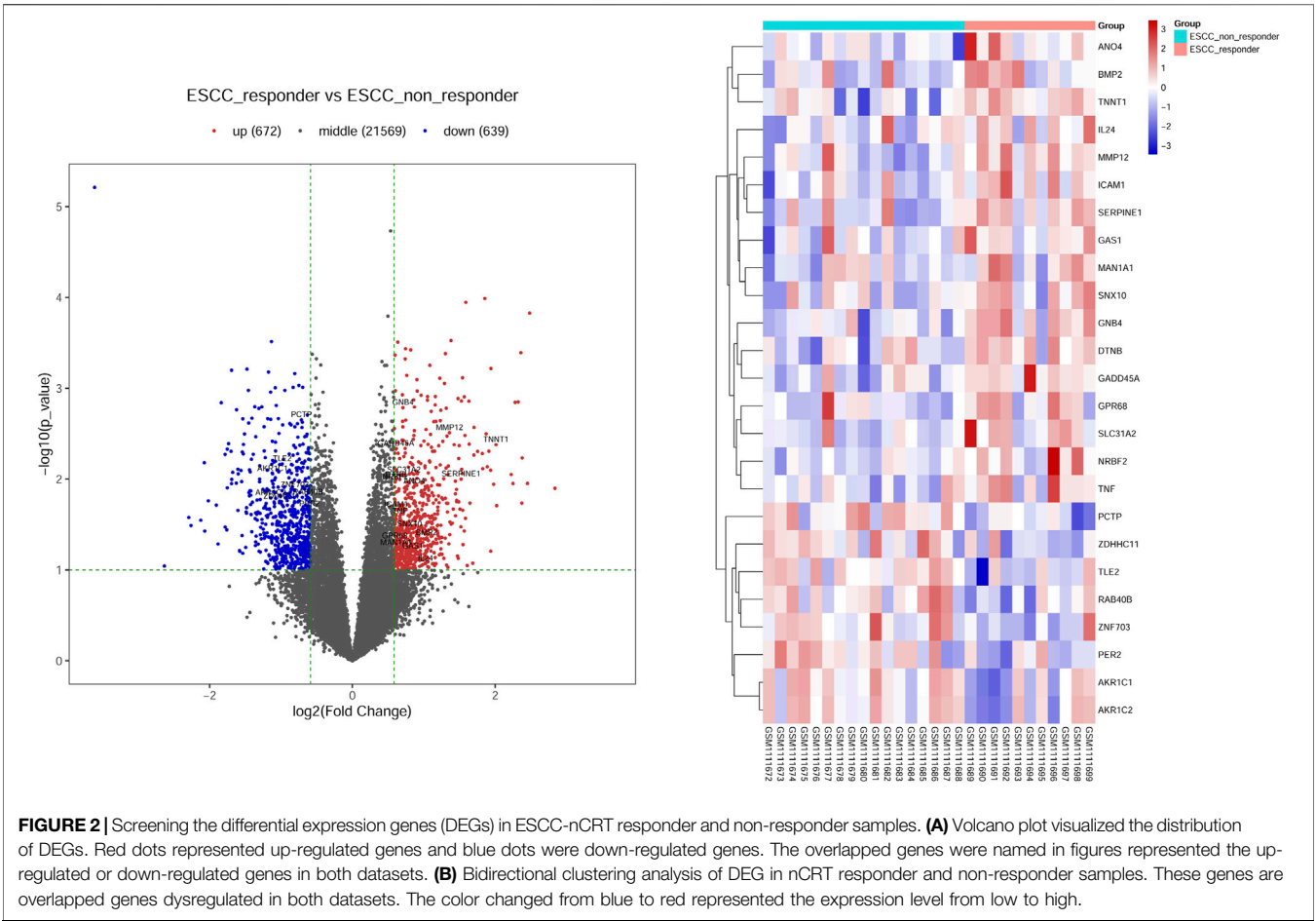


**TABLE 1 |** Twenty five DEGs were identified from two mRNA profiles (GSE45670 dataset and GSE137867 dataset), including 17 upregulated genes and 8 down-regulated genes in the ESCC responder groups compared with control non-responder groups.

DEGs	Gene names
Up-regulated	ANO4, BMP2, DTNB, GADD45A, GAS1, GNB4, GPR68, ICAM1, IL24, MAN1A1, MMP12, NRBF2, SERPINE1, SLC31A2, SNX10, TNF, TNNT1
Down-regulated	AKR1C1, AKR1C2, PCTP, PER2, RAB40B, TLE2, ZDHHC11, ZNF703

**TABLE 2 |** Fifty nine differential expressed miRNAs were identified from miRNA profiles (GSE59974 dataset), including 44 upregulated genes and 15 down-regulated genes in the ESCC responder groups compared with control groups.

miRNAs	Gene names
Up-regulated	hsa-miR-106b-3p, hsa-miR-122-5p, hsa-miR-1252, hsa-miR-127-5p, hsa-miR-1295a, hsa-miR-1343, hsa-miR-137, hsa-miR-155-3p, hsa-miR-18a-3p, hsa-miR-195-3p, hsa-miR-196a-5p, hsa-miR-206, hsa-miR-222-5p, hsa-miR-299-3p, hsa-miR-3144-5p, hsa-miR-323b-5p, hsa-miR-330-3p, hsa-miR-34b-3p, hsa-miR-3617-5p, hsa-miR-363-5p, hsa-miR-373-3p, hsa-miR-3975, hsa-miR-3978, hsa-miR-424-5p, hsa-miR-4448, hsa-miR-4528, hsa-miR-4645-3p, hsa-miR-4670-5p, hsa-miR-4704-5p, hsa-miR-4709-3p, hsa-miR-4715-5p, hsa-miR-4717-5p, hsa-miR-4773, hsa-miR-4774-5p, hsa-miR-4789-5p, hsa-miR-4798-5p, hsa-miR-503-5p, hsa-miR-504, hsa-miR-5189, hsa-miR-539-3p, hsa-miR-5579-3p, hsa-miR-637, hsa-miR-7-5p, hsa-miR-924
Down-regulated	hsa-miR-138-1-3p, hsa-miR-144-3p, hsa-miR-144-5p, hsa-miR-192-3p, hsa-miR-3145-5p, hsa-miR-3972, hsa-miR-486-5p, hsa-miR-489, hsa-miR-499a-5p, hsa-miR-550b-2-5p, hsa-miR-551b-3p, hsa-miR-5585-5p, hsa-miR-5690, hsa-miR-640, hsa-miR-675-3p

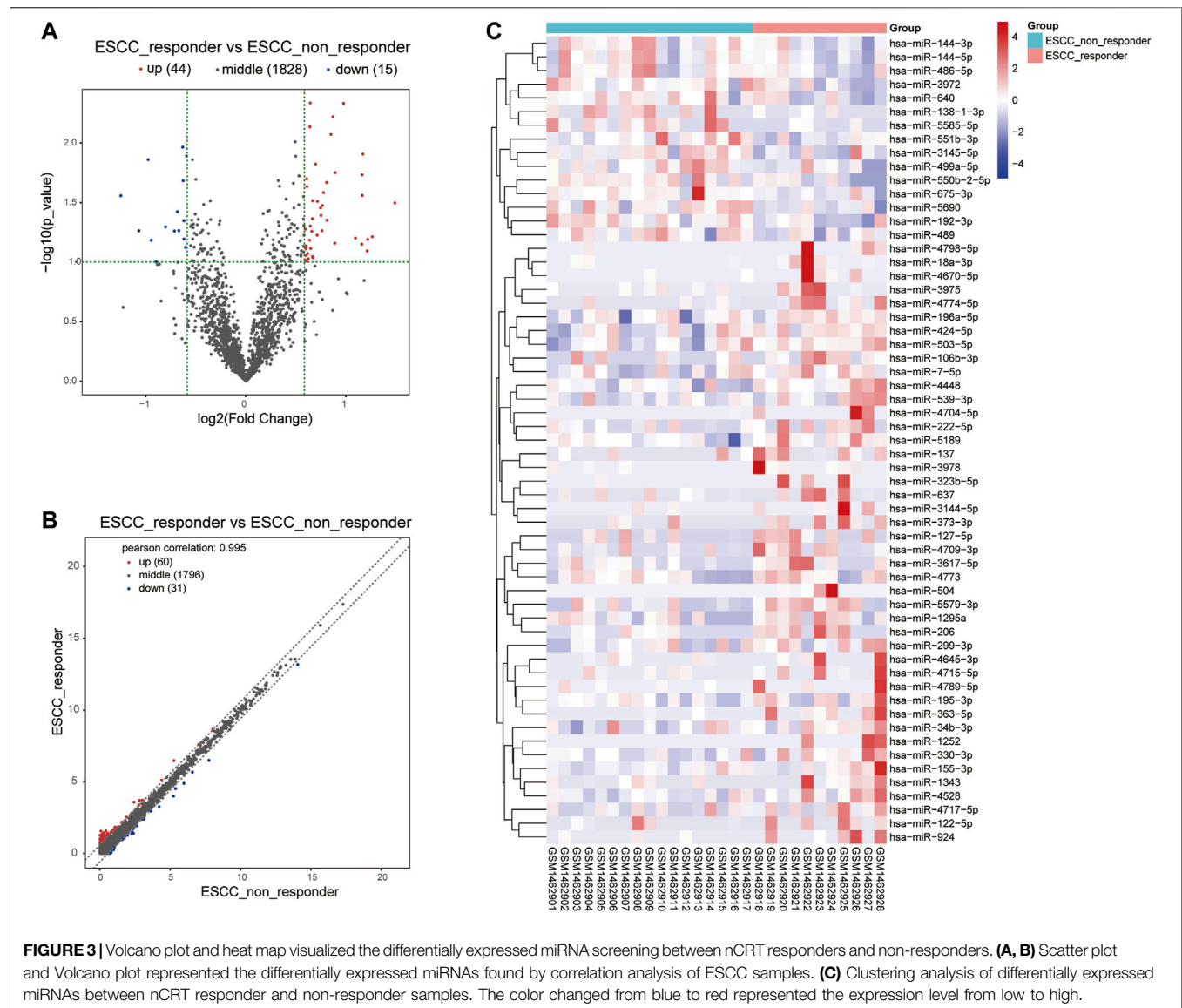


**FIGURE 3 |** Volcano plot and heat map visualized the differentially expressed miRNA screening between nCRT responders and non-responders. **(A, B)** Scatter plot and Volcano plot represented the differentially expressed miRNAs found by correlation analysis of ESCC samples. **(C)** Clustering analysis of differentially expressed miRNAs between nCRT responder and non-responder samples. The color changed from blue to red represented the expression level from low to high.

**TABLE 3 |** Gene Ontology analysis of differentially expressed genes associated with ESCC (Top ten biological process terms).

Category	Description	Count	p value	FDR
BP	GO:0071396~cellular_response_to_lipid	6	2.80e-06	0.001617666
BP	GO:0050896~response_to_stimulus	18	2.84e-06	0.001617666
BP	GO:0071395~cellular_response_to_jasmonic_acid_stimulus	2	3.63e-06	0.001617666
BP	GO:0023051~regulation_of_signaling	12	6.06e-06	0.001658521
BP	GO:0010033~response_to_organic_substance	11	7.33e-06	0.001658521
BP	GO:0071310~cellular_response_to_organic_substance	10	7.44e-06	0.001658521
BP	GO:0009966~regulation_of_signal_transduction	11	1.32e-05	0.002048231
BP	GO:0071222~cellular_response_to_lipopolysaccharide	4	1.46e-05	0.002048231
BP	GO:0030155~regulation_of_cell_adhesion	6	1.46e-05	0.002048231
BP	GO:2000351~regulation_of_endothelial_cell_apoptotic_process	3	1.54e-05	0.002048231

Category stands for GO terms and BP refers to biological process.

**TABLE 4 |** KEGG pathway analysis of differentially expressed genes in ESCC.

Category	Description	Count	p value	FDR	Genes
KEGG	hsa04933~AGE-RAGE_signaling_pathway_in_diabetic_complications Homo_sapiens_(human)	3	5.23e-04	0.058021807	ICAM1/ SERPINE1/TNF
KEGG	hsa05143~African_trypanosomiasis Homo_sapiens_(human)	2	1.63e-03	0.08638883	ICAM1/TNF
KEGG	hsa05144~Malaria Homo_sapiens_(human)	2	2.85e-03	0.08638883	ICAM1/TNF
KEGG	hsa05169~Epstein-Barr_virus_infection Homo_sapiens_(human)	3	3.91e-03	0.08638883	GADD45A/ ICAM1/TNF
KEGG	hsa00140~Steroid_hormone_biosynthesis Homo_sapiens_(human)	2	4.24e-03	0.08638883	AKR1C1/AKR1C2
KEGG	hsa05217~Basal_cell_carcinoma Homo_sapiens_(human)	2	4.67e-03	0.08638883	BMP2/GADD45A
KEGG	hsa04115~p53_signaling_pathway Homo_sapiens_(human)	2	6.06e-03	0.095935394	GADD45A/SERPINE1
KEGG	hsa05323~Rheumatoid_arthritis Homo_sapiens_(human)	2	9.54e-03	0.095935394	ICAM1/TNF
KEGG	hsa04350~TGF-beta_signaling_pathway Homo_sapiens_(human)	2	0.01	0.095935394	BMP2/TNF
KEGG	hsa04713~Circadian_entrainment Homo_sapiens_(human)	2	0.01	0.095935394	GNB4/PER2

total of 1311 DEGs from nCRT responders and non-responders. We found 672 upregulated and 639 down-regulated genes. The same cutoff criteria were applied for RNA-Seq profile GSE137867, and numerous DEGs were screened in specimens before and after nCRT.

Moreover, we integrated the overlapped DEGs between RNA-Seq profile and GEO datasets. Of these gene overlaps, 17 genes were both upregulated in two datasets while eight genes were both downregulated in two datasets (Table 1). Volcano plot and bidirectional clustering analysis were performed for these DEGs, and results were shown in Figure 2. Furthermore, the differentially expressed miRNAs were identified by setting the thresholds of  $P < 0.1$  and fold change  $> 1.5$  ( $|\log_2FC| > 0.585$ ). Scatter plot and volcano plot were used to visualize the results. Finally, we identified 44 upregulated miRNAs and 15 downregulated miRNAs from the nCRT responders compared with non-responders. The differentially expressed miRNAs are listed in Table 2 and heatmaps are visualized in Figure 3.

## GO and KEGG Analysis for These Candidate Genes

The GO analysis results revealed that these dysregulated DEGs were mainly associated with several biological processes (Table 3), such as “response to stimulus” (count = 18, FDR = 0.001617666), “regulation of signaling” (count = 12, FDR = 0.001658521), “response to organic substance” (count = 11, FDR = 0.001658521), “cellular response to organic substance” (count = 11, FDR = 0.001658521), and “regulation of signal transduction” (count = 11, FDR = 0.002048231). The KEGG pathways (Table 4) enriched by these genes were “AGE-RAGE signaling pathway in diabetic complications” (count = 3,  $p = 5.23e-04$ ), “Epstein-Barr virus infection” (count = 3,  $p = 3.91e-03$ ), “steroid hormone biosynthesis” (count = 2,  $p = 3.91e-03$ ), “African trypanosomiasis” (count = 2,  $p = 1.63e-03$ ) and “malaria” (count = 2,  $p = 2.85e-03$ ).

## PPI Network Analysis and Prediction of miRNA-Gene Interactions

By predicting the target genes of the upregulated miRNAs and downregulated miRNAs, we built two miRNA-target networks

for upregulated miRNAs (Figure 4A) and downregulated miRNAs (Figure 4B). In the regulatory networks, several molecules were identified as hub genes for high degree of connectivity, including PER2 (degree = 6), PCTP (degree = 6), and hsa-miR-486-5p (degree = 6).

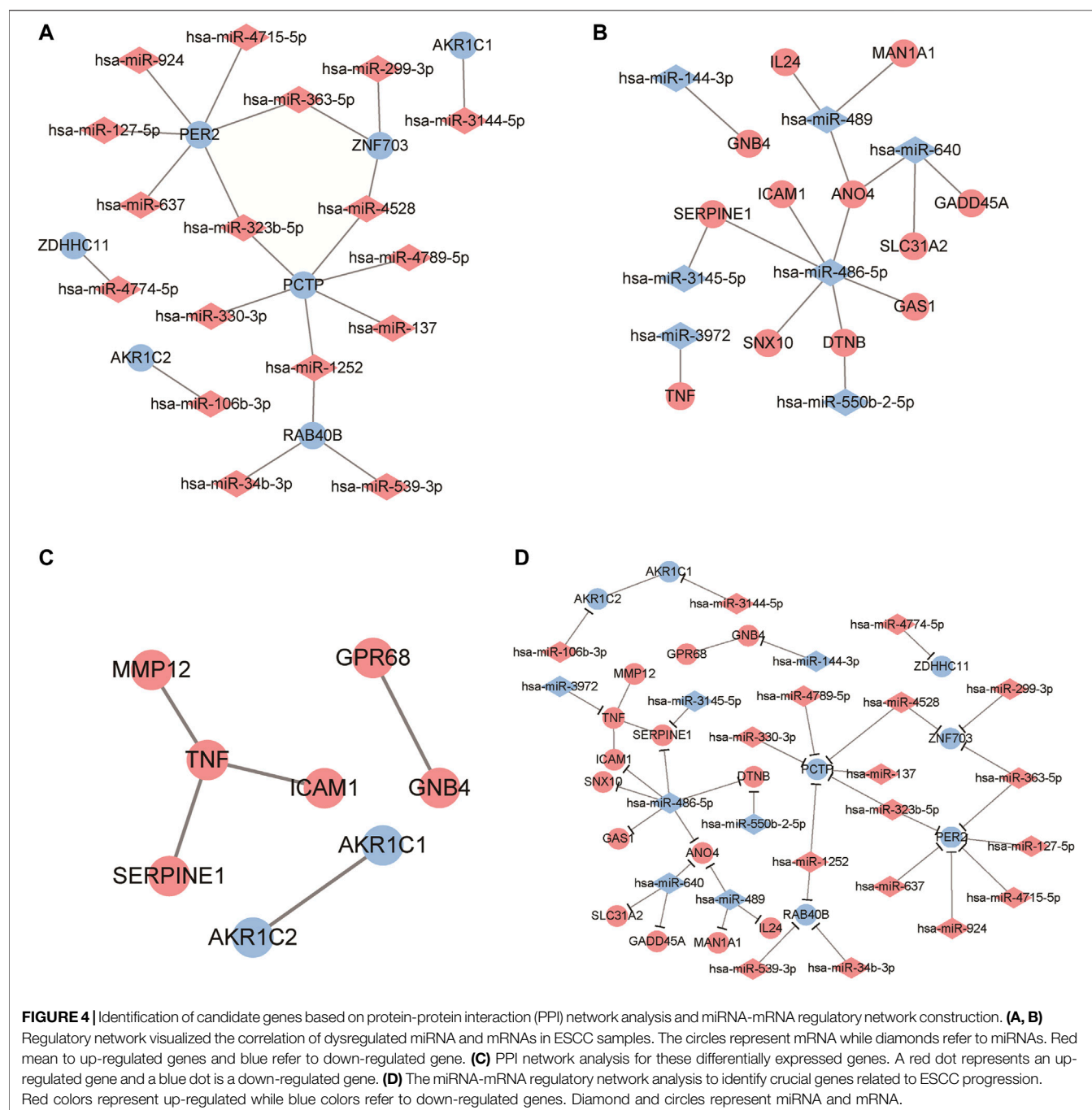
Using the online tool STRING and Cytoscape software, we constructed a PPI network for DEGs (Table 5; Figure 4C) and obtained five interaction pairs among eight genes, including tumor necrosis factor (TNF), Aldo-keto reductase family one member C1 (AKR1C1), AKR1C2, intercellular adhesion molecule 1 (ICAM1), ovarian cancer G-protein coupled receptor 1 (GPR68), guanine nucleotide-binding protein subunit beta-4 (GNB4), plasminogen activator inhibitor-1 (SERPINE1) and matrix metalloproteinase-12 (MMP12).

By integrating PPI network and miRNA-mRNA network, we finally constructed a regulatory network that consisted with miRNAs and genes. Among these genes, PER2, PCTP, TNF and hsa-miR-486-5p exhibited higher interactions than other genes. Thus, these genes were identified as hub genes related to ESCC progression.

## Identifying Crucial Genes with Prognostic Values in nCRT Responders

We conducted a survival analysis on independent cohort of patients (the data were derived from TCGA database) to analyze the prognostic significance of 8 genes in ESCC patients. The analyzed signatures included genes TNF, AKR1C1, AKR1C2, and ICAM1, et al. (Figure 5) The patients were divided into high expression group and low expression group according to the median of gene expression. Survival probability was compared between two groups to predict candidate genes with prognostic value. The results revealed that patients with high level of MMP-12 exhibited poorer prognosis than patients in low expression groups (hazardous ratio for survival probability, 1.737;  $p < 0.05$ ).

Moreover, univariate cox regression analysis and survival analysis were performed for these differentially expressed miRNAs, such as hsa-miR-34b-3p, hsa-miR-127-5p, hsa-miR-144-3p, and hsa-miR-486-5p et al. However, the results revealed that there was no significant correlation between any



dysregulated miRNAs and prognosis of ESCC patients (Figure 6).

## DISCUSSION

In this study, we attempted to identify potential tumor biomarkers for prediction of nCRT-response in patients with ESCC. After integrating overlapped genes between RNA sequencing dataset and GEO datasets, we identified 17 genes

that were upregulated, and eight genes that were downregulated in these two datasets. After verification of the data set samples used in the project analysis and the actual number of samples included in the analysis, no samples were excluded from the project, and all samples were analyzed. Functional enrichment analysis showed that dysregulated genes were mainly involved in “response to stimulus”, “regulation of signal transduction”, “AGE-RAGE signaling pathway in diabetic complications”, “steroid hormone biosynthesis”. According to analysis of PPI network and miRNA-mRNA network, we identified eight



**TABLE 5 |** Protein-protein interaction network analysis for differential expressed genes in ESCC samples based on connectivity degrees evaluation.

Gene	Degree
TNF	3
AKR1C1	1
AKR1C2	1
ICAM1	1
GPR68	1
GNB4	1
SERPINE1	1
MMP12	1

Only AKR1C1 and AKR1C2 were down-regulated genes while other genes were upregulated.

candidate genes, TNF, AKR1C1, AKR1C2, ICAM1, GPR68, GNB4, SERPINE1 and MMP12, that were associated with progression of ESCC progression. Finally, univariate regression analysis in ESCC patients revealed that high expression of MMP12 was significantly correlated to poor prognosis.

Previous studies have explored the difference of gene expression between nCRT responder and non-responder

samples for prediction of nCRT response in esophageal cancer. Maher et al. (2009) identified eight genes that were differentially expressed in patients responded to treatment. Based on analysis using predictive model, five genes were able to predict response to nCRT with high accuracy (95%) in a large proportion of esophageal cancer patients. In a recent study (Chen et al., 2015), researchers identified nine dysregulated genes between treatment responders and non-responders. Functional enrichment analysis showed that four of the genes, miR-422, CDK4, Cyclin D2, and E2F3, were mainly related to G1/S checkpoint which could regulate tumor sensitivity to nCRT. Els Visser et al. (2017) assessed the association of gene expression and clinical outcome in 22 studies of esophageal cancer, and they found a large heterogeneity in gene expression, response to nCRT, and lymph node metastasis.

Our results demonstrated that eight genes, including TNF, AKR1C1, AKR1C2, ICAM1, GPR68, GNB4, SERPINE1 and MMP12, were candidate genes associated with ESCC progression. AKR1C1/C2 encodes enzymes belong to aldo/keto reductase superfamily. These enzymes are crucial in drug resistance of cancer cells and related to metabolism of polycyclic aromatic hydrocarbons (Selga et al., 2008). AKR1C1

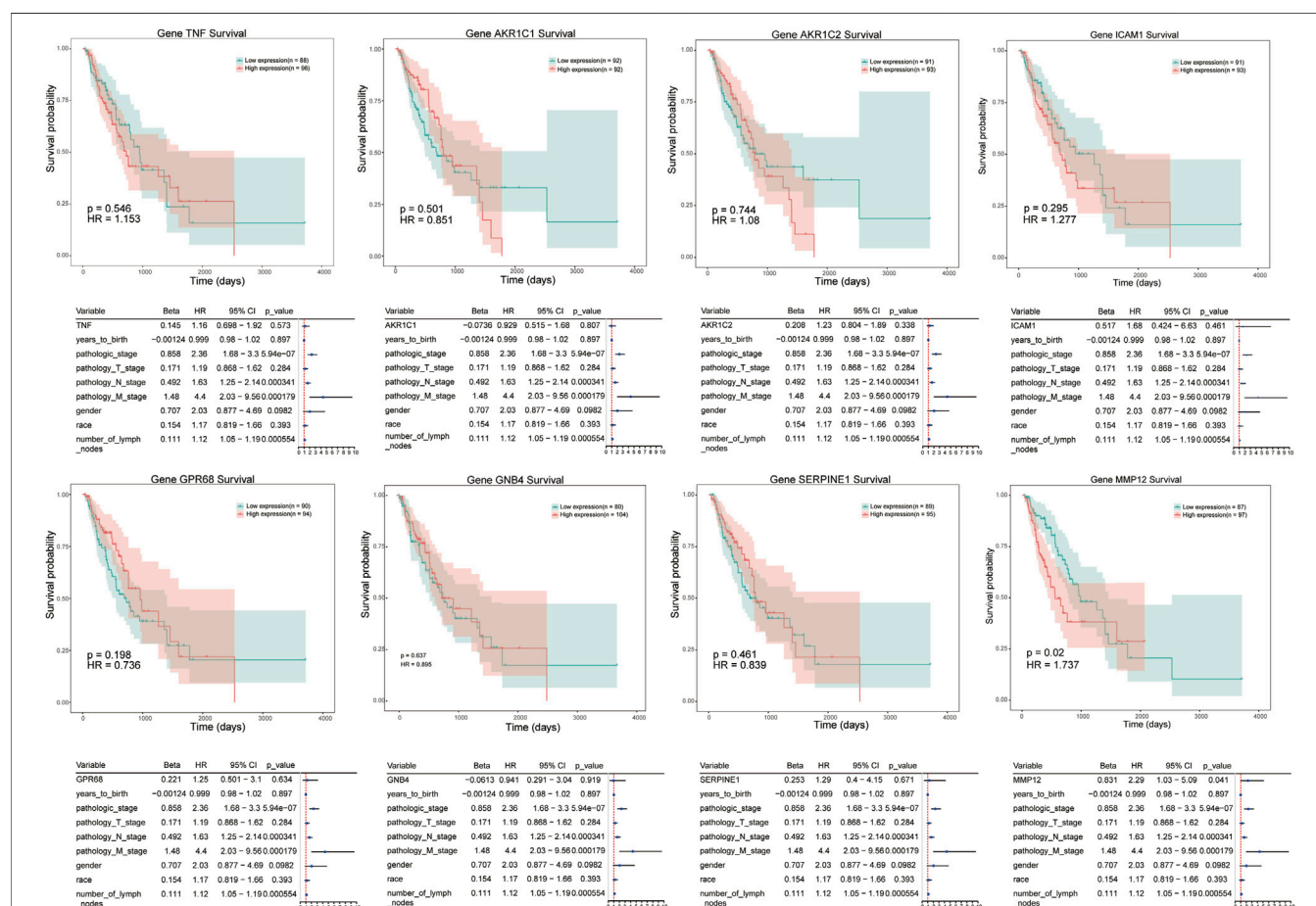


**FIGURE 5 |** Kaplan-Meier survival curves of candidate genes in ESCC, including TNF, AKR1C1, ICAM1, MMP12, et al. Red line represents high expression of crucial genes while green line refers to low expression genes. The X axis represent overall survival time (day), and Y axis means survival probability.

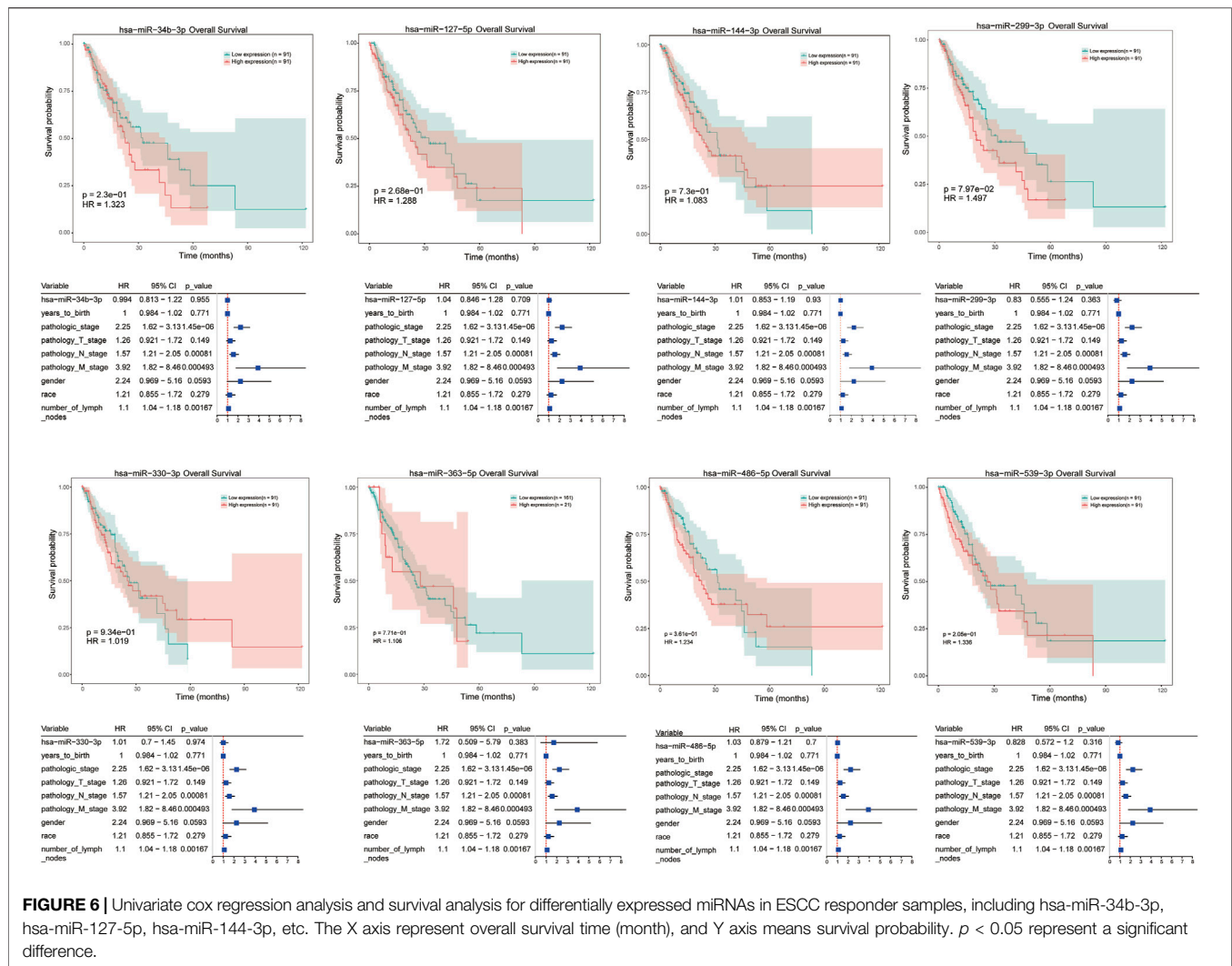


**FIGURE 6 |** Univariate cox regression analysis and survival analysis for differentially expressed miRNAs in ESCC responder samples, including hsa-miR-34b-3p, hsa-miR-127-5p, hsa-miR-144-3p, etc. The X axis represent overall survival time (month), and Y axis means survival probability.  $p < 0.05$  represent a significant difference.

and AKR1C2 share a high degree of homology in AKR1C subfamily and were different in seven amino acids. Previous study showed that AKR1C1/C2 were associated with EDHB-induced inhibition of esophageal cancer cell proliferation and this might promote treatment of esophageal cancer using EDHB, a substrate of the enzymes (Li et al., 2016).

In the miRNA-mRNA regulatory network, we identified PER2, PCTP, TNF and hsa-miR-486-5p as hub genes related to disease progression. MiRNA have been confirmed to have a major role in cancer development by regulating the expression of oncogenes or cancer suppressor genes. Aberrant expression of special miRNAs have been detected in ESCC patients such as upregulated of miR-10b (Tian et al., 2010), miR-21 (Mathe et al., 2009), miR-26a (Shao et al., 2016) and downregulated miR-125b, miR-203, and miR-205 (Matsushima et al., 2011; Hu et al., 2016; Fan et al., 2018). A recent study showed that downregulation of miR-486-5p was reported in esophageal carcinoma samples and it might function as a tumor suppressor gene in disease metastasis via regulating cellular migration (Yi et al., 2016). By tissue microarrays analysis of 185 ESCCs samples, Ren et al. also found that decreased miR-486-5p was identified in 66.2% of cases

and abnormal expression of miR-486-5p were related to prognosis of esophageal carcinoma (Ren et al., 2016). Our results predicted down-regulated miR-486-5p, interact with target gene ICAM1 played critical roles in ESCC progression. ICAM1 or CD54 is a 90 kDa glycosylated transmembrane protein highly expressed on endothelial cells and mesenchymal stem cells. It plays major roles in cell metastasis, proliferation and multiple cellular immune response. Dysregulation of ICAM1 has been confirmed in liver cancer and ESCC stem cells (Liu et al., 2013; Tsai et al., 2015). ICAM1 promotes epithelial-to-mesenchymal transition by regulating metastasis-related genes in ESCC cells. ICAM1 was identified as a target gene of lncRNA-ECM and involved in development and progression of ESCC (Yao et al., 2018). However, the role of ICAM1 and miR-486-5p remains unclear, especially the interaction of the two molecules. A previous study reported that down-regulation of miR-486-5p could suppress tumor metastasis by regulating metastatic mediator of ICAM-1 in breast cancer (Abdallah et al., 2017). It is speculated that ICAM-1 might be regulated by miR-486-5p and played a crucial role in development and metastasis of ESCC. Therefore, inhibition of ICAM-1 might be a potential strategy for ESCC treatment.

In addition to hsa-miR-486-5p, survival analysis was performed for several other differentially expressed miRNAs, such as hsa-miR-34b-3p, hsa-miR-127-5p, and hsa-miR-144-3p, et al. in tumor samples. However, there was no significant correlation between any dysregulated miRNAs and prognosis of ESCC patients. According to literature, miR-127 was downregulated in several types of cancers, including gastric cancer (Guo et al., 2013), glioblastoma (Jiang et al., 2014), and hepatocellular carcinoma (Huan et al., 2016). In ESCC patients, Gao et al. revealed that miR-127 acted as a tumor suppressor in tumors by regulating oncogene Formin-like 3 (FMNL3) (Gao et al., 2016). In another study, seven serum miRNAs were identified as ESCC biomarkers, including miR-127-3p (Zhang et al., 2010). Also, tissue or serum miR-144 expression were evaluated in gastric cancer and low miR-144 expression was found to predict a poor prognosis in gastrointestinal cancer (Liu et al., 2017). Moreover, miRNA-34b played an oncogenic role in ESCC development, the polymorphisms of rs4938723/primiR-34b/c were associated with ESCC susceptibility based on an analysis on a large number of Chinese population (Harata et al., 2010; Zhang et al., 2014). Thus, the potential role of these miRNAs in response to nCRT in ESCC warrants further studied.

Protein of MMP-12 is known as human macrophage metalloelastase (HME) or macrophage elastase (ME), and belongs to the MMPs family. MMP12 is associated with elastin degradation and macrophage migration in various diseases, such as chronic obstructive pulmonary disease, skin diseases and cancers (Kerkela et al., 2000; Hunninghake et al., 2009). However, the function of MMP12 in tumors is controversial. Aberrant expression of MMP12 was reported in several types of cancers, including hepatocellular carcinoma (He et al., 2018), lung cancer (Roman, 2017), colon cancer (Klupp et al., 2016) and nasopharyngeal carcinoma (Chung et al., 2014). Overexpression of HME/MMP12 mRNA in patients with colorectal carcinoma exhibited a significantly better survival outcome compared with patients with normal HME/MMP12 mRNA expression (Yang et al., 2001). Cheng et al. observed a high level of MMP12/HME protein in patients with gastric carcinoma, and overexpression of MMP12 represented a better survival rate (Cheng et al., 2010). The anti-tumorigenic effect of MMP12 might be due to the generation of angiostatin, which is induced by MMP12 and could prevent tumor angiogenesis. However, in other types of cancers, upregulated MMP12 were reported to involve in short survival times. When grouping samples, the analysis is based on the average gene expression to distinguish high and low expression, so the sample size of high and low expression is different. The longest survival time of high expression group is around 2000 days, which is also consistent with the survival trend of grouping according to the median. To our knowledge, the potential role of MMP12 in ESCC remains uncertain. A recent study showed that overexpression of MMP12 was identified in cohorts of resectable tumor tissues compared with normal squamous epithelium, and overexpression of MMP12 was correlated with poor overall survival in ESCCs (Han et al., 2017). Consistent with the previous study, our results also demonstrated that overexpression of MMP12 was correlated with clinical stage and poor survival outcomes by cox regression analysis. In miRNA-mRNA

regulatory network, MMP12 interacting with TNF was identified as hub genes related to disease progression. A previous study have reported that the expression and secretion of MMP-12 can be regulated by IL-1 $\beta$  and TNF- $\alpha$  in human airway smooth muscle cells, and thereby participated in diseases of the airway, such as chronic asthma or chronic obstructive pulmonary diseases (COPD) (Xie et al., 2005). Yu et al. showed that TNF $\alpha$ -activated mesenchymal stromal cells can recruit CXCR2+ neutrophils to tumor microenvironment, resulting in upregulation of MMP12 and other metastasis-related genes in tumor cells, such as MMP13 and TGF $\beta$ , that promoted breast cancer metastasis (Yu et al., 2017). However, there is few study on the interactions of MMP12 and TNFs in cancer development. Our findings suggested that MMP12 might interact with TNFs and play a role in ESCC progression.

There were some limitations in our study. Experimental validation should be conducted to identify the exact biological behaviors of candidate DEGs or miRNAs in ESCC development. Meanwhile, the number of ESCC specimen was limited. Further validation in larger cohorts is necessary to investigate the disease predictive value of these genes.

## CONCLUSION

In conclusion, we identified eight genes, including TNF, AKR1C1, AKR1C2, ICAM1, GPR68, GNB4, SERPINE1, and MMP12, as candidate genes by performing integrative analysis on gene expression profiles of microarray datasets. We found that abnormal expression of MMP12 was significantly correlated with pathological degree, TNM stage, lymph nodes metastasis, survival time of ESCC patients. Further basic experiments and large-scale multi-center clinical research studies are required to validate our results since our study was conducted based on data analysis.

## DATA AVAILABILITY STATEMENT

The datasets presented in this study can be found in online repositories. The names of the repository/repositories and accession number can be found below: <https://www.ncbi.nlm.nih.gov/GSE137867>.

## ETHICS STATEMENT

The studies involving human participants were reviewed and approved by the Ethics Committee of Changzhou Second Hospital Affiliated to Nanjing Medical University. The patients/participants provided their written informed consent to participate in this study.

## AUTHOR CONTRIBUTIONS

Data curation: JW, Formal analysis: ZS, Funding acquisition: JW and JY. Resources: PY. Software: JW, JL, and ZS. Writing—original draft: JW. Writing—review and editing: JW and JY.



## FUNDING

We thanked the support from National Natural Science Foundation of China (11705095); Young Talent Development Plan of Changzhou Health Commission (CZQM2020074);

Changzhou Sci and Tech Program (CJ20200053); The Key Research and Development Program of Jiangsu Province (BE2020637); Wuxi double hundred young and middle-aged medical and health top-notch talent project (No. 202014) and 3333 High-level personnel training Project (BRA2019025).

## REFERENCES

- Abdallah, R., Youness, R. A., El Meckawy, N., El Sebaei, A. F., Abdelmotaal, A., and Assal, R. A. (2017). 77PDown-regulated miR-486-5p acts as a tumor suppressor in breast cancer patients by targeting the metastatic mediator ICAM-1. *Ann. Oncol.* 28. doi:10.1093/annonc/mdx711.058
- Agarwal, V., Bell, G. W., Nam, J.-W., and Bartel, D. P. (2015). Predicting effective microRNA target sites in mammalian mRNAs. *eLife* 4, e05005. doi:10.7554/eLife.05005
- Ashburner, M., Ball, C. A., Blake, J. A., Botstein, D., Butler, H., et al. Ontology: Tool for the unification of biology. *Nat. Genet.* 25, 25–29. doi:10.1038/75556
- Berger, A. C., Farma, J., Scott, W. J., Freedman, G., Weiner, L., Cheng, J. D., et al. (2005). Complete response to neoadjuvant chemoradiotherapy in esophageal carcinoma is associated with significantly improved survival. *J. Clin. Oncol. Official J. Am. Soc. Clin. Oncol.* 23, 4330–4337. doi:10.1200/jco.2005.05.017
- Bray, F., Ferlay, J., Soerjomataram, I., Siegel, R. L., Torre, L. A., and Jemal, A. (2018). Global cancer statistics 2018: GLOBOCAN estimates of incidence and mortality worldwide for 36 cancers in 185 countries. *CA: Cancer J. Clin.* 68, 394–424. doi:10.3322/caac.21492
- Chen, W., Zheng, R., Baade, P. D., Zhang, S., Zeng, H., Bray, F., et al. (2016). Cancer statistics in China, 2015. *CA: Cancer J. Clin.* 66, 115–132. doi:10.3322/caac.21338
- Chen, X., Veigl, M., Barnholtz-Sloan, J., Xin, W., Chen, Y., and Dorth, J. A. (2015). Prediction of response to chemoradiation by gene expression profiling in esophageal squamous cell carcinoma. *Int. J. Radiat. Oncol. Biol. Phys.* 93, S218–S219. doi:10.1016/j.ijrobp.2015.07.527
- Cheng, P., Jiang, F. H., Zhao, L. M., Dai, Q., Yang, W. Y., Zhu, L. M., et al. (2010). Human macrophage metalloelastase correlates with angiogenesis and prognosis of gastric carcinoma. *Dig. Dis. Sci.* 55, 3138–3146. doi:10.1007/s10620-010-1127-3
- Chih-Hung, C., Sirjana, S., Chi-Dung, Y., Nai-Wen, C., Yu-Ling, L., Kuang-Wen, L., et al. (2017). miRTarBase update 2018: a resource for experimentally validated microRNA-target interactions. *Nucl. Acids Res.* 46 (D1), D296–D302. doi:10.1093/nar/gkx1067
- Christian, V. M., Martijn, H., Daniel, J., Steffen, S., Peer, B., and Berend, S. (2003). STRING: a database of predicted functional associations between proteins. *Nucl. Acids Res.* 31, 258–261. doi:10.1093/nar/gkg034
- Chung, I. C., Chen, L. C., Chung, A. K., Chao, M., Huang, H. Y., Hsueh, C., et al. (2014). Matrix metalloproteinase 12 is induced by heterogeneous nuclear ribonucleoprotein K and promotes migration and invasion in nasopharyngeal carcinoma. *BMC Cancer* 14, 1471–2407. doi:10.1186/1471-2407-14-348
- Cox, D. R. (1972). Regression Models and Life-Tables. *J. R. Stat. Soc. Series B Stat. Methodol.* 34, 187–202. doi:10.1111/j.2517-6161.1972.tb00899.x
- Doron, B., Manda, W., Aaron, G., Marks, D. S., and Chris, S. (2008). The microRNA.org resource: targets and expression. *Nucl. Acids Res. suppl.* 1 36, D149–53. doi:10.1093/nar/gkm995
- Ellsworth, S. G., Rabatic, B. M., Chen, J., Zhao, J., Campbell, J., Wang, W., et al. (2017). Principal component analysis identifies patterns of cytokine expression in non-small cell lung cancer patients undergoing definitive radiation therapy. *PLoS One* 12, e0183239. doi:10.1371/journal.pone.0183239
- Fan, Y. X., Bian, X. H., Qian, P. D., Chen, Z. Z., Wen, J., Luo, Y. H., et al. (2018). MicroRNA-125b inhibits cell proliferation and induces cell apoptosis in esophageal squamous cell carcinoma by targeting BMF. *Oncol. Rep.* 40, 61–72. doi:10.3892/or.2018.6413
- Fu, J., Luo, K., Liu, H., Liu, S., Lin, G., Hu, Y., et al. (2016). MiRNA Expression Analysis of Pretreatment Biopsies Predicts the Pathological Response of Esophageal Squamous Cell Carcinomas to Neoadjuvant Chemoradiotherapy. *Ann. Surg.* 263, 942–948. doi:10.1097/sla.0000000000001489
- Gao, X., Wang, X., Cai, K., Wang, W., Ju, Q., Yang, X., et al. (2016). MicroRNA-127 is a tumor suppressor in human esophageal squamous cell carcinoma through the regulation of oncogene FMNL3. *Eur. J. Pharmacol.* 791, 603–610. doi:10.1016/j.ejphar.2016.09.025
- Guo, L.-H., Li, H., Wang, F., Yu, J., and He, J.-S. (2013). The Tumor suppressor roles of miR-433 and miR-127 in gastric Cancer. *IJMS* 14, 14171–14184. doi:10.3390/ijms140714171
- Han, F., Zhang, S., Zhang, L., and Hao, Q. (2017). The overexpression and predictive significance of MMP-12 in esophageal squamous cell carcinoma. *Pathol. Res. Pract.* 213, 1519–1522. doi:10.1016/j.prp.2017.09.023
- Harata, K., Ishiguro, H., Kuwabara, Y., Kimura, M., Mitsui, A., Ogawa, R., et al. (2010). MicroRNA-34b has an oncogenic role in esophageal squamous cell carcinoma. *Oncol. Lett.* 1, 685–689. doi:10.3892/ol.00000120
- He, J. M., Chang, A. M., Chen, Y. Z., Yuan, X. L., and Li, F. (2016). Regulatory Role of miR-203 in Occurrence and Progression of Kazakh Esophageal squamous cell carcinoma. *Scientific Rep.* 6, 23780. doi:10.1038/srep23780
- He, M. K., Le, Y., Zhang, Y. F., Ouyang, H. Y., Jian, P. E., Yu, Z. S., et al. (2018). Matrix metalloproteinase 12 expression is associated with tumor FOXP3+ regulatory T cell infiltration and poor prognosis in hepatocellular carcinoma. *Oncol. Lett.* 16, 475–482. doi:10.3892/ol.2018.8642
- He, Y., Li, D., Li, D., Shan, B., Liang, D., Shi, J., et al. (2019). Incidence and mortality of esophagus cancer in China, 2008–2012. *Chin. J. Cancer Res.* 31, 426–434. doi:10.21147/j.issn.1000-9604.2019.03.04
- Huan, L., Bao, C., Chen, D., Li, Y., Lian, J., Ding, J., et al. (2016). MicroRNA-127-5p targets the biliverdin reductase B/nuclear factor- $\kappa$ B pathway to suppress cell growth in hepatocellular carcinoma cells. *Cancer Sci.* 107, 258–266. doi:10.1111/cas.12869
- Hunninghake, G. M., Cho, M. H., Tesfayig, Y., Soto-Quiros, M. E., Avila, L., Lasky-Su, J., et al. (2009). MMP12, lung function, and COPD in high-risk populations. *N. Engl. J. Med.* 361, 2599–2608. doi:10.1056/nejmoa0904006
- Jiang, H., Jin, C., Liu, J., Hua, D., Zhou, F., Lou, X., et al. (2014). Next Generation Sequencing Analysis of miRNAs: MiR-127-3p Inhibits Glioblastoma Proliferation and Activates TGF- $\beta$  Signaling by Targeting SKI. *OMICS: J. Integr. Biol.* 18, 196–206. doi:10.1089/omi.2013.0122
- Kerkelä, E., Ala-Aho, R., Jeskanen, L., Rechardt, O., Grénman, R., Shapiro, S. D., et al. (2000). Expression of human macrophage metalloelastase (MMP-12) by tumor cells in skin cancer. *J. Invest. Dermatol.* 114, 1113–1119. doi:10.1046/j.1523-1747.2000.00993.x
- Klupp, F., Neumann, L., Kahlert, C., Diers, J., Halama, N., Franz, C., et al. (2016). Serum MMP7, MMP10 and MMP12 level as negative prognostic markers in colon cancer patients. *BMC Cancer* 16, doi:10.1186/s12885-016-2515-7
- Li, W., Hou, G., Zhou, D., Lou, X., Xu, Y., Liu, S., et al. (2016). The roles of AKR1C1 and AKR1C2 in ethyl-3,4-dihydroxybenzoate induced esophageal squamous cell carcinoma cell death. *Oncotarget* 7, 21542–21555. doi:10.18632/oncotarget.7775
- Liu, S., Li, N., Yu, X., Xiao, X., Cheng, K., Hu, J., et al. (2013). Expression of intercellular adhesion molecule 1 by hepatocellular carcinoma stem cells and circulating tumor cells. *Gastroenterology* 144, 1031–1041. doi:10.1053/j.gastro.2013.01.04610.1053/j.gastro.2013.01.046
- Liu, S., Suo, J., Wang, C., Sun, X., Wang, D., He, L., et al. (2017). Prognostic significance of low miR-144 expression in gastric cancer. *Cbm* 20, 547–552. doi:10.3233/cbm-170351
- Maher, S. G., Gillham, C. M., Duggan, S. P., Smyth, P. C., Miller, N., Muldoon, C., et al. (2009). Gene expression analysis of diagnostic biopsies predicts pathological response to neoadjuvant chemoradiotherapy of esophageal Cancer. *Ann. Surg.* 250, 729–737. doi:10.1097/sla.0b013e3181bce7e1
- Mathe, E. A., Nguyen, G. H., Bowman, E. D., Zhao, Y., Budhu, A., Schetter, A. J., et al. (2009). MicroRNA expression in squamous cell carcinoma and adenocarcinoma of the esophagus: associations with survival. *Clin. Cancer Res.* 15, 6192–6200. doi:10.1158/1078-0432.ccr-09-1467



- Matsushima, K., Isomoto, H., Yamaguchi, N., Inoue, N., Machida, H., Nakayama, T., et al. (2011). MiRNA-205 modulates cellular invasion and migration via regulating zinc finger E-box binding homeobox 2 expression in esophageal squamous cell carcinoma cells. *J. Transl. Med.* 9, 1479–5876. doi:10.1186/1479-5876-9-30
- Meyerson, M., Gabriel, S., and Getz, G. (2010). Advances in understanding cancer genomes through second-generation sequencing. *Nat. Rev. Genet.* 11, 685–696. doi:10.1038/nrg2841
- Nathan, W., and Wang, X. (2014). miRDB: an online resource for microRNA target prediction and functional annotations. *Nucl. Acids Res.* 43, D146–52. doi:10.1093/nar/gku1104
- Ogata, H., Goto, S., Sato, K., Fujibuchi, W., Bono, H., and Kanehisa, M. (2000). KEGG: Kyoto encyclopedia of genes and genomes. *Nucl. Acids Res.* 27, 29–34. doi:10.1093/nar/28.1.27
- Ren, C., Chen, H., Han, C., Fu, D., Zhou, L., Jin, G., et al. (2016). miR-486-5p expression pattern in esophageal squamous cell carcinoma, gastric cancer and its prognostic value. *Oncotarget* 7, 15840–15853. doi:10.18632/oncotarget.7417
- Ringnér, M. (2008). What is principal component analysis?, *Nat. Biotechnol.* 26: 303–304. doi:10.1038/nbt0308-303
- Ritchie, M. E., Phipson, B., Wu, D., Hu, Y., Law, C. W., Shi, W., et al. (2015). limma powers differential expression analyses for RNA-sequencing and microarray studies. *Nucl. Acids Res.* 43, e47. doi:10.1093/nar/gkv007
- Rohatgi, P., Swisher, S. G., Correa, A. M., Wu, T.-T., Liao, Z., Komaki, R., et al. (2005). Characterization of pathologic complete response after preoperative chemoradiotherapy in carcinoma of the esophagus and outcome after pathologic complete response. *Cancer* 104, 2365–2372. doi:10.1002/cncr.21439
- Roman, J. (2017). On the "TRAIL" of a Killer: MMP12 in Lung Cancer. *Am. J. Respir. Crit. Care Med.* 196, 262–264. doi:10.1164/rccm.201704-0668ed
- Ross, J. S., and Cronin, M. (2011). Whole cancer genome sequencing by next-generation methods. *Am. J. Clin. Pathol.* 136, 527–539. doi:10.1309/ajcpr1svt1vhugxw
- Selga, E., Noé, V., and Ciudad, C. J. (2008). Transcriptional regulation of aldo-keto reductase 1C1 in HT29 human colon cancer cells resistant to methotrexate: role in the cell cycle and apoptosis. *Biochem. Pharmacol.* 75, 414–426. doi:10.1016/j.bcp.2007.08.034
- Shaheen, O., Ghibour, A., and Alsaid, B. (2017). Esophageal Cancer metastases to unexpected sites: a systematic review. *Gastroenterol. Res. Pract.* 2017, 1657310. doi:10.1155/2017/1657310
- Shannon, P., Markiel, A., Ozier, O., Baliga, N. S., Wang, J. T., Ramage, D., et al. (2003). Cytoscape: a software environment for integrated models of biomolecular interaction networks. *Genome Res.* 13, 2498–2504. doi:10.1101/gr.1239303
- Shao, Y., Li, P., Zhu, S.-T., Yue, J.-P., Ji, X.-J., Ma, D., et al. (2016). MiR-26a and miR-144 inhibit proliferation and metastasis of esophageal squamous cell cancer by inhibiting cyclooxygenase-2. *Oncotarget* 7, 15173–15186. doi:10.18632/oncotarget.7908
- Siegel, R. L., Miller, K. D., and Jemal, A. (2020). Cancer statistics, 2020. *CA A. Cancer J. Clin.* 70, 7–30. doi:10.3322/caac.21590
- Tian, Y., Luo, A., Cai, Y., Su, Q., Ding, F., Chen, H., et al. (2010). MicroRNA-10b promotes migration and invasion through KLF4 in human esophageal cancer cell lines. *J. Biol. Chem.* 285, 7986–7994. doi:10.1074/jbc.m109.062877
- Tsai, S. T., Wang, P. J., Liou, N. J., Lin, P. S., Chen, C. H., and Chang, W. C. (2015). ICAM1 is a potential Cancer stem cell marker of esophageal squamous cell carcinoma. *PLoS One* 10, e0142834. doi:10.1371/journal.pone.0142834
- Visser, E., Franken, I. A., Brosens, L. A. A., Ruurda, J. P., and van Hillegersberg, R. (2017). Prognostic gene expression profiling in esophageal cancer: a systematic review. *Oncotarget* 8, 5566–5577. doi:10.18632/oncotarget.13328
- Wen, J., Yang, H., Liu, M. Z., Luo, K. J., Liu, H., Hu, Y., et al. (2014). Gene expression analysis of pretreatment biopsies predicts the pathological response of esophageal squamous cell carcinomas to neo-chemoradiotherapy. *Ann. Oncol.* 25, 1769. doi:10.1093/annonc/mdu201
- Xie, S., Issa, R., Sukkar, M. B., Oltmanns, U., Bhavsar, P. K., Papi, A., et al. (2005). Induction and regulation of matrix metalloproteinase-12 in human airway smooth muscle cells. *Respir. Res.* 6, 1465–9921. doi:10.1186/1465-9921-6-148
- Yang, W., Arii, S., Gorrin-Rivas, M. J., Mori, A., Onodera, H., and Imamura, M. (2001). Human macrophage metalloelastase gene expression in colorectal carcinoma and its clinicopathologic significance. *Cancer* 91, 1277–1283. doi:10.1002/1097-0142(20010401)91:7<1277::aid-cncr1129>3.0.co;2-h
- Yao, J., Shen, X., Li, H., Xu, J., Shao, S., Huang, J. X., et al. (2018). LncRNA-ECM is overexpressed in esophageal squamous cell carcinoma and promotes tumor metastasis. *Oncol. Lett.* 16, 3935–3942. doi:10.3892/ol.2018.9130
- Yi, Y., Lu, X., Chen, J., Jiao, C., Zhong, J., Song, Z., et al. (2016). Downregulated miR-486-5p acts as a tumor suppressor in esophageal squamous cell carcinoma. *Exp. Ther. Med.* 12, 3411–3416. doi:10.3892/etm.2016.3783
- Yu, P. F., Huang, Y., Han, Y. Y., Lin, L. Y., Sun, W. H., Rabson, A. B., et al. (2017). TNF $\alpha$ -activated mesenchymal stromal cells promote breast cancer metastasis by recruiting CXCR2+ neutrophils. *Oncogene* 36, 482–490. doi:10.1038/ncr.2016.217
- Zhang, C., Wang, C., Chen, X., Yang, C., Li, K., Wang, J., et al. (2010). Expression profile of microRNAs in serum: a fingerprint for esophageal squamous cell carcinoma. *Clin. Chem.* 56, 1871–1879. doi:10.1373/clinchem.2010.147553
- Zhang, J., Huang, X., Xiao, J., Yang, Y., Zhou, Y., Wang, X., et al. (2014). , Pri-miR-124 rs531564 and pri-miR-34b/c rs4938723 polymorphisms are associated with decreased risk of esophageal squamous cell carcinoma in Chinese populations. *Plos One* 9, e100055. doi:10.1371/journal.pone.0100055

**Conflict of Interest:** The authors declare that the research was conducted in the absence of any commercial or financial relationships that could be construed as a potential conflict of interest.

Copyright © 2021 Wang, Yu, Luo, Sun, Yu and Wang. This is an open-access article distributed under the terms of the Creative Commons Attribution License (CC BY). The use, distribution or reproduction in other forums is permitted, provided the original author(s) and the copyright owner(s) are credited and that the original publication in this journal is cited, in accordance with accepted academic practice. No use, distribution or reproduction is permitted which does not comply with these terms.



# LCT-3d Induces Oxidative Stress-Mediated Apoptosis by Upregulating Death Receptor 5 in Gastric Cancer Cells

## OPEN ACCESS

### Edited by:

Haichang Li,  
The Ohio State University,  
United States

### Reviewed by:

Taeg Kyu Kwon,  
Keimyung University Dongsan Medical  
Center, South Korea  
Jin Won Hyun,  
Jeju National University, South Korea  
Dong-Hua Yang,  
St. John's University, United States

### \*Correspondence:

Cheng-yun Jin  
cyj@zzu.edu.cn  
Hai-wei Xu  
Xhwei01@126.com  
Zhengya Wang  
zhenyawang@zzu.edu.cn

<sup>†</sup>These authors have contributed  
equally to this work and share  
first authorship

### Specialty section:

This article was submitted to  
Pharmacology of Anti-Cancer Drugs,  
a section of the journal  
Frontiers in Oncology

Received: 26 January 2021

Accepted: 22 March 2021

Published: 16 April 2021

### Citation:

Wang M, Wu X, Yu L, Hu Z-y,  
Li X, Meng X, Lv C-t, Kim G-Y,  
Choi YH, Wang Z, Xu H-W and Jin C-Y  
(2021) LCT-3d Induces Oxidative  
Stress-Mediated Apoptosis by  
Upregulating Death Receptor 5  
in Gastric Cancer Cells.  
Front. Oncol. 11:658608.  
doi: 10.3389/fonc.2021.658608

Menglin Wang<sup>1†</sup>, Xinxin Wu<sup>1†</sup>, Lu Yu<sup>1†</sup>, Zi-yun Hu<sup>1†</sup>, Xiaobo Li<sup>1</sup>, Xia Meng<sup>1</sup>,  
Chun-tao Lv<sup>1</sup>, Gi-Young Kim<sup>2</sup>, Yung Hyun Choi<sup>3</sup>, Zhengya Wang<sup>1\*</sup>, Hai-Wei Xu<sup>1\*</sup>  
and Cheng-Yun Jin<sup>1,4\*</sup>

<sup>1</sup> Key Laboratory of Advanced Technology for Drug Preparation, Ministry of Education, School of Pharmaceutical Sciences, Zhengzhou University, Zhengzhou, China, <sup>2</sup> Department of Marine Life Sciences, Jeju National University, Jeju, South Korea, <sup>3</sup> Department of Biochemistry, College of Oriental Medicine, Dong-Eui University, Busan, South Korea, <sup>4</sup> State Key Laboratory of Esophageal Cancer Prevention & Treatment, Zhengzhou University, Zhengzhou, China

Gastric cancer is a global health problem. In this study, we investigate the role of a novel Indole derivative, named LCT-3d, in inhibiting the growth of gastric cancer cells by MTT assay. The Western blotting results showed that LCT-3d modulated the mitochondrial-related proteins and Cleaved-Caspases 3/9, to induce cell apoptosis. The up-regulation of Death receptor 5 (DR5) in MGC803 cells was observed with LCT-3d treatment. Knockdown of DR5 on MGC803 cells partially reversed the LCT-3d-induced mitochondrial apoptosis. The level of Reactive Oxygen Species (ROS) in MGC803 cells was increased with LCT-3d treatment and could be blocked with the pretreatment of the ROS inhibitor N-Acetylcysteine (NAC). The results demonstrate that the elevating ROS can up-regulate the expression of DR5, resulting in apoptosis via mitochondrial pathway. Although the nuclear factor erythroid-2 related factor 2 (Nrf2) pathway served an important role in protecting gastric cancer cells against the injury of ROS, it can't reverse LCT-3d-induced cell apoptosis. Taken together, our study showed that LCT-3d induced apoptosis via DR5-mediated mitochondrial apoptotic pathway in gastric cancer cells. LCT-3d could be a novel lead compound for development of anti-cancer activity in gastric cancer.

**Keywords:** LCT-3d, DR5, reactive oxygen species, Nrf2, apoptosis, gastric cancer

## INTRODUCTION

Gastric cancer remains the third leading cause of death in spite of the decreasing incidence and mortality (1). Many people in China are diagnosed with gastric cancer every year, and once diagnosed, most of them are in the advanced stage with metastasis (2). Currently, chemotherapy for gastric cancer is limited due to serious side effects and low efficacy (3). The development of drug resistance in tumors is a major obstacle of chemotherapy (4–7). Hence, developing novel effective strategies for treatment of gastric cancers is warranted.

Drugs with Indole skeleton shows good efficacy for cancer therapy (8), such as vincristine (9), Indole-3-carbinol (I3C) (10), BPR0L075 (11), as well as JKA97 (12). All of them have exhibited good effects on anti-tumor through inducing cell apoptosis *via* a variety of signaling pathways.

In the previous work, we synthesized a potent Lysine (K)-Specific Demethylase 1A (LSD1) inhibitor, named LCT-9e (Figure 1B), which effectively inhibits the macrophages (THP-1 cells) growth (13). LCT-9e is the first irreversible LSD1 inhibitor, which is not derived from monoamine oxidase inhibitors. Hence, LCT-9e was chosen to be a lead compound for optimization. Unexpectedly, when the heterocyclic group was introduced to C-5 position of the Indole, the LSD1 inhibitors such as compound LCT-3d kept the anti-proliferation activity in gastric cancer cells with low cytotoxicity. In this study, we explored the role of LCT-3d in gastric cancer cells and its molecular mechanism. The results suggested that LCT-3d induced the generation of Reactive Oxygen Species (ROS), which subsequently led to gastric cancer cell apoptosis *via* up-regulating the expression of Death receptor 5 (DR5). Meanwhile, LCT-3d activated the nuclear factor erythroid-2 related factor 2 (Nrf2) pathway, which attenuated LCT-3d-induced cell apoptosis. This is the first report on Indole derivative in inducing apoptosis in gastric cancer cells through DR5-mediated pathway.

## MATERIALS AND METHODS

### Reagents and Antibodies

LCT-3d was synthesized in our group and was dissolved in DMSO. RPMI-1640, Fetal bovine serum (FBS), and penicillin-streptomycin were purchased from HyClone (Victoria, Australia). DCFH-DA (2, 7-dichlorodihydrofluorescein diacetate), the Nuclear and Cytoplasmic Protein Extraction Kit, and Annexin V- FITC Apoptosis Detection Kit were purchased from Beyotime Biotechnology (Shanghai, China). The primary antibodies for Caspase 3 (sc-7272), PARP (sc-7150), DR5 (sc-65314), Caspase 9 (sc-7885), Bim (sc-11425), Bad (sc-8044), Bax (sc-493), DR4 (sc-7863), and  $\beta$ -actin (sc-1615) were purchased from Santa Cruz Biotechnology (Santa Cruz, CA, USA). Bid (#2002), Bcl-xL (#2764), and XIAP (#14334) were purchased from Cell Signaling Technology (Danvers, MA, USA). The secondary antibodies anti-goat, anti-rabbit, and anti-mouse were purchased from Bioss (Shanghai, China). The pan-Caspase inhibitor Z-VAD-FMK was purchased from Selleck. The Nrf2 inhibitor ML385 was purchased from MCE (NJ, USA). The ECL (enhanced chemiluminescence) kit was purchased from Thermo Fisher (Waltham, MA, USA). Anti-DR5 (ab1675) antibody for flow cytometry was purchased from Abcam (Cambridge, MA, USA). NAC (N-acetyl-L-cysteine), MTT [3-(4, 5-dimethylthiazol-2-yl) - 2, 5-diphenyltetrazolium

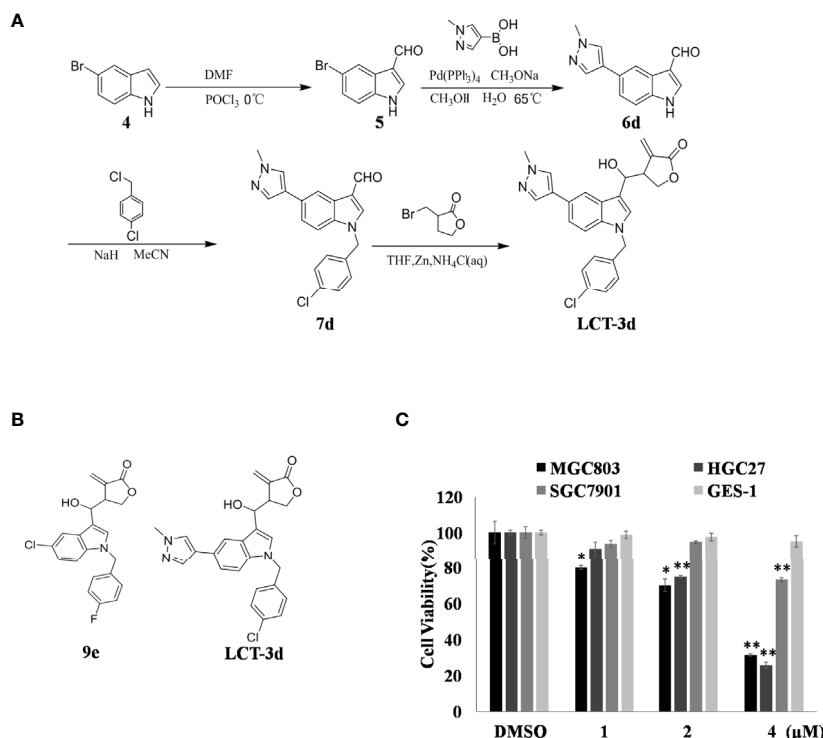


**FIGURE 1 |** LCT-3d inhibited the cell proliferation of gastric cancer cells. (A) LCT-3d synthetic procedure. (B) Structure of LCT-3d. (C) Cytotoxic effect of LCT-3d on gastric cancer cells measured by MTT assay. Cells were treated with increasing concentration of LCT-3d for 48 h. \* $P < 0.05$ , \*\* $P < 0.01$ , significantly different compared with control.

bromide], and JC-1 fluorescent dye were purchased from Sigma-Aldrich (St. Louis, MO, USA).

## Cell Lines and Culture

Gastric cancer cells MGC803, HGC27, SGC7901 and normal gastric cells GES-1 were from the American Type Culture Collection. These cells were cultured in cell medium supplemented with 10% FBS in an incubator with 5% CO<sub>2</sub> at 37°C. The DR5 knockout cell line of MGC803 was previously constructed by our team (14).

## Cell Viability Assay

The viability of gastric cancer cells and GES-1 cells were examined by MTT assay. After cells were incubated with LCT-3d for 48 h, 20  $\mu$ l MTT (5 mg/ml) was added into each well. Subsequently, cells were incubated for another 2–4 h, the cell culture medium was removed, and then 150  $\mu$ l DMSO was added into each well. Optical density for MTT assay was detected at 490 nm with a microplate reader (Synergy H1, BioTek, VT, USA). The dose of DMSO has no effect on cell viability in all groups of cells in this study.

## Apoptosis Analysis

MGC803 and HGC27 cells were treated with LCT-3d at different concentrations. After incubating for 48 h, the cells were collected and stained with Annexin V and PI for 20 min. Next, cells were measured by a flow cytometer (BD LSRFortessa™ Cell Analyzer, Becton, Dickinson and Company, NJ, USA). The data was quantified by the FlowJo software.

## Measurement of Mitochondrial Membrane Potential (MMP, $\Delta\Psi$ )

MGC803 and HGC27 cells were treated with LCT-3d at different concentrations. After incubating for 48 h, the cells were collected and then incubated with JC-1 (2.5  $\mu$ g/ml) for 10 min at 37°C. Next, cells were measured by a flow cytometer. The data was quantified by the FlowJo software (15).

## Analysis of DR5 Expression by a Flow Cytometer

Wild type MGC803 and DR5<sup>-/-</sup> MGC803 cells were seeded in a six-well plate and treated with LCT-3d for 24 h. The cells were collected and fixed by 1% paraformaldehyde at 4°C for 30 min. Then the cells were incubated with normal goat serum, DR5 antibody, and Goat anti-mouse IgG successively. Next, the cells were measured by a flow cytometer. The data was quantified by FlowJo software.

## Measurement of ROS

MGC803 and HGC27 cells were treated with LCT-3d for indicated time. Then cells were collected and stained with DCFH-DA for 20 min. Next, the cells were measured by a flow cytometer. The data was quantified by FlowJo software.

## Total/Nuclear Protein Extraction

MGC803 cells were treated with LCT-3d for indicated time. Then the cells were collected and proteins were extracted according to instruction of the Nuclear and Cytoplasmic

Protein Extraction Kit. The protein concentration was determined by the micro-BCA protein assay kit.

## Western Blotting

MGC803 and HGC27 cells were treated with agents for indicated time. The total proteins were collected and quantified by the micro-BCA protein assay kit (P0012, Beyotime, Shanghai, China). Then the proteins were subjected to immunoblotting as previously described (16).

## Immunofluorescence

Cells were treated with agents for indicated time, then immunofluorescence analysis was performed as reported previously (17).

## Statistical Analysis

All experiments were repeated at least three times. The data were presented as mean  $\pm$  SD. Differences between the experimental groups were determined by paired or unpaired Student's t test, \* and \*\* represent  $P < 0.05$  and  $P < 0.01$ , respectively.

# RESULTS

## LCT-3d Reduced the Cell Viability of Human Gastric Cancer Cells but Not Normal Cells

The process of synthesize LCT-3d as shown in **Figure 1A**. The effect of LCT-3d on three human gastric cancer cells (MGC803, HGC27, SGC7901) and normal cell GES-1 were evaluated by MTT assay. The results showed that the viability of MGC803 and HGC27 cells were reduced in a dose-dependent manner after treatment with LCT-3d (**Figure 1C**). In addition, MGC803 and HGC27 cells exhibited more sensitivity to LCT-3d than SGC7901 cells, with the inhibitory rate of 68.83 and 74.41% at 4  $\mu$ M, respectively. LCT-3d showed little inhibition on the viability of GES-1 cells after treatment with LCT-3d. These results demonstrated that LCT-3d decreased the growth of human gastric cancer cells but not normal cells.

## LCT-3d Induced Cell Apoptosis Dependent on Caspases

In order to determine whether LCT-3d induced cell apoptosis, the apoptotic rate of MGC803 and HGC27 cells was detected by flow cytometry. The apoptotic rate was increased in a concentration-dependent manner in both cells (**Figure 2A**). Then some Caspase-related proteins were tested (**Figure 2B**). Western blotting results demonstrated that LCT-3d promoted the expression of Cleaved-PARP and Cleaved-Caspase 3/9 in MGC803 and HGC27 cells.

To further confirm whether Caspase family proteins regulated LCT-3d-induced apoptosis, the cells were pretreated with a pan-Caspase inhibitor Z-VAD-FMK (100  $\mu$ M) for 1 h, and subsequently incubated with LCT-3d (4  $\mu$ M) for an additional 48 h. The flow cytometry analysis showed that pretreatment with Z-VAD-FMK (100  $\mu$ M) partially reversed LCT-3d-induced



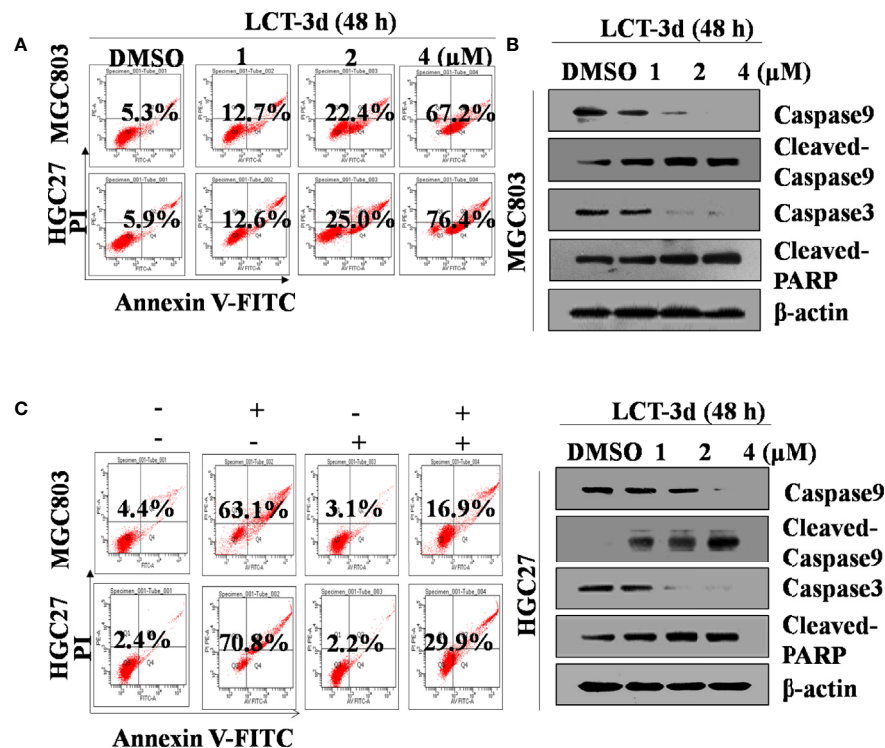


**FIGURE 2 |** LCT-3d triggered Caspase mediated apoptotic pathway in gastric cancer cells. **(A)** MGC803 cells and HGC27 were cells treated with various concentrations of LCT-3d for 48 h and apoptosis analyzed by flow cytometry. **(B)** Cells were treated as in **(A)** and the expression of Cleaved-Caspase and Cleaved PARP was analyzed by Western blotting. **(C)** MGC803 cells and HGC27 cells were pretreated with a pan-Caspase inhibitor, Z-VAD-FMK (100 μM) for 1 h, followed by incubation with LCT-3d (4 μM) for 48 h. Flow cytometric analysis on the effect of Z-VAD-FMK on LCT-3d-induced cells apoptosis.

apoptosis in MGC803 and HGC27 cells (**Figure 2C**). These results suggested that LCT-3d induced apoptosis of the gastric cancer cells through a Caspase-dependent manner.

### LCT-3d Regulated the Expression of Bcl-2 Family Proteins and Reduced the Mitochondrial Membrane Potential (MMP/ΔΨ)

To further explore the underlying mechanism of LCT-3d-induced apoptosis, the change of mitochondrial membrane potential (ΔΨ) and the level of proteins involved in apoptosis were investigated. It was found that LCT-3d reduced the mitochondrial membrane potential in MGC803 and HGC27 cells (**Figure 3A**). Furthermore, LCT-3d down-regulated the expression of anti-apoptotic proteins Bcl-2, Bcl-xl, Bid, and XIAP, and up-regulated the pro-apoptotic proteins Bax, Bad, and Bim in MGC803 cells (**Figure 3B**). These results demonstrated that LCT-3d induced apoptosis of gastric cancer cells via the mitochondrial pathway.

### DR5 Was Involved in LCT-3d-Induced Apoptosis in MGC803 Cells

Then, the role of DR5 was evaluated on LCT-3d-induced apoptosis. It was found that LCT-3d significantly up-regulated the expression of DR5 in MGC803 cells (**Figure 4A**). To further

confirm whether DR5 is necessary for LCT-3d-induced apoptosis, the DR5 knocked down MGC803 cells were used for investigation. Flow cytometry analysis showed that the expression of DR5 was reduced in DR5 knocked down MGC803 cells (**Figure 4B**). The LCT-3d-induced cell death was partially reversed in DR5 knocked down MGC803 cells (**Figures 4C, D**). The Cleaved-Caspase 9 and Cleaved-PARP were decreased in DR5 knocked down MGC803 cells compared with wild type MGC803 cells (**Figure 4E**). LCT-3d-induced mitochondrial depolarization was partially reversed in DR5 knocked down MGC803 cells (**Figure 4F**). Collectively, these results suggested that LCT-3d-induced apoptosis was mediated by DR5.

### LCT-3d Induced ROS Production and Activated Nrf2 Pathway in MGC803 Cells

To explore whether ROS was related to LCT-3d-induced apoptosis, the levels of ROS were detected after treatment with LCT-3d by flow cytometry. The results showed that the level of ROS was markedly increased in a time-dependent manner in MGC803 and HGC27 cells (**Figure 5A**). Next, we detected the role of Nrf2 in LCT-3d-induced ROS generation in MGC803 cells. The results showed that LCT-3d up-regulated p-Nrf2 and its downstream targets HO-1 and NQO1 in MGC803 cells (**Figure 5B**). Moreover, levels of Nrf2 in the nuclear fraction

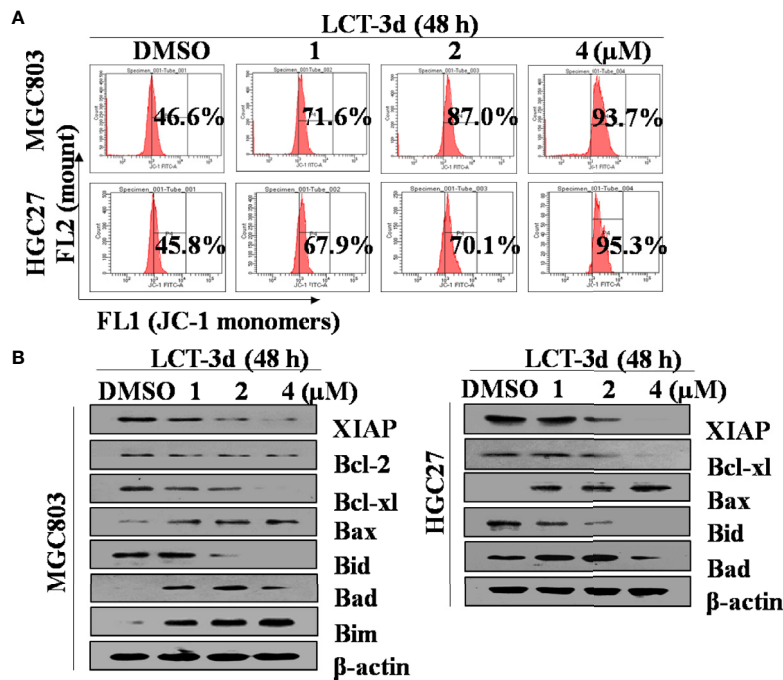


**FIGURE 3** | LCT-3d-induced apoptosis was associated with mitochondrial pathway in gastric cancer cells. **(A)** MGC803 cells and HGC27 cells were treated with various concentrations of LCT-3d for 48 h and the membrane potential was measured by JC-1 dye retention using flow cytometry. **(B)** Cells were treated as in **(A)** and the expression of Bax, Bad, Bim, Bid, Bcl-xl, Bcl-2, and XIAP proteins was determined by Western blotting.

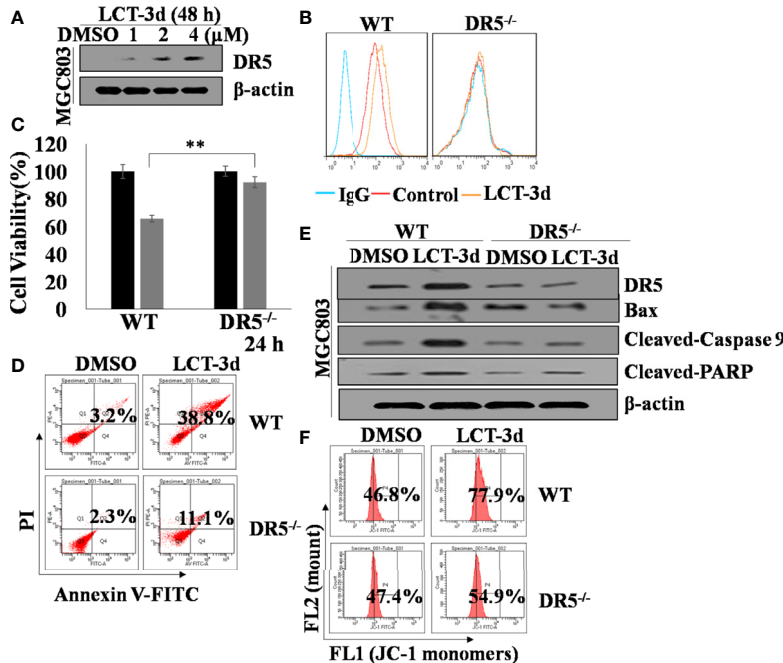


**FIGURE 4** | LCT-3d-induced apoptosis is associated with extrinsic pathway in gastric cancer cells. Both wild type and DR5<sup>-/-</sup> MGC803 cells were treated with 4 μM LCT-3d or indicated concentration. **(A)** Western blotting assay showed reduced expression of DR5 in a dose-dependent manner in MGC803 cells. **(B)** MGC803 cells and DR5<sup>-/-</sup> MGC803 cells were treated with 4 μM LCT-3d for 24 h and DR5 protein expressions in MGC803 cells determined by flow cytometry. **(C)** MTT assay showed the cell viability after treatment with 4 μM LCT-3d for 24 h. \*\**P* < 0.01, significantly different compared with control. **(D)** Flow cytometric analysis showed the ratios of apoptotic cells after treatment with 4 μM LCT-3d for 24 h. **(E)** Western blotting assay showed the expression of the apoptosis-related proteins after treatment with 4 μM LCT-3d for 24 h. **(F)** Flow cytometric analysis demonstrated the reduction of MMP (ΔΨ) after treatment with 4 μM LCT-3d for 24 h.

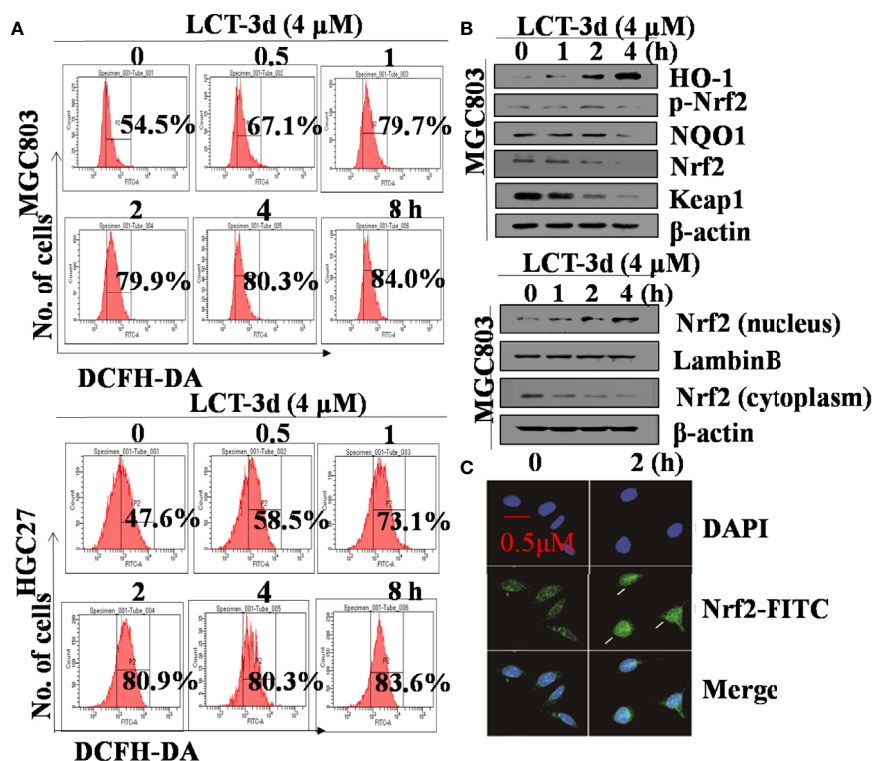


**FIGURE 5** | LCT-3d increased the level of ROS in gastric cancer cells. **(A)** MGC803 cells and HGC27 cells were treated with LCT-3d (4 μM) for indicated times and the level of ROS was detected by DCFH-DA with flow cytometry. **(B)** Western blotting assay showed Nrf2 nuclear-translocation and the changes of LCT-3d-induced protein expression at indicated time points. **(C)** MGC803 cells were treated with LCT-3d (4 μM) for 2 h. The treated and untreated samples are stained with Nrf2 antibody (Green) and DAPI (Blue) (magnification, 400×). The arrows indicate Nrf2 nuclear translocation.

were significantly increased, whereas levels of Nrf2 in the cytoplasm were decreased, indicating that Nrf2 translocated into the nucleus and activated its downstream target genes (Figure 5B). To support this point, the immunofluorescence assay was conducted and similar result was observed (Figure 5C). These results suggested that LCT-3d induced the production of ROS and triggered the Nrf2 pathway to inhibit apoptosis of gastric cancer cells.

### LCT-3d-Induced Apoptosis Depends on ROS but Not Nrf2 in Gastric Cancer Cells

To explore whether ROS contributed to the apoptosis induction, MGC803 and HGC27 cells were pretreated with NAC for 1 h followed by the treatment with LCT-3d (4 μM) for an additional 48 h. The pretreatment with NAC reversed the cell death in MGC803 and HGC27 cells (Figures 6A, B). The effect of ROS on cell apoptosis-related proteins was investigated by Western blotting. The results showed that NAC markedly reversed the changes of expression of apoptosis-related proteins, as well as abrogated mitochondrial depolarization. These results were similar in HGC27 cells to MGC803 cells (Figures 6C, D). However, the pretreatment with ML385 rarely reversed the cell death in MGC803 cells (Figure 6E). These results suggested that

LCT-3d-induced apoptosis depended on ROS but not Nrf2 in gastric cancer cells.

## DISCUSSION

The death rate of patients suffering from gastric cancer is increasing. The emergence of side effects and multi-drug resistance to chemotherapeutic drugs usually lead to the failure of chemotherapies (18). In this study, a new Indole compound LCT-3d was discovered, which had selective cytotoxicity against gastric cancer cells with no apparent cytotoxicity against non-malignant gastric epithelial cells. ROS level was detected by flow cytometry in gastric cancer cells. The cells pretreated with NAC for 1 h blocked the production of ROS and prevented the up-regulation of DR5, as well as mitochondria JNK-CHOP pathway (18). ROS triggered apoptosis by activating death receptors and the mitochondria pathway (19, 20). Mechanistically, the data demonstrated that LCT-3d induced gastric cell apoptosis through DR5-mediated mitochondrial pathway.

The activation of Caspase family proteins is an important event leading to cell apoptosis (21). At the early stage of apoptosis, Caspase 3 and Caspase 9 were activated, and they served as biomarker proteins of apoptosis (22). Caspase 3,

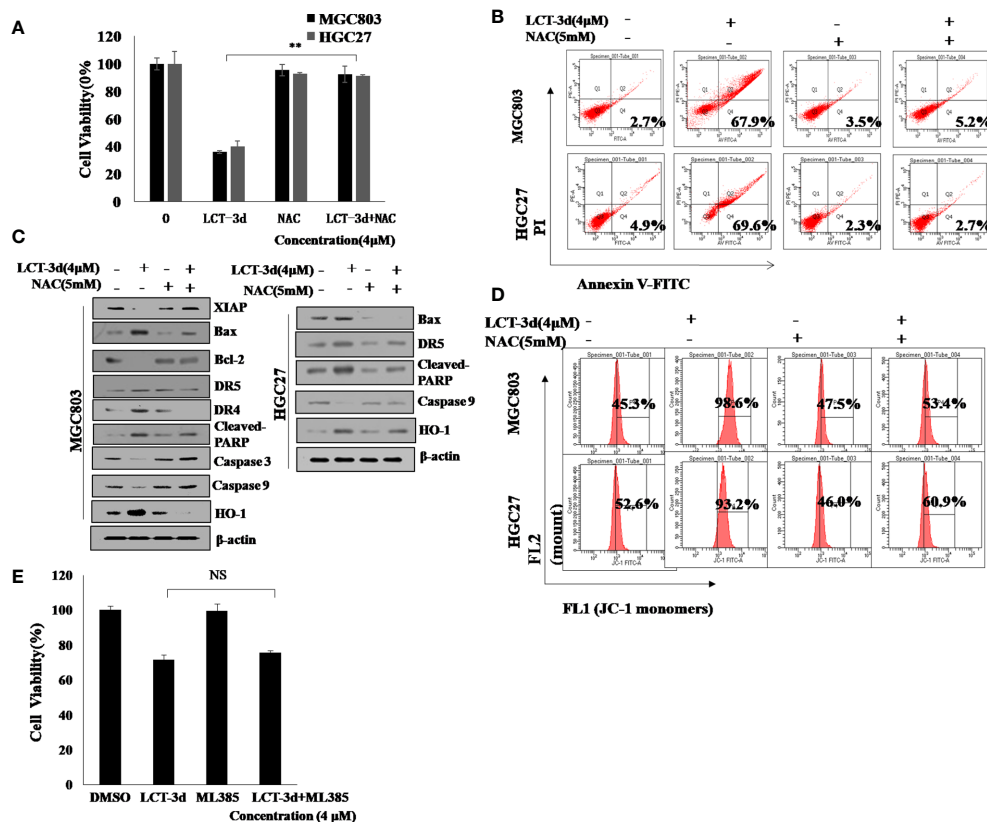


**FIGURE 6** | LCT-3d-induced apoptosis is associated with the rising ROS in gastric cancer cells. **(A)** MGC803 cells and HGC27 cells were pretreated with NAC (5 mM) for 1 h, followed by incubation with LCT-3d (4 μM) for 48 h. The effect of NAC on LCT-3d-induced cell death was analyzed by MTT assay. \*\* $P < 0.01$ , significantly different compared with control. **(B)** Flow cytometric analysis demonstrated the effects of NAC (5 mM) on LCT-3d (4 μM)-induced cell apoptosis of the gastric cancer cells. **(C)** Western blotting assay showed the effect of NAC (5 mM) on LCT-3d (4 μM)-induced change of protein expression at 48 h. **(D)** Flow cytometric analysis showed the effect of NAC (5 mM) on LCT-3d (4 μM)-induced loss of MMP ( $\Delta\psi$ ) in gastric cancer cells. **(E)** MGC803 cells pretreated with ML385 for 1 h followed by the treatment with LCT-3d (4 μM) for an additional 48 h. The pretreatment with ML385 rarely reversed the cell death in MGC803 and HGC27 cells.

the key execution enzyme, was activated by Caspase 9, which is the primary initiator Caspase (23). The cleavage of PARP was regarded as an important indicator of apoptosis (24). Therefore, the expression of these proteins was measured by Western blotting. The results showed the activation of Cleaved-Caspase 3/9 and Cleaved-PARP after treatment with LCT-3d. The reversal of the process by Z-VAD-FMK confirmed that LCT-3d induced apoptosis dependent on Caspases.

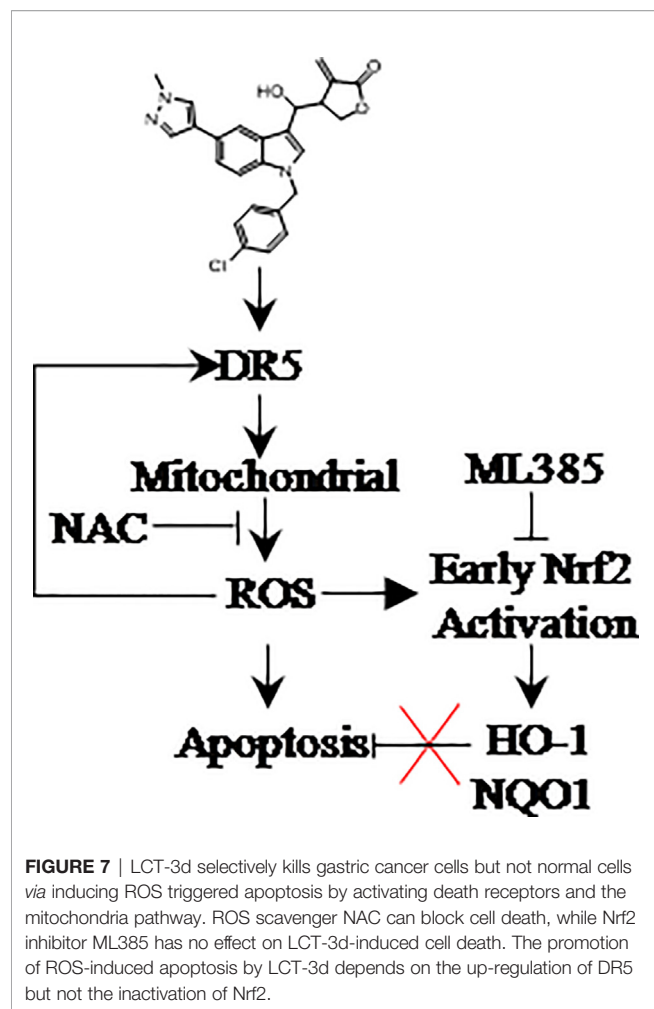
It has long been reported that mitochondria is an important factor in the process of apoptosis (25). To further confirm whether LCT-3d treatment activated mitochondrial pathway, we detected mitochondria-related proteins in gastric cancer cells. Bcl-2 family proteins are the major regulators and effectors of the mitochondrial apoptotic pathway, which include anti-apoptotic proteins such as Bcl-2 and pro-apoptotic proteins such as Bax (26–29). The oligomerization of Bax and Bak proteins promote the increase of the mitochondrial membrane permeability, which leading to the release of cytochrome c into the cytosol, subsequently cell apoptosis occurred through Caspase cascade. In this work, mitochondrial membrane potential and the levels of Bcl-2 and Bcl-xL were

decreased upon LCT-3d treatment. Meanwhile, pro-apoptotic protein Bax, Bad, and Bim were increased after LCT-3d treatment. Collectively, the findings demonstrated that LCT-3d induced apoptosis of gastric cancer cells *via* mitochondrial pathway.

The role of DR5 in LCT-3d-induced apoptosis was investigated. MTT assay showed that LCT-3d-induced cell death was partially reversed in MGC803-DR5<sup>-/-</sup> cells, suggesting that DR5 is an important factor for inducing cell apoptosis upon LCT-3d treatment. Moreover, compared with wild type MGC803 cells, the apoptotic rate and the decline of MMP as well as the cleavage of PARP and Caspase 9 were reversed in MGC803-DR5<sup>-/-</sup> cells. These results demonstrated that activation of mitochondrial pathway was associated with DR5.

ROS can trigger the mitochondria-mediated intrinsic apoptotic pathway (19, 30). In this work, the elevating ROS in the process of LCT-3d-induced apoptosis was observed. In addition, NAC markedly inhibited the activation of Caspase 3/9, the up-regulation of DR5, the modulation of Bcl-2 family proteins, as well as the cancellation of MMP decrease. These results suggested that NAC blocked the effect of ROS on gastric cancer cells,





indicating that ROS triggered cell death through DR5-mediated mitochondrial apoptosis pathway (31).

ROS are the key molecules in the process of apoptosis (32, 33). It is reported that moderate level of ROS can increase the ability of cell survival (34). It is well known that Nrf2 can protect cells from injury by oxidative stress through separating from Keap1 and subsequently translocating into the cell nucleus (35, 36). In this study, it was confirmed that the elevating ROS activated Nrf2, which then translocated into the nucleus, subsequently up-regulated its downstream target genes such as HO-1, NQO1, leading to inhibition of apoptosis, which is in consistent with the previous work (31, 37).

## REFERENCES

1. Thrift AP, El-Serag HB. Burden of Gastric Cancer. *Clin Gastroenterol Hepatol* (2020) 18:534–42. doi: 10.1016/j.cgh.2019.07.045
2. Cao J, Zhang X, Xu P, Wang H, Wang S, Zhang L, et al. Circular RNA circLMO7 acts as a microRNA-30a-3p sponge to promote gastric cancer progression via the WNT2/beta-catenin pathway. *J Exp Clin Cancer Res* (2021) 40:6. doi: 10.1186/s13046-020-01791-9
3. Shen X, Wang J, Yan X, Ren X, Wang F, Chen X, et al. Predictive value of GSTP1 Ile105Val polymorphism in clinical outcomes of chemotherapy in

## CONCLUSION

A novel Indole derivative LCT-3d was found to induce apoptosis in gastric cancer cells through DR5-mediated mitochondrial apoptotic pathway (13, 31). LCT-3d modulated the Bcl-2 family proteins and Cleaved-Caspases 3/9, and resulted in cell apoptosis in MGC803 and HGC27 cells. Nrf2 played an important role in protecting gastric cancer cells from the injury of oxidative stress after LCT-3d treatment, but it could not reverse LCT-3d-induced cell apoptosis (**Figure 7**). This study suggested that LCT-3d could be a potential lead compound for the development of anti-gastric cancer agents.

## DATA AVAILABILITY STATEMENT

The original contributions presented in the study are included in the article/supplementary material. Further inquiries can be directed to the corresponding authors.

## AUTHOR CONTRIBUTIONS

MW, XW, LY, and Z-YH performed majority experiments, analyzed data, and wrote original draft. XL, XM, and C-TL synthesized the compound LCT-3d. G-YK and YC knocked down the DR5. C-YJ, H-WX, and ZW conceived and designed the experiments and revised the draft of manuscript. All authors contributed to the article and approved the submitted version.

## FUNDING

The work was supported by the National Natural Science Foundation of China (Project No. 81973529 for C-YJ), “13th five-year plan of China”: Major Projects of National Science and Technology on New Drug Creation and Development (Project No. HX2018ZX09711001-005-026 for HX), and Fang’s family (Hong Kong) foundation (ZW).

## ACKNOWLEDGMENTS

The author would like to thank Dr. Cheng-yun Jin, Dr. Hai-wei Xu, and Dr. Zheng-ya Wang for providing technical support.

- gastric and colorectal cancers: a systematic review and meta-analysis. *Cancer Chemother Pharmacol* (2016) 77:1285–302. doi: 10.1007/s00280-016-3047-1
4. Gao HL, Gupta P, Cui Q, Ashar YV, Wu ZX, Zeng L, et al. Sunitinib Reverses Anticancer Drug Resistance in Colon Cancer Cells Overexpressing the ABCB1 Transporter. *Front Oncol* (2020) 10:574861. doi: 10.3389/fonc.2020.574861
  5. Lei ZN, Teng QX, Zhang W, Fan YF, Wang JQ, Cai CY, et al. Establishment and Characterization of a Topotecan Resistant Non-small Cell Lung Cancer NCI-H460/TPT10 Cell Line. *Front Cell Dev Biol* (2020) 8:607275. doi: 10.3389/fcell.2020.607275

6. Wang JQ, Teng QX, Lei ZN, Ji N, Cui Q, Fu H, et al. Reversal of Cancer Multidrug Resistance (MDR) Mediated by ATP-Binding Cassette Transporter G2 (ABCG2) by AZ-628, a RAF Kinase Inhibitor. *Front Cell Dev Biol* (2020) 8:601400. doi: 10.3389/fcell.2020.601400
7. Zhang H, Xu H, Ashby CJ, Assaraf YG, Chen ZS, Liu HM. Chemical molecular-based approach to overcome multidrug resistance in cancer by targeting P-glycoprotein (P-gp). *Med Res Rev* (2021) 41:525–55. doi: 10.1002/med.21739
8. Munakarmi S, Chand L, Shin HB, Jang KY, Jeong YJ. Indole-3-Carbinol Derivative DIM Mitigates Carbon Tetrachloride-Induced Acute Liver Injury in Mice by Inhibiting Inflammatory Response, Apoptosis and Regulating Oxidative Stress. *Int J Mol Sci* (2020) 21:2048. doi: 10.3390/ijms21062048
9. Igarashi T, Kishi S, Hosono N, Higashi T, Iwao T, Yano R, et al. Population pharmacokinetic model development and exposure-response analysis of vincristine in patients with malignant lymphoma. *Cancer Chemother Pharmacol* (2021) 87. doi: 10.1007/s00280-020-04220-y
10. Lee CM, Park SH, Nam MJ. Anticarcinogenic effect of indole-3-carbinol (I3C) on human hepatocellular carcinoma SNU449 cells. *Hum Exp Toxicol* (2019) 38:136–47. doi: 10.1177/0960327118785235
11. Wang X, Wu E, Wu J, Wang TL, Hsieh HP, Liu X. An antimetabolic and antivascular agent BPRO1075 overcomes multidrug resistance and induces mitotic catastrophe in paclitaxel-resistant ovarian cancer cells. *PloS One* (2013) 8:e65686. doi: 10.1371/journal.pone.0065686
12. Yang X, Wang W, Qin JJ, Wang MH, Sharma H, Buolamwini JK, et al. JKA97, a novel benzylidene analog of harmine, exerts anti-cancer effects by inducing G1 arrest, apoptosis, and p53-independent up-regulation of p21. *PloS One* (2012) 7:e34303. doi: 10.1371/journal.pone.0034303
13. Kim SY, Hwang S, Choi MK, Park S, Nam KY, Kim I. Molecular mechanisms underlying the effects of the small molecule AMC-04 on apoptosis: Roles of the activating transcription factor 4-C/EBP homologous protein-death receptor 5 pathway. *Chem Biol Interact* (2020) 332:109277. doi: 10.1016/j.cbi.2020.109277
14. Yu H, Wu CL, Wang X, Ban Q, Quan C, Liu M, et al. SP600125 enhances C-2-induced cell death by the switch from autophagy to apoptosis in bladder cancer cells. *J Exp Clin Cancer Res* (2019) 38:448. doi: 10.1186/s13046-019-1467-6
15. Jin CY, Molagoda I, Park C, Kwon TK, Yun SJ, Kim WJ, et al. Piceatannol-Induced Apoptosis Is Reversed by N-Acetyl-L-cysteine through Restoration of XIAP Expression. *Biol Pharm Bull* (2018) 41:1372–8. doi: 10.1248/bpb.b18-00157
16. Xu HW, Jia S, Liu M, Li X, Meng X, Wu X, et al. A low toxic CRM1 degrader: Synthesis and anti-proliferation on MGC803 and HGC27. *Eur J Med Chem* (2020) 206:112708. doi: 10.1016/j.ejmech.2020.112708
17. Kim SO, Cha HJ, Park C, Lee H, Hong SH, Jeong SJ, et al. Cordycepin induces apoptosis in human bladder cancer T24 cells through ROS-dependent inhibition of the PI3K/Akt signaling pathway. *Biosci Trends* (2019) 13:324–33. doi: 10.5582/bst.2019.01214
18. Naveen SM, Sivanandhan D, Gajendran C, Tantry S, Dewang P, Murugan K, et al. Novel dual LSD1/HDAC6 inhibitors for the treatment of multiple myeloma. *Bioorg Med Chem Lett* (2020) 34:127763. doi: 10.1016/j.bmcl.2020.127763
19. Kim SY, Jin CY, Kim CH, Yoo YH, Choi SH, Kim GY, et al. Isorhamnetin alleviates lipopolysaccharide-induced inflammatory responses in BV2 microglia by inactivating NF-kappaB, blocking the TLR4 pathway and reducing ROS generation. *Int J Mol Med* (2019) 43:682–92. doi: 10.3892/ijmm.2018.3993
20. Zingue S, Cisolotto J, Fogang R, Tchoupang EN, Ndinteh DT, Tchuengue FN, et al. The antimammmary tumor effects of ethanolic extract of propolis from Adamawa region (Cameroon) are by apoptosis via reactive oxygen species-mediated mitochondrial pathway. *Environ Toxicol* (2021) 36:861–73. doi: 10.1002/tox.23089
21. Wu Y, Xu J, Liu Y, Zeng Y, Wu G. A Review on Anti-Tumor Mechanisms of Coumarins. *Front Oncol* (2020) 10:592853. doi: 10.3389/fonc.2020.592853
22. Shakeri R, Kheirollahi A, Davoodi J. Apaf-1: Regulation and function in cell death. *Biochimie* (2017) 135:111–25. doi: 10.1016/j.biochi.2017.02.001
23. Jiang W, Chen Y, Li B, Gao S. DBA-induced caspase-3-dependent apoptosis occurs through mitochondrial translocation of cyt-c in the rat hippocampus. *Mol Biosyst* (2017) 13:1863–73. doi: 10.1039/c7mb00246g
24. Noh S, Choi E, Hwang CH, Jung JH, Kim SH, Kim B. Dietary Compounds for Targeting Prostate Cancer. *Nutrients* (2019) 11:11. doi: 10.3390/nu11102401
25. Jezek J, Cooper KF, Strich R. The Impact of Mitochondrial Fission-Stimulated ROS Production on Pro-Apoptotic Chemotherapy. *Biol (Basel)* (2021) 10:983. doi: 10.3390/biology10010033
26. Suraweera CD, Hinds MG, Kvensakul M. Poxviral Strategies to Overcome Host Cell Apoptosis. *Pathogens* (2020) 10:6. doi: 10.3390/pathogens10010006
27. Rachakhom W, Banjerdpongchai R. Effect of Calomelanone, a Dihydrochalcone Analogue, on Human Cancer Apoptosis/Regulated Cell Death in an In Vitro Model. *BioMed Res Int* (2020) 2020:4926821. doi: 10.1155/2020/4926821
28. Negi A, Murphy PV. Development of Mcl-1 inhibitors for cancer therapy. *Eur J Med Chem* (2021) 210:113038. doi: 10.1016/j.ejmech.2020.113038
29. Quezada MJ, Picco ME, Villanueva MB, Castro MV, Barbero G, Fernandez NB, et al. BCL2L10 Is Overexpressed in Melanoma Downstream of STAT3 and Promotes Cisplatin and ABT-737 Resistance. *Cancers (Basel)* (2020) 13:78. doi: 10.3390/cancers13010078
30. Fu Y, Ye Y, Zhu G, Xu Y, Sun J, Wu H, et al. Resveratrol induces human colorectal cancer cell apoptosis by activating the mitochondrial pathway via increasing reactive oxygen species. *Mol Med Rep* (2021) 23:1. doi: 10.3892/mmr.2020.11809
31. Zhang S, Li T, Zhang L, Wang X, Dong H, Li L, et al. A novel chalcone derivative S17 induces apoptosis through ROS dependent DR5 up-regulation in gastric cancer cells. *Sci Rep* (2017) 7:9873. doi: 10.1038/s41598-017-10400-3
32. Yogeswari S, Kamalraj S, Jayabaskaran C. A novel synergistic anticancer effect of fungal cholestanol glucoside and paclitaxel: Apoptosis induced by an intrinsic pathway through ROS generation in cervical cancer cell line (HeLa). *Toxicol In Vitro* (2021) 72:105079. doi: 10.1016/j.tiv.2021.105079
33. Wang YY, Lee KT, Lim MC, Choi JH. TRPV1 Antagonist DWP05195 Induces ER Stress-Dependent Apoptosis through the ROS-p38-CHOP Pathway in Human Ovarian Cancer Cells. *Cancers (Basel)* (2020) 12:1702. doi: 10.3390/cancers12061702
34. Cao X, Chen XM, Xiao WZ, Li B, Zhang B, Wu Q, et al. ROS-mediated hypomethylation of PRDX5 promotes STAT3 binding and activates the Nrf2 signaling pathway in NSCLC. *Int J Mol Med* (2020) 47:573–82. doi: 10.3892/ijmm.2020.4819
35. Kamble D, Mahajan M, Dhat R, Sitasawad S. Keap1-Nrf2 Pathway Regulates ALDH and Contributes to Radioresistance in Breast Cancer Stem Cells. *Cells Basel* (2021) 10:83. doi: 10.3390/cells10010083
36. Volpe C, Villar-Delfino PH, Dos AP, Nogueira-Machado JA. Cellular death, reactive oxygen species (ROS) and diabetic complications. *Cell Death Dis* (2018) 9:119. doi: 10.1038/s41419-017-0135-z
37. Jin CY, Molagoda I, Karunaratne W, Kang SH, Park C, Kim GY, et al. TRAIL attenuates sulforaphane-mediated Nrf2 and sustains ROS generation, leading to apoptosis of TRAIL-resistant human bladder cancer cells. *Toxicol Appl Pharmacol* (2018) 352:132–41. doi: 10.1016/j.taap.2018.05.022

**Conflict of Interest:** The authors declare that the research was conducted in the absence of any commercial or financial relationships that could be construed as a potential conflict of interest.

The reviewer JH declared a shared affiliation with one of the authors, G-YK, to the handling editor at time of review.

Copyright © 2021 Wang, Wu, Yu, Hu, Li, Meng, Lv, Kim, Choi, Wang, Xu and Jin. This is an open-access article distributed under the terms of the Creative Commons Attribution License (CC BY). The use, distribution or reproduction in other forums is permitted, provided the original author(s) and the copyright owner(s) are credited and that the original publication in this journal is cited, in accordance with accepted academic practice. No use, distribution or reproduction is permitted which does not comply with these terms.



# TP53-Activated lncRNA GHRLOS Regulates Cell Proliferation, Invasion, and Apoptosis of Non-Small Cell Lung Cancer by Modulating the miR-346/APC Axis

Ke Ren<sup>1,2†</sup>, Jinghui Sun<sup>1†</sup>, Lingling Liu<sup>1,2†</sup>, Yuping Yang<sup>3</sup>, Honghui Li<sup>4</sup>, Zhichao Wang<sup>1</sup>, Jingzhu Deng<sup>1</sup>, Min Hou<sup>1</sup>, Jia Qiu<sup>1</sup> and Wei Zhao<sup>1,5\*</sup>

<sup>1</sup> School of Laboratory Medicine/Sichuan Provincial Engineering Laboratory for Prevention and Control Technology of Veterinary Drug Residue in Animal-origin Food, Chengdu Medical College, Chengdu, China, <sup>2</sup> Development and Regeneration Key Laboratory of Sichuan Province, Chengdu Medical College, Chengdu, China, <sup>3</sup> Department of Pulmonary and Critical Care Medicine, The First Affiliated Hospital of Chengdu Medical College, Chengdu, China, <sup>4</sup> Department of Refractive Surgery, Chengdu Aier Eye Hospital, Chengdu, China, <sup>5</sup> Department of Biomedical Sciences, City University of Hong Kong, Hong Kong, China

## OPEN ACCESS

### Edited by:

Dong-Hua Yang,  
St. John's University,  
United States

### Reviewed by:

Haishi Qiao,  
China Pharmaceutical University,  
China  
Yunwen Yang,  
Nanjing Children's Hospital, China

### \*Correspondence:

Wei Zhao  
zw198626520@126.com

<sup>†</sup>These authors have contributed  
equally to this work

### Specialty section:

This article was submitted to  
Pharmacology of Anti-Cancer Drugs,  
a section of the journal  
Frontiers in Oncology

**Received:** 04 March 2021

**Accepted:** 29 March 2021

**Published:** 21 April 2021

### Citation:

Ren K, Sun J, Liu L, Yang Y, Li H,  
Wang Z, Deng J, Hou M, Qiu J and  
Zhao W (2021) TP53-Activated  
lncRNA GHRLOS Regulates Cell  
Proliferation, Invasion, and Apoptosis  
of Non-Small Cell Lung Cancer by  
Modulating the miR-346/APC Axis.  
Front. Oncol. 11:676202.  
doi: 10.3389/fonc.2021.676202

Non-small cell lung cancer (NSCLC) is the main type of lung cancer with high mortality worldwide. To improve NSCLC therapy, the exploration of molecular mechanisms involved in NSCLC progression and identification of their potential therapy targeting is important. Long noncoding RNAs (lncRNAs) have shown important roles in regulating various tumors progression, including NSCLC. We found lncRNA GHRLOS was decreased in NSCLC cell lines and tissues which correlated with poor prognosis of NSCLC patients. However, the role and underlying mechanisms of lncRNA GHRLOS in NSCLC progression remains elusive. The expression of lncRNA GHRLOS was examined in NSCLC cell lines and biopsy specimens of patients with NSCLC by quantitative real time polymerase chain reaction (qRT-PCR). The effects of GHRLOS on proliferation, invasion and apoptosis of NSCLC cells were determined by both *in vitro* and *in vivo* experiments. The interaction between GHRLOS and TP53 was determined by dual-luciferase reporter assay and chromatin immunoprecipitation (ChIP) combined with qRT-PCR analysis. RNA immunoprecipitation (RIP) was conducted to validate the binding between GHRLOS and microRNA-346 (miR-346). Dual-luciferase reporter assays were also carried out to reveal the interaction between miR-346 and the 3' untranslated region (3'UTR) of adenomatous polyposis coli (APC) mRNA. Our data demonstrated that overexpression of lncRNA GHRLOS suppressed cancer cell proliferation and invasion as well as promoted cell apoptosis by regulating the expression of CDK2, PCNA, E-cadherin, N-cadherin, Bax, and Bcl-2 in NSCLC cells. Moreover, lncRNA GHRLOS was upregulated by the binding of TP53 to the GHRLOS promoter. The binding target of lncRNA GHRLOS was identified to be miR-346. Impressively, overexpression of miR-346 promoted cell proliferation and invasion, as well as inhibited cell apoptosis, however, these effects can be blocked by

overexpression of lncRNA GHRLOS both *in vitro* and *in vivo*. In summary, this study reveals lncRNA GHRLOS, upregulated by TP53, acts as a molecule sponge of miR-346 to cooperatively modulates expression of APC, a miR-346 target, and potentially inhibits NSCLC progression via TP53/lncRNA GHRLOS/miR-346/APC axis, which represents a novel pathway that could be useful in targeted therapy against NSCLC.

**Keywords:** NSCLC, TP53, lncRNA GHRLOS, miR-346, APC

## INTRODUCTION

Lung cancer has been the leading cause of cancer-associated death globally (1–3). Non-small cell lung cancer (NSCLC) is the main sub-type of lung cancer (4–6), and its 5-year survival probability remains less than 15% as a result of recurrence and deficient treatment options (7, 8). To improve NSCLC therapy, it is critical to understand the molecular mechanisms involved in NSCLC progression. Therefore, a better interpretation of the potential molecular events in regulating NSCLC would offer novel prognostic and therapeutic biomarkers.

Long noncoding RNAs (lncRNAs) were once considered as “noise” in genomes, however, their functions in a variety of cancers, including NSCLC, are recently appreciated (9–14). It was reported that actin filament-associated protein 1 antisense RNA 1 (AFAP1-AS1) aggravates tumorigenesis and drug resistance in NSCLC (15–17). Overexpression of long non-coding RNA maternally expressed gene 3 (MEG3) resulted in increased apoptosis in NSCLC by regulating microRNA-7-5p (18). Small nucleolar RNA host gene 7 (SNHG7) is upregulated in NSCLC and indicates a poor prognosis. SNHG7 serves as a competitive endogenous RNA (ceRNA) by sponging miR-193b to increase expression of Fas apoptotic inhibitory molecule 2 (FAIM2) (19). Therefore, investigation of the role of lncRNAs in NSCLC could contribute to better treatment for NSCLC patients.

Ghrelin opposite strand/antisense RNA (GHRLOS) is the antisense strand of the ghrelin (*GHL*) gene, which encodes active peptides such as ghrelin, a multifunctional peptide hormone involved in cancer development, insulin release, glucose metabolism, and gut motility (20–22). The level of lncRNA GHRLOS is reduced in human colorectal cancer tissues, and its high expression suggests a better prognosis (23). A recent study suggests that lncRNA GHRLOS is an inhibitor of cancer progression and may serve as a candidate biomarker of tumor metastasis and a prognostic indicator in colorectal cancer (24).

In cancer cells, lncRNAs were found to regulate gene expression at epigenetic, transcriptional and post-transcriptional levels by gene imprinting, histone modification, chromatin remodeling, transcriptional activation, transcriptional interference, nuclear

transport and others (25). Emerging data suggests that lncRNAs work as sponges by binding competitively to microRNAs (miRNAs) and consequently repressing their function in lung cancer cells (26). Various miRNAs have been reported to play multiple roles in regulating tumor progression of NSCLC through the interaction with lncRNAs in many researches (27–29). However, the biofunction of miRNA-346, which dysregulated expression in NSCLC cells and tissues found in this study, was still not clear. Accumulating evidence shows that lncRNA GHRLOS and miRNA-346 play important roles in cancers. However, the functions of lncRNA GHRLOS and miRNA-346 in NSCLC remains largely unknown.

As one of the well-known tumor suppressor, tumor protein p53 (TP53) has been reported to play important role in association with cancer progressions such as proliferation, invasion and metastasis, as well as resistance to chemo- or radio-therapy (30). However, TP53 also has mutant alleles in about 50% of all cancers (31), which seriously affects its function in tumor suppression. Beyond the loss of gene copies, the mutation of TP53 often occurs in the DNA-binding domain (32). These TP53 mutations lead to decreased ability that transactivate downstream genes, and dysregulation of target genes accelerates NSCLC development (33, 34). Although a number of lncRNAs were reported to be regulated by TP53 (35), whether TP53 modulates lncRNA GHRLOS in NSCLC is unknown.

Here, we explored the lncRNA GHRLOS involved molecular signal in NSCLC progression, and suggested lncRNA GHRLOS as a promising therapeutic target for NSCLC.

## MATERIALS AND METHODS

### Specimens Collection and Overall Survival Analysis

A total of 134 pairs of NSCLC tissues and adjacent non-cancerous tissues were collected from the Department of pulmonary and critical care medicine in the First Affiliated Hospital of Chengdu Medical College (Chengdu, China). All participants signed an informed consent form. No patients were given chemotherapy and radiotherapy before surgery. The clinical samples were stored in liquid nitrogen before used for analysis. This study was approved by the Ethics Committee of the First Affiliated Hospital of Chengdu Medical College Chengdu. The overall survival rate was evaluated by Kaplan–Meier analysis according to lncRNA GHRLOS expression using Kaplan–Meier Plotter (36).

**Abbreviations:** NSCLC, Non-small cell lung cancer; GHRLOS, Ghrelin opposite strand/antisense RNA; TP53, Tumor protein p53; APC, Adenomatous polyposis coli; lncRNAs, long non-coding RNAs; miRNA, microRNA; ChIP, chromatin immunoprecipitation; RIP, RNA Binding Protein Immunoprecipitation; H&E, Hematoxylin and eosin; CCK-8, Cell counting kit-8; CDK2, Cyclin-dependent kinase 2; PCNA, Proliferating cell nuclear antigen; qRT-PCR, Quantitative polymerase chain reaction; UTR, Untranslated region.



## H&E Staining

Briefly, the clinical samples were fixed in 4% paraformaldehyde, embedded in paraffin and sectioned similar to our previous study (16). After dewaxing in dimethylbenzene, the slides were rehydrated in graded ethanol. Then, they were stained with hematoxylin for 15 min, and with eosin for 3 min. Finally, the stained sections were subjected to dehydration and mounting. They were observed using a Carl Zeiss microscope (Axio Observer A1, Jena, Germany).

## Cell Culture

The pulmonary epithelial cell line BEAS-2B cells and NSCLC cell lines including A549, PC-9, NCI-H460, and NCI-H1975 cells were bought from the national biomedical experimental cell resource bank (Beijing, China). The cells were maintained in RPMI 1640 basic medium (Gibco/Thermo Fisher Scientific, Shanghai, China) containing 100 U/ml penicillin, 100 mg/ml streptomycin (Biological Industries, Hertzliya Pituach, Israel), and supplemented with 10% fetal bovine serum (Gibco/Thermo Fisher Scientific). They were placed in a humidified incubator with 5% CO<sub>2</sub> at 37°C.

## Plasmids Construction and Interfering RNA Fragment Preparation

The Lv-GHRLOS contained full length of lncRNA GHRLOS (UCSC ID: ENST00000439539.3) for overexpression of GHRLOS, and Lv-sh-GHRLOS expressed 5'-GCUCCAUAUAGAACAUGUUU-3' for knockdown of GHRLOS whereas the control vector expressed 5'-AGA UCG ACG UGG CGU AAU CCA-3' (named Lv-sh-NC-lnc). Meanwhile, Lv-TP53 contained full length of TP53 (NCBI Reference Sequence: NM\_000546.5) for overexpression of TP53, and Lv-sh-TP53 expressed 5'-GCAC AGAGGAAGAGAAUCUUU-3', and Lv-vector was used as a negative control. Lv-sh-APC expressed the sequences: 5'-CCUG CAAAUAGCAGAAUAUU-3', and Lv-sh-NC expressed: 3'-ACGGUCAAU UCCUCGAUAUC-3'. Then, the GHRLOS promoter (-1500bp, +50bp) and its corresponding mutants (as illustrated in **Figure 3H**) were constructed into pmirGLO vector for luciferase reporter assays, and they were named pmirGLO-PF, pmirGLO-ΔE1, and pmirGLO-ΔE2. The full length of GHRLOS and its mutants were inserted into pmirGLO empty vector for dual luciferase reporter assays, and they were termed pmirGLO-GHRLOS-WT and pmirGLO-GHRLOS-mut, respectively. Similarly, the APC 3'-UTR and its mutants were constructed into pmirGLO-vector for dual luciferase reporter assays, and they were named pmirGLO-APC-3'UTR-WT and pmirGLO-APC-3'UTR-mut, respectively. In this study, The Mock, mimic, and inhibitor for miR-346 were constructed into lentiviruses. The Lv-Mock expressed 5'-UCACAACCUCCUAGAAAGAGUAGA-3', and Lv-miR-346 mimic expressed 5'-UGUCUGCCCGCAUG CCUGCCUCU-3', and Lv-miR-346 inhibitor expressed 5'-AGAGGCAGCGCGGGGCAGACA-3'. In this study, the lentivirus vectors were from Addgene (Watertown, MA, USA), and pGLO vector, also named pmirGLO, was bought from Promega (Madison, USA). Here, lentivirus was added into cells medium as our previous report (16).

## Quantitative Real Time PCR (qRT-PCR) Analysis

TRIzol reagent (Thermo Fisher Scientific) was applied to extract the total RNAs from clinical tissues or lung cell lines. 0.5 µg total RNA was prepared for reverse transcription into complementary DNA (cDNA) using SMART MMLV Reverse Transcriptase (Takara Bio, Inc., Dalian, Liaoning). Quantitative real-time PCR was performed to determine the gene expression in tissues and cells using AceQ qPCR SYBR GreenMaster Mix (Vazyme, Nanjing, China) on a CFX96 Real-Time PCR Detection System (Bio-Rad Laboratories, Inc., Hercules, USA). The primers were shown in **Table S1** and **Table S2** in **Supplementary Materials**.

## Western Blot

The tissues and cells were lysed with RIPA buffer to prepare proteins (Thermo Fisher Scientific). The 30 µg protein supernatant was separated by sodium dodecyl sulfate-polyacrylamide gel electrophoresis (SDS-PAGE), and transferred onto a nitrocellulose membrane (Bio-Rad, Hercules, CA, USA). The membranes were blocked with 5% no-fat milk for 0.5 h, and incubated with primary antibodies at 4°C overnight, then followed by incubating with the secondary antibodies at room temperature for 1 h. Finally, the protein bands on membranes were captured using a luminescence instrument (Tanon, Shanghai, China), and the gray density of protein bands were determined by Image J software (Media Cybernetics, Bethesda, MD). The primary antibodies were listed below, anti-APC (Cat. no. ab40778, abcam), anti-β-catenin (Cat. no. #9562, Cell Signal Technology), anti-Phospho-β-catenin (Cat. no. #2009, Cell Signal Technology), anti-GAPDH (Cat. no. #MB9231, Bioworld Technology). The secondary antibodies were bought from Bioworld, horseradish peroxidase (HRP)-labeled goat anti-rabbit or -mouse secondary antibody (Cat. no. # BS13278 or #BS12478, Shanghai, China). All other agents were purchased from Sigma (St. Louis, MO, USA).

## CCK-8 Assays and Colony Formation Assays

After transfection for 48 h, A549 and NCI-H460 cells were planted in a 96-well plate. At the indicated time, 10 µl CCK-8 solution (Sigma) was added into each well. After 1.5 h incubation, the OD value at 450 nm was measured using a microplate reader (Thermo Fisher Scientific). The experiments were conducted in quadruplicate and repeated three times.

In the cancer cell colony formation assay, cancer cells were infected with the indicated lentivirus for 48 h. Then,  $1 \times 10^3$  infected cells were planted into 6-well plates incubating for 14 days. The colonies were stained with 0.3% crystal violet for imaging using a light microscope. The experiments were conducted in quadruplicate and repeated three times.

## Trans-Well Assays

The lentivirus infected cancer cells ( $2 \times 10^4$ ) were planted in the top chamber coated with matrigel (Cat. no. # 354230, Corning, Shanghai, China), and incubated in serum-free RPMI 1640 basic

medium. The lower chamber was placed with FBS-containing medium. After 24 h, the invading cells in lower chamber were fixed with 4% formaldehyde, and stained with 0.3% crystal violet. The invading cells were counted under a light microscope (Carl Zeiss, Axio Observer A1). The experiments were conducted in quadruplicate and repeated three times.

## Apoptosis Assays

After infection for 48h, A549 and NCI-H460 cells were collected using trypsin. The cells were incubated with annexin V and propidium iodide (PI) (Cat. no. #C1062L, Beyotime) for 15 min. The apoptotic cells were measured on the Becton Dickinson flow cytometer (Becton Dickinson, USA). The cells both annexin V and PI positive staining indicated cells in necrosis (post-apoptotic necrosis or late apoptosis), the cells Annexin V positive but PI negative staining indicated cells in early apoptosis, as well as the cells both annexin V and PI negative staining indicated cells were healthy (37). The experiments were conducted in quadruplicate and repeated three times.

## Dual-Luciferase Reporter Assays

The cancer cells were seeded in 24-well plate at the density of  $5 \times 10^4$  cells/well. The cells were infected according to experimental design in this study. Briefly, to determine the effect of TP53 on transcriptional activity of GHRLOS promoter, the cells were transfected with the lentivirus containing either the wild-type promoter (WT, also named pmirGLO-PF) or mutated GHRLOS promoters (pmirGLO- $\Delta$ E1 or pmirGLO- $\Delta$ E2). To investigate the reciprocal regulation between GHRLOS and miR-346, the cells were infected with lentivirus containing miR-346 mimic, inhibitor or Mock for 48 h, and transfected with wild type GHRLOS in pmirGLO vector (pmirGLO-GHRLOS-WT), mutated GHRLOS (pmirGLO-GHRLOS-mut), wild type of APC 3'UTR (APC 3'UTR-WT) or mutated APC 3'UTR (pmirGLO-APC-3'UTR-mut). After transfection for 48 h, luciferase activity was analyzed using the Dual-Luciferase Assay Kit on a GloMax 20/20 Luminometer (Promega). The experiments were conducted in quadruplicate and repeated three times.

## Subcellular Fractionation Assays

The cytoplasm and nucleus were separated using the PARIS Kit (Cat. no. # AM1921, Life Technologies, MA, USA). qRT-PCR analysis was conducted on the content of miR-346 and GHRLOS in nucleus or cytoplasm. GAPDH was used as a cytoplasmic control for GHRLOS whereas U6 was taken as a nuclear control. The experiments were repeated three times.

## Chromatin Immunoprecipitation Assays (ChIP) and RNA Immunoprecipitation Assay (RIP)

To determine the binding between TP53 and GHRLOS, ChIP assay was performed using the SimpleChIP® Enzymatic Chromatin IP Kit (Cell Signaling Technology, #9002) according to manufacturer's instructions. Briefly, cancer cells were treated with 4% formaldehyde and sequentially incubated

with glycine to quench the reaction of formaldehyde fixation, after rinse with ice-cold PBS, the cells were collected using cell lysis buffer. The chromatin in the mixture is fragmented by partial digestion with Micrococcal Nuclease to obtain chromatin fragments of 1 to 5 nucleosome. The enzymatic fragmentation of chromatin was used immediately for immunoprecipitation. Anti-TP53 (Cat. no. ab1101, abcam) and anti-IgG (Cat. no. I4131, Sigma) were incubated with Dyna beads Protein G (Life Technologies). Then, the protein-DNA complexes were precipitated with an indicated antibody and protein G beads at 4°C for overnight. After reversal of protein-DNA cross-links, the DNA is purified using DNA purification spin columns. In addition, the possible contaminating RNAs and proteins in obtained DNA were removed by using RNase and proteinase K, respectively. Finally, the immunoprecipitated and purified DNA was detected using qRT-PCR analysis. The used primers for ChIP were listed as below:

GHRLOS, 5'-TTGGAGGCCCTCCCACGAACC TTCTCCCAT-3' (Forward), 5'-GAGGGGCTCAGCTCCC TGTGCATTC-3' (Reverse); and 5'-GGCGCAGGGGCT GCCCCTCACCCAG-3' (Forward), 5'-GCTCTGCTGGTCTC GCACGACTTCTG-3' (Reverse). The experiments were repeated three times.

To investigate the interaction between GHRLOS and miR-346, RIP analysis was conducted using a Magna RIP™ RNA-Binding Protein Immunoprecipitation Kit (Millipore, Billerica, MA, USA). The cell lysates were incubated overnight at 4°C in RIP buffer containing magnetic beads conjugated anti-Ago-2 (Cat. no. SAB4301150, Sigma) or anti-IgG as a control (Cat. no. I4131, Sigma). Before isolating the immunoprecipitated RNAs, the harvested magnetic beads, which enriched RNAs, were first treated with Proteinase K buffer at 4°C for 3 h. Finally, the content of GHRLOS and miR-346 in immunoprecipitated RNAs was examined by qRT-PCR (primers were listed in above section). The experiments were repeated three times.

## NSCLC Xenograft Model

To establish the NSCLC xenograft model, 5x10<sup>6</sup> lentivirus infected NCI-H460 cells were collected at 100 g  $\times$  5 min, and were inoculated into 6-week old BALB/c nude mice (Model Animal Research Center of Nanjing University, Nanjing, China). Then, the volume of tumor was calculated every 4 days for 28 days by using the formula: volume=length  $\times$  width<sup>2</sup>/2. Finally, the mice were sacrificed on the 28th day according to the animal protocol approved by the Research Ethics Committee of Chengdu Medical College (ID: SYXK2020196).

## Statistical Analysis

The results were presented as mean  $\pm$  standard deviation (S.D.). The data were analyzed using GraphPad Prism 6 (CA, USA) and SPSS software (version 19.0, SPSS Inc., NY, USA). Statistical significance was tested by Two-tailed Student's *t*-test for two groups comparisons and one-way analysis of variance (ANOVA) test with post-hoc analysis contrasts for multi-groups comparisons. A *p* value <0.05 was considered significant.

## RESULTS

### LncRNA GHRLOS Expression Was Decreased in NSCLC Cells and Tissues, and Correlated With Poor Prognosis of NSCLC Patients

The NSCLC tissues and adjacent non-tumor tissues were collected and confirmed by H&E staining (Figure 1A). Quantitative RT-PCR was performed to evaluate the level of GHRLOS in these tissues. It was found that lncRNA GHRLOS was significantly downregulated in NSCLC tumors tissues and cancer cells compared with adjacent non-tumor tissues and the normal lung BEAS-2B cells (Figures 1B, C). The patients were separated into high- and low- lncRNA GHRLOS expression groups using median value as a cut point. Kaplan–Meier analysis was used to evaluate the overall survival in these patients following lncRNA GHRLOS expression. The results showed that high lncRNA GHRLOS expression was associated with better NSCLC prognosis (Figure 1D). These data indicated that lncRNA GHRLOS might function as a tumor suppressor in the progression of NSCLC.

### Overexpression of lncRNA GHRLOS Inhibited Cell Proliferation and Invasion and Increased Cell Apoptosis

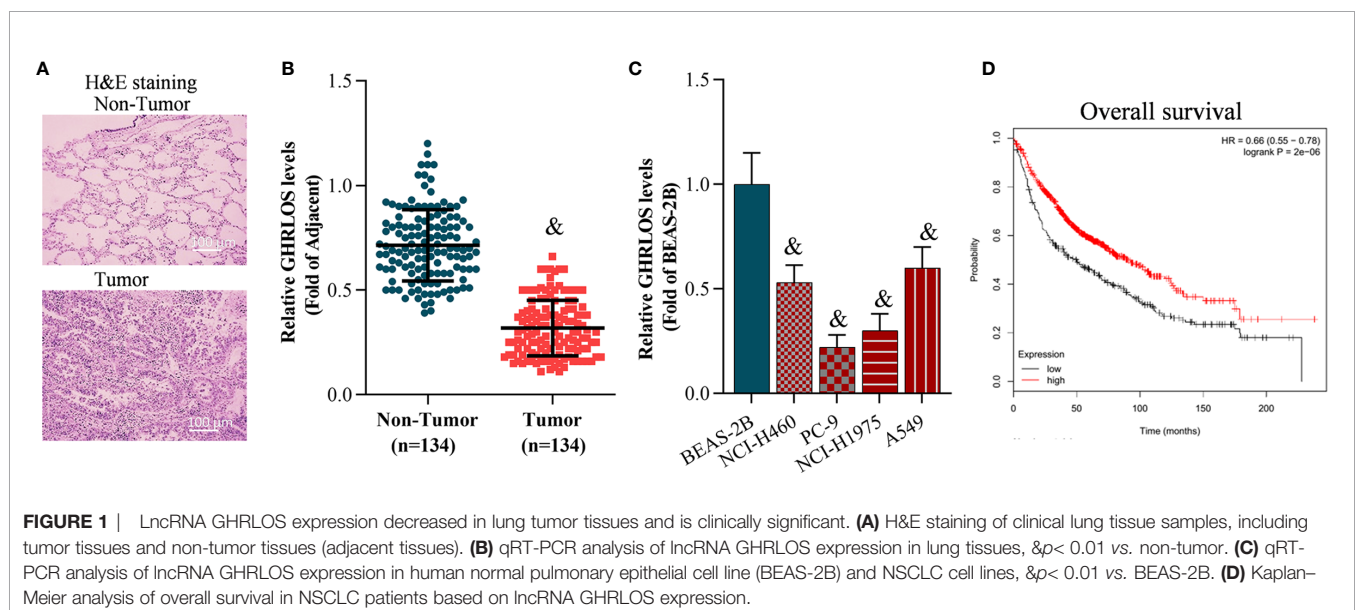
To investigate the role of lncRNA GHRLOS in cancer cell proliferation, invasion, and apoptosis, we overexpressed lncRNA GHRLOS in A549 and NCI-H460 cells by lentivirus infection (Figure 2A). Overexpression of lncRNA GHRLOS obviously inhibited A549 and NCI-H460 cell proliferation, as evidenced by CCK-8 and colony formation assays (Figures 2B–D). Overexpression of lncRNA GHRLOS significantly downregulated the expression of cell growth biomarkers, including PCNA and CDK2, in NSCLC cells (Figure 2E). lncRNA GHRLOS overexpression suppressed cancer cell invasion (Figures 2F, G)

with downregulation of N-cadherin and upregulation of E-cadherin, that are epithelial-to-mesenchymal transition (EMT) associated biomarkers (Figure 2H). Finally, lncRNA GHRLOS overexpression markedly promoted A549 and NCI-H460 cell apoptosis (Figures 2I, J). Furthermore, lncRNA GHRLOS repressed Bcl-2 and upregulated Bax expression in cancer cell lines (Figure 2K). These results indicated that lncRNA GHRLOS functions as tumor suppressor by inhibiting proliferation and inducing apoptosis in NSCLC cells.

### TP53 Stimulated the Transcriptional Activation of lncRNAGHRLOS

To explore the genes that regulated lncRNAGHRLOS in NSCLC cells, online prediction tools JASPAR (38) was used to predict the potential binding sites of the lncRNA GHRLOS promoter. TP53 was identified as the transcription factor with the highest binding potential based on the highest scores (Figure 3A) with several TP53 binding sites were predicted. In order to understand the relationship of TP53 and lncRNA GHRLOS, the expression of lncRNA GHRLOS was evaluated by qRT-PCR with inhibition of TP53. It was found that lncRNA GHRLOS expression was suppressed when TP53 was blocked, and upregulated when TP53 was overexpressed in NSCLC cells (Figures 3B–E). TP53 was found to bind to the GHRLOS promoter at “-667 to -681 (E2)” region, as evidenced by CHIP assays (Figures 3F, G). Dual luciferase reporter assays validated that the E2 site is the required binding region of TP53. As depicted in Figure 3H, the luciferase reporter plasmids, including PF (pGLO-PF), ΔE1, or ΔE2, were transfected into NSCLC cells. Luciferase assays revealed that TP53 failed to activate luciferase activity of the GHRLOS promoter without E2 region (Figures 3H–J). Collectively, TP53 is suggested to be a transcriptional factor in regulating lncRNA GHRLOS expression.

To evaluate the role of the TP53/lncRNA GHRLOS axis in cancer development, we overexpressed TP53 and silenced lncRNA





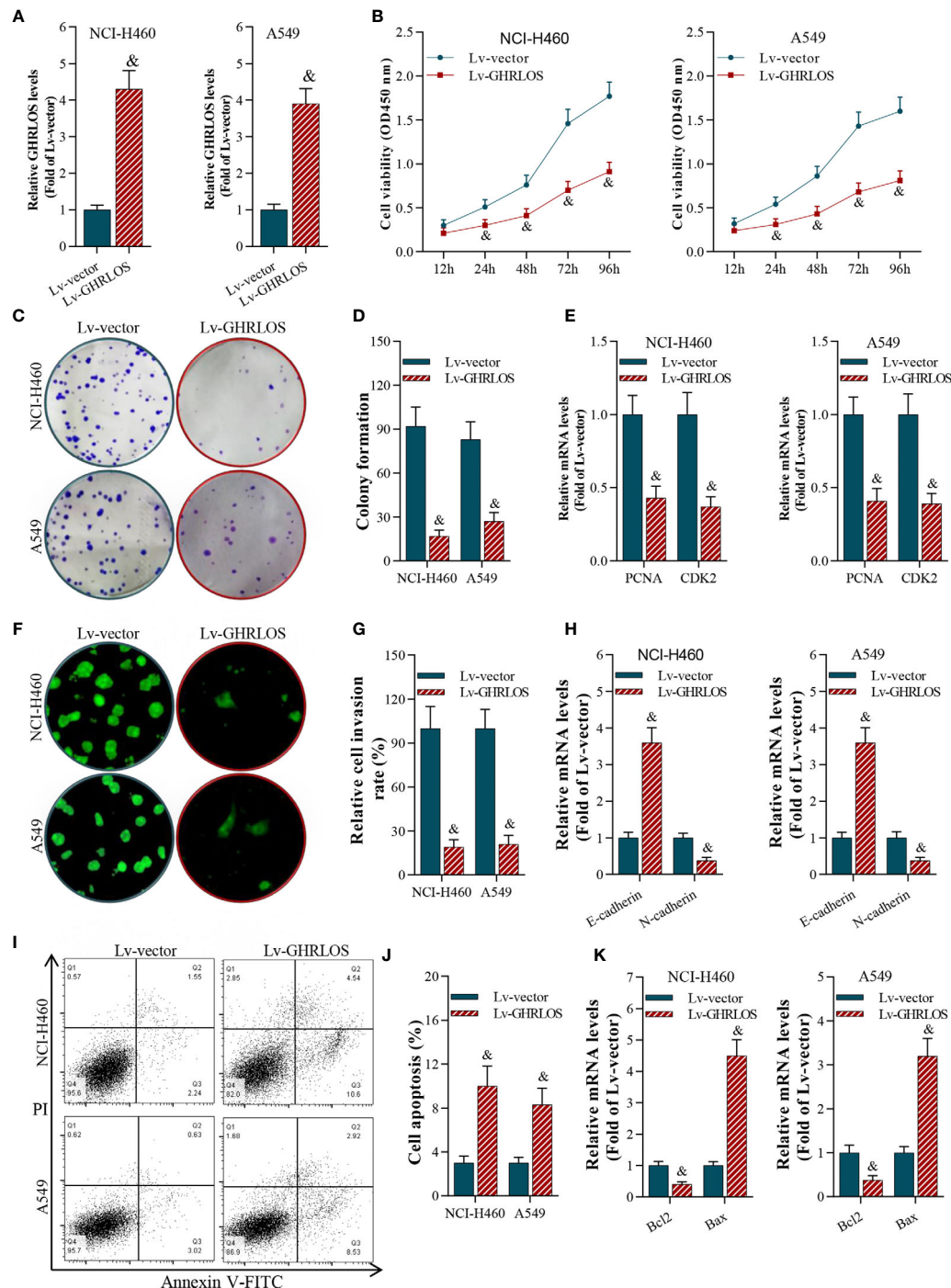


**FIGURE 2 |** LncRNA GHRLOS inhibited NSCLC cell growth and invasion, and increased apoptosis. **(A)** qRT-PCR determination on lentivirus-induced overexpression of lncRNA GHRLOS at 48 h in A549 and NCI-H460 cells, &p < 0.01 vs. Lv-vector. **(B)** CCK-8 assay on the effect of lncRNA GHRLOS on cancer cell proliferation after lentivirus infection at the indicated time points, &p < 0.01 vs. Lv-vector. **(C, D)** Colony formation assay on the effect of lncRNA GHRLOS on growth of cancer cells after 14 days of culture, &p < 0.01 vs. Lv-vector. **(E)** qRT-PCR analysis on the expression of cell growth-associated genes, PCNA and CDK2, in A549 and NCI-H460 cells after overexpressed lncRNA GHRLOS for 48 h, &p < 0.01 vs. Lv-vector. **(F, G)** Trans-well assay analysis on the effect of lncRNA GHRLOS on the invasion of cancer cells, &p < 0.01 vs. Lv-vector. **(H)** qRT-PCR analysis on cell adhesion-related genes, including E-cadherin and N-cadherin, in A549 and NCI-H460 cells after infection for 48 h, &p < 0.01 vs. Lv-vector. **(I, J)** Annexin V-FITC/PI analysis on the effect of lncRNA GHRLOS on cancer cell apoptosis, &p < 0.01 vs. Lv-vector. **(K)** qRT-PCR analysis on the expression of cell apoptosis related genes, Bax and Bcl-2, in NSCLC cells infected by lentivirus for 48 h, &p < 0.01 vs. Lv-vector.



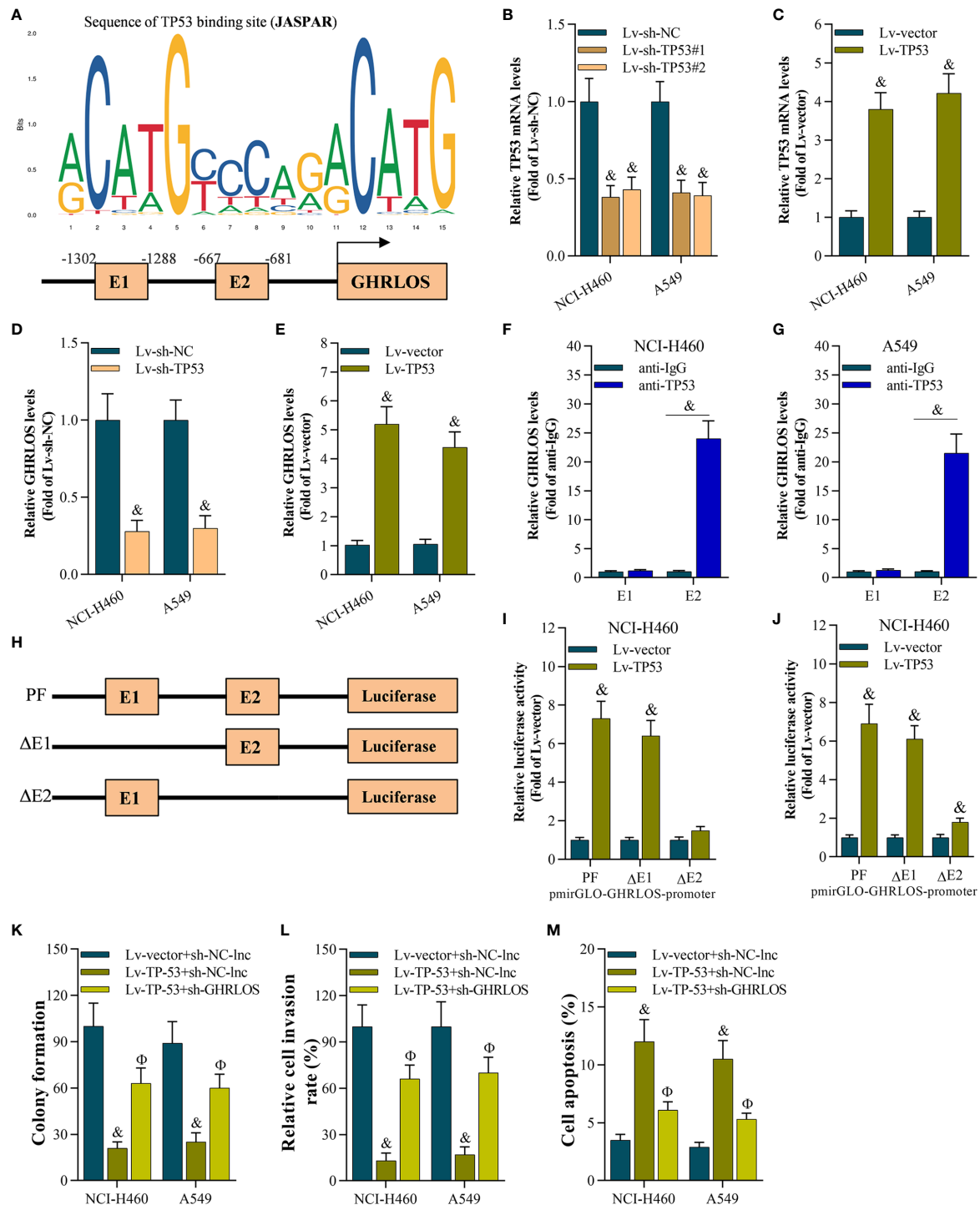


**FIGURE 3 |** The TP53 activated lncRNA GHRLOS transcription in NSCLC cells. **(A)** The predicted binding motif of TP53 in the human lncRNA GHRLOS promoter based on analysis using JASPAR. **(B, C)** qRT-PCR analysis of TP53 expression after knockdown or overexpression of TP53 for 48 h in NSCLC cells,  $&p < 0.01$  vs. Lv-sh-NC or Lv-vector. **(D, E)** qRT-PCR analysis on lncRNA GHRLOS expression after knockdown or overexpression of TP53 for 48 h in NSCLC cells,  $&p < 0.01$  vs. Lv-sh-NC or Lv-vector. **(F, G)** ChIP assays evaluated TP53 binding sites,  $&p < 0.01$  vs. anti-IgG. **(H)** Schematic diagram of plasmids used for luciferase reporter assays. **(I, J)** Dual luciferase reporter assays examined luciferase activity,  $&p < 0.01$  vs. Lv-vector. **(K)** Colony formation assay on the growth of cancer cells infected with indicated lentivirus for 48 h followed by 14 days of culture,  $&p < 0.01$  vs. Lv-vector,  $\Phi p < 0.01$  vs. Lv-TP53. **(L)** Transwell assays on invasion of cancer cells 48 h after infection,  $&p < 0.01$  vs. Lv-vector,  $\Phi p < 0.01$  vs. Lv-TP53. **(M)** Annexin V-FITC/PI analysis on cancer cell apoptosis after infection for 48 h,  $&p < 0.01$  vs. Lv-vector,  $\Phi p < 0.01$  vs. Lv-TP53.

GHRLOS expression in A549 and NCI-H460 cells. lncRNA GHRLOS knockdown significantly reversed TP53-mediated cell growth, invasion and apoptosis in NSCLC cells (Figures 3K–M).

## lncRNA GHRLOS Is a Molecular Sponge of miR-346 in NSCLC Cells

To analyze the subcellular location of lncRNA GHRLOS in NSCLC cells, the nucleus and cytoplasm of these cells were separated, and qRT-PCR were performed. Interestingly, lncRNA GHRLOS is primarily distributed in the cytoplasm of NSCLC cells (Figure 4A), suggesting that lncRNA GHRLOS could function as a ceRNA in NSCLC. The target miRNA of lncRNA GHRLOS was predicted using DIANA tools (39). It was found that miR-346 was a potential target of lncRNA GHRLOS and its binding sites were showed in Figure 4B. Furthermore, the expression of miR-346 was found to be elevated in NSCLC tissues (Figure 4C). Moreover, lncRNA GHRLOS interacted with miR-346, as evidenced by RIP assays (Figure 4D). Furthermore, dual luciferase reporter assays revealed that a miR-346 mimic efficiently repressed the luciferase activity of wild-type GHRLOS (pGLO-GHRLOS-WT), whereas a miR-346 mimic did not significantly affect the luciferase activity of mutant GHRLOS (pGLO-GHRLOS-mut) (Figure 4E). Finally,

miR-346 expression was negatively regulated by lncRNA GHRLOS in NSCLC cells (Figure 4F). These results demonstrated that lncRNA GHRLOS is a molecular sponge of miR-346 in NSCLC cells.

## Overexpression of miR-346 Partly Reversed Overexpression of lncRNA GHRLOS-Mediated Cell Proliferation, Invasion, and Apoptosis Both *In Vitro* and *In Vivo*

The above data indicated that lncRNA GHRLOS could be a potential tumor suppressor and a molecular sponge of miR-346 in NSCLC cells. Colony formation and transwell assays demonstrated that miR-346 significantly increased cancer growth and cell invasion, but this effect was overturned by concomitant overexpression of lncRNA GHRLOS (Figures 5A, B). Similarly, lncRNA GHRLOS partly blocked miR-346 mimic-mediated regulation on the expression of PCNA, CDK2, E-cadherin, and N-cadherin in NSCLC cells (Figures 5C, D). In addition, lncRNA GHRLOS also partly abolished miR-346 mimic-mediated dysregulation on mRNA of Bcl-2 and Bax in A549 and NCI-H460 cells (Figure 5E).

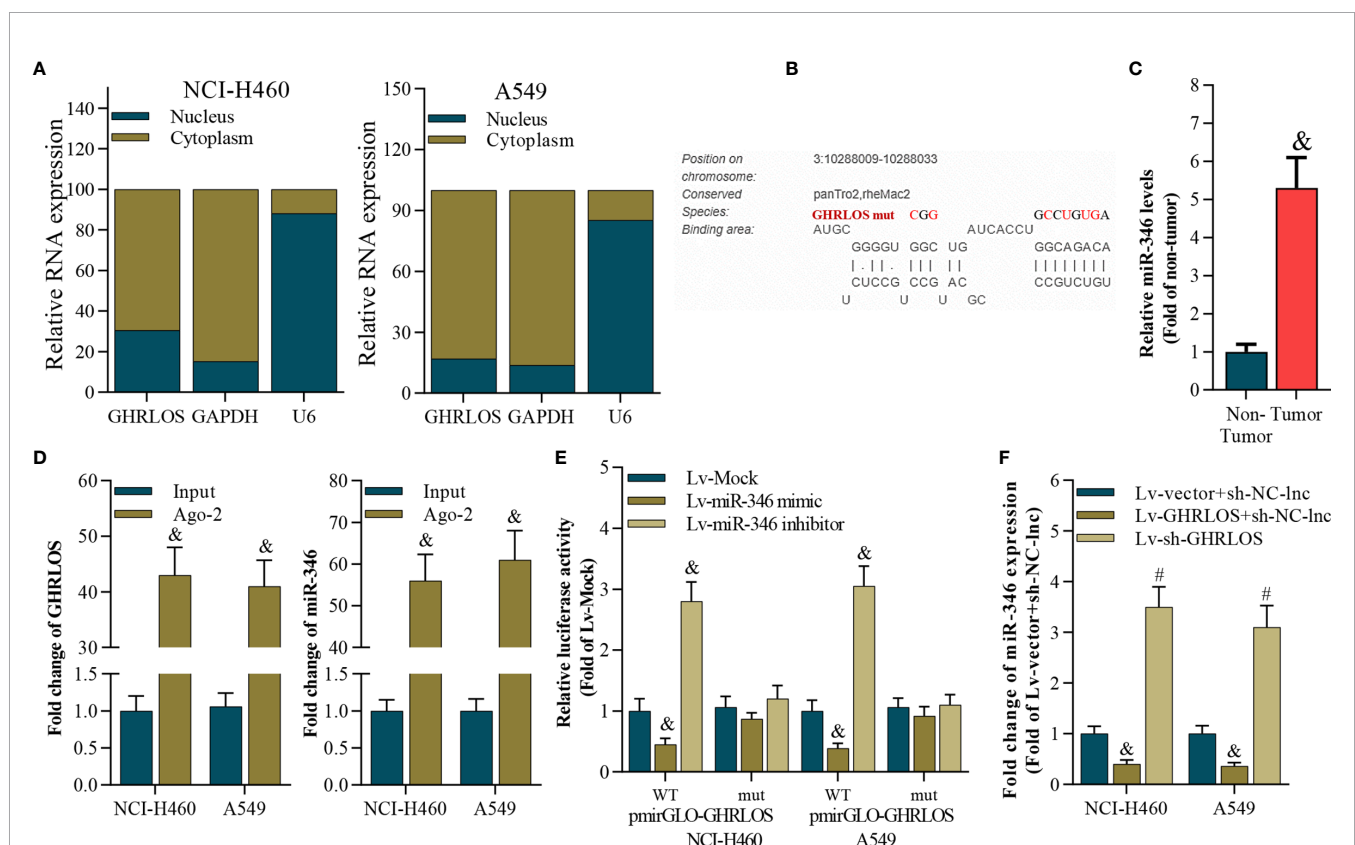


**FIGURE 4 |** lncRNA GHRLOS is a molecular sponge of miR-346. **(A)** qRT-PCR analysis of subcellular localization of lncRNA GHRLOS. GAPDH was used as an internal cytoplasmic control, and U6 served as an internal nuclear control. **(B)** qRT-PCR analysis of miR-346 in clinical NSCLC tissues,  $p < 0.01$  vs. non-tumor. **(C)** The predicted binding site between lncRNA GHRLOS and miR-346 was obtained. **(D)** qRT-PCR analysis on the expression of lncRNA GHRLOS and miR-346 after anti-Ago2-mediated RIP assays in A549 and NCI-H460 cells,  $p < 0.01$  vs. input. **(E)** Dual luciferase reporter assay on the interaction between lncRNA GHRLOS and miR-346 after infection with Mock, miR-346 mimic, or miR-346 inhibitor for 48 h,  $p < 0.01$  vs. Lv-Mock. **(F)** qRT-PCR analysis of miR-346 after indicated infection for 48 h in A549 and NCI-H460 cells,  $p < 0.01$  vs. Lv-vector.

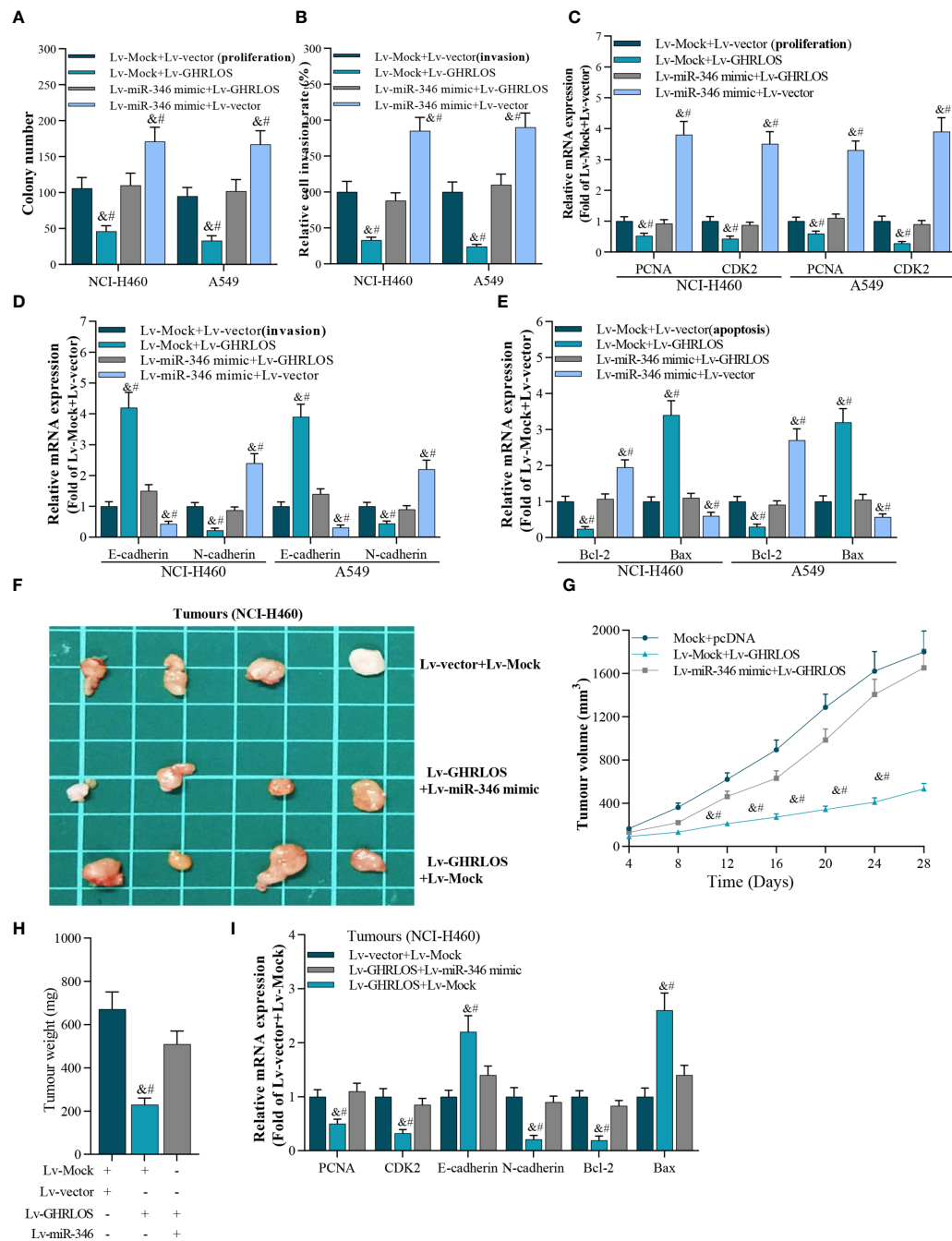


**FIGURE 5 |** The interaction between lncRNA GHRLOS and miR-346 in cancer cell proliferation, invasion, and apoptosis. **(A)** Colony formation assay showed reciprocal suppression between lncRNA GHRLOS and miR-346 on the growth of transfected cancer cells after 14 days culture, &#p< 0.01 vs. Lv-Mock+Lv-vector, #p< 0.01 vs. Lv-miR-346+Lv-GHRLOS. **(B)** Trans-well assays on invasion of lentivirus infected cancer cells, &#p< 0.01 vs. Lv-Mock+Lv-vector, #p< 0.01 vs. Lv-miR-346+Lv-GHRLOS. **(C)** qRT-PCR on the expression of cell growth biomarkers, PCNA and CDK2, in A549 and NCI-H460 cells after infected with indicated lentivirus for 48 h, &#p< 0.01 vs. Lv-Mock+Lv-vector, #p< 0.01 vs. Lv-miR-346+Lv-GHRLOS. **(D)** qRT-PCR on the expression of cell adhesion biomarkers, including E-cadherin and N-cadherin, in A549 and NCI-H460 cells, &#p< 0.01 vs. Lv-Mock+Lv-vector, #p< 0.01 vs. Lv-miR-346+Lv-GHRLOS. **(E)** qRT-PCR analysis on the expression of cell apoptosis-associated genes, Bax and Bcl-2, in cancer cells after lentivirus infection for 48 h, &#p< 0.01 vs. Lv-Mock+Lv-vector, #p< 0.01 vs. Lv-miR-346+Lv-GHRLOS. **(F)** Photo of tumors in nude mice after inoculation for 28 days. **(G)** The tumor volume of each group (n=6) measured at the indicated time points after inoculation of NCI-H460 cells. **(H)** The weight of tumors in nude mice after inoculation for 28 days, &#p< 0.01 vs. Lv-Mock+Lv-vector, #p< 0.01 vs. Lv-miR-346+Lv-GHRLOS. **(I)** qRT-PCR analysis on the expression of PCNA, CDK2, E-cadherin, N-cadherin, Bcl-2, and Bax in xenografted tumors, &#p< 0.01 vs. Lv-Mock+Lv-vector, #p< 0.01 vs. Lv-miR-346+Lv-GHRLOS.

The reciprocal inhibition between lncRNA GHRLOS and miR-346 was also investigated *in vivo*. lncRNA GHRLOS overexpression significantly inhibited tumor growth (Figures 5F, G) and decreased tumor weight in nude mice (Figure 5H). However, miR-346 overexpression markedly reversed lncRNA GHRLOS-induced suppression on tumor volume and weight (Figures 5F–H). Profoundly, miR-346 overexpression attenuated changes in gene expression induced by lncRNA GHRLOS, including PCNA, CDK2, E-cadherin, and N-cadherin, Bcl-2, and Bax (Figure 5I). These data showed that lncRNA GHRLOS and miR-346 play reciprocally modulated tumor suppressor and oncogenic roles, respectively, in NSCLC cells.

## APC Is a Direct Target of miR-346 and Is Regulated by Interaction Between lncRNA GHRLOS and miR-346

It was demonstrated that APC is a suppressor of the canonical Wnt/ $\beta$ -catenin pathway, which increases the transcriptional activation of oncogenes in NSCLC (40). Here, APC was identified to be a target of miR-346 by STARBASE online tools (41) (Figure 6A). We found that the expression of APC reduced

in NSCLC tissues (Figure 6B). Dual luciferase reporter assays revealed that miR-346 inhibited the luciferase activity of APC 3'UTR in NSCLC cells, whereas miR-346-induced inhibition is significantly alleviated by lncRNA GHRLOS (Figure 6C). Moreover, lncRNA GHRLOS elevated the luciferase activity of APC 3'UTR in A549 and NCI-H460 cells, whereas the lncRNA GHRLOS-induced elevation was significantly reversed by miR-346 overexpression (Figure 6C). Similarly, lncRNA GHRLOS significantly reversed the effects of miR-346 on the expression of APC mRNA and protein, as demonstrated by qRT-PCR and Western blot (Figures 6D, E). These findings showed that APC is a direct target of miR-346, and its expression is modulated by the interaction between lncRNA GHRLOS and miR-346.

## Knockdown of APC Blocked miR-346 Inhibitor- or lncRNA GHRLOS Overexpression-Induced Expression of Genes Involved in the Growth, Invasion, and Apoptosis of NSCLC Cells

As the downstream molecule of lncRNA GHRLOS/miR-346 axis, APC was interfered in NSCLC cells, and its effect was evaluated.

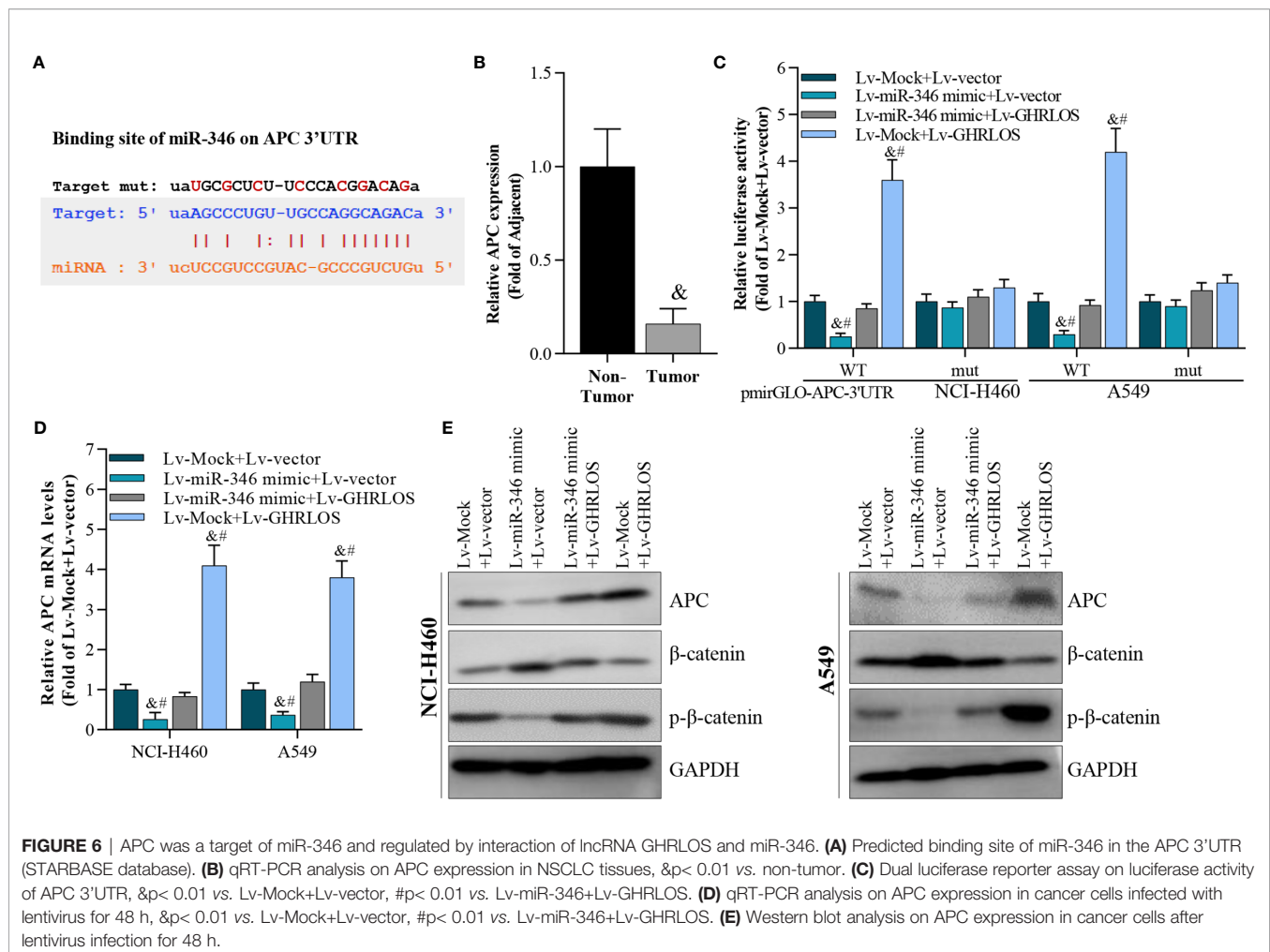


**FIGURE 6** | APC was a target of miR-346 and regulated by interaction of lncRNA GHRLOS and miR-346. (A) Predicted binding site of miR-346 in the APC 3'UTR (STARBASE database). (B) qRT-PCR analysis on APC expression in NSCLC tissues, &#p< 0.01 vs. non-tumor. (C) Dual luciferase reporter assay on luciferase activity of APC 3'UTR, &#p< 0.01 vs. Lv-Mock+Lv-vector, &#p< 0.01 vs. Lv-miR-346+Lv-GHRLOS. (D) qRT-PCR analysis on APC expression in cancer cells infected with lentivirus for 48 h, &#p< 0.01 vs. Lv-Mock+Lv-vector, &#p< 0.01 vs. Lv-miR-346+Lv-GHRLOS. (E) Western blot analysis on APC expression in cancer cells after lentivirus infection for 48 h.



The data showed that inhibition of APC expression blocks miR-346-induced genes dysregulation, including PCNA, CDK2, E-cadherin, N-cadherin, Bcl-2, and Bax (Figures 7A, B). Moreover, downregulation of APC also abolished the regulation of gene expression mediated by GHRLOS (Figures 7C, D). Therefore, the role of lncRNA GHRLOS and miR-346 in regulating cell proliferation, invasion, and apoptosis might require APC participation.

## APC Expression Is Regulated by TP53-Mediated lncRNA GHRLOS and miR-346

To determine whether TP-53 was required for the regulation of APC expression in NSCLC cells, TP53 was overexpressed or knocked down by lentivirus infection (Figure 8A). qRT-PCR analysis demonstrated that TP53 overexpression upregulated the expression of both lncRNA GHRLOS and APC but repressed the expression of miR-346 (Figure 8B). Most impressively, APC expression was increased in response to TP53. In contrast, APC expression was decreased by knockdown of TP53 (Figure 8C). These results suggest that TP53 controls lncRNA GHRLOS- and miR-346-regulated APC expression.

Taken together, these results suggest that by competitively absorbing miR-346, lncRNA GHRLOS upregulates APC and

further regulates cancer cell proliferation, invasion, and apoptosis in NSCLC (Figure 8D).

## DISCUSSION

NSCLC is the most common type of lung cancer worldwide (1, 3–6). Increasing evidence has demonstrated that lncRNAs play essential roles in NSCLC tumorigenesis and progression. Our previous works showed that AFAP1-AS1 (16), DHRS4-AS1 (42) and KTN1-AS1 (43) participate in NSCLC progression via regulating diverse molecular mechanisms involved in cancer cell behaviors. Here, we reported a new NSCLC suppressor lncRNA, lncRNA GHRLOS. We found that lncRNA GHRLOS was downregulated in NSCLC tissues and cells, and its downregulation predicts a poor overall survival in patients. lncRNA GHRLOS significantly inhibited cell proliferation and invasion and increased apoptosis in NSCLC cells. These findings demonstrate that lncRNA GHRLOS exerts tumor inhibitory activity in the development of NSCLC, suggesting that overexpression of lncRNA GHRLOS could be used for treatment in patients with NSCLC.

A number of studies have revealed that lncRNA are regulated by TP53, a well-known transcription factor and tumor suppressor

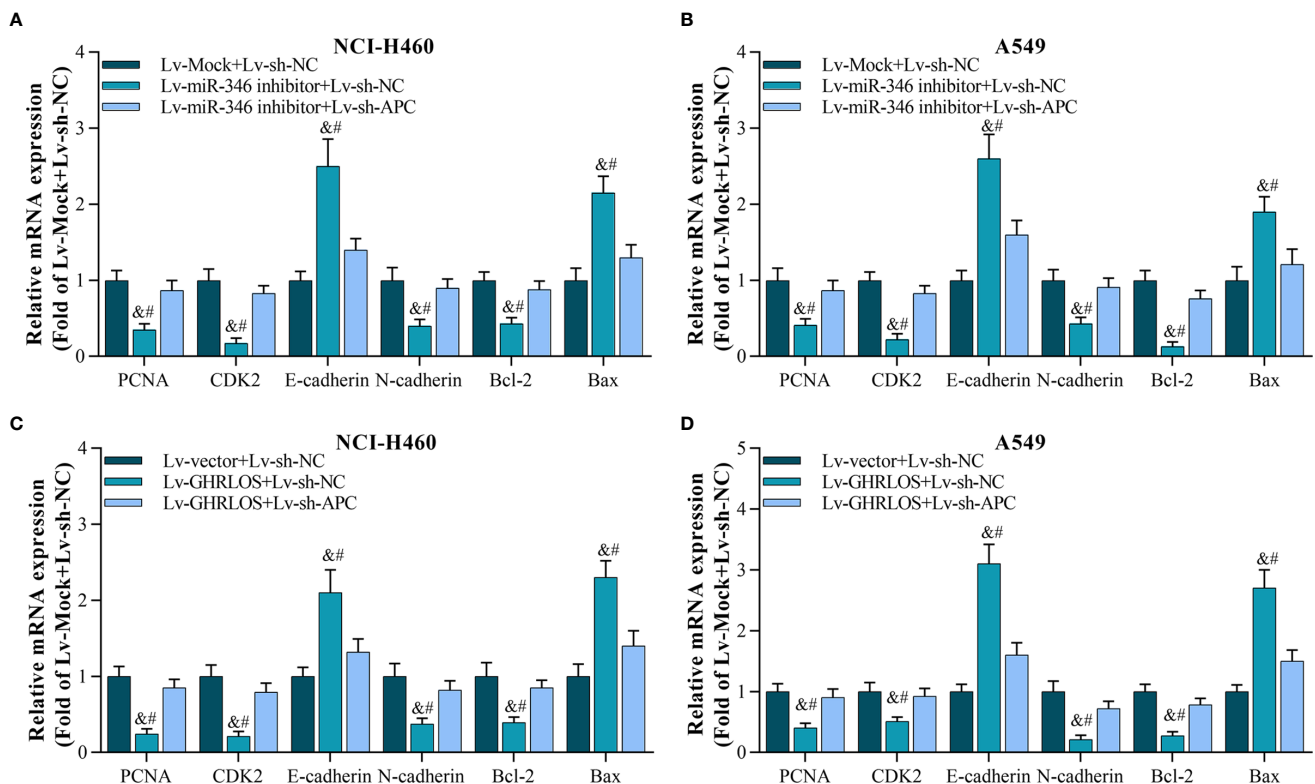


**FIGURE 7 |** Silencing APC blocked miR-346 knockdown- or lncRNA GHRLOS overexpression-controlled gene expression on biomarkers of cell proliferation, invasion, and apoptosis. (A, B) qRT-PCR analysis on gene expression after lentivirus infection for 48 h in A549 and NCI-H460 cells, &#p< 0.01 vs. Lv-Mock+Lv-sh-NC, &#p< 0.01 vs. Lv-miR-346+Lv-sh-APC. (C, D) qRT-PCR analysis on gene expression in NSCLC cells with lentivirus infection for 48 h, &#p< 0.01 vs. Lv-Mock+Lv-sh-NC, &#p< 0.01 vs. Lv-miR-346+Lv-sh-APC.

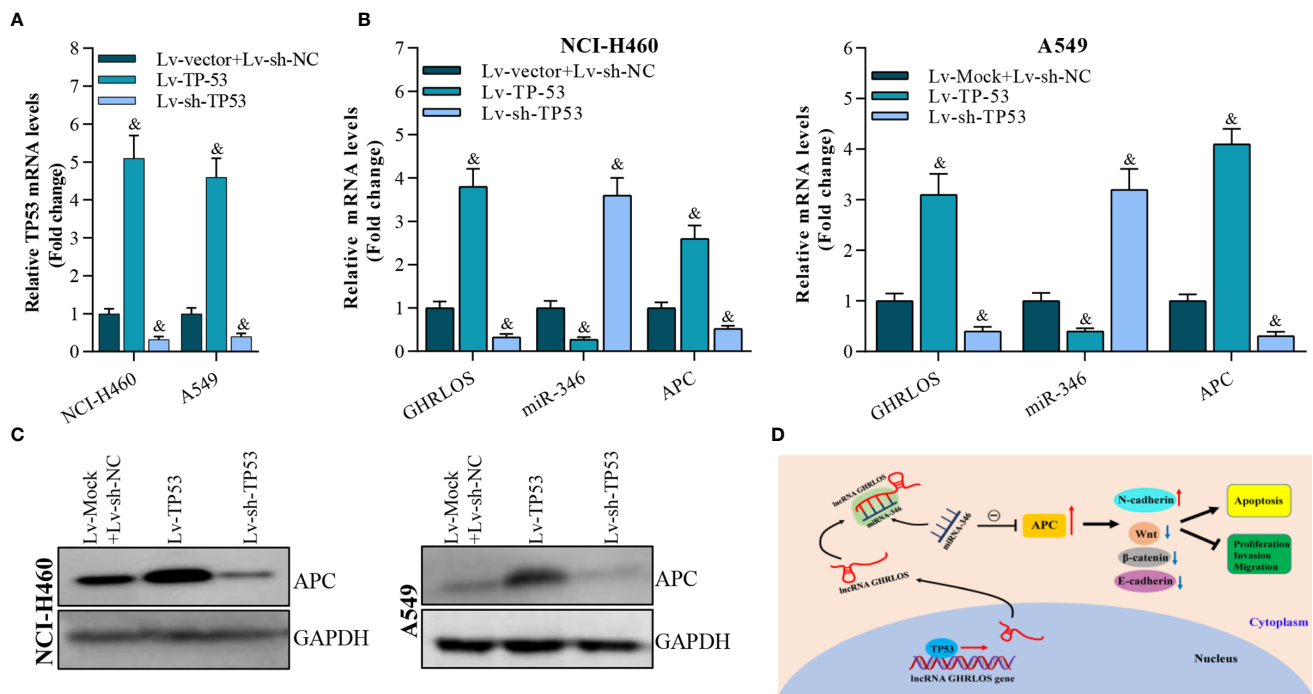


**FIGURE 8 |** APC expression is modulated by overexpression or interference with TP53 expression. **(A)** qRT-PCR analysis on TP53 expression after overexpressed- or knockdown-TP53 for 48 h, &  $p < 0.01$  vs. Lv-vector. **(B)** qRT-PCR analysis on APC, lncRNA GHRLOS, and miR-346 expression after indicated lentivirus infection for 48 h in A549 and NCI-H460 cells, &  $p < 0.01$  vs. Lv-vector. **(C)** Western blot analysis on APC expression in A549 and NCI-H460 cells with indicated infection. **(D)** Schematic presentation of molecular mechanism of lncRNA GHRLOS mediated cell proliferation, invasion and apoptosis in NSCLC.

(35). We found that TP53 activates the transcription of lncRNA GHRLOS by binding to its promoter. In contrast, interruption of TP53 expression decreases lncRNA GHRLOS level in NSCLC cells. Therefore, the downregulation of lncRNA GHRLOS is most likely caused by loss of DNA-binding domain of TP53 gene, which are common events in NSCLC. TP53 is encoded by the *TP53* gene, and it is the most frequently mutated gene in human cancers of many types mutations are common in NSCLC, and *TP53* mutations have been reported associate with poor prognosis of NSCLC patients (44, 45). Whether the occurrence of *TP53* gene mutation could affect the binding of TP53 with *GHRLOS* promoter, and hence inducing the loss of function of lncRNA GHRLOS in inhibiting the progression of NSCLC still required to verified. Therefore, make further efforts to estimate the influence of different *TP53* gene mutation on the binding with the promoter of gene encoding lncRNA, like GHROS, and explore the underlying regulatory mechanism in NSCLC progression are urgently needed.

In this study, it was found that lncRNA GHRLOS was mainly located in the cytoplasm of NSCLC cells, and lncRNA GHRLOS acts as a molecular sponge of miR-346. Previous studies have demonstrated that miR-346 may be regulated by lncRNA NBAT1 (46), DGCR5 (47), and circFBLIM1 (48) in cancers. Moreover, miR-346 facilitates NSCLC growth and metastasis and inhibits cell apoptosis via controlling XPC/ERK/Snail/E-cadherin signaling pathway (49). Consistent with these studies,

our data demonstrated that miR-346 is overexpressed in NSCLC tissues, and miR-346 regulates the mRNA expression of PCNA, CDK2, E-cadherin, N-cadherin, Bcl-2, and Bax in NSCLC cells. These findings demonstrated that lncRNA GHRLOS and miR-346 reciprocally controlled the activities of tumor suppressor and oncogenes, respectively. However, whether other lncRNAs are involved in the regulation of miR-346 in NSCLC is not addressed in this study.

APC is a negative regulator of Wnt/β-catenin signaling, which promotes the transcriptional activation of oncogenes in cancers (40, 50–52). Here, our results showed that TP53 significantly increased APC expression by regulating lncRNA GHRLOS/miR-346 pathway in NSCLC cells. Jaiswal *et al.* reported that phosphorylated p53 can up-regulate the APC promoter activity with other transcriptional factors through direct binding (53). Therefore, TP53 might directly or indirectly regulate APC, and lncRNA GHRLOS/miR-346 axis might be an indirect pathway for TP53 to regulate APC.

In summary, we identified a novel transcription factor-mediated lncRNA-miRNA-mRNA axis in NSCLC cells in this study. The downregulation of lncRNA GHRLOS caused by TP53 mutation not only correlates with poor clinical outcome, but also promotes cancer progression of NSCLC. TP53 regulates APC expression through lncRNA GHRLOS/miR-346 axis. Thus, the components of the TP53/lncRNA GHRLOS/miR-346/APC signaling pathway could represent novel targets for NSCLC therapies.

## DATA AVAILABILITY STATEMENT

The original contributions presented in the study are included in the article/**Supplementary Material**. Further inquiries can be directed to the corresponding author.

## ETHICS STATEMENT

The studies involving human participants were reviewed and approved by the ethics committee of first affiliated hospital of Chengdu Medical College. The patients/participants provided their written informed consent to participate in this study. The animal study was reviewed and approved by the Ethics Committee of Animal Experiments of Chengdu Medical College.

## AUTHOR CONTRIBUTIONS

WZ designed this research. KR and JS performed experiments and drafted this manuscript. YY and LL participated in most of the experiments, collected tissues samples, and analyzed clinical data. HL, ZW, JD, MH, and JQ assisted with part of cell and animal experiments. WZ edited the manuscript. All authors contributed to the article and approved the submitted version.

## REFERENCES

1. Siegel RL, Miller KD, Jemal A. Cancer statistics, 2020. *CA Cancer J Clin* (2020) 70(1):7–30. doi: 10.3322/caac.21590
2. Feng RM, Zong YN, Cao SM, Xu RH. Current cancer situation in China: good or bad news from the 2018 Global Cancer Statistics? *Cancer Commun (Lond)* (2019) 39(1):22. doi: 10.1186/s40880-019-0368-6
3. Chen W, Zheng R, Baade PD, Zhang S, Zeng H, Bray F, et al. Cancer statistics in China, 2015. *CA Cancer J Clin* (2016) 66(2):115–32. doi: 10.3322/caac.21338
4. Herbst RS, Morgensztern D, Boshoff C. The biology and management of non-small cell lung cancer. *Nature* (2018) 553(7689):446–54. doi: 10.1038/nature25183
5. Hill A, Gupta R, Zhao D, Vankina R, Amanam I, Salgia R. Targeted Therapies in Non-small-Cell Lung Cancer. *Cancer Treat Res* (2019) 178:3–43. doi: 10.1007/978-3-030-16391-4\_1
6. Reck M, Rabe KF. Precision Diagnosis and Treatment for Advanced Non-Small-Cell Lung Cancer. *N Engl J Med* (2017) 377(9):849–61. doi: 10.1056/NEJMra1703413
7. Garon EB, Hellmann MD, Rizvi NA, Carcereny E, Leighl NB, Ahn MJ, et al. Five-Year Overall Survival for Patients With Advanced NonSmall-Cell Lung Cancer Treated With Pembrolizumab: Results From the Phase I KEYNOTE-001 Study. *J Clin Oncol* (2019) 37(28):2518–27. doi: 10.1200/JCO.19.00934
8. Hirsch FR, Scagliotti GV, Mulshine JL, Kwon R, Curran WJ Jr, Wu YL, et al. Lung cancer: current therapies and new targeted treatments. *Lancet* (2017) 389(10066):299–311. doi: 10.1016/S0140-6736(16)30958-8
9. Chang ZW, Jia YX, Zhang WJ, Song LJ, Gao M, Li MJ, et al. LncRNA-TUSC7/miR-224 affected chemotherapy resistance of esophageal squamous cell carcinoma by competitively regulating ESC1. *J Exp Clin Cancer Res CR* (2018) 37(1):56. doi: 10.1186/s13046-018-0724-4
10. Bautista RR, Gomez AO, Miranda AH, Dehesa AZ, Villarreal-Garza C, Avila-Moreno F, et al. Correction to: Long non-coding RNAs: implications in targeted diagnoses, prognosis, and improved therapeutic strategies in human

## FUNDING

This work was supported by the National Natural Science Foundation of China (81602636 and 31800154), the Nanjing medical science and technology development project (ZKX15049), the Key project of science of Sichuan Education Department (18ZA0164), the Natural Science Foundation of Chengdu Medical College (CYZ18-01, CYZ18-04), the Technology Innovation R&D Project of Chengdu Science and Technology Bureau (2018-YFYF-00158-SN), the Open fund of Development and Regeneration Key Laboratory of Sichuan Province (SYS18-08, SYS20-07), the Natural Science Foundation of Laboratory Medicine School in Chengdu Medical College (JYZK201701) and the Miaozi project of science and Technology Department of Sichuan Province (2018RZ0095).

## ACKNOWLEDGMENTS

The authors wish to thank the patients enrolled in this study.

## SUPPLEMENTARY MATERIAL

The Supplementary Material for this article can be found online at: <https://www.frontiersin.org/articles/10.3389/fonc.2021.676202/full#supplementary-material>

- non- and triple-negative breast cancer. *Clin Epigenet* (2018) 10(1):106. doi: 10.1186/s13148-018-0537-5
11. Chan JJ, Tay Y. Noncoding RNA:RNA Regulatory Networks in Cancer. *Int J Mol Sci* (2018) 19(5):1310. doi: 10.3390/ijms19051310
12. Kopp F, Mendell JT. Functional Classification and Experimental Dissection of Long Noncoding RNAs. *Cell* (2018) 172(3):393–407. doi: 10.1016/j.cell.2018.01.011
13. Chen Z, Lei T, Chen X, Gu J, Huang J, Lu B, et al. Long non-coding RNA in lung cancer. *Clin Chim Acta* (2020) 504:190–200. doi: 10.1016/j.cca.2019.11.031
14. Fang C, Wang L, Gong C, Wu W, Yao C, Zhu S. Long non-coding RNAs: How to regulate the metastasis of non-small-cell lung cancer. *J Cell Mol Med* (2020) 24(6):3282–91. doi: 10.1111/jcmm.15054
15. Yin D, Lu X, Su J, He X, De W, Yang J, et al. Long noncoding RNA AFAP1-AS1 predicts a poor prognosis and regulates non-small cell lung cancer cell proliferation by epigenetically repressing p21 expression. *Mol Cancer* (2018) 17(1):92. doi: 10.1186/s12943-018-0836-7
16. Huang N, Guo W, Ren K, Li W, Jiang Y, Sun J, et al. LncRNA AFAP1-AS1 Suppresses miR-139-5p and Promotes Cell Proliferation and Chemotherapy Resistance of Non-small Cell Lung Cancer by Competitively Upregulating RRM2. *Front Oncol* (2019) 9:1103. doi: 10.3389/fonc.2019.01103
17. Liu Y, Hu Q, Wang X. AFAP1-AS1 induces cisplatin resistance in non-small cell lung cancer through PI3K/AKT pathway. *Oncol Lett* (2020) 19(1):1024–30. doi: 10.3892/ol.2019.11175
18. Zhao Y, Zhu Z, Shi S, Wang J, Li N. Long non-coding RNA MEG3 regulates migration and invasion of lung cancer stem cells via miR-650/SLC34A2 axis. *BioMed Pharmacother* (2019) 120:109457. doi: 10.1016/j.biopha.2019.109457
19. Kalemkerian GP, Loo BW, Akerley W, Attia A, Bassetti M, Boumber Y, et al. NCCN Guidelines Insights: Small Cell Lung Cancer, Version 2.2018. *J Natl Compr Cancer Netw JNCCN* (2018) 16(10):1171–82. doi: 10.6004/jnccn.2018.0079
20. Nikolopoulos D, Theocharis S, Kouraklis G. Ghrelin's role on gastrointestinal tract cancer. *Surg Oncol* (2010) 19(1):e2–e10. doi: 10.1016/j.suronc.2009.02.011

21. Poher AL, Tschop MH, Muller TD. Ghrelin regulation of glucose metabolism. *Peptides* (2018) 100:236–42. doi: 10.1016/j.peptides.2017.12.015
22. Yanagi S, Sato T, Kangawa K, Nakazato M. The Homeostatic Force of Ghrelin. *Cell Metab* (2018) 27(4):786–804. doi: 10.1016/j.cmet.2018.02.008
23. Wu S, Liu J, Wang X, Li M, Chen Z, Tang Y. Aberrant Expression of the Long Non-coding RNA GHRLOS and Its Prognostic Significance in Patients with Colorectal Cancer. *J Cancer* (2017) 8(19):4040–7. doi: 10.7150/jca.21304
24. Zhang J, Wei J, Wang Z, Feng Y, Wei Z, Hou X, et al. Transcriptome hallmarks in *Helicobacter pylori* infection influence gastric cancer and MALT lymphoma. *Epigenomics* (2020) 12(8):661–71. doi: 10.2217/epi-2019-0152
25. Bhan A, Soleimani M, Mandal SS. Long Noncoding RNA and Cancer: A New Paradigm. *Cancer Res* (2017) 77(15):3965–81. doi: 10.1158/0008-5472.CAN-16-2634
26. Seo D, Kim D, Chae Y, Kim W. The ceRNA network of lncRNA and miRNA in lung cancer. *Genomics Inf* (2020) 18(4):e36. doi: 10.5808/GI.2020.18.4.e36
27. Hong W, Xue M, Jiang J, Zhang Y, Gao X. Circular RNA circ-CPA4/let-7 miRNA/PD-L1 axis regulates cell growth, stemness, drug resistance and immune evasion in non-small cell lung cancer (NSCLC). *J Exp Clin Cancer Res* (2020) 39(1):149. doi: 10.1186/s13046-020-01648-1
28. Gao L, Yan SB, Yang J, Kong JL, Shi K, Ma FC, et al. MiR-182-5p and its target HOXA9 in non-small cell lung cancer: a clinical and in-silico exploration with the combination of RT-qPCR, miRNA-seq and miRNA-chip. *BMC Med Genomics* (2020) 13(1):3. doi: 10.1186/s12920-019-0648-7
29. Liang G, Meng W, Huang X, Zhu W, Yin C, Wang C, et al. miR-196b-5p-mediated downregulation of TSPAN12 and GATA6 promotes tumor progression in non-small cell lung cancer. *Proc Natl Acad Sci U S A* (2020) 117(8):4347–57. doi: 10.1073/pnas.1917531117
30. Labbe C, Cabanero M, Korpanty GJ, Tomasini P, Doherty MK, Mascaux C, et al. Prognostic and predictive effects of TP53 co-mutation in patients with EGFR-mutated non-small cell lung cancer (NSCLC). *Lung Cancer* (2017) 111:23–9. doi: 10.1016/j.lungcan.2017.06.014
31. Levine AJ. Targeting Therapies for the p53 Protein in Cancer Treatments. *Annu Rev Cancer Biol* (2019) 3(1):21–34. doi: 10.1146/annurev-cancerbio-030518-055455
32. Yue X, Zhao Y, Xu Y, Zheng M, Feng Z, Hu W. Mutant p53 in Cancer: Accumulation, Gain-of-Function, and Therapy. *J Mol Biol* (2017) 429(11):595–606. doi: 10.1016/j.jmb.2017.03.030
33. Shi Y, Norberg E, Vakifahmetoglu-Norberg H. Mutant p53 as a Regulator and Target of Autophagy. *Front Oncol* (2021) 10:607149. doi: 10.3389/fonc.2020.607149
34. Chou CW, Lin CH, Hsiao TH, Lo CC, Hsieh CY, Huang CC, et al. Therapeutic effects of statins against lung adenocarcinoma via p53 mutant-mediated apoptosis. *Sci Rep* (2019) 9(1):20403. doi: 10.1038/s41598-019-56532-6
35. Chen S, Thorne RF, Zhang XD, Wu M, Liu L. Non-coding RNAs, guardians of the p53 galaxy. *Semin Cancer Biol* (2020) S1044-579(20):30190–5. doi: 10.1016/j.semcancer.2020.09.002
36. Barakat A, Mittal A, Ricketts D, Rogers BA. Understanding survival analysis: actuarial life tables and the Kaplan-Meier plot. *Br J Hosp Med (Lond)* (2019) 80(11):642–6. doi: 10.12968/hmed.2019.80.11.642
37. Kabakov AE, Gabai VL. Cell Death and Survival Assays. *Methods Mol Biol* (2018) 1709:107–27. doi: 10.1007/978-1-4939-7477-1\_9
38. Fornes O, Castro-Mondragon JA, Khan A, van der Lee R, Zhang X, Richmond PA, et al. JASPAR 2020: update of the open-access database of transcription factor binding profiles. *Nucleic Acids Res* (2020) 48(D1):D87–92. doi: 10.1093/nar/gkz1001
39. Karagkouni D, Paraskevopoulou MD, Tastsoglou S, Skoufos G, Karavangeli A, Pierros V, et al. DIANA-LncBase v3: indexing experimentally supported miRNA targets on non-coding transcripts. *Nucleic Acids Res* (2020) 48(D1):D101–D10. doi: 10.1093/nar/gkz1036
40. Huang P, Yan R, Zhang X, Wang L, Ke X, Qu Y. Activating Wnt/beta-catenin signaling pathway for disease therapy: Challenges and opportunities. *Pharmacol Ther* (2019) 196:79–90. doi: 10.1016/j.pharmthera.2018.11.008
41. Li JH, Liu S, Zhou H, Qu LH, Yang JH. starBase v2.0: decoding miRNA-ceRNA, miRNA-ncRNA and protein-RNA interaction networks from large-scale CLIP-Seq data. *Nucleic Acids Res* (2014) 42(Database issue):D92–7. doi: 10.1093/nar/gkt1248
42. Yan F, Zhao W, Xu X, Li C, Li X, Liu S, et al. LncRNA DHRS4-AS1 Inhibits the Stemness of NSCLC Cells by Sponging miR-224-3p and Upregulating TP53 and TET1. *Front Cell Dev Biol* (2020) 8:585251. doi: 10.3389/fcell.2020.585251
43. Li C, Zhao W, Pan X, Li X, Yan F, Liu S, et al. LncRNA KTN1-AS1 promotes the progression of non-small cell lung cancer via sponging of miR-130a-5p and activation of PDPK1. *Oncogene* (2020) 39(39):6157–71. doi: 10.1038/s41388-020-01427-4
44. Petitjean A, Achatz MI, Borresen-Dale AL, Hainaut P, Olivier M. TP53 mutations in human cancers: functional selection and impact on cancer prognosis and outcomes. *Oncogene* (2007) 26(15):2157–65. doi: 10.1038/sj.onc.1210302
45. Mogi A, Kuwano H. TP53 mutations in nonsmall cell lung cancer. *J BioMed Biotechnol* (2011) 2011:583929. doi: 10.1155/2011/583929
46. Xue S, Wang S, Li J, Guan H, Jiang S, Guo Y, et al. LncRNA NBAT1 suppresses cell proliferation and migration via miR-346/GSK-3beta axis in renal carcinoma. *IUBMB Life* (2019) 71(11):1720–28. doi: 10.1002/iub.2111
47. Wang YG, Liu J, Shi M, Chen FX. LncRNA DGCR5 represses the development of hepatocellular carcinoma by targeting the miR-346/KLF14 axis. *J Cell Physiol* (2018) 234(1):572–80. doi: 10.1002/jcp.26779
48. Bai N, Peng E, Qiu X, Lyu N, Zhang Z, Tao Y, et al. circFBLIM1 act as a ceRNA to promote hepatocellular cancer progression by sponging miR-346. *J Exp Clin Cancer Res* (2018) 37(1):172. doi: 10.1186/s13046-018-0838-8
49. Sun CC, Li SJ, Yuan ZP, Li DJ. MicroRNA-346 facilitates cell growth and metastasis, and suppresses cell apoptosis in human non-small cell lung cancer by regulation of XPC/ERK/Snail/E-cadherin pathway. *Aging* (2016) 8(10):2509–24. doi: 10.18632/aging.101080
50. El-Sahli S, Xie Y, Wang L, Liu S. Wnt Signaling in Cancer Metabolism and Immunity. *Cancers* (2019) 11(7):904. doi: 10.3390/cancers11070904
51. Rajagopal C, Lankadasari MB, Aranjani JM, Harikumar KB. Targeting oncogenic transcription factors by polyphenols: A novel approach for cancer therapy. *Pharmacol Res* (2018) 130:273–91. doi: 10.1016/j.phrs.2017.12.034
52. Clevers H, Nusse R. Wnt/beta-catenin signaling and disease. *Cell* (2012) 149(6):1192–205. doi: 10.1016/j.cell.2012.05.012
53. Jaiswal AS, Narayan S. p53-dependent transcriptional regulation of the APC promoter in colon cancer cells treated with DNA alkylating agents. *J Biol Chem* (2001) 276(21):18193–9. doi: 10.1074/jbc.M101298200

**Conflict of Interest:** The authors declare that the research was conducted in the absence of any commercial or financial relationships that could be construed as a potential conflict of interest.

Copyright © 2021 Ren, Sun, Liu, Yang, Li, Wang, Deng, Hou, Qiu and Zhao. This is an open-access article distributed under the terms of the Creative Commons Attribution License (CC BY). The use, distribution or reproduction in other forums is permitted, provided the original author(s) and the copyright owner(s) are credited and that the original publication in this journal is cited, in accordance with accepted academic practice. No use, distribution or reproduction is permitted which does not comply with these terms.





# PROTAC: An Effective Targeted Protein Degradation Strategy for Cancer Therapy

Si-Min Qi<sup>1†</sup>, Jinyun Dong<sup>2†</sup>, Zhi-Yuan Xu<sup>2</sup>, Xiang-Dong Cheng<sup>2\*</sup>, Wei-Dong Zhang<sup>3\*</sup> and Jiang-Jiang Qin<sup>1,2\*</sup>

<sup>1</sup>School of Pharmaceutical Sciences, Zhejiang Chinese Medical University, Hangzhou, China, <sup>2</sup>The Cancer Hospital of the University of Chinese Academy of Sciences (Zhejiang Cancer Hospital), Institute of Basic Medicine and Cancer (IBMC), Chinese Academy of Sciences, Hangzhou, China, <sup>3</sup>School of Pharmacy, Naval Medical University, Shanghai, China

## OPEN ACCESS

### Edited by:

Haichang Li,  
The Ohio State University,  
United States

### Reviewed by:

Hongwei Guo,  
Guangxi Medical University, China  
Panagiotis J. Vlachostergios,  
Cornell University, United States

### \*Correspondence:

Xiang-Dong Cheng  
chengxd516@126.com  
Wei-Dong Zhang  
wdzhangy@hotmail.com  
Jiang-Jiang Qin  
jqin@zcmu.edu.cn

<sup>†</sup>These authors have contributed  
equally to this work

### Specialty section:

This article was submitted to  
Experimental Pharmacology and Drug  
Discovery,  
a section of the journal  
Frontiers in Pharmacology

**Received:** 08 April 2021

**Accepted:** 26 April 2021

**Published:** 07 May 2021

### Citation:

Qi S-M, Dong J, Xu Z-Y, Cheng X-D,  
Zhang W-D and Qin J-J (2021)  
PROTAC: An Effective Targeted  
Protein Degradation Strategy for  
Cancer Therapy.  
Front. Pharmacol. 12:692574.  
doi: 10.3389/fphar.2021.692574

Proteolysis targeting chimeric (PROTAC) technology is an effective endogenous protein degradation tool developed in recent years that can ubiquitinate the target proteins through the ubiquitin-proteasome system (UPS) to achieve an effect on tumor growth. A number of literature studies on PROTAC technology have proved an insight into the feasibility of PROTAC technology to degrade target proteins. Additionally, the first oral PROTACs (ARV-110 and ARV-471) have shown encouraging results in clinical trials for prostate and breast cancer treatment, which inspires a greater enthusiasm for PROTAC research. Here we focus on the structures and mechanisms of PROTACs and describe several classes of effective PROTAC degraders based on E3 ligases.

**Keywords:** PROTAC, E3 ubiquitin ligase, protein degradation, ubiquitin-proteasome system, cancer therapy

## INTRODUCTION

As a traditional treatment method, chemotherapy plays an irreplaceable role in the cancer treatment process. The main disadvantages of traditional anticancer drugs are that most of them have poor selectivity and are easy to develop drug resistance (Mangal et al., 2017; Dong et al., 2020; Yuan et al., 2020). As a result, the targeted therapy of cancer has attracted people's attention (Zhou Y. et al., 2020; Qi et al., 2020; Yu et al., 2020). On this basis, the discoveries of new targets and small molecule inhibitors (SMIs) become powerful treatment strategies (Dong et al., 2018). In particular, the development of small molecule kinase inhibitors has become one of the most widely pursued fields in the process of drug discovery and has made great achievements in cancer treatment (Wu et al., 2015). However, after the success, the treatment strategy also faces the same problem of drug resistance as chemotherapy (Dong et al., 2020; Xu et al., 2020). Therefore, drug resistance is the main limitation for cancer therapy and needs to be solved urgently.

In recent years, a novel strategy that targets disease-related proteins for degradation has gained tremendous attention. Proteolysis targeting chimerics (PROTACs), also known as bivalent chemical protein degraders, are heterobifunctional molecules that degrade specific endogenous proteins through the E3 ubiquitin ligase pathway (Potjewyd et al., 2020). It structurally connects the protein of interest (POI)-binding ligand and the E3 ubiquitin ligase (E3) ligand through an appropriate linker (Buckley et al., 2015; Zhang et al., 2019; Kregel et al., 2020; Vollmer et al., 2020). The potential advantages of PROTAC technology may compensate for the shortcomings of traditional drug therapy, which promotes its rapid development (Toure and Crews, 2016; Sun and Rao, 2020). This paper focuses on introducing the mechanisms and the research progress of PROTAC technology, as well as summarizing the advantages of this degradation method.

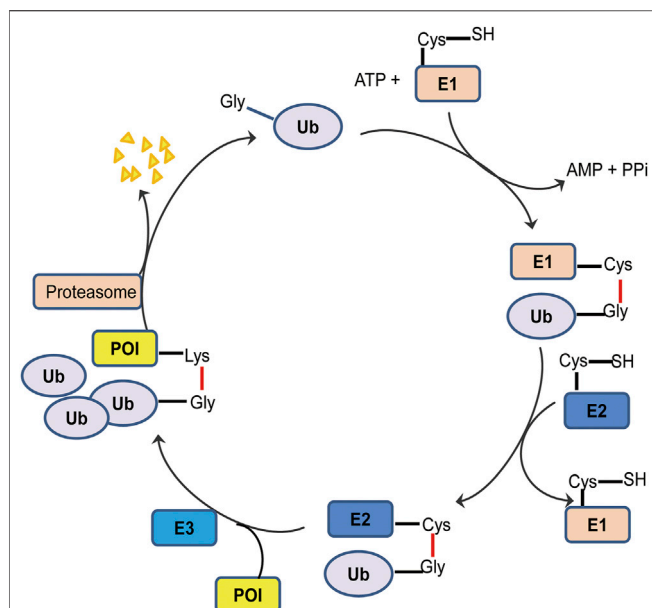


**FIGURE 1 |** Schematic diagram of ubiquitination process. The ubiquitin tag first binds to an E1 ubiquitin activating enzyme, transfers to an E2 ubiquitin binding enzyme, and then relies on an E3 ubiquitin ligase to deliver its ubiquitin to the target protein. Ubiquitin labeled proteins are specifically recognized and degraded by proteasome.

## UBIQUITIN-PROTEASOME SYSTEM AND MECHANISM OF PROTEOLYSIS TARGETING CHIMERIC TECHNOLOGY

There are many approaches to protein degradation, which is very important to maintain the homeostasis of cell proteins and to regulate numerous cell processes, such as gene transcription, DNA pairing, cell cycle control, and apoptosis (Cyrus et al., 2011). Among them, the ubiquitin-proteasome system is a crucial way to specifically degrade proteins that are involved in various metabolic activities, mainly including cyclin, spindle related proteins, cell surface receptors (epidermal growth factor receptor, etc.), transcription factors (NF- $\kappa$ B, etc.), tumor suppressor factors such as p53, oncogene products, and intracellular denaturing proteins, whose deregulation is related to the pathogenesis of many diseases (Nam et al., 2017). UPS relies on ATP and consists of two steps: polyubiquitination of target protein and proteolysis of polyubiquitin by 26S proteolytic enzyme complex (Nandi et al., 2006).

The ubiquitin-activating enzyme E1 could form a high-energy sulfur lipid bond between the C-terminal Gly residue of the ubiquitin molecule and its own Cys residue by using ATP, and the activated ubiquitin is transferred to a ubiquitin binding enzyme E2 (Zhou L. et al., 2020). In the presence of a ubiquitin ligase E3, the ubiquitin molecule transfers from E2 to the target protein, to form an isopeptide bond with  $\epsilon$ -NH<sub>2</sub> of the Lys residue of the target protein, and then the C-terminal of the next ubiquitin molecule connects to the former at Lys48, leading to polyubiquitination (Figure 1) (Nandi et al., 2006). The ubiquitinated protein can be

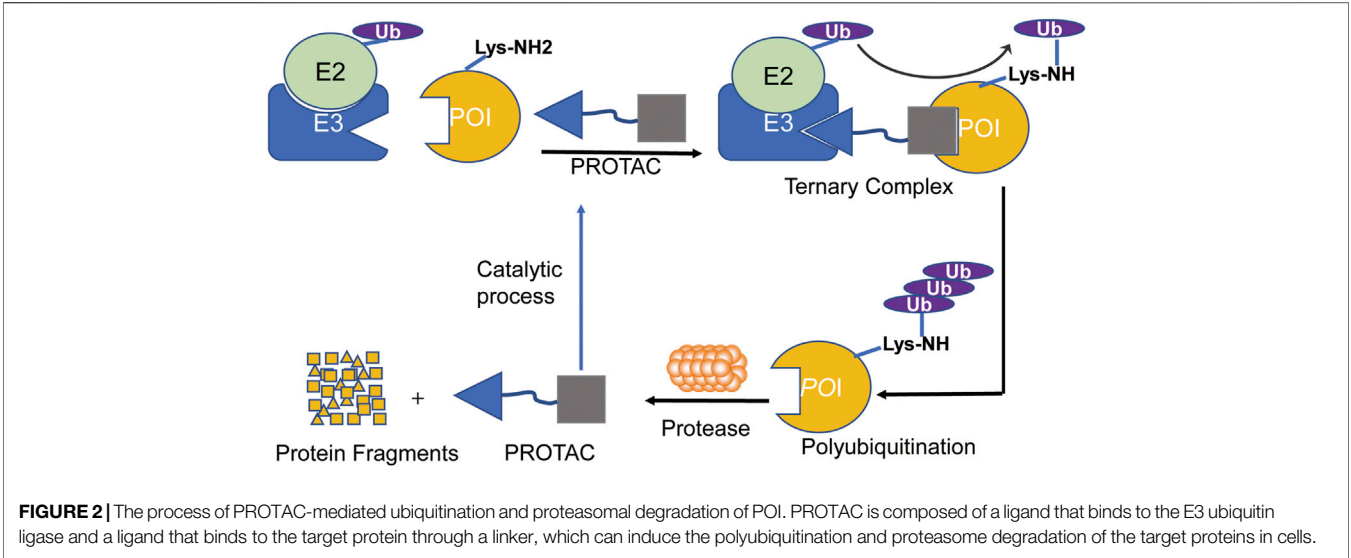
recognized by the cap-like regulatory particles of 26S proteasome, transported to the cylindrical core of 20S, hydrolyzed into oligopeptides by a variety of enzymes, and finally released from the proteasome to achieve the degradation of the target protein. The ubiquitin molecule, on the other hand, dissociates from the substrate and returns to the cytoplasm for reutilization (Myeku et al., 2016).

The mechanism of PROTACs is to use the UPS system to ubiquitinate and degrade the target protein (Wang et al., 2020b). Once the PROTAC molecules combine the target protein with E3 ligase together to form a ternary complex, which induces E3 ligase ubiquitinating the target protein to initiate the degradation process (Zou et al., 2019). The ubiquitinated target protein is recognized and degraded by 26S proteasome, which is a part of the eukaryotic cells of UPS (Figure 2). The ability of PROTACs to induce the degradation of the target protein is not limited to the binding site within the kinase domain, and it may also be achieved when the kinase activity is not the singular action of the target protein (Burslem et al., 2019).

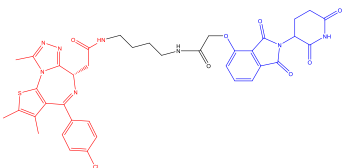
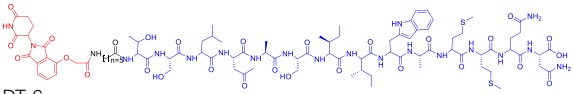
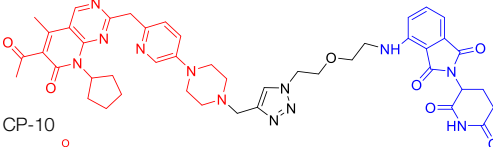
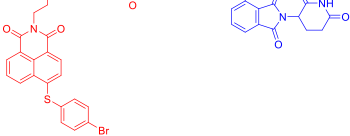
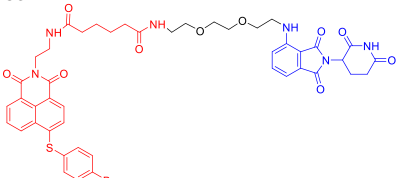
## COMPARISON AMONG PROTEOLYSIS TARGETING CHIMERICS, SMALL MOLECULE INHIBITORS AND MONOCLONAL ANTIBODIES

As two conventional treatment methods, SMIs and monoclonal antibodies (mAbs) have suffered from some inherent limitations, due to their ways of actions (Ohashi et al., 2013; Coats et al., 2019; Wolska-Washer and Robak, 2019; Lu et al., 2020). The SMIs can inhibit the biological activity of protein targets according to the action of specific active sites (Qin J. J. et al., 2017; Wang W. et al., 2019; Wang et al., 2020a). Until now, FDA has approved 62 SMIs that target about 20 different protein kinases (Roskoski, 2020). However, for most protein kinases, there is a lack of suitable active sites to target. In addition, molecule-targeted therapy is easy to induce drug resistance. All of these factors limit the development of SMIs in cancer treatment (Liu et al., 2020). mAbs are the highly uniform antibodies produced by a single B cell clone with high purity, high sensitivity, strong specificity, less cross reaction, and low cost. However, mAbs have a large molecular weight and mainly target proteins located at the plasma membrane. Besides, they need certain requirements for technology (Coats et al., 2019; Wolska-Washer and Robak, 2019).

The ligand of the target protein in PROTAC does not necessarily bind to the active site of the target protein, which overcomes the disadvantage of SMIs (Neklesa et al., 2017; Guo et al., 2019; Schapira et al., 2019). Owing to the existence of E3 ligase, PROTACs execute their functions by degrading the target proteins rather than inhibiting them, which is different from that of SMIs. Therefore, PROTAC has a great superiority in overcoming resistance caused by target mutation or overexpression when compared with SMIs. To date, PROTAC technology is applied to a variety of targets, including AR, ER, BTK, BET, and BCR-ABL to overcome resistance (Sun and Rao, 2020).

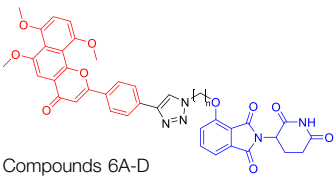
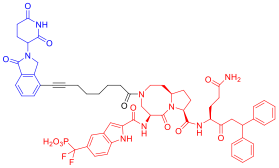
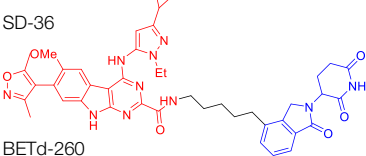
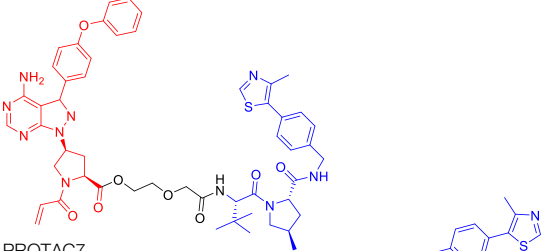
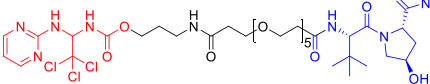
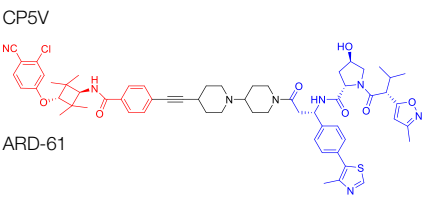
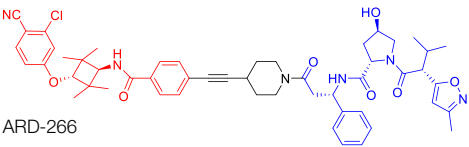
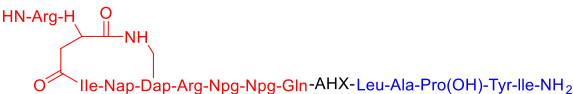


**TABLE 1 |** Representative small-molecule PROTACs under development.

PROTAC structure	Target	E3 ligase	IC <sub>50</sub> (nM)	EC <sub>50</sub> (nM)	DC <sub>50</sub> (nM)	References
 dBET1	BRD	CRBN	20	—	—	Winter et al. (2015)
 DT-6	TGF-β1	CRBN	—	—	—	Feng et al. (2020)
 CP-10	CDK6	CRBN	—	—	2.1	Su et al. (2019)
 C3	Mcl-1	CRBN	—	—	700	Wang et al. (2019b)
 C5	Bcl-2	CRBN	—	—	3,000	Wang et al. (2019b)

(Continued on following page)

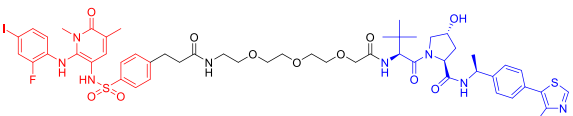
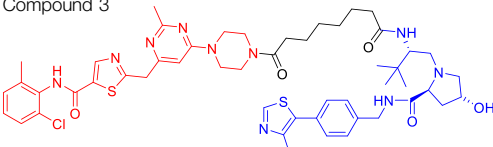
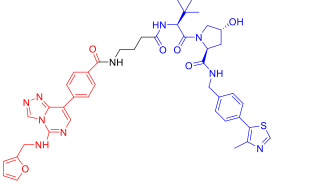
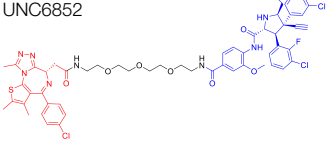
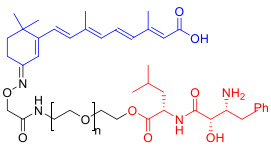
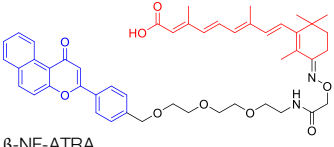
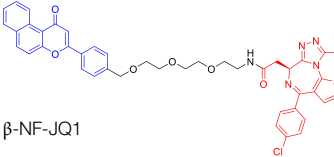
**TABLE 1 |** (Continued) Representative small-molecule PROTACs under development.

PROTAC structure	Target	E3 ligase	IC <sub>50</sub> (nM)	EC <sub>50</sub> (nM)	DC <sub>50</sub> (nM)	References
 <p>Compounds 6A-D</p>	CYP1B1	CRBN	—	—	—	Zhou et al. (2020b)
 <p>SD-36</p>	STAT3	CRBN	13	—	60	Zhou et al. (2019)
 <p>BETd-260</p>	BET	CRBN	—	1.8 1.1	—	Shi et al. (2019)
 <p>PROTAC7</p>	BTK BLK	VHL VHL	— —	— —	136 220	Wang et al. (2019b) Wang et al. (2019b)
	Cdc20	VHL	2,600 1,990	—	1,600	Chi et al. (2019)
 <p>ARD-61</p>	AR	VHL	2	—	7.2	Han et al. (2019)
 <p>ARD-266</p>	AR	VHL	2	—	0.5	Han et al. (2019)
 <p>Compound I-6</p>	ERα	VHL	9,700	—	—	Dai et al. (2020)

(Continued on following page)



**TABLE 1 |** (Continued) Representative small-molecule PROTACs under development.

PROTAC structure	Target	E3 ligase	IC <sub>50</sub> (nM)	EC <sub>50</sub> (nM)	DC <sub>50</sub> (nM)	References
 Compound 3	MEK	VHL	—	—	—	Vollmer et al. (2020)
 SIAIS178	BCR-ABL	VHL	24	—	8.5	Zhao et al. (2019)
 UNC6852	PRC2	VHL	247	—	—	Potjewyd et al. (2020)
 A1874	BRD4	MDM2	—	—	32	Hines et al. (2019)
 Compounds 4	CRABPs	clAP1	—	—	—	Itoh et al. (2010)
 β-NF-ATRA	CRABPs	AhR	—	—	—	Ohoka et al. (2019a)
 β-NF-JQ1	BRD	AhR	—	—	—	Ohoka et al. (2019a)

## DESIGN AND DEVELOPMENT OF PROTEOLYSIS TARGETING CHIMERICS

The concept of PROTAC was developed by Crews and Deshaies groups in 2001, and then it has been successfully applied to multiple targets with different subcellular localization, especially in the hijacking of cancer-related kinases (Sakamoto et al., 2001; Sakamoto et al., 2003). The team first proposed a peptide-based PROTAC-1, wherein the ligand ovalbumin binds to the target protein methionine

aminopeptidase-2 (MetAP-2), while the IκB, a phosphopeptide (DRHDpSGLDSM) is responsible for recruiting SCF<sup>β-TrCP</sup> E3 ligase to ubiquitinate MetAP-2, leading to its degradation. In addition, the Crews and Deshaies team also verified that MetAP-2 can be degraded by *Xenopus* extract through the endogenous ubiquitin-proteasome pathway (Sakamoto et al., 2001). This research has opened the door of PROTAC technology, opened up a new era different from the traditional drug treatment, and paved the way for future science (Sakamoto et al., 2001).

Although there are more than 600 E3 ligases, only a few E3 ligases can be used to degrade target proteins by present PROTAC technology, including SCF<sup>β-TrCP</sup>, VHL (Von Hippel-Lindau), MDM2 (Murine double minute 2), IAPs (inhibitor of apoptosis proteins), and CRBN (cereblon) (Zhao et al., 2019). However, with the deepening of research, more and more E3 ligases may be developed in the future to achieve the desired degradation results. In this paper, we classify PROTACs according to E3 ligase and summarize the PROTAC degradation strategies for different target proteins (Table 1).

## Cereblon-Based Proteolysis Targeting Chimerics

CRBN, a component of a cullin-RING ubiquitin ligase (CRL) complex, is the target of thalidomide (Girardini et al., 2019). After binding to CRBN, thalidomide and its analogs inhibit the activity of CRL4<sup>CRBN</sup> E3 ubiquitin ligase in human cells (Fink et al., 2018). BRD4 is a critical protein that is overexpressed in human cancer and promotes the growth and survival of cancer cells (Donati et al., 2018; Zhang F. et al., 2020). In 2015, the Bradner group has developed the first CRBN-based PROTAC, with the structure of pomalidomide capturing CRBN and BRDs inhibitor JQ1 as POI ligand. The resulting compound dBET1 has been shown to induce highly selective CRBN-dependent BET protein degradation *in vitro* and *in vivo* and delay the progression of leukemia in mice. They have demonstrated the high efficiency and specificity of dBET1 in degrading BRD family members, such as BRD2, BRD3, and BRD4, by using large-scale proteomic methods (Winter et al., 2015).

TGF-β1 is a pleiotropic cytokine and plays an important role in tumor progression (e.g., colorectal and prostate cancer). Also, it is one of the key factors of tumor cell immune escape (Sun D.-Y. et al., 2019; Dai et al., 2019). Feng's team has developed a CRBN-based PROTAC DT-6 to degrade TGF-β1. The TGF-β1 ligand is derived from its direct inhibitor P144, and CRBN is recruited by the widely used ligand thalidomide. It has been shown that DT-6 can effectively degrade TGF-β1 in cells and reduce its secretion, which is of great significance for diseases that are correlated with the TGF-β1 signaling (Feng et al., 2020).

In light of the large effect of structure on degradation efficacy, Su's team has designed a series of PROTACs with varying CDK6 targeting ligands, E3 ligases, and linkers. Considering that the terminal ligands of E3 ligase can also deeply affect the interaction angle between the target protein and the ligase, they have introduced flexible and rigid groups such as alkyl and alkyne into the ligand pomalidomide. To predict which ligase matches CDK6, they have also designed nutlin-3b, VH032, and Bestatin to recruit the E3 ligases MDM2, VHL, and cIAP, respectively. Three FDA-approved CDK4/6 inhibitors (palbociclib, ribociclib, and abemaciclib) have been selected as the binding ligands of the target protein CDK6, which have a strong binding ability to CDK6 with different terminal directions. Finally, it has been found that only CRBN-based PROTAC can degrade CDK6. PROTACs with shorter linkers have shown a higher capacity in CDK6 degradation, suggesting that these shorter molecules have better CRBN recruitment ability on CDK6 (Su et al., 2019).

There are many PROTACs that have been designed with pomalidomide as the CRBN ligand to degrade various POIs, such as MCL-1/BCL-2, BCL-xL, HDAC6, and BTK (Myeku et al., 2016; Sun et al., 2018; Wang X. et al., 2019; Chi et al., 2019; Yang et al., 2019; Xue et al., 2020). Protein-protein interaction (PPI) is involved in most cell processes, including cell differentiation, apoptosis, signal transduction, and transcription (Ryan and Matthews, 2005). Therefore, the role of PPI should not be underestimated, and it has been believed that the target of PPI is the next breakthrough point in disease treatment. Ye's team has used two different BCL-2/MCL-1 inhibitors S1-6 and Nap-1 to develop two different series of PROTACs, C3 and C5 (Wang X. et al., 2019). These PROTACs have shown strong ability in PPI target degradation with DC<sub>50</sub> (The 50% of maximum degradation) of 0.7 and 3.0 μM, respectively. This study has verified that PROTACs can extend the "target space" to the PPI target. It provides a selective chemical intervention for BCL-2 family protein in chemical biology research and drug discovery.

BTK, a non-receptor cytoplasmic tyrosine kinase, is involved in B cell receptor (BCR) signaling pathway and plays a key role in B cell lymphoma, so its degradation is particularly important (Hendriks et al., 2014). There are many reports on the degradation of BTK by PROTAC. Using CRBN as the E3 ligase, Crews's team has found that MT802 can effectively degrade BTK. It has excellent degradation characteristics *in vitro* but shows a high clearance rate and short half-life *in vivo*. They have further replaced the CRBN ligand with the VHL ligand. Unfortunately, the resulting compound have shown low degradation efficiency. Finally, the structure modification of the CRBN ligand has led to the identification of SJF620, with improved druggability compared with MT802 (Jaime-Figueroa et al., 2020).

Multiple E3 ubiquitin ligases have been selected to degrade the target proteins. Ibrutinib and PLS-123, two covalent inhibitors of BTK, have been chosen as the binding part of BTK due to the high affinity and different folding structures. CRBN and VHL have been selected as the E3 ligase, which were recruited by pomalidomide and VH032, respectively. Once irreversibly combined with target kinase, an excellent degradation efficiency has been observed in living cells (Xue et al., 2020). Different from Pan's team, CRBN and MDM2 have been selected as the E3 ligases in Rao's study (Sun et al., 2018; Xue et al., 2020). In addition to the recruitment of CRBN by pomalidomide, RG-7112 has been designed as the ligand for MDM2 recruitment and ibrutinib and spebrutinib have been selected as the BTK ligands. It has been found that CRBN is generally more effective as E3 ligase than MDM2 (Sun et al., 2018). Besides BTK, CRBN- and VHL-PROTAC can also effectively degrade EGFR, BRD4, PLK1, and CDK2 (Zhou F. et al., 2020; Zhang H. et al., 2020; Mu et al., 2020).

In addition, Li et al. have developed a PROTAC that can degrade the cell cycle kinase Wee1 and provided a new direction for targeted cancer therapy (Jaeger and Winter, 2020; Li et al., 2020). Winzker et al. have described that PDEδ-based PROTACs can effectively and selectively reduce the level of phosphodiesterase-δ (PDEδ) in cells (Winzker et al., 2020). At the same time, it has also increased the expression of various lipid-related enzymes and the level of cholesterol precursor. The results have also shown that PDEδ plays a role in the regulation of

**TABLE 2 |** PROTACs in clinical stage.

Drug	NCT numbers	Target	Lead indication	Phase	Toxicity profile	Preliminary efficacy data
ARV-110	NCT03888612	Androgen receptor	Prostate cancer	Phase 2	ARV-110 has an acceptable safety profile; however, co-administration of rosuvastatin with ARV-110 could produce toxic side effects.	Two of 15 patients had a PSA reduction of more than 50% (140 mg dose group); two of five patients (40%) with T878 or H875 mutations in AR had PSA reductions over 50%; two of 15 patients (13%) with wild-type AR also had PSA reductions over 50%
ARV-471	NCT04072952	Oestrogen receptor	Breast cancer	Phase 2	ARV-471 is well tolerated at all tested dose levels; no treatment-related grade 3 or 4 adverse events, and DLTs were reported. The most common treatment-related grade 1–2 adverse events are nausea (24%), arthralgia (19%), fatigue (19%), and decreased appetite (14%)	One patient (totally 21 adult patients) in ARV-471 trial had a 51% reduction in target lesion size (confirmed PR), two patients had unconfirmed PRs, and one additional patient showed stable disease, with a target lesion reduction of more than 50%; five of 12 patients (42%) achieved CBR
KT-474	NCT04772885	IRAK4	Autoimmune including AD, HS and RA	Phase 1	NR	NR
NX-2127	NCT04830137	BTK	B cell malignancies	Phase 1	NR	NR

NR, not reported yet (Recruiting Status).

sterol synthesis (Winzker et al., 2020). Signal transducer and activator of transcription 3 (STAT3) activation is beneficial to the survival, reproduction, metastasis, and immune escape of tumor cells (Furtek et al., 2016). STAT3 is closely related to the adverse prognosis of human cancer and has become a promising therapeutic target for cancer and other diseases. Zhou et al. have developed SD-36 as a highly selective and potent PROTAC degrader of STAT3. SD-36 can inhibit the growth of leukemia and lymphoma cell lines with highly phosphorylated STAT3 at low nanomolar concentrations *in vitro*. SD-36 can also completely and persistently regress the tumor growth in mice bearing the Molm-16 xenografts. SD-36 has been found to rapidly induce the degradation of STAT3 but has no significant effect on other STAT isoforms (Zhou et al., 2019).

Bromodomain and Extra-Terminal domain (BET) family proteins are epigenetic regulatory factors related to the expression of multiple oncogenes (Stathis and Bertonni, 2018). BETd-260 is an effective PROTAC degradation agent synthesized on the basis of BET SMIs. The *in vivo* and *in vitro* experiments have shown that it can induce a large amount of apoptosis in osteosarcoma (OS) cells and OS xenograft tumor tissues and ultimately lead to the depth and sustained inhibition of tumor growth in both mouse OS cell line-derived xenograft and patient-derived xenograft (PDX) models (Shi et al., 2019).

## Von Hippel-Lindau-Based Proteolysis Targeting Chimerics

VHL, an important tumor suppressor of clear cell renal cell carcinoma (ccRCC), is a part of the E3 ubiquitin ligase complex (Zhang et al., 2018). Its regulatory pathway involves the activity of E3 ligase, which can target hypoxia inducible factors  $\alpha$  (including HIF1 $\alpha$  and HIF2 $\alpha$ ) for proteasomal degradation (Pezzuto and Carico, 2018). Recent studies have shown that VHL possesses additional HIF-independent

functions. For example, in VHL-deficient ccRCC, the assembly of VHL-mediated intercellular junctions is achieved through HIF-independent mechanisms (Calzada et al., 2006; Zhang and Zhang, 2018). Accordingly, there are many PROTACs that use VHL as the E3 ubiquitin ligase to degrade the target protein.

Kim's team has also recruited CRBN and VHL by using pomalidomide and VH032, respectively (Kim et al., 2019). They are dedicated to knowing whether the E3 ligase itself can be ubiquitinated and degraded by another E3 ligase when two different E3 ligases are put together. Therefore, they have designed PROTACs to target CRBN or VHL itself. However, in all cases, the results have shown that the level of CRBN is decreased while the level of VHL is unchanged or increased, indicating that RPOTAC can ubiquitously degrade CRBN itself (Kim et al., 2019).

Chronic myeloid leukemia (CML) is a kind of malignant tumor that affects blood and bone marrow. It is characterized by the production of a large number of immature leukocytes to inhibit the normal hematopoiesis of bone marrow. BCR-ABL1 is a critical kinase in CML, which drives the over production and expansion of white blood cells in bone marrow and finally squeezes out normal cells in the bone marrow (Burslem et al., 2019). Crews lab has developed a series of PROTACs for BCR-ABL1 protein. They have used their previously developed E3 ligase VHL ligand to degrade the fusion protein (Buckley et al., 2012a; Buckley et al., 2012b). Their research further proves the great ability of the PROTAC technique, for it is not only a potential therapeutic method but also a tool to explore basic biology (Burslem et al., 2019).

Mitosis is the primary mechanism of cell proliferation, and thus inhibition of cancer proliferation can be achieved by blocking the process of mitosis. Cell division cycle 20 (Cdc20) is a key factor in mitosis, and targeting Cdc20 has been considered as a novel cancer therapeutic strategy (Wang et al., 2015). A PROTAC molecule named CP5V has been designed to induce the degradation of Cdc20, with PEG5 being used to connect the Cdc20 ligand and the VHL ligand. CP5V can effectively degrade

Cdc20 and eventually overcome cell division slippage, which is the main reason for drug resistance of taxane in breast cancer treatment (Chi et al., 2019).

Overexpression of anti-apoptotic proteins such as BCL-2 and BCL-XL will promote the development and progression of cancer (Singh et al., 2019). Many SMIs targeting the BCL-2 family have been developed, such as ABT263 (a BCL-2 and BCL-xL dual inhibitor) and ABT199 (a BCL-2 selective inhibitor) (Chang et al., 2016; Naqvi et al., 2017). However, ABT263 has the obvious disadvantages of on-target toxicity and dose-limiting thrombocytopenia, which greatly limits its clinical application. Although ABT199 has become the only BCL-2 family anticancer drug approved by the FDA, it cannot be used in the treatment of solid tumors because most solid tumor cells do not rely on BCL-2 expression. The shortcomings of traditional inhibitors prompted Khan's team to develop a PROTAC, DT2216, which can target BCL-xL protein degradation by the VHL E3 ligase (Khan et al., 2019). Compared with ABT263 (BCL-xL inhibitor), DT2216 not only has strong inhibitory effects on all kinds of BCL-xL-dependent leukemia and cancer cells *in vitro* but also has much less toxicity to platelets because of the poor expression of VHL in platelets. DT2216, either as a single drug or combined with other chemotherapeutic drugs, can effectively inhibit the tumor growth in several xenograft mouse models without causing significant thrombocytopenia *in vivo*. Their research has shown that DT2216 may have a great potential to replace the traditional SMIs as a safe and effective anticancer drug targeting the BCL-2 family (Khan et al., 2019).

Androgen receptor (AR) antagonists play a pivotal role in the treatment of metastatic castration-resistant prostate cancer (mCRPC), but they still face the problem of drug resistance. Using PROTAC technology, Han et al. have developed several AR degraders by using four different AR antagonists as the AR ligands, of which ARD-61 with ARI-16 as the AR ligand is the most effective one (Han et al., 2019). Compared with AR antagonists, ARD-61 has a better inhibitory effect on cancer cell proliferation and can overcome drug resistance, suggesting that PROTAC-mediated degradation of AR has great clinical potential. In addition, the team has also proved that even if the E3 ligands have a micromolar binding affinity to ubiquitin ligase E3, the obtained PROTAC products can still effectively degrade the target protein, which contributes to overwhelming the difficulty of seeking high active ligands for E3 ligands complex (Han et al., 2019).

It has been reported that polycomb repressive complex 2 (PRC2) is both a carcinogenic gene and a tumor suppressor gene (Gan et al., 2018). The catalytic activity of PRC2 depends on the embryonic ectodermal development (EED), enhancer of zeste homolog (EZH1) or EZH2, and suppressor of zeste homolog 12 (SUZ12) (Margueron and Reinberg, 2011). PRC2 is located at histone 3 lysine 27 (H3K27), and H3K27 trimethylation (H3K27me3) is the key mechanism for transcriptional repression (Ferrari et al., 2014). EZH2 is up-regulated in a variety of cancer types, such as breast, colorectal, and prostate cancer. The overexpression of EZH2 and the increase in the H3K27me3 level contribute to cancer cell proliferation and chemotherapy resistance, leading to a low survival rate in

clinical practice. EED, EZH2, and SUZ12 are also susceptible to cancer mutations. Therefore, targeting EED and EZH2 can effectively block the catalytic activity of PRC2. UNC6852 is a PROTAC designed using the EED ligand EED226. It has been shown that UNC6852 has time- and concentration-dependent inhibitory effects on EED, EZH2, and SUZ12 of PRC2 in HeLa cells in a VHL-dependent manner, with a reduced level of H3K27me3 (Potjewyd et al., 2020).

## Murine Double Minute 22-Based Proteolysis Targeting Chimerics

p53 is an indispensable tumor suppressor that regulates cell cycle, apoptosis, DNA damage repair, and other processes (Qin J.-J. et al., 2017; Qin et al., 2018). MDM2 is one of the main inhibitors of p53; it can bind to p53 through its N-terminal domain (region I) to form the MDM2-p53 complex and reduce the activity and level of p53 (Hou et al., 2019; Wang et al., 2020a). MDM2 gene exists in the cell genome of human malignant tumors such as lung and colon cancer (Mendoza et al., 2014). Overexpressed MDM2 can be detected in many malignant tumors, so MDM2 has become an effective target for the development of anticancer drugs (Nag et al., 2013). With the emergence of PROTAC, MDM2 has also been developed as an E3 ligase to degrade AR (Sun X. et al., 2019) and BRD4 (Groppe, 2019). Nutlin-3a and Idasanutlin are usually selected as the E3 ligase ligands. Although nutlin-3a specifically binds to MDM2 with a high binding affinity, there are few PROTACs that are designed and developed based on nutlin-3a. A1874, a BRD4 PROTAC based on nutlin-3a, degraded 98% of its target protein at nanomolar concentrations and activated the p53 signaling pathway. This study has also shown that for the same target protein (e.g., BRD4), MDM2-based PROTAC has a better degrading effect than CRBN-based PROTAC (provided that in the context of wild-type p53) (Hines et al., 2019).

## Inhibitor of Apoptosis Proteins-Based Proteolysis Targeting Chimerics

Available data have confirmed that IAPs are involved in cancer and other human diseases and have been considered as a potential target for cancer treatment (LaCasse et al., 2008). Mammalian IAP protein family includes at least 8 members, among which cIAP1 and cIAP2 function as E3 ubiquitin ligases to mediate the ubiquitination of target proteins (Fulda, 2017). In 2010, Hashimoto's team has hijacked cIAP1-E3 ligase using bestatin-methyl ester MeBS and used all-trans retinoic acid (ATRA) as a warhead to develop the first cIAP1-based PROTAC (compounds 4) to degrade cellular retinoic acid binding protein (CRABP-I/-II) (Itoh et al., 2010). Compounds 4 has been shown to induce the selective loss of CRABP-I and -II proteins in cells in a concentration-dependent manner. With the deepening of research, more and more IAP1-based PROTACs have been developed. Interestingly, unlike other PROTACs, IAP-based PROTACs have dual functions of degradation of POI and IAP, which is beneficial to the anti-tumor function and also suggests that it should be careful in design to avoid unexpected side effects (Ohoka et al., 2019b; Liu et al., 2020).



## CLINICAL RESEARCH ON PROTEOLYSIS TARGETING CHIMERICS

Currently, several PROTACs have entered clinical trials (Table 2), and some of them have shown encouraging results, such as ARV-110 and ARV-471. ARV-110, an oral protein degradation agent, binds AR specifically and mediates its degradation (Neklesa et al., 2018). ARV-110 completely degraded AR ( $DC_{50} < 1$  nM) in all tested cell lines (Neklesa et al., 2019) and Oral ARV-110 (10 mg/kg) significantly inhibited the growth of enzalutamide-insensitive tumors in the PDX model (Wang et al., 2020b). ARV-110 degrades clinically relevant mutant AR proteins and retains activity in a hyperandrogen environment. The early reported data (by January 2020) from the first-in-human, phase I study of ARV-110 demonstrated its safety and tolerability in patients with metastatic castrate-resistant prostate cancer (mCRPC) (Petrylak et al., 2020). ARV-110 was administered to 18 patients at four doses, including 35 mg ( $N = 3$ ), 70 mg ( $N = 4$ ), 140 mg ( $N = 8$ ) and 280 mg ( $N = 3$ ). Among them, 12 patients received ARV-110 combined with enzalutamide (ENZ)/abiraterone (ABI), and 14 patients received prior chemotherapy. One patient administered ARV-110 280 mg experienced Grade (GR) 4 elevated AST/ALT followed by an acute renal failure while taking together with rosuvastatin (ROS). Similarly, another patient developed GR3 AST/ALT while taking ROS. Their plasma concentrations of ROS were increased accompanied by AST/ALT elevations, suggesting that concurrent ROS could produce toxic side effects. For other patients, no related GR 3/4 adverse events were reported. Generally, ARV-110 possesses an acceptable safety profile. 15 of 18 patients were evaluable for prostate specific antigen (PSA) response. Of these, two patients had a PSA reduction of more than 50% (140 mg dose group), and both of them received prior therapy including ENZ and ABI, chemotherapy, bicalutamide, radium-223 and others.

According to the recent interim clinical data released by Arvinas (<https://ir.arvinas.com/>), in the phase I clinical trial, ARV-110 shows promising activity in a very late-line mCRPC patients, with PSA reductions over 50% at doses greater than 280 mg. Previous studies have shown that multiple pre-treatments will lead to tumor resistance to targeted AR therapy, and improve the heterogeneity of tumor, resulting in a decreased efficacy of AR targeted therapy. Molecular biological analysis of patients treated with ARV-110 showed that 84% of patients carried non-AR gene mutations. Among the highly heterogeneous phase I patients, Arvinas has identified an advanced population with a molecular definition that has a particularly strong response to ARV-110. Of the five patients with T878 or H875 mutations in AR, two (40%) had a PSA reduction of more than 50%, including one with PR confirmed by RECIST and tumor size reduction of 80%. Additionally, two of 15 patients (13%) with wild-type AR also had PSA reductions over 50%. These results suggest ARV-110 has great potentials in molecularly defined population (T878/H875) and in wild-type patients.

ARV-471 is an estrogen receptor (ER) alpha PROTAC molecule that degrades ER in ER-positive breast cancer cell

lines with  $DC_{50}$  around 1 nM. It can decrease the expression of classically regulated ER-target genes and suppress the growth of ER-dependent cell lines (including cell lines expressing ESR1 variants such as Y537S and D538G) via degradation of ER. Oral administration of single agent ARV-471 (3, 10, and 30 mpk/day) shows significant anti-tumor activity in estradiol-dependent MCF7 xenografts along with ER protein reductions of over 90%. Excitingly, more pronounced tumor growth inhibition is observed (131% TGI) in the MCF7 xenograft model, accompanied by significant reductions in ER protein levels when combined with a CDK4/6 inhibitor palbociclib. Furthermore, the combination of ARV-471 and CDK4/6 inhibitor palbociclib showed great superiority over the combination of fulvestrant with palbociclib in tumor regressions. Also, ARV-471 (10 mpk) completely inhibited growth and markedly reduced mutant ER protein levels in ESR1 mutant hormone-independent PDX model (Flanagan et al., 2019). These promising results translate well into clinical trials. Recently, Arvinas has also announced ARV-471 for the treatment of locally advanced or metastatic ER-positive/HER2-negative breast cancer, and its phase I clinical trials have started in the second half of 2019 (<https://ir.arvinas.com/>). Analysis of the mid-term trial showed that ARV-471 could significantly reduce ER expression level in tumor tissues, with an average of 62% and a maximum of 90%. Moreover, ARV-471 could degrade both wild-type ER and mutant ER. According to the RECIST evaluation, one patient (a total of 21 adult patients) in the ARV-471 trial had a 51% reduction in target lesion size (confirmed PR), two patients had unconfirmed PRs, and one additional patient showed stable disease, with a target lesion reduction of more than 50%. In the clinical benefit rate (CBR) evaluation, five of the 12 patients (42%) achieved CBR (defined as PRS + complete response + stable disease at 6 months).

## CONCLUSION AND PERSPECTIVES

Different from the traditional SMIs, PROTAC is a new strategy of inducing the ubiquitination degradation of target proteins. However, it is worth noting that up to now, less than 10 of more than 600 E3 ubiquitin ligases have been used to degrade target proteins, which reminds scholars to expand their knowledge in this area.

Although the PROTAC technology has made remarkable achievements since its development in 2001, there are still some problems in the process of design and application of PROTAC. For example, the effectiveness of PROTAC depends not only on the ligands of POIs and E3 ligases but also on the length and chemical properties of the linkers connecting the ligands. In addition, the binding strength of ligands, spatial orientation, cell permeability, and other factors will have important impacts on the efficacy of PROTACs. Therefore, how these factors work together to achieve the highest efficiency is a major scientific problem to be addressed. Although the PROTACs can target protein for degradation, it cannot actively locate at the target tumor tissue and may have the off-target effects. Therefore, the safety is another challenge for

PROTACs that should be taken into account. Considering the different expression of E3 ligase at different time and in different tissues, high selectivity can be achieved through tissue-specific E3 protein. After the completion of the theoretical design, several rounds of experiments are needed to optimize the structures of PROTACs and finally locate the ligands of the POIs and the E3 ligases into an appropriate spatial structure to form ternary degradation complex. It takes much time and manpower, so the application of new design strategies or technologies (e.g., CADD and AI) has a huge importance in rational design of PROTACs.

One of the biggest advantages of PROTAC technology is its great potential to target “undruggable” proteins. Because small molecule ligands can well bind to the target proteins, most of the successful PROTACs currently use SMIs as ligands to target druggable proteins. Additionally, studies by ARV-471 have clearly shown that PROTAC could produce a synergistic effect on tumor inhibition when combined with kinase inhibitors including CDK4/6 inhibitors. It suggests that combination of PROTAC either with targeted inhibitors or with chemotherapy/antibody drugs may represent a good alternative strategy for cancer therapy. It is believed that it will open up a broad road for the development of PROTAC technology and the discovery of new anticancer drugs once these problems mentioned above are solved.

## REFERENCES

- Buckley, D. L., Gustafson, J. L., Van Molle, I., Roth, A. G., Tae, H. S., Gareiss, P. C., et al. (2012a). Small-Molecule Inhibitors of the Interaction between the E3 Ligase VHL and HIF1 $\alpha$ . *Angew. Chem. Int. Ed.* 51, 11463–11467. doi:10.1002/anie.201206231
- Buckley, D. L., Van Molle, I., Gareiss, P. C., Tae, H. S., Michel, J., Noblin, D. J., et al. (2012b). Targeting the von Hippel-Lindau E3 Ubiquitin Ligase Using Small Molecules To Disrupt the VHL/HIF-1 $\alpha$  Interaction. *J. Am. Chem. Soc.* 134, 4465–4468. doi:10.1021/ja209924v
- Buckley, D. L., Raina, K., Darricarrere, N., Hines, J., Gustafson, J. L., Smith, I. E., et al. (2015). HaloPROTACS: Use of Small Molecule PROTACs to Induce Degradation of HaloTag Fusion Proteins. *ACS Chem. Biol.* 10, 1831–1837. doi:10.1021/acscchembio.5b00442
- Burslem, G. M., Schultz, A. R., Bondeson, D. P., Eide, C. A., Savage Stevens, S. L., Druker, B. J., et al. (2019). Targeting BCR-ABL1 in Chronic Myeloid Leukemia by PROTAC-Mediated Targeted Protein Degradation. *Cancer Res.* 79, 4744–4753. doi:10.1158/0008-5472.can-19-1236
- Calzada, M. J., Esteban, M. A., Feijoo-Cuaresma, M., Castellanos, M. C., Naranjo-Suárez, S., Temes, E., et al. (2006). von Hippel-Lindau tumor suppressor protein regulates the assembly of intercellular junctions in renal cancer cells through hypoxia-inducible factor-independent mechanisms. *Cancer Res.* 66, 1553–1560. doi:10.1158/0008-5472.can-05-3236
- Chang, J., Wang, Y., Shao, L., Laberge, R.-M., Demaria, M., Campisi, J., et al. (2016). Clearance of Senescent Cells by ABT263 Rejuvenates Aged Hematopoietic Stem Cells in Mice. *Nat. Med.* 22, 78–83. doi:10.1038/nm.4010
- Chi, J., Li, H., Zhou, Z., Izquierdo-Ferrer, J., Xue, Y., Wavelet, C. M., et al. (2019). A Novel Strategy to Block Mitotic Progression for Targeted Therapy. *EBioMedicine*. 49, 40–54. doi:10.1016/j.ebiom.2019.10.013
- Coats, S., Williams, M., Keble, B., Dixit, R., Tseng, L., Yao, N.-S., et al. (2019). Antibody-Drug Conjugates: Future Directions in Clinical and Translational Strategies to Improve the Therapeutic Index. *Clin. Cancer Res.* 25, 5441–5448. doi:10.1158/1078-0432.ccr-19-0272
- Cyrus, K., Wehenkel, M., Choi, E.-Y., Han, H.-J., Lee, H., Swanson, H., et al. (2011). Impact of Linker Length on the Activity of PROTACs. *Mol. Biosyst.* 7, 359–364. doi:10.1039/c0mb00074d
- Dai, G., Sun, B., Gong, T., Pan, Z., Meng, Q., and Ju, W. (2019). Ginsenoside Rb2 Inhibits Epithelial-Mesenchymal Transition of Colorectal Cancer Cells by Suppressing TGF- $\beta$ /Smad Signaling. *Phytomedicine*. 56, 126–135. doi:10.1016/j.phymed.2018.10.025
- Dai, Y., Yue, N., Gong, J., Liu, C., Li, Q., Zhou, J., et al. (2020). Development of Cell-Permeable Peptide-Based PROTACs Targeting Estrogen Receptor  $\alpha$ . *Eur. J. Med. Chem.* 187, 111967. doi:10.1016/j.ejmech.2019.111967
- Donati, B., Lorenzini, E., and Ciarrocchi, A. (2018). BRD4 and Cancer: Going beyond Transcriptional Regulation. *Mol. Cancer*. 17, 164. doi:10.1186/s12943-018-0915-9
- Dong, J., Qin, Z., Zhang, W.-D., Cheng, G., Yehuda, A. G., Ashby, C. R., Jr., et al. (2020). Medicinal Chemistry Strategies to Discover P-Glycoprotein Inhibitors: An Update. *Drug Resist. Updates*. 49, 100681. doi:10.1016/j.drup.2020.100681
- Dong, J., Zhang, Q., Wang, Z., Huang, G., and Li, S. (2018). Recent Advances in the Development of Indazole-Based Anticancer Agents. *ChemMedChem*. 13, 1490–1507. doi:10.1002/cmdc.201800253
- Feng, Y., Su, H., Li, Y., Luo, C., Xu, H., Wang, Y., et al. (2020). Degradation of Intracellular TGF- $\beta$ 1 by PROTACs Efficiently Reverses M2 Macrophage Induced Malignant Pathological Events. *Chem. Commun.* 56, 2881–2884. doi:10.1039/c9cc08391j
- Ferrari, K. J., Scelfo, A., Jammula, S., Cuomo, A., Barozzi, I., Stützer, A., et al. (2014). Polycomb-dependent H3K27me1 and H3K27me2 Regulate Active Transcription and Enhancer Fidelity. *Mol. Cell*. 53, 49–62. doi:10.1016/j.molcel.2013.10.030
- Fink, E. C., Mcconkey, M., Adams, D. N., Haldar, S. D., Kennedy, J. A., Guirguis, A. A., et al. (2018). Crbn I391V Is Sufficient to Confer In Vivo Sensitivity to Thalidomide and its Derivatives in Mice. *Blood*. 132, 1535–1544. doi:10.1182/blood-2018-05-852798
- Flanagan, J., Qian, Y., Gough, S., Andreoli, M., Bookbinder, M., Cadelina, G., et al. (2019). Abstract P5-04-18: ARV-471, an Oral Estrogen Receptor PROTAC Degradar for Breast Cancer. *Cancer Res.* 79, P5-P04-18. doi:10.1158/1538-7445.SABCS18-P5-04-18

## AUTHOR CONTRIBUTIONS

J-JQ, X-DC, and W-DZ conceptualized the manuscript. S-MQ, JD, Z-YX, X-DC, W-DZ, and J-JQ collected the literature, wrote the manuscript, and made the figures. J-JQ edited and made significant revisions to the manuscript. All authors read and approved the final manuscript.

## FUNDING

This work was supported by grants from Zhejiang Provincial Natural Science Foundation of China (LQ21B020003, LR21H280001), Program of Zhejiang Provincial TCM Sci-tech Plan (2020ZZ005), and National Natural Science Foundation of China (81903842).

## ACKNOWLEDGMENTS

We thank the current and former members of our laboratories and collaborators for their contributions to the publications cited in this review article. The research field in PROTAC is rapidly growing, and we apologize for not being able to cite all the recent publications, due to space limitation.

- Fulda, S. (2017). Smac Mimetics to Therapeutically Target IAP Proteins in Cancer. *Int. Rev. Cel Mol Biol.* 330, 157–169. doi:10.1016/bs.ircmb.2016.09.004
- Furtek, S. L., Backos, D. S., Matheson, C. J., and Reigan, P. (2016). Strategies and Approaches of Targeting STAT3 for Cancer Treatment. *ACS Chem. Biol.* 11, 308–318. doi:10.1021/acscchembio.5b00945
- Gan, L., Yang, Y., Li, Q., Feng, Y., Liu, T., and Guo, W. (2018). Epigenetic Regulation of Cancer Progression by EZH2: from Biological Insights to Therapeutic Potential. *Biomark Res.* 6, 10. doi:10.1186/s40364-018-0122-2
- Girardini, M., Maniaci, C., Hughes, S. J., Testa, A., and Ciulli, A. (2019). Cereblon versus VHL: Hijacking E3 Ligases against Each Other Using PROTACs. *Bioorg. Med. Chem.* 27, 2466–2479. doi:10.1016/j.bmc.2019.02.048
- Groppe, J. C. (2019). Induced Degradation of Protein Kinases by Bifunctional Small Molecules: a Next-Generation Strategy. *Expert Opin. Drug Discov.* 14, 1237–1253. doi:10.1080/17460441.2019.1660641
- Guo, J., Liu, J., and Wei, W. (2019). Degrading Proteins in Animals: “PROTAC”tion Goes In Vivo. *Cell Res.* 29, 179–180. doi:10.1038/s41422-019-0144-9
- Han, X., Zhao, L., Xiang, W., Qin, C., Miao, B., Xu, T., et al. (2019). Discovery of Highly Potent and Efficient PROTAC Degraders of Androgen Receptor (AR) by Employing Weak Binding Affinity VHL E3 Ligase Ligands. *J. Med. Chem.* 62, 11218–11231. doi:10.1021/acs.jmedchem.9b01393
- Hendriks, R. W., Yuvaraj, S., and Kil, L. P. (2014). Targeting Bruton’s Tyrosine Kinase in B Cell Malignancies. *Nat. Rev. Cancer.* 14, 219–232. doi:10.1038/nrc3702
- Hines, J., Lartigue, S., Dong, H., Qian, Y., and Crews, C. M. (2019). MDM2-Recruiting PROTAC Offers Superior, Synergistic Antiproliferative Activity via Simultaneous Degradation of BRD4 and Stabilization of P53. *Cancer Res.* 79, 251–262. doi:10.1158/0008-5472.can-18-2918
- Hou, H., Sun, D., and Zhang, X. (2019). The Role of MDM2 Amplification and Overexpression in Therapeutic Resistance of Malignant Tumors. *Cancer Cel Int.* 19, 216. doi:10.1186/s12935-019-0937-4
- Itoh, Y., Ishikawa, M., Naito, M., and Hashimoto, Y. (2010). Protein Knockdown Using Methyl Bestatin–Ligand Hybrid Molecules: Design and Synthesis of Inducers of Ubiquitination-Mediated Degradation of Cellular Retinoic Acid-Binding Proteins. *J. Am. Chem. Soc.* 132, 5820–5826. doi:10.1021/ja100691p
- Jaeger, M. G., and Winter, G. E. (2020). Expanding the Degradable Proteome: Designing PROTACs by the Book. *Cel Chem. Biol.* 27, 14–16. doi:10.1016/j.chembiol.2019.12.009
- Jaime-Figueroa, S., Buhimschi, A. D., Toure, M., Hines, J., and Crews, C. M. (2020). Design, Synthesis and Biological Evaluation of Proteolysis Targeting Chimeras (PROTACs) as a BTK Degraders with Improved Pharmacokinetic Properties. *Bioorg. Med. Chem. Lett.* 30, 126877. doi:10.1016/j.bmlc.2019.126877
- Khan, S., Zhang, X., Lv, D., Zhang, Q., He, Y., Zhang, P., et al. (2019). A Selective BCL-XL PROTAC Degradator Achieves Safe and Potent Antitumor Activity. *Nat. Med.* 25, 1938–1947. doi:10.1038/s41591-019-0668-z
- Kim, K., Lee, D. H., Park, S., Jo, S. H., Ku, B., Park, S. G., et al. (2019). Disordered Region of Cereblon Is Required for Efficient Degradation by Proteolysis-Targeting Chimera. *Sci. Rep.* 9, 19654. doi:10.1038/s41598-019-56177-5
- Kregel, S., Wang, C., Han, X., Xiao, L., Fernandez-Salas, E., Bawa, P., et al. (2020). Androgen Receptor Degraders Overcome Common Resistance Mechanisms Developed during Prostate Cancer Treatment. *Neoplasia.* 22, 111–119. doi:10.1016/j.neo.2019.12.003
- Lacasse, E. C., Mahoney, D. J., Cheung, H. H., Plenchette, S., Baird, S., and Korneluk, R. G. (2008). IAP-targeted Therapies for Cancer. *Oncogene.* 27, 6252–6275. doi:10.1038/onc.2008.302
- Li, Z., Pinch, B. J., Olson, C. M., Donovan, K. A., Nowak, R. P., Mills, C. E., et al. (2020). Development and Characterization of a Wee1 Kinase Degradator. *Cel Chem. Biol.* 27, 57–65. doi:10.1016/j.chembiol.2019.10.013
- Liu, J., Ma, J., Liu, Y., Xia, J., Li, Y., Wang, Z. P., et al. (2020). PROTACs: A Novel Strategy for Cancer Therapy. *Semin. Cancer Biol.* 67, 171–179. doi:10.1016/j.semcancer.2020.02.006
- Lu, X., Smail, J. B., and Ding, K. (2020). New Promise and Opportunities for Allosteric Kinase Inhibitors. *Angew. Chem. Int. Ed.* 59, 13764–13776. doi:10.1002/anie.201914525
- Mangal, S., Gao, W., Li, T., and Zhou, Q. (2017). Pulmonary Delivery of Nanoparticle Chemotherapy for the Treatment of Lung Cancers: Challenges and Opportunities. *Acta Pharmacol. Sin.* 38, 782–797. doi:10.1038/aps.2017.34
- Margueron, R., and Reinberg, D. (2011). The Polycomb Complex PRC2 and its Mark in Life. *Nature.* 469, 343–349. doi:10.1038/nature09784
- Mendoza, M., Mandani, G., and Momand, J. (2014). The MDM2 Gene Family. *Biomol. Concepts.* 5, 9–19. doi:10.1515/bmc-2013-0027
- Mu, X., Bai, L., Xu, Y., Wang, J., and Lu, H. (2020). Protein Targeting Chimeric Molecules Specific for Dual Bromodomain 4 (BRD4) and Polo-like Kinase 1 (PLK1) Proteins in Acute Myeloid Leukemia Cells. *Biochem. Biophysical Res. Commun.* 521, 833–839. doi:10.1016/j.bbrc.2019.11.007
- Myeku, N., Clelland, C. L., Emrani, S., Kukushkin, N. V., Yu, W. H., Goldberg, A. L., et al. (2016). Tau-driven 26S Proteasome Impairment and Cognitive Dysfunction Can Be Prevented Early in Disease by Activating cAMP-PKA Signaling. *Nat. Med.* 22, 46–53. doi:10.1038/nm.4011
- Nag, S., Qin, J., Srivenugopal, K. S., Wang, M., and Zhang, R. (2013). The MDM2-P53 Pathway Revisited. *J. Biomed. Res.* 27, 254–271. doi:10.7555/JBR.27.20130030
- Nam, T., Han, J. H., Devkota, S., and Lee, H. W. (2017). Emerging Paradigm of Crosstalk between Autophagy and the Ubiquitin-Proteasome System. *Mol. Cell.* 40, 897–905. doi:10.14348/molcells.2017.0226
- Nandi, D., Tahiliani, P., Kumar, A., and Chandu, D. (2006). The Ubiquitin-Proteasome System. *J. Biosci.* 31, 137–155. doi:10.1007/bf02705243
- Naqvi, K., Konopleva, M., and Ravandi, F. (2017). Targeted Therapies in Acute Myeloid Leukemia: a Focus on FLT-3 Inhibitors and ABT199. *Expert Rev. Hematol.* 10, 863–874. doi:10.1080/17474086.2017.1366852
- Neklesa, T. K., Winkler, J. D., and Crews, C. M. (2017). Targeted Protein Degradation by PROTACs. *Pharmacol. Ther.* 174, 138–144. doi:10.1016/j.pharmthera.2017.02.027
- Neklesa, T., Snyder, L. B., Willard, R. R., Vitale, N., Pizzano, J., Gordon, D. A., et al. (2019). ARV-110: An Oral Androgen Receptor PROTAC Degradator for Prostate Cancer. *J. Clin. Oncol.* 37, 259. doi:10.1200/jco.2019.37.7\_suppl.259
- Neklesa, T., Snyder, L. B., Willard, R. R., Vitale, N., Raina, K., Pizzano, J., et al. (2018). Abstract 5236: ARV-110: An Androgen Receptor PROTAC Degradator for Prostate Cancer. *Cancer Res.* 78, 5236. doi:10.1158/1538-7445.AM2018-5236
- Ohashi, K., Maruvka, Y. E., Michor, F., and Pao, W. (2013). Epidermal Growth Factor Receptor Tyrosine Kinase Inhibitor-Resistant Disease. *J. Clin. Oncol.* 31, 1070–1080. doi:10.1200/jco.2012.43.3912
- Ohoka, N., Tsuji, G., Shoda, T., Fujisato, T., Kurihara, M., Demizu, Y., et al. (2019a). Development of Small Molecule Chimeras that Recruit AhR E3 Ligase to Target Proteins. *ACS Chem. Biol.* 14, 2822–2832. doi:10.1021/acscchembio.9b00704
- Ohoka, N., Ujikawa, O., Shimokawa, K., Sameshima, T., Shibata, N., Hattori, T., et al. (2019b). Different Degradation Mechanisms of Inhibitor of Apoptosis Proteins (IAPs) by the Specific and Nongenetic IAP-dependent Protein Eraser (SNIPER). *Chem. Pharm. Bull.* 67, 203–209. doi:10.1248/cpb.c18-00567
- Petrylak, D. P., Gao, X., Vogelzang, N. J., Garfield, M. H., Taylor, I., Dougan Moore, M., et al. (2020). First-in-human Phase I Study of ARV-110, an Androgen Receptor (AR) PROTAC Degradator in Patients (Pts) with Metastatic Castrate-Resistant Prostate Cancer (mCRPC) Following Enzalutamide (ENZ) And/or Abiraterone (ABI). *J. Clin. Oncol.* 38, 3500. doi:10.1200/jco.2020.38.15\_suppl.3500
- Pezzuto, A., and Carico, E. (2018). Role of HIF-1 in Cancer Progression: Novel Insights. A Review. *Curr. Mol. Med.* 18, 343–351. doi:10.2174/1566524018666181109121849
- Potjewyd, F., Turner, A.-M. W., Beri, J., Rectenwald, J. M., Norris-Drouin, J. L., Cholensky, S. H., et al. (2020). Degradation of Polycomb Repressive Complex 2 with an EED-Targeted Bivalent Chemical Degradator. *Cel Chem. Biol.* 27, 47–56. doi:10.1016/j.chembiol.2019.11.006
- Qi, S. M., Cheng, G., Cheng, X. D., Xu, Z., Xu, B., Zhang, W. D., et al. (2020). Targeting USP7-Mediated Deubiquitination of MDM2/MDMX-P53 Pathway for Cancer Therapy: Are We There yet?. *Front Cel Dev Biol.* 8, 233. doi:10.3389/fcell.2020.00233

- Qin, J. J., Li, X., Wang, W., Zi, X., and Zhang, R. (2017). Targeting the NFAT1-MDM2-MDMX Network Inhibits the Proliferation and Invasion of Prostate Cancer Cells, Independent of P53 and Androgen. *Front. Pharmacol.* 8, 917. doi:10.3389/fphar.2017.00917
- Qin, J.-J., Wang, W., and Zhang, R. (2017). Experimental Therapy of Advanced Breast Cancer: Targeting NFAT1-MDM2-P53 Pathway. *Prog. Mol. Biol. Transl. Sci.* 151, 195–216. doi:10.1016/bs.pmbts.2017.07.005
- Qin, J.-J., Li, X., Hunt, C., Wang, W., Wang, H., and Zhang, R. (2018). Natural Products Targeting the P53-MDM2 Pathway and Mutant P53: Recent Advances and Implications in Cancer Medicine. *Genes Dis.* 5, 204–219. doi:10.1016/j.gendis.2018.07.002
- Roskoski, R., Jr. (2020). Properties of FDA-Approved Small Molecule Protein Kinase Inhibitors: A 2020 Update. *Pharmacol. Res.* 152, 104609. doi:10.1016/j.phrs.2019.104609
- Ryan, D., and Matthews, J. (2005). Protein-protein Interactions in Human Disease. *Curr. Opin. Struct. Biol.* 15, 441–446. doi:10.1016/j.sbi.2005.06.001
- Sakamoto, K. M., Kim, K. B., Kumagai, A., Mercurio, F., Crews, C. M., and Deshaies, R. J. (2001). Protacs: Chimeric Molecules that Target Proteins to the Skp1-Cullin-F Box Complex for Ubiquitination and Degradation. *Proc. Natl. Acad. Sci.* 98, 8554–8559. doi:10.1073/pnas.141230798
- Sakamoto, K. M., Kim, K. B., Verma, R., Ransick, A., Stein, B., Crews, C. M., et al. (2003). Development of Protacs to Target Cancer-Promoting Proteins for Ubiquitination and Degradation. *Mol. Cell Proteomics.* 2, 1350–1358. doi:10.1074/mcp.t300009-mcp200
- Schapiro, M., Calabrese, M. F., Bullock, A. N., and Crews, C. M. (2019). Targeted Protein Degradation: Expanding the Toolbox. *Nat. Rev. Drug Discov.* 18, 949–963. doi:10.1038/s41573-019-0047-y
- Shi, C., Zhang, H., Wang, P., Wang, K., Xu, D., Wang, H., et al. (2019). PROTAC Induced-BET Protein Degradation Exhibits Potent Anti-osteosarcoma Activity by Triggering Apoptosis. *Cell Death Dis.* 10, 815. doi:10.1038/s41419-019-2022-2
- Singh, R., Letai, A., and Sarosiek, K. (2019). Regulation of Apoptosis in Health and Disease: the Balancing Act of BCL-2 Family Proteins. *Nat. Rev. Mol. Cell Biol.* 20, 175–193. doi:10.1038/s41580-018-0089-8
- Stathis, A., and Bertoni, F. (2018). BET Proteins as Targets for Anticancer Treatment. *Cancer Discov.* 8, 24–36. doi:10.1158/2159-8290.cd-17-0605
- Su, S., Yang, Z., Gao, H., Yang, H., Zhu, S., An, Z., et al. (2019). Potent and Preferential Degradation of CDK6 via Proteolysis Targeting Chimera Degraders. *J. Med. Chem.* 62, 7575–7582. doi:10.1021/acs.jmedchem.9b00871
- Sun, D. Y., Wu, J.-Q., He, Z.-H., He, M.-F., and Sun, H.-B. (2019). Cancer-associated Fibroblast Regulate Proliferation and Migration of Prostate Cancer Cells through TGF- $\beta$  Signaling Pathway. *Life Sci.* 235, 116791. doi:10.1016/j.lfs.2019.116791
- Sun, X., Gao, H., Yang, Y., He, M., Wu, Y., Song, Y., et al. (2019). PROTACs: Great Opportunities for Academia and Industry. *Signal. Transduct. Target. Ther.* 4, 64. doi:10.1038/s41392-019-0101-6
- Sun, X., and Rao, Y. (2020). PROTACs as Potential Therapeutic Agents for Cancer Drug Resistance. *Biochemistry.* 59, 240–249. doi:10.1021/acs.biochem.9b00848
- Sun, Y., Zhao, X., Ding, N., Gao, H., Wu, Y., Yang, Y., et al. (2018). PROTAC-induced BTK Degradation as a Novel Therapy for Mutated BTK C481S Induced Ibrutinib-Resistant B-Cell Malignancies. *Cel Res.* 28, 779–781. doi:10.1038/s41422-018-0055-1
- Toure, M., and Crews, C. M. (2016). Small-Molecule PROTACs: New Approaches to Protein Degradation. *Angew. Chem. Int. Ed.* 55, 1966–1973. doi:10.1002/anie.201507978
- Vollmer, S., Cunoosamy, D., Lv, H., Feng, H., Li, X., Nan, Z., et al. (2020). Design, Synthesis, and Biological Evaluation of MEK PROTACs. *J. Med. Chem.* 63, 157–162. doi:10.1021/acs.jmedchem.9b00810
- Wang, L., Zhang, J., Wan, L., Zhou, X., Wang, Z., and Wei, W. (2015). Targeting Cdc20 as a Novel Cancer Therapeutic Strategy. *Pharmacol. Ther.* 151, 141–151. doi:10.1016/j.pharmthera.2015.04.002
- Wang, W., Cheng, J.-W., Qin, J.-J., Hu, B., Li, X., Nijampatnam, B., et al. (2019). MDM2-NFAT1 Dual Inhibitor, MA242: Effective against Hepatocellular Carcinoma, Independent of P53. *Cancer Lett.* 459, 156–167. doi:10.1016/j.canlet.2019.114429
- Wang, X., He, Q., Wu, K., Guo, T., Du, X., Zhang, H., et al. (2019). Design, Synthesis and Activity of Novel 2,6-disubstituted Purine Derivatives, Potential Small Molecule Inhibitors of Signal Transducer and Activator of Transcription 3. *Eur. J. Med. Chem.* 179, 218–232. doi:10.1016/j.ejmech.2019.06.017
- Wang, W., Qin, J. J., Rajaei, M., Li, X., Yu, X., Hunt, C., et al. (2020a). Targeting MDM2 for Novel Molecular Therapy: Beyond Oncology. *Med. Res. Rev.* 40, 856–880. doi:10.1002/med.21637
- Wang, W., Yang, J., Liao, Y.-Y., Cheng, G., Chen, J., Mo, S., et al. (2020b). Aspetereurone A, a Cytotoxic Dihydrobenzofuran-Phenyl Acrylate Hybrid from the Deep-Sea-Derived Fungus *Aspergillus terreus* CC-S06-18. *J. Nat. Prod.* 83, 1998–2003. doi:10.1021/acs.jnatprod.0c00189
- Winter, G. E., Buckley, D. L., Paulk, J., Roberts, J. M., Souza, A., Dhe-Paganon, S., et al. (2015). Phthalimide Conjugation as a Strategy for In Vivo Target Protein Degradation. *Science.* 348, 1376–1381. doi:10.1126/science.aab1433
- Winzler, M., Friese, A., Koch, U., Janning, P., Ziegler, S., and Waldmann, H. (2020). Development of a PDE $\delta$ -Targeting PROTACs that Impair Lipid Metabolism. *Angew. Chem. Int. Ed.* 59, 5595–5601. doi:10.1002/anie.201913904
- Wolska-Wascher, A., and Robak, T. (2019). Safety and Tolerability of Antibody-Drug Conjugates in Cancer. *Drug Saf.* 42, 295–314. doi:10.1007/s40264-018-0775-7
- Wu, P., Nielsen, T. E., and Clausen, M. H. (2015). FDA-approved Small-Molecule Kinase Inhibitors. *Trends Pharmacol. Sci.* 36, 422–439. doi:10.1016/j.tips.2015.04.005
- Xu, J. L., Yuan, L., Tang, Y. C., Xu, Z. Y., Xu, H. D., Cheng, X. D., et al. (2020). The Role of Autophagy in Gastric Cancer Chemoresistance: Friend or Foe?. *Front. Cell Dev. Biol.* 8, 621428. doi:10.3389/fcell.2020.621428
- Xue, G., Chen, J., Liu, L., Zhou, D., Zuo, Y., Fu, T., et al. (2020). Protein Degradation through Covalent Inhibitor-Based PROTACs. *Chem. Commun.* 56, 1521–1524. doi:10.1039/c9cc08238g
- Yang, H., Lv, W., He, M., Deng, H., Li, H., Wu, W., et al. (2019). Plasticity in Designing PROTACs for Selective and Potent Degradation of HDAC6. *Chem. Commun.* 55, 14848–14851. doi:10.1039/c9cc08509b
- Yu, D. H., Xu, Z. Y., Mo, S., Yuan, L., Cheng, X. D., and Qin, J. J. (2020). Targeting MDMX for Cancer Therapy: Rationale, Strategies, and Challenges. *Front. Oncol.* 10, 1389. doi:10.3389/fonc.2020.01389
- Yuan, L., Xu, Z. Y., Ruan, S. M., Mo, S., Qin, J. J., and Cheng, X. D. (2020). Long Non-coding RNAs towards Precision Medicine in Gastric Cancer: Early Diagnosis, Treatment, and Drug Resistance. *Mol. Cancer.* 19, 96. doi:10.1186/s12943-020-01219-0
- Zhang, F., Wu, Z., Chen, P., Zhang, J., Wang, T., Zhou, J., et al. (2020). Discovery of a New Class of PROTAC BRD4 Degraders Based on a Dihydroquinazolinone Derivative and Lenalidomide/pomalidomide. *Bioorg. Med. Chem.* 28, 115228. doi:10.1016/j.bmc.2019.115228
- Zhang, H., Zhao, H.-Y., Xi, X.-X., Liu, Y.-J., Xin, M., Mao, S., et al. (2020). Discovery of Potent Epidermal Growth Factor Receptor (EGFR) Degraders by Proteolysis Targeting Chimera (PROTAC). *Eur. J. Med. Chem.* 189, 112061. doi:10.1016/j.ejmech.2020.112061
- Zhang, J., Wu, T., Simon, J., Takada, M., Saito, R., Fan, C., et al. (2018). VHL Substrate Transcription Factor ZHX2 as an Oncogenic Driver in Clear Cell Renal Cell Carcinoma. *Science* 361, 290–295. doi:10.1126/science.aap8411
- Zhang, J., and Zhang, Q. (2018). VHL and Hypoxia Signaling: Beyond HIF in Cancer. *Biomedicines.* 6, 35. doi:10.3390/biomedicines6010035
- Zhang, X., Thummuri, D., He, Y., Liu, X., Zhang, P., Zhou, D., et al. (2019). Utilizing PROTAC Technology to Address the On-Target Platelet Toxicity Associated with Inhibition of BCL-XL. *Chem. Commun.* 55, 14765–14768. doi:10.1039/c9cc07217a
- Zhao, Q., Ren, C., Liu, L., Chen, J., Shao, Y., Sun, N., et al. (2019). Discovery of SIAIS178 as an Effective BCR-ABL Degradable by Recruiting Von Hippel-Lindau (VHL) E3 Ubiquitin Ligase. *J. Med. Chem.* 62, 9281–9298. doi:10.1021/acs.jmedchem.9b01264
- Zhou, H., Bai, L., Xu, R., Zhao, Y., Chen, J., Mceachern, D., et al. (2019). Structure-Based Discovery of SD-36 as a Potent, Selective, and Efficacious PROTAC



- Degrader of STAT3 Protein. *J. Med. Chem.* 62, 11280–11300. doi:10.1021/acs.jmedchem.9b01530
- Zhou, F., Chen, L., Cao, C., Yu, J., Luo, X., Zhou, P., et al. (2020). Development of Selective Mono or Dual PROTAC Degradable Probe of CDK Isoforms. *Eur. J. Med. Chem.* 187, 111952. doi:10.1016/j.ejmech.2019.111952
- Zhou, L., Chen, W., Cao, C., Shi, Y., Ye, W., Hu, J., et al. (2020). Design and Synthesis of  $\alpha$ -naphthoflavone Chimera Derivatives Able to Eliminate Cytochrome P450 (CYP)1B1-mediated Drug Resistance via Targeted CYP1B1 Degradation. *Eur. J. Med. Chem.* 189, 112028. doi:10.1016/j.ejmech.2019.112028
- Zhou, Y., Chen, R., Luo, X., Zhang, W. D., and Qin, J. J. (2020). The E2 Ubiquitin-Conjugating Enzyme UbcH5c: an Emerging Target in Cancer and Immune Disorders. *Drug Discov. Today* 25 (11), 1988–1997. doi:10.1016/j.drudis.2020.09.015
- Zou, Y., Ma, D., and Wang, Y. (2019). The PROTAC Technology in Drug Development. *Cell Biochem Funct.* 37, 21–30. doi:10.1002/cbf.3369
- Conflict of Interest:** The authors declare that the research was conducted in the absence of any commercial or financial relationships that could be construed as a potential conflict of interest.
- Copyright © 2021 Qi, Dong, Xu, Cheng, Zhang and Qin. This is an open-access article distributed under the terms of the Creative Commons Attribution License (CC BY). The use, distribution or reproduction in other forums is permitted, provided the original author(s) and the copyright owner(s) are credited and that the original publication in this journal is cited, in accordance with accepted academic practice. No use, distribution or reproduction is permitted which does not comply with these terms.



# Pharmacological Vitamin C Treatment Impedes the Growth of Endogenous Glutamine-Dependent Cancers by Targeting Glutamine Synthetase

Yali Long<sup>†</sup>, Jia Qiu<sup>†</sup>, Bing Zhang<sup>†</sup>, Peng He, Xinchong Shi, Qiao He, Zhifeng Chen, Wanqing Shen, Zhoulei Li<sup>\*</sup> and Xiangsong Zhang<sup>\*</sup>

Department of Nuclear Medicine, The First Affiliated Hospital of Sun Yat-Sen University, Guangzhou, China

## OPEN ACCESS

### Edited by:

Dong-Hua Yang,  
St. John's University, United States

### Reviewed by:

Lu Yang,  
University at Buffalo,  
United States  
Xiao-Feng Li,  
Jinan University, China

### \*Correspondence:

Zhoulei Li  
lizhlei3@mail.sysu.edu.cn  
Xiangsong Zhang  
zhxiangs@mail.sysu.edu.cn

<sup>†</sup>These authors have contributed  
equally to this work

### Specialty section:

This article was submitted to  
Pharmacology of Anti-Cancer Drugs,  
a section of the journal  
Frontiers in Pharmacology

**Received:** 24 February 2021

**Accepted:** 29 March 2021

**Published:** 11 May 2021

### Citation:

Long Y, Qiu J, Zhang B, He P, Shi X,  
He Q, Chen Z, Shen W, Li Z and  
Zhang X (2021) Pharmacological  
Vitamin C Treatment Impedes the  
Growth of Endogenous Glutamine-  
Dependent Cancers by Targeting  
Glutamine Synthetase.  
Front. Pharmacol. 12:671902.  
doi: 10.3389/fphar.2021.671902

**Purpose:** Glutamine synthetase (GS) is the only currently known enzyme responsible for synthesizing endogenous glutamine (Gln). GS exerts a critical role in the oncogenesis of endogenous Gln-dependent cancers, making it an attractive target for anti-tumor therapies. A mixed-function oxidation system consisting of vitamin C (VC), oxygen, and trace metals can oxidize GS and promote its degradation. The current study aims to explore the effect of pharmacological VC treatment on GS.

**Methods:** Endogenous Gln-dependent cancer lines (breast cancer MCF7 and prostate cancer PC3) were selected to establish chronic Gln-deprived MCF7 and PC3 cell models. The expression of GS in parental and chronic Gln-deprived tumor cells exposed to VC treatment and control was determined by Western blot analysis. The anti-cancer effects of VC on parental and chronic Gln-deprived tumor cells were assessed by CCK-8 and annexin V-FITC/PI FACS assays. In addition, changes in cellular reactive oxygen species (ROS), glutathione (GSH) levels and NADPH/NADP<sup>+</sup> ratio were analyzed to explore the underlying mechanisms. Moreover, BALB/c nude mice xenografting with parental and chronic Gln-deprived prostate cancer cells were constructed to evaluate the *in vivo* therapeutic effect of VC. Finally, tumor <sup>13</sup>N-ammonia uptake in mice bearing prostate cancer xenografts was analyzed following treatment with VC and the expression of GS in xenografts were detected by immunohistochemistry.

**Results:** Cells overexpressing GS were obtained by chronic Gln deprivation. We found that the cytotoxic effect of VC on cancer cells was positively correlated with the expression of GS. Additionally, VC treatment led to a significant increase in ROS production, as well as GSH depletion and NADPH/NADP<sup>+</sup> reduction. These changes could be reversed by the antioxidant N-acetyl-L-cysteine (NAC). Furthermore, pharmacological VC treatment exhibited a more significant therapeutic effect on xenografts of prostate cancer cells overexpressing GS, that could be well monitored by <sup>13</sup>N-ammonia PET/CT imaging.

**Abbreviations:** VC, vitamin C; GS, glutamine synthetase; NAC, N-acetyl-L-cysteine; Gln, glutamine; NADPH, nicotinamide adenine dinucleotide phosphate; GSH, glutathione; ROS, reactive oxygen species; LIP, labile iron pool; ATP, adenosine triphosphate; DCF, dichloro-fluorescein; PET/CT, positron emission tomography/computed tomography.

**Conclusion:** Our findings indicate that VC can kill cancer cells by targeting glutamine synthetase to induce oxidative stress. VC could be used as an anti-cancer treatment for endogenous glutamine-dependent cancers.

**Keywords:** vitamin C, glutamine synthetase, redox stress, endogenous glutamine-dependent cancer,  $^{13}\text{N}$ -ammonia PET/CT

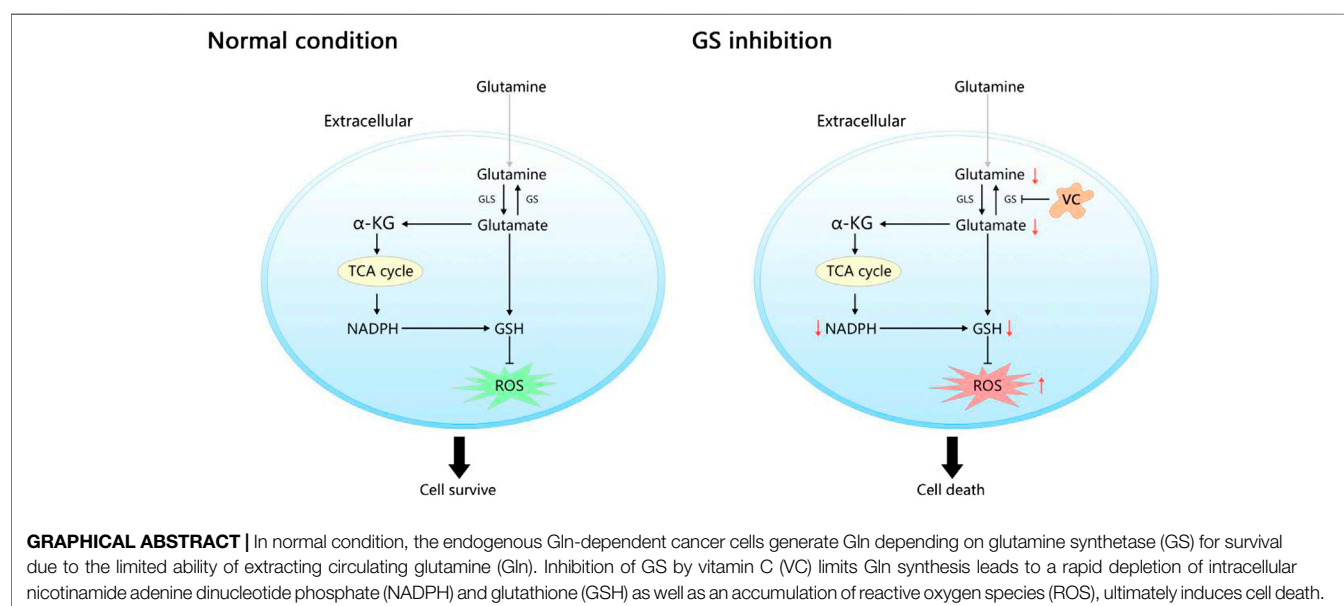
## INTRODUCTION

Vitamin C (VC) is an essential micronutrient for human beings, and serves as a cofactor for a large number of biosynthetic enzymes (Padayatty et al., 2003; Padayatty and Levine, 2016). Numerous pioneering studies have highlighted that pharmacological VC treatment exhibits selective toxicity to cancer cells both *in vivo* and *in vitro*. Additionally, early clinical trials have documented that intravenous VC treatment could relieve symptoms and improve survival in patients with advanced cancers (Cameron and Pauling, 1976; Cameron and Pauling, 1978; Chen et al., 2005; Chen et al., 2008; van der Reest and Gottlieb, 2016). Moreover, recent studies have shown that the anti-cancer effect of VC may be closely associated with its pro-oxidative function, which leads to increased levels of  $\text{H}_2\text{O}_2$  and labile iron pool (LIP), consequently resulting in intracellular oxidative stress and induction of cell death (Yun et al., 2015; Schoenfeld et al., 2017; Cimmino et al., 2018). However, the biological functions of VC are highly diverse and can target multiple critical pathways in various cancers. The molecular mechanism underlying the cytotoxicity of VC remains to be established (Ngo et al., 2019).

The increased usage of glutamine (Gln) is a key feature of metabolic reprogramming in various types of cancers (Wise and Thompson, 2010; Ward and Thompson, 2012). In addition, Gln is the richest conditionally essential amino acid in plasma, accounting for as much as 20% of the total amino acid

content. Moreover, it serves as a precursor for the synthesis of numerous amino acids, proteins, nucleotides, and other important biological molecules, in addition to being important in other processes such as supporting energy generation, modulating signaling pathways, and maintaining redox status (Stumvoll et al., 1999; DeBerardinis and Cheng, 2010; Hensley et al., 2013; Lyssiotis et al., 2013; Altman et al., 2016; Bott A. et al., 2019). However, due to highly fibrotic and poorly vascular diffusivity of tumor microenvironment, the ability of cells to uptake Gln from the tumor microenvironment is limited and depends on the supply of endogenous Gln. As the only known enzyme that catalyzes the synthesis of endogenous Gln from glutamate and ammonia in an adenosine triphosphate (ATP)-dependent pathway, glutamine synthetase (GS) has been reported to be generally overexpressed in breast, prostate and pancreatic cancers, where it maintains the proliferation and survival of cancer cells when the source of Gln is limited (Listrom et al., 1997; Pissimissis et al., 2009; Kung et al., 2011; Yuneva et al., 2012; Shi et al., 2014; Bott et al., 2015). In the endogenous Gln-dependent cancers, inhibition of GS expression is associated with a reduction in Gln and later leads to cell death. Therefore, targeting GS is a conceivable strategy against cancer metastasis and to improve the survival of patients with malignant tumors (Loeppen et al., 2002; Tardito et al., 2015; Yang et al., 2016; Bott A. J. et al., 2019).

Several studies have suggested that the GS enzyme is sensitive to oxidative stress. A mixed-function oxidation system



comprising of O<sub>2</sub>, ascorbate, and trace metal, was previously demonstrated to be capable of modifying GS by altering one of its sixteen histidine residues/subunit, consequently causing the degradation of intracellular proteolytic enzymes (Fucci et al., 1983; Levine, 1983a; Levine, 1983b; Daggett, 1987). In this study, we investigate whether VC could selectively kill cancer cells by promoting GS proteolytic digestion. Our results showed that the cancer cells overexpressing GS were more sensitive to VC treatment, which reduces GS expression, and induces cell apoptosis and intracellular redox imbalance. Our findings indicate that VC has a positive therapeutic effect in endogenous Gln-dependent cancers through disrupting intracellular redox homeostasis by targeting GS.

## MATERIALS AND METHODS

### Cells and Cell Culture

The endogenous Gln-dependent prostate cancer cell line PC3 and breast cancer cell line MCF7 were purchased from the Cell Bank of the Chinese Academy of Sciences (Shanghai, China). The obtained cells were cultured in RPMI 1640 (GIBICO, Grand Island, NY, United States) medium or DMEM medium (GIBICO, Grand Island, NY, United States) containing 10% FBS (GIBICO, Grand Island, NY, United States) and 1% penicillin/streptomycin (MRC, Changzhou, China) in a humidified incubator with 5% CO<sub>2</sub> at 37°C. Chronic Gln-deprived PC3 and MCF7 cells were obtained by progressive Gln deprivation as previously reported (He et al., 2016): at each passage, half of the PC3 or MCF7 cells were seeded in a new culture medium with a Gln concentration half of that in the previous culture medium until cells grew at a Gln concentration of 0.06 mmol/L, and defined as 0.06PC3 and 0.06MCF7 cells.

### CCK-8 Assay

The CCK-8 assays were performed according to the manufacturer's instructions (DOJINDO Laboratories, Kumamoto, Japan). Briefly, the cells were seeded in 96-well plates at a density of  $1 \times 10^4$  cells/well, and incubated with different doses (0, 0.5, 1, 2, 4, 8 mM) of VC (Alfa Aesar, Ward Hill, MA, United States) for 3, 6, and 9 h. Then, 100 µl CCK-8 solution was added to each well. After that the cells were incubated for an additional 1–2 h. Finally, the light absorbance values were recorded at 450 nm using a Multiskan FC apparatus (Thermo Fisher Scientific, Waltham, MA, United States) and cell viability was calculated.

### Flow Cytometry

Cells were incubated in 6-well plates at a density of  $4 \times 10^5$  cells/well with different doses (0, 0.5, 1, 2, 4, 8 mM) of VC at 37°C. After 16 h, the cells were harvested with 0.05% trypsin solution, rinsed twice with PBS and centrifuged at 1500 U/min for 5 min. Next, the cells were stained with fluorescein isothiocyanate-labelled Annexin V (BD Pharmingen, San Jose, CA, United States) and counterstained with propidium iodide (PI; BD Pharmingen, San Jose, CA, United States). Finally, the cells were resuspended in binding solution (BD Pharmingen) and

analyzed using a flow cytometer (CytoFLEX S, Beckman Coulter, Fullerton, CA, United States).

### Western Blot Analysis

The drug-treated cells were washed, collected and lysed. The proteins were separated with 10% sodium dodecyl sulfate polyacrylamide gel electrophoresis (SDS-PAGE) and then transferred onto a polyvinylidene fluoride (PVDF) membrane. After blocking with 5% skimmed milk for 1 h, the membrane was incubated with primary rabbit anti-GS antibody (Abcam, Cambridge, United Kingdom) at 4°C overnight, while the mouse anti-β-tubulin was used as the internal reference protein. Next, the membrane was washed and incubated with the secondary antibody at room temperature for 1 h. The resulting blots were developed using a Pierce Fast Western Blot Kit (Thermo Fisher, Rockford, IL, United States) and exposed to film.

### ROS Assay

Cells were incubated in 6-well plates (at a density of  $4 \times 10^5$  cells/well) with or without 8 mM VC treatment for 2–4 h. After that, the cells were washed and incubated in serum-free medium containing 10 µM/ml H<sub>2</sub>DCF-DA (GeneCopoeia, Rockville, MD, United States) for 30 min at 37°C in the dark. Next, the cells were collected after trypsinization and resuspended in 400 µl serum-free medium. Finally, the fluorescence-stained cells were measured using a flow cytometer (CytoFLEX S, Beckman Coulter, Fullerton, CA, United States).

### GSH Assay

The GSH assay was conducted based on the protocols provided by the GSH-Glo™ Glutathione Assay kit (Promega, Madison, WI, United States). Cells were seeded in 96-well white opaque plates at a density of  $1 \times 10^4$  cells/well and incubated with or without 8 mM VC for 3 h. After removing the drug from the wells and rinsing with PBS, the cells were incubated with 100 µl mixed GSH-Glo™ reagent for 30 min and 100 µl reconstituted luciferin detection reagent for another 15 min. Finally, intracellular luminescent signals were measured using a SPECTRAMaxM5 apparatus (Molecular Devices, Sunnyvale, CA, United States).

### The ratio of NADPH to NADP+

Cellular NADPH/NADP + ratio assay was performed according to the manufacturer's instructions (Abbkine, Wuhan, China). Cells treated with 8 mM VC were collected after trypsinization. Next, the intracellular NADP+ and NADPH were extracted, placed on ice and added with 80 µl working solution quickly. Then, the solution was mixed gently and the light absorbance was measured at 565 nm using a Multiskan FC apparatus. After incubation for 30 min at room temperature, the light absorbance values were measured again and the NADPH/NADP + ratio was calculated as the instructions described.

### Xenograft Model in Nude Mice

BALB/c male nude mice (4–5 weeks old) were purchased from the Model Animal Research Center of Nanjing University (Nanjing,



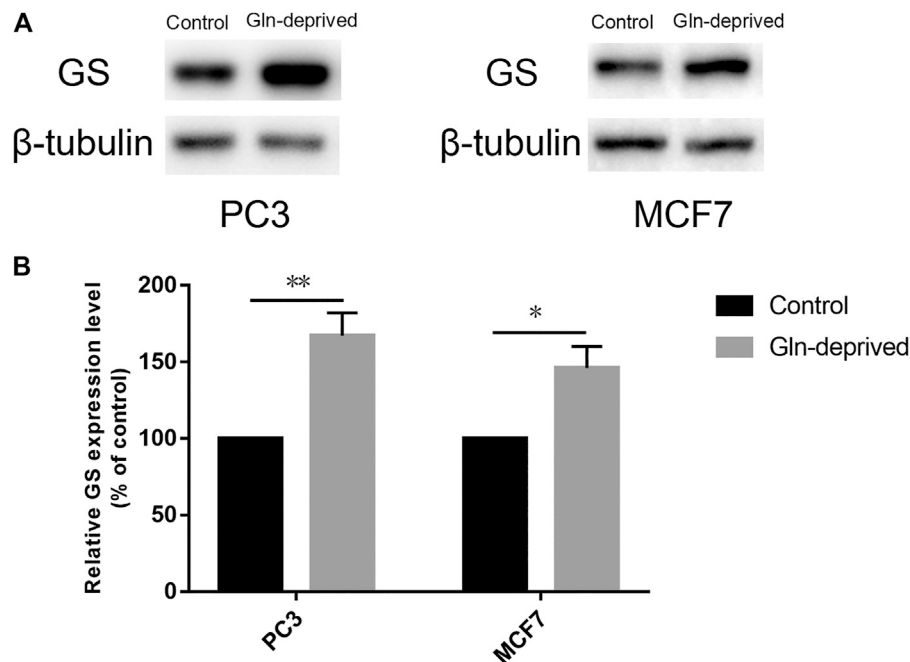


**FIGURE 1 |** Chronic Gln deprivation augments the levels of GS in MCF7 and PC3 cells. **(A)** GS protein in cancer cells (MCF7, PC3, 0.06MCF7, 0.06PC3) analyzed by Western blotting. **(B)** Relative GS protein contents were evaluated with  $\beta$ -tubulin as a loading control. All data are presented as means  $\pm$  SEM, \* $p$  < 0.05, \*\* $p$  < 0.01,  $n$  = 3. GS, glutamine synthetase.

China). All animal experiments were approved by the Ethics Committee for Clinical Research and Animal Trials of the First Affiliated Hospital of Sun Yat-sen University and conformed to the Guide for the Care and Use of Laboratory Animals of the Ministry of Science and Technology of the People's Republic of China. Firstly, 10 BALB/c male nude mice were randomly divided into two groups. Each nude mouse was subcutaneously injected with  $2 \times 10^6$  PC3 cells (right) and 0.06PC3 (left) cells in the two flank regions. Once the tumors reached a size of 50–80 mm<sup>3</sup>, the mice were respectively administered with saline or VC (4 g/kg, twice a day). Tumor sizes (length  $\times$  width<sup>2</sup>  $\times$  0.5) were measured once every 2 days using a Vernier caliper. After 16 days of treatment, the tumors were excised, weighed and analyzed by immunohistochemistry.

### Radiosynthesis of 13N-Ammonia

The 13N-ammonia was synthesized according to our published method (Xiangsong et al., 2006). We have done a purification step in our study. Radiochemical purity was obtained through IC-OH column to remove anions, and the radiochemical purity of 13N-ammonia was greater than 99%.

This part of the work and subsequent related operations strictly conformed to the Basic Standards for Protection Against Ionizing Radiation and for Safety of Radiation Sources of the People's Republic of China (GB 18871–2002) and the safety management measures for laboratories of Sun Yat-sen University (NO. 2014–34).

### Positron Emission Tomography Imaging

13N-ammonia was administered *via* tail vein injection (100  $\mu$ l) at an activity dose of 1 mCi per mouse 1 day before and 3 days after

treatment initiation. CT scanning was started immediately after the injection, and then PET imaging was performed after 10 min using a micro-PET system (Inveon, SIEMENS, Germany). The emission protocol involved a 15 min static scan. Regions of interest were drawn around tumors and the contralateral normal tissues, and the tumor-to-background ratios (TBR) were calculated.

### Immunohistochemistry

Tumor specimens were obtained at the end of the treatment course. Cell proliferation were analyzed based on Ki-67 (Sevicebio, Palo Alto, CA, United States) staining. GS expression was analyzed after microPET/CT imaging. The immunohistochemical staining was carried out according to the previously described procedures (He et al., 2016; Zheng et al., 2020). Positive rate of Ki-67 was analyzed using Image-pro plus 6.0 (Media Cybernetics, United States). GS expression was quantified based on H-scores. The score is obtained by the following formula: 3  $\times$  the percentage of strongly stained nuclei + 2  $\times$  the percentage of moderately stained nuclei + 1  $\times$  the percentage of weakly stained nuclei. The range of H-scores is 0–300.

### Statistical Analysis

Comparisons between two groups were carried out using Student's *t* test or analysis of variance (ANOVA) with Bonferroni post-hoc test. All analyses were performed in GraphPad Prism (GraphPad Software, Inc., La Jolla, CA, United States). Each experiment was repeated at least in triplicates, and the mean  $\pm$  standard error of the mean (SEM) was calculated for each value. For all analyses, significance was

determined at  $p < 0.05$ . \*, \*\*, \*\*\* or \*\*\*\* represent significant difference between drug exposure conditions.

## RESULTS

### Chronic Glutamine Deprivation Significantly Increases Glutamine Synthetase Expression in MCF7 and PC3 Cells

Overexpression of GS has been documented in a wide array of cancers, wherein it maintains exogenous Gln independently and promotes the proliferative potential of cancer cells (Listrom et al., 1997; Yuneva et al., 2012; Pissimissis et al., 2009; Shi et al., 2014; Bott et al., 2015; Kung et al., 2011). We firstly applied Western blot analysis to determine the expression of GS protein in human prostate cancer cell line PC3 and breast cancer cell line MCF7. The results suggested that GS was expressed in both cell lines (Figure 1A). Previous studies have suggested that chronic Gln deprivation can augment the expression of GS both *in vitro* and *in vivo* (Collins et al., 1997; Kung et al., 2011; Tardito et al., 2015; Issaq et al., 2019). Based on this, in order to explore the anti-cancer effect of pharmacological VC on cancer cells with different GS protein expression levels, chronic Gln-deprived cell lines (0.06PC3, 0.06MCF7) were established and Western blot analysis was performed to examine their GS expression. It was found that elevated level of GS was seen in chronic Gln-deprived 0.06PC3 and 0.06MCF7 cells, as compared to their parental PC3 and MCF7 cells (Figures 1A,B).

### Cancer Cells Overexpressing Glutamine Synthetase are More Sensitive to Vitamin C Treatment

The expression of GS has been reported to be closely associated with progression and metastasis in numerous cancers (Son et al., 2013; Alberghina and Gaglio, 2014). Although several studies have demonstrated that a mixed-function oxidation system consists of  $O_2$ , ascorbate, and trace metal may oxidize GS enzyme and consequently lead to degradation of the protein, the relationship between the selective toxicity of VC and the expression of GS protein remains unclear (Fucci et al., 1983; Levine, 1983a; Levine, 1983b; Daggett, 1987). Therefore, we established cell models of chronic Gln-deprivation using breast cancer MCF7 and prostate cancer PC3 cells. It was found that the cells with chronic Gln-deprivation, named 0.06MCF7 and 0.06PC3 cells had up-regulated expression of GS. The different response of chronic Gln-deprived tumor cells (0.06MCF7 and 0.06PC3) and their parental cells (MCF7 and PC3) upon VC treatment was tested. We found that all cells (MCF7, PC3 and 0.06MCF7, 0.06PC3) exhibited time- and dose-dependent inhibition of cell proliferation under VC treatment in CCK-8 assay (Figures 2A,B). We assessed the IC<sub>50</sub> values of VC in these cells, and notably, the 0.06MCF7 and 0.06PC3 cells were found to be more sensitive to VC treatment. As shown in

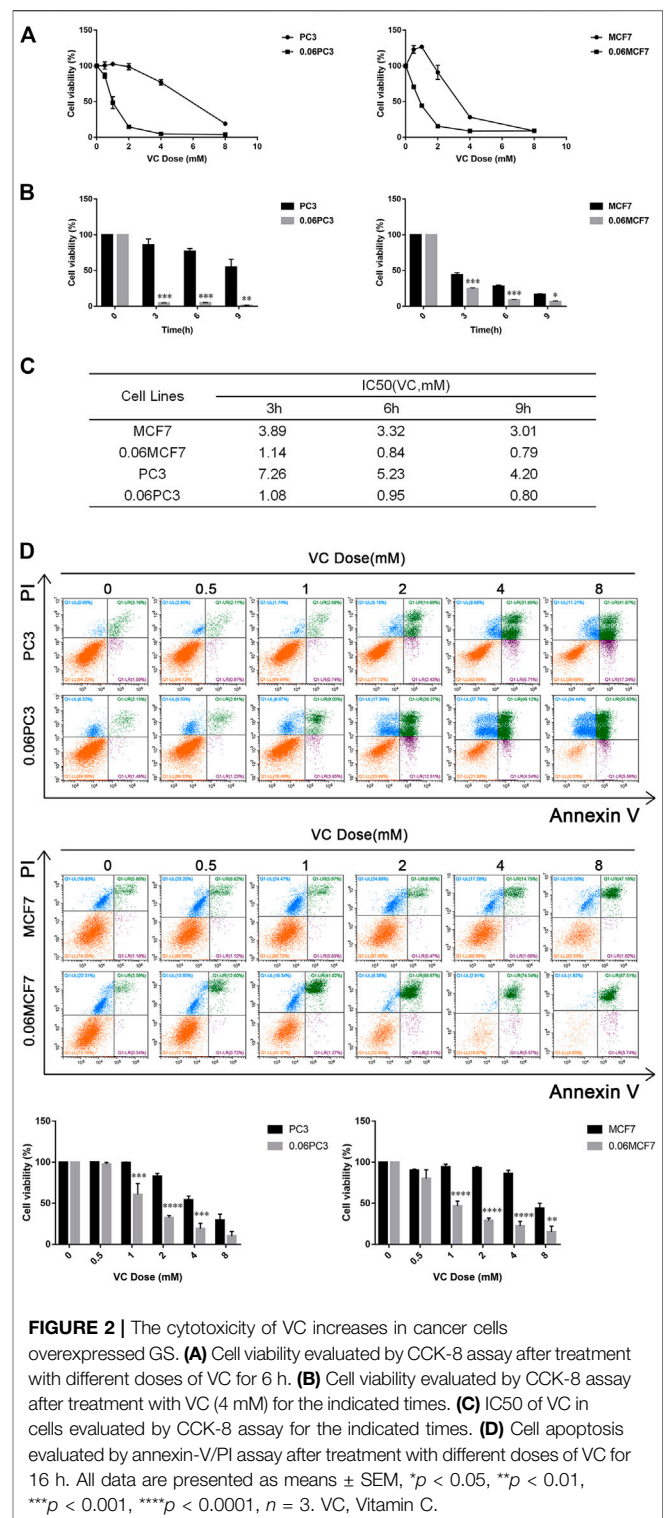


**FIGURE 2 |** The cytotoxicity of VC increases in cancer cells overexpressed GS. (A) Cell viability evaluated by CCK-8 assay after treatment with different doses of VC for 6 h. (B) Cell viability evaluated by CCK-8 assay after treatment with VC (4 mM) for the indicated times. (C) IC<sub>50</sub> of VC in cells evaluated by CCK-8 assay for the indicated times. (D) Cell apoptosis evaluated by annexin-V/PI assay after treatment with different doses of VC for 16 h. All data are presented as means  $\pm$  SEM, \* $p < 0.05$ , \*\* $p < 0.01$ , \*\*\* $p < 0.001$ , \*\*\*\* $p < 0.0001$ ,  $n = 3$ . VC, Vitamin C.

Figure 2C, for MCF7 and 0.06MCF7 cells, the IC<sub>50</sub> values of VC at 3, 6 and 9 h were calculated to be 3.89, 3.32, 3.01 and 1.14, 0.84, 0.79 mM, respectively. As for PC3 and 0.06PC3 cells, the IC<sub>50</sub> values of VC at 3, 6 and 9 h were calculated to be 7.26, 5.23, 4.20 mM and 1.08, 0.95, 0.80 mM, respectively. In addition, flow cytometric

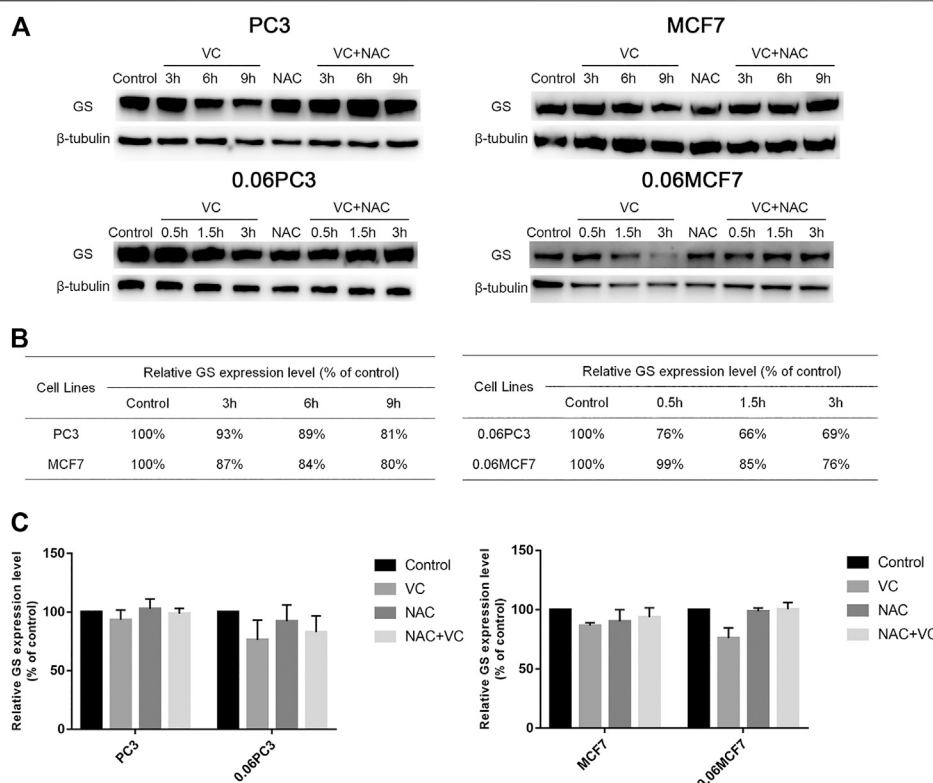


**FIGURE 3 |** Cancer cells overexpressing GS show augmented protein degradation under VC treatment, which is reversed by NAC. **(A)** GS protein in cancer cells (MCF7, PC3, 0.06MCF7, 0.06PC3) analyzed by Western blotting under treatment with VC(4 mM), NAC(5 mM), VC(4 mM) + NAC(5 mM) for indicated times. **(B)** The relative GS contents of cancer cells (MCF7, 0.06MCF7, PC3, 0.06PC3) under treatment with VC(4 mM) for indicated times were calculated with  $\beta$ -tubulin as a loading control. **(C)** The relative expression of GS in cancer cells (MCF7, 0.06MCF7, PC3, 0.06PC3) under treatment with VC(4 mM), NAC(5 mM), VC(4 mM) + NAC(5 mM) for 3 h. All data are presented as means  $\pm$  SEM,  $n = 3$ . VC, VitaminC; GS, glutaminesynthetase; NAC, N-acetyl-L-cysteine.

analysis revealed that pharmacological dose of VC conferred stronger cytotoxic effect on 0.06PC3 and 0.06MCF7 cells compared to PC3 and MCF7 cells, as reflected by an obvious increase in Annexin V/PI positive cells and a remarkable decrease in Annexin V/PI negative cells (Figure 2D). Taken together, these findings indicate that the cytotoxic effects of VC increased in cancer cells with high GS expression.

### Cancer Cells Overexpressing Glutamine Synthetase Show Augmented Protein Degradation Under Vitamin C Treatment

In order to clarify whether the cytotoxic effects of VC on tumor cells were related to the expression of GS, Western blot analysis was applied to quantify the changes in GS levels in tumor cells under 4 mM VC treatment at different times. As shown in Figure 3, the expression of GS decreased in a time-dependent manner in VC-treated cancer cells, as compared with the untreated cancer cells, and the GS degradation caused by VC was found to be reversed following pretreatment with the antioxidant N-acetyl-L-cysteine (NAC). In addition, the degradation level of GS was more significant in 0.06MCF7 and 0.06PC3 cells relative to MCF7 and PC3 cells. As shown in

Figures 3B,C, after 3 h treatment with 4 mM VC, the expression of GS decreased to 76 and 69% in 0.06MCF7 and 0.06PC3 cells, respectively, in contrast to 87 and 93% in MCF7 and PC3 cells. When VC treatment went on for 9 h, the GS levels in MCF7 and PC3 cells decreased to 80 and 81%, respectively. These results together with the CCK-8 assay-based data suggested that cancer cells with up-regulated GS expression were more sensitive to VC treatment.

### Cancer Cells Overexpressing Glutamine Synthetase Show Augmented Redox Imbalance Under Vitamin C Treatment

It was reported that Gln metabolism-sustained redox homeostasis is extremely critical, wherein inhibition of any component enzyme in this pathway can lead to an increased production of reactive oxygen species (ROS) and a decrease in reduced glutathione (GSH) (Lyssiotis et al., 2013). VC treatment induces toxicity in cancer cells due to disrupted redox balance, whereas the toxic mechanism and possible targets remain uncharacterized. We investigated whether VC treatment induces cancer cell apoptosis is associated with oxidative stress by targeting GS. Cellular ROS levels were detected by dichloro-

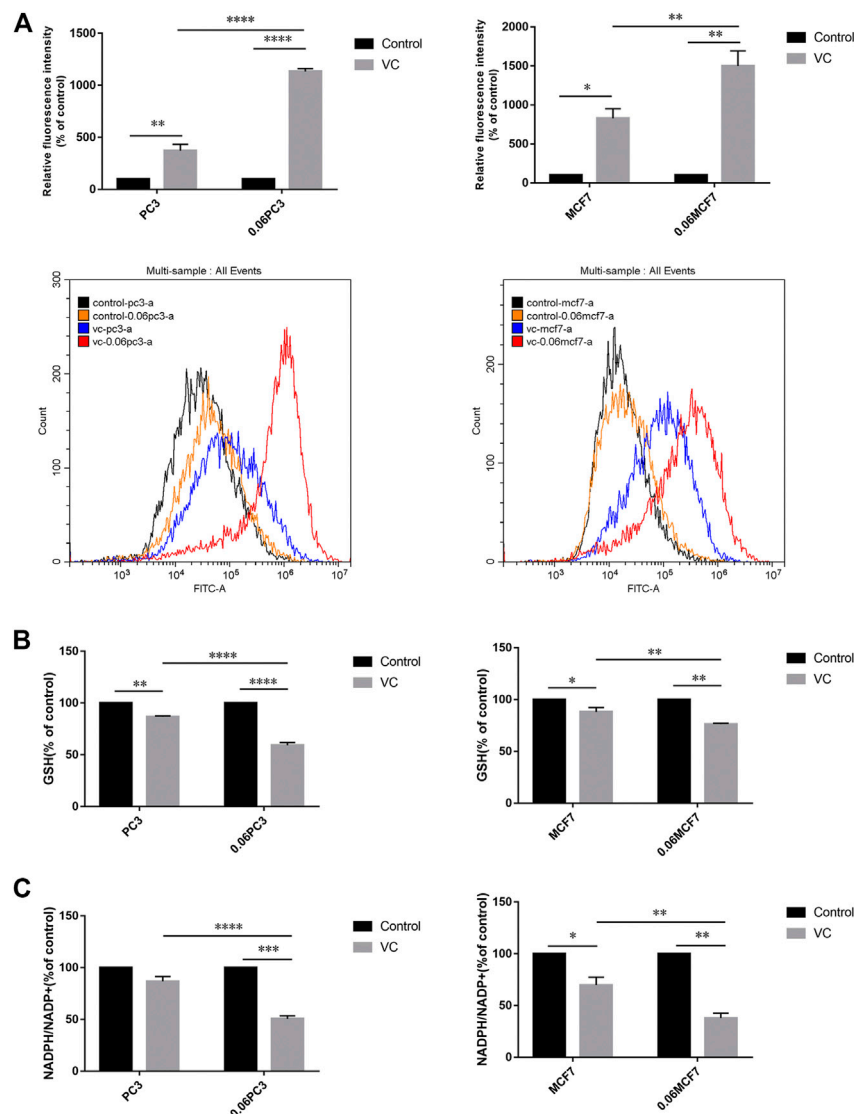


**FIGURE 4 |** Cancer cells overexpressing GS show augmented redox imbalance under VC treatment. **(A)** Quantitative bar graphs of cellular ROS levels before and after treatment with VC (8mM, 3 h). **(B)** Quantitative bar graphs of cellular GSH levels before and after treatment with VC (8mM, 3 h). **(C)** Quantitative bar graphs of cellular NADPH/NADP<sup>+</sup> ratio before and after treatment with VC (8mM, 3 h). All data are presented as means  $\pm$  SEM, \* $p$  < 0.05, \*\* $p$  < 0.01, \*\*\* $p$  < 0.001, \*\*\*\* $p$  < 0.0001,  $n$  = 3. VC, Vitamin C.

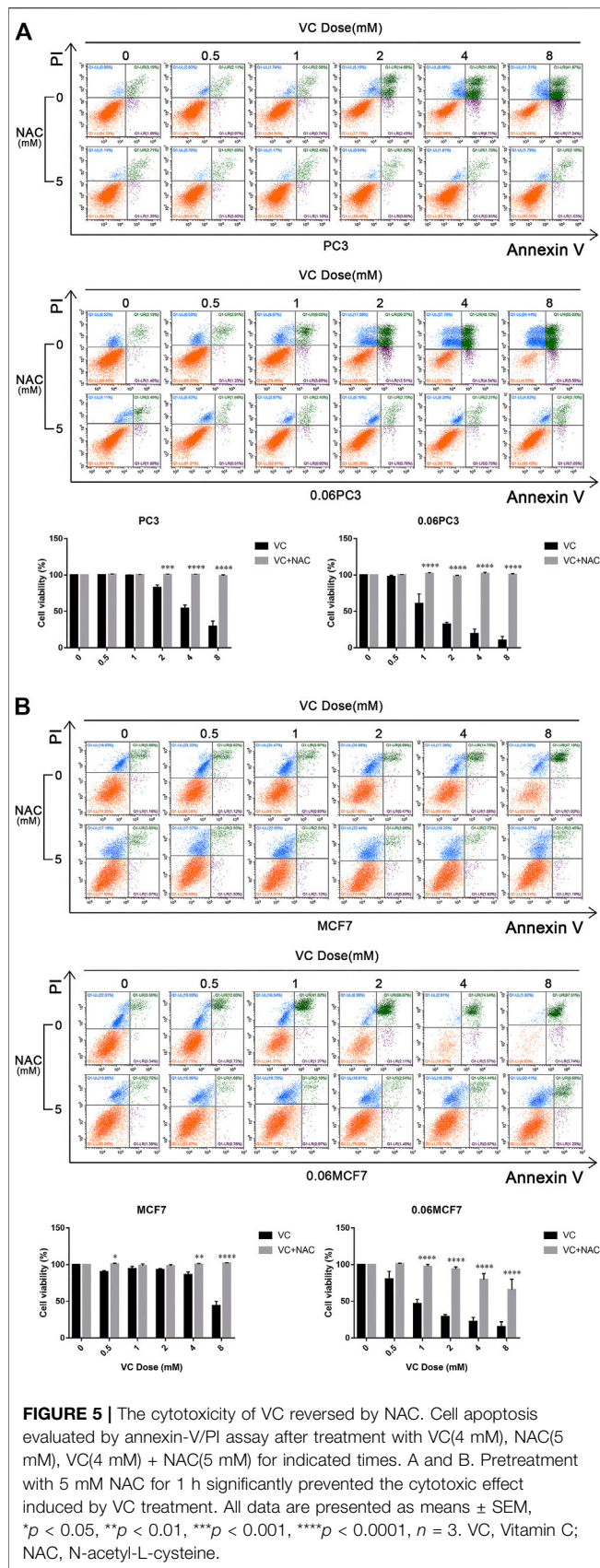
fluorescein (DCF) staining after treatment with 8 mM VC for 3 h. As expected, the ROS production was found increased in all cells following VC treatment. Interestingly, the accumulation of ROS was more significant in 0.06MCF7 and 0.06PC3 cells, as compared with their parental MCF7 and PC3 cells. As shown in **Figure 4A**, the accumulation of ROS in 0.06MCF7 was about 1.8 times as that of MCF7 cells, whereas ROS accumulation in 0.06PC3 was 3.0 times of PC3 cells. Furthermore, we observed that changes in GSH depletion and NADPH/NADP<sup>+</sup> reduction were also obvious in 0.06MCF7 and 0.06PC3 cells, relative to MCF7 and PC3 cells (**Figures 4B,C**). Interestingly, the cell death and GS degradation could be reversed by pre-treatment with the antioxidant NAC (5 mM for 1 h) (**Figure 3, Figure 5**). These

findings suggest that VC may lead to redox imbalance by targeting GS.

### Xenografts of Cells Overexpressing Glutamine Synthetase Show Slow Tumor Growth Under Vitamin C Treatment

In order to determine the relationship between the *in vivo* anti-tumor activity of VC and GS expression in cancer cells, BALB/c male nude mice bearing xenograft tumors of PC3 and 0.06PC3 cells were intraperitoneally (i.p.) treated with 4 g/kg VC or saline (control) twice daily for 16 days. As shown in **Figures 6A**, VC treatment brought a remarkable reduction in tumor growth in





tumors regardless of being derived from PC3( $p = 0.0093$ ) or 0.06PC3( $p = 0.0433$ ) cells, when compared to the control group. Moreover, VC conferred a more significant inhibition on tumor growth in the 0.06PC3 cell xenograft compared to PC3 cell xenograft ( $p = 0.0347$ ). In addition, immunohistochemistry was employed to observe whether VC treatment could change the expression of proliferative index Ki-67 *in vivo*. It was found that the expression of Ki-67 decreased in response to VC treatment. Furthermore, the changes were found to be more significant in the 0.06PC3 cell xenograft model (Figure 6B). These findings confirm that pharmacological dose of VC has a more significant suppressive effect on prostate cancer xenograft of cells overexpressing GS by inhibiting cell proliferation *in vivo*.

## Tumor Xenografts Show a Significant Reduction in $^{13}\text{N}$ -Ammonia Uptake Under Vitamin C Treatment

Functional  $^{13}\text{N}$ -ammonia-PET/CT imaging was performed to evaluate the therapeutic response following VC treatment. BALB/c male nude mice bearing PC3 cell xenografts were intraperitoneally injected with 4 g/kg VC for 3 days when the volume of tumors had grown to 250–300 mm<sup>3</sup>, and the mice were intravenously injected with 1 mCi  $^{13}\text{N}$ -ammonia. As shown in Figure 7,  $^{13}\text{N}$ -ammonia-PET imaging revealed a visible reduction in  $^{13}\text{N}$ -ammonia uptake after 3 days of VC treatment compared with that before pretreatment, whereas the control group exhibited a slight increase in  $^{13}\text{N}$ -ammonia uptake. Subsequently, GS expression patterns in xenografts from the control group and VC treatment group were examined using immunohistochemistry, which demonstrated the weakened GS-positive staining in VC-treated sections (Figure 7B), suggesting that VC treatment could induce GS degradation. This result indicated that  $^{13}\text{N}$ -ammonia PET/CT imaging could be a useful tool in monitoring the therapeutic response.

## DISCUSSION

Cancers are complex diseases involving numerous common signaling pathways and molecular metabolic alterations (Shenoy et al., 2018; Su et al., 2019). There have been a surge in the number of reports stating that some cancer cell proliferation relies on the increased consumption of Gln to support cell growth and maintain redox homeostasis (Hanahan and Weinberg, 2000; DeBerardinis et al., 2008; Gaglio et al., 2011). GS and the glutaminase (GLS) are commonly found enzymes that participate in Gln metabolism. GS possesses the ability to catalyze endogenous Gln production from glutamate and ammonia, which is the reverse reaction of glutaminolysis catalyzed by GLS. It was speculated that mutual suppressive action may exist between these two enzymes, that avoid their simultaneous up-regulation (Kung et al., 2011; Yuneva et al., 2012). Targeting GLS has been explored and documented to be beneficial for cancer therapy. However, some studies have found that inhibiting GLS does not always bring about desired results, especially in cancers with poor vascularization and limited

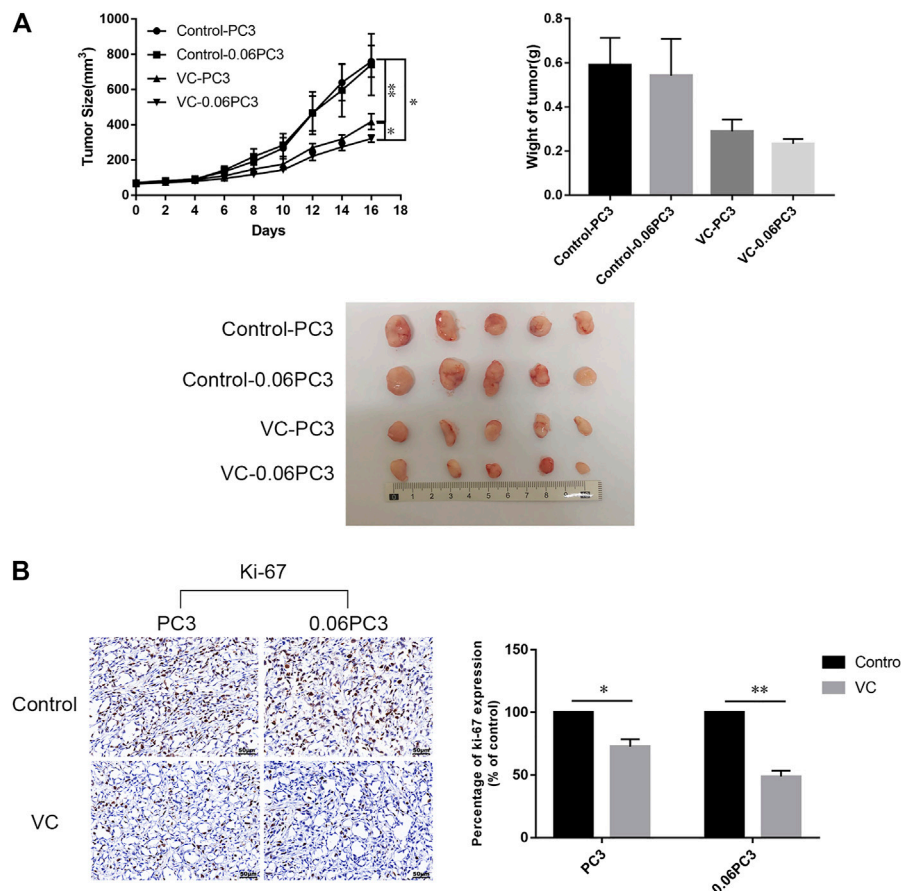
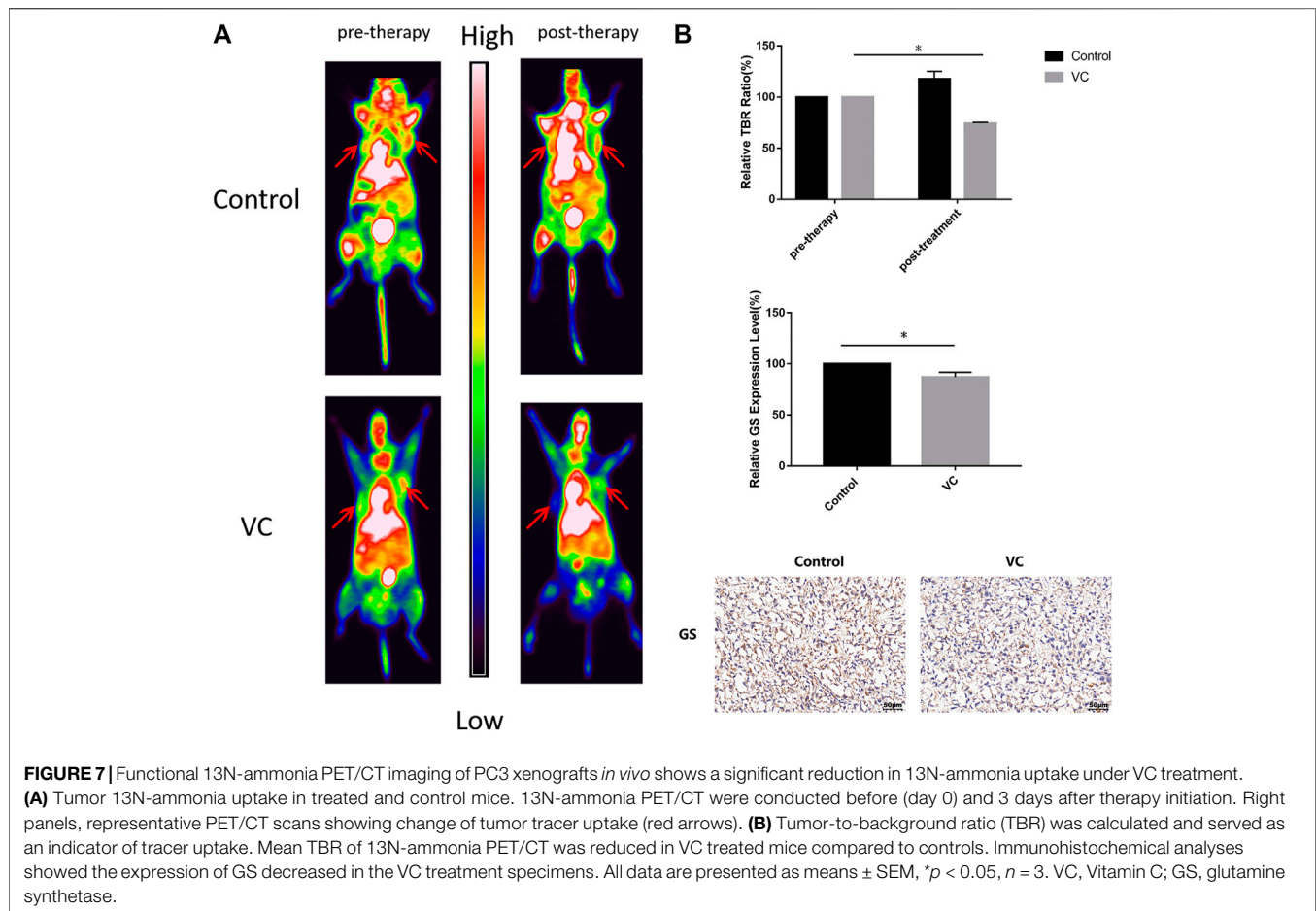


**FIGURE 6 |** Xenografts of cells overexpressing GS show slow tumor growth under VC treatment. BALB/c nude mice (4–5 weeks old/male) were subcutaneously (s.c.) injected with  $2 \times 10^6$  PC3 cells. When the tumor sizes reached 50–80 mm<sup>3</sup>, ascorbate sodium (4 g/kg, twice a day) were intraperitoneally (i.p.) administered to the mice. After 16 days, all mice were euthanized and the tumors were analyzed. **(A)** Tumor volume and weight changed after treatment with VC. **(B)** Immunohistochemical analyses showed the expression of Ki-67 (proliferation marker) decreased in the VC treatment groups, with more obvious change in the 0.06PC3 group. All data are presented as means  $\pm$  SEM, \* $p < 0.05$ , \*\* $p < 0.01$ ,  $n = 3$ . VC, Vitamin C.

ability of extracting circulating Gln, where they depend on the increased expression of GS to synthesize *de novo* Gln autonomously (Tardito et al., 2015; Bott A. J. et al., 2019). In addition, some other reports have indicated that many human cancers exhibit markedly elevated levels of GS, wherein GS enables cell growth independent on extracellular Gln. Silencing GS or using GS inhibitors can considerably suppress cell proliferation and tumor growth in preclinical models. However, there is no safe and specific drug targeting GS approved for clinical trials (Collins et al., 1997; Brusilow and Peters, 2017). In the current study, we found that 0.06PC3 and 0.06 MCF7 cells, that were derived from progressive Gln deprivation in PC3 and MCF7 cells, showed GS up-regulation and could grow normally in low-Gln medium. Moreover, the addition of VC could effectively inhibit cell proliferation and lead to GS degradation, which was more obvious in 0.06PC3 and 0.06 MCF7 cells with overexpression of GS, indicating that VC can kill cancer cells by targeting GS, especially in cells depending on GS expression. This study confirmed that Gln deprivation could up-regulate the

expression of GS, which has been demonstrated and is one of the most commonly applied method for the regulation of GS expression (Collins et al., 1997; Tardito et al., 2015; He et al., 2016).

In the early 1970s, Cameron and Rotman first proposed that high-dose VC might confer anti-cancer property. Later on, numerous researches have also reported that VC exhibits selectively toxic effects on various types of cancer cells and holds immense application potential (Cameron and Pauling, 1976; Cameron and Pauling, 1978; van der Reest and Gottlieb, 2016; Shenoy et al., 2018). With further exploration on the role of VC, newly found evidences revealed that the selective anti-cancer toxicity of pharmacological VC treatment was regulated by the production of ascorbic acid radical and H<sub>2</sub>O<sub>2</sub> in the extracellular fluid, a process driven by the depletion of NADPH and GSH (Chen et al., 2005; Yun et al., 2015; Schoenfeld et al., 2017). However, the targets and pathways of VC-mediated cell apoptosis are multiple, while the therapeutic effect of VC varies among different cancers. Notably, studies have reported that a system comprising of O<sub>2</sub>, VC and trace meta is capable of inducing GS



degradation (Fucci et al., 1983; Levine, 1983a; Levine, 1983b; Daggett, 1987). In addition, it is also known that sustaining protein homeostasis is critical for cell growth and the balance between protein synthesis and degradation must be discretely regulated to maintain sound functioning of the system. As a result, highly selected strategies aimed at down-regulation of targeted proteins have become increasingly popular in therapeutic anti-cancer applications (Luh et al., 2020). In the current study, we demonstrated that VC could induce cell death *in vitro* and inhibit tumor growth *in vivo*. Additionally, our findings revealed that the cancer cells overexpressed GS were significantly more sensitive to VC treatment. GS is the only identified enzyme that can drive the process of endogenous Gln biosynthesis. As we know, a critical function of Gln metabolism is to produce reducing equivalents in the form of NADPH, which may sustain redox balance and support cell survival (Shenoy et al., 2018; Su et al., 2019). Based on this, we investigated the effects of VC on cellular homeostasis to elucidate its potential anti-tumor mechanisms. We found that VC treatment could lead to a cellular redox imbalance *via* several aspects that include accumulation of ROS, depletion of GSH and reduction in the NADPH/NADP<sup>+</sup> ratio. Moreover, the changes in redox imbalance were positively associated with cell death as well as GS degradation, that were more obvious in

GS overexpressing cells. Furthermore, the above effects altered by VC treatment could be rescued through media supplementation with the antioxidant NAC. Collectively, these data indicate that VC exerts its anti-cancer effects by inducing GS degradation, which could be a novel approach to target malignancies. It holds a tremendous application potential in some specific cancers that depend on the high expression of GS to produce endogenous Gln.

GS upregulation is prevalent in multiple human cancers, with significant differences in expression patterns between tumors. Therefore, evaluation of GS expression profiles in tumors may be necessary for predicting therapeutic responses. Previous studies have reported that  $^{13}\text{N}$ -ammonia serves as a useful PET tracer in several types of cancers, including malignant lymphomas, brain tumors and prostate cancers (Shi et al., 2013a; Shi et al., 2013b; Shi et al., 2015). Recently, Shi *et al.* associated the accumulation of  $^{13}\text{N}$ -ammonia in prostate cancers with GS expression levels, while He *et al.* demonstrated that  $^{13}\text{N}$ -ammonia functions as a potential tracer for the evaluation of GS as it can be trapped by cancer cells through the synthesis of *de novo* Gln (Shi et al., 2014). In the current study, we established prostate cancer xenografts through subcutaneous injection of PC3 cells into nude mice, treated mice with VC for 3 days when tumor volume reached about 250–300 mm<sup>3</sup> and monitored the therapeutic effects of VC using  $^{13}\text{N}$ -ammonia-



PET/CT imaging. Our findings illustrated that <sup>13</sup>N-ammonia-PET/CT imaging could accurately identify the location of xenografts, and was suitable for monitoring the therapeutic response of VC. Furthermore, we observed that VC treatment precipitated a visible reduction in <sup>13</sup>N-ammonia accumulation in prostate cancer xenografts. Moreover, xenografts derived from VC-treated nude mice presented with lower GS expression levels relative to saline-treated mice. These findings indicate that <sup>13</sup>N-ammonia PET/CT imaging is useful for the evaluation of GS expression, and suitable for monitoring the therapeutic effects of VC treatment in patients with high GS expression.

Taken together, our data indicate that VC treatment induces redox stress by targeting GS in tumor cells. This study suggests that VC possesses specific anti-tumor property in endogenous Gln-dependent cancers that rely on GS to promote its growth and survival. Furthermore, the application of <sup>13</sup>N-ammonia PET/CT imaging could be useful for monitoring and predicting the therapeutic response in cancers overexpressing GS.

## DATA AVAILABILITY STATEMENT

The original contributions presented in the study are included in the article/**Supplementary Material**, further inquiries can be directed to the corresponding authors.

## ETHICS STATEMENT

The animal study was reviewed and approved by Ethics Committee for Clinical Research and Animal Trials of the First Affiliated Hospital of Sun Yat-sen University.

## AUTHOR CONTRIBUTIONS

Conception and design: YL, ZL, and XZ. Development of the methodology: YL, JQ, BZ, ZL, and XZ. Data acquisition (provided

animals, acquired and managed patients, provided facilities, etc.): YL, JQ, BZ, PH, XS, QH, WS, ZL, and XZ. Analysis and interpretation of the data (e.g., statistical analysis, biostatistics, computational analysis): YL, BZ, JQ, PH, ZC, ZL, and XZ. Writing, review, and/or revision of the manuscript: YL, BZ, JQ, XS, ZL, and XZ. Administrative, technical, or material support (i.e., reporting or organizing data, constructing databases): BZ, ZL, and XZ. Study supervision: ZL and XZ. All authors contributed to the article and approved the submitted version.

## FUNDING

This study was supported by the National Science Foundation of China (grant numbers 81602701 and 81901793), the Science and Technology Planning Project of Guangdong Province (2017B020210001), the Training program of the Major Research Plan of Sun Yat-Sen University (17ykjc10), the Science and Technology Program of Guangzhou (201607010353), Young teacher training program of Sun Yat-sen University (19ykpy55).

## ACKNOWLEDGMENTS

We are grateful to all members of the XZ group for their contributions to this project. We thank Dr. Qiao Su, Wuguo Li and all members of the animal care facility of the First Affiliated Hospital of Sun Yat-Sen University for animal management. We thank Yali Tang, Tong Zhang and Qingqiang Tu from the core facility for research equipment at Sun Yat-Sen University for technical support for FACS analysis.

## SUPPLEMENTARY MATERIAL

The Supplementary Material for this article can be found online at: <https://www.frontiersin.org/articles/10.3389/fphar.2021.671902/full#supplementary-material>

## REFERENCES

- Alberghina, L., and Gaglio, D. (2014). Redox control of glutamine utilization in cancer. *Cell Death Dis.* 5 (12), e1561. doi:10.1038/cddis.2014.513
- Altman, B. J., Stine, Z. E., and Dang, C. V. (2016). From Krebs to clinic: glutamine metabolism to cancer therapy. *Nat. Rev. Cancer* 16 (10), 619–634. doi:10.1038/nrc.2016.71
- Bott, A. J., Peng, I.-C., Fan, Y., Faubert, B., Zhao, L., Li, J., et al. (2015). Oncogenic myc induces expression of glutamine synthetase through promoter demethylation. *Cell Metab.* 22 (6), 1068–1077. doi:10.1016/j.cmet.2015.09.025
- Bott, A., Maimouni, S., and Zong, W.-X. (2019). The pleiotropic effects of glutamine metabolism in cancer. *Cancers* 11 (6), 770. doi:10.3390/cancers11060770
- Bott, A. J., Shen, J., Tonelli, C., Zhan, L., Sivaram, N., Jiang, Y.-P., et al. (2019). Glutamine anabolism plays a critical role in pancreatic cancer by coupling carbon and nitrogen metabolism. *Cell Rep.* 29 (5), 1287–1298.e6. doi:10.1016/j.celrep.2019.09.056
- Brusilow, W. S. A., and Peters, T. J. (2017). Therapeutic effects of methionine sulfoximine in multiple diseases include and extend beyond inhibition of glutamine synthetase. *Expert Opin. Ther. Targets* 21 (5), 461–469. doi:10.1080/14728222.2017.1303484
- Cameron, E., and Pauling, L. (1976). Supplemental ascorbate in the supportive treatment of cancer: prolongation of survival times in terminal human cancer. *Proc. Natl. Acad. Sci.* 73 (10), 3685–3689. doi:10.1073/pnas.73.10.3685
- Cameron, E., and Pauling, L. (1978). Supplemental ascorbate in the supportive treatment of cancer: reevaluation of prolongation of survival times in terminal human cancer. *Proc. Natl. Acad. Sci.* 75 (9), 4538–4542. doi:10.1073/pnas.75.9.4538
- Chen, Q., Espey, M. G., Krishna, M. C., Mitchell, J. B., Corpe, C. P., Buettner, G. R., et al. (2005). Pharmacologic ascorbic acid concentrations selectively kill cancer cells: action as a pro-drug to deliver hydrogen peroxide to tissues. *Proc. Natl. Acad. Sci.* 102 (38), 13604–13609. doi:10.1073/pnas.0506390102
- Chen, Q., Espey, M. G., Sun, A. Y., Pooput, C., Kirk, K. L., Krishna, M. C., et al. (2008). Pharmacologic doses of ascorbate act as a prooxidant and decrease growth of aggressive tumor xenografts in mice. *Proc. Natl. Acad. Sci.* 105 (32), 11105–11109. doi:10.1073/pnas.0804226105
- Cimmino, L., Neel, B. G., and Aifantis, I. (2018). Vitamin C in stem cell reprogramming and cancer. *Trends Cell Biol.* 28 (9), 698–708. doi:10.1016/j.tcb.2018.04.001



- Collins, C. L., Wasa, M., Souba, W. W., and Abcouwer, S. F. (1997). Regulation of glutamine synthetase in human breast carcinoma cells and experimental tumors. *Surgery* 122 (2), 451–464. doi:10.1016/s0039-6060(97)90039-8
- Daggett, V. (1987). Protein degradation: the role of mixed-function oxidases. *Pharm. Res.* 04 (4), 278–284. doi:10.1023/a:1016484901485
- DeBerardinis, R. J., and Cheng, T. (2010). Q's next: the diverse functions of glutamine in metabolism, cell biology and cancer. *Oncogene* 29 (3), 313–324. doi:10.1038/onc.2009.358
- DeBerardinis, R. J., Lum, J. J., Hatzivassiliou, G., and Thompson, C. B. (2008). The biology of cancer: metabolic reprogramming fuels cell growth and proliferation. *Cell Metab.* 7 (1), 11–20. doi:10.1016/j.cmet.2007.10.002
- Fucci, L., Oliver, C. N., Coon, M. J., and Stadtman, E. R. (1983). Inactivation of key metabolic enzymes by mixed-function oxidation reactions: possible implication in protein turnover and ageing. *Proc. Natl. Acad. Sci.* 80 (6), 1521–1525. doi:10.1073/pnas.80.6.1521
- Gaglio, D., Metallo, C. M., Gameiro, P. A., Hiller, K., Dana, L. S., Balestrieri, B., et al. (2011). Oncogenic K-Ras decouples glucose and glutamine metabolism to support cancer cell growth. *Mol. Syst. Biol.* 7, 523. doi:10.1038/msb.2011.56
- Hanahan, D., and Weinberg, R. A. (2000). The hallmarks of cancer. *Cell* 100 (1), 57–70. doi:10.1016/s0092-8674(00)81683-9
- He, Q., Shi, X., Zhang, L., Yi, C., Zhang, X., and Zhang, X. (2016). De novo glutamine synthesis. *Mol. Imaging* 15, 153601211664544. doi:10.1177/1536012116645440
- Hensley, C. T., Wasti, A. T., and DeBerardinis, R. J. (2013). Glutamine and cancer: cell biology, physiology, and clinical opportunities. *J. Clin. Invest.* 123 (9), 3678–3684. doi:10.1172/JCI69600
- Issaq, S. H., Mendoza, A., Fox, S. D., and Helman, L. J. (2019). Glutamine synthetase is necessary for sarcoma adaptation to glutamine deprivation and tumor growth. *Oncogenesis* 8 (3), 20. doi:10.1038/s41389-019-0129-z
- Kung, H.-N., Marks, J. R., and Chi, J.-T. (2011). Glutamine synthetase is a genetic determinant of cell type-specific glutamine independence in breast epithelia. *PLoS Genet.* 7 (8), e1002229. doi:10.1371/journal.pgen.1002229
- Levine, R. L. (1983a). Oxidative modification of glutamine synthetase. I. Inactivation is due to loss of one histidine residue. *J. Biol. Chem.* 258 (19), 11823–11827. doi:10.1016/s0021-9258(17)44305-5
- Levine, R. L. (1983b). Oxidative modification of glutamine synthetase. II. Characterization of the ascorbate model system. *J. Biol. Chem.* 258 (19), 11828–11833. doi:10.1016/s0021-9258(17)44306-7
- Listrom, D. C., Morizono, H., Rajagopal, S. B., McCann, T. M., Tuchman, M., and Allewell, M. N. (1997). Expression, purification, and characterization of recombinant human glutamine synthetase. *Biochem. J.* 328 (Pt 1), 159–163. doi:10.1042/bj3280159
- Loeppen, S., Schneider, D., Gaunitz, F., Gebhardt, R., Kurek, R., Buchmann, A., et al. (2002). Overexpression of glutamine synthetase is associated with beta-catenin-mutations in mouse liver tumors during promotion of hepatocarcinogenesis by phenobarbital. *Cancer Res.* 62 (20), 5685–5688.
- Luh, L. M., Scheib, U., Juenemann, K., Wortmann, L., Brands, M., and Cromm, P. M. (2020). Prey for the proteasome: targeted protein degradation-A medicinal chemist's perspective. *Angew. Chem. Int. Ed.* 59 (36), 15448–15466. doi:10.1002/anie.202004310
- Lyssiotis, C. A., Son, J., Cantley, L. C., and Kimmelman, A. C. (2013). Pancreatic cancers rely on a novel glutamine metabolism pathway to maintain redox balance. *Cell Cycle* 12 (13), 1987–1988. doi:10.4161/cc.25307
- Ngo, B., Van Riper, J. M., Cantley, L. C., and Yun, J. (2019). Targeting cancer vulnerabilities with high-dose vitamin C. *Nat. Rev. Cancer* 19 (5), 271–282. doi:10.1038/s41568-019-0135-7
- Padayatty, S. J., Katz, A., Wang, Y., Eck, P., Kwon, O., Lee, J.-H., et al. (2003). Vitamin C as an antioxidant: evaluation of its role in disease prevention. *J. Am. Coll. Nutr.* 22 (1), 18–35. doi:10.1080/07315724.2003.10719272
- Padayatty, S., and Levine, M. (2016). Vitamin C: the known and the unknown and goldilocks. *Oral Dis.* 22 (6), 463–493. doi:10.1111/odi.12446
- Pissimissis, N., Papageorgiou, E., Lembessis, P., Armakolas, A., and Koutsilieris, M. (2009). The glutamatergic system expression in human PC-3 and LNCaP prostate cancer cells. *Anticancer Res.* 29 (1), 371–377.
- Schoenfeld, J. D., Sibenaller, Z. A., Mapuskar, K. A., Wagner, B. A., Cramer-Morales, K. L., Furqan, M., et al. (2017). O2- and H2O2-mediated disruption of Fe metabolism causes the differential susceptibility of NSCLC and GBM cancer cells to pharmacological ascorbate. *Cancer Cell* 32 (2), 268. doi:10.1016/j.ccell.2017.07.008
- Shenoy, N., Creagan, E., Witzig, T., and Levine, M. (2018). Ascorbic acid in cancer treatment: let the phoenix fly. *Cancer Cell* 34 (5), 700–706. doi:10.1016/j.ccell.2018.07.014
- Shi, X., Liu, Y., Zhang, X., Yi, C., Wang, X., Chen, Z., et al. (2013a). The comparison of 13N-ammonia and 18F-FDG in the evaluation of untreated gliomas. *Clin. Nucl. Med.* 38 (7), 522–526. doi:10.1097/RLU.0b013e318295298d
- Shi, X., Zhang, X., Yi, C., Wang, X., Chen, Z., and Zhang, B. (2013b). The combination of 13N-ammonia and 18F-FDG in predicting primary central nervous system lymphomas in immunocompetent patients. *Clin. Nucl. Med.* 38 (2), 98–102. doi:10.1097/RLU.0b013e318279b6cc
- Shi, X., Yi, C., Wang, X., Zhang, B., Chen, Z., Tang, G., et al. (2015). 13N-ammonia combined with 18F-FDG could discriminate between necrotic high-grade gliomas and brain abscess. *Clin. Nucl. Med.* 40 (3), 195–199. doi:10.1097/RLU.0000000000000649
- Shi, X., Zhang, X., Yi, C., Liu, Y., and He, Q. (2014). 13N-ammonia positron emission tomographic/computed tomographic imaging targeting glutamine synthetase expression in prostate cancer. *Mol. Imaging* 13, 1–10. doi:10.2310/7290.2014.00048
- Son, J., Lyssiotis, C. A., Ying, H., Wang, X., Hua, S., Ligorio, M., et al. (2013). Glutamine supports pancreatic cancer growth through a KRAS-regulated metabolic pathway. *Nature* 496 (7443), 101–105. doi:10.1038/nature12040
- Stumvoll, M., Perriello, G., Meyer, C., and Gerich, J. (1999). Role of glutamine in human carbohydrate metabolism in kidney and other tissues. *Kidney Int.* 55 (3), 778–792. doi:10.1046/j.1523-1755.1999.055003778.x
- Su, X., Shen, Z., Yang, Q., Sui, F., Pu, J., Ma, J., et al. (2019). Vitamin C kills thyroid cancer cells through ROS-dependent inhibition of MAPK/ERK and PI3K/AKT pathways via distinct mechanisms. *Theranostics* 9 (15), 4461–4473. doi:10.7150/thno.35219
- Tardito, S., Oudin, A., Ahmed, S. U., Fack, F., Keunen, O., Zheng, L., et al. (2015). Glutamine synthetase activity fuels nucleotide biosynthesis and supports growth of glutamine-restricted glioblastoma. *Nat. Cell Biol.* 17 (12), 1556–1568. doi:10.1038/ncb3272
- van der Reest, J., and Gottlieb, E. (2016). Anti-cancer effects of vitamin C revisited. *Cell Res.* 26 (3), 269–270. doi:10.1038/cr.2016.7
- Ward, P. S., and Thompson, C. B. (2012). Metabolic reprogramming: a cancer hallmark even warburg did not anticipate. *Cancer Cell* 21 (3), 297–308. doi:10.1016/j.ccr.2012.02.014
- Wise, D. R., and Thompson, C. B. (2010). Glutamine addiction: a new therapeutic target in cancer. *Trends Biochem. Sci.* 35 (8), 427–433. doi:10.1016/j.tibs.2010.05.003
- Xiangsong, Z., Changhong, L., Weian, C., and Dong, Z. (2006). PET Imaging of cerebral astrocytoma with 13N-ammonia. *J. Neurooncol.* 78 (2), 145–151. doi:10.1007/s11060-005-9069-x
- Yang, L., Achreja, A., Yeung, T.-L., Mangala, L. S., Jiang, D., Han, C., et al. (2016). Targeting stromal glutamine synthetase in tumors disrupts tumor microenvironment-regulated cancer cell growth. *Cell Metab.* 24 (5), 685–700. doi:10.1016/j.cmet.2016.10.011
- Yun, J., Mullarky, E., Lu, C., Bosch, K. N., Kavalier, A., Rivera, K., et al. (2015). Vitamin C selectively kills KRAS and BRAF mutant colorectal cancer cells by targeting GAPDH. *Science* 350 (6266), 1391–1396. doi:10.1126/science.aaa5004
- Yuneva, M. O., Fan, T. W. M., Allen, T. D., Higashi, R. M., Ferraris, D. V., Tsukamoto, T., et al. (2012). The metabolic profile of tumors depends on both the responsible genetic lesion and tissue type. *Cell Metab.* 15 (2), 157–170. doi:10.1016/j.cmet.2011.12.015
- Zheng, Z., Luo, G., Shi, X., Long, Y., Shen, W., Li, Z., et al. (2020). The Xc- inhibitor sulfasalazine improves the anti-cancer effect of pharmacological vitamin C in prostate cancer cells via a glutathione-dependent mechanism. *Cell Oncol.* 43 (1), 95–106. doi:10.1007/s13402-019-00474-8

**Conflict of Interest:** The authors declare that the research was conducted in the absence of any commercial or financial relationships that could be construed as a potential conflict of interest.

Copyright © 2021 Long, Qiu, Zhang, He, Shi, He, Chen, Shen, Li and Zhang. This is an open-access article distributed under the terms of the Creative Commons Attribution License (CC BY). The use, distribution or reproduction in other forums is permitted, provided the original author(s) and the copyright owner(s) are credited and that the original publication in this journal is cited, in accordance with accepted academic practice. No use, distribution or reproduction is permitted which does not comply with these terms.



# Functionalized Selenium Nanotherapeutics Synergizes With Zoledronic Acid to Suppress Prostate Cancer Cell Growth Through Induction of Mitochondria-Mediated Apoptosis and Cell Cycle S Phase Arrest

## OPEN ACCESS

### Edited by:

Dong-Hua Yang,  
St. John's University, United States

### Reviewed by:

Cundong Fan,  
Shandong First Medical University,  
China  
Yinghua Li,  
Guangzhou Medical University, China  
Pranav Gupta,  
Albert Einstein College of Medicine,  
United States  
Vinoth Kumar Lakshmanan,  
Medical Centre, Sri Ramachandra  
Institute of Higher Education and  
Research, India

### \*Correspondence:

Jianfu Zhao  
zhaojianfu@jnu.edu.cn

### Specialty section:

This article was submitted to  
Pharmacology of Anti-Cancer Drugs,  
a section of the journal  
Frontiers in Oncology

**Received:** 25 March 2021

**Accepted:** 10 May 2021

**Published:** 08 June 2021

### Citation:

An Y and Zhao J (2021) Functionalized  
Selenium Nanotherapeutics  
Synergizes With Zoledronic Acid to  
Suppress Prostate Cancer Cell  
Growth Through Induction of  
Mitochondria-Mediated Apoptosis  
and Cell Cycle S Phase Arrest.  
Front. Oncol. 11:685784.  
doi: 10.3389/fonc.2021.685784

Yulin An and Jianfu Zhao\*

Research Center of Cancer Diagnosis and Therapy, Department of Oncology, The First Affiliated Hospital, Jinan University, Guangzhou, China

The use of established drugs in new therapeutic applications has great potential for the treatment of cancers. Nanomedicine has the advantages of efficient cellular uptake and specific cell targeting. In this study, we investigate using lentinan-functionalized selenium nanoparticles (LET-SeNPs) for the treatment of prostate cancer (PCa). We used assays to demonstrate that a combination of LET-SeNPs and zoledronic acid (ZOL) can reduce PCa cell viability *in vitro*. Stability and hemocompatibility assays were used to determine the safety of the combination of LET-SeNPs and ZOL. The localization of LET-SeNPs was confirmed using fluorescence microscopy. JC-1 was used to measure the mitochondrial membrane potential, while the cellular uptake, cell cycle and apoptosis were evaluated by flow cytometry. Finally, cell migration and invasion assays were used to evaluate the effects of the combination treatment on cell migration and invasion. Under optimized conditions, we found that LET-SeNPs has good stability. The combination of LET-SeNPs and ZOL can effectively inhibit metastatic PCa cells in a concentration-dependent manner, as evidenced by cytotoxicity testing, flow cytometric analysis, and mitochondria functional test. The enhanced anti-cancer effect of LET-SeNPs and ZOL may be related to the regulation of BCL2 family proteins that could result in the release of cytochrome C from the inner membranes of mitochondria into the cytosol, accompanied by induction of cell cycle arrest at the S phase, leading to irreversible DNA damage and killing of PCa cells. Collectively, the results of this study suggest that the combination of SeNPs and ZOL can successfully inhibit the growth of PCa cells.

**Keywords:** selenium, nanomedicine, zoledronic acid, prostate cancer, apoptosis

## INTRODUCTION

Prostate cancer (PCa) is one of the leading causes of cancer-related death among men worldwide, with an incidence and mortality of approximately 11% and 2.5%, respectively (1–3). The high morbidity and mortality of PCa have aroused great concern among scientists. PCa is common in middle-aged and elderly patients with urinary tract obstruction. In addition, disease relapse with metastasis is common. However, diagnosis of PCa is challenging in the vast majority of patients because of the insidious symptoms in the early stage of disease. The cases of advanced stage of cancer have lost the opportunity for radical treatment at the time of diagnosis (4, 5). According to the recommendations of National Comprehensive Cancer Network guideline, endocrine therapy alone or in combination with radiotherapy have been used in clinical practice for the treatment of PCa with T3–T4 stage in the TNM classification. Such treatment can easily lead to castration-resistant prostate cancer (CRPC) (6, 7). Based on the characteristics of high degree of malignancy, short median survival time, high mortality, and insensitivity to a variety of chemotherapeutic drugs, clinicians use endocrine therapy combined with chemotherapy, targeted therapy, or immunotherapy for patients with distant bone metastases supplemented with local treatment and supportive therapy (e.g., nutrition to enhance immunity, pain relief, et al) (8). The goal in the treatment of PCa is to improve the quality of life and prognosis of patients with advanced PCa. The development of a more effective treatment strategy against PCa is urgently warranted.

In recent years, zoledronic acid (ZOL), a third-generation nitrogen-containing bisphosphate drug, has been used in the treatment of Paget's disease and osteoporosis (9–11). Clinical studies have confirmed the clinical efficacy of this drug in relieving bone metastasis of malignant tumors (12, 13). Numerous studies have shown that ZOL can delay bone metastasis of PCa, increase the number and activity of osteoblasts, and effectively inhibit the proliferation and activity of osteoclasts (14). Moreover, it can reduce the risk of osteoporosis (which reduced the risk of osteoporosis by 70% during a 3-year observation period), pathological fracture, and hypercalcemia (15, 16). It is generally accepted that ZOL inhibits the growth of tumor cells by inducing the isopentenylolation of cellular proteins through the mevaleric acid pathway. This effect has been confirmed in *in vitro* experiments in osteosarcoma and breast cancer. However, the therapeutic effect and potential mechanism of ZOL in the treatment of primary cancer with high risk for bone metastasis or PCa with bone metastasis warrant further investigation. In addition, ZOL is used in the treatment of bone metastatic cancer and common diseases, such as osteoporosis (17). Adjusting the annual cycle to a monthly cycle increases the occurrence of common side effects of drugs, such as headache, dizziness, bone pain, gastrointestinal reactions, nephrotoxicity, et al. Also, there is insufficient evidence to support continuous use of the drug for more than three years (18). Hence, the current clinical application status limits the use of ZOL.

Selenium (Se) is one of the essential and unique trace elements in the human body. It is mainly present in the form

of selenocysteine in protein and participates in immunity, reproduction, and other important functions of the body (19, 20). Selenoprotein is present in the 21st amino acid selenocysteine (SeC) (21). The human genome contains 25 selenoprotein genes, suggesting that Se plays an important role in the human body. Synthetic Se-containing compounds, including SeNPs and organic Se, have a wide range of biological functions, such as anti-oxidative and anti-tumor effects (22–24). These functions depend on the high level of intracellular reactive oxygen species caused by the high proliferation and metabolism of cancer cells, which increases sensitivity to Se oxidation damage. However, Se nanoparticles (SeNPs) have attracted considerable attention due to their optical, magnetic, and structural properties that molecules or bulk solids lack, as well as the low toxicity, faster absorption, and good biological activity (25, 26). Owing to their unique physicochemical properties, Se nanomaterials as drug carriers or therapeutic agents with good biocompatibility have demonstrated great potentials in the treatment of cancer in recent studies (27–31). SeNPs exert an anti-cancer effect at the nutritional level; however, high-level intake will convert it into an oxidant and lead to high toxicity. Interestingly, we found that lentinan-modified SeNPs have low toxicity, high permeability, and low blood clearance and could achieve efficient drug delivery to tumors and assist in the clinical treatment of solid tumors (32). However, determining the optimal nutritional concentration of SeNPs to effectively exert its anti-cancer effect is challenging. The present study investigated the anti-PCa effect of lentinan-functionalized SeNPs (LET-SeNPs) in combination with ZOL in the treatment of PCa.

## MATERIALS AND METHODS

### Materials

Sodium selenite ( $\text{Na}_2\text{SeO}_3$ ), chitosan (CS), polyvinylpyrrolidone (PVP), lentinan (LET), and vitamin C (Vc) were purchased from Guangzhou Chemical Reagent Factory (Guangzhou, China). Thiazolyl blue tetrazolium bromide (MTT), propidium iodide (PI), 4',6-diamino-2-phenylindole (DAPI), 5,5',6,6'-Tetrachloro-1,1',3,3'-tetraacetyl carbocyanine iodide (JC-1), Lyso-tracker, Hoechst 33342, Annexin V-fluorescein isothiocyanate (Annexin V-FITC), vascular endothelial growth factor (VEGF), Matrigel, and Giemsa dye solution were purchased from Sigma-Aldrich (St. Louis, MO, USA). Ultra-pure water, purified by Millipore's Milli-Q water purification system, was used in all experiments.

### Preparation of Different Modified SeNPs

Firstly, 1 mL of (10 mg/mL) CS, PVP, LET storage solution, and 1 mL of (10 mM) sodium selenite ( $\text{Na}_2\text{SeO}_3$ ) storage solution were added to a glass bottle. Next, 1 mL of (40 mM) Vc and 2 mL of ultra-pure water were added. The mixture was stirred at room temperature overnight and dialyzed in Milli-Q ultra-pure water for 24 h. Subsequently, the concentration of Se was measured by inductively coupled plasma atomic emission spectroscopy (ICP-AES). This study used coumarin 6-labeled

SeNPs to investigate the process of drug absorption by cells. The synthetic process was similar to that of SeNPs, adding coumarin 6 (20  $\mu\text{g/mL}$ ) prior to the addition of Vc.

## Structural Characterization of Different Modified SeNPs

The morphology and size of the nanoparticles were observed using transmission electron microscopy (TEM, Philips TECNAL-10). The hydrodynamic size and Zeta potential of different modified SeNPs were measured using a Malvern particle size analyzer. The energy dispersive spectroscopy (EDS, x-MaxTEM) element was analyzed by high-resolution TEM. The outer valence electron transition of the molecule was detected through the ultraviolet spectrum, and the skeleton structure of SeNPs was determined. The vibration of functional groups was detected by Fourier transform infrared spectroscopy.

## Stability of Different modified SeNPs Under Physiological Conditions

The stability and hemocompatibility of SeNPs were evaluated as previously described (33). Different modified SeNPs (0.5 mL) were incubated in phosphate-buffered saline (PBS), Dulbecco's modified Eagle's medium (DMEM), and human serum (0.5 mL). Changes in the hydrodynamic size of different modified SeNPs within 72 h were recorded using a Malvern nano-size analyzer (Zetasizer, Malvern Instruments, UK) to investigate their stability. To understand the biological safety of different modified SeNPs under physiological conditions, we simulated the changes in the physiological state of erythrocytes after administration. A volume of 0.5 mL of different modified SeNPs solutions (LET-SeNPs, CS-SeNPs, PVP-SeNPs; final concentration: 20  $\mu\text{M}$  and 40  $\mu\text{M}$ ) and only ZOL solution (final concentration: 10  $\mu\text{M}$  and 20  $\mu\text{M}$ ) were incubated with 0.5 mL of human erythrocyte suspension (centrifuged at 4°C and re-diluted with PBS) at 37°C for 4 h. A positive control group was formed using Triton  $\times$  100 (10 g Compact L, 0.5 mL) incubated with erythrocyte suspension (0.5 mL). Finally, the morphological changes in erythrocytes were observed using a light microscope (40 $\times$ , Nikon ECLIPSE Ts2, Japan). At the same time, the supernatant of the mixture was added into a 96-well plate, and fluorescence was measured at 540 nm.

## Cell Culture and MTT Assay for Cell Viability

The prostate cancer cell line (PC3) used in this study was purchased from ATCC Global Biology Co., Ltd. (ATCC, Manassas, VA, USA). The cells were cultured in DMEM medium containing 10% fetal bovine serum and 1% double antibody (mixture of 50 U/mL streptomycin and 100 U/mL penicillin) and incubated under the following conditions: 37°C, 5% CO<sub>2</sub>, 95% relative humidity. Briefly,  $2 \times 10^4$  cells/mL PC3 cells were seeded into 96-plate. After 24 h, the cells were pretreated with SeNPs for 8 h, then cells were treated with different concentration ZOL for 72 h. Finally, the cell viability was determined by MTT assay. The synergistic effect of the drugs was analyzed using the equivalent line method (34, 35).

## Cellular Uptake and Localization of LET-SeNPs *In Vitro*

The uptake of green fluorescence-labeled LET-SeNPs by PC3 cells was measured and analyzed by flow cytometry assay (Beckman Coulter), while the subcellular localization was analyzed using a fluorescence microscope (Cytation 5, Bio Tek, USA). PC3 cells in the logarithmic growth phase were inoculated into 6-cm cell Petri dishes (cell density:  $6 \times 10^4$  cells/mL, 5 mL/dish). After allowing the cells to adhere to the wall for 24 h, the cells were incubated with coumarin 6-labeled LET-SeNPs (final concentration: 40  $\mu\text{M}$ ) for different treatment durations (0, 1, 2, 4, 6, 8, and 12 h), and the culture medium was discarded. Subsequently, the cells were washed with PBS and collected. Following horizontal centrifugation and re-suspension of the cells in PBS, the fluorescence value of the forward scatter area channel was detected using a flow cytometry assay (Beckman Coulter) and the absorption of the drug by PC3 cells was analyzed. Following treatment, the cells were incubated with Lyso-tracker (Red, 80 nM) for 2 h to label the intracellular lysosome, and treated with Hoechst 33342 (Blue, 1 mg/mL) for 20 min to label the nucleus. The lysosome was labeled with Lyso-tracker and showed red fluorescence, the nucleus was labeled with Hoechst 33342 and showed blue fluorescence, and the drug emitted green fluorescence. After staining, the medium was discarded, and the cells were rinsed thrice with pre-cooled PBS to remove any free drug and dyes. The fluorescence signals of cells were detected using a fluorescence microscope (Cytation 5, Bio Tek, USA), and the cell images with different fluorescence channels were captured.

## Cell Cycle Analysis

Cell cycle distribution was determined by flow cytometry (36). PC3 cells in the logarithmic growth phase were inoculated into 6-cm dishes ( $2 \times 10^4$  cell/mL, 5 mL/dish) and cultured for 24 h until the cells adhered to the wall. A total of nine experimental groups were prepared as follows: blank control group, two different concentrations of ZOL (2.5 and 5  $\mu\text{M}$ ), two groups of LET-SeNPs alone (5 and 10  $\mu\text{M}$ ), two groups of LET-SeNPs (10  $\mu\text{M}$ ) combined with two different concentrations of ZOL (2.5 and 5  $\mu\text{M}$ ), and two groups of LET-SeNPs (5  $\mu\text{M}$ ) combined with two different concentrations of ZOL (2.5 and 5  $\mu\text{M}$ ). The experimental groups were pretreated with LET-SeNPs (final concentration: 5 and 10  $\mu\text{M}$ ) for 8 h, and the groups were cultured with different concentrations of ZOL (2.5, and 5  $\mu\text{M}$ ) for 72 h. After incubation, the cells were digested with 0.25% trypsin for 2–3 min, and the reaction was terminated by adding medium. Next, the cells were collected in a 15-mL centrifuge tube and centrifuged with washing solution (horizontal centrifuge: 1500 rpm, 10 min). Following centrifugation, the supernatant was discarded, pre-cooled 70% ethanol (1–2 mL) was added to each tube, and the tubes were placed in a refrigerator at  $-20^\circ\text{C}$  overnight. The next day, the cell mixture was centrifuged (horizontal centrifuge: 1500 rpm, 10 min), washed with PBS, centrifuged in an Eppendorf tube (1.5 mL), resuspended in PBS, mixed with 300  $\mu\text{L}$  of PI working solution (final concentration: 5  $\mu\text{M}$ ), and stained for 15 min at room temperature. Subsequently, the cells were washed and resuspended in PBS. The samples were



analyzed using BD flow cytometry ( $\geq 10000$  cells/sample), and the intracellular DNA content was detected using the FlowJo software (Phoenix Flow Systems, San Diego, CA, USA). The cell cycle at the Sub G0/G1, S, and G2/M phases, as well as the proportion of apoptotic peaks, were determined.

### Apoptosis Analysis

The effects of LET-SeNPs and ZOL on cell apoptosis were quantitatively analyzed by flow cytometry (37). PC3 cells in the logarithmic growth phase were inoculated into 6-cm dish ( $2 \times 10^4$  cell/mL, 5 mL/dish) and cultured for 24 h until the cells adhered to the wall. Subsequently, the experimental groups were pretreated with LET-SeNPs (final concentration: 5 and 10  $\mu\text{M}$ ) for 8 h, and the groups were cultured with different concentrations of ZOL (2.5 and 5  $\mu\text{M}$ ) for 72 h. Following incubation, the cell culture medium was collected in a 15-mL centrifuge tube, and the cells were washed once with PBS. Next, the cells were digested with 0.25% trypsin solution (without ethylenediaminetetraacetic acid) for 2–3 min. The reaction was terminated with the addition of DMEM, followed by centrifugation of the collected culture medium, washing solution and cell mixture (horizontal centrifuge: 1500 rpm). Subsequently, the cells were washed once with PBS and centrifuged to remove the supernatant. The cells were re-mixed with binding buffer (100  $\mu\text{L}$ ), and mixed with Annexin V-FITC and PI staining solution (2.5  $\mu\text{L}$  respectively). After thorough mixing, the cells were incubated at room temperature in the dark for 15 min. PBS (200  $\mu\text{L}$ ) was added to the flow tube cell suspension and flow cytometry assay (Beckman Coulter) was performed.

### Analysis of the Mitochondrial Membrane Potential

The decrease of the mitochondrial membrane potential is an important index which reflects cell apoptosis. When the mitochondrial membrane potential is high, the JC-1 dye accumulates in the matrix of the mitochondria to form polymers and produce red fluorescence. When the mitochondrial membrane potential is low, the JC-1 dye is a monomer producing green fluorescence. We measured the change of the mitochondrial potential based on the change of color and calculate the ratio of monomer to polymer to understand the cell damage caused by drugs. In the JC-1 membrane potential detection experiment, PC3 cells in the logarithmic growth phase were inoculated in 6-cm-cell dishes for 24 h (inoculation density:  $1 \times 10^5$  cells/mL; 5 mL/dish). The experimental groups were prepared as in the cell cycle experiment. The experimental groups were pretreated with LET-SeNPs (final concentration: 5 and 10  $\mu\text{M}$ ) for 8 h, and the groups were cultured with different concentrations of ZOL (2.5 and 5  $\mu\text{M}$ ) for 12 h. Subsequently, the culture medium was discarded, and the cells were digested with 0.25% trypsin. Next, the cells were washed twice with pre-cooled PBS and centrifuged to remove the supernatant (1500 rpm, 5 min); this was following by the addition of JC-1 dye (500  $\mu\text{L}$ ; working concentration: 10  $\mu\text{g/mL}$ , PBS dilution) to an Eppendorf tube (1.5 mL) and incubation at 37°C for 30 min. The cell populations (JC-1 aggregation and JC-1 monomer states) were analyzed by flow

cytometry assay (Beckman Coulter). The number of cells recorded in each experimental group was  $\geq 10000$ .

### Cell Invasion

The matrix gel was dissolved at 4°C, diluted with fetal bovine serum-free medium, evenly added to the Transwell chamber (pore diameter: 8  $\mu\text{M}$ , 30  $\mu\text{L}$ /well), and placed into the incubator at 37°C for 4 h for solidification. PC3 cells in the logarithmic growth phase were added to the upper chamber covered with the matrix gel (serum-free medium mixed with  $15 \times 10^4$  cell/mL, 100  $\mu\text{L}$ /well). Medium with 10% fetal bovine serum (500  $\mu\text{L}$ ) and 50 ng/mL VEGF were added in the lower chamber. The same concentration of drug was added in the upper and lower chambers, and the cells were incubated for 24 h. The following eight experimental groups were prepared: Control group; LET-SeNPs 5  $\mu\text{M}$  alone group; two ZOL (2.5 and 5  $\mu\text{M}$ ) groups; and two LET-SeNPs 5  $\mu\text{M}$  combined with different concentrations of ZOL (2.5 and 5  $\mu\text{M}$ ) groups. After 12 h of culture, cells in the upper chamber were fixed for 10 min with 4% paraformaldehyde. Subsequently, the fixative was removed, and the cells were stained with Giemsa stain and washed with ultra-pure water. Next, the non-invading cells and matrix gel in the chamber were gently removed using a cotton swab, and the cell invasion rate was observed and recorded under a microscope (Cytation 5, Bio Tek, USA).

### Cell Scratch Test

PC3 cells in the logarithmic growth phase were inoculated into 6-well plates ( $25 \times 10^4$  cell/mL, 2 mL/well) for cell adhesion. When the cells reached almost 100% confluence, the combined experimental group was pretreated with LET-SeNPs (final concentration: 5  $\mu\text{M}$ ) for 8 h and Hoechst 33342 (50 ng/mL) stain was added for 15 min. Subsequently, the medium was removed, and scratches were made at the bottom of the vertical plate with a 200- $\mu\text{L}$  pipette tip. The nonadherent cells were washed thrice with PBS. The cell images were captured using a fluorescence microscope (Cytation 5, Bio Tek, USA) and the state of cells was recorded. At the end of this step, ZOL at different concentrations (2.5 and 5  $\mu\text{M}$ ) diluted in serum-free medium containing VEGF (50 ng/mL) was added to each well. Next, the cells were cultured in an incubator. At 24 h and 48 h, the cell migration was observed and recorded using a fluorescence microscope (Cytation 5, Bio Tek, USA), and the scratch distance following migration was measured.

## RESULTS

### Synthesis and Characterization of LET-SeNPs

The LET-SeNPs have a spherical two-layer structure formed by Se atoms under the coating of lentinan. Lentinan is modified on the surface of the Se ball by intermolecular interaction. The morphology of the three types of modified SeNPs was observed by TEM. As shown in **Figure 1A**, the SeNPs modified by PVP, CS, and LET were spherical-like particles with different particle sizes. The TEM results showed that the particle size of CS-SeNPs

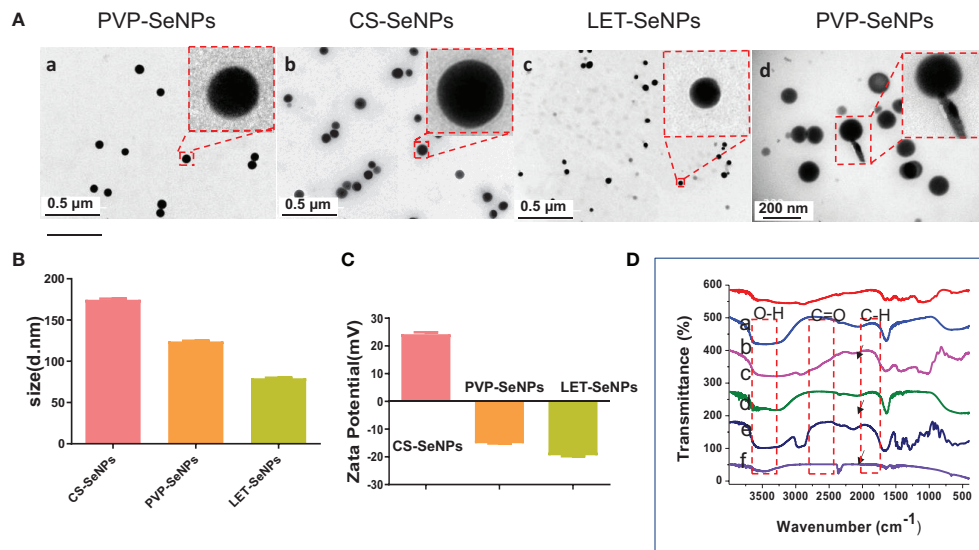


**FIGURE 1 | (A)** Transmission electron micrographs of SeNPs modified by polyvinylpyrrolidone (PVP, a and d), chitosan (CS, b), and lentinan (LET, c). **(B)** Columnar chart of the particle size and **(C)** potential diagram of three different modified SeNPs. **(D)** Fourier transform infrared spectroscopy (FT-IR) diagram, and the dotted lines indicate CS, CS-SeNPs, LET-SeNPs, PVP, and PVP-SeNPs, respectively. The arrowhead denotes the position of the functional groups.

was >150 nm, while that of PVP-SeNPs ranged between 100 and 150 nm. LET-SeNPs are colloids with a particle size <100 nm. As shown in **Figure 1Ac**. We analyzed the three types of SeNPs using the Zetasizer particle size analyzer (**Figure 1B**). We found that PVP-SeNPs and LET-SeNPs with relatively small particle sizes had a negative potential, whereas CS-SeNPs with a larger particle size were positively charged (**Figure 1C**). Fourier transform infrared spectroscopy (FT-IR) (as shown in **Figure 1D**) revealed that CS, LET and PVP have corresponding stretching oscillatory peaks around  $3300\text{ cm}^{-1}$ ,  $2350\text{ cm}^{-1}$ , and  $1385\text{ cm}^{-1}$ , respectively. These characteristic absorption peaks are simultaneously shown in their respective infrared spectra of modified SeNPs. In addition, we also found the characteristic absorption peak of SeNPs at  $1610\text{ cm}^{-1}$  on the infrared spectra of CS-, LET- and PVP-modified SeNPs. Moreover, as illustrated in **Figure 2**, the red Se atoms accumulated to form nanospheres. Also, the purple N element in the modified polymer was clearly visible, indicating the successful modification of various polysaccharides on the surface of SeNPs. The above results showed that the modification of SeNPs by polysaccharides was successful. Smaller particles size is more conducive to the cellular uptake of LET-SeNPs. Moreover, the sufficient negative charge of LET-SeNPs at -19.42 kept the nanosystems stable in complicated physiological environment. Hence, LET-SeNPs was more suitable than PVP-SeNPs and CS-SeNPs for cancer therapy.

## Enhancement of the Stability and Hemocompatibility of SeNPs

Under physiological conditions, the stability of SeNPs modified by different polysaccharides is a very important aspect for the evaluation of their medical application (38). To investigate the

stability of SeNPs modified by different polysaccharides, their size was measured in different solution environments using the dynamic light scattering method to evaluate changes in the hydration state. As shown in **Figures 3A–C**, the SeNPs modified by three different polysaccharides showed different degrees of stability in different solutions. LET-SeNPs and PVP-SeNPs were relatively stable in three different solution environments, whereas CS-SeNPs particle size exhibited greater instability in DMEM with 10% FBS. Among the three types of SeNPs modified by different polymers, the least change of particle size was the LET-SeNPs, followed by PVP-SeNPs, while CS-SeNPs were relatively unstable among the three solutions. Thus, LET-SeNPs have the best stability among the three types of SeNPs spheres, supporting its potential application in the field of medicine. The advantages offered by nanomedicines for biological application in the human body include a good biosafety profile and reliable *in vivo* circulation properties (39). However, under human physiological conditions, the hematocrit in blood reaches 37–45%. Thus, foreign NPs may cause some physiological stress reactions after entering the human body (40). Therefore, in this study, we tested the hemocompatibility of SeNPs functionalized with different polysaccharides (41). The hemolysis rates of ZOL and SeNPs with different surface modification were <5%, indicating their favorable safety profile (**Figures 3D, E**). For instance, the hemolysis of ZOL alone at the concentration of  $10\text{ }\mu\text{M}$  was approximately 0.66%. The rate of hemolysis for CS-SeNPs, LET-SeNPs, and PVP-SeNPs was 0.08%, 0.13%, and 0.13%, respectively, without visible damage to the red blood cells. We observed that the red blood cells showed a smooth double concave disk shape. These results demonstrated that SeNPs have good blood compatibility.

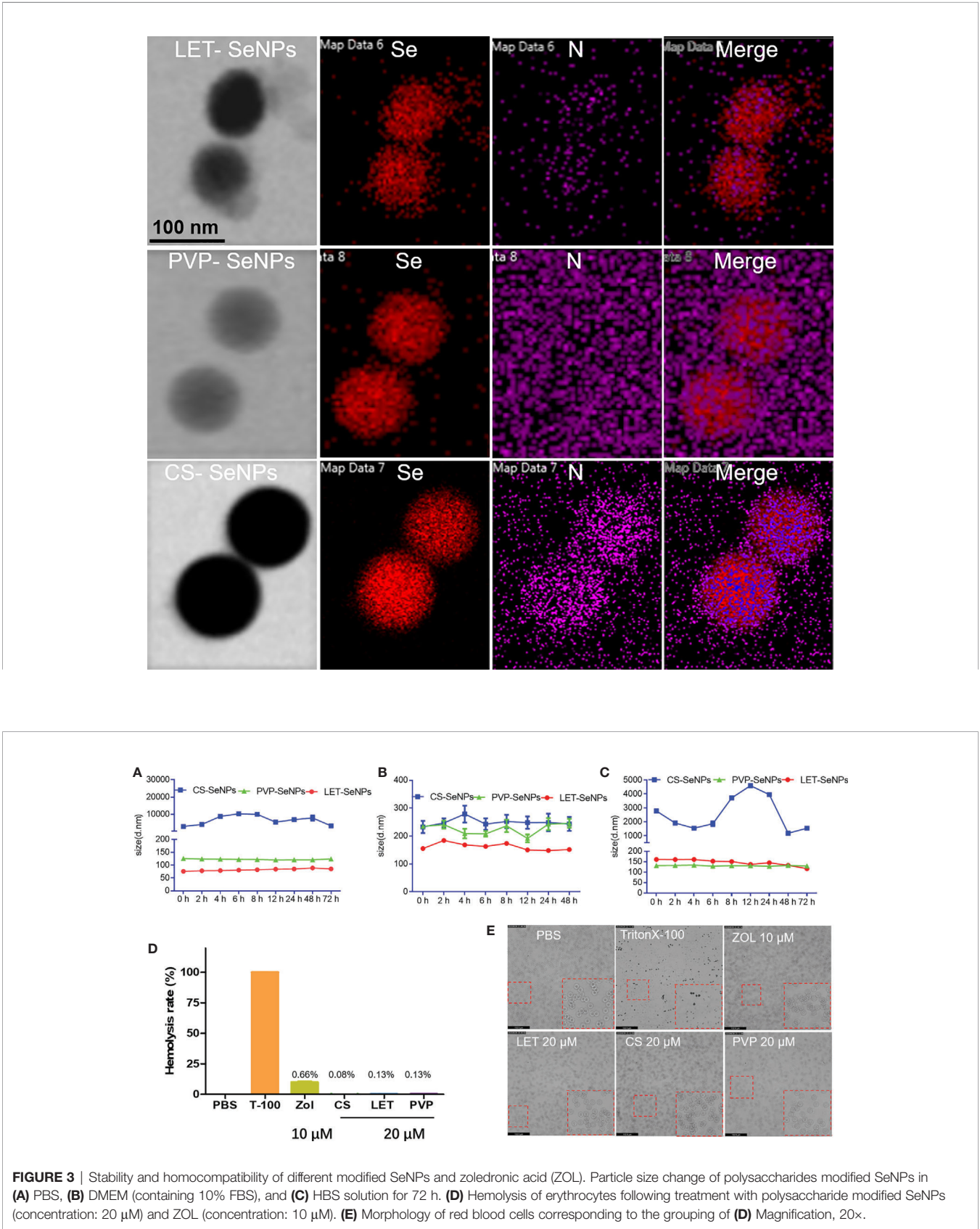


**FIGURE 3 |** Stability and homocompatibility of different modified SeNPs and zoledronic acid (ZOL). Particle size change of polysaccharides modified SeNPs in (A) PBS, (B) DMEM (containing 10% FBS), and (C) HBS solution for 72 h. (D) Hemolysis of erythrocytes following treatment with polysaccharide modified SeNPs (concentration: 20  $\mu$ M) and ZOL (concentration: 10  $\mu$ M). (E) Morphology of red blood cells corresponding to the grouping of (D) Magnification, 20 $\times$ .



## Cellular Uptake of LET-SeNPs

Drug absorption and half-life time are very important indicators that affect the drug efficacy. Therefore, we used flow cytometric analysis to analyze the absorption effect of LET-SeNPs alone and in combination with ZOL. The absorption of coumarin 6-labeled LET-SeNPs increased gradually from 1 h to 6 h, reached the absorption peak at 6 h and, subsequently, showed a downward trend (**Figures 4A, D**). **Figures 4B, E** illustrate that the fluorescence intensity increased in parallel with the concentration, indicating that the absorption of LET-SeNPs is concentration-dependent. It was known that SeNPs is disassembled by lysozyme (42). We found that PCas internalized coumarin 6-labeled LET-SeNPs in a time dependent manner. However, the cellular uptake of coumarin 6-labeled LET-SeNPs showed a downward trend after 6 h, which may account for the reason that LET-SeNPs begins to metabolize into other products to exhibit its anticancer activities. According to **Figures 4C, F**, after the addition of ZOL (2.5 and 5  $\mu$ M), the absorption of coumarin 6-labeled LET-SeNPs did not change significantly compared with that of LET-SeNPs alone but remained concentration-dependent. This result showed that addition of ZOL did not affect the absorption of SeNPs.

## Localization and Bio-response of LET-SeNPs

Next, we used fluorescence microscopy to examine the subcellular localization of LET-SeNPs after absorption. PC3 PCa cells were treated with coumarin 6-labeled LET-SeNPs and its distribution were observed at 0, 1, 2, 6, and 12 h. The red lysosome and blue

nucleus were observed without drug absorption at 0 h (**Figure 5A**). From 1 h, the green SeNPs were gradually observed in the lysosome, and reached the peak at 4 and 6 h; moreover, the morphology of LET-SeNPs-filled lysosomes was clearly observed. The drug fluorescence decreased gradually at 12 h, indicating that the cell may have the drug metabolized. In the process of drug transport and metabolism, we observed the different morphological changes of SeNPs by TEM. There was no significant change in the particle size and appearance of LET-SeNPs in the simulated intravascular blood environment (pH=7.4) (**Figure 5Ba**). In the tumor microenvironment (pH=6.8), the particle size of LET-SeNPs expanded and the irregular edge of the particle sphere dissolved (**Figure 5Bb**). As the drug continued to be transported to the cellular lysosomal environment (pH=5.3) (**Figure 5Bc**), the NPs were dissolved into small particles of different sizes, and clusters and flocs were blurred with cellular proteins appearing after cell lysis and death (**Figure 5Bd**). In this metabolic process, SeNPs were relatively stable during transportation, and final degradation occurred only when they reached the tumor cells. These results suggest that, surface decoration with LET can enhance the stability and bio-response of SeNPs, and might reduce the development of undesirable side effects on human body.

## Synergistic Anti-Cancer Action of ZOL and SeNPs

We used the MTT assay to evaluate the survival rate of cells treated with SeNPs and ZOL. Following treatment, the survival rate of PC3 cells decreased with the increase in the concentration of

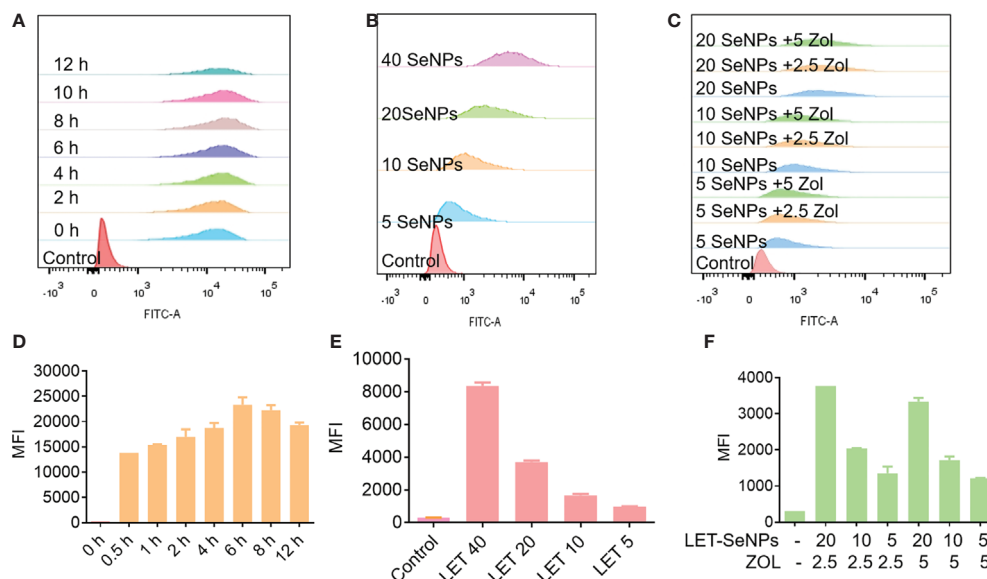


**FIGURE 4 |** Cellular uptake of coumarin 6-labeled LET-SeNPs in PC3 cells analyzed by flow cytometry. **(A)** Cellular uptake of LET-SeNPs at different time points (0, 0.5, 1, 2, 4, 6, 8, and 12 h) at 40  $\mu$ M. **(B)** Cellular uptake of coumarin 6-labeled LET-SeNPs at different concentrations (5, 10, 20, and 40  $\mu$ M) for 6 h. **(C)** Cellular uptake of LET-SeNPs combined with ZOL at different concentrations for 6 h. Mean fluorescence intensity (MFI) of coumarin 6-labeled LET-SeNPs at **(D)** different time points, **(E)** different concentrations, and **(F)** different concentrations combined with ZOL.



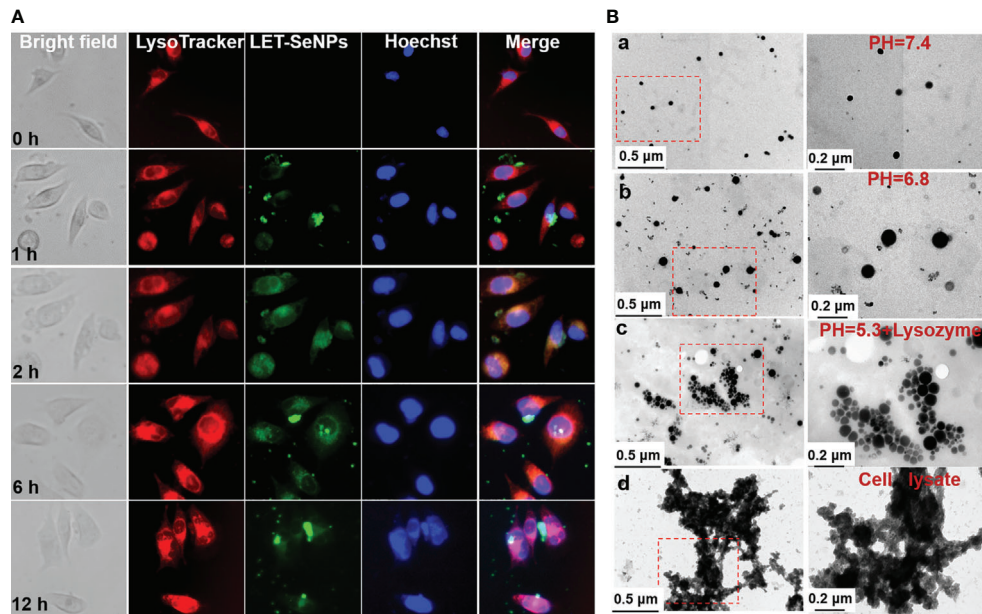


**FIGURE 5 |** Localization of LET-SeNPs in PC3 cells. **(A)** Cellular localization of LET-SeNPs (10  $\mu$ M) after incubation for different periods of time in PC3 cells. Nanoparticles (green), Lyso-tracker (red), and nucleus (blue). Scale: 50  $\mu$ m; magnification: 400 $\times$ . **(B)** TEM images of LET-SeNPs after incubation in different buffers (pH=7.4, a; pH=6.8, b; pH=5.3 + lysozyme, c; and cell lysate, d).

LET-SeNPs, PVP-SeNPs, and CS-SeNPs in a concentration-dependent manner (**Figures 6A–C**). The LET-SeNPs showed higher efficacy in killing cancer cells, most likely due to the anticancer activity of lentinan polysaccharide (43, 44). We also analyzed the synergistic effect using the equivalent line method. The results showed that, when IC60 was used, the concentration of LET-SeNPs alone and ZOL alone was 61.8  $\mu$ M and 10.3  $\mu$ M, respectively (**Figures 6D–F**). There was a synergistic effect of fixed concentration of LET-SeNPs at 10  $\mu$ M with ZOL at 1.25, 2.5, and 5  $\mu$ M (**Figures 6G–I**). Hence, LET-SeNPs at 5  $\mu$ M in combination with ZOL was selected for further examination of the mechanisms of action.

### Induction of Cell Apoptosis and Cell Cycle Arrest at the S Phase by ZOL and SeNPs

Further studies were performed to examine the anti-cancer modes of action of LET-SeNPs and ZOL in PC-3 cells. **Figures 7A, B** suggest that there is a certain dose-dependent increase of apoptosis in cells exposed to different concentrations of LET-SeNPs combined with ZOL. The apoptosis in the drug combination group was higher than that observed in the single drug control group. Specifically, the apoptotic cell of LET-SeNPs (10  $\mu$ M) and ZOL (5  $\mu$ M) was 7.04%. Thus, the co-treatment of LET-SeNPs and ZOL effectively induced PC-3 cells apoptosis. Furthermore, treatment with LET-SeNPs and ZOL either alone or in combination led to cell cycle arrest at the S phase, and the degree of cell cycle arrest increased in a drug concentration-dependent manner (**Figures 7C, D**). Correspondingly, the mitochondrial membrane potential also showed the same

trend, and the proportion of green monomers representing early cell death gradually increased. The monomer ratio of individual ZOL 5  $\mu$ M and LET-SeNPs 5  $\mu$ M was 40% and 69%, respectively, and the combined use of drugs almost reached 76% (**Figure 7E**). These results suggest that, the combination of LET-SeNPs and ZOL may induce apoptosis and cell cycle arrest at the S phase. Firstly, LET-SeNPs with ZOL inhibited cell proliferation through S phase block, then co-treatment damaged mitochondria and subsequently caused mitochondrial membrane diffusion, and eventually induces apoptosis to achieve effectively cancer therapy.

### Inhibition of Cancer Cell Migration and Invasion by ZOL and SeNPs

PCa cells are characterized by their ability to invade surrounding tissues. Moreover, they show a good cloning ability and can break through the basement membrane from carcinoma *in situ* to form metastatic foci and worsen the disease through the invasion-metastasis cascade reaction. We investigated whether the combination of ZOL and SeNPs could effectively inhibit the growth of tumor cells by inhibiting the migration and invasion of tumor cells (45, 46). According to the literature, ZOL in the concentration range of 1–100  $\mu$ M is sufficient to inhibit the adhesion, migration, and bone resorption of PCa cells. The invasion experiment showed that the effect of the drug combination was significantly better than that of any single drug and positively correlated with the drug concentration (**Figures 8A, B**). ZOL alone (2.5 and 5  $\mu$ M) exerted an inhibitory effect; however, this effect was more pronounced

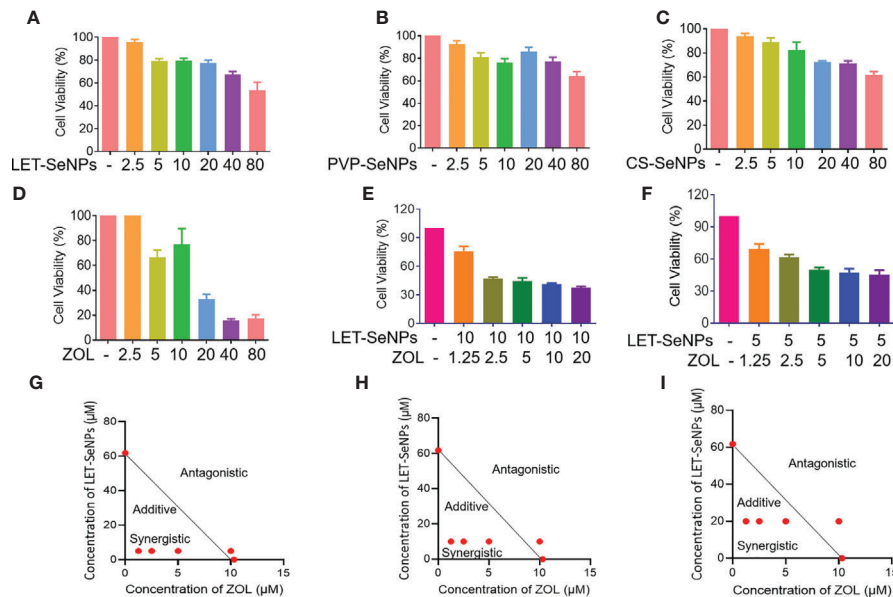


**FIGURE 6 |** Synergistic anti-cancer activities of SeNPs and ZOL against prostate cancer PC3 cells. **(A–D)** Cytotoxic effects of LET-SeNPs, PVP-SeNPs, CS-SeNPs, and ZOL on PC3 cells for 24 h. **(E, F)** Synergistic effects of SeNPs with ZOL on PC3 cells. The cells were pretreated with ZOL for 8 h, then were treated with different concentration SeNPs for 24 h. **(G–I)** Isobologram analysis of the synergistic anti-proliferative effect of combined SeNPs (10, 5, and 20 μM, respectively) with ZOL on PC3 cells. The data points in the isobologram correspond to a 60% inhibition of growth in cells with combined treatment.

when ZOL was combined with LET-SeNPs. This effect was also reflected in the results of the cell migration experiments (**Figures 8C, D**). Therefore, ZOL and LET-SeNPs can effectively inhibit the invasion and migration of PCa cells.

## DISCUSSION

Combination chemotherapy has been postulated as a promising treatment strategy for cancer therapy. There are many advantages for combined treatment therapy, such as increasing drug efficiency and decreasing toxicity. A number of studies have demonstrated the benefit of chemotherapy strategy in combination with selenium, such as Selenocystine in combination with 5-fluorouracil, auranofin and doxorubicin, methylseleninic acid and cisplatin (47–50). Overall, the findings of this study improve the current understanding of the anti-tumor effect of Se. At present, there are numerous Se species available for anti-cancer applications, including inorganic Se, organic Se, and SeNPs. However, different types of Se species exert different biological effects due to their different morphology, chemical structure, specific metabolic pathways in cells and tissues, and variety of intracellular targeting molecules. SeNPs are nanoscale particles with unique advantages (e.g., low toxicity and fast absorption) compared with other Se (51, 52). The biocompatibility, bio-safety and excellent biological activities of Selenium particles have been confirmed to be superior than inorganic and organic selenium species, which indicates its potential application for cancer

treatment. Additionally, lentinan has a lot of biological and physiological activities. Lentinan is a non-specific immune stimulant, which stimulates the proliferation of mononuclear macrophages and enhance the activity of T and NK cells. Additionally, the autoimmunity of patients with advanced prostate cancer is low. Therefore, the choice of LET-SeNPs may help to modulate the immune system of PCas and enhance the therapeutic efficiency ZOL. Further exploration and determination of the reference value are warranted for the clinical use of LET-SeNPs.

The results of our study showed that the anti-tumor effect of the combination of these two drugs was significantly enhanced. This is in consistent with the evidence regarding Se compounds previously reported in the literature. At present, the conventional chemotherapy drugs used in clinical practice are accompanied by severe gastrointestinal reactions, hair loss, and other side effects (41). Multi-cycle chemotherapy leads to a decline in patient compliance and affects the final treatment effect (42). The combination of drugs used in this study exerted a good anti-cancer effect, and can effectively overcome the issue of poor compliance. SeNPs are commercially available as a health product used to enhance immunity. However, when combined with ZOL (which acts through S-phase blockade), SeNPs can achieve the same or better anti-tumor effect. This simple dual-drug regimen can reduce the side effects caused by multiple drugs.

Evidences have shown that triggering ROS overproduction thereby activating p53 and MAPKs pathways to induce apoptosis is one of the important mechanisms of SeNPs in cancer therapy (53). Additionally, ROS overproduction triggering DNA damage

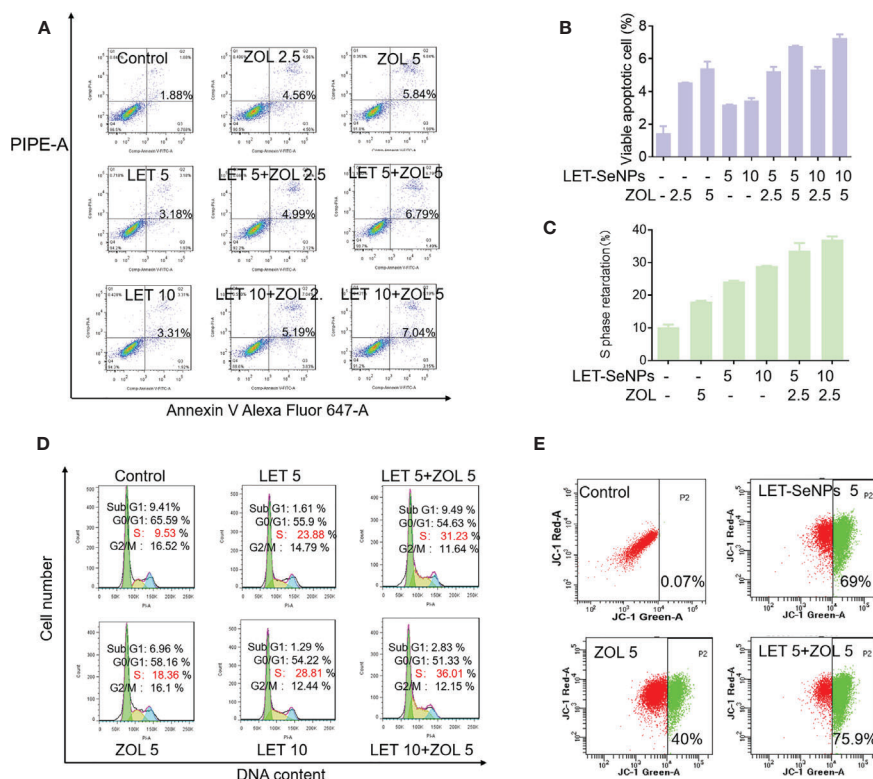


**FIGURE 7 |** Induction of cell apoptosis and cell cycle arrest at S phase by ZOL and SeNPs. **(A, B)** Annexin V-PI co-staining assay to evaluate apoptosis in PC3 cells induced by LET-SeNPs (5 and 10 μM) and ZOL (2.5 and 5 μM). **(C, D)** Cell cycle distribution analysis of PC3 cells treated with LET-SeNPs (5 and 10 μM) and ZOL (5 μM). **(E)** Mitochondrial membrane potential in PC-3 cells following treatment with LET-SeNPs (5 μM) and ZOL (5 μM).

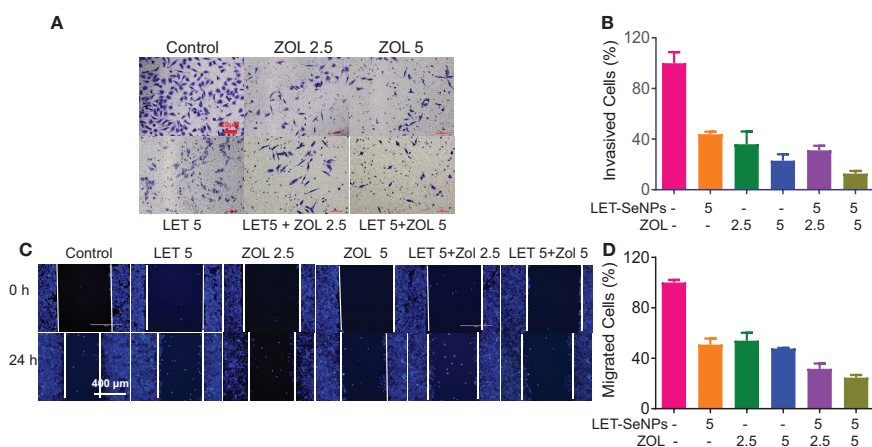


**FIGURE 8 |** Inhibition of cancer cell invasion and migration of ZOL with SeNPs. **(A)** Wound healing assay and **(C)** anti-invasion effects of ZOL with LET-SeNPs on PC3 cells. The relative reduction in the width of the wound by the healing cells and the numbers of invaded cells suggested a remarkable anti-metastasis effect of combined treatment. **(B)** The migration cells in **(A, D)** invasion cells in **(C)** The quantitative data were analyzed by manual counting (% of control).

and mitochondria malfunction thereby inducing apoptosis have also been confirmed to be the most important role of selenium for cancer therapy (54). Therefore, ROS-mediated signaling pathway may also contribute to the anticancer activities of LET-SeNPs and

ZOL. We suggested that the killing of tumor cells by the combined drugs may be related to mitochondrial damage, and the imbalance between the BCL family and BCL family-related proteins. These effects induce the release of cytochrome C, leading

to irreversible damage in cancer cells, DNA damage, nuclear fragmentation, decrease in cell size, and finally death.

Nevertheless, our study has limitations. This study is currently not supported by *in vivo* data, including animal and human experiments. In addition, there is no quantitative study on the specific mechanism of combined drug use.

Collective, this study revealed the good anti-tumor effect of the combination of LET-SeNPs and ZOL on PCa. The results will provide a rationale for the application of nanomedicine for the diagnosis and treatment of PCa.

## DATA AVAILABILITY STATEMENT

The original contributions presented in the study are included in the article/supplementary material. Further inquiries can be directed to the corresponding author.

## REFERENCES

- Fenton JJ, Weyrich MS, Durbin S, Liu Y, Bang H, Melnikow J. Prostate-Specific Antigen-Based Screening for Prostate Cancer: Evidence Report and Systematic Review for the US Preventive Services Task Force. *JAMA* (2018) 319(18):1914–31. doi: 10.1001/jama.2018.3712
- Force U.S.P.S.T., Grossman DC, Curry SJ, Owens DK, Bibbins-Domingo K, Caughey AB, et al. Screening for Prostate Cancer: US Preventive Services Task Force Recommendation Statement. *JAMA* (2018) 319(18):1901–13. doi: 10.1001/jama.2018.3710
- Underwood W. Racial Regional Variations in Prostate Cancer Survival Must Be Viewed in the Context of Overall Racial Disparities in Prostate Cancer. *JAMA Netw Open* (2020) 3(3):e201854. doi: 10.1001/jamanetworkopen.2020.1854
- Sharma S, Zapatero-Rodriguez J, O'Kennedy R. Prostate Cancer Diagnostics: Clinical Challenges and the Ongoing Need for Disruptive and Effective Diagnostic Tools. *Biotechnol Adv* (2017) 35(2):135–49. doi: 10.1016/j.biotechadv.2016.11.009
- Litwin MS, Tan HJ. The Diagnosis and Treatment of Prostate Cancer A Review. *Jama Journal Of Am Med Assoc* (2017) 317(24):2532–42. doi: 10.1001/jama.2017.7248
- Cornford P, Bellmunt J, Bolla M, Briers E, De Santis M, Gross T, et al. EAU-Estrogen-Siog Guidelines on Prostate Cancer. Part II: Treatment of Relapsing, Metastatic, and Castration-Resistant Prostate Cancer. *Eur Urol* (2017) 71(4):630–42. doi: 10.1016/j.eururo.2016.08.002
- Zhou M, Wang XY, Xia J, Cheng YT, Xiao LC, Bei Y, et al. A Mansonone Derivative Coupled With Monoclonal Antibody 4d5-Modified Chitosan Inhibit AKR1C3 to Treat Castration-Resistant Prostate Cancer. *Int J Of Nanomed* (2020) 15:3087–98. doi: 10.2147/IJn.S241324
- Wan Z, Xie FY, Wang L, Zhang GQ, Zhang H. Preparation and Evaluation of Cabazitaxel-Loaded Bovine Serum Albumin Nanoparticles for Prostate Cancer. *Int J Of Nanomed* (2020) 15:5333–44. doi: 10.2147/IJn.S258856
- Viereck V, Emons G, Lauck V, Frosch KH, Blaschke S, Grundker C, et al. Bisphosphonates Pamidronate and Zoledronic Acid Stimulate Osteoprotegerin Production by Primary Human Osteoblasts. *Biochem And Biophys Res Commun* (2002) 291(3):680–6. doi: 10.1006/bbrc.2002.6510
- Rosen LS, Gordon DH, Dugan W, Major P, Eisenberg PD, Provencher L, et al. Zoledronic Acid Is Superior to Pamidronate for the Treatment of Bone Metastases in Breast Carcinoma Patients With at Least One Osteolytic Lesion. *Cancer* (2004) 100(1):36–43. doi: 10.1002/cncr.11892
- Chen K, Wang Y, Liu J, Kang J, Ge Y, Huang W, et al. In Situ Preparation of a CsPbBr<sub>3</sub>/Black Phosphorus Heterostructure With an Optimized Interface and Photodetector Application. *Nanoscale* (2019) 11(36):16852–9. doi: 10.1039/C9NR06488E
- Wilson C, Bell R, Hinsley S, Marshall H, Brown J, Cameron D, et al. Adjuvant Zoledronic Acid Reduces Fractures in Breast Cancer Patients; an AZURE (BIG 01/04) Study. *Eur J Cancer* (2018) 94:70–8. doi: 10.1016/j.ejca.2018.02.004
- Lu Y, Li M, Li L, Wei S, Hu X, Wang X, et al. High-Activity Chitosan/Nano Hydroxyapatite/Zoledronic Acid Scaffolds for Simultaneous Tumor Inhibition, Bone Repair and Infection Eradication. *Mater Sci Eng C Mater Biol Appl* (2018) 82:225–33. doi: 10.1016/j.msec.2017.08.043
- Chen L, Ding Y, Wang Y, Liu X, Babu R, Ravis W, et al. Codelivery of Zoledronic Acid and Doublestranded RNA From Core-Shell Nanoparticles. *Int J Nanomed* (2013) 8:137–45. doi: 10.2147/IJn.S38928
- Black DM, Delmas PD, Eastell R, Reid IR, Boonen S, Cauley JA, et al. Once-Yearly Zoledronic Acid for Treatment of Postmenopausal Osteoporosis. *N Engl J Med* (2007) 356(18):1809–22. doi: 10.1056/NEJMoa067312
- Coleman R, Cook R, Hirsh V, Major P, Lipton A. Zoledronic Acid Use in Cancer Patients More Than Just Supportive Care? *Cancer* (2011) 117(1):11–23. doi: 10.1002/cncr.25529
- Yang Q, Liu DZ, Liu M, Ji QF, Mei QB, Cheng Y, et al. Bone-Targeted Calcium Phosphate-Polymer Hybrid Nanoparticle Co-Deliver Zoledronate and Docetaxel to Treat Bone Metastasis of Prostate Cancer. *J Of Pharm Sci* (2021) 110(2):876–87. doi: 10.1016/j.xphs.2020.11.005
- Li PF, Zhao ZM, Wang LT, Jin XH, Shen YX, Nan CR, et al. Minimally Effective Concentration of Zoledronic Acid to Suppress Osteoclasts *In Vitro*. *Exp And Ther Med* (2018) 15(6):5330–6. doi: 10.3892/etm.2018.6120
- Hoffmann PR, Berry MJ. The Influence of Selenium on Immune Responses. *Mol Nutr Food Res* (2008) 52(11):1273–80. doi: 10.1002/mnfr.200700330
- Cao W, Wang L, Xu HP. Selenium/Tellurium Containing Polymer Materials in Nanobiotechnology. *Nano Today* (2015) 10(6):717–36. doi: 10.1016/j.nantod.2015.11.004
- Shrimali RK, Irons RD, Carlson BA, Sano Y, Gladyshev VN, Park JM, et al. Selenoproteins Mediate T Cell Immunity Through an Antioxidant Mechanism. *J Of Biol Chem* (2008) 283(29):20181–5. doi: 10.1074/jbc.M802559200
- Wang CB, Xia Y, Huo SC, Shou DW, Mei Q, Tang WJ, et al. Silencing of MEF2D by siRNA Loaded Selenium Nanoparticles for Ovarian Cancer Therapy. *Int J Of Nanomed* (2020) 15:9759–70. doi: 10.2147/IJn.S270441
- He LZ, Lai HQ, Chen TF. Dual-Function Nanosystem for Synergetic Cancer Chemo-/Radiotherapy Through ROS-Mediated Signaling Pathways. *Biomaterials* (2015) 51:30–42. doi: 10.1016/j.biomaterials.2015.01.063
- Huang YY, Fu YT, Li MT, Jiang DW, Kuttyreff CJ, Engle JW, et al. Chirality-Driven Transportation and Oxidation Prevention by Chiral Selenium Nanoparticles. *Angewandte Chemie Int Ed* (2020) 59(11):4406–14. doi: 10.1002/anie.201910615

## AUTHOR CONTRIBUTIONS

JZ: conception, design of research, edited, revised, and approved final version of manuscript. YA: performed experiments, analyzed data, prepared figures, drafted manuscript, and interpreted results of experiments. All authors contributed to the article and approved the submitted version.

## FUNDING

This work was supported by the Science and Technology Program of Guangzhou (202102010083), Guangdong Science and Technology Plan Project (2017ZC0005), the Guangdong Science and Technology Research Project of Traditional Chinese Medicine (20182020), and the Cultivation Program of the First Affiliated Hospital of Jinan University (802226).



25. Liu T, Lai LH, Song ZH, Chen TF. A Sequentially Triggered Nanosystem for Precise Drug Delivery and Simultaneous Inhibition of Cancer Growth, Migration, and Invasion. *Adv Funct Mater* (2016) 26(43):7775–90. doi: 10.1002/adfm.201604206
26. Zhang ZH, Du YX, Liu T, Wong KH, Chen TF. Systematic Acute and Subchronic Toxicity Evaluation of Polysaccharide-Protein Complex-Functionalized Selenium Nanoparticles With Anticancer Potency. *Biomater Sci* (2019) 7(12):5112–23. doi: 10.1039/c9bm01104h
27. Yang YH, Xie Q, Zhao ZN, He LZ, Chan L, Liu YX, et al. Functionalized Selenium Nanosystem as Radiation Sensitizer of I-125 Seeds for Precise Cancer Therapy. *ACS Appl Mater Interfaces* (2017) 9(31):25857–69. doi: 10.1021/acsami.7b07167
28. Huang J, Huang W, Zhang Z, Lin X, Lin H, Peng L, et al. Highly Uniform Synthesis of Selenium Nanoparticles With EGFR Targeting and Tumor Microenvironment-Responsive Ability for Simultaneous Diagnosis and Therapy of Nasopharyngeal Carcinoma. *ACS Appl Mater Interfaces* (2019) 11(12):11177–93. doi: 10.1021/acsami.8b22678
29. Li T, Pan S, Gao S, Xiang W, Sun C, Cao W, et al. Diselenide-Pemetrexed Assemblies for Combined Cancer Immuno-, Radio-, and Chemotherapies. *Angew Chem Int Ed Engl* (2020) 59(7):2700–4. doi: 10.1002/anie.201914453
30. Liu T, Xu LG, He LZ, Zhao JF, Zhang ZH, Chen Q, et al. Selenium Nanoparticles Regulates Selenoprotein to Boost Cytokine-Induced Killer Cells-Based Cancer Immunotherapy. *Nano Today* (2020) 35:100975. doi: 10.1016/j.nantod.2020.100975
31. Gao SQ, Li TY, Guo Y, Sun CX, Xianyu BR, Xu HP. Selenium-Containing Nanoparticles Combine the NK Cells Mediated Immunotherapy With Radiotherapy and Chemotherapy. *Adv Mater* (2020) 32(12):1907568. doi: 10.1002/Adma.201907568
32. Yang F, Huang JR, Liu HX, Lin WQ, Li XL, Zhu XQ, et al. Lentinan-Functionalized Selenium Nanosystems With High Permeability Infiltrate Solid Tumors by Enhancing Transcellular Transport. *Nanoscale* (2020) 12(27):14494–503. doi: 10.1039/d0nr02171g
33. Liu T, Shi CZ, Duan LQ, Zhang ZH, Luo LP, Goel S, et al. A Highly Hemocompatible Erythrocyte Membrane-Coated Ultrasmall Selenium Nanosystem for Simultaneous Cancer Radiosensitization and Precise Antiangiogenesis. *J Of Mater Chem B* (2018) 6(29):4756–64. doi: 10.1039/c8tb01398e
34. He LZ, Huang GN, Liu HX, Sang CC, Liu XX, Chen TF. Highly Bioactive Zeolitic Imidazolate Framework-8-Capped Nanotherapeutics for Efficient Reversal of Reperfusion-Induced Injury in Ischemic Stroke. *Sci Adv* (2020) 6(12):eaay9751. doi: 10.1126/sciadv.aay9751
35. Wu ZX, Yang Y, Zeng L, Patel H, Bo L, Lin L, et al. Establishment and Characterization of an Irinotecan-Resistant Human Colon Cancer Cell Line. *Front Oncol* (2020) 10:624954. doi: 10.3389/fonc.2020.624954
36. Li YD, Mao Y, Dong XD, Lei ZN, Yang YQ, Lin LZ, et al. Methyl-Cantharidinimide (MCAS) Has Anticancer Efficacy in ABCB1-and ABCG2-Overexpressing and Cisplatin Resistant Cancer Cells. *Front Oncol* (2020) 10:932. doi: 10.3389/fonc.2020.00932
37. Wu ZX, Peng Z, Yang YQ, Wang JQ, Teng QX, Lei ZN, et al. M3814, a DNA-PK Inhibitor, Modulates Abcg2-Mediated Multidrug Resistance in Lung Cancer Cells. *Front Oncol* (2020) 10:674. doi: 10.3389/fonc.2020.00674
38. Huang W, He LZ, Ouyang J, Chen Q, Liu C, Tao W, et al. Triangle-Shaped Tellurium Nanostars Potentiate Radiotherapy by Boosting Checkpoint Blockade Immunotherapy. *Matter* (2020) 3(5):1725–53. doi: 10.1016/j.matt.2020.08.027
39. Hosnedlova B, Kepinska M, Skalickova S, Fernandez C, Ruttkay-Nedecky B, Peng QM, et al. Nano-Selenium and Its Nanomedicine Applications: A Critical Review. *Int J Of Nanomed* (2018) 13:2107–28. doi: 10.2147/Ijn.S157541
40. Wu LP, Wang DY, Li ZB. Grand Challenges in Nanomedicine. *Mater Sci Eng C Mater Biol Appl* (2020) 106:110302. doi: 10.1016/J.Msec.2019.110302
41. Neu M, Germershaus O, Behe M, Kissel T. Bioreversibly Crosslinked Polyplexes of PEI and High Molecular Weight PEG Show Extended Circulation Times *In Vivo*. *J Of Controlled Release* (2007) 124(1-2):69–80. doi: 10.1016/j.jconrel.2007.08.009
42. Liu T, Lai L, Song Z, Chen T. A Sequentially Triggered Nanosystem for Precise Drug Delivery and Simultaneous Inhibition of Cancer Growth, Migration, and Invasion. *Adv Funct Mater* (2016) 26(43):7775–90. doi: 10.1002/adfm.201604206
43. Yang F, Huang J, Liu H, Lin W, Li X, Zhu X, et al. Lentinan-Functionalized Selenium Nanosystems With High Permeability Infiltrate Solid Tumors by Enhancing Transcellular Transport. *Nanoscale* (2020) 12(27):14494–503. doi: 10.1039/D0NR02171G
44. Song Z, Luo W, Zheng H, Zeng Y, Wang J, Chen T. Translational Nanotherapeutics Reprograms Immune Microenvironment in Malignant Pleural Effusion of Lung Adenocarcinoma. *Adv Healthcare Mater* (2021) e2100149. doi: 10.1002/adhm.202100149
45. Jacob K, Webber M, Benayahu D, Kleinman HK. Osteonectin Promotes Prostate Cancer Cell Migration and Invasion: A Possible Mechanism for Metastasis to Bone. *Cancer Res* (1999) 59(17):4453–7.
46. Dong W, Luo Y, Zhang G, Zhang H, Liang Y, Zhuo Y, et al. Carbon Nanospheres Exert Antitumor Effects Associated With Downregulation of 4E-BP1 Expression on Prostate Cancer. *Int J Nanomed* (2020) 15:5545–59. doi: 10.2147/IJN.S257522
47. Fan C, Chen J, Wang Y, Wong Y-S, Zhang Y, Zheng W, et al. Selenocystine Potentiates Cancer Cell Apoptosis Induced by 5-Fluorouracil by Triggering Reactive Oxygen Species-Mediated DNA Damage and Inactivation of the ERK Pathway. *Free Radical Biol Med* (2013) 65:305–16. doi: 10.1016/j.freeradbiomed.2013.07.002
48. Fan C, Zheng W, Fu X, Li X, Wong Y, Chen T. Enhancement of Auranofin-Induced Lung Cancer Cell Apoptosis by Selenocystine, a Natural Inhibitor of TrxR1 *In Vitro* and *In Vivo*. *Cell Death Dis* (2014) 5(4):e1191–1. doi: 10.1038/cddis.2014.132
49. Fan C, Zheng W, Fu X, Li X, Wong Y-S, Chen T. Strategy to Enhance the Therapeutic Effect of Doxorubicin in Human Hepatocellular Carcinoma by Selenocystine, A Synergistic Agent That Regulates the ROS-Mediated Signaling. *Oncotarget* (2014) 5(9):2853. doi: 10.18632/oncotarget.1854
50. Zhang Y, Zheng S, Zheng J-S, Wong K-H, Huang Z, Ngai S-M, et al. Synergistic Induction of Apoptosis by Methylseleninic Acid and Cisplatin, the Role of ROS-ERK/AKT-p53 Pathway. *Mol Pharm* (2014) 11(4):1282–93. doi: 10.1021/mp400749f
51. Zheng L, Li C, Huang X, Lin X, Lin W, Yang F, et al. Thermosensitive Hydrogels for Sustained-Release of Sorafenib and Selenium Nanoparticles for Localized Synergistic Chemoradiotherapy. *Biomaterials* (2019) 216:119220. doi: 10.1016/j.biomaterials.2019.05.031
52. Liu T, Zeng L, Jiang W, Fu Y, Zheng W, Chen T. Rational Design of Cancer-Targeted Selenium Nanoparticles to Antagonize Multidrug Resistance in Cancer Cells. *Nanomedicine* (2015) 11(4):947–58. doi: 10.1016/j.nano.2015.01.009
53. Liu T, Zeng L, Jiang W, Fu Y, Zheng W, Chen T. Rational Design of Cancer-Targeted Selenium Nanoparticles to Antagonize Multidrug Resistance in Cancer Cells. *Nanomed: Nanotechnol Biol Med* (2015) 11(4):947–58. doi: 10.1016/j.nano.2015.01.009
54. Fernandes AP, Gandin V. Selenium Compounds as Therapeutic Agents in Cancer. *Biochim Biophys Acta (BBA) General Subj* (2015) 1850(8):1642–60. doi: 10.1016/j.bbagen.2014.10.008

**Conflict of Interest:** The authors declare that the research was conducted in the absence of any commercial or financial relationships that could be construed as a potential conflict of interest.

Copyright © 2021 An and Zhao. This is an open-access article distributed under the terms of the Creative Commons Attribution License (CC BY). The use, distribution or reproduction in other forums is permitted, provided the original author(s) and the copyright owner(s) are credited and that the original publication in this journal is cited, in accordance with accepted academic practice. No use, distribution or reproduction is permitted which does not comply with these terms.



# A Novel Mice Model for Studying the Efficacy and IRAEs of Anti-CTLA4 Targeted Immunotherapy

Shengchao Xu<sup>1†</sup>, Xi Yan<sup>2†</sup>, Gan Dai<sup>3</sup> and Chengke Luo<sup>1\*</sup>

<sup>1</sup> Department of Neurosurgery, Xiangya Hospital of Central South University, Changsha, China, <sup>2</sup> Health Management Center, Xiangya Hospital of Central South University, Changsha, China, <sup>3</sup> Department of Microbiology, Xiangya School of Medicine, Central South University, Changsha, China

## OPEN ACCESS

### Edited by:

Haichang Li,  
The Ohio State University,  
United States

### Reviewed by:

Shouheng Lin,  
Chinese Academy of Sciences  
(CAS), China  
Gamal Eldein Fathy Abd-Elatef  
Abd-Elrahman,  
National Research Centre, Egypt

### \*Correspondence:

Chengke Luo  
ck\_luo@csu.edu.cn

<sup>†</sup>These authors have contributed  
equally to this work

### Specialty section:

This article was submitted to  
Pharmacology of Anti-Cancer Drugs,  
a section of the journal  
Frontiers in Oncology

Received: 08 April 2021

Accepted: 20 May 2021

Published: 10 June 2021

### Citation:

Xu S, Yan X, Dai G and Luo C (2021) A  
Novel Mice Model for Studying the  
Efficacy and IRAEs of Anti-CTLA4  
Targeted Immunotherapy.  
Front. Oncol. 11:692403.  
doi: 10.3389/fonc.2021.692403

**Background:** Patient-derived orthotopic xenograft (PDOX) is a popular animal model for translational cancer research. Immunotherapy is a promising therapy against glioblastoma (GBM). However, the PDOX model is limited to evaluating immune-related events. Our study aims to establish GBM humanized PDOX (HPDOX) mice models to study the mechanism of anti-CTLA4 immunotherapy and immune-related adverse events (IRAEs).

**Methods:** HPDOX models were established by culturing GBM tissues and intracranially implanting them in NSG mice. Meanwhile, peripheral blood mononuclear cells (PBMCs) were separated from peripheral blood and of GBM patients and administrated in corresponding mice. The population of CD45+, CD3+, CD4+, CD8+, and regulatory T (Treg) cells was estimated in the peripheral blood or tumor.

**Results:** T cells derived from GBM patients were detected in HPDOX mice models. The application of anti-CTLA4 antibodies (ipilimumab and tremelimumab) significantly inhibited the growth of GBM xenografts in mice. Moreover, residual patient T cells were detected in the tumor microenvironment and peripheral blood of HPDOX mice and were significantly elevated by ipilimumab and tremelimumab. Additionally, Treg cells were decreased in mice with IRAEs. Lastly, the proportion of CD4+/CD8+ T cells dramatically increased after the administration of ipilimumab. And the degree of IRAEs may be related to CD56+ expression in HPDOX.

**Conclusions:** Our study established HPDOX mice models for investigating the mechanism and IRAEs of immunotherapies in GBM, which would offer a promising platform for evaluating the efficacy and IRAEs of novel therapies and exploring personalized therapeutic strategies.

**Keywords:** glioblastoma, humanized patient-derived orthotopic xenograft, immune-related adverse events, anti-CTLA4 immunotherapy, regulatory T cells

## BACKGROUND

Glioblastoma (GBM) is one of the most malignant primary brain cancers. The median overall survival of GBM patients is only 14.6 months, despite the satisfactory surgery and concomitant chemoradiotherapy (1–3). Therefore, there is a clear urgent to reveal the mechanism of tumorigenesis and development and develop novel therapeutic agents against GBM. However, recent clinical trials without appropriate mice models in this area have resulted in dissatisfactory and inconsistent therapeutic effects. It cannot reflect the tumor microenvironment, principal histologic, and genetic characteristics of GBM. In this context, the development of accurate and reproducible animal models is essential.

The patient-derived orthotopic xenograft (PDOX) has attracted more and more attention to facilitate biologic studies, preclinical drug evaluation, and biomarker identification (4–8). Nevertheless, clinically relevant PDOX models are not fully capable of recapitulating patients' immune systems, which impedes the evaluation of immunotherapy efficacy. In recent years, although the co-cultures combined GBM organoids with immune cells such as human peripheral blood mononuclear cells (PBMCs) have been of great concern, which could be an ideal platform for immunotherapy selection (9), since the tumor-derived spheres are still not in the same conditions such as hypoxia or immune microenvironment, as to those occur in intracranial. Besides, the co-culture conditions combined GBM organoids with immune cells are not the optimum one for each cell type according to compromise strategy (10, 11). Meanwhile, immune-related adverse events (IRAEs) arising under immunotherapy forcing us potentially without precedent to think of strategies to maintain the immune system. Therefore, revealing the mechanism of T cells from PBMCs in the action of IRAEs and anti-tumor immunity is essential to balancing the immune system in developing a cancer immunotherapy strategy.

Humanized PDOX models (HPDOX) were regarded as the next-generation PDOX. Although humanized mice were reported in few tumors such as myeloma and hepatocellular carcinoma, humanized GBM mice models were seldom studied in recent literature (12). Those models were essential to study the potential and limitations for differential immune-enhancing approaches, as well as contribute to refining the framework of emerging immunotherapy strategies and related IRAEs against GBM. Our study was conducted to establish humanized GBM mice models and investigate the efficacy and IRAEs of anti-CTLA4 immunotherapy. Our studies aimed to provide a platform to develop effective strategies to minimize immune therapeutic IRAEs without impeding anti-tumor immunity in the future.

## MATERIALS AND METHODS

### Human GBM Tissue Specimens

Fresh GBM specimens were obtained from patients who received surgery in the Department of Neurosurgery, Xiangya Hospital

from 2016 to 2020. All clinical samples were collected with informed consent obtained from the patients. All procedures were conducted following the Declaration of Helsinki (1964).

### Peripheral Blood

All procedures were approved by the Ethics Committee of Xiangya Hospital. Peripheral blood (PB) specimens were collected from patients who received surgery in the Department of Neurosurgery, Xiangya Hospital from 2016 to 2020 with written informed consent obtained. PBMCs were isolated using Lymphoprep (Stem Cell Technologies) according to the manufacturer's instructions.

### T Cell Reconstitution and Anti-CTLA4 Antibodies

The reconstitution of CD4+ and CD8+ T cells of PB from mice was monitored every week. A total of  $1 \times 10^6$  GBM patients' PBMCs were implanted into sub-lethally irradiated (0.5 Gy) 4–6-week-old male NSG mice by tail vein. The anti-CTLA4 antibodies (ipilimumab, ipilimumab with N298A mutation, and tremelimumab) were generous gifts from Huntsman Cancer Institute, University of Utah, USA.

### Generation of HPDOX Mice Model

Some 4–6-week-old male NSG (NOD.Cg-*Prkdc*<sup>scid</sup> *Il2rg*<sup>tm1Wjl</sup>/SzJ) mice were used in this study. All animal experiments were obtained and performed at the Laboratory Animal Center of the Central South University and all procedures were approved by the Ethics Committee of Xiangya Hospital following the Guide for the Care and Use of Laboratory Animals. PDOX was established from surgically resected specimens in NSG mice. Fresh surgical specimens were rinsed with Hank's solution three times. Then the tumor tissue was cut into several 1–3 mm<sup>3</sup> pieces. The tissue was incubated with accutase for 30 min at 37°C and dissociated into single cells. Cells were cultured in serum-free medium (Canada, Stemcell Technologies) in an incubator. Before transplantation, cells were digested and resuspended in the medium with a density of  $1 \times 10^8$ /ml. The injection was located at the skull 1–2 mm lateral and 1 mm anterior to the bregma. Each time, 5 µl of cell suspension was aspirated using the Hamilton syringe and slowly injected into the brain at a depth of 2–3 mm with a rate of 1 µl/min. After the completion of the injection, maintain the needle for 3 min before withdrawing to reduce the backflow of the injected cells spillover. After 14 days of PDOX established, the mice with criterion can be incorporated for further study: (a) The weight loss is no more than 10%; (b) Motor function is normal, without hypokinesia; (c) Hair's clean and shiny, without ruffings; (d) The bowel and bladder functions are normal; and (e) No signs of infection or any other illness. To estimate the tumor volume, the simple random sampling method was employed to select three mice from each group for sacrifice. The tumor volume was calculated according to the HE slides with the greatest cross-sectional area. Tumor volume was determined using the following equation: length (L)  $\times$  width<sup>2</sup> (W)  $\times$  0.5. Tumor volume of the three mice was within our expectation, whereas some mice were excluded because the mice failed to meet the standard as described

previously. There is no significant difference in tumor volume at this time point (**Figure S1**,  $P > 0.05$ ). Afterward, the HPDOX mice model was established by injecting PBMCs from GBM patients at 4 h after irradiation (13). The antibodies were given twice a week after PBMCs transplantation. The mice in our study were monitored for up to 3 months for weight, health, or immune status. HPDOX suffered systemic IRAEs were assessed by the criterion of mice graft-versus-host disease (GVHD) clinical scoring system including weight loss, posture, activity, fur texture, and skin integrity (14). The mouse's total score was estimated twice a week. Mice were sacrificed according to the following criteria: weight loss of 20–25%; tumor weight reached 10% of mice weight; appetite loss of more than 24 h; depression and hypothermia. The observation endpoint was defined as 104 days (14 days for model establishment and 3 months for observation).

## Flow Cytometry

PB containing the anticoagulant sodium heparin was centrifuged at 1,500 rpm for 5 min at room temperature. Red blood cells were lysed by Red Blood Cell Lysis Buffer (Sigma), and the white blood cells were pelleted at 300g for 3 min. Flow cytometric analysis was performed using the LSR FORTRESSA device (BD Biosciences, San Jose, CA, USA). The samples were incubated with the following antibodies to identify T and regulatory T (Treg) cells: anti-human CD3 FITC (BD Biosciences), anti-human CD4 Pacific Blue (BD Biosciences), anti-human CD8 APC (BD Biosciences), anti-human CD45 PE (BD Biosciences), IFN $\gamma$ -APC (BioLegend), CD45RA- PE (BD Biosciences), CD45RO-APC-cy7 (BD Biosciences), anti-human FOXP3 PE (BD Biosciences), CFSE FITC (BD Biosciences), CD25 PE (BD Biosciences), CD127 PE-cy7 (BD Biosciences), CD56 PE (BD Biosciences), and HLA-DR PE-cy7 (BD Biosciences). The following controls were used: unstained cells and single-stained cells; and dead cells, which in conjunction with AutoComp software were used to set accurate compensation and

data analysis. Cells were counted per sample, and the data were analyzed with FlowJo V10.

## Statistical Analyses

Statistical analyses were conducted using GraphPad Prism v8.0. One-way ANOVA or unpaired two-tailed Student's t-test was used to estimate the difference between two or more groups. Kaplan–Meier analysis was used to evaluate the survival difference between two groups. Two-sided  $p < 0.05$  was considered as statistical significance.

## RESULTS

### Establishment of GBM HPDOX Mice Models

Establishment of GBM PDOX from patient's tissues. The establishment of the PDOX model was conducted by injecting patients' tumor-derived GBM cells into female immune-deficient nude mice. Candidate mice for PDOX models could be NSG, NOD-SCID, and nude. Herein we investigated *in vitro* culture of 26 PDOX generated and/or passaged in NSG mice. The workflow was shown in **Figure 1**, and details were described above. The demographic information of patients from whom PDOX was generated was summarized in **Table 1**. The age of patients ranged from 22 to 76 years old with a mean of  $58 \pm 12.05$  years old, and 11 patients were women and 15 were men. The tumor volume varied from 4.88 to 115.33 cm<sup>3</sup>, with a mean of  $48 \pm 26.60$  cm<sup>3</sup>. GBM cells from each specimen were injected into five mice, in which 12 specimens successfully inherited in mice. The overall engraftment rate of GBM PDOX in NSG mice was 46.15% (60/130). The total time of PDOX establishment ranged from 44 to 126 days, with a mean of  $62 \pm 17.5$  days. Humanized GBM PDOX by transplanting the same patient's PBMCs. Firstly, we established

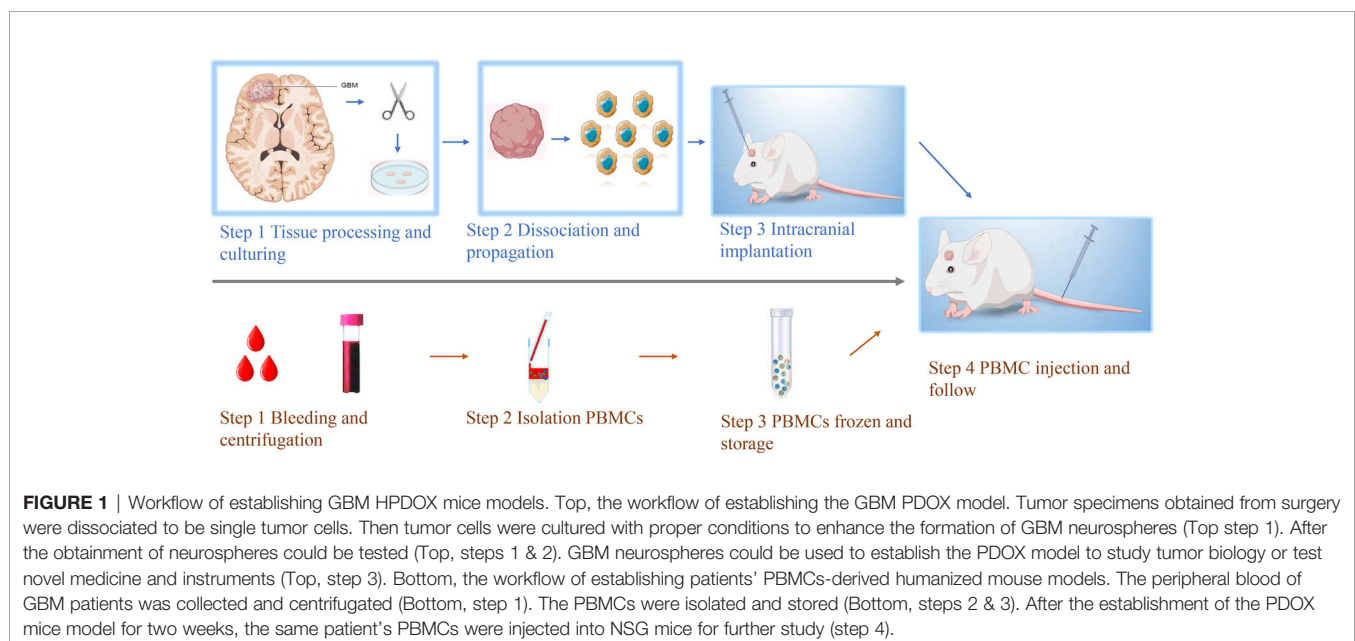




**TABLE 1** | The demographic and clinical information for patients of PDOX models.

Case ID	Age	Sex	Race	Pathology	Grades	Tumor Volume (cm <sup>3</sup> )	Smoke status	Pretreatment	Passage	In vivo Days
1	62	Male	Han	GBM	IV	11.76	Current	NO	–	–
2	70	Male	Tujia	GBM	IV	27.95	Former	NO	–	–
3	61	Female	Han	GBM	IV	31.4	Current	NO	F1	53
4	73	Male	Han	GBM	IV	115.33	Former	NO	F1	88
5	46	Female	Han	GBM	IV	15.17	Current	NO	F1	67
6	52	Male	Han	GBM	IV	100.68	Current	NO	F1	48
7	39	Female	Zhuang	GBM	IV	4.88	Never	NO	F1	44
8	22	Male	Han	GBM	IV	42.47	Never	Surgery/RT/CT	F1	56
9	64	Male	Han	GBM	IV	78.44	Current	NO	F1	68
10	67	Male	Han	GBM	IV	59.59	Current	NO	–	–
11	63	Female	Han	GBM	IV	29.97	Former	NO	F1	67
12	58	Male	Han	GBM	IV	47.38	Current	NO	F1	46
13	55	Female	Han	GBM	IV	47.36	Former	NO	F1	126
14	57	Female	Han	GBM	IV	56.76	Never	NO	F1	57
15	56	Male	Han	GBM	IV	62.2	Former	NO	F1	59
16	76	Female	Han	GBM	IV	105.13	Never	NO	F1	48
17	54	Male	Han	GBM	IV	29.47	Former	NO	F1	76
18	67	Female	Han	GBM	IV	33.43	Former	NO	F1	68
19	72	Male	Han	GBM	IV	41.79	Former	NO	–	–
20	73	Female	Han	GBM	IV	40.71	Current	NO	F1	67
21	64	Male	Tujia	GBM	IV	47.47	Former	NO	–	53
22	68	Female	Han	GBM	IV	18.54	Former	NO	F1	57
23	61	Male	Han	GBM	IV	35.87	Former	NO	F1	51
24	57	Female	Miao	GBM	IV	40.22	Current	NO	F1	49
25	43	Male	Han	GBM	IV	61.94	Former	NO	–	–
26	40	Male	Han	GBM	IV	49.39	Current	NO	F1	52

GBM, glioblastoma; RT, radiotherapy; CT, chemotherapy.

GBM PDOX mice. Two weeks later, the HPDOX models were established by engrafting the same patient's PBMCs (Figure 1, bottom).

## Patients' T Cells Reconstituted Well in GBM HPDOX Mice

Timepoint of the construction of HPDOX mice model. PBMCs were collected from GBM patients and the HPDOX model was constructed in PDOX mice bearing tumors derived from the same patients (Figure 2A). Flow cytometry of CD4+ and CD8+ T cells in HPDOX to explore the differentiated T cells within transplanted PBMCs (Figure 2B). The population of CD4+ (Figure 2C) and CD8+ (Figure 2D) T cells in GBM HPDOX mice. Our results showed both CD4+ and CD8+ T cells reconstituted well in GBM HPDOX mice.

## Evaluation of Antitumor Effects of Anti-CTLA4 Antibodies in HPDOX Mice Model

GBM07 and GBM22 were selected as the representation since they had a high expression of CTLA4 (Table S1 and Figure 3A). After the construction of the HPDOX model, mice were treated with anti-CTLA4 antibody ipilimumab and tremelimumab twice weekly as the workflow described before. Results showed that tumor volume was significantly reduced after the application of ipilimumab and tremelimumab ( $P < 0.05$ ) (Figures 3B, C). After the intervention, residual human T cells (CD45+, CD3+) could be detected and their levels were significantly elevated in the tumor microenvironment and PB in HPDOX mice ( $P < 0.05$ ) (Figures 3D–G). Then we explored the population of the subgroups of the T cells. The

activated T cells were presented with a higher expression of IFN- $\gamma$ + and CD25+. The population of the activated T cells was increased significantly after the treatment of anti-CTLA4 antibodies ( $P < 0.01$ , Figures S2A–C). The exhausted T cells presented the lower expression of IFN- $\gamma$ + (Figure S2B). The exhausted T could differentiate into the activated T cells in certain conditions. The effector T cells are usually CD45RA positive, which was increased dramatically after treatment ( $P < 0.001$ , Figures S2A, D). The memory T cells are CD45RO positive, which showed no significant difference between the groups (Figures S2A, E). The P value of the survival data of the HPDOX 07, and HPDOX 22 was 0.0082 and 0.0003 respectively, which indicated the significant difference between the treatment groups (Figures 3H, I). However, for the tremelimumab, the P value was 0.1118 and 0.0102 respectively, which indicated the significant difference between the treatment groups only in HPDOX 22 instead of HPDOX 07. These results indicated that CTLA4 played an inhibitory role in immune surveillance and HPDOX models could be appropriate approaches for revealing antitumor mechanisms and effects of anti-CTLA4 immunotherapy.

## FOXP3+ and Ratio of CD4+/CD8+ T Cells Were Associated With IRAEs

To prolong the period for evaluation of the efficacy and IRAEs of immunotherapy, the detail of PBMCs transplantation is essential for the success of HPDOX (Table 2). The period can be prolonged to  $47.90 \pm 17.91$  days engrafted with the decreased number ( $1 \times 10^6$  vs  $>1 \times 10^7$  normally) of autologous patients' PBMCs (Figure S3 and Table 1). Further, we detected the effect of ipilimumab at different

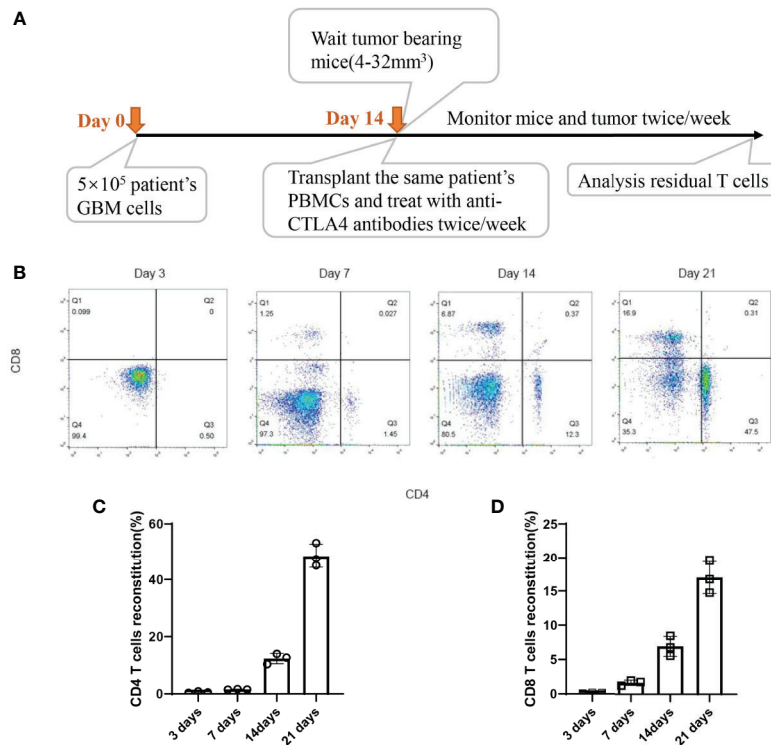


**FIGURE 2** | The reconstitution of T cells derived from GBM patients in HPDOX mice model. **(A)** Timepoint of the construction of HPDOX mice model. **(B)** Flow cytometry analysis of CD4<sup>+</sup> and CD8<sup>+</sup> T cells in NSG mice with transplanted PBMCs. **(C, D)** The population of CD4<sup>+</sup> **(C)** and CD8<sup>+</sup> **(D)** T cells in NSG mice with transplanted PBMCs. Each experiment was repeated at least three times, and three repeats were included each time.

doses in HPDOX mice models. The construction of HPDOX was detailed as before and GBM26 was taken as an example. Ten mice in each group were administrated with a high dose (10  $\mu\text{g/g}$ ) and normal dose (3  $\mu\text{g/g}$ ) of ipilimumab respectively. IRAEs were detected in 7/10 in the high dose group, only 1/10 in the normal dose group within the next two months (Table 3). After the intervention, we found that CD4<sup>+</sup> and CD8<sup>+</sup> T cells reconstituted well in GBM HPDOX26 mice (Figures 4A top and B), and the ratio of CD4<sup>+</sup>/CD8<sup>+</sup> T cells was dramatically increased in mice with IRAEs ( $P < 0.05$ ) (Figure 4C). For the mice without IRAEs, the CD4/CD8 ratio after therapy was  $2.34 \pm 2.12$ , which is the normal range of human. But for the mice with IRAEs, the ratio shifts to  $8.06 \pm 2.69$ . The CD4/CD8 ratio increased because the percentage of CD4 T cells increased, while the percentage of CD8 T cells decreased in PB. Moreover, the FOXP3<sup>+</sup> Treg cells were decreased in mice with IRAEs ( $P < 0.05$ ) (Figures 4A bottom and D). These results indicated that the promotion of CD4<sup>+</sup> T cells and the suppression of CD8<sup>+</sup> and FOXP3<sup>+</sup> Treg cells were associated with the occurrence of IRAEs. The construction of the HPDOX mice model could provide a platform for assessing adverse events of immunotherapies.

### The Degree of IRAEs in HPDOX May Be Related to CD56<sup>+</sup> Cells

After the treatment of ipilimumab, the HPDOX with mild or severe IRAEs were accessed by flow cytometry to detect the

possible mechanism of IRAEs. The whole blood was collected at the 7th and 35th days after the autologous PBMCs transplantation. As is shown in Figure 5, HPDOX suffered systemic IRAEs were assessed by the criterion of mouse GVHD clinical scoring system including weight loss, posture, activity, fur texture, and skin integrity (14). The CD4, CD8, CD25, CD127, CD56, and HLA-DR were detected to evaluate the expression of CD4, CD8 in T cells, the CD25<sup>+</sup> CD127<sup>-</sup> Treg cells, CD56, and HLA-DR (Figures 5A, B). Those results showed, after the treatment of ipilimumab, there was no significant difference in the CD56 expression in the mild IRAEs group (Figure 5C), although increased in the severe IRAEs group. It indicates that the degree of IRAEs in HPDOX may be related to CD56<sup>+</sup> cells. Similarly, the CD25<sup>+</sup>CD127<sup>-</sup> Treg cells were significantly decreased, while the HLA-DR expression was increased in both mild and severe IRAEs groups (Figures 5D, E).

## DISCUSSION

During the past decades, various animal models have been developed to study brain tumor (15). Although established cell lines such as U87 and U251 have inherited most of the genetic and genomic features of GBM, they bear nothing in common with the actual patients' GBM such as invasion histologic hallmarks (6). the development of severely

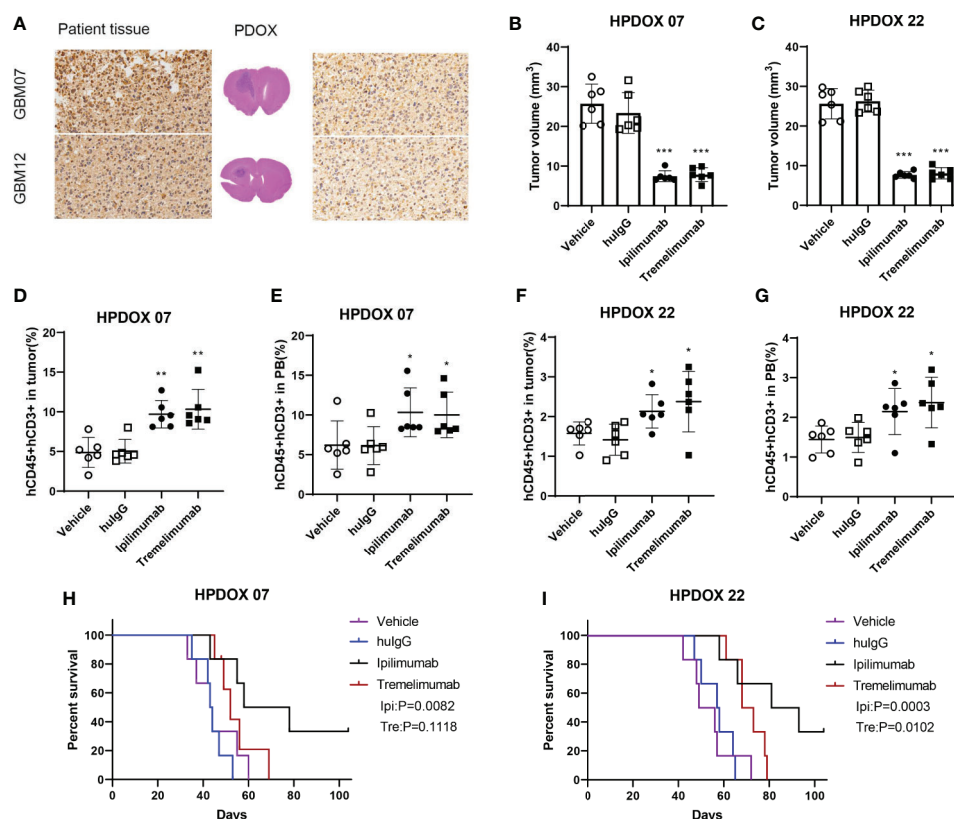


**FIGURE 3 |** Evaluating the antitumor effect of anti-CTLA4 monoclonal antibodies in HPDOX. **(A)** IHC analyzes anti-CTLA4 in HPDOX 07, HPDOX 22; Scale bar: 20  $\mu$ m (sides)/1,000  $\mu$ m (middle). **(B, C)** Tumor volume of GBM xenograft in mice treated with Vehicle, hulgG, ipilimumab, and tremelimumab. **(D–G)** The population of T cells in GBM tissues **(D, F)** and peripheral blood **(E, G)** in mice treated with Vehicle, hulgG, ipilimumab, and tremelimumab. **(H, I)** The survival data of the HPDOX 07, and HPDOX 22 was presented after the treatment respectively. There were six mice in each group. Data were represented as mean  $\pm$  SD. \* $P < 0.05$ , \*\* $P < 0.01$ , \*\*\* $P < 0.001$ .

**TABLE 2 |** Establishing autologous GBM HPDOX.

	Materials	Characteristics and delivery routes in the immunodeficient mouse	Analyses performed for HPDOX
Immunity	PBMCs by intraperitoneal	Human cells or cytokines by intravenous	Mature and function T cells and Treg Graft-versus-host disease
GBM	Patient derived orthotopic xenograft (PDOX)	Preclinical study of drugs and cells by intravenous	Weight loss Tumor growth Mutation Access therapeutic drugs
TME	PDOX +Autologous PBMCs by intraperitoneal	Preclinical study of drugs, cells, ICIs, and Vaccination by intravenous	Weight/hair loss Tumor growth Mutation Access therapeutic drugs Immune response IRAEs

TME, tumor microenvironments; ICIs, immune checkpoint inhibitors; IRAEs, immune-related adverse events.

immunocompromised mice has laid a solid foundation of PDOX, which has attracted more and more attention to facilitating biologic studies, preclinical drug evaluation, and biomarker identification (4–8). There are two main methods we have tried to obtain single cells for establishing the PDOX mice model: firstly, GBM tumor tissue right after they obtain from surgery is dissociated into single cells by treatment with Accutase™ solution

to digest the extracellular material; secondly, the primary GBM cultures of tissue-derived cells which may acquire purer GBM cells but the resemblance disappeared with passages increasingly (6). The primary GBM culture conditions are also be used for the culture of GBM stem cells, which can enhance the success of produce those phenotypes from patients' tissue in PDOX via few cells with enlarging tumor-initiating potential (4).

**TABLE 3** | Evaluating the IRAEs under the treatment of ipilimumab.

IRAEs	Mild	Severe	Total	P-value
Low dose	10	2	12	0.0306
High dose	2	10	12	
Total	12	12	24	

IRAEs, immune-related adverse events.

Therefore, PDOX can reproduce biological features of GBM, such as brain invasion, microvascular proliferation, and anti-tumor therapy. Moreover, PDOX can simulate an appropriate microenvironment for cancer research compared with heterotopic extracranial implantation (16, 17). However, a limitation of PDOX should be addressed that it cannot be used in the researches on the immune of the microenvironment because of the requirement for immune-deficient nude mice as hosts (18).

Therefore, the HPDOX mice model was developed, which was a promising approach to facilitate the understanding of human immunity and the evaluation of the efficacy and IRAEs of immunotherapy *in vivo*. Stem-like cells derived HPDOX was reported with a low occurrence of IRAEs such as GVHD but represent few features of cancer in patients (19). HPDOX derived from patients' PBMCs is the easiest way, which has limited application in following antigenic immune responses, but still is applied to access human immunosuppressive reagents (19). Although the novel mouse strains have been developed to inhibit the IRAEs such as GVHD by MHC complex-deficient mouse (20, 21), the immune cell differentiation and response could also be impeded. In this study, we established HPDOX mice models and evaluated the potential mechanism of anti-CTLA4 immunotherapy

in GBM. Patients' PBMCs could be engrafted into PDOX to reconstitute T cells for humanizing. Usually, the GVHD occurs 2–4 weeks after PBMC transfer. To prolong the period for evaluation of the efficacy and IRAEs of immunotherapy, the detail of PBMCs transplantation is essential for the success of HPDOX. The period can be prolonged after engrafted with the decreased number of autologous patients' PBMCs. Specifically, IRAEs were assessed by weight loss, posture, activity, fur texture, and skin integrity. Although PBMCs derived humanized mice have been thought to be an appropriate platform to evaluate the efficacy of targeted therapy or immunotherapy, no previous literature has described its application in assessing the efficacy and IRAEs of immunotherapies in the GBM HPDOX mice model. The reconstitution of PBMCs to T cells is faster than stem-like cells, and it has higher veracity as a model (22). Similarly, our study revealed that the application of PBMCs could efficiently construct the HPDOX mice model to investigate the antitumor activities and IRAEs of anti-CTLA4 antibodies.

Immune checkpoint inhibitors (ICIs) enhance the anti-tumor immune response by blocking Treg-mediated immunosuppression. Why the T cells in the tumor microenvironment are few and non-sensitive still unrevealed. Recently, HPDOX has become a brand-new tool to assess cancer immunotherapy, which sets a robust foundation for cancer immune-related researches (23). In our study, we aim to demonstrate that HPDOX mice are appropriate to investigate the efficacy and IRAEs of anti-CTLA4 antibody therapies against GBM. Thus, this model can be used as a platform to evaluate whether patients benefit from certain targeted immunotherapy or not, which may provide a solid basis for clinical decisions. As one of the most common ICIs, anti-CTLA4 antibodies such as ipilimumab and tremelimumab have

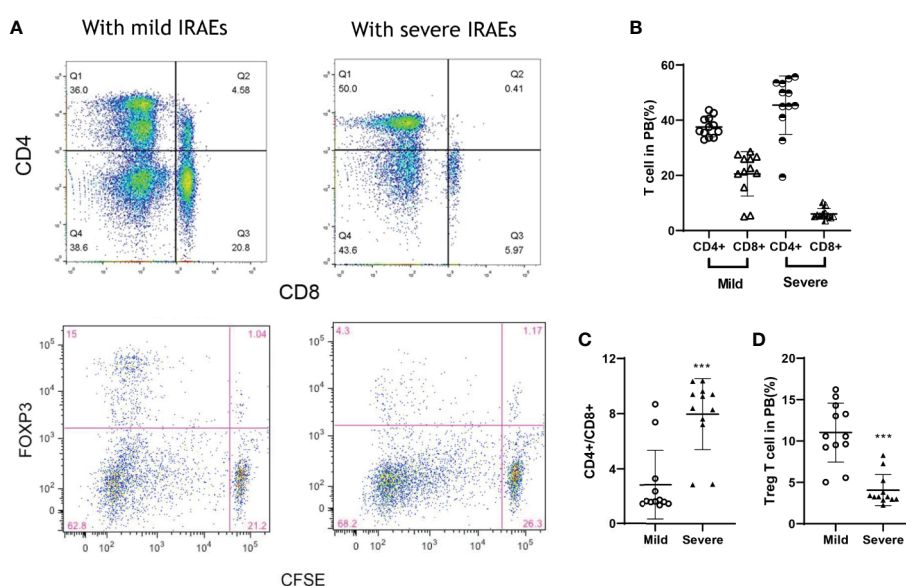


**FIGURE 4** | FOXP3<sup>+</sup> and CD4<sup>+</sup>/CD8<sup>+</sup> T cells were associated with IRAEs during anti-CTLA4 immunotherapy. **(A)** The population of CD4<sup>+</sup>, CD8<sup>+</sup>, and FOXP3<sup>+</sup> T cells after the intervention of ipilimumab. **(B, C)** The population of T cells **(B)** and Treg cells **(C)** in peripheral blood of mice with IRAEs or not. **(D)** The ratio of CD4<sup>+</sup>/CD8<sup>+</sup> T cells in peripheral blood of the HPDOX mice with IRAEs and not. There were twelve mice in each group. Data were represented as mean ± SD. \*\*\**P* < 0.001.



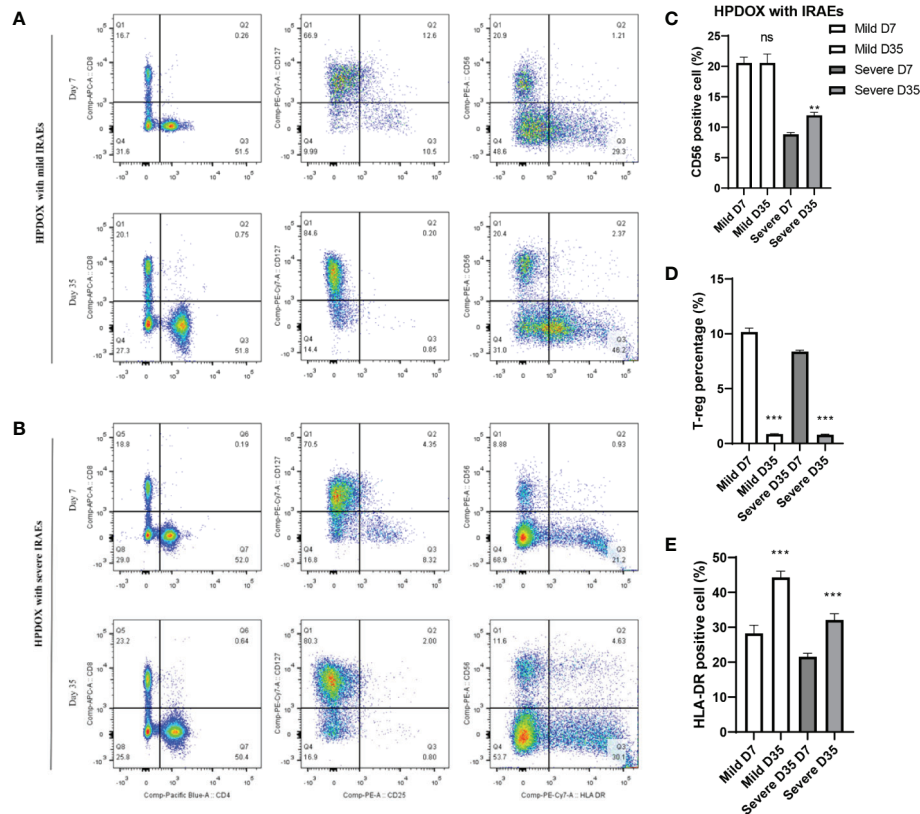


**FIGURE 5 |** The degree of IRAEs may be related to CD56+ expression in HPDOX. (A, B) The population of CD4+, CD8+, the CD25+CD127– Treg cells, CD56, and HLA-DR in both mild and severe IRAEs groups after the intervention of ipilimumab. (C) There was no significant difference in the CD56 expression in the mild IRAEs group, although increased in the severe IRAEs group. (D, E) The CD25+CD127– Treg cells were significantly decreased, while the HLA-DR expression was increased in both mild and severe IRAEs groups. There were six mice in each group. Data were represented as mean  $\pm$  SD. \*\* $P < 0.01$ , \*\*\* $P < 0.001$ .

enhanced the anti-tumor immune response in both preclinical and clinical research and achieved unprecedented success. The achievement of ICIs mainly on account of two essential factors: 1) attenuate highly immunosuppressive tumor microenvironment by lowering frequencies of Treg cells; and 2) T effective cells are activated in tumor microenvironments (TME) by certain mechanisms, which play a critical role in anti-tumor in cellular immunity (24). Base on those points, anti-CTLA-4 antibodies might weaken their immunosuppressive effects *via* inhibiting the activated Treg cells.

Anti-CTLA4 antibodies block the CTLA4 molecules enhancing the anti-tumor immune response *via* inhibiting Treg-mediated immunosuppression in HPDOX. We observed the CTLA4 was blocked by anti-CTLA4 antibodies and rescued the T cell exhaustion phenotype in the GBM HPDOX mouse model. Persistent exposure to high levels of antigen such as cancer or chronic infections may drive functional exhaustion of T cells (25). Recently, more and more researches focused on reversing T cell depletion abrogates the control of the proliferation of cancer. The critical role of CTLA4 in T cell exhaustion has been reported (26, 27). These findings warrant the clinical trial of CTLA4-targeted immunotherapy for GBM patients (NCT04606316). However, some patients do not benefit from anti-CTLA4 immunotherapy,

which might because only a few T cells arrived in TME, which is not enough to reverse the immunosuppressive effects (28). In our study, ipilimumab, an anti-CTLA4 antibody that binds to CTLA4 specifically, showed the anti-GBM efficacy in inhibiting tumor growth *via* at least partly preserving T cells in the HPDOX model.

IRAEs showed a negative relationship with Treg numbers or percentages in the HPDOX model. This model may provide an emerging and promising tool to reveal the mechanism of clinical efficacy as well as IRAEs of immune-related therapies. IRAEs occurred in more than 90% of patients during the treatment with anti-CTLA4 antibody (29). Systemic administration of ICIs is usually not only influence by T cells in TME but also all T cells across the body. ICIs administrated by vein could induce IRAEs *via* unbalancing the T effect and Treg cells in normal tissues such as guts and skin. Those possible reasons reported for IRAEs during ICIs. On one side, Treg, expression of CTLA4, was inhibited by ADCC, which mediated by FcR expressing cells such as natural killer cells or macrophages in TME. On the other, T effective cells were activated and sustained *via* blocking the CTLA4 pathway. IRAEs could be induced by losing the functions or numbers of Treg, which are critical for maintaining tolerance (30). Based on those points, the dual roles of Treg are presented. On one hand, Treg cells can impede anti-tumor immunity to enhance immune evasion of tumor cells;

On the other, Treg cells sustain an immune tolerance state and prevent from IRAEs. It reported that a negative relationship between Treg and IRAEs has been demonstrated in preclinical models, but not in GBM. Our study showed the patients' PBMCs can co-exist in GBM HPDOX mice, which may be a useful platform for investigating the mechanism and role of the immune-related factors in IRAEs. In theory, it is a promising area to reform anti-CTLA4 antibodies and enhance its efficacy of cancer immunotherapy. To weaken ADCC and CDC effects, the N298A (Human IgG control) mutation was designed to prevent immune cells from IRAEs. However, our study showed N298A mutation did not affect the IRAEs of anti-CTLA4 antibodies, which might because patients' natural killer cells or complement were not well restored in the HPDOX mice model (**Figure S4** and **Table S2**). And the degree of IRAEs may be related to CD56+ expression in HPDOX.

The challenge of immunotherapy is to prevent IRAEs while preserving anti-tumor efficacy. In theory, the immunosuppressors or corticosteroids probably maintain immune tolerance in normal organs and tissues, which could also impede the antitumor efficacy. But they are not weakening the antitumor efficacy of ICIs. Interestingly, some clinical trials showed a positive relationship between the IRAEs and antitumor responses (31, 32). It's a promising direction to study this mechanism in the future (33, 34). In the future, our study will also aim to make the current anti-CTLA4 immunotherapy more effective *via* inhibiting Treg cells and weaken their immunosuppressive effects. In the meanwhile, activating T effective cells by ICIs or vaccine in TME.

However, some important limitations should be considered. In the first place, in the tissues and plasma of mice, there are only low levels of human factors and cytokines resulted in a decreased number of myeloid cells and Treg cells. With the presence of GM-CSF, IL-6, IL-3, and M-CSF, the differentiation of T, B, and NK cells were more actively (35, 36). Secondary, although the novel mouse strains have been developed to inhibit the GVHD by mouse MHC complex, the immune cell types and responses in HPDOX still need to be further studied (12, 37). Thirdly, accessing the change in the transcriptome and epigenome of the patient tumor tissues is passaged in the HPDOX models (19, 38). Lastly, personalized medicine strategies will be needed to allow higher tumor infiltration and anti-tumor responses.

## CONCLUSIONS

In conclusion, our study established HPDOX mice models for investigating the mechanism and IRAEs of immunotherapies in GBM, which would offer a promising platform for evaluating the efficacy and IRAEs of novel therapies and exploring personalized therapeutic strategies.

## DATA AVAILABILITY STATEMENT

The original contributions presented in the study are included in the article/**Supplementary Material**. Further inquiries can be directed to the corresponding author.

## ETHICS STATEMENT

The studies involving human participants were reviewed and approved by the Ethics Committee of Xiangya Hospital. The patients/participants provided their written informed consent to participate in this study. The animal study was reviewed and approved by the Ethics Committee of Xiangya Hospital.

## AUTHOR CONTRIBUTIONS

CL conceived, designed, and supervised the study. SX and XY drafted the manuscript. SX and XY performed data analysis. SX, XY, and GD collected the data. All authors contributed to the article and approved the submitted version.

## FUNDING

This work was supported by the National Natural Science Foundation of China (81902553); Natural Science Foundation of Hunan Province (2019JJ50942).

## ACKNOWLEDGMENTS

We would like to show our gratitude to Prof. Chen (Huntsman Cancer Institute, University of Utah, USA) for providing CTLA4-specific antibodies (ipilimumab and tremelimumab).

## SUPPLEMENTARY MATERIAL

The Supplementary Material for this article can be found online at: <https://www.frontiersin.org/articles/10.3389/fonc.2021.692403/full#supplementary-material>

**Supplementary Figure 1** | The tumor volume before antibodies treatment. **(A)** The tumor volume of PDOX 07; **(B)** The tumor volume of PDOX 22. There were three mice in each group. Data were represented as mean  $\pm$  SD. ns:  $P > 0.05$ .

**Supplementary Figure 2** | The subgroups of T cells. **(A–C)** The activated T cells were presented with the higher expression of IFN- $\gamma$  and CD25+. **(B)** The exhausted T cells presented the lower expression of IFN- $\gamma$ . **(a & d)** The effector T cells are CD45RA positive. **(a & e)** The memory T cells are CD45RO positive.

**Supplementary Figure 3** | HPDOX with IRAEs such as graft-versus-host disease (GVHD). **(left)** The normal autologous GBM HPDOX without IRAEs like GVHD. **(right)** The autologous GBM HPDOX mice suffered IRAEs and/or GVHD. Specifically, IRAEs was assessed by weight and hair loss, posture, activity, fur texture and skin integrity.

**Supplementary Figure 4** | Evaluating the antitumor effect of ipilimumab without and with the N298A mutation in HPDOX. **(A, B)** Tumor volume of GBM xenograft in mice treated with Vehicle, hulgG, ipilimumab, and ipilimumab with N298A. **(C, E)** The population of T cells in GBM tissues and **(D, F)** peripheral blood in mice treated with Vehicle, hulgG, ipilimumab, and ipilimumab with N298A. There were six mice in each group. Data were represented as mean  $\pm$  SD. ns, no significant difference.

## REFERENCES

- Stupp R, Mason WP, van den Bent MJ, Weller M, Fisher B, Taphoorn MJ, et al. Radiotherapy Plus Concomitant and Adjuvant Temozolomide for Glioblastoma. *N Engl J Med* (2005) 352(10):987–96. doi: 10.1056/NEJMoa043330
- Chinot OL, Wick W, Mason W, Henriksson R, Saran F, Nishikawa R, et al. Bevacizumab Plus Radiotherapy-Temozolomide for Newly Diagnosed Glioblastoma. *N Engl J Med* (2014) 370(8):709–22. doi: 10.1056/NEJMoa1308345
- Gilbert MR, Dignam JJ, Armstrong TS, Wefel JS, Blumenthal DT, Vogelbaum MA, et al. A Randomized Trial of Bevacizumab for Newly Diagnosed Glioblastoma. *N Engl J Med* (2014) 370(8):699–708. doi: 10.1056/NEJMoa1308573
- Singh SK, Hawkins C, Clarke ID, Squire JA, Bayani J, Hide T, et al. Identification of Human Brain Tumour Initiating Cells. *Nature* (2004) 432(7015):396–401. doi: 10.1038/nature03128
- Bao S, Wu Q, McLendon RE, Hao Y, Shi Q, Hjelmeland AB, et al. Glioma Stem Cells Promote Radioresistance by Preferential Activation of the DNA Damage Response. *Nature* (2006) 444(7120):756–60. doi: 10.1038/nature05236
- Lee J, Kotliarova S, Kotliarov Y, Li A, Su Q, Donin NM, et al. Tumor Stem Cells Derived From Glioblastomas Cultured in bFGF and EGF More Closely Mirror the Phenotype and Genotype of Primary Tumors Than do Serum-Cultured Cell Lines. *Cancer Cell* (2006) 9(5):391–403. doi: 10.1016/j.ccr.2006.03.030
- Hidalgo M, Amant F, Biankin AV, Budinska E, Byrne AT, Caldas C, et al. Patient-Derived Xenograft Models: An Emerging Platform for Translational Cancer Research. *Cancer Discov* (2014) 4(9):998–1013. doi: 10.1158/2159-8290.CD-14-0001
- Tentler JJ, Tan AC, Weekes CD, Jimeno A, Leong S, Pitts TM, et al. Patient-Derived Tumour Xenografts as Models for Oncology Drug Development. *Nat Rev Clin Oncol* (2012) 9(6):338–50. doi: 10.1038/nrclinonc.2012.61
- Ye W, Luo C, Li C, Huang J, Liu F. Organoids to Study Immune Functions, Immunological Diseases and Immunotherapy. *Cancer Lett* (2020) 477:31–40. doi: 10.1016/j.canlet.2020.02.027
- Klein E, Hau AC, Oudin A, Golebiewska A, Niclou SP. Glioblastoma Organoids: Pre-Clinical Applications and Challenges in the Context of Immunotherapy. *Front Oncol* (2020) 10:604121. doi: 10.3389/fonc.2020.604121
- Bar-Ephraim YE, Kretzschmar K, Clevers H. Organoids in Immunological Research. *Nat Rev Immunol* (2020) 20(5):279–93. doi: 10.1038/s41577-019-0248-y
- Byrne AT, Alferez DG, Amant F, Annibaldi D, Arribas J, Biankin AV, et al. Interrogating Open Issues in Cancer Precision Medicine With Patient-Derived Xenografts. *Nat Rev Cancer* (2017) 17(4):254–68. doi: 10.1038/nrc.2016.140
- King MA, Covassin L, Brehm MA, Racki W, Pearson T, Leif J, et al. Human Peripheral Blood Leucocyte non-Obese Diabetic-Severe Combined Immunodeficiency Interleukin-2 Receptor Gamma Chain Gene Mouse Model of Xenogeneic Graft-Versus-Host-Like Disease and the Role of Host Major Histocompatibility Complex. *Clin Exp Immunol* (2009) 157(1):104–18. doi: 10.1111/j.1365-2249.2009.03933.x
- Lai HY, Chou TY, Tzeng CH, Lee OK. Cytokine Profiles in Various Graft-Versus-Host Disease Target Organs Following Hematopoietic Stem Cell Transplantation. *Cell Transplant* (2012) 21(9):2033–45. doi: 10.3727/096368912X653110
- Huszthy PC, Daphu I, Niclou SP, Stieber D, Nigro JM, Sakariassen PO, et al. In Vivo Models of Primary Brain Tumors: Pitfalls and Perspectives. *Neuro Oncol* (2012) 14(8):979–93. doi: 10.1093/neuonc/nos135
- Jamal M, Rath BH, Tsang PS, Camphausen K, Tofilon PJ. The Brain Microenvironment Preferentially Enhances the Radioresistance of CD133 (+) Glioblastoma Stem-Like Cells. *Neoplasia* (2012) 14(2):150–8. doi: 10.1593/neo.111794
- Camphausen K, Purow B, Sproull M, Scott T, Ozawa T, Deen DF, et al. Orthotopic Growth of Human Glioma Cells Quantitatively and Qualitatively Influences Radiation-Induced Changes in Gene Expression. *Cancer Res* (2005) 65(22):10389–93. doi: 10.1158/0008-5472.CAN-05-1904
- Oh T, Fakurnejad S, Sayegh ET, Clark AJ, Ivan ME, Sun MZ, et al. Immunocompetent Murine Models for the Study of Glioblastoma Immunotherapy. *J Transl Med* (2014) 12:107. doi: 10.1186/1479-5876-12-107
- Striepecke R, Munz C, Schuringa JJ, Bissig KD, Soper B, Meeham T, et al. Innovations, Challenges, and Minimal Information for Standardization of Humanized Mice. *EMBO Mol Med* (2020) 12(7):e8662. doi: 10.15252/emmm.201708662
- Yaguchi T, Kobayashi A, Inozume T, Morii K, Nagumo H, Nishio H, et al. Human PBMC-transferred Murine MHC Class I/II-deficient NOG Mice Enable Long-Term Evaluation of Human Immune Responses. *Cell Mol Immunol* (2018) 15(11):953–62. doi: 10.1038/cmi.2017.106
- Brehm MA, Kenney LL, Wiles MV, Low BE, Tisch RM, Burzenski L, et al. Lack of Acute Xenogeneic Graft- Versus-Host Disease, But Retention of T-cell Function Following Engraftment of Human Peripheral Blood Mononuclear Cells in NSG Mice Deficient in MHC Class I and II Expression. *FASEB J* (2019) 33(3):3137–51. doi: 10.1096/fj.201800636R
- Lin S, Huang G, Cheng L, Li Z, Xiao Y, Deng Q, et al. Establishment of Peripheral Blood Mononuclear Cell-Derived Humanized Lung Cancer Mouse Models for Studying Efficacy of PD-L1/PD-1 Targeted Immunotherapy. *MAbs* (2018) 10(8):1301–11. doi: 10.1080/19420862.2018.1518948
- Jespersen H, Lindberg MF, Donia M, Soderberg EMV, Andersen R, Keller U, et al. Clinical Responses to Adoptive T-cell Transfer can be Modeled in an Autologous Immune-Humanized Mouse Model. *Nat Commun* (2017) 8(1):707. doi: 10.1038/s41467-017-00786-z
- Tanaka A, Sakaguchi S. Regulatory T Cells in Cancer Immunotherapy. *Cell Res* (2017) 27(1):109–18. doi: 10.1038/cr.2016.151
- Mueller SN, Ahmed R. High Antigen Levels are the Cause of T Cell Exhaustion During Chronic Viral Infection. *Proc Natl Acad Sci U S A* (2009) 106(21):8623–8. doi: 10.1073/pnas.0809818106
- Zarour HM. Reversing T-cell Dysfunction and Exhaustion in Cancer. *Clin Cancer Res* (2016) 22(8):1856–64. doi: 10.1158/1078-0432.CCR-15-1849
- Farhood B, Najafi M, Mortezaee K. CD8(+) Cytotoxic T Lymphocytes in Cancer Immunotherapy: A Review. *J Cell Physiol* (2019) 234(6):8509–21. doi: 10.1002/jcp.27782
- Havel JJ, Chowell D, Chan TA. The Evolving Landscape of Biomarkers for Checkpoint Inhibitor Immunotherapy. *Nat Rev Cancer* (2019) 19(3):133–50. doi: 10.1038/s41568-019-0116-x
- Michot JM, Bigenwald C, Champiat S, Collins M, Carbonnel F, Postel-Vinay S, et al. Immune-Related Adverse Events With Immune Checkpoint Blockade: A Comprehensive Review. *Eur J Cancer* (2016) 54:139–48. doi: 10.1016/j.ejca.2015.11.016
- Kumar P, Saini S, Prabhakar BS. Cancer Immunotherapy With Check Point Inhibitor can Cause Autoimmune Adverse Events Due to Loss of Treg Homeostasis. *Semin Cancer Biol* (2020) 64:29–35. doi: 10.1016/j.semcancer.2019.01.006
- Baik CS, Rubin EH, Forde PM, Mehnert JM, Collyar D, Butler MO, et al. Immuno-Oncology Clinical Trial Design: Limitations, Challenges, and Opportunities. *Clin Cancer Res* (2017) 23(17):4992–5002. doi: 10.1158/1078-0432.CCR-16-3066
- Chang LS, Barroso-Sousa R, Tolaney SM, Hodi FS, Kaiser UB, Min L. Endocrine Toxicity of Cancer Immunotherapy Targeting Immune Checkpoints. *Endocr Rev* (2019) 40(1):17–65. doi: 10.1210/er.2018-00006
- Sanmamed MF, Chen L. A Paradigm Shift in Cancer Immunotherapy: From Enhancement to Normalization. *Cell* (2018) 175(2):313–26. doi: 10.1016/j.cell.2018.09.035
- Ye Q, Zhang Y, Cao Y, Wang X, Guo Y, Chen J, et al. Frenolicin B Targets Peroxiredoxin 1 and Glutaredoxin 3 to Trigger Ros/4e-Bp1-Mediated Antitumor Effects. *Cell Chem Biol* (2019) 26(3):366–77.e12. doi: 10.1016/j.chembiol.2018.11.013
- Yu H, Borsotti C, Schickel JN, Zhu S, Strowig T, Eynon EE, et al. A Novel Humanized Mouse Model With Significant Improvement of Class-Switched, Antigen-Specific Antibody Production. *Blood* (2017) 129(8):959–69. doi: 10.1182/blood-2016-04-709584
- Bryce PJ, Falahati R, Kenney LL, Leung J, Bebbington C, Tomasevic N, et al. Humanized Mouse Model of Mast Cell-Mediated Passive Cutaneous Anaphylaxis and Passive Systemic Anaphylaxis. *J Allergy Clin Immunol* (2016) 138(3):769–79. doi: 10.1016/j.jaci.2016.01.049
- De La Rochere P, Guil-Luna S, Decaudin D, Azar G, Sidhu SS, Piaggio E. Humanized Mice for the Study of Immuno-Oncology. *Trends Immunol* (2018) 39(9):748–63. doi: 10.1016/j.it.2018.07.001

38. Brendel C, Rio P, Verhoeyen E. Humanized Mice are Precious Tools for Evaluation of Hematopoietic Gene Therapies and Preclinical Modeling to Move Towards a Clinical Trial. *Biochem Pharmacol* (2020) 174:113711. doi: 10.1016/j.bcp.2019.113711

**Conflict of Interest:** The authors declare that the research was conducted in the absence of any commercial or financial relationships that could be construed as a potential conflict of interest.

Copyright © 2021 Xu, Yan, Dai and Luo. This is an open-access article distributed under the terms of the Creative Commons Attribution License (CC BY). The use, distribution or reproduction in other forums is permitted, provided the original author(s) and the copyright owner(s) are credited and that the original publication in this journal is cited, in accordance with accepted academic practice. No use, distribution or reproduction is permitted which does not comply with these terms.





# Post-Diagnostic Beta Blocker Use and Prognosis of Ovarian Cancer: A Systematic Review and Meta-Analysis of 11 Cohort Studies With 20,274 Patients

Zhao-Yan Wen<sup>1,2</sup>, Song Gao<sup>3</sup>, Ting-Ting Gong<sup>3</sup>, Yu-Ting Jiang<sup>1,2</sup>, Jia-Yu Zhang<sup>1,2</sup>, Yu-Hong Zhao<sup>1,2</sup> and Qi-Jun Wu<sup>1,2\*</sup>

## OPEN ACCESS

### Edited by:

Yingyan Yu,  
Shanghai Jiao Tong University, China

### Reviewed by:

Xiuli Dan,  
National Institute on Aging (NIH),  
United States  
Haichen Lv,  
Dalian Medical University, China

### \*Correspondence:

Qi-Jun Wu  
wuqj@sj-hospital.org

### Specialty section:

This article was submitted to  
Pharmacology of Anti-Cancer Drugs,  
a section of the journal  
Frontiers in Oncology

**Received:** 08 February 2021

**Accepted:** 19 May 2021

**Published:** 17 June 2021

### Citation:

Wen Z-Y, Gao S, Gong T-T, Jiang Y-T,  
Zhang J-Y, Zhao Y-H and Wu Q-J  
(2021) Post-Diagnostic Beta Blocker  
Use and Prognosis of Ovarian  
Cancer: A Systematic Review  
and Meta-Analysis of 11 Cohort  
Studies With 20,274 Patients.  
Front. Oncol. 11:665617.  
doi: 10.3389/fonc.2021.665617

<sup>1</sup> Department of Clinical Epidemiology, Shengjing Hospital of China Medical University, Shenyang, China, <sup>2</sup> Clinical Research Center, Shengjing Hospital of China Medical University, Shenyang, China, <sup>3</sup> Department of Obstetrics and Gynecology, Shengjing Hospital of China Medical University, Shenyang, China

**Objectives:** Previous experimental studies have indicated that exposure to beta blocker provides protective effects against ovarian cancer (OC). However, findings from epidemiologic studies have still been controversial. Therefore, we carried out a meta-analysis to update and quantify the correlation between post-diagnostic beta blocker usage and OC prognosis.

**Methods:** The meta-analysis had been registered at PROSPEPO. The number of registration is CRD42020188806. A comprehensive search of available literatures in English prior to April 16, 2020, was conducted in PubMed, EMBASE, and the Web of Science databases. Random-effects models were used to calculate overall hazard ratios (HRs) and 95% confidence intervals (CIs). Publication bias assessments, and subgroup, sensitivity, and meta-regression analyses were also performed.

**Results:** Of the 637 initially identified articles, 11 retrospective cohort studies with 20,274 OC patients were included. The summary HRs did not reveal any statistically significant associations between post-diagnostic beta blocker use and OC prognosis characteristics, such as total mortality (HR = 1.08, 95% CI = 0.92–1.27,  $I^2$  = 76.5%,  $n$  = 9), cancer-specific mortality (HR = 1.22, 95% CI = 0.89–1.67,  $I^2$  = 88.1%,  $n$  = 3), and progression-free survival (HR = 0.88, 95% CI = 0.75–1.05,  $I^2$  = 0,  $n$  = 4). No evidence of publication bias was observed in current analysis. In our subgroup analyses, the majority of results were consistent with the main findings. However, several positive correlations were detected in studies with  $\geq 800$  cases (HR = 1.20, 95% CI = 1.05–1.37), no immortal time bias (HR = 1.28, 95% CI = 1.10–1.49), and adjustment for comorbidity (HR = 1.20,

95% CI = 1.05–1.37). In the meta-regression analysis, no evidence of heterogeneity was detected in the subgroups according to study characteristics and confounding factors.

**Conclusions:** Post-diagnostic beta blocker use has no statistical correlation with OC prognosis. More prospective cohort studies are necessary to further verify our results.

**Systematic Review Registration:** Identifier (CRD42020188806).

**Keywords:** beta blocker, meta-analysis, ovarian cancer, post-diagnostic, survival, systematic review

## INTRODUCTION

Ovarian cancer (OC) is one of the deadliest cancer types of gynecological reproductive system, with over 200,000 new cases and 150,000 deaths globally in 2018 (1). Over 70% of OCs are discovered at advanced stages (stages III–IV) and with fast-growing metastases in the peritoneal cavity, largely because of unnoticed early symptoms and the lack of effective diagnostic approaches (2). For stage III and IV OC patients, survival rates of 5 years are only 42% and 26%, respectively (3). Therefore, some strategies that will have a beneficial impact on the treatment outcome of patients with OC should be developed to improve OC prognosis.

Beta blockers are medicines commonly used in a range of cardiovascular diseases, for example, coronary artery diseases or hypertension because of their function on the adrenergic system *via* inhibiting beta receptors (4, 5). Beta blocker treatment may prevent metastasis by inhibiting tumor cell invasion, tumor-associated inflammation, and vasculature remodeling to limit tumor cell dissemination (6–8). In recent years, *vitro* researches have indicated a positive correlation of beta blocker on the prognosis of OC (9–11). However, the differences in metabolism between human beings and other species preclude the extrapolation of data from cell and animal studies to human biology (12, 13).

In view of systematic review and meta-analysis, including available literatures up until September 2017, Yap et al. (14) was unable to show statistically relationship between beta blocker use (pre- and post-diagnostic) on OC prognosis (hazard ratio [HR] = 0.73, 95% confidence interval [CI] = 0.43–1.23). However, these findings were generated on the basis of a combined study of pre- and post-diagnosis beta blocker use on OC prognosis, which is not ideal because such an association could differ between these two phases. Majidi et al. (15) investigated the relationship between common medications and the survival of OC patients (including beta blockers) in a systematic review and meta-analysis of available literatures up until May 2019. The authors were unable to find a statistically significant relationship between beta blocker use and OC patients survival (HR = 0.97, 95% CI = 0.84–1.11) after adjusting for immortal time bias. However, this meta-analysis also explored mixed effects of pre- or post-diagnostic beta blocker use, and no further subgroup analyses, such as age at diagnosis, sample size, or study quality, were performed to explore possible sources of heterogeneity. Interestingly, results from a meta-analysis, including five studies (16–20) with 3,140 OC patients until September 2017

by Na et al. (21) revealed that use of post-diagnostic beta blocker was significantly related with improved survival of OC patients (HR = 0.59, 95% CI = 0.36–0.96). However, this meta-analysis had substantial heterogeneity ( $I^2 = 88.0\%$ ), which was not further explored through subgroup analyses.

During the last 2 years, many of high-quality studies with additional potential confounder adjustments have been published (22–25). Several studies have indicated that post-diagnostic beta blocker use increased OC mortality (22, 25), while other studies did not show an association (23, 24). In 2020, a large prognostic cohort study with 6,197 OC patients showed that post-diagnostic beta blocker use increased mortality (25). In contrast, no association was observed in a study by Harding et al. involving 2,195 OC patients (24). These inconsistencies could be attributed to the differences in the type of beta blockers used, the health status of OC patients, sample sizes, and adjustments for potential confounding factors. A more latest meta-analysis of existing evidence may further reveal the true effect of beta blocker in the treatment of OC. The source of heterogeneity has been further analyzed by subgroup, sensitivity, and meta-regression analyses. As far as we know, there are currently no published literatures comprehensively analyzing the data on post-diagnostic beta blocker use and OC survival. Consequently, we carried out an updated systematic review and meta-analysis of existing cohort studies to further identify the correlation between post-diagnostic beta blocker usage and OC prognosis.

## METHODS

### Data Sources and Searches

The systematic review and meta-analysis was carried out in accordance with Preferred Reporting Items for Systemic Reviews and Meta-Analyses guidelines (26) and Meta-Analysis of Observational Studies in Epidemiology guidelines (27). Prior to study selection, the protocol of this meta-analysis was registered through the International Prospective Register of Systematic Reviews (registration number: CRD42020188806).

Two authors (Z-YW and T-TG) independently searched PubMed, EMBASE, and Web of Science databases for all relevant literatures published up until April 30, 2021. The following key words were included in our literature search: (“beta blocker” OR “beta blockers” OR “atenolol” OR “propranolol” OR “metoprolol” OR “arotinolol” OR “betaxolol” OR “bevantolol” OR “bisoprolol” OR “carteolol” OR “carvedilol” OR “celiprolol”) AND (“ovarian” OR “ovary”)

AND (“neoplasm” OR “carcinoma” OR “cancer” OR “tumor”) AND (“survival” OR “mortality” OR “death”). The list of references included in the study was further screened to determine other publications.

## Study Selection

We put the retrieved citations into the reference management database and delete the literatures by automatic and manual methods. The judgment standard is based on the inclusion criteria determined before the search.

Studies that meet the following criteria will be included in our analysis (1): observational study or randomized controlled trial (2); exposure defined as use of beta blocker after diagnosis for OC patients (3); survival (such as disease-specific survival, progression-free survival, cancer-specific survival, overall survival) or mortality as outcome (such as all-cause mortality); and (4) analyses with HR or relative risk and 95% CI, or provided data suitable for risk estimates and 95% CI calculation.

Literatures, which meet the following criteria, were excluded (1): meeting abstracts, studies performed in animals, or non-original studies, including commentaries, editorials review articles, systemic reviews, meta-analyses (2); lack of sufficient risk estimates or related data in calculating risk estimates; and (3) studies were written in non-English.

## Data Extraction and Quality Assessment

Two authors (Z-YW and T-TG) extracted basic data of literatures by standardized form. Inconsistency was solved by a third author (J-YZ). The following data were extracted from the included articles: last name of first author, year of publication, country of origin, follow-up length, OC cases and events' number, stage of cancer, classification of outcomes, and covariates matched in the study design or confounding factors adjusted in the primary statistical analysis.

In order to better identify the quality of included studies, we applied the Newcastle-Ottawa Scale (NOS) to evaluate quality of literatures for observational studies (28). The NOS scale comprises eight categories divided into three fields for selection, comparability, and outcome. In addition to the item Control for important factors or additional factors, each study could be given every item a maximum of one star. These studies, which obtained full stars in at least two classifications of selection, comparability, or outcome assessment, were classified as low risk of having bias (29, 30).

## Statistical Analysis

Since the differences in the populations and conditions among different studies might not exactly explain a common effect, a random-effects model was applied for summarizing HR in our analysis (30). The heterogeneity of all studies by calculating  $I^2$  statistics, which assesses meta-analysis variability caused by differences between all studies instead of sampling errors (31). Using >75%, 50% to 75%, and <50% as the demarcation points indicated high, medium, and low levels of heterogeneity (31). We carried out subgroup analyses to probe into heterogeneous sources by using prespecified variables, for example, region, median number of cases, study quality, International Federation

of Obstetrics and Gynecology (FIGO) stage of OC, length of follow-up, and adjustment for potential confounder factors such as age at diagnosis, stage of FIGO, comorbidities, residual diseases, histology, chemotherapy, and use of non-beta blocker drugs. We carried out sensitivity analyses to explore the impact of a single research on the summary HR *via* ruling out one research every time in the analysis (32). In addition, a meta-regression model was applied for identifying heterogeneous sources between subgroups. Finally, we evaluated publication bias through Egger's linear regression (33), Begg's rank correlation method (34), and visual inspection of funnel plots. All analyses were conducted using Stata version 11.0 software (StataCorp, College Station, TX). A two-tailed P value < 0.05 was regarded statistically significant.

## RESULTS

### Search Results, Study Characteristics, and Quality Assessment

Of the 637 articles that were reviewed, 621 were removed following review of the titles and abstracts. After full-text screening of the remaining 16 articles, five articles (14, 15, 21, 35, 36) were excluded. Two of the excluded articles (14, 21) examined the impact of beta-blockers on cancer prognosis, and one article (15) analyzed the relationship between common medications and survival of OC patients. The remaining two articles were excluded because one article (35) did not provide the 95% CI and one article (36) included pre-diagnostic beta blocker use for OC prognosis. In the end, 11 published literatures were included for the main analysis (**Figure 1**).

**Table 1** reveals the major features of the included literatures. All of the included literatures were published between 2012 and 2020, with a scope of 123 to 6,626 OC cases each study. Five of the studies were performed in the United States (17, 18, 20, 22, 24), three of the studies were performed in Europe (16, 25, 38), two studies were performed in Korea (23, 37), and one study was conducted (19) across Belgium, Canada, and Germany. All of the cohort studies were retrospectively designed, with a median follow-up duration between 17 and 91 months. **Table 2** outlines the potential confounder adjustments in the preliminary analysis of the included literatures. Majorities of the studies adjusted for potentially important confounder factors, such as age at diagnosis ( $n = 10$ ) and FIGO stage ( $n = 8$ ). A limited number of studies adjusted for comorbidity ( $n=6$ ), histology ( $n=4$ ), chemotherapy use ( $n = 3$ ), residual disease ( $n = 3$ ), race ( $n = 3$ ), and grade ( $n = 3$ ).

The results the quality assessment in view of the NOS are summarized in **Table 3**. One study (19) was graded as high risk, and 10 studies (16–18, 20, 22–25, 37, 38) were graded as low risk. For “selection” classification, three studies (16, 17, 20) were not assigned to full stars. For the item of “control for important factor or additional factor”, two studies (19, 37) were not awarded two stars since these studies had adjusted for less than two important confounder factors. For classification of “outcome”, one study (19) was not assigned to full stars because of insufficient duration of follow-up.

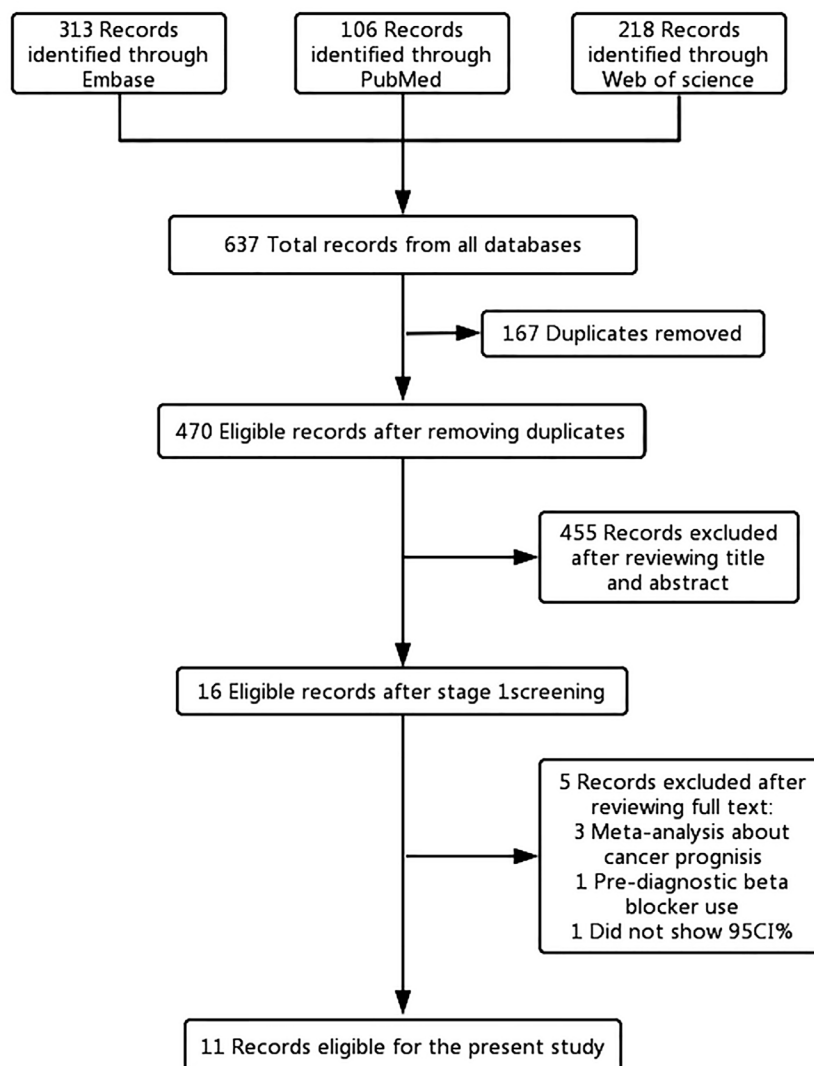


**FIGURE 1 |** Flowchart of the study selection. The flowchart shows the process used to select studies for our meta-analyses focusing on the association between post-diagnostic beta blocker use and ovarian cancer (OC) prognosis.

**TABLE 1 |** Characteristics of included studies.

First author, reference, year	Country	No. of cases/event	Patient stage	Follow-up	Outcome
Cho et al. (23), 2020	Korea	878/470	I–IV	33.9 months (median)	Progression-free survival
Gonzalez et al. (22), 2020	USA	534/NA	III–IV	32 months (median)	Overall survival
Couttenier et al. (25), 2019	Belgium	6197/2918	I–IV	3.49 years (median)	All-cause mortality Cancer-specific mortality
Harding et al. (24), 2019	USA	2195/796	I–IV	2.2 years (median)	Cancer-specific mortality
Baek et al. (37), 2018	Korea	866/381	NA	6.35 years (median)	Overall survival
Al-Niaimi et al. (17), 2016	USA	185/123	I–IV	91 months (median)	Progression-free survival Overall survival
Heitz et al. (16), 2016	Germany	801/682	I–IV	40 months (median)	Progression-free survival Overall survival
Watkins et al. (18), 2015	USA	1425/NA	III–IV	44.9 months (median)	Overall survival Disease-specific survival
Johannesdottir et al. (38), 2013	Denmark	6626/NA	NA	2.55 years (median)	All-cause mortality
Heitz et al. (19), 2013	Germany Belgium Canada	381/267	NA	17 months (median)	Progression-free survival Overall survival
Diaz et al. (20), 2012	USA	248/NA	III–IV	27 months (median)	Overall survival

NA, not available.



**TABLE 2 |** Adjustment potential confounders of included studies.

First author, reference, year	Adjustment for potential confounders in the primary analysis
Cho et al. (23), 2020	Age, FIGO stage, histologic type, residual disease status after PDS, platinum resistance, comorbidity, cytoreduction status
Gonzalez et al. (22), 2020	Age, race, CCI, FIGO stage, PDS vs NACT, residual disease status, statin use, metformin use, aspirin use
Couttenier et al. (25), 2019	Age at diagnosis, year of diagnosis, FIGO stage, grade, cancer histology, diabetes, and pulmonary comorbidities
Harding et al. (24), 2019	Age at diagnosis, year of diagnosis, race/ethnicity, marital status, census tract poverty level, location of residence, tumor histology, FIGO stage at diagnosis, receipt of surgery, receipt of chemotherapy, Charlson comorbidity score, diagnosis of diabetes and hypertension
Baek et al. (37), 2018	N/A
Al-Niaimi et al. (17), 2016	Age, stage, grade, cytoreduction status, BMI, presence or absence of diabetes
Heitz et al. (16), 2016	Age, ECOG, Charlson comorbidity score, tumor residuals, histology, BMI, FIGO stage
Watkins et al. (18), 2015	Age, race, stage, BMI, neoadjuvant therapy, diabetes, hypertension
Johannesdottir et al. (38), 2013	Age, comorbidity level, prior use of diuretics, year of diagnosis, aspirin, statins
Heitz et al. (19), 2013	Age, platinum free-interval, study treatment arms, ECOG performance status
Diaz et al. (20), 2012	Age, FIGO stage, grade, suboptimal cytoreduction

BMI, body mass index; CCI, Charlson comorbidity index; ECOG, Eastern Cooperative Oncology Group; FIGO, International Federation of Gynecology and Obstetrics; N/A, not available; NACT, neoadjuvant chemotherapy; PDS, primary debulking surgery.

**TABLE 3 |** Methodological quality of cohort studies included in the meta-analysis.

First author, reference, publication year	Selection				Comparability	Outcome			Risk of bias <sup>d</sup>
	Representativeness of the exposed cohort	Selection of the unexposed cohort	Ascertainment of exposure	Outcome of interest not present at start of study	Control for important factor or additional factor <sup>a</sup>	Assessment of outcome	Follow-up long enough for outcomes to occur <sup>b</sup>	Adequacy of follow-up of cohorts <sup>c</sup>	
Cho et al. (23), 2020	*	*	*	*	**	*	*	*	Low risk
Gonzalez et al. (22), 2020	*	*	*	*	**	*	*	*	Low risk
Couttenier et al. (25), 2019	*	*	*	*	**	*	*	*	Low risk
Harding et al. (24), 2019	*	*	*	*	**	*	*	*	Low risk
Baek et al. (37), 2018	*	*	*	*	—	*	*	*	Low risk
Al-Niaimi et al. (17), 2016	*	—	*	*	**	*	*	*	Low risk
Heitz et al. (16), 2016	—	*	—	*	**	*	*	*	Low risk
Watkins et al. (18), 2015	*	*	*	*	**	*	*	*	Low risk
Johannesdottir et al. (38), 2013	*	*	*	*	**	*	*	*	Low risk
Heitz et al. (19), 2013	*	*	*	*	*	*	—	*	High risk
Diaz et al. (20), 2012	—	*	*	*	**	*	*	*	Low risk

<sup>a</sup>A study could be awarded a maximum of one star for each item except for the item Control for important factor or additional factor.

The definition/explanation of the Newcastle-Ottawa Scale in each column is available from [http://www.ohri.ca/programs/clinical\\_epidemiology/oxford.asp](http://www.ohri.ca/programs/clinical_epidemiology/oxford.asp).

<sup>b</sup>A maximum of two stars could be awarded for this item. Studies that controlled for age at diagnosis received one star, whereas studies that controlled for other important confounders such as FIGO stage, comorbidity received an additional star.

<sup>c</sup>A cohort study with a follow-up time >24 months was assigned one star.

<sup>d</sup>A cohort study with a follow-up rate >75% was assigned one star.

<sup>e</sup>Studies that obtained a full scores at least two domains were considered to have a low risk of bias, other situations were considered as high risk.

## Association of Post-Diagnostic Beta Blocker Usage With OC Prognosis

Nine studies (16–20, 22, 25, 37, 38), including 17,201 OC patients and 4,433 events were used to estimate the summary

relationship between post-diagnostic beta blocker usage and total mortality of OC patients. The overall HR was 1.08 (95% CI = 0.92–1.27) with high heterogeneity ( $I^2 = 76.5\%$ ) (**Figure 2**). No publication bias was discovered (**Supplementary Figure S1**)

(Egger's  $P = 0.22$  and Begg's  $P = 0.05$ ). Three (18, 24, 25) studies were applied for assessing the overall effects of post-diagnostic beta blocker usage on cancer-specific mortality ( $HR=1.22$ , 95%  $CI=0.89-1.67$ ,  $I^2 = 88.1\%$ ), and four (16, 17, 19, 23) studies were applied for assessing the overall effects of post-diagnostic beta blocker use on progression-free survival ( $HR = 0.88$ , 95%  $CI = 0.75-1.05$ ,  $I^2 = 0\%$ ).

The results of subgroup and meta-regression analyses are presented in **Table 4**. Most of these findings were consistent with the main results. Notably, in the stratified analysis, we observed significant positive associations in studies with  $\geq 800$  cases ( $HR = 1.20$ , 95%  $CI = 1.05-1.37$ ), no immortal time bias ( $HR = 1.28$ , 95%  $CI = 1.10-1.49$ ) and adjustment for comorbidity ( $HR = 1.20$ , 95%  $CI = 1.05-1.37$ ). Furthermore, no evidence of heterogeneity source was detected in meta-regression model on the base of the variables mentioned.

When each study was removed from the major analysis in turn, the summary results did not change substantially in the sensitivity analysis (**Supplementary Figure S2**). The resulting HR of total mortality ranged from a low of 1.03 (95%  $CI = 0.82-1.29$ ;  $I^2 = 78.7\%$ ) after removing the study by Couttenier et al. (25) to a high of 1.14 (95% $CI = 0.97-1.33$ ;  $I^2 = 73.0\%$ ) after removing the study by Al-Niaimi et al. (17).

## DISCUSSION

The present updated meta-analysis based on eleven cohort studies, including 20,274 OC patients and 5,699 events were unable to observe a significant association between post-diagnostic beta blocker use and OC prognosis. These null findings were consistently detected in numerous subgroup and sensitivity analyses. To our knowledge, the current analysis is the most comprehensive meta-analysis of the available cohort

studies estimating the aforementioned relationship between post-diagnostic beta blocker use and OC prognosis.

Compared with two previous published systematic reviews and meta-analyses (14, 15), our present study revealed consistent results. Yap et al. (14) indicated no statistical association between beta blocker use on OC prognosis. Majidi et al. (15) was also unable to find a statistically significant relationship between beta blocker use and OC patients' survival. These two reports had common limitations in exploring mixed effects of pre- or post-diagnostic beta blocker use and failed to provide information regarding subgroup analyses stratified by geographic locations, study quality and whether adjustments were made for confounders. The present meta-analysis included several relevant high-quality studies (22–25) with additional potential confounder adjustments during the past 2 years. To explore sources of study heterogeneity, subgroup analysis and meta-regression analysis were conducted based on study characteristics and confounding factors. Further investigation of relationships between beta blocker use and total mortality, cancer-specific mortality and progression-free survival as outcomes revealed no significant correlation.

Although we were unable to observe significant result in the subgroup analysis stratified by geographic location, the point estimate was slightly different (1.03 for U.S. vs. 1.10 for non-U.S.). This observation could partly be attributed to different rates of beta blocker use in OC patients. For example, Watkins et al. (18) reported that the usage rate was 18.9% in the U.S. based on 1,425 OC patients from 2004 to 2010, whereas Couttenier et al. (25) reported this rate as 38.3% in Belgium based on 6,197 OC patients from 2004 to 2014.

In the subgroup analysis layered by immortal time bias, we detected positive correlation between use of beta blocker after diagnosis and total mortality for OC patients in studies without immortal time bias. The probability of accidental results could not be excluded because limited studies were included in this

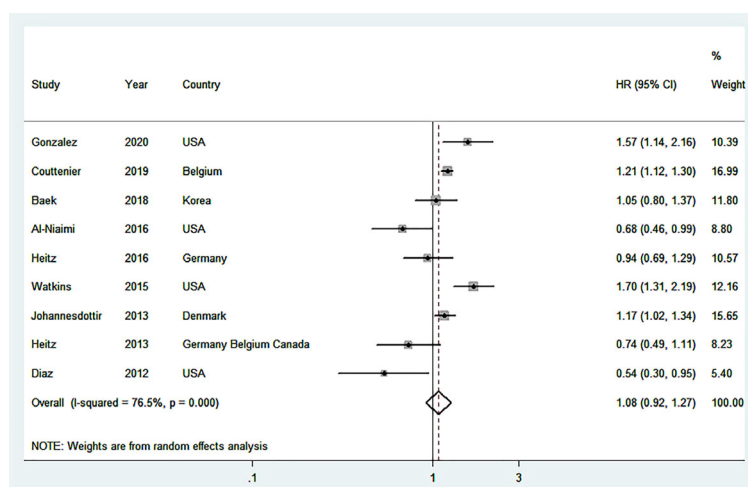


**FIGURE 2** | Forest plot (random-effects model) of the association between post-diagnostic beta blocker use and total mortality of OC patients. Squares indicate study-specific hazard ratios (HR), where the size of the square reflects the study-specific statistical weight; horizontal lines indicate the 95% confidence interval (CI); diamonds denote the summary hazard ratio with 95% CI.

**TABLE 4 |** Summary risk estimates of the association between post-diagnostic beta blocker use and prognosis of ovarian cancer (user vs. non-user).

	No. of study	HR (95%CI)	I <sup>2</sup> (%)	P*	P**
<b>Total mortality</b>	9	1.08 (0.92–1.27)	76.5	<0.01	
<b>Cancer-specific mortality</b>	3	1.22 (0.89–1.67)	88.1	<0.01	
<b>Progression-free survival</b>	4	0.88 (0.75–1.05)	0	0.773	
<b>Subgroup analyses for total mortality</b>					
<b>Type of beta blocker</b>					0.877
Non-selective beta blocker	3	1.24 (0.90–1.71)	68.9	0.04	
Selective beta blocker	4	1.21 (0.94–1.55)	76.0	0.006	
<b>Region</b>					0.888
USA	4	1.03 (0.61–1.74)	88.1	<0.01	
Non-USA	5	1.10 (0.98–1.24)	50.6	0.088	
<b>Number of cases</b>					0.183
<800	4	0.83 (0.51–1.36)	82.9	0.001	
≥800	5	1.20 (1.05–1.37)	61.9	0.033	
<b>Study quality</b>					0.375
Low risk	8	1.12 (0.95–1.31)	75.8	<0.01	
High risk	1	0.74 (0.49–1.11)	N/A	N/A	
<b>FIGO stage</b>					0.535
I-IV (All)	3	0.96 (0.68–1.34)	80.7	0.006	
III-IV (Advanced)	3	1.21 (0.71–2.05)	84.6	0.002	
<b>Immortal time bias</b>					0.118
Yes	6	0.90 (0.68–1.19)	72.3	0.003	
No	3	1.28 (1.10–1.49)	70.5	0.034	
<b>Adjustment for potential confounders</b>					
<b>Age at diagnosis</b>					0.984
Yes	8	1.08 (0.90–1.29)	79.0	<0.01	
No	1	1.05 (0.80–1.37)	NA	NA	
<b>FIGO stage</b>					0.778
Yes	6	1.09 (0.84–1.40)	82.1	<0.01	
No	3	1.03 (0.83–1.29)	55.6	0.105	
<b>Comorbidity</b>					0.289
Yes	4	1.20 (1.07–1.34)	42.7	0.155	
No	5	0.90 (0.60–1.35)	84.8	<0.01	
<b>Residual disease</b>					0.541
Yes	2	1.21 (0.73–2.01)	80.2	0.025	
No	7	1.04 (0.87–1.25)	79.3	<0.01	
<b>Histology</b>					0.880
Yes	2	1.12 (0.89–1.41)	57.8	0.124	
No	7	1.04 (0.81–1.34)	80.9	<0.01	
<b>Chemotherapy</b>					0.262
Yes	1	1.57 (1.14–2.16)	N/A	N/A	
No	8	1.03 (0.87–1.22)	77.3	<0.01	
<b>Non-beta blocker drug use</b>					0.276
Yes	2	1.31 (0.99–1.73)	63.7	0.097	
No	7	0.98 (0.78–1.23)	80.5	<0.01	

\*P-Value for heterogeneity within each subgroup.

\*\*P-Value for heterogeneity between subgroups with meta-regression analysis.

subgroup analysis. Immortal time bias was first described by Suissa (39), and refers to drug usage classification based on data about usage of beta blocker after the beginning of follow-up. Herein, OC patients had to survive until follow-up before they would to be defined as exposed group. This immortal time bias can result in overestimating survival rate of the exposed group and may interpret why survival rate of beta blocker users has increased. For example, two studies (17, 20) reported improved survival among beta blocker users. However, both results were probably affected by immortal time bias. On the contrary, three other studies (18, 25, 38) avoided immortal time bias in the study design and showed no evidence that the use of beta blocker was beneficial for ovarian survival. Therefore, future primary studies should address this issue of immortal time bias.

Beta blocker are generally prescribed for hypertension. OC patients with hypertension were more likely to take beta blocker as prescription drugs, whereas OC patients without hypertension may also use beta blocker for perioperative treatment. Baek et al. (37) described a increase in survival with post-diagnostic beta blocker use among OC patients with hypertension (HR = 0.65, 95% CI = 0.45–0.93); however, no statistically correlated was found for OC patients and normal blood pressure levels (HR = 0.60, 95% CI = 0.34–1.07). Therefore, there may be differences in underlying disease, which could be a source of bias for the resulting analysis. In addition, there could also be confounding variables associated with the severity of the health status during treatment, if OC patients with high blood pressure also has comparatively more serious malignant tumors, they are

less likely to keep on using beta blocker following diagnosis (40). Information on stage and grade are not widely obtained and do not grasp the whole condition of the severity of disease. Therefore, a low evaluation of the mortality for beta blocker users could have happened.

Clinical studies presented that the use of beta blocker has been confirmed to decrease total mortality and tumor proliferation in some malignant tumors (41, 42). The underlying biological mechanisms by which beta blocker use after diagnosis may alter the survival rate of those with OC have been explored in certain researches. Beta blockers exert antineoplastic effects on the cyclic adenosine monophosphate pathway, causing down regulation of adhesion receptors and upregulation of tumor suppressor genes (43). In addition, beta blockers decrease expression of the pro-proliferative protein Ki-67 and pro-survival protein Bcl-2 and increase expression of pro-apoptotic p53 protein expression (44). Studies have shown that OC patients with better social support produce less vascular endothelial growth factor (VEGF) (11). Orepinephrine, epinephrine, and isoproterenol significantly increased VEGF production *via* SKOV3 cells, and the effects of these pathways were inhibited by the beta blocker called propranolol (11). Selective beta blockers inhibited phosphorylation of the mitogenic signaling regulators p44/42 MAPK, p38 MAPK, JNK, and CREB, and promoted phosphorylation of the cell survival/apoptosis regulators AKT, p53, and GSK3 $\beta$ 42 (45).

The advantages of this study deserve to be emphasized. This study investigated the association between different exposures (type of post-diagnostic beta blocker use) and outcomes (total mortality, cancer-specific mortality, progression-free survival) of OC patients. In consideration of study features and main adjustments for confounding variables, subgroup, sensitivity, meta-regression analyses were conducted to probe into possible sources of heterogeneity. Moreover, majorities of the included articles had a low risk of bias after using the NOS to assess the literature quality of all included articles.

The disadvantages of this study deserve to be outlined. First, we relied on prescription records to define medication use without information on compliance. This method could not make an accurate evaluation of medications used if patients are prescribed medication but not taking these drugs. Second, included cohort studies were all retrospective, which may endure potential risks of information and selection biases. This could lead to exposure group selection if inappropriate and if information is incomplete. Third, because of the features of observational studies, it is not enough to rule out the possibility of residual confounding effects of incomplete or unmeasured factors. Post-diagnostic beta blocker use is usually related to different clinical and non-clinical factors, for example, age at diagnosis, cancer stage, comorbidities, chemotherapy administration, and use of non-beta blocker drugs. However, not all of the currently included studies have adjusted for the abovementioned potential confounder factors (37). Fourth, due to limited information supplied by the included literatures, we were unable to determine the categories (beta-1 blocker on cardiac ventricular myocytes, beta-2 blocker on bronchial epithelium and systemic vascular, and beta-3 blocker on

adipocytes), dose, intensity, duration of post-diagnostic beta blocker use and OC prognosis in our meta-analysis. Finally, we merely included and analyzed openly published literatures; however, other unpublished literatures and gray literatures content with our criteria might have been ignored.

## CONCLUSIONS

The current meta-analysis reveals that post-diagnostic beta blocker use does not have an association with prognosis of OC patients. Further large-scale, prospective, and randomized controlled trials are necessary to verify the therapeutic effect of beta blockers and other factors, such as intensity, dose, duration, and type of beta blocker use on OC patients.

## DATA AVAILABILITY STATEMENT

The data analyzed in this study are subject to the following licenses/restrictions: The data that support the findings of this study are available from the corresponding author upon reasonable request. Requests to access these datasets should be directed to wuqj@sj-hospital.org.

## AUTHOR CONTRIBUTIONS

Q-JW and Y-HZ conceived and designed the study. Z-YW and T-TG performed the literature search and reviewed the search results for study inclusion. Z-YW and Y-TJ performed the data curation and formal analysis. Z-YW, SG, T-TG, Y-TJ, and J-YZ participated in writing the original draft. Z-YW and SG contributed equally to this work. All authors contributed to the article and approved the submitted version.

## FUNDING

This study was supported by grants from the National Key R&D Program of China (2017YFC0907401 to Y-HZ), the Natural Science Foundation of China (82073647 and 81602918 to Q-JW), the China Postdoctoral Science Foundation Funded Project (2018M641752 to Q-JW), the LiaoNing Revitalization Talents Program (XLYC1907102 to Q-JW and XLYC1802095 to Y-HZ), Shenyang high level innovative talents support program (RC190484 to Q-JW), and 345 Talent Project to Q-JW (M0268).

## SUPPLEMENTARY MATERIAL

The Supplementary Material for this article can be found online at: <https://www.frontiersin.org/articles/10.3389/fonc.2021.665617/full#supplementary-material>



## REFERENCES

- Bray F, Ferlay J, Soerjomataram I, Siegel RL, Torre LA, Jemal A. Global Cancer Statistics 2018: GLOBOCAN Estimates of Incidence and Mortality Worldwide for 36 Cancers in 185 Countries. *CA Cancer J Clin* (2018) 68:394–424. doi: 10.3322/caac.21492
- Ledermann JA, Raja FA, Fotopoulou C, Gonzalez-Martin A, Colombo N, Sessa C. Newly Diagnosed and Relapsed Epithelial Ovarian Carcinoma: ESMO Clinical Practice Guidelines for Diagnosis, Treatment and Follow-Up. *Ann Oncol* (2013) 24:vi24–32. doi: 10.1093/annonc/mdt333
- Torre LA, Trabert B, DeSantis CE, Miller KD, Samimi G, Runowicz CD, et al. Ovarian Cancer Statistics, 2018. *CA Cancer J Clin* (2018) 68:284–96. doi: 10.3322/caac.21456
- Ong HT. Beta Blockers in Hypertension and Cardiovascular Disease. *BMJ* (2007) 334:946–9. doi: 10.1136/bmj.39185.440382.47
- Bristow MR. Mechanism of Action of Beta-Blocking Agents in Heart Failure. *Am J Cardiol* (1997) 80:26L–40L. doi: 10.1016/s0002-9149(97)00846-1
- Le CP, Nowell CJ, Kim-Fuchs C, Botteri E, Hiller JG, Ismail H, et al. Chronic Stress in Mice Remodels Lymph Vasculature to Promote Tumour Cell Dissemination. *Nat Commun* (2016) 7:10634. doi: 10.1038/ncomms10634
- Pon CK, Lane JR, Sloan EK, Halls ML. The Beta2-Adrenoceptor Activates a Positive cAMP-Calcium Feedforward Loop to Drive Breast Cancer Cell Invasion. *FASEB J* (2016) 30:1144–54. doi: 10.1096/fj.15-277798
- Sloan EK, Priceman SJ, Cox BF, Yu S, Pimentel MA, Tangkanangnukul V, et al. The Sympathetic Nervous System Induces a Metastatic Switch in Primary Breast Cancer. *Cancer Res* (2010) 70:7042–52. doi: 10.1158/0008-5472.CAN-10-0522
- Shahzad MM, Arevalo JM, Armaiz-Pena GN, Lu C, Stone RL, Moreno-Smith M, et al. Stress Effects on FosB- and Interleukin-8 (IL8)-Driven Ovarian Cancer Growth and Metastasis. *J Biol Chem* (2010) 285:35462–70. doi: 10.1074/jbc.M110.109579
- Thaker PH, Han LY, Kamat AA, Arevalo JM, Takahashi R, Lu C, et al. Chronic Stress Promotes Tumor Growth and Angiogenesis in a Mouse Model of Ovarian Carcinoma. *Nat Med* (2006) 12:939–44. doi: 10.1038/nm1447
- Lutgendorf SK, Cole S, Costanzo E, Bradley S, Coffin J, Jabbari S, et al. Stress-Related Mediators Stimulate Vascular Endothelial Growth Factor Secretion by Two Ovarian Cancer Cell Lines. *Clin Cancer Res* (2003) 9:4514–21.
- Bracken MB. Why Animal Studies are Often Poor Predictors of Human Reactions to Exposure. *J R Soc Med* (2009) 102:120–2. doi: 10.1258/jrsm.2008.08k033
- Rueluis HW. Extrapolation From Animals to Man: Predictions, Pitfalls and Perspectives. *Xenobiotica* (1987) 17:255–65. doi: 10.3109/00498258709043936
- Yap A, Lopez-Olivo MA, Dubowitz J, Pratt G, Hiller J, Gottumukkala V, et al. Effect of Beta-Blockers on Cancer Recurrence and Survival: A Meta-Analysis of Epidemiological and Perioperative Studies. *Br J Anaesth* (2018) 121:45–57. doi: 10.1016/j.bja.2018.03.024
- Majidi A, Na R, Dixon-Suen S, Jordan SJ, Webb PM. Common Medications and Survival in Women With Ovarian Cancer: A Systematic Review and Meta-Analysis. *Gynecol Oncol* (2020) 157:678–85. doi: 10.1016/j.ygyno.2020.03.028
- Heitz F, Hengsbach A, Harter P, Traut A, Ataseven B, Schneider S, et al. Intake of Selective Beta Blockers has No Impact on Survival in Patients With Epithelial Ovarian Cancer. *Gynecol Oncol* (2017) 144:181–6. doi: 10.1016/j.ygyno.2016.11.012
- Al-Niaimi A, Dickson EL, Albertin C, Karnowski J, Niemi C, Spencer R, et al. The Impact of Perioperative Beta Blocker Use on Patient Outcomes After Primary Cytoreductive Surgery in High-Grade Epithelial Ovarian Carcinoma. *Gynecol Oncol* (2016) 143:521–5. doi: 10.1016/j.ygyno.2016.09.019
- Watkins JL, Thaker PH, Nick AM, Ramondetta LM, Kumar S, Urbauer DL, et al. Clinical Impact of Selective and Nonselective Beta-Blockers on Survival in Patients With Ovarian Cancer. *Cancer-Am Cancer Soc* (2015) 121:3444–51. doi: 10.1002/cncr.29392
- Heitz F, du Bois A, Harter P, Lubbe D, Kurzeder C, Vergote I, et al. Impact of Beta Blocker Medication in Patients With Platinum Sensitive Recurrent Ovarian Cancer-A Combined Analysis of 2 Prospective Multicenter Trials by the AGO Study Group, Ncic-CTG and EORTC-GCG. *Gynecol Oncol* (2013) 129:463–6. doi: 10.1016/j.ygyno.2013.03.007
- Diaz ES, Karlan BY, Li AJ. Impact of Beta Blockers on Epithelial Ovarian Cancer Survival. *Gynecol Oncol* (2012) 127:375–8. doi: 10.1016/j.ygyno.2012.07.102
- Na Z, Qiao X, Hao X, Fan L, Xiao Y, Shao Y, et al. The Effects of Beta-Blocker Use on Cancer Prognosis: A Meta-Analysis Based on 319,006 Patients. *Onco Targets Ther* (2018) 11:4913–44. doi: 10.2147/OTT.S167422
- Gonzalez R, Gockley AA, Melamed A, Sugrue R, Clark RM, Del CM, et al. Multivariable Analysis of Association of Beta-Blocker Use and Survival in Advanced Ovarian Cancer. *Gynecol Oncol* (2020) 157:700–5. doi: 10.1016/j.ygyno.2020.03.012
- Cho MA, Jeong SY, Sohn I, Kim MS, Kang JH, Paik ES, et al. Impact of Angiotensin Receptor Blockers, Beta Blockers, Calcium Channel Blockers and Thiazide Diuretics on Survival of Ovarian Cancer Patients. *Cancer Res Treat* (2020) 52:645–54. doi: 10.4143/crt.2019.509
- Harding BN, Delaney JA, Urban RR, Weiss NS. Post-Diagnosis Use of Antihypertensive Medications and the Risk of Death From Ovarian Cancer. *Gynecol Oncol* (2019) 154:426–31. doi: 10.1016/j.ygyno.2019.05.030
- Couttenier A, Lacroix O, Silversmit G, Vaes E, De Schutter H, Robert A. Beta-Blocker Use and Mortality Following Ovarian Cancer Diagnosis: A Population-Based Study. *Cancer Epidemiol* (2019) 62:101579. doi: 10.1016/j.canep.2019.101579
- Moher D, Liberati A, Tetzlaff J, Altman DG. Preferred Reporting Items for Systematic Reviews and Meta-Analyses: The PRISMA Statement. *PLoS Med* (2009) 6:e1000097. doi: 10.1371/journal.pmed.1000097
- Stroup DF, Berlin JA, Morton SC, Olkin I, Williamson GD, Rennie D, et al. Meta-Analysis of Observational Studies in Epidemiology. *JAMA* (2000) 283:2008–12. doi: 10.1001/jama.283.15.2008
- Wells GA, Shea B, O'Connell D, Peterson J, Welch V, Losos M, et al. The Newcastle-Ottawa Scale (NOS) for Assessing the Quality of Nonrandomised Studies in Meta-Analyses. (2013). (Accessed on May 2020).
- Jiang YT, Gong TT, Zhang JY, Li XQ, Gao S, Zhao YH, et al. Infertility and Ovarian Cancer Risk: Evidence From Nine Prospective Cohort Studies. *Int J Cancer* (2020) 147:2121–30. doi: 10.1002/ijc.33012
- Gong TT, Wu QJ, Lin B, Ruan SK, Kushima M, Takimoto M. Observational Studies on the Association Between Post-Diagnostic Metformin Use and Survival in Ovarian Cancer: A Systematic Review and Meta-Analysis. *Front Oncol* (2019) 9:458. doi: 10.3389/fonc.2019.00458
- Higgins JP, Thompson SG. Quantifying Heterogeneity in a Meta-Analysis. *Stat Med* (2002) 21:1539–58. doi: 10.1002/sim.1186
- Trikalinos TA, Salanti G, Khoury MJ, Ioannidis JP. Impact of Violations and Deviations in Hardy-Weinberg Equilibrium on Postulated Gene-Disease Associations. *Am J Epidemiol* (2006) 163:300–9. doi: 10.1093/aje/kwj046
- Egger M, Davey SG, Schneider M, Minder C. Bias in Meta-Analysis Detected by a Simple, Graphical Test. *BMJ* (1997) 315:629–34. doi: 10.1136/bmj.315.7109.629
- Begg CB, Mazumdar M. Operating Characteristics of a Rank Correlation Test for Publication Bias. *Biometrics* (1994) 50:1088–101. doi: 10.2307/2533446
- Diaz ES, Karlan BY, Li AJ. Impact of Beta Blockers on Epithelial Ovarian Cancer Survival. *Obstetrical Gynecol Survey* (2013) 68:109–10. doi: 10.1097/01.ogx.0000427623.57640.65
- Shah SM, Carey IM, Owen CG, Harris T, Dewilde S, Cook DG. Does  $\beta$ -Adrenoceptor Blocker Therapy Improve Cancer Survival? Findings From a Population-Based Retrospective Cohort Study. *Brit J Clin Pharmacol* (2011) 72:157–61. doi: 10.1111/j.1365-2125.2011.03980.x
- Baek MH, Kim DY, Kim SO, Kim YJ, Park YH. Impact of Beta Blockers on Survival Outcomes in Ovarian Cancer: A Nationwide Population-Based Cohort Study. *J Gynecol Oncol* (2018) 29:e82. doi: 10.3802/jgo.2018.29.e82
- Johannesdottir SA, Schmidt M, Phillips G, Glaser R, Yang EV, Blumenfeld M, et al. Use of  $\beta$ -Blockers and Mortality Following Ovarian Cancer Diagnosis: A Population-Based Cohort Study. *BMC Cancer* (2013) 13:85. doi: 10.1186/1471-2407-13-85
- Suissa S. Immortal Time Bias in Pharmaco-Epidemiology. *Am J Epidemiol* (2008) 167:492–9. doi: 10.1093/aje/kwn324
- van Nordennen RT, Lavrijsen JC, Heesterbeek MJ, Bor H, Vissers KC, Koopmans RT. Changes in Prescribed Drugs Between Admission and the End of Life in Patients Admitted to Palliative Care Facilities. *J Am Med Dir Assoc* (2016) 17:514–8. doi: 10.1016/j.jamda.2016.01.015

41. Rains SL, Amaya CN, Bryan BA. Beta-Adrenergic Receptors are Expressed Across Diverse Cancers. *Oncoscience* (2017) 4:95–105. doi: 10.18632/oncoscience.357
42. Armaiz-Pena GN, Allen JK, Cruz A, Stone RL, Nick AM, Lin YG, et al. Src Activation by Beta-Adrenoreceptors Is a Key Switch for Tumour Metastasis. *Nat Commun* (2013) 4:1403. doi: 10.1038/ncomms2413
43. Lang K, Drell TT, Lindecke A, Niggemann B, Kaltschmidt C, Zaenker KS, et al. Induction of a Metastatogenic Tumor Cell Type by Neurotransmitters and Its Pharmacological Inhibition by Established Drugs. *Int J Cancer* (2004) 112:231–8. doi: 10.1002/ijc.20410
44. Montoya A, Varela-Ramirez A, Dickerson E, Pasquier E, Torabi A, Aguilera R, et al. The Beta Adrenergic Receptor Antagonist Propranolol Alters Mitogenic and Apoptotic Signaling in Late Stage Breast Cancer. *BioMed J* (2019) 42:155–65. doi: 10.1016/j.bj.2019.02.003
45. Montoya A, Amaya CN, Belmont A, Diab N, Trevino R, Villanueva G, et al. Use of Non-Selective Beta-Blockers Is Associated With Decreased Tumor

Proliferative Indices in Early Stage Breast Cancer. *Oncotarget* (2017) 8:6446–60. doi: 10.18632/oncotarget.14119

**Conflict of Interest:** The authors declare that the research was conducted in the absence of any commercial or financial relationships that could be construed as a potential conflict of interest.

Copyright © 2021 Wen, Gao, Gong, Jiang, Zhang, Zhao and Wu. This is an open-access article distributed under the terms of the Creative Commons Attribution License (CC BY). The use, distribution or reproduction in other forums is permitted, provided the original author(s) and the copyright owner(s) are credited and that the original publication in this journal is cited, in accordance with accepted academic practice. No use, distribution or reproduction is permitted which does not comply with these terms.



# Berberine Sensitizes Human Hepatoma Cells to Regorafenib via Modulating Expression of Circular RNAs

Kunyuan Wang<sup>1†</sup>, Ganxiang Yu<sup>1†</sup>, Jiaen Lin<sup>1†</sup>, Zhilei Wang<sup>1</sup>, Qianting Lu<sup>1</sup>, Chengxin Gu<sup>1</sup>, Tao Yang<sup>1</sup>, Shiming Liu<sup>2</sup> and Hui Yang<sup>1\*</sup>

<sup>1</sup>Department of Gastroenterology, The Second Affiliated Hospital of Guangzhou Medical University, Guangzhou, China,

<sup>2</sup>Guangzhou Institute of Cardiovascular Disease, The Second Affiliated Hospital of Guangzhou Medical University, Guangzhou, China

## OPEN ACCESS

### Edited by:

Dong-Hua Yang,  
St. John's University, United States

### Reviewed by:

Zhi Shi,  
Jinan University, China  
Gui-Qiang Wang,  
Peking University First Hospital, China

### \*Correspondence:

Hui Yang  
yanghui@gzhmu.edu.cn

<sup>†</sup>These authors have contributed  
equally to this work

### Specialty section:

This article was submitted to  
Pharmacology of Anti-Cancer Drugs,  
a section of the journal  
Frontiers in Pharmacology

Received: 22 November 2020

Accepted: 08 March 2021

Published: 17 June 2021

### Citation:

Wang K, Yu G, Lin J, Wang Z, Lu Q,  
Gu C, Yang T, Liu S and Yang H (2021)  
Berberine Sensitizes Human  
Hepatoma Cells to Regorafenib via  
Modulating Expression of  
Circular RNAs.  
Front. Pharmacol. 12:632201.  
doi: 10.3389/fphar.2021.632201

Regorafenib resistance is a key limiting factor in the treatment of advanced hepatocellular carcinoma (HCC). Increasing evidence has demonstrated that Berberine (BBR) can synergistically enhance the therapeutic effect of various chemotherapeutic agents. However, the contribution of BBR on regorafenib therapy remains unclear. The purpose of this study was to explore the combined treatment effect of berberine and regorafenib in HCC. We found that BBR enhanced the cytotoxicity of regorafenib in HCC cells. Compared with regorafenib alone, the combined treatment of BBR and regorafenib significantly inhibited the proliferation of HCC cells and induced cellular apoptosis. Meanwhile, the combined treatment group with BBR (10mg/kg/day) and regorafenib (5mg/kg/day) had a dramatic inhibitory effect on the growth of HCC xenograft tumors in nude mice. The increased apoptosis of xenograft tumors was seen in the combined treatment group. Moreover, a comprehensive circular RNA sequencing was performed to identify differentially expressed circRNAs in HCC cells after exposure to 100μM BBR and 5μM regorafenib. The volcano plot and scatter plot analyses revealed that there were 58 up-regulated and 19 down-regulated differentially expressed circRNAs between the combination treatment and control groups. Among them, the expression of hsa\_circ\_0032029 and hsa\_circ\_0008928 were up-regulated in HCC cells after treatment with 100μM BBR and 5μM regorafenib. Taken together, this study demonstrated that BBR enhanced the anti-HCC effect of regorafenib both *in vitro* and *in vivo*. The synergistic anti-tumor effect of BBR and regorafenib might be related to the up-regulation of hsa\_circ\_0032029 and hsa\_circ\_0008928 in HCC cells.

**Keywords:** berberine, regorafenib, hepatocellular carcinoma, proliferation, apoptosis, circular RNAs

## INTRODUCTION

Hepatocellular carcinoma (HCC) is a major health problem with increasing incidence and mortality (Bray et al., 2018; Forner et al., 2018). Although the treatment of HCC has improved over the past decade, the therapeutic options for patients with advanced HCC are very limited (Vogel and Saborowski, 2020). Regorafenib, an oral multi-kinase inhibitor, has become a therapeutic agent which significantly improves overall survival after the treatment failure of sorafenib, and receives the

approval as a second line treatment for advanced HCC in 2017 (Bruix et al., 2017; Duffy and Greten, 2017). However, regorafenib also faces the risk of drug resistance and subsequent progression of HCC after treatment (Wang et al., 2019). Therefore, it is needed to find novel agents that can increase the sensitivity of HCC cells to regorafenib treatment.

Chinese medicine has been used worldwide as a supplement and alternative medicine for the treatment of cancers. The experimental studies and clinical trials have shown that Berberine (BBR) can exert anti-cancer activity by inhibiting cellular proliferation and inducing cell apoptosis in various cancers (Fondevila et al., 2019; Lagoa et al., 2020). Recently, a randomized double-blinded, placebo-controlled trial shows that BBR reduces the risk of colorectal adenoma and recurrence of polypoid lesion in patients after polypectomy (Chen et al., 2020). By using Janus nanocarrier containing doxorubicin (DOX) and BBR simultaneously, BBR can drastically enhance the anti-tumor activity of DOX and suppress HCC recurrence (Zhang et al., 2019). In addition, our previous study has proved that BBR makes HCC cells sensitive to sorafenib (Huang et al., 2018). However, it is unclear whether BBR can enhance the anti-HCC activity of regorafenib.

Circular RNAs (circRNAs) belong to the endogenous non-coding RNAs with a closed loop structure, which have multiple biological functions in regulating the occurrence and progression of cancer (Liu et al., 2019). Studies have shown that circRNA is involved in regulating the resistance of chemotherapeutic drugs (Abu et al., 2019; Hua et al., 2019). In the present study, we aimed to investigate the contribution of BBR to the anti-HCC activity of regorafenib and its underlying mechanism. Our data demonstrated that BBR could synergistically enhanced the anti-HCC effect of regorafenib both *in vitro* and *in vivo*. The expression of hsa\_circ\_0032029 and hsa\_circ\_0008928 were up-regulated in HCC cells after treatment with 100 $\mu$ M BBR and 5 $\mu$ M regorafenib. These findings suggest that hsa\_circ\_0032029 and hsa\_circ\_0008928 may be associated with the synergistic anti-tumor effect of BBR and regorafenib in HCC cells.

## MATERIALS AND METHODS

### Cell Culture and Reagents

Human HCC cell lines Hep3B and SMMC-7721 were obtained from the Cell Bank of Type Culture Collection (Chinese Academy of Sciences, Shanghai, China) and the American Type Culture Collection (Manassas, VA, USA), respectively. HCC cells were cultivated at 37°C in a 5% CO<sub>2</sub> incubator with the high-glucose Dulbecco's modified Eagle's medium (Thermo Fisher Scientific, Inc., Waltham, MA, United States), supplemented with 10% (V/V) fetal bovine serum. Regorafenib and BBR were obtained from Selleck Chemicals (Houston, TX, United States; cat. no. S1178 and S2271).

### Cell Viability Assay

HCC cells were seeded into a 96-well plate with 5,000 cells per well. After overnight incubation, HCC cells were treated with the indicated concentrations of regorafenib, BBR or their combination for 24h or 48h. The viability of HCC was

examined by MTS Assay (Promega, United States; cat. no. G3588) and Synergy H1/Epoch microplate reader (BioTek Instruments, Inc., Winooski, VT, United States). The cell survival rate was calculated as follows: viability (%) = (average OD value of drug-treated sample/average OD value of control sample)  $\times$  100%. The drug concentration (IC<sub>50</sub>) that inhibited cell growth by 50% was calculated via Probit Regression.

### Combined Effect Evaluation

The interaction between regorafenib and BBR was quantified by Com-puSyn software (ComboSyn, Inc., Paramus, NJ, <http://www.combosyn.com/feature.html>) and determined by the combination index (CI). CI value < 1, = 1 and >1 represented synergistic, additive and antagonistic effects, respectively.

### EdU Incorporation Assay and Apoptosis Assay

The Cell-Light™ EdU ApolloR567 *In Vitro* Imaging Kit (RiboBio, Guangzhou, China) was used to detect the level of cell proliferation. The Annexin V-FITC/PI Apoptosis Detection Kit (Thermo Fisher, USA) and DeadEnd™ Fluorometric TUNEL System assay (Promega, cat. no. G3250; United States) were used to measure cellular apoptotic level. The EVOS FL High Content Imaging System (Invitrogen, Carlsbad, CA, United States) was performed to obtain and analyze images.

### Western Blot Assay

The extraction of total protein lysate and SDS-PAGE were performed as previously described (Huang et al., 2018). After protein extracts were transferred onto methanol-activated polyvinylidene fluoride (PVDF) membranes in 1.5h at 90V condition, the PVDF membranes were blocked with 5% non-fat milk for 1h at 25°C. The membranes were probed with primary antibodies at 4°C for 12h, including anti-poly (ADP-ribose) polymerase (PARP; 1:1,000; cat. no. 9532; Cell Signaling Technology, Inc.), anti-BCL-2 (1:1,000; cat. no. 2870; Cell Signaling Technology, Inc.), and anti-GAPDH (1:1,000; cat. no. 2118; Cell Signaling Technology, Inc.). The membranes were subsequently incubated with horseradish peroxidase-conjugated anti-rabbit or anti-mouse IgG secondary antibody (1:5,000; cat. no. 7074 or 7,076; Cell Signaling Technology, Inc.) for 1h at 25°C. Then, the protein bands were detected by enhanced chemiluminescence (SuperSignal West Pico Chemiluminescent Substrate; Pierce; Thermo Fisher Scientific, Inc.). ImageJ software (National Institutes of Health, Bethesda, MD, United States) was used to scanned and analyzed the protein bands.

### *In vivo* Tumor Assays

Male BALB/c nude mice at 4 weeks old were subcutaneously injected with 1 $\times$ 10<sup>7</sup> SMMC-7721 cells in the underarm region. When tumor size reached 5  $\times$  5mm<sup>2</sup>, mice were randomly divided into four groups (n = 5 in each group). Regorafenib (5mg/kg/day, 5 days per week) and BBR (10mg/kg/day, 2 days per week) were administered by gavage and intraperitoneal injection, respectively. The tumor volume of nude mice was measured by a caliper and calculated according to the formula (width<sup>2</sup>  $\times$  length)/2. *In vivo* experiments were performed according to the guidelines for



the use of laboratory animals that was approved by the Second Affiliated Hospital of Guangzhou Medical University.

## Circular RNA Sequencing, Differential Expression Analysis and Target miRNA Prediction

Trizol reagent (Invitrogen, Carlsbad, CA, United States) was used to extract the total RNAs from SMMC-7721 cells cultured in DMSO, regorafenib, BBR or their combination. The RNA-Seq libraries were constructed according to Illumina standard protocols and sequenced with Illumina HiSeq 3,000 through Genengy Biotechnology Co., Ltd (Shanghai, China). CircRNAs expression levels were quantified by the number of reads spanning back-spliced junctions (circular reads). CircRNAs expression was expressed as BSRP (back-spliced reads per million mapped reads), which circular reads was normalized to per million mapped reads. The DESEQ software package was used to identify differentially expressed circRNAs in the two groups (DMSO and the combination of regorafenib and BBR) with *t* test *p*-value < 0.05 and fold change >2. The top 77 expressed circRNAs were log2 transformed, gene mean centered and visualized as heatmaps using the Multi Experiment Viewer. Differentially expressed circRNAs were used to predict the potential binding sites of miRNAs by miRanda with threshold parameters as follows: single-residue-pair match scores >150,  $\Delta G < -20$  kcal/mol and demand strict 5' seed pairing.

## Real-Time PCR Validation

To detect the expression of circRNAs observed by high-throughput sequencing, five circRNAs were chosen for real-time PCR. Total RNA was extracted from HCC cell samples from DMSO, regorafenib, BBR and combination treatment groups using Trizol reagent. CircRNA levels were quantified by using the Prime Script RT Reagent Kit (TaKaRa, Dalian, China) and SYBR Premix Ex Taq (TaKaRa, Dalian, China). Then, Real-time PCR was performed on ABI Prism 7,300 real-time PCR system (Applied Biosystems, Foster City, CA, United States). Relative quantification was calculated based on the comparative CT method. GAPDH was used as an internal control to normalize the data. Primer sequences are shown in **Supplementary Table S1** in Supporting Information.

## Statistical Analysis

Statistical analyses were conducted by SPSS version 16.0 software (SPSS Inc. Chicago, IL, United States). The quantitative data was shown as means  $\pm$  SD from three independent experiments. Statistical analysis was performed using Student's *t*-test or one-way ANOVA. A value of *p* < 0.05 indicated a significant difference.

## RESULTS

### BBR Synergistically Enhances the anti-HCC Effect of Regorafenib *in vitro*

To explore the anti-HCC effect of regorafenib and BBR, the cellular viability was evaluated by MTS assay after HCC cells were

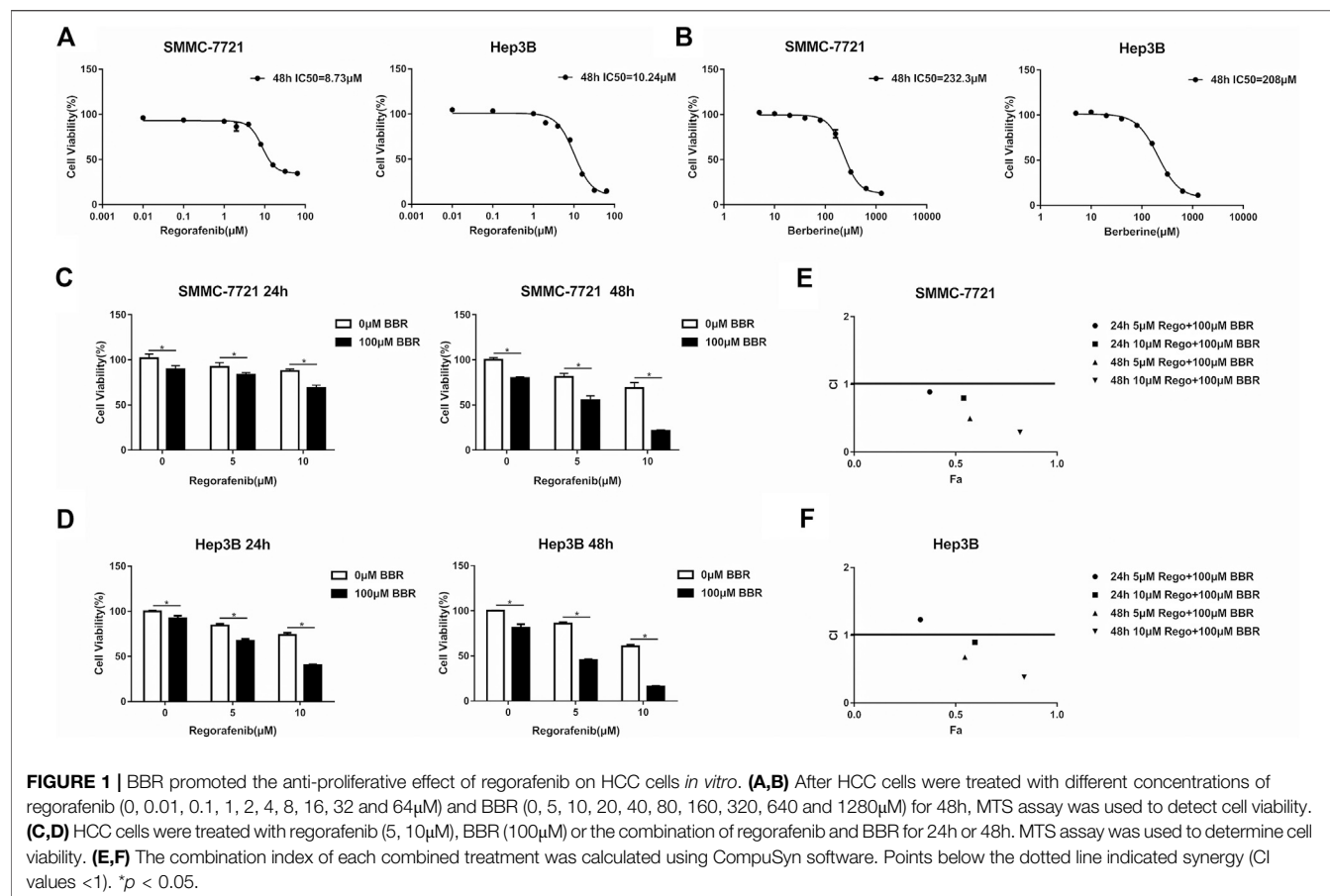
treated with regorafenib or BBR at different concentrations. The results showed that regorafenib or BBR alone could inhibit the proliferation of HCC cells in a dose-dependent manner (**Figures 1A,B**). The IC<sub>50</sub> value of regorafenib in SMMC-7721 and Hep3B cells were 8.73 and 10.24  $\mu$ M, respectively (**Figure 1A**). The IC<sub>50</sub> of BBR was 232.3  $\mu$ M in SMMC-7721 cells and 208  $\mu$ M in Hep3B cells (**Figure 1B**). Moreover, the IC<sub>50</sub> of BBR in normal hepatocytes L02 cells was 408.9  $\mu$ M, indicating that BBR at a concentration of 100  $\mu$ M had no obvious inhibitory effect on normal liver cells (**Supplementary Figure S1A**). Since the trough blood concentration of regorafenib in patients receiving regorafenib 40–160 mg/day was 318–9467 ng/ml (Taguchi et al., 2020), which was equivalent to 0.612–18.231  $\mu$ M, we first detected the combined effect of 1  $\mu$ M regorafenib and 100  $\mu$ M BBR. The results showed that 100  $\mu$ M BBR had a cytotoxic effect on HCC cells, while 1  $\mu$ M regorafenib had no influence on HCC cell viability (**Supplementary Figure S1B**). And the CI values of 1  $\mu$ M regorafenib and 100  $\mu$ M BBR combination in SMMC-7721 and hep3B cells were both greater than 1 (**Supplementary Figure S1C**). Therefore, regorafenib (5 and 10  $\mu$ M) and 100  $\mu$ M BBR were selected for further study. We found that the anti-proliferative effect caused by the combined treatment of regorafenib and BBR was significantly greater than that by a single agent treatment (**Figures 1C,D**). As shown in **Figure 1E**, regardless of 24h or 48h treatment, the CI values of different drug combinations in SMMC-7721 cells were all less than 1. In Hep3B cells, except for the combination of 5  $\mu$ M regorafenib and 100  $\mu$ M BBR for 24h, the CI values of other combined groups was less than 1 (**Figure 1F**). The above results indicate that there is a synergistic interaction between BBR and regorafenib in inhibiting the proliferation of HCC cells.

### Combined Treatment of BBR and Regorafenib Significantly Inhibits the Proliferation of HCC Cells

Then, we applied EdU assay to detect the anti-proliferative effect of BBR and regorafenib. We observed that compared with regorafenib or BBR alone, the combined therapy of regorafenib and BBR obviously inhibited the proliferation of HCC cells (**Figures 2A,B**). The combined treatment with 10  $\mu$ M regorafenib and 100  $\mu$ M BBR suppressed HCC cells proliferation more obviously than that with 5  $\mu$ M regorafenib and 100  $\mu$ M BBR. Meanwhile, the group treated with 10  $\mu$ M regorafenib and 100  $\mu$ M BBR for 48h has a stronger proliferation inhibitory effect when compared with other groups (**Figures 2C,D**). These results demonstrate that a longer drug exposure time will produce a stronger inhibitory effect.

### Co-Treatment of BBR and Regorafenib Induces HCC Cells Apoptosis

To investigate cellular apoptosis induced by BBR and regorafenib, HCC cells were treated with BBR and regorafenib alone or in combination. We found that the combined treatment of BBR and regorafenib significantly induced HCC cells apoptosis when cells



were cultured over 48h (**Figure 3A**). The protein expression of cleaved PARP was up-regulated, while the expression of anti-apoptotic protein BCL-2 was down-regulated in BBR and regorafenib combined treatment group (**Figure 3B**).

Meanwhile, Annexin V-FITC/PI co-staining was performed to further confirm the apoptosis-inducing effect of the combined treatment. After 48h of exposure to the series of treatments, we observed an increase in the percentage of Annexin V-positive cells in the cells treated with combined 10  $\mu$ M regorafenib and 100  $\mu$ M BBR (**Figure 4A**). Compared with the control group, the monotherapy or combination treatment group of 5  $\mu$ M regorafenib and 100  $\mu$ M BBR, the fluorescence intensity of Q2 and Q3 regions showed that the number of apoptotic cells was the highest in the combinational treatment group of 10  $\mu$ M regorafenib and 100  $\mu$ M BBR (**Figure 4B**). These results suggested that the combined treatment of regorafenib and BBR had synergistic effect in inducing cell apoptosis.

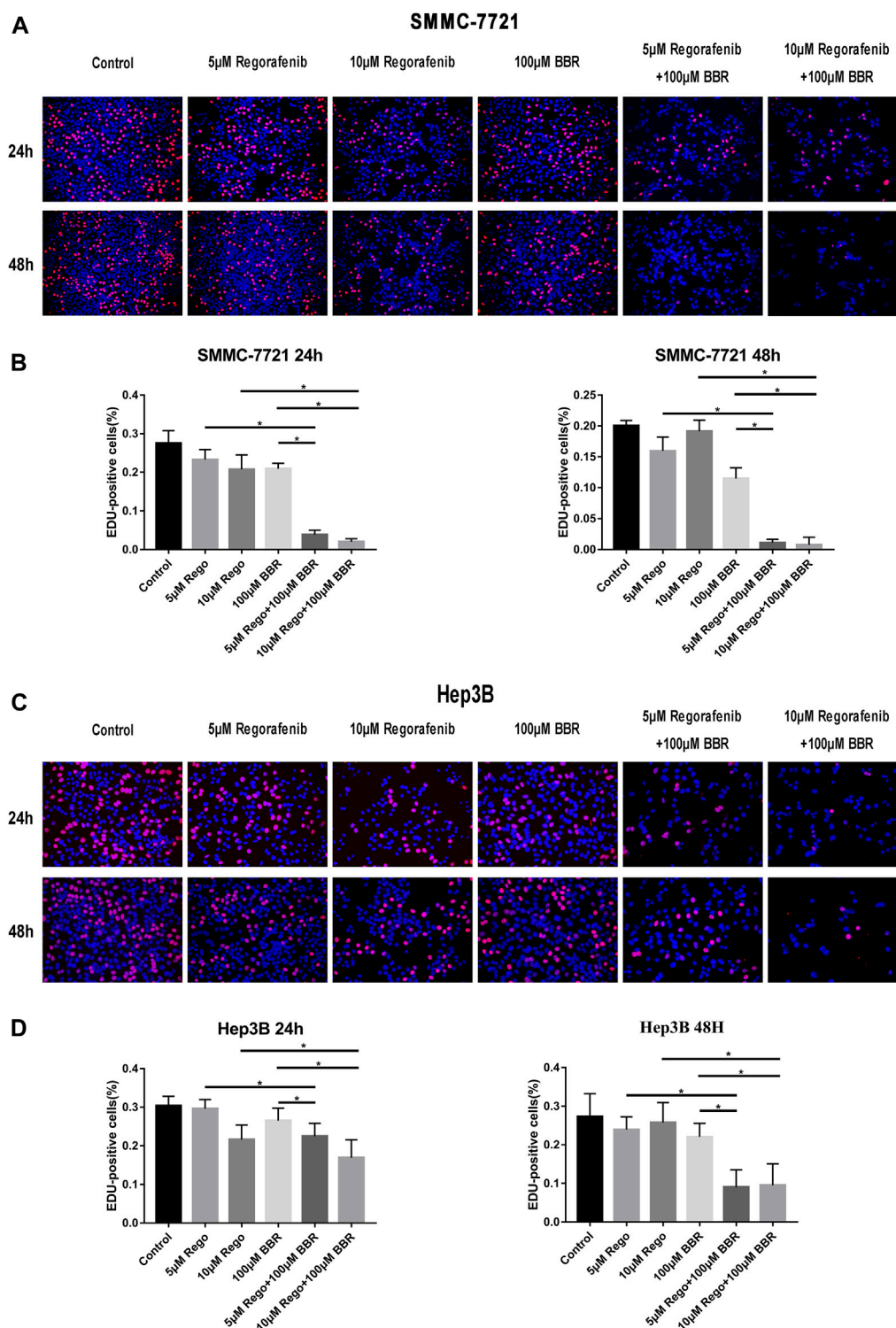
## BBR Enhances the Anti-Tumor Effect of Regorafenib *in vivo*

Next, we applied a subcutaneous xenograft tumor model to validate the anti-HCC effect of BBR and regorafenib *in vivo*. Tumor xenograft was established by transplanting SMMC-7721 cells into nude mice. BBR (10mg/kg/day) and regorafenib

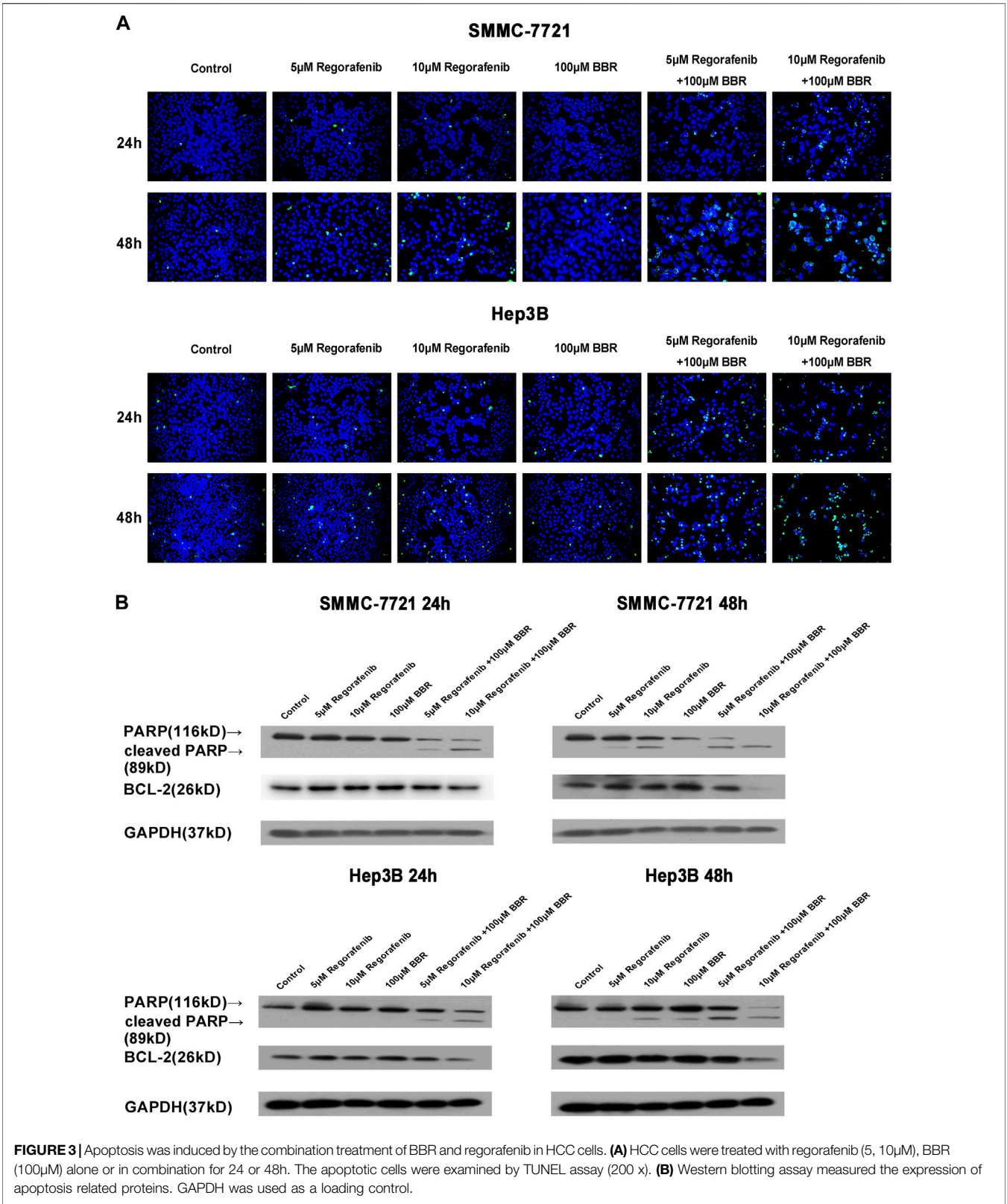
(5mg/kg/day) were administered to tumor-bearing mice alone or in combination. The results showed that the tumor size was smaller in the mice of combined treatment group compared with that in the DMSO group, BBR alone group and regorafenib alone group (**Figure 5A**). The tumor volume and weight of nude mice were dramatically reduced in the combined treatment group as compared with other groups ( $p$  < 0.05; **Figures 5B,C**). Moreover, the protein expression of cleaved PARP was up-regulated in xenograft tumor tissues in the BBR and regorafenib combined treatment group, while the protein expression of BCL-2 was down-regulated (**Figure 5D**). We also found that, as shown by TUNEL staining, the apoptosis level of xenograft tumors was much higher in the combination treatment group (**Figure 5E**). These results indicated that the combined treatment of BBR and regorafenib suppressed HCC cells growth and induced apoptosis *in vivo*.

## Expression Profiles of circRNAs in HCC Cells Treated with BBR and Regorafenib

To investigate the potential mechanism of BBR and regorafenib combination, we initiated a comprehensive circular RNA sequencing to identify differentially expressed circRNAs in HCC cells after exposure to 100  $\mu$ M BBR and 5  $\mu$ M regorafenib. DEGseq analysis was applied to search for the



**FIGURE 2 |** The combination of BBR and regorafenib reduced the proliferative capacity of HCC cells. **(A,B)** The proliferative capacity of SMMC-7721 cells detected by Edu assay after treatment with regorafenib (5, 10μM), BBR (100μM) alone or in combination for 24 or 48h. **(C,D)** The combination of BBR and regorafenib reduced the proliferative capacity of Hep3B cells, as determined by Edu assay (magnification, ×200). \**p* < 0.05.





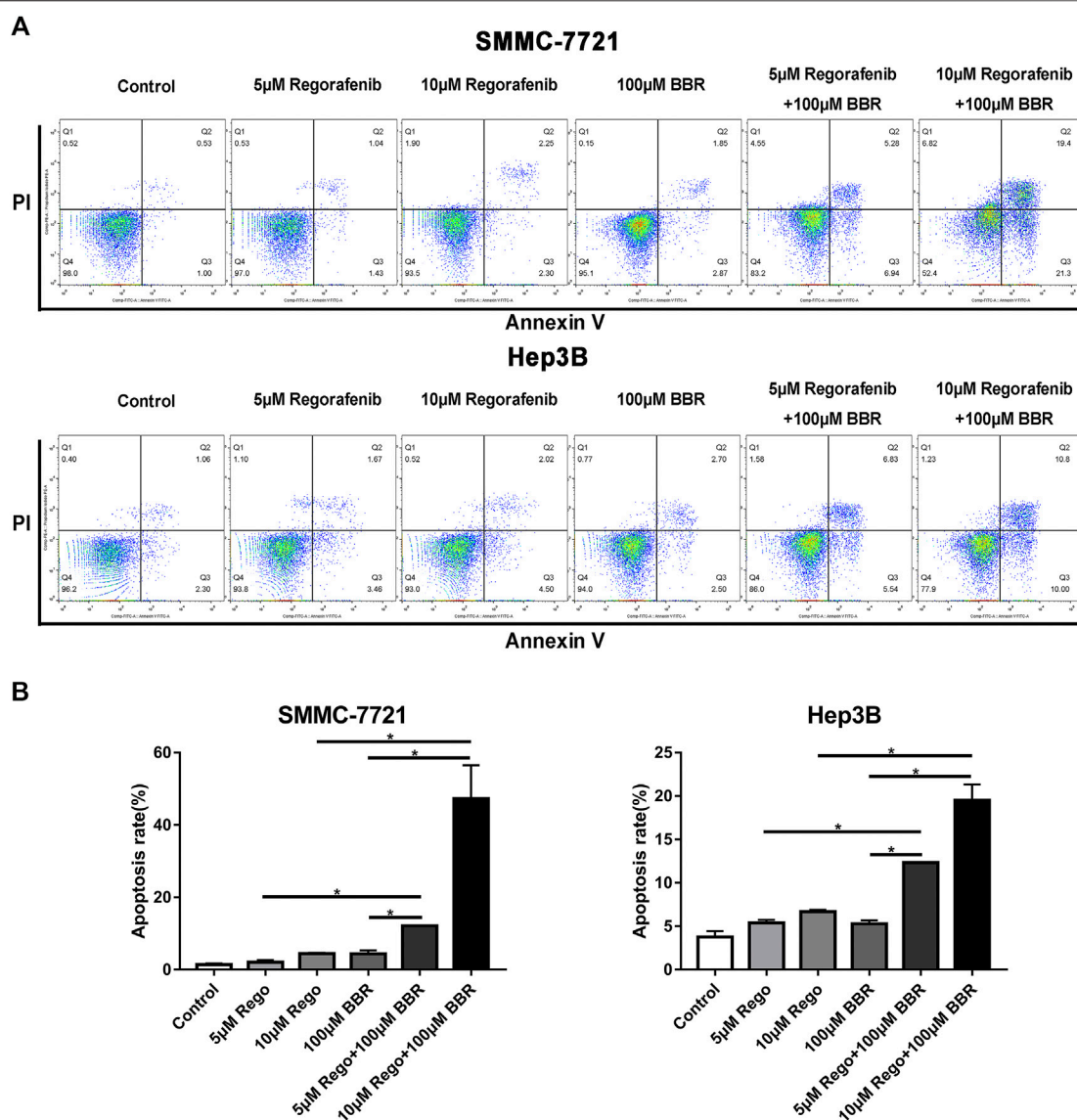
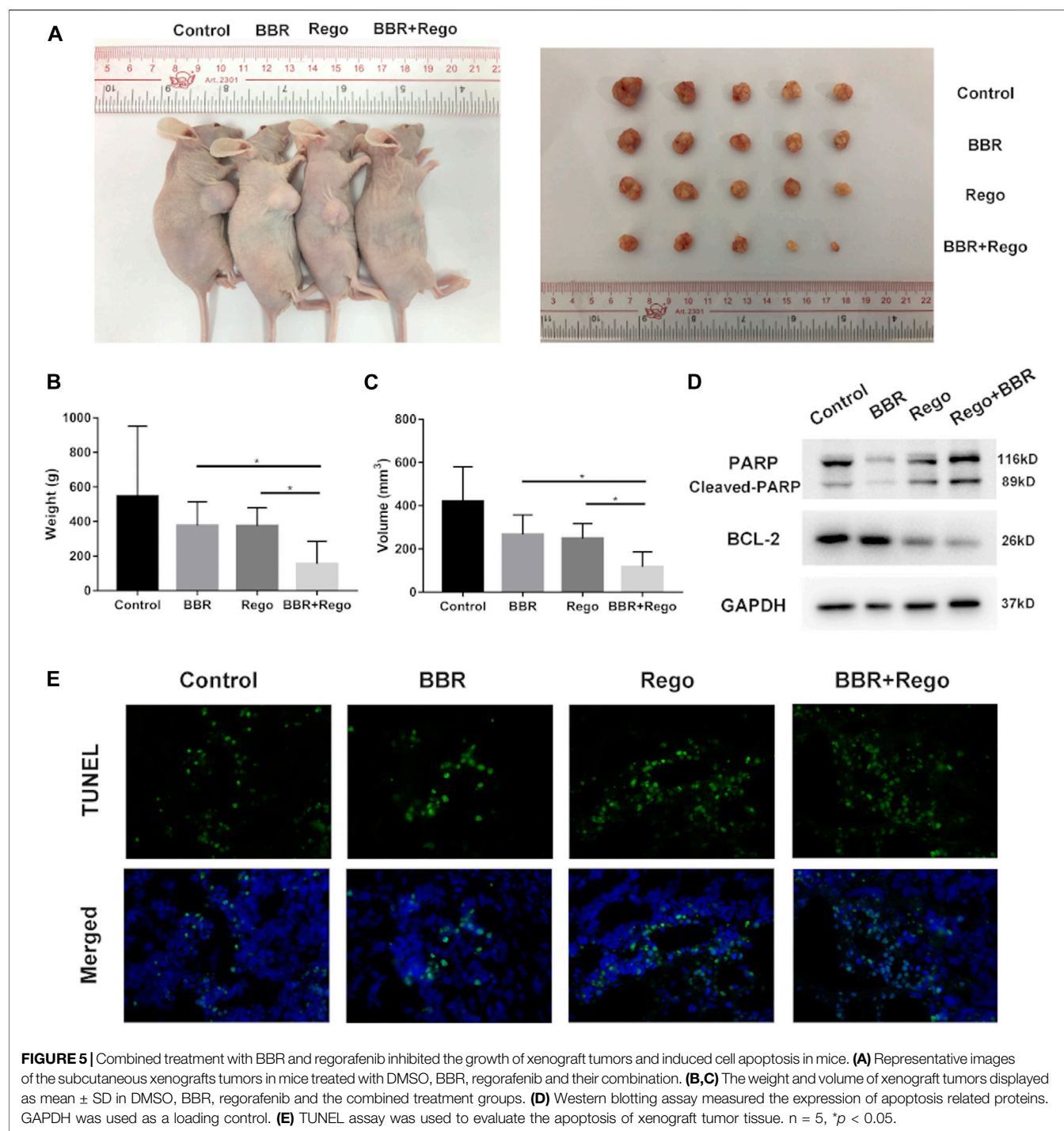


**FIGURE 4 |** BBR enhanced regorafenib induced apoptosis in HCC cells. **(A)** Flow cytometric assay analyzed the apoptotic rate of SMMC-7721 and Hep3B cells induced by BBR and regorafenib. After HCC cells were treated with BBR (100μM), regorafenib (5, 10μM) or their combination for 48h, they were stained with Annexin V/PI. **(B)** Histogram displayed the apoptotic rates in different groups from three independent experiments. \**p* < 0.05.

differentially expressed circRNAs, and clustered according to their expression profiles (**Figure 6A**). As presented in **Figures 6B,C**, volcano plot and scatter plot analyses revealed that there were 58 up-regulated and 19 down-regulated differentially expressed circRNAs between the combination treatment and control groups. To validate the results of circular RNA sequencing, we used qPCR assay to detect the expression level of five circRNAs (hsa\_circ\_0032029, hsa\_circ\_0008928, hsa\_circ\_0001346, hsa\_circ\_0006702, hsa\_circ\_0008039) that were up-regulated in HCC cells after treatment with 100μM BBR and 5μM regorafenib. The results showed that the expression of hsa\_circ\_0032029 and hsa\_circ\_0008928 were up-regulated (**Figure 6D**), and there

was no change on the expression hsa\_circ\_0001346, hsa\_circ\_0006702 and hsa\_circ\_0008039 (**Supplementary Figure S2**).

In addition, we predicted the miRNA binding sites for differential expressed circRNAs using miRanda software. According to the *p*-value ranking information, the top 50 target circRNAs that were differentially expressed in the control and combination treatment groups were selected. We then matched them to 50 potential target miRNAs. Finally, an interactive network map was constructed based on these data (**Figure 6E**). These up-regulated circRNAs will be candidates for further study on the mechanism of the combination treatment with BBR and regorafenib.



## DISCUSSION

Drug resistance and toxicity remain key issues in the treatment of advanced HCC. Although regorafenib treatment can significantly improve the overall survival of patients with HCC, resistance to regorafenib is inevitable (Bangaru et al., 2020). Novel strategies are needed to enhance the efficacy of regorafenib in HCC

treatment. In this study, we explore the effect of BBR in sensitizing HCC cells to regorafenib both *in vitro* and *in vivo*.

As a multi-kinase inhibitor, regorafenib plays its anti-tumor role by blocking the activity of multiple protein kinases that involve in cancer cell proliferation, metastasis, angiogenesis and tumor microenvironment (Teufel et al., 2019). Regorafenib alone has been reported to inhibit the proliferation of HCC cells.

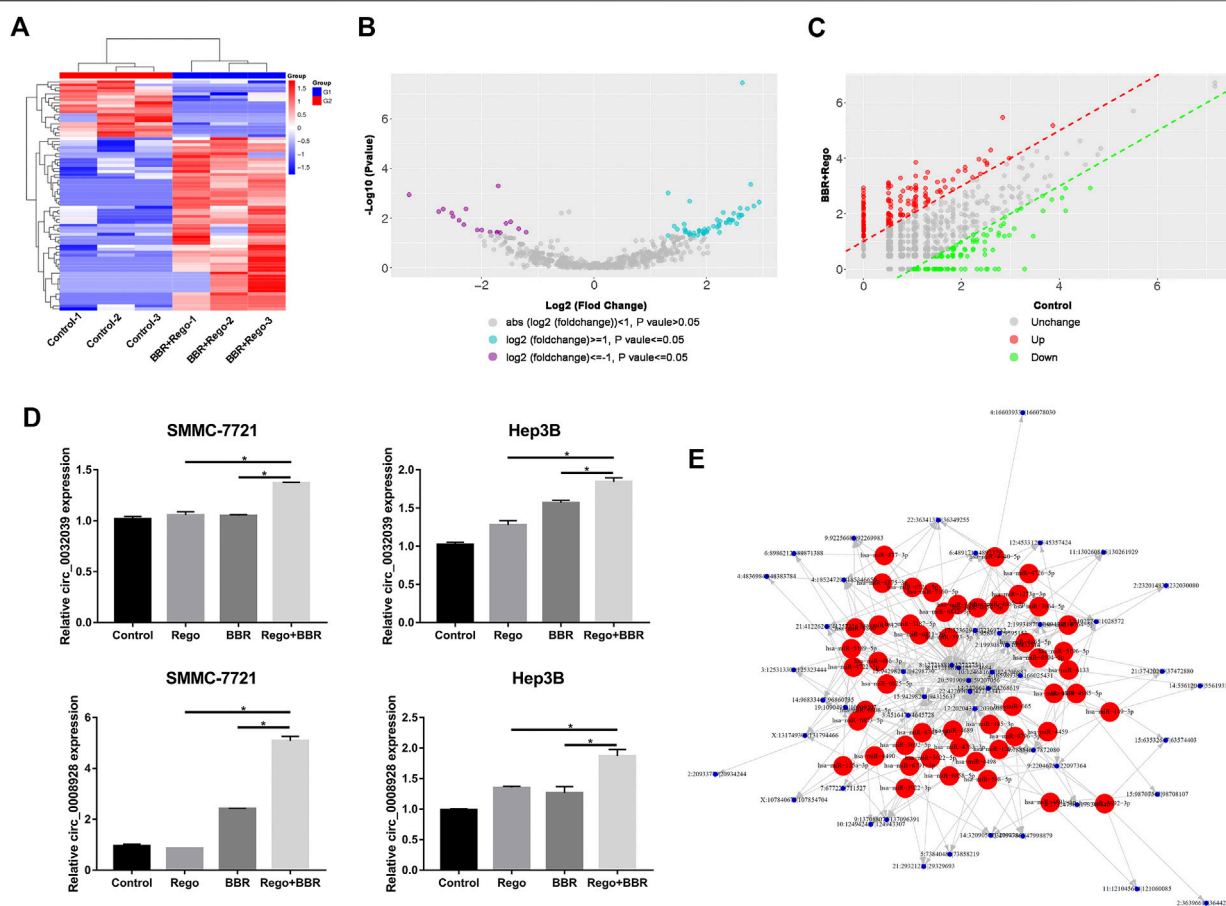


**FIGURE 6 |** Differential expression of circRNAs in SMMC-7721 cells treated with BBR and regorafenib. **(A)** Different circRNA expression profiles among samples from the RNA sequencing data shown by heat map. Three DMSO samples and three combined samples of BBR and regorafenib were examined. **(B,C)** In the volcano and scatter plots, 58 circRNAs were increased and 19 were decreased in the combination treatment group. **(D)** qRT-PCR performed on the validation of two differentially expressed circRNAs in control, BBR, regorafenib and the combination groups. **(E)** Interaction network of circRNAs and their potential target miRNAs \* $p < 0.05$ .

Similar to previous studies (Refolo et al., 2018; Wang et al., 2020), our data indicated that regorafenib dramatically inhibited the proliferation of HCC cells in a time- and dose-dependent manner. Several preclinical studies have shown that some chemotherapeutic agents can effectively improve the anti-tumor efficacy of regorafenib. Chlorogenic acid can enhance the inhibitory effect of regorafenib in cell growth and motility, and potentiate regorafenib-induced apoptosis in HCC cells (Refolo et al., 2018). B. Wang et al. observed that regorafenib and ginsenoside combined treatment significantly suppressed the proliferation of liver cancer cells (Wang et al., 2020). Researchers found that ramucirumab and GSK183705A (VEGFR2 and IGF1R inhibitors) increased the sensitivity of HCC cells to the combination of sorafenib and regorafenib at low concentrations (D'Alessandro et al., 2019).

Numerous studies demonstrated the beneficial role of BBR in preventing cancer and enhancing chemotherapeutic effect when combined with BBR in HCC treatment (Liu et al., 2019a). BBR can inhibit HCC cell proliferation *in vitro* and tumor xenografts growth *in vivo* (Chuang et al., 2017; Zhang et al., 2019a). We found that BBR alone suppressed the proliferation

of SMMC-7721 and hep3B cells in a concentration-dependent manner in this research. Furthermore, BBR has exhibited the ability to overcome multidrug resistance. BBR sensitized the cells to paclitaxel, and combination of BBR and paclitaxel resulted in potentiation, that inhibited the growth of tumors and elicited apoptosis of cancer cells (Cheng and Ji, 2020). BBR could also sensitize MDA-MB-231 cells to camptothecin, cisplatin and methyl methanesulfonate (Gao et al., 2019). Our study indicated that BBR and regorafenib combined treatment had a remarkable anti-HCC effect via inhibiting cellular proliferation and inducing cell apoptosis both *in vitro* and *in vivo*. Simultaneously, we found this phenomenon was more pronounced in the combinational of 10 $\mu$ M regorafenib and 100 $\mu$ M BBR than in combination of 5 $\mu$ M regorafenib and 100 $\mu$ M BBR alone group, suggesting that the synergic effect of regorafenib and BBR was concentration-dependent. This study further proves that BBR has the potential to improve chemotherapeutic efficacy.

Previous studies have identified various differentially expressed circRNAs in multiple diseases, particularly in human cancers (Liu et al., 2019). Some dysregulated

circRNAs are related to chemotherapeutic resistance (Hua et al., 2019). It had been reported that circRNA-104797 was up-regulated in sorafenib-resistant HCC cells, and the depletion of circRNA-104797 increased the sensitivity of sorafenib in HCC cells (Xu et al., 2020). Su et al. identified circELP3, a hypoxia-elevated circular RNA, contributed to bladder cancer progression and cisplatin resistance (Su et al., 2019). CircPVT1 was up-regulated in chemo-resistant osteosarcoma cells, and knockdown of circPVT1 could impair the resistance of osteosarcoma cells to doxorubicin and cisplatin (Kun-Peng et al., 2018). Additionally, Chen et al. found that circ-0003418 exerted an anti-tumor role in HCC and increased the sensitivity of HCC cells to cisplatin (Chen et al., 2019). RNA sequencing is a technology that can be applied to detect potential biomarkers or candidate therapeutic targets in various diseases. In this study, we performed circular RNA sequencing to identify differentially expressed circRNAs in HCC cells after cells were treated with 100 $\mu$ M BBR and 5 $\mu$ M regorafenib. The results demonstrated that the expression of hsa\_circ\_0032029 and hsa\_circ\_0008928 were up-regulated after cells were treated with 100 $\mu$ M BBR and 5 $\mu$ M regorafenib, suggesting that these circRNAs may play a role in modulating the anti-tumor activity of the combination of BBR and regorafenib. CircRNAs can regulate tumor cell phenotype by acting as a miRNA sponge, transcription regulator or by protein interaction, that correlate with the subcellular location of circRNAs (Cui et al., 2020). Usually, circRNAs that were predominantly localized in the cytoplasm serve as molecular sponges of miRNAs or proteins, while circRNAs localized in the nucleus play their role by regulating transcription. Currently, it was demonstrated that circARNT2 was localized in the cytoplasm of HCC cells and could regulate cell proliferation, apoptosis and cisplatin resistance in HCC through acting as a sponge for miR-155-5p (Li et al., 2020). CircRNA-104797 regulated the cell-killing ability of sorafenib in HCC via binding to YBX1 in the cytoplasm and preventing the degradation of YBX1 mediated by PRP19 (Xu et al., 2020). Yang et al. found that Circ-CTNNB1 was predominantly localized in the nucleus and promoted cancer progression via DDX3-mediated transactivation of YY1 (Yang et al., 2019). Although circRNAs are generally regarded as non-coding RNAs, several protein-coding circRNAs have been identified (Liu et al., 2020; Wu et al., 2021). The peptides encoded by circRNAs are usually truncated, and their functions are similar to their full-length protein counterparts (Zhou et al., 2020). In the follow-up study, we will detect the sub-cellular localization of hsa\_circ\_0032029 and hsa\_circ\_0008928, and investigate how these two circRNAs regulate the synergistic effect of BBR and regorafenib in inhibiting HCC growth.

In summary, our study has demonstrated that the combination of BBR and regorafenib inhibits cellular proliferation and induces apoptosis of HCC cells both *in vitro*

and *in vivo*. Both hsa\_circ\_0032029 and hsa\_circ\_0008928 could be potential biological targets involved in regulating the synergistic effect of BBR and regorafenib. This research provides evidence for the combinational use of BBR and regorafenib as a novel chemotherapeutic strategy for HCC treatment.

## DATA AVAILABILITY STATEMENT

The datasets presented in this study can be found in online repositories. The names of the repository/repositories and accession number(s) can be found below: NCBI BioProject PRJNA701123.

## ETHICS STATEMENT

*In vivo* experiments were performed in accordance with the guidelines for the use of laboratory animals and approved by the Animal Ethics Committee of the Second Affiliated Hospital of Guangzhou Medical University.

## AUTHOR CONTRIBUTIONS

KW, GY and JL generated, analyzed, and interpreted the data and prepared the manuscript. ZW, QL, CG, TY and SL generated, analyzed, and interpreted the data. HY generated the idea, designed the study, analyzed and interpreted the data, and edited the manuscript. All authors read and approved the final manuscript.

## FUNDING

This study was supported by grants from the General Project of Guangdong Natural Science Foundation (2021A1515010795, 2020A1515011255), the National Natural Science Foundation of China (no. 81372634), the Key projects of universities of Guangdong Province Office of Education (no. 2019KZDXM006), the Doctoral Research Project of the Second Affiliated Hospital of Guangzhou Medical University, the Scientific research project of Guangdong Bureau of Traditional Chinese Medicine (20201212), the Medical Science and Technology Research Foundation of Guangdong Province (A2020522), and the Guangzhou Health Science and Technology Project (20201A010056).

## SUPPLEMENTARY MATERIAL

The Supplementary Material for this article can be found online at: <https://www.frontiersin.org/articles/10.3389/fphar.2021.632201/full#supplementary-material>.



## REFERENCES

- Abu, N., Hon, K. W., Jeyaraman, S., Yahaya, A., Abdullah, N. M., Mustangin, M., et al. (2019). Identification of differentially expressed circular rnas in chemoresistant colorectal cancer. *Epigenomics* 11 (8), 875–884. doi:10.2217/epi-2019-0042
- Bangaru, S., Marrero, J. A., and Singal, A. G. (2020). Review article: new therapeutic interventions for advanced hepatocellular carcinoma. *Aliment. Pharmacol. Ther.* 51 (1), 78–89. doi:10.1111/apt.15573
- Bray, F., Ferlay, J., Soerjomataram, I., Siegel, R. L., Torre, L. A., and Jemal, A. (2018). Global cancer statistics 2018: globocan estimates of incidence and mortality worldwide for 36 cancers in 185 countries. *CA: A Cancer J. Clinicians* 68, 394–424. doi:10.3322/caac.21492
- Bruix, J., Qin, S., Merle, P., Granito, A., Huang, Y.-H., Bodoky, G., et al. (2017). Regorafenib for patients with hepatocellular carcinoma who progressed on sorafenib treatment (resorce): a randomised, double-blind, placebo-controlled, phase 3 trial. *The Lancet* 389, 56–66. doi:10.1016/S0140-6736(16)32453-9
- Chen, H., Liu, S., Li, M., Huang, P., and Li, X. (2019). circ\_0003418 inhibits tumorigenesis and cisplatin chemoresistance through wnt/ $\beta$ -catenin pathway in hepatocellular carcinoma. *Onco Targets Ther.* 12, 9539–9549. doi:10.2147/OTT.S229507
- Chen, Y. X., Gao, Q. Y., Zou, T. H., Wang, B. M., Liu, S. D., et al. (2020). Berberine versus placebo for the prevention of recurrence of colorectal adenoma: a multicentre, double-blinded, randomised controlled study. *Lancet Gastroenterol. Hepatol.* 5 (3), 267–275. doi:10.1016/S2468-1253(19)30409-1
- Cheng, Y., and Ji, Y. (2020). Mitochondria-targeting nanomedicine self-assembled from gsh-responsive paclitaxel-ss-berberine conjugate for synergetic cancer treatment with enhanced cytotoxicity. *J. Controlled Release* 318, 38–49. doi:10.1016/j.jconrel.2019.12.011
- Chuang, T.-Y., Wu, H.-L., Min, J., Diamond, M., Azziz, R., and Chen, Y.-H. (2017). Berberine regulates the protein expression of multiple tumorigenesis-related genes in hepatocellular carcinoma cell lines. *Cancer Cel Int.* 17, 59. doi:10.1186/s12935-017-0429-3
- Cui, C., Yang, J., Li, X., Liu, D., Fu, L., and Wang, X. (2020). Functions and mechanisms of circular rnas in cancer radiotherapy and chemotherapy resistance. *Mol. Cancer* 19 (1), 58. doi:10.1186/s12943-020-01180-y
- D'Alessandro, R., Refolo, M. G., Iacovazzi, P. A., Pesole, P. L., Messa, C., and Carr, B. I. (2019). Ramucirumab and gsk1838705a enhance the inhibitory effects of low concentration sorafenib and regorafenib combination on hcc cell growth and motility. *Cancers (Basel)* 11 (6), 787. doi:10.3390/cancers11060787
- Duffy, A. G., and Greten, T. F. (2017). Liver cancer: Regorafenib as second-line therapy in hepatocellular carcinoma. *Nat. Rev. Gastroenterol. Hepatol.* 14 (3), 141–142. doi:10.1038/nrgastro.2017.7
- Fondevila, F., Méndez-Blanco, C., Fernández-Palanca, P., González-Gallego, J., and Mauriz, J. L. (2019). Anti-tumoral activity of single and combined regorafenib treatments in preclinical models of liver and gastrointestinal cancers. *Exp. Mol. Med.* 51 (9), 1–15. doi:10.1038/s12276-019-0308-1
- Forner, A., Reig, M., and Bruix, J. (2018). Hepatocellular carcinoma. *The Lancet* 391, 1301–1314. doi:10.1016/S0140-6736(18)30010-2
- Gao, X., Wang, J., Li, M., Wang, J., Lv, J., Zhang, L., et al. (2019). Berberine attenuates XRCC1-mediated base excision repair and sensitizes breast cancer cells to the chemotherapeutic drugs. *J. Cel Mol Med.* 23 (10), 6797–6804. doi:10.1111/jcmm.14560
- Hua, X., Sun, Y., Chen, J., Wu, Y., Sha, J., Han, S., et al. (2019). Circular rnas in drug resistant tumors. *Biomed. Pharmacother.* 118, 109233. doi:10.1016/j.biopha.2019.109233
- Huang, Y., Wang, K., Gu, C., Yu, G., Zhao, D., Mai, W., et al. (2018). Berberine, a natural plant alkaloid, synergistically sensitizes human liver cancer cells to sorafenib. *Oncol. Rep.* 40 (3), 1525–1532. doi:10.3892/or.2018.6552
- Kun-Peng, Z., Xiao-Long, M., and Chun-Lin, Z. (2018). Overexpressed circpvt1, a potential new circular rna biomarker, contributes to doxorubicin and cisplatin resistance of osteosarcoma cells by regulating abcb1. *Int. J. Biol. Sci.* 14 (3), 321–330. doi:10.7150/ijbs.24360
- Lagoa, R., Silva, J., Rodrigues, J. R., and Bishayee, A. (2020). Advances in phytochemical delivery systems for improved anticancer activity. *Biotechnol. Adv.* 38, 107382. doi:10.1016/j.biotechadv.2019.04.004
- Li, Y., Zhang, Y., Zhang, S., Huang, D., Li, B., Liang, G., et al. (2021). circRNA circARNT2 suppressed the sensitivity of hepatocellular carcinoma cells to cisplatin by targeting the miR-155-5p/PDK1 Axis. *Mol. Ther. - Nucleic Acids* 23, 244–254. doi:10.1016/j.omtn.2020.08.037
- Liu, D., Meng, X., Wu, D., Qiu, Z., and Luo, H. (2019). A natural isoquinoline alkaloid with antitumor activity: studies of the biological activities of berberine. *Front. Pharmacol.* 10, 9. doi:10.3389/fphar.2019.00009
- Liu, J., Li, D., Luo, H., and Zhu, X. (2019a). Circular rnas: the star molecules in cancer. *Mol. Aspects Med.* 70, 141–152. doi:10.1016/j.mam.2019.10.006
- Liu, Y., Li, Z., Zhang, M., Zhou, H., Wu, X., Zhong, J., et al. (2020). Rolling-translated egfr variants sustain egfr signaling and promote glioblastoma tumorigenicity. *Neuro Oncol.* noaa279. doi:10.1093/neuonc/noaa279
- Refolo, M., Lippolis, C., Carella, N., Cavallini, A., Messa, C., and D'Alessandro, R. (2018). Chlorogenic acid improves the regorafenib effects in human hepatocellular carcinoma cells. *Ijms* 19 (5), 1518. doi:10.3390/ijms19051518
- Su, Y., Yang, W., Jiang, N., Shi, J., Chen, L., Zhong, G., et al. (2019). Hypoxia-elevated circelp3 contributes to bladder cancer progression and cisplatin resistance. *Int. J. Biol. Sci.* 15 (2), 441–452. doi:10.7150/ijbs.26826
- Taguchi, D., Inoue, M., Fukuda, K., Yoshida, T., Shimazu, K., Fujita, K., et al. (2020). Therapeutic drug monitoring of regorafenib and its metabolite m5 can predict treatment efficacy and the occurrence of skin toxicities. *Int. J. Clin. Oncol.* 25 (4), 531–540. doi:10.1007/s10147-019-01593-w
- Teufel, M., Seidel, H., Köchert, K., Meinhardt, G., Finn, R. S., Llovet, J. M., et al. (2019). Biomarkers associated with response to regorafenib in patients with hepatocellular carcinoma. *Gastroenterology* 156 (6), 1731–1741. doi:10.1053/j.gastro.2019.01.261
- Vogel, A., and Saborowski, A. (2020). Current strategies for the treatment of intermediate and advanced hepatocellular carcinoma. *Cancer Treat. Rev.* 82, 101946. doi:10.1016/j.ctrv.2019.101946
- Wang, B., Wang, F., Ding, A., Zhao, H., and Bu, X. (2020). Regorafenib and ginsenoside combination therapy: inhibition of hepg2 cell growth through modulating survivin and caspase-3 gene expression. *Clin. Transl Oncol.* 22 (9), 1491–1498. doi:10.1007/s12094-019-02283-9
- Wang, J., Zhang, N., Han, Q., Lu, W., Wang, L., Yang, D., et al. (2019). Pin1 inhibition reverses the acquired resistance of human hepatocellular carcinoma cells to regorafenib via the gli1/snail/e-cadherin pathway. *Cancer Lett.* 444, 82–93. doi:10.1016/j.canlet.2018.12.010
- Wu, X., Xiao, S., Zhang, M., Yang, L., Zhong, J., Li, B., et al. (2021). A novel protein encoded by circular smo rna is essential for hedgehog signaling activation and glioblastoma tumorigenicity. *Genome Biol.* 22 (1), 33. doi:10.1186/s13059-020-02250-6
- Xu, J., Ji, L., Liang, Y., Wan, Z., Zheng, W., Song, X., et al. (2020). Circrna-sore mediates sorafenib resistance in hepatocellular carcinoma by stabilizing ybx1. *Sig Transduct Target. Ther.* 5 (1), 298. doi:10.1038/s41392-020-00375-5
- Yang, F., Fang, E., Mei, H., Chen, Y., Li, H., Li, D., et al. (2019). Cis-acting circ-CTNNB1 promotes  $\beta$ -catenin signaling and cancer progression via DDX3-mediated transactivation of YY1. *Cancer Res.* 79 (3), 557–571. doi:10.1158/0008-5472.CAN-18-1559
- Zhang, F., Jia, Y., Zheng, X., Shao, D., Zhao, Y., Wang, Z., et al. (2019). Janus nanocarrier-based co-delivery of doxorubicin and berberine weakens chemotherapy-exacerbated hepatocellular carcinoma recurrence. *Acta Biomater.* 100, 352–364. doi:10.1016/j.actbio.2019.09.034
- Zhang, P., Wang, Q., Lin, Z., Yang, P., Dou, K., and Zhang, R. (2019a). Berberine inhibits growth of liver cancer cells by suppressing glutamine uptake. *Onco Targets Ther.* 12, 11751–11763. doi:10.2147/OTT.S235667
- Zhou, W.-Y., Cai, Z.-R., Liu, J., Wang, D.-S., Ju, H.-Q., and Xu, R.-H. (2020). Circular rna: metabolism, functions and interactions with proteins. *Mol. Cancer* 19 (1), 172. doi:10.1186/s12943-020-01286-3

**Conflict of Interest:** The authors declare that the research was conducted in the absence of any commercial or financial relationships that could be construed as a potential conflict of interest.

Copyright © 2021 Wang, Yu, Lin, Wang, Lu, Gu, Yang, Liu and Yang. This is an open-access article distributed under the terms of the Creative Commons Attribution License (CC BY). The use, distribution or reproduction in other forums is permitted, provided the original author(s) and the copyright owner(s) are credited and that the original publication in this journal is cited, in accordance with accepted academic practice. No use, distribution or reproduction is permitted which does not comply with these terms.



# A PD-1 Inhibitor Induces Complete Response of Advanced Bladder Urothelial Carcinoma: A Case Report

Jianzheng Wang<sup>1†</sup>, Qingli Li<sup>2†</sup>, Huifang Lv<sup>1</sup>, Caiyun Nie<sup>1</sup>, Beibei Chen<sup>1</sup>, Weifeng Xu<sup>1</sup>, Tiejun Yang<sup>3</sup>, Yinping Zhang<sup>4</sup>, Shuiping Tu<sup>2\*</sup> and Xiaobing Chen<sup>1\*</sup>

<sup>1</sup> Department of Medical Oncology, Affiliated Cancer Hospital of Zhengzhou University, Henan Cancer Hospital, Zhengzhou, China, <sup>2</sup> Department of Oncology, Renji Hospital, School of Medicine, Shanghai Jiaotong University, Shanghai, China, <sup>3</sup> Department of Urology Surgery, Affiliated Cancer Hospital of Zhengzhou University, Henan Cancer Hospital, Zhengzhou, China, <sup>4</sup> Department of Pathology, Affiliated Cancer Hospital of Zhengzhou University, Henan Cancer Hospital, Zhengzhou, China

## OPEN ACCESS

### Edited by:

Dong-Hua Yang,  
St. John's University, United States

### Reviewed by:

Changjiang Guo,  
Rutgers, The State University of New  
Jersey, United States  
Xiaohua Jiang,  
The Chinese University of Hong Kong,  
China

### \*Correspondence:

Xiaobing Chen  
zlyychenxb0807@zzu.edu.cn  
Shuiping Tu  
tushuiping@yahoo.com

<sup>†</sup>These authors have contributed  
equally to this work

### Specialty section:

This article was submitted to  
Pharmacology of  
Anti-Cancer Drugs,  
a section of the journal  
Frontiers in Oncology

Received: 23 February 2021

Accepted: 07 April 2021

Published: 18 June 2021

### Citation:

Wang J, Li Q, Lv H, Nie C, Chen B,  
Xu W, Yang T, Zhang Y, Tu S and  
Chen X (2021) A PD-1 Inhibitor  
Induces Complete Response of  
Advanced Bladder Urothelial  
Carcinoma: A Case Report.  
Front. Oncol. 11:671416.  
doi: 10.3389/fonc.2021.671416

The prognosis of patients with advanced urothelial carcinoma is dismal. Platinum-based chemotherapy is still the main first-line treatment for advanced urothelial carcinoma, while immunotherapy can be used as a first-line treatment option for people who cannot tolerate platinum. Immunotherapy is preferred in the second-line treatment of bladder urothelial carcinoma. PD-1 inhibitors (Pembrolizumab, nivolumab and atezolizumab) and PD-L1 inhibitors (Ddurvalumab and avelumab) have not been approved for the treatment of advanced urothelial cancer in China. We describe a patient with advanced urothelial carcinoma experienced disease progression after gemcitabine chemotherapy. Following a treatment of domestic PD-1 inhibitor (sintilimab), the patient achieved a durable complete response with mild toxicity. This case indicates that PD-1 inhibitor sintilimab might be a second-line treatment choice for advanced urothelial carcinoma.

**Keywords:** PD-1, complete response, advanced, urothelial carcinoma, case report

## BACKGROUND

Bladder urothelial carcinoma is the most common malignant tumor of the urinary system in China. Advanced urothelial carcinoma is sensitive to platinum-based chemotherapy, with an effective rate of up to 50% (1, 2). However, some patients cannot tolerate cisplatin-based chemotherapy. Therefore, the treatment of advanced urothelial carcinoma is divided into non-cisplatin chemotherapy and cisplatin chemotherapy according to platinum tolerance. In general, most of the non-cisplatin chemotherapy is not satisfied. Therefore, for those who cannot tolerate cisplatin therapy, cisplatin-free chemotherapy or other treatments are recommended. Gemcitabine, as one of the chemotherapeutic drugs for advanced urothelial carcinoma, is used alone for the first-line treatment of bladder urothelial carcinoma. The results of a phase 2 study showed that the objective effective rate was 24%-44%, of which the complete remission rate was 8%-17%, and the median overall survival time was 8-13.5 months (3). For patients with advanced bladder urothelial carcinoma who cannot tolerate platinum-based chemotherapy, immunotherapy is also recommended.

Immune checkpoint inhibitors represented by PD-1/PD-L1inhibitors significantly improve the objective and effective rate of the second-line treatment of advanced urothelial carcinoma compared with traditional chemotherapy, and opened a new chapter in the second-line treatment of advanced bladder cancers. In particular, the randomized controlled phase 3 clinical study of pembrolizumab and chemotherapy (KEYNOTE045) showed that immunotherapy improved the overall survival, and established the status of immunotherapy in the second-line treatment of advanced urothelial carcinoma (4). Sintilimab is a monoclonal antibody against programmed cell death protein 1. It is developed by Innovent Biologics and Eli Lilly and Company and has been approved to treat relapsed or refractory classical Hodgkin lymphoma in patients who have undergone two or more lines of systemic chemotherapy by the National Medical Products Administration of China. It has been reported in number of literature and shows satisfying anti-tumor effect (5).

## CASE PRESENTATION

Here, we present a case of advanced bladder urothelial carcinoma. A 66-year-old female patient was diagnosed with bladder occupying mass, left hydronephrosis, and left ureter dilatation in a local hospital due to painless hematuria for 2 months. The patient was then hospitalized in Henan Cancer Hospital. The results of enhanced CT (2019.4.4) showed: 1. Thickening of the lower ureter and nodules at the entrance of the vesicoureter, about 25mm\*22mm in size, with fluid in the dilated upper ureter and renal pelvis, and possible atypical cell carcinoma. 2. There are multiple lymph nodes in the retroperitoneum and between the liver and stomach. 3. Multiple metastases in both lungs. 4. There are multiple swollen lymph nodes in the running area of the left iliac vessels (**Figure 1A**). Renal dynamic imaging and glomerular filtration rate were measured with 99m-Tc-DTPA. Diagnostic considerations: 1. No obvious abnormality in blood perfusion of the right kidney. 2. The right glomerular filtration function is normal. 3. Poor excretion in the upper right urinary tract. 4. No function in the left kidney (**Figure 1B**). In order to relieve the symptoms of left kidney compression, a percutaneous external renal pelvic drainage tube was placed on April 11, 2019. Cystoscopy was performed, and the pathological results of biopsy showed urothelial carcinoma. There was no clear muscle infiltration in the submitted tissues(**Figure 1C**). Immunohistochemistry: P63+,CK20+,CK7+, CyclinD1+, Ki-67: 80% (**Supplementary Figure 1**). The final diagnosis was stage IV bladder urothelial carcinoma with multiple lung metastases. Because the patient has only one normal kidney left. According to the patient's age, physical fitness score and considering the nephrotoxicity of cisplatin, we choose gemcitabine (1000mg/m<sup>2</sup>, d1, 8, q21d) as a single agent for the first-line treatment. After two cycles of gemcitabine treatment, the efficacy of chemotherapy was evaluated as SD (stable disease) (**Figure 2A**). The efficacy of chemotherapy remained as SD after four cycles of treatment (**Figure 2B**) and

it became PD (progression disease) after six cycles of treatment (**Figure 2C**).

According to the patient's age, economic status, PD-1 donation policy and family's wishes, Sintilimab (200mg, on day1, q21d) was used for the second-line treatment for three cycles on 2019.9.20、2019.10.16 and 2019.11.12. The treatment

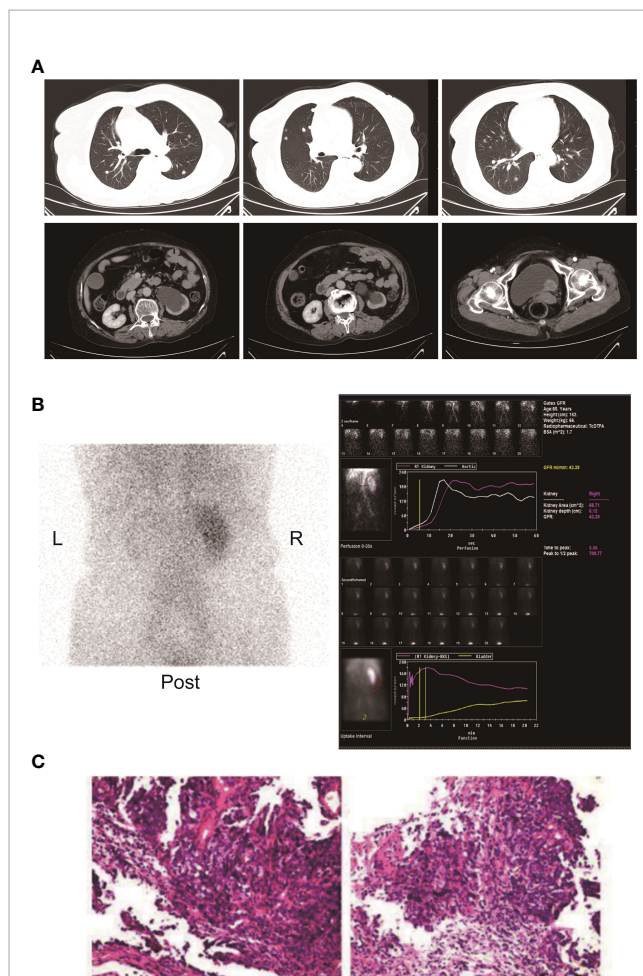


**FIGURE 1 | (A)** Enhanced CT of the chest and pelvis showed multiple round nodules in both lungs with clear boundaries. A dense mass of soft tissue is seen at the entrance of the ureter on the left side of the bladder. The size is about 25mm\*22mm. **(B)** Renal dynamic imaging and glomerular filtration. 1. Renal blood perfusion image: After intravenous "projectile" injection of imaging agent 99m-Tc-DTPA, renal blood perfusion imaging was performed. After imaging of the abdominal aorta, the right kidney was immediately imaged, and the position, shape and the size is roughly normal, and the radioactivity distribution is roughly even; the left kidney is not seen. 2. Renal function shows: After renal blood flow perfusion, the left kidney is not visible; the shadow of the right kidney gradually increases, and the imaging of right kidney reaches a peak at 3.35 minutes. After that, the shadow of the renal cortex diminishes, the shadow of the renal medulla increases, and the renal excretion process. There was no abnormal reflex concentration in the right renal pelvis; after 5 hours of delay, the right kidney was lightened, there was no radioactive concentration in the right renal pelvis and ureter, and the left kidney was slightly developed. 3. Renal functional curve shows: the curve of the right kidney is roughly normal; the peak time of the right kidney is 3.35min; the GFR of the right kidney is: 43.39ml/min. **(C)** Pathological results of HE staining on cystoscopy biopsy.



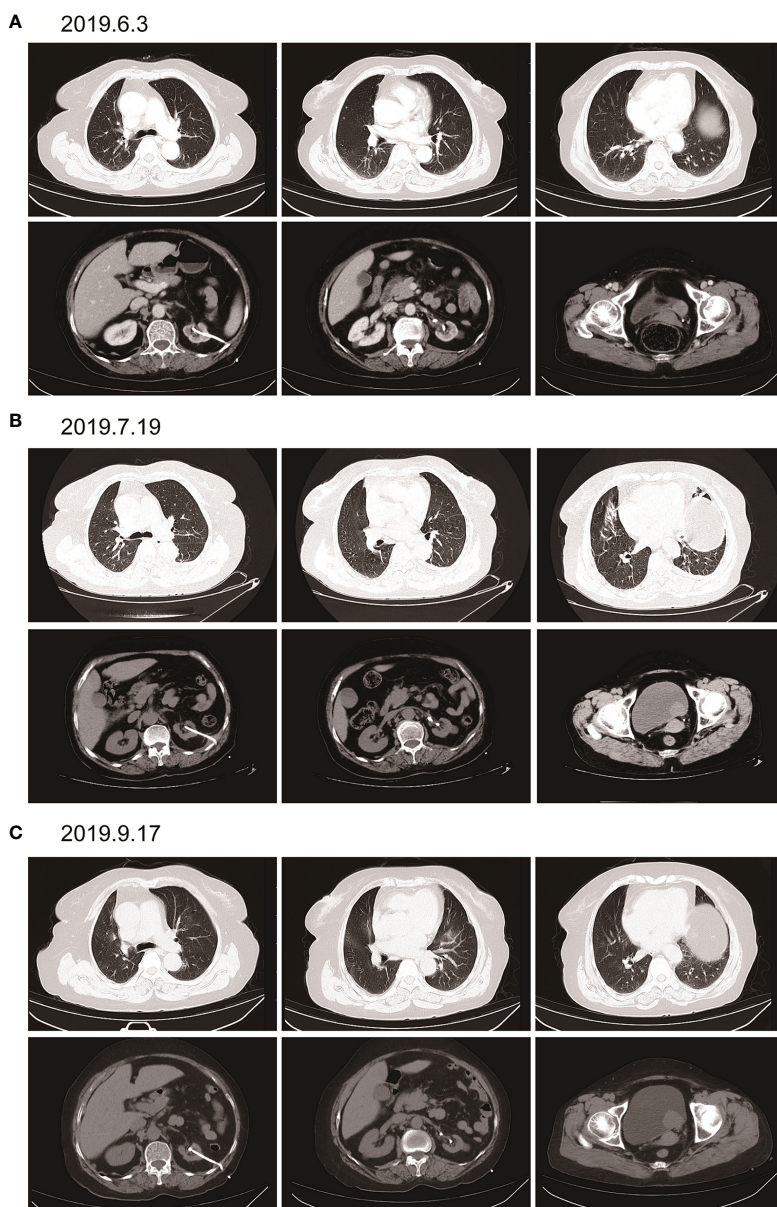


**FIGURE 2** | Imaging examination after single-agent gemcitabine chemotherapy. **(A)** (2019.6.3) after two cycles of gemcitabine. Multiple round small nodules are seen in both lungs, with clear borders and reduced size compared to the previous ones. A dense mass of soft tissue at the entrance of the ureter on the left side of the bladder, with a size of about 25mm\*22mm, and a clear boundary. **(B)** (2019.7.19) after 4 cycles of gemcitabine. Multiple round-shaped nodules in both lungs, with clear boundaries and slightly smaller than before. A dense mass of soft tissue at the entrance of the ureter on the left side of the bladder, with a size of about 25mm\*22mm, with a clear boundary. **(C)** (2019.9.17) after 6 cycles of gemcitabine. Multiple round nodules in both lungs, with clear boundaries, and some were slightly larger than before. The soft tissue density mass at the entrance of the ureter on the left side of the bladder is shadowed, about 37mm\*30mm in size, with a clear boundary and larger than before.

efficacy is evaluated as PR (Partial response) (**Figure 3**). Then Sintilimab was given for the fourth cycle of immunotherapy on 2019.12.04. One week later, on December 10, 2019, the patient developed chest tightness and shortness of breath, accompanied by gradual increase in dyspnea. The local hospital gave oxygen inhalation and anti-asthmatic treatment, but the symptoms did not alleviate. Chest CT examination considered infectious lesions

of both lungs. Serological examination ruled out tuberculosis or Aspergillus infections. Subsequently, the patient was transferred to our hospital for further treatment. On admission, her blood oxygen saturation was 75%, and his skin was cyanotic. The breath sound of auscultation in both lungs is thick, and the wheezing sound can be heard. The results of chest CT examination on 2019.12.26 showed pneumonia in both lungs,



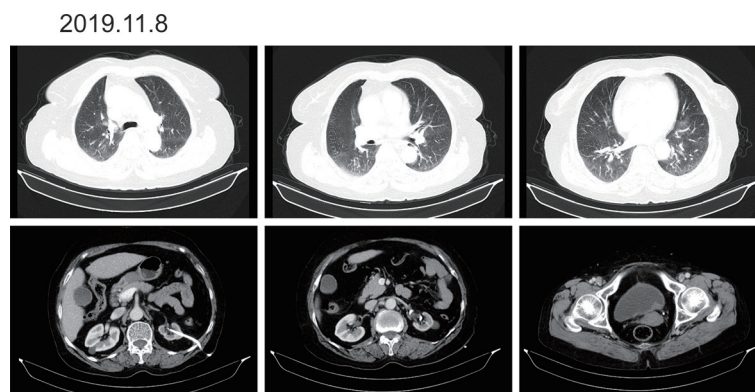


**FIGURE 3** | Imaging after three cycles of Sintilimab immunotherapy. There are multiple round-shaped nodules in both lungs, with clear boundaries, and some are smaller than before. The local soft tissue shadow at the entrance of the ureter on the left side of the bladder thickens, forming soft tissue nodules, the size is about 24mm\*10mm, which is smaller than before.

that are more severe than earlier images (**Figure 4**). The patient was suspected to have developed grade 3 immunotherapy-related pneumonia, and was given an intravenous infusion of methylprednisolone at 1 mg/(Kg.d) for 72 hours. After 3 days, the patient's chest tightness symptoms improved, and oxygen saturation reached 94%. The methylprednisolone was changed to oral administration and the dose was gradually reduced by 5-10mg per week. By March 23, 2020, methylprednisolone was reduced to 10mg/d orally, at which time the blood oxygen saturation had reached 96%. We performed chest CT to observe the changes of pneumonia, and the results showed that pneumonia of both lungs had improved significantly (**Figure 4B**). On January 14, 2021, the patient underwent whole-body enhanced CT evaluation. To our surprise, the results showed that the patient's lung metastases disappeared, and the local soft tissue shadow at the entrance of the ureter on the left side of the bladder disappeared completely (**Figure 5A**). The patient achieved progression-free survival for more than one year (**Figure 5B**). The current condition is generally good.

## DISCUSSION

Bladder cancer refers to a malignant tumor occurred on the bladder mucosa. It is the most common malignant tumor of the urinary system and one of the ten most common tumors in the body. Bladder cancer is the number one urogenital tumors in China (6). Cisplatin-based chemotherapy is the standard therapy for stage IV bladder malignancy, which can increase the overall survival but rarely results in complete remission. The most significant breakthrough in cancer therapy over the last decade was the development of immunotherapy (7). Immunotherapy is approved as a second-line treatment for metastatic urothelial carcinoma. Its use as a first-line agent is limited to patients who are ineligible for cisplatin-based treatments. Five drugs are approved by the Food and Drug Administration of USA for metastatic urothelial carcinoma including three Programmed cell-death protein 1 (PD-1) inhibitors

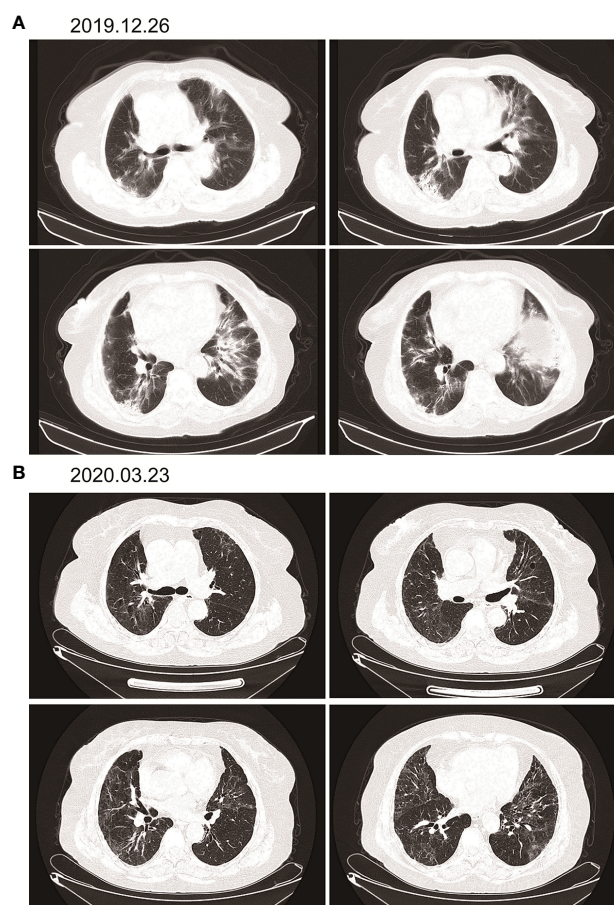
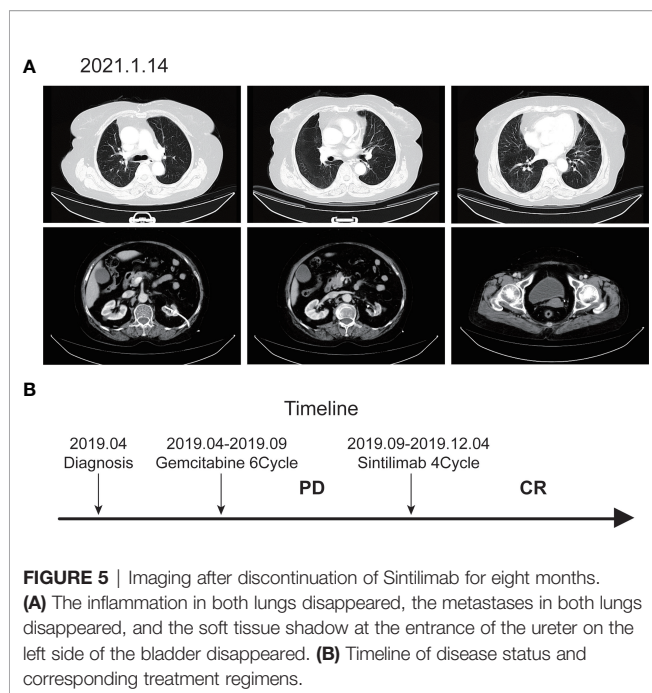


**FIGURE 4** | Immunotherapy-related pneumonia before and after methylprednisolone therapy. **(A)** There are cords and patchy shadows in both lungs, with blurred boundaries and inflammatory changes, that are bigger than before. **(B)** Frequent strand shadows and patchy shadows are seen in both lungs, and the boundary is blurred, and the area is smaller than before.



and two programmed cell-death ligand 1 (PD-L1) inhibitors for patients whose tumor progressed during or after platinum-based therapy. However, only two drugs were approved based on phase III clinical trials—pembrolizumab and atezolizumab, of which only KEYNOTE study performed with pembrolizumab showed overall survival benefits.

Atezolizumab and pembrolizumab are the Food and Drug Administration–approved checkpoint inhibitors in cisplatin-ineligible patients. However, the PD-1 antibody approved in China to treat classical Hodgkin's lymphoma is sintilimab, which is still under clinical trials to test its efficacy and safety in solid tumors (8, 9). There is no report on the clinical effect of this immune checkpoint inhibitor (ICI) sintilimab in advanced bladder cancer. Considering the age of the patient and the wishes of his family members, it is recommended that immunotherapy be performed as soon as possible. As a representative domestic PD-1 monoclonal antibody, sintilimab has a 10 times and 50 times higher affinity for human PD-1 receptors than pembrolizumab and nivolumab, respectively (10).

Immune checkpoint blockade can cause inflammatory reaction by enhancing the activity of the immune system, and these side effects are often referred to as immune-related adverse events (11). Immune-related pneumonia is a rare but fatal serious adverse event. Data from clinical studies show that the incidence of pneumonia in patients treated with PD-1/PD-L1 inhibitors is less than 5%, and the incidence of pneumonia above grade 3 is up to 1.5% (12–16). PD-1 inhibitors and PD-L1 inhibitors caused 3.6% and 1.3% of all grades of pneumonia, respectively, and the incidence of severe pneumonia was 1.1% and 0.4% (15, 17). So far, there is no convincing evidence that PD-1 inhibitors and PD-L1 inhibitors have a significant difference in the incidence of adverse events in the respiratory

system. Immune-related pneumonia may occur at any time, but compared with other irAEs, pneumonia occurs relatively late, with a median occurrence time of 2.8 months. This patient developed immunotherapy-related pneumonia 90 days later after treatment. In general, the onset of pneumonia in patients with combination therapy occurs earlier. Also, the onset of pneumonia in patients with NSCLC occurs later than that of malignant melanoma (18). The high-risk population of immune-related pneumonia include: 1. NSCLC patients with positive driver gene sensitive mutations treated with EGFR-TKI combined with immune checkpoint inhibitors (19, 20); and 2. Previously diagnosed with chronic obstructive pulmonary disease (COPD), pulmonary fibrosis or patients with active lung infections (13, 20, 21). Gemcitabine can damage the lungs and cause lung diseases such as interstitial pneumonia (22). This patient was treated with gemcitabine in first-line chemotherapy. Whether there is a connection between gemcitabine and immunotherapy-related pneumonia caused by subsequent use of immune checkpoint inhibitor is worthy of further exploration.

At present, the mechanism of immune-related adverse reactions has not been fully understood. It is generally thought to be the inflammatory response of the immune system to specific organs and tissues. The adverse reactions related to immunotherapy may have a certain correlation with the treatment efficacy, but they are not positively correlated. Immune-related adverse reactions, especially rash or itching, may implicate better efficacy. The predictor of efficacy of immunotherapy has always been a hot research topic. Some previous retrospective analyses have suggested that adverse reactions related to immunotherapy can predict the efficacy of treatment. Early appearance of rash and itching is a strong predictor of the efficacy of nivolumab (23). Whether immunotherapy-associated pneumonia is positively correlated with the curative effect is currently inconclusive. However, there are some case reports that the appearance of immunotherapy-related pneumonia suggests better efficacy, even complete remission, and long-term survival of patients (24, 25). The mechanism by which irAEs can predict the efficacy of PD-1/PD-L1 needs to be further clarified in the future.

In performing immunotherapy, attentions must not only be paid to its efficacy, but also its side effects. There are evidence show that some patients might not benefit from immunotherapy, instead, the tumor grows bigger and their survival time might shortened after receiving immunotherapy. This phenomenon is called hyperprogressive disease (HPD) (26, 27). MDM2/4 gene and DNMT3A gene mutations are closely related to HPD. However, these HPD indicators are very immature and need a lot of clinical data to support (28).

In conclusion, complete regression of advanced bladder cancer following immunotherapy is an extremely rare but spectacular event. The precise mechanism of this phenomenon remains a mystery, and no specific factor seems to be responsible for tumor regression. Additional research is warranted to explain the possible mechanisms. Knowledge of these mechanisms may help elucidate the nature of bladder cancer and the disease management.

## DATA AVAILABILITY STATEMENT

The original contributions presented in the study are included in the article/**Supplementary Material**. Further inquiries can be directed to the corresponding authors.

## AUTHOR CONTRIBUTIONS

JW, XC, and TY treated the patient. JW, HL, CN, BC, and WX collected the data. JW, QL, YZ, and ST analyzed the data and wrote the original draft. All authors contributed to the article and approved the submitted version.

## REFERENCES

- Gunlusoy B, Arslan M, Vardar E, Degirmenci T, Kara C, Ceylan Y, et al. The Efficacy and Toxicity of Gemcitabine and Cisplatin Chemotherapy in Advanced/Metastatic Bladder Urothelial Carcinoma. *Actas Urol Esp* (2012) 36(9):515–20. doi: 10.1016/j.acuroe.2012.03.007
- von der Maase H, Hansen SW, Roberts JT, Dogliotti L, Oliver T, Moore MJ, et al. Gemcitabine and Cisplatin Versus Methotrexate, Vinblastine, Doxorubicin, and Cisplatin in Advanced or Metastatic Bladder Cancer: Results of a Large, Randomized, Multinational, Multicenter, Phase III Study. *J Clin Oncol* (2000) 18(17):3068–77. doi: 10.1200/JCO.2000.18.17.3068
- von der Maase H. Gemcitabine in Transitional Cell Carcinoma of the Urothelium. *Expert Rev Anticancer Ther* (2003) 3(1):11–9. doi: 10.1586/14737140.3.1.11
- Bellmunt J, de Wit R, Vaughn DJ, Fradet Y, Lee JL, Fong L, et al. Pembrolizumab as Second-Line Therapy for Advanced Urothelial Carcinoma. *N Engl J Med* (2017) 376(11):1015–26. doi: 10.1056/NEJMoa1613683
- Zhang L, Mai W, Jiang W, Geng Q. Sintilimab: A Promising Anti-Tumor Pd-1 Antibody. *Front Oncol* (2020) 10:594558. doi: 10.3389/fonc.2020.594558
- Bray F, Ferlay J, Soerjomataram I, Siegel RL, Torre LA, Jemal A. Global Cancer Statistics 2018: GLOBOCAN Estimates of Incidence and Mortality Worldwide for 36 Cancers in 185 Countries. *CA Cancer J Clin* (2018) 68(6):394–424. doi: 10.3322/caac.21492
- Konala VM, Adapa S, Aronow WS. Immunotherapy in Bladder Cancer. *Am J Ther* (2019). doi: 10.1097/mjt.0000000000000934
- Ansell SM. Sintilimab: Another Effective Immune Checkpoint Inhibitor in Classical Hodgkin Lymphoma. *Lancet Haematology* (2019) 6(1):e2–3. doi: 10.1016/S2352-3026(18)30210-2
- Hoy SM. Sintilimab: First Global Approval. *Drugs* (2019) 79(3):341–6. doi: 10.1007/s40265-019-1066-z
- Deng M. The Approval of Sintilimab for Classical Hodgkin's Lymphoma: Views and Perspectives of Anti-PD-1/PD-L1 Antibodies in China. *Antibody Ther* (2019) 2(2):54–5. doi: 10.1093/abt/tbz005
- Postow MA, Sidlow R, Hellmann MD, Med NEJ. Immune-Related Adverse Events Associated With Immune Checkpoint Blockade. *N Engl J Med* (2018) 378(2):158–68. doi: 10.1056/NEJMra1703481
- Naidoo J, Page D, Li B, Connell L, Schindler K, Lacouture M, et al. Toxicities of the Anti-PD-1 and Anti-PD-L1 Immune Checkpoint Antibodies. *Ann Oncol* (2016) 27(7):1362. doi: 10.1093/annonc/mdw141
- Suresh K, Voong K, Shankar B, Forde P, Ettinger D, Marrone K, et al. Pneumonitis in Non-Small Cell Lung Cancer Patients Receiving Immune Checkpoint Immunotherapy: Incidence and Risk Factors. *J thoracic Oncol* (2018) 13(12):1930–9. doi: 10.1016/j.jtho.2018.08.2035
- Khunger M, Jain P, Rakshit S, Pasupuleti V, Hernandez A, Stevenson J, et al. Safety and Efficacy of PD-1/PD-L1 Inhibitors in Treatment-Naive and Chemotherapy-Refractory Patients With Non-Small-Cell Lung Cancer: A Systematic Review and Meta-Analysis. *Clin Lung Cancer* (2018) 19(3):e335–48. doi: 10.1016/j.clcc.2018.01.002
- Nishino M, Giobbie-Hurder A, Hatabu H, Ramaiya N, Hodi F. Incidence of Programmed Cell Death 1 Inhibitor-Related Pneumonitis in Patients With Advanced Cancer: A Systematic Review and Meta-Analysis. *JAMA Oncol* (2016) 2(12):1607–16. doi: 10.1001/jamaoncol.2016.2453
- Naidoo J, Wang X, Woo K, Iyriboz T, Halpenny D, Cunningham J, et al. Pneumonitis in Patients Treated With Anti-Programmed Death-1/Programmed Death Ligand 1 Therapy. *J Clin Oncol* (2017) 35(7):709–17. doi: 10.1200/jco.2016.68.2005
- Pillai R, Behera M, Owonikoko T, Kamphorst A, Pakkala S, Belani C, et al. Comparison of the Toxicity Profile of PD-1 Versus PD-L1 Inhibitors in Non-Small Cell Lung Cancer: A Systematic Analysis of the Literature. *Cancer* (2018) 124(2):271–7. doi: 10.1002/cncr.31043
- Delaunay M, Cadranet J, Lusque A, Meyer N, Gounant V, Moro-Sibilot D, et al. Immune-Checkpoint Inhibitors Associated With Interstitial Lung Disease in Cancer Patients. *Eur Respir J* (2017) 50(2):1700050. doi: 10.1183/13993003.01319-2017
- Ahn MJ, Yang J, Yu H, Saka H, Oxnard GR. 136o Osimertinib Combined With Durvalumab in EGFR-Mutant Non-Small Cell Lung Cancer: Results From the TATTON Phase Ib Trial. *J Thoracic Oncol* (2016) 11(4):S115. doi: 10.1016/S1556-0864(16)30246-5
- Oshima Y, Tanimoto T, Yuji K, Tojo A. EGFR-TKI-Associated Interstitial Pneumonitis in Nivolumab-Treated Patients With Non-Small Cell Lung Cancer. *JAMA Oncol* (2018) 4(8):1112–5. doi: 10.1001/jamaoncol.2017.4526
- Cho JY, Kim J, Lee JS, Kim YJ, Kim SH, Lee YJ, et al. Characteristics, Incidence, and Risk Factors of Immune Checkpoint Inhibitor-Related Pneumonitis in Patients With Non-Small Cell Lung Cancer. *Lung Cancer* (2018) 125:150–6. doi: 10.1016/j.lungcan.2018.09.015
- Ma W, Li H, Tian Z, Wang S, Zheng X, Hou J. Complete Regression of Pulmonary Squamous Carcinoma in IPF Following Gemcitabine Plus Cisplatin: A Case Report and Literature Review. *BMC Pulmonary Med* (2020) 20(1):69. doi: 10.1186/s12890-020-1094-1
- Teraoka S, Fujimoto D, Morimoto T, Kawachi H, Ito M, Sato Y, et al. Early Immune-Related Adverse Events and Association With Outcome in Advanced Non-Small Cell Lung Cancer Patients Treated With Nivolumab: A Prospective Cohort Study. *J Thoracic Oncol* (2017) 12(12):1798–805. doi: 10.1016/j.jtho.2017.08.022
- Mendiola V, Kesireddy M, Jana B. Nivolumab-Induced, Late-Onset, Steroid-Sensitive, High-Grade Pneumonitis and Durable Tumor Suppression in Metastatic Renal Cell Carcinoma: A Case Report. *Case Rep Oncol Med* (2019) 2019:6759472. doi: 10.1155/2019/6759472
- Ashinuma H, Mizuno S, Yoshida Y, Shingyoji M. A Case of Long-Term Survival After Checkpoint Inhibitor Pneumonitis in a Patient With Squamous Cell Lung Cancer. *Case Rep Oncol Med* (2019) 2019:1–4. doi: 10.1155/2019/4836404
- Kim C, Kim C, Yoon SE, Kim KH, Choi SJ, Kang B, et al. Hyperprogressive Disease During PD-1 Blockade in Patients With Advanced Hepatocellular Carcinoma. *J Hepatol* (2020) 74(2):350–9. doi: 10.1016/j.jhep.2020.08.010
- Faure M, Rochigneux P, Olive D, Taix S, Brenot-Rossi I, Gilbert M. Hyperprogressive Disease in Anorectal Melanoma Treated by PD-1 Inhibitors. *Front Immunol* (2018) 9:797. doi: 10.3389/fimmu.2018.00797
- Kato S, Goodman A, Walavalkar V, Barkauskas D, Sharabi A, Kurzrock R. Hyperprogressors After Immunotherapy: Analysis of Genomic Alterations

## FUNDING

This work was financially supported by the Science and Technique Foundation of Henan Province (No. 202102310121 for JW), 1000 Talents Program of Central plains (No. 204200510023 for XC), State Key Laboratory of Esophageal Cancer Prevention & Treatment (No. Z2020000X for XC).

## SUPPLEMENTARY MATERIAL

The Supplementary Material for this article can be found online at: <https://www.frontiersin.org/articles/10.3389/fonc.2021.671416/full#supplementary-material>



Associated With Accelerated Growth Rate. *Clin Cancer Res* (2017) 23 (15):4242–50. doi: 10.1158/1078-0432.CCR-16-3133

**Conflict of Interest:** The authors declare that the research was conducted in the absence of any commercial or financial relationships that could be construed as a potential conflict of interest.

Copyright © 2021 Wang, Li, Lv, Nie, Chen, Xu, Yang, Zhang, Tu and Chen. This is an open-access article distributed under the terms of the Creative Commons Attribution License (CC BY). The use, distribution or reproduction in other forums is permitted, provided the original author(s) and the copyright owner(s) are credited and that the original publication in this journal is cited, in accordance with accepted academic practice. No use, distribution or reproduction is permitted which does not comply with these terms.





# Feiyanning Formula Induces Apoptosis of Lung Adenocarcinoma Cells by Activating the Mitochondrial Pathway

Li-Min Zhu<sup>1</sup>, Hai-Xia Shi<sup>2\*</sup>, Masahiro Sugimoto<sup>3</sup>, Kenjiro Bandow<sup>4</sup>, Hiroshi Sakagami<sup>5</sup>, Shigeru Amano<sup>5</sup>, Hai-Bin Deng<sup>1</sup>, Qing-Yu Ye<sup>1</sup>, Yun Gai<sup>6</sup>, Xiao-Li Xin<sup>1</sup> and Zhen-Ye Xu<sup>1\*</sup>

## OPEN ACCESS

### Edited by:

Dong-Hua Yang,  
St. John's University, United States

### Reviewed by:

Xiaodong Zhao,  
Shanghai Jiao Tong University, China  
Juan Zhang,  
Henan University of TCM, China

### \*Correspondence:

Hai-Xia Shi  
haixia.0101@163.com  
Zhen-Ye Xu  
xuzhenye1947@126.com

### Specialty section:

This article was submitted to  
Pharmacology of Anti-Cancer Drugs,  
a section of the journal  
Frontiers in Oncology

**Received:** 04 April 2021

**Accepted:** 09 June 2021

**Published:** 02 July 2021

### Citation:

Zhu L-M, Shi H-X, Sugimoto M,  
Bandow K, Sakagami H, Amano S,  
Deng H-B, Ye Q-Y, Gai Y, Xin X-L and  
Xu Z-Y (2021) Feiyanning Formula  
Induces Apoptosis of Lung  
Adenocarcinoma Cells by Activating  
the Mitochondrial Pathway.  
Front. Oncol. 11:690878.  
doi: 10.3389/fonc.2021.690878

<sup>1</sup> Department of Oncology, Longhua Hospital, Shanghai University of Traditional Chinese Medicine, Shanghai, China,

<sup>2</sup> Department of Traditional Chinese Medicine, Shanghai Ninth People's Hospital, Shanghai Jiao Tong University School of Medicine, Shanghai, China, <sup>3</sup> Research and Development Center for Minimally Invasive Therapies, Institute of Medical

Science, Tokyo Medical University, Shinjuku, Japan, <sup>4</sup> Division of Biochemistry, Meikai University School of Dentistry, Saitama, Japan, <sup>5</sup> Meikai University Research Institute of Odontology (M-RIO), Meikai University School of Dentistry, Saitama, Japan, <sup>6</sup> Department of Oncology, The Seventh People's Hospital, Shanghai University of Traditional Chinese Medicine, Shanghai, China

Feiyanning formula (FYN) is a traditional Chinese medicine (TCM) prescription used for more than 20 years in the treatment of lung cancer. FYN is composed of *Astragalus membranaceus*, *Polygonatum sibiricum*, *Atractylodes macrocephala*, *Cornus officinalis*, *Paris polyphylla*, and *Polistes olivaceous*, etc. All of them have been proved to have anti-tumor effect. In this study, we used the TCM network pharmacological analysis to perform the collection of compound and disease target, the prediction of compound target and biological signal and the Kyoto Encyclopedia of Genes and Genomes (KEGG) pathway enrichment analysis. It was found that the activation of mitochondrial pathway might be the molecular mechanism of the anti-lung cancer effect of FYN. The experimental results showed that FYN had an inhibitory effect on the growth of lung cancer cells in a dose-dependent and time-dependent manner. Moreover, FYN induced G<sub>2</sub>/M cell cycle arrest and apoptotic cell death as early as 6 h after treatment. In addition, FYN significantly induced mitochondrial membrane depolarization and increased calreticulin expression. Metabolomics analysis showed the increase of ATP utilization (assessed by a significant increase of the AMP/ATP and ADP/ATP ratio, necessary for apoptosis induction) and decrease of polyamines (that reflects growth potential). Taken together, our study suggested that FYN induced apoptosis of lung adenocarcinoma cells by promoting metabolism and changing the mitochondrial membrane potential, further supporting the validity of network pharmacological prediction.

**Keywords:** FYN, A549 cells, apoptosis, NSCLC, mitochondrial pathway, metabolomics analysis, ATP utilization

## INTRODUCTION

Lung cancer has the highest morbidity and mortality worldwide (1). Major lung cancer types include small cell lung cancer (SCLC) and non-small cell lung cancer (NSCLC), with the latter being further divided into adenocarcinoma, squamous cell carcinoma, and large cell carcinoma, accounting for 85 to 90% of all lung cancers (2). Most lung cancers usually produce no specific symptoms at the early stage, and this disease is consequently diagnosed at later stage with poor outcomes. With a 5-year survival rate of only 16.6%, the prognosis for lung cancer is poor. The 5-year survival of lung cancer is less than 4% when distant metastases are discovered at diagnosis (3).

At present, common therapies for lung cancer include surgery, chemotherapy, radiotherapy, targeted therapy, and immunotherapy (4). However, adverse effects such as mucositis, neurotoxicity, and extravasation are often caused by chemotherapy and radiotherapy. Moreover, chemotherapy and targeted therapy easily produce drug resistance. Also, limited benefit of immunotherapy happens in some patients. In China, traditional Chinese medicines (TCMs) are commonly prescribed as an adjuvant therapy to conventional cancer treatments to reduce such adverse reactions to radiotherapy and chemotherapy and improve the efficacy of treatment, thus improving the quality of life of patients and prolonging their survival. Various mechanisms of TCM have been proposed (5) with published evidence that TCM can improve general symptoms and even prolong the survival of cancer patients (6). However, in many instances, TCM is prescribed without objective evidence of mechanism.

Here we sought to better define the activity of Feiyaning formula (FYN), a proprietary prescription developed by Z-YX, a prominent TCM practitioner in Shanghai. The prescription has been used clinically for more than 20 years. Our previous randomized placebo-controlled study showed its benefits in prolonging the patient's survival and improving the quality of life with limited toxicity and side effects (7). In this study, the Chinese medicine network pharmacology method was adopted to analyze lung cancer as the research object to complete the collection of compounds and disease targets, the prediction of compound targets, the enrichment analysis of biological signals and KEGG pathways to predict the possible role of FYN recipe in lung cancer. To verify the network pharmacological prediction, we performed mitochondrial pathway-related functional verification by observing the effect of FYN on lung cancer cells *in vitro*.

## METHODS

### Network Pharmacological Analysis of FYN Collection of Compound Data of 11 Traditional Chinese Medicines

FYN was composed of 11 traditional Chinese medicines. According to the Traditional Chinese Medicine Systems

Pharmacology Database and Analysis Platform (TCMSP) (<https://tcmspw.com/tcmsp.php>), a Bioinformatics Analysis Tool for Molecular mechanism of Traditional Chinese Medicine (BATMAN-TCM) database (<http://bionet.ncpsb.org.cn/batman-tcm/>) and literature review, their compositional and structural information was collected. In TCMSP data query, the parameters are set as ob  $\geq 30\%$  and dl  $\geq 0.18$ . In BATMAN data query, the parameter setting score cutoff is 20; adjusted *p*-value is 0.05. The obtained compounds were de-duplicated, and the structural files and SMILES codes of 282 compounds were downloaded from PubChem for the following research.

### Prediction of Targets of Compounds in 11 Traditional Chinese Medicines

Two methods were used to predict compound targets. First, by Seaware, prediction software of compound activity, 282 compounds were identified. The screening conditions were set for human targets, and potential targets were obtained through calculation and prediction. Second, by SMILES code of compounds, compound targets were predicted from Swiss Target Prediction database (<http://www.swisstargetprediction.ch/>). The results were obtained by integrating these two methods; the Uniprot database (<https://www.uniprot.org/>) was used to correct all targets of official gene names.

### Searching for Anti-Lung Cancer Targets

Anti-lung cancer targets were searched through Comparative Toxicogenomics Database (CTD) (<http://ctdbase.org/>) with keywords such as "Carcinoma, Non-Small-Cell Lung", "Carcinoma, Small Cell" and "Small Cell Lung Carcinoma". Gene names were unified through the Uniprot database. The lung cancer related targets were matched with the potential targets that were calculated in *Prediction of Targets of Compounds in 11 Traditional Chinese Medicines*, thus the potential action targets of the compound against lung cancer were obtained.

### Gene Enrichment Analysis

GO (gene ontology) analysis and KEGG analysis were carried out on the targets for the compounds collected through the Database for Annotation, Visualization, and Integrated Discovery (DAVID) (<https://david.ncifcrf.gov/>, Version 6.8). The biological process (BP), molecular function (MF), and cellular component (CC) are selected for pathway analysis, and the top 20 genes of BP, MF, CC, and KEGG pathways are selected by scoring the *p* values, and the results of pathway enrichment analysis are visualized by R software.

## Experimental Verification

### Materials and Methods

#### Reagents

FYN prescription powder was provided by the Longhua Hospital Affiliated to Shanghai University of Traditional Chinese Medicine. Dulbecco's modified Eagle medium (DMEM) was used to dilute the powder to the required concentrations.

cisplatin was purchased from Sigma-Aldrich Inc. (St. Louis, MO, USA), and stock solution was prepared with 0.9% sodium chloride.

### Cell Culture

Lung cancer cell lines, LC-1/sq (squamous cell carcinoma), A549 (adenocarcinoma), WA-hT (small cell carcinoma), and A904 (large cell carcinoma) were purchased from the RIKEN BRC Cell Bank (Tsukuba, Japan). All cell lines were maintained in high glucose DMEM (Thermo Fischer Scientific, Waltham, MA, USA) containing 10% heat-inactivated fetal bovine serum (Fischer Scientific; A3160802), 100 U/ml penicillin G, and 100 µg/ml streptomycin sulfate at 37°C, with a humidified 5% CO<sub>2</sub> atmosphere. Cells were routinely passaged every 2–3 days, and cells in logarithmic growth phase were used for experiments.

### Preparation of FYN

FYN is composed of *Astragalus membranaceus*, *Polygonatum sibiricum*, *Atractylodes macrocephala*, *Cornus officinalis*, *Paris polyphylla*, *Polistes olivaceous*, *Salvia chinensis*, *Pseudobulbus cremastrae seu pleiones*, *Corium bufonis*, *Ganoderma lucidum*, and *Epimedium folium*. These herbs were purchased from the Longhua Hospital Affiliated to Shanghai University of TCM (Shanghai, China). The following components were combined as follows: 2,200 ml water was added to the herb mix and soaked for 60 min and filtered with four layers of gauze into 1.8 L filtrate. Then the filtrate was dried directly at –70°C to obtain the lyophilized powder (FYN-M) 41.813 g. Then 500 mg of FYN-M was dissolved in 15 ml of pure water and applied to the activated RP-C<sub>18</sub> solid phase extraction column (5 g RP-C<sub>18</sub>). The column was washed with 15 ml water to remove carbohydrates and other water-soluble components. Then 15 mg of FYN-M-SPE was eluted with 15 ml chromatographic grade methanol and dissolved with 3 ml methanol/water = 1:1 to make the concentration of 5 mg/ml and dissolved by ultrasonic wave. FYN-M-SPE was further diluted to make 1 mg/ml solution, centrifuged at 15,000 rpm to remove debris. The supernatant was used for the analysis.

### Cell Proliferation Assays

MTT assays were used to determine the relative viable cell number (8). Briefly, cells were seeded into 96 well plates (4,000 cells/100 µl per well) and allowed to attach before discarding the original medium. Thereafter, 200 µl culture medium (control) or drug-containing medium was added to each well (n = 5 replicates/treatment). Final concentration of FYN was 16, 31, 63, 125, 250, 500, and 1,000 µg/ml. Final concentration of cisplatin was 16, 31, 63, 125, 250, 500, and 1,000 µM. After incubation for 24, 48, and 72 h, the relative viable cell number was determined by MTT method. Cells were incubated for 2 h with 0.2 mg/ml MTT and lysed with dimethyl sulfoxide (DMSO). The absorbance of the cell lysate was then measured at 560 nm, using a microplate reader (Infinite F50R; Tecan, Männedorf, Switzerland). Control cells were treated with the same amounts of DMSO and the cell damage induced by DMSO was subtracted from that induced by test agents. The concentration of compound that reduced the viable cell

number by 50% (CC<sub>50</sub>) was determined from the dose-response curve, and the mean value of CC<sub>50</sub> for each cell type was calculated from triplicate assays.

### Cell Cycle and Apoptosis Assays

Flow cytometric based analyses were used to measure the effects of FYN on cell cycle and apoptosis using the annexin V-FITC/PI apoptosis detection Kit (Sigma, Aldrich; A9210). Six-well plates were seeded with  $5 \times 10^5$  A549 cells and cultured overnight. The culture medium was removed and replaced with either: (1) fresh DMEM (blank control) group; (2) 1 mM cisplatin treatment group; or (3) different concentrations of FYN (50, 100, or 200 µg/ml) groups. After 48 h, all cells were collected, washed three times with PBS and then re-suspended with 500 µl binding buffer. Thereafter, 5 µl annexin V-FITC reagent was added and incubated for 15 min at 4°C before adding 5 µl PI solution for 5 min. Cells were then analyzed using flow cytometry (SH800S, Sony Imaging Products & Solutions, Kanagawa, Japan), and cell apoptosis rate was determined using the BD software (9, 10).

### Metabolomics Analysis

A549 cells were washed twice with 10 ml of 5% mannitol after treating with FYN at different concentrations (10, 30, 60, 100 µg/ml) for 24 h. Aliquots of the cells were trypsinized, and the viable cell number was counted with a hemocytometer after staining with trypan blue. The remaining cells were washed twice with 5 ml of ice-cold 5% D-mannitol and then immersed for 10 min in 1 ml of methanol containing internal standards [25 µM each of methionine sulfone, 2-(N-morpholino)-ethane sulfonic acid and D-camphor-10-sulfonic acid]. The methanol extract (supernatant) was collected. The aqueous layer was filtered to remove large molecules by centrifugation through a 5-kDa cutoff filter (Millipore, Billerica, MA) at  $9,100 \times g$  for 2.5 h at 4°C. The 320 µl of the filtrate was concentrated by centrifugation and dissolved in 50 µl of Milli-Q water containing reference compounds (200 µM each of 3-aminopyrrolidine and trimesate) immediately before capillary electrophoresis-time-of-flight-mass spectrometry (CE-TOF-MS) analysis. The parameters of the measurement instrument and data processing were described previously. The concentrations of intracellular metabolites were expressed as amol/cell (11).

### Mitochondrial Membrane Potential

A549 cells were treated with different concentrations of FYN (50, 100 or 200 µg/ml) for 6 h, washed with PBS, and incubated at 37°C for 20 min in 0.5 ml medium containing the JC-1 probe (mitochondrial membrane potential detection kit, Thermo Fisher Scientific, Waltham, MA, USA, T3168). The image was taken with a Zeiss LSM 800 confocal microscope (Carl Zeiss, Oberkochen, Germany) and analyzed with Image J software (<https://imagej.nih.gov/ij/>).

### Calreticulin Detection

Cell expression of calreticulin was detected by immunofluorescence staining and flow cytometry. A549 cells were treated with different

concentrations of FYN (50, 100 or 200  $\mu\text{g/ml}$ ) or cisplatin (1 mM). After 4 h of incubation, the cells were collected and pelleted by centrifugation at 1,200 rpm for 5 min, resuspended with buffer containing Dylight 488 conjugated anti-calreticulin antibody (Enzo Life Sciences, Lausen, Switzerland; ADI-SPA-601-488-D), and incubated for 30 min at 4°C in the dark. Thereafter, cells were resuspended in 500  $\mu\text{l}$  buffer and immediately analyzed by flow cytometer.

### Statistics

SPSS 22.0 software (IBM, Armonk, NY, USA) was used for statistical analyses, and Prism 6.0 software (GraphPad Software, San Diego, CA, USA) was used for preparing plots. Each experiment was independently repeated three times with data expressed as Mean  $\pm$  SD. Univariate analysis of variance was used for comparison among groups, and the LSD-t test was used for pairwise comparison within groups. Differences of  $p < 0.05$  were considered statistically significant.

## RESULTS

### Results of Pharmacological Analysis of FYN Network

#### Collection of Target Points

A total of 1,701 potential targets of TCM components were obtained after the prediction and screening by Seaware reverse target searching and Swiss Target Prediction database. Six hundred forty-six genes related to lung cancer were collected in CTD database. One hundred twenty-four common targets were obtained by intersection of compound targets and human lung adenocarcinoma targets. These 124 common targets are considered as potential targets for the treatment of lung cancer.

#### Network Construction and Analysis

Protein-protein interaction (PPI) graph is obtained from String database, which contains 124 nodes and 1,485 edges. Using Network Analyzer to analyze the node degree and related

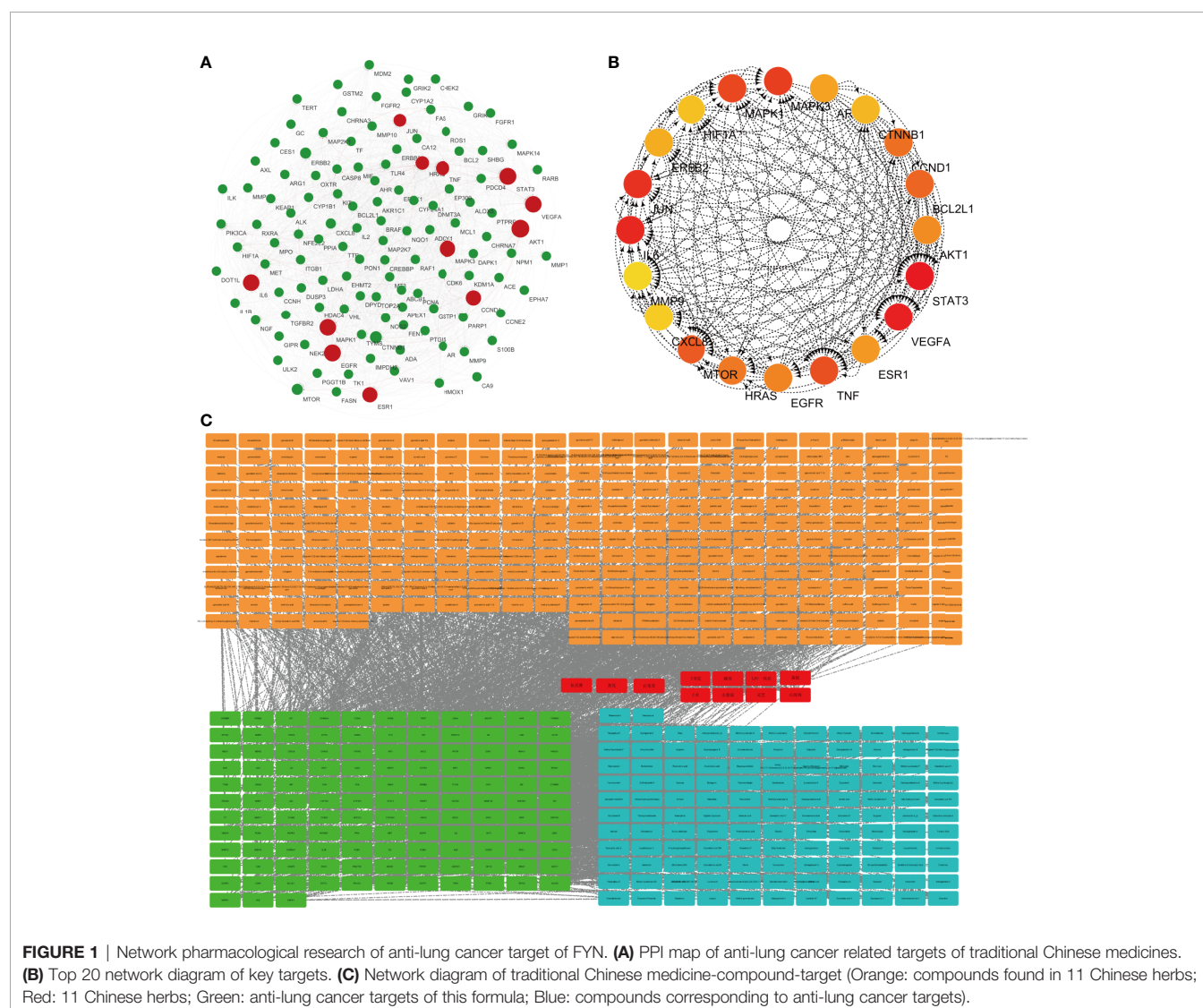


**FIGURE 1 |** Network pharmacological research of anti-lung cancer target of FYN. **(A)** PPI map of anti-lung cancer related targets of traditional Chinese medicines. **(B)** Top 20 network diagram of key targets. **(C)** Network diagram of traditional Chinese medicine-compound-target (Orange: compounds found in 11 Chinese herbs; Red: 11 Chinese herbs; Green: anti-lung cancer targets of this formula; Blue: compounds corresponding to anti-lung cancer targets).



parameters, the average node degree is 24, and the average local clustering coefficient is 0.656, as shown in **Figure 1A**.

Traditional Chinese medicine-component-target network diagram is constructed by Cytoscape, as shown in **Figure 1B**. The network includes 540 nodes and 2,751 edges. Among them, nodes represent compounds or targets corresponding to traditional Chinese medicine, while edges indicate the interactions between traditional Chinese medicine and compounds or between compounds and targets. It can be seen from the network diagram that there are phenomena that multiple compounds correspond to one target or one traditional Chinese medicine corresponds to multiple compounds, and there are also situations that multiple targets correspond to one compound or one compound corresponds to multiple traditional Chinese medicines. It indicates that there are pharmacological similarities among several compounds, and it is possible that a single compound can produce anti-lung cancer therapeutic effect through multiple targets. At the same time, side reaction is essential for every traditional Chinese medicine in the anti-lung cancer effect of this prescription.

The CytoHubba module in Cytoscape was used to obtain the top 20 network diagrams of the core target point. The nodes change from orange to red, and the degree value gradually increases from small to large. The importance of the target point was judged according to the degree of value, as shown in **Figure 1C**. The information of top 20 targets was shown in **Table 1**. It can be seen from the network diagram that STAT3, VEGFA, IL6, JUN, and MAPK3 may be the five key targets of the eleven traditional Chinese medicines against lung cancer. Eleven of these targets were associated with apoptosis in lung cancer cells; the result was shown in **Table 2**.

### Target-Pathway Network Analysis Diagram

The top 20 pathways were analyzed and the target-pathway analysis diagram was obtained (**Figure 2**). It can be seen from the network diagram that 16 of the top 20 pathways are enriched in

**TABLE 1** | Degree information of top 20 targets.

Sort	Target spot	Scoring value
1	STAT3	9.00E+18
2	VEGFA	9.00E+18
3	IL6	9.00E+18
4	JUN	9.00E+18
5	MAPK3	9.00E+18
6	MAPK1	9.00E+18
7	TNF	9.00E+18
8	MTOR	8.98E+18
9	BCL2L1	8.98E+18
10	CCND1	8.63E+18
11	HRAS	8.62E+18
12	EGFR	8.59E+18
13	AKT1	8.49E+18
14	ESR1	8.25E+18
15	AR	7.08E+18
16	ERBB2	6.85E+18
17	CTNNB1	6.50E+18
18	HIF1A	5.60E+18
19	CXCL8	5.53E+18
20	MMP9	5.53E+18

**TABLE 2** | Apoptosis-related targets in lung cancer cells.

Sort	Target spot	Scoring value
1	STAT3	9.00E+18
2	JUN	9.00E+18
3	TNF	9.00E+18
4	MTOR	8.98E+18
5	BCL2L1	8.98E+18
6	CCND1	8.63E+18
7	HRAS	8.62E+18
8	EGFR	8.59E+18
9	AKT1	8.49E+18
10	HIF1A	5.60E+18
11	MMP9	5.53E+18

the anti-lung cancer genes. Among the 124 potential targets against lung cancer of 11 traditional Chinese medicines, 68 targets were enriched in related pathways.

### Gene Enrichment Analysis

The functional annotation and pathway enrichment analysis of genes corresponding to 282 compounds were carried out by DAVID platform, and the data of top 20 targets were analyzed according to *p* value and visualized by R software. The results are shown in **Figure 3**. The larger the dots in the figures, the greater the number of enriched genes, and the color of the dots corresponds to *p* value.

From the enrichment results, the biological processes of 282 compounds mainly include: positive regulation of RNA polymerase II promoter transcription, negative regulation of apoptosis process, positive regulation of cell proliferation, positive regulation of gene expression and drug reaction (**Figure 3A**); cell composition mainly includes cell nucleus, cytoplasm, nucleoplasm, and extracellular space (**Figure 3B**). Molecular functions mainly involve protein binding, ATP binding, identical protein binding, enzyme binding, and transcription factor binding (**Figure 3C**).

According to the results of DAVID pathway enrichment analysis, the pathway of top 20 was visualized by R software according to *p* value. The main pathways enriched included cancer pathway, cancer proteoglycan, hepatitis B, prostate cancer, and HIF-1 signaling pathway (**Figure 3D** and **Table 3**).

### Pathway Analysis

In recent years, the clinical practice of traditional Chinese medicine has become one of the new approaches for the treatment of cancer (12). We found that the mitochondrial apoptosis pathway is closely related to tumor development. This pathway plays a key role in the process of apoptosis, and the release of cytochrome c (cyt c) is the key link in the mitochondrial apoptosis pathway (13).

According to literature research and pathway map **Figure S1**, it can be found that Bcl-2, an anti-apoptotic protein, forms heterodimer with Bax, and Bak in the mitochondrial apoptotic pathway prevents the oligomerization of Bax and Bak, reduces the permeability of mitochondrial membrane, and leads to the retention of pro-apoptotic factor cyt c in mitochondria, thus reducing the pro-apoptotic effect. After therapy, the ratio of Bax,



**TABLE 3 |** KEGG analysis of top 20 pathways.

Access	Number of genes	p-Value
hsa05200: Pathways in cancer	44	1.27E-26
hsa05205: Proteoglycans in cancer	28	8.45E-19
hsa04151: PI3K-Akt signaling pathway	27	6.45E-12
hsa05206: MicroRNAs in cancer	25	4.93E-12
hsa05161: Hepatitis B	23	1.71E-16
hsa05215: Prostate cancer	21	1.12E-18
hsa04066: HIF-1 signaling pathway	20	1.42E-16
hsa04510: Focal adhesion	19	1.69E-09
hsa04015: Rap1 signaling pathway	19	2.31E-09
hsa04010: MAPK signaling pathway	19	4.40E-08
hsa05142: Chagas disease (American trypanosomiasis)	18	1.92E-13
hsa04068: FoxO signaling pathway	17	1.45E-10
hsa05164: Influenza A	17	7.17E-09
hsa05166: HTLV-I infection	17	1.39E-06
hsa04919: Thyroid hormone signaling pathway	16	1.61E-10
hsa05219: Bladder cancer	15	4.30E-16
hsa05223: Non-small cell lung cancer	15	6.01E-14
hsa05230: Central carbon metabolism in cancer	15	4.48E-13
hsa05212: Pancreatic cancer	15	5.63E-13
hsa05211: Renal cell carcinoma	15	7.06E-13

Bak, and Bcl-2 is unbalanced, or the conformational change and oligomerization of Bax and Bak occur, which caused cyt c to leak into the cytoplasm from mitochondria and then combine with Apaf-1 to form a complex to shear and activate caspase-9, resulting in the activation of downstream caspase-3, thus inducing apoptosis. Therefore, activation of the mitochondrial pathway may be the molecular mechanism of the anti-lung cancer effect of TCM (14).

### Identification of Major Component of FYN

FYN was analyzed by high resolution mass spectrometry with cationic (A, B) and anionic (C, D) total-ion exchange chromatograms (UPLC- Thermo Q) with standard (**Figure 4**). The most abundant compound identified by cationic ion exchange chromatograms was atractylenolide II, followed by atractylenolide I, bufogenin, calycosin 7-O- $\beta$ -D-glucopyranoside, loganin, morronside, militarine, and epmedin (A, B). The most abundant compound identified by anionic ion exchange chromatograms was gallic acid, component unit of tannin, followed by protocatechuic acid, rosmarinic acid, polyphyllin VI, and ganoderic acid B (C, D).

## Experimental Results

### FYN Inhibits Human Lung Cancer Cell Proliferation

The analysis of FYN by high resolution mass spectrometry was shown in **Figure 4**. The growth inhibitory effects of FYN were evaluated against four lung cancer cell lines representing the major lung cancer types/subtypes. Analyses using MTT assays showed that the growth of the LC-1/sq squamous cell line, the A549 adenocarcinoma line, WA-hT small cell carcinoma line, and A904 large cell carcinoma line were all significantly reduced after FYN treatment compared to the control group ( $p < 0.01$ ; **Figure 5A**). The inhibitory effects were dose- and time-dependent with maximal inhibition at 72 h. Among the cell lines, FYN showed the strongest inhibitory effect against A549

cells and to a lesser extent in WA-hT cells, and these effects were clearly evident in the first 24 h (**Figure 5A**). In comparison, cisplatin effects were also dose- and time-dependent for all cell lines with WA-hT being the most sensitive (**Figure 5B**). Further research was carried out to compare the cytotoxicity of FYN and cisplatin against A549 cells (**Figure 5C**). The IC<sub>50</sub> values at each time point are shown in **Figure 5D**. Since A549 was much more sensitive to FYN than cisplatin, A549 cells were selected to further study the mechanism of action of FYN.

### Effect of FYN on Apoptosis of A549 Cells

The rapid reduction in cell proliferation observed after 24 h treatment of A549 cells with FYN suggested the occurrence of cell cycle arrest and other types of cell death might occur. Therefore, to determine if FYN induced cell cycle arrest and apoptosis, A549 cells were treated with different concentrations of FYN (25, 50, 100  $\mu$ g/ml) for 48 h and flow cytometric analyses were performed to measure the cell cycle distribution. Cisplatin (1 mM) was used as a positive control. Compared with control cells, FYN treatment decreased the number of cells in the G<sub>1</sub> phase while increasing cells in the G<sub>2</sub>/M phase ( $p < 0.01$ ; **Figure 5E**), suggesting that FYN causes G<sub>2</sub> cell cycle arrest, similar to the effects of cisplatin. We next investigated the effects of FYN on cell apoptosis. The 24 h FYN treatment of A549 cells promoted both early apoptotic cells (Annexin V+, PI-) and late apoptotic cells (Annexin V+, PI+) in a dose-dependent manner (**Figure 5F**). Collectively, these results indicate that FYN rapidly induces cell cycle arrest and induces apoptosis in A549 lung cancer cells.

### Metabolomics Analyses of A549 Cells Treated With FYN

Metabolomics was used to determine the changes in the intracellular concentration of metabolites in A549 cells after treatment with FYN. One hundred sixty three metabolites were detected (**Table S1**). **Figure 6B** showed the heat map of metabolites upregulated (red color) or downregulated (blue color), normalized by mean of control samples or mean of total samples. First, there was a significant decrease in putrescine and spermidine in the polyamine pathway (**Figure 6A**). This may reflect the growth inhibition accompanied with apoptosis. ATP cellular content also decreased with accompanying increases in AMP and ADP, suggesting the increased utilization of ATP. Similarly, UTP levels were also decreased with accompanying increases in UMP and UDP, suggesting the increased utilization of UTP. The increased utilization of ATP and UTP, donors of cellular energy, may relate to the stimulated apoptosis induction (**Figure 6A**).

### Effect of FYN on Mitochondrial Membrane Potential in A549 Cells

Mitochondrial membrane potential is known to break down in apoptotic or metabolically stressed cells. In view of the fact that FYN can induce rapid apoptosis and also disturbs cellular metabolism, we anticipated there would be accompanying changes in mitochondrial membrane potential. FYN treatment

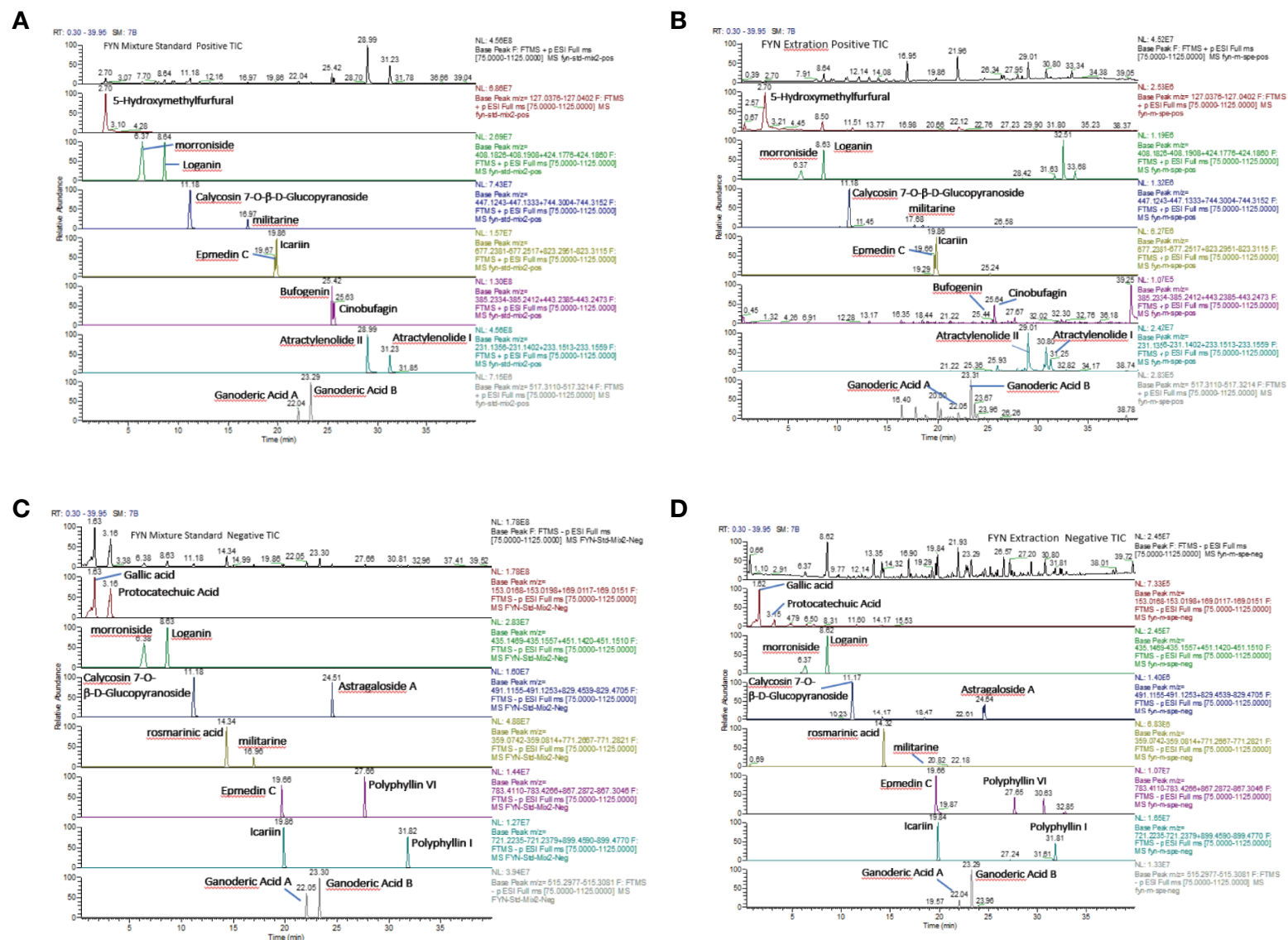


**FIGURE 4** | Analysis of FYN by high resolution mass spectrometry. **(A)** Positive total-ion chromatograms of standard by Waters Acquity UPLC-Thermo Q/Exactive HRMS with the mixture standard solution. **(B)** Positive total-ion chromatograms of standard by Waters Acquity UPLC-Thermo Q/Exactive HRMS with FYN extract solution. **(C)** Negative total-ion chromatograms of standard by Waters Acquity UPLC-Thermo Q/Exactive HRMS with the mixture standard solution. **(D)** Negative total-ion chromatograms of standard by Waters Acquity UPLC-Thermo Q/Exactive HRMS with the FYN extract solution.



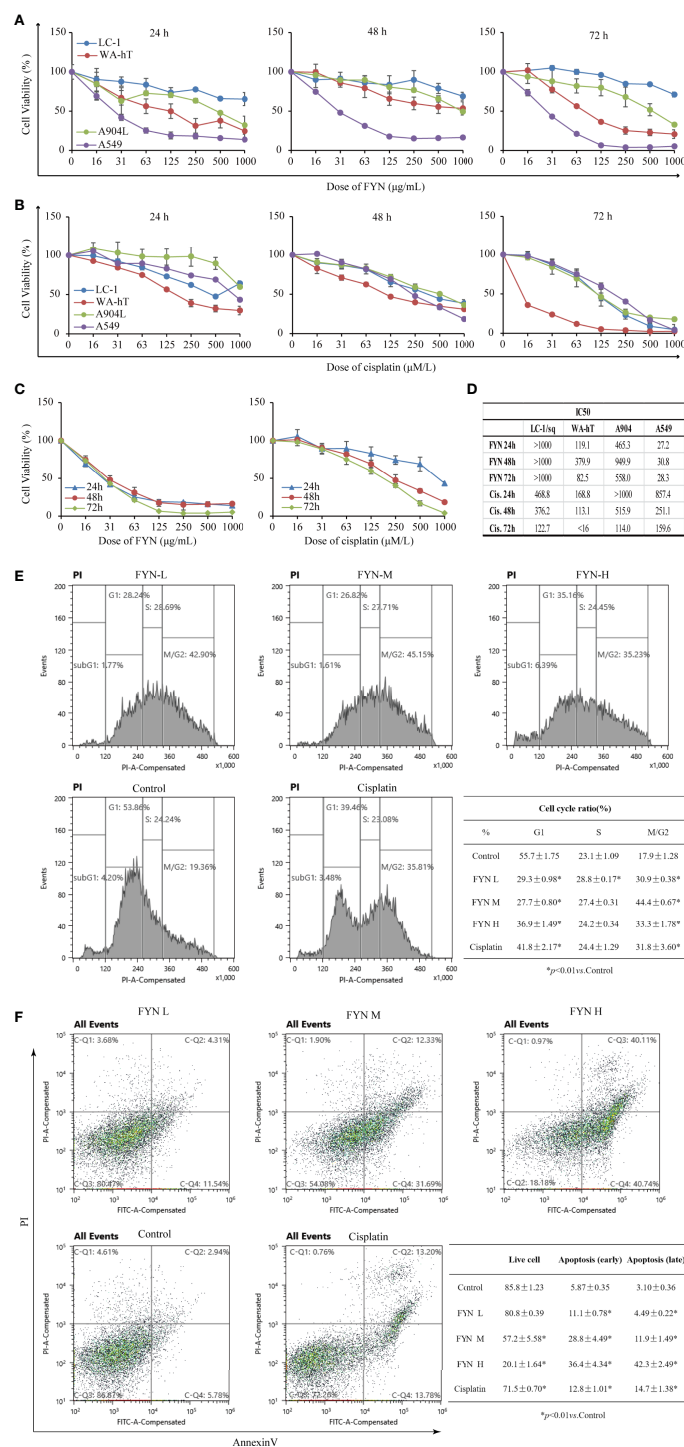


**FIGURE 5 |** FYN inhibits the proliferation of human lung cancer cells and induces cell cycle arrest and apoptosis. **(A)** Time and dose responses of four lung cancer cell lines to FYN ( $\mu\text{g/ml}$ ). **(B)** Time and dose responses of the indicated lung cancer cell lines to cisplatin ( $\mu\text{M}$ ). **(C)** Comparison of FYN versus cisplatin effects on A549 cells. **(D)** The IC50 values at each time point of FYN versus cisplatin. **(E)** The cell cycle analysis of A549 lung cancer cells after FYN treatment. Flow cytometric profiles of PI staining in A549 cells after treatments without (control) or with FYN, cisplatin. The percentages of cells in the G<sub>1</sub>, S, and G<sub>2</sub>/M phases displayed in the flow cytometric histogram represent one of the three repeated experiments. These data are statistically processed and shown in a table. **(F)** FYN induces apoptosis in A549 lung cancer cells. The cells treated without (control) or with FYN, or cisplatin and stained by FITC-conjugated Annexin V and PI. Then, the cells were analyzed by dual parameter flow cytometry. The percentages of quadrant fractions displayed in the flow cytometric plots represent one of the three repeated experiments. These data are statistically processed and shown in a table.

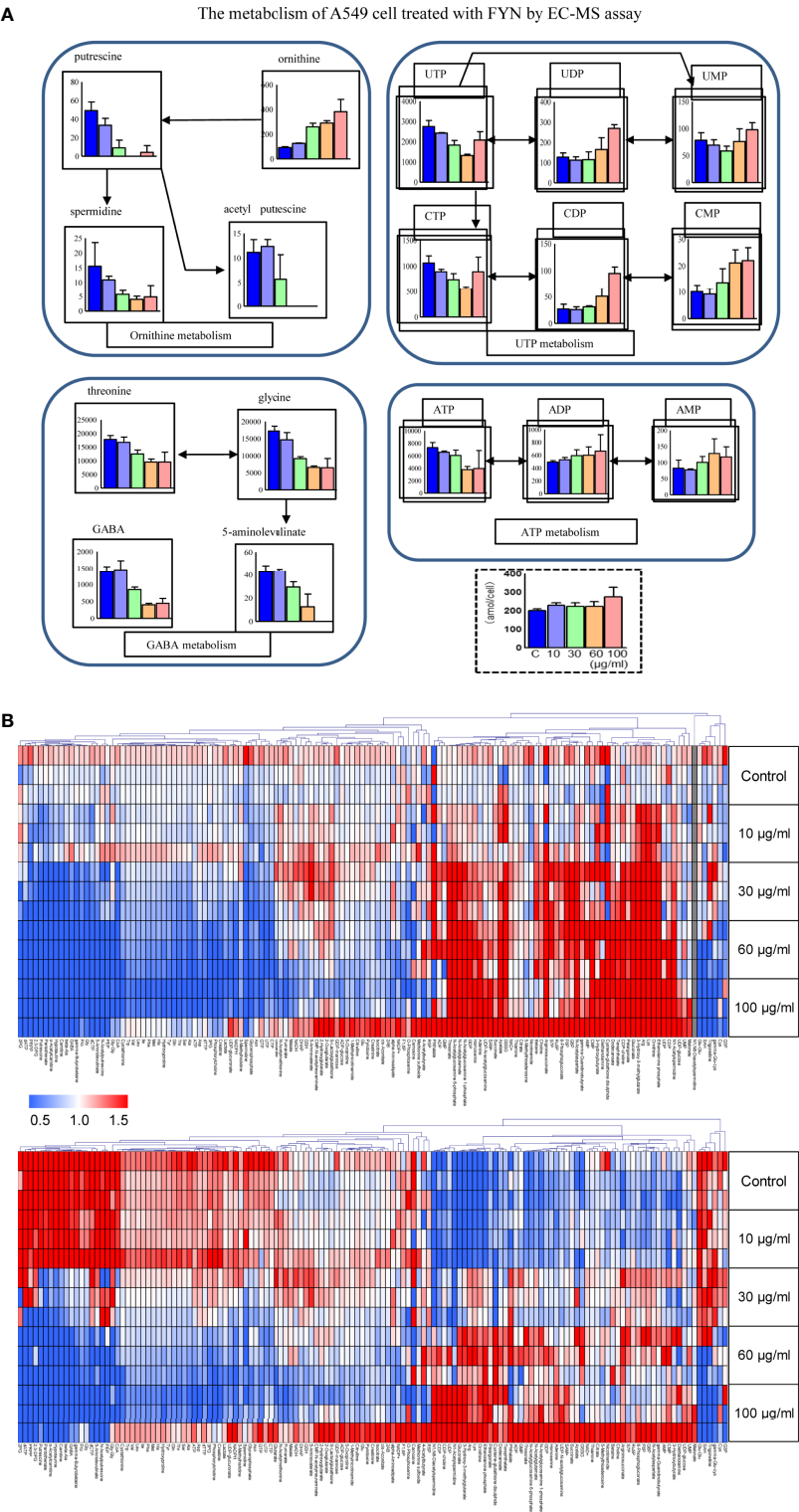


**FIGURE 6 |** Metabolomics analyses of A549 cells treated with FYN. **(A)** Changes in common cellular metabolites in A549 cells were measured using CE-MS assay after the indicated treatments. A549 cells were treated with different concentrations of FYN (10, 30, 60, 100 µg/ml) for 24 h, and CE-MS was performed to measure cell metabolites (amol/cell). **(B)** Metabolome heat map. Blue, white, and red indicate the fold changes of 0, 1, and 2, respectively, compared to the average of control samples. For undetectable substances in the control group, the half value of the minimum concentration of all samples was used.

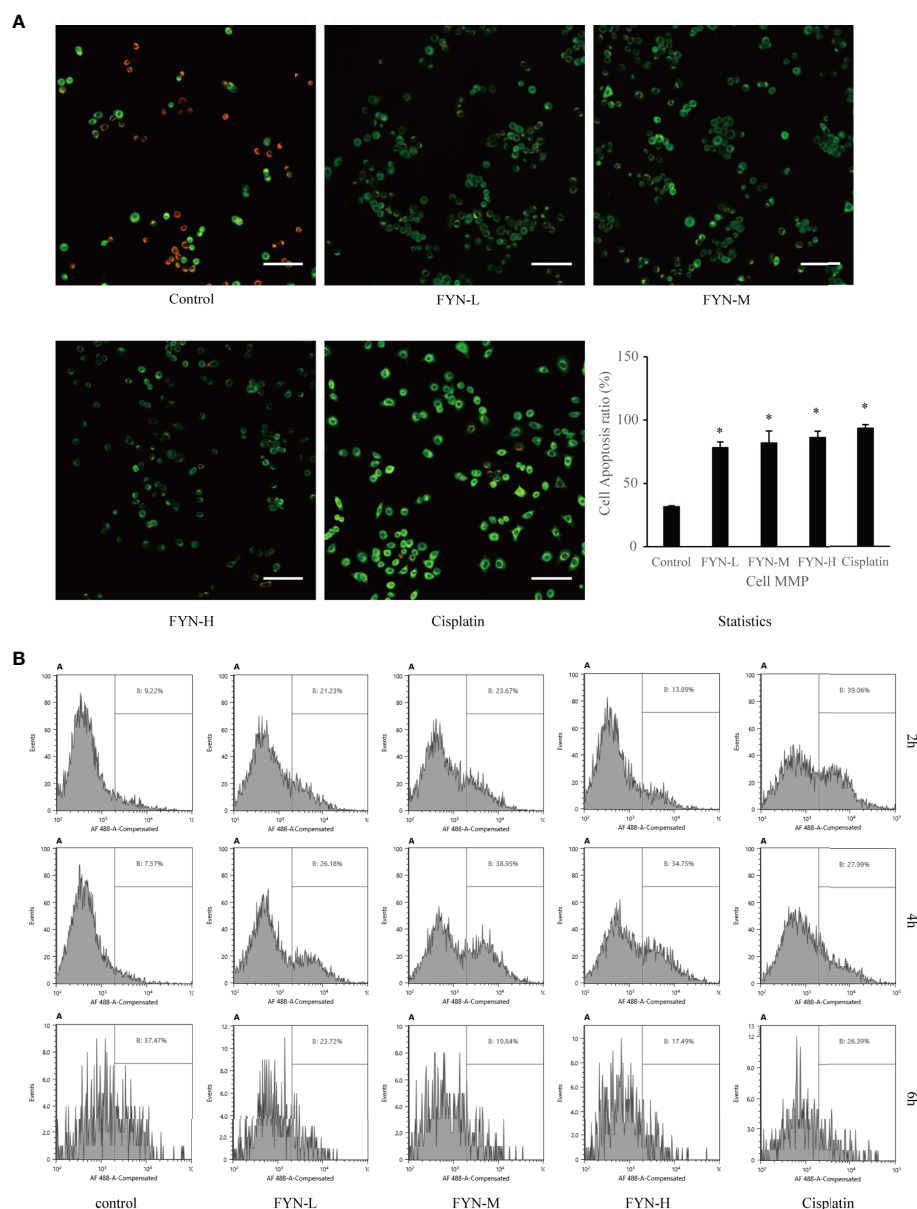


**FIGURE 7** | Mitochondrial membrane potential and calreticulin surface expression of A549 cells treated with FYN. **(A)** FYN induces mitochondrial depolarization in A549 cells. A549 cells were treated with different concentrations of FYN for 6 h, and MMP was assessed using JC-1 staining (scale bar: 100  $\mu$ m). \*Significant difference from the value of control group ( $p < 0.05$ ). **(B)** Surface translocation of calreticulin in A549 cells treated with FYN. Flow cytometric profiles of calreticulin staining in A549 cells after the indicated treatments with control, FYN, or cisplatin.

of A549 cells induced significant and dose-dependent decreases in membrane mitochondrial potentials, comparable to cisplatin (**Figure 7A**).

### The Effect of FYN on Calreticulin Surface Expression

Cellular stress can result in the altered distribution of some intracellular proteins including calreticulin to the cell surface (15). To determine if FYN-induced cell injury causes the translocation of calreticulin to the cell surface, we used a flow cytometric assay. As shown in **Figure 7B**, the surface expression

of calreticulin in A549 cells was significantly higher than the untreated control group after FYN treatment, albeit less prominent than after cisplatin treatment (**Figure 7B**).

## DISCUSSION

Lung cancer is the fastest growing malignant tumor in China in terms of morbidity and mortality, which seriously threatens the life of patients (16). Toxicity-based side effects of Western medicines

are very common, and drug resistance often develops during repeated courses of treatment. In recent years, targeted therapies and immunotherapy have emerged, but drug resistance still occurs, and the high costs limit availability to many patients. These factors limit the application of cutting-edge Western medicines, particularly in developing countries. The increasing prosperity of China allows more treatment options, but nonetheless, the use of TCM remains high, even in younger generations. Therefore, there is a need to rationally determine the effectiveness and mechanism of action of TCM formulations (17).

FYN has established benefits for the treatment of NSCLC. Previous clinical studies showed that FYN combined with conventional chemotherapy improves reductions in serum tumor biomarkers CA125 and CYFRA21-1, reduces the impact of chemotherapy on the level of peripheral blood lymphocytes, and improves cancer-related fatigue and quality of life scores of patients (18, 19). The clinical effectiveness and disease control rates using FYN were significantly better than those of placebo (20). Our previous basic experiments established that FYN combined with chemotherapeutic drugs induces apoptosis in lung cancer cells (21) and moreover, downregulates the side population (SP) of lung cancers cells, which was reflected by the inhibition of ABCG2 protein expression (22). Furthermore, FYN can inhibit the invasion of A549 lung cancer cells by downregulating Malat1 to inhibit the Wnt/ $\beta$ -catenin/EMT signaling axis (23). In this study, we firstly predicted the possible action pathway of FYN through network pharmacology of traditional Chinese medicine, and then demonstrated the direct anticancer effect and its pathway of FYN through *in vitro* experiments. We now build on this foundation to provide a more detailed assessment of the anticancer effects of FYN.

We first completed the compound collection involved in FYN, disease target collection, compound target prediction, and KEGG pathway enrichment analysis. It was found that the main targets of FYN were related to the apoptosis of lung cancer cells (24–34) and predicted that the inhibition of FYN on lung cancer growth may be related to the mitochondrial pathway, and then performed *in vitro* experiments. The result showed that in the four representative subtypes of lung cancer, the A549 adenocarcinoma cells were most sensitive to inhibition of cell proliferation by FYN, while FYN inhibited the growth of the WA-hT small cell carcinoma to a lesser extent. Indeed, cell proliferation assays indicated reductions in cell number, possibly by apoptosis, known as physiological process of autonomous cell death. Subsequently, we confirmed that FYN induces cell cycle arrest in the G<sub>2</sub>/M phase resulting in apoptosis. Apoptotic changes were evident as early as 6 h after treatment and notably, the rates of apoptosis at 48 h were similar for 200  $\mu$ g/ml dose of FYN and the established cytotoxic agent cisplatin. Thus, FYN alone can induce cell cycle arrest and apoptosis in lung cancer cells.

The mitochondria act as the “power house” of cells because of their role in producing energy through aerobic respiration (35). Cellular apoptosis can proceed through the extrinsic and intrinsic pathways, the latter often called the mitochondrial

apoptotic pathway (36). When cells are stimulated by DNA damage and/or ATP depletion, mitochondrial membrane swelling and increased permeability can occur to cause the irreversible activation of apoptosis (37). Here mitochondrial stress, defined as the loss of mitochondrial membrane potential, is a key event determining the fate of cells (38). We show here that one of the actions of FYN was the depolarization of mitochondrial membrane potential. Mitochondrial stress signals to activate calcineurin, and many Ca<sup>2+</sup> response factors, including RYR1, calreticulin, and calcium chelating, are upregulated, as shown in our study (39). Thus, the induction of apoptosis in A549 cells which accompanies the inhibition of cell proliferation by FYN involves the mitochondrial pathway. Accompanying metabonomic profiling of these cells also provided evidence of widespread disturbances in metabolism. FYN decreased the polyamines such as putrescine and spermidine, which is related to growth stimulation (40), accompanied by apoptosis induction. Since apoptosis is an energy-dependent process, an increase in ATP may stimulate the execution of apoptosis (41). This point was further potentiated by our finding that FYN increased the ATP utilization, which is necessary for apoptosis induction.

Finally, we explored the effect of FYN on the translocation of calreticulin to the cell surface. Calreticulin is a calcium binding protein in the endoplasmic reticulum which affects a variety of vital homeostatic processes and plays important roles in cell proliferation, differentiation, and apoptosis (42). Calreticulin is mutated or downregulated in a variety of tumors, and the loss of its function is closely associated with the progression of tumors and the poor treatment prognosis (43). Calreticulin, also known as angiostatin, can inhibit the formation of microvessels and inhibit the growth of tumors. Cellular stress conditions including apoptosis can result in the altered distribution of calreticulin to the cell surface (44). This has also been proposed to facilitate the clearance of dead and dying tumor cells by phagocytes (45). We found that the localization of calreticulin on the cell surface significantly increased, suggesting that calreticulin exposure through FYN-mediated apoptosis may contribute to its anti-cancer properties. However, to determine whether FYN-induced cell injury can prime the lung cancer cells' removal or can inhibit the blood vessel growth requires further investigation.

In conclusion, we found that FYN can directly induce apoptosis in human lung cancer cells by promoting energy metabolism and change in mitochondrial membrane potential changes. This study provides a rational basis for further investigations on the use of FYN for the treatment of non-small cell lung cancer and other cancers. This finding further supports the validity of network pharmacological prediction.

## DATA AVAILABILITY STATEMENT

The original contributions presented in the study are included in the article/Supplementary Material. Further inquiries can be directed to the corresponding authors.



## AUTHOR CONTRIBUTIONS

L-MZ was responsible for the design and drafting of the article. L-MZ and H-XS acquired, analyzed, and interpreted the data. H-BD provided FYN lyophilized powder. L-MZ, H-XS, MS, KB, HS, and SA participated in data analysis and paper revision of cell experiments. Q-YY, YG, and X-LX were involved in checking the details of the paper format. H-XS and Z-YX gave the final approval and overall responsibility for the published work. All authors contributed to the article and approved the submitted version.

## FUNDING

The research was funded by the Shanghai Science and Technology Commission Development Foundation, award number is 16ZR1437500; the Shanghai Health and Family Planning Commission of Medical Science and Technology

Innovation Project, award number is ZYKC201701009; and The project of “the Sixth Batch of Inheritance of Academic Experience of National Old Chinese Medicine Experts” of the State Administration of Traditional Chinese Medicine, award number is zyryjf [2017] No. 29.

## ACKNOWLEDGMENTS

The authors would like to appreciate all the participating centers and members.

## SUPPLEMENTARY MATERIAL

The Supplementary Material for this article can be found online at: <https://www.frontiersin.org/articles/10.3389/fonc.2021.690878/full#supplementary-material>

## REFERENCES

- Romaszko AM, Doboszynska A. Multiple Primary Lung Cancer: A Literature Review. *Adv Clin Exp Med* (2018) 27(5):725–30. doi: 10.17219/acem/68631
- Ettinger DS, Wood DE, Aisner DL, Akerley W, Bauman J, Chirieac LR, et al. Non-Small Cell Lung Cancer, Version 5.2017, NCCN Clinical Practice Guidelines in Oncology. *J Natl Compr Canc Netw* (2017) 15(4):504–35. doi: 10.6004/jnccn.2017.0050
- Duma N, Santana-Davila R, Molina JR. Non-Small Cell Lung Cancer: Epidemiology, Screening, Diagnosis, and Treatment. *Mayo Clin Proc* (2019) 94(8):1623–40. doi: 10.1016/j.mayocp.2019.01.013
- Rafei H, El-Bahesh E, Finianos A, Nassereldine S, Tabbara I. Immune-Based Therapies for Non-Small Cell Lung Cancer. *Anticancer Res* (2017) 37(2):377–87. doi: 10.21873/anticancer.11330
- Xiang M, Li R, Zhang Z, Song X. Advances in the Research of the Regulation of Chinese Traditional Medicine Monomer and Its Derivatives on Autophagy in Non-Small Cell Lung Cancer. *Zhongguo Fei Ai Za Zhi* (2017) 20(3):205–12. doi: 10.3779/j.issn.1009-3419.2017.03.10
- Liao YH, Li CL, Lin CC, Lin JG, Chiang JH, Li TC. Traditional Chinese Medicine as Adjunctive Therapy Improves the Long-Term Survival of Lung Cancer Patients. *J Cancer Res Clin Oncol* (2017) 143(12):2425–35. doi: 10.1007/s00432-017-2491-6
- Gong Y, Xu Z, Jin C, Deng H, Wang Z, Zhou W, et al. Treatment of Advanced Non-Small-Cell Lung Cancer With Qi-Nourishing Essence-Replenishing Chinese Herbal Medicine Combined With Chemotherapy. *Biol Proced Online* (2018) 20:9. doi: 10.1186/s12575-018-0074-9
- Soga T, Igarashi K, Ito C, Mizobuchi K, Zimmermann HP, Tomita M. Metabolomic Profiling of Anionic Metabolites by Capillary Electrophoresis Mass Spectrometry. *Anal Chem* (2009) 81(15):6165–74. doi: 10.1021/ac900675k
- Traitcheva N, Berg H. Electroporation and Alternating Current Cause Membrane Permeation of Photodynamic Cytotoxins Yielding Necrosis and Apoptosis of Cancer Cells. *Bioelectrochemistry* (2010) 79(2):257–60. doi: 10.1016/j.bioelectrochem.2010.02.005
- Kupcho K, Shultz J, Hurst R, Hartnett J, Zhou W, Machleidt T, et al. A Real-Time, Bioluminescent Annexin V Assay for the Assessment of Apoptosis. *Apoptosis* (2019) 24(1–2):184–97. doi: 10.1007/s10495-018-1502-7
- Garcia-Contreras R, Sugimoto M, Umemura N, Kaneko M, Hatakeyama Y, Soga T, et al. Alteration of Metabolomic Profiles by Titanium Dioxide Nanoparticles in Human Gingivitis Model. *Biomaterials* (2015) 57:33–40. doi: 10.1016/j.biomaterials.2015.03.059
- Yan Z, Lai Z, Lin J. Anticancer Properties of Traditional Chinese Medicine. *Comb Chem High Throughput Screen* (2017) 20(5):423–9. doi: 10.2174/1386207320666170116141818
- Balachandran C, Sangeetha B, Duraipandiyar V, Raj MK, Ignacimuthu S, Al-Dhabi NA, et al. A Flavonoid Isolated From *Streptomyces* Sp. (ERINLG-4) Induces Apoptosis in Human Lung Cancer A549 Cells Through p53 and Cytochrome C Release Caspase Dependant Pathway. *Chem Biol Interact* (2014) 224:24–35. doi: 10.1016/j.cbi.2014.09.019
- Wang TL, Ouyang CS, Lin LZ. beta-Asarone Suppresses Wnt/beta-catenin Signaling to Reduce Viability, Inhibit Migration/Invasion/Adhesion and Induce Mitochondria-Related Apoptosis in Lung Cancer Cells. *BioMed Pharmacother* (2018) 106:821–30. doi: 10.1016/j.biopha.2018.07.009
- Wang YJ, Fletcher R, Yu J, Zhang L. Immunogenic Effects of Chemotherapy-Induced Tumor Cell Death. *Genes Dis* (2018) 5(3):194–203. doi: 10.1016/j.gendis.2018.05.003
- Hong QY, Wu GM, Qian GS, Hu CP, Zhou JY, Chen LA, et al. Prevention and Management of Lung Cancer in China. *Cancer* (2015) 121 Suppl 17:3080–8. doi: 10.1002/cnrc.29584
- Li JX, Huang JM, Jiang ZB, Li RZ, Sun A, Lai-Han Leung E, et al. Current Clinical Progress of PD-1/PD-L1 Immunotherapy and Potential Combination Treatment in Non-Small Cell Lung Cancer. *Integr Cancer Ther* (2019) 18:1534735419890020. doi: 10.1177/1534735419890020
- Liu C, Zhao XZ, Wang ZQ, Deng HB, Cai YJ, Xu ZY. Clinical Study on Feiyanning Recipe Combined With Kangliu Zengxiao Recipe on Cancer-Related Fatigue, Immune Function and Tumor Markers in Patients With Intermediate-Terminal Lung Adenocarcinoma After Chemotherapy. *Shanghai J Tradit Chin Med* (2019) 53(6):49–53. doi: 10.16305/j.1007-1334.2019.06.013
- Xu ZY, Jin CJ, Zhou CC, Wang ZQ, Zhou WD, Deng HB, et al. Treatment of Advanced Non-Small-Cell Lung Cancer With Chinese Herbal Medicine by Stages Combined With Chemotherapy. *J Cancer Res Clin Oncol* (2011) 137(7):1117–22. doi: 10.1007/s00432-011-0975-3
- Wang LF, Cai YJ, Zhou H, Xu ZY, Wang ZQ, Deng HB, et al. Clinical Study of Feiyanning Granule in the Treatment of Advanced Lung Adenocarcinoma With Syndrome of Deficiency of Both Essence and Qi. *Shanghai J Tradit Chin Med* (2018) 52(4):49–52. doi: 10.16305/j.1007-1334.2018.04.014
- Zheng Z, Ma Y, Wang LF, Deng HB, Wang ZQ, Li JW, et al. Chinese Herbal Medicine Feiyanning Cooperates With Cisplatin to Enhance Cytotoxicity to Non-Small-Cell Lung Cancer by Inhibiting Protective Autophagy. *J Ethnopharmacol* (2021) 276(8):114196. doi: 10.1016/j.jep.2021.114196
- Zheng Z, Ma Y, Wang Q, Xu ZY. Feiyanning Down-Regulates the Side Population of Lung Cancer Cells and Its Selective Anti-Cancer Mechanism. *Tumor* (2018) 38(8):742–49. doi: 10.3781/j.issn.1000-7431.2018.11.195
- Kang XH, Wang Y, Cui HY, Kou WZ, Cao F, Miao ZH, et al. Mechanism Study on FYN Inhibiting Invasion of A549 Lung Cancer Cells by Regulating

- MALAT1. *Shanghai J Tradit Chin Med* (2019) 53(03):77–82. doi: 10.16305/j.1007-1334.2019.03.019
24. Wang M, Meng B, Liu Y, Yu J, Chen Q, Liu Y. Mir-124 Inhibits Growth and Enhances Radiation-Induced Apoptosis in Non-Small Cell Lung Cancer by Inhibiting Stat3. *Cell Physiol Biochem* (2017) 44(5):2017–28. doi: 10.1159/000485907
  25. Lu C, Xiong M, Luo Y, Li J, Zhang Y, Dong Y, et al. Genome-Wide Transcriptional Analysis of Apoptosis-Related Genes and Pathways Regulated by H2AX in Lung Cancer A549 Cells. *Apoptosis* (2013) 18(9):1039–47. doi: 10.1007/s10495-013-0875-x
  26. Hu J, Wang H, Gu J, Liu X, Zhou X. Trail Armed Oncolytic Poxvirus Suppresses Lung Cancer Cell by Inducing Apoptosis. *Acta Biochim Biophys Sin (Shanghai)* (2018) 50(10):1018–27. doi: 10.1093/abbs/gmy096
  27. Chatterjee P, Seal S, Mukherjee S, Kundu R, Bhuyan M, Barua NC, et al. A Carbazole Alkaloid Deactivates mTOR Through the Suppression of Rictor and That Induces Apoptosis in Lung Cancer Cells. *Mol Cell Biochem* (2015) 405(1–2):149–58. doi: 10.1007/s11010-015-2406-2
  28. Chou YT, Lee CC, Hsiao SH, Lin SE, Lin SC, Chung CH, et al. The Emerging Role of SOX2 in Cell Proliferation and Survival and Its Crosstalk With Oncogenic Signaling in Lung Cancer. *Stem Cells* (2013) 31(12):2607–19. doi: 10.1002/stem.1518
  29. Sun CC, Li SJ, Li DJ. Hsa-miR-134 Suppresses Non-Small Cell Lung Cancer (NSCLC) Development Through Down-Regulation of CCND1. *Oncotarget* (2016) 7(24):35960–78. doi: 10.18632/oncotarget.8482
  30. Liu H, Liang Y, Li Y, Li Y, Wang J, Wu H, et al. Gene Silencing of BAG-1 Modulates Apoptotic Genes and Sensitizes Lung Cancer Cell Lines to Cisplatin-Induced Apoptosis. *Cancer Biol Ther* (2010) 9(10):832–40. doi: 10.4161/cbt.9.10.11589
  31. Oh HN, Lee MH, Kim E, Yoon G, Chae JI, Shim JH. Licochalcone B Inhibits Growth and Induces Apoptosis of Human Non-Small-Cell Lung Cancer Cells by Dual Targeting of EGFR and MET. *Phytomedicine* (2019) 63:153014. doi: 10.1016/j.phymed.2019.153014
  32. Zhao X, Wu X, Wang H, Yu H, Wang J. USP53 Promotes Apoptosis and Inhibits Glycolysis in Lung Adenocarcinoma Through FKBP51-AKT1 Signaling. *Mol Carcinog* (2020) 59(8):1000–11. doi: 10.1002/mc.23230
  33. Li X, Liu X, Xu Y, Liu J, Xie M, Ni W, et al. KLF5 Promotes Hypoxia-Induced Survival and Inhibits Apoptosis in Non-Small Cell Lung Cancer Cells via HIF-1 $\alpha$ . *Int J Oncol* (2014) 45(4):1507–14. doi: 10.3892/ijo.2014.2544
  34. Vaikundamoorthy R, Sundaramoorthy R, Krishnamoorthy V, Vilwanathan R, Rajendran R. Marine Steroid Derived From Acropora Formosa Enhances Mitochondrial-Mediated Apoptosis in Non-Small Cell Lung Cancer Cells. *Tumour Biol* (2016) 37(8):10517–31. doi: 10.1007/s13277-016-4947-8
  35. Chan DC. Mitochondrial Dynamics and Its Involvement in Disease. *Annu Rev Pathol* (2020) 15:235–59. doi: 10.1146/annurev-pathmechdis-012419-032711
  36. Whitley BN, Engelhart EA, Hoppins S. Mitochondrial Dynamics and Their Potential as a Therapeutic Target. *Mitochondrion* (2019) 49:269–83. doi: 10.1016/j.mito.2019.06.002
  37. Ganta KK, Mandal A, Chaubey B. Depolarization of Mitochondrial Membrane Potential Is the Initial Event in Non-Nucleoside Reverse Transcriptase Inhibitor Efavirenz Induced Cytotoxicity. *Cell Biol Toxicol* (2017) 33(1):69–82. doi: 10.1007/s10565-016-9362-9
  38. Hussain S. Measurement of Nanoparticle-Induced Mitochondrial Membrane Potential Alterations. *Methods Mol Biol* (2019) 1894:123–31. doi: 10.1007/978-1-4939-8916-4\_7
  39. Biswas G, Guha M, Avadhani NG. Mitochondria-to-Nucleus Stress Signaling in Mammalian Cells: Nature of Nuclear Gene Targets, Transcription Regulation, and Induced Resistance to Apoptosis. *Gene* (2005) 354:132–9. doi: 10.1016/j.gene.2005.03.028
  40. Park MH, Igarashi K. Polyamines and Their Metabolites as Diagnostic Markers of Human Diseases. *Biomol Ther (Seoul)* (2013) 21(1):1–9. doi: 10.4062/biomolther.2012.097
  41. Halestrap A. Biochemistry: A Pore Way to Die. *Nature* (2005) 434(7033):578–9. doi: 10.1038/434578a
  42. Sun J, Mu H, Dai K, Yi L. Calreticulin: A Potential Anti-Cancer Therapeutic Target. *Pharmazie* (2017) 72(9):503–10. doi: 10.1691/ph.2017.7031
  43. Zamanian M, Veerakumarasivam A, Abdullah S, Rosli R. Calreticulin and Cancer. *Pathol Oncol Res* (2013) 19(2):149–54. doi: 10.1007/s12253-012-9600-2
  44. Scholnik-Cabrera A, Oldak B, Juarez M, Cruz-Rivera M, Flisser A, Mendlovic F. Calreticulin in Phagocytosis and Cancer: Opposite Roles in Immune Response Outcomes. *Apoptosis* (2019) 24(3–4):245–55. doi: 10.1007/s10495-019-01532-0
  45. Lopez J, Tait SW. Mitochondrial Apoptosis: Killing Cancer Using the Enemy Within. *Br J Cancer* (2015) 112(6):957–62. doi: 10.1038/bjc.2015.85

**Conflict of Interest:** The authors declare that the research was conducted in the absence of any commercial or financial relationships that could be construed as a potential conflict of interest.

The reviewer XZ declared a shared affiliation with one of the authors, H-XS, to the handling editor at time of review.

Copyright © 2021 Zhu, Shi, Sugimoto, Bandow, Sakagami, Amano, Deng, Ye, Gai, Xin and Xu. This is an open-access article distributed under the terms of the Creative Commons Attribution License (CC BY). The use, distribution or reproduction in other forums is permitted, provided the original author(s) and the copyright owner(s) are credited and that the original publication in this journal is cited, in accordance with accepted academic practice. No use, distribution or reproduction is permitted which does not comply with these terms.



# Exploring the Significance of the Exon 4-Skipping Isoform of the ZNF217 Oncogene in Breast Cancer

Aurélie Bellanger<sup>1,2†</sup>, Diep T. Le<sup>1,3†</sup>, Julie Vendrell<sup>4</sup>, Anne Wierinckx<sup>1,2,5</sup>, Lőrinc S. Pongor<sup>6,7</sup>, Jérôme Solassol<sup>4,8</sup>, Joël Lachuer<sup>1,2,5</sup>, Philippe Clezardin<sup>1,3</sup>, Balázs Györfy<sup>6,7</sup> and Pascale A. Cohen<sup>1,2,3,5\*</sup>

## OPEN ACCESS

### Edited by:

Olivier Cuvillier,  
UPR8241 Laboratoire de Chimie de  
Coordination (LCC), France

### Reviewed by:

Qing Cong,  
Fudan University, China  
Paul Yaswen,  
Lawrence Berkeley National  
Laboratory, United States

### \*Correspondence:

Pascale A. Cohen  
pascale.cohen@univ-lyon1.fr

<sup>†</sup>These authors have contributed  
equally to this work

### Specialty section:

This article was submitted to  
Pharmacology of  
Anti-Cancer Drugs,  
a section of the journal  
Frontiers in Oncology

Received: 29 January 2021

Accepted: 31 May 2021

Published: 02 July 2021

### Citation:

Bellanger A, Le DT, Vendrell J,  
Wierinckx A, Pongor LS, Solassol J,  
Lachuer J, Clezardin P, Györfy B  
and Cohen PA (2021) Exploring  
the Significance of the Exon  
4-Skipping Isoform of the ZNF217  
Oncogene in Breast Cancer.  
Front. Oncol. 11:647269.  
doi: 10.3389/fonc.2021.647269

<sup>1</sup> Université Lyon 1, Lyon, France, <sup>2</sup> CRCL-Centre de Recherche en Cancérologie de Lyon-Inserm U1052-CNRS U5286, Lyon, France, <sup>3</sup> INSERM, UMR1033 LYOS, Lyon, France, <sup>4</sup> Département de Pathologie et Oncobiologie, Laboratoire de Biologie des Tumeurs Solides, CHU Montpellier, Univ. Montpellier, Montpellier, France, <sup>5</sup> ProfileXpert, SFR-Est, CNRS UMR-S3453, INSERM US7, Lyon, France, <sup>6</sup> Department of Bioinformatics, Semmelweis University, Budapest, Hungary, <sup>7</sup> TTK "TermészetTudományi Kutatóközpont" Momentum Cancer Biomarker Research Group, Institute of Enzymology, Budapest, Hungary, <sup>8</sup> Institut de Recherche en Cancérologie de Montpellier (IRCM), INSERM U1194, Univ. Montpellier, Montpellier, France

Oncogene alternative splicing events can create distinct functional transcripts that offer new candidate prognostic biomarkers for breast cancer. ZNF217 is a well-established oncogene but its exon 4-skipping isoform (ZNF217- $\Delta$ E4) has never been investigated in terms of clinical or biological relevance. Using *in silico* RNA-seq and RT-qPCR analyses, we demonstrated for the first time the existence of ZNF217- $\Delta$ E4 transcripts in primary breast tumors, and a positive correlation between ZNF217- $\Delta$ E4 mRNA levels and those of the wild-type oncogene (ZNF217-WT). A pilot retrospective analysis revealed that, in the Luminal subclass, the combination of the two ZNF217 variants (the ZNF217- $\Delta$ E4-WT gene-expression signature) provided more information than the mRNA expression levels of each isoform alone. Ectopic overexpression of ZNF217- $\Delta$ E4 in breast cancer cells promoted an aggressive phenotype and an increase in ZNF217-WT expression levels that was inversely correlated with DNA methylation of the ZNF217 gene. This study provides new insights into the possible role of the ZNF217- $\Delta$ E4 splice variant in breast cancer and suggests a close interplay between the ZNF217-WT and ZNF217- $\Delta$ E4 isoforms. Our data suggest that a dual signature combining the expression levels of these two isoforms may serve as a novel prognostic biomarker allowing better stratification of breast cancers with good prognosis and aiding clinicians in therapeutic decisions.

**Keywords:** ZNF217, isoform, splice variant, prognosis, breast cancer

**Abbreviations:** ZNF217-WT, ZNF217 wild-type; ZNF217- $\Delta$ E4, exon 4-skipping ZNF217 isoform; E3, exon 3; E3-E4, exon 3 – exon 4 junction; E3 – E5, exon 3 – exon 5 junction; ER, Estrogen Receptor alpha; ER-, ER-negative; HER2, Human epidermal growth factor receptor 2; PR, Progesterone receptor; RT-qPCR, Real-Time quantitative Polymerase Chain Reaction; RFS, relapse free survival; ASE, alternative splicing events; KLF, Krüppel-like factor; AA, amino acids; SBR grade, Scarff-Bloom-Richardson grade.

## INTRODUCTION

Breast cancer is the most frequent cancer in women, with an estimated 2.2 million new cases being diagnosed in 2020 worldwide, and the leading cause of cancer death in women (> 684,000 cases in 2020) (1). The *ZNF217* gene is located on chromosome 20q13.2, a region frequently amplified in many tumors, including those of the breast (2). The encoded protein is an oncogenic transcription factor belonging to the Krüppel-like zinc finger transcription factors family. Previous studies highlighted that the *ZNF217* oncogene is involved in both early and late stages of tumor progression [for review (3)]. Our previous work contributed to the demonstration that breast cancer cells possessing high *ZNF217* expression levels display a more aggressive phenotype (e.g. increased cell proliferation, increased invasive properties and resistance to chemotherapy) (4, 5). High *ZNF217* mRNA levels in primary breast tumors are also of bad prognosis and associated with shorter relapse free survival (RFS) and metastasis development (5, 6), with the most discriminatory prognostic power observed in Luminal breast cancers (7).

Alternative splicing is now considered as a hallmark of cancer (8), participating in tumor progression through the expression of distinct isoforms. Key splicing events targeting important factors in tumorigenesis have been identified in breast cancer (e.g., *TP53*, *HER2*, *BRCA1*, *FGFR*, *BIRC5/survivin*,...). Alternative splicing events (ASE) in breast cancer thus represent candidate biomarkers and candidate therapeutic targets [for review (9)]. Considering the *ZNF217* oncogene, only little is known about the existence of its splice variants. In the original study discovering the human *ZNF217* gene (2), the *in silico* alignment of cDNAs from colon carcinoma and HeLa cell lines suggested a possible alternative processing of the 133-base pairs exon 4. The corresponding putative exon 4-skipping *ZNF217* (*ZNF217-ΔE4*) mRNA would encode for a *ZNF217* protein isoform with a C-terminus sequence [1013-1061 amino acids (aa)] distinct from that of *ZNF217* wild-type (*ZNF217-WT*) protein (1013-1048 aa sequence) (2). Nevertheless, since the original description (2), the *ZNF217-ΔE4* variant has never been studied, either in terms of expression in human tumor samples or in terms of biological relevance.

Considering the key role of the *ZNF217* oncogene in breast cancer and its strong biomarker value, the *ZNF217-ΔE4* transcript is thus of utmost interest. The main objectives of the present work were to newly investigate: (i) whether *ZNF217-ΔE4* is expressed in primary breast cancers; (ii) if so, whether *ZNF217-ΔE4* mRNA levels possess any clinical relevance; and (iii) whether increased expression levels of *ZNF217-ΔE4* functionally affect the phenotype of breast cancer cells.

By performing *in silico* RNAseq and real-time quantitative polymerase chain reaction (RT-qPCR) investigations, our study highlights the existence of *ZNF217-ΔE4* transcripts in primary breast tumors. Interestingly, *ZNF217-ΔE4* mRNA levels were significantly correlated with those of *ZNF217-WT* in tumor samples. A pilot retrospective analysis revealed that, in the Luminal subclass, the combination of the two *ZNF217* variants (the *ZNF217-ΔE4-WT* gene-expression signature) provided

more information than the mRNA expression levels of each isoform alone. Strikingly, the ectopic overexpression of *ZNF217-ΔE4* in breast cancer cells led to: (i) a more aggressive phenotype, similar to that previously observed with *ZNF217-WT* (4, 5); (ii) increased expression of endogenous *ZNF217-WT*; and (iii) decreased DNA methylation on key CpG sites within the *ZNF217* gene.

## MATERIALS AND METHODS

### Analysis of RNA-seq Data

A total of 1,097 RNA-seq aligned BAM files were obtained from the TCGA repository (10). Samples were filtered to include only primary tumor samples in women. The ratio of the exon 4 skipping isoform of the *ZNF217* gene in each sample was calculated based on the number of reads that had spliced alignments from exon 3 to exon 4 junction (E3-E4) compared to all reads mapped to the exon 3 to exon 5 junction (E3-E5). The ratio was used to quantify the isoform expression from the DESeq2 normalized data for each sample separately. Expression for exon 3 was computed using the following formula:  $\text{Exon}_3\_DESeq = (\text{Exon}_3\_reads / \text{Total\_reads}) * \text{Gene\_DESeq}$ . A minimal expression of 1,000 was used as a cutoff to designate patients as those positive for the *ZNF217* exon 4-skipping isoform. Kruskal-Wallis test was used to compare breast cancer subclasses distribution. The correlation of expression was tested using the Pearson correlation coefficient. Statistical significance was set at  $p < 0.05$ .

### ZNF217 Isoforms Plasmid Constructs

The pcDNA6-*ZNF217-WT* plasmid has been previously described and established (4). The pcDNA6 plasmid (Invitrogen, Cergy Pontoise, Paris) containing *ZNF217* exon4 skipping isoform DNA sequence (pcDNA6-*ZNF217-ΔE4*) was produced as follows: the DNA sequence specific for *ZNF217-ΔE4* was obtained after polymerase chain reaction (PCR) amplification from breast cancer cells using specific primers, then ligated into the restriction enzymes pre-digested pcDNA6-*ZNF217-WT* plasmid to replace the DNA region specific for *ZNF217-WT* with that of *ZNF217-ΔE4*.

### RT-qPCR Amplification of ZNF217 Isoforms

Total RNA extraction, reverse transcription, and RT-qPCR measurements were performed as described previously (4, 5). CFX96 equipment with the SsoAdvanced Universal SYBR green supermix (BioRad, Hercules, USA) was designed for RT-qPCR measurements, according to the manufacturer's recommendations. Specific primers were used to amplify the DNA sequence for *ZNF217* isoforms. The 5'-AGTCCAAATCCCTGCCATCT-3' and 5'-GGGGAAACACTGGTTTTAGG-3' primers amplify a region within exon 3 (E3). The 5'-CTCGACGTTAGAAGGAAAAAG-3' and 5'-TGGTCGATAATGTGCATTCC-3' primers were used to explore *ZNF217-WT* (exon 3 – exon 4 junction, E3-E4). The 5'-GTGGCTGACTGTTTCAGAAAGCCC-3' and 5'-GACATCCA CCAAGACCTTCTA-3' primers are specific for the *ZNF217-ΔE4*



isoform (exon 3 – exon 5 junction, E3-E5). For investigation in breast tumor samples and MDA-MB-231 stable transfectants, all measurements were normalized to the ribosomal 28S gene expression using the 5'-CGATCCATCATCCGCAATG-3' and 5'-AGCCAAGCTCAGCGCAAC-3' primers.

## Primary Breast Tumor Cohort

Women with primary breast tumors (n = 107) and known clinical follow-up who had not received any therapy before surgery and who relapsed, or not, while receiving endocrine therapy and/or chemotherapy were recruited from the BB-0033-00050, Biological Resources Center (CRB) Centre Léon Bérard, Lyon France (**Supplementary Table 1**). This study has been approved by the local ethics committee (CRB Centre Léon Bérard, France). The CRB Centre Léon Bérard is quality certified according to NFS96-900 French standard and ISO 9001 for clinical trials, ensuring scientific rigor for sample conservation, traceability, and quality, as well as ethical rules observance and defined rules for transferring samples for research purposes (Ministry of Health for activities authorization no AC-2019-3426 and DC-2008-99). The material used in the study has been collected in agreement with all applicable laws, rules, and requests of French and European government authorities, including the patients' informed written consents. Extraction of total RNA from frozen tumor samples and RT-qPCR measurements were performed as previously described (5). Univariate (log-rank) analysis, multivariate analysis and all statistical analyses were performed using the SPSS<sup>TM</sup> Software (IBM, USA). For univariate analyses, the data were divided at the median value of *ZNF217-E3*, *ZNF217-WT* (E3-E4), or *ZNF217-ΔE4* (E3-E5) mRNA expression into two groups with either high or low expression levels. A  $p < 0.05$  was considered statistically significant.

## Establishment of MDA-MB-231- ZNF217-ΔE4 Stable Transfectants

MDA-MB-231 breast cancer cells were grown according to recommendations in DMEM medium supplemented with 10% fetal bovine serum (Invitrogen). MDA-MB-231 cells were stably transfected with pcDNA6 or pcDNA6-ZNF217-ΔE4 plasmids, then selected in the presence of 20 μg/ml blasticidin. MDA-MB-231-ZNF217-WT cells have been previously established (4, 5).

## Western Blotting

Western blot experiments were performed as previously described (5) with a commercial anti-ZNF217 antibody produced against a peptide comprised within the 1000-1048 aa sequence of ZNF217-WT (#48133; Abcam, Paris, France), a home-made rabbit polyclonal antibody directed against the C-terminus 1045-1060 aa sequence specific for ZNF217-ΔE4 isoform (RM217 Ab, Covalab, Lyon, France), the home-made polyclonal Cov-2 antibody directed against the C-terminus 1035-1048 aa sequence specific for ZNF217-WT isoform (Covalab) and anti-α-tubulin antibody (#T5168; Sigma, St Louis, MO, USA).

## Cell Proliferation

Cells (20,000 cells per well) were plated in triplicates into a 24-well plate then grown up to 96h. The medium was changed

every 2 days. Proliferating cells were analyzed using the Scepter<sup>TM</sup> 2.0 Cell Counter (Merck Millipore, Billerica, USA).

## Cytotoxicity Assay

As previously described (4), cells (8,000 cells per well) were plated onto a 96-well plate, treated for 4 days with  $10^{-12}$  to  $10^{-6}$  M of paclitaxel (Paxene<sup>®</sup>, Ivax, Miami, USA). Cell viability was assessed with the CellTiter 96 AQueous One Solution Cell Proliferation assay (Promega, Madison, WI, USA).

## Soft-Agar Colony-Formation Assay

The experiment was performed as previously described using 10,000 cells (11). Fifteen days later, the cells were stained with 0.005% Cristal violet (Sigma-Aldrich) for 1 h.

## Methylome

For each cell line, genomic DNA was extracted from two independent cell cultures using the QIAamp DNA mini kit (Qiagen, Hilden, Germany). The Illumina Infinium MethylationEPIC Beadchip was used to obtain DNA methylation profiles according to the manufacturer's instructions. Briefly, 500 ng of gDNA (QuantiFluor<sup>®</sup> dsDNA System, Promega) were bisulfite-modified using EZ-DNA Methylation-Gold Kit (Zymo Research) and then used for the genome-wide methylation assays. The iDat's files were obtained by scanning the array on iScan scanner (Illumina).

## Pyrosequencing Analysis

Genomic DNA (500 ng) was used in bisulfite conversion reactions with the EpiTect<sup>®</sup> Bisulfite Kit (Qiagen), according to the manufacturer's protocol. The bisulfite converted DNA was amplified using the PyroMark PCR kit (Qiagen) using the 5'-GTTATTTGTTAAGAAGTGAAGGAAT-3' and the 5'-biotin-CCTTACTACTAAATAACTTAAAATC-3' primers for the two following CpG: chr20:52198378 (cg01692482) and chr20:52198279 (cg00703481). PCR products were used for CpG quantification using a PyroMark Q24 (Qiagen) as the supplier's recommendation. The percentage of methylation of the two CpG sites was calculated using the PyroMark Q24 Advanced software (Qiagen).

## RESULTS

### *In Silico* RNA-seq Analysis Reveals the Expression of ZNF217 Exon 4-Skipping Isoform in Primary Breast Tumor Samples

RNA-seq files obtained from the TCGA repository (10) were used to decipher whether the *ZNF217-ΔE4* isoform is expressed in 1,097 primary breast tumors. Identification of reads mapped to the exon 3 to exon 4 junction (E3-E4) of the *ZNF217* gene corresponds to the expression of *ZNF217-WT* isoform in breast tumor samples. Our analysis further discovered spliced alignments from exon 3 to exon 5 (exon 4-skipping, E3-E5), revealing the expression of the *ZNF217-ΔE4* isoform in primary breast cancers. The distribution of *ZNF217-WT* (E3-E4) and

*ZNF217-ΔE4* (E3-E5) mRNA levels in the primary breast tumors highlighted that the *ZNF217-ΔE4* isoform mRNA expression levels are globally weaker than those of the *ZNF217-WT* isoform (Figures 1A, B). *ZNF217-ΔE4* expression levels ranged from 0 to

6,000, with 42.1% of the patients expressing the *ZNF217-ΔE4* isoform over 1,000, while *ZNF217-WT* expression levels ranged from 0 to 27,000 (Figures 1A, B). The *ZNF217-ΔE4* (E3-E5) expression levels represented more than 10% of *ZNF217-WT*

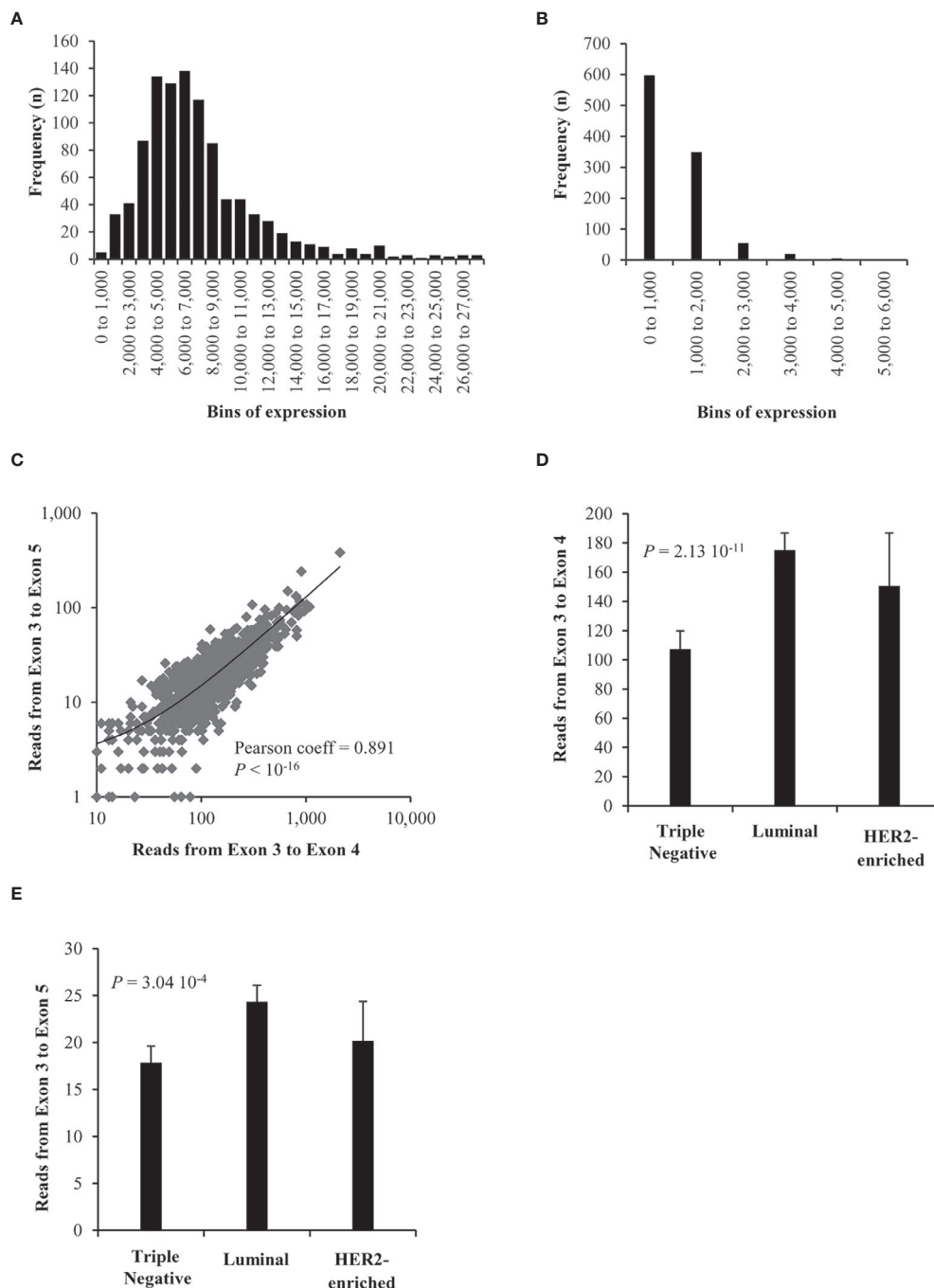


**FIGURE 1** | RNAseq expression of *ZNF217* isoforms in breast cancer. **(A)** *ZNF217-WT* (E3-E4) expression and **(B)** *ZNF217-ΔE4* (E3-E5) expression, in bins of thousands. **(C)** A high correlation was observed when correlating the expression of splice reads mapped to exon 3 – exon 5 junction versus those mapped to exon 3 – exon 4 junction. There is a significant expression difference between breast cancer molecular subtypes of both **(D)** exon 3 – exon 4 reads and **(E)** exon 3 – exon 5 reads.

expression levels in 76% of the patients (between 10% and 20% in 61.5% of the patients, and higher than 20% in 14.5% of the patients (data not shown)).

Importantly, **Figure 1C** reveals that *ZNF217-WT* (*E3-E4*) and *ZNF217-ΔE4* (*E3-E5*) mRNA levels are significantly positively correlated (Pearson coefficient = 0.891,  $p < 10^{-16}$ ). The 1,097 patients were then stratified according to molecular subtypes into Luminal, Triple negative, HER2-enriched subclasses (12–14). **Figures 1D, E** show that both *ZNF217-WT* (*E3-E4*) and *ZNF217-ΔE4* (*E3-E5*) display significant expression differences between the molecular subtypes ( $p = 2.13 \cdot 10^{-11}$  and  $p = 3.04 \cdot 10^{-4}$ , respectively, Kruskal-Wallis test).

Altogether, the RNA-seq data analysis newly demonstrated: (i) the existence of the exon 4-skipping variant of the *ZNF217* oncogene in primary breast cancers, expressed at weaker mRNA levels than those of *ZNF217-WT*; (ii) correlated mRNA expression levels of *ZNF217-ΔE4* and *ZNF217-WT* isoforms in primary breast tumor.

### Establishment of Primers for Specific RT-qPCR Investigation of *ZNF217* Isoforms

With the aim of further specifically investigating *ZNF217-ΔE4* (*E3-E5*) mRNA expression in clinical samples, three specific primer pairs were designed to discriminate the *ZNF217-WT* (*E3-E4*) and *ZNF217-ΔE4* (*E3-E5*) mRNA expression levels (**Supplementary Figure 1A**). The primer pair 1 amplifies within the sequence of *ZNF217*'s exon 3, a region common to both *ZNF217-WT* and *ZNF217-ΔE4* isoforms. The isoforms thus detected with primer pair 1 will be named *ZNF217-E3*. The primer pair 2 detects the *ZNF217-WT* isoform since the forward primer is located at the *E3-E4* junction. The primer pairs 3 detects *ZNF217-ΔE4* isoform, with the reverse primer hybridizing to the *E3-E5* junction. The PCR efficiency calculated from standard curves validated that the three primer pairs led to similar and high PCR efficiency values (data not shown).

RT-qPCRs were performed to assess the three primer pairs' specificity within a complex DNA mixture containing different proportions of pcDNA6-*ZNF217-WT* and/or pcDNA6-*ZNF217-ΔE4* plasmids. **Supplementary Figure 1B** shows a steady number of *ZNF217-E3* copies corresponding to a constant number of pcDNA6-*ZNF217* plasmids copies in the mixture. Importantly, primer pair 2 or primer pair 3 were able to discriminate and quantify the number of, respectively, pcDNA6-*ZNF217-WT* or pcDNA6-*ZNF217-ΔE4* copies actually deposited in the mixture (**Supplementary Figure 1B**). Altogether, these results validated that these pairs of primers are specific and sensitive for each isoform, even within a mixture of *ZNF217* isoforms.

### RT-qPCR Validation of *ZNF217-WT* and *ZNF217-ΔE4* Expression in an Independent Cohort of Primary Breast Tumors

We performed RT-qPCR analyses to explore *ZNF217-WT* (*E3-E4*) and *ZNF217-ΔE4* (*E3-E5*) mRNA expression levels in a cohort of 107 human primary breast tumor samples (**Supplementary**

**Table 1**). The patterns of distribution of *ZNF217-WT* (*E3-E4*) and *ZNF217-ΔE4* (*E3-E5*) mRNA levels over the 107 primary breast tumors (**Supplementary Figures 1C, D**) were very similar to those observed in **Figures 1A, B**. Overall, the *ZNF217-ΔE4* (*E3-E5*) mRNA levels were 6–8 fold weaker than those of *ZNF217-WT* (*E3-E4*) within a particular primary breast tumor (data not shown). The *ZNF217-ΔE4* (*E3-E5*) mRNA levels represented less than 10% of *ZNF217-WT* expression levels in 25% of the patients, 10–30% in 44% of the patients, and higher than 30% in 31% of the patients (data not shown). In accordance with what we have observed by RNAseq analyses, the RT-qPCR investigation found *ZNF217-WT* (*E3-E4*) and *ZNF217-ΔE4* (*E3-E5*) mRNA levels significantly and positively correlated (Pearson coefficient = 0.807,  $p < 10^{-4}$ ). Again, both *ZNF217-WT* (*E3-E4*) and *ZNF217-ΔE4* (*E3-E5*) isoforms display significant mRNA expression differences between the breast cancer molecular subtypes ( $p = 0.007$  and  $p = 0.056$ , respectively, Kruskal-Wallis Test, data not shown).

### The *ZNF217-ΔE4-WT* Gene Expression Signature Indicates Poor Prognosis in Luminal Breast Cancers

We have previously reported that high mRNA levels of *ZNF217* are of poor prognosis and represent an early indicator of relapse in breast cancer, with the most powerful prognostic value observed in Luminal subtypes (5, 7). However, at the time when those studies were conducted, the possible expression of the *ZNF217-ΔE4* isoform in breast tumors was unknown. The primer pair used in our previous studies (5, 7) targets exon 3 of the *ZNF217* gene (primer pair 1, *ZNF217-E3*), thus exploring in reality both *ZNF217-WT* and *ZNF217-ΔE4* mRNA expression levels. Taking advantage of the specificity of primer pair 2 and primer pair 3, we thus aimed at investigating in a pilot study the prognostic value of *ZNF217-WT* (*E3-E4*) and *ZNF217-ΔE4* (*E3-E5*) mRNA expression levels, alone or in combination, in the molecular subtypes of breast cancer.

In accordance with our previous work (5, 7), the present retrospective analysis of the cohort composed of 107 human primary breast tumor samples confirmed that high *ZNF217-E3* mRNA levels: (i) were significantly associated with shorter relapse free survival (RFS) in the whole cohort ( $p = 0.031$  **Table 1**) and in the Luminal subclass ( $p = 0.030$ , **Table 1** and **Supplementary Figure 2A**); (ii) were not informative in the HER2-enriched, or Triple negative subclasses (**Table 1**). In the whole cohort, *ZNF217-ΔE4* (*E3-E5*) mRNA levels were significantly associated with shorter RFS ( $p = 0.025$ , **Table 1**). In the Luminal subclass, high mRNA levels of *ZNF217-WT* (*E3-E4*) and high mRNA levels of *ZNF217-ΔE4* (*E3-E5*) did not reach significance after 10 years of retrospective analysis, while a tendency could be observed (**Table 1** and **Supplementary Figures 2B, C**). We then constructed a gene expression signature based on *ZNF217-WT* (*E3-E4*) and *ZNF217-ΔE4* (*E3-E5*) mRNA expression levels by dividing patients into three groups: patients who expressed low *ZNF217-WT* (*E3-E4*) and low *ZNF217-ΔE4* (*E3-E5*) mRNA levels (group 1); patients who expressed high *ZNF217-WT* (*E3-E4*) or high *ZNF217-ΔE4*

**TABLE 1 |** Univariate analyses (10 years-retrospective analysis) of the ZNF217 isoforms mRNA expression levels with regards to relapse-free survival.

	All tumor samples (n = 107)			Luminal subclass <sup>d</sup> (ER+ and/or PR+) (n = 72)			HER2-enriched subclass <sup>d</sup> (ER-/PR-/HER2+) (n = 15)			Triple negative subclass <sup>d</sup> (ER-/PR-/HER2-) (n = 20)		
	HR <sup>a</sup>	95% CI <sup>b</sup>	p <sup>c</sup>	HR <sup>a</sup>	95% CI <sup>b</sup>	p <sup>c</sup>	HR <sup>a</sup>	95% CI <sup>b</sup>	p <sup>c</sup>	HR <sup>a</sup>	95% CI <sup>b</sup>	p <sup>c</sup>
<b>ZNF217-E3 mRNA levels</b>	4.62	0.85-5.52	0.031	4.72	1.04-13.20	0.030	0.026	0.17-4.57	NS (0.872)	0.024	0.05-12.87	NS (0.876)
<b>ZNF217-WT (E3-E4) mRNA levels</b>	3.32	0.76-4.56	NS (0.068)	2.86	0.82-8.23	NS (0.091)	1.01	0.41-13.63	NS (0.314)	0.001	0.06-15.18	NS (0.970)
<b>ZNF217-ΔE4 (E3-E5) mRNA levels</b>	5.05	0.93-6.05	0.025	3.00	0.84-8.33	NS (0.083)	0.216	0.27-8.21	NS (0.642)	0.161	N/A <sup>e</sup>	NS (0.204)
<b>ZNF217-WT-ΔE4 signature</b>	5.12	0.95-8.29	0.024	5.11	1.07-21.23	0.023	1.54	0.41-30.84	NS (0.214)	1.296	N/A <sup>e</sup>	NS (0.255)

<sup>a</sup>HR, Hazard ratio.<sup>b</sup>95% CI, 95% confidence interval.<sup>c</sup>p was considered significant when  $p < 0.05$ . NS, not significant.<sup>d</sup>subclasses of breast cancer were determined (ER, PR, HER2) according to the St Gallen recommendation (12-14).<sup>e</sup>N/A, not applicable as all the cases are censored in the low ZNF217-ΔE4 (E3-E5) mRNA level and in the low ZNF217-WT-ΔE4 signature groups.

(E3-E5) mRNA levels (group 2); patients who expressed high ZNF217-WT (E3-E4) and high ZNF217-ΔE4 (E3-E5) mRNA levels (group 3). **Supplementary Figure 2D** illustrate that: (i) 83.3% (60 out of 72) of the patients in the Luminal subclass belonged either to group 1 or to group 3, again supporting correlated mRNA levels of ZNF217-WT and ZNF217-ΔE4 in human primary breast tumors; (ii) the resulting Kaplan Meier curves for RFS in Luminal subclasses showed patients' stratification into diverse prognostic classes ( $p = 0.05$ ), with the patients belonging to group 1 having the better prognosis (and Kaplan Meier curves for RFS for group 2 and group 3 close). Consequently, we further constructed a ZNF217-WT-ΔE4 gene expression signature based on two new groups: patients who expressed low ZNF217-WT (E3-E4) and low ZNF217-ΔE4 (E3-E5) mRNA levels; patients who expressed high ZNF217-WT (E3-E4) and/or high ZNF217-ΔE4 (E3-E5) mRNA levels. Strikingly, the prognostic value of the ZNF217-WT-ΔE4 gene expression signature for RFS was demonstrated to be significant in the Luminal subclasses ( $p = 0.023$ , **Table 1** and **Supplementary Figure 2E**), and not informative in the HER2-enriched, or Triple negative subclasses (**Table 1**).

To investigate the clinical relevance of our findings, we also investigated by univariate analysis the classical prognostic parameters usually studied in breast cancer. **Supplementary Table 2** and **Table 1** indicated that in the whole cohort, the prognostic value of ZNF217-E3 or of ZNF217-WT-ΔE4 gene expression signature for RFS was more informative than conventional biomarkers (age, SBR grade, Lymph node status, Macroscopic tumor size, ER status, PR status, HER2 status). In the Luminal subclass (ER+ and/or PR+), the prognostic value of ZNF217-E3 mRNA levels or of ZNF217-WT-ΔE4 gene expression signature for RFS was more informative than age, SBR grade, Lymph node status, Macroscopic tumor size, and HER2 status (**Table 1** and **Supplementary Table 2**). However, ER status and PR status were associated with shorter RFS ( $p = 0.025$  and  $p = 0.032$ , respectively, **Supplementary Table 2**). Prognostic factors for RFS in the Luminal subclass with a 0.05 significance level in univariate analysis were then entered in a multivariate Cox model. When entering ZNF217-E3 mRNA

levels, ER status, PR status in the multivariate analysis, only ZNF217-E3 mRNA levels persisted in the model ( $p = 0.04$ , HR = 3.71; 95%CI = 1.04-13.18, data not shown). Similarly, when entering ZNF217-WT-ΔE4 gene expression signature, ER status, PR status in the multivariate analysis, only ZNF217-WT-ΔE4 gene expression signature persisted in the model ( $p = 0.04$ , HR = 4.78; 95%CI = 1.07-21.23, data not shown). Finally, no association was found between ZNF217-E3, ZNF217-WT, ZNF217-ΔE4 or ZNF217-WT-ΔE4 gene expression signature with age, invaded lymph nodes, macroscopic tumor size, ER status, PR status and HER2 status (**Supplementary Table 3**). Considering SBR grade, while the p value was significant ( $p = 0.002$ ), the distribution of ZNF217-WT mRNA levels did not reflect any association between high ZNF217-WT mRNA levels and high grade, or vice versa (**Supplementary Table 3**). With the aim to clarify the association between ZNF217-WT-ΔE4 gene expression signature and SBR grade ( $p = 0.024$ , **Supplementary Table 3**), we performed univariate analyses in both SBRI+II ( $n = 45$ ) and SBRIII ( $n = 61$ ) subclasses. Strikingly, ZNF217-WT-ΔE4 gene expression signature was significantly associated with shorter RFS in the SBRI+II subclass ( $p = 0.005$ , data not shown), but not in the SBRIII subclass ( $p = 0.64$ , data not shown), indicating that the ZNF217-WT-ΔE4 gene expression signature could allow the re-stratification of patients with breast cancers of low/intermediate grade.

Altogether, our pilot study suggests that: (i) at least in the Luminal subclass, the ZNF217-WT-ΔE4 gene expression signature has a better prognostic value than that of ZNF217-WT mRNA levels alone, ZNF217-ΔE4 mRNA levels alone or that of the other conventional prognostic parameters of breast cancer; and (ii) in the Luminal subclass, the prognostic value of the ZNF217-WT-ΔE4 gene expression signature recapitulates that of ZNF217-E3 mRNA levels.

## Constitutive Expression of ZNF217-ΔE4 In Breast Cancer Cells Promotes An Aggressive Phenotype

We have previously described the deleterious effect of ZNF217-WT expression after stably transfecting MDA-MB-231 cells, a



relevant breast cancer cell model because possessing low endogenous levels of ZNF217 (4, 5). With the aim to study the impact of *ZNF217-ΔE4* expression on breast cancer cells phenotype, we established stable MDA-MB-231 cells constitutively overexpressing the ZNF217-ΔE4 protein. Two cell clones (ZNF217-ΔE4-1G3 and ZNF217-ΔE4-2C2), overexpressing *ZNF217-ΔE4* mRNA (**Figure 2A**) and ZNF217-ΔE4 protein (**Figure 2B**), were selected under blasticidin, and their phenotype was compared with that of MDA-MB-231-pcDNA6 control cells and of previously established ZNF217-WT cells (4, 5). ZNF217-WT cells did not display any significant increase in ZNF217-ΔE4 expression levels (**Supplementary Figure 3**). Our previous work demonstrated that ectopic expression of ZNF217-WT in MDA-MB-231 cells triggers an aggressive phenotype [increased cell proliferation, increased anchorage-independent growth, resistance to paclitaxel (4, 5)], as illustrated in **Figures 2C–F**. We newly found that the constitutive expression of ZNF217-ΔE4 led to a significant increase in proliferation of both ZNF217-ΔE4-1G3 and ZNF217-ΔE4-2C2 cells, compared to MDA-MB-231-pcDNA6 control cells or to ZNF217-WT cells (**Figure 2C**). To investigate whether ZNF217-ΔE4 alters the response to the chemotherapeutic drug paclitaxel, we performed dose-response experiments to measure IC50 values. Strikingly, constitutive expression of ZNF217-ΔE4 led to significant increase in cell viability in the presence of paclitaxel (**Figure 2D**), with a relative resistance of 3.2- and 3.8-fold, respectively, for ZNF217-ΔE4-1G3 and ZNF217-ΔE4-2C2 cells ( $IC_{50}^{MDA-MB-231-pcDNA6} = 1.8 \pm 0.3 \times 10^{-9}$  M,  $IC_{50}^{ZNF217-ΔE4-1G3} = 5.7 \pm 0.4 \times 10^{-9}$  M,  $IC_{50}^{ZNF217-ΔE4-2C2} = 7.0 \pm 1.0 \times 10^{-9}$  M). The relative resistance developed by the ZNF217-WT cells was of 2.3 (with an  $IC_{50}^{ZNF217-WT} = 4.2 \pm 0.85 \times 10^{-9}$  M). Anchorage-independent growth is a phenotype commonly associated with aggressiveness and metastasis. We found that the number and the size of colonies formed in soft agar when ZNF217-ΔE4 was constitutively overexpressed were significantly higher in ZNF217-ΔE4-1G3 and ZNF217-ΔE4-2C2 cells than in control cells or than in ZNF217-WT cells ( $p < 0.001$ , **Figures 2E, F**). Altogether, these data demonstrate that overexpression of ZNF217-ΔE4 in breast cancer cells enhances their aggressiveness and that the impact of ZNF217-ΔE4 expression on the phenotype of breast cancer cells seems to be at least as or more efficient than that of ZNF217-WT.

### Ectopic Over-Expression of ZNF217-ΔE4 Is Associated With Increased Expression of ZNF217-WT

Having demonstrated that ectopic and constitutive overexpression of ZNF217-ΔE4 in MDA-MB-231 cells confers a phenotype similar to that previously described when ZNF217-WT is constitutively overexpressed (4, 5), we sought to clarify the expression levels of endogenous ZNF217-WT in ZNF217-ΔE4-1G3 and ZNF217-ΔE4-2C2 cells. Strikingly, both cell lines displayed increased mRNA levels and protein levels of endogenous ZNF217-WT (**Figures 3A, B**). The molecular mechanisms regulating the transcription of the *ZNF217* gene

are barely known. We cloned the -2110 base pairs to +300 base pairs region of the *ZNF217* gene into a firefly luciferase reporter plasmid, but we did not observe any increased firefly signal when pcDNA6-ZNF217-ΔE4 plasmid was co-transfected (data not shown), ruling out a positive direct transcriptional regulation by the ZNF217-ΔE4 isoform. Converging epigenetic data stress out that the methylation status at CpG sites within the *ZNF217* locus correlates with inverse *ZNF217* expression levels (7, 15–18). We thus investigated the DNA methylation status at the *ZNF217* CpG sites in both ZNF217-ΔE4-1G3 and ZNF217-ΔE4-2C2 cell lines, in comparison with control MDA-MB-231-pcDNA6 cells. Our methylome analyses revealed in both ZNF217-ΔE4-1G3 and ZNF217-ΔE4-2C2 cells (but not in ZNF217-WT cells) the demethylated DNA status of three sites belonging to a CpG island included in exon 1 (GRCh37/hg19) of the *ZNF217* gene: chr20:52198378 (cg01692482), chr20:52198279 (cg00703481), and chr20:52198225 (cg12032027). Heat map visualizing the DNA methylation status at the three identified CpG sites (cg01692482, cg00703481, and cg12032027) illustrates the consensus clustering result, demonstrating DNA demethylated status in both ZNF217-ΔE4-1G3 and ZNF217-ΔE4-2C2 cell lines compared to MDA-MB-231-pcDNA6 control cells or ZNF217-WT cells (**Figure 3C**). Pyrosequencing analyses validated this finding for cg01692482 and cg00703481 (**Figure 3D**). Specific primers targeting cg12032027 could not be designed, thus not allowing to explore this CpG site by pyrosequencing analysis. Altogether, our data highlighted that ectopic overexpression of ZNF217-ΔE4 leads to increased expression on endogenous ZNF217-WT correlated with an inverse DNA methylation status of the *ZNF217* gene.

## DISCUSSION

A growing body of evidence suggests that ASE significantly affect tumor progression, including in the breast. Several studies have indicated that breast cancer-specific ASE include the generation of proteins with new functions (8, 9, 19, 20). Such studies have also underscored the richness of ASE as a source of biomarkers for breast cancer and attempted to define transcript isoform signatures that are associated with molecular subtypes, tumor grade, ER status, or metastasis (8, 9, 19–22).

The first key finding of our study was the identification of *ZNF217-ΔE4* mRNA in primary breast tumors, indicating that the exon 4-skipping process of the *ZNF217* pre-mRNA occurs in breast cancer. This was thoroughly validated by RNAseq or RT-qPCR analyses in primary breast tumors from independent cohorts. Alternative splicing of other members of the Krüppel-like factor (KLF) gene family, including the KLF6 tumor suppressor and the KLF4 regulator of stem cell pluripotency, has been previously described and shown to result in the production of several isoforms with specific biological functions and biomarker value (22–25). Our study thus highlights ZNF217 as a further member of the KLF family that is susceptible to splicing modulation in a tumorigenic context, generating distinct isoforms. We next sought to explore the

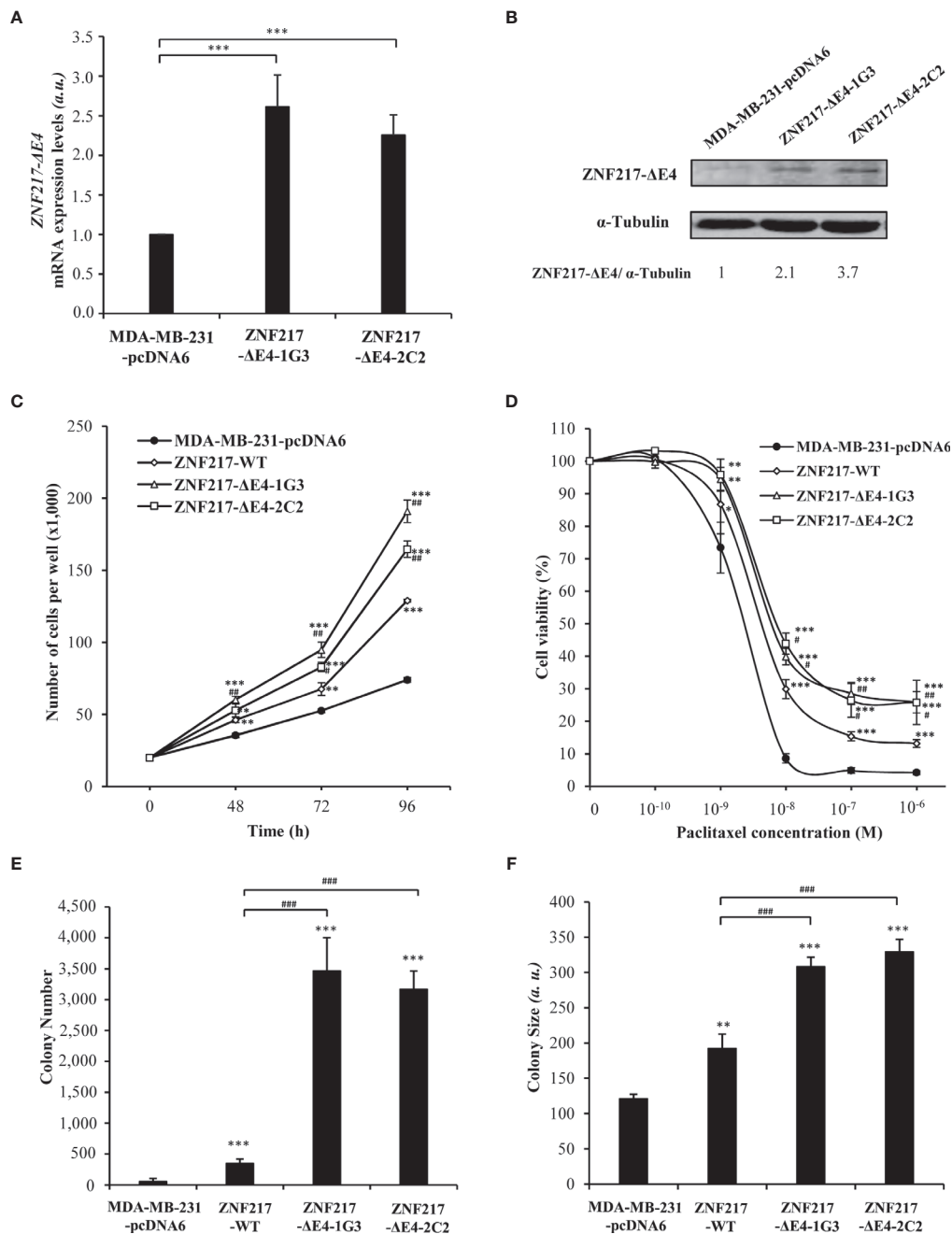


**FIGURE 2** | Constitutive expression of *ZNF217-ΔE4* enhances cell proliferation, paclitaxel resistance and anchorage-independent growth of MDA-MB-231 cells. **(A)** RT-qPCR analysis of *ZNF217-ΔE4* (E3-E5) mRNA expression levels in MDA-MB-231-ΔE4 cell lines and MDA-MB-231-pcDNA6 control cells (mean  $\pm$  SD from three independent experiments, a.u., arbitrary units). **(B)** Representative Western blot analysis of ZNF217-ΔE4 expression levels in MDA-MB-231-ΔE4 cell lines versus control cells using RM217 antibody. **(C)** Cell proliferation assessment of the two MDA-MB-231-ΔE4 cell lines (means  $\pm$  SD of three independent experiments). **(D)** Cell viability after 96 hours of paclitaxel exposure as assessed by MTS cytotoxicity assay. **(E)** Average number of colonies per well, and **(F)** average size of the colonies in soft agar. (a.u.), arbitrary units. Data illustrated in **(E, F)** represent mean  $\pm$  SD of three independent experiments. In **(A, C-F)**: \* $p$  < 0.05, \*\* $p$  < 0.01 and \*\*\* $p$  < 0.001 versus MDA-MB-231-pcDNA6 cells (Student's t-test). In **(C-F)**: # $p$  < 0.05, ## $p$  < 0.01 and ### $p$  < 0.001 versus ZNF217-WT cells (Student's t-test).

clinical and functional relevance of *ZNF217-ΔE4* expression in breast cancer.

Using a primer pair targeting exon 3, we have previously demonstrated that the *ZNF217* mRNA expression level of a

breast tumor is informative and provides a powerful biomarker of poor prognosis, in particular in the Luminal subclass (5, 7). The present pilot retrospective study with 10-years follow-up provided evidence that the novel *ZNF217-WT-ΔE4* gene

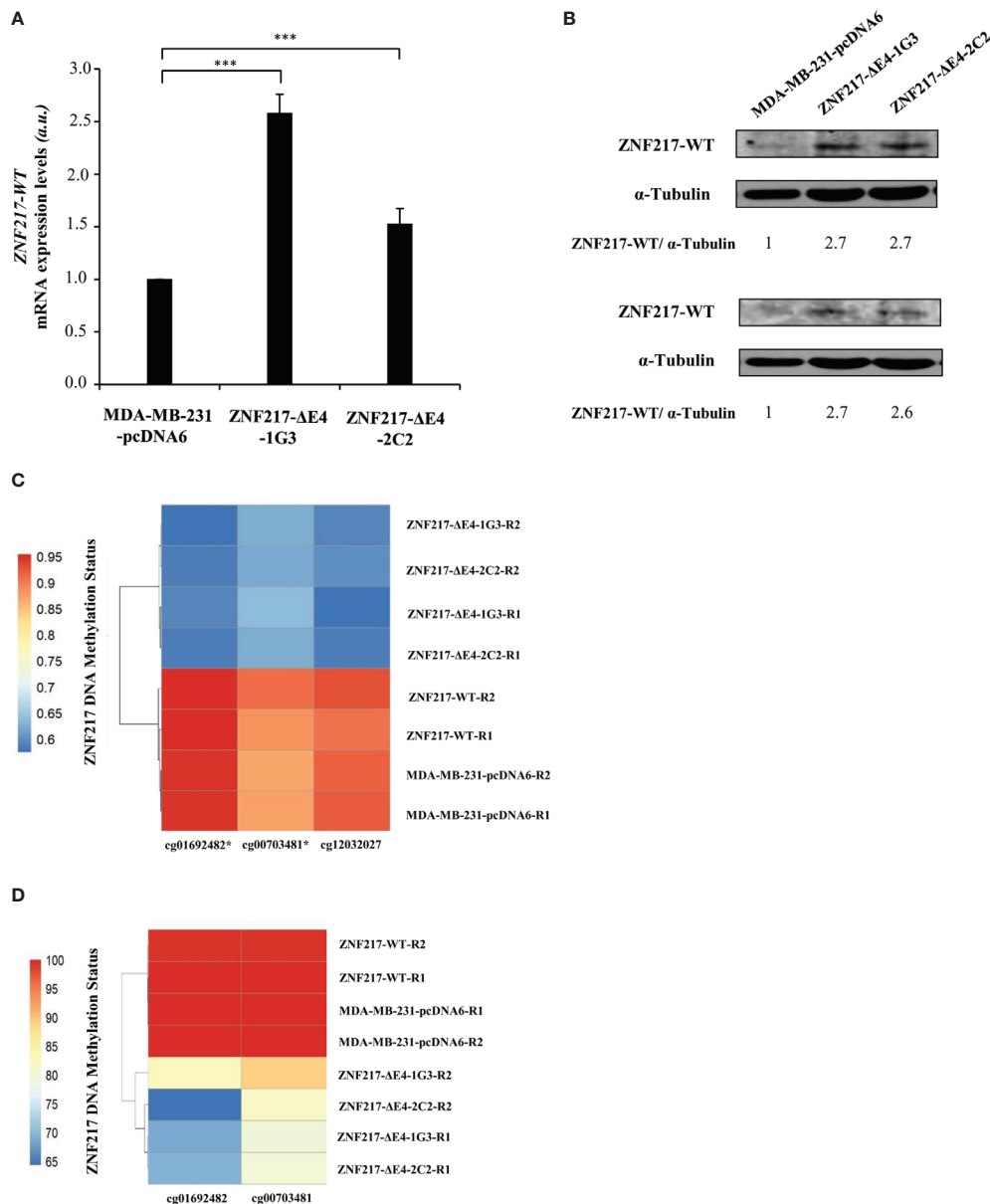


**FIGURE 3** | Constitutive *ZNF217-ΔE4* expression leads to increased expression of *ZNF217-WT* and demethylated DNA status of the *ZNF217* gene. **(A)** RT-qPCR analysis of *ZNF217-WT* (*E3-E4*) mRNA expression levels in MDA-MB-231-ΔE4 cell lines and MDA-MB-231-pcDNA6 control cells (mean ± SD from three independent experiments, a.u., arbitrary units) \*\*\* $p < 0.001$ , in Student *t*-test. **(B)** Representative Western blot analysis of ZNF217 WT protein expression levels using Abcam #48133 (upper panel) and Covalab 2 antibodies (lower panel). **(C)** β-values of 3 CpG sites located in the first Exon of the *ZNF217* gene in MDA-MB-231-pcDNA6 control cells, in MDA-MB-231-ZNF217-ΔE4 and in MDA-MB-231-ZNF217-WT cell lines were calculated after genome-wide methylation analysis with Illumina Infinium MethylationEPIC Beadchip. R1 and R2, independent genomic replicates. Heatmaps were realized with pheatmap package (Version: 1.0.12) in RStudio (Version 1.4.1106). Demethylated positions validated by pyrosequencing are indicated by an asterisk. **(D)** Heatmap of pyrosequencing analysis of cg01692482 and cg00703481 in MDA-MB-231-pcDNA6 control cells and in MDA-MB-231-ZNF217-ΔE4 and in MDA-MB-231-ZNF217-WT cell lines. R1 and R2, independent genomic replicates.

expression signature, which combines the expression of the two isoforms, retained clinical significance, and was significantly associated with shorter RFS in the Luminal subclass. The *ZNF217-WT-ΔE4* signature is thus capable of resuming the prognostic value of *ZNF217-E3* mRNA levels by allowing the stratification of the “good prognosis” Luminal subclass into good

or poor/intermediate outcome. When considering the “good prognosis” SBRI+II subgroup, again the *ZNF217-WT-ΔE4* signature could be used to refine the categorization of patients into good or poor/intermediate outcome. Our gene expression signature, however, was not informative in the “bad prognosis” subclasses such as HER2-enriched, Triple-negative, or SBRIII

subgroups. Importantly, our univariate and multivariate analyses conducted in the Luminal subclass demonstrated that the prognostic value of the *ZNF217-WT-ΔE4* dual signature was more powerful than the expression levels of each isoform only, or than any of the usual clinical prognostic parameters. Altogether, our pilot retrospective study indicates the need to assess the mRNA expression levels of the two *ZNF217* isoforms to obtain the most powerful prognostic biomarker value. Regarding the TCGA RNAseq data, the high proportion of censored cases (90%) prevented us from performing univariate analysis. While future work on an independent cohort is needed to confirm our findings, the results of our clinical investigation strongly suggest that the protein encoded by *ZNF217-ΔE4* has a functional role.

Our study additionally pinpoints the existence of intricate molecular mechanisms involving *ZNF217-WT* and *ZNF217-ΔE4*. First, both the RNA-seq and RT-qPCR investigations, conducted on independent primary breast tumor cohorts, identified a positive correlation between *ZNF217-ΔE4* and *ZNF217-WT* mRNA levels. Second, our *in vitro* data revealed that ectopic overexpression of the *ZNF217-ΔE4* isoform in breast cancer cells leads to: (i) increased endogenous mRNA and protein levels of the *ZNF217-WT* isoform; and (ii) features of cell aggressiveness (increased cell proliferation, increased anchorage-independent growth and resistance to paclitaxel) previously described when *ZNF217-WT* is ectopically overexpressed (4, 5). Our study thus indicates that the *ZNF217-ΔE4* isoform triggers, directly or indirectly, a poor phenotype in breast cancer cells that may involve dysregulated *ZNF217-WT* expression levels. Little is known regarding the molecular mechanisms governing *ZNF217* transcription. Converging epigenetic data, however, show that the methylation status at CpG sites within the *ZNF217* locus correlates with inverse *ZNF217* expression levels (7, 15–18). Importantly, our methylome investigation revealed that constitutive expression of the *ZNF217-ΔE4* isoform (but not of *ZNF217-WT*) is paired with decreased DNA methylation status on three CpG sites located on a key exon on the *ZNF217* gene. In a case-control study involving 1,083 blood samples (healthy women *versus* breast cancer patients), lack of methylation of the same *ZNF217* exon predicted increased breast cancer risk (26), allowing the authors to propose the DNA methylation status at this *ZNF217* locus to be a surrogate biomarker of breast cancer risk. We thus propose a model where the *ZNF217-ΔE4* isoform plays a biologically relevant role in breast cancer, at least by impacting epigenetic-driven mechanisms governing the expression of *ZNF217-WT*. In future work, it would thus be of great interest to investigate the expression levels of both *ZNF217-ΔE4* and *ZNF217-WT* as well as the DNA methylation status of the *ZNF217* gene in breast cancer tissues from patients.

The predicted amino acid (aa) sequence encoded by the *ZNF217-ΔE4* transcript shows that it shares a common region (aa 1 to 1012) with the *ZNF217-WT* protein, but the C-terminal region (49 aa) encoded by exon 5 is different from that present in *ZNF217-WT* protein and encoded by most of exon 4 (36 aa). The C-terminal region of *ZNF217* is of the greatest interest because: (i) it possesses the transcriptional repressor domain (27) and a

proline-rich domain (2) that might be involved in the *ZNF217*'s transcriptional activator properties; and (ii) it binds to CtBP1 and CtBP2 transcriptional co-repressors (27, 28) and to the ER, modulating ER-signaling (7). Future work is thus required to determine how the *ZNF217-ΔE4* interferes with the epigenetic machinery and whether it retains any transcriptional activity.

Little is known about the molecular mechanisms governing ASE in specific biological contexts. However, while the detailed mechanisms are still elusive, many recent studies have revealed that RNA N<sup>6</sup>-methyladenosine (m<sup>6</sup>A) modification serves as a mark for the recruitment of splicing factors and then affects ASE (20, 29). Interestingly, one elegant study has deciphered that the *ZFP217* transcription factor (the murine ortholog of the human *ZNF217*) catalyzes m<sup>6</sup>A methylation at key transcripts, of which was the *ZFP217* RNA itself (at exon3 and exon 5) (30). One thus cannot exclude that such *ZNF217-WT*-driven mechanisms may control splice events leading to the production of the *ZNF217-ΔE4* isoform.

Overall, our new findings have important medical applications. Indeed, we have provided insights into the biological and clinical significance of the novel exon4-skipping *ZNF217* isoform in breast cancer. Our pilot retrospective analysis emphasized the need to assess both *ZNF217-WT* and *ZNF217-ΔE4* expression levels to obtain the most powerful biomarker value, and suggested a key biological function of the encoded *ZNF217-ΔE4* protein isoform. Our *in vitro* data supported our clinical data and reported for the first time that the *ZNF217-ΔE4* protein drives cell aggressiveness and increased *ZNF217-WT* expression levels. In conclusion, our data highlight that assessing the expression levels of *ZNF217-WT* and *ZNF217-ΔE4* isoforms may serve as a novel prognostic biomarker allowing a better stratification of breast cancers with good prognosis and helping clinicians in therapeutic decisions. Future studies on the biological activities of *ZNF217-ΔE4* protein and its interplay with *ZNF217-WT* will lead to a better understanding of *ZNF217* oncogenic machinery.

## DATA AVAILABILITY STATEMENT

Publicly available datasets were analyzed in this study. This data can be found here: <https://www.nature.com/articles/nature11412>.

## ETHICS STATEMENT

This study has been approved by the local ethics committee (CRB Centre Léon Bérard, France). The CRB Centre Léon Bérard is quality certified according to NFS96-900 French standard and ISO 9001 for clinical trials, ensuring scientific rigor for sample conservation, traceability, and quality, as well as ethical rules observance and defined rules for transferring samples for research purposes (Ministry of Health for activities authorization no AC-2019-3426 and DC-2008-99). The material used in the study has been collected in agreement with all applicable laws, rules, and requests of French and



European government authorities. All subjects gave written informed consent. The patients/participants provided their written informed consent to participate in this study.

## AUTHOR CONTRIBUTIONS

BG and LP performed the biostatistical analyses of the RNAseq data. AB validated the *ZNF217* isoforms specific primers and performed *in vitro* experiments. DL and PAC performed the biostatistical analyses of the 107-breast tumor cohort. AW and JL performed and analyzed the methylome study. JV and JS performed the pyrosequencing experiments and analysis. JV and PC participated in scientific discussions. DL, BG, and PAC wrote the manuscript. PAC designed and supervised the study. All authors contributed to the article and approved the submitted version.

## FUNDING

This research program was supported by grants from the Pack Ambition International 2020 (Région Rhône-Alpes, France) and the French Ligue Contre le Cancer (committee 71). DL was funded by France Excellence Scholarship Program of the French Embassy in Vietnam. AB was supported by a Ph.D. grant from the French Ligue Nationale contre le Cancer. BG and LP were financed by the 2018-2.1.17-TET-KR-00001 and 2018-1.3.1-VKE-2018-00032 grants and the Higher Education Institutional Excellence Programme (2020-4.1.1.-TKP2020) of the Ministry for Innovation and Technology in Hungary, within the framework of the Bionic thematic programme of the Semmelweis University.

## ACKNOWLEDGMENTS

We thank Dr. H. Mattock for her kind help in the edition. The authors thank the Centre de Ressources Biologiques (CRB) of the Centre Léon Bérard (BB-0033-00050). The authors wish to acknowledge the support of ELIXIR Hungary ([www.elixir-hungary.org](http://www.elixir-hungary.org)). We are grateful to Dr. Nguyen for generating the pcDNA6-ZNF217-ΔE4 plasmid and Miss S. Crose for technical help in methylome studies.

hungary.org). We are grateful to Dr. Nguyen for generating the pcDNA6-ZNF217-ΔE4 plasmid and Miss S. Crose for technical help in methylome studies.

## SUPPLEMENTARY MATERIAL

The Supplementary Material for this article can be found online at: <https://www.frontiersin.org/articles/10.3389/fonc.2021.647269/full#supplementary-material>

**Supplementary Figure 1 |** The sequence-specific primers for *ZNF217*-WT (*E3-E4*) and *ZNF217*-ΔE4 (*E3-E5*) isoforms with high specificity and sensitivity. **(A)** Binding sites of the primer pair 1, 2, and 3 used to specifically detect the *ZNF217*-E3, *ZNF217*-WT (*E3-E4*), and *ZNF217*-ΔE4 (*E3-E5*) isoforms, respectively. The primer pair 1 hybridized within the sequence of *ZNF217*'s exon 3. The forward primer of pair 2 hybridized onto the exon 3 - exon 4 junction of *ZNF217*-WT (*E3-E4*) isoform. The reverse primer of pair 3 hybridized onto the exon 3 - exon 5 junction of *ZNF217*-ΔE4 (*E3-E5*) isoform. **(B)** RT-qPCR detection of *ZNF217* isoforms in mixtures containing 1,000 copies of different ratios of pcDNA6-ZNF217-WT and/or pcDNA6-ZNF217-ΔE4 plasmids amplified by RT-qPCR using the primer pair 1 (black bar), primer pair 2 (grey bar), or primer pair 3 (white bar). All data represent as mean ± standard deviation of two independent experiments conducted in triplicate. Frequency of **(C)** *ZNF217*-ΔE4 (*E3-E5*) mRNA levels and of **(D)** *ZNF217*-ΔE4 (*E3-E5*) mRNA levels among the 107 primary breast tumors.

**Supplementary Figure 2 |** The *ZNF217*-WT-ΔE4 gene expression signature is of poor prognosis and is associated with shorter relapse-free survival in the Luminal breast cancer subclass. Kaplan-Meier analyses (univariate analyses) for RFS in Luminal subclass (ER+ and/or PR +) of **(A)** *ZNF217*-E3 mRNA expression levels; **(B)** *ZNF217*-WT (*E3-E4*) mRNA expression levels; **(C)** *ZNF217*-ΔE4 (*E3-E5*) mRNA expression levels; **(D)** the 3-groups *ZNF217*-WT-ΔE4 gene expression signature defined by: (group 1), low *ZNF217*-WT (*E3-E4*) and low *ZNF217*-ΔE4 (*E3-E5*) mRNA levels; (group 2), high *ZNF217*-WT (*E3-E4*) or high *ZNF217*-ΔE4 (*E3-E5*) mRNA levels; (group 3), high *ZNF217*-WT (*E3-E4*) and high *ZNF217*-ΔE4 (*E3-E5*) mRNA levels; **(E)** *ZNF217*-WT-ΔE4 gene expression signature.  $p < 0.05$ .

**Supplementary Figure 3 |** Characterization of MDA-MB-231-ZNF217-WT cells. **(A)** RT-qPCR analysis of *ZNF217*-WT (*E3-E4*) mRNA expression levels in MDA-MB-231-ZNF217-WT cell line and MDA-MB-231-pcDNA6 control cells (mean ± SD from three independent experiments, a.u., arbitrary units) \*\*\* $p < 0.001$ , in Student *t*-test. **(B)** Representative Western blot analysis of ZNF217 WT protein expression levels using Abcam #48133 (upper panel) and Covalab 2 antibodies (lower panel). **(C)** RT-qPCR analysis of *ZNF217*-ΔE4 (*E3-E5*) mRNA expression levels in MDA-MB-231-ZNF217-WT cell line and in MDA-MB-231-pcDNA6 control cells (mean ± SD from three independent experiments, a.u., arbitrary units). **(D)** Representative Western blot analysis of ZNF217-ΔE4 expression levels in MDA-MB-231-ZNF217-WT cell line versus control cells using RM217 antibody.

## REFERENCES

1. Ferlay J, Ervik M, Lam F, Mery L, Piñeros M, Znaor A, et al. *Global Cancer Observatory: Cancer Today* (2020). Lyon, France: International Agency for Research on Cancer. Available at: <https://gco.iarc.fr/today> (Accessed 23/12/2020).
2. Collins C, Rommens JM, Kowbel D, Godfrey T, Tanner M, Hwang SI, et al. Positional Cloning of ZNF217 and NABC1: Genes Amplified at 20q13.2 and Overexpressed in Breast Carcinoma. *Proc Natl Acad Sci USA* (1998) 95 (15):8703–8. doi: 10.1073/pnas.95.15.8703
3. Cohen PA, Donini CF, Nguyen NT, Lincet H, Vendrell JA. The Dark Side of ZNF217, A Key Regulator of Tumorigenesis With Powerful Biomarker Value. *Oncotarget* (2015) 6(39):41566–81. doi: 10.18632/oncotarget.5893
4. Thollet A, Vendrell JA, Payen L, Ghayad SE, Ben Larbi S, Grisard E, et al. ZNF217 Confers Resistance to the Pro-Apoptotic Signals of Paclitaxel and Aberrant Expression of Aurora-a in Breast Cancer Cells. *Mol Cancer* (2010) 9:291. doi: 10.1186/1476-4598-9-291
5. Vendrell JA, Thollet A, Nguyen NT, Ghayad SE, Vinot S, Bièche I, et al. ZNF217 Is a Marker of Poor Prognosis in Breast Cancer That Drives Epithelial-Mesenchymal Transition and Invasion. *Cancer Res* (2012) 72 (14):3593–606. doi: 10.1158/0008-5472.CAN-11-3095
6. Bellanger A, Donini CF, Vendrell JA, Lavaud J, Machuca-Gayet I, Ruel M, et al. The Critical Role of the ZNF217 Oncogene in Promoting Breast Cancer Metastasis to the Bone. *J Pathol* (2017) 242(1):73–89. doi: 10.1002/path.4882
7. Nguyen NT, Vendrell JA, Poulard C, Gyorffy B, Goddard-Leon S, Bièche I, et al. A Functional Interplay Between ZNF217 and Estrogen Receptor Alpha Exists in Luminal Breast Cancers. *Mol Oncol* (2014) 8(8):1441–57. doi: 10.1016/j.molonc.2014.05.013
8. Ladomery M. Aberrant Alternative Splicing is Another Hallmark of Cancer. *Int J Cell Biol* (2013) 2013:463786. doi: 10.1155/2013/463786

9. Martinez-Montiel N, Anaya-Ruiz M, Perez-Santos M, Martinez-Contreras RD. Alternative Splicing in Breast Cancer and the Potential Development of Therapeutic Tools. *Genes (Basel)* (2017) 8(10):217. doi: 10.3390/genes8100217
10. Koboldt DC, Fulton RS, McLellan MD, Schmidt H, Kalicki-Verizer J, McMichael JF, et al. Comprehensive Molecular Portraits of Human Breast Tumours. *Nature* (2012) 490(7418):61–70. doi: 10.1038/nature11412
11. Stephenson JR, Axelrad AA, McLeod DL, Shreeve MM. Induction of Colonies of Hemoglobin-Synthesizing Cells by Erythropoietin *In Vitro*. *Proc Natl Acad Sci USA* (1971) 68(7):1542–6. doi: 10.1073/pnas.68.7.1542
12. Gnatt M, Harbeck N, Thomssen C. St. Gallen 2011: Summary of the Consensus Discussion. *Breast Care (Basel)* (2011) 6(2):136–41. doi: 10.1159/000328054
13. Goldhirsch A, Wood WC, Coates AS, Gelber RD, Thürlimann B, Senn HJ, et al. Strategies for Subtypes—Dealing With the Diversity of Breast Cancer: Highlights of the St. Gallen International Expert Consensus on the Primary Therapy of Early Breast Cancer 2011. *Ann Oncol* (2011) 22(8):1736–47. doi: 10.1093/annonc/mdr304
14. Goldhirsch A, Winer EP, Coates AS, Gelber RD, Piccart-Gebhart M, Thürlimann B, et al. Personalizing the Treatment of Women With Early Breast Cancer: Highlights of the St Gallen International Expert Consensus on the Primary Therapy of Early Breast Cancer 2013. *Ann Oncol* (2013) 24(9):2206–23. doi: 10.1093/annonc/mdt303
15. Etcheverry A, Aubry M, de Tayrac M, Vauleon E, Boniface R, Guenot F, et al. DNA Methylation in Glioblastoma: Impact on Gene Expression and Clinical Outcome. *BMC Genomics* (2010) 11:701. doi: 10.1186/1471-2164-11-701
16. Leu YW, Yan PS, Fan M, Jin VX, Liu JC, Curran EM, et al. Loss of Estrogen Receptor Signaling Triggers Epigenetic Silencing of Downstream Targets in Breast Cancer. *Cancer Res* (2004) 64(22):8184–92. doi: 10.1158/0008-5472.CAN-04-2045
17. Ness C, Katta K, Garred O, Kumar T, Olstad OK, Petrovski G, et al. Integrated Differential DNA Methylation and Gene Expression of Formalin-Fixed Paraffin-Embedded Uveal Melanoma Specimens Identifies Genes Associated With Early Metastasis and Poor Prognosis. *Exp Eye Res* (2021) 203:108426. doi: 10.1016/j.exer.2020.108426
18. Renner M, Wolf T, Meyer H, Hartmann W, Penzel R, Ulrich A, et al. Integrative DNA Methylation and Gene Expression Analysis in High-Grade Soft Tissue Sarcomas. *Genome Biol* (2013) 14(12):r137. doi: 10.1186/gb-2013-14-12-r137
19. Trincado JL, Sebestyen E, Pages A, Eyra E. The Prognostic Potential of Alternative Transcript Isoforms Across Human Tumors. *Genome Med* (2016) 8(1):85. doi: 10.1186/s13073-016-0339-3
20. Yang Q, Zhao J, Zhang W, Chen D, Wang Y. Aberrant Alternative Splicing in Breast Cancer. *J Mol Cell Biol* (2019) 11(10):920–9. doi: 10.1093/jmcb/mjz033
21. Venables JP, Klinck R, Bramard A, Inkel L, Dufresne-Martin G, Koh C, et al. Identification of Alternative Splicing Markers for Breast Cancer. *Cancer Res* (2008) 68(22):9525–31. doi: 10.1158/0008-5472.CAN-08-1769
22. Yang Y, Xiong J, Wang J, Ruan Y, Zhang J, Tian Y, et al. Novel Alternative Splicing Variants of Klf4 Display Different Capacities for Self-Renewal and Pluripotency in Mouse Embryonic Stem Cells. *Biochem Biophys Res Commun* (2020) 532(3):377–84. doi: 10.1016/j.bbrc.2020.08.054
23. Syafruddin SE, Mohtar MA, Wan Mohamad Nazarie WF, Low TY. Two Sides of the Same Coin: The Roles of KLF6 in Physiology and Pathophysiology. *Biomolecules* (2020) 10(10):1378. doi: 10.3390/biom10101378
24. Wang L, Shen F, Stroehlein JR, Wei D. Context-Dependent Functions of KLF4 in Cancers: Could Alternative Splicing Isoforms Be the Key? *Cancer Lett* (2018) 438:10–6. doi: 10.1016/j.canlet.2018.09.005
25. Zhang N, Yan QQ, Lu L, Shao JB, Sun ZG. The KLF6 Splice Variant KLF6-SV1 Promotes Proliferation and Invasion of Non-Small Cell Lung Cancer by Up-Regulating PI3K-AKT Signaling Pathway. *J Cancer* (2019) 10(22):5324–31. doi: 10.7150/jca.34212
26. Widschwendter M, Apostolidou S, Raum E, Rothenbacher D, Fiegl H, Menon U, et al. Epigenotyping in Peripheral Blood Cell DNA and Breast Cancer Risk: A Proof of Principle Study. *PLoS One* (2008) 3(7):e2656. doi: 10.1371/journal.pone.0002656
27. Cowger JJM, Zhao Q, Isovich M, Torchia J. Biochemical Characterization of the Zinc-Finger Protein 217 Transcriptional Repressor Complex: Identification of a ZNF217 Consensus Recognition Sequence. *Oncogene* (2007) 26(23):3378–86. doi: 10.1038/sj.onc.1210126
28. Quinlan KGR, Nardini M, Verger A, Francescato P, Yaswen P, Corda D, et al. Specific Recognition of ZNF217 and Other Zinc Finger Proteins At a Surface Groove of C-Terminal Binding Proteins. *Mol Cell Biol* (2006) 26(21):8159–72. doi: 10.1128/MCB.00680-06
29. Adhikari S, Xiao W, Zhao YL, Yang YG. M<sup>5</sup>A: Signaling for mRNA Splicing. *RNA Biol* (2016) 13(9):756–9. doi: 10.1080/15476286.2016.1201628
30. Aguilo F, Zhang F, Sancho A, Fidalgo M, Di Cecilia S, Vashisht A, et al. Coordination of m<sup>6</sup>A mRNA Methylation and Gene Transcription by ZFP217 Regulates Pluripotency and Reprogramming. *Cell Stem Cell* (2015) 17(6):689–704. doi: 10.1016/j.stem.2015.09.005

**Conflict of Interest:** The authors declare that the research was conducted in the absence of any commercial or financial relationships that could be construed as a potential conflict of interest.

Copyright © 2021 Bellanger, Le, Vendrell, Wierinckx, Pongor, Solassol, Lachuer, Clezardin, Györfy and Cohen. This is an open-access article distributed under the terms of the Creative Commons Attribution License (CC BY). The use, distribution or reproduction in other forums is permitted, provided the original author(s) and the copyright owner(s) are credited and that the original publication in this journal is cited, in accordance with accepted academic practice. No use, distribution or reproduction is permitted which does not comply with these terms.



# The Role of Long Noncoding RNA AL161431.1 in the Development and Progression of Pancreatic Cancer

Gang Ma, Guichen Li, Wufeng Fan, Yuanhong Xu, Shaowei Song, Kejian Guo and Zhe Liu\*

Department of Pancreatic-Biliary Surgery, First Hospital of China Medical University, Shenyang, China

## OPEN ACCESS

### Edited by:

Pascale Cohen,  
Université Claude Bernard Lyon 1,  
France

### Reviewed by:

Zhongjie Shi,  
Wayne State University, United States  
Dong Pan,  
Duke University, United States

### \*Correspondence:

Zhe Liu  
liuzhe4321@126.com

### Specialty section:

This article was submitted to  
Pharmacology of Anti-Cancer Drugs,  
a section of the journal  
Frontiers in Oncology

**Received:** 01 June 2021

**Accepted:** 25 June 2021

**Published:** 30 July 2021

### Citation:

Ma G, Li G, Fan W, Xu Y, Song S,  
Guo K and Liu Z (2021) The Role of  
Long Noncoding RNA AL161431.1 in  
the Development and Progression of  
Pancreatic Cancer.  
Front. Oncol. 11:666313.  
doi: 10.3389/fonc.2021.666313

Pancreatic cancer is known for its notorious fast progression and poor prognosis. Long noncoding RNA (lncRNA) AL161431.1 has been reported to be involved in the pathogenesis of different cancers. In this study, we explored the role of lncRNA AL161431.1 in the development and progression of pancreatic cancer by bioinformatic analysis, *in vitro* and *in vivo* experiments in pancreatic cancer BxPC-3 and SW1990 cells, as well as clinical samples. We found that lncRNA AL161431.1 was highly expressed in pancreatic cancer cells and tissues. Knock down of lncRNA AL161431.1 led to increased cancer cell death and cell cycle arrest. Xenograft growth of SW1990 cells with stable knockdown of lncRNA AL161431.1 in mice was significantly slower than that of SW1990 cells with scrambled control shRNA. Finally, we showed the involvement of lncRNA AL161431.1 in pancreatic cancer was related to its promotion of epithelial mesenchymal transition process.

**Keywords:** long noncoding RNA, pancreatic cancer, epithelial mesenchymal transition (EMT), bioinformatics, diagnosis

## INTRODUCTION

In the United States, pancreatic cancer represents about 3% of cancers and 7% of cancer-related deaths (1). About 57,600 people were predicted to be diagnosed with pancreatic cancer, with 47,050 deaths according to the estimate for pancreatic cancer for 2020 from the American Cancer Society in the United States. The 5-year relative survival rate of patients with pancreatic cancers at all stages was only 9% based on the survey on patients diagnosed with pancreatic cancer between 2009 and 2015 (2). Furthermore, pancreatic cancer often presents at late stage, and only 20% of patients showed surgically resectable lesions at diagnosis (3). Therefore, better understanding the mechanisms of tumorigenesis and development of pancreatic cancer is pivotal to its early diagnosis and improved prognosis.

Long noncoding RNAs (lncRNAs) are mRNA transcripts longer than 200 nucleotides that are not destined to be translated into proteins (4). Although thought to be non-functional for decades, more and more evidence has shown that lncRNAs are critical regulators of pathogenesis, progression, and metastasis of a broad scope of cancers (5). Many lncRNAs are promising diagnostic and prognostic biomarkers for cancers, including pancreatic cancer (6), whereas lncRNA AL161431.1 has been reported to be involved in the pathogenesis of endometrial carcinoma (7), hypoxic TCGA-BRCA tumors (8), and lung squamous cell carcinoma (9).

In the present study, we explored the role of lncRNA AL161431.1 in the development and progression of pancreatic cancer by employing bioinformatic analysis and *in vitro* and *in vivo* experiments in two different pancreatic cancer cell lines as well as clinical samples. We showed that lncRNA AL161431.1 was highly expressed in pancreatic cancer cell lines and clinical tissues. Knocking down of lncRNA AL161431.1 led to increased cancer cell death and cell cycle arrest. The involvement of lncRNA AL161431.1 in pancreatic cancer progression was related to its promotion of the epithelial mesenchymal transition (EMT) process.

## MATERIALS AND METHODS

### Bioinformatic Analysis

The transcriptome sequencing data of 181 samples were generated by the R package in The Cancer Genome Atlas- Pancreatic adenocarcinoma (TCGA-PAAD) dataset obtained from the TCGA biolinks (<https://bioconductor.org/packages/release/data/experiment/vignettes/TCGAbiolinksGUI.data/inst/doc/vignettes.html>). Differential mRNA abundance analyses were carried out using DESeq2 (<http://www.r-project.org/>). Genes with reads < 5 in any sample were filtered out from the final quantitative analysis. Heatmap and volcano plot were constructed by normalized gene expression *via* R package. The normalized gene expressions were subjected to Gene Set Variation Analysis (GSVA, a non-parametric, unsupervised method for estimating variation of gene set enrichment through the samples of an expression dataset). R package survival was used for overall survival analysis. Cox proportional hazard (PH) model was executed by the functions of survival and survminer in R package. The best-scanned cutoff points are defined as the one with the most significant (log-rank test) split. R package survival ROC was used for Receiver Operating Characteristic (ROC) curve and Area Under Curve (AUC) plotted for different durations of survival analysis.

### Patients

Ethical approval was obtained from the Ethical Committee of the First Affiliated Hospital of China Medical University (a tertiary hospital and regional cancer center in Shenyang, China). Written informed consent was obtained from all patients at admission. The diagnosis of pancreatic cancer was based on the National Comprehensive Cancer Network Guidelines (NCCN 2018), and no patient received preoperative chemotherapy. Pancreatic cancer tissues and adjacent normal tissue from the same patients were obtained during pancreaticoduodenectomy at the First Affiliated Hospital of China Medical University from June 1, 2018 to May 31, 2019, who had no bacterial or viral infections, chronic diseases such as hypertension, cardiovascular diseases, diabetes, or other cancers. Tissue samples were cryopreserved in liquid nitrogen immediately after surgical resection until further experiments.

### Cell Culture

All experiments were performed with mycoplasma-free cells. Human pancreatic adenocarcinoma cell lines PANC-1 (RRID :

CVCL\_0480), BxPC-3 (RRID : CVCL\_0186), and SW1990 (RRID : CVCL\_1723) were purchased from Shanghai Zhong Qiao Xin Zhou Biotechnology Co., Ltd (Shanghai, China). Cells were cultured in Dulbecco's modified Eagle's medium (DMEM, Gibco, Thermo Fisher Scientific, Inc.) supplemented with 10% fetal bovine serum (FBS, Gibco), 10 mM HEPES (Gibco), 2 mM L-glutamine (Gibco), 1 mM pyruvate sodium (Gibco), 100 U/ml penicillin and 100 µg/ml streptomycin (Gibco) at 37°C with 5% CO<sub>2</sub>.

### Stable lncRNA-Knockdown Cell Line Construction

A specific SW1990 cell line (SW1990-LNC-KD) with stable knockdown of lncRNA AL161431.1 or control SW1990 cell line was constructed using a lnc-shRNA sequence targeting 5'-GCAGTATTCCTGCACTTCT-3' or scramble control sequence 5'-TTCTCCGAACGTGTCACGT-3' cloned into the pLV3(H1/GFP&Puro) vector (**Figure S1**), and transfected into 293T cells (Shanghai GenePharma China). After 72 h incubation, cell supernatants were collected, and used for transfection (24 h) of SW1990s (10). SW1990 cells containing the lnc-shRNA were selected by media containing 5 µg/ml puromycin (Sigma, St. Louis, MO), and were used for Xenograft tumor growth experiments (11).

### Transfection of siRNAs

Small interfering RNAs (siRNAs) and scrambled negative control for lncRNA were provided by Shanghai GenePharma (Shanghai, China). The siRNAs (30 nM of each, sequences listed in **Table S1**) were transfected with X-tremeGENE siRNA transfection reagent (Roche Applied Science, Shanghai, China) according to the manufacturer's manual.

### Total RNA Extraction and qRT-PCR

Fresh cells or frozen tissues were homogenized in TRIzol reagent (Thermo Fisher Scientific, Inc.) for total RNA extraction following the manual's instructions. The purified RNAs were quantified by a NanoDrop 2000 Spectrophotometers (Thermo Fisher Scientific, Inc.), reverse transcribed using an RT reagent Kit (Nachuan Bio-Tech Co., Binzhou, China) based on the manufacturer's instructions. qRT-PCR analysis was performed in an Exicycle 96 Real-Time Quantitative Thermal Block (Bioneer) using SYBR Green Master Mix (Nachuan Bio-Tech Co.) according to the manufacturer's protocol (sequence of primers listed in **Table S1**). Reactions were performed in 96-well plates in 10 µL total volume including 1x SYBR Green Master mix, cDNA (10 ng), and primers (75 nM of forward and reverse primers each). The average of triplicate qRT-PCR results of target lncRNA expression from each sample was normalized by  $\beta$ -actin of the same sample, and the relative expression was calculated using  $2^{-\Delta\Delta Ct}$ .

### Cell Count Kit-8 Assay for Cell Proliferation

Cell proliferation was detected using a CCK-8 assay kit (DOJINDO, Japan). Cells were seeded into 96-well plates (1 x



10<sup>4</sup>/well). At 10 am, 10 µl CCK-8 reagent in 100 µl medium was added to each well. The light absorbance at 450 nm of each well was measured after 2 hour incubation at 37°C with an Epoch microplate spectrophotometer (BioTek China, Beijing). Cell viability was monitored in triplicate experiments and expressed as a percentage of that of the control cells.

## Flow Cytometry

Forty-eight hours after siRNA transfection, cell death/apoptosis or cell cycle was analyzed by flow cytometry (LSR, BD Biosciences) using Annexin V-FITC/PI Apoptosis Detection Kit (Beyotime Institute of Biotechnology, Shanghai, China) or Propidium Iodide (PI; Solarbio Biotech, China), respectively, according to the manufacturer's instructions. For cell death/apoptosis, cells were collected, washed three times with cold PBS, stained in 500 µl staining buffer (Annexin V-FITC/PI in PBS) at room temperature for 30 min in the dark. For cell cycle analysis, cells were collected, washed three times with cold PBS, fixed in precooled anhydrous ethanol at 4°C for 30 min, and stained with 50 µg/mL PI in 500 µl PBS in the dark. All experiments were triplicated.

## Immunofluorescence Staining

Cells were grown on sterile glass slides, fixed with 4% paraformaldehyde for 30 min, blocked with 1% BSA for 30 min, incubated with primary antibodies against CDH1 (E-cadherin, AF0131, 1:500; Affinity Biosciences LTD.), CDH2 (N-cadherin AF4039, 1:200; Affinity Biosciences LTD.), and VIM (Vimentin AF7013, 1:250; Affinity Biosciences LTD.) at 4°C overnight, followed by incubation with Alexa Fluor<sup>®</sup> 594 conjugated Affinipure Goat Anti-Rabbit IgG (H + L) secondary antibodies (Jackson ImmunoResearch Laboratories, PA) for 1 hour. Nuclei were counterstained with DAPI. Images were captured with Olympus IX81 inverted fluorescence microscope (Olympus, Beijing, China).

## Western Blotting

Anti-beta actin (AF7018, 1:3000), anti-E-cadherin (AF0131, 1:10000), anti-Vimentin (AF7013, 1:1000), anti-N-cadherin (AF4039, 1:1000) were obtained from Affinity Biosciences LTD., and the secondary antibody concentration was 1:5000 (S0001, Affinity Biosciences LTD.). Forty-eight hours after siRNA transfection, cells were lysed in RIPA lysis buffer (Merck Group, Germany) for 30 min on ice. Sample protein concentrations were quantified using a BCA assay kit (Solarbio, China). Equal amounts of proteins were separated by SDS-polyacrylamide gel electrophoresis, transferred to polyvinylidene difluoride membranes, and probed with the antibodies of interest. The intensity of bands was quantified using ImageJ, using β-actin as internal loading control.

## Xenograft Tumor Growth in Nude Mice

Animal experiment protocols were approved by the Institutional Ethical Committee, and animals were properly treated in accordance with the institutional ethical requirements of experimental animals. Male nude mice were kept in a temperature-controlled specific-pathogen-free animal

laboratory, with a 12h light/dark cycle. All animals had free access to food and water. SW1990-LNC-KD cells (1.5 × 10<sup>6</sup> cells in 0.1 ml sterile PBS, with stable knockdown of lncRNA AL161431.1), or SW1990-LNC-NC cells (with scrambled shRNA) were subcutaneously injected into the left flank of mice at 8 weeks of age. The volume of tumor was measured every morning by length x width x depth in mm. The mice were euthanized 2 weeks after cancer cell injection, and the growth of subcutaneous tumors were compared (n=7 in each group).

## Immunohistochemistry

PCNA immunohistochemical staining was performed on 10 µm sections of paraffin-embedded tissue samples. In brief, the slides were incubated in PCNA antibody (AF0239, Affinity Biosciences LTD.; at 1:100 dilution) at 4°C overnight followed by the secondary antibody (S0001, Affinity Biosciences LTD.; at 1:200 dilution) at 37°C for 1 hours. Nuclei were counterstained with hematoxylin. PCNA positive cells were quantified using the IHC Profiler (12).

## Transwell Assay

Twenty-four hours after transfection, SW1990 (1 × 10<sup>5</sup>) or BxPC-3 (1 × 10<sup>5</sup>) cells were resuspended in 100 µl serum-free medium and seeded into the upper chamber with 12 µm pore polycarbonate membranes pre-coated with Matrigel Basement Membrane Matrix (BD Biosciences, Bedford, MA). The lower chamber was filled with 600 µl of 1640 medium supplemented with 20% FBS. After 24 hours of incubation at 37°C with 5% CO<sub>2</sub>, cells remaining in the upper membrane surface were removed with a cotton swab, whereas invaded cells were fixed and stained with 0.5% crystal violet (13).

## Wound-Healing Assay

Twenty-four hours after transfection, cells were seeded in 24-well plates at 1 × 10<sup>5</sup> cells/well. Cells were cultured in medium containing 5% FBS with 5% CO<sub>2</sub> for 24 h. A 1-mm wide scratch was made in the confluent cultures with a pipette tip, followed by wash twice with PBS to remove debris. The area of the scratch was measured using images taken by a phase-contrast microscope (14).

## Statistics

Statistical analysis was performed using SPSS software (version 24, Armonk, NY: IBM Corp.). Quantitative data are presented as mean ± SD. Differences in the mean of two samples were analyzed by Student's t-test. All 2-tailed statistical tests were considered significant when p < 0.05.

## RESULTS

### LncRNA AL161431.1 Was Overexpressed in Pancreatic Adenocarcinoma

In order to identify lncRNAs that are most relevant to pancreatic cancer, we obtained data on tumor (PAAD) transcriptome-level 3 (including 177 pancreatic cancer tissues and 4 normal

pancreatic tissues) from the TCGA database (15). The expression of lncRNA AL161431.1 (also named RP11-54H7.4) in pancreatic cancer tissues was found to be significantly higher than that of normal pancreatic tissues (**Figures 1A–C**) by DESeq2 software package (16) analysis. We further analyzed the data of TCGA-PAAD cohort by dividing the samples into a high- and a low-lncRNA AL161431.1 expression groups using the median as the cut-off value. Using GEPIA online tool (17) and R language survival analysis, it was found that patients in the high lncRNA AL161431.1 expression group had a shorter survival period (**Figures 1D, E**), and lncRNA AL161431.1 was shown to be positively correlated with the prognosis of pancreatic adenocarcinoma (**Figure 1F**). Pancreatic cancer tissues (n=26) and paired adjacent normal tissue from the same patients (n=26) were obtained from 14 male and 12 female patients admitted in our hospital aged between 43 and 63 (mean age  $53.8 \pm 6.0$  years) and analyzed by qRT-PCR. According to the eighth edition of the AJCC-TNM staging system for pancreatic cancer, there were 6 cases in the first stage, 12 cases in the second stage, 7 cases in the third stage, and 1 case in the fourth stage. Among the 26 cases, 10 were poorly differentiated, 8 were moderately differentiated, and 8 were highly differentiated. The level of lncRNA AL161431.1 was significantly higher in cancer tissues than that of the normal tissues ( $p < 0.05$ , **Figure 1G**). The above results suggested that lncRNA AL161431.1 was highly expressed in pancreatic cancer

tissues, and overexpression of lncRNA AL161431.1 could indicate a poor prognosis.

## Knocking Down of lncRNA AL161431.1 Inhibited the Growth, Invasion and Migration of Pancreatic Adenocarcinoma Cells

The expression of lncRNA AL161431.1 in pancreatic cancer cell lines PANC-1, SW1990 and BxPC-3 cells was determined by qRT-PCR, and was found to be significantly higher in SW1990 and BxPC-3 cells compared to that in PANC-1 cells (**Figure 2A**). In order to study the function of AL161431.1, we tested specific siRNAs to knock down the expression of lncRNA AL161431.1, and found both siRNA1 and siRNA2 had significant knockdown effect ( $p < 0.05$  for both, **Figure 2B**). siRNA1 was selected for the following knockdown experiments. CCK-8 assay showed that the cell proliferative activity in the AL161431.1 siRNA knockdown group was significantly lower than that in the control group in both SW1990 and BxPC-3 cell lines (**Figure 2C**). Wound healing and Transwell experiments showed that after knocking down lncRNA AL161431.1, cell migration and invasion was significantly inhibited (**Figures 2D, E**). Compared with the scrambled control group, siRNA knock down of AL161431.1 significantly promoted cell death (**Figure 2F**), and the cells in the knockdown group accumulated in G1/S phase (**Figure 2G**).

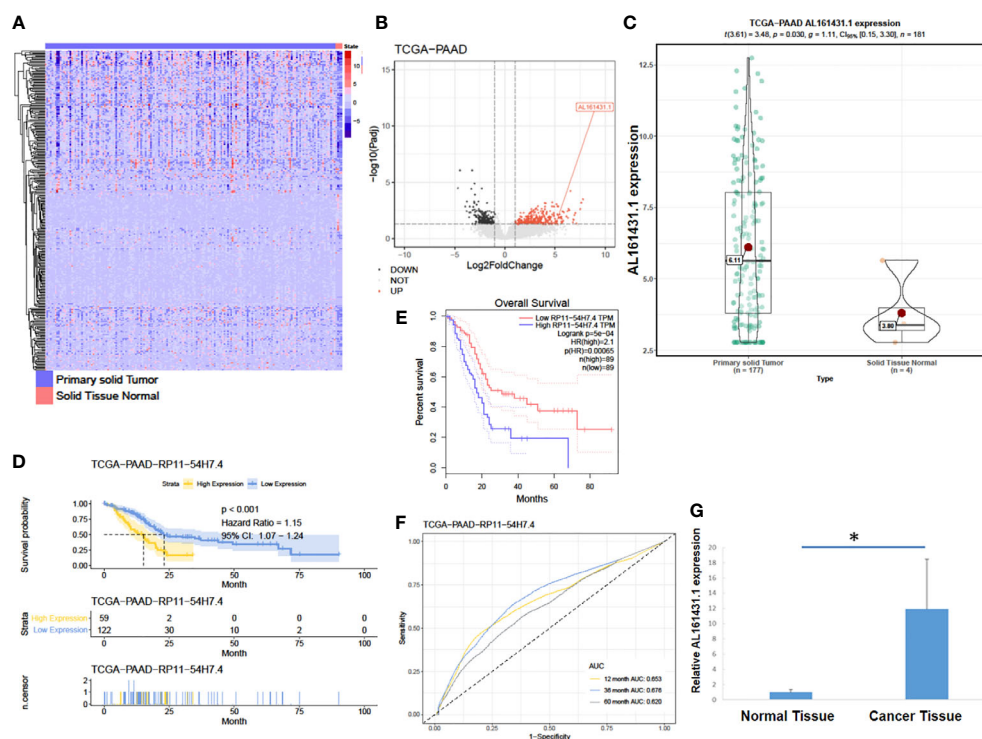


**FIGURE 1 |** LncRNA AL161431.1 was overexpressed in pancreatic adenocarcinoma. **(A)** Heatmap of TCGA-PAAD transcriptome; **(B)** Volcano plot of different gene expressions in TCGA-PAAD; **(C)** LncRNA AL161431.1 expression in the TCGA-PAAD cohort; **(D, E)** Kaplan-Meier curves of the overall survival in the TCGA-PAAD cohort; **(F)** ROC curves of patients in the TCGA-PAAD cohort; **(G)** Relative AL161431.1 expression in pancreatic cancer and normal tissues from clinical samples (qRT-PCR). \* $p < 0.05$ .

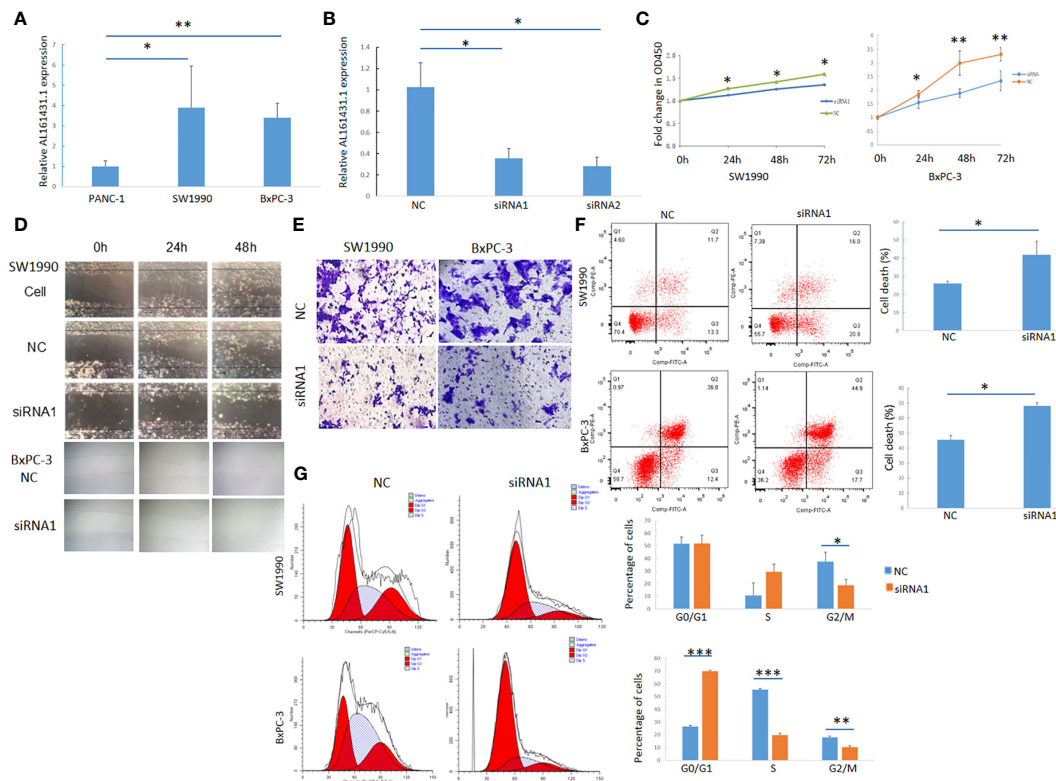


**FIGURE 2 |** Knockdown of lncRNA AL161431.1 inhibited the growth, invasion and migration and promoted apoptosis in pancreatic adenocarcinoma cells.

(A) Relative AL161431.1 expression in PANC-1, SW1990, and BxPC-3 cells analyzed by qRT-PCR; (B) Relative AL161431.1 expression in SW1990 cells after siRNA transfection analyzed by qRT-PCR; (C) CCK-8 assay showing fold change at OD450, representing growth curve of SW1990 and BxPC-3 cells at 24, 48, and 72 hours after siRNA1 transfection; (D) Wound healing assay in naïve, scramble siRNA, or siRNA1 transfected SW1990 or BxPC-3 cells at 0, 24, and 48 hours post scratching (100x); (E) Transwell assay in scramble siRNA or siRNA1 transfected SW1990 or BxPC-3 cells (100x); (F) Cell death (Q2+Q3) in scramble siRNA or siRNA1 transfected SW1990 and BxPC-3 cells analyzed by flow cytometry; (G) Cell cycle analysis of SW1990 and BxPC-3 cells after transfection of scramble siRNA or siRNA1 by flow cytometry. NC: scramble siRNA or shRNA. \* $p < 0.05$ , \*\* $p < 0.01$ , \*\*\* $p < 0.001$ .

These results suggested that knocking down lncRNA AL161431.1 can inhibit the growth, invasion and migration, and promote apoptosis in pancreatic adenocarcinoma cells.

## LncRNA AL161431.1 in Nude Mice Xenografts

The above experiments have demonstrated that knockdown of lncRNA AL161431.1 can inhibit cell growth *in vitro*. In order to further evaluate the role of AL161431.1 *in vivo*, we constructed the lncRNA AL161431.1 stable knockdown cell line (SW1990-LNC-KD cells) using specific shRNA. The cells in the 8th passage was found to have minimum residual level of lncRNA AL161431.1 compared with the 3rd and 5th passages by qRT-PCR analysis (data not shown), and was injected into nude mice for xenograft tumor growth analysis. The size of xenograft tumor in the stable knockdown group was significantly smaller than that of the control group at 2 weeks post injection (Figure 3A). The knockdown group also showed slower tumor growth (Figure 3B). The expression of lncRNA AL161431.1 in the tumor tissue was lower in the knockdown group (Figure 3C). HE staining and PCNA (cell proliferation index) immunohistochemical staining showed

reduced cell atypia and fewer PCNA-positive cells in the knockdown group (Figures 3D, E). There was significant lower number of PCNA-positive cells in SW1990-LNC-KD cell xenograft tumor tissue ( $p < 0.01$ ; Figure 3F). These results suggested that knocking down of lncRNA AL161431.1 inhibited the growth of xenograft tumors.

## Predicting the Function of lncRNA AL161431.1 in Pancreatic Cancer Cells

The above *in vivo* and *in vitro* studies suggested that lncRNA AL161431.1 promoted cell growth. Using the median of lncRNA AL161431.1 as the cut-off value threshold, the expression of differential genes was analyzed by the DEseq2 (Figures 4A, B), and GSEA (Figure 4C). The enrichment of differentially expressed genes and the known gene set was analyzed by the GSEA software. It was found that genes that were upregulated in pancreatic cancer were highly enriched in the AL161431.1 high expression group. Through GO enrichment analysis (18), AL161431.1 was found to play roles in various cellular functions and processes such as cell-cell junction and extracellular microenvironment (Figures 4D, E).

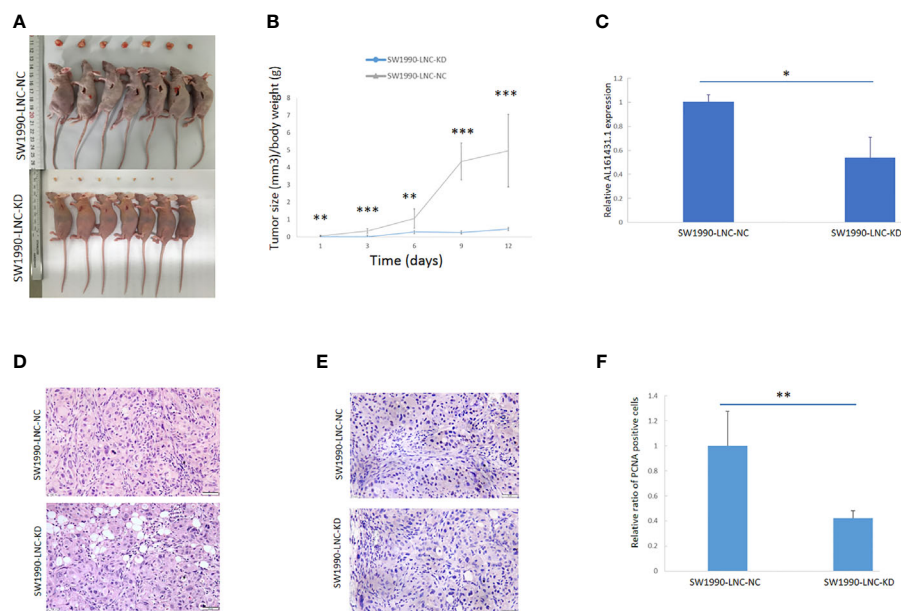


**FIGURE 3 |** Knockdown of lncRNA AL161431.1 inhibited the growth of tumor xenografts. **(A)** Size of SW1990 tumor xenografts with SW1990-LNC-KD or SW1990-LNC-NC cells at 14 days after injection; **(B)** Time course of in vivo xenografts growth measured in mm<sup>3</sup>; **(C)** Relative AL161431.1 expression in engrafted tumors with SW1990-LNC-NC cell or SW1990-LNC-KD cell; **(D)** HE staining of tumor xenografts; **(E)** PCNA immunohistochemistry in tumor xenografts; **(F)** Relative ratio of PCNA positive cells in the engrafted tumors with SW1990-LNC-NC cell or SW1990-LNC-KD cell. \*p < 0.05, \*\*p < 0.01, \*\*\*p < 0.001.

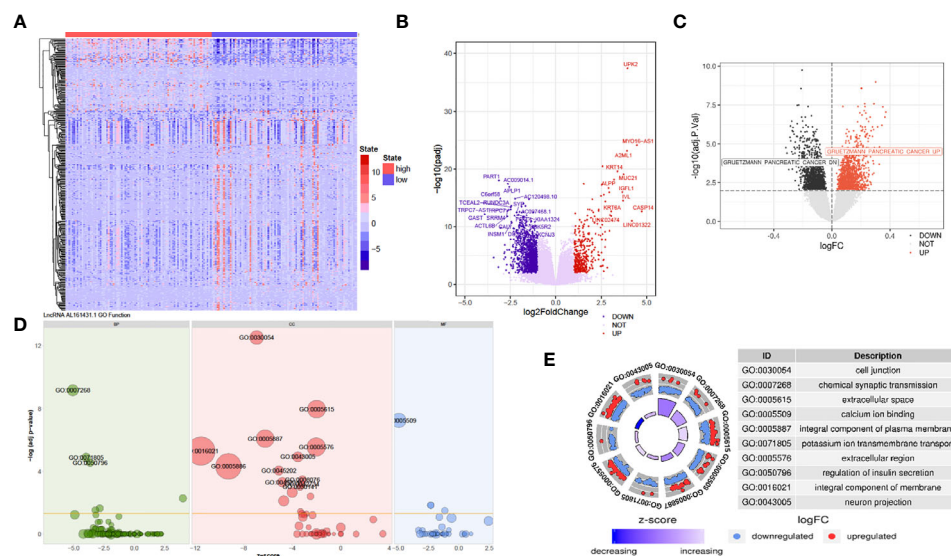


**FIGURE 4 |** Prediction of the function of lncRNA AL161431.1 in cells. Heatmap **(A)** and Volcano plot **(B)** of different gene expression between high- and low-AL161431.1 expression patients in the TCGA-PAAD cohort; **(C)** GSEA analysis of lncRNA AL161431.1 effect on pancreatic adenocarcinomas in TCGA cohort; **(D, E)** GO function analysis of AL161431.1.

## The Mechanism of lncRNA AL161431.1 in Regulating Cell Function

The above analysis indicated that lncRNA AL161431.1 regulated cell migration and infiltration. We further analyzed the role of

lncRNA AL161431.1 in regulating cell-cell junctions, and extracellular region. We found that there was an interaction network centered by lncRNA AL161431.1 (**Figures 5A, B**). Moreover, through GSEA analysis, we found that the differential genes of the high lncRNA AL161431.1 expression



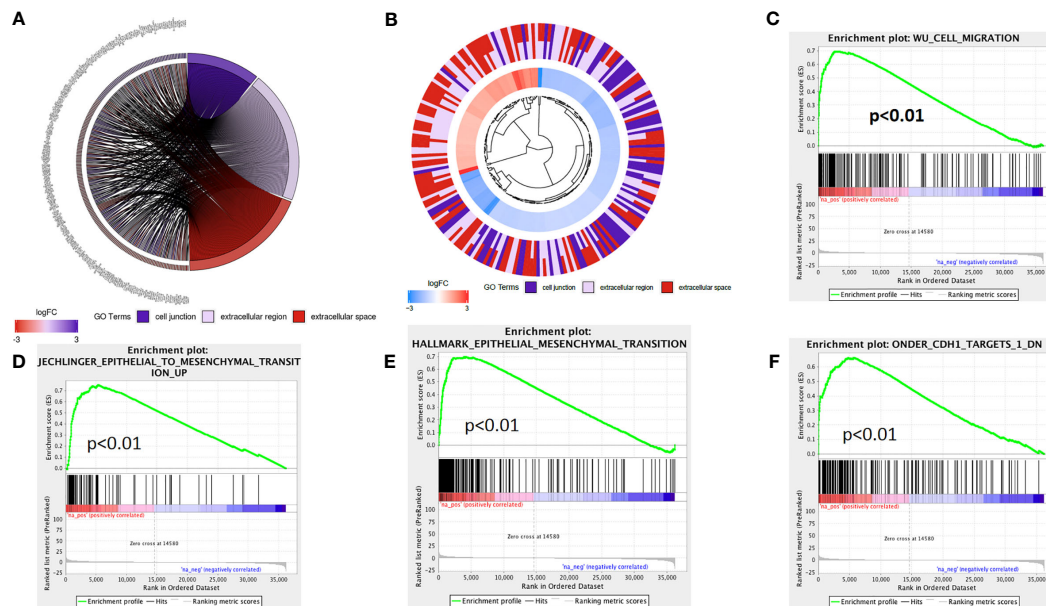


**FIGURE 5** | The mechanism of lncRNA AL161431.1 in regulating cell function. GO function relative genes (A) and fold changes (B); (C–F) GSEA analysis for different gene expression in patients with high- and low- AL161431.1 expression in TCGA-PAAD.

groups were highly enriched in the WU\_CELL\_MIGRATION gene set (Figure 5C), which was closely associated with the EMT (Figures 5D–F) and involved in cell migration and invasion. These bioinformatic analysis suggested that lncRNA AL161431.1 could potentially regulate the migration and invasion of pancreatic cancer cells through EMT process.

In order to further verify the above bioinformatic findings on the role of lncRNA AL161431.1 in cell migration and invasion, we knocked down the expression of lncRNA AL161431.1 with siRNA1 in both SW1990 and BxPC-3 cells and the gene knockdown efficiency was confirmed by qRT-PCR (Figure 6A). Using qRT-PCR (Figure 6A), Western blot (Figure 6B) and immunofluorescence (Figure 6C) analyses, we found significant increase in the expression of CDH1 (E-cadherin), and decrease in the expression of CDH2 (N-cadherin) and VIM (Vimentin) in both mRNA and protein level after knocking down of lncRNA AL161431.1. These results suggested that lncRNA AL161431.1 promoted cell migration and invasion by promoting EMT process.

## DISCUSSION

lncRNAs have been shown to be involved in the development and progression of pancreatic cancer. A search using the key words of lncRNA and pancreatic cancer in PubMed on July 28, 2020 yielded 589 publications, with the most relevant one dating back in 2011 (19). Most lncRNAs have been reported to promote the proliferation of pancreatic cancer through different signaling pathways (20–23). In the case of lncRNA AL161431.1, its identified targets include miR-1252-5p, and the pathways include MAPK signaling in endometrial carcinoma and a competing

endogenous RNA network in lung squamous cell carcinoma (7, 9; Table S2).

The employment of bioinformatics analyses was beneficial in identifying both candidate lncRNAs and lncRNAs-associated signaling pathways for mechanistic and therapeutic studies. Based on the analysis of TCGA-PAAD dataset, we found an increase of lncRNA AL161431.1 in clinical pancreatic cancer tissues, as well as in pancreatic cancer SW1990 and BxPC-3 cells. To test if this phenomenon was an coincidence, siRNA or shRNA were used to knock down lncRNA AL161431.1 in those cells, with the finding of significantly more cell death and cell cycle arrest, indicating that lncRNA AL161431.1 is truly involved in pancreatic cancer growth and progression.

EMT is crucial in tumorigenesis by enhancing metastasis and cancer cell stemness. The signature of EMT is the upregulation of Vimentin and N-cadherin accompanied by the downregulation of E-cadherin. EMT is a process which is regulated by a complicated network of signaling pathways and transcription factors, including the TGF- $\beta$  signaling pathway, the MAPK signaling pathway, the JAK/STAT signaling pathway, the Hedgehog signaling pathway, the Wnt signaling pathway, the Hippo-YAP/TAZ signaling pathway, etc. (24). E-cadherin plays an important role in the initiation and maintenance of EMT, where cleavage of E-cadherin leads to the destabilization of cell-cell junctions as well as the release of  $\beta$ -catenin as a transcriptional activator for cell proliferation (25). Increased level of vimentin and decreased level of E-cadherin was evident in lung cancer cells (26). Vimentin has been reported as the main intermediate filament protein of normal mesenchymal tissue (27) with a major role of sustaining cellular integrity (28). Furthermore, vimentin expression was a potential independent adverse prognostic molecular biomarker in patients with

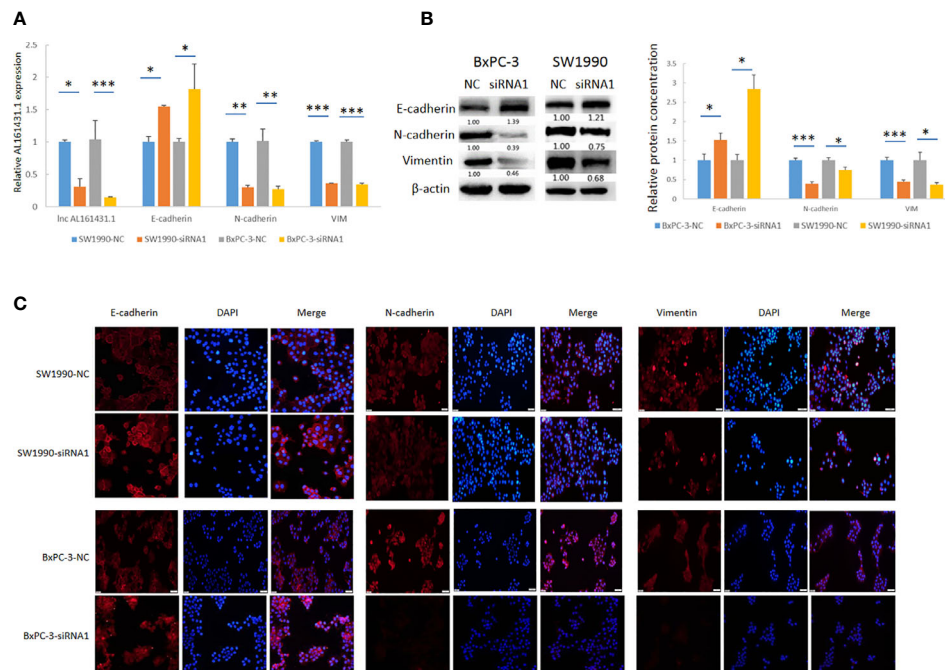


**FIGURE 6 |** Knockdown of lncRNA AL161431.1 inhibited EMT. **(A)** qRT-PCR showing the knock down of lncRNA AL161431.1, and the corresponding changes in E-cadherin, N-cadherin, and vimentin in SW1990 and BxPC-3 cells; **(B)** Western blots showing the changes in protein level in E-cadherin, N-cadherin, and vimentin in SW1990 and BxPC-3 cells after transfection of scrambled siRNA or siRNA1; **(C)** Immunofluorescence analysis showing the change of expression of E-cadherin, N-cadherin, and vimentin in SW1990 and BxPC-3 cells after transfection of scrambled siRNA or siRNA1 (200x). \* $p < 0.05$ , \*\* $p < 0.01$ , \*\*\* $p < 0.001$ .

pancreatic ductal adenocarcinoma (29). Similar to our recent findings of lncRNA ELFN1-AS1 (30), the finding of increased E-cadherin accompanied by decreased N-cadherin and vimentin in lncRNA AL161431.1 knockdown pancreatic cancer cells clearly indicated that lncRNA AL161431.1 is critical in the EMT process.

In summary, we showed by bioinformatics analysis, *in vivo* and *in vitro* experiments that lncRNA AL161431.1 was involved in the pathogenesis of pancreatic cancer by promoting EMT. lncRNA AL161431.1 could be a potential prognostic predictor and treatment target in pancreatic cancer.

## DATA AVAILABILITY STATEMENT

The original contributions presented in the study are included in the article/**Supplementary Material**. Further inquiries can be directed to the corresponding author.

## ETHICS STATEMENT

The studies involving human participants were reviewed and approved by Ethical Committee of the First Affiliated Hospital of China Medical University. The patients/participants provided their written informed consent to participate in this study. The animal study was reviewed and approved by Ethical Committee of the First Affiliated Hospital of China Medical University.

## AUTHOR CONTRIBUTIONS

GM and ZL designed the study, analyzed and interpreted patient data, and were major contributors in writing the manuscript. GL and WF performed the cell culture, qRT-PCR and Western blot experiments. YX and SS performed flow cytometry, IF, and IHC experiments. KG performed xenografts experiments. All authors contributed to the article and approved the submitted version.

## FUNDING

(I) Liaoning Provincial Department of Education science research project (L2014299); (II) National Natural Science Foundation of China (81572360).

## SUPPLEMENTARY MATERIAL

The Supplementary Material for this article can be found online at: <https://www.frontiersin.org/articles/10.3389/fonc.2021.666313/full#supplementary-material>

**Supplementary Table 1 |** Primers for qRT-PCR and siRNAs.

**Supplementary Table 2 |** The roles of LNC RNA AL161431.1 in different steps/mechanisms of the development and progression of different cancers.

## REFERENCES

- (2019). The American Cancer Society Medical and Editorial Content Team. About Pancreatic Cancer. Retrieved July 20, 2020. Available at: <https://www.cancer.org/content/dam/CRC/PDF/Public/8778.00.pdf> (Accessed February 11).
- (2020). The American Cancer Society medical and editorial content team. Survival Rates for Pancreatic Cancer. Retrieved July 20, 2020. Available at: <https://www.cancer.org/cancer/pancreatic-cancer/detection-diagnosis-staging/survival-rates.html> (Accessed January 8).
- Saad AM, Turk T, Al-Husseini MJ, Abdel-Rahman O. Trends in Pancreatic Adenocarcinoma Incidence and Mortality in the United States in the Last Four Decades; a SEER-Based Study. *BMC Cancer* (2018) 18(1):688. doi: 10.1186/s12885-018-4610-4
- Engreitz JM, Haines JE, Perez EM, Munson G, Chen J, Kane M, et al. Local Regulation of Gene Expression by lncRNA Promoters, Transcription and Splicing. *Nature* (2016) 539(7629):452–5. doi: 10.1038/nature20149
- Wang JJ, Wang X, Song YX, Zhao JH, Sun JX, Shi JX, et al. Circulating Noncoding RNAs Have a Promising Future Acting as Novel Biomarkers for Colorectal Cancer. *Dis Markers* (2019) 2019:2587109. doi: 10.1155/2019/2587109
- Huang X, Zhi X, Gao Y, Ta N, Jiang H, Zheng J. LncRNAs in Pancreatic Cancer. *Oncotarget* (2016) 7(35):57379–90. doi: 10.18632/oncotarget.10545
- Gu ZR, Liu W. The LncRNA AL161431.1 Targets miR-1252-5p and Facilitates Cellular Proliferation and Migration via MAPK Signaling in Endometrial Carcinoma. *Eur Rev Med Pharmacol Sci* (2020) 24(5):2294–302. doi: 10.26355/eurrev\_202003\_20495
- De Troyer L, Zhao P, Pastor T, Baietti MF, Barra J, Vendramin R, et al. Stress-Induced lncRNA LASTR Fosters Cancer Cell Fitness by Regulating the Activity of the U4/U6 Recycling Factor SART3. *Nucleic Acids Res* (2020) 48(5):2502–17. doi: 10.1093/nar/gkz1237
- Ju Q, Zhao YJ, Ma S, Li XM, Zhang H, Zhang SQ, et al. Genome-Wide Analysis of Prognostic-Related lncRNAs, miRNAs and mRNAs Forming a Competing Endogenous RNA Network in Lung Squamous Cell Carcinoma. *J Cancer Res Clin Oncol* (2020) 146(7):1711–23. doi: 10.1007/s00432-020-03224-8
- Wang Y, Gao R, Li J, Tang S, Li S, Tong Q, et al. Circular RNA Hsa\_Circ\_0003141 Promotes Tumorigenesis of Hepatocellular Carcinoma via a miR-1827/UBAP2 Axis. *Aging (Albany NY)* (2020) 12(10):9793–806. doi: 10.18632/aging.103244
- Wei L, Ye H, Li G, Lu Y, Zhou Q, Zheng S, et al. Cancer-Associated Fibroblasts Promote Progression and Gemcitabine Resistance via the SDF-1/SATB-1 Pathway in Pancreatic Cancer. *Cell Death Dis* (2018) 9(11):1065. doi: 10.1038/s41419-018-1104-x
- Varghese F, Bukhari AB, Malhotra R, De A. IHC Profiler: An Open Source Plugin for the Quantitative Evaluation and Automated Scoring of Immunohistochemistry Images of Human Tissue Samples. *PLoS One* (2014) 9(5):e96801. doi: 10.1371/journal.pone.0096801
- Pijuan J, Barceló C, Moreno DF, Maiques O, Sisó P, Martí RM, et al. In Vitro Cell Migration, Invasion, and Adhesion Assays: From Cell Imaging to Data Analysis. *Front Cell Dev Biol* (2019) 7:107. doi: 10.3389/fcell.2019.00107
- Jonkman JEN, Cathcart JA, Xu F, Bartolini ME, Amon JE, Stevens KM, et al. An Introduction to the Wound Healing Assay Using Live-Cell Microscopy. *Cell Adh Migr* (2014) 8(5):440–51. doi: 10.4161/cam.36224
- Genomic Data Commons Data Portal. Available at: <https://portal.gdc.cancer.gov/projects/TCGA-PAAD>.
- Bioconductor. Available at: <https://bioconductor.org/packages/release/bioc/html/DESeq2.html>.
- Tang Z, Li C, Kang B, Gao G, Li C, Zhang Z. GEPIA: A Web Server for Cancer and Normal Gene Expression Profiling and Interactive Analyses. *Nucleic Acids Res* (2017) 45(W1):W98–102. doi: 10.1093/nar/gkx247
- The Gene Ontology Consortium. The Gene Ontology Resource: 20 Years and Still GOing Strong. *Nucleic Acids Res* (2019) 47(D1):D330–D8. doi: 10.1093/nar/gky1055
- Tahira AC, Kubrusly MS, Faria MF, Dazzani B, Fonseca RS, Maracaja-Coutinho V, et al. Long Noncoding Intronic RNAs Are Differentially Expressed in Primary and Metastatic Pancreatic Cancer. *Mol Cancer* (2011) 10:141. doi: 10.1186/1476-4598-10-141
- Zhou X, Gao W, Hua H, Ji Z. LncRNA-BLACAT1 Facilitates Proliferation, Migration and Aerobic Glycolysis of Pancreatic Cancer Cells by Repressing CDKN1C via EZH2-Induced H3K27me3. *Front Oncol* (2020) 10:539805. doi: 10.3389/fonc.2020.539805
- Gong R, Jiang Y. Non-Coding RNAs in Pancreatic Ductal Adenocarcinoma. *Front Oncol* (2020) 10:309. doi: 10.3389/fonc.2020.00309
- Ros G, Pegoraro S, De Angelis P, Sgarra R, Zucchini S, Gustincich S, et al. HMGA2 Antisense Long Non-Coding RNAs as New Players in the Regulation of HMGA2 Expression and Pancreatic Cancer Promotio. *Front Oncol* (2020) 9:1526. doi: 10.3389/fonc.2019.01526
- Lu Y, Tang L, Zhang Z, Li S, Liang S, Ji L, et al. Long Noncoding RNA TUG1/miR-29c Axis Affects Cell Proliferation, Invasion, and Migration in Human Pancreatic Cancer. *Dis Markers* (2018) 2018:6857042. doi: 10.1155/2018/6857042
- Loh CY, Chai JY, Tang TF, Wong WF, Sethi G, Shanmugam MK, et al. The E-Cadherin and N-Cadherin Switch in Epithelial-To-Mesenchymal Transition: Signaling, Therapeutic Implications, and Challenge. *Cells* (2019) 8(10):1118. doi: 10.3390/cells8101118
- Niehrs C. The Complex World of WNT Receptor Signalling. *Nat Rev Mol Cell Biol* (2012) 13(12):767–79. doi: 10.1038/nrm3470
- Chen H, Zhou X, Shi Y, Yang J. Roles of P38 MAPK and JNK in TGF- $\beta$ 1-Induced Human Alveolar Epithelial to Mesenchymal Transition. *Arch Med Res* (2013) 44(2):93–8. doi: 10.1016/j.arcmed.2013.01.004
- Leader M, Collins M, Patel J, Henry K. Vimentin: An Evaluation of Its Role as a Tumour Marker. *Histopathology* (1987) 11(1):63–72. doi: 10.1111/j.1365-2559.1987.tb02609.x
- Fuchs E, Weber K. Intermediate Filaments: Structure, Dynamics, Function, and Disease. *Annu Rev Biochem* (1994) 63:345–82. doi: 10.1146/annurev.bi.63.070194.002021
- Myoteri D, Dellaportas D, Lykoudis PM, Apostolopoulos A, Marinis A, Zizi-Sermpetzoglou A. Prognostic Evaluation of Vimentin Expression in Correlation With Ki67 and CD44 in Surgically Resected Pancreatic Ductal Adenocarcinoma. *Gastroenterol Res Pract* (2017) 2017:9207616. doi: 10.1155/2017/9207616
- Ma G, Li G, Gou A, Xiao Z, Xu Y, Song S, et al. Long Non-Coding RNA ELFN1-AS1 in the Pathogenesis of Pancreatic Cancer. *Ann Transl Med* (2021) 9(10):877. doi: 10.21037/atm-21-2376

**Conflict of Interest:** The authors declare that the research was conducted in the absence of any commercial or financial relationships that could be construed as a potential conflict of interest.

**Publisher's Note:** All claims expressed in this article are solely those of the authors and do not necessarily represent those of their affiliated organizations, or those of the publisher, the editors and the reviewers. Any product that may be evaluated in this article, or claim that may be made by its manufacturer, is not guaranteed or endorsed by the publisher.

Copyright © 2021 Ma, Li, Fan, Xu, Song, Guo and Liu. This is an open-access article distributed under the terms of the Creative Commons Attribution License (CC BY). The use, distribution or reproduction in other forums is permitted, provided the original author(s) and the copyright owner(s) are credited and that the original publication in this journal is cited, in accordance with accepted academic practice. No use, distribution or reproduction is permitted which does not comply with these terms.



# Case Report and Literature Review: Primary Pulmonary NUT-Midline Carcinoma

Yunxiang Zhang<sup>1</sup>, Kai Han<sup>1</sup>, Xiaotong Dong<sup>1</sup>, Qian Hou<sup>1</sup>, Tianbao Li<sup>2</sup>, Li Li<sup>3</sup>, Gengyin Zhou<sup>3</sup>, Xia Liu<sup>4\*</sup>, Guifeng Zhao<sup>5\*</sup> and Wei Li<sup>6\*</sup>

<sup>1</sup> Pathology Department, Weifang People's Hospital, Weifang, China, <sup>2</sup> Scientific Research Department, Qingdao Geneis Institute of Big Data Mining and Precision Medicine, Qingdao, China, <sup>3</sup> Pathology Department, Qilu Hospital of Shandong University, Jinan, China, <sup>4</sup> Ophthalmology Department, Affiliated Hospital of Weifang Medical University, Weifang, China, <sup>5</sup> Prenatal Diagnosis Department, Weifang People's Hospital, Weifang, China, <sup>6</sup> Thoracic Surgery Department, Weifang People's Hospital, Weifang, China

## OPEN ACCESS

### Edited by:

Dong-Hua Yang,  
St. John's University, United States

### Reviewed by:

Tianshun Zhang,  
University of Minnesota Twin Cities,  
United States  
Xiaoping Lin,  
Sun Yat-Sen University Cancer Center  
(SYSUCC), China

### \*Correspondence:

Wei Li  
wflwei0213@163.com  
Guifeng Zhao  
wfrmgzf@126.com  
Xia Liu  
liuxia1978@163.com

### Specialty section:

This article was submitted to  
Pharmacology of Anti-Cancer Drugs,  
a section of the journal  
Frontiers in Oncology

**Received:** 26 April 2021

**Accepted:** 06 August 2021

**Published:** 30 August 2021

### Citation:

Zhang Y, Han K, Dong X, Hou Q, Li T,  
Li L, Zhou G, Liu X, Zhao G and Li W  
(2021) Case Report and Literature  
Review: Primary Pulmonary  
NUT-Midline Carcinoma.  
Front. Oncol. 11:700781.  
doi: 10.3389/fonc.2021.700781

Nuclear protein of the testis (NUT) carcinoma is a very rare and aggressive carcinoma characterized by chromosomal rearrangement. NUT-midline carcinoma (NMC) can occur anywhere in the body, but most of the tumors are found in the midline anatomic structure or mediastinum. Pulmonary-originated NMC is extremely rare and often difficult to be distinguished from other poorly differentiated tumors, making the diagnosis awfully challenged in clinical practice. There are less than 100 cases of NUT carcinoma reported so far. In this study, the diagnosis and molecular mechanisms of reported NUT carcinoma cases were reviewed. Furthermore, a case of primary pulmonary NUT-midline carcinoma and its pathological features was reported. The process of pathological identification and genomic analysis for establishing the diagnosis was discussed. We found that NUT carcinoma could be identified by combining CT, H&E staining, immunohistochemistry (IHC), and molecular tests. The development of NUT carcinoma might be associated with mutation of *MYC*, *p63*, and *MED24* genes and the Wnt, MAPK, and PI3K signaling pathways. Our study provided a detailed molecular mechanistic review on NMC and established a procedure to identify pulmonary NMC.

**Keywords:** bromodomain-containing protein 4 (BRAD4), lung, genomic analysis, nuclear protein of the testis (NUT), NUT-midline carcinoma (NMC)

## INTRODUCTION

Nuclear protein of the testis (NUT) carcinoma is a very rare and aggressive carcinoma characterized by chromosomal rearrangement. NUT-midline carcinoma (NMC) was originally named proline-rich undifferentiated carcinoma (PRUC) because of the genetic build-up of proline (1). NMC is an aggressive malignant epithelial neoplasia and its average survival is less than 1 year. NMC is characterized by rearrangement on the NUT gene, which is located on chromosome 15q14, resulting in the bromodomain-containing protein 4 (BRAD4)-NUT fusion oncogene. NMC primarily occurs in children and young adults. In the USA, the first case was reported in a 12-year-old girl with an epiglottitis mass. She did not respond to antibiotics treatment and died shortly due to tumor recurrence that closed her airway. This tumor is usually diagnosed by positive karyotyping for t(15;19) and confirmed by



fluorescence *in situ* hybridization (FISH) (2). The histological feature cannot be used as diagnostic criteria since the morphology is a poorly differentiated carcinoma and tends to be pleomorphic. NMC is considered a genetically defined disease and does not arise from a specific organ. Most of them are found in midline anatomic structure and mediastinum, within the upper aerodigestive tract and thymus. Some NMCs might arise in bone (3), bladder (4), abdominal retroperitoneum (5), pancreas, and salivary glands (5, 6), and pulmonary origin NMC is extremely rare.

Pulmonary NMC is classified as a type of novel disease at the WHO lung cancers. This carcinoma was recognized in the thymus in 2004 (7). At present, literatures about pulmonary NMC are rare. Tanaka et al. described only two possible pediatric cases of pulmonary NMC in their 41-year investigation (8). Haruki et al. screened 128 lung cancer tissues using fluorescence *in situ* hybridization, but none of the screened tumors showed t(15;19) (9). Sholl et al. reported eight cases of primary pulmonary NMC and used NUT immunohistochemical screening. The result suggested that although primary pulmonary NMC is rare, it has highly clinical, imaging, and pathological features (10). NMC is often undiagnosed or misdiagnosed due to a lack of comprehensive knowledge of NMC and the lack of reagents and expertise needed to diagnose the disease. A case previously misdiagnosed as Ewing's sarcoma (ES) (11)/primitive neuroectodermal tumor (PNET) (12) was reported, which was later confirmed as NUT carcinoma by next generation sequencing (NGS). Stelow et al. investigated the incidence and expression of NUT rearrangement in a series of undifferentiated carcinomas of the upper aerodigestive tract (UCUAT) in the diagnostic significance and described the histological characteristics of these tumors in detail (13). Hellquist et al. used immunohistochemistry, FISH, and reverse transcription-polymerase chain reaction (RT-PCR) to observe NUT rearrangement to diagnose NMC. They found three previously published cases and added the 4th one of their own (14). Bishop et al. identified all NMC specimens (confirmed by molecular testing and/or NUT immunoreactivity) in two academic centers and identified 26 NMC cytopathological samples from 13 patients. The results showed that the cytological characteristics of NMC overlapped with other tumors to a certain extent (15). Recently, a rare case of NMC in an 8-year-old Turkish boy was reported by immunoreactivity to nut antibody (FISH), suggesting that NMC should be considered in the differential diagnosis of undifferentiated carcinoma located in the midline (16).

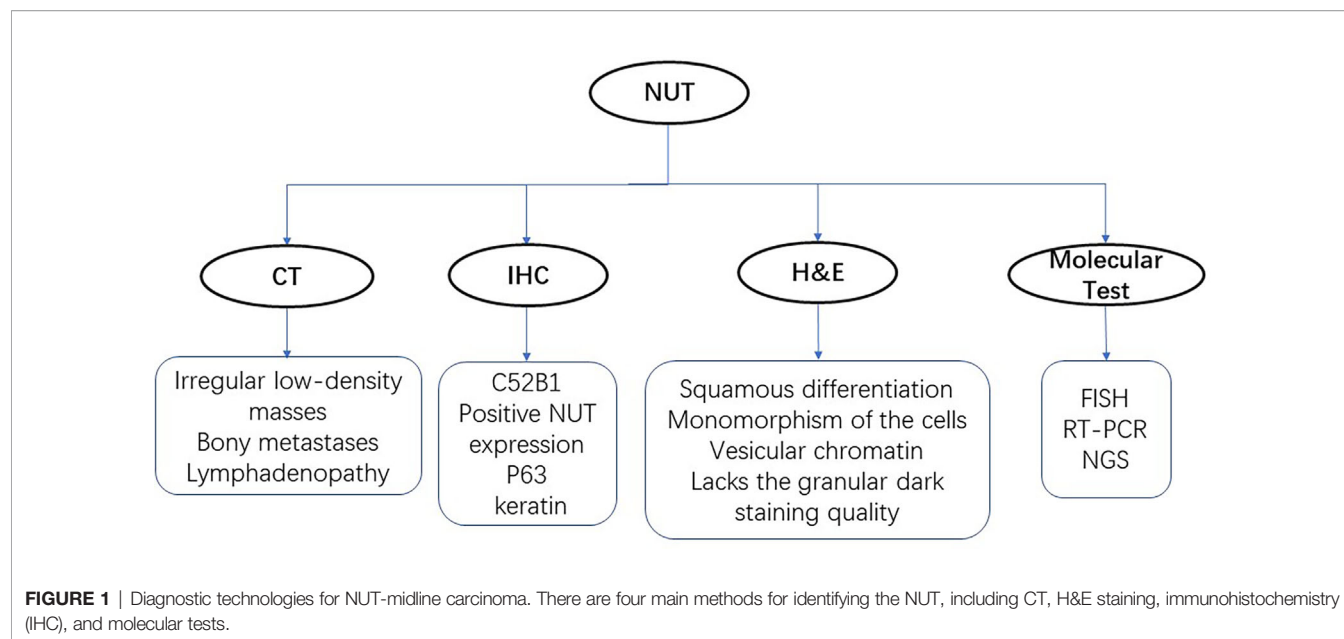
So far, only a small number of case series and rare case reports have described the cytopathological features of NMC. Pulmonary-originated NMC is rare and often difficult to identify from other poorly differentiated tumors. Thereby, it is a challenge to make an accurate diagnosis. In this study, we investigate the pathological feature of primary pulmonary NMC and report a case of a 16-year-old boy with a growing pulmonary mass in the upper lobe of his right lung. The tumor is diagnosed as pulmonary NMC by immune-histological examination and qPCR-assisted assay.

## Diagnosis and Molecular Mechanism of NMC

NUT-midline carcinoma can be diagnosed by testing a monoclonal antibody to NUT (C52B1) with immunohistochemical (IHC)

nuclear staining (17, 18). However, mutation types of NUT rearrangements are unknown in a monoclonal antibody test. For targeted therapy, exact fusion partner gene should be identified by FISH, RT-PCR, and next-generation sequencing technology. Imaging examination of digital radiography (DR), computed tomography (CT) scans, and positron emission tomography (PET)/CT for patients are available methods for diagnosis, including head CT, 18F fluorodeoxyglucose (FDG) PET/CT, abdominal CT, and bone scintigraphy if needed (**Figure 1**). Chest CT scans were applied to assess the characteristics of lung lesion, involvement of the contralateral lung, lymphadenopathy, and pleural and osseous abnormalities. Other imaging examinations were used to identify the extrathoracic metastasis. CT imaging masses of primary lung NMC were mostly located in the center of the lung lobe, especially in the right lung and lower lobe. Primary pulmonary NMC usually showed large and irregular soft tissue masses with low density and fused with ipsilateral hilar and mediastinal lymph nodes. Patients with primary lung NMC often accompanied by pleural effusion, pleural thickening and obstructive atelectasis. Lymph node metastasis was seen in most patients, and the contralateral lung of patients was often not invaded. Extrathoracic metastasis of tumors was common, and bone is the most frequently metastatic site of the lung NMC. It was reported that one patient showed multiple bone metastases on CT and PET-CT, but the results of bone imaging were negative (19). This observation is consistent with other published studies, suggesting that negative bone imaging may not accurately exclude the bone metastasis of the tumor (20). In addition to bone, liver, breast, retroperitoneum, soft tissue, and adrenal glands are also important sites for NUT cancer metastasis. Imaging examination plays a significant role in the early diagnosis of pulmonary (NUT)-midline carcinoma.

Histologic appearances of NUT-midline carcinoma often overlap with many other poorly differentiated tumors. Differential diagnosis should be followed. Firstly, lymphoid epithelioid carcinoma has similar histological features; however, lymphoid epithelioid carcinoma often shows aggregates of cells, the margin is not clear and the nucleus often has prominent nucleoli, necrosis, and interstitial fibrous tissue hyperplasia are uncommon. Negative NUT antibody staining with positive expression of EBER fluorescent *in situ* hybridization are the most diagnostic characteristics. Secondly, the histology and morphology of pulmonary small cell carcinoma share some features with midline carcinoma. The immunohistochemical staining shows neuroendocrine biomarkers, high CD56 and TTF-1 expression, and positive NUT antibody staining. Thirdly, lymphocytic tumors are the most difficult to make differentiated diagnosis, because of its similar morphology, especially high-grade B-cell lymphoma. The tumor cells are usually scattered and diffusely arranged which is difficult to identify by immunohistochemical staining. The immunohistochemical staining would show negative NUT staining, LCA is positive, myeloid sarcoma biomarker CD 117 is positive, and CK staining is negative. In addition, primitive neuroectodermal tumor (PNET) should also be differentiated. The immunohistochemical staining of CD99 biomarker is diffusely positive, while CK is generally negative and NUT antibody biomarker is negative. FISH test can confirm the



existence of EWS-FL1-1 gene fusion. Finally, the incidence of germ cell tumor (GCT) in the thoracic organs such as the mediastinum is relatively higher than upper respiratory track. The cell arrangement of NUT carcinoma and infiltration of interstitial lymphocytes are necessary to distinguish NMC from seminoma and embryonal cancer. Immunohistochemical staining assay of GCT would show negative CK staining and NUT focal nucleus (<5%), while NUT carcinoma is positive for CK and the nuclei is diffusely distributed (>50%).

*NUTM1* gene with unknown function on chromosome 15 is usually expressed solely in testis tissue, and rearrangement of which is the main cause of NUT-midline carcinoma. BRD4 in BET family is the most common fusion partner gene, and BRD4-NUT fusion oncogene can be identified in two-thirds of the cases (21). Other relatively common fusion partner genes are NDS3 and BRD3. Moreover, MXD1, CIC, ZNF532, ZNF592, MXD4, BCORL1, and MGA have been reported recently (22–28). BRD4 is associated with many types of tumors and plays a crucial part in cell cycle regulation, transcriptional regulation, cell growth, and chromatin structure. Two key domains of BRD4 was retained in BRD4-NUT fusion oncoprotein. One is bromodomain which binds to acetylated histone, and the other is ET domain which binds to chromatin-modifying proteins. The acidic domain of NUT in fusion protein bound with histone acetyltransferase p300 can lead to histone acetylation. Furthermore, BRD4-NUT fusion oncoprotein, acetylated chromatin, and p300 form several huge regions that include the regulatory regions of MYC, p63, and MED24, which regulate cell transformation, differentiation, growth, and proliferation (Figure 2). Multiple studies have proved that p63 plays a key role in cell proliferation, survival, apoptosis, differentiation, cancer progression, and cancer metastasis. *MED24* gene, encoded as a transcriptional coactivator complex, is usually involved in gene expression. MYC, a transcription factor overexpressed in various types of cancer cells, has been proven to

be a key inducer of many oncogenic pathways, such as the Wnt, mitogen-activated protein kinase (MAPK), and phosphatidylinositol 3-kinase (PI3K) signaling pathways (29–33). MYC gene regulates organ morphogenesis during embryogenesis and tissue repair. Wnt signaling is associated with various types of cancers such as colorectal, breast, and lung cancer. Compared with other signaling pathways, MAPK and PI3K pathways are involved in complex biological processes like cell proliferation, differentiation, transformation, apoptosis, and metabolism, which are closely associated with human diseases.

## Case Description: Primary Pulmonary NUT-Midline Carcinoma

A 16-year-old male patient presented with a pulmonary mass in the upper lobe of the right lung for 10 days. Lab examination results show NSE was high (16.93 ng/ml). Lung enhanced CT showed a round soft tissue density shadow in the upper lobe of the lung, the size was about 6.3 × 6.2 cm, and the edge is smooth. The enhanced CT scan showed the value of the mass was about 46 HU and the adjacent bronchus is compressed. The distal lung tissue showed strips of ground-glass opacity shadow (Figures 3A, B).

## Surgical Findings

During the surgery, no adhesion was found in the thoracic cavity. The pleura was smooth and there was no significant effusion in the thoracic cavity. Pulmonary fissure developed normally. The tumor was located at the upper lobe of the right lung with a size of 6 × 5 cm. The tissue texture is hard and red. The mass was closed to the pleura. The tumor mass was relatively large, therefore, right upper lobectomy combined with lymph node dissection was performed.

## Gross and Microscopic Pathological Findings

One lobe from lobectomy. A mass is seen in the lung. The size of the lung lobe is about 11 cm × 9 cm × 4.5 cm. The mass is located

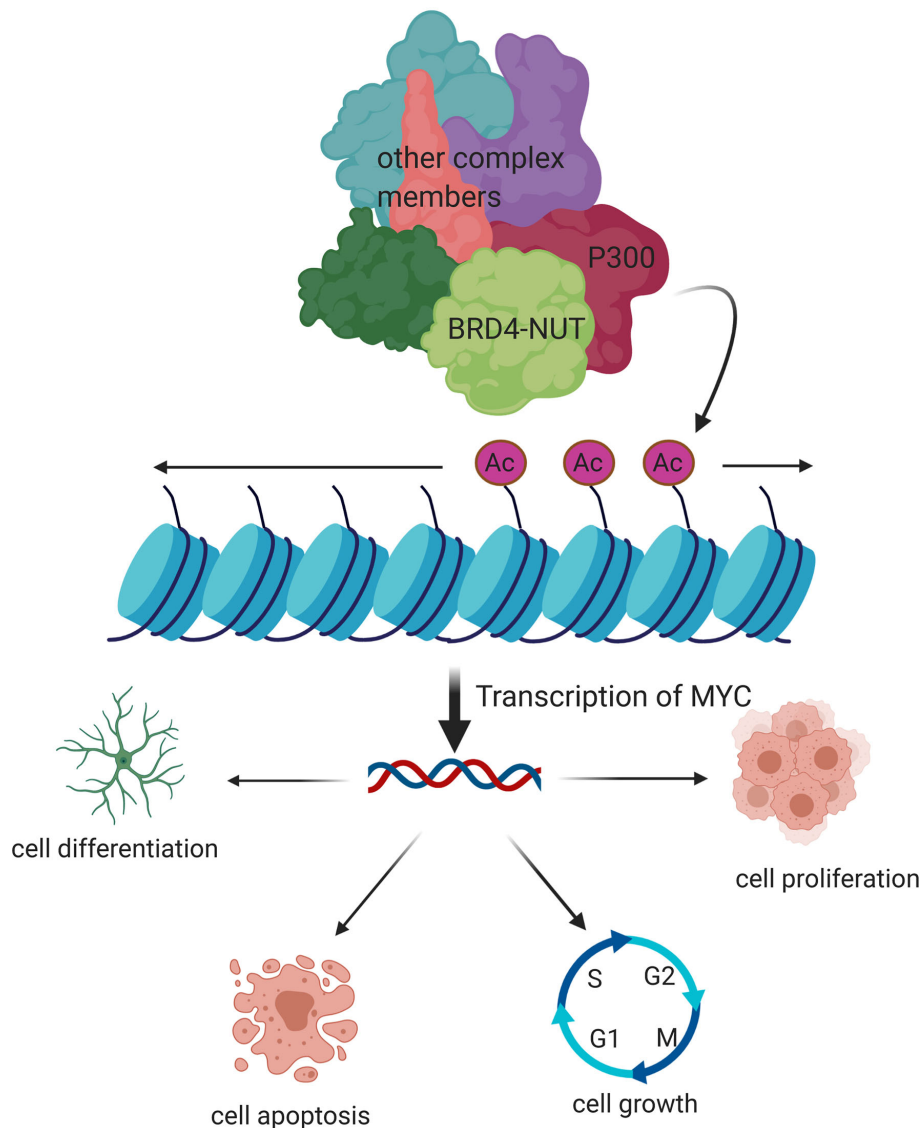


**FIGURE 2** | Molecular mechanism of pathogenesis of NUT-midline carcinoma. BRD4-NUT fusion oncoprotein, acetylated chromatin, and p300 form several huge regions that include the regulatory regions of MYC, p63, and MED24, which regulate cell transformation, differentiation, growth, and proliferation.

0.6 cm away from the end of bronchial anastomosis, close to the lung capsule with a total size of 7 cm × 6 cm × 5 cm. The section surface is gray and gray-red, the texture is slightly brittle, the margin is not clear, bleeding, shows a cystic change, and easy to be broken. The gross image of pulmonary mass includes the following: the section is gray and gray-red, bleeding, and shows a cystic change (**Figure 3C**). Under the microscope, the tumor cells are extreme poorly differentiated, round, medium size, nested, or scattered. It is similar to the morphology of small cell carcinoma or lymphoid epithelioid carcinoma. Few fibrous connective tissues were seen between the cell nests. There are multiple foci and slice-like necrosis. The adhesion of tumor cells is relatively poor. Most nuclei is round or oval-round shape and medium size. The size of cells is about two to threefold over

lymphocyte. The ratio of the nucleus over cytoplasm is high; the nuclei are irregular and atypical. The chromatin is fine or granular, vesicle shaped, and its nucleoli are prominent. Mitotic figures and apoptotic body are commonly seen; however, there is no significant “squamous differentiation” pattern in the stained slice. Focal infiltration of interstitial lymphocytes is seen and arrange in a flaky, scattered, or nested pattern (**Figures 3D–H**).

### Immunohistochemical Staining

Immunohistochemical staining was performed on a broad spectrum of biomarkers (**Table 1**). In addition to NUT, several positively stained biomarkers have been identified. CKpan (partial+), NUT (nuclear positive), P63 (mostly+), TTF-1(few+), CK7(few+), CK5/P40(few+), CD5/6(few+), Syn (partial+), CD30 (few weak+),



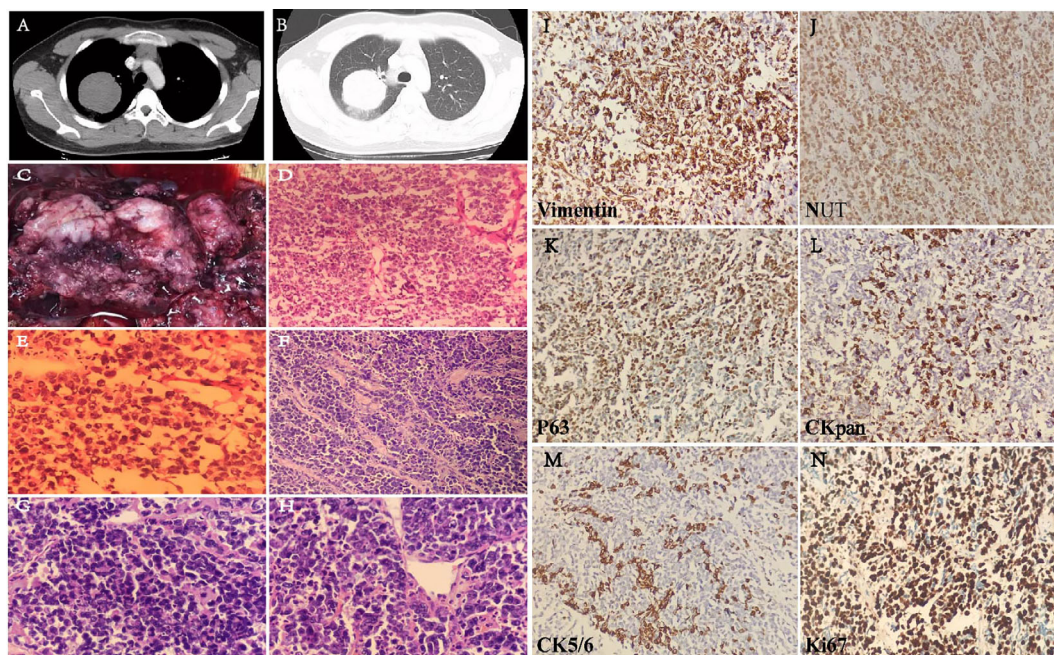


**FIGURE 3** | Lung CT image of the patient with soft tissue window **(A)** and lung window **(B)**. Gross sample and H&E images. **(C)** The gross image of pulmonary mass. **(D)** Frozen H&E section  $\times 20$ . **(E)** Frozen H&E section  $\times 40$ . **(F)** Paraffin H&E sections  $\times 20$ . **(G, H)** Paraffin H&E sections  $\times 40$ . Immunohistochemical staining **(I–N)** on six biomarkers. Vimentin (+), NUT (nuclear positive), P63 (mostly+), CK7 (few+), CK5/6 (few+), and Ki-67 index (80%).

EMA (few weak+), Vimetin (+), CD99 (few weak+), HMB45, MelanA, CD3, CD20, CgA, CD31, CD34, Desmin, LCA, MyOD1, S-100, WT-1, PLAP,  $\alpha$ -inhibin, CD138, CD38, MUM-1, TdT, ALK, Ki-67 index (80%), and fluorescence *in situ* hybridization EBEB (–). Some of the representative stainings are shown in **Figures 3I–N**.

### Genomic Analysis of Primary Pulmonary NUT-Midline Carcinoma

Quantitative PCR was performed, and the result indicated that the patient was positive for NUT carcinoma. Dye-based qPCR was

used to identify NUT gene product, and lung adenocarcinoma and water were used as reference. The design of amplification probes: forward probe is located in exon 10 and reverse probe is located in exon 2 of the *NUMT1* gene. The result showed that the CT value of sample is 26.34 which indicated a strong amplification. Moreover, the dissolution curve showed the product is specific. The CT value of reference sample is  $\geq 34$  which indicated a weak amplification. The dissolution curve showed nonspecific amplification which mostly was primer dimer. The results of Sanger sequencing showed positive for NUT rearrangement.

**TABLE 1** | Immunohistochemical staining of biomarkers.

Antibody name	Expression level	Antibody name	Expression level
CKpan	Partial+	CD3	Negative
NUT	Nuclear positive	CD20	Negative
P63	Mostly+	CgA	Negative
TTF-1	Few+	CD31	Negative
CK7/6	Few+	CD34	Negative
CK5/P40	Few+	Desmin	Negative
CD56	Few+	LCA	Negative
Syn	Partial+	MyOD1	Negative
CD30	Few weak+	S-100	Negative
EMA	Few weak+	WT-1	Negative
Vimetin	+	PLAP	Negative
CD99	Few weak +	$\alpha$ -inhibin	Negative
HMB45	Negative	CD138	Negative
MelanA	Negative	CD38	Negative
TdT	Negative	MUM-1	Negative
ALK	Negative	Ki-67 index	Ki-67 index (80%)



The probe design: forward probe is located in exon 10 of the *BRD4* gene and reverse probe is located in exon 2 of the *NUMT1* gene. Amplification Sanger sequencing further confirmed that the translocation occurs between the *NUMT1* and *BRD4* genes (**Supplementary Figure S1**).

### Related Tumor Signaling Pathway and Gene Annotation

Using the high-throughput gene sequencing technique, we have identified KIFB-related heterozygous mutations and gene changes that are associated with multiple tumor-related pathways (**Supplementary Table S1**). Some signaling pathways are associated with NMC. To be specific, most of the KIFB mutation leads to a dysfunction of those signaling pathways that are related to cell metabolism and differentiation. The dysfunction of these genes would lead to an increase in the risk of tumor development. Since NMC patients are often diagnosed in advanced stage, the surgical intervention is usually not an option. Thereby, biopsy sample from the surgery is relatively few. In 70% of the cases, translocation occurs with the juxtaposition of *NUT* (15q14) and *BRD4* (19p13.1) genes or *BRD3* (9q34.2, 6% of cases) and other unknown genes (24%). Usually, gene sequencing test was performed to evaluate the possible gene variants (**Supplementary Table S2**) in order to find possible gene mutations.

### Follow-Up and Outcome

This patient was transferred to multiple places in Ji Nan (Shandong Province) and Beijing for medical consultation, and he received two traditional chemotherapies. The outcome of this case was unfortunately fatal, and the patient died 3 months after diagnosis.

## DISCUSSION

Presently, less than 100 cases of NMC were reported worldwide. NMC can occur at any age; however, it has more likely been seen in young adults and children with no significant gender difference. NUT carcinoma is frequently diagnosed at advanced stage, thereby sample from surgical resection are relatively few. NUT carcinoma is characterized by *NUT* gene rearrangement. In 70% of the cases, the juxtaposition of *NUT* (15q14) and *BRD4* (19p13.1) genes, the *BRD3* (9q34.2, 6% of cases) and other unknown genes (24%), results in translocation products (34–36). The NUT carcinoma is generally misdiagnosed as squamous cell carcinomas (especially basal cell-like squamous cell carcinoma), undifferentiated carcinomas, small cell carcinoma, Aden squamous carcinoma, Ewing's sarcoma or lymphoma, metastatic germ cell tumor, and acute lymphoma. The diagnosis of NMC is made by demonstration of NUT expression or NUT rearrangement by immunohistochemistry assay. NUT carcinoma is highly aggressive, and there is no effective therapy. The mean survival of NUT carcinoma is only 7 months (36, 37).

In NMCs, the primary tumor is mostly located in the upper digestive tract and mediastinum, and the lung NMC was very rare (38–40). The pathological characteristics of the tumor tissue are insignificant for diagnosis. Cases of NUT-midline carcinoma

with cryptic translocation are likely to be overlooked. A 13-year-old girl once was misdiagnosed with germ cell tumor in earlier publication (41). Detailed examination plays a key role in the diagnosis and treatment of NUT-midline carcinoma.

Sustainable and effective treatment plans for NUT-midline carcinoma are still in exploration and research. Without standard therapeutic option for NMCs, this case in study received two traditional chemotherapies, while outcome of the case was not satisfactory (42, 43). According to previous literatures, radiotherapy and complete tumor resection is critical to improve progression-free survival (PFS) and overall survival (OS); however, chemotherapy has no benefit in OS outcome (21, 44). Once diagnosed as Ewing's sarcoma, a NMC patient survived for 13 years after receiving local radiotherapy, while similar treatment strategies have no perceptible effect on other NMC patients (2). Although radiotherapy or chemotherapy can affect tumor progression within a brief period for some NMC patients, the average overall survival of patients is very short. As there are not enough clinical evidences, the prognostic effectiveness of surgery, radiotherapy, and chemotherapy is unclear.

Target therapy plays an increasingly important part in NMC treatment. Histone deacetylase inhibitors (HDACi) was reported to be a key inhibitor of tumor cell differentiation and growth (45). The response of a 10-year-old male NMC patient to HDACi vorinostat seemed good after 5 weeks of treatment. Because of severe nausea and vomiting, the therapy was forced to terminate. Unfortunately, the tumor continued to grow and deteriorated, and the boy died 11 months after diagnosis (46). As significant members in the bromodomain and extraterminal motif (BET) protein family, BRD3 and BRD4 are the most important fusion partners of NUTM1. A serial of anticancer compounds that targeted BTE were developed. Bromodomain inhibitors (BETis) can directly bind to the bromodomain and target the BRD3/4-NUTM1 fusion proteins expressed in tumor tissue. Efficacy of BETi was proved to be better in NMC cell lines with BRD4-NUTM1 ex11:ex2 fusion than those with BRD4-NUTM1 ex15:ex2 or ex14:ex2 fusions (47). Although HDACi and BETi may dramatically prolong OS of NMC patients, toxicity, side effect, and acquisition of these inhibitors are major challenges that cannot be underestimated (48, 49).

As a rare and aggressive malignant tumor, NUT-midline carcinoma can be identified by combining PET/CT, H&E staining, IHC, and molecular tests. The development of NUT carcinoma might be associated with MYC, p63, and MED24 and the Wnt, MAPK, and PI3K signaling pathways. Our study provided a detailed molecular mechanistic review on NMC and established a procedure to identify pulmonary NMC. Early identification, timely symptomatic treatment, and progressive targeted treatment for NMC patients are an extremely urgent need.

## DATA AVAILABILITY STATEMENT

The original contributions presented in the study are included in the article/**Supplementary Material**. Further inquiries can be directed to the corresponding authors.

## ETHICS STATEMENT

The studies involving human participants were reviewed and approved by the Weifang People's Hospital. The patients/participants provided their written informed consent to participate in this study.

## AUTHOR CONTRIBUTIONS

WL, XL, and GFZ conceived and designed the experiments. YZ, XD, LL, QH, GYZ, and KH performed the experiments. YZ and TL analyzed the data. YZ wrote the first draft. All authors contributed to the article and approved the submitted version.

## REFERENCES

- French CA. NUT Midline Carcinoma. *Cancer Genet Cytogenet* (2010) 203 (1):16–20. doi: 10.1016/j.cancergencyto.2010.06.007
- Mertens F, Wiebe T, Adlercreutz C, Mandahl N, French CA. Successful Treatment of a Child With T (15; 19)-Positive Tumor. *Pediatr Blood Cancer* (2007) 49(7):1015–7. doi: 10.1002/pbc.20755
- French CA, Kutok JL, Faquin WC, Toretsky JA, Antonescu CR, Griffin CA, et al. Midline Carcinoma of Children and Young Adults With NUT Rearrangement. *J Clin Oncol* (2004) 22(20):4135–9. doi: 10.1200/JCO.2004.02.107
- den Bakker MA, Beverloo BH, van den Heuvel-Eibrink MM, Meeuwis CA, Tan LM, Johnson LA, et al. NUT Midline Carcinoma of the Parotid Gland With Mesenchymal Differentiation. *Am J Surg Pathol* (2009) 33(8):1253–8. doi: 10.1097/PAS.0b013e3181abe120
- Ziai J, French CA, Zambrano E. NUT Gene Rearrangement in a Poorly-Differentiated Carcinoma of the Submandibular Gland. *Head Neck Pathol* (2010) 4(2):163–8. doi: 10.1007/s12105-010-0174-6
- Travis WD, Brambilla E, Burke AP, Marx A, Nicholson AG. WHO Classification of Tumours of the Lung, Pleura. *Thymus Heart* (2015) 4.
- Mao N, Liao Z, Wu J, Liang K, Wang S, Qin S, et al. Diagnosis of NUT Carcinoma of Lung Origin by Next-Generation Sequencing: Case Report and Review of the Literature. *Cancer Biol Ther* (2019) 20(2):150–6. doi: 10.1080/15384047.2018.1523852
- Tanaka M, Kato K, Gomi K, Yoshida M, Niwa T, Aida N, et al. NUT Midline Carcinoma: Report of 2 Cases Suggestive of Pulmonary Origin. *Am J Surg Pathol* (2012) 36(3):381–8. doi: 10.1097/PAS.0b013e31824230a8
- Haruki. Cloned Fusion Product From a Rare T(15;19)(Q13.2;P13.1) Inhibit S Phase In Vitro. *J Med Genet* (2005) 42(7):558–64. doi: 10.1136/jmg.2004.029686
- Sholl LM, Nishino M, Pokharel S, Mino-Kenudson M, French CA, Janne PA, et al. Primary Pulmonary NUT Midline Carcinoma: Clinical, Radiographic, and Pathologic Characterizations. *J Thorac Oncol* (2015) 10(6):951–9. doi: 10.1097/JTO.0000000000000545
- Balamuth NJ, Womer RB. Ewing's Sarcoma. *Lancet Oncol* (2010) 11(2):184–92. doi: 10.1016/S1470-2045(09)70286-4
- Lessnick SL, Ladanyi M. Molecular Pathogenesis of Ewing Sarcoma: New Therapeutic and Transcriptional Targets. *Annu Rev Pathol* (2012) 7:145. doi: 10.1146/annurev-pathol-011110-130237
- Stelow EB, Bellizzi AM, Taneja K, Mills SE, Legallo RD, Kutok JL, et al. NUT Rearrangement in Undifferentiated Carcinomas of the Upper Aerodigestive Tract. *Am J Surg Pathol* (2008) 32(6):828–34. doi: 10.1097/PAS.0b013e31815a3900
- Hellquist H, French CA, Bishop JA, Coca-Pelaz A, Propst EJ, Paiva Correia A, et al. NUT Midline Carcinoma of the Larynx: An International Series and Review of the Literature. *Histopathology* (2017) 70(6):861–8. doi: 10.1111/his.13143
- Bishop JA, French CA, Ali SZ. Cytopathologic Features of NUT Midline Carcinoma: A Series of 26 Specimens From 13 Patients. *Cancer Cytopathol* (2016) 124(12):901–8. doi: 10.1002/cncy.21761

## FUNDING

This work was supported by the Project of Key R&D Program of Shandong Province (2015GSF118168), the Project of Soft Science & Development program of Weifang Bureau of Science and Technology (2019RKX039), and the Project of Medical and Health Technology Development of Shandong Province (2017WS807).

## SUPPLEMENTARY MATERIAL

The Supplementary Material for this article can be found online at: <https://www.frontiersin.org/articles/10.3389/fonc.2021.700781/full#supplementary-material>

- Büra Yaprak B, Demir Kürat Y, Uur D, Funda O, Christopher AF: Nuclear Protein in Testis Midline Carcinoma in a Turkish Boy: A Case Report. *Asian Biomed* (2020) 14(5):203–208. doi: 10.1515/abm-2020-0029
- French CA. NUT Carcinoma: Clinicopathologic Features, Pathogenesis, and Treatment. *Pathol Int* (2018) 68 (11):583–95. doi: 10.1111/pin.12727
- Haack H, Johnson LA, Fry CJ, Crosby K, Polakiewicz RD, Stelow EB, et al. Diagnosis of NUT Midline Carcinoma Using a NUT-Specific Monoclonal Antibody. *Am J Surg Pathol* (2009) 33(7):984–91. doi: 10.1097/PAS.0b013e318198d666
- He X, Shi L, Zhang Z, Li J. Clinical Diagnosis and Treatment of Primary Lung NUT Midline Carcinoma. *Cancer Res Prev Treat* (2019) 46(11):1040–3. doi: 10.3971/j.issn.1000-8578.2019.19.0322
- Bair RJ, Chick JF, Chauhan NR, French C, Madan R. Demystifying NUT Midline Carcinoma: Radiologic and Pathologic Correlations of an Aggressive Malignancy. *Am J Roentgenol* (2014) 203(4):W391–9. doi: 10.2214/AJR.13.12401
- Chau NG, Hurwitz S, Mitchell CM, Aserlind A, Grunfeld N, Kaplan L, et al. Intensive Treatment and Survival Outcomes in NUT Midline Carcinoma of the Head and Neck. *Cancer* (2016) 21:3632–40. doi: 10.1002/cncr.30242
- French CA, Ramirez CL, Kolmakova J, Hickman TT, Cameron MJ. BRD–NUT Oncoproteins: A Family of Closely Related Nuclear Proteins That Block Epithelial Differentiation and Maintain the Growth of Carcinoma Cells. *Oncogene* (2008) 27:2237–42. doi: 10.1038/sj.onc.1210852
- French CA, Rahman S, Walsh EM, Kuhnle S, Grayson AR, Lemieux ME, et al. NSD3–NUT Fusion Oncoprotein in NUT Midline Carcinoma: Implications for a Novel Oncogenic Mechanism. *Cancer Discov* (2014) 4(8):928. doi: 10.1158/2159-8290.CD-14-0014
- Shiota H, Elya JE, Alekseyenko AA, Chou PM, French CA. "Z4" Complex Member Fusions in NUT Carcinoma: Implications for a Novel Oncogenic Mechanism. *Mol Cancer Res* (2018) 16(12):1826–33. doi: 10.1158/1541-7786.MCR-18-0474
- Tamura R NH, Yoshihara K. Novel MXD4–NUTM1 Fusion Transcript Identified in Primary Ovarian Undifferentiated Small Round Cell Sarcoma. *Genes Chromosomes Cancer* (2018) 57:557–63. doi: 10.1002/gcc.22668
- Stevens TM, Morlote D, Xiu J, Swensen J, Brandwein-Weber M, Miettinen MM, et al. NUTM1–Rearranged Neoplasia: A Multi-Institution Experience Yields Novel Fusion Partners and Expands the Histologic Spectrum. *Modern Pathol* (2019) 32:764–73. doi: 10.1038/s41379-019-0206-z
- Schaefer IM, Dal Cin P, Fletcher CDM, Hanna GJ, French CA. Cancer: CIC–NUTM1 Fusion: A Case Which Expands the Spectrum of NUT–Rearranged Epithelioid Malignancies. *Genes Chromosomes Cancer* (2018) 57:446–51. doi: 10.1002/gcc.3
- Diolaiti D, DCFS, Gundem G. A Recurrent Novel MGA–NUTM1 Fusion Identifies a New Subtype of High-Grade Spindle Cell Sarcoma. *Mol Case Stud* (2018) 4:2373–873. doi: 10.1101/mcs.a003194
- Wu C-H, Van Riggelen J, Yetil A, Fan AC, Bachireddy P, Felsner DW. Cellular Senescence Is an Important Mechanism of Tumor Regression Upon C-Myc Inactivation. *Proc Natl Acad Sci* (2007) 104(32):13028–33. doi: 10.1073/pnas.0701953104
- Shachaf CM, Kopelman AM, Arvanitis C, Karlsson Å, Beer S, Mandl S, et al. MYC Inactivation Uncovers Pluripotent Differentiation and Tumour

- Dormancy in Hepatocellular Cancer. *Nature* (2004) 431(7012):1112–7. doi: 10.1038/nature03043
31. Jain M, Arvanitis C, Chu K, Dewey W, Leonhardt E, Trinh M, et al. Sustained Loss of a Neoplastic Phenotype by Brief Inactivation of MYC. *Science* (2002) 297(5578):102–4. doi: 10.1126/science.1071489
  32. Felsner DW, Bishop JM. Reversible Tumorigenesis by MYC in Hematopoietic Lineages. *Mol Cell* (1999) 4(2):199–207. doi: 10.1016/S1097-2765(00)80367-6
  33. Casey SC, Tong L, Li Y, Do R, Walz S, Fitzgerald KN, et al. MYC Regulates the Antitumor Immune Response Through CD47 and PD-L1. *Science* (2016) 352(6282):227–31. doi: 10.1126/science.aac9935
  34. Edelbrock MA, Kaliyaperumal S, Williams KJ. Structural, Molecular and Cellular Functions of MSH2 and MSH6 During DNA Mismatch Repair, Damage Signaling and Other Noncanonical Activities. *Mutat Res/Fundamental Mol Mech Mutagenesis* (2013) 743:53–66. doi: 10.1016/j.mrfmmm.2012.12.008
  35. Fontebasso AM, Schwartzentruber J, Khuong-Quang D-A, Liu X-Y, Sturm D, Korshunov A, et al. Mutations in SETD2 and Genes Affecting Histone H3K36 Methylation Target Hemispheric High-Grade Gliomas. *Acta Neuropathol* (2013) 125(5):659–69. doi: 10.1007/s00401-013-1095-8
  36. Williams GJ, Lees-Miller SP, Tainer JA. Mre11–Rad50–Nbs1 Conformations and the Control of Sensing, Signaling, and Effector Responses at DNA Double-Strand Breaks. *DNA Repair* (2010) 9(12):1299–306. doi: 10.1016/j.dnarep.2010.10.001
  37. Bian L, Meng Y, Zhang M, Li D. MRE11–RAD50–NBS1 Complex Alterations and DNA Damage Response: Implications for Cancer Treatment. *Mol Cancer* (2019) 18(1):1–14. doi: 10.1186/s12943-019-1100-5
  38. Stelow EB, French CA. Carcinomas of the Upper Aerodigestive Tract With Rearrangement of the Nuclear Protein of the Testis (NUT) Gene (NUT Midline Carcinomas). *Adv Anat Pathol* (2009) 16(2):92–6. doi: 10.1097/PAP.0b013e31819923e4
  39. Bishop JA, Westra WH. NUT Midline Carcinomas of the Sinonasal Tract. *Am J Surg Pathol* (2012) 36(8):1216–21. doi: 10.1097/PAS.0b013e318254ce54
  40. Sholl LM, Nishino M, Pokharel S, Mino-Kenudson M, Lathan C. Primary Pulmonary NUT-Midline Carcinoma: Clinical, Radiographic, and Pathologic Characterization. *J Thorac Oncol* (2015) 10(6):951–9. doi: 10.1097/JTO.0000000000000545
  41. Puliyl MM, Mascarenhas L, Zhou S, Sapra A, Venkatramani R. Nuclear Protein in Testis Midline Carcinoma Misdiagnosed As Adamantinoma. *J Clin Oncol* (2014) 32(15):e57. doi: 10.1200/JCO.2012.48.5300
  42. Tan E, Mody M, Saba NF. Systemic Therapy in Non-Conventional Cancers of the Larynx. *Oral Oncol* (2018) 82:61–8. doi: 10.1016/j.oraloncology.2018.05.005
  43. Cao J, Chen D, Fan Y, Yao J, Zhao C. NUT Midline Carcinoma as a Primary Lung Tumor: A Case Report. *J Thorac Dis* (2017) 9(12):E1045–9. doi: 10.21037/jtd.2017.11.50
  44. Bauer DE, Mitchell CM, Strait KM, Lathan CS, Stelow EB, Luer SC, et al. Clinicopathologic Features and Long-Term Outcomes of NUT Midline Carcinoma. *Clin Cancer Res Off J Am Assoc Cancer Res* (2012) 18(20):5773. doi: 10.1158/1078-0432.CCR-12-1153
  45. Schwartz BE, Hofer M, Lemieux ME, Bauer DE, Cameron MJ, West NH, et al. Differentiation of NUT Midline Carcinoma by Epigenomic Reprogramming. *Cancer Res* (2011) 71(7):2686–96. doi: 10.1158/0008-5472.CAN-10-3513
  46. Fujioka N, French CA, Cameron MJ, Kratzke RA. Long-Term Survival of a Patient With Squamous Cell Carcinoma Harboring NUT Gene Rearrangement. *J Thoracic Oncol* (2010) 5(10):1704–5. doi: 10.1097/JTO.0b013e3181ebaa20
  47. Stirnweis A, Oommen J, Kotecha RS, Kees UR, Beesley AH. Molecular-Genetic Profiling and High-Throughput *In Vitro* Drug Screening in NUT Midline Carcinoma—An Aggressive and Fatal Disease. *Oncotarget* (2017) 8(68):112313–29. doi: 10.18632/oncotarget.22862
  48. Liao S, Ophélia M, Karen C, Elledge SJ. Genetic Modifiers of the BRD4-NUT Dependency of NUT Midline Carcinoma Uncovers a Synergism Between BETs and CDK4/6. *Genes Dev* (2018) 32(17–18):1188–200. doi: 10.1101/gad.315648.118
  49. Amorim S, Stathis A, Gleeson M, Iyengar S, Magarotto V, Leleu X, et al. Bromodomain Inhibitor OTX015 in Patients With Lymphoma or Multiple Myeloma: A Dose-Escalation, Open-Label, Pharmacokinetic, Phase 1 Study. *Lancet Haematol* (2016) 2016:e196–204. doi: 10.1016/S2352-3026(16)00021-1

**Conflict of Interest:** TL is an employee of the Qingdao Geneis Institute of Big Data Mining and Precision Medicine.

The remaining authors declare that the research was conducted in the absence of any commercial or financial relationships that could be construed as a potential conflict of interest.

**Publisher's Note:** All claims expressed in this article are solely those of the authors and do not necessarily represent those of their affiliated organizations, or those of the publisher, the editors and the reviewers. Any product that may be evaluated in this article, or claim that may be made by its manufacturer, is not guaranteed or endorsed by the publisher.

Copyright © 2021 Zhang, Han, Dong, Hou, Li, Li, Zhou, Liu, Zhao and Li. This is an open-access article distributed under the terms of the Creative Commons Attribution License (CC BY). The use, distribution or reproduction in other forums is permitted, provided the original author(s) and the copyright owner(s) are credited and that the original publication in this journal is cited, in accordance with accepted academic practice. No use, distribution or reproduction is permitted which does not comply with these terms.

# Advantages of publishing in Frontiers



## OPEN ACCESS

Articles are free to read  
for greatest visibility  
and readership



## FAST PUBLICATION

Around 90 days  
from submission  
to decision



## HIGH QUALITY PEER-REVIEW

Rigorous, collaborative,  
and constructive  
peer-review



## TRANSPARENT PEER-REVIEW

Editors and reviewers  
acknowledged by name  
on published articles

## Frontiers

Avenue du Tribunal-Fédéral 34  
1005 Lausanne | Switzerland

**Visit us:** [www.frontiersin.org](http://www.frontiersin.org)

**Contact us:** [frontiersin.org/about/contact](http://frontiersin.org/about/contact)



## REPRODUCIBILITY OF RESEARCH

Support open data  
and methods to enhance  
research reproducibility



## DIGITAL PUBLISHING

Articles designed  
for optimal readership  
across devices



## FOLLOW US

@frontiersin



## IMPACT METRICS

Advanced article metrics  
track visibility across  
digital media



## EXTENSIVE PROMOTION

Marketing  
and promotion  
of impactful research



## LOOP RESEARCH NETWORK

Our network  
increases your  
article's readership